2012

Proceedings of the 2012 Monitoring Research Review:
Ground-Based Nuclear Explosion Monitoring Technologies

Proceedings of the 2012 Monitoring Research Review: Ground-Based Nuclear Explosion Monitoring Technologies

September 18–20, 2012

Albuquerque, New Mexico

Volume I

Seismic Regional Characterization and Wave Propagation
Seismic Event Detection and Location
Seismic Identification and Source Characterization

Approved for Public Release; further dissemination unlimited.

National Nuclear Security Administration

AIR FORCE RESEARCH LABORATORY

LA-UR-12-24325

ACKNOWLEDGEMENTS

The National Nuclear Security Administration (NNSA) and the Air Force Research Laboratory (AFRL) gratefully acknowledge the important contributions of the following people for their work to produce the ***Proceedings of the 2012 Monitoring Research Review: Ground-Based Nuclear Explosion Monitoring Technologies***.

Authors of papers for excellent research, technical documentation, and cooperation with electronic submission processes.

Dr. G. Eli Baker, Mr. Robert J. Raistrick, and ***Dr. Frederick R. Schult,*** AFRL/RVBYE; ***Dr. Anton M. Dainty,*** Universal Technology Corporation; and the 377th Airbase Wing Public Affairs Office, for review and clearance of abstracts and papers related to AFRL awards.

Ms. Brenda K. Vaughan, Advanced Logistics Support Corporation, for facilitating production of the Proceedings and supporting communications with authors through the Monitoring Research Review meeting website, http://monitoringresearchreview.com.

Dr. Michael L. Begnaud, Los Alamos National Laboratory (LANL), for design of the CD label.

Ms. Brenda M. DeVargas, LANL, for composition of the hardcopy cover and the CD label.

Ms. Jody Benson and ***Ms. Marisa N. Sandoval,*** LANL, for editorial assistance with papers.

Mr. Marvin A. Wetovsky, LANL, Managing Editor of the Proceedings and Aide-de-camp.

SAFE 1 Classification Group, LANL, for reviewing papers for clearance.

Dr. Stanley D. Ruppert, Ms. Laura M. Long, and ***Ms. Arleen L. Allsup,*** Lawrence Livermore National Laboratory (LLNL), for testing files and ensuring that the CDs could be read on a variety of platforms and for burning the CDs.

Ms. Leslie A. Casey, NNSA, for review and clearance of abstracts and papers related to NNSA awards and for NNSA overall support of the Proceedings.

Ms. Sonal Joshi, NNSA Nonproliferation Graduate Fellow, for review of papers related to NNSA awards.

The NNSA/NA-22 webAPPS Team: Mr. Nickolas T. Torres, Ms. Sue A. Medeiros, Ms. Guadalupe (Lupe) Massoth, and ***Mr. Owen J. Yaklin,*** Sandia National Laboratories (SNL), for implementing web-based technology for abstract and paper submission, on-line review and approval tools, and creation of the master files for the hardcopy and CD versions of the Proceedings.

Dr. Robert J. Mellors, Dr. Stephen C. Myers, Dr. Michael E. Pasyanos, Dr. Stanley D. Ruppert, and ***Dr. William R. Walter,*** LLNL; ***Dr. Dale N. Anderson, Dr. Michael L. Begnaud,*** and ***Dr. Ken R. Rehfeldt,*** LANL; ***Dr. Theodore W. Bowyer, Dr. James C. Hayes,*** and ***Dr. Martin E. Keillor,*** Pacific Northwest National Laboratory; and ***Mr. Marcus C. Chang, Dr. Timothy S. McDonald,*** and ***Dr. Christopher J. Young,*** SNL, for a myriad of internal management and technical reviews of NNSA abstracts and papers.

PROCEEDINGS

Year	Title of the Proceedings
2012	Proceedings of the 2012 Monitoring Research Review: Ground-Based Nuclear Explosion Monitoring Technologies, LA-UR-12-24325
2011	Proceedings of the 2011 Monitoring Research Review: Ground-Based Nuclear Explosion Monitoring Technologies, LA-UR-11-04823
2010	Proceedings of the 2010 Monitoring Research Review: Ground-Based Nuclear Explosion Monitoring Technologies, LA-UR-10-05578
2009	Proceedings of the 2009 Monitoring Research Review: Ground-Based Nuclear Explosion Monitoring Technologies, LA-UR-09-05276
2008	Proceedings of the 30th Monitoring Research Review: Ground-Based Nuclear Explosion Monitoring Technologies, LA-UR-08-05261
2007	Proceedings of the 29th Monitoring Research Review: Ground-Based Nuclear Explosion Monitoring Technologies, LA-UR-07-5613
2006	Proceedings of the 28th Seismic Research Review: Ground-Based Nuclear Explosion Monitoring Technologies, LA-UR-06-5471
2005	Proceedings of the 27th Seismic Research Review: Ground-Based Nuclear Explosion Monitoring Technologies, LA-UR-05-6407
2004	Proceedings of the 26th Seismic Research Review: Trends in Nuclear Explosion Monitoring, LA-UR-04-5801
2003	Proceedings of the 25th Seismic Research Review: Nuclear Explosion Monitoring: Building the Knowledge Base, LA-UR-03-6029
2002	Proceedings of the 24th Seismic Research Review: Nuclear Explosion Monitoring: Innovation and Integration, LA-UR-02-5048
2001	Proceedings of the 23rd Seismic Research Review: Worldwide Monitoring of Nuclear Explosions, LA-UR-01-4454
2000	Proceedings of the 22nd Annual DoD/DoE Seismic Research Symposium: Planning for Verification of and Compliance with the Comprehensive Nuclear-Test-Ban Treaty (CTBT)
1999	Proceedings of the 21st Seismic Research Symposium: Technologies for Monitoring the Comprehensive Nuclear-Test-Ban Treaty, LA-UR-99-4700

The Proceedings are available to the public from 2012 back to 1999 in PDF at the DOE Office of Scientific and Technical Information (OSTI) Information Bridge http://www.osti.gov/bridge ; suggested words for the keyword search are, in quotes, “monitoring research review”. Proceedings from 1998 to 1985 are available at the Defense Technical Information Center (DTIC) http://www.dtic.mil/dtic ; suggested words for the keyword search are “seismic research symposium”. Be advised that these archival electronic copies are large files [greater than 45MB] and will take significant time to download and open.

Table of Contents - Volume I

1. Seismic Regional Characterization and Wave Propagation 1

1-01 **Bergman, E., C. Rowe, and M. Maceira**
Crustal and Upper Mantle Structure from Joint Inversion of Body Wave and Gravity Data 3

1-02 **Fisk, M. and W. Phillips**
Constraining Source Terms, Regional Attenuation Models, Geometric Spreading, and Site Effects for Eurasia 13

1-03 **Gök, R., S. Herzog, K. Nakanishi, M. Pasyanos, R. Mellors, A. Rodgers, D. Harris, and E. Vergino**
Lithospheric Models of the Middle East to Improve Seismic Source Parameter Determination/Event Location Accuracy 23

1-04 **Hipp, J., A. Encarnacao, C. Young, S. Ballard, M. Begnaud, and W. Phillips**
Calculating Path-Dependent Travel Time Prediction Variance and Covariance for a Global Tomographic P-Velocity Model 31

1-05 **Maceira, M., C. Larmat, R. Porritt, and D. Higdon**
Validation and Uncertainty Assessment of Ground-Based Nuclear Explosion Monitoring Models 41

1-06 **Mackey, K., H. Hartse, D. Burk, K. Fujita, and M. Pasyanos**
Seismic and Geophysical Characterization of Northern Asia 50

1-07 **Mayeda, K., W. Phillips, C. Rowe, M. Pasyanos, R. Gök, and W. Walter**
Transitioning the Coda Methodology to Full 2-D for P and S Codas 61

1-08 **Nyblade, A., J. Julià, E. Matzel, A. Raveloson, and A. Rodgers**
Developing Regionalized Models of Lithospheric Thickness and Velocity Structure Across Eurasia and the Middle East from Jointly Inverting P-wave and S-wave Receiver Functions with Rayleigh Wave Group and Phase Velocities 66

1-09 **Pulliam, J., M. Sen, M. Agrawal, U. Dutta, R. Ghosh, F. Sepulveda, R. Mellors, and M. Pasyanos**
Joint, Non-Linear Modeling of Receiver Functions, Surface Wave Dispersion, and Waveforms with Formal Assessments of Constraints 75

1-10 **Reiter, D., W. Rodi, and S. Myers**
Estimating the Uncertainty and Predictive Capabilities of Three-Dimensional Earth Models 85

1-11 **Sandvol, E., A. Kaviani, W. Ku, R. Gök, and G. Rumpker**
High-Resolution Regional Phase Attenuation Models of the Iranian Plateau and Zagros 95

1-12 **Sandvol E., T. Hearn, J. Ni, S. Ceylan, W. Ku, X. Bao, X. Liang, and W. Phillips**
High-Resolution Seismic Velocity and Attenuation Models of Eastern Tibet 105

1-13 **Savage, B., D. Peter, B. Covellone, C. Morency, A. Rodgers, and J. Tromp**
Short-Period, Anelastic and Anisotropic, Waveform-Based 3D Middle East Model to Improve Nuclear Explosion Monitoring 114

1-14 **Shen, Y. and W. Zhang**
Full-Wave Tomography of the Eastern Hemisphere 121

1-15 **Snelson, C., V. Chipman, R. White, R. Emmitt, M. Townsend, D. Barker, and P. Lee**
An Overview of the Source Physics Experiment at the Nevada National Security Site 130

1-16 **Song, X., R. Weaver, and X. Yang**
Surface Wave Attenuation in the Tibetan Plateau From Ambient Noise 135

1-17 **Song, X., Z. Xu, L. Zhu, and Y. Zhou**
Joint Inversion of Crustal And Uppermost Mantle Structure in Western China 143

1-18 **van der Hilst, R., H. Zhang, M. Maceira, C. Rowe, H. Yao**
3D Variations in Seismic Wavespeed and Mass Density in the Crust and Upper Mantle of SE Asia from Joint Inversion of Seismic and Gravity Data 150

1-19 **van der Lee, S., S. Chang, M. Witek, T. Kang, and M. Feng**
Joint Inversion of Multiple Seismic Data for Three-Dimensional Velocity Structure Beneath Southern and Eastern Asia 160

1-20 **Vorobiev, O., H. Xu, I. Lomov, E. Herbold, T. Antoun, and L. Glenn**
Analysis and Simulation of Near-Field Ground Motion from the Source Physics Experiment 166

1-21 **Worthington, L., K. Miller, H. Hartse, W. Phillips, S. Harder, and A. Sheehan**
Crustal Velocity Heterogeneity and Assessment of Regional Explosion Discriminants in North-Central Wyoming: Results from the Bighorns Arch Seismic Experiment (BASE) 176

2. Seismic Event Detection and Location 189

2-01 **Arora, N., J. Given, E. Tomuta, S. Russell, and S. Spiliopoulos**
Analyst Evaluation of Model-Based Bayesian Seismic Monitoring at the CTBTO 191

2-02 **Begnaud, M., S. Ballard, C. Young, J. Hipp, A. Encarnacao, W. Phillips, E. Chael, and C. Rowe**
Validating a Global 3D P-Velocity Model of the Earth's Crust and Mantle for Improved Event Location 200

2-03 **Brazier, R., K. Boomer, J. O' Donnell, A. Nyblade, S. Myers, J. Kokoska, and S. Liu**
From Craton to Rift: Empirically Based Ground Truth Criteria for Regional Networks 210

2-04 **Draelos, T., S. Ballard, C. Young, and R. Brogan**
Refinement and Testing of the Probabilistic Event Detection, Association, and Location Algorithm 221

2-05 **Flanagan, M., S. Myers, and N. Simmons**
Model-Based Corrections To Observed Back Azimuth And Slowness Observations From a Dipping Mohorovicic Discontinuity 232

2-06 **Fourguette, D., V. Ötügen, L. Larocque, U. Ayaz, and G. Ritter**
Optical MEMS-Based Seismometer 241

2-07 **Heck, S., B. Hamlet, E. Chael, C. Young, W. Walter, and D. Anderson**
A New Network Modeling Tool for the Ground-Based Nuclear Explosion Monitoring Community 247

2-08 **Mackey, K. and K. Fujita**
Improvement of GT Classification of Soviet PNEs 254

2-09 **Moore, D., K. Mayeda, S. Myers, M. Seo, and S. Russell**
Progress in Signal-Based Bayesian Monitoring 263

2-10 **Myers, S. and G. Johannesson**
Extension of the Bayesloc Multiple-Event Location Algorithm to Include Differential Travel-Time Measurements 274

2-11 **Nábelek, J., J. Braunmiller, E. Riddle, P. Monigle, and W. Phillips**
Source and Path Calibration in Regions of Poor Crustal Propagation Using Temporary, Large-Aperture, High-Resolution Seismic Arrays 282

2-12 **Ritzwoller, M., A. Levshin, and M. Barmin**
Exploiting Ambient Noise for Source Characterization of Regional Seismic Events 291

2-13 **Rodi, W., D. Reiter, S. Myers, and N. Simmons**
A Unified Approach to Joint Regional/Teleseismic Calibration and Event Location with a 3D Earth Model 302

2-14 **Rowe, C., R. Stead, M. Begnaud, and E. Morton**
Seismic Signal Analysis for Event Detection and Categorization 312

2-15 **Simmons, N., S. Myers, G. Johannesson, and E. Matzel**
Global P-Wave Tomography for Improved Travel-Time Predictions and Event Locations 321

2-16 **Taylor, S., P. Harben, S. Jarpe, and D. Harris**
Development of Mine Explosion Ground Truth Smart Sensors 331

3. Seismic Identification and Source Characterization 343

3-01 **Biasi, G., D. von Seggern, J. Anderson, and I. Tibuleac**
Investigation of an Unusually Shallow Earthquake Sequence in Mogul, NV from a Discrimination Perspective 345

3-02 **Bonner, J. and D. Russell**
Estimating Yield Using Short-Period Surface Waves 355

3-03 **Bonner, J., R. Herrmann, and D. Russell**
A Synthetic Study of Surface Wave Magnitudes 365

3-04 **Dreger, D., A. Chiang, S. Ford, and W. Walter**
Refinement of Regional Distance Seismic Moment Tensor and Uncertainty Analysis for Source-Type Identification 377

3-05 **Ford, S., W. Walter, S. Ruppert, E. Matzel, T. Hauk, and R. Gök**
An Empirically-Based Parametric Explosion Spectral Model 387

3-06 **Hartse, H., G. Randall, D. Anderson, W. Phillips, and S. Arrowsmith**
Regional Event Identification Research in Central Asia 397

3-07 **Knight, E., E. Rougier, A. Zubelewicz, A. Sussman, D. Coblentz, D. Steedman, W. Brunish, and C. Bradley**
Hydrodynamic Analysis of the Effect of a Non-Uniform Weathered Layer on Free Surface Acceleration Signals 407

3-08 **Lay, T., M. Avants, X. Xie, and A. Rodgers**
Effects of 3D Surface Topography on Regional and Teleseismic Signals from Underground Explosions 419

3-09 **Martin, R., P. Boyd, A. Stroujkova, M. Leidig, J. Lewkowicz, and J. Bonner**
Anisotropy of the Barre Granite in the Vicinity of the NEDE 428

3-10 **Mayeda, K. and S. Yoo**
Absolute Amplitude vs Explosion Yield Scaling For P and S-Codas: On the Path to Removing Test Site Bias and Constraining Source Phenomenology 441

3-11 **Mayeda, K., S. Yoo, W. Walter, and L. Malagnini**
Local Micro-Calibration for Ground-Truth Source Spectral Database in Broad Regions of Monitoring Interest 447

3-12 **Mayeda, K., S, Yoo, W. Walter, R. Gök, and L. Malagnini**
Improved High Frequency Discrimination: A New Approach to Correct for Regional Source Scaling Variations 453

3-13 **Pasyanos, M., W. Walter, E. Matzel, R Gök, S. Ford, H. Xu, and K. Mayeda**
Integrating Work in Seismic Attenuation, Coda Decay, and Source Models for Event Identification and Characterization 459

3-14 **Patton, H., C. Larmat, E. Rougier, C. Rowe, and X. Yang**
Seismic Studies of Source Physics Experiments Conducted at the Nevada National Security Site Using Close-In (< 2 km) Waveforms 469

3-15 **Patton, H., G. Randall, and S. Taylor**
Analytical Explosion Models Including Source Medium Damage: Implications for Teleseismic P Waves and Regional Phase Excitation 479

3-16 **Phillips, W., X. Yang, R. Stead, M. Begnaud, H. Hartse, D. Anderson, M. Fisk, and K. Mayeda**
Model Building for Amplitude Prediction 487

3-17 **Pollitz, F., W. Ellsworth, and J. Rubinstein**
Analysis and Modeling of the Shear Waves Generated by Explosions at the San Andreas Fault Observatory at Depth 496

3-18 **Rodgers, A., H. Xu, N. Petersson, B. Sjogreen, I. Lomov, and O. Vorobiev**
Progress On Seismic Ground Motion Simulations for Nuclear Explosion Monitoring Using Hydrodynamic And Anelastic Modeling 507

3-19 **Steedman, D., D. Coblentz, C. Bradley, and A. Sussman**
Simulating the Response of a Faulted Test Site with a Fully Coupled Euler-Lagrange Hydrocode 518

3-20 **Stevens, J. and M. O'Brien**
Seismic Wave Generation and Propagation from Complex 3D Explosion Sources 524

3-21 **Stroujkova, A. and J. Bonner**
Topographic Scattering at Local Distances: Insights from Modeling of SPE-Arizona Data 534

3-22 **Stroujkova, A., J. Bonner, M. Leidig, A. Ferris, W. Kim, T. Rath, M. Carnevale, and J. Lewkowicz**
Effect of Rock Damage on Seismic Amplitudes from Explosions 544

3-23 **Townsend, M., H. Huckins-Gang, L. Prothro, and D. Reed**
Geologic Assessment of the Damage Zone from the Second Test of the Source Physics Experiment in Nevada 553

Seismic Regional Characterization and Wave Propagation

CRUSTAL AND UPPER MANTLE STRUCTURE FROM JOINT INVERSION OF BODY WAVE AND GRAVITY DATA

Eric A. Bergman[1], Charlotte Rowe[2], and Monica Maceira[2]

University of Colorado[1] and Los Alamos National Laboratory[2]

Sponsored by the Air Force Research Laboratory and the National Nuclear Security Administration

Award Nos. FA9453-11-1-0233[1] and DE-AC52-06NA25396[2]
Proposal No. BAA11-46

ABSTRACT

We present a preliminary model of the three-dimensional seismic structure of the Iran region obtained via simultaneous, joint inversion of body wave travel time and gravity observations. The body wave data set is derived from location calibration efforts and includes a large (>1000 events) subset of GT5-level events. The arrival time data sets for these events include many readings of direct crustal P and S phases, as well as regional (Pn and Sn) and teleseismic phases. These data have been groomed to identify and remove outlier readings; empirical reading errors are estimated for most arrivals from multiple event relocation analysis.

We use both free-air and Bouguer gravity anomalies derived from the global gravity model of the GRACE satellite mission. The gravity data provide information on shallow density variations with short spatial wavelengths, and deeper density structures with longer spatial wavelengths. To increase the usefulness of the gravity data, we apply high-pass filtering, yielding gravity anomalies that possess higher resolving power for crustal and lithospheric structures. To integrate both data sets into a single inversion a functional relationship between seismic velocities and density is required. We first use a combination of two empirical relations: one most appropriate for sedimentary rocks, and a linear Birch's Law that is more applicable to basement rocks. These relationships, however, assume a constant Poisson ratio throughout the inversion. We therefore also apply a method that allows the Poisson ratio to vary by mapping densities to V_P and V_S independently for different earth materials.

Final results of the simultaneous inversion will help us to better understand the crustal and lithospheric structures associated with early-stage continental collision. Such models also provide an important starting model for computationally more expensive and time-consuming fully 3D waveform inversions.

OBJECTIVES

Our objective in this project is to gain increased understanding of the lateral variations of velocity structure in the crust and upper mantle of the region expressing the continental collision between the Arabian and Eurasian plates. Our strategy is to combine different types of geophysical data sets, in this case, body wave travel time data and gravity data, in a formal joint inversion for velocity structure. Preliminary work has shown that body wave data and gravity data can be combined to yield improved resolution of the variability of crustal and upper mantle velocities. A key element to this success is careful filtering of the gravity data so that the signal source region corresponds to the depth range that is sampled by the seismic data.

Our choice of region for this study is driven in part by the availability of an exceptional data set of body wave travel time data that results from a series of research projects on calibrated locations in the region. No other area of monitoring interest is so well sampled by ground truth events. This project is one effort to make maximum use of this unique data set.

RESEARCH ACCOMPLISHED

We have made progress in all major areas of this project, acquiring the earthquake and gravity data sets, development of the joint inversion code, and performing preliminary inversions.

Calibrated Earthquake Dataset

We have imported a large data set of calibrated earthquake locations and associated station information and arrival times into the Ground Truth Database that is maintained at Los Alamos National Laboratory (LANL). This data set was developed in several previous projects in the Nuclear Explosion Monitoring Research and Development (NEM R&D) research program (Bergman et al., 2009). These are all available calibrated events for the study region at this time, although we expect to be able to add some additional calibrated clusters during the project.

By “calibrated” we mean that the hypocenters have been estimated with a specialized multiple event relocation process that removes systematic location errors from clusters of earthquakes, by establishing the location of the cluster using only near-source data that are insensitive to unknown velocity structure. Such data includes seismic recordings at short epicentral distances, field mapping of faulting, and remote sensing analyses of ground displacements such as Interferometric Synthetic Aperture Radar (InSAR). The accuracy of relative locations of clustered events is also improved in the relocation analysis. The majority of events in the data set qualify as $GT5_{90}$ and many qualify at lower levels of location accuracy. In the relocation process the arrival time data sets are groomed to remove outlier readings and to estimate empirical reading errors.

The import process required extensive review of station codes and coordinates to maintain the correct associations with station information and associated arrival time data already in the database. The calibrated earthquake data set is now easily accessible for input to the joint inversion code that is maintained at LANL, and it is also easy to incorporate other (non-calibrated) earthquake data in the region in the inversion as needed. The calibrated earthquake data set includes 1902 events recorded at 376 stations, yielding 26,043 P readings and 6,390 S readings that we have used in the joint inversion. The distribution of calibrated events is shown in Figure 1 and the ray coverage for the Pn phase is shown in Figure 2.

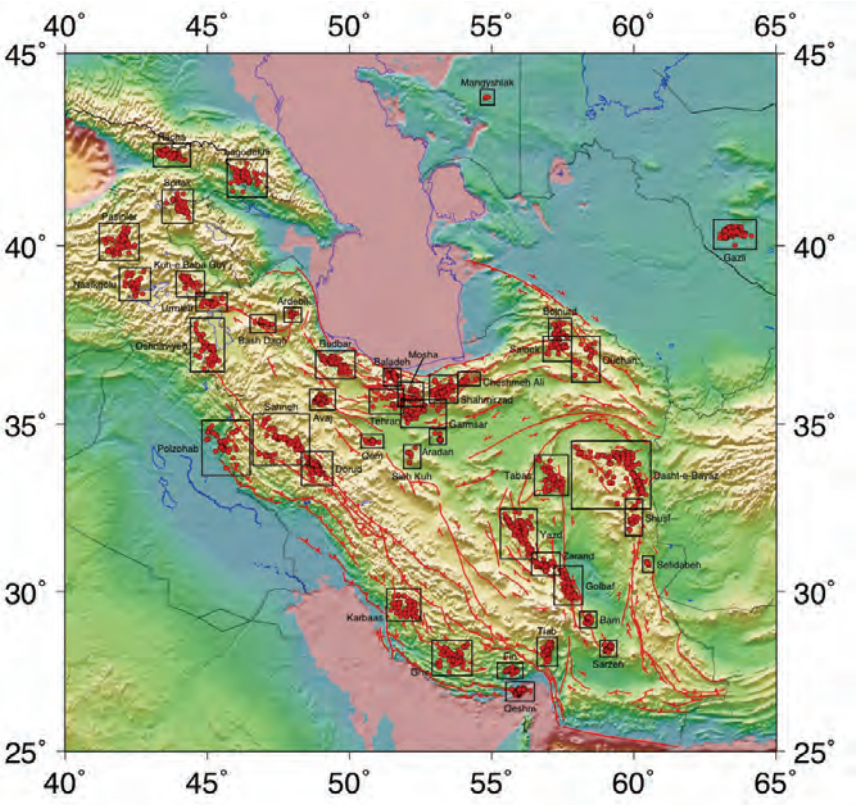


Figure 1. Map of the study region, showing the locations of earthquakes with calibrated locations that are used in this study. Calibrated relocations have been done with a multiple event analysis applied to clusters. The bounding boxes of the clusters are shown.

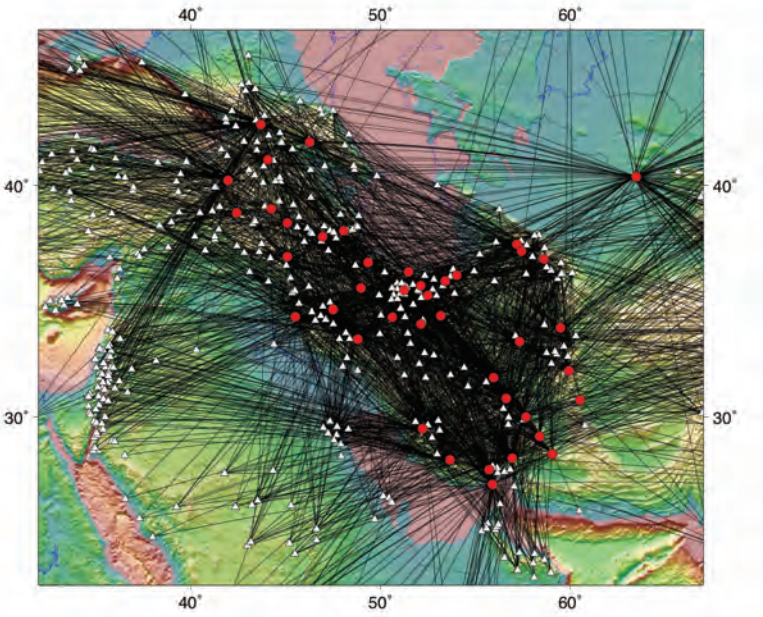


Figure 2. Pn raypaths in the calibrated earthquake data set. The data set also contains Sn arrivals, as well as crustal (Pg, Sg) and teleseismic arrivals. The raypaths shown are summary rays from individual clusters (Figure 1), shown as red circles, to stations (white triangles). Most raypaths are sampled many times, providing useful information on variability of the input data.

Gravity Data

We used gravity observations extracted from the global gravity model derived from the Gravity Recovery and Climate Experiment (GRACE) satellite mission. A detailed description of the satellite data and the computation of the gravity field are given by Tapley et al. (2005). The new gravity field is more accurate than previous data and reveals previously unobserved tectonic features. Figure 3 shows the free-air gravity anomalies for the study region. Blue colors represent gravity highs and gravity lows are represented in red. Free-air gravity anomalies contain information not only of the subsurface density but also topography. While in flat regions this may not be a problem, in areas of high topographic relief this effect needs to be removed; thus, we converted free-air anomalies into Bouguer anomalies assuming a standard density for crustal rocks of 2670 kg/m^3.

To increase the usefulness of the gravity data for investigating 3-D seismic structure, we are exploring high-pass gravity filtering. Though commonly applied in gravity forward modeling (e.g., Simiyu and Keller, 1997), such techniques are not usually applied in joint inversion studies (e.g., Zeyen and Achauer 1997; Tiberi et al., 2003; Maceira and Ammon, 2009). Filtered gravity anomalies are expected to possess their highest resolving power at short wavelengths and thus enhance resolution of lithospheric structure. Maceira et al. (2011) have shown the possible benefits of filtering. After high-pass filtering, the remaining short-wavelength signal can be assigned with greater confidence to structures within the crust, reducing the mutually degrading effects of smearing between crustal and mantle structures. To high-pass filter the Bouguer gravity data we follow the filtering parameter choices of Tessema and Antoine (2004), who use an upward continuation method and demonstrate correlation with crustal geology.

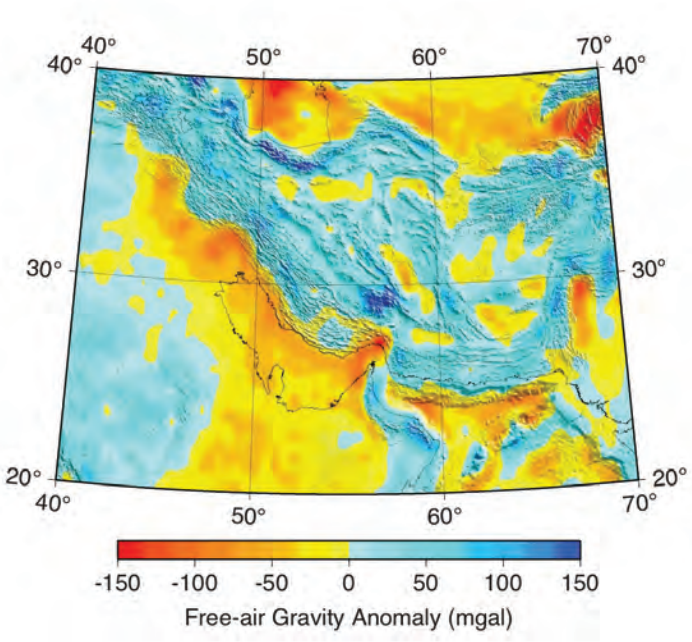


Figure 3. Free Air gravity anomaly field in the study area.

Joint Inversion Code

During a previous project in the NEM R&D research program and in collaboration with MIT, we developed an algorithm named JointTomoDD (Maceira et al., 2010), which is a modification of the Maceira and Ammon (2009) joint inversion code, in combination with the double-difference tomography program tomoFDD (Zhang and Thurber, 2003, 2006), with a fast LSQR solver operating on the gridded values jointly. The model representation is a combination of columns of rectangular prisms (needed for the gravity forward modeling) embedded in a grid whose nodes are located at the center of each prism.

Preliminary Inversions

We first performed several runs using only the seismic body waves (P and S) arrival times. The resulting 3D model depends strongly on the initial model. Figure 4 shows the P and S velocity fields obtained when using ak135 as the starting velocity model. Figure 5 shows the corresponding Moho isosurface (choosing a velocity of 8 km/s) in which quite unrealistically deep Moho depths can be seen. Figure 6 shows the velocity fields obtained by starting with a modified ak135 model in which the Moho is set to ~ 50 km depth (as compared to 35 km in ak135), which is known to be a more reasonable average Moho depth for this region. Figure 7 shows the corresponding Moho isosurface, which is still too deep in some places.

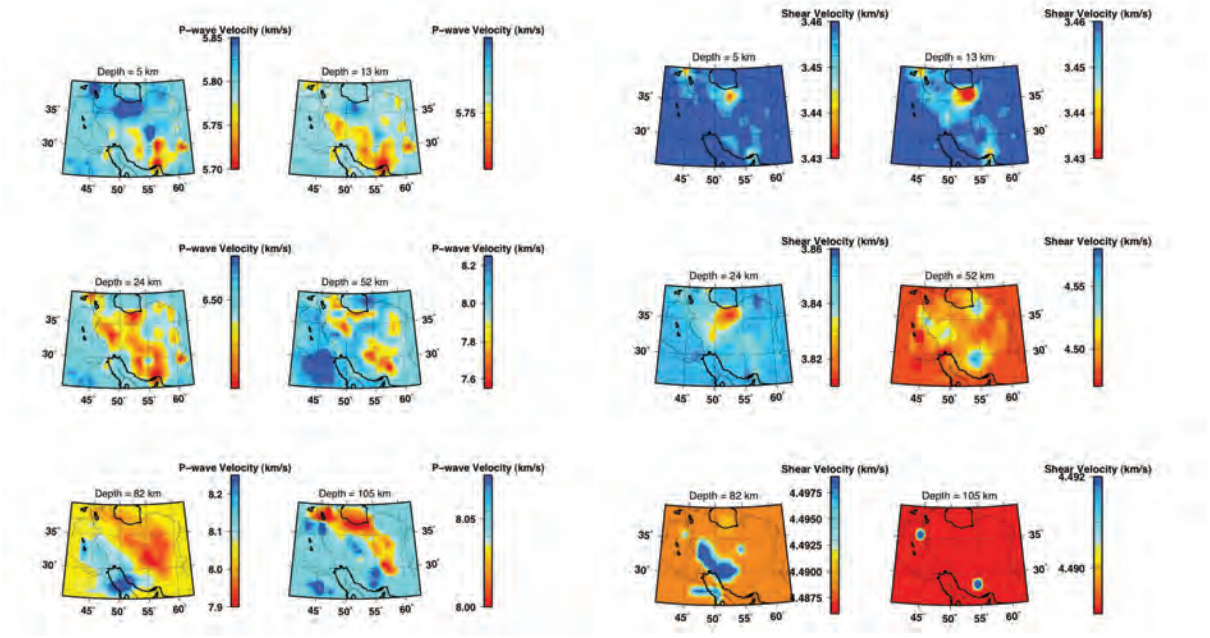


Figure 4. Results of inversion of the seismic data only (P velocities on the left, S velocities on the right), shown at depths of 5, 13, 24, 52, 82 and 105 km. The starting model is ak135.

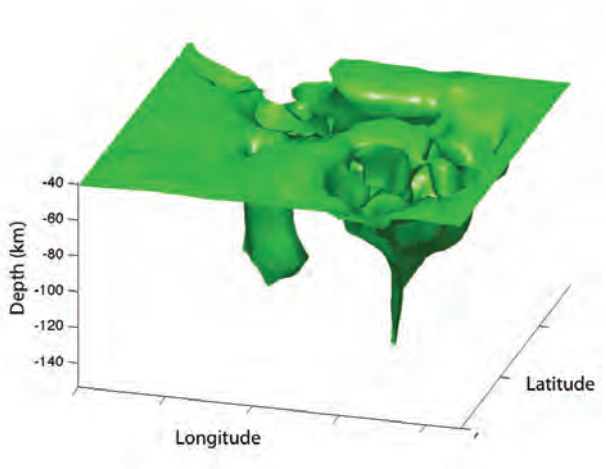


Figure 5. Moho isosurface (at 8 km/s) derived from the velocity model of the inversion using only seismic data (Figure 4).

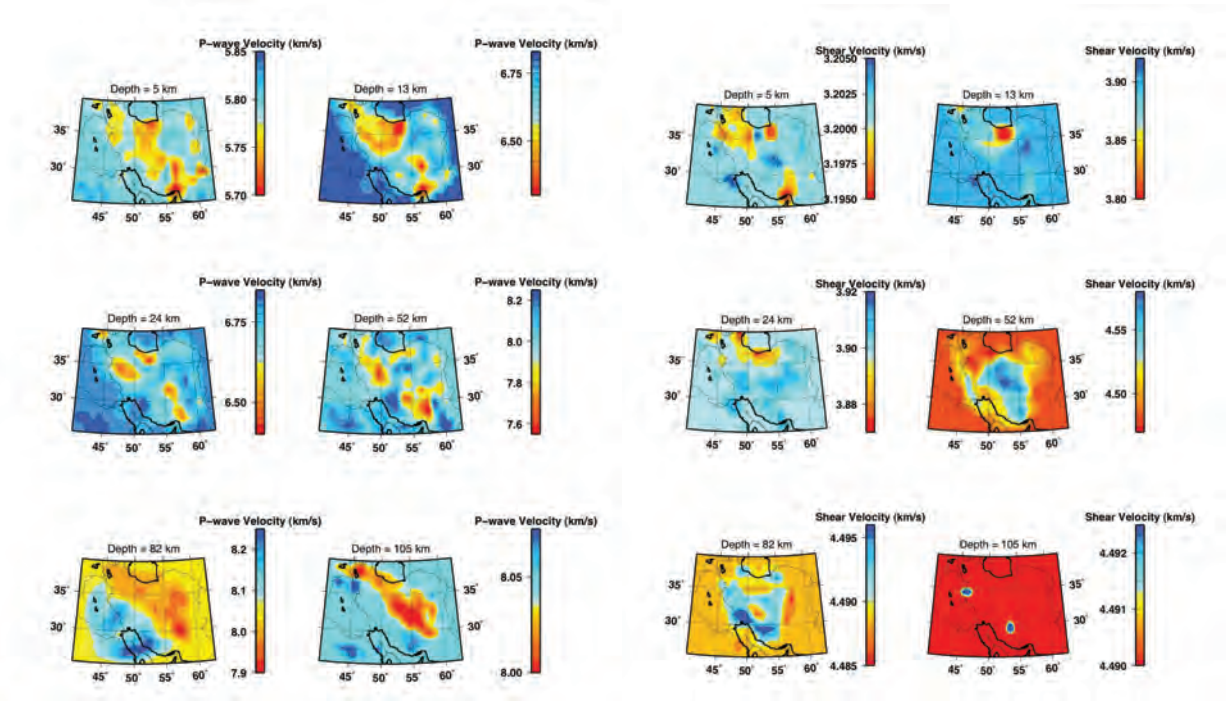


Figure 6. Results of inversion of the seismic data only, with a modified version of ak135 (Moho at 50 km) as the starting model. Otherwise, as Figure 4.

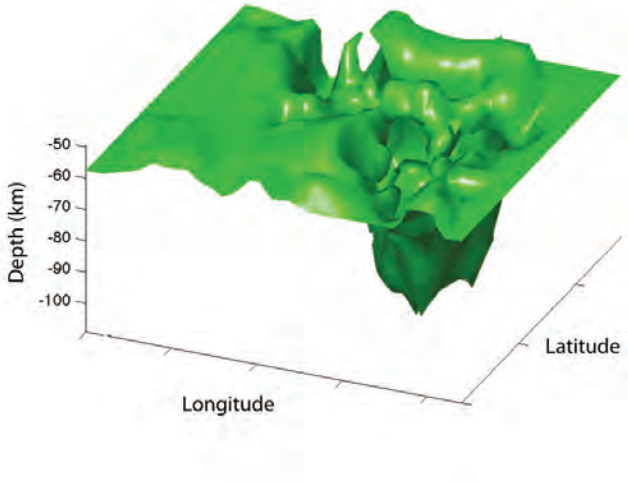


Figure 7. Isosurface of the Moho derived from the inversion of seismic data alone, using a modified version of ak135 (with Moho at 50 km) as the starting model (Fig. 6).

In either case, the fit of the gravity field inferred from the final velocity model to the observed gravity field is very poor (Figure 8). In fact there appears to be a significant degree of anti-correlation.

We then performed some initial joint inversions combining the seismic data with the free-air gravity anomalies for the region and using the modified version of ak135 as the initial model. Figure 9 shows the compressional (left) and shear-wave (right) velocity models from the joint inversion. The Moho isosurface derived from this inversion is shown in Figure 10. These results are very preliminary so we do not attempt an interpretation. Even though the fit to the gravity data has greatly improved (compare Figures 8 and 11), we can already see signs of leakage of the high

wavenumber gravity signal into the upper mantle velocity structure. Gravity filtering of the Bouguer anomalies will help alleviate this problem and we are now in the process of performing those runs.

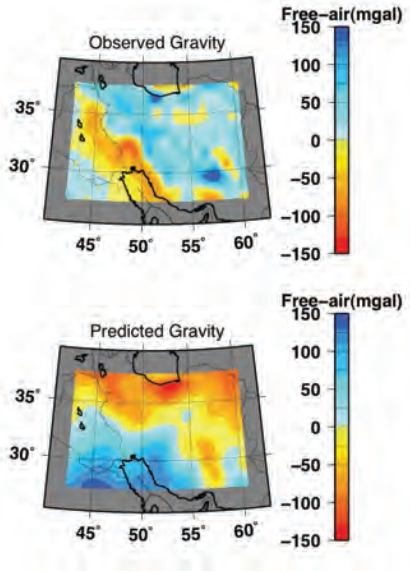


Figure 8. Comparison of the gravity field predicted from the velocity model shown in Figure 6 with the observed gravity field. There is a significant degree of anti-correlation.

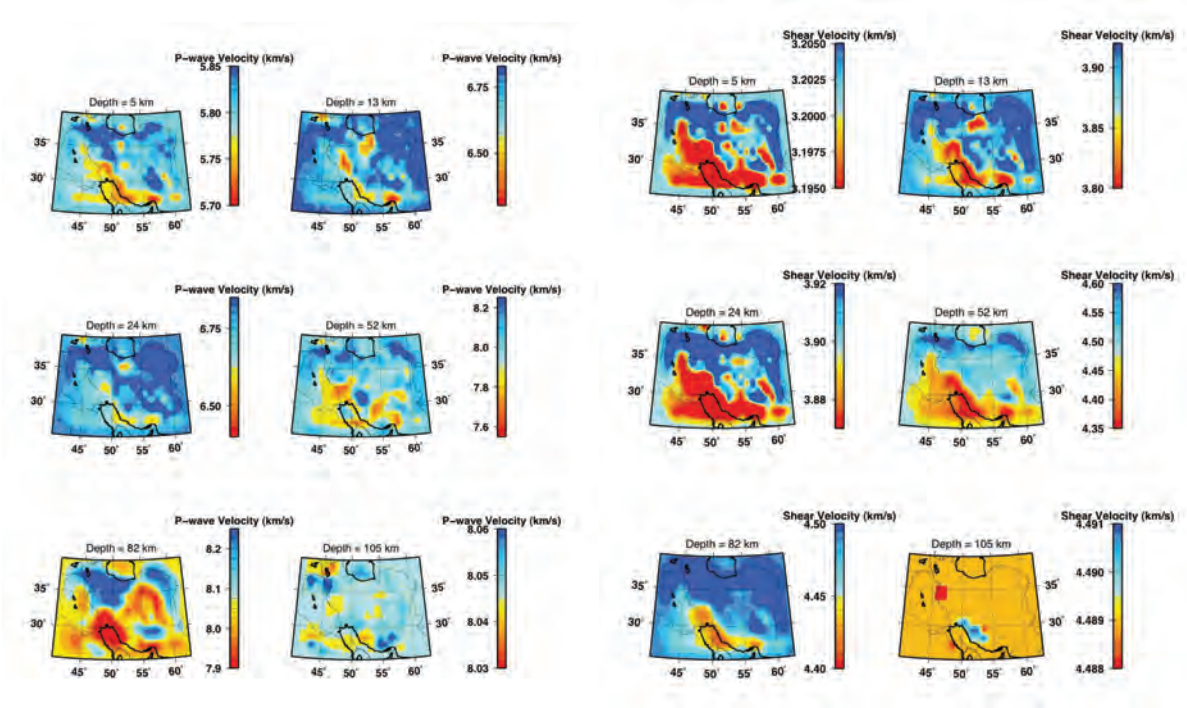


Figure 9. Results of the joint inversion of seismic and gravity data (P velocities on the left, S velocities on the right), shown at depths of 5, 13, 24, 52, 82 and 105 km. The starting model is ak135, modified to have a 50 km thick crust.

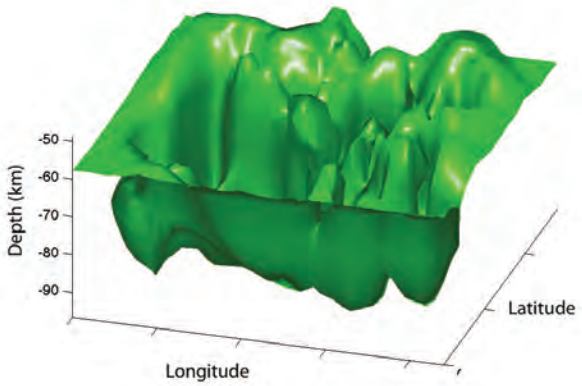


Figure 10. Isosurface of the Moho (8 km/s) based on the velocity field from joint inversion of seismic and gravity data (Figure 9).

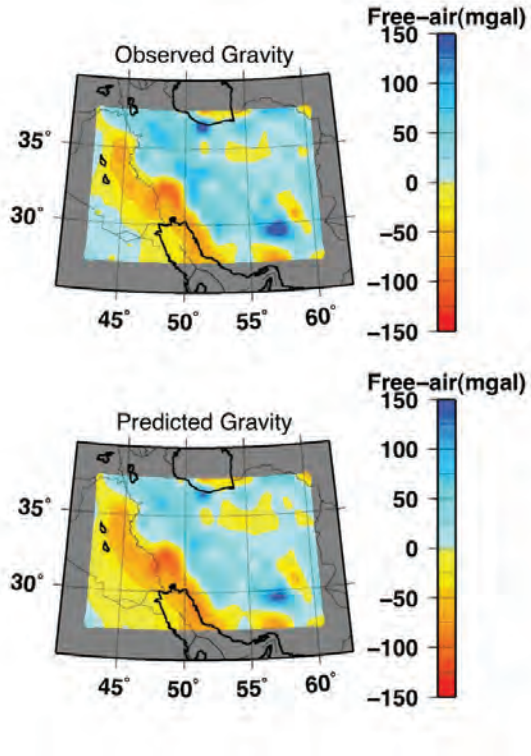


Figure 11. Comparison of the gravity field predicted from the velocity model shown in Figure 9 (joint inversion of seismic and gravity data) with the observed gravity field. The agreement is, unsurprisingly, much better than the case where the velocity model is determined using only seismic data (Figure 8).

In our modeling we couple seismic and gravity data through a density-velocity relationship. This is an ambiguous relationship, however, because seismic wavespeeds are governed not only by rock density but also by bulk and shear moduli, which vary independently and are influenced by many factors, including lithology, temperature and

lithostatic pressure. Our initial inversions have used a combination of traditional empirical relationships: one appropriate for sedimentary rocks (after Nafe and Drake, 1963) and one for basement rock (Birch, 1961). Both require the additional assumption of a fixed Poisson ratio in order to obtain shear wave velocity. In subsequent modeling we are employing a shear velocity vs. density relationship proposed by Ludwig et al. (1970), as implemented in a code provided by D.G. Harkrider. This method allows us to treat Poisson's ratio as a variable in the joint inversion, although the degree to which the data will permit this variable to be resolved needs to be explored.

CONCLUSIONS AND RECOMMENDATIONS

We have set up the seismic (body wave travel times) and gravity data sets, finished modification and testing of the code for the joint inversion, and begun running inversions to learn how best to combine these types of data to infer features of the 3-D velocity structure of a continental collision zone. We have performed inversions using only the seismic data, finding that they are inadequate to accurately image the 3-D velocity field in the study region, except perhaps for a few areas with especially good coverage. Adding the unfiltered gravity data to the inversion leads to results that are far more consistent with the observed gravity field, as expected, but much work will be needed to explore issues of resolution and uniqueness for the seismic velocity fields determined in this type of inversion.

We are also exploring the usefulness of filtering the gravity data to create data sets whose signal is dominated by certain ranges in depth that can be associated with specific seismic phases and epicentral distance ranges. Our code is also able to incorporate seismic surface wave data and we will consider this as a way to improve the sampling coverage by seismic data in the study region.

ACKNOWLEDGEMENTS

We acknowledge the assistance of Richard Stead in importing the data set of calibrated earthquake locations and arrival time data into the database used for the joint inversions.

REFERENCES

Bergman, E. A., E. R. Engdahl, M. H. Ritzwoller, and S. C. Myers (2009). Crustal structure from in-country and ground-truth data, in *Proceedings of the 2009 Monitoring Research Review: Ground-Based Nuclear Explosion Monitoring Technologies*, Vol. 1, pp. 22-31.

Birch, F. (1961). The velocity of compressional waves in rocks to 10 kilobars, part 2, *J. Geophys. Res*. **66**, 2199–2224.

Ludwig, W.J., J.E. Nafe, and C.L. Drake (1970). Seismic refraction, in *The Sea*, Part I, v.4., A.E. Maxwell (ed.), Wiley-Interscience, New York.

Maceira, M. and C. J. Ammon (2009). Joint inversion of surface wave velocity and gravity observations and its application to Central Asian basins shear velocity structure, *J. Geophys. Res*. **114**, B02314, doi:10.1029/2007JB005157.

Maceira, M., H. Zhang, R. Modrak, C. Rowe, and M. Begnaud (2010). Advanced Multivariate Inversion Techniques for High Resolution 3D Geophysical Modeling, in *Proceedings of the 2010 Monitoring Research Review: Ground-Based Nuclear Explosion Monitoring Technologies*, Vol. 1, pp. 97-107.

Maceira, M., H. Zhang, C. Larmat, C. Rowe, and M. Begnaud (2011). Advanced Multivariate Inversion Techniques for High Resolution 3D Geophysical Modeling, in *Proceedings of the 2011 Monitoring Research Review: Ground-Based Nuclear Explosion Monitoring Technologies*, Vol. 1, pp. 98-108.

Nafe, J. E., and C. L. Drake (1963). Physical properties of marine sediments, in *The Sea*, vol. 3, edited by M. N. Hill, pp. 794–815, Interscience, New York.

Tapley, B.D., S. Bettadpur, J.C. Ries, P.F. Thompson, and M.M. Watkins (2005). GRACE measurements of mass variability in the Earth system, *Science* **305**, 503–505.

Tessema, A., and L. A. G. Antoine (2004). Processing and interpretation of the gravity field of the East African Rift: Implication for crustal extension, *Tectonophysics* **394**, 87-110.

Tiberi, C., M. Diament, J. Déverchère, C. Petit-Mariani, V. Mikhailov, S. Tikhhotsky, and U. Achauer (2003). Deep structure of the Baikal rift zone revealed by joint inversion of gravity and seismology, *J. Geophys. Res*. **108**, (B3), 2133, doi:10.1029/2002JB001880.

Simiyu, S. M., and G. R. Keller (1997). An integrated analysis of lithospheric structure across the East Africa plateau based on gravity anomalies and recent seismic studies, *Tectonophysics* **278**, 291-313.

Zeyen, H., and U. Achauer (1997). Joint inversion of teleseismic delay times and gravity anomaly data for regional structures, in: K. Fuchs (ed.), *Upper Mantle Heterogeneities from Active and Passive Seismology*, Kluwer Academic Publishers, Dordrecht, 1997, 155-169.

Zhang, H., and C. H. Thurber (2003). Double-Difference Tomography: The Method and Its Application to the Hayward Fault, California, *Bull. Seismol. Soc. Am* **93**, 1875-1889.

Zhang, H., and C. Thurber (2006). Development and applications of double-difference tomography, *Pure and Applied Geophys.* **163**, 373-403, doi:10.1007/s00024-005-0021-y.

CONSTRAINING SOURCE TERMS, REGIONAL ATTENUATION MODELS, GEOMETRIC SPREADING, AND SITE EFFECTS FOR EURASIA

Mark D. Fisk[1] and W. Scott Phillips[2]

Alliant Techsystems[1] and Los Alamos National Laboratory[2]

Sponsored by the Air Force Research Laboratory[1] and the National Nuclear Security Administration[2]

Award Nos. FA8718-09-C-0005[1] and LA09-BAA09-01-NDD03[2]
Proposal No. BAA09-01

ABSTRACT

Reliable use of regional seismic phases for discrimination and magnitude estimation requires accurate corrections. Procedures that simultaneously invert for source, attenuation, spreading, and site parameters have many trade-offs, resulting in large errors for source and distance corrections. This motivated our development and testing of methods to constrain the trade-offs, to improve the accuracy of these parameters. We have processed many thousands of spectra of Pn, Pg, Sn, Lg, and coda envelopes. We compute and fit relative spectra for nearby, similar event pairs of different moments, to cancel path, site, and focal mechanism effects, and estimate reliable corner frequencies and relative moments. The results indicate the benefits of incorporating multiple, independent measurements of coda and direct-phases, to provide a large set of corroborated source terms for earthquakes throughout Eurasia. Discrepancies between source parameter estimates from coda versus direct phases indicate problems, often due to data quality issues. We then correct the spectra for source terms and fit source-corrected spectra to estimate site and distance-related terms for Lg, Sn, Pn, and Pg. This is a distinct approach from amplitude tomography, in which the path dependence of Q is estimated for fixed frequency bands. Comparing results from independent measurements and inversion methods verifies paths with reliable Q estimates and identifies needed improvements. Q_0 estimates from the two approaches generally agree reasonably well, particularly for areas with good station coverage. We provide overall comparisons for various phases and highlight some representative cases in detail. Discrepancies in the Q estimates are usually for higher frequencies, in low Q regions and/or at the edges of the tomography grid. We also describe how the fits of source-corrected spectra are used to estimate the geometric spreading rate for each phase, and also provide a way to estimate a very consistent set of absolute moments for the earthquakes. We find that constant power-law models (Street et al., 1975) fit the Lg, Sn, and Pg data quite well, and yield similar spreading exponents to previous studies. Pn clearly departs from constant power-law spreading behavior at far regional distances (beyond about 1500 km), due to sphericity, upper mantle triplication, and other propagation effects. Recently, we have corrected the spectra for source, Q, and spreading terms, and computed the median spectral residual, to estimate frequency-dependent site effects. We compare our results to independent site terms estimated from Lg coda tomography. We are in the process of also applying the site corrections to the spectra, to quantify residual variances versus frequency, partitioned by physical contributions. From this work, we have identified three critical ways that Q and spreading models must be improved and evaluated. First, tomography results are unreliable near grid edges, particularly important for the Middle East, where data sampling issues (i.e., limited crossing ray paths, particularly for higher frequencies) lead to large errors for tomography, but not our method. Tomography can be adapted to use our results as direct constraints. Second, data quality has a direct impact on calibration. Existing signal-to-noise tests do not exclude enough bad data, while retaining a majority of good data, particularly for secondary phases that are in the coda of preceding phases. We describe enhanced (physically-based) data quality criteria to determine useful frequency ranges. Third, Pn is the most complicated regional phase, with the least reliable tomography results. Although Pg is typically more stable than Pn, there is only a fraction of Pg observations compared to Pn. Thus, improving and validating Pn Q and spreading models are paramount for application of P/S discriminants to broad areas. We show order-of-magnitude errors that directly impact P/S discrimination results and describe plans to rectify these issues.

OBJECTIVES

We are developing, applying, and evaluating innovative methods to improve the accuracy of source, attenuation, geometric spreading, site terms, and their uncertainties for regional phases in Eurasia, by constraining trade-offs among the parameters at various stages of the analysis. The approach breaks up the inversion into controllable pieces, canceling certain physical effects (e.g., distance and site) to reliably estimate others (e.g., source), and then correcting for the latter to then reliably estimate the former. A key aspect of this work is to use independent measurements and methods to validate the corrections. We use spectra of Pn, Pg, Sn, and Lg, and independent coda envelopes, to corroborate source terms. We then fit source-corrected spectra to estimate Q and compare to independent amplitude tomography results. We estimate geometric spreading from constants of the spectral fits and show how they are also used to estimate a consistent set of absolute moments. Applying source, Q, and spreading corrections, we estimate site terms from the median spectral residuals for each station and phase, and compare them to independent site terms from coda tomography. We have compared and delivered our results for use as constraints for amplitude tomography runs at LANL. We are quantifying and partitioning uncertainties for the various physical parameters.

RESEARCH ACCOMPLISHED

Following Sereno et al. (1988), Taylor et al. (2002), and many others, the amplitude spectrum for a given phase and station, for event *i*, is modeled by

$$A_i(f) = S_i(f;M_0,f_c)G(r_i;r_0,\eta)\exp\left(-\frac{\pi f^{1-\gamma}}{Q_0 v}r_i\right)P(f), \quad \text{(EQ 1)}$$

where $S_i(f)$ is the source spectrum with moment M_0 and corner frequency f_c; $G(r_i;r_0,\eta)$ is geometric spreading; $Q_0 f^{\gamma}$ represents attenuation, r_i is distance; v is group velocity; and $P(f)$ is a site term. Methods that invert for all parameters simultaneously have many trade-offs and instabilities (e.g., Taylor and Hartse, 1998; Fisk and Taylor, 2006; Fisk and Phillips, 2009), that can result in deleterious discrimination errors (shown below).

Estimating Source Terms

In our approach, we start by computing and fitting relative spectra for similar event pairs of different moments, to cancel path and site effects, and estimate reliable corner frequencies and relative moments. That is, for a pair of nearby earthquakes with similar radiation patterns, the relative spectra for a given seismic phase type is modeled (Brune, 1970) by

$$\frac{A_1(f)}{A_2(f)} = \frac{S_1(f)}{S_2(f)} = \frac{M_0^{(1)}[1+(f/f_c^{(2)})^2]}{M_0^{(2)}[1+(f/f_c^{(1)})^2]}. \quad \text{(EQ 2)}$$

There are many repeating events throughout Eurasia (Schaff and Richards, 2004) to which this approach can be applied. Mayeda et al. (2007) showed that coda is less sensitive to focal mechanism, event separation, and station coverage, not requiring similar events, augmenting the number of pairs for which we can estimate source terms. Thus, in addition to fitting relative spectra of direct regional phases, we compute coda envelopes using the method of Mayeda et al. (2003) and Phillips et al. (2008), compute a pseudo relative spectrum as the median ratio of coda envelopes in 16 frequency bands, and fit it. Figure 1 illustrates relative spectra at a single station, and fits of Eq. (2) for an earthquake pair in southwestern Siberia. Distinct measurements and methods for direct-phase spectra and coda envelopes are used to corroborate the moment and corner frequency estimates. Discrepancies flag problems, most often due to data quality issues. For example, MKAR waveforms for the same larger (Mw 6.7) event are badly clipped, which varies by phase, leading to relative spectra in Figure 2

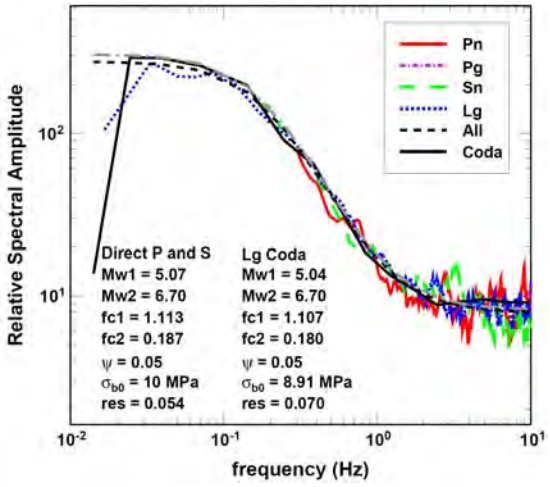


Figure 1. Relative spectra of Pn, Sn, Lg, and Lg coda, using data from a single station (CHKZ) for an event pair in southwestern Siberia. Model fits and source parameter estimates agree very well.

We acquired IRIS data for events listed in PDE from 1989 to 2009 with epicenter estimates within 50 km of another event, a magnitude difference of at least 0.7 m.u., and the larger (*master*) event of each pair at least mb 5. The set includes 46,495 such pairs, corresponding to 9,395 unique events (Figure 3). We processed about 2,000,000 spectra of regional phases and about 10,000,000 coda envelopes, computed network-median relative spectra, and fit Eq. (2) to each pair. We also computed waveform cross-correlations for all pairs, to assess similarity of focal mechanisms. We reviewed the results for $Mw \geq 5.4$ master events, and smaller events in areas of interest. Bright markers in Figure 3 depict

events with consistent source estimates from coda and direct phases (cf. Fisk and Phillips, 2011). Faint markers correspond to smaller processed pairs that need further review. Figure 3 also shows ray paths to regional IRIS stations for events with corroborated source terms, indicating good coverage for much of Eurasia. Unlike tomography, our approach does not require crossing ray paths to estimate the parameters of Eq. (1), providing constraints for many paths and extending calibration to the edges (e.g., Russia, India, and the Middle East). Below, we discuss the importance of this issue.

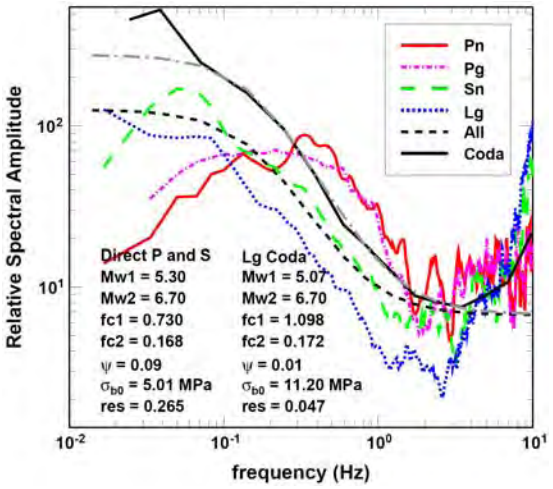


Figure 2. Similar to Figure 1, but for MKAR data that are clipped for the larger event.

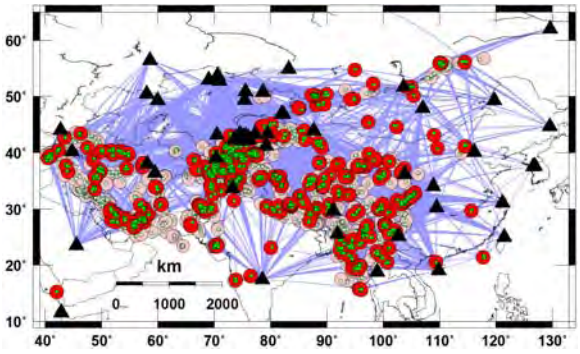


Figure 3. Map of earthquakes listed in the PDE from 1989 to 2009 for which we processed and fit relative spectra. Red circles indicate larger events within 50 km of smaller events (green circles). Bright markers and ray paths are shown for events with consistent source terms from coda and direct phases.

Fisk and Phillips (2010) presented investigations that (1) confirm the stability of coda, (2) give similar source terms estimated from coda and direct-phases for a large set of event pairs, (3) agree with published studies based on local networks, and (4) indicate discrepancies due to various data quality issues and focal mechanism effects. Although Lg coda is very stable, it is more prone to data quality problems because signal-to-noise is lower than for direct Lg, and measurement windows are longer, increasing the probability of including spurious signals. The results show the benefits of incorporating multiple, independent measurements of coda and direct-phase in our approach, to provide a large set of corroborated source terms for earthquakes throughout Eurasia.

Estimating Distance and Site Terms

Given this set of source terms, we fit source-corrected spectra to estimate distance and site terms, using the following equation for each station/path and phase:

$$\log A(f)/S(f) = \log G + b + \log\varepsilon(f) - \frac{\pi f^{1-\gamma}}{Q_0 v} r \quad \text{(EQ 3)}$$

where G is frequency-independent spreading, b is a constant site factor, ε(f) is the residual site frequency-dependence, and the last term represents attenuation. Figure 4 illustrates source-corrected Lg (3C) spectra and the fit at VOS for an earthquake in Kazakhstan. Such fits estimate effective Q as a function of frequency for fixed paths. This is distinct from tomography that estimates the path dependence of Q for fixed frequency bands. Comparing results of independent measurements and methods confirms paths with reliable Q estimates and identifies discrepancies, where improvements are needed. To compare Q_0 and γ estimates of the two methods, we average Q^{-1} from tomography over grid cells along each path, for each of 12 frequency bands. We regress log $Q(f)$ = log Q_0 + γ log f to the tomography $Q(f)$ values to estimate Q_0 and γ for each path. Fisk and Phillips (2011) found many paths with good agreement, particularly where ray-path sampling is good, needed for tomography, but not for fitting source-corrected spectra.

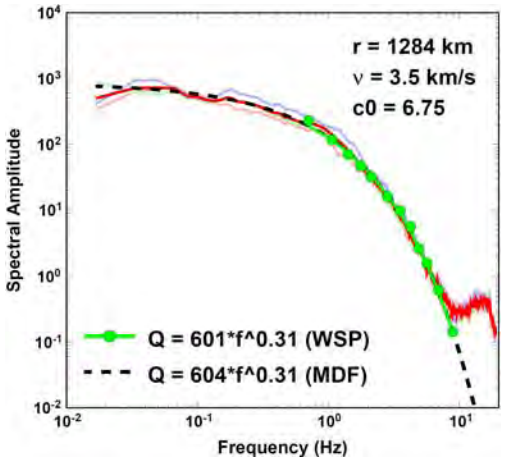


Figure 4. Source-corrected Lg spectra at VOS for an earthquake in eastern Kazakhstan, the fit (dashed curve), and Q estimates. The green circles are Lg Q tomography results for this path.

We processed and fit source-corrected spectra of Lg, Sn, Pn, and Pg (as available), for the paths shown in Figure 3. We interpolate the pathwise *Q* estimates using a code that inverts *Q* estimates for a suite of paths into a grid. Figure 5 compares Lg *Q* grids at 1 Hz. They are similar, both showing higher Lg Q_0 for the Kazakh Platform and India, low values for Tibet, and intermediate for eastern China. The fits of source-corrected spectra give lower *Q* than tomography in Iran and nearby areas, at the edge of the grid. Figure 6 compares Lg *Q* at 5 Hz, showing even lower *Q* estimates from spectral fitting than amplitude tomography for the Middle East. (We also generated *Q* grids for other phases.) Fisk and Phillips (2011) verified *Q* estimates for many paths and investigated various discrepancies, most of which can be attributed to grid edge effects and data quality issues in higher frequency bands, that impact tomography results, and strong site effects for some stations (e.g., KMI, NIL), that impact *Q* estimates from fitting source-corrected spectra.

To better visual the spatial dependence of differences in *Q* estimates from our spectral-fitting approach and from amplitude tomography, we also computed difference *Q* grids, given in percentage, for various phases and frequencies. For example, Figure 7 shows the percent difference of Sn *Q* at 1 Hz and 5 Hz. The upper plot for 1 Hz shows some modest differences. The lower plot for 5 Hz indicates differences as large as 200% in some areas, generally to the west and south of most IRIS stations, systematically biased higher for tomography, mostly due to edge effects and data quality issues.

Figure 8 shows a prevalent problem where tomography *Q(f)* results agree with the source-corrected spectrum for lower bands (less than 3 Hz, in this case), but deviate in higher bands, due to noise effects. (As shown below, over-estimating *Q* for regional S phases biases P/S ratios high, i.e., making earthquakes seem more explosion-like.) Signal-to-noise (S/N) criteria used for tomography (pre-Pn S/N>2 and pre-phase S/N>1.1) are intentionally lax, to utilize more data. If S/N tests are too stringent, data sampling issues arise. Excluding the tomography *Q(f)* values in higher bands, Figure 9 shows that the Q_0 and γ estimates now agree. Many amplitudes, especially at higher frequencies for low *Q* paths, are corrupted by noise. Results of our distinct methods can be reconciled to corroborate *Q* estimates. Note that our spectral fit (black curve) in Figures 8 and 9 is automatic, including determining the frequency range of the fit. The inflection at about 2 Hz, where noise starts biasing the spectrum high from expected decay, is usually straightforward to find. Although not all cases are easy, examination and fitting of thousands of spectra suggests that such valid frequency ranges can be found for most, which could be used to improve data quality before performing amplitude tomography.

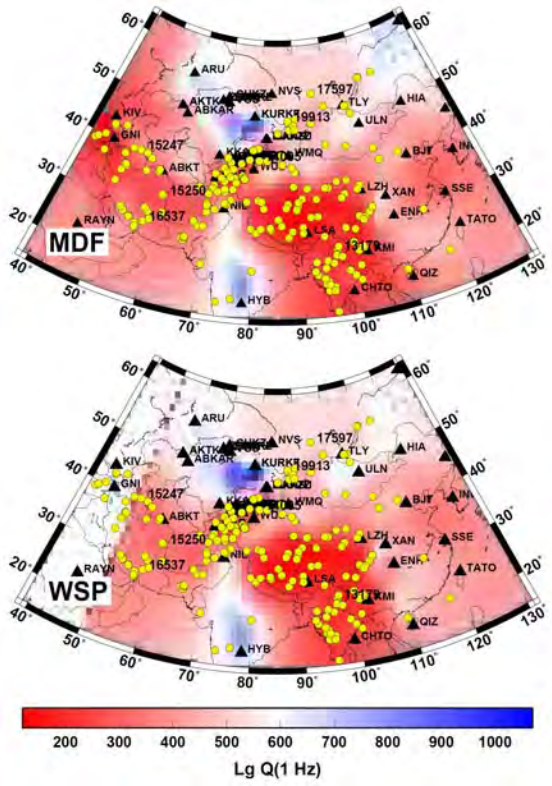


Figure 5. Lg Q_0 (1 Hz) grids from spectral fitting (top) and amplitude tomography (bottom).

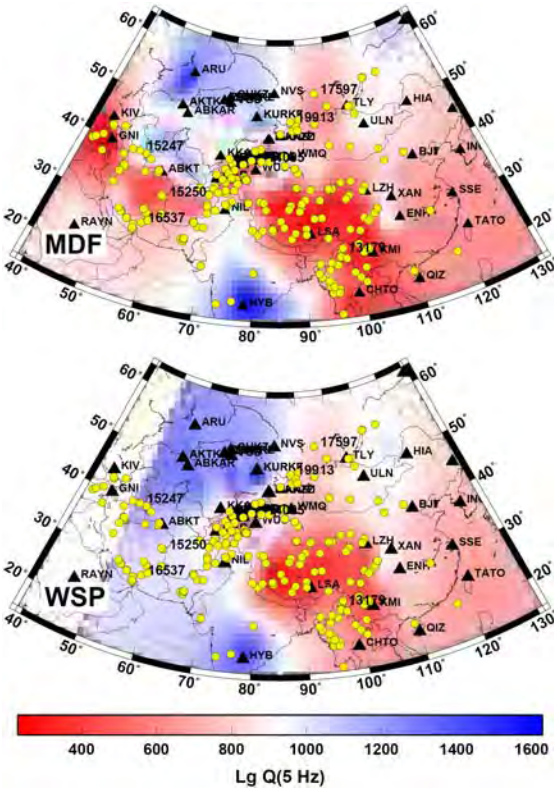


Figure 6. Similar to Figure 5, but for Lg Q at 5 Hz.

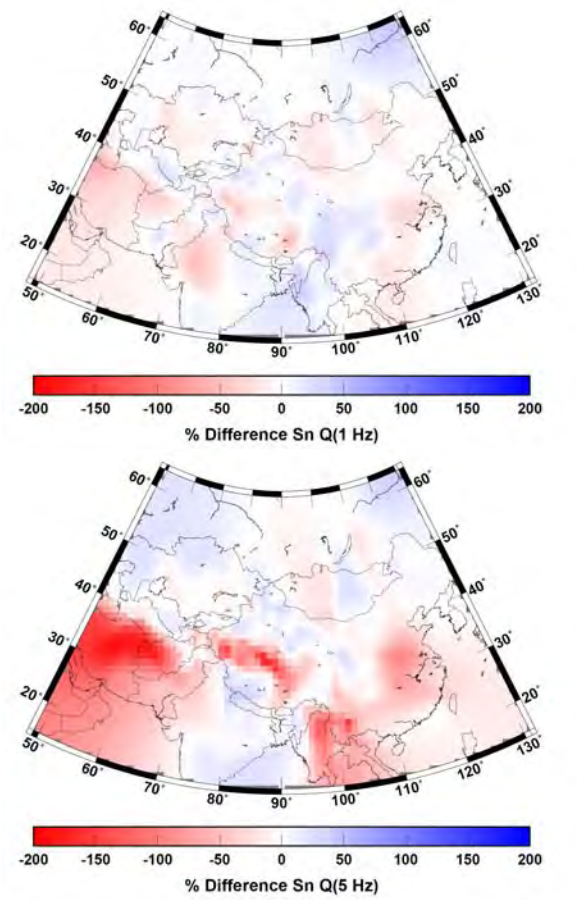


Figure 7. Percent difference of Sn *Q* estimates from tomography and fitting source-corrected spectra at 1 Hz (top) and 5 Hz (bottom).

Geometric Spreading

The fits of source-corrected spectra also give constants (viz. *c0* in Figure 4), related to spreading and site factor (the first two terms on the right-hand side of Eq. (3)), as well as Mw errors. Using Street et al. (1975), frequency-independent geometric spreading, beyond a transition distance r_0 is represented by

$$G(r) = r_0^{-1}(r_0/r)^{\eta} \text{ for } r \geq r_0 . \qquad \text{(EQ 4)}$$

For purposes of fitting data recorded at distances beyond 100 km, we can linearly regress

$$c_0 = -\eta \log r + b + (\eta - 1)\log r_0 , \qquad \text{(EQ 5)}$$

where the last two terms are independent of distance, *r*. Figure 10 shows Lg spectral constants versus distance for Eurasia. The initial results (gray squares) have large scatter, mainly due to PDE Mw errors and data quality issues. For example, red "+" markers for an earthquake near the Lop Nor Test Site (LNTS) are all shifted low relative to the Eurasian average, indicating a PDE Mw error of 0.5 m.u. (one of the largest). The red circles show those constants after correcting Mw. Green circles show the Lg results after addressing most problems, giving a spreading rate (beyond 100 km) of 0.59.

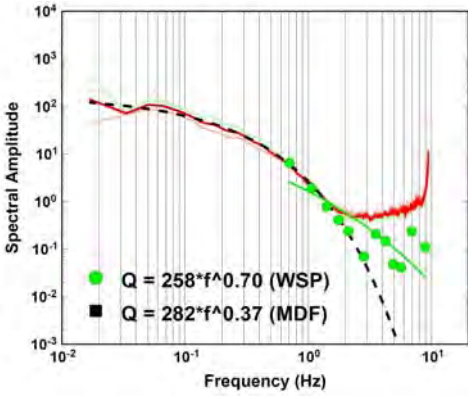


Figure 8. Comparison of Sn *Q* for an earthquake in Tibet to CHTO. Tomography *Q(f)* results are biased very high by noise in bands above 3 Hz.

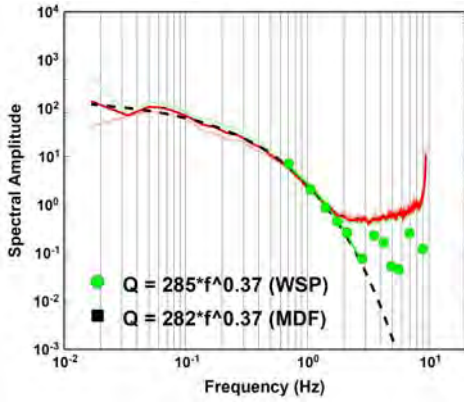


Figure 9. Same as Figure 8, but excluding the amplitude tomography Q results in bands > 3 Hz.

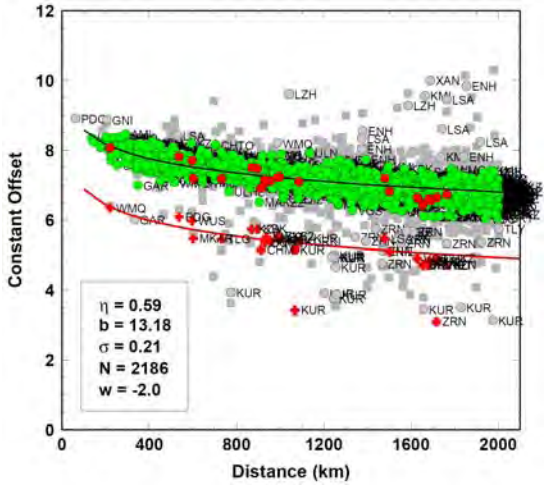


Figure 10. Lg spreading results based on 2183 paths. Gray (green) markers show initial (reviewed) results. The black curve is the regression fit giving η = 0.59.

Figure 11 shows regression of Sn spectral fit constants versus distance, giving a spreading rate of 1.06. This plot has much less scatter than the initial results for Lg because PDE Mw errors are now redressed; e.g., the red circles are Sn constants for the same event as in Figure 10. Gray circles correspond to data quality problems (e.g., gain errors). We also reviewed the fits of source-corrected Pg spectra. Because Pg does not propagate as far as other regional phases, there are many fewer paths and worse spatial coverage. As for Sn and Lg, Pg Q_0 grids of the two methods (not shown) are similar. The largest differences in *Pg Q* are at the western boundary of the grid, including the Middle East, where there are few or no crossing ray paths. Figure 12 shows Pg spectral fit constants versus distance for the 714 paths. Regression estimates a geometric spreading rate of 0.68.

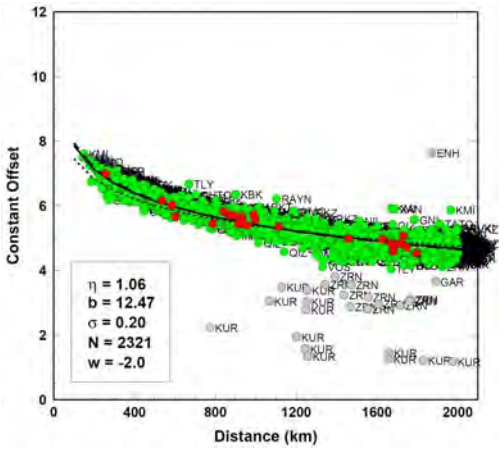


Figure 11. Sn geometric spreading results for 2321 paths. The estimated spreading exponent is η = 1.06.

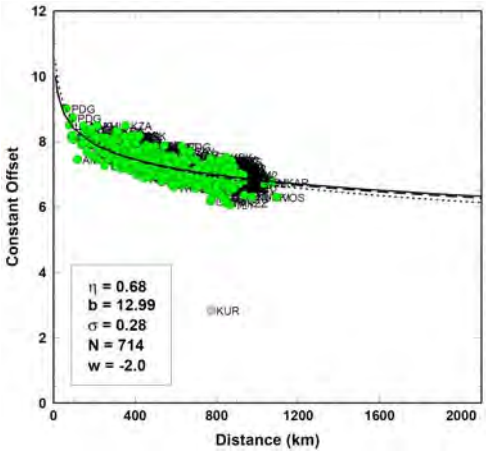


Figure 12. Pg spreading results for 714 paths. The estimated spreading exponent is η = 0.68.

We have also been reviewing Pn (checking picks, data quality, and spectral fits) for 2672 paths. Pn spectra for distances less than ~300 km are complicated by short time windows and ones that measure noise or Pg, depending on actual versus predicted arrival times. Pn spectra are the most variable and most time consuming to review. Although Pg/Lg typically has the lowest variance of various P/S discriminants, Pn/Lg and Pn/Sn discriminate better for calibrated areas (e.g., Fisk et al., 2001). In addition, for broad area monitoring, the ratio of Pg to Pn observations is roughly 1:4 (e.g., 714 versus 2672) for the same set of events. This is why it is so important to obtain good calibration for Pn. The green circles in Figure 13 are Pn spectral fit constants versus distance for 2237 reviewed paths, so far. Fitting Eq. (5) to all points out to 2000 km gives $\sigma = 0.37$. Fitting data out to 1500 km, gives $\eta = 1.06$ and $\sigma = 0.28$. For farther distances, the spectral constants are higher, on average, than the black curve. This is not a noise effect for these relatively large earthquakes. It is a physical departure from constant power-law spreading, due to sphericity, upper mantle triplication, and other propagation effects. We have also tested quadratic and piecewise fits.

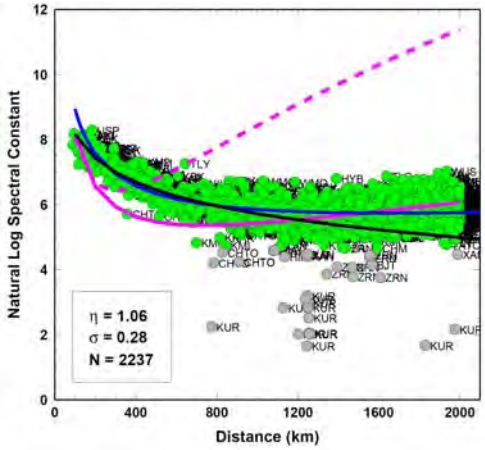


Figure 13. Pn spreading results for 2237 paths. The black curve is the fit of Eq. (5) out to 1500 km. The blue curve is a quadratic fit out to 2000 km. Magenta curves are the spreading model of Yang (2011) for frequencies of 1 Hz (solid) and 10 Hz (dashed).

The magenta curves in Figure 13 show the Pn spreading predictions of Yang (2011) for 1 Hz and 10 Hz, based on elastic simulations by Yang et al. (2007), using a spherical, two-layer, homogeneous model. Comparing models with or without frequency dependence is complicated, but note that the magenta curves predict elastic 10-Hz Pn amplitudes at 1500 km a factor of 36 larger than at 300 km, and 73 times larger than 1-Hz Pn at 1500 km. Y2007 explain this as whispering gallery effects and argue that their spreading simulations lead to reasonable Pn *Q*, assuming that the generic source corrections they applied are valid. Using our verified source terms (Figure 3), we can directly test whether the Y2011, or any other, spreading corrections really yield

reasonable Pn *Q*. For example, Figure 14 shows Pn *Q* results for paths from an earthquake at LNTS to 25 stations. Except for TLY and LSA, the *Q* estimates from tomography and fits of source-corrected Pn spectra agree very well. Figure 15 compares results for AAK and TLY, indicating the range of agreement and the need for improvements. The plots also show the Y2011 spreading predictions versus frequency. For AAK (at a distance of 1158 km), if we apply that correction prior to fitting for *Q*, it gives $Q(f) = 68\, f^{0.67}$, very inconsistent with the spectral behavior and *Q* estimates in Figure 15. Avants et al. (2011) note that fully inclusive spreading would consider elastic scattering in a heterogeneous earth. They find that mantle lid velocity gradients alter frequency-dependent spreading from that found for constant velocity, and random lateral heterogeneities in the uppermost mantle give Pn spreading approaching power-law behavior as the RMS strength increases.

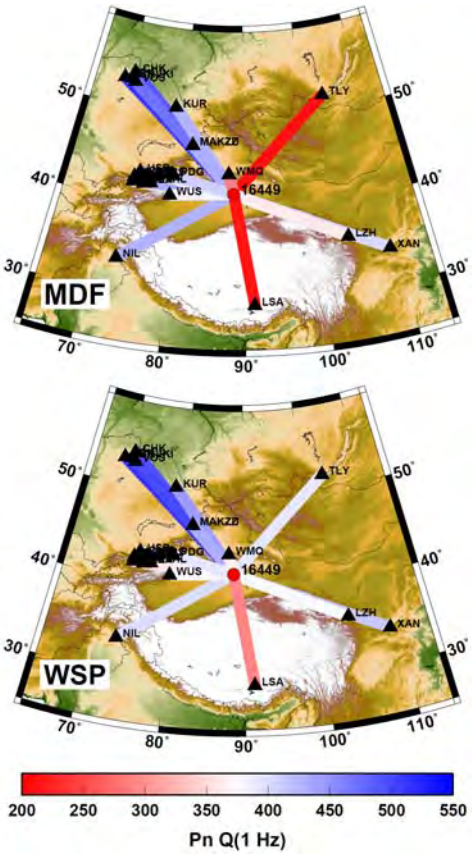


Figure 14. Comparison of Pn Q estimates at 1 Hz from spectral fitting (top) and tomography (bottom) for regional paths from an earthquake at LNTS.

Frequency-Dependent Site Effects

We have also corrected the spectra for source, Q, and spreading terms, and computed the median residual, to estimate the site frequency dependence, ε(f) in Eq. (3), of Lg, Sn, Pg, and Pn. Figure 16 shows Sn site effects for various channels of TLY and HYB. Magenta and cyan circles are vertical and horizontal site terms in discrete bands from Lg coda tomography, showing similar behavior from independent analysis. Not all compare this well; Figure 17 is a similar plot for HYB, showing agreement for lower frequencies; at higher frequencies the coda results are biased very high by noise. Figure 18 shows examples of Pg site terms at four stations. Also shown are the Lg coda site terms for those stations. Site terms for Pg and Lg coda do not always, or necessarily have to, agree this well, but it is interesting that they do for many stations. A remaining step is to also apply the site corrections, to quantify residual variances versus frequency, and partition them by physical contributions.

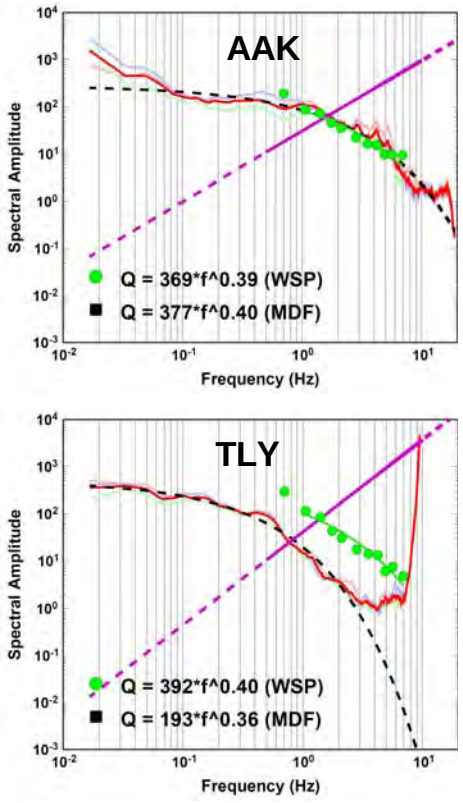


Figure 15. Source-corrected Pn spectrum, Q model fits, and tomography Q results at AAK and TLY for an earthquake at LNTS. The magenta curves are the Pn spreading predictions from Yang (2011).

Tomography Edge Effects on P/S Discrimination

An important issue we have noted previously is that amplitude tomography results have large errors near the boundaries, where there are insufficient crossing ray paths to resolve various physical effects. Now that we have estimated *Q* for regional S and P phases, and given that some key areas are near grid edges, it is interesting

to assess how those errors impact P/S discrimination. Figure 19 depicts earthquake clusters in or near Iran. We have processed some, including those labeled by master orid. Figure 20 compares Lg (left) and Pn or Pg (right) *Q* results for two paths at the western edge of LANL's grid. Tomography results generally agree better with ours for paths with higher *Q* and better station coverage. Differences are progressively larger for lower *Q* and worse ray-path sampling. The bottom left plot of Figure 20 is one of the largest γ discrepancies we found. Note that the lower bands of the tomography results (green circles) agree with the source-corrected spectra, but deviate higher for higher bands (important for P/S discrimination), due to worse sampling (fewer crossing paths) at higher frequencies. Blue curves in the lower plots are corrected LANL amplitude data, showing that our independent measurements of amplitudes and spectra are consistent. Our results, which do not depend on sampling issues (e.g., crossing ray paths), can be used to improve tomography results at grid edges. A key question is how these errors affect P/S discrimination.

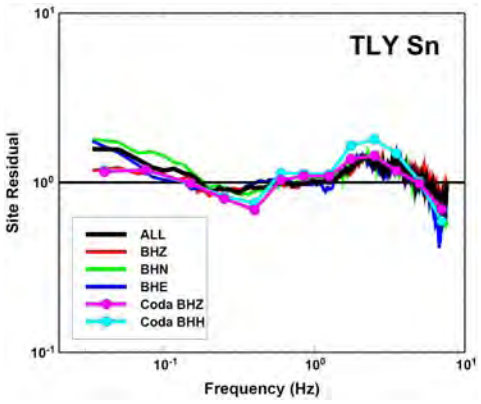


Figure 16. Sn site frequency dependence for various channels of TLY, and estimates from Lg coda.

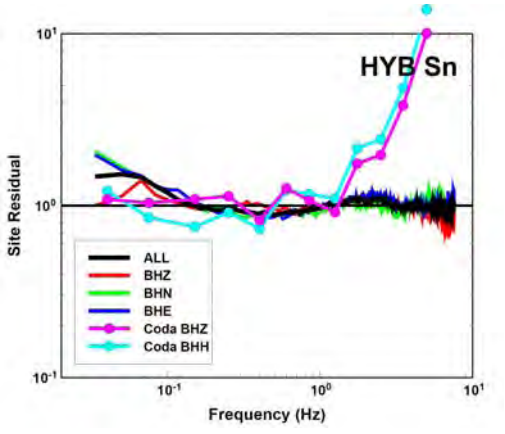


Figure 17. Similar to Figure 16, but for HYB. For bands higher than about 1.5 Hz, the coda site terms are biased high by noise.

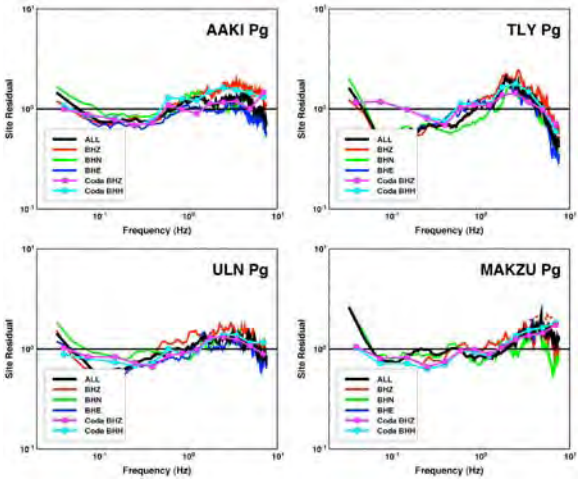


Figure 18. Similar to Figure 16, but Pg site terms at four stations, compared to coda site terms.

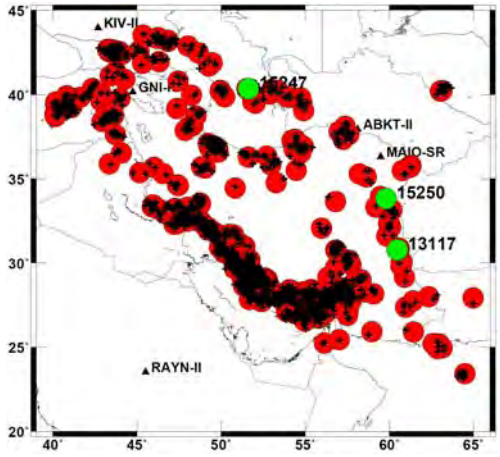


Figure 19. Map of earthquake clusters in or near Iran. Events considered in Figure 20 are labeled.

Figure 21 (top) shows Pn/Lg and Pn/Sn ratios at AKT for orid 15250. The corresponding tomography *Q* predictions (cf. Figure 20) are both higher than the source-corrected Lg and Pn spectra at high frequencies, but the errors largely cancel, giving corrected P/S ratios near one, appropriate for earthquakes. Figure 21 (bottom) shows that the errors do not cancel for any of the P/S ratios using tomography *Q* corrections from either LANL or LLNL, leading to P/S ratios as high as 10-20 at higher frequencies, i.e., very explosion-like. For comparison, the corrected Pn/Lg(6-8 Hz) mean for Nevada Test Site explosions is 5.8 (Fisk et al., 2010). To avoid false alarms, large uncertainties can be assigned to the tomography *Q* estimates. However, given the errors and reasonable uncertainties, no event in this area would be discriminated. Given the importance of this region and the investment in tomography work, this problem must be fixed, providing *Q* estimates that are verified by multiple methods and datasets.

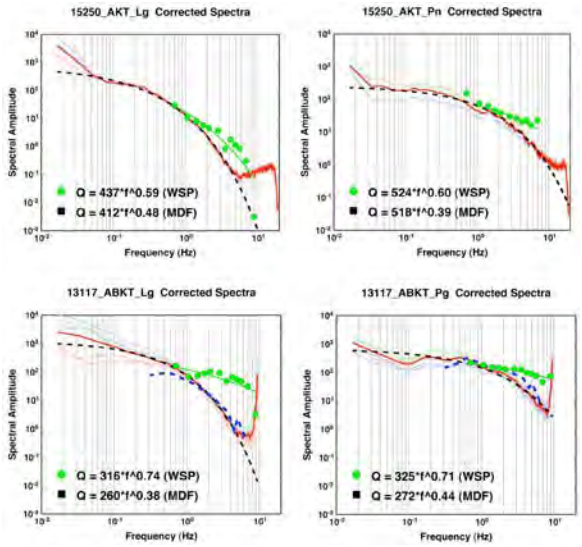


Figure 20. Comparisons of Lg (left) and Pn or Pg (right) spectral fits and tomography results for two clusters in Iran. The dashed blue curves are source-corrected amplitudes from LANL.

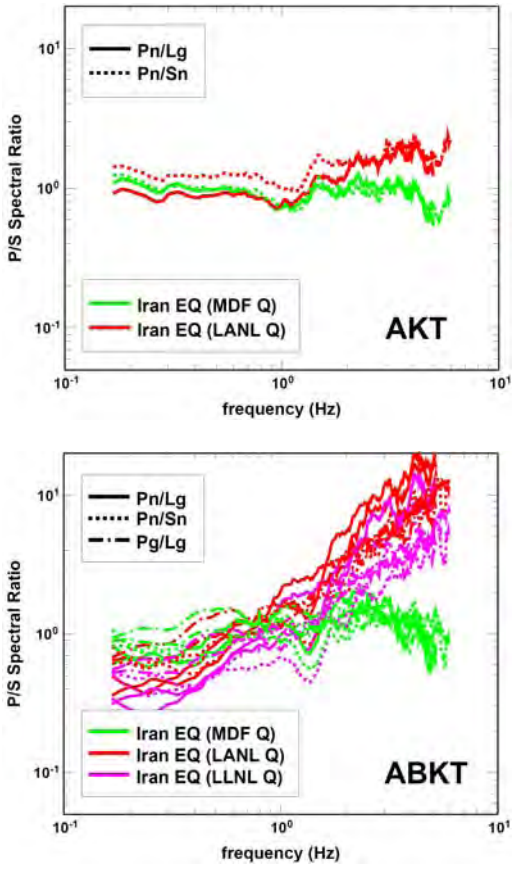


Figure 21. P/S spectral ratios at AKT for orid 15250 (top) and ABKT for orid 13117 (bottom), using my Q corrections from fitting source-corrected spectra, and from tomography by LANL and LLNL (see legends).

CONCLUSIONS AND RECOMMENDATIONS

We have shown that traditional inversion methods have many trade-offs, leading to large errors in distance and source corrections. This motivated our development of innovative techniques to constrain the terms. Our unique use of coda and direct phases has provided a large set of corroborated source terms. Our independent *Q* estimates from source-corrected spectra corroborate tomography results for many paths and various phases. Likewise, our estimates of site terms compare well with coda methods for many stations. We also used fits of source-corrected spectra to estimate geometric spreading rates for Lg, Sn, Pg, and Pn, and showed how this information can be used to obtain a consistent set of absolute moments.

Note that at the outset of our analysis, we fit relative spectra for event pairs to estimate corner frequencies and relative moments. We tied the absolute moments to PDE Mw's for the larger events, assumed to be better recorded and more accurate. This does not affect our f_c estimates, which, in turn, does not affect our *Q(f)* estimates. A high/low Mw simply shifts all source-corrected spectra for the event low/high. Our ultimate goal is to improve tomography results, which can be affected by Mw errors. Thus, we started with minimal assumptions, but have now updated the results to give a consistent set of absolute moments, corner frequencies, *Q* estimates, and spreading rates. We delivered these to LANL for future use as constraints on tomography.

By comparing results of independent measurements and methods, we have also found critical ways that *Q* and spreading models must be improved and evaluated. First, given that some key areas are near grid edges, where tomography results are known to have significant errors, we need to incorporate our source and Q constraints in tomography runs at LANL and LLNL. Second, data quality directly impacts calibration. S/N tests do not exclude sufficient bad data, while retaining a majority of good data, particularly for secondary phases that are in the coda of preceding phases. We have shown that the useful frequency range of spectra can be found.

Third, while Pg is typically more stable than Pn, there are only a fraction of Pg observations compared to Pn. The results indicate the importance of Pn and the need to improve Pn spreading and *Q* models. Using reviewed data with well-constrained source terms, Pn clearly departs from constant power-law spreading (cf. Figure 13). Pn *Q* estimates are verified for many paths, but there are also many large differences (e.g., for TLY), much more so for areas lacking good ray-path sampling. Calibration of Pn is a very hard problem because of its variability from a host of complicated effects. However, more accurate, robust, and compact Pn *Q* and spreading

models are attainable than currently exist. These three problems are not minor; we showed order-of-magnitude errors that directly impact P/S discrimination results. Rectifying them and incorporating the enhancements in calibrations are essential.

ACKNOWLEDGEMENTS

Seismic data from IRIS were used in this study.

REFERENCES

Avants, M., T. Lay, X.-B. Xie, and X. Yang (2011). Effects of 2D random velocity heterogeneities in the mantle lid and Moho topography on Pn geometric spreading, *Bull. Seismol. Soc. Am.* **101,** 126–140.

Brune, J. N. (1970). Tectonic stress and the spectra of seismic shear waves from earthquakes, *J. Geophys. Res.* **75,** 4997–5009.

Fisk, M. D., S. Bottone, and G. D. McCartor (2001). Regional Seismic Event Characterization Using Bayesian Calibration, MRC-R-1621, Mission Research Corp., Santa Barbara, CA.

Fisk, M. D., G. D. McCartor, and S. R. Taylor (2008). Robust Magnitude, Distance, and Path-Specific Corrections for Regional Seismic Phases by Constrained Inversion and Enhanced Kriging Methods, ATK/NCR-0608-501, Final Report.

Fisk, M. D. and W. S. Phillips (2011). Constraining source terms, regional attenuation models, and site effects, *in Proceedings of the 2011 Monitoring Research Review: Ground-Based Nuclear Explosion Monitoring Technologies*, LA-UR-11-04823, Vol. 1, pp. 59–68

Fisk, M. D. and W. S. Phillips (2010). A stepwise, iterative procedure to constrain stress drop, regional attenuation models, and site effects, *in Proceedings of the 2010 Monitoring Research Review: Ground-Based Nuclear Explosion Monitoring Technologies*, LA-UR-10-05578, Vol. 1, pp. 57–66.

Fisk, M. D. and W. S. Phillips (2009). A stepwise, iterative procedure to constrain stress drop, regional attenuation models, and site effects, *in Proceedings of the 2009 Monitoring Research Review: Ground-Based Nuclear Explosion Monitoring Technologies*, LA-UR-09-05276, Vol. 1, pp. 52–61.

Fisk, M. D. and S. R. Taylor (2006). Robust magnitude and path corrections for regional seismic phases in Eurasia by constrained inversion and enhanced kriging techniques, *in Proceedings of the 28th Monitoring Research Review, Ground-Based Nuclear Explosion Monitoring Technologies*, LA-UR-06-5471, Vol. 1, pp. 15–24.

Fisk, M. D., S. R. Taylor, W. R. Walter, and G. E. Randall (2010). Seismic Event Discrimination and Modeling Using Two-Dimensional Grids of Regional P/S Spectral Ratios, ATK-R-1744, Final Technical Report, NNSA Contract DE-AC52-07NA28116.

Mayeda, K. M., A. Hofstetter, J. L. O'Boyle, and W. R. Walter (2003). Stable and Transportable Regional Magnitudes Based on Coda-Derived Moment-Rate Spectra, *Bull. Seismol. Soc. Am.* **93** 224–239.

Mayeda, K. M., L. Malagnini, and W. R. Walter (2007). A new spectral ratio method using narrow band coda envelopes: evidence for non-self-similarity in the Hector Mine sequence, *Geophys. Res. Lett.* **34** L11303.

Phillips, W. S., R. J. Stead, G. E. Randall, H. E. Hartse and K. Mayeda (2008). Source effects from broad area network calibration of regional distance coda waves, in *Scattering of Short Period Waves in the Heterogeneous Earth*, H. Sato and M.C. Fehler, Editors.

Schaff, D. P. and P. G. Richards (2004). Repeating seismic events in China, *Science* **303,** 1176–1178.

Sereno T. J., S. R. Bratt and T. C. Bache (1988). Simultaneous inversion of regional wave spectra for attenuation and seismic moment in Scandinavia, *J. Geophys. Res.* **93,** 2019–2035.

Street, R., R. Herrmann, and O. Nuttli (1975). Spectral characteristics of Lg wave generated by central United States earthquakes, Geophys. *J. R. Astron. Soc.* **41**: 51–63.

Taylor, S. R., and H. E. Hartse (1998). A procedure for estimation of source and propagation amplitude corrections for regional seismic discriminants, *J. Geophys. Res.* **103,** 2781–2789.

Taylor, S. R., A. A. Velasco, H. E. Hartse, W. S. Phillips, W. R. Walter, and A. J. Rodgers (2002). Amplitude corrections for regional seismic discriminants, *Pure Appl. Geophys.* **159,** 623–650.

Yang, X. (2011). A Pn spreading model constrained with observed amplitudes in Asia, *Bull. Seismol. Soc. Am* **101,** 2201-2211.

Yang, X., T. Lay, X.-B. Xie, and M.S. Thorne (2007). Geometric spreading of Pn and Sn in a spherical Earth model, *Bull. Seismol. Soc. Am.* **97** 2053–2065.

LITHOSPHERIC MODELS OF THE MIDDLE EAST TO IMPROVE SEISMIC SOURCE PARAMETER DETERMINATION/EVENT LOCATION ACCURACY

Rengin Gök[1], Stephen Herzog[2], Keith Nakanishi[1], Michael E. Pasyanos[1], Rob J. Mellors[1], Arthur J. Rodgers[1], David B. Harris[1], and Eileen S. Vergino[1]

Lawrence Livermore National Laboratory[1] and the National Nuclear Security Administration[2]

Sponsored by the National Nuclear Security Administration and the U.S. Department of State

Award Nos. DE-AC52-07NA27344/24.2.3.2 and DOS_SIAA-11-AVC/NMA-1

ABSTRACT

The Middle East is a tectonically complex and seismically active region. The ability to accurately locate earthquakes and other seismic events in this region is complicated by tectonics, the uneven distribution of natural earthquakes, and the fact that countries run separate national seismic networks without well-developed data-sharing agreements. We report here on a variety of scientific efforts to enhance knowledge of the lithospheric velocity structure in the Middle East, making use of data from national networks in Saudi Arabia, Oman, and Kuwait to improve seismic location accuracy for events throughout the region.

Collaborative seismology engagements with research institutes in the Middle East have produced several important findings. Studies of regional seismic structure revealed that the Arabian Shield and the Arabian Platform have fundamental differences in velocity structure. The earth's crust is relatively thicker than average in Kuwait and Iraq as a result of the Mesopotamian Foredeep, characterized by 8-10 km thick sediments. Ophiolites dominate the southeastern margin of the Arabian Peninsula, where the crust is thicker and seismic velocities are faster. In Kuwait, seismic activity is intensified near oil fields, and seismic source parameters show that this activity comes from tectonic events.

This work is informed by continuous or event-based regional seismic data obtained from 68 seismic stations from national networks, and this number is expected to grow in the future. A current effort is focused on using regional seismic data to develop better and more accurate seismic magnitude scales based on coda for stations in these national networks. Data and derived measurements from stations are integrated into lithospheric velocity and attenuation models to increase resolution, improve event location accuracy and source parameter determination, and advance tectonic understanding of the region.

OBJECTIVES

We engage in mutually beneficial bilateral and multilateral seismology arrangements in the Middle East that provide important data coverage of the region's complex geophysical structures, thereby improving location accuracy for lithospheric velocity and attenuation models. These models can then be used to improve earthquake hazard mitigation, tsunami warning systems, and Comprehensive Nuclear-Test-Ban Treaty (CTBT) monitoring.

The Middle East is part of the Alpine-Himalayan system, where the Iranian and Turkish Plateaus meet at the Arabian Plate, and the divergent plate boundary is at the Red Sea and convergent plate boundary is at the Zagros Mountains. In addition to this geophysical complexity, seismological studies of the region typically suffer from a lack of available data. Data availability issues result from an uneven distribution of seismic stations due to logistical, financial, and even political reasons. Consequently, seismic event data distribution is highly uneven, strongly sampling from some parts of the region, while minimally sampling from others. Seismicity is also unevenly scattered throughout the region, with the highest concentration found near the eastern Zagros Mountains.

Location accuracies and lithospheric models are greatly influenced and oftentimes limited by these geophysical and data availability factors. Specifically, small event detection and identification for seismic hazard mitigation and CTBT monitoring poses a significant challenge in the region due to the complicated tectonic regime and uneven distribution of both seismic sources and seismic stations. Openly available regional data through the CTBT International Monitoring System (IMS) and other sources like the Global Seismographic Network (GSN), operated by Incorporated Research Institutions for Seismology (IRIS), is fairly limited (Figure 1a). However, national seismic networks run by governments, universities, and non-governmental organizations and research institutes enhance the quality of potential data and increase the number of seismic stations in the region (Figure 1b). These stations are used for various purposes such as seismic hazard mitigation, tsunami warning systems, and studies of oil field-related seismicity. Seismic source, attenuation, and 3-D velocity models can be improved by incorporating national network data from the greater Middle East region. Incorporating data from these stations—which is usually absent from but essential for higher quality lithospheric models—will greatly improve scientific knowledge of event locations and source characteristics in the Middle East.

To improve lithospheric models of the Middle East and build regional seismological capacity, the U.S. Department of Energy (DOE) began sponsoring Lawrence Livermore National Laboratory (LLNL) in cooperation with research institutes in the Middle East in 1996. Since 2006, this work has been pursued by the National Nuclear Security Administration's (NNSA) Confidence-Building Measures (CBM) Program and includes seismic data-sharing, joint data analysis, technical training, and seismic station installation (Figure 1b). In 1998, LLNL began collaborating with the Jordan Seismological Observatory (JSO), which involved the deployment of two broadband seismometers, exchange visits of seismologists, and joint research projects. And in 1999, with LLNL technical support, DOE initiated seismic cooperation with King Saud University in Riyadh, Saudi Arabia. The longstanding LLNL relationship with King Saud University has resulted in temporary deployments of seismic stations, as well as ongoing technical cooperation in seismological research. This scope of work continued through relationships with the Kuwait Institute for Scientific Research and the Earthquake Monitoring Center at Sultan Qaboos University in Muscat, Oman. Further, CBM worked with the University of Sharjah in the United Arab Emirates to begin a regional seismology meeting called the Gulf Seismic Forum (GSF), which completed its seventh iteration in Jeddah, Saudi Arabia in January 2012. CBM also provides assistance to the Reducing Earthquake Losses in the Extended Mediterranean Region (RELEMR) workshops run by the United Nations Educational, Scientific, and Cultural Organization (UNESCO) and the U.S. Geological Survey (USGS).

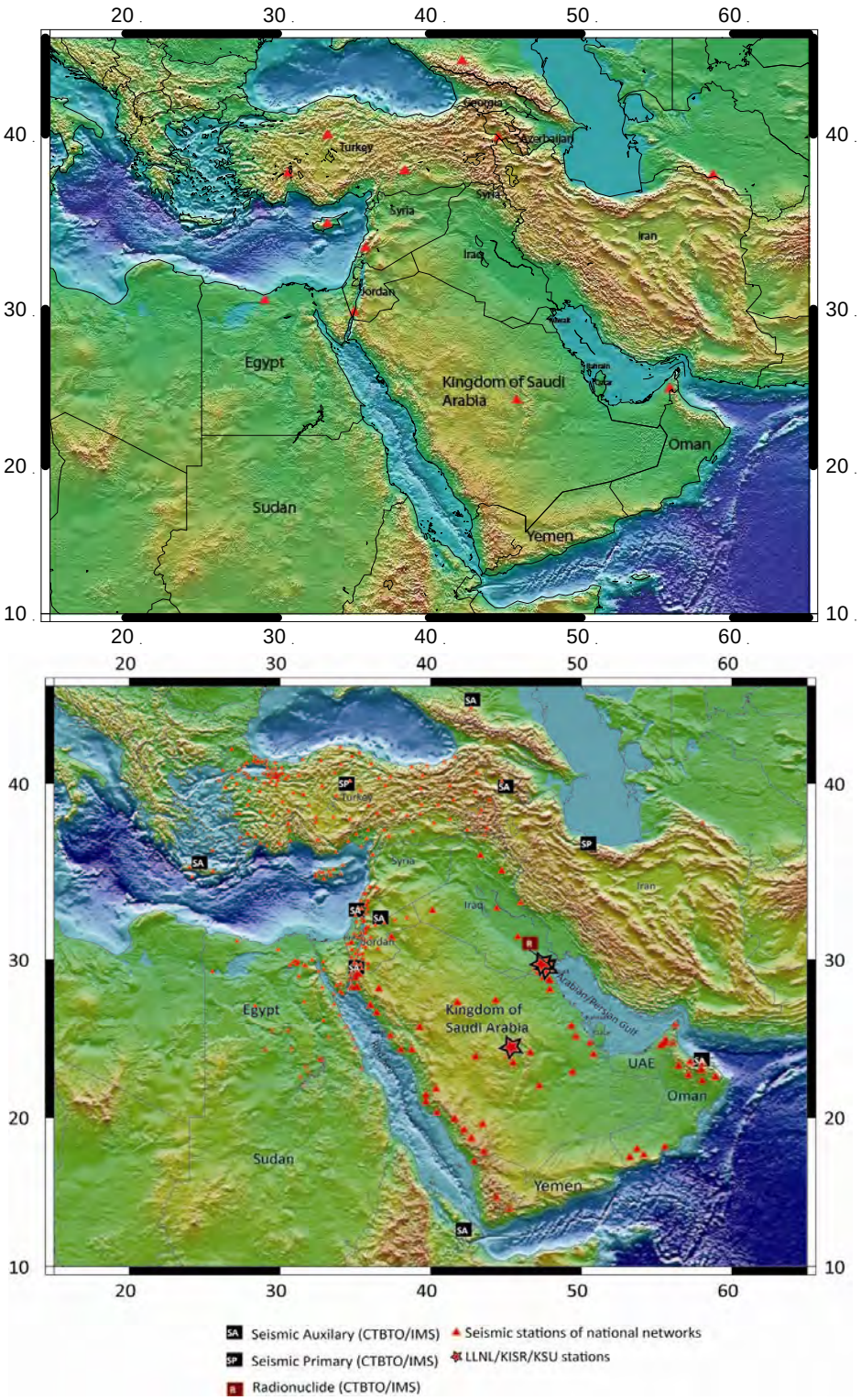


Figure 1. (Top) Operational International Monitoring System (IMS) Seismic Stations and Global Seismographic Network (GSN) Stations. (Bottom) National network stations, IMS Seismic Stations, and stations collaboratively operated by Lawrence Livermore National Laboratory (LLNL) with the Kuwait Institute for Scientific Research (KISR) and King Saud University (KSU).

RESEARCH ACCOMPLISHED

We perform data analysis that increases scientific understanding of regional seismicity in the Middle East. In doing so, we use several techniques for estimating the velocity models in the crust and upper mantle. One key technique that we use is to jointly invert receiver functions with surface waves (Gök et al., 2006; Tkalčić et al., 2006), which is a technique that has wide applicability in various parts of the world. The new velocity models from our data analysis are used for improving seismic network location accuracy and/or informing seismic hazard studies. Seismic waveform modeling studies for source parameter estimates also benefit from these new velocity models that help to calculate Green's function.

Joint work in Saudi Arabia includes data analysis and collaboration that has resulted in a number of papers in leading, peer-reviewed seismological journals (e.g. Rodgers et al., 2006; Tkalčić et al., 2006; Hansen et al., 2008; Park et al., 2007; Al-Damegh et al., 2009). Data analyzed through these efforts samples various tectonic environments on the Arabian Peninsula, including both active continental rifting and more stable environments. The resultant velocity models confirm rapid crustal thinning of the Arabian Shield toward the Red Sea (Tkalčić et al., 2006). Lithospheric thickness on the Arabian Peninsula varies considerably, with thin lithosphere centered on the rift axis, thickening toward the Arabian interior (Hansen et al., 2008). A nine-element seismic array is jointly sponsored by LLNL and King Saud University (KSU) for small event detection and joint data analysis purposes. The array was originally installed at Ar-Rayn, Saudi Arabia in 2010 (Figure 2) but was moved to Al-Quwaiyah in 2012 to strengthen data collection efforts. Initial beam-forming results demonstrate that the Al-Quwaiyah array will provide improved estimates of P-wave arrival times and waveforms for small events in the region (Al-Amri et al., 2011). We currently have seismic attenuation and ambient noise correlation data analysis projects with KSU to study the crust and upper mantle structure of Saudi Arabia through data collection from broadband stations.

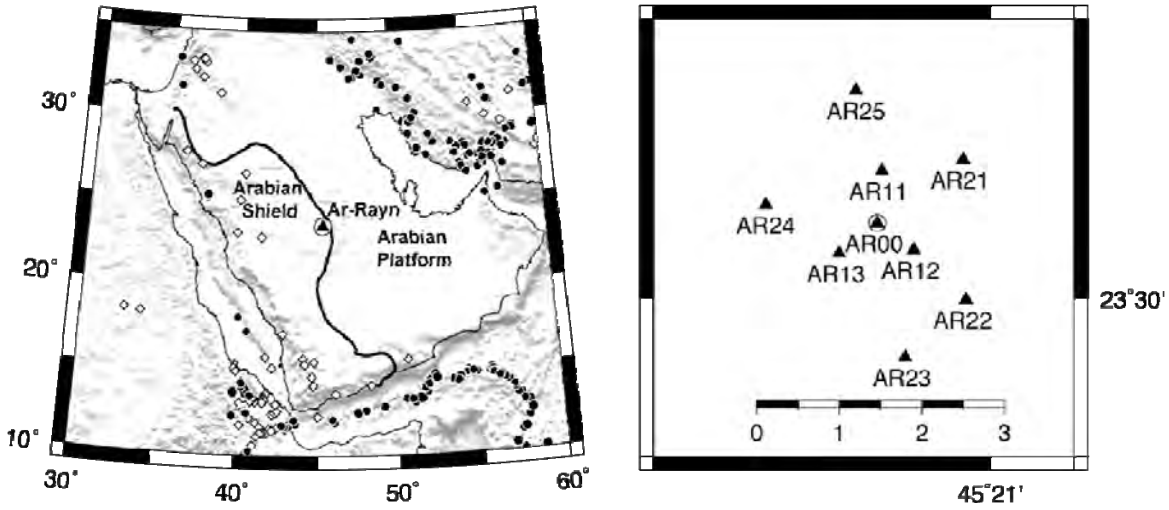


Figure 2. (Left) Map of Arabian Plate showing major tectonic elements of Arabian Shield and Arabian Platform and position of Ar-Rayn seismic array (triangle): earthquakes greater than magnitude 5 for period 2000-2010 and volcanic centers (black circles and white diamonds, respectively). (Right) Array geometry: broadband sensor (STS-2) at center (triangle with circle), surrounded by two rings of short-period sensors (triangles).

Collaboration with the Kuwait Institute for Scientific Research (KISR) began in 1999 when the Kuwait National Seismic Network (KNSN) had few stations and difficulties with network operations. Two jointly written, peer-reviewed papers were published on the seismic structure and the source characteristics of earthquakes in the Persian Gulf region (Pasyanos et al., 2007; Rodgers et al., 2006). Seismic source studies demonstrated that the location of earthquakes is predominantly confined to the upper crust, and they also showed the features of tectonic events

(Figure 3). Due to Kuwaiti concerns about seismicity and whether oil field activities were triggering earthquakes, a cooperative project between KISR and LLNL began in May 2010. Two broadband, three-component seismic stations were successfully deployed in the existing vaults for KNSN sites MIB (Mutribah) and UMR (Umm ar Rimam). The average crustal thickness in the sampled area is 43-45 km.

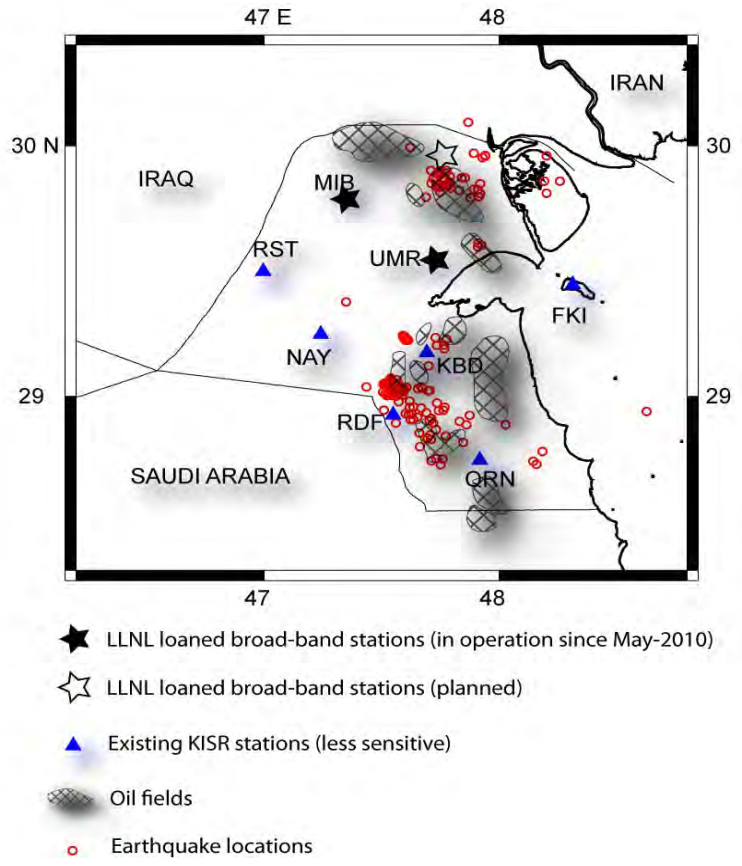


Figure 3. Seismicity and seismic station locations in Kuwait: notice proximity of earthquakes to oil fields.

Additionally, two temporary broadband stations were deployed in Bagdad (BHD) and Mosul (MSL) in early 2005. The stations were equipped with Guralp CMG-3ESPD digital broadband seismometers. Despite the fact that the sites were prone to background noise due to their location near major Iraqi cities, we were able to estimate the crustal thickness under stations BHD and MSL (Gök et al., 2007) (Figure 4). Our results indicated that crustal thicknesses increase toward the south correlated with increasing sedimentary thickness due to the Mesopotamian Foredeep. Ignoring the sediments of the Mesopotamian Foredeep, crustal velocities and thicknesses are remarkably similar between northern and southern Iraq near Kuwait, suggesting that the crustal structure of the proto-Arabian Platform in northern Iraq was uniform before subsidence and deposition of the sediments in the Cenozoic.

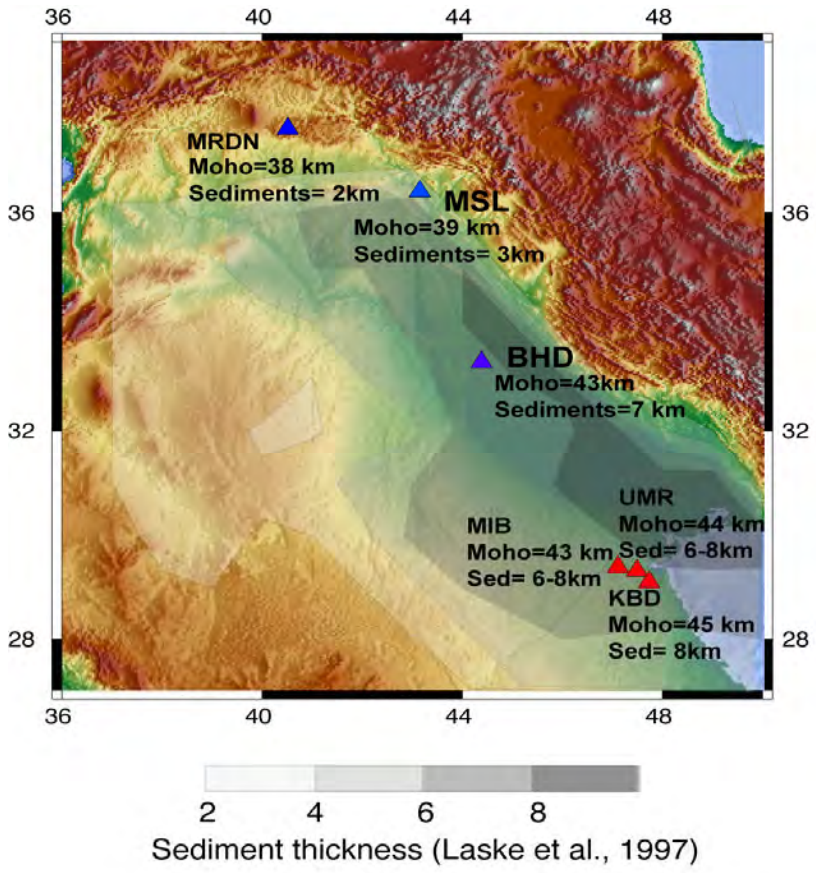


Figure 4. Estimated crustal thicknesses overlaid on sediment thickness model.

Another productive scientific collaboration is between LLNL and the Earthquake Monitoring Center (EMC) of Sultan Qaboos University (SQU) in Oman to study the lithospheric structure of the southeastern Arabian Peninsula by analyzing teleseismic P-receiver functions recorded at broadband and short-period seismic stations of the Oman Seismological Network (Al-Hashmi et al., 2011). Lithospheric structure is obtained by jointly inverting receiver functions and Rayleigh wave group velocities derived from continental-scale surface tomography. We observed relatively thick crust (40-48 km) within the ophiolite-formed mountains in northern Oman. The crustal thickness is about 35 km within the passive continental margin of the southern Dhofar region (Figure 5). Uppermost (<5 km) crustal shear wave velocities are faster in the northern ophiolite regions compared to the southern Dhofar region, while shear velocities in the middle crust are faster in the Dhofar region compared to the ophiolite region. This observation coincides well with Cretaceous to Eocene marine platform sequences overlying the Precambrian to Cambrian basement of the southern region. Joint inversion analysis shows that the Moho depth within the southeastern Arabian Peninsula varies from 34 km in the southern region to 48 km in the northern part. Currently, studies are underway to supplement this effort with ambient noise cross-correlation for Green's function and coda-magnitude calibration. Our goal is to calibrate the magnitudes of smaller events in the country to meet Omani operational needs.

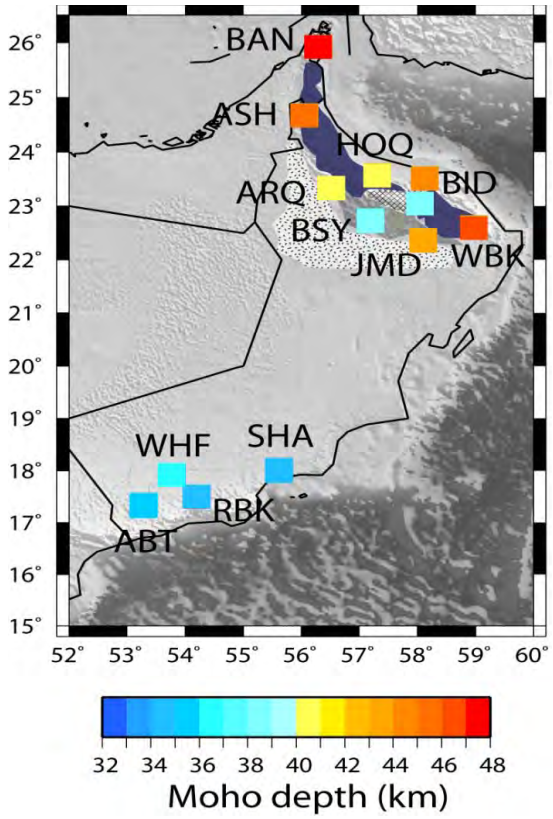


Figure 5. Moho depths color-coded at each Oman Seismological Network Station.

CONCLUSIONS AND RECOMMENDATIONS

Our research results demonstrate that, as expected, significant tectonic and seismic complexity is observed in the geophysical structure of the Middle East. These large variations in structural complexity—combined with limited event data availability—provide the dominant reason for seismic source and event location inaccuracies that constrain current lithospheric models. Open source seismological data-sharing mechanisms are highly useful for scientists and other researchers interested in studying the lithospheric structure of the Middle East and regional seismic wave propagation patterns. However, both national investments in seismic instrumentation and formal data-sharing agreements between states in this region of high seismicity are limited. LLNL collaboration with research institutes in the Middle East has enhanced the ability of partner countries to operate national seismic networks and strengthened regional seismic expertise. These scientific and technical relationships have improved lithospheric velocity and attenuation models of the Middle East by revealing information about the complexity of the crustal and upper mantle structure in the region.

Further scientific and technical cooperation in seismic monitoring with research institutes and universities in the Middle East can help to build upon these models, increasing station coverage and event data availability. In turn, new data and velocity models will increase our lithospheric knowledge of the Arabian Peninsula and other structures, enhancing seismic source parameter determination and event location accuracy. This will benefit geophysical studies, city planning and development efforts, civilian and military disaster responses, mining and oil drilling activities, and CTBT monitoring.

ACKNOWLEDGEMENTS

The authors would like to thank several individuals for their programmatic contributions to this research:

Preparatory Committee of the Comprehensive Nuclear-Test-Ban Treaty Organization: John Coyne, Belkacem Djermouni, and Lassina Zerbo. Sultan Qaboos University: Issa El-Hussain. King Saud University: Abdullah Al-Amri. Kuwait Institute for Scientific Research: Abdullah Al-Enezi. Lawrence Livermore National Laboratory: William Walter and Jay Zucca. National Nuclear Security Administration: Paula Alfonso, Leslie Casey, Michele Dash-Pauls, Tim Evans, Edward Fei, Wayne Mei, Mike Newman, and Anne Phillips. United States Department of State: John Godfrey and Terrill Ray.

REFERENCES

Al-Amri, A.M.S., D.B. Harris, M. Fnais, A.J. Rodgers, and M. Hemaida (2011). A Regional Seismic Array of Three-Component Stations in Central Saudi Arabia, *Seismol. Res. Lett*. **83**, 49–58.

Al-Damegh, K.S., K.M. Abou Elenaen, H.M. Hussein, and A.J. Rodgers (2009). Source mechanism of June 2004 Tabuk earthquake sequence, Eastern Red Sea margin, Kingdom of Saudi Arabia, *J. Seismology*. **13**, 561–576.

Al-Hashmi, S., R. Gök, K. Al-Toubi, Y. Al-Shijbi, I. El-Hussain, and A.J. Rodgers (2011). Seismic velocity structure at the southeastern margin of the Arabian Peninsula, *Geophys. J. Int*. **186**, 782–792.

Gök, R.**,** M. E. Pasyanos and E. Zor, (2006). Lithospheric Structure of the Continent-Continent Collision Zone: Eastern Turkey, *Geophys. J. Int.* **169**, 1079–1088.

Gök, R., H. Mahdi, H. Al-Shukri, and A.J. Rodgers (2007). Crustal structure of Iraq from receiver functions and surface wave dispersion: Implications for understanding the deformation history of the Arabian–Eurasian collision, *Geophys J. Int*. **172**, 1179–1187.

Hansen, S., J. Gaherty, S. Schwartz, A. Rodgers, and A. Al-Amri (2008). Seismic velocity structure and depth-dependence of anisotropy in the Red Sea and Arabian shield from surface wave analysis, *J. Geophys. Res*. **113**, B10307.

Laske, G., and G. Masters (1997). A Global Digital Map of Sediment Thickness, *Eos Trans. Am. Geophys. Union.* **78**, 483.

Park, Y., A. Nyblade, A. Rodgers, and A. Al-Amri (2007). Upper mantle structure beneath the Arabian Peninsula from regional body-wave tomography: Implications for the origin of Cenozoic uplift and volcanism in the Arabian Shield, *Geophysics, Geochemistry and Geosystems.* **8**, Q07020.

Pasyanos, M. E., H. Tkalčić, R. Gök, A. Al-Enezi, and A.J. Rodgers (2007). Seismic structure of Kuwait, *Geophys. J. Int*. **170**, 299–312.

Rodgers, A., A.R. Fowler, A.M.S. Al-Amri, and A. Al-Enezi (2006). The March 11, 2002 Masafi, United Arab Emirates Earthquake: Insights into the Seismotectonics of the Northern Oman Mountains, *Tectonophysics*. **415**, 57–64.

Tkalčić, H., M.E. Pasyanos, A.J. Rodgers, R. Gök, W.R. Walter, and A. Al-Amri (2006). A multi-step approach in joint modeling of surface wave dispersion and teleseismic receiver functions: Implications for lithospheric structure of the Arabian Peninsula, *J. Geophys. Res.* **111**, B11311.

CALCULATING PATH-DEPENDENT TRAVEL TIME PREDICTION VARIANCE AND COVARIANCE FOR A GLOBAL TOMOGRAPHIC P-VELOCITY MODEL

Jim R. Hipp[1], Andre V. Encarnacao[1], Chris J. Young[1], Sandy Ballard[1], Mike L. Begnaud[2], and W. Scott Phillips[2]

Sandia National Laboratories[1] and Los Alamos National Laboratory[2]

Sponsored by the National Nuclear Security Administration

Award Nos. DE-AC04-94AL85000/SL12-Signal_Propagation-NDD02[1] and
DE-AC52-06NA25396/LA12-Signal_Propagation-NDD02[2]

ABSTRACT

Several studies have shown that global 3D models of the compression wave speed in the Earth's mantle can provide superior first P travel time predictions at both regional and teleseismic distances. However, given the variable data quality and uneven data sampling associated with this type of model, it is essential that there be a means to calculate high-quality estimates of the path-dependent variance and covariance associated with the predicted travel times of ray paths through the model. In this paper, we show path dependent uncertainty results for various receivers. The results were calculated using our previously defined methodology that exploits the full model covariance matrix.

Typical global 3D models have on the order of half a million nodes, so the challenge in calculating the covariance matrix is formidable: 0.9 TB storage for one half of a symmetric matrix, necessitating an Out-Of-Core (OOC) blocked matrix solution technique. With our approach the tomography matrix (G which includes Tikhonov regularization terms) is multiplied by its transpose (G^TG) and written in a blocked sub-matrix fashion. We employ a distributed parallel solution paradigm that solves for $(G^TG)^{-1}$ by assigning blocks to individual processing nodes for matrix decomposition update and scaling operations. We first find the Cholesky decomposition of G^TG which is subsequently inverted. Next, we employ OOC matrix multiplication methods to calculate the model covariance matrix from $(G^TG)^{-1}$ using prior data and model covariance vectors. Given the model covariance matrix we solve for the travel-time covariance associated with arbitrary ray-paths by integrating the model covariance along both ray paths. Setting the paths equal yields the variance for that path.

OBJECTIVES

The development of global 3D P-velocity models capable of producing high-quality travel time predictions is a significant accomplishment, but such models cannot be routinely used for locating seismic events until they are accompanied by appropriate, path dependent uncertainty estimates. In this paper, we show a methodology for calculating travel time variance and covariance for ray paths through 3D velocity models by exploiting the full model covariance matrix, a product of the tomograhic inversion process. For all but the crudest models, this is a computationally intensive calculation, necessitating the use of OOC solution techniques, which add an additional layer of complexity to the problem. These methods were defined in the 2011 version of this paper (Hipp et al., 2011). In this paper we concentrate on results obtained with these methods using our most recent version of the SNL/LANL SALSA3D global 3D tomographic P-velocity model.

RESEARCH ACCOMPLISHED

Introduction

The ready availability of large data sets and powerful computers has made the production of 3D global tomographic geophysical models increasingly common. These models can provide important insight into the structure of the Earth, but more importantly for the monitoring community, they can also improve the quality of our seismic event locations by providing higher fidelity predictions of the observables used to locate events. Perhaps of most direct use for seismic monitoring are global 3D P-velocity models that can be used to predict first P travel times, the observables upon which seismic locations are generally based. Many such models have been produced over the past few decades, but only recently has it been clearly demonstrated that such models can provide superior travel time predictions over broad geographic regions (Ballard et al., 2010; Simmons et al., 2011). This is an important milestone, and the routine use of 3D models for event location now seems inevitable, but there are still important problems that must be addressed. Arguably the most important of these is the calculation of variance and covariance associated with travel time predictions through these models. For tomographic models especially, the uncertainty associated with different ray paths can be vary widely, reflecting the data coverage. Hence, travel times calculated through such a model are of limited utility without accompanying uncertainty estimates.

In the following sections we summarize the theory for calculating travel time variance and covariance for paths through 3D Earth models, and then we apply our theory to the most recent version of the SNL/LANL SALSA3D model. We first review the calculation of the model covariance matrix for a tomographic velocity model, and then show how this matrix can be used to calculate variance and covariance for arbitrary ray paths through the model.

Calculation of the Model Covariance Matrix

Assume that we have a simple ray-theory tomographic problem of the form:

$$A\Delta s = \Delta d \tag{1}$$

where A is the $M \times N$ matrix of path geometries (the "data kernel"), Δs is the $N \times 1$ array of slowness changes, and Δd is the $M \times 1$ array of data residuals (observed – predicted travel times). M is the number of observations, and N is the number of slowness nodes in our model. The typical problem is both over and under-determined, so we solve using damped least-squares. The damping implies adding additional constraints that attempt to impose zero change in the slowness solution:

$$\begin{bmatrix} C_d^{-1/2} A \\ \alpha C_s^{-1/2} \end{bmatrix} \Delta s = \begin{bmatrix} C_d^{-1/2} \Delta d \\ 0 \end{bmatrix} \tag{2}$$

where α is the damping factor, $C_d^{-1/2}$ is an $M \times M$ diagonal scaling matrix of inverse uncorrelated *a priori* data variances (pick uncertainties), $C_s^{-1/2}$ is an $N \times N$ diagonal scaling matrix of assumed inverse uncorrelated *a priori* model variances, and the 0 on right hand side is an $N \times 1$ array of zeros. Thus, the right hand side is now a $(M + N) \times 1$ extended data vector.

Scaling the least squares solution given in (2) by both the *a priori* data and model covariance is a common approach (Tarantola, 2005; Aster, et.al., 2005; Nolet, 2008) and helps to both stabilize the solution and acts to reduce the complexity of the covariance calculation considerably (see Equation 7 below). The difficulty with least squares problems formulated this way is that the *a priori* model covariance is seldom if ever known. On the other hand, since the quantity multiplies the Tikhonov constraint matrix (damping and smoothing), considerable latitude in its definition is afforded. We describe our approach to setting the *a priori* model covariance later in this paper.

The constrained set of equations given by (2) is simultaneously trying to solve for slowness changes that better fit the data, while also trying to minimize those changes relative to the values defined in the *a priori* model. For paths with travel times not fit well by the starting model, these goals are in competition and the solution will be a compromise. A higher damping value amplifies the zero slowness change constraints, and hence leads to models that deviate less from the starting model.

Let $G_w = \begin{bmatrix} C_d^{-1/2} A \\ \alpha C_s^{-1/2} \end{bmatrix}$ and $\Delta d_w = \begin{bmatrix} C_d^{-1/2} \Delta d \\ 0 \end{bmatrix}$ from which (2) can be re-written as

$$G_w \Delta s = \Delta d_w \tag{3}$$

To find the least squares solution, we multiply both sides by the transpose of the bracketed matrix on the-left hand side:

$$G_w^T G_w \Delta s = G_w^T \Delta d_w \tag{4}$$

The least squares solution follows as

$$\Delta s = (G_w^T G_w)^{-1} G_w^T \Delta d_w \tag{5}$$

To assess the ability of the data to resolve Δs in the inversion, we replace Δd with $A\Delta s^{true}$ (Equation 1), where Δs^{true} represents the unknown true solution. We get

$$\Delta s = (G_w^T G_w)^{-1} A^T C_d^{-1} A \Delta s^{true} = R \Delta s^{true} \tag{6}$$

where $R = (G_w^T G_w)^{-1} A^T C_d^{-1} A$ is the $N \times N$ model resolution matrix.

From the definition of covariance for a linear operator and Equation5, one finds the expression for model covariance to be

$$\mathrm{C_M} = (G_w^T G_w)^{-1} G_w^T Cov(\Delta d_w) G_w (G_w^T G_w)^{-1} \tag{7}$$

Since $Cov(\Delta d_w) = I$ because of the normalized *a priori* data and model scaling we obtain

$$\mathrm{C_M} = (G_w^T G_w)^{-1} \tag{8}$$

Path-Dependent Travel Time Uncertainty Derivation

Once we have the model covariance matrix calculated, we can follow the standard methodology for propagation of uncertainty in a linear relation[1] to calculate variance and covariance for ray paths through the model.

$$\sigma_{TT_{ij}} = \int_{P_i} dx\, a_i(x) \int_{P_j} dx'\, C_M(x, x') a_j(x') \tag{9}$$

[1] e.g., http://en.wikipedia.org/wiki/Propagation_of_uncertainty

where $\boldsymbol{x}$ indicates the position along the *i*th ray path (P_i), $\boldsymbol{x}'$ indicates the position along the *j*th ray path (P_j), $a_i(\boldsymbol{x})$ is the data kernel, or weight, for the *i*th path at position $\boldsymbol{x}$, $a_j(\boldsymbol{x})$ is the data kernel for the *j*th path at position $\boldsymbol{x}'$,and $C_{\mathrm{M}}(\boldsymbol{x}, \boldsymbol{x}')$ is the model covariance between points $\boldsymbol{x}$ and $\boldsymbol{x}'$ along the two paths *i* and *j*. If $i = j$, then this equation gives variance along a single ray path; if $i \neq j$ then covariance between the ray paths is calculated. Discretizing (9) and transforming from the path specific domain to the SALSA3D grid domain yields

$$\sigma_{\mathrm{ij}} = W_i C_{\mathrm{M}} W_j^T \tag{10}$$

where W_i and W_j are data kernel vectors for the *i*th and *j*th paths, respectively. For a set of arbitrary ray paths, all of the variances and covariances can be calculated at once as

$$\mathrm{C_{TT}} = W C_{\mathrm{M}} W^T \tag{11}$$

where W is the data kernel matrix for all rays to be evaluated with one row per ray path.

Model Resolution and Traditional Checkerboard Tests

The ability of a tomographic model to resolve features of the model space has historically been assessed using checkerboard tests. In these tests, the velocity field in the model is perturbed from its final tomographic value by some small amount with the sign of the perturbation varying in some regular pattern such as a checkerboard. Then the observed travel times used in tomography are replaced with travel time predictions computed through the perturbed model, and the tomographic inversion is repeated. The velocity model thus obtained can be compared to the actual final tomography model. In areas with good resolution the pattern of the checkerboard perturbations will be accurately retrieved while the pattern will not be discernible in areas with poor resolution. A checkerboard test applied to a recent version of the SALSA3D model at a depth of 820 km is shown in Figure 1a. Figure 1b shows a map of the diagonal elements of the model resolution matrix computed according to Equation 6. Both images suggest that the resolution of the model is best in central Europe, the western Pacific and western North America, which correspond to the regions of the model that are best sampled by the available data. The model resolution matrix is more informative however, providing a more quantitative rather than qualitative estimate of the ability of the model to resolve features of the tomographic model.

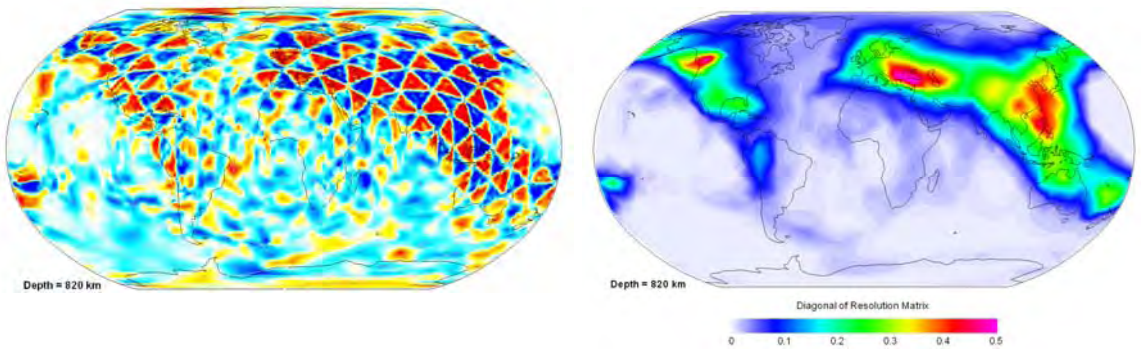


Figure 1. Evaluating resolution for the SALSA3D model at a depth of 820 km. a) Traditional checkerboard test. b) Diagonal elements of the model Resolution matrix.

***A priori* model covariance**

The procedure for determining the model covariance matrix described above is basically a Bayesian process where we iteratively:

1. Make an *a priori* estimate of the general distribution of covariance in the model space;
2. Perform tomography using Equation 5;
3. Calculate the *a posteriori* model covariance matrix (Equation 8);
4. Compute travel time prediction uncertainties for a substantial data set of interest (Equation 11);

5. Compare the resulting travel time prediction uncertainties with estimates determined with other techniques;
6. Stop when reasonable values travel time prediction uncertainties are obtained.

Our *a priori* estimate of the model covariance is simple: the diagonal terms decrease linearly with depth in the mantle and the off-diagonal elements are all zero. We adjust the overall magnitude of the diagonal elements and the slope of the mantle gradient until we obtain travel time uncertainty estimates that satisfy two criteria. The first is to compare the computed path-dependent travel time uncertainties to travel time uncertainties estimated using traditional 1D distance dependent uncertainty calculations. The premise in this case is that 1D distance dependent uncertainties at teleseismic distances for sources in areas of the world with high seismicity are probably reasonable estimates of the actual uncertainty. Computed path-dependent uncertainties for teleseismic paths from sources in seismically active areas should compare reasonably well with 1D distance dependent uncertainties under these conditions.

To implement this comparison, we first identified 79 widely distributed points around the globe that were all in high seismicity areas (Figure 2a). Then we computed path-dependent travel time uncertainty estimates from every station in the International Monitoring System network to each of the points in high seismicity areas and plotted travel time uncertainty versus distance considering only ray paths in the teleseismic distance range from 30° to 95°. The results we obtained with our final estimates of the *a priori* variance are compared to a traditional 1D distance dependent uncertainty curve in Figure 2b. When the magnitudes of our *a priori* variance values were higher than the final values, the path dependent uncertainties were too high relative to the 1D distance dependent values. When the decrease in *a priori* slowness variance with depth was too strong, we observed a decrease in travel time uncertainty with distance that did not match the 'flatness' of the 1D distance dependent uncertainty trend with distance.

We plan to test our final travel time uncertainty estimates with a second criterium but have not yet implemented this comparison. Our intention is to relocate a substantial set of seismic events whose true locations are known with high accuracy and compute uncertainty coverage ellipses using our path dependent travel time uncertainty estimates. The metric for success will be that close to 95% of the known event locations fall within the computed 95% coverage ellipses. We will adjust our *a priori* model covariance estimates to ensure that this criterion is satisfied.

While our *a priori* estimates of model covariance are of a very simple form, the *a posteriori* model covariance exhibits much richer complexity (Figure 3) and the derived path-dependent travel time uncertainties are even more interesting. Both exhibit lower uncertainty for paths through the Earth that are well sampled by data in the tomographic inversion and higher uncertainty for poorly represented paths.

Variance, Covariance, and Resolution Comparison

Figure 3 shows the diagonal elements of the model covariance matrix at a depth of 820 km. Comparing this to the diagonal elements of the model resolution matrix illustrated in Figure 1 we see that the two are inversely related – in well sampled areas where the model resolution is high, the variance is low, and vice versa. The variance values in poorly sampled, high-variance regions are controlled, to a significant degree, by the *a priori* estimates of delta slowness variance, C_s, in Equation 2.

Next we turn our attention to cross-sections through our model. The positions of these cross-sections are shown in Figure 3: one through Sarajevo in central Europe and the other through Hawaii. These present interesting opportunities to assess the implications of the covariance structure of the SALSA3D model. The cross-sections themselves are shown in Figure 4. For each, we show the diagonal of the model resolution matrix, the diagonal of the model covariance matrix (i.e., the variances), and the covariances for nodes located at a depth of 100 km below centers of each map cross-section (i.e., beneath Sarajevo and Hawaii).

Situated in the middle of the Pacific Ocean, Hawaii has stations that observe seismic events around the Pacific Rim but there are few events at intermediate distances from the island. Most importantly, the shallow mantle beneath the Pacific Ocean is poorly sampled by the available data and there are relatively few crossing rays in that part of the model. This is evident in the low values of the diagonal elements of the model resolution matrix beneath the Pacific, including Hawaii. The diagonal elements of the model covariance matrix are the mirror image of the resolution values, with very high variance beneath the Pacific Ocean indicating relatively high uncertainty in the value of

P velocity in that portion of the model. For the covariance, we note that the paths through the model that are well sampled, such as the path from Hawaii to the Philippines, are characterized by relatively high negative covariance values compared to paths that are more poorly sampled, suggesting that the model velocity along these paths are not independent. If the velocity at the node below Hawaii were to be increased for some reason, the velocity at other points along the path to the Philippines would have to be reduced in order to compensate. These observations suggest that even though the variance of the mantle velocity along well sampled paths may be very high, the integrated covariance along the path, i.e. the uncertainty of the predicted travel time along the path, may end up being lower that it would be otherwise due to the substantial values of model covariance along the path.

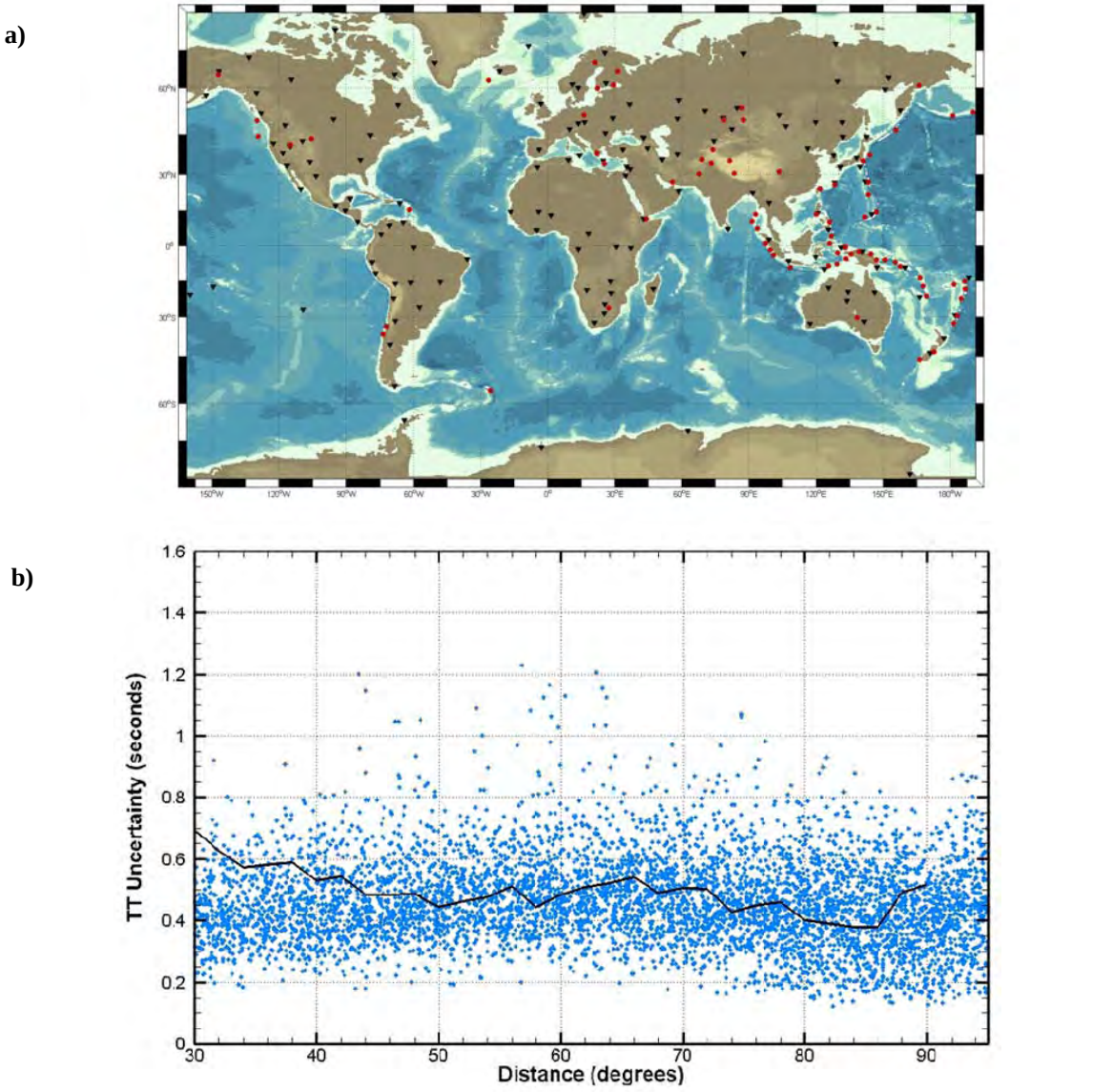


Figure 2. Information used to refine initial estimates of the *a priori* model covariance matrix. a) red dots reflect the positions of 79 hypothetical surface sources in high seismicity areas and black triangles are the locations of stations in the IMS network. b) Blue dots are path dependent travel time uncertainties calculated for every source-receiver pair in a) in the distance range of 30 to 90 degrees. The black curve is a 1D distance dependent uncertainty curve calculated for SALSA3D using traditional methods.

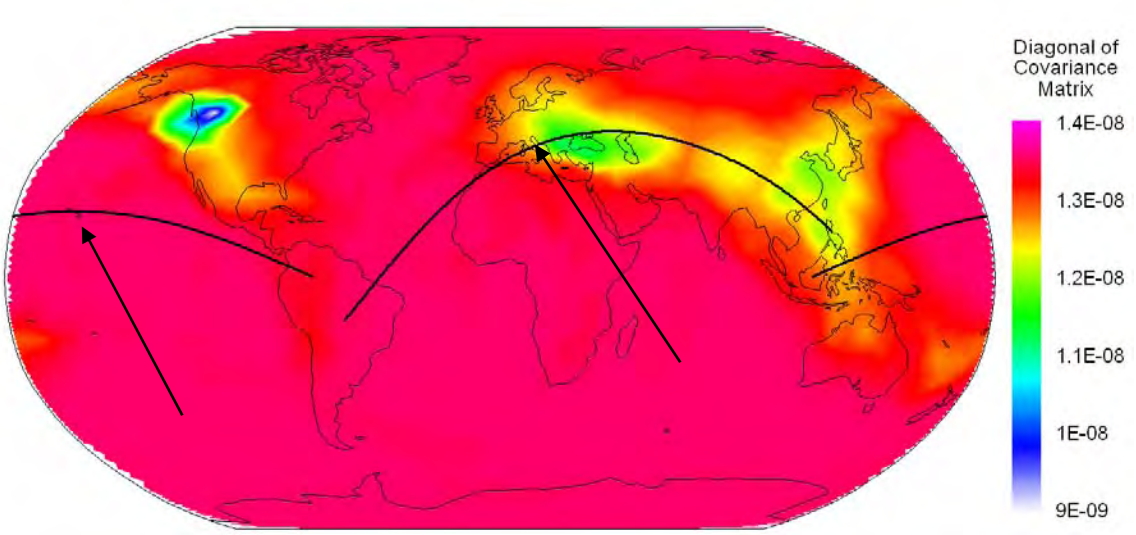


Figure 3 Diagonal of model covariance at 820 km depth. The bold black lines indicate position of cross-section views shown in Figure 4.

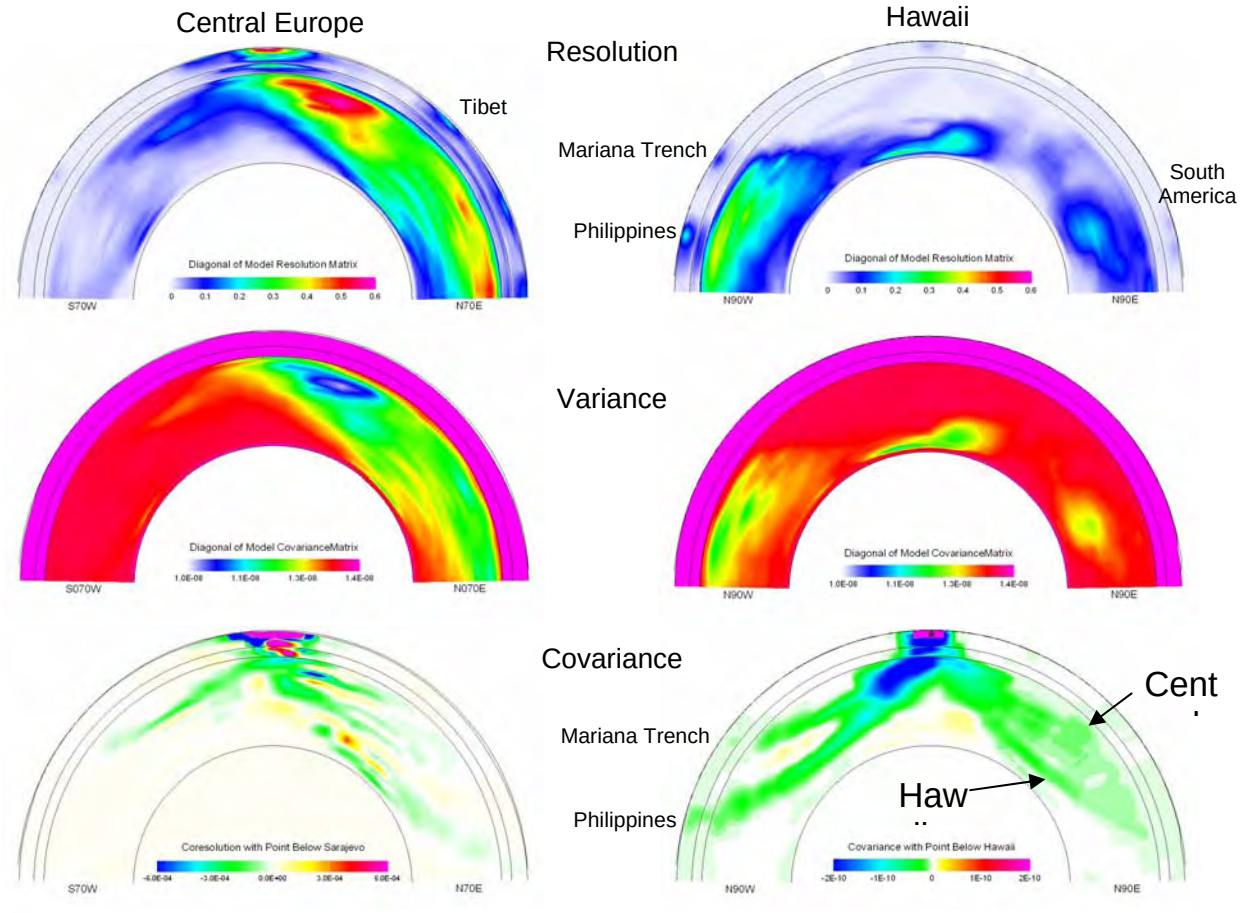


Figure 4. Resolution, variance, and covariance for the cross-sections shown in Figure 3.

For Sarajevo, we can see that our model is very well resolved for the portion of the cross-section to the east, hence the model variance is low. To the west, the resolution is poorer, and hence the variance is higher. For the covariance, we can still see negative covariance along ray paths both to the west and the east, suggesting that tradeoffs occur even in relatively well-sampled parts or our model. Integrating covariance along these ray paths will lead to low variance travel times, as would be expected given that this part of the model is well sampled by many crossing ray paths.

Station-Centric Ray Uncertainty

In this section we illustrate the results of performing the ray uncertainty calculation defined by Equation 11. Figure 5 shows the decomposition of the model covariance for the specific receiver ALAR located in Alaska. Note the strong negative covariance magnitude for the off-diagonal component in regions where we have abundant data (Figure 5c). Generally speaking, regions with significant seismicity tend to have substantial negative off-diagonal terms in the model covariance matrix resulting in lower travel time uncertainty than would be the case if the travel time uncertainty were computed with only the diagonal elements of the model covariance matrix.

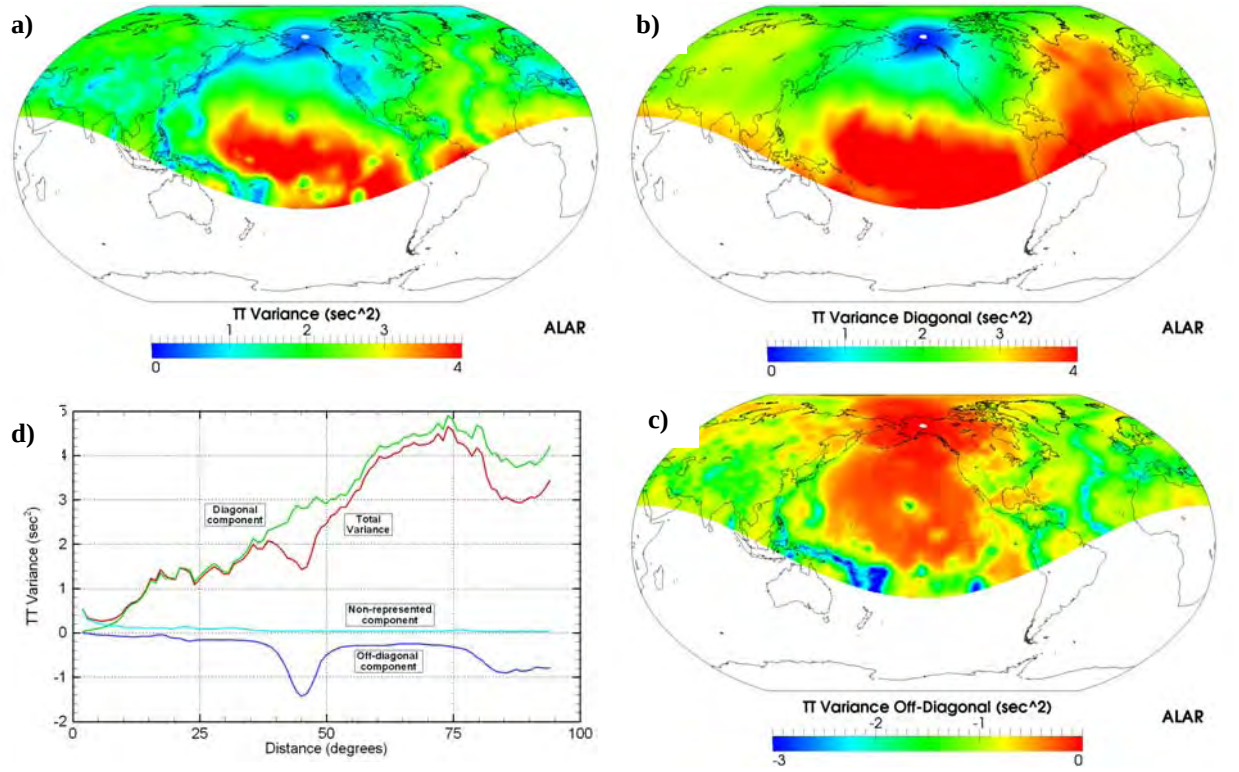


Figure 5. Travel time covariance decomposition for receiver ALAR located in Alaska. a) total path dependent travel time variance. b) travel time variance computed using only the diagonal elements of the model covariance matrix. c) travel time variance computed using only the off-diagonal elements of the model covariance matrix. The values in a) are the sum of the values in b) and c). d) transect from station ALAR through Hawaii.

The last set of Figures (6 - 9) show the calculated uncertainty for four other receivers including ILAR, ESDC, WRA, and VNDA. Each Figure has two sub-panels where: a) shows the new path dependent uncertainty calculated using the methods described in this paper, and b) shows the traditional 1D distance dependent uncertainty for comparison. The path dependent uncertainties exhibit much more variability geographically and properly reflect the correlation between uncertainty and the amount and quality of data that were used to develop the tomographic model. Well sampled paths in the Earth exhibit lower uncertainty compared with paths that were not well represented in the tomographic data set. This is in stark contrast to the 1D distance dependent uncertainty estimates which display the same uncertainty over broad areas. The 1D distance dependent uncertainty estimates probably accurately

characterize the uncertainty in areas of high seismicity since those are the data that contributed to their development. They likely severely underestimate the uncertainty in aseismic and low-seismicity regions, however.

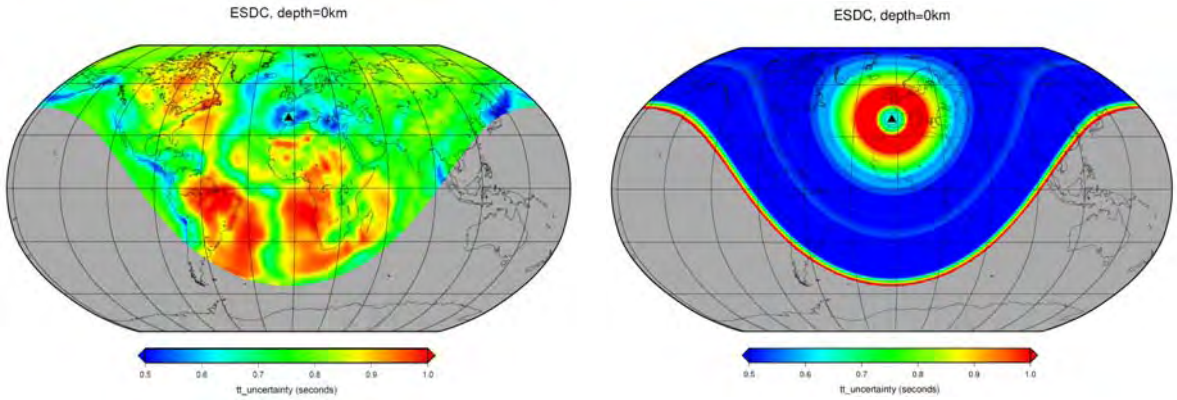


Figure 6. Comparison of a) path dependent travel time uncertainty and b) 1D distance dependent travel time uncertainty for station ESDC.

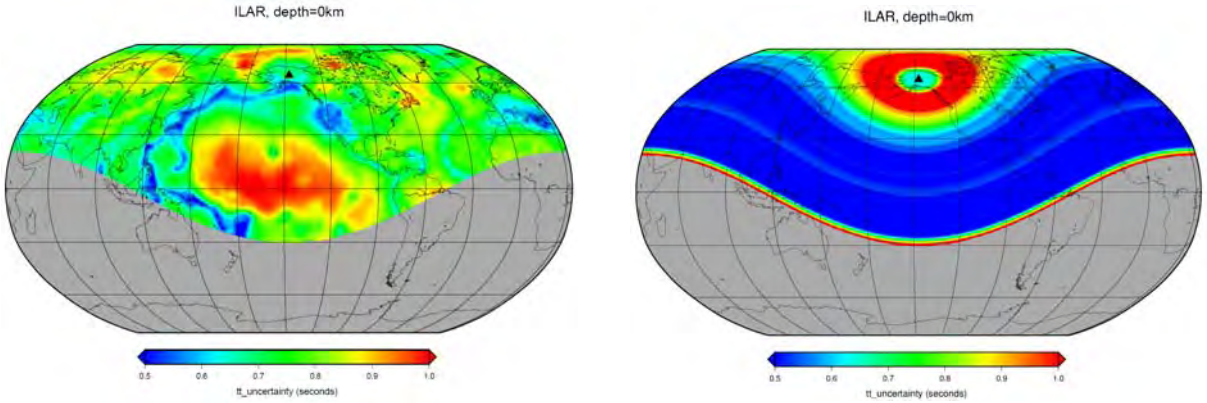


Figure 7. Comparison of a) path dependent travel time uncertainty and b) 1D distance dependent travel time uncertainty for station ILAR.

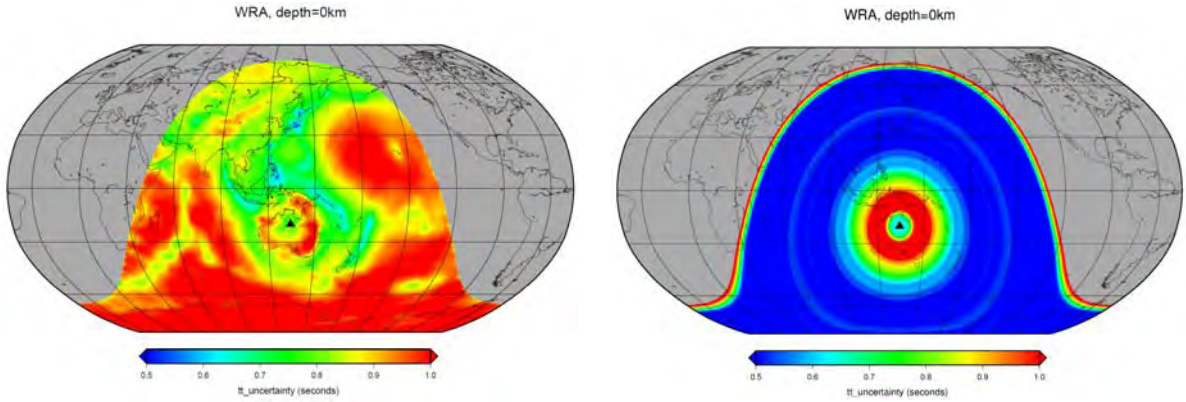


Figure 8. Comparison of a) path dependent travel time uncertainty and b) 1D distance dependent travel time uncertainty for station WRA.

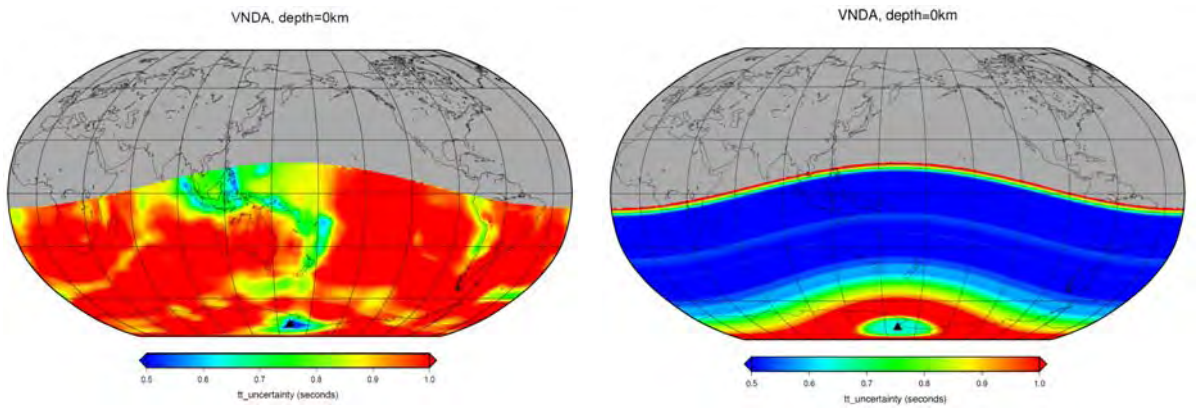


Figure 9. Comparison of a) path dependent travel time uncertainty and b) 1D distance dependent travel time uncertainty for station VNDA.

CONCLUSIONS AND RECOMMENDATIONS

The use of 3D global tomographic models to predict travel times for locating seismic events seems to be inevitable, yet there are several important problems that must be solved to bring this about. Perhaps foremost among these is the need to be able to produce realistic, path-dependent uncertainties for travel times calculated through these types of models, uncertainty estimates that accurately reflect the very uneven data sampling in the data sets from which these models are derived. In this paper, we have shown how one can first derive the model resolution and model covariance matrices, and from the latter, how path-dependent travel time uncertainties can be estimated. Both the calculation of those matrices and of the travel time uncertainties require huge numbers of calculations and huge amounts of memory making out-of-core methods a necessity if direct solvers are used. We have developed such methods and used them with the SALSA3D model to calculate model resolution, model covariance, and path dependent travel time uncertainty estimates.

REFERENCES

Aster, R. C., B. Borchers, and C. H. Thurber (2005). *Parameter Estimation and Inverse Problems*, Elsevier Academic Press, ISBN: 0-12-065604-3.

Ballard, S., M.A. Begnaud, C.J.Young, J.R. Hipp, M. Chang, A. Enacarnacao, C.A. Rowe, W.S.Phillips, and L.K. Steck (2010). SALSA3D -- a global 3D P-velocity model the Earth's crust and mantle for improved event location, presentation at the Fall 2010 American Geophysical Union Meeting.

Gunter, B.C. and W.C. Reiley (2001). Parallel Out-Of-Core Cholesky and QR Factorizations with POOCLAPACK, 15th International Parallel and Distributed Processing Symposium (IPDPS'01), San Francisco, Ca., USA, September 2001, ISBN: 0-7695-0990-8.

Hipp, J.R., A. Encarnacao, C.J. Young, S. Ballard, M. Chang, M.A. Begnaud, and W.S. Phillips (2011). Calculating Path-Dependent Travel Time Prediction Variance and Covariance for a Global Tomographic P-Velocity Model. need citation, presentation at the 2011 Seismological Society of America Meeting.

Nolet, G. (2008). A Breviary of Seismic Tomography, Cambridge University Press, ISBN: 978-0-521-88244-6

Simmons, N.A., S.C. Myers, and G. Johannesson (2011). The LLNL-3D global P-wave velocity model and its performance in seismic event location, presentation at the 2011 Seismological Society of America Meeting.

Tarantola, A. (2005). Inverse Problem Theory and Methods for Model Parametric Estimation, SIAM, ISBN: 0-89871-572-5

.

VALIDATION AND UNCERTAINTY ASSESSMENT OF GROUND-BASED NUCLEAR EXPLOSION MONITORING MODELS

Monica Maceira[1], Carene S. Larmat[1], Rob Porritt[2], and David M. Higdon[1]

Los Alamos National Laboratory[1] and University of California, Berkeley[2]

Sponsored by the National Nuclear Security Administration

Award No. DE-AC52-06NA25396/LA12-Signal_Propagation-NDD02

ABSTRACT

Since the beginning of tomography studies in the 1970s, geoscientists have mastered the art of inferring an image of the underground solid Earth from a collection of observables recorded at the surface. In particular and for the last years, the National Nuclear Security Administration (NNSA) has been focusing on addressing the Earth's 3D heterogeneities and complexities toward high-resolution 3D seismic models in programmatic areas. The goal is to improve the reliability of event location, which is critical to detection of banned nuclear tests at regional scale. However it is difficult to assess how accurate these velocity models are, especially concerning seismic source parameters. Model validation is typically done using resolution tests that assume the imaging theory used is accurate and thus only considers the impact of the data coverage for resolution. In the last years, new horizons have opened up in earth structure imaging, with the advent of new numerical and mathematical methods in computational seismology and statistical sciences. We are taking advantage of these newly applied to seismology methods and combining them to start tackling the question of uncertainty quantification.

During this first year, we have focused on an independent assessment of the prediction capability of the investigated models using a purely numerical method for wave propagation modeling. To test the codes and the proper implementation of our ideas, we are first focusing on the "best-case scenario": the western USA, where state of the art imaging techniques together with an unprecedented seismic station coverage are providing the best ever seismic models. We have collected several models for the Western USA (DNA models) generated using both ray-theoretical and finite-frequency methods. In this manner we do not validate just the model but also the imaging technique. We evaluate the model performances by comparing synthetic seismograms and observed data, and using different measurement techniques for different parts of the signal. Results show that both, finite-frequency and ray-theoretical DNA09 models, predict the observations well. Waveform cross-correlation coefficients show a difference in performance between models obtained with the finite-frequency or ray-theory limited to smallest periods (<15s), with no perceptible difference at longer periods (50-200s). At those shortest periods, and based on S-wave phase delay measurements, finite-frequency shows an improvement over ray theory. Implementation of the method for a densely instrumented region such as that covered by the Dynamic North America models provides a useful testbed for the validation methods that we will subsequently apply to other areas of programmatic interest.

OBJECTIVES

The main objective of this research is to provide a new tool that will improve the reliability of event location, which is critical to detection of banned nuclear tests at regional scale. A lot of effort has been directed toward high-resolution 3D seismic models in programmatic areas to address this mission need. However it is difficult to assess how accurate these velocity models are, especially concerning seismic source parameters. Model validation is typically done using resolution tests that assume the imaging theory used is accurate and thus only considers the impact of the data coverage for resolution. We are developing a more rigorous approach to this problem of model validation based on spectral-element and adjoint methods (Komatitsch and Tromp, 2002; Tromp et al., 2005; Tape et al., 2009). This new approach will provide assessment of the location error related to uncertainty in current 3D high-resolution models and will also advance our understanding of wave propagation in programmatic areas.

RESEARCH ACCOMPLISHED

To accomplish the above mentioned objective and during this first year of the project, we have focused on the independent assessment of the prediction capability of the investigated models using a purely numerical method for wave propagation modeling, the Spectral Element Method (SEM). To test the codes and the proper implementation of our ideas, we are first focusing on the "best-case scenario": the western USA, where state of the art imaging techniques together with an unprecedented seismic station coverage are providing the best ever seismic models. We have collected several models for the Western USA (Dynamic North America, DNA, models) generated using both ray-theoretical and finite-frequency methods. In this manner we do not validate just the model but also the imaging technique.

Background

Since the beginning of tomography studies in the 70s (Aki et al., 1977; Sengupta and Toksöz, 1977; Dziewonski et al., 1977), geoscientists have mastered the art of inferring an image of the underground solid Earth from a collection of observables recorded at the surface. While the best current inversion techniques are providing 3D seismic structure models with the best resolution ever, there is a severe lack of proper methodology to Uncertainty Quantification (UQ) in 3D Earth imaging. Theoretically, this will require testing the entire range of possible values for each parameter to get a complete "picture" of the solution space, in addition to questioning the fidelity of the imaging method (in this case, the seismic wave propagation scheme used to predict waveforms). In most tomography studies, UQ is limited to resolution checks such as checkerboard and spike tests. The checkerboard test considers arbitrary, alternately positive and negative structures with the same wavelengths. There are several problems with this approach: (1) they are falsely interpreted as resolution test while they only indicate which parts of the model is potentially well resolved. In other words, they give information about the data coverage, ray geometry and data errors such as phase picking errors but not on the range of possible values for elastic parameters; (2) they do not always provide meaningful quantifications of nonuniqueness (Menke, 1989; Lévêque et al., 1993); (3) visual inspection between input and output is inadequate because of the very efficient psychological tendency to mistake the great detail seen in the models as an indicator of comparatively high resolution when, in fact, small-scale features may be not well resolved.

In the last ten years, new horizons have opened up in earth structure imaging, with major instrumentation efforts (e.g., NSF funded Earthscope) as well as with major developments in computational power with the establishment of machines now allowing to reach the petaflop. Motivated by these recent developments that now allow us to model the full-waveform propagation in 3D heterogenous media with unprecedented accuracy, we first validate state of the art seismic models developed for North America in a first robust attempt to UQ in seismology. Making use of the SEM, which is now emerging as the prime method for full-waveform seismic modeling in complex media (Komatitsch and Vilotte, 1998; Komatitsch et al., 2002), we are also able to independently validate the seismic imaging method used to generate the models. In the following, we will assess the advantages and disadvantages of the more recently developed finite-frequency approach to tomography over the more traditional and more approximate ray theoretical approach. Implementation of the method for a densely instrumented region such as that covered by the DNA models provides a useful testbed for the validation methods that we subsequently plan to apply to other study areas. These regions are less instrumented but are of interest to our national security mission to more confidently and accurately detect and locate small events to improve our monitoring capabilities for the Comprehensive Nuclear-Test-Ban Treaty.

The DNA09 model

Recent theoretical developments in seismic wave propagation through the Earth now provide the basis for a new generation of geophysical models. Finite-frequency (FF) methods have replaced ray-theoretical (RT) methods that assumed any observed travel time delay at a station was the result of velocity anomalies along an infinitely narrow ray path between the source and the receiver. In addition, seismic waveform datasets from dense continental-scale deployments are now available in the United States (USArray component of NSF funded Earthscope project) as well as in other countries, providing the opportunity to apply finite-frequency tomography on a regional or continental scale and compare the results with traditional ray-theoretical models for the same regions.

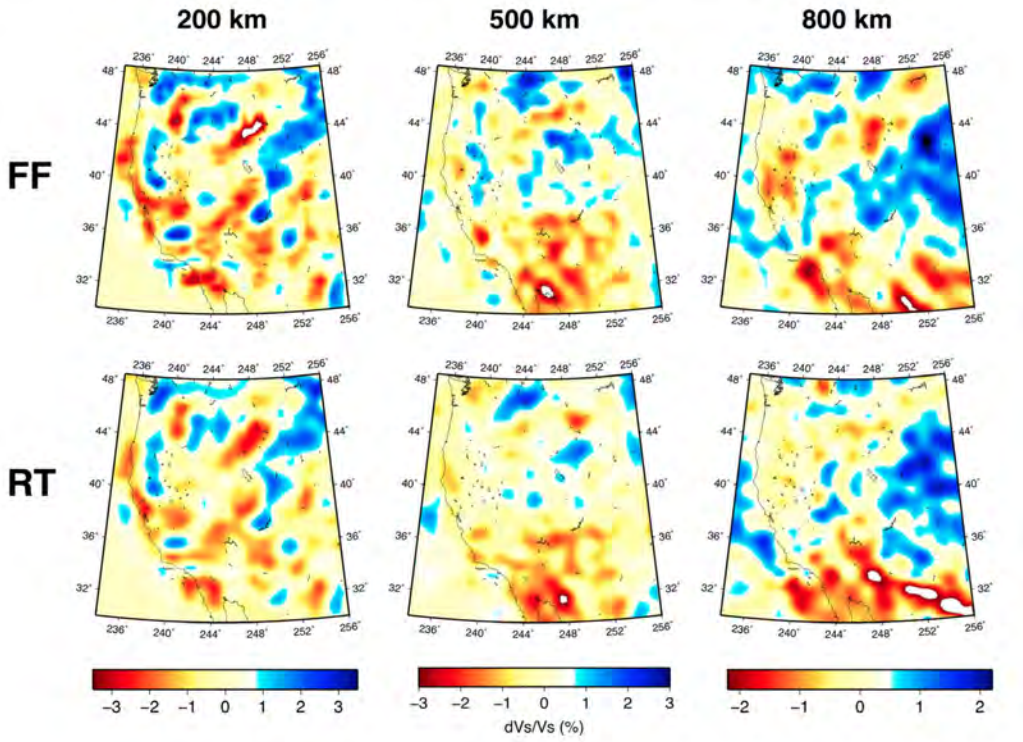


Figure 1. Maps of the seismic velocity anomalies obtained by the RT and FF imaging methods at different depths. The two models display the same features at long wavelength but show some clear discrepancies for the shortest wavelengths.

We initially focus on 3D geophysical models developed for North America through the continental-scale Earthscope project. Professor Allen's research group (University of California, Berkeley) has developed a high-resolution model of the western United States (Dynamic North America model, DNA) using both the body-wave finite-frequency approach (Xue and Allen, 2010; Obrebski et al., 2010) and the more classical ray theory approach (see figure 1 for a comparison of both models). The DNA09 models are derived from relative delay times of body waves (direct P, direct S, and SKS) recorded with the USArray. The arrival time windows are hand picked and the delays are refined via the multi-channel cross-correlation of VanDecar and Crosson, 1990. These delays are accumulated along a raypath, which is used to populate the inversion matrix. The inverse problem is then solved with standard least squares regression utilizing damping and smoothing regularization to stabilize the solution. Additionally, event and station static corrections are solved for in order to account for small errors in the timing and location of the events and to absorb the structure of the upper 100km where teleseismic raypaths do not cross before reaching the station. The differences between the RT and FF models are manifested in the inversion matrix. In the RT case, the sensitivity is evenly distributed along the center of the ray to the resolution limit of the grid cells. The FF model uses the single scatterer (Born) approximation to calculate the frequency dependent sensitivity along the raypath, which has a null at the center and a sinusoidal cross-section extending to approximately the square root of the dominant wavelength from the center. Due to this inherently smooth sensitivity kernel, the FF inversion does not use smoothing regularization.

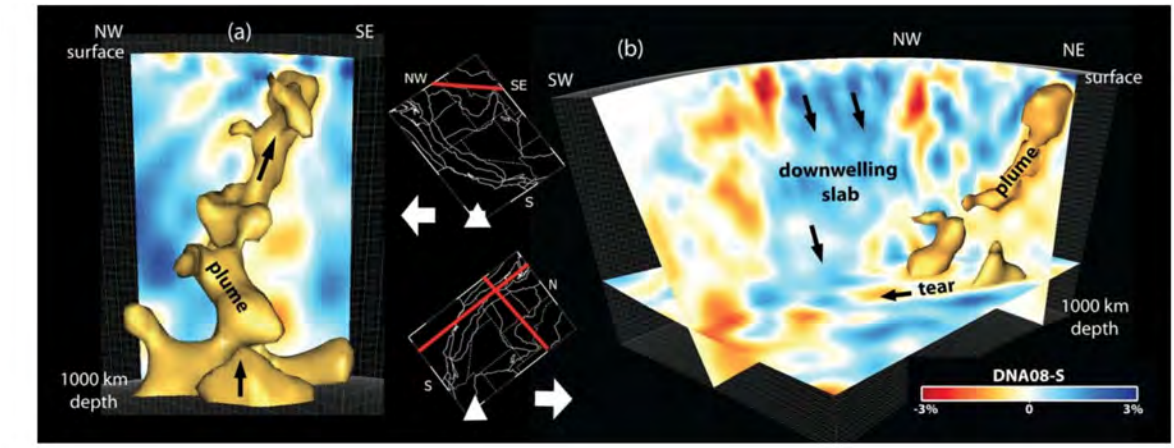


Figure 2. Images of 3D velocity structure beneath the western US. Yellow shows low velocity regions interpreted as hot upwellings; blue is high velocity interpreted as cold downwellings. Red lines on insert maps indicate location of cross sections. (a) Cross section beneath Yellowstone hotspot showing upwelling conduit from greater than 1000 km depth. (b) The subducting slab (blue) is torn by the plume.

Obrebski et. al., 2010 interpreted the model as illustrative of the interactions between the Yellowstone Plume and the Juan de Fuca plate (Figure 2). Three-dimensional views show a relatively intact slab to the west aside from a low velocity hole occupied by the Yellowstone Plume. East of the continuous slab, fragments of high velocity material suggest slab breakup attributed to interaction with the Yellowstone Plume. This interpretation is bolstered by the observed volcanic chemistry at Yellowstone Caldera, the relatively young age of the slab, the lack of seismicity, and the offshore evidence for internal deformation of the Juan de Fuca plate.

The SEM

In order to validate the 3D models with synthetic seismograms generated as independent forward calculations (Bozdag and Trampert, 2010), we chose to work with SEM that is emerging as a prime numerical method for full 3D waveform propagation. SEM makes no assumptions about the theory used to generate the models but it requires substantial computational resources, such as the ones available at LANL. SEM solves the wave equation in its integral form on customized meshes adapted to realistic Earth models and made of hexahedral elements (see Figure 3). It employs a high order finite-element method with exponential convergence for smooth solutions while maintaining the geometric flexibility of finite elements (Komatitsch and Vilotte, 1998; Komatitsch & Tromp, 2002). It accounts for heterogeneity in the crust and mantle, topography, anisotropy, attenuation, fluid-solid interactions, self-gravitation, rotation, and the oceans. We use a modeling package called SPECFEM3D (Komatitsch et al., 2002), whose scalability to petaflop calculations is promising to open up new horizons in Earth imaging. Thanks to its computing power and accuracy, SEM makes it possible to exploit all of the information contained in regional and teleseismic seismograms and has already lead to the first full-waveform 3D models (Tape et al., 2009; Fichtner et al., 2009; Lekic and Romanowicz, 2011).

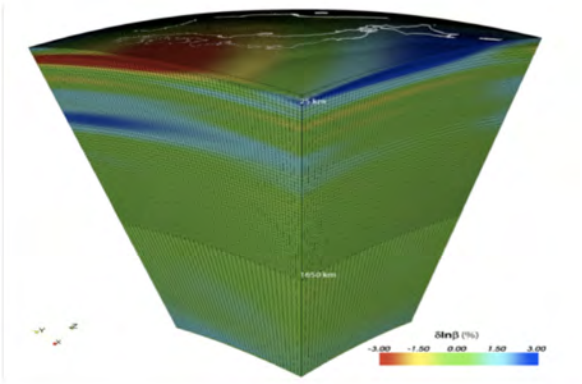


Figure 3. Using HPC to address Earth's 3D heterogeneity and complexity. Example of a mesh used by the SPECFEM3D modeling package for a regional scale modeling superimposed to the S wave velocity variations of the 3D S20RTS of Ritsema and Van Heijst (2000) (Figure from SPECFEM3D user guide, version 5.0, "Tiger.")

The Validation Set and Synthetic Seismograms

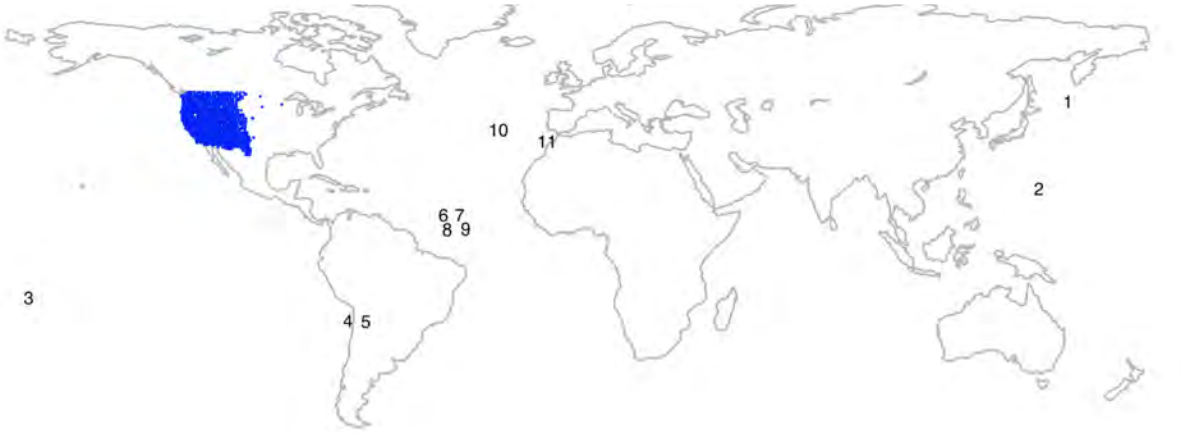


Figure 4. Locations of the 11 seismic events used for evaluating the RT and FF DNA09 models. The blue points in the western U.S. mark the locations of monitoring stations used in this evaluation.

We chose a validation set consisting of 11 seismic events of different types and magnitudes and making sure of a good azimuthal coverage (see figure 4 for their location). For each of them we compute synthetic seismograms through both the Finite-frequency (FF) and Ray-theory (RT) DNA09 models. We then performed waveform cross-correlation analysis for two different period bands between synthetics and observations and between FF and RT synthetics (see figure 5 for an example). Preliminary conclusions from these analyses are that, (1) for the period band between 50-200s, both FF and RT DNA09 models predict the observations well; data and synthetic seismograms fit the best for the horizontal components and smaller epicentral distances; (2) we can't see perceptible difference in performance between FF and RT models at intermediate periods; differences start to appear, however, at higher frequencies.

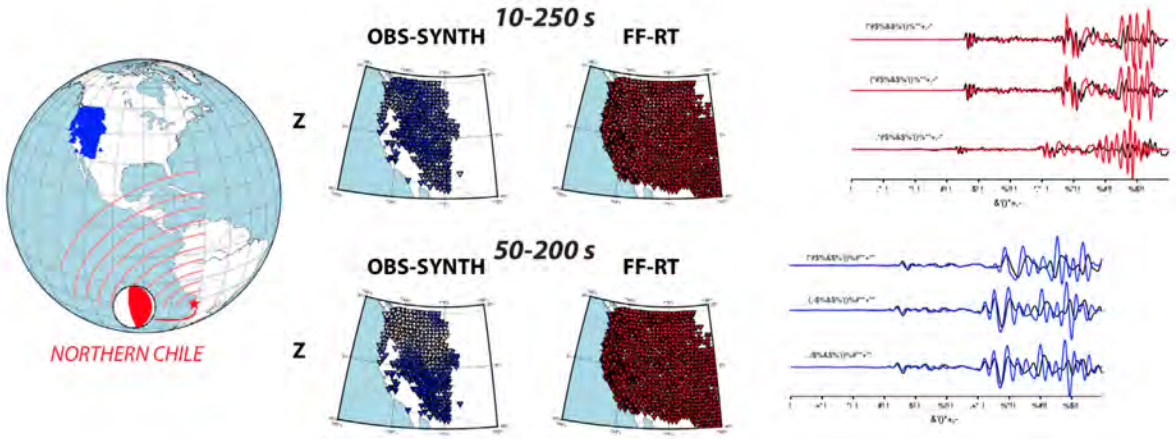


Figure 5. Waveform cross-correlation analyses. (left) Location of event under study (red star) and recording seismic station (blue triangles); (middle) waveform cross-correlation coefficients for two period bands between observed data and synthetic seismograms and between FF and RT synthetics; (right) observed seismograms (black) and synthetics filtered between 10-250 s (red) and 50-250 s (blue).

These analyses were performed for the whole waveform meanwhile the models were created using only body waves, so in order to fairly assess the quality of the RT and FF models, we treat synthetic seismograms in the same way we do the real observations. We utilize new software to rotate the data from the Vertical-North-East coordinate frame into the P-SV-SH coordinate frame using the slowness parameter computed for the iasp91 model with TauP. The direct SV and SH arrivals (the synthetic seismograms are accurate up to 10 s so they do not contain enough higher frequencies to focus on P arrivals) are handpicked independently on the synthetics from the RT and FF models. The set of picks on synthetic data are then joined with the set of stations with acceptable picks for the real data and the multi-channel cross-correlation is repeated for the synthetic and real datasets to normalize the basis function of the model space. We then compare the observed delay times from the real data with the observed delay times from each of the synthetic datasets (Figure 6).

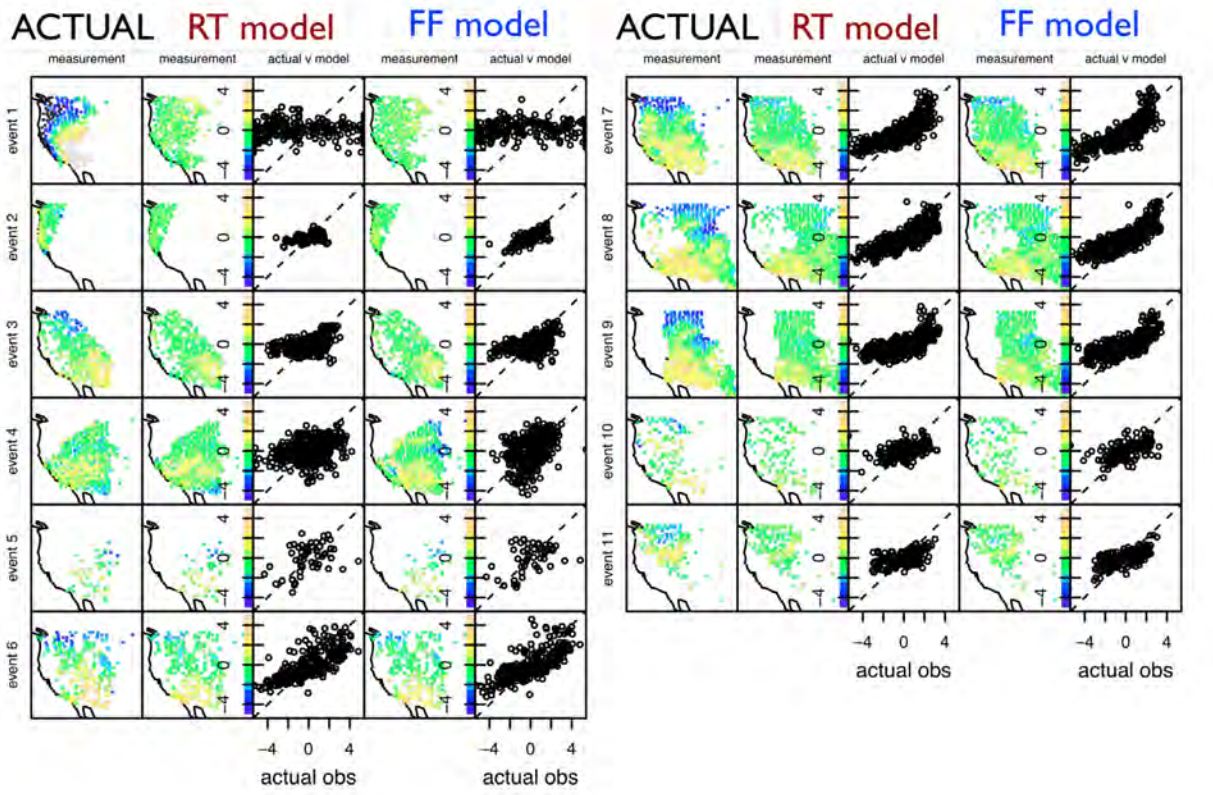


Figure 6. A comparison of actual and modeled S-phase arrival times. The plots show the actual and modeled measurements at their spatial locations as well as actual measured arrival times (x-axis) plotted against the modeled arrival times (y-axis).

Figure 6 indicates it is clear that the time delays produced by the two models are more similar to each other than they are to the actual delays. The mean absolute residuals between the actual and model-based delay times are shown in Figure 7. Clearly, the ability of the models to reproduce the actual delay times depends on the event. Both models do a poor job with event 1, while the results for events 2, 6, and 8 are much more in line with the actual observations. From events 1,3,6,7, 8, and 9, it is apparent that the models have difficulty reproducing the small actual delays present in the northern stations given by the blue, purple and black pixels of the first column of Figure 6. The models do somewhat better reproducing the large delays given by the light/yellow pixels in the figure.

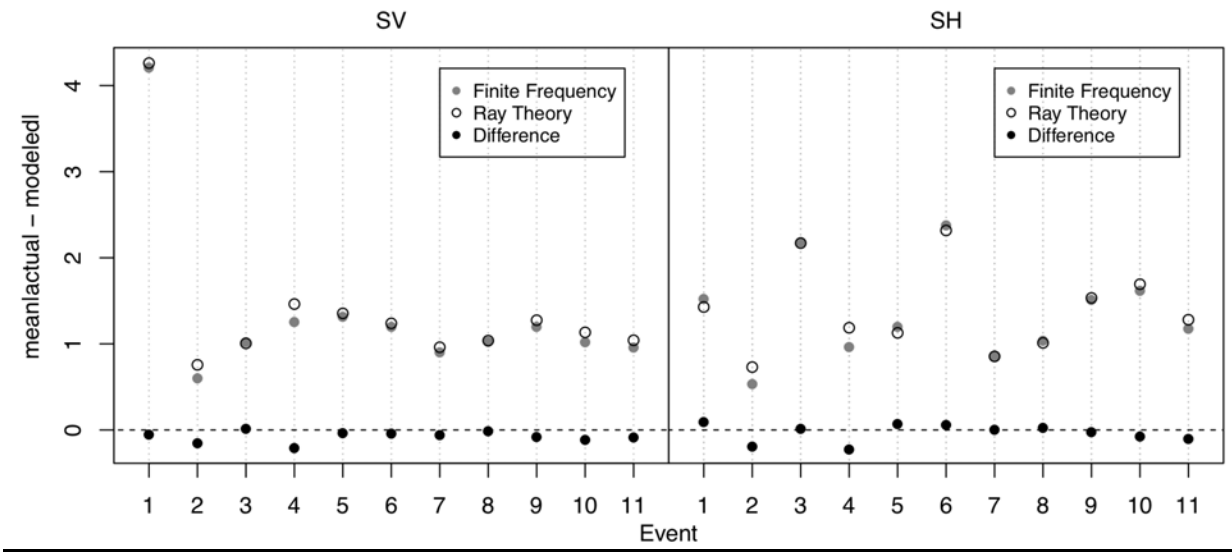


Figure 7. For each station measurement, the misfit between actual and modeled arrival measurements is summarized by the mean of the absolute deviations. The differences resulting from each pair of models for the 11 events are given by the black dots. The models are statistically different for SV measurements but there is no significant difference between the two models for SH measurements based on this summary.

On average, the delay times produced by the FF model are about a half second closer to the actual delay times for both SV and SH. A simple paired t-test can be used to assess the significance of this observed difference. The difference is significant for the SV arrival times (p=0.003) and not for the SH arrival times (p=0.4). These differences are shown graphically by the black dots in Figure 7.

Focusing on only the S-phase, we repeated the waveform cross-correlation analyses and stacked the horizontal components coefficient values for each station. Results are shown in Figure 8, which shows that FF approaches make a difference for large amplitude low-velocity anomalies such as mantle plumes (e.g., the Yellowstone area).

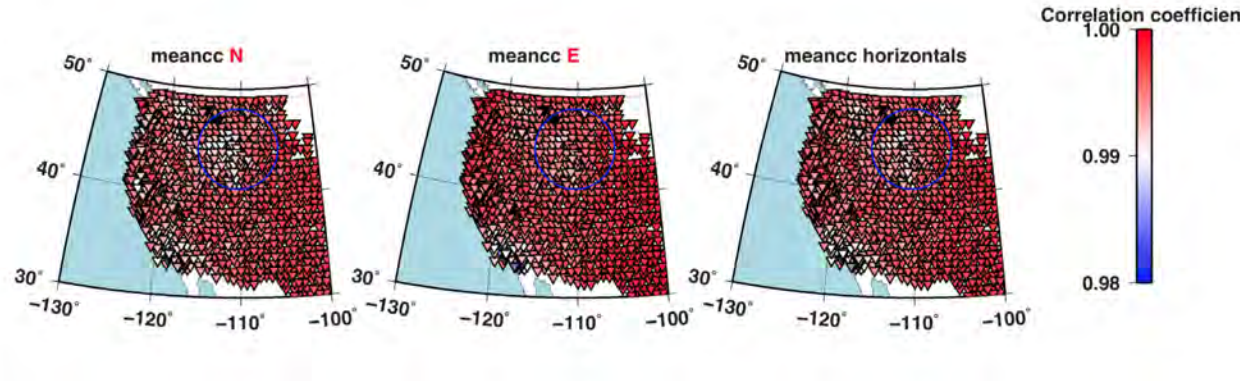


Figure 8. Stack of waveform cross-correlation coefficients between RT and FF synthetic seismograms for all 11 events and per seismic station. (left) for the N-S horizontal component; (middle) for the E-W horizontal component; (right) the mean of both horizontal components. The blue circle marks the location of the Yellowstone area.

CONCLUSIONS AND RECOMMENDATIONS

While the best current inversion techniques are providing 3D seismic structure models with the best resolution ever, there is a severe lack of proper methodology to UQ in 3D Earth imaging. In the last ten years, new horizons have opened up in earth structure imaging, with major developments in computational power as well as the advent of new numerical and mathematical methods in the disparate fields of the physics of wave propagation and statistical sciences. LANL is the ideal institution to nurture the frontiers science of UQ with its remarkable HPC resources combined with world-renowned expertise on 3D modeling for various science areas. We are using the SEM for generating a large database of synthetic seismograms and validate seismic models as well as seismic imaging techniques. We will, in the coming years, combine it with a Bayesian hierarchical modeling approach to probabilistically describe error, so that the latter can be back-projected to estimate event location error. With this type of study we are also paving the way for a more effective integration of science and decision-making.

ACKNOWLEDGEMENTS

We thank Richard Allen for kindly providing us the DNA09 models. Peter Loxley and Yasuyuki Kato provided useful discussion regarding the use of statistics for the purpose of models validation. We also thank Wessel and Smith (1991), the developers of the Generic Mapping Tools software, which we use to create many of the illustrations of our research. Our thanks to M. Wetovsky for editorial assistance.

REFERENCES

Aki, K., A. Christoffersson, and E. S. Husebye (1977). Determination of the three-dimensional seismic structure of the lithosphere, *J. Geophys. Res*. **82,** 277–296.

Dziewonski, A. M., B. H. Hager, and R. J. O'Connell (1977). Large-Scale Heterogeneities in the Lower Mantle, *J. Geophys. Res*. **82**(2), 239–255, doi:10.1029/JB082i002p00239.

Fichtner, A., B. L. N. Kennett, H. Igel, and H-P Bunge (2009). Full seismic waveform tomography for upper-mantle structure in the Australasian region using adjoint methods, *Geophys. J. Int*. **179**, 1703–1725.

Komatitsch, D. and J.-P. Vilotte (1998). The spectral element method: an effective tool to simulate the seismic response of 2D and 3D geological structures, *Bull. Seismol. Soc. Am*. **88**, 368–392.

Komatitsch, D. and J. Tromp (2002). Spectral-element simulations of global seismic wave propagation: II. Three-dimensional models, oceans, rotation and self-gravitation, *Geophys. J. Int*. **150**, 303–318.

Komatitsch, D., J. Ritsema, and J. Tromp (2002). The spectral-element method, Beowulf computing, and global seismology, *Science* **298**, (5599), 1737.

Lekic, V. and B. Romanowicz (2011). Inferring mantle structure by full waveform tomography using the Spectral Element Method, *Geophys. J. Int*. **185**, 799–831, doi: 10.1111/j.1365-246X.2011.04969.x.

Lévêque, J. J., L. Rivera, and G. Wittlinger (1993). On the use of the checkerboard test to assess the resolution of tomographic inversions, *Geophys. J. Int*. **115**, 313–318.

Menke, W. (1989). *Geophysical Data Analysis: Discrete Inverse Theory*, Academic Press.

Obrebski, M., R. M. Allen, M. Xue, and S.-H. Hung (2010). Slab␣ plume interaction beneath the Pacific Northwest, *Geophys. Res. Lett.* **37**, L14305, doi:10.1029/2010GL043489.

Sengupta M.K, and M.N.Toksöz (1977). Three- dimensional model of seismic velocity variation in the Earth's mantle, *Geophys. Res. Lett*. **3,** 84–86.

Tape, C., Q. Liu, A. Maggi, and J. Tromp (2009). Adjoint tomography of the southern California crust, *Science*, **325**(5943), 988.

Tromp, J., C. Tape, and Q. Liu (2005). Seismic tomography, adjoint methods, time-reversal and banana-doughnut kernels, *Geophys. J. Int.* **160**, 195–216.

VanDecar, J.C. and R.S. Crosson (1990). Determination of teleseismic relative phase arrival times using multi-channel cross-correlation and least squares, *Bull. Seismol. Soc. Am*. **80** (1), 150–169.

Wessel, P. and W. H. F. Smith (1991). Free software helps map and display data, EOS, *Trans. Am. Geophys. Union* **72**, 441–445.

Xue, M. and R. M. Allen (2010). Mantle structure beneath the western United States and its implications for convection processes, *J. Geophys. Res*. **115,** B07303, doi:10.1029/2008JB006079.

SEISMIC AND GEOPHYSICAL CHARACTERIZATION OF NORTHERN ASIA

Kevin G. Mackey[1], Hans E. Hartse[2], Daniel R. Burk[1], Kazuya Fujita[1], and Michael E. Pasyanos[3]

Michigan State University[1], Los Alamos National Laboratory[2], and Lawrence Livermore National Laboratory[3]

Sponsored by the National Nuclear Security Administration

Award Nos. DE-AC52-09NA29323[1], DE-AC52-06NA25396[2], and DE-AC52-07NA27344[3]
Proposal No. BAA09-19

ABSTRACT

Over the past year Michigan State University (MSU) and Los Alamos National Laboratory (LANL) undertook a major update of the Eastern Russia Database (ERDB). This effort involved parsing Russian seismicity bulletins into standard database tables, merging origin time, magnitude, arrival, and amplitude information into the existing ERDB, and applying quality-control checks on all data. Bulletins and catalogs parsed were from the following regions: Chukotka, Yakutia, Kamchatka, Kuril Islands, Sakhalin, Amur-Primoria, Baikal , and Altai-Sayan. New bulletins added were primarily from the years 2006-2010. In some cases MSU workers hand-entered information from hard-copy Russian bulletins prior to parsing. The ERDB now holds events through December 31, 2010. New or updated entries include: 81,453 events, 84,444 origin times, 276,448 arrival times, 118,422 phase amplitudes, and 134,671 network magnitudes. Over 1,000 new mining explosions were also added. In total, the ERDB (1960-2010) now holds: 336,571 events, 462,322 origins, and 2,423,448 arrival times.

We are now formally addressing the calibration of seismic stations in northern Asia. Most seismic stations in the region use short period SKM and SM-3 mechanical seismometers that were designed to be used with analog recording systems having a galvanometer and recording to photopaper. During the late 1990s, digital recording systems were paired with these seismometers and established calibration methodologies became invalid and regional networks were left to their own devices to figure new ones out. Across the networks of the Former Soviet Union (FSU), many different digital recording systems have been introduced, with different sample rates, resolution, voltage ranges, amplification, and input impedance, all of which affect the calibration of the seismic station. The problem is apparent after observing data from several networks that operate digital instruments. In particular, we have noted shifts in K-class value determinations. For example, in the past, K-class values for earthquakes along network boundaries were often determined independently by both networks. In the analog era, values were generally consistent to within 0.2 units. In the digital era, the difference is often larger, and sometimes exceeds a full unit. We are developing a calibration system that can be conducted in the field. Our idea is to artificially excite the seismometer mass at different periods, then physically measure displacements of the mass using a laser positioning system. The laser positioning system voltage is recorded on one channel of the Analog to Digital (A/D) converter so that the actual mass position, and thus true displacement, is known. This can then be compared to the output of the seismometer coil to precisely know what mass movement produces what signal on the recorder. This procedure generates a full system calibration curve, which can be converted to poles and zeros, that is sufficient for many analyses.

We are developing an accessible database for our CD archive of continuous and event specific waveforms, which spans approximately 22 digital stations and twelve years. At present, we have transferred to hard disc over 1,700,000 files and 300GB of data, with a considerable amount remaining to process. We expect close to twelve million files representing a terabyte of waveform data within the system when complete, representing many thousands of events. We are modeling our seismic database after other mainstream centers by utilizing the Datascope database structure as found in Antelope 5.1-64. We note that much of the archived waveform data has gross timing errors endemic from the original recording systems. The data does, however, contain an analog representation of the GPS timing marks so it is possible to correct the errors in post-processing. To that end, we are developing a program for a timing validation and correction.

OBJECTIVES

The objectives of this project are to characterize the seismicity and geophysical parameters of northern Asia. This project is a continuation of the long-running cooperative program between MSU, LANL, Lawrence Livermore National Laboratory (LLNL), and several foreign institutes and organizations, primarily in Russia.

RESEARCH ACCOMPLISHED

We continue to expand and quality control both our database on eastern Russian seismicity (Eastern Russia Database, ERDB), as well as our archive of digital waveforms, with the goal of establishing a centralized data source that is accessible, and compatible with major research software packages. We have also focused our efforts in the development of a calibration system for the primary types of sensors operating in eastern Russia, SKMs and SM-3s, and the improvement of SKM sensor output for use with high-impedance input amplifiers to improve signal to noise ratios.

Eastern Russia Database

The Eastern Russia Database now includes events up through December 31, 2010. The primary geographic regions covered by the ERDB include Chukotka, Yakutia, Kamchatka, the Kuril Islands, Sakhalin, Amur-Primoria, Baikal, and Altai-Sayan. The ERDB holds detailed seismic event and phase information, primarily obtained from regional seismic networks via collaborations between Michigan State University, Russian network operators, and LANL researchers. New or updated entries (mostly from 2006-2010) added in this reporting period (Figure 1) include 81,453 event lines, 84,444 origin times, 276, 448 arrivals, 118, 422 amplitudes, and 134,671 magnitudes. Over 1,000 new mining explosions have been added. The ERDB now covers a fifty year period starting in 1960 and contains 336,571 events, 462,322 origin times and coordinates, and 2,423,448 arrivals.

Additional work to update the seismic station tables for the ERDB is ongoing.

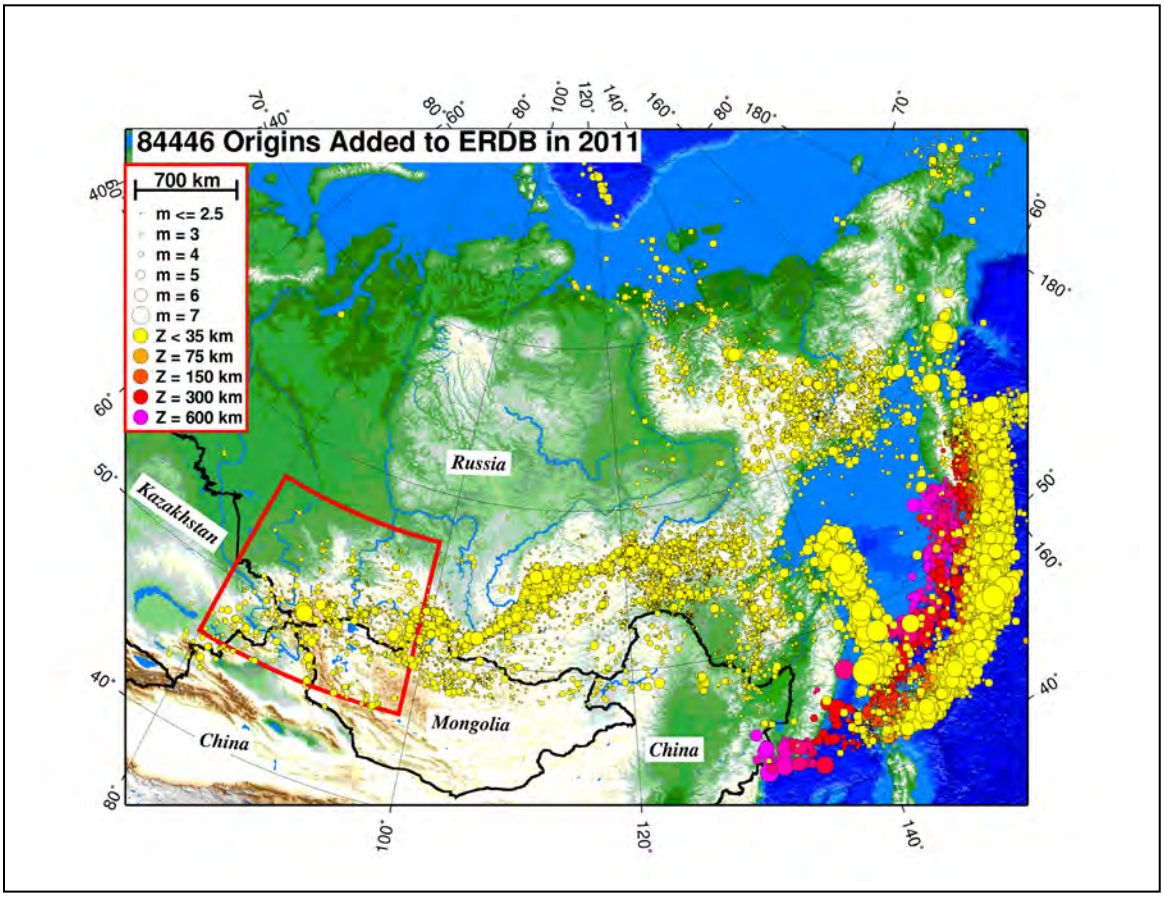


Figure 1. Additions to the ERDB. The red box represents expanded coverage into the Altai-Sayan region.

Waveform Collection

We have collected digitized seismic data from about 50 different stations from1999 - 2012. A good portion of the data resides at MSU in the form of CD-ROMs, which are actively being transferred to redundant hard drives for ease of access and conversion and preservation. The archived waveform collection currently contains well over 300GB and 2 million files, most of which represents a record of approximately 3.6 minutes (a total of 120,000 hours). This total is increasing as we continue the transfer of data from the CD-ROMs. Additional seismograms include event-only waveforms for many thousands of additional events as recorded at stations for which we do not hold continuous data. Additional data is available from the Russian networks and can be accessed as needed via electronic files. The waveform collection generally consists of a four-channel dataset in varying formats, although the majority of the data is formatted in various versions of the Symmetric Research .OUT data format. This data typically contains three channels of broadband (BHN, BHE, BHZ) or short period (SHN, SHE, SHZ) and one channel of digitized GPS timing marks (TIME). For some stations and time periods, the data is continuous with very few gaps, for other stations and times, only specific events of interest are available.

The collection has a considerable number of timing errors that are embedded within the file start time that requires correction during the validation and conversion process. Fortunately, the timing channel can be used to validate and correct these errors. The collection also has issues in terms of station calibration; Many stations in some of the Russian seismic networks, since conversion to from analog to digitized recording, are no longer routinely calibrated, but instead rely upon a standardized instrument response that may not match actual responses. Changes to the station instrumentation, such as gain changes or instrument adjustments have only been sporadically documented, and even then, not necessarily used to update station calibration sheets. Therefore the response of each station must remain suspect until a method of station response validation and correction is developed (see below). In the meantime, some form of “standard” estimate of calibration must be created in order to generate a dataless SEED file for use with other seismic analysis software packages.

The waveform collection remains a large, un-indexed collection of seismic data. To be useful, an efficient method of handling and serving data must be developed. To that end, we have acquired the BRTT Antelope 5.1 software package. We plan to develop a Datascope database that will enable us to index, validate, convert, and serve the EDRB collection as a series of .miniSEED files compatible with mainstream data analysis packages.

Development of Calibration methods for SKM and SM-3

As noted above, the routine calibration and documentation of the seismic stations within northern Asia has proven to be problematic over the past decade. As stations converted from analog to digital recording methods, the calibration methodologies that were used for the galvanometer-based analog systems were no longer applicable. Analog to digital converters were introduced, along with a host of various (and different) amplifier and signal conditioning configurations resulting in input impedance and gain changes that affected the response of the sensor, which was typically designed to operate in conjunction with the lower input impedance of the old, standardized analog system. Unfortunately, the regional networks were left without a calibration methodology for their newly configured digital seismic stations. Compounding the problem was that many different digital recording systems were introduced across the networks of the FSU with no standardization in terms of sample rate, resolution, range, amplification, input impedance, and amplification. These factors are critical when translating the raw counts of digitized signal into sensor output voltage, mass velocity, and ultimately, actual ground motion.

Amplitude deviations are not a problem if the primary objective (as it is for most FSU networks) is to locate the epicenter. However, if one attempts to determine the size and energy of an earthquake, the amplitude becomes of greater importance. In looking at data from the ERDB, it has become apparent that shifts in the K-class value determinations have occurred as they moved from analog into digitial data. When calibrations were regularly conducted in the analog era, a typical deviation of 0.2 units occurred between networks, recent (digital) data now shows a deviation of up to a full unit in K-class.

As we study the digital data within the collection it became apparent that many station calibrations supplied with the data use default parameters, or something to ‘fill in space for the parameter’. This results in a large variation in the quality of the individual station calibration. It is likely that the expertise to create an effective system calibration methodology at the regional level does not exist.

If we are to improve the quality of future data in the network, a modern calibration methodology is required that can be easily understood and implemented at the station level. The system should not require complex mathematics beyond the comprehension of the station engineers or different methodologies or parameters for different digitizers. Ideally, we envision an easy to implement 'full system' calibration where we look at measured ground motion input and relate it directly to digitizer output without excessively worrying about impedance mismatch, amplifier gain settings, etc. A complex field calibration procedure will fail at the local level and will also not be adaptable to equipment upgrades or station changes. To that end, we have begun to develop a simplified full system calibration methodology.

Most of the digital stations operated in conjunction with MSU now employ a version of the Symmetric Research PAR24CH digital seismic recording system, a 24-bit data acquisition system with between four and eight channels. Other similar systems commonly employed are the Baikal series of digitizers and DAS recorders. Most systems are configured to record two channels of horizontal data, one channel of vertical data, and one channel of timing data. The sample rate is software programmable. It is possible that for calibration, one of the channels can be reassigned to record a reference signal, and the sample rate increased in order to ensure a good 10:1 oversampling ratio when exciting the system.

We are developing a procedure to artificially excite the seismometer mass at different periods, then to physically measure displacements of the mass using a laser positioning system (Figure 2). The laser positioning system voltage is then recorded on one channel of the Analog to Digital (A/D) converter so that the actual mass position, and thus true displacement, is known. This displacement can then be compared to the output of the seismometer coil to precisely know what mass movement produces what signal on the recorder. It is also easy to measure the phase shift at different frequencies.

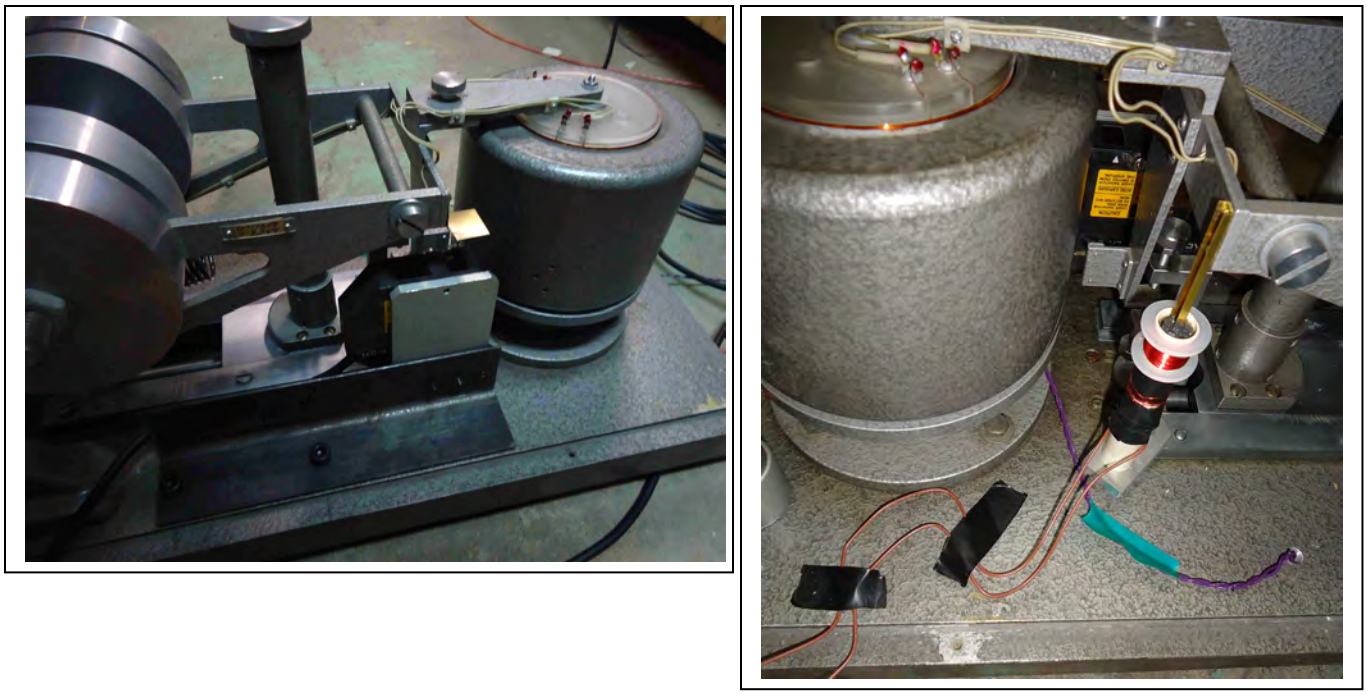


Figure 2. Left - Laser position measurement system mounted on an SKM vertical seismometer. Right – Calibration coil mounted on the same seismometer.

We have an SKM seismometer and a Symmetric Research PAR24CH available at MSU for development of instrumentation, fixture design, and procedures for the calibration of a typical Russian seismic station. The calibration tools will consist of a Keyence LK-031 laser position sensor that can resolve to 1 micron of mass movement, a signal generator, a precision potentiometer for precisely setting the appropriate critical damping resistance, and an add-on calibration coil. Fixturing, in the case of the SKM, is basic and can be fabricated with minimal machining.

A step-by-step method of calibration is actively being developed to determine:

1) The voltage sensitivity (microvolts per count) for each digitized channel.
2) The sensitivity of the laser position sensor to ensure linearity over the measurement range (mV/micron).
3) The resistance necessary for critical damping of the instrument.
4) The position shift of the mass relative to a DC voltage as applied to the calibration coil.
5) The position shift of the mass relative to ground motion amplitude for both SKM and SM-3 seismometers.
6) A signal frequency sweep to the calibration coil over the established frequency response of the sensor in which sensor output is measured in tandem with calibration input voltage and laser position.

By tracking the seismometer output, laser determined displacement, calibration coil input, and relating them to the mass displacement from ground motion, we will be able to create a full system response in terms of signal output versus ground motion, and provide a full station calibration. Figure 3 shows a plot of calibration coil input, measured mass displacement, and seismometer output from our test SKM seismometer. Assuming that no significant instrumentation changes have occurred in the recent past, it may be possible to apply the new calibration to previous un-calibrated data within the collection to yield a better estimate of actual recorded ground motion, and the resulting K-class of seismic events derived from this data.

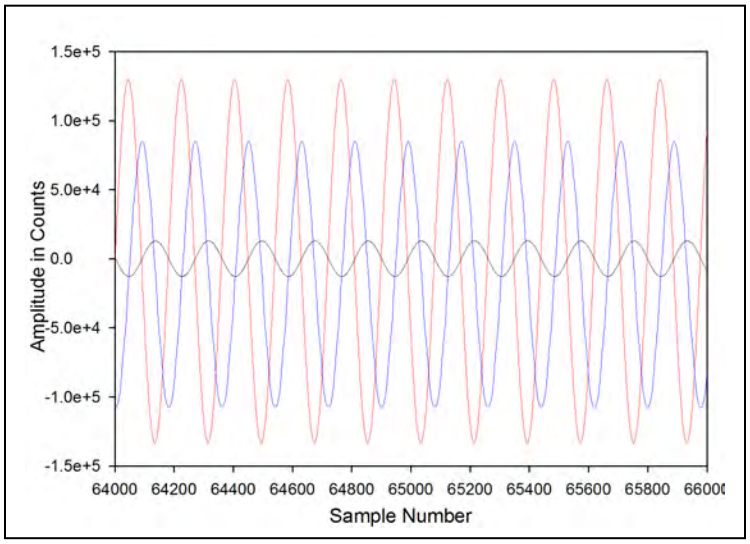


Figure 3. Plot showing the relation of calibration coil input (red), mass displacement (blue) and seismometer output in velocity (black) from our test SKM instrument. The velocity output of the seismometer relative to mass displacement is clear, as is the phase delay relative to the calibration coil input. Note that this plot was generated during systems testing of the Keyence laser positioning instrumentation and operation of the calibration coil and does not represent a meaningful calibration.

Improvement of SKM sensor output for use with high-impedance input amplifiers

The seismic networks of the Former Soviet Union have in-place a considerable number of SKM as well as SM-3 seismometers, which are the backbone instrument of their regional digital systems. These sensors were developed well before the advent of digital data acquisition, as well as before the high-impedance, high-gain instrumentation amplifiers that form the front-end of most modern data acquisition equipment. The SKM in particular, is equipped with a dual-coil mass of 30 awg wire. One of the coils is typically used for damping the instrument whereas the other is typically connected to the input channel of the data acquisition system. Nominal coil resistance is approximately 38 ohms on each coil, and testing indicates that the two coils are identical in terms of winding length. Therefore in the harsh conditions of a Siberian seismic station, it is possible to swap the input wires between the damping coil and the signal coil if you experience noise or other technical problems with the seismometer. Though the result would be uncalibrated with an unknown damping coefficient, at least it would be possible to record some form of ground motion. Unfortunately, the SKM and the SM-3, when installed on modern data acquisition systems, provide a very low signal output relative to actual ground motion. Studies have shown that

most modern seismic recording systems will perform at their optimum when the coil impedance approaches several thousand ohms, typically within the range of 2000 to 4000 ohms (Rogers, 1993).

With this in mind, we have started experimenting with winding replacement coils for the SKM-series of seismometers that use a finer gage wire, which will boost the number of turns within the coil as well as the coil winding resistance. We expect that the re-designed coil will improve the signal to noise ratio resulting in improved sensitivity of the station. This improvement, coupled with an improved calibration methodology, should yield new usefulness to the sensors already emplaced within the field, as well as improve the sensitivity and accuracy of the network.

Improved K-class relations and their determinations

We have been working to better understand the Soviet K-class determinations for the energy of earthquakes. We initially published an explanation of the system for the western audience (Rautian et al, 2007), but have worked to further expand the study. Part of our work was to establish a relation between Me and K, and part was an investigation on how the determination of K-class has changed with the change to digital recording.

We expanded on Rautian et al. (2007) by calculating regressions between Me, as calculated by the US Geological Survey and K-class determinations. Such regressions could only be calculated for a limited number of areas in the FSU due to the small overlap in the magnitude range over which both Me and K are calculated and thus the number of events (N(Me) in Table 1). A reliable regression which could be compared with USGS determinations could only be made for the Kamchatka region (Figure 4).

Table 1. Regressions between K class and magnitudes*

Region	mb	Ms	Me	N(Me)	Me r^2**
Carpathians	5.54 + 0.397 (K-14)	5.92 + 0.661 (K-14)			
Crimea	6.20 + 0.699 (K-14)	Insufficient Data			
Caucasus	5.60 + 0.391 (K-14)	6.02 + 0.782 (K-14)	6.49 + 0.547 (K-14)	8	0.61
N-Caucasus			5.23 + 0.635 (K-14)	3	1.00
Kopetdag	5.53 + 0.467 (K-14)	5.71 + 0.781 (K-14)	5.15 + 0.672 (K-14)	5	0.93
Central Asia	5.53 + 0.449 (K-14)	5.36 + 0.594 (K-14)	5.73 + 0.218 (K-14)	15	0.10
Altai - Sayan	5.47 + 0.482 (K-14)	5.37 + 0.633 (K-14)	5.79 + 0.517 (K-14)	5	0.59
Baikal	5.23 + 0.434 (K-14)	5.54 + 0.828 (K-14)	5.13 + 0.474 (K-14)	5	0.60
Yakutia	5.49 + 0.427 (K-14)	5.55 + 0.539 (K-14)	Insufficient data		
Northeast	5.33 + 0.445 (K-14)	Insufficient Data	Insufficient data		
Amur	5.01 + 0.394 (K-14)	5.10 + 0.755 (K-14)			
Sakhalin	7.25 + 0.669(K_S-14)	7.57+0.773 (K_S-14)	Insufficient data		
Kurile***	6.30 + 0.460(K_S-14)	6.56+0.642 (K_S-14)	6.93 + 0.729 (K-14)	18(39)	0.85
Kamchatka	6.11+ 0.552 (K_F-14)	6.47+0.838 (K_F-14)	6.26 + 0.657 (K-14)	52	0.66

* mb and Ms correlations from Rautian et al. (2007).

** r^2 is Pearson's correlation coefficient squared.

*** see Rautian et al. (2007) for calculation methodology; for N(M_e) the number of bins is given, the number of total data points is in parentheses.

We also investigated the typical periods of waves used for K-class determinations in the FSU. As noted in Rautian et al. (2007), regional networks in the FSU used only the maximum horizontal displacement amplitudes to determine K-class, usually at distances up to about 600 km, since the amplitude of Sg (or Lg) dominates that of Pg; Sg and Lg are not differentiated and simply referred to as Sg in Russian bulletins, even at distances up to 1500 km where Lg is often observed on the craton. These arrivals typically have dominant periods below 2.5 s. Operationally, the typical range of periods measured for determining K-class values today is 0.2 to 1.1 s (Figure 5). For more information on the expansion of our K-class work, please see Bormann et al. (in press).

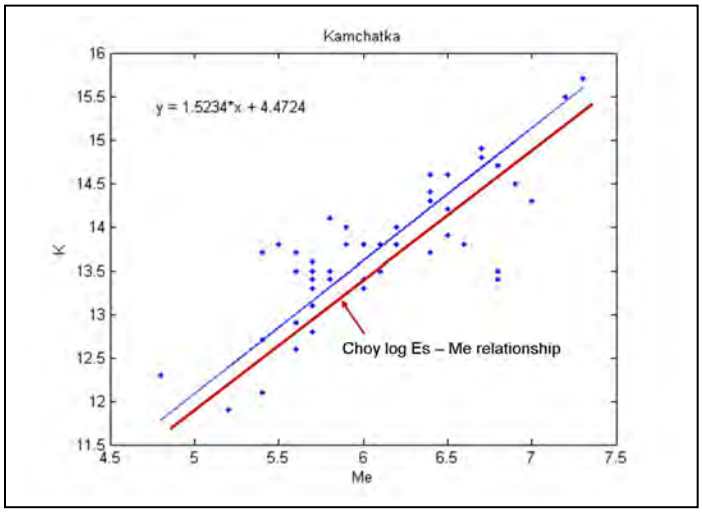


Figure 4. Orthogonal regression relationship between K measured for Kamchatka earthquakes and the related teleseismic E_S -Me(USGS) relationship.

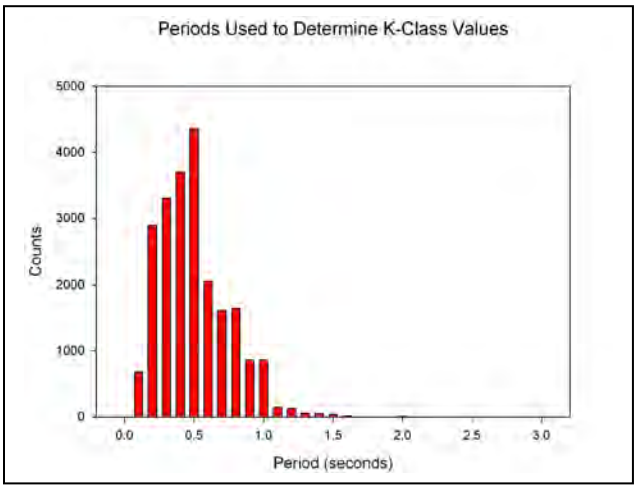


Figure 5. Average histogram of periods at which P and/or S-wave amplitudes were measured by local networks in the FSU for estimating the K-class between 1978 and 2009.

In addition to causing problems with station calibrations as discussed above, the conversion from analog to digital based recording in the former Soviet networks has caused problems in seismogram analysis. Looking at the station specific K-class determinations from station Stekolnyi (International code MGD) in eastern Russia, we can make three temporal based divisions in the periods used (Figure 6). Station Stekolnyi operated SKM instruments and analog recording up through 1994, and the distribution of periods used to calculate K-class is normal with respect to the response of the instrument. From 1994 through September 2004, the seismometers were changed to SM-3s but recording remained analog. Again, considering the response of the instruments, the distribution of periods measured is reasonable. In September 2004, the SM-3 seismometer recording was changed from analog to digital. In this change, there was no significant alteration in the response of the seismometers, but the periods measured (which should represent the period of maximum amplitude) for determining K-class changed significantly and became restricted to a narrow high frequency zone. This seems to be the result of measuring periods (and amplitudes) after filtering data intended to improve the signal to noise ratio. Unfortunately this type of analysis error, which initiated

with digital recording, is difficult to track without intimate knowledge of the analysis procedures of each network. Combined with the lack of calibrations at seismic stations as discussed above, the current determinations of K-class and magnitudes from some regional networks of the Former Soviet Union may not be reliable.

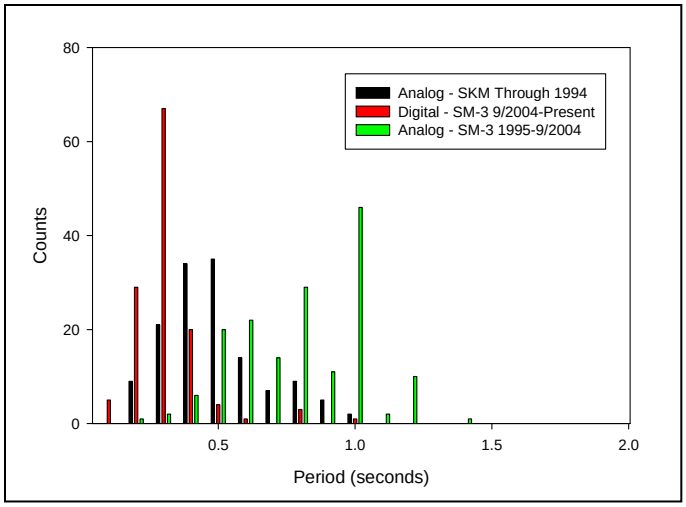


Figure 6. Histogram of periods used to determine K-class values for station Stekolnyi in eastern Russia. The typical period measured changed when seismometer types were changed, which would be expected, as well as when digital recording was introduced, which would not be expected.

Ground Truth Determination of PNE Detonation Sites

In 1969 and 1970, three PNEs were detonated in the Mangyshlak region of western Kazakhstan (Figure 7).

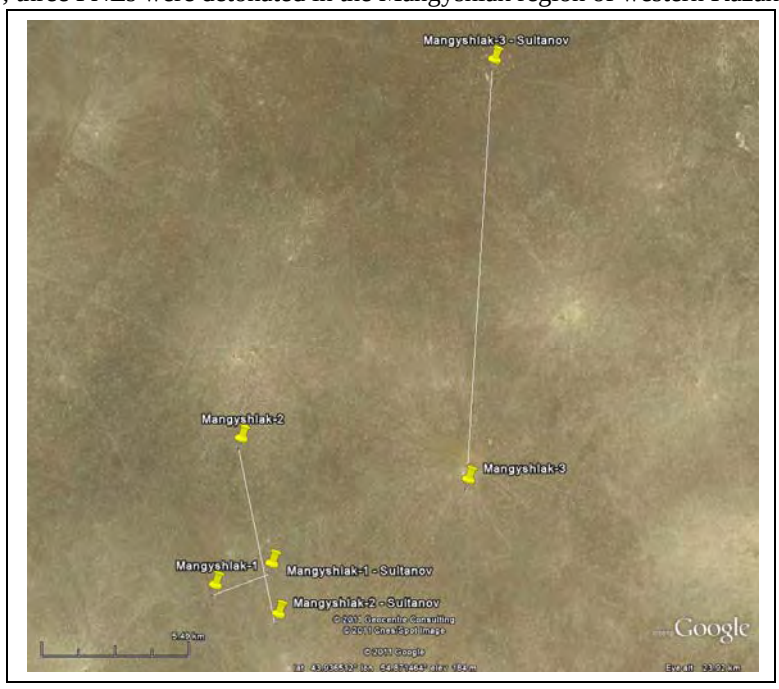


Figure 7. Locations of the Mangyshlak PNEs from Sultanov et al. (1999) and this study. The new locations for Mangyshlak 1 and 2 are identified by collapse craters visible on Google Earth Imagery while Mangyshlak 3 is based on a relative location.

The source parameters for the sequence are published in Sultanov et al. (1999) and the Mangyshlak-1 and -3 explosions are considered GT-1 or better; Mangyshlak-2 is an instrumentally derived location with a presumed GT5-GT10. We have identified the collapse craters of the Mangyshlak-1 and -2 explosions (Figures 8 and 9) on satellite imagery and associated digital topography. Using the collapse craters as calibration points, we determined a new relative location and possible detonation site for the Mangyshlak-3 explosion (Figure 10). Some 300 m to the south and east is a region of disturbed ground which we propose is the true detonation site. The new locations for Mangyshlak-1 and -3 are not within with the GT-1 or better accuracy as reported by Sultanov et al. (1999), with errors being 2.3 and 15.7 km respectively and Mangyshlak-2 is discrepant by about 7 km. Revised coordinates are presented in Table 2.

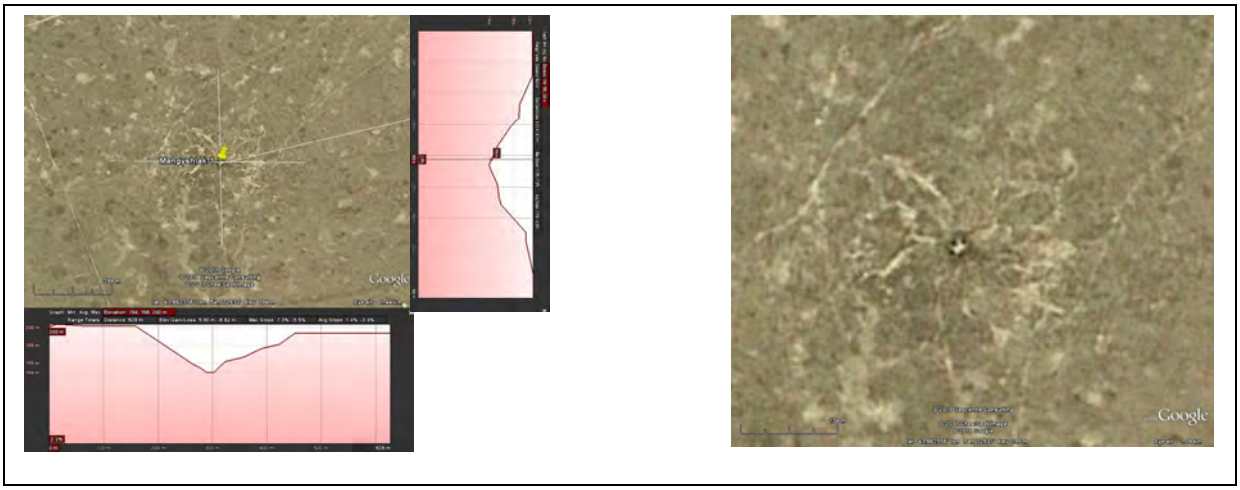


Figure 8. Left – The southern collapse crater structure (Mangyshlak-1) and associated topographic profiles. Right - Close up visuals of the collapse crater. Imagery and topographic profiles from Google Earth.

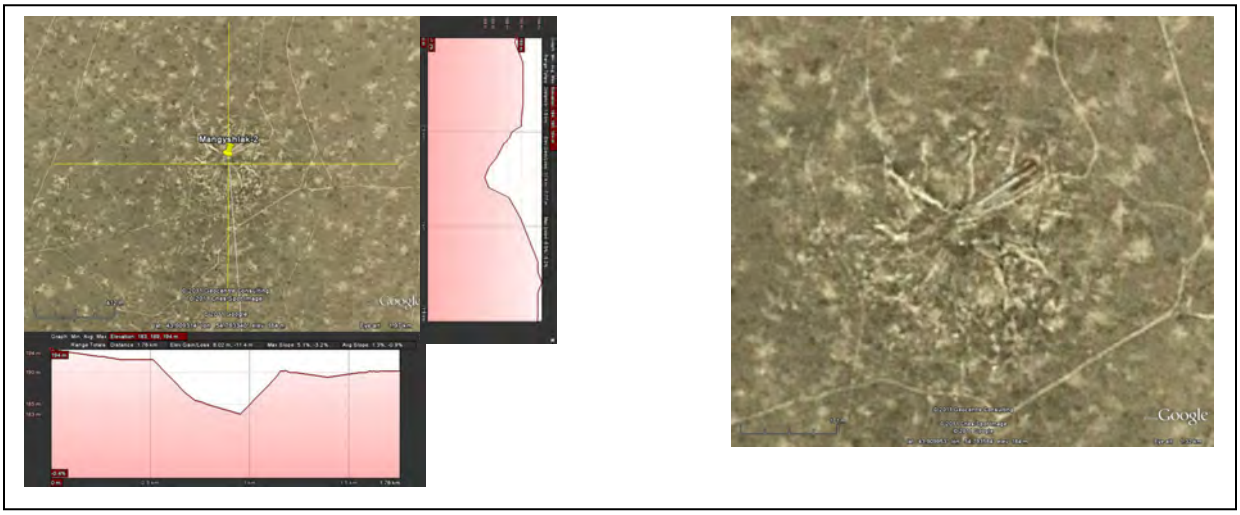


Figure 9. Left – The southern collapse crater structure (Mangyshlak-2) and associated topographic profiles. Right - Close up visuals of the collapse crater. Imagery and topographic profiles from Google Earth.

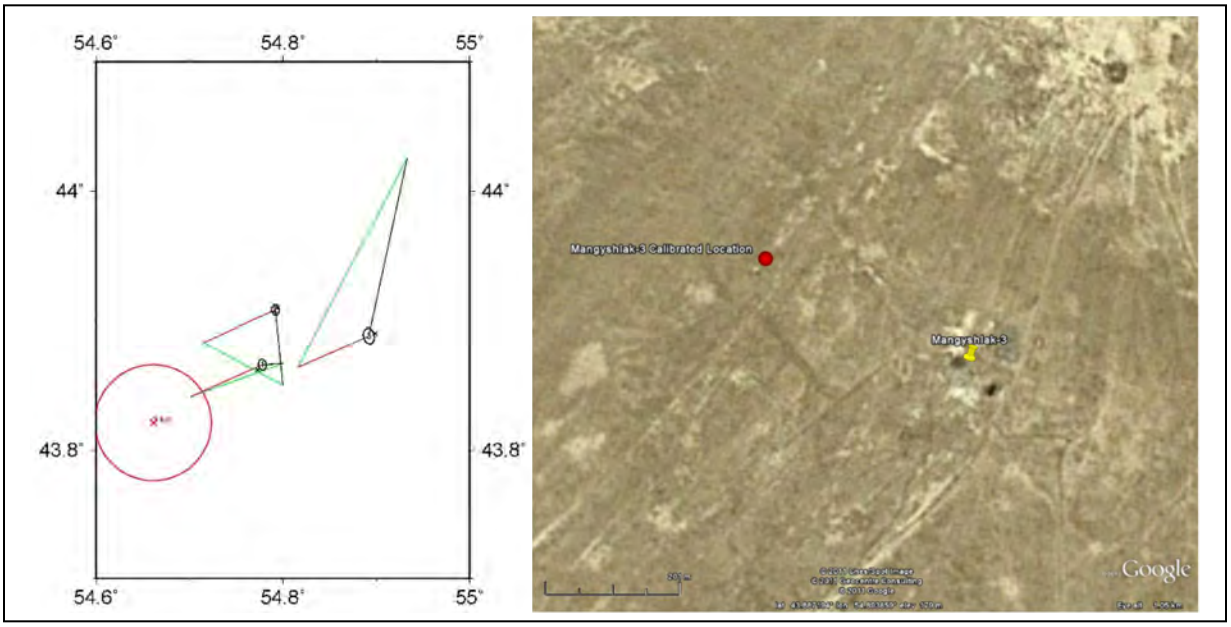


Figure 10. Left - Relocation of the Mangyshlak PNEs. The intersection of the black and green lines are the original Sultanov et al. (1999) locations. The intersection of the green and red lines are the new calculated locations. The red lines represent the static calibration location correction to arrive at the best fit of Mangyshlak 1 and 2 to the collapse craters shown by the x's Final calibrated locations are at the intersection of the red and black lines. The small circles represent the location uncertainty for each event. Right - The Mangyshlak-3 calibrated location is shown by the red dot. We propose that a disturbed area approximately 300m to the east and south, represents the true detonation site of the Mangyshlak 3 PNE.

Table 2. Revised GT locations of the Mangyshlak 1 and 2 PNEs.

PNE (Date)	Proposed Coordinates		Sultanov Coordinates		Difference (km)	Proposed GT
	Latitude (ºN)	Longitude (ºE)	Latitude (ºN)	Longitude (ºE)		
Mangyshlak-1 (06-12-1969)	43.8623	54.7726	43.867	54.800	2.3	GT0
Mangyshlak-2 (12-12-1970)	43.9099	54.7933	43.85	54.80	6.7	GT0
Mangyshlak-3 (12-23-1970)	43.8865	54.8957	44.025	54.933	15.7	GT1

CONCLUSIONS AND RECOMMENDATIONS

This project will improve our knowledge on many geophysical aspects of northern Asia. As summarized here, this is inclusive of seismic characterization, analysis of Peaceful Nuclear Explosion data, improving the GT classification of events, database expansion, and establishing better calibration of seismic stations.

ACKNOWLEDGEMENTS

We thank the Geophysical Survey, Russian Academy of Sciences and its affiliated branches, and the Geophysical Survey, Siberian Branch, Russian Academy of Sciences and its affiliated branches for making this project possible.

We also thank Eric Bergman for determining the relative locations of the three Mangyshlak PNEs.

REFERENCES

Bormann, P., K. Fujita, K. G. Mackey, and A. Gusev, in press. The Russian K-class system, its relationships to magnitudes and its potential for future development and application, Information Sheet 3.7, in P. Borman (editor), *IASPEI New Manual of Seismological Observatory Practice (NMSOP-2, 2nd Web Edition)*: GFZ German Research Centre for Geosciences, Potsdam; http://nmsop.gfz-potsdam.de; DOI: 10.2312/GFZ.NMSOP-2 urn:nbn:de:kobv:b103-NMSOP-2.

Rautian, T., Khalturin, V., Fujita, K., Mackey, K., and Kendall, A. (2007). Origins and methodology of the Russian energy K-class system and its relationship to magnitude scales: *Seismol. Res. Lett.* **78**, 579–590.

Rogers, P. W. (1993). Maximizing the signal-to-noise ratio of the electromagnetic seismometer: The optimum coil resistance, amplifier characteristics, and circuit, *Bull. Seismol. Soc. Am.* **83**, 561–582.

Sultanov, D. D., J. R. Murphy, and K. D. Rubinstein (1999). A seismic source summary for Soviet peaceful nuclear explosions, *Bull. Seismol. Soc. Am.* **89**, 640–647.

TRANSITIONING THE CODA METHODOLOGY TO FULL 2-D FOR P AND S CODAS

Kevin M. Mayeda[1] , William Scott Phillips[2], Charlotte A. Rowe[2], Michael E. Pasyanos[3], Rengin M. Gök[3], and William R. Walter[3]

Weston Geophysical Corporation[1], Los Alamos National Laboratory[2], Lawrence Livermore National Laboratory[3]

Sponsored by the Air Force Research Laboratory

Award Nos. FA9453-10-C-0255 and DE-AC52-06NA25396
Proposal No. BAA10-72

ABSTRACT

In limited regions, small-scale 1-D coda calibrations have proven sufficient and yield very low variance spectral estimates but for the broader, increasingly complex regions, it is unfeasible to perform a patch-work of small-scale 1-D calibrations due to lack of stations and events. The project objectives are straightforward and can be broken down into two parts. First, we planned to transition the 1-D coda methodology to a full 2-D capability including both P-coda and S-coda, including the ability to account for frequency-dependent phase blockage, as well as 2-D variations in peak envelope velocity and site-transfer corrections. Second, our goal was to improve upon the way we make amplitude measurements and tie to an absolute scale. This will include improved synthetic envelope functions and fitting, which to date has been overly simplified using a model derived for a homogeneous full-space (i.e., the single-scattering model). 2-D path (Q) corrections are necessary because it was clear that 2-D variations in the *other* coda calibration parameters are significant and their inclusion in the coda method is necessary to significantly reduce variance in broad-area coda calibrations. Specifically, lateral variations in coda shape (envelope decay), peak P and S velocity, including coda type, and site-transfer corrections must be accounted for. Our objective is to improve the regional methodology for both *P*-coda and *S*-coda by upgrading models and transitioning to full 2-D. For example, the parameterization of the synthetic coda envelope shapes has been based on a simplistic single-scattering formulation for a homogeneous full-space. We plan to test formulations that better predict the effects of multiple scattering as well as develop 2-D empirical models. Increasingly, monitoring needs require both local and broad-area regional to far-regional calibration, usually in complex regions where we observe frequency-dependent phase blockage. For example, regions of the Middle East and Central Asia present strong 2-D variations in attenuation, velocity, and phase blockage effects, and we must adjust to the dominant coda type on the fly. The recent North Korean nuclear tests illustrate that even a seemingly simple region requires 2-D corrections for L_g-coda.

OBJECTIVES

The regional shear-wave coda methodology has evolved over time; originally inspired by Aki's (1969) local single-scattering model, the method has undergone some recent modification, but is mostly used under the assumption of 1-D, radially symmetric Earth centered on each station. The methodology has had great success at local and near-regional distances for simple regions, for crustal *S* transitioning to L_g coda types, and at longer distances for small source regions such as test sites and aftershock zones, using codas associated with *P*, S_n or L_g, depending on the dominant coda type for each individual path. Despite recent successes in small-scale 1-D coda calibrations, there are a number of reasons to make significant enhancements to the coda methodology to encompass laterally complex regions. The use of the 1-D coda is effective in small regions; however, there is a need to extend to the broader regions which have larger lateral complexity. Regions that have been calibrated under the 1-D assumption (Mayeda et al., 2003) have either been small and/or uniformly complicated (e.g., Yellow Sea/Korean Peninsula (YSKP), Kuwait, eastern Mediterranean, northern Italy, Northern California) or broad regions that are more or less uniform (e.g., European Arctic, Turkey, South Africa). In each of the above-mentioned cases, we recognize that performance was limited mostly by oversimplified parameterization and that better results could have been obtained. For example in the YSKP region, calibration to the east of the peninsula requires completely different velocity, coda shape, and attenuation corrections because the path is dominated by oceanic S_n propagation, whereas the YSKP is comprised of L_g continental propagation. In fact, the recent North Korean tests illustrate this point as we found partial blockage for paths towards the south because of short (but significant) propagation through the oceanic crust that reduced broadband amplitudes by nearly a factor of two-to-three on the L_g coda. Such effects in other areas of low crustal Q and Lg blockage are critical for yield estimation For example, Turkey is geophysically complicated, but for lower frequencies, between 0.05 and ~1 Hz, the whole country can be treated as if it were homogeneous (e.g., Eken et al., 2004). However for the higher frequencies, 2-D corrections are required for path corrections, envelope shapes (due to varying S_n and L_g levels, and subsequent coda) and peak envelope velocity.

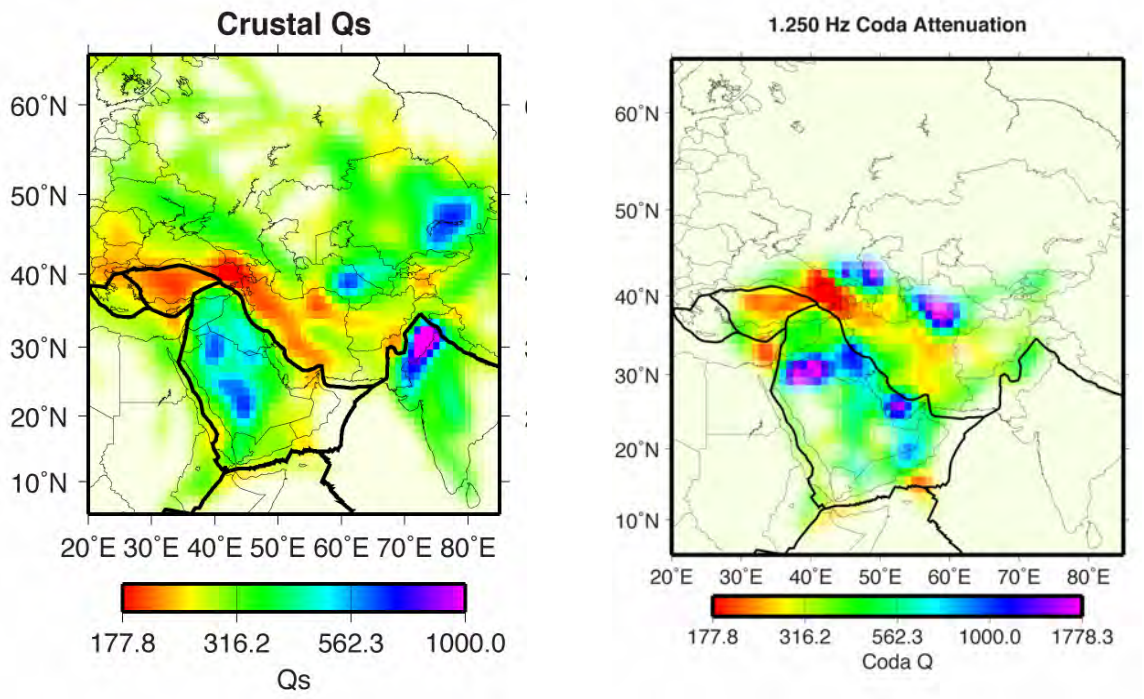


Figure 1. A comparison of crustal *Qs* in the 1-2-Hz passband from the tomography of direct phase amplitudes (left) to *Q* of coda envelope amplitudes (right). The maps are extremely similar, although the absolute *Q* levels are different. The crustal *Qs* maps are primarily sensitive to the amplitudes of *Lg* phases, while the coda maps in this frequency are primarily sensitive to *Lg*-coda.

With regard to Asia and the Middle East, we are also faced with mixing of phase types in addition to strong lateral changes in attenuation. We need to improve the coda method so that it is general enough to handle any region, including those that have lateral changes in phase type and/or blockage. This will require enhancing all aspects of coda calibration to full 2-D. Figure 1 illustrates that both direct Lg and coda attenuation appear to share a similar trend, though their absolute levels are different. This is encouraging because there might be a way to use 2-D direct Lg attenuation as a surrogate for 2-D coda attenuation.

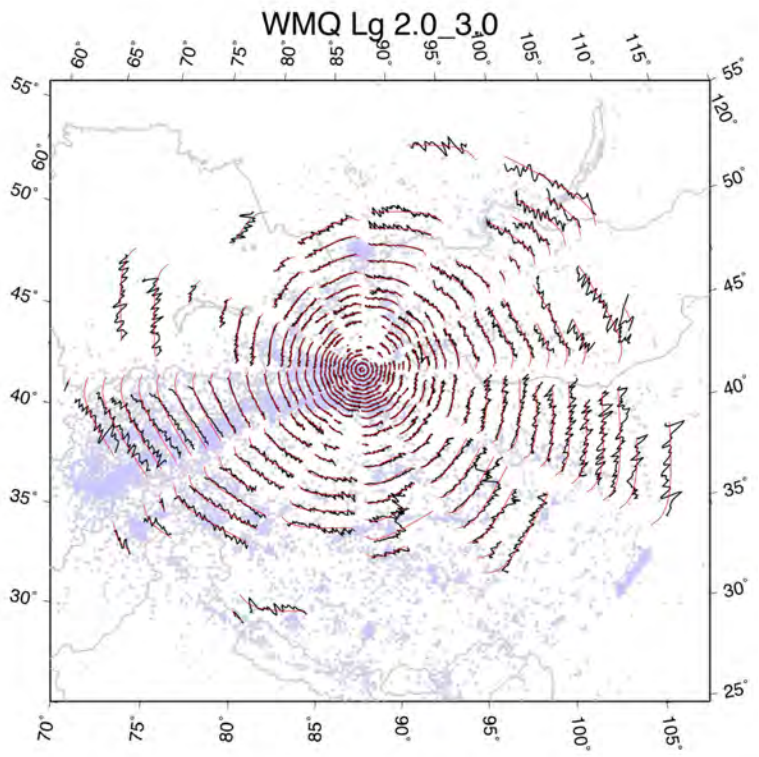


Figure 2. Radially and distant dependent envelopes are shown for station WMQ. Black envelopes are the result of stacking in bins and the red lines are synthetic fits. This region is particularly complicated and highlights the need for 2-D coda calibration.

In addition to spatial Q variation shown in Figure 1, in Figure 2 above we show 2.0-3.0-Hz coda stacks for station WMQ as a function of both distance and azimuth. Stacking was performed for events in azimuth-distance bins, and results are plotted at each bin center. Codas are plotted in polar format with time increasing tangentially in the CCW direction, and amplitude increasing radially inward. Axes not shown. Fits for a distance dependent coda shape model for broad area Asia are plotted in red. Event distribution is shown in the background. Note the smooth stacks in areas of high event density. 2-D variations can be seen in the model fits. Tien Shan coda are shallower than the model predicts, thus experience lower attenuation, possibly due to influence of the Tarim basin and Kazakh platform. Codas from the southeast are steeper than the model, reflecting higher attenuation along those azimuths.

The motivation for making a change to the methodology is quite simple. First, regions of monitoring interest are rarely tectonically simple and in fact, most appear to require 2-D corrections for velocity, path, and envelope function. Figure 3 shows a result of coda wave *Q* for central Asia (*Q* from amplitude decrease with distance, rather than temporal decay of coda) and illustrates the strong lateral changes that need to be accounted for. The partial blockage for paths from the Korean test can be seen in the *Q* map, although the smoothness enforced on this large-scale result decreases its effectiveness for such short paths.

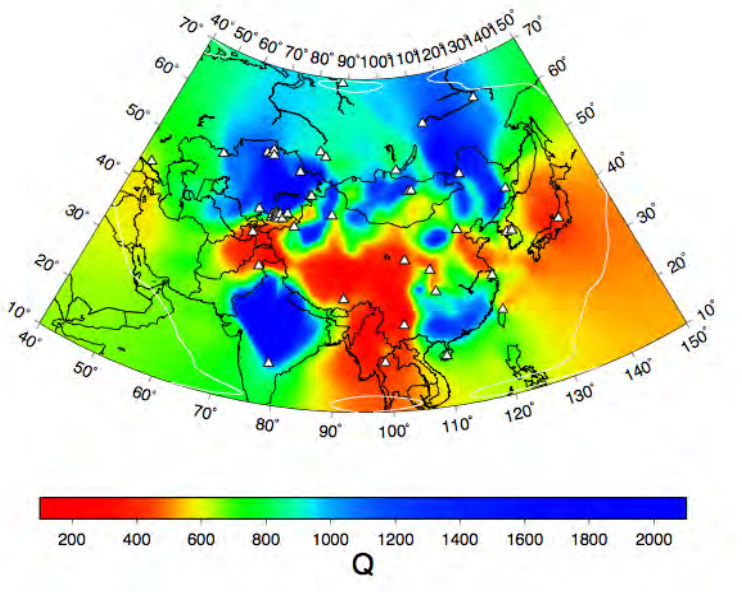


Figure 3. Coda wave apparent *Q* for central Asia for the 0.7-1.0 Hz band. This 2-D inversion was performed over a very broad region and emphasizes the need for 2-D path corrections. Stations are represented by triangles and a liberal model error (1/*Q*) indicating raypath coverage is represented by the white contour. *Q* becomes poorly resolved as the coverage contour is approached. Note: Coda wave apparent Q is not to be confused with coda Q as defined by Aki (1969).

Finally, using a data set of 85 narrowband envelopes at a single station in the Hindu Kush region, we show a first attempt at cross correlation to look for similarities and differences in the envelope shapes that might help us identify (quantitatively) spatial variations.

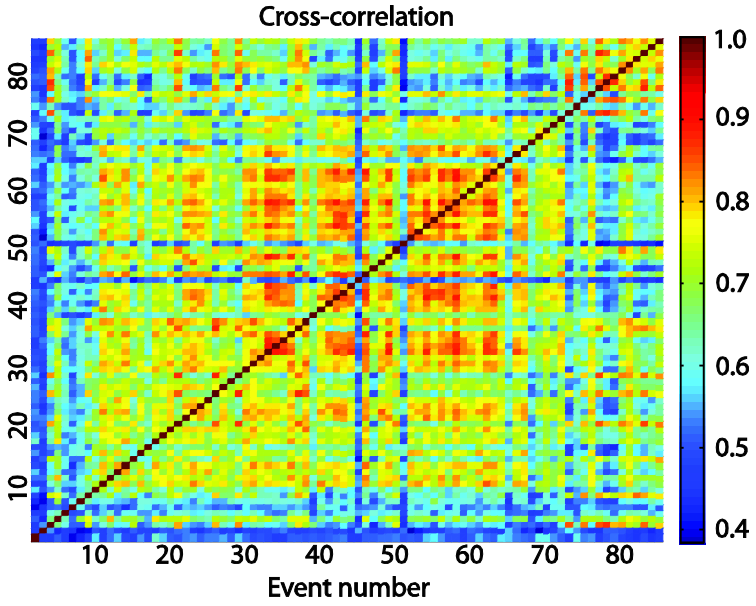


Figure 4. A cross-correlation on a suite of 85 waveforms and generated a correlation matrix of each envelope correlated with every other envelope. The color bar at the right shows the cross-correlation value achieved. Raw envelope correlation came back with almost all values of near to 1.0. This is likely due to the envelope shapes being dominated by the quasi-triangular decay function that is very similar among all events, irrespective of the details contained in the envelope.

CONCLUSIONS AND RECOMMENDATIONS

Aside from some preliminary project planning and cross correlation tests completed during this current year, we summarize our project tasks. Our plan is to improve the coda methodology by upgrading models and transitioning to full 2-D for both *P*-coda and *S*-codas. For example, the parameterization of the synthetic envelopes has been based on a simplistic single-scattering formulation for a homogeneous full-space. We plan on testing multiple scattering formulations as well as developing other empirical models. In addition, *ad-hoc* 1-D path corrections were developed, mostly because the regions of study were relatively small and/or had P_n-codas, S_n-codas or L_g-codas, but not a mixture. Increasingly however, monitoring needs require both local and broad-area regional to far-regional calibration, usually in complex regions where we observe frequency-dependent phase blockage.

We are leveraging existing data holdings at both institutions and also use new results that stem from local background coda models, earthquake source scaling studies, and more sophisticated scattering models in the literature.

The following lists our planned tasks for this project.

1) Evaluate error improvement when we account for 2-D variations in coda type for both *P* and *S*-codas. This will involve developing and testing methods that account for multiple coda types in 2-D sense.

2) Evaluate error improvement when we change from 1-D to 2-D for peak envelope velocity. This will initially involve a 1-D background model of peak velocity, then using 2-D corrections that are obtained either through a 2-D tomography or station-centric lookup table. We will evaluate both approaches and make recommendations based on error.

3) Evaluate error improvement when we change from 1-D to 2-D for envelope shape. Again, we will have a 1-D background model, then test tomography and station-centric lookup methods for exponential decay (*b*) and spreading terms that describe coda shape. This is similar to what we plan to do for peak envelope velocity in (2).

4) Evaluate advanced 1-D models for envelope shape that account for multiple scattering or shifts to mantle coda with increased lapse time. There are a number of theoretical formulations in the literature that model scattering mean-free path changing as a function of depth as well as multiple scattering models in 1-D varying velocity structure.

5) Blend 2-D calibrations for *P* and *S*-coda from central and east Asia networks with Middle East calibrations. Our goal is to have a seamless calibration that is consistent with Knowledge Base deliveries from one year to the next and allows for re-calibration when new stations and waveform data become available.

6) Evaluate error improvement transitioning from 1-D to 2-D coda transfer function corrections (i.e., empirical Green's function). We will test tomography methods that invert for source-region specific transfer functions. For example, the *P*-to-coda and *S*-to-coda transfer functions may be region-specific due to crustal structural variations (e.g., impedance contrast and scattering efficiency differences from one source region to the next).

7) Evaluate error improvement using theoretical source models as calibration events versus Empirical Green's Function approach outlined in Mayeda et al., (2003).

REFERENCES:

Aki, K. (1969). Analysis of the seismic coda of local earthquakes as scattered waves, *J. Geophys. Res*. **74**, 615–631.

Eken, T., K. Mayeda, A. Hofstetter, R. Gök, G. Örgülü and N. Turkelli (2004). An application of the coda methodology for moment-rate spectra using broadband stations in Turkey, *Geophys. Res. Lett*. **31**, 11, L11609.

Mayeda, K., A. Hofstetter, J.L. O'Boyle, and W.R. Walter (2003). Stable and transportable regional magnitudes based on coda-derived moment-rate spectra, *BSSA*, **93**, 224–239.

DEVELOPING REGIONALIZED MODELS OF LITHOSPHERIC THICKNESS AND VELOCITY STRUCTURE ACROSS EURASIA AND THE MIDDLE EAST FROM JOINTLY INVERTING P-WAVE AND S-WAVE RECEIVER FUNCTIONS WITH RAYLEIGH WAVE GROUP AND PHASE VELOCITIES

Andrew A. Nyblade[1], Jordi Julià[1], Eric M. Matzel[2], Andriamiranto H. Raveloson[1], and Arthur J. Rodgers[2]

Penn State University[1] and Lawrence Livermore National Laboratory[2]

Sponsored by the National Nuclear Security Administration

Award Nos. DE-AC52-09NA29322[1] and DE-AC52-07NA27344[2]
Proposal No. BAA09-13

ABSTRACT

The main goal of this project is to develop models of lithospheric velocity structure for Eurasia and the Middle East in order to improve capabilities to accurately predict travel-times for local and regional phases, as well as travel-times for body-waves at upper mantle triplication distances. Velocity models of the lithosphere are not only key for accurately modeling travel-times, but also surface-wave dispersion velocities and full waveforms at regional (2º-15º) and far-regional (15º-25º) distances. The models are being developed following a two-step approach: first, 1-D velocity models for select broadband stations are obtained by jointly inverting P- and S-wave receiver functions and fundamental-mode group and phase dispersion velocities; second, regionalized velocity models are constructed by combining the 1-D joint inversion models within UNIFIED/Western Eurasia and North Africa (WENA) regions and validated through regional waveform modeling. We expect the velocity models will also help inform and strengthen ongoing and future efforts to develop 3-D velocity models for Eurasia and the Middle East, assist in obtaining model-based predictions where no empirical data are available, and improve event locations in regions with sparse network coverage.

So far, we have obtained a total of 69 joint inversion models in Eurasia and the Middle East: 35 for Europe, 10 for the Middle East, and 24 for Asia. To develop these models we have considered permanent broadband stations with open access, and with waveforms archived at the Data Management Center (DMC) of the Incorporated Research Institutes for Seismology (IRIS). The station distribution is quite uneven among the UNIFIED/WENA regions, and the selected stations have been complemented with open stations archived at other data centers when available. P-wave receiver functions have been computed for all the selected stations at overlapping frequency bands of $f < 0.5$ Hz and $f < 1.25$ Hz, totaling 78,267 in the low-frequency band and 80,218 in the high-frequency band. S-wave receiver functions have been computed for $f < 0.5$ Hz, totaling 5,868. And fundamental-mode, Rayleigh-wave, group velocities have been obtained from an independent surface-wave tomography study for Eurasia and North Africa, for periods between 10 and 100 s. The velocity models obtained from the joint inversion of these datasets reveal important differences in lithospheric structure among UNIFIED/WENA regions. In the cratonic regions of eastern Europe no sharp velocity decrease is observed down to ~250 km depth, while in the tectonic regions of western Europe and the Middle East, low-velocity zones in the lithospheric mantle are common. In the cratonic areas of Asia, on the other hand, some stations do display well-defined low-velocity channels within the lithosphere.

We have also developed regionalized velocity models for UNIFIED/WENA regions in Europe and the Middle East. The models have been constructed after combining 1D velocity models from the joint inversion of P- and S-wave receiver functions and dispersion velocities within the regions. The regionalized models have been verified by modeling regional waveforms from the LLNL Seismic Research Database for events with well-determined source parameters and ray-paths predominately within the UNIFIED/WENA region (pure path propagation). The validation exercise reveals that the body-wave portion of the regional waveforms is correctly predicted by the regionalized models, but the surface-wave portion requires modification. We are now investigating why models constrained by teleseismic surface-wave dispersion velocities are not capable of predicting regional surface-wave phases and amplitudes.

OBJECTIVES

The main objective of this project is to develop models of lithospheric thickness and velocity structure for a wide variety of tectonic regions throughout Eurasia and the Middle East. The new models will improve NNSA labs abilities to accurately predict travel times for local and regional phases, such as Pg, Pn, Sn and Lg, as well as travel times for body-waves at upper mantle triplication distances. They will also help inform and strengthen ongoing and future efforts to develop 3-D velocity models for Eurasia and the Middle East. Importantly, the new velocity models will assist in obtaining model-based predictions where no empirical data are available (e.g., Flanagan et al., 2006), and in improving locations from sparse networks (e.g., Schultz et al., 1998; Myers and Schultz, 2000).

The new velocity models are being developed following a two-step approach. In the first step, local velocity-depth profiles are obtained by jointly inverting up to 3 different seismic data sets: (i) P-wave receiver functions (PRFs), (ii) S-wave receiver functions (SRFs), and (iii) fundamental-mode Rayleigh-wave group velocities. In the second step, regionalized 1-D velocity models are developed after averaging joint inversion models within tectonic regions of Eurasia and the Middle East. PRFs constrain detailed crust and uppermost mantle velocity variations through S-P travel-times and velocity contrast across discontinuities. SRFs constrain detailed lithospheric mantle structure, including lithospheric thickness, through P-S travel times and velocity contrasts across discontinuities. And surface-wave group velocities constrain large-scale average velocity structure at frequency-dependent depth-ranges across the crust and upper mantle. All three datasets are mainly sensitive to S-wave velocity, and provide complementary sets of constraints that bridge resolution gaps among them. The joint inversion approach integrates those constraints, producing S-wave velocity-depth profiles with the high-resolution details constrained by the receiver functions superimposed to an average background velocity model constrained by the surface-wave dispersion velocities (Julià et al., 2000).

The regionalized models are evaluated through 1-D waveform of waveforms from events with well-determined source parameters (depth, seismic moment, and focal mechanism) and ray-paths predominately within a single geologic/tectonic region. The model validation effort focuses on regions where there is good event-station coverage (i.e., pure path propagation with a region) over a range of local and regional distances and includes an investigation of the misfits between data and synthetics to understand how the regionalized models need to be perturbed to improve the fits in phase and amplitude. These waveforms have sensitivity to crustal and uppermost mantle shear velocity structure through the surface waves. For larger regions we focus on modeling body-waves (Pnl and upper mantle triplication P- and S-waves). Pnl waveforms have sensitivity to crustal P-wave structure through the shear-coupled P-wave (PL) and lithospheric thickness, velocities and velocity gradient through the timing and amplitude of the first-arriving P-wave (Pn). Triplication waveforms have great sensitivity to lithospheric structure through the timing and amplitude of different branches.

The tectonic regions for which regionalized velocity models are being produced are outlined in Figure 1, and correspond to the regions proposed in the UNIFIED model of Pasyanos et al. (2003; 2004). The UNIFIED models were constructed from *a priori* information in the published literature and subdivide Eurasia and the Middle East into tectonically distinct regions, each of which are characterized by multiple sediment, crustal, and upper mantle layers with specified thicknesses, compressional and shear velocities, densities, and attenuation factors (Pasyanos et al., 2003; 2004). Our "regionalized" velocity models will characterize the average structure within the same tectonic regions, and will include estimates of lithospheric thickness, velocity structure of the lithospheric mantle, and the structure of the low-velocity zone beneath the lithospheric lid.

The regionalized velocity models developed for the UNIFIED regions will aid ongoing efforts to develop 3-D velocity models for Eurasia and the Middle East, such as the Seismic Lithosphere Base Model (SLBM). In the SLBM models, each point is parameterized as a crust with variable velocity and thickness over a mantle half-space with a constant sub-Moho velocity and velocity gradient. Because the mantle lithosphere is parameterized as infinitely thick with a constant velocity gradient, the model cannot accurately model rays that penetrate below the lithosphere. As such the current SLBM is limited, and cannot be used for travel time predictions or waveform modeling much beyond a distance of about 12^o. The new models will add the necessary details about the velocity structure of the lithospheric mantle, the thickness of the lithosphere, and the structure of the low velocity zone under the lithosphere to extend prediction and modeling capabilities beyond 12^o.

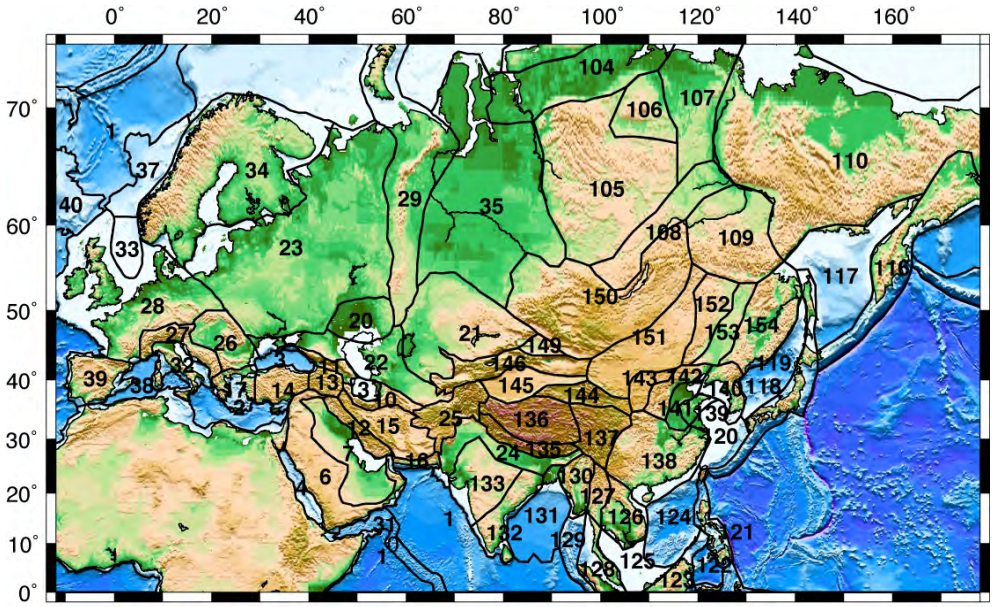


Figure 1.The UNIFIED model, with contributions from both LLNL and LANL. The numbered areas mark tectonically distinct regions defined by Pasyanos et al. (2003; 2004).

RESEARCH ACCOMPLISHED

We have now completed the gathering of teleseismic P- and S-waveforms at open broadband stations in Eurasia and the Middle East as well as the computation of PRFs and SRFs from the collected waveforms. We have also completed the development of joint inversion models for Europe and the Middle East and are now completing the development of joint inversion models for Asia. The first steps of the modeling process involving the joint inversion of PRFs and dispersion measurements have been completed for 10 new stations in Asia and work is underway to add the SRFs to the inversion for those stations. Regionalized models for UNIFIED regions in Europe and the Middle East are being developed from the joint inversion models developed during the first year.

Data gathering

During the third year of application of this project, we completed the gathering of teleseismic P and S waveforms for the computation of PRFs and SRFs in Asia. The dataset consists of 226,584 P-waveforms corresponding to in the $30^o < \Delta < 90^o$ distance range and magnitude above 5.5 and 51,124 S-waveforms corresponding to events in the $60^o < \Delta < 82^o$ distance range and magnitude above 5.7, as recorded at 143 open broadband stations in the region (Figure 2). The waveforms have been downloaded from the IRIS archive using the Standard Order for Data (SOD) utility of Owens et al. (2004).

Fundamental-mode, Rayleigh-wave group velocities in Europe and the Middle East were obtained from the surface-wave tomography study of Pasyanos (2005). In that study, local dispersion curves were obtained for Eurasia, the Middle East, and North Africa by inverting fundamental-mode, Rayleigh-wave group velocities measured along more than 30,000 source-station paths with a conjugate-gradient method with variable smoothness. The resulting surface-wave tomography maps highlight lateral variations across the region for periods between 7 and 100 s with a resolution approaching 1º.

A number of regional events with well-determined source parameters and ray-paths predominately contained within terranes defined in the UNIFIED models have been identified for Europe and the Middle East. The terranes sampled by the 1D joint inversion models include regions number 06, 13, 14, 22, 23, 26, 27, 28, 29, 32, 34 and 39 (Figure 1). The regional waveforms were selected from the LLNL Seismic Research Database and will be utilized to evaluate the average velocity models that will be developed for the geologic/tectonic terrains from the local 1D models.

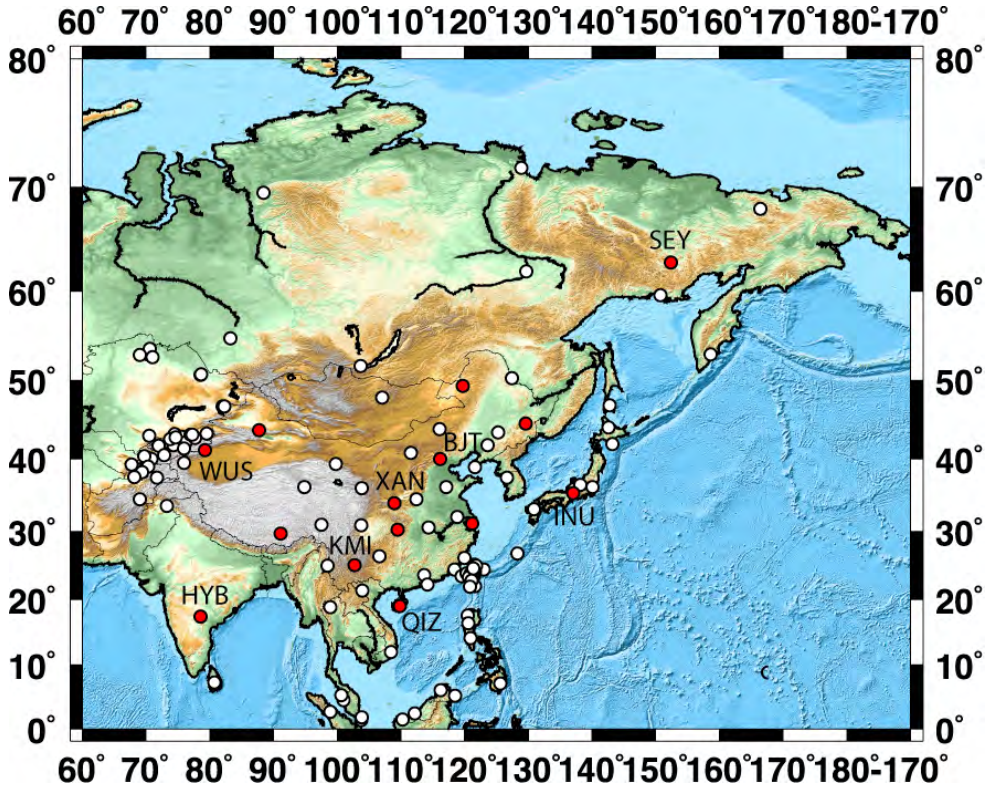


Figure 2. Topographic map of Asia showing the 143 permanent broadband stations (white circles) considered in this work. Some stations overlap and will be combined for a single estimate of the 1D velocity models with the joint inversion procedure. The red circles denote stations for which joint inversion models are being developed.

Receiver Function Computation

During the 3rd year of application we have completed the computation of PRFs for selected permanent broadband stations in Asia (Figure 2). The PRFs were obtained in the ZRT coordinate system by deconvolving the vertical component of the teleseismic P-waveforms from the corresponding radial component, using the iterative time-domain procedure of Ligorría & Ammon (1999) with 500 iterations. PRFs were computed at two overlapping frequency bands of f < 1.2 Hz and f < 0.5 Hz. A first-pass quality control was applied to the PRFs by convolving them back with the corresponding vertical component and comparing predicted and observed radial waveforms. Only those reproducing at least 85% of the original radial component were selected, yielding a total of 9,145 PRFs for the high-frequency band and 9,537 PRFs for the low-frequency band.

We have also completed the computation of SRFs for the same selection of permanent broadband stations. Following standard SRF computation practices (e.g., Hansen et al., 2007), SRFs have been obtained in the local ray-coordinate system after deconvolving the Q component (SV-wave) of teleseismic S-waveforms from the corresponding L component (P-wave). The deconvolution has been performed through the iterative time-domain procedure of Ligorría & Ammon (1999), with 500 iterations, after low-pass filtering below 0.5 Hz. Similar to PRFs, a first-pass quality control has been applied to the computed SRFs by convolving them back with the corresponding L component and comparing predicted and observed waveforms. Only those reproducing at least 85% of the original radial component have been selected, yielding a total of 5,579 SRFs. This number will likely be reduced after visual inspection of the selected SRF waveforms.

The receiver function computation effort (for both PRFs and SRFs) in Eurasia and the Middle East has thus been finalized. Additional stations with open data access from other data centers might be included in the future in order to improve the sampling of UNIFIED regions with little data coverage from the IRIS-Data Management Center database.

Development of Joint Inversion Models

During the 3rd year of application we started the development of 1D S-velocity models from the joint inversion of PRFs, SRFs, and group velocities at broadband stations in Asia. We concentrated on permanent broadband stations with operating times over 5 years in order to develop robust receiver function averages and be able to inspect for azimuthal variations around the station. Using large data sets is especially important for obtaining reliable SRF estimates, as events must be within epicentral distance ranges that are narrower than those for PRFs (Wilson et al., 2006), and the deconvolution process is more unstable.

The joint inversion procedure utilized follows the iterative, linearized approach of Julià et al. (2003). The approach is described by the following system of equations:

$$\begin{bmatrix} \sqrt{\frac{p}{w_s^2}}\, D_s \\ \sqrt{\frac{q}{w_b^2}}\, D_b \\ \sigma\Delta \\ A \end{bmatrix} \vec{m} = \begin{bmatrix} \sqrt{\frac{p}{w_s^2}}\, \vec{r}_s \\ \sqrt{\frac{q}{w_b^2}}\, \vec{r}_b \\ \vec{0} \\ A\,\vec{m}_a \end{bmatrix} + \begin{bmatrix} \sqrt{\frac{p}{w_s^2}}\, D_s \\ \sqrt{\frac{q}{w_b^2}}\, D_b \\ \vec{0} \\ \vec{0} \end{bmatrix} \vec{m}_o$$

where D_s and D_b are partial derivative matrices for the dispersion and the receiver function estimates, respectively, $\mathbf{r}_s$ and $\mathbf{r}_b$ are the corresponding vectors of residuals, w_s^2 and w_b^2 are weights that equalize the data sets, the vector $\mathbf{m}$ contains the velocities of fixed thickness layers overlying a half-space, and $\mathbf{m}_0$ contains an initial estimate for the velocities. The matrix Δ constructs the second difference model and makes the resulting profiles vary smoothly, and the diagonal matrix W contains constraint weights to the *a priori* velocity values $\mathbf{m}_a$. The influence factor p controls the trade-off between fitting the receiver functions and the dispersion curves, and the smoothness parameter σ controls the trade-off between fitting the data and model smoothness. The parameter q=1-p, with $0 \leq p \leq 1$, so that p = 0 means inverting receiver function data only and p = 1 means inverting dispersion data only. The weights w_s^2 and w_b^2 were computed as $N\sigma^2$, where N is the number of data points and σ^2 is the variance of the observations, to account for differences in the number of data points and physical units.

Figure 3 displays an example at station XAN, located in UNIFIED region #143 (Figure 1). PRFs and SRFs were grouped by back-azimuth and ray parameter (or, equivalently, incidence angle) before the inversion, in order to investigate lateral variations in velocity structure around the recording station. The influence factor was given a value of p=0.5, so that each dataset contributes similarly to the combined L2 misfit function, and the smoothness parameter was chosen to provide the highest resolution possible while keeping the inversion stable. Velocities below ~250 km depth were constrained to be PREM-like (Dziewonski and Anderson, 1981) to account for the partial sensitivity of long-period dispersion velocities to deeper structure. The resulting velocity model is simple and displays a 38-40 km thick crust, consisting of a 8-10 km thick upper crust with S-velocity around 3.1 km/s and a ~30 km thick lower crust with uniform S-velocity ~3.7 km/s down to 30 km depth overlying a sharp gradational increase up to 4.5 km/s at Moho depths. The mantle is PREM-like and does not display any velocity decrease suggestive of a lithosphere-asthenosphere boundary (LAB). The inverted model satisfactorily predicts the dispersion velocities and the main features in the receiver function waveforms. Nonetheless, some secondary arrivals in the high-frequency PRFs are not matched and the amplitudes in one of the SRF waveforms are clearly underestimated. We think this is the result of lateral variations of Earth structure around the station, as station XAN is located near the boundaries with UNIFIED regions #144 and #151.

Figure 4 displays a subset of the joint inversion models developed in Asia, corresponding to those under stations operated by the French GEOSCOPE global network and the New China Digital Seismographic Network (CDSN). Crustal thicknesses range between 32 km under station HYB to more than 50 km under station WUS, in good agreement with independent studies (e.g. Chen et al., 2010). The lithospheric structure, as revealed by the computed SRF waveforms, generally includes a velocity drop at depths around 100 km or shallower; this velocity drop might correspond to the lithosphere-asthenosphere boundary (LAB) or some other intra-lithopsheric discontinuity (e.g., Rychert et al., 2009). Under stations HYB and KMI, however, no clear seismic discontinuities are imaged in the lithospheric mantle.

These results contrast with the findings we reported previously for Europe, where consistent differences in lithospheric structure were observed between the East European craton and Phanerozoic Western Europe. The lithosphere under East Europe was characterized by the lack of a sharp velocity decrease above 250 km depth that could mark the location of the LAB, while the lithosphere under Western Europe was rich in seismic discontinuities that could be interpreted as the boundaries of a low velocity channel. These two types of structures are observed for the Asian lithosphere, but their correlation with continental age is less clear.

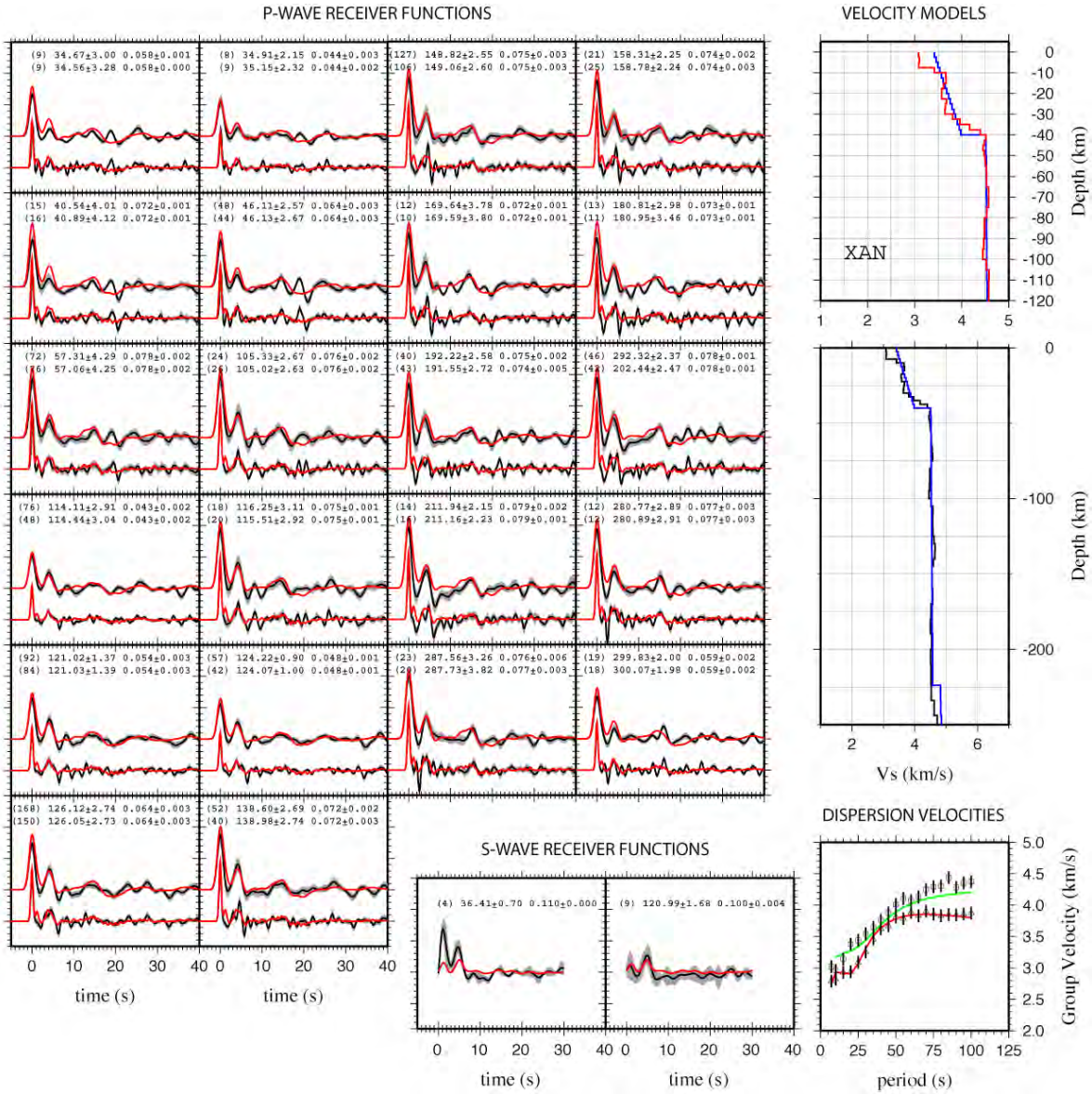


Figure 3. Joint inversion results for station XAN, China. Each PRF and SRF panel contains receiver function averages for the back-azimuth and ray-parameter values noted on top. The number of waveforms contributing to the average stack is noted in parenthesis. Observations and predictions are represented by black and red lines in the receiver function panels, respectively, and triangles and red lines in the group velocity panel, respectively. The velocity models for the crust and lithosphere are shown to the right.

(A)

(B)

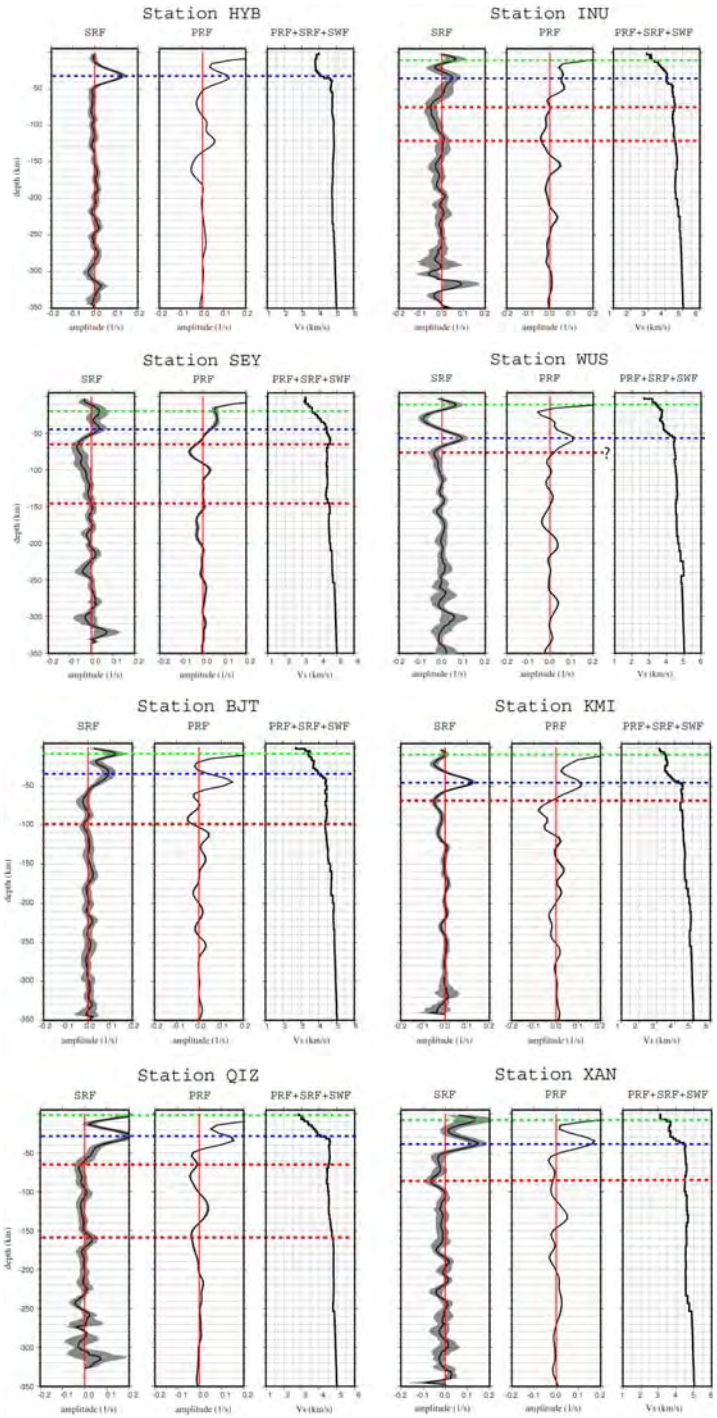


Figure 4. Joint inversion results for GEOSCOPE (A) and China Digital Seismographic Network (B) stations in Asia. The PRF and SRF waveforms have been migrated to depth using the ak135 earth model to allow for a better comparison to the velocity-depth profiles. The models were inverted down to 250 km depth and constrained to be PREM below. The low velocity channel is bounded by the red dotted lines, the Moho is marked by the blue dotted line, and some intra-crustal discontinuities are marked by green dotted lines.

Development of Regionalized Models

We have continued to work on developing regionalized models for the UNIFIED regions (Pasyanos et al., 2003) in Europe and the Middle East by combining the joint inversion models developed during the 1st and 2nd years of application of this project. As a first step, the joint inversion models within each UNIFIED region were tested through modeling of regional waveforms with ray-paths within UNIFIED regions. Figure 5 displays the results for an event with waveforms recorded at stations in and around Turkey (UNIFIED region #14). The joint inversion models do a good job matching the timing and amplitude of the body wave arrivals, but the surface wave trains are more poorly fit. Figure 5 also shows that fitting the full waveforms requires significant changes in the lower crustal structure.

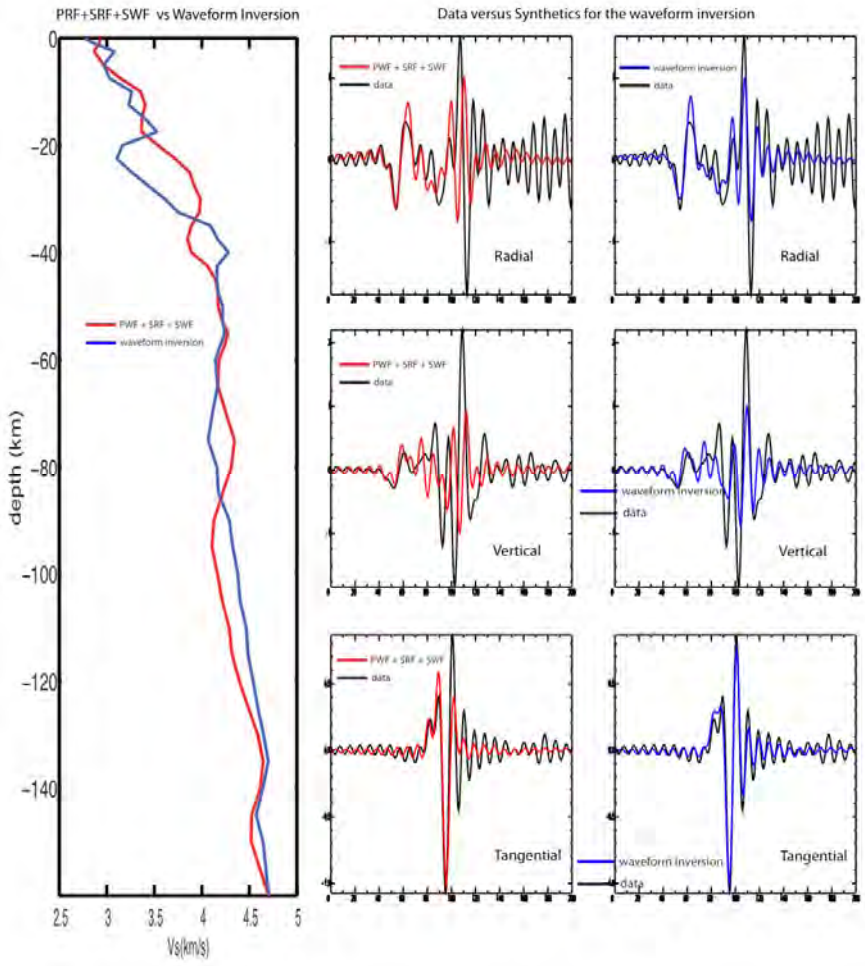


Figure 5. Forward modeling of regional waveforms at station ANTO, in UNIFIED region #14. The velocity models (left) and the corresponding predictions (middle and right) are shown in red for the joint inversion and in blue for the regional modeling. The joint inversion model satisfactorily matches the body-wave train, but needs modification to produce a similar match to the surface-wave train. The synthetic seismograms were computed with the reflectivity method (Randall et al. (1994); Zhu and Rivera, 2002).

CONCLUSIONS AND RECOMMENDATIONS

We have completed the development of 1-D joint inversion models for open broadband stations in Europe and the Middle East, and are working towards completing the development of joint inversion models for open broadband stations in Asia. Overall, we have developed 59 joint inversion models: 35 for Europe, 10 for the Middle East, and

14 for Asia, plus we have joint inversion results using PRFs and dispersion measurements for another 10 stations in Asia. Our results show that, as anticipated, SRFs control the location of seismic discontinuities in the lithospheric mantle, and that the joint inversion models provide a more satisfactory representation of the lithospheric and sub-lithospheric mantle than the existing UNIFIED and/or SLBM velocity models.

The development of new average 1-D models from the joint inversion models for the UNIFIED regions in Eurasia and the Middle East is underway. The first step has been the validation of the joint inversion models through regional waveform modeling. Preliminary results in UNIFIED region #14 have shown that the joint inversion models cannot correctly predict surface-wave amplitudes for regional events. We suspect that crustal and lithospheric heterogeneity within UNIFIED region, which favors distortion of the surface-wave train by multi-pathing effects, is most likely responsible. Average 1-D models can still be developed for surface-wave propagation at low frequencies, but modeling of higher frequencies will likely require accounting for 3-D structures.

ACKNOWLEDGEMENTS

We would like to thank the IRIS DMC and GEOFON Data Center for their role in the archiving and distribution of seismic data utilized for this project.

REFERENCES

Chen, Y.L., F.L. Niu, R.F. Liu, Z.B. Huang, H. Tkalcic, L. Sun, & W. Chan (2010). Crustal structure beneath China from receiver function analysis, *J. Geophys. Res*. **115**, B03307, doi:10.1029/2009JB006386.

Dziewonski, A.M, and D.L. Anderson (1981). Preliminary Reference Earth Model, *Phys. Earth Planet. Inter*. **25**, 297–356.

Flanagan, M., S. Myers, and K. Koper (2006). Regional travel-time uncertainty and seismic location improvement using a three-dimensional a priori velocity model, *EOS Trans. AGU* **87**, S31B-0194.

Hansen, S., A. Rodgers, S. Schwartz, and A. Al-Amri (2007). Imaging ruptured lithosphere beneath the Red Sea and Arabian Peninsula, *Earth Planet. Sci. Lett.* **259**, 256–265.

Julià, J., C.J. Ammon, R.B. Herrmann, and A.M. Correig (2000). Joint inversion of receiver function and surface wave dispersion observations, *Geophys. J. Int.* **143**, 99–112.

Julià, J., C. Ammon, and R. Herrmann (2003). Lithospheric structure of the Arabian Shield from the joint inversion of receiver functions and surface-wave group velocities, *Tectonophysics* **371**, 1–21.

Ligorría, J., and C. Ammon (1999). Poisson's ratio variations of the crust beneath North America, *Seismol. Res. Lett.* **89**, 1395–1400.

Myers, S. and C. Schultz (2000). Improving sparse network seismic location with Bayesian kriging and teleseismically constrained calibration events, *Bull. Seismol. Soc. Am.* **90**, 199–211.

Owens, T.J., H.P. Crotwell, C. Groves, and P. Oliver-Paul (2004). Standing Order for Data, *Seismol. Res. Lett.* **75**, 515–520.

Pasyanos, M., W. Walter, and M. Flanagan (2003). Geophysical models for nuclear explosion monitoring, in *Proceedings of the 25th Seismic Research Review—Nuclear Explosion Monitoring: Building the Knowledge Base,* LA-UR-03-6029, Vol. 1, pp. 125–134.

Pasyanos, M., W. Walter, M. Flanagan, P. Goldstein, and J. Bhattacharyya (2004). Building and testing an a priori geophysical model for western Eurasia and North America, *Pure Appl. Geophys* **161**, 235–281.

Pasyanos, M. (2005). A variable resolution surface wave dispersion study of Eurasia, North Africa, and surrounding regions, *J. Geophys. Res.* **110**, doi: 10.1029/2005JB003749.

Randall, G. (1994), Efficient calculation of complete differential seismograms for laterally homogeneous earth models, *Geophy. J. Int.* **118**, 245–254.

Rychert, C.A. and P.M. Shearer (2009). A global view of the lithosphere-asthenosphere boundary, *Science* **324**, 495–498.

Schultz, C., S. Myers, J. Hipp, and C. Young (1998). Nonstationary Bayesian kriging; a predictive technique to genereate spatial corrections for seismic detection, location, and identification, *Bull. Seismol. Soc. Am.* **88**, 1275–1288.

Wilson, D., D. Angus, J. Ni, and S. Grand (2006). Constraints on the interpretation of *S*-to-*P* receiver functions, *Geophys. J. Int.*, **165**: 969–980.

Zhu, L. and L. Rivera (2002). A note on the dynamic and static displacements from a point source in multi-layered media, *Geophys. J. Int.* **148**, 619–627.

JOINT, NON-LINEAR MODELING OF RECEIVER FUNCTIONS, SURFACE WAVE DISPERSION, AND WAVEFORMS WITH FORMAL ASSESSMENTS OF CONSTRAINTS

Jay Pulliam[1,2], Mrinal K. Sen[2], Mohit Agrawal[1], Utpal Dutta[3], Ranjana Ghosh[1], Frank Sepulveda[1], Rob J. Mellors[4], and Michael E. Pasyanos[4]

Baylor University[1], University of Texas at Austin[2], University of Alaska, Anchorage[3], and Lawrence Livermore National Laboratory[4]

Sponsored by the National Nuclear Security Administration

Award Nos. DE-AC52-09NA29327 and DE-AC52-09NA27344
Proposal No. BAA09-58

ABSTRACT

Our goal is to develop optimal procedures for the use of multiple datasets. Specifically, our objective is to jointly model surface wave dispersion, receiver functions, and characteristics of the waveform that appear in a window around the direct S arrival. Optimization is done using a three part objective function that allows the user to vary both the relative weights of different data types and the norm used to measure data misfit. The algorithm is very general in that the weights can change with iteration, and misfit norms can take different values for the three different parts of the objective function. Note that the same model is used to compute synthetic waveforms, surface wave dispersion and receiver functions. Forward modeling is done using a reflectivity algorithm and optimization is carried out using variant of simulated annealing. The code therefore runs efficiently on multiple processors using MPI routines.

We have coded the algorithm, validated the implementation, and performed synthetic tests to confirm the method's effectiveness and tractability and to demonstrate the usefulness of associated model assessment tools. More recently we conducted a search for shear-coupled PL waveforms among broadband seismic data available to us from the Middle East and discovered that this phase is quite rare in this region. In the past year we focused on developing a general processing tool to produce P-to-S and S-to-P receiver functions, in order to explore the Middle East for receiver functions that are suitable for modeling. Sp (converted at the Mohorovičić discontinuity [Moho]) and SsPmP phases are occasionally prominent and modeling their characteristics, including amplitude and arrival times relative to the direct S phase, can constrain structural models of the Earth's crust and uppermost mantle.

We will show results of both synthetic tests and applications to real broadband data from the region and use assessment tools, including Posterior Probability Distribution (PPD) and model parameter correlation matrices, to show the advantages of joint modeling via forward modeling with simulated annealing. These statistical tools allow us to evaluate the relative strength of constraints placed on model parameters by each type of data in addition to the portions of the model that are well, or poorly, constrained.

OBJECTIVES

Our goal is to develop optimal procedures for the use of multiple datasets. Due to the inherent variability, inconsistency, and peculiarities of disparate datasets and the well-known nonlinearity and non-uniqueness associated with geophysical modeling, such procedures must include methods for evaluating the performance and contribution of each dataset to the final results.

We use quantitative assessment tools and a formal Bayesian approach to explore and evaluate each step of the modeling process, rather than to simply toss all constraints into a simultaneous fitting procedure to find the single solution that satisfies particular criteria. The procedure we propose is best characterized as velocity analysis via optimization; it is analogous to velocity analysis in exploration seismology, rather than "inversion." It provides quantitative error measures of structural parameter estimates that can then be translated to earthquake location errors, and thus guide seismologists toward the most effective and efficient ways to improve model reliability.

Additional goals include efforts to determine the optimal functionals to model in order to provide useful estimates of P and S velocity and density models for a particular locale, optimal weighting schemes for modeling, and to determine optimal pre-processing strategies for identifying and preparing data for modeling.

RESEARCH ACCOMPLISHED

Knowledge of crust and upper mantle velocity structure is essential to locating seismic events and, specifically, for constraining event focal depths. Seismic locations, discriminants, and yield estimates are all affected negatively by errors in seismic velocity models. Accurately assessing and quantitatively describing model errors is a critical component of estimating velocity and attenuation structure and such assessment is especially difficult in nonlinear modeling. We are developing a multi-step modeling procedure for the estimation of crust and upper mantle velocity models using distinct types of regional and teleseismic waveform data.

Our overall approach is to jointly model receiver functions, surface wave dispersion, and windowed portions of waveforms through a forward modeling approach driven by a variant of simulated annealing. Each of these functionals is described below, followed by comments concerning our progress in incorporating them into our multi-objective optimization technique.

Receiver functions. The isolated response of the crust and upper mantle beneath a seismic station that is produced by deconvolving the vertical component of the P wave from the radial component is commonly called a receiver function. Receiver functions tend to be sensitive to changes in seismic velocities, such as discontinuities, but only weakly sensitive to absolute velocities (Julia et al., 2000). Velocity structure obtained through inversion of receiver functions alone is also highly non-unique (Ammon, 1991). Receiver functions have been used to model Earth structure by inversion (Ammon, 1991) or by iterative forward methods, such as grid search (Sandvol et al., 1998), genetic algorithms (Shibutani et al., 1996), simulated annealing (Zhao and Frohlich, 1996), or the neighborhood algorithm of Sambridge (Sambridge, 1999).

We have focused, until recently, on P-to-S receiver functions (which we call PRFs). We have been fairly successful in modeling PRFs, both individually and jointly with surface wave dispersion and windowed waveforms, but have learned, as have others before us, that modeling PRFs alone produces highly non-unique models. Nevertheless, certain characteristics of the model, such as average velocities over portions of the stack and impedance contrasts across certain layers, are constrained by PRFs. Which portions of the stack and which layer impedance contrasts depends on the models themselves. Only layers with strong impedance contrasts can produce significant peaks in the receiver function (although they will not produce significant peaks at all epicentral distances), so the portions of the model that are well-constrained by PRFs are model- and observation-dependent. This points to the conclusion that PRFs are most useful when they are modeled jointly with other functionals that provide constraints on other aspects of the models.

Surface wave dispersion. The speed of propagation of seismic surface waves is a function of the waves' frequency, i.e., the seismic surface waves are dispersive. Put another way, individual harmonic components of the surface wave seismogram (individual modes) propagate over the globe at different speeds. For any given source-receiver pair, one can isolate from the seismogram each harmonic component, and measure the speed between source and receiver. Dispersion can either be characterized by phase velocity (the velocity of an individual peak or trough) or group velocity (which is the velocity of the surface wave energy). Here, we will be considering only group velocities because they are easier to measure (no knowledge of the source phase needed) and can be measured for shorter periods that we will need to sample the crust.

Our results suggest that group velocity surface wave dispersion is sensitive to bulk characteristics, such as thickness of a high-velocity lid/crust and average velocities in the model. Also, the smoothness of the dispersion curve allows us to tailor the weight assigned to its fit in a unique way. Increasing the weight assigned to surface wave dispersion stabilizes the inversion because it pushes the results toward smoother models. Whether or not this is a desirable result is a decision that must be made by the operator.

Windowed portions of waveforms. Phases that arrive near the direct S phase, including Sp (converted at the base of the Moho), SsPmP (reflected once from the topside of the Moho), and shear-coupled PL (SPL) waves, collectively sample the Earth's crust and upper mantle at oblique angles and therefore have the potential to produce an accurate lateral average of structural properties than teleseismic P waves. SPL waves essentially mimic the propagation characteristics of regional PL phases, with the important difference that the number of events available for modeling is often greater for relatively aseismic regions, since sources are located at teleseismic distances.

SPL waves are sensitive to crust and upper mantle structure, including seismic velocity gradients, Vp/Vs, impedance contrast across the Moho, and layer thicknesses (Gangopadhyay et al., 2007). However, SPL waves require a well-established low-velocity zone beneath the crust to propagate efficiently. This appears to be missing beneath the Middle East region, as will be discussed further below. Sp and SsPmP waves require a fairly large impedance contrast across the Moho to have large amplitudes. They do appear across the Middle East but relatively high noise levels render them less than ideal candidates for modeling.

Multi-Objective Optimization for Multiple Data Functionals

Our optimization algorithm is expected to minimize misfit of each of the data functionals using three different objective or cost functions. The process of optimizing systematically and simultaneously a collection of objective functions is called multi-objective optimization (MOO) or vector optimization. An objective function is minimized subject to constraints. In our application, we use standard constraints such as bounds and negativity.

A general objective function allows for different measures of error and varying weights to the datasets. There are at least three fundamental questions that we need to resolve:

- What measures of error do we use?
- Can they be different for various datasets?
- How do we choose the three weights?

In practice, and with noisy data and unmodeled sources of complexity (such as 3D heterogeneity, seismic anisotropy, topography, etc.), these questions do not have simple answers. Weights have to be determined by trial and error. In order to make the relative weighting of functional fits objective and explicit we use the following normalized objective function:

$$\boldsymbol{Error} = 1 - \frac{2\sum \left| \boldsymbol{d}_{\boldsymbol{obs}}^{\boldsymbol{i}} - \boldsymbol{d}_{\boldsymbol{syn}}^{\boldsymbol{i}} \right|^{\boldsymbol{\alpha}}}{\sum \left| \boldsymbol{d}_{\boldsymbol{obs}}^{\boldsymbol{i}} + \boldsymbol{d}_{\boldsymbol{syn}}^{\boldsymbol{i}} \right|^{\boldsymbol{\alpha}} + \sum \left| \boldsymbol{d}_{\boldsymbol{obs}}^{\boldsymbol{i}} - \boldsymbol{d}_{\boldsymbol{syn}}^{\boldsymbol{i}} \right|^{\boldsymbol{\alpha}}}$$

where the sum is taken over all the data points and the parameter α is equivalent to the norm. We initially chose $\alpha=1$ for all three objective functions but experimented with variations with a goal of producing good fits to all data functionals, rather than excellent fits for one or two and lesser fits to others.

Modeling the Middle East

A second goal of our project is to model the crust and upper mantle beneath stations located in the Middle East. To this end we have obtained Rayleigh and Love wave group velocity dispersion curves for selected stations in the region, computed PRFs, and conducted a broad search for shear-coupled PL waves in the region. Figures 1 and 2 summarize modeling results via MOO using teleseismic data recorded at stations DESE and KIV, respectively.

Station DESE. An example of waveform modeling is shown in Figure 1 for station DESE (located in Dese, Ethiopia, Russia, located at 11.12°N, 39.63°E and at 2538 meter elevation), along with assessments. Figure 1a shows, in the leftmost panel, the search bounds (dashed lines), the P-wave receiver function model (green line) from which the search bounds were determined, and the final model determined through optimizations. Variances are indicated by shading. Subsequent panels show results for S-wave velocity, density and Poisson ratio. Layer thickness is also a free parameter and its search range is indicated through the upper and lower depth bounds of the search bounds. Note that the P velocity model that is used nominally as a "starting model" is found from the PRF and is assumed to be proportional to the S velocity model. We have found that allowing Poisson's ratio to serve as a free parameter, along with S-wave velocity, layer thickness, and density, produces a more stable inversion. The P velocity results shown here are computed from the results for the other parameters.

Note also that the initial ("starting") model is used only to establish search bounds; models are drawn from within the search range as guided by temperature schedule set by the user. Final results do not depend on the choice of a first model to be tested. Note that there are numerous instances in which layers are either removed (effectively or entirely) by dramatically reducing the velocity contrast across the boundary or are introduced by dramatically increasing the contrast. Note that the Possion ratio does not vary as strongly as suggested by the highly magnified scale. All values are quite reasonable for the crust and upper mantle. Note also the absence of a clear Moho from these results. A gradient leads from crustal velocities to mantle velocities without an abrupt increase. This offers an explanation for why SPL is not observed in this region, as well as an explanation for fairly weak converted phases.

Figure 1b shows the waveform fits from this optimization run. Note that our objective function measures correlation between synthetics and data, so it serves to prioritize timing of phases and waves over amplitudes. Also, attenuation (Q) is not a free parameter, so amplitude is in principle more difficult to fit than phase. Nevertheless, amplitudes match reasonably well.

To characterize uncertainty in the estimation we perform multiple runs of a variant of Simulated Annealing (called "very fast" simulated annealing or VFSA) with different starting random models and use all the models sampled along to compute approximate marginal PPD and posterior correlation matrices. Figure 1c shows the posterior parameter correlation matrix, one of two critical assessment tools for the MOO procedure. Each axis represents the four free parameters (Poission ratio, S-velocity, layer thickness, and density) for each layer. For example, "40" represents density for layer 10. Colors indicate correlation on a scale of -1 (blue), representing perfect anti-correlation, to 1 (red), represent perfect correlation. Values that fall on the diagonal represent auto-correlations and should all have values of "1". If our procedure were able to resolve each parameter independently, all off-diagonal values would be zero (green). This is not the case—nor will it ever be for inversions of real data for the real Earth—but this tool allows us to examine trade-offs, particularly, between parameters in the same, and in different, layers. It can serve as a guide to the confidence we should have in our result as we address the critical questions: "Have we successfully modeled the structure beneath this station?" and "Can we move on to the next location?" Note also that correlation matrices, such as this one, are symmetric so, only one half—divided by the auto-correlation diagonal—need be plotted.

Figure 1d shows the marginal PPD for the S-wave velocity beneath station DESE for this run. The PPD plot offers a visual guide to the confidence we should have in the model we retrieved for each parameter. Each depth interval shows the probability of S-velocity values in that layer. Only colored portions were sampled. It is possible that the true velocity lies in the white portion; we had to limit the search range in order to pose a tractable problem. Ideally the distribution for the parameter should be single-valued and highly peaked. The least satisfactory result would be one in which the probability is evenly distributed across the range of sampled values, meaning our data impose no constraint on (and therefore we have no idea of) the parameter's true value in that depth range. Multiple peaks reveal the nature of the inverse problem in this case: that there are multiple local solutions. Ideally one of the solutions should offer a clear global minimum; it would then be our preferred solution. Regardless, a PPD plot such as the one in Figure 1d allows us to characterize the nature of the problem, whether it is a simple or complex problem. This characterization can not only help us address the questions posed in the previous paragraph but can also provide guidance as to what type of data might be helpful in resolving the ambiguities that are identified here. In the case of

station DESE, for example, data that are sensitive to the shallowest structure are needed to resolve the ambiguity posed by two peaks for the S-velocity, and data that are sensitive to the depth range 30-40 km are needed to resolve ambiguities in those layers. For the latter issue, observations of SPL, if they could be found, would be helpful. For the shallowest layers, it is unlikely any teleseismic data would resolve this issue, but active-source studies conducted locally could provide hard constraints. Lastly, note that the search bounds for the depth range 50-60 km should be expanded to the left and the modeling should be run again. These adjustments are examples of the sort of guidance that the PPD can offer.

Station KIV. We applied our MOO methodology to data available from the IRIS Data Management Center for station KIV (Kislovodosk, Russia, located at 43.96°N, 42.69°E and at 1054 meter elevation). The waveform windowed about the S arrival for three component seismograms, surface wave dispersion and receiver function are generated from the collected data following a sequence of operations that include filtering the data within the desired frequency range, rotation to great-circle path, deconvolving vertical component from the radial component (for the P-wave receiver function), etc. Model search parameters are Poisson ratio, Vs, layer thickness and density for twenty-three layers.

Figure 2 shows the result from a joint inversion in which all three weights are equal. Figures 2a-c demonstrate that observed datasets match the synthetics well. The model produced (Figure 2d) from our joint inversion method shows a low velocity zone at ~10 km depth and the crust-mantle boundary (Moho) is at 40 km depth. We have also compared models from joint inversions with the models obtained separately from inversion of receiver function and surface wave. Figure 2e shows the posterior probability density distribution for the S-wave velocity.

New Directions

Unfortunately, our search for SPL in the Middle East has not been very productive, as noted previously. SPL requires a well-established low velocity zone beneath a lithospheric or crustal lid in order to propagate and the correct structure apparently does not exist in the Middle East region. Further, crustal phases such as Sp and SsPmP are also either rare, emergent, or noisy in the cases we have found, so we have focused our efforts on producing, and ultimately modeling, S-to-P receiver functions (SRFs) for selected event-station pairs for which the signal-to-noise ratios are acceptably high.

SRFs are similar to PRFs in that the represent the band-limited seismic response of a stack of layers but differ in several important ways. First, S waves, and the converted phases they produce, arrive well after the initial P-wave arrivals and associated coda, so signal-to-noise ratios are usually lower for SRFs than for PRFs. Further, useful SRFs are limited to a more restricted range of epicentral distances. However, on the positive side, SRFs are relatively free of multiple reflections, making it easier to identify for studying seismic discontinuities at lithospheric depths.

However, for teleseismic S waves, incidence angles become critical for certain epicentral distances, so there are no S-to-P wave conversions for those distances. Synthetics computed for standard Earth models reveal that S-to-P conversions should be most efficient in the 55°-100° distance range, although the absolute value of the transmission coefficients increases with increasing slowness (decreasing epicentral distance). This presents an opportunity in our case because the most common source-receiver pairs we have found in the Middle East (for intermediate and deep events, which are the cleanest and most conducive to modeling) occur in the range 60°-80°, the range for which the transmission coefficients nearly reach their maxima.

In order to augment our set of data functionals, and to replace the waveform modeling when SPL is absent, we decided to compute and, ultimately model S-to-P (or S-wave) receiver functions, which we call SRFs. For this purpose we downloaded three-component data around S-wave arrivals for stations DESE and KIV, among others. Events were selected with a moment magnitude greater than 5.5, depth greater than 50 km and epicentral distance in the range $40 \leq \Delta \leq 105°$. Slowness and backazimuth values for each raypath were computed using the AK135 (Kennett et al., 1995) velocity model. The seismograms are processed to remove the mean and trend, then bandpass filtered using a third order Butterworth filter with corner frequencies 0.02 and 1.5 Hz.

For each three-component seismogram, we cut a time window of 200 s, starting 100 s before the onset of S phases, and visually inspect all the S phases and retain the records with clear S phases to calculate the SRFs. Calculation of SRFs mainly involves coordinate rotation and deconvolution (Yuan et al. 2006; Zhao et al. 2010). We rotate the ZNE (Z, N–S and E–W) components to the ZRT (vertical, radial and transverse) system based upon the theoretical

backazimuth and then further to the P-SV-SH system with incidence angle determined by minimizing the amplitude within a window of ±1 s at the S-phases arrival time on the P component. This coordinate rotation ensures optimal isolation of the Sp converted waves from the incident S phases. Subsequently, SRFs are conducted by deconvolving the SV components from the P components by a Wiener filtering approach in the time domain. Prior to deconvolution, a bandpass filter is applied to the data. Following the conventions of others, and to make the SRFs more comparable to conventional PRFs we reverse the time axis and the polarity of the SRFs. In the resulting SRFs, as for PRFs, positive amplitudes indicate increasing velocity with depth across a discontinuity, and vice versa.

Figure 3 shows the result of the processing described above for a single event recorded by station DESE in Ethiopia. This SRF shows a significant number of arrivals, suggesting that the Earth beneath DESE can be represented effectively by a stack of layers that have large impedance contrasts between them. The appearance of such a series of effective P-to-S "scatterers" or "conversion horizons" offers hope that this SRF will provide constraints for modeling, but whether these constraints augment the constraints offered by PRFs and surface wave dispersion, can only be answered by a series of trials. That set of trials is one of our next steps. On a separate note, the relatively consistent amplitudes of the peaks suggest that the impedance contrasts are fairly consistent across the set of layer boundaries, reinforcing our conclusion from prior modeling (Figure 1) that there the Moho (and other discontinuities) are not abrupt in this region.

A more hopeful SRF, in that it shows greater variations in amplitudes of its peaks, is show in Figure 4 for station KIV. This SRF follows a pattern observed commonly in PRFs in that the amplitudes of peaks decrease with time. This indicates that the shallower discontinuities are more efficient in converting energy. There are exceptions, however, in that discontinuities at 410 and 660 km depth are known to have substantial impedance contrasts. Incorporating these, and other, SRFs into our MOO methodology is the next step in our research.

CONCLUSIONS AND RECOMMENDATIONS

No single data type carries with it the constraints needed to produce accurate and sufficiently detailed models of the Earth's crust and uppermost mantle. Multiple data types must be used, yet the optimal strategies for modeling disparate, inconsistent, and noisy data are not clear. It is clear that a broad search of set of possible models must be conducted and assessment tools must be produced that a) allow a user to evaluate the results of a particular modeling run and b) provides guidance to the user concerning ways to improve the results. Geophysical modeling is intrinsically non-linear, so linear methods are likely to both mis-identify a model that represents a local minimum as the "true" model and to overestimate the degree of confidence we should have in that model. Global search methods that incorporate multiple data types must be preferred to linear methods that propose to model a single data functional. Global searches, however, pose problems of tractability.

We have made substantial progress in our attempts to formalize Multi-Objective Optimization (MOO) for multiple data functionals while posing computational problems that are tractable. Further, we have been able to demonstrate the relative usefulness of a variety of data functionals:

- Group velocity surface wave dispersion is sensitive to bulk characteristics, such as thickness of a high-velocity lid/crust and average velocities in the model. Also, the smoothness of the dispersion curve allows us to tailor the weight assigned to its fit in a unique way. Increasing the weight assigned to surface wave dispersion stabilizes the inversion because it pushes the results toward smoother models.
- Modeling SPL waves can help constrain seismic velocity gradients, Vp/Vs, impedance contrast across the Moho, and layer thicknesses. Sp and SsPmP waves require a fairly large impedance contrast across the Moho to have large amplitudes.
- Characteristics of the model such as average velocities over portions of the stack and impedance contrasts across certain layers, are constrained by PRFs, although the particular portions of the stack and layer impedance contrasts that are constrained depend on the model (and the epicentral distance at which an observation is made). The important implication is that PRFs are most useful when they are modeled jointly with other functionals.

However, SPL appears rarely in the Middle East and Sp SsPmP are often subject to high noise levels, rendering modeling difficult and error-prone. We are therefore pursuing a strategy of modeling SRFs in place of, or, where possible, in addition to, windowed portions of the waveform.

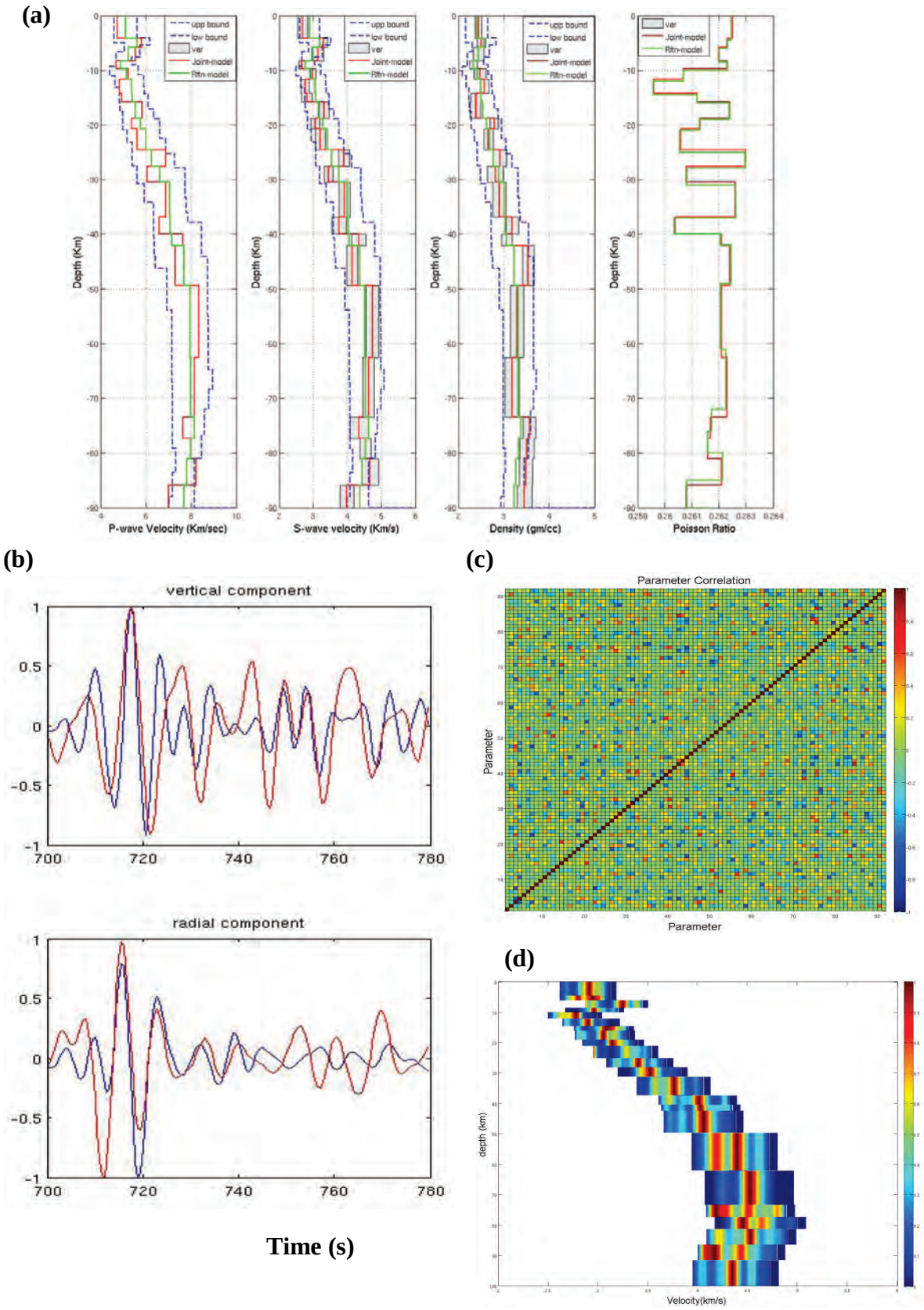


Figure 1. Station DESE: (a) Model obtained from inversion, (b) waveform fitting (data-blue, synthetic-red), (c) correlation matrix, (d) PPD plot (S-wave velocity).

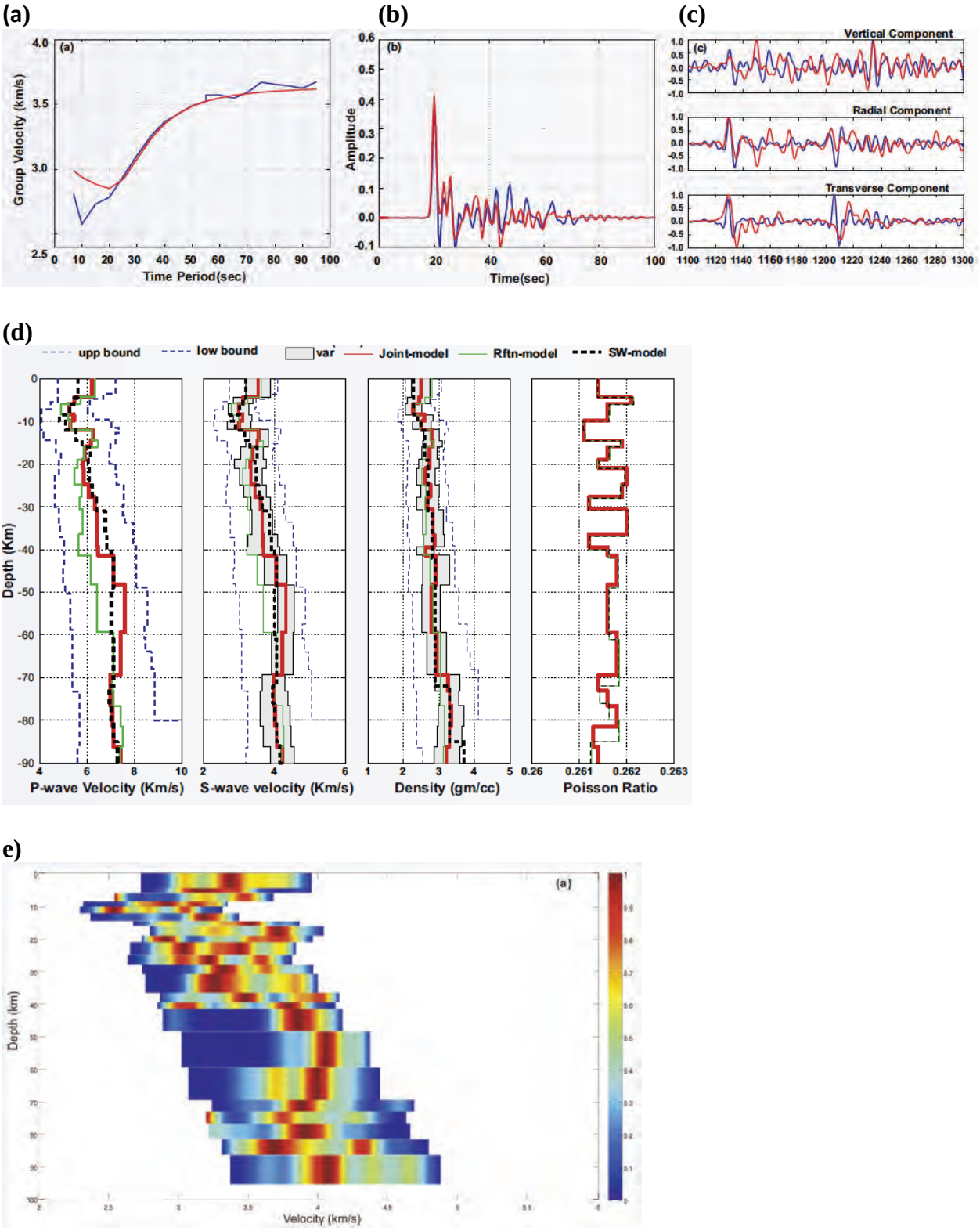


Figure 2. Station KIV MOO results: (a) Surface wave dispersion fit (data-blue, synthetic-red), (b) P-wave receiver function fit, (c) waveform fit, (d) models produced and, (e) PPD plot for S-wave velocity.

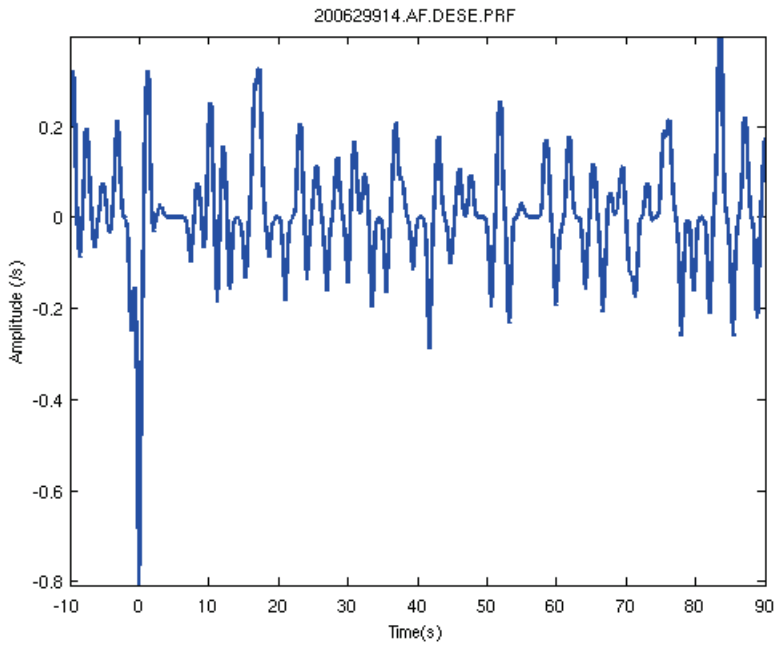


Figure 3. S-wave receiver function for station DESE. See text for details concerning data processing. Our next step is to incorporate this S-wave receiver function into the inversion described in Figure 1.

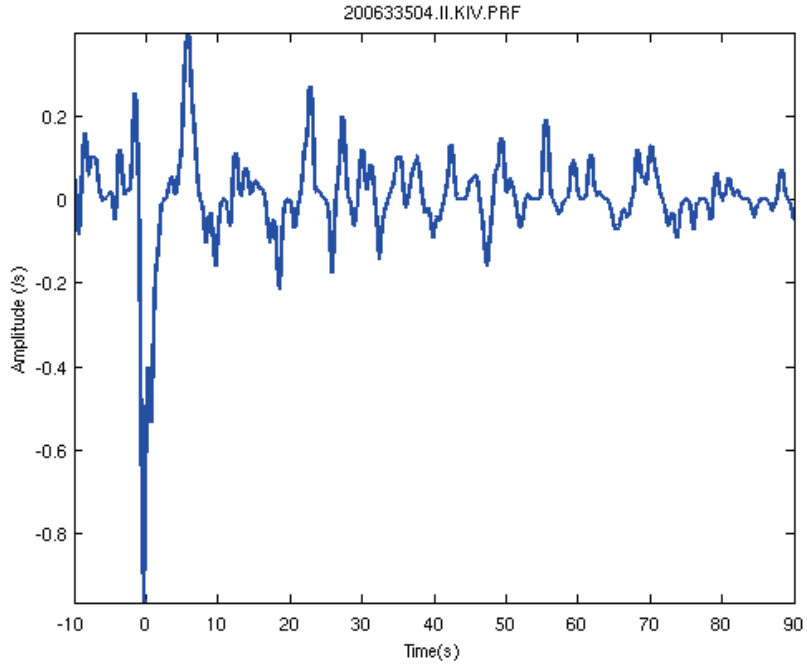


Figure 4. S-wave receiver function for station KIV. See text for details concerning data processing. Our next step is to incorporate this S-wave receiver function into the inversion described in Figure 2.

REFERENCES

Ammon, C.J. (1991). The isolation of receiver effects from teleseismic P waveforms. *Bull. Seismol. Soc. Am*. **81**, 2504–2510.

Gangopadhyay, A., Pulliam, J. and Sen, M.K. (2007). Waveform Modeling of Teleseismic S, SP, SsPmP, and Shear-Coupled PL Waves for Crust and Upper Mantle Velocity Structure Beneath Africa. *Geophys. J. Int*. **170**, 1210–1226.

Julia, J., Ammon, C.J., Herrmann, R.B. and Correig, A.M. (2000). Joint inversion of receiver function and surface wave dispersion observations. *Geophys. J. Int*. **143**(1), 99–112.

Kennett, B.L.N. Engdahl, E.R. & Buland R. (1995). Constraints on seismic velocities in the Earth from travel times, *Geophys J Int* **122**, 108–124

Sambridge, M. (1999). Geophysical inversion with a neighborhood algorithm; I, Searching a parameter space. *Geophys. J. Int*. **138,** 479–494.

Sandvol, E., Seber, D., Calvert, A. and Barazangi, M. (1998). Grid search modeling of receiver functions; implications for crustal structure in the Middle East and North Africa. *J. Geophys. Res.* **103**(11): 26,899–26,917.

Shibutani, T., Sambridge, M. and Kennett, B. (1996). Genetic algorithm inversion for receiver functions with application to crust and uppermost mantle structure beneath eastern Australia, *Geophys. Res. Lett*. **23**, 1829–1832.

Zhao, L.-S. and Frohlich, C. (1996). Teleseismic body waveforms and receiver structures beneath seismic stations. *Geophys. J. Int*. **124**, 525–540.

ESTIMATING THE UNCERTAINTY AND PREDICTIVE CAPABILITIES OF THREE-DIMENSIONAL EARTH MODELS

Delaine T. Reiter[1], William L. Rodi[2], and Stephen C. Myers[3]

Weston Geophysical Corp.[1], Massachusetts Institute of Technology[2], and Lawrence Livermore National Laboratory[3]

Sponsored by the Air Force Research Laboratory and the National Nuclear Security Administration

Award Nos. FA8718-09-C-0013[1,2] and DE-AC52=-07NA27344[3]
Proposal No. BAA09-73

ABSTRACT

In recent years many models of 3D seismic velocity structure in Eurasia have been developed, using a variety of techniques and data. Most of these models are not accompanied by quantitative estimates of uncertainty, either in the model parameters themselves (e.g. seismic velocities) or in geophysical observables predicted by the models (e.g., body-wave travel times). Moreover, the various 3D models produced by these studies have not been compared to one another in their predictive capabilities in any meaningful way within the monitoring research community. To address these issues we are developing and applying evaluation metrics that robustly quantify and compare the uncertainty and predictive capability of 3D seismic velocity models.

There are two major elements in our approach. First, we are performing a comprehensive evaluation of a set of 3D velocity models for Eurasia based on previously developed data misfit and event mislocation metrics. These metrics are computed using a ground-truth (GT) data set available at the International Seismic Centre (ISC). We present the results from applying a comprehensive set of metrics to the models in our study.

Second, we are investigating a new approach to evaluating velocity models based on a Bayesian framework for model uncertainty in the travel-time tomography problem. In this approach, geostatistical parameters describing velocity heterogeneity in the Earth are estimated from travel-time residuals observed along a set of event-station paths. The parameters include the velocity variance, which quantifies the strength of velocity heterogeneity, and vertical and horizontal correlation lengths, which quantify the spatial smoothness of velocity heterogeneity. The inferred geostatistical parameters characterize the discrepancy between the Earth's velocity and the velocity of the reference model used to calculate the travel-time residuals. That is, they quantify the uncertainty of the reference model and thus serve as metrics for model evaluation. In addition, as we have shown in previous projects, geostatistical parameters can be used to calculate the uncertainty in travel times predicted by the reference model for arbitrary paths.

OBJECTIVES

The main objective of our project is to develop meaningful measures of the predictive capabilities of 3D seismic velocity models that have been developed over recent years by the nuclear monitoring research community. While our current focus is on regional-scale seismic velocity models, we intend for our general approach to be applicable as well to global Earth models and models of other geophysical parameters such as attenuation and density.

Our project consists of two major elements. First, we collected a set of regional 3D velocity models for Asia and are performing a comprehensive and methodical evaluation of their travel-time prediction behavior using data misfit and event mislocation metrics. Metrics were evaluated for each model based on a common ground-truth data set comprising GT5 events and their arrival picks. A large part of this effort was spent developing standardized methods for model parameterization, forward modeling (e.g., ray tracing), and event relocation. Some of the tools we needed for these tests are available to us in-house from our previous tomography and location projects, but others were gathered from outside sources.

The second element of our project has been the investigation of a new approach for estimating the uncertainty and predictive capability of 3D velocity models. Our approach will quantify model uncertainty in terms of spatially variable geostatistical parameters fit to second-order statistics of travel-time residuals, and then convert these parameters into the uncertainty in travel-time or other geophysical predictions. To do this requires covariance modeling capabilities we developed for travel times in an earlier project (Rodi and Myers, 2010) and which can be extended to other observables.

RESEARCH ACCOMPLISHED

Traditional Residual Analysis Techniques to Examine Model Performance

As part of our first major project task, we collected a set of 3D seismic velocity models and have developed tools to compare them in a straightforward manner. Our test-bed model for the project is the Joint Weston/MIT (JWM) inversion model (Reiter and Rodi, 2009). JWM is result of a joint inversion of regional P travel times and Rayleigh fundamental-mode group velocities. It consists of the P and S velocities and density of the crust and upper mantle for a broad region of Asia (defined in a geographic box from 0 – 60°N, 30 – 120°E). In addition to the JWM model, we obtained the CUB2.0 surface-wave inversion model with density (Ritzwoller et al., 2002); the Stevens et al. (2008) surface-wave inversion model; the EAVP11 inversion model from the group headed by Suzan van der Lee at Northwestern University (Chang et al., 2011); and a new P-velocity inversion model (LLNL_G3D) from Nathan Simmons and Stephen Myers (Simmons et al., 2011). We also have access to an *a priori* regionalized model known as the DOE Unified Model (Begnaud et al., 2004; Pasyanos et al., 2004), as well as the Regionalized Seismic Travel Time model (RSTT; Myers et al, 2010), which comprises a velocity model with its required companion forward modeling capability.

A significant effort was required to convert all the models in the study (except for RSTT) to a single common format. There is still no standardized format for model exchange in the nuclear monitoring research community, which has hampered an understanding of the differences between 3D models that are constructed for use in predicting nuclear monitoring observables. Our in-house model format represents a 3D model as a geographic grid of 1D profiles, with each profile sharing a common parameterization with respect to depth. For example, in the JWM model the crust at each latitude/longitude point is divided into vertically homogeneous layers corresponding to the those of the CRUST2.0 model: water overlying two sediment layers (soft and hard sediments) overlying three metamorphic/igneous layers (upper, middle and lower crust). The upper mantle is represented vertically by piecewise linear parameter functions sampled at multiple nodes distributed between the Moho discontinuity and a depth of 410 km. The versatility of this model format allows discontinuities and homogeneous layers to be accurately captured, and no special software is necessary to allow the models to be exchanged between researchers. Most of the models in our study can be represented in this format, although some conversion is necessary in certain cases (LP2008; Stevens et al., 2008).

Following the conversion of the six models in our study to our in-house format, we examined a wide variety of existing metrics to determine the models' prediction capabilities using a database of GT0-5 events in Eurasia (IASPEI Reference Event List; ISC, 2008). There are many possible metrics that can be calculated; for example, we

can measure the ability of a model to fit the observed path arrival times for the GT hypocenters. We predict the travel time using a modified Podvin-Lecomte ray tracing algorithm (Podvin and Lecomte, 1991), subtract it from the observed time, and bin the results as a function of epicentral distance from station to event. The results of this exercise for our six 3D models as well as the AK135 1-D model are shown in Figure 1. It is clear that some models (JWM, G3D, EAPV11) fit the regional GT arrivals better than others. However, this is only one snapshot of the GT residual behavior with respect to the models, and we note that all azimuth and geographic information (e.g., one particular station to a particular event cluster) has been collapsed out of the plots.

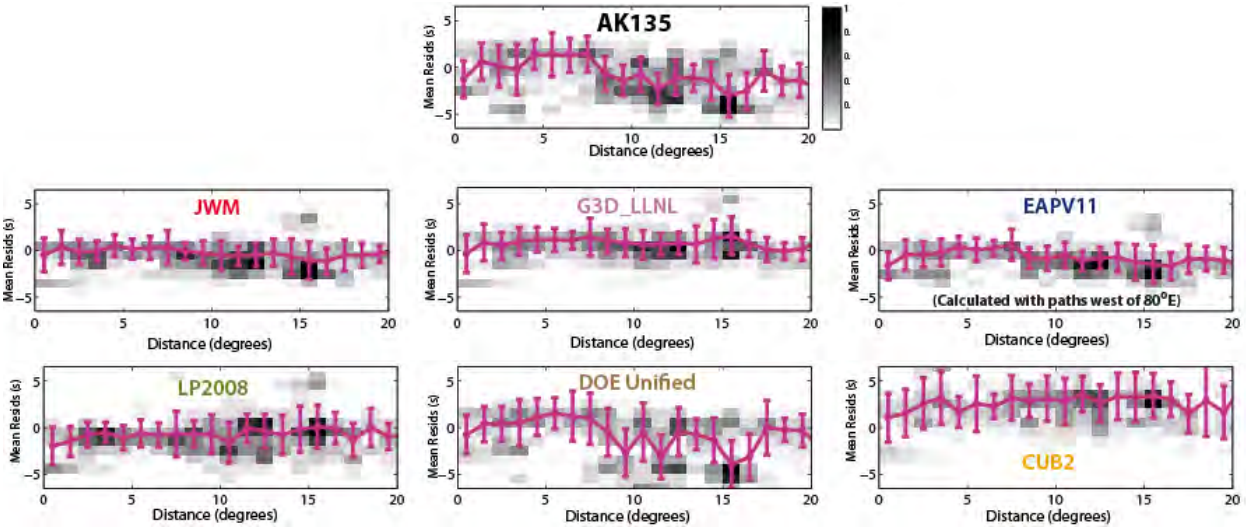


Figure 1. In the panels above we show the fit to our GT database path times as a function of distance between station and event, following binning and normalization across all models. The magenta error bars show the mean and standard deviation at 1° epicentral distance intervals.

Next we can examine travel-time fits as both a function of event-to-station distance and as station corrections for the same set of GT data. We predict travel times to all paths and then use our location algorithm to additionally calculate a bulk shift in time at each station in the data set, holding the hypocenter and origin time to the GT values. The station corrections do not absorb the entire misfit for each station-to-event path (unless there is only one path in the database), and therefore we must still examine the misfit as a function of distance to understand each model's results.

The results from this exercise are consequently more complex to understand and display. In Figure 2 we display color-coded and sized corrections on maps from the 25 stations in the GT database with the highest number of arrival (inside the box [10 - 60°N, 30 - 110°E]). Table 2 shows the details of the station corrections as a function of model, with highlighted cells showing the models with the best and worst fits at each station. Finally, in Figure 3 we show the binned and normalized residuals as a function of distance - these represent the 'remainder' misfits after station corrections are removed.

There are additional levels of travel-time misfit metrics that can be assessed. Each adds another layer of complexity to the analysis. We can also examine the models' performance in relocation exercises, which convolve in the network geometry as well as the path prediction. These exercises quickly become very convoluted to perform and harder to interpret easily.

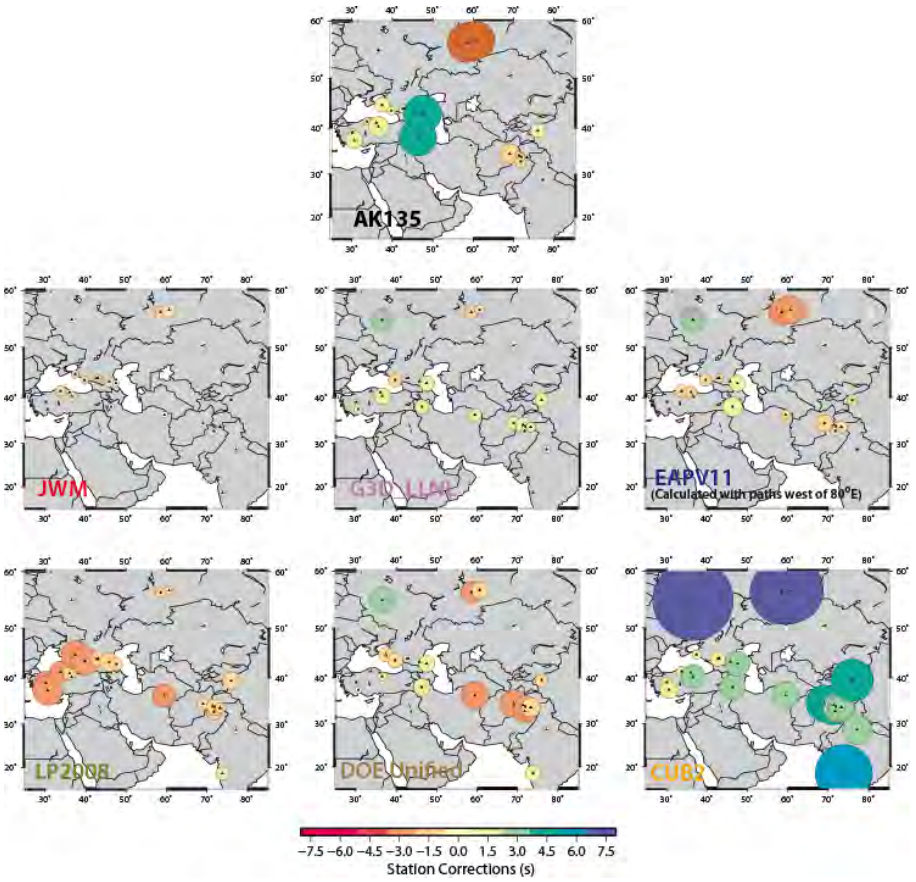


Figure 2. Model-specific maps of station corrections for the 25 stations in the GT database with the highest number of arrivals (inside a latitude-longitude box [10 - 60°N, 30 - 110°E]). Table 1 provides details of the station corrections as a function of model, with highlighted cells showing the models with the best and worst fits at each station.

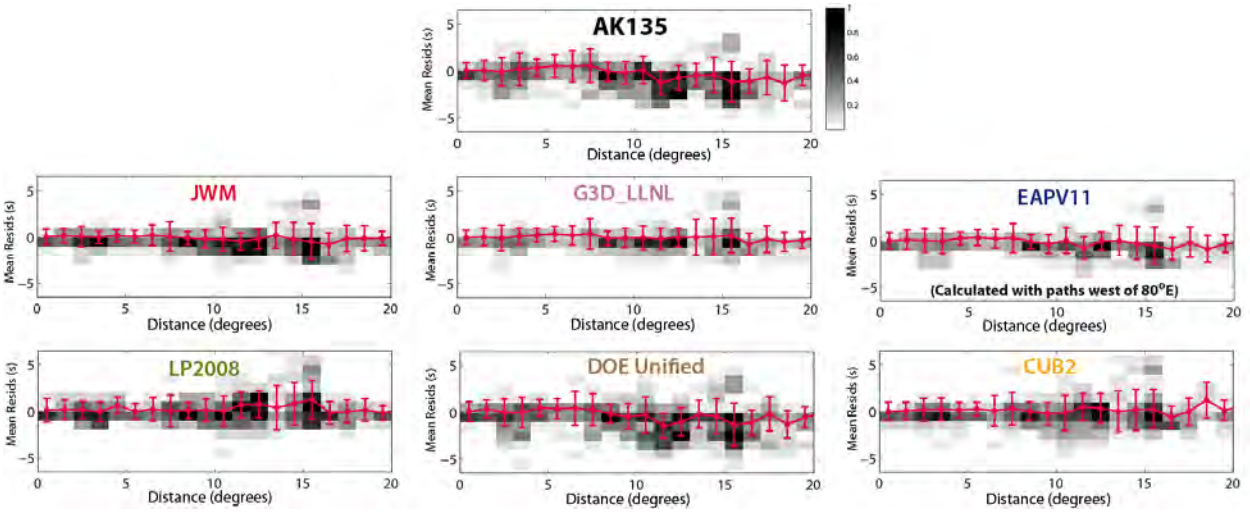


Figure 3. In the panels above we show the fit to the GT path times as a function of distance between station and event, following binning and normalization. This version shows the corrections *after* the station correction component has been included in the travel-time prediction exercise. The red error bars show the mean and standard deviation at 1° epicentral distance intervals.

Table 1. Station corrections as a function of 3D model for the twenty-five stations with the highest number of phase readings in the GT bulletin; models with the smallest corrections are shaded green, largest corrections are shaded orange.

				Station Corrections by Model (in seconds)						
Station Name	**Lat. (°N)**	**Long. (°E)**	**# GT Pn Phases**	**JWM**	**G3D**	**EAVP11**	**LP2008**	**CUB2**	**DOE Unified**	**AK135**
CEP	33.82	71.91	120	-0.38	0.70	2.58	-1.72	2.74	-2.27	3.89
OBN	55.11	36.57	111	0.67	2.36	-1.26	0.55	8.42	2.71	1.41
THW	32.79	71.74	110	-0.65	0.79	-1.22	-1.64	2.16	-2.45	-0.56
CHCP	33.66	73.26	107	-0.36	1.00	-1.77	-1.09	2.58	-2.01	-3.95
KVT	41.08	36.05	107	-0.61	-0.06	-0.72	-1.32	0.86	-0.52	1.54
NDI	28.68	77.22	106	-0.51	0.78	-0.45	0.64	3.08	-0.49	-4.14
NIL	33.65	73.25	104	-0.40	1.00	-1.07	-0.63	2.92	-1.83	0.91
KBL	34.54	69.04	102	-0.14	1.43	-0.37	-1.21	3.83	-2.85	0.87
ALT	39.06	30.11	91	0.32	0.58	-1.37	-2.40	1.19	0.34	-0.81
ANN	44.80	37.43	88	-0.82	-0.44	0.44	-2.96	0.96	-1.53	3.90
KAS	41.37	33.77	88	-1.13	0.26	-0.63	-2.25	1.12	-0.36	1.80
MAIO	36.31	59.47	83	-0.69	1.31	-1.06	-2.42	2.86	-2.89	0.60
TOKT	40.32	36.54	80	0.95	1.73	-0.13	0.04	2.52	0.95	2.11
PYA	44.03	43.06	79	-0.78	-0.67	-0.86	-1.48	-0.20	-0.57	-0.64
BCK	37.46	30.59	75	0.34	0.94	-0.45	-3.13	1.84	0.70	1.57
MAK	42.96	47.51	73	0.61	1.58	1.70	-1.37	2.59	1.70	0.81
WRS	34.15	71.40	68	-0.30	1.59	-0.57	0.26	4.02	-2.03	0.83
SOC	43.58	39.72	67	-0.80	-1.42	-1.28	-2.90	0.11	-1.60	-2.08
ARU	56.43	58.56	66	-1.29	-1.30	-2.78	-1.08	6.68	-2.19	-0.46
KIV	43.96	42.69	66	-0.29	0.19	-0.42	-0.47	1.58	-0.16	0.07
KSH	39.52	75.97	64	-0.26	1.44	-1.15	-1.84	4.41	-1.37	-0.27
GRO	43.32	45.75	62	-1.13	-0.24	-0.19	-1.92	0.05	-0.22	0.92
POO	18.53	73.85	62	-0.47	0.43	0.61	1.39	5.97	1.64	-1.16
SVE	56.83	60.64	62	-1.41	-1.09	-2.97	-1.04	6.90	-1.68	-0.31
TAB	38.07	46.33	61	0.60	1.46	2.00	-0.27	2.65	1.75	-0.80

Another useful metric that does not require GT residuals compares travel time predictions from various models as a function of geographic position using a single event (or station) position. The results from this type of calculation resemble source-specific station corrections (SSSCs), which examine the differences between 3D regional velocity models and standard background 1-D global models (e.g., Murphy et al., 2005). Our application differs from the computation of a traditional SSSC, however, in that we examine how 3D models vary from one another with respect to predicted first-arrival P times. We select a surface point of interest, ray trace through a set of 3D models to points on the earth's surface at a range of distances and azimuths, and form travel-time difference maps. There are many potential applications of this simple idea. For instance, if we use a single 3D model and several ray tracing algorithms, we can examine the effects of the prediction algorithms. Conversely, we can analyze the differences between two 3D models using a single ray tracing code, or the differences between two models that are tied to specific modeling codes.

This last case is illustrated in Figure 4, in which we predict the first-arriving P times from the epicenter of the May 1998 Pakistan nuclear test using two models and ray tracers: 1) the JWM model and the Podvin-Lecomte ray tracer; 2) the Regional Seismic Travel Time (RSTT) model and its inherent ray tracer (a variant of Zhao and Xie, 1993). The travel time differences at distances up to approximately 12° from the event's epicenter are color-coded and mapped as a function of latitude and longitude. The results indicate that both models produce travel times within a second of each other in many areas surrounding the event position. However, there are also larger differences (up to +2.5s) within 600-700 km of the source point in southwestern Pakistan. The source of the differences can sometimes be traced to differences in the depth to and shape of the Moho discontinuity or the crustal layers beneath the event position. However, the differences in other cases are not so clear-cut to interpret.

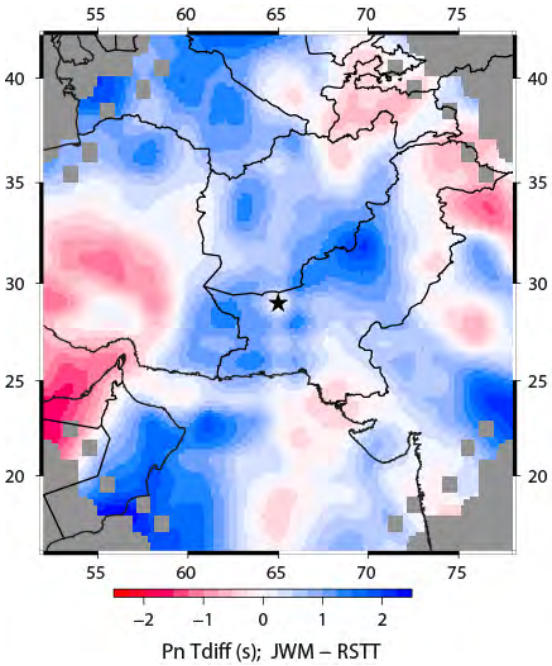


Figure 4. Map showing differences in predicted Pn travel times between the JWM and RSTT models for one of the 1998 Pakistan nuclear tests. Travel times were predicted from the event position to points on the earth's surface for the distance ranges at which RSTT is valid. The maximum travel time difference is +2.5s at a distance of approximately 5.4° away.

New Model Uncertainty Metrics

In the second task of our project we are attempting to develop new metrics that directly quantify the error, or uncertainty, in a velocity model compared to the Earth's true velocity. In the context of an inverse problem, model uncertainty is associated with an optimal estimate of the Earth's velocity derived from a given data set. Our context is different: we seek to measure the uncertainty of a given, fixed model, one that may or may not be an optimal inversion model and the details of whose construction may not even be available.

The new metrics we are developing will ultimately, like traditional travel-time and event-mislocation metrics, reflect how well the travel times predicted by the velocity model of concern fit ground-truth travel times observed along various event-station paths. However, we are attempting to define metrics that better isolate travel-time prediction capability from confounding effects like pick errors in the ground-truth data, poor network geometry (affecting mislocation tests) and errors in the ground-truth event locations. To the extent this is achieved, larger data sets based on weaker ground-truth criteria can be used to derive the metrics. Moreover, we are attempting to define metrics that are localized within the Earth, allowing one to assess a velocity model as a function of depth and geographical location. Hand-in-hand with this goal, the metrics we seek will be usable for extrapolating travel-time prediction capability away from the ground-truth paths.

Our progress to date on this task has exclusively been in the mathematical formulation of our new approach and, what has turned out to be a real challenge, the development of a practical numerical algorithm for executing the approach. Our focus has been on estimating the velocity variance of a model, averaged over various portions of the model, based on the scatter in the ground-truth travel-time residuals produced by the model. Implicit in this problem is isolating the residual scatter due to model prediction errors from that caused by pick errors. The following subsections describe our theoretical approach to the general problem of model uncertainty metrics and the mathematical and computational techniques we have developed thus far.

Geostatistical Formulation: Letting v_{ref} denote the velocity of a reference model we wish to evaluate, and letting v_{tru} denote the Earth's true velocity, both functions of position $\mathbf{r}$, we denote the error in the reference *slowness* as m, defined by

$$m(\mathbf{r}) = \frac{1}{v_{tru}(\mathbf{r})} - \frac{1}{v_{ref}(\mathbf{r})} \quad (1)$$

Our approach assumes that *m* is a Gaussian random field with second order statistics given by

$$E[m(\mathbf{r})] = 0 \quad (2)$$
$$E[m(\mathbf{r})m(\mathbf{r}')] = C(\mathbf{r}, \mathbf{r}') \quad (3)$$

(where E[ ] denotes the expected value of a random variable). That is, *m* has zero mean at each point and the covariance between its value at any two points is determined by the covariance kernel, *C*. We parameterize *C* in terms of three functions of position: the standard deviation of slowness σ_m, a horizontal correlation length λ_h, and a vertical correlation length λ_v. The kernel *C* is determined by these three geostatistical parameters and an assumed functional dependence on its position arguments. Here, we take this dependence to be an exponential decay with spatial separation, **r** - **r**'. When the correlation lengths are constant with position, this yields

$$C(\mathbf{r}, \mathbf{r}') = \sigma_m(\mathbf{r})\,\sigma_m(\mathbf{r}')\exp\left\{-\left[\frac{(x-x')^2}{\lambda_h^2} + \frac{(y-y')^2}{\lambda_h^2} + \frac{(z-z')^2}{\lambda_v^2}\right]^{1/2}\right\}, \quad (4)$$

where *x*, *y* and *z* (depth) are local Cartesian coordinates. When the correlation lengths vary spatially, and when other complexities are desired, such as allowing *m* to decorrelate across the Moho or other velocity discontinuities in the Earth, it is possible to specify *C* indirectly as the Green's function of a differential operator *D*, such that

$$D\,C(\mathbf{r}, \mathbf{r}') = \delta(\mathbf{r} - \mathbf{r}') \quad (5)$$

(Rodi and Myers, 2010).

Our approach takes the three geostatistical parameters – σ, λ_h and λ_v – to be model uncertainty metrics. The problem to be solved is how to estimate these parameters from ground-truth travel-time data.

The Variance Estimation Problem: To describe our approach to the estimation of model covariance parameters, it is convenient to consider a discrete representation of the slowness error function *m*. Let **m** be a finite-dimensional vector containing, for example, samples of *m* on a 3D grid. The stochastic assumptions about **m** corresponding to Eqs. (2) and (3) are

$$E[\mathbf{m}] = 0 \quad (6)$$
$$E[\mathbf{m}\,\mathbf{m}^T] = \mathbf{C}, \quad (7)$$

where the covariance matrix **C** serves as a discrete approximation to the covariance kernel *C*. We assume that **C** depends on a set of geostatistical parameters γ_1, γ_2, …, which are a discrete representation of the model variance and correlation length functions (σ, λ_h and λ_v). The problem at hand now can be stated as estimating the γ_k .

Now let **d** be a vector of travel-time residuals, relative to the reference velocity model under consideration, observed from a set of well-located (ground-truth) seismic events at various stations. To first order in **m**, we have

$$\mathbf{d} = \mathbf{A}\mathbf{m} + \mathbf{e}, \quad (8)$$

where **A** is a travel-time sensitivity matrix (evaluated at the reference model) and **e** is a vector of measurement (pick) errors. This equation dismisses contributions to the residuals from errors in the event hypocenters and origin times, which can be accounted for with a more general formulation than the one we present here. We assume the pick errors are zero-mean and have a diagonal covariance matrix, which we denote **V**:

$$E[\mathbf{m}\mathbf{e}] = 0 \quad (9)$$
$$E[\mathbf{e}\,\mathbf{e}^T] = \mathbf{V}, \quad (10)$$

We allow **V** to depend on unknown parameters θ_1, θ_2, …. For example, if the pick-error variance depends on event-station distance in an unknown way, each θ_j could be the variance assigned to a particular distance range.

Eqs. (6) – (10) imply that

$$E[\mathbf{d}] = 0 \quad (11)$$
$$E[\mathbf{d}\mathbf{d}^T] = \mathbf{A}\mathbf{C}\mathbf{A}^T + \mathbf{V} \equiv \mathbf{T}. \quad (12)$$

The right-hand side of this last equation represents the total variance of the residuals, denoted **T**, which has a contribution from the model-error variance (**C**) and the pick-error variance (**V**). The equation shows that estimates of the pick-error variance parameters θ_j and geostatistical parameters γ_k will ultimately be derived from the second-order statistics of the travel-time residuals.

Maximum-Likelihood Variance Estimates: We are pursuing a maximum-likelihood approach to estimating the variance parameters θ_j and γ_k. The likelihood function for these parameters, denoted *L,* is determined by the probability density function (p.d.f.) of the residual vector **d**, which in turn is determined by the joint p.d.f. of the error vectors **e** and **m**. We will assume **e** and **m** are independent and that each has a Gaussian p.d.f. Then, by virtue of Eq. (8), **d** is Gaussian and the likelihood function becomes

$$\log L = \text{const} - \frac{1}{2}[\log(\det \mathbf{T}) + \mathbf{d}^T\mathbf{T}^{-1}\mathbf{d}], \tag{13}$$

where "det" denotes the determinant of a matrix. It is understood that **T**, and thus *L*, depend on the θ_j and γ_k. The maximum-likelihood estimates of these parameters, in maximizing *L*, satisfy the stationarity conditions: $\partial L/\partial\,\theta_j = 0,\ \partial L/\,\partial\,\gamma_k = 0$. Given (12) and the properties of matrix determinants, the stationarity conditions become

$$\text{tr}\,\mathbf{T}^{-1}\frac{\partial \mathbf{V}}{\partial \theta_j} = \mathbf{d}^T\mathbf{T}^{-1}\frac{\partial \mathbf{V}}{\partial \theta_j}\mathbf{T}^{-1}\mathbf{d} \tag{14}$$

$$\text{tr}\,\mathbf{T}^{-1}\mathbf{A}\frac{\partial \mathbf{C}}{\partial \theta_j}\mathbf{A}^T = \mathbf{d}^T\mathbf{T}^{-1}\mathbf{A}\frac{\partial \mathbf{C}}{\partial \gamma_j}\mathbf{A}^T\mathbf{T}^{-1}\mathbf{d} \tag{15}$$

where "tr" denotes the trace of a matrix. The maximum-likelihood estimates of θ_j and γ_k can be obtained by solving these nonlinear, coupled equations. Unfortunately, the equations do not admit analytical solutions except in very simple situations.

***Block Variances*:** To date, we have only considered the solution of Eqs. (14) and (15) for the case of *block variance* parameters, i.e. variances assigned to subsets of the pick errors and model errors. In the case of pick errors, we can expand the variance matrix **V**, which is diagonal, in terms of block variances as

$$\mathbf{V} = \sum_j \theta_j^2\,\mathbf{P}_j \tag{16}$$

where each matrix $\mathbf{P}_j$ is a partition, or block, of the data-space identity matrix. If the partitions are defined by epicentral distance bins, for example, θ_j^2 would then be the pick-error variance for the *j*th bin. In the case of model errors, a double sum over model partitions is needed to allow for correlations between model parameters. We thus write

$$\mathbf{C} = \sum_{kk'} \gamma_k\gamma_{k'}\mathbf{Q}_k\mathbf{\Gamma}\mathbf{Q}_{k'} \tag{17}$$

where **Γ** is the model-error correlation matrix, having ones along its diagonal, and $\mathbf{Q}_k$ is a partition of the model-space identity matrix selecting parameters in a portion of the velocity model, all of whose variances are given as γ_k^2.

From (16) and (17) it is not difficult to derive that

$$\theta_j\frac{\partial \mathbf{V}}{\partial \theta_j} = 2\mathbf{P}_j\mathbf{V} \tag{18}$$

$$\gamma_k\frac{\partial \mathbf{C}}{\partial \gamma_k} = \mathbf{Q}_k\mathbf{C} + \mathbf{C}\mathbf{Q}_k. \tag{19}$$

Applying these formulas in the stationarity conditions of Eqs. (14) and (15) yields, after some manipulation,

$$\text{tr}\,\mathbf{P}_j\mathbf{V}\mathbf{T}^{-1} = \mathbf{d}^T\mathbf{T}^{-1}\mathbf{V}\mathbf{P}_j\mathbf{T}^{-1}\mathbf{d} \tag{20}$$

$$\text{tr}\,\mathbf{Q}_k\mathbf{C}\mathbf{A}^T\mathbf{T}^{-1}\mathbf{A} = \mathbf{d}^T\mathbf{T}^{-1}\mathbf{A}\mathbf{C}\mathbf{Q}_k\mathbf{A}^T\mathbf{T}^{-1}\mathbf{d}. \tag{21}$$

We can simplify these equations by making use of the tomographic inversion results implied by Eq. (8) and the stochastic assumptions we have made. That is, the maximum a posteriori (MAP) estimate of **m**, and its data residual vector, are given by

$$\tilde{\mathbf{m}} = \mathbf{C}\mathbf{A}^T\mathbf{T}^{-1}\mathbf{d} \tag{22}$$

$$\tilde{\mathbf{e}} \equiv \mathbf{d} - \mathbf{A}\tilde{\mathbf{m}} = \mathbf{V}\mathbf{T}^{-1}\mathbf{d}. \tag{23}$$

Eqs. (20) and (21) can then be rewritten as

$$\text{tr } \mathbf{P}_j\mathbf{V}\mathbf{T}^{-1} = \tilde{\mathbf{e}}^T\mathbf{P}_j\mathbf{V}^{-1}\tilde{\mathbf{e}} \quad (24)$$

$$\text{tr } \mathbf{Q}_k\mathbf{C}\mathbf{A}^T\mathbf{T}^{-1}\mathbf{A} = \tilde{\mathbf{m}}^T\mathbf{Q}_k\mathbf{C}^{-1}\tilde{\mathbf{m}}. \quad (25)$$

We can simplify the stationarity equations even further by installing the definitions of the influence matrix, **S**, and resolution matrix, **R**, for this inverse problem, which can be expressed as

$$\mathbf{S} = \mathbf{A}\mathbf{C}\mathbf{A}^T\mathbf{T}^{-1} = \mathbf{I} - \mathbf{V}\mathbf{T}^{-1} \quad (26)$$

$$\mathbf{R} = \mathbf{C}\mathbf{A}^T\mathbf{T}^{-1}\mathbf{A}. \quad (27)$$

Using these, (24) and (25) become

$$\text{tr } \mathbf{P}_j(\mathbf{I} - \mathbf{S}) = \tilde{\mathbf{e}}^T\mathbf{P}_j\mathbf{V}^{-1}\tilde{\mathbf{e}} \quad (28)$$

$$\text{tr } \mathbf{Q}_k\mathbf{R} = \tilde{\mathbf{m}}^T\mathbf{Q}_k\mathbf{C}^{-1}\tilde{\mathbf{m}}. \quad (29)$$

The matrix trace on the left-hand side of Eq. (28) can be recognized to be the number of degrees of freedom available in the *j*th block of data, while the right-hand side is the portion of the data misfit (defined as $\tilde{\mathbf{e}}^T\mathbf{V}^{-1}\tilde{\mathbf{e}}$) attributable to the *j*th data block. Similarly, (29) equates the number of independent parameters in the *k*th block of the model to its contribution to the total model roughness ($\tilde{\mathbf{m}}^T\mathbf{C}^{-1}\tilde{\mathbf{m}}$).

***Variance Estimation Algorithm*:** We are developing an iterative algorithm to solve Eqs. (24) and (25) and thus obtain maximum-likelihood estimates of block data variances (θ_j^2) and block model variances (γ_k^2). Each step of the algorithm entails four sub-steps:

1. Evaluate the variance matrices **V** and **C** with Eqs. (16) and (17), using the current values of θ_j and γ_k.
2. Use the current **V** and **C** (and the travel-time data vector **d**) to compute a tomographic model ($\tilde{\mathbf{m}}$) and its data residual vector ($\tilde{\mathbf{e}} = \mathbf{d} - \mathbf{A}\tilde{\mathbf{m}}$).
3. For each data and model partition, calculate the matrix traces:

$$K_j = \text{tr } \mathbf{P}_j\,\mathbf{V}\mathbf{T}^{-1} \quad (30)$$

$$L_k = \text{tr } \mathbf{Q}_k\mathbf{C}\mathbf{A}^T\mathbf{T}^{-1}\mathbf{A} \quad (31)$$

4. Rescale the variance of each data and model partition:

$$\theta_j^2 \leftarrow \theta_j^2\,\frac{\tilde{\mathbf{e}}^T\mathbf{P}_j\mathbf{V}^{-1}\tilde{\mathbf{e}}}{K_j} \quad (32)$$

$$\gamma_k^2 \leftarrow \gamma_k^2\,\frac{\tilde{\mathbf{m}}^T\mathbf{Q}_k\mathbf{C}^{-1}\tilde{\mathbf{m}}}{L_k} \quad (33)$$

The four sub-steps are repeated until a convergence is reached.

Many algorithms for computing a tomographic model ($\tilde{\mathbf{m}}$) from very large data sets, including ours, perform the computations with an iterative updating technique like conjugate gradients, rather than with matrix inversion. In this case, the matrix $\mathbf{T}^{-1}$ used in the equations above is not available. As a result, the most challenging task in our variance estimation algorithm is computation of the matrix traces in Eqs. (30) and (31). The variance estimation algorithm we are developing accomplishes this with an approximate method due to Hutchinson (1990), which works as follows. Let **u** be a random data vector whose elements are either +1 (with .5 probability) or -1 (with .5 probability). Then

$$\text{E}[\mathbf{u}] = 0 \quad (34)$$

$$\text{E}[\mathbf{u}\mathbf{u}^T] = \mathbf{I}. \quad (35)$$

Therefore,

$$\text{E}\left[\mathbf{u}^T\,\mathbf{P}_j\mathbf{V}\mathbf{T}^{-1}\mathbf{u}\right] = \text{E}\left[\text{tr } \mathbf{P}_j\mathbf{V}\mathbf{T}^{-1}\mathbf{u}\mathbf{u}^T\right] = \text{tr } \mathbf{P}_j\mathbf{V}\mathbf{T}^{-1}\text{E}[\,\mathbf{u}\mathbf{u}^T] = \text{tr } \mathbf{P}_j\mathbf{V}\mathbf{T}^{-1}. \quad (36)$$

This implies that, for a sequence of random realizations of **u**, denoted $\mathbf{u}_n$, $n = 1, \ldots, N$, we have

$$\text{tr } \mathbf{P}_j\mathbf{V}\mathbf{T}^{-1} \approx \frac{1}{N}\sum_{n=1}^{N}\mathbf{u}_n^T\,\mathbf{P}_j\mathbf{V}\mathbf{T}^{-1}\mathbf{u}_n. \quad (37)$$

The main chore in this technique is the computation of $\mathbf{V}\mathbf{T}^{-1}\mathbf{u}_n$ for each realization. Eq. (23) shows that this can be accomplished by performing tomography with $\mathbf{u}_n$ as the data vector, in lieu of **d**: the desired vector will be the residual vector, $\tilde{\mathbf{e}}$, that results.

A similar technique finds L_k. Letting $\mathbf{v}_n$ be a realization of a model vector with random components ±1, we have

$$\text{tr } \mathbf{Q}_k\mathbf{C}\mathbf{A}^T\mathbf{T}^{-1}\mathbf{A} \approx \frac{1}{N}\sum_{n=1}^{N} \mathbf{v}_n^T \mathbf{Q}_k\mathbf{C}\mathbf{A}^T\mathbf{T}^{-1}\mathbf{A}\mathbf{v}_n. \quad (38)$$

The main computation is of $\mathbf{C}\mathbf{A}^T\mathbf{T}^{-1}\mathbf{A}\mathbf{v}_n$, which Eq. (22) shows will be the inversion model resulting from performing tomography with $\mathbf{d}$ replaced by $\mathbf{A}\mathbf{v}_n$.

CONCLUSIONS AND RECOMMENDATIONS

Our project demonstrates that the use of traditional travel-time prediction (i.e., residual fits) and relocation metrics can reveal differences between 3D regional seismic velocity models. However, one significant problem with this approach is that the validation database (GT events and their accompany phase arrival bulletins) must be impeccable, otherwise the results have limited power to discriminate between models.

In addition, we have developed the theoretical framework for new metrics that will allow us to directly quantify the error in a given, fixed velocity model, whether or not we have the details of how it may have been constructed. We continue work on a practical numerical algorithm to assess our theoretical approach, one that will ultimately separate the travel-time prediction capability of a model from other confounding effects like pick errors in the ground-truth data, poor network geometry (affecting mislocation tests) and errors in the ground-truth event locations.

REFERENCES

Begnaud, M. L., C. A. Rowe, and L. K. Steck (2004). Validating three-dimensional velocity models in China and East-Asia for use in regional seismic event location, *EOS Trans. AGU*, Fall Meet. Suppl.

Chang, S.-J., S. Van der Lee, and M. P. Flanagan (2011)**.** P-velocity model along the Tethyan margin using regional and teleseismic P- and PKP-arrival times and S-velocity joint inversion model, submitted to *Phys. Earth and Planet Int.*

Hutchinson, M. F. (1990). A stochastic estimator of the trace of the in influence matrix for Laplacian smoothing splines, *Communications in Statistics, Simulation and Computation, 19,* 433–450.

International Seismological Centre, Reference Event Bulletin, http://www.isc.ac.uk (2008). Int. Seis. Cent., Thatcham, United Kingdom, 2008.

Murphy, J.R., W. Rodi, M. Johnson, D. D. Sultanov, T. J. Bennett, M. N. Toksöz, et al. (2005). Calibration of International Monitoring System (IMS) stations in Central and Eastern Asia for improved seismic event location, *Bull. Seismol. Soc. Am*. **95**, 1535–1560.

Myers, S. C., M. L. Begnaud, S. Ballard, M. E. Pasyanos, W. S. Phillips, A. L. Ramirez, M. S. Antolik, K. D. Hutchenson, G. S. Wagner, J. J. Dwyer, C. A. Rowe, and D. R. Russell (2010). A crust and upper mantle model of Eurasia and North Africa for Pn travel time calculation, *Bull. Seismol. Soc. Am.* **100** (2), 640–656.

Pasyanos, M. E., W. R. Walter, M. P. Flanagan, P. Goldstein, and J. Bhattacharyya (2004). Building and testing an a priori geophysical model for Western Eurasia and North Africa, *Pure Appl. Geophys*. **161**, 234–281.

Podvin, P. and I. Lecomte (1991). Finite difference computation of travel times in very contrasted velocity models: a massively parallel approach and its associated tools, *Geophys. J. Int.* **105,** 271–284.

Ritzwoller, M. H., N. M. Shapiro, M. P. Barmin and A. L. Levshin (2002). Global surface wave diffraction tomography, *J. Geophys. Res*. **107,** doi: 10.1029/2002JB001777.

Reiter, D. T. and W. L. Rodi (2009). Validated 3D velocity models in Asia from joint regional body- and surface-wave tomography, *Final Report*, Contract FA8718-04-C-0027, AFRL-RV-HA-TR-2009-1009.

Rodi, W. L. and S. C. Myers (2010). Modeling travel-time correlations based on sensitivity kernels and correlated velocity anomalies, *Final Technical Report*, DOE National Nuclear Security Administration, contract no. DE-FC52-05NA26603.

Simmons, N. A., Myers, S. C., and G. Johannesson (2011). Global-scale *P* wave tomography optimized for prediction of teleseismic and regional travel times for Middle East events: 2. Tomographic inversion, *J. Geophys. Res*. **116**, B04305, doi:10.1029/2010JB007969.

Stevens, J. L., H. Xu, J. W. Given, and G. E. Baker (2008). Development of surface wave dispersion and attenuation maps and improved methods for measuring surface waves, *Final Report*, Contract FA8718-05-C-0023, AFRL-RV-HA-TR-2008-1106.

Zhao, L.-S. and J. Xie (1993). Lateral variations in compressional velocities beneath the Tibetan Plateau from Pn traveltime tomography, *Geophys. J. Int*. **115**, 1070–1084.

HIGH-RESOLUTION REGIONAL PHASE ATTENUATION MODELS OF THE IRANIAN PLATEAU AND ZAGROS

Eric A. Sandvol[1], Ayoub Kaviani[2], Wenfei Ku[1], Rengin Gök[3], and Georg Rumpker[2]

University of Missouri[1], Johann Wolfgang Goethe-Universität [2],
and Lawrence Livermore National Laboratory[3]

Sponsored by the Air Force Research Laboratory

Award Nos. FA9453-11-C-0235[1,2] and DE-AC52-07NA27344[3]
Proposal No. BAA11-13

ABSTRACT

Development of high-resolution seismic attenuation models of the Iranian plateau and the Zagros mountains are critical to monitoring efforts in the Middle East due to the lack of high quality regional waveform data with reliable instrument response information. Furthermore, prior studies have suggested a complexity in the crustal and uppermost mantle attenuation structure beneath much of the Iranian plateau and the surrounding regions. Regional seismic phases show strong lateral variability in amplitude and frequency content due to this very complex structure. Using data collected by a series of deployments which consisted of approximately 140 temporary and permanent seismic stations in the Iranian Plateau, we have created a frequency dependent Lg Q model that covers most of the Iranian plateau using the two station method that eliminates the contributions from the source. Furthermore, we have combined this data set with our existing two station measurements that cover much of the Anatolian plateau so that we now have a model that extends from the western Anatolian plate to the eastern edge of the Iranian plateau. In general we have found that our model is consistent with other more regional scale models as well as the regional geology. One of the largest features of our models is the large Lg Q contrast across the Zagros suture. We have, however, found unexpected results, including a high Q zone that rings the Caspian Sea. Initially we thought this was an artifact of stations coverage, instead it seems to originate from energy that is bending around the south Caspian Sea oceanic crust. We have also found a region of high Q in the easternmost Iranian plateau.

We have analyzed Sn waveform data in order to characterize uppermost mantle shear wave attenuation. Sn is a relatively weak phase across much of the Anatolian-Iranian plateau, however, we have been able to identify a sufficient number of Sn phases to construct two-station Q maps for much of the Anatolian plateau and we are working to extend this model to the Iranian plateau. We are also working to create a catalog of well located events that have reliable source spectra determined using coda. This work will increase the number of seismic events with reliable source spectral and thereby significantly improve the ground truth database in Middle East.

OBJECTIVES

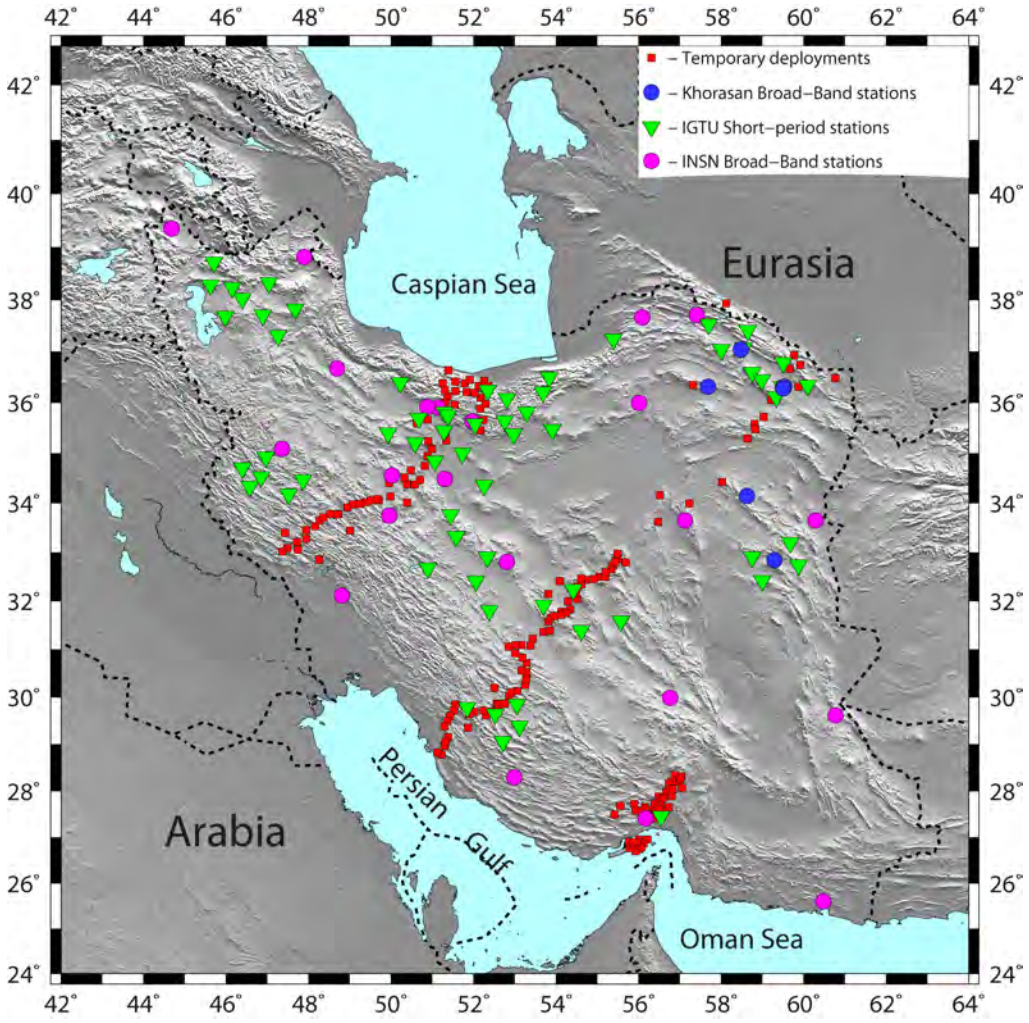


Figure 1. A regional topographic map showing the broadband (circles) and short-period stations (triangles) from all of the temporary and permanent networks that have been deployed across the Iranian plateau and Zagros mountains. These stations are nearly all three-component.

RESEARCH ACCOMPLISHED

The objective of this project, which has just begun, is to construct and validate regional wave (Pg, Sn, and Lg) attenuation models for the crust and upper mantle throughout the Iranian plateau and surrounding regions. Our research should increase ray path coverage of critical areas in the Middle East and help to create robust regional phase amplitude and attenuation models. This work will involve using new data collected by 31 permanent broadband and 70 short-period stations and another 204 temporary-broadband, intermediate-band, and short-period stations (Figure 1) distributed throughout Iran and across most of the major tectonic boundaries with the Iranian plateau. Furthermore, we have determined that these data are suitable for all types of regional phase attenuation studies. We are working to create a catalog of seismic events in and around Iran with reliable source spectra as well as a tested regional phase attenuation maps for the Zagros and Iranian plateau. These integrated Iranian arrays (Figure 1) cover much all of central Iran and the Zagros. The location of

these stations are ideal for studying aspects of monitoring research since there is a large number of broadband seismic stations across a complex tectonic environment. We are utilizing this relatively uniform coverage of permanent broadband stations along with the temporary deployments to study the propagation of the regional phases Pn, Pg, Sn, and Lg.

Data Collection

We have compiled waveform data from 70 permanent short-period stations operated by the Institute of Geophysics of Tehran University (IGTU), 23 permanent broad-band stations operated by the International Institute of Earthquake Engineering and Seismology (IIEES), 8 broad-band stations of the Khorasan Seismological Network in NE of Iran operated by the Earthquake Research Center of the Ferdowsi University of Mashhad (EQRC). All short-period stations are equipped with the SS1 sensor. All the broad-band stations are equipped with CMG-3T sensors. WE have also included the data available several temporary deployments of stations across the Zagros and Iranian Plateau. These temporary deployments include 204 broadband and sort-period stations. The collected waveforms of the regional events by our Iranian stations cover 21528 ray paths from 2453 regional events of magnitude greater than 4.0. We have verified that we have correctly normalized the instrument responses by comparing noise spectra for selected stations across Iran.

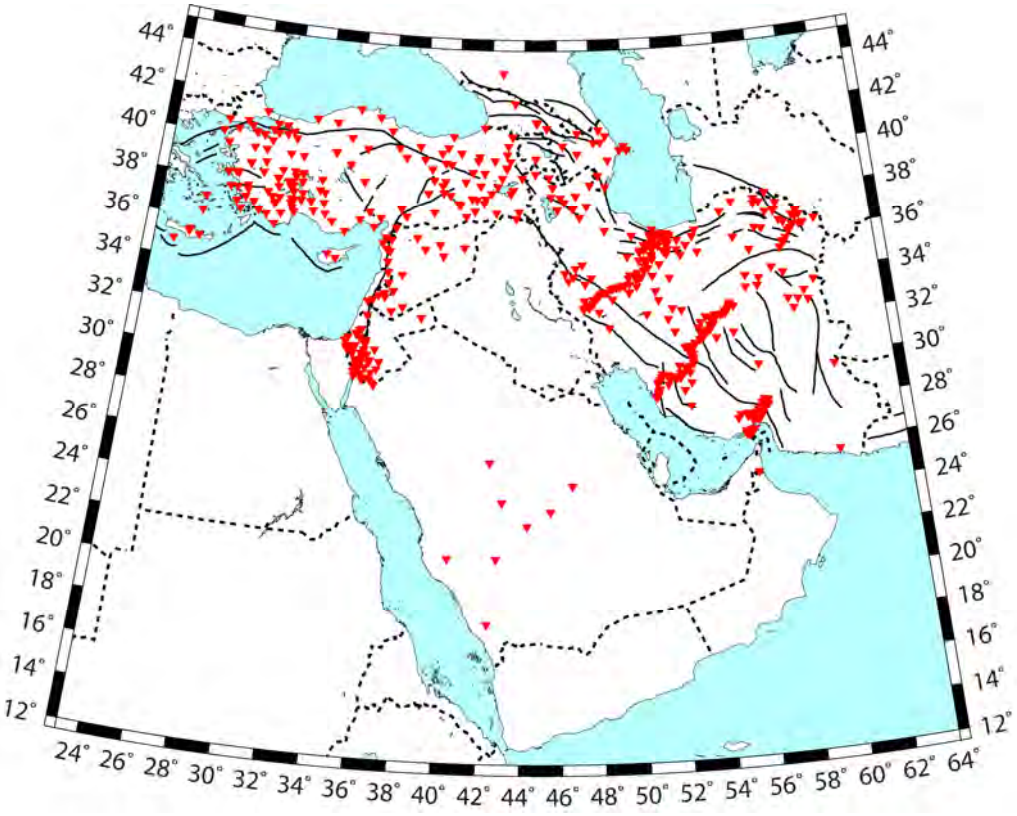


Figure 2. Location of all the stations in the Middle East used in this study.

We have also combined these data with data from numerous networks across Turkey, Georgia, Azerbaijan, Syria, Jordan, and Saudi Arabia. In total we have collected data from more than 250 stations that when combined with the data from Iran gives us waveforms from over 550 stations spanning most of the Northern Middle East. Figure 2 shows the location map of all the stations in the Middle East used in this study.

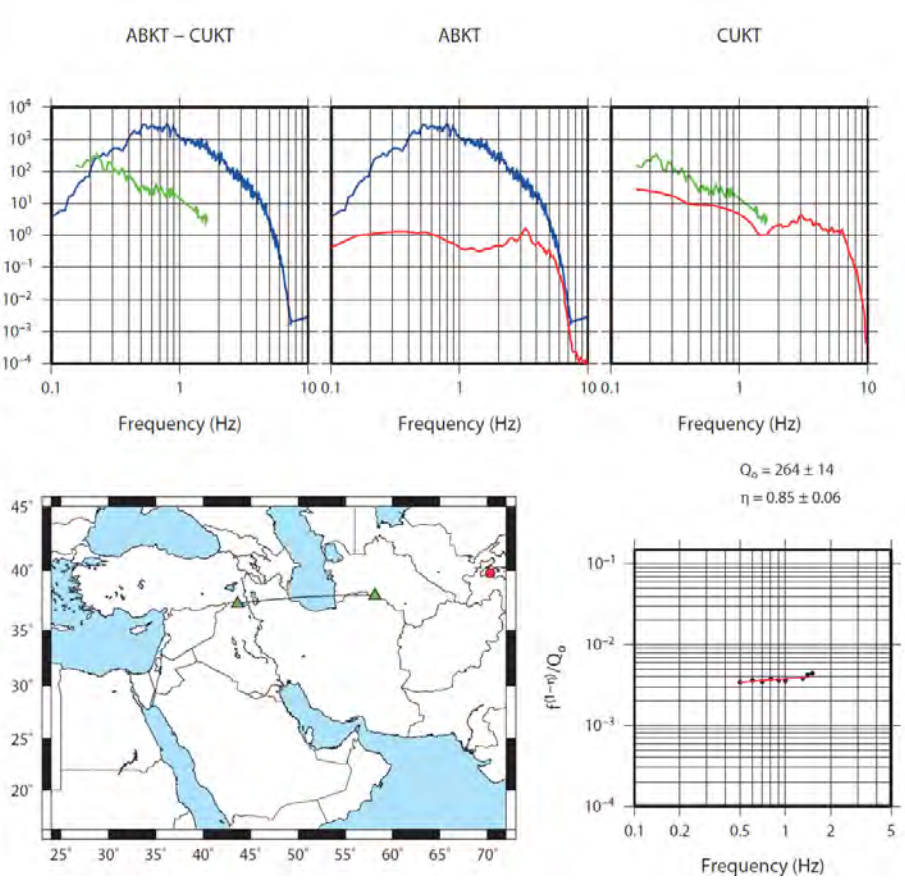


Figure 3. An example of Lg two-station analysis for a path that is cross the southern edge of the Caspian Sea. This may be an example of Lg energy bending around the south Caspian ocean crust.

The contemporaneous coverage of the stations is needed in the two-station method. By taking into account this criterion, we could have 7389 two-station paths (Figure 4) over the Iranian and Turkish Plateau from 830 events yielding sufficient ray coverage suitable for the tomographic imaging of Lg and Pg attenuation.

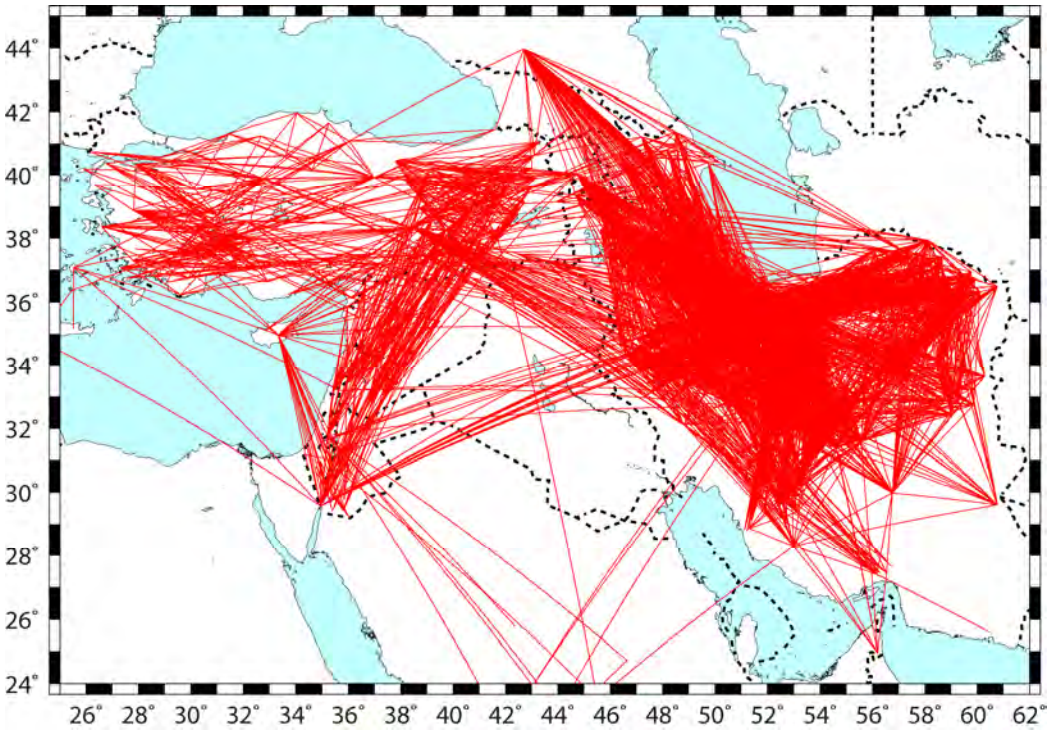


Figure 4. Two station paths over the Middle East, Turkey and Iran used for the tomographic imaging of Lg Q.

Regional phase Attenuation Analysis-Two-Station Approach

Using the dense coverage of the combined Iranian-Northern Middle Eastern database we have constructed detailed maps of regional phase attenuation for the Iranian and Anatolian Plateaus. We have created a model that can be compared with other independent techniques such as amplitude tomography (e.g., Pasaynos et al., 2009). Regional discriminants use high frequency regional phase amplitudes, thus it is critically important to be able to develop a reliable model for the direct phase amplitudes. They are also essential to investigations into regional phase yield estimation, however, coverage has been difficult to obtain for high frequencies as they decay into noise more quickly, and can be obscured by the coda of prior phases at distance.

Methodology

The amplitude of a seismic wave may be described by an exponential attenuation equation that accounts for both geometric spreading and attenuation,

$$A(f) = I(f)E(f)S(f)G(\Delta)\exp\left(-\frac{\pi f \Delta}{vQ(f)}\right) \qquad (1)$$

where A is the observed amplitude between source and receiver for a wave of frequency f recorded at distance Δ. Here, I is the instrument response, E is the source amplitude, S is the site amplification response, v is the wave group speed, and G is the geometric spreading function that is described primarily by an exponent. Q(f) is attenuation coefficient that represents the decay of the amplitude due to both anelastic absorption and scattering of seismic energy.

Attenuation (Q) Tomography

Our Attenuation (Q) tomography relies on two-station methods for measuring inter-station Q. We apply a two-station method to estimate Lg Q_0 (Q at 1 Hz) and the power-law frequency dependence η using the relationship (Xie and Mitchell, 1990, Xie, 2002; and Zor et al., 2007)

$$\ln\left(\frac{A_i(f)}{A_j(f)}\right) = -m\ln\frac{\Delta_i}{\Delta_j} + \frac{f^{1-\eta}}{Q_0}\frac{\pi\Delta_{i,j}}{V}. \qquad (2)$$

The first term on the right side represents the inter-station geometrical spreading by a parameter m, and the second term represents the inter-station seismic attenuation. V is the empirical Lg group velocity of 3.3 km/sec. Δ_i, Δ_j and $\Delta_{i,j}$ are the epicentral distance to each station and the inter-station distance, respectively. A_i and A_j are Lg amplitude from each station in the frequency domain. The amplitude ratio in the frequency domain from two stations' waveforms for each event, represented in left term of equation (2), is obtained using spectrum from each station calculated in the Lg window with the group velocity range from 3.6 km/sec to 3.0 km/sec. The maximum acceptable signal/noise ratio is set at 2 in this study by using the pre-Pn noise window.

To select the two-station paths, the maximum difference in source-station azimuths $\delta\theta$ for each two-station path is set at 15°, the minimum inter-station distance Δ_{ij} between the two stations is 100km to reduce modeling errors to less than 20%, and the minimum epicentral distance is set at 2° to guarantee measured Lg as a regional phase For Lg, the critical inter-station distance will be determined by

$$\frac{\delta Q_0}{Q_0} = \frac{V_{Lg}}{\pi f_0}\left(\frac{Q_0}{\Delta_{ij}}\right)\delta x. \qquad (3)$$

If the modeling error δx is assumed to be 0.2 and the Q error is to be kept less than 20%, the inter-station distance should be more than 100km.

Our two-station Lg attenuation model shown in Figure 5 shows the great deal of large variations in Lg Q especially associated with plate boundaries. All measurements used to construct this model were manually reviewed in order to verify the presence of Lg (i.e., Lg efficiency) as well as to determine the optimal Lg group velocity window. We believe this part of the work is essential to quality control our Lg amplitude data. In general we observe very consistent patterns in Lg attenuation that correspond to the Arabian-Eurasian plate boundary. We generally observe large Lg Q (~400) within the Arabian plate and Low Lg Q (~150) within the Iranian and Anatolian plateaus. This can be clearly seen by the very abrupt change in Lg Q across the eastern margin of the Zagros which marks the suture between the Arabian and Eurasian plates. This model is a clear indication of the well know Lg blockage zone across the Zagros. We also see that there is higher attenuation within the Anatolian plateau, especially in eastern Anatolia, than that in the Iranian plateau. The Lg Q variation within the Iranian plateau seems to correspond weakly to sediment thickness.

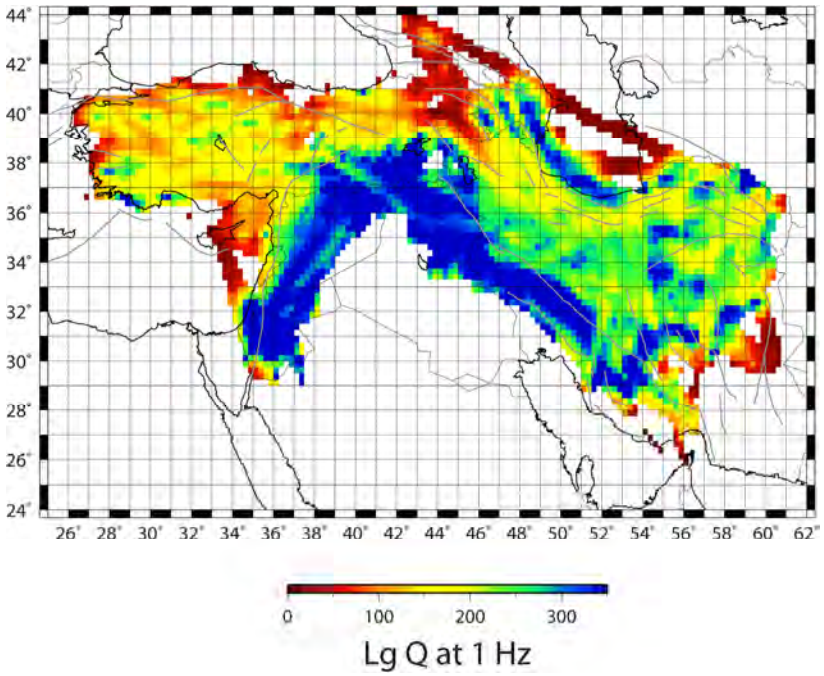


Figure 5. Our Lg Qo map for the northern Middle East, including the Iranian and Anatolian plateaus. This model only includes analysis of efficient and inefficient Lg phases (no blocked paths).

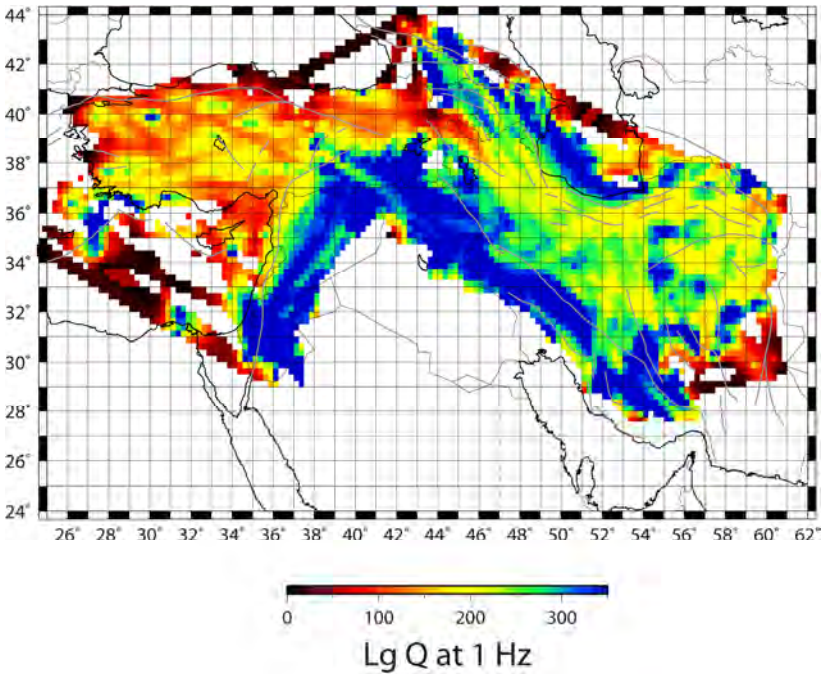


Figure 6. Our Lg Qo map for the northern Middle East that includes blocked paths in the tomographic model. We estimated a minimum Lg Q required to eliminate 90% of the Lg signal and included these estimates in our Lg Q tomography.

One potential problem with our approach in only using waveforms with inefficient or efficient Lg phases is that we are systematically censoring a portion of our data set that will bias our Lg Q model upwards. In order to explore the effects of this we have included blocked paths in our Lg Q models by estimating a minimum Q

value required to eliminate 90% of the Lg phase, similar to the technique we used for our Sn efficiency tomography. Figure 6 shows the result of this approach. We see strong attenuation across both the South Caspian and Black Seas; however, we continue to see evidence of efficient Lg propagation around the western edge of the South Caspian basin. As we can see from Figure 3 this appears to be real. We speculate that Lg energy is not propagating only along a great circle path but is propagating efficiently along the Alborz mountains along the western edge of the Caspian Sea.

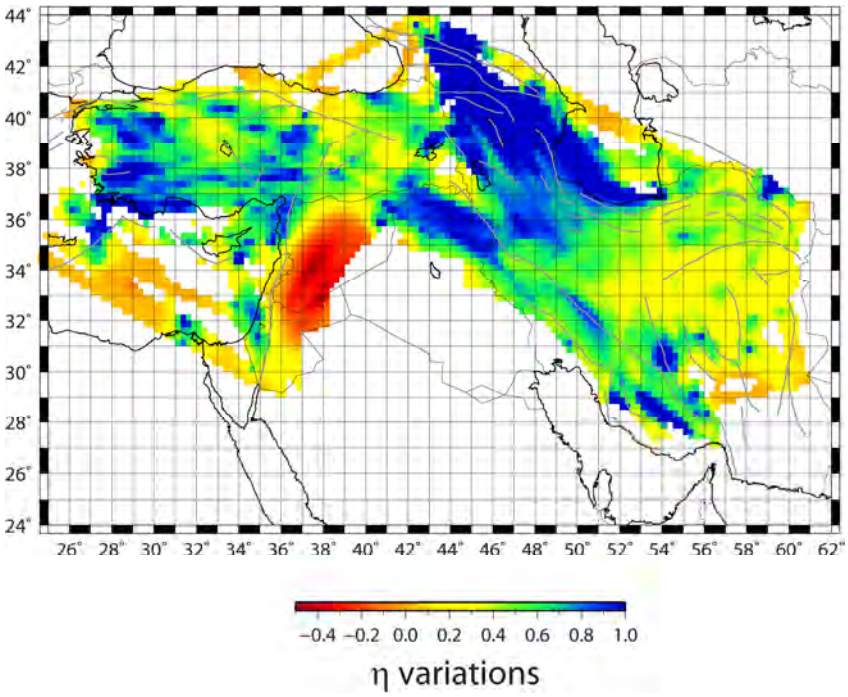


Figure 7. Map of frequency dependence of Q for the 1 Hz Q values over the Iranian and Turkish Plateau shown in Figure 6.

Sn Q tomography

In addition to Lg we have also created attenuation models for Sn. This is a far more challenging job than Lg propagation because of the lack of high frequency Sn paths across much of the Anatolian and Iranian plateaus. We have computed a preliminary Sn Q model shown in Figure 8 using only efficient and inefficient Sn phases all of which have been manually reviewed. The relatively small number of two station paths (825) is due to the effective blockage of high frequency Sn throughout much of the study region (Figure 9). Our preliminary Sn Q estimate to first order correlate with Pn velocity estimates in the region. We see high Sn Q values within the Arabian plate and throughout much of the central Anatolian plate. The low Q values in central Anatolian correlate with region with active Quaternary volcanism and low Pn velocities. This correlation is encouraging despite the potential problems with focusing and defocusing caused by changes in uppermost mantle velocity gradients. We also observe low Q values in the Isparta angle where there is a well established slab tear where the Cyprean and Hellenic arcs intersect. This also gives us some confidence that we are preliminary model is reliable. We are working to expand our Sn Q model by identifying low frequency Sn propagation and thereby allowing us to apply a reverse two station approach to Sn Q.

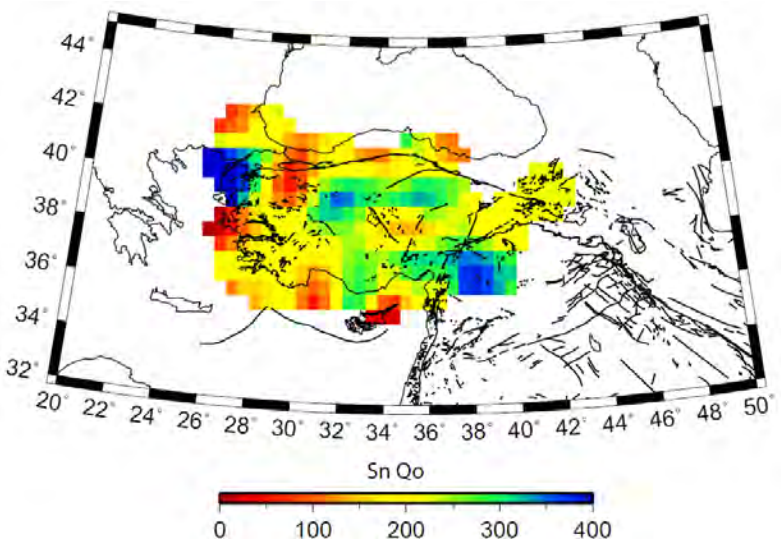


Figure 8. A preliminary Sn Q map for western and central Anatolia. This Q map was created using efficient and inefficient high frequency Sn phases visually inspected from over 100 stations spread throughout Anatolia.

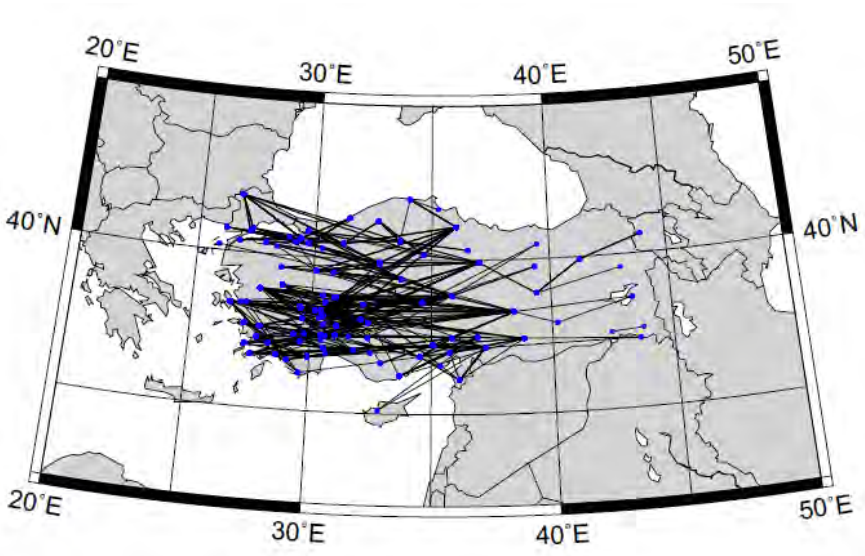


Figure 9. The two station paths used in our preliminary Sn Q model.

CONCLUSIONS AND RECOMMENDATIONS

In order to develop transportable seismic source discriminants it is very important that we develop method to account for source and site effect; our two station method should effectively eliminate the source term, however we are left with the site term. We are now working on this problem by extending our two station model to reverse two station measurements. The reverse two station measurements will effectively isolate the site as well as source term as well as provide some of the most accurate regional phase Q estimate (Ford et al., 2008). In order to expand the number of two station Sn measurements we are working at identifying low frequency Sn phases throughout the Middle East. We are apply a low pass filter at 0.5 Hz and visually inspecting approximately 5,000 waveform recorded in and around the Iranian plateau Furthermore, this will allow us to create a robust model that can be use to predict seismic amplitudes and thereby contribute important model base information to DOE's MDAC amplitude corrections

ACKNOWLEDGEMENTS

We are grateful to all the Iranian and international scientists and engineers who helped to deploy and service both the permanent and temporary seismic networks across Iran.

REFERENCES

Ford. S. R., D. S. Dreger, K. Mayeda, W. R. Walter, L. Malagnini, and W. S. Phillips (2008). Regional Attenuation in Northern California: A Comparison of Five 1D *Q* Methods, *Bull. Seismol. Soc. Am.* **98**, 2033–2046, 2008.

Pasyanos, M.E., Walter, W.R., and Matzel, E.M. (2009). A simultaneous multiphase approach to determine P-Wave and S-Wave attenuation of the crust and upper mantle, *Bull. Seismol. Soc. Am.* **99** (6), 3314–3325.

Sandvol, E., K. Al-Damegh, A. Calvert, D. Seber, M. Barazangi, Mohamad, R, R. Gök, N. Turkelli, and C. Gurbuz (2001). Tomographic imaging of Lg and Sn propagation in the Middle East, *Pure Appl. Geophys.* **158**, 1121–1163.

Xie, J., and B. J. Mitchell (1990). A back-projection method for imaging large-scale lateral variations of Lg coda Q with application to continental Africa, *Geophys. J. Int.* **100,** 161–181.

Xie, J. (1998). Spectral inversion of Lg from earthquakes; a modified method with applications to the 1995, western Texas earthquake sequence, *Bull. Seismol. Soc. Am.* **88**, (6), 1525–1537.

Xie, J. (2002). Source scaling of Pn, Lg spectra and their ratios from explosions in central Asia: Implications on identification of small seismic events at regional distances, *J. Geophys. Res.* (B7), 10.1029/2001JB000509.

Zor, E., E. Sandvol, J. Xie, N. Türkelli, B. Mitchell, A. Gasanov, and G. Yetirmishli (2006). Crustal Attenuation within the Turkish Plateau and Surrounding Regions, *Bull. Seismol. Soc. Am.*, in review.

HIGH-RESOLUTION SEISMIC VELOCITY AND ATTENUATION MODELS OF EASTERN TIBET

Eric A. Sandvol[1], Tom M. Hearn[2], James F. Ni[2], Savas Ceylan[1], Wenfei Ku[1], Xueyang Bao[1], Xiaofeng Liang[1], and W. Scott Phillips[3]

University of Missouri[1], New Mexico State University[2], and Los Alamos National Laboratory[3]

Sponsored by the Air Force Research Laboratory

Award Nos. FA9453-10-C-0256 and DE-AC52-06NA25396
Proposal No. BAA10-61

ABSTRACT

High-resolution seismic velocity and attenuation models of the Tibetan Plateau are critical to monitoring seismology efforts in eastern Eurasia. We have used three different but complimentary seismic methods to determine the velocity structure in this region: P_n velocity tomography, body-wave finite-frequency tomography, and Rayleigh and Love surface wave tomography. We observed consistent anomalies in the crust and upper mantle using all of these methods. These anomalies include a low velocity in northern Qiangtang Terrane and the Songpan-Ganzi fold belt and the high velocity in the Qaidam Basin. We have done a quantitative comparison between these three models and found that although all of these anomalies exist in our velocity models, the position differs slightly from model to model. Q_{Lg} and Q_{Pg} models have been determined using a Reverse Two-station/event Method, which shows a high seismic attenuation zone along the Kunlun Mountains. We have also obtained Q_{Sn} model using long period Sn propagation across the northern Tibetan Plateau. High-frequency Sn phases are almost never observed for stations within the northern Tibetan Plateau, however, we do observe long period Sn for some ray paths. It is important to note that we also observe long period Sn blockage for paths that travel through a great length in the northern Qiangtang terranes. Our long period Q_{Sn} shows a low Q zone below the Songpan-Ganzi Terrane. We have also observed significant azimuthal anisotropy in Lg Q that strongly correlates with seismic velocity anisotropy. The origin of the Lg Q anisotropy is probably related to deflection of the Lg wave along the Kunlun Mountains. We are working to compare our reverse two station Q models with the other single station models of regional phase Q that covers the Tibetan Plateau.

OBJECTIVES

The objectives of this project are to establish high-resolution three-dimensional seismic velocity models and regional wave attenuation models for the crust and upper mantle in Tibetan Plateau and adjacent regions of western China. The Tibetan Plateau and adjacent areas have been focused by many studies of seismic velocity structure (e.g., Kind et al., 2002; Tilmann et al., 2003; Li et al., 2008) and seismic attenuation structure (e.g., McNamara et al., 1996; Phillips et al., 2000; Xie, 2002). Reliable high-resolution images of the crustal and mantle of this region is very important but limited by insufficient data sets and mutually independent techniques. Our research involves new waveform database, which have increased the coverage of the northern Tibet and Qaidam Basin (Figure 1). All stations are equipped with broadband CMG-3T, CMG-ESP, and STS-2 sensors. Based on the results of last year's research review (Sandvol et al., 2010), we have applied this new data set and various techniques to estimate the seismic velocity and Q variations within this area.

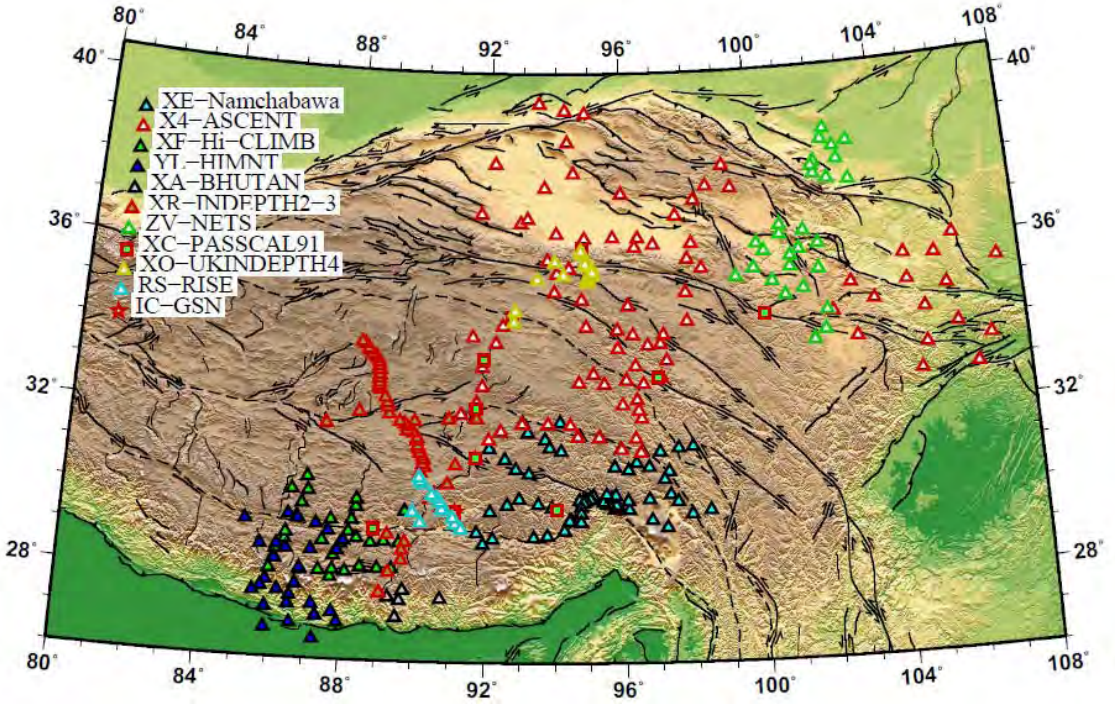


Figure 1. A map showing the broadband stations from all permanent and temporary networks whose data are used in our project. Open red triangles represent the station location of the ASCENT experiment and open light green triangles represent NETS. Also included are large numbers of both phase and waveform data from US and Chinese temporary seismic stations.

RESEARCH ACCOMPLISHED

Using both travel-time body and surface wave tomography, we have created a Pn velocity model, 3-D P and S wave velocity models, and Rayleigh waves phase velocity models for the crust and upper mantle of this region. We have also generated 2-D Q_{Lg} and Q_{Pg} models with site and source responses are isolated and resolved as well. A significant azimuthal anisotropy of Lg Q is dramatically observed and solved in 2-D tomography.

Seismic Velocity Models

Pn waves mainly travel within the mantle-lid that lie beneath the Moho discontinuity, and thus its velocity model mainly represents the velocity structure of the uppermost mantle. We have applied the method of Hearn et al. (1991) to generate the Pn velocity tomographic model (Figure 2). The Pn velocity varies from 7.8 km/s to 8.3 km/s with an average of 8.1 km/s. We have used Pn arrivals from many seismic

experiments and networks in Tibet and surrounding regions to image the structure of the mantle-lid. Previous Pn tomography studies have remarked on the contrast between high velocities beneath southern Tibet and low velocities beneath northern Tibet. We find that this model is oversimplified. Longer raypaths show a vastly different velocity structure than do the shorter raypaths, thus there is significant vertical variation in the velocity structure (and thickness) of the mantle lid. Only longer raypaths show low velocity beneath northern Tibet. The lowest velocities occur beneath the central Qiangtang and Songpan-Ganzi terranes, but are not coincident with the Bangong-Nujiang suture that separates northern and southern Tibet.

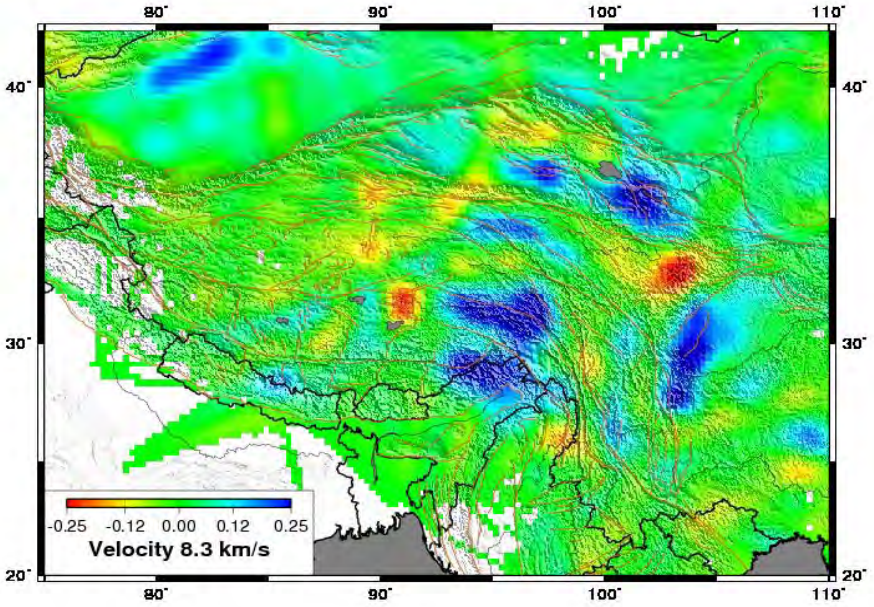


Figure 2a. Pn wave velocity structure in the northeastern Tibetan Plateau. High Pn velocity anomalies are located to the north of the Kunlun range and around the Eastern Himalayan Syntaxis. Low Pn velocity anomalies are mainly observed in central Qiangtang and northern Songpan-Ganzi terrain. These Pn measurements were made for distances between 3 and 6 degree.

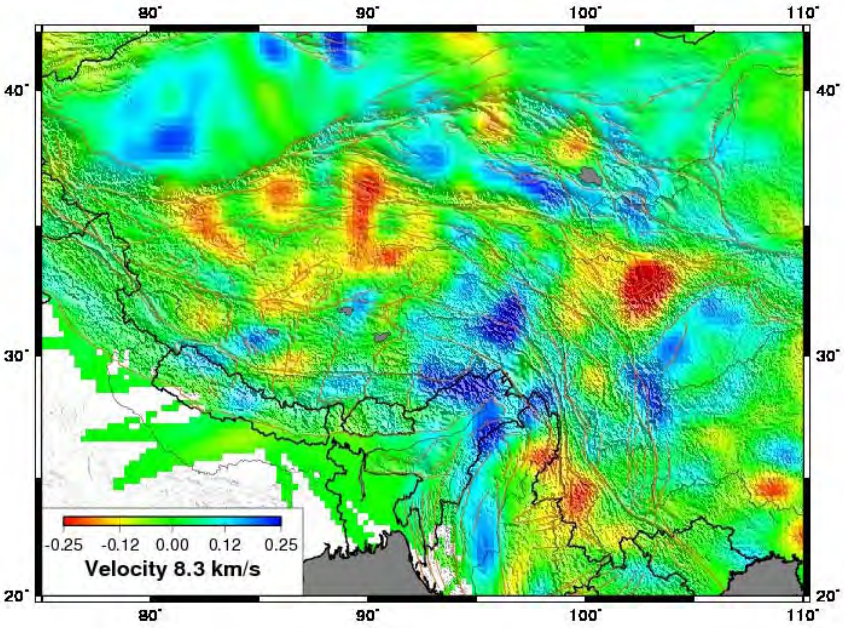


Figure 2b. Pn wave velocity structure in the northeastern Tibetan Plateau taken from Pn measurements between 6 and 12 degrees.

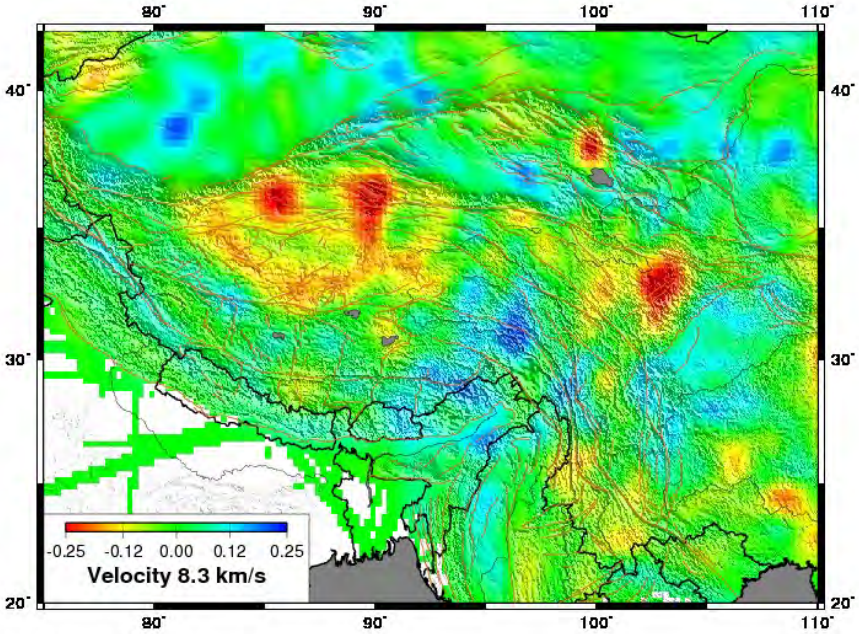


Figure 2c. Pn wave velocity structure in the northeastern Tibetan Plateau taken from Pn measurements between 9 and 15 degrees.

These deep low velocity zones suggest a thin lithosphere there beneath most parts of the northern Tibetan Plateau. There is also low velocity mantle beneath the northeast Songpan-Ganzi Terrane (in Gansu province). Shorter ray paths image the top of the mantle lid and show two distinct high velocity zones beneath the Himalayas. Several similar high velocity regions occur north of the eastern Himalayan syntaxis beneath the Lhasa, Qiangtang, and Songpan-Ganzi terranes. Most of the high velocity anomalies that lie south of the Bangong Nujiang Suture are probably related to the underthusted and segmented Indian continental lithosphere. A shallow mantle-lid high velocity anomaly in the central Songpan-Ganzi Terrane (between 93°E and 98°E) is probably related to a fossil subducted oceanic slab or continental lithosphere during the closure of the Lhasa Terrane and the Qiangtang Terrane (Yue et al., 2012). The east-west variability of Pn velocity beneath the Himalayas and southern Tibet indicates that the underthrusted Indian continental lithosphere is not a homogeneous body. Qaidam Basin along with the Gonghe and Xining Basins east of it show an east-west high velocity anomaly. We interpret this as a preexisting cratonic core that deformed little while the Tibetan Plateau to the south and the Qilian Shan to the north did.

We have applied a finite-frequency tomography method (e.g., Hung et al., 2004; Liang et al., 2011) to generate three-dimensional P and S body wave velocity models for the lithosphere of the eastern Tibet (Figure 3). A contrast between a widespread slow velocity northern Tibet and heterogeneous southern Tibet is significant in the upper mantle velocity structure. The homogeneous low P- and S- velocity anomalies in the crust and upper mantle of the northern Qiangtang and Songpan-Ganzi Terranes probably penetrate at least 250 km into the upper mantle. High P- and S-wave velocity anomalies are generally distributed within the mantle beneath the Qaidam Basin and southern Tibet to a depth of more than 250 km. A few N-S oriented low velocity bands are observed beneath southern Tibet and appear to extend to at least 150 km depth.

A three-dimensional model of shear-wave velocities derived from Rayleigh wave phase velocity measurements is also presented for the lithosphere of the eastern Tibet (Figure 3). Like Pn and body wave results, low velocity anomalies occur across and within most major strike-slip fault zones in the Qiangtang and Songpan-Ganzi portion of the northern Tibet. A high velocity anomaly, mainly observed along the Bangong-Nujiang Suture at 65 km depth (33°N and 92°E), probably is a portion of the underthrusting Indian plate. This high velocity below the Bangong-Nujiang Suture appears in both models to extend to depths of at least 300 to 400 km depths and is oriented vertically. In general the upper mantle, from the

Main Frontal Thrust to central Tibet around ~33°N, exhibits laterally variable P- and S-wave velocity anomalies extending to at least 250 km in depth. Significant alternating low and high velocity anomalies are observed beneath southern Tibet, elongated in a north-south direction and extending to at least 150 km depth, possibly deeper. Quantitative comparison of the overlapping regions of the body and surface wave models of the shear wave velocity show that although we can observe the same features in both the surface and body wave tomographic models, the position of these anomalies is different suggesting some systematic difference in the way these different waves are sampling the Tibetan crust and upper mantle.

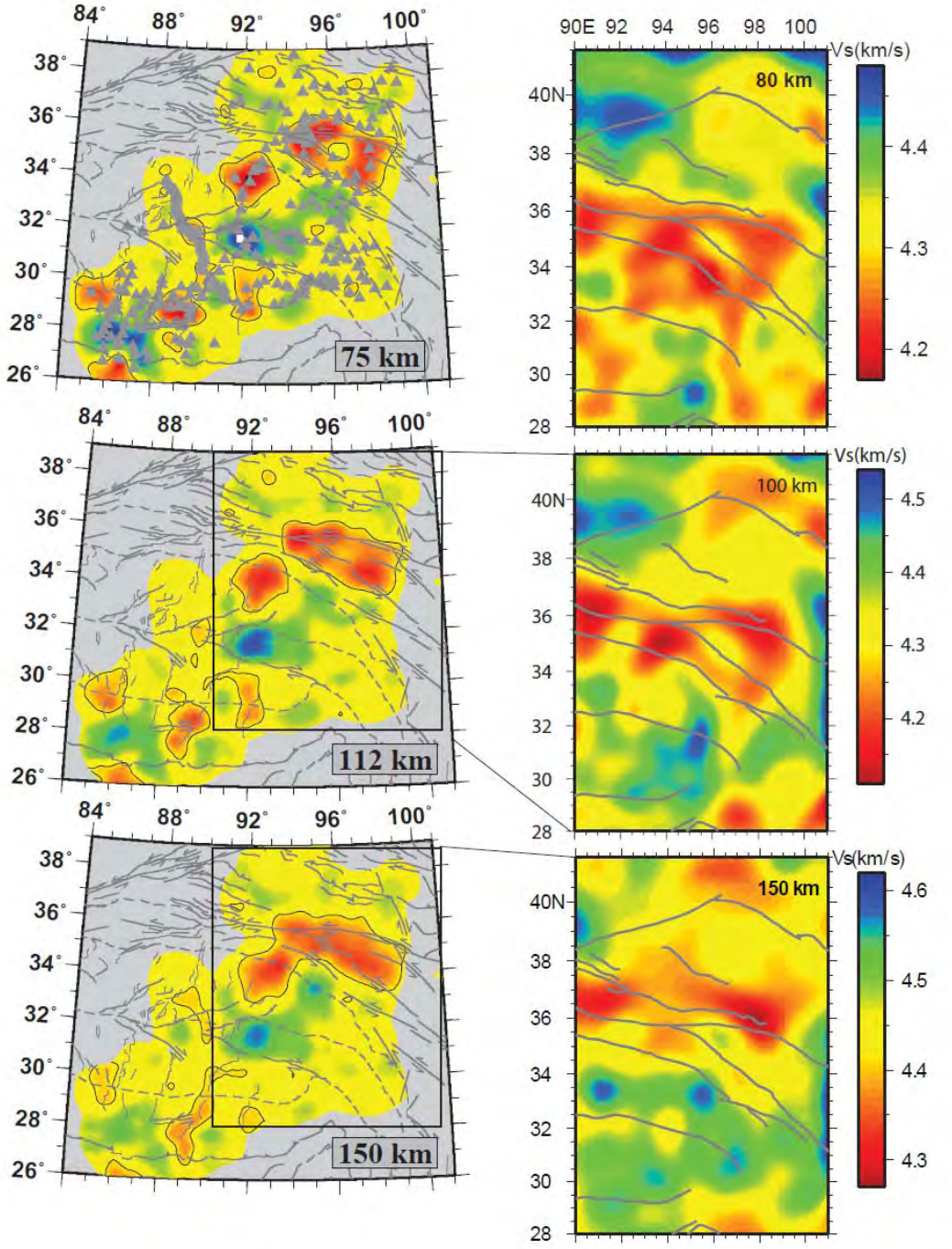


Figure 3. A comparison of our shear wave velocity model derived from body waves (on the right) and surface waves (on the left). Nearly all of the features in both models are observed, however, the position of the anomalies is different in each of the two models.

All of the methods individual results consistently show a low velocity zone in the northern Qiangtang and Songpan-Ganzi Terranes, and relatively high velocity in southern Tibet and Qaidam Basin. The strong correlation between the independent methods suggests that, at least to first order, these models are relatively robust. Further studies, such as joint inversion o body and surface wave, are expected to see if these models will help to improve sparse network earthquake locations.

Seismic Attenuation

Q_{Lg} is typically assumed as an approximation or proxy for shear wave Q of the crust and can help serve as a physically based model to predict regional phase amplitudes. We used a Reverse Two-station/event Method (RTM) (Chun et al., 1987) to measure accurate path-based $1/Q_{Lg}$ values (Figure 5). This method is an improvement upon the Two-Station Method (TSM) and includes two specific cases: Reverse Two Station (RTS) path and Reverse Two Event (RTE) path. In theory, it eliminates the contribution on spectral amplitude from the source excitation function, radiation pattern, instrument response, and site response, and has been presented as the most accurate method in Q measurement (Ford et al., 2008). Because of its rigorous geometrical requirement and the specific propagation characteristics of Lg, the application of this method still requires extensive seismic network deployed contemporaneously throughout Tibet (Fan and Lay, 2003).

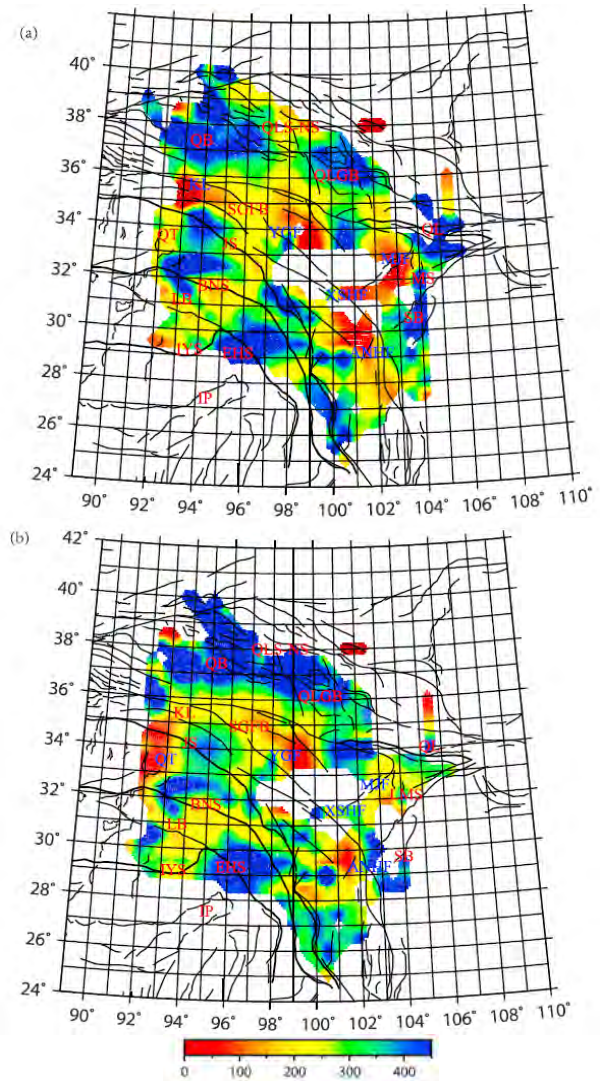


Figure 4. A comparison of our Lg (top) and Pg (bottom) models for eastern Tibet. These values are taken from our reverse two station measurements.

Similar to Q_{Lg} being used as a proxy of crustal Q_{β}, the Q_{Pg} can be assumed to be a proxy of crustal *Q in P-wave*$_{\alpha}$. We apply a very similar data processing and inversion method to the *Pg* data as we do with the *Lg* data; while some parameters, such as the group velocity window, the geometrical spreading coefficient, the threshold of maximum inter-station distance, etc, have been revised to appropriate values for *Pg* (Bao et al., 2011a). The calculated RTM Q_{Pg} tomographic map is strongly correlated with the RTM Q_{Lg} model (Figure 5) with high attenuation regions throughout most of the north and northeastern TP and low attenuation regions surrounding the TP. We observe differences in the relative attenuation structure between *Pg* and *Lg* in part of Qiangtang terrane that may indicate strong crustal heterogeneity causing different degrees of scattering attenuation effects on *Pg* and *Lg*.

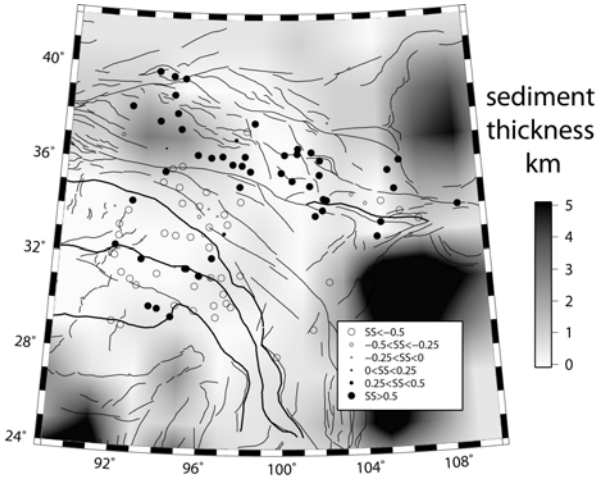


Figure 5. The lateral variations of site responses and sediment thickness for eastern Tibet. The sediment thicknesses are taken from crust 2.0 (Bassin et al., 2000).

We also use the RTM to solve the site response and source response. The site responses have a strong spatial structure across the Tibean Plateau (Figure 6). We consistently observe high site responses within the Qaidam basin and low site responses within the Tibetan Plateau at different frequencies. The lateral variation does not correlate with either the difference in instrument response or the surface shear-velocity down (the Vs for the upper 30 meters) in this area (Wald and Allen, 2007). Alternatively, it is possible that the site response strongly varies with the change in topography (Figure 1). Meanwhile, the site response may be affected by near-surface geological structures (Su et al., 1992). Our result of high site responses within the Qaidam basin, which has widespread sediment thicker than 10 km, suggests that thick sedimentary basins probably help to enhance the site amplification (Figure 5). However, we do not observe a perfect correlation between sediment thickness and thus there are other factors that effect the local site response such as topography and the upper crustal velocity structure.

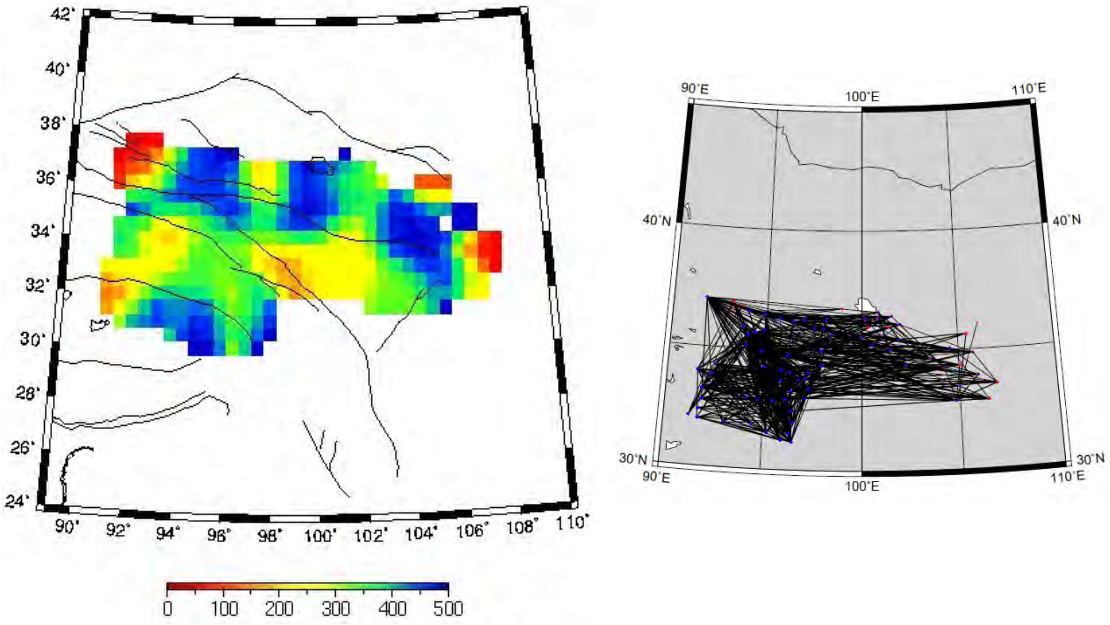


Figure 6. (left) Our preliminary estimate of Sn Q at 1 Hz using two station measurements of only efficient long period Sn across the Tibetan plateau and (right) the available two station paths used to compute these Sn Q estimates.

We have manually reviewed approximately 12,000 separate Sn waveforms recorded by the ASCENT and NETS arrays covering the northeastern Tibetan plateau. We have bandpassed filtered the data between 0.2 and .05 Hz in order to try and identify efficient and inefficient long period Sn waveforms across the Tibetan plateau. We were able to identify approximately 2,000 efficient paths that we used to build a two station Q_{Sn} model (Figure 7). We have found similar patterns in Sn Q as we have observed in Lg and Pg Q suggesting a vertical coherence in the seismic attenuation structure across northeastern Tibet.

CONCLUSIONS AND RECOMMENDATIONS

In this project, we are moving towards comparing and testing our velocity and attenuation models. We are nearly finished constructing regional Q models for Lg, Pg, and Sn. We are working to finalize our Sn Q map and test the how distance dependence our Sn Q measurements are. Furthermore, it is important to note that we still find a large number of blocked Sn paths events for the lower frequencies for Sn. The three separate velocity models show consistent results including a low velocity in the northern Qiangtang and the Kunlun belt and a high velocity anomaly within the Qaidam Basin. This suggests a strong lateral variation and vertical coherency of the relative velocity structures for the whole lithosphere in eastern Tibet and adjacent regions. We suggest that this structure is vertically coherent because it originates in from the large strike slip faults in northern Tibet. A high seismic attenuation zone is also observed along the Kunlun belt for Lg, Pg, and Sn. The consistency between the preliminary Sn Q measurements and Lg Q suggests that like velocity, seismic attenuation is also vertically coherent in this region. Our Sn mesaurements are considered preliminary because we have not accounted for the potentially strong effect of the uppermost mantle velocity gradient. In future work we would like to attempt to correct our Sn Q estimates for this effect.

ACKNOWLEDGEMENTS

We are grateful to all members of the INDEPTH IV and NETS teams, as well the IRIS DMC for providing other seismic data.

REFERENCES

Bao, X., E. Sandvol, J. Ni, T. Hearn, Y. J. Chen, and Y. Shen (2011). High resolution regional seismic attenuation tomography in eastern Tibetan Plateau and adjacent regions, *Geophys. Res. Lett.* **38** (16), 1–5, doi:10.1029/2011GL048012.

Bassin, C., Laske, G. and Masters, G., (2000), The Current Limits of Resolution for Surface Wave Tomography in North America, EOS Trans AGU, **81**, F897.

Chun, K.-Y., G. F. West, R. J. Kokoski, and C. Samson (1987). A novel technique for measuring Lg attenuation-results from eastern Canada between 1 to 10 Hz, *Bull. Seismol. Soc. Am.* **77**, 398–419.

Fan, G.W. and T. Lay (2003). Strong Lg wave attenuation in the Northern and Eastern Tibetan Plateau measured by a two-station/two-event stacking method, *Geophys. Res. Lett.* **30**, 1530, doi: 10.1029/2002GL016211.

Ford, S. R., D. S. Dreger, K. Mayeda, W. R. Walter, L. Malagnini, and W. S. Phillips (2008), Regional attenuation in northern California: a comparison of five 1D Q methods, *Bull. Seismol. Soc. Am.* **98**, 2033–2046, doi:10.1785/0120070218.

Hearn, T. M., M. N. Beghoul, and M. Barazangi (1991), Tomography of the western United States from regional arrival times, *J. Geophys. Res.* **89**, 1843–1855.

Hung, S.-H., Y. Shen, and L.-Y., Chiao (2004). Imaging seismic velocity structure beneath the Iceland hot spot: A finite frequency approach, *J. Geophys. Res.* **109**, B0835, doi: 10.1029/2003JB002889.

Kind, R., X. Yuan, J. Saul, D. Nelson, S. V. Sobolev, J. Mechie, W. Zhao, G. Kosarev, J. Ni, U. Achauer, M. Jiang (2002). Seismic images of crust and upper mantle beneath Tibet: Evidence for Eurasian plate subduction, *Science* **298**, 1219–1221.

Li, C., R. D. Van der Hilst, A. S. Meltzer, R. Sun, and E. R. Engdahl (2008). Subduction of the Indian lithosphere beneath the Tibetan Plateau and Burma, *Earth Planet. Sci. Lett.* **274** 157–168.

Liang, X., Y. Shen, Y. J. Chen, and Y. Ren (2011). Crustal and mantle velocity models of southern Tibet from finite frequency tomography, *J. Geophys. Res.* **116**: B02408, doi: 10.1029/2009/2009JB007159.

McNamara, D.E., T. J. Owens, and W. R. Walter (1996). Propagation characteristics of Lg across the Tibetan Plateau, *Bull. Seismol. Soc. Am.* **86**, 457–469.

Phillips, W. S., H. E. Hartse, S. R. Taylor, and G. E. Randall (2000). 1 Hz Lg Q tomography in central Asia, *Geophys. Res. Lett.* **27**, 3425–3428.

Sandvol, E. A., X. Bao, J. Ni, T. Hearn, and S. Phillips (2010), High-resolution seismic velocity and attenuation models of western China, in *Proceedings of the 2010 Monitoring Research Review: Ground-Based Nuclear Explosion Monitoring Technologies*, LA-UR-10-05578, Vol. 1, pp. 197–206.

Su, F., K. Aki, T. Teng, Y. Zeng, S. Koyanagi, and K. Mayeda (1992). The relation between site amplification factor and surficial geology in central California, *Bull. Seismol. Soc. Am* **82** (2), 580–602.

Tilmann, F., Ni, J., and INDEPTH III Seismic Team (2003). Seismic imaging of the downwelling Indian lithosphere beneath central Tibet, *Science* **300**, 1424–1427, doi: 10.1126/science.1082777.

Wald, D. J. and T. I. Allen (2007). Topographic slope as a proxy for seismic site conditions and amplification, *Bull. Seismol. Soc. Am.* **97** (5), 1379–1395, doi:10.1785/0120060267.

Xie, J. (2002a). Lg Q in the eastern Tibetan Plateau, *Bull. Seismol. Soc. Am*. **92**, 871–876.

Yue, Han, Y.J. Chen, E. Sandvol, J. Ni, T. Hearn, S. Zhou, Y. Feng, Z. Ge, A. Trujillo, Y. Wang, G. Jin, M. Jiang, Y. Tang, X. Liang, S. Wei, H. Wang, W. Fan, and Z. Liu (2012). Lithospheric and upper mantle structure of the northeastern Tibetan Plateau, *J. Geophys. Res*. **117**, B05307.

SHORT-PERIOD, ANELASTIC AND ANISOTROPIC, WAVEFORM-BASED 3D MIDDLE EAST MODEL TO IMPROVE NUCLEAR EXPLOSION MONITORING

Brian Savage[1], Daniel Peter[2], Brian M. Covellone[1], Christina E. Morency[3], Arthur J. Rodgers[3], and Jeroen Tromp[2]

University of Rhode Island[1], Princeton University[2], and Lawrence Livermore National Laboratory[3]

Sponsored by the Air Force Research Laboratory and the National Nuclear Security Administration

Award Nos. FA9453-12-C-0208[1,2] and DE-AC52-07NA27344[3]
Proposal No. BAA12-29

ABSTRACT

Utilization of the full, seismic-waveform based techniques for discrimination purposes is currently effective and efficient for large magnitude, > M 4.5, well-recorded events. However, a need to reduce the magnitude threshold requires predictive capabilities at shorter periods, < 10 seconds, if waveform based techniques are to be used in routine event evaluations. Recent efforts to improve the seismic waveform, prediction capabilities of existing models have proven successful by reducing an acceptable period for prediction to 15 – 20 seconds. As models begin to accurately predict shorter periods, they will begin to incorporate higher order structures, i.e. larger and sharper wave speed contrasts, and they will also be effective in source discrimination at shorter periods and high noise environments. However, as the minimum period continues to drop, effects of attenuation and anisotropy will become more significant and require quantification. As such, current generation models lack both heterogeneous anelastic attenuation and a more robust treatment of anisotropy. We plan on pushing the predictive capabilities of the current 3D Middle East wave speed model to approximately 2 seconds. In doing so, 3D anleastic attenuation and anisotropic models will be incorporated into a seamless seismic Earth model of the region. Anelastic attenuation will be embedded along side a 3D wave speed model and the anisotropic component will be parameterized as transverse isotropy with a variably oriented symmetry axis.

Achieving these ambitious goals will require a waveform based, tomographic inversion capable of handling seismic waveform propagation at 2 seconds, 3D variations in attenuation, and general anisotropy. As with previous efforts use of the SPECFEM3D Globe and its adjoint tomographic capabilities will perform the necessary forward and time-reversed calculations. Demands required by the 2 second minimum period requires use of large clustered computer systems and improved / state-of-the-art computational units to efficiently simulate the seismic wavefield. Initial steps will gather seismic waveform and source data to evaluate the sources and stations in the region. Our recent experience with source characterization demonstrated that this step is invaluable to accurately predict waveform amplitudes with minimal change to the source moment tensor. Predicting wave-field amplitudes are increasingly important, as anelastic attenuation is highly dependent on variations in seismic amplitudes. Initial inversions for seismic wave speeds will begin at longer periods, 15 - 20 seconds, and later inversions will include additional shorter period energy. As with studies of a similar methodology, we anticipate wave speed anomalies to localize and strengthen in amplitude; similar effects for attenuation and anisotropy are also expected. The final model, with predictive capabilities at 2 seconds period, 3D anelastic attenuation, and anisotropy with a variably oriented symmetry axis will be a major advance for the Nuclear Explosion Monitoring community for event discriminate at smaller magnitudes.

OBJECTIVES

Source studies that utilize full-waveform seismic data are quite robust at discriminating between a variety of source types (e.g., Liu et al, 2004; Minson and Dreger, 2008; Ford et al., 2009; Kim et al., 2011). However, their use is limited by a requirement of high quality, well-recorded seismic data and Earth models that accurately predict the path-specific Green's functions. High quality seismic data must be well recorded azimuthally and have good signal to noise. Due to the limited predictive capabilities of wave speed models, they are only used at periods greater than 30 – 50 seconds depending on the epicentral distance. Use of these long periods necessitates sources to be a minimum magnitude, nominally > 4.5 Mw. Efforts to enhance the waveform predictive capabilities of wave speed models have recently begun to shift the minimum period to ~15 seconds (Savage et al., 2011) at regional distances. The recent and future improvement of these full waveform predictive models will allow the investigation of sources at even lower magnitudes, ~ 3.0 Mw, dependent on epicentral distance.

Efforts to extend the period range to even shorter periods requires higher resolution images of the wave speeds in the region, plus increasingly important effects of anelastic attenuation, Q^{-1}, and anisotropy. As the period range decreases these second order effects at long period, > 30 seconds, become increasingly important and can radically change seismic paths and recorded responses. The goal of this effort is to further improve models of seismic wave speeds, Vs and Vp, to predict seismic waveforms at periods approaching 2 seconds. In addition, anelastic attenuation and anisotropy will also be accounted for through improved use of amplitude anomalies and parameterization.

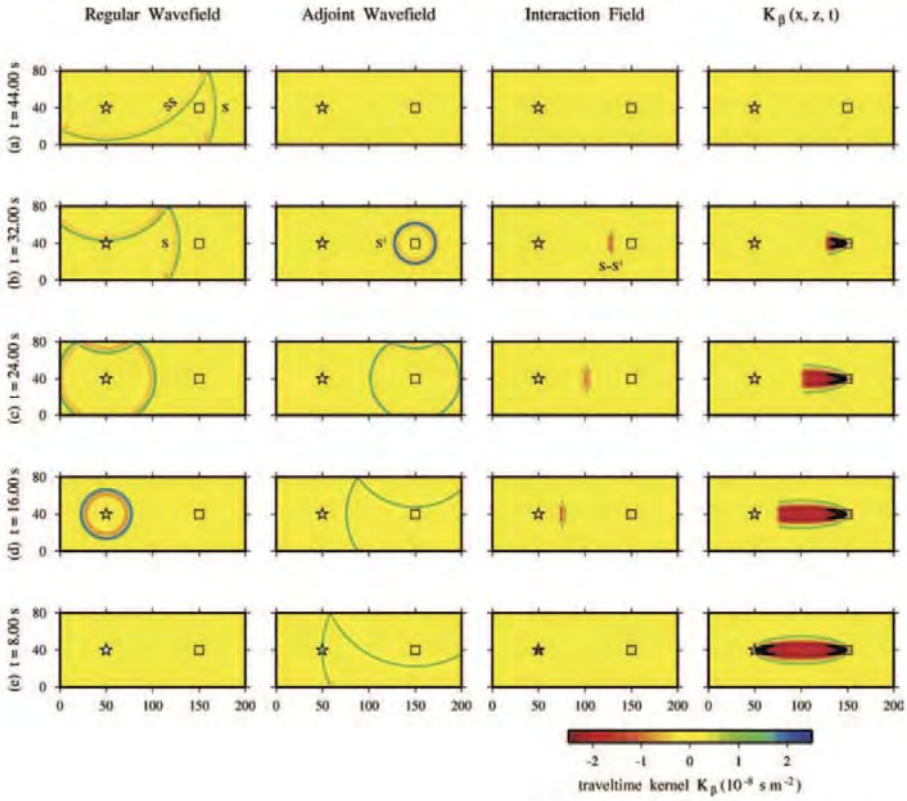


Figure 1. Simple example of the adjoint tomography method, where time increases in each row starting from the bottom, the first two columns are the regular and adjoint wavefields, the third column is the interaction, or multiplication, between the first two columns and the fourth column is the kernel, or time summation of the third column. Notice the regular wavefield propagates from the source, star, to the receiver, box, in forward time (bottom row to top row) and the adjoint field propagates from the receiver to the station, but in reverse time (top row to bottom row). From Tromp et al. (2005)

Extending the predictive period range of the Middle East model will be undertaken using the adjoint capabilities of SPECFEM3D. Essential to the adjoint tomographic method (Tromp et al., 2005) and improving 3D Earth model is the ability to calculate the waveform regular field and the waveform adjoint field of an existing 3D Earth model. The

waveform regular field is defined as the displacement at all points for all times from a traditional seismic source. While the waveform adjoint field is defined as the displacement at all points for all reversed times from a waveform adjoint sources. A waveform adjoint sources is a user-defined measure between the true response at a seismic station, the data, and the predicted response, the synthetic. This measure can be as simple as a difference between the data and synthetics, a least squares differences, a metric isolating travel time or amplitude differences, or any combination. Frechét kernels are created by summing the regular and adjoint fields over time isolating deficiencies in the current model or where the model requires improvement. Adjoint techniques use full seismic wave propagation physics and incorporates finite frequency effects of propagation. These methods have been used with impressive results in the Middle East (Savage et al., 2011), Southern California (Tape et al., 2009), and Europe (Zhu et al., 2012). Many of the current advanced seismic tomographic techniques include various fundamentals of the adjoint methodology, but do not exploit the full waveform to improve the predictive response of surface waves and body waves in tandem. A simple example of creating the kernels is displayed in Figure 1 with a single source and single receiver. The kernel created is a travel time version.

This new adjoint tomography experiment will increase the seismic data by ~30% through the inclusion of more recent seismic events (Figure 2). The data set will also vastly increase due to the ability to model smaller magnitude events at shorter periods. Event and station distributions (Figure 2) have not changed much from the initial experiment, but regions of interest tectonically have instrumentally expanded thus adding more seismic data.

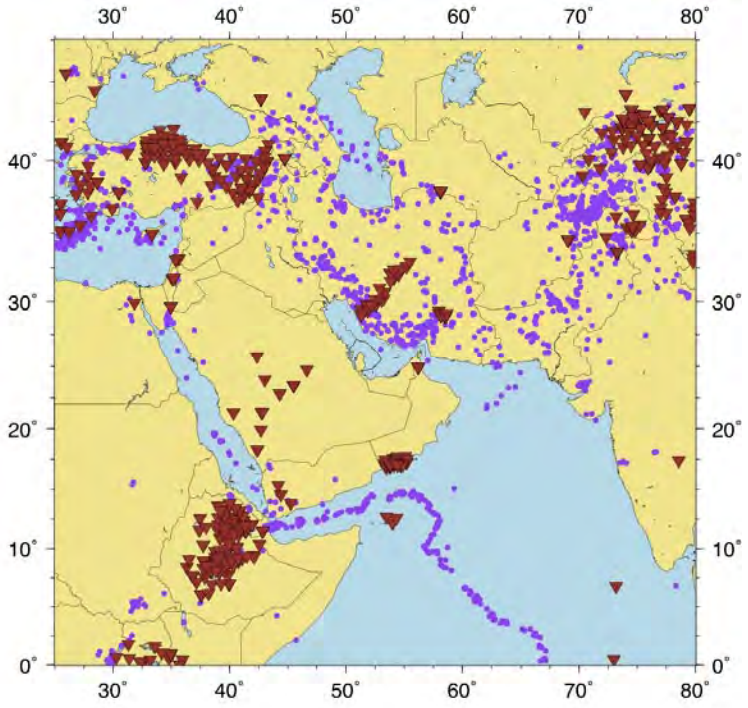


Figure 2. Map of available broadband stations (inverted triangles) and events (dots) from 1990 – 2012 larger than M 5.25. A number of the stations included here are very temporary deployments, < 6 months. The events and stations from 1990-2007 were used in a previous adjoint tomography and source reevaluation study successfully. An extra 5 years worth of seismic data increases the data set by ~30% over previous work. This increase does not include the emergence and availability of temporary deployments in the center of the study area.

RESEARCH ACCOMPLISHED

Previous work to improve the wave speed model in the Middle East (Vp and Vs and transverse isotropy with a vertical symmetry axis) proved successful in predicting waveforms at a minimum period of 15 seconds (Savage et al., 2011). As expected, wave speed anomalies in the initial model were reduced in geographic size and increased in wave speed perturbation, producing more localized and stronger wave speed anomalies. As the

iterations in the inversion progressed, travel time anomalies were reduced but amplitude anomalies, not specifically parameterized, did not improve substantially (Figure 3). The initial starting model (S2.9EA, Kustowski et al., 2008) is quite well constrained, and major, unaccounted for, travel time anomalies were minimal. The demonstrated changes to the model did reduce the overall travel time variation for the full waveform data set, including surface waves, Rayleigh and Love, and body waves.

During the initial improvement of the minimum period from 30 seconds to 15 seconds, inclusion of simple anisotropy was required to stabilize the adjoint inversion from iteration to iteration. Parameterizing the model as wholly isotropic required the Love and Rayleigh waves to be fit using the same shear wave speeds. As we have known for some decades (PREM, Dwizwonski and Anderson, 1981) that the mantle wave speeds are anisotropic, the isotropic parameterization did not allow the adjoint inversion to incrementally improve the waveform fits with successive iterations. The addition of anisotropy to the model facilitated the adjoint iteration's improvement of traveltimes and waveform fits. An example of the current model compared to the initial model is show in Figure 4. The addition of anisotropy was essential to stabilizing the inversion and localizing wave speed structures in the model. Anisotropy was parameterized as transverse isotropy with a vertical symmetry axis allowing only two shear wave speeds, Vsv and Vsh. While this was sufficient for longer period arrivals, the rapidly decreasing minimum period will expose errors in this parameterization as identified in the isotropic case. Newer models will allow the symmetry axis to vary and capture the complex anisotropy within the continental lithosphere and near the edges of the many plate boundaries in the Middle East region.

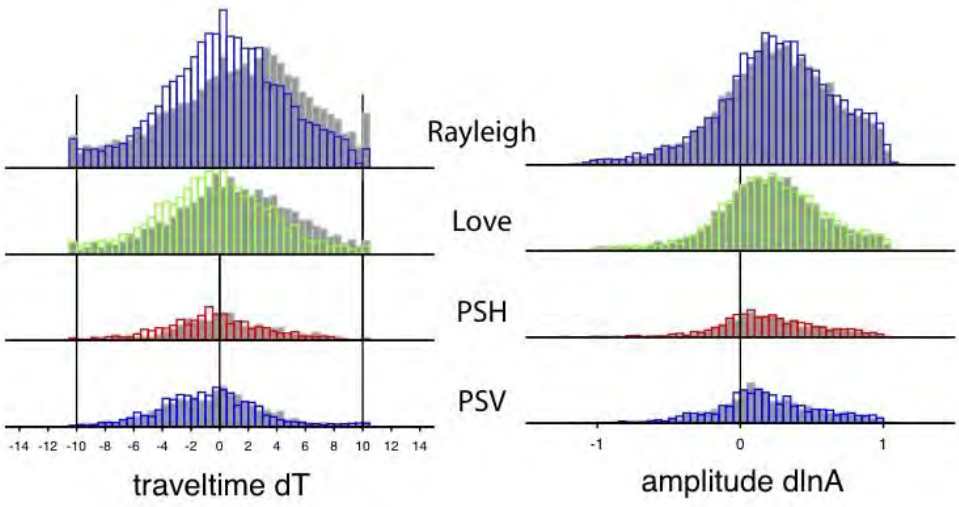


Figure 3. Travel time (left) and amplitude (right) variations between the initial model (gray background histograms) and current iteration model (colored foreground histograms). Travel times were grouped into surface and body waves. Shown are measurements for a band-pass from 60 s to 80 s. Amplitude anomalies shown in the right column have so far not been used in our inversions, and the predicted amplitudes are currently consistently too large. Including 3D attenuation and more general transverse isotropy should help improve amplitude fits.

Unlike predicting traveltimes, our initial attempts at improving the predictive capabilities of the Middle East Adjoint Tomography Model did not show large improvement to the original amplitude mismatches. This initial adjoint inversion only attempted to improve the seismic wave speeds in the region and held the anelastic attenuation constant for all iterations. While we did expect some improvement to the amplitude anomalies due to seismic wave speed induced wavefront bending, the initial model (S2.9EA, Kustowski et al., 2008) did quite well at reproducing the amplitudes at longer periods, > 30 seconds. Our improvements to the wave speed model to predict waveforms at 2 seconds period will require a 3D anelastic attenuation model throughout the crust and mantle. Shorter period wave will be affected greatly by the localized elastic and anelastic crustal and mantle structures in the Middle East. Anelastic attenuation of large scale, but localized structures, including the Caspian Sea sedimentation and Zagros Mountains salt tectonics, will dramatically modify wavefields that propagate through or near these structures. Use of the amplitude anomalies of these paths, along side the seismic wave speeds will aid in improving the anelastic attenuation models.

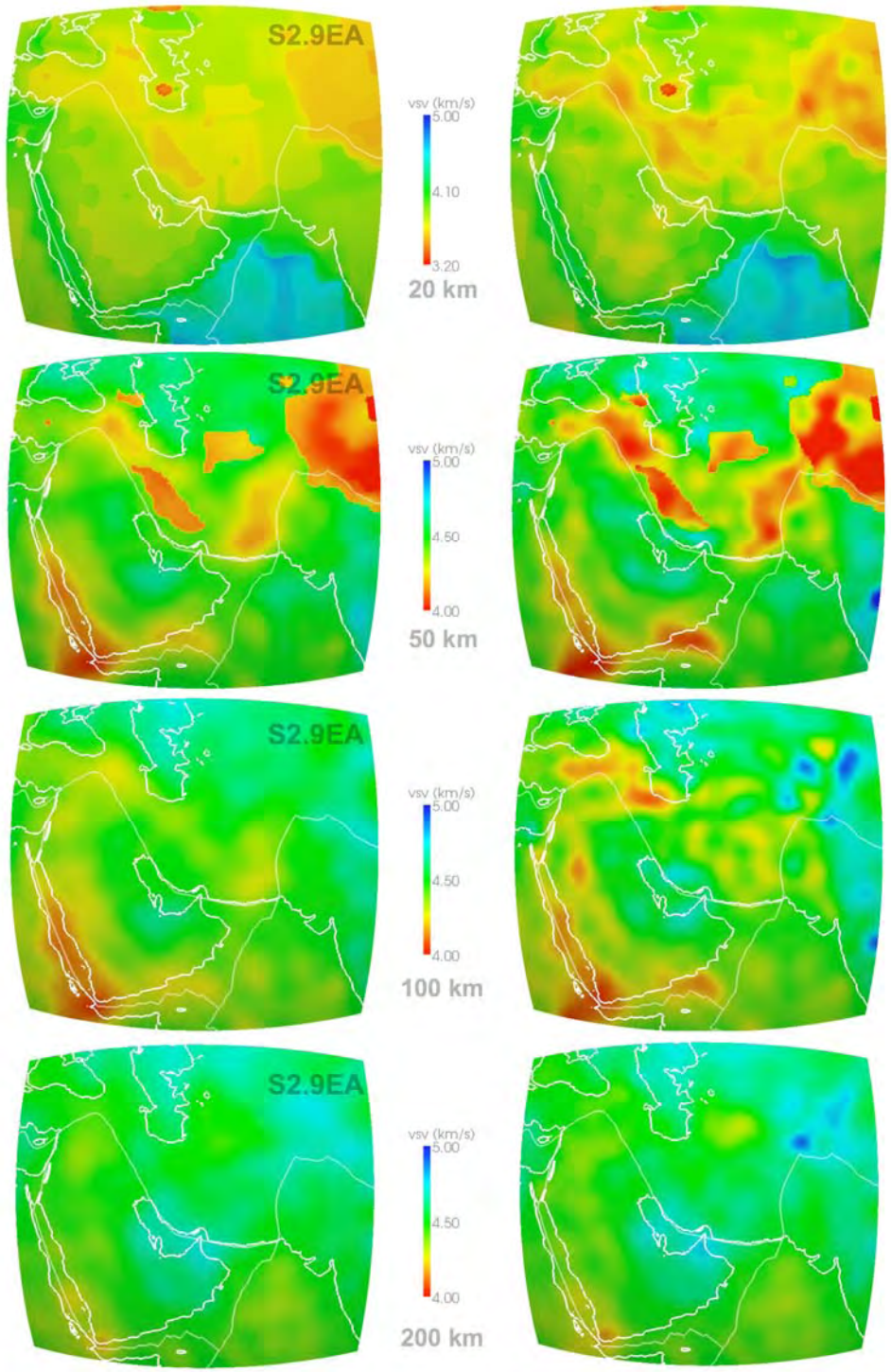


Figure 4. Comparison of the initial wave speed model (left column) to the current iteration wave speed model (right column) at a selection of depths; 20 km, 50 km, 100 km, and 200 km. All image are displayed as absolute Vsv wave speed. Larger amplitude and localized structures are evident between the initial and current model primarily at 50 km and 100 km depths.

As an added benefit, moment tensor analysis of sources in the Middle East (Covellone and Savage, 2012) demonstrated an overall improvement to the source catalog based on metrics of waveform fit and significant increase in the double-couple component for the entire data set. Overall, moment tensors did not change appreciably, but variance reduction was substantially improved. These changes were primarily due to the improvement of near nodal stations that result in major waveform changes, as the moment tensor was refined. Near nodal stations can show large waveform variation with moment tensor, and small changes this component can dramatically modify the response at near nodal stations. Changes in azimuth can also cause similar behavior, but were not a factor here as the events were not relocated. The percent double couple of the moment tensor, %DC, was substantially increased for the entire data set (Figure 5) when the 3D model (S2.9EA, Kustowski et al., 2008) was used in place of the 1D model (PREM, Dwizwonski and Anderson, 1981). This improvement of %DC demonstrates an improved discrimination potential through the use of predictive 3D models in source studies using full waveforms, provided the wave speed model is well calibrated.

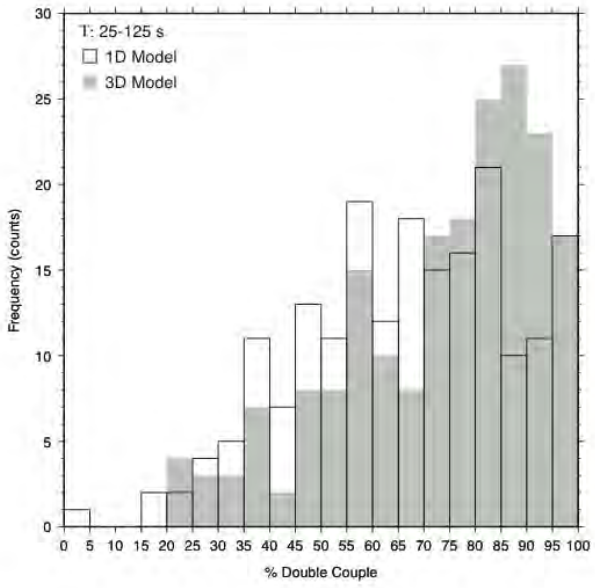


Figure 5. Comparison of recovered percent double couple when using a 1D model and a 3D model. Moment tensors calculated in a 3D model show a significantly larger percent double couple than those in a 1D model.

CONCLUSIONS AND RECOMMENDATIONS

Our initial attempts to improve the seismic waveform predictive capabilities for the Middle East adjoint tomography model demonstrated that improvements were possible up to 15 seconds. Full waveforms and adjoint techniques were used to identify deficiencies in the wave speed model. To progress to a minimum period of 15 seconds, transverse isotropy with a vertical symmetry axis was used in the mantle to stabilize the inversion. Travel times of all types of seismic waves showed the largest variance reduction, whereas there was minimal improvement of amplitude variations. Moreover, use of 3D wave speed models in source studies showed a dramatic improvement in the percent double couple of moment tensors over the entire data set.

Future work will continue to improve the seismic waveform predictive capability of the Middle East adjoint tomography model. We hope to eventually push down the minimum period to 2 seconds allowing for use of shorter period arrivals, smaller sized sources, and data with smaller signal to noise ratios. To reach periods of 2 seconds, the 3D anelastic attenuation variations will become increasingly important and will be incorporated into the Middle East model. At shorter periods knowledge of the 3D anelastic attenuation structure will improve the fitting of the amplitudes. Incorporation of 3D anisotropy will also be essential as the minimum period continues to decrease. We

will relax the current constraint of a vertical symmetry axis for transverse isotropy in an attempt to recover the anisotropy in the Asian continental lithosphere and surrounding microplates.

Improved methods for routinely computing seismic waveforms down to periods approaching 2 seconds will require GPU and large clustered systems, and improved, highly optimized algorithms and routines to reduce unnecessary computation. Waveforms at periods of 2 seconds will be computed from the start of the inversions and used later on in the iterations to avoid local minima. This scheme was used effectively for previous adjoint inversions (Savage et al., 2011).

REFERENCES

Covellone, B. M., and B. Savage (2012). A quantitative comparison between 1D and 3D source inversion methodologies: application to the Middle East, *Bull. Seismol. Soc. Am*., in press.

Dziewonski, A. and D. Anderson (1981). Preliminary reference Earth model, *Phys. Earth. Planet. Int.* **25**, 297–356.

Ford, S. R., D. S Dreger,. and W. R. Walter (2009). Identifying isotropic events using a regional moment tensor inversion, J. *geophys. Res*. **114**, B01306, doi:10.1029/2008JB005743.

Kim, Y., Q. Liu, and J. Tromp (2011). Adjoint Centroid-Moment Tensor inversions. *Geophys. J. Int.* **186**, 264–278. doi: 10.1111/j.1365-246X.2011.05027.x.

Kustowski, B., G. Ekstrom, and A. Dziewonski (2008). The shear-wave velocity structure in the upper mantle beneath eurasia, *Geophys. J. Int*. **174**, 978–992, doi:10.1111/j.1365-246X.2008.03865.x.

Liu, Q., J. Polet,, D. Komatitsch, and J. Tromp (2004). Spectral-element moment tensor inversions for earthquakes in southern California. *Bull. Seismol. Soc. Am.* **94**, 1748–1761. doi: 10.1785/012004038.

Minson, S. E. and D. S. Dreger (2008). Stable inversions for complete moment tensors, *Geophys. J. Int.* **174**, 585–592.

Savage, B., D. B. Peter, B. M. Covellone, A. J. Rodgers, and J. Tromp (2011). Next generation, waveform based three-dimensional models and metrics to improve nuclear explosion monitoring in the Middle East, in *Proceedings of the 2011 Monitoring Research Review: Ground-Based Nuclear Explosion Monitoring Technologies*, LA-UR-11-04823, Vol. 1, pp. 161–167.

Tape, C., Q. Liu, A. Maggi, and J. Tromp (2009). Adjoint tomography of the Southern California crust, *Science* **325**, 988–992, doi: 10.1126/science.1175298.

Tromp, J., C. Tape, and Q. Liu (2005). Seismic tomography, adjoint methods, time reversal and banana-doughnut kernels, *Geophys. J. Int*. **160** (1), 195–216.

Zhu, H., E. Bozdağ, D. Peter, and J. Tromp (2012). Structure of the European upper mantle revealed by adjoint tomography, *Nat. Geosci.*, doi: doi:10.1038/ngeo1501.

FULL-WAVE TOMOGRAPHY OF THE EASTERN HEMISPHERE

Yang Shen and Wei Zhang

University of Rhode Island

Sponsored by the Air Force Research Laboratory

Award No. FA9453-10-C-0217
Proposal No. BAA10-62

ABSTRACT

Advances in computation and numerical method have made it possible to simulate increasingly broadband, full wave propagation in 3D Earth models and use the resulting waveforms to image the Earth structure and characterize seismic sources. Here we report the development of multi-grid full-wave tomography and moment tensor inversion based on 3D strain Green's tensor databases. We collected and processed up to 21 years continuous seismic data from broadband seismic stations in the eastern hemisphere (latitude 55°S-55°N; longitude 30°W-157°E). We developed a new method to significantly improve the extraction of Empirical Green's Functions (EGF) from ambient seismic noise. Compared to the commonly used one-bit normalization, the new method improves the signal-to-noise ratio of EGFs by a factor of ~2 and thus increases the effective data recording duration by a factor of 4, assuming random local and instrument noise. It yields useful Rayleigh waves at periods up to 300 s for PASSCAL-type deployments of broadband stations and 600 s for permanent stations with very broadband sensors. We overcome the challenge of computing full-wave propagation in 3D models with a multi-grid approach that allows wave-speed solutions to be passed from coarse to fine wave-simulation (and inversion) grids, and vice versa. The result is a comprehensive P and S velocity model of the crust and upper mantle for the eastern hemisphere that contains regions with variable resolutions. In the upper mantle transition zone, the major findings to date include a deep-rooted low-velocity anomaly beneath the Eastern African Rift and Afar, the Tethyan slab, and a broad low-velocity anomaly beneath northern Eurasia. In the mid upper mantle, the model reveals various depth extents of the cratonic roots, and the remnant cratonic mantle in the wake of the Indian plate. In regions with fine grids and dense temporary arrays (e.g., southern Tibet), we observe details such as ductile extrusion of high-grade metamorphic rocks on the southern slope of the Himalaya. On-going work includes integration of earthquake arrivals and ambient noise data.

OBJECTIVES

The main objectives of this project are to construct hierarchical, multi-grid (resolution) joint P and S velocity models of the Middle East and East Eurasia and the corresponding finite-difference strain Green's tensors (FDSGT) for rapid earthquake/explosion moment determination.

RESEARCH ACCOMPLISHED

Improvements in tomographic resolution come from two main sources: (1) More and/or better seismic data, and (2) a more accurate theory that relates data to the Earth structure. To this end, we have developed a new method to extract very-broadband Empirical Green's functions from ambient seismic record (Shen et al., 2012) and adapted the full-wave method to ambient noise tomography (Gao and Shen, 2012b). We applied the new method to obtain a joint P and S velocity model of the eastern hemisphere (latitude 55°S-55°N, longitude 30°W-157°E). In order to assess the quality of various velocity models, including the results of this project, we developed a new method to quantitatively validate velocity models (Gao and Shen, 2012a). In the following, we begin with a brief introduction to the project and the approach we take. We report the preliminary results of full-wave ambient noise tomography of the eastern hemisphere and conclude with plans for remaining work.

Introduction

There is a general consensus that the use of 3D models improves seismic characterization (Antoun et al., 2008). Advances in computation and numerical methods have made it possible to capture increasingly broadband, full wave generation and propagation in 3D Earth models. But it is still impractical to routinely simulate forward wave propagation from the source in 3D regional models in real time. One way to overcome this computational challenge is to take advantage of an important property in seismic wave propagation, the source-receiver reciprocity. The use of the reciprocity property and Green's functions can drastically reduce computational costs when the sources outnumber the stations (e.g., Eisner and Clayton, 2001; Graves and Wald, 2001). More importantly, with 3D Green's functions pre-calculated and saved in a database, they can be extracted quickly from the database after a seismic event and used to determine seismic moments (Zhao et al., 2006; Shen et al., 2011).

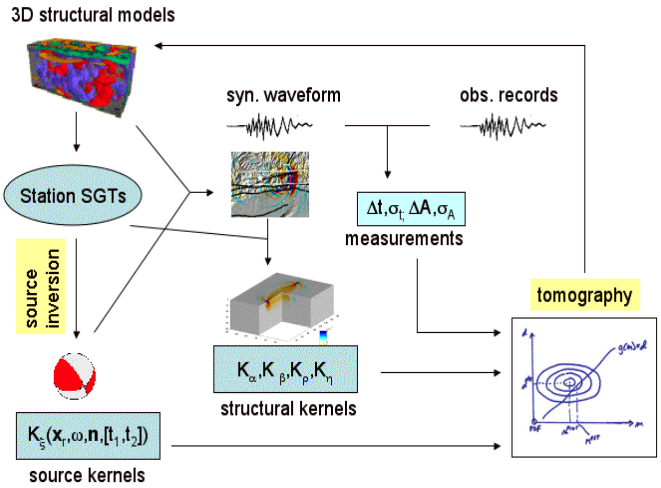


Figure 1. Flow chart of the unified tomography and moment tensor inversions based on 3D FDSGT databases.

Figure 1 is a schematic illustration of the unified tomography and source moment inversion based on 3D Strain Green Tensor (SGT) databases. Station SGTs are constructed from 3D reference models by finite-difference simulation of the responses to orthogonal unit impulsive point forces acting at stations. By extracting SGTs in a small volume surrounding the source reference location, we can invert for source moment tensors and location in a global optimization scheme. Travel time and amplitude anomalies are measured from the observed and synthetic waveforms at stations. The forward wave field from the source and SGTs are used to calculate finite-frequency

sensitivities of the measurements to perturbations in Vp, Vs (Zhao et al., 2005; Zhang et al., 2007; Zhang and Shen, 2008). Together with the sensitivities to source parameters, the measurements and sensitivity kernels are used to invert for the Earth structure (e.g., Chen et al., 2007; Shen and Zhang, 2010). The inversion results and additional constraints (e.g., receiver function solutions) are added to the 3D model. This process can be repeated to progressively improve the solutions. For full-wave tomography using ambient noise, the source moment inversion is omitted and the synthetic waveforms at stations and sensitivity kernels are all calculated from SGTs.

One of the main challenges in full-wave tomography is the intense computation associated with simulating wave propagation in 3D models. To reduce computational cost, which often scales linearly with the number of discrete nodes in numerical methods, we adapt a multigrid/multilevel method (Briggs, 1987) to solve the wave propagation and inversion problem using a hierarchy of discretization (Figure 2). We use three levels of finite-difference computational grids at the hemispherical, regional-, and local-scales to progressively construct a hierarchical, multi-resolution model. Data analysis correspondingly evolves from long period waves for teleseismic observations to broadband waves for regional and local observations.

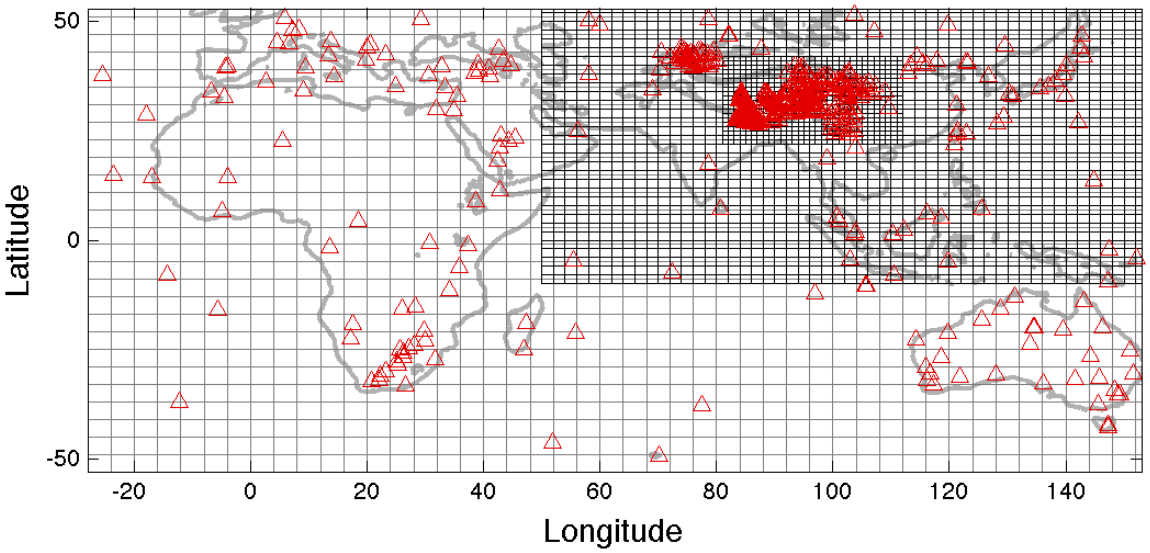


Figure 2. A hierarchical, multi-grid (resolution) approach to develop a joint P and S velocity model in the eastern hemisphere. The three levels of grid represent the finite-difference grids used in simulation of wave propagation in 3D models at the three scales. The finest grid has a grid spacing of 2.5 km. For legibility, the grids shown have been down-sampled to approximately every 20 grids. Triangles mark the permanent and temporary seismic stations used in the full-wave ambient noise tomography.

Full-Wave Ambient Noise Tomography of the Eastern Hemisphere

Reference Model and Wave Propagation Simulation

The initial 3D reference model is composed of CRUST 2.0 (Bassin et al., 2000) for the crust and AK135 (Kennett et al., 1995) for the mantle. The choice of an average Earth model for the mantle instead of one of the current 3D models (e.g., Ritsema and van Heijst, 2000; Ritzwoller et al., 2002; Antolik et al., 2003) is a tradeoff between finding a good starting model and the need to explore a wide enough model space and validate the final solution.

We use a non-staggered grid to simulate wave propagation in a spherical coordinate (Figure 3, Zhang et al., 2012). The DRP/opt MacCormack scheme, which alternately uses forward and backward finite-difference operators, is implemented in the calculation. The solution is optimized for both dispersion error and dissipation error, and has a 4th-order dispersion accuracy. In order to increase the efficiency of the finite-difference algorithm, we use a grid with non-uniform grid spacing to discretize the computational domain. The grid varies continuously with smaller

spacing in low velocity layers and with larger spacing otherwise. The computational domain is surrounded by complex-frequency shifted Perfect Matched Layers (PMLs) implemented through auxiliary differential equations (Zhang and Shen, 2010).

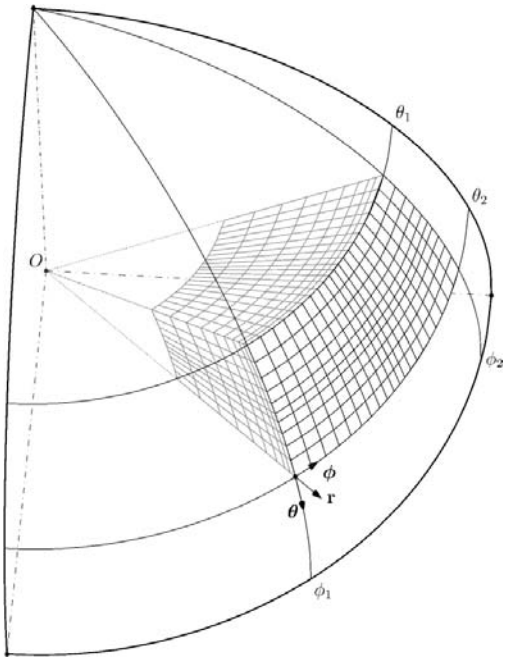


Figure 3. Geometry of non-uniform, non-staggered finite-difference grid in a spherical coordinate system.

For the lowest-level grid, the computational domain covers the eastern hemisphere (latitude 55°S-55°N; longitude 30°W-158°E) with a lateral grid spacing of 0.2°, and a non-uniform grid from the surface to ~2100 km depth (3 km near surface, and gradually increasing to ~40 km near the bottom of the model). There are 12 PML layers surrounding the model boundaries except the free surface. The two higher-level grids for Asia and the Tibetan plateau are spaced at 0.1° and 0.025°, respectively. Figure 3 shows a snapshot of simulated seismic response to a vertical force at station BJI (Beijing).

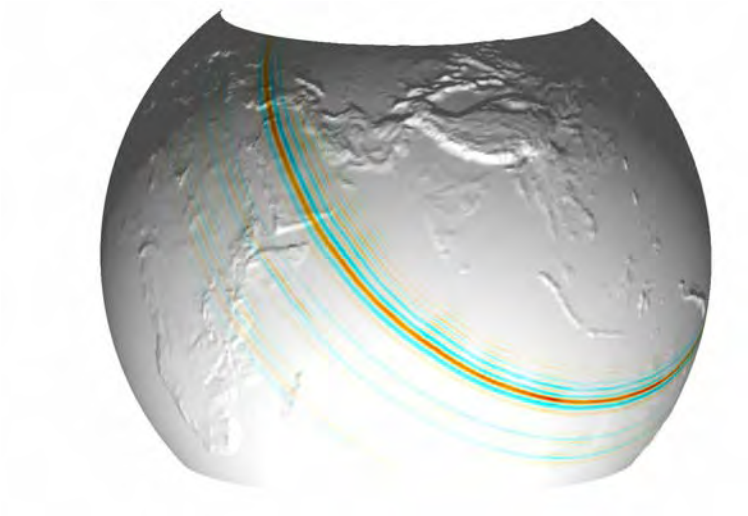


Figure 4. A snapshot of the seismic response at the surface (vertical ground-motion velocity) to a vertical force at station BJT (Beijing).

Empirical Green's Functions

We collected continuous data recorded by broadband seismic stations in the eastern hemisphere during 1990 to 2011. For the lowest-level grid and hemisphere-scale inversion, we selected 257 stations having at least 300 days of continuous records for further analysis. We developed a new method to extract Empirical Green's Functions (EGFs) from the continuous records (Shen et al., 2012). Figure 5 shows an example of EGFs from cross correlation of vertical-vertical component of permanent seismic stations. Our results confirm that Rayleigh waves can be clearly extracted from seismic "hum", or earth's background free oscillation (Nishida et al., 2009). Furthermore we extend the useful period from 400 s (Nishida et al., 2009) up to 600 s! Notice the remarkably good symmetry of very-long period (>100 s) EGFs for the positive and negative time lags. Examples of EGFs from PASSCAL stations can be found in Shen et al. (2012). These long-period waves help extend surface wave constraints to all depths of the upper mantle and uppermost lower mantle.

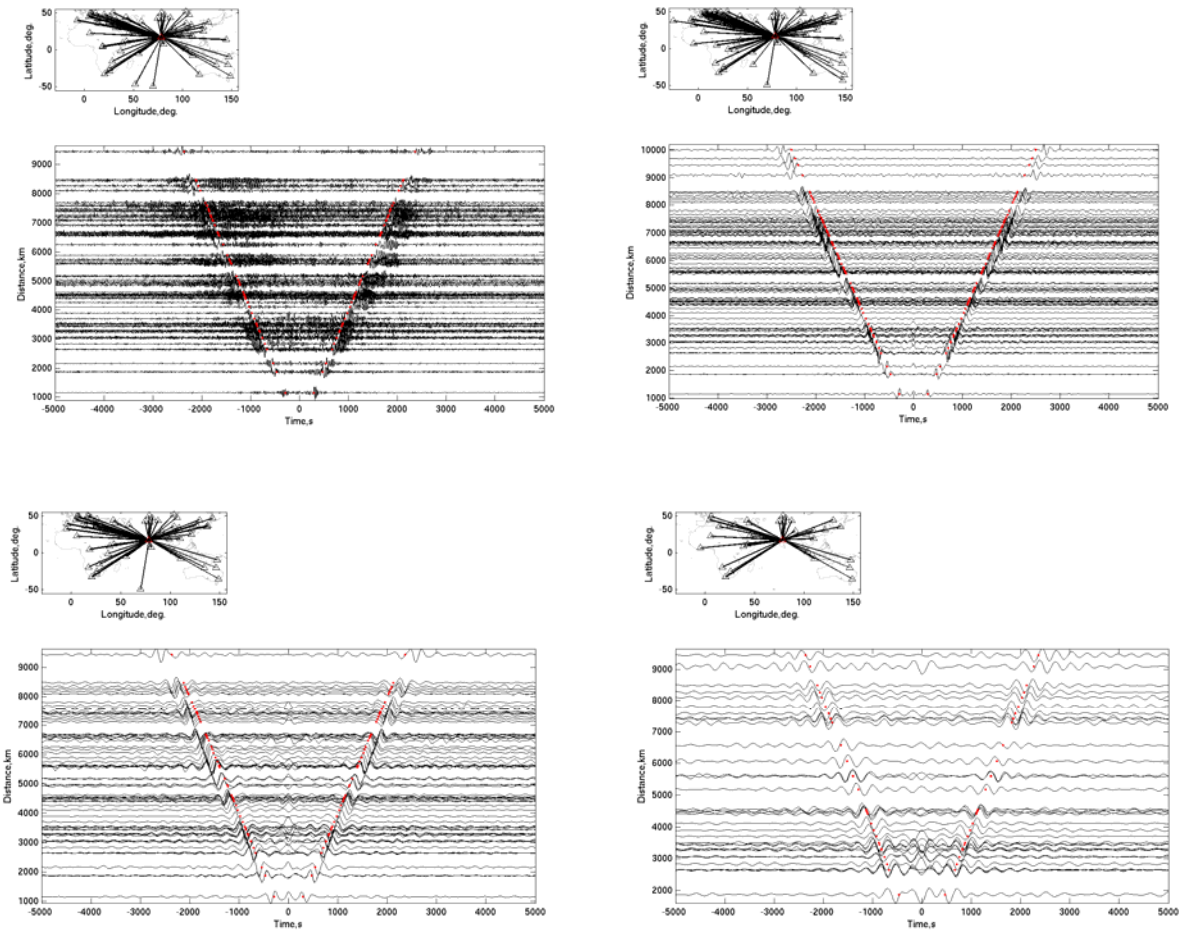


Figure 5. Example of EGFs derived ambient noise (Earth "hum") with various wave periods (upper left: 50-600 s; upper right: 100-600 s; lower left: 200-600 s; and lower right: 300-600 s). The lines in the accompanying maps show the paths with high signal-to-noise arrivals from the virtual source (station HYB) to other receivers in the eastern hemisphere. The red dots mark a wave propagating at a velocity of 3.9 km/s.

We measure Rayleigh wave phase delays by cross-correlating observed and synthetic Green's functions. For the lowest-level grid, the waveforms are band-pass filtered in six period ranges (50-100, 75-150, 100-200, 150-300, 200-400, and 300-600 s). A total of ~23,000 phase delay measurements meet our data selection criteria

(waveform correlation coefficient greater than 0.7 and signal-to-noise ratio greater than 5). Most of the propagation paths with useful waves are in the northern hemisphere (Figure 6).

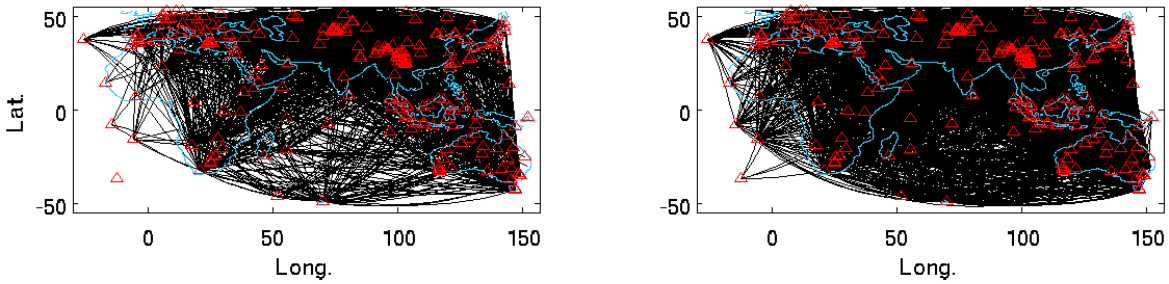


Figure 6. Great circle paths of useful Rayleigh wave delays from EGFs at 200-400 s (left), and 75-150 s (right) periods. Triangles mark the locations of seismic stations. Eurasia, northern Africa and Australia are well sampled at all periods used.

Finite-Frequency Sensitivity Kernels

The cross-correlation of vertical-vertical component yields predominantly Rayleigh waves in the time window and frequency of our interest. Although commonly neglected in surface wave tomography, P-wave speed affects Rayleigh waves (Figure 7). The sensitivity to P-wave speed is near the surface (the depth of sensitivity increases with period) and at a level comparable to the Vs kernel near the surface.

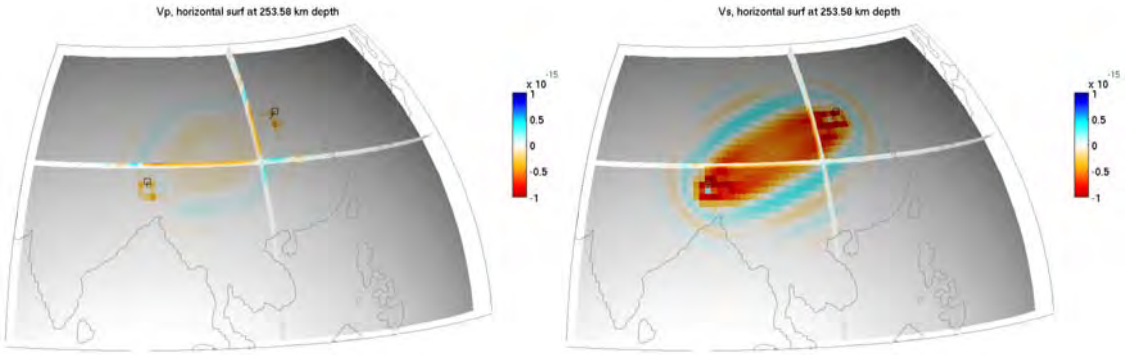


Figure 7. Finite-frequency sensitivity of long-period EGFs between BJT (Beijing) and LSA (Lhasa) to Vp (left) and Vs (right) perturbations. The Rayleigh wave period is 150-300 s. The horizontal slice is at ~250 km depth. Notice that the sensitivity to Vp is mostly in the upper 100 km. The unit of the sensitivity kernel is s/m^3.

Inversion and the Preliminary Velocity Model

We represent the Rayleigh wave delays as a joint Vp and Vs inverse problem linearized relative to an iteratively updated 3D model,

$$\delta \mathbf{t} = \int [K_\alpha(\mathbf{m}_0, x)\Delta \mathbf{m}_\alpha + K_\beta(\mathbf{m}_0, x)\Delta \mathbf{m}_\beta] dV \qquad (1)$$

where δt is the travel time delay relative to the synthetics for the 3D model m_0, Δm_α and Δm_β perturbations to P-wave and S-wave speeds, respectively, K_α and K_β the sensitivity kernels to P-wave and S-wave speeds, respectively. The integration is for the 3D volume of the model.

The above equation is discretized into inversion cells. For the hemisphere-scale inversion, we use 2°x2° blocks as the inversion cells. The thickness of the blocks changes from ~14 km near the surface to ~80 km at ~1600 km depth. The inversion block size is reduced for the higher-level grids (Asia and Tibet) to capture sharp velocity changes. The size of the inversion cells for Tibet is 0.5°x0.5°. The thickness of the blocks is proportional to the lateral dimension.

The inverse problem is solved with LSQR (Paige and Saunders, 1982) with damping and smoothness constraints. The damping and smoothness constraints are gradually reduced until the data misfit is consistent with the estimated data uncertainty (normalized χ^2~1), as in Montelli et al. (2004).

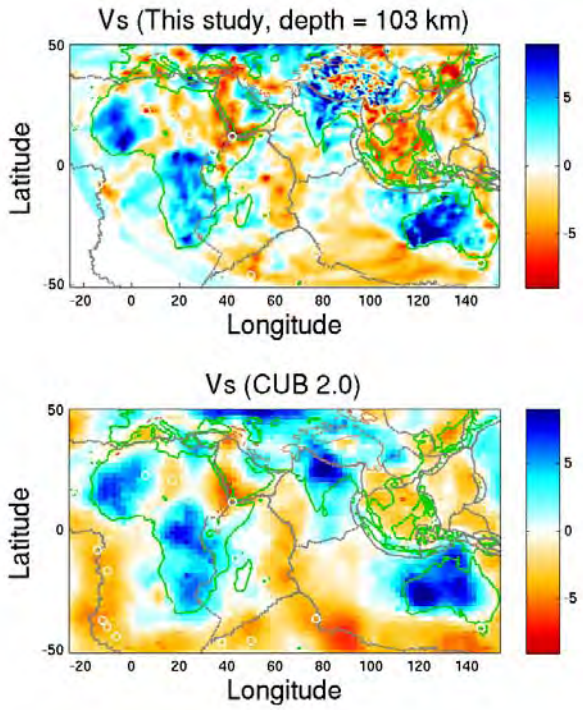


Figure 8. Comparison of the shear-wave velocity models at 103 km depth from full-wave ambient noise tomography (upper panel) and CUB 2.0 (lower panel, Shapiro and Ritzwoller, 2002). Color indicates the perturbation in percentage relative to the average at the depth.

Figure 8 is a comparison of the Vsv model from this study and that of Shapiro and Ritzwoller (2002), which was derived from group and phase velocities of earthquake surface wave arrivals. There are notable similarities and differences between the two models. For example, the African cratons and the west Australian craton exhibit high velocity anomalies in both models. The Afar and Eastern Africa Rift are prominent low velocity anomalies in both models. The full-wave ambient noise model reveals far more detailed structure than in CUB2.0, particularly in the Tibetan plateau (Figure 9), where full-wave ambient noise tomography with fine grids and dense PASSCAL stations yields unprecedented high resolution.

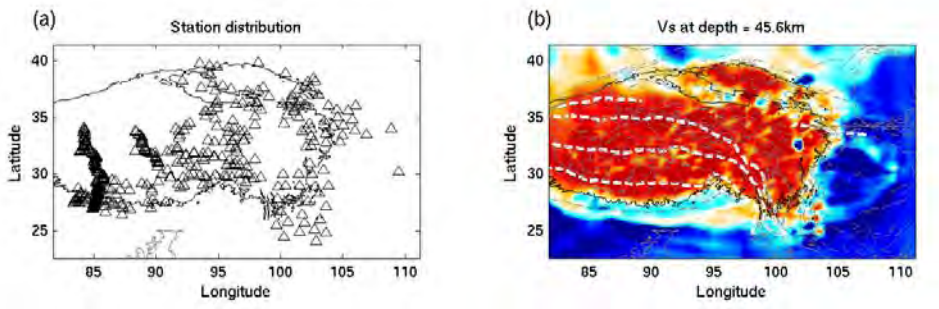


Figure 9 (a) Broadband seismic stations (triangles) used in full-wave ambient noise tomography of the Tibetan plateau. The 3000-m contour outlines the plateau. (b) The shear-wave velocity at depth of ~46 km. The color scale (red to blue) is between 3.59-4.59 km/s. Dashed white lines are the sutures in Tibet, while dashed grey lines are faults. The velocity structures closely follow the geological features. As an indication of resolution, the ductile extrusion of high-grade metamorphic rocks on the southern slope of the Himalaya is images as a band of high velocity anomaly.

CONCLUSIONS

We collected and processed up to 21 years continuous seismic data from broadband seismic stations in the eastern hemisphere (latitude 55°S-55°N; longitude 30°W-158°E). Empirical Green's functions derived from ambient seismic noise show clear Rayleigh waves over a wide frequency range. The very broadband Rayleigh waves extend Vs resolution through the entire upper mantle. The new model provides constraints on several geological processes in the region, such as the origin of the East African Rift, the extent of underthrustisng of the Indian lithosphere beneath Tibet, and recycling of water by subducted slabs. Each of these geological processes warrants detailed studies that will be accomplished by the integration of ambient noise and earthquake data and the development of a hierarchical, multi-grid (resolution) model.

ACKNOWLEDGEMENTS

We acknowledge the IRIS DMC for making seismic data available. Seismic Analysis Code (SAC) is used for data processing. A major part of the computation in this study was carried out on a Beowulf PC cluster purchased with a grant from the National Science Foundation (NSF OCE 0727919).

REFERENCES

Antolik, M., Y. Gu, G. Ekstrom, and A. Dizwonski (2003). J362D28: a new joint model of compressional and shear velocity in the Earth's mantle, *Geophys. J. Int*. **153**, 443–466.

Antoun, T., D. Harris, T. Lay, S.C. Myers, M.E. Pasyanos, P. Richards, A.J. Rodgers, W.R. Walter, and J.J. Zucca (2008). The prospect of using three-dimensional earth models to improve nuclear explosion monitoring and ground motion hazard assessment, Lawrence Livermore National Laboratory Technical Report LLNL-TR-401312.

Bassin C, G. Laske, and G. Masters (2000). The current limits of resolution for surface wave tomography in North America, *Eos Trans AGU* **81**, F897.

Briggs, W.L. (1987). *A multigrid Tutorial*. Denver: University of Colorado.

Chen, P., L. Zhao, and T.H. Jordan (2007). Full 3D tomography for crustal structure of the Los Angeles Region, *Bull. Seismol. Soc. Am.* **97** (4), 1094–1120, doi: 10.1785/0120060222.

Eisner, L. and R.W. Clayton (2001). A reciprocity method for multiple-source simulations, *Bull. Seismol. Soc. Am.* **91**, 553–560.

Gao, H. and Y. Shen (2012a). Validation of shear-wave velocity models of the Pacific Northwest, *Bull. Seismol. Soc. Am*., in press.

Gao, H. and Y. Shen (2012b). Seismic evidence for 3D decompressional melting at the Cascadia subduction zone, submitted to *Nature*.

Graves, R.W. and D.J. Wald, (2001). Resolution analysis of finite fault source inversion using one- and three-dimensional Green's functions, 1, Strong motions, *J. Geophys. Res*. **106**, 8745–8766.

Kennet B L N, E.R. Engdahl, and R. Buland (1995). Constraints on seismic velocities in the Earth from traveltimes. *Geophys. J. Int*. **122**, 108–124.

Montelli, R., G. Nolet, G. Masters, F.A. Dahlen, and S.-H. Hung (2004). Global P and PP traveltime tomography: rays versus waves, *Geophys. J. Int*. **158**, 637–654.

Nishida, K., J.-P. Montagner, H. Kawakatsu (2009). Global surface wave tomography using seismic hum, *Science*, **326**, 112.

Paige, C.C. and M.A. Saunders (1982). LSQR: An algorithm for sparse linear equations and sparse least squares, *ACM Trans. Math. Software*, **8**(1), 43–71.

Ritsema, J. and H.J. van Heijst (2000). Seismic imaging of structural heterogeneity in Earth's mantle: Evidence for large-scale mantle flow, *Science Progress* **83**, 243–259.

Ritzwoller, M.H., NM. Shapiro, M.P. Barmin, and A.L. Levshin (2002), Global surface wave diffraction tomography, *J. Geophys. Res*. **107**, DOI: 10.1029/2002JB001777.

Shapiro, N.M. and M.H. Ritzwoller (2002). Monte-Carlo inversion for a global shear velocity model of the crust and upper mantle, *Geophys. J. Int.* **151**, 88–105.

Shen**,** Y**.,** Y. Ren, H. Gao, and B. Savage (2012). An Improved Method to Extract Very Broadband Empirical Green's Functions From Ambient Seismic Noise, *Bull. Seismol. Soc. Am*., in press.

Shen, Y. and W. Zhang (2010). Full-wave ambient noise tomography of the northern Cascadia, SSA meeting (abstract), *Seismol. Res. Lett*. **81**, 300.

Shen, Y., Z. Zhang, W. Zhang (2011). Moment inversions of earthquakes in the southeast Tibetan plateau using finite-difference strain Green tensor database, submitted to *Geophys. J. Int.*

Zhang, W. and Y. Shen (2010). Unsplit complex frequency shifted PML implementation using auxiliary differential equation for seismic wave modeling, *Geophys*. **75** (4), 141–154.

Zhang, W., Y. Shen, and L. Zhao (2012). 3D seismic wave modeling in spherical coordinate by a non-staggered finite difference method, *Geophys. J. Int.*, **188**, 1359–1381, doi: 10.1111/j.1365-246X.2011.05331.x.

Zhang, Z. and Y. Shen (2008), Cross-dependence of finite-frequency compressional waveforms to shear seismic wave-speeds, *Geophys. J. Int.* **174**, 941–948, doi:10.1111/j.1365-246X.2008.03840.x.

Zhang, Z., Y. Shen, and L. Zhao (2007). Finite-frequency sensitivity kernels for head waves, *Geophys. J. Int.* **171**, 847–856.

Zhao, L., T.H. Jordan, K.B. Olsen, and P. Chen (2005). Fréchet kernels for imaging regional earth structure based on three-dimensional reference models, *Bull. Seismol. Soc. Am.* **95**, 2066–2080.

Zhao, L., P. Chen and T.H. Jordan (2006). Strain Green tensor, reciprocity, and their applications to seismic source and structure studies, *Bull. Seismol. Soc. Am.* **96**, 1753–1763, doi:10.1785/0120050253.

AN OVERVIEW OF THE SOURCE PHYSICS EXPERIMENT AT THE NEVADA NATIONAL SECURITY SITE

Catherine M. Snelson, Veraun D. Chipman, Robert L. White, Ryan F. Emmitt, Margaret J. Townsend, Dennis L. Barker, and Ping Lee

National Security Technologies, LLC

Sponsored by the National Nuclear Security Administration

Award No. DE-AC52-06NA25946/NST11-NCNS-TM-EXP-PD15

ABSTRACT

Understanding the changes in seismic energy as it travels from the near field to the far field is the ultimate goal in monitoring for explosive events of interest. This requires a clear understanding of explosion phenomenology as it relates to seismic, infrasound, and acoustic signals. Although there has been much progress in modeling these phenomena, this has been primarily based in the empirical realm. As a result, the logical next step in advancing the seismic monitoring capability of the United States is to conduct field tests that can expand the predictive capability of the physics-based modeling currently under development.

The Source Physics Experiment (SPE-N) at the Nevada National Security Site (NNSS) is the first step in this endeavor to link the empirically based with the physics-based modeling. This is a collaborative project between National Security Technologies (NSTec), Lawrence Livermore National Laboratory (LLNL), Los Alamos National Laboratory (LANL), Sandia National Laboratories (SNL), the Defense Threat Reduction Agency (DTRA), and the Air Force Technical Applications Center (AFTAC). The test series require both the simple and complex cases to fully characterize the problem, which is to understand the transition of seismic energy from the near field to the far field; to understand the development of S-waves in explosives sources; and how anisotropy controls seismic energy transmission and partitioning. The current series is being conducted in a granite body called the Climax Stock. This location was chosen for several reasons, including the fairly homogenous granite; the location of previous nuclear tests in the same rock body; and generally the geology has been well characterized.

The simple geology series is planned for 7 shots using conventional explosives in the same shot hole surrounded by Continuous Reflectometry for Radius vs. Time Experiment (CORRTEX), Time of Arrival (TOA), Velocity of Detonation (VOD), down-hole accelerometers, surface accelerometers, infrasound, and a suite of seismic sensors of various frequency bands from the near field to the far field. This allows for the use of a single test bed in the simple geology case instead of multiple tests beds to obtain the same results. The shots are planned at various depths to obtain a Green's function, scaled-depth of burial data, nominal depth of burial data and damage zone data.

SPE-1 was conducted in May 2011 as a 220 lb (100 kg) TNT equivalent calibration shot at a depth of 180 ft (55 m). SPE-2 was conducted in October 2011 as a 2200 lb (1000 kg) TNT equivalent calibration shot at a depth of 150 ft (46 m). SPE-3 was conducted in July 2012 as a 2200 lb (1000 kg) TNT equivalent calibration shot at a depth of 150 ft (46 m) in the damaged zone. Over 400 data channels were recorded for each of these shots and data recovery was about 95% with high signal to noise ratio.

Once the simple geology site data has been utilized, a new test bed will be developed in a complex geology site to test these physics based models. Ultimately, the results from this project will provide the next advances in the science of monitoring to enable a physics-based predicative capability.

OBJECTIVES

The ability of the United States to detect low-yield nuclear explosions is critical in supporting the monitoring and verification community. The current United States capability for detecting low-yield nuclear explosions has been primarily empirically based. Thus, the SPE-N is designed to bridge the current predicative capability from empirically based to a physics-based approach. The first series of SPE-N tests is currently taking place in the Climax Stock, a highly fractured granite body. This location was chosen because of the proximity to historic nuclear tests (Pile Driver and Hard Hat) where legacy data can be used as a direct comparison to the new data and also because it was noted during these tests that there were intriguing data that could not be explained at that time (Simmons et al., 2003). In particular, the S-waves seem to be sensitive to the discontinuities within the formation, a phenomenon best studied at the field scale, rather than only on laboratory-scale tests (Antoun, 2010). For these reasons, the Climax site is an ideal location to study the effects of anisotropy in the near-field and wave propagation into the far-field. In addition, the geology of the test bed is well documented, which provides additional constraints in the models. To study these phenomenonology a multi-disciplinary, multi-institutional team was assembled, which includes NSTec, LLNL, LANL, SNL, and DTRA.

RESEARCH ACCOMPLISHED

The SPE-N test bed was built in 2011, with a shot hole (ground zero – GZ) of 0.91 m in diameter and 61 m deep in the granitic rocks of the Climax Stock (Figure 1). The GZ borehole intersects two high-angle faults, and core from the hole and image log data show the formation to be highly fractured. There are three high-angle fracture sets, including a conjugate pair, and one low-angle set. In addition, the formation contains a perched water table that resides within the interconnected fractures. There are series of instrument holes, each 20 cm in diameter and 58 m deep, placed in two concentric rings around GZ at lateral distances of 10 m and 20 m. Characterization studies of the test bed include geophysical logs in all holes (density, velocity, image), material properties measurements on core samples from the GZ borehole, and high-resolution seismic refraction/reflection studies.

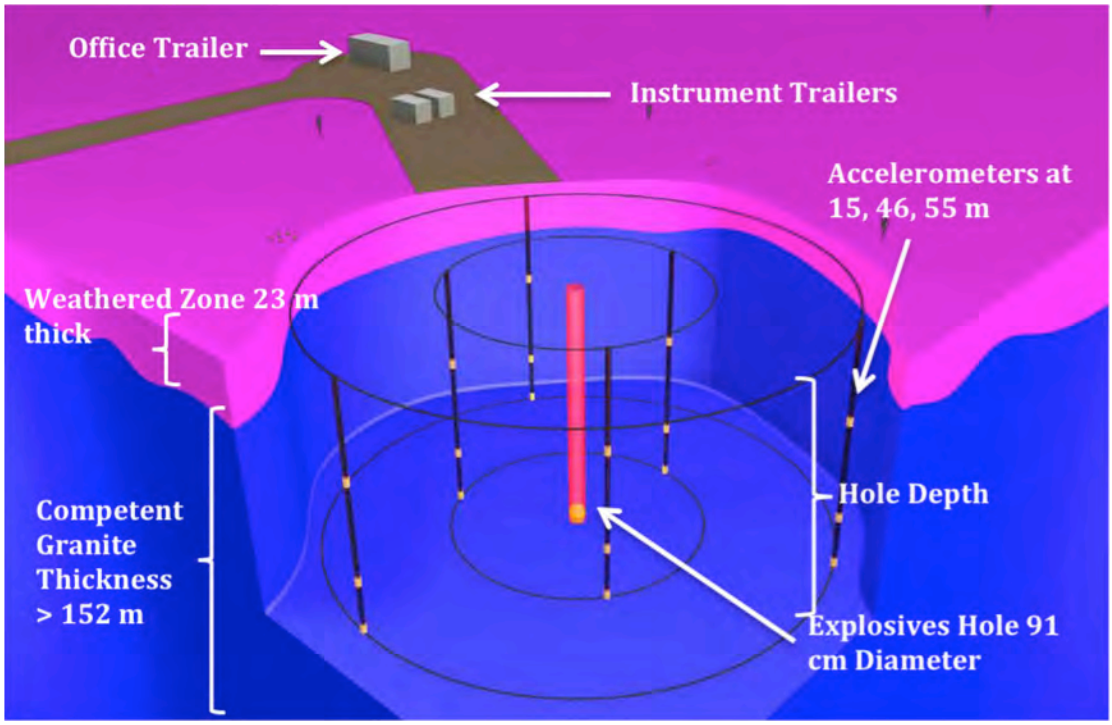


Figure 1. Conceptual drawing of the SPE-N test bed. The red line is the location of GZ and the black lines are the instrument holes. The yellow dots are the accelerometer packages.

To characterize the near-field, initially 6 instrument holes were drilled, which contained 3-component accelerometer packages set at 15-, 46-, and 55-m depths, pointing to GZ. The inner and outer ring instrument holes are offset from each other to maximize azimuthal coverage. On SPE-1 there were two sets of surface accelerometers placed at GZ and every 10 m out to 50 m, inline at an azimuth of WSW with gauges of 100 and 500 g sensitivity. On SPE-2, an

additional instrumentation hole was added due to channel failures in the first suite of holes. In addition, the surface accelerometers were moved and placed in rings around GZ every 10 m and a linear array was placed in the same azimuth as SPE-1 out to 90 m to understand the spall of the test bed. On SPE-3, four additional accelerometer packages were installed to provide additional coverage in areas of interest and where channels failed. In particular, a package was installed at 45 m from GZ to assess attenuation. An angled-core hole was acquired that intersected GZ, to characterize the damage zone with material testing techniques. Other diagnostics in the near-field include CORRTEX (Continuous Reflectometry Radius versus Time Experiment), TOA (Time of Arrival), and VOD (Velocity of Detonation) and were installed in and on the explosives canister in GZ. These diagnostics provide a sense of the symmetry of the blast and that can be used to distinguish between the blast effects and discontinuities within the formation. In addition, visual observation data has been acquired over SPE-N such as LIDAR (Light Detection and Ranging), Hyperspectral imaging (both ground-based as well as air), and satellite imagery data. These data will be used to develop change detection capabilities.

To characterize the far-field, geophones were placed starting at 100 m from GZ and continuing out to 2 km at 100-m station spacing, in five radials around GZ (Figure 2). Broadband, short period, rotational, and infrasound sensors were placed at various locations near GZ and out several tens of km.

In May 2011, SPE-1 was a calibration shot using 100 kg of SHANFO (Sensitized Heavy Ammonium Nitrate Fuel Oil) as the energy source. The SHANFO was loaded into an aluminum canister to simulate a point source and was placed at a depth of 55 m. In October 2011, SPE-2 was a 1000 kg SHANFO shot placed at 45 m in the same GZ hole. This shot was fully confined and the surface spalled with permanent deformation up to 3.5 cm in some places. In July 2012, SPE-3 will be placed at 45 m depth in the damage zone; this is in an effort to distinguish differences in the seismic signal from the deformation from SPE-2.

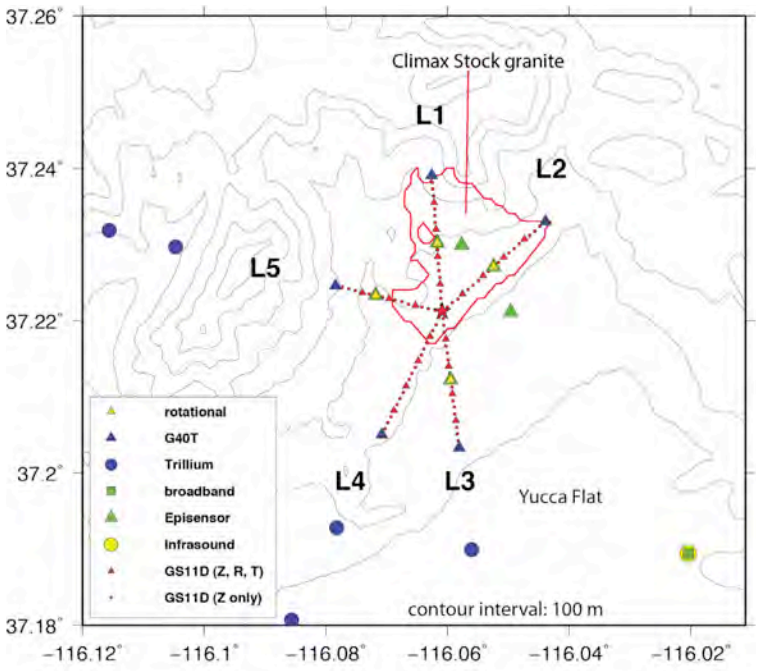


Figure 2. Location map of the seismic and infrasound stations deployed to record the SPE shots.

Data recovery has been on the order of 95% for all data with over 400 channels recorded, one of the largest data sets acquired on the NNSS to date. Overall, the data quality was high and analysis has been underway (see additional SPE-N papers, these Proceedings) (Figure 3).

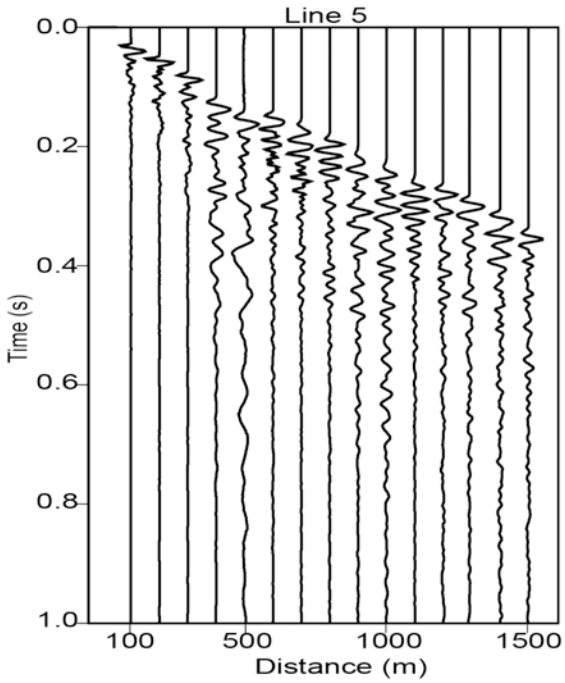


Figure 3. Geophone (GS11) shot gather from Line 5 for SPE-2.

CONCLUSIONS AND RECOMMENDATIONS

As the data from SPE-1 and SPE-2 continue to be analyzed, SPE-3 data from the July 2011 shot will be included. The same GZ borehole will be used for all shots in this series in the granitic geology. Four additional tests are planned for this series at granite site (Figure 4). Eventually, we will reach a point where we will simulate the conditions of a nuclear explosion. Once this GZ has been exhausted, the experiment will move to a new location with a more complicated geology, and the tests will continue and exercise the modeling capabilities.

Yield, ton	DOB (m)	SDOB (m)	Medium	Short Description and Scientific Basis
SPE-1 – 0.1	60	1026	Granite	Initial ~Green function (GF) shot in a simple geology. Simulation capability R&D for non-isotropic effects.
SPE-2 – 1.0	45	357	Granite	Increase shot size to record signals to 100 km. Investigate depth of burial (DOB) effects with SPE-5 and SPE-6.
SPE-3 – 1.0	45	357	Granite	Investigate damage zone effects relative to SPE-2.
SPE-4 – 0.1	110	1881	Granite	Minimize spall, ~GF for SPE-5, DOB relative to SPE-1
SPE-5 – ~5.0	100	464	Granite	Increase shot size to record signals to 300 km
SPE-6 – 1.0	30	238	Granite	DOB investigation with SPE-2 and SPE-7, middle depth
SPE-7 – 1.0	15	119	Granite	Final granite SPE, standard DOB for nuclear test shot
Beyond SPE	TBD	TBD	TBD	Complex geologies and other analogs

Figure 4. Chart of the planned SPE-N tests.

The SPE-N is a unique opportunity to acquire data at a previously characterized nuclear event site with modern instrumentation and modern modeling capabilities. For the first time, we will be able to model the seismic waveforms in a physics-based model both in the near and far-field. The tests are undertaken in a systematic approach so that the modeling can be tested in the most robust manner to obtain models that can be applied in the monitoring regime. In addition, a main goal is to couple the near-field into the far-field and understand how the waveforms change in this transitional region, thereby providing predictive capability that has not existed previously.

ACKNOWLEDGEMENTS

Many hands have helped make the project successful, we would like to thank those people that have been involved from the inception to the execution of these tests.

REFERENCES

Antoun, T. (2010). Wave propagation in jointed geologic media, in *Ground Shock in Faulted Media (GSFM) Workshop Final Report,* DTRA-TR-10-27.

Simmons, D. A., L. A. Glenn, and T. Carney (2003). Review of ground shock calculations in hard rock, in *Hard Rock Database Review (final report)* and *Proceedings of the HRDR Workshop, Volume I: Unclassified Material*.

SURFACE WAVE ATTENUATION IN THE TIBETAN PLATEAU FROM AMBIENT NOISE

Xiaodong Song[1], Richard L. Weaver[1], and Xiaoning (David) Yang[2]

University of Illinois at Urbana-Champaign[1] and Los Alamos National Laboratory[2]

Sponsored by the Air Force Research Laboratory[1] and the National Nuclear Security Administration[2]
Award Nos. FA9453-12-C-0209[1] and DE-AC52-06NA25396[2]
Proposal No. BAA12-43

ABSTRACT

In this project, we explore the methodologies to extract amplitude information from the Empirical Green Functions (EGF) derived from ambient noise correlations and to map the attenuation of the surface waves. Our objectives are: (1) To develop methods for extracting attenuation from ambient noise; (2) To develop methods for practical applications using the Tibetan Plateau as a test bed; (3) To develop preliminary surface wave attenuation maps of the Tibetan Plateau.

This is a project that we have just started. Our approaches are to combine theoretical derivations, numerical simulations, and practical considerations. A particular problem in retrieving amplitudes from noise is that seismic ambient noise source is not uniform and it changes with time. Theoretical insights show that even in the case of incompletely diffuse noise fields, we can robustly recover not only just travel times, but also ray arrival amplitudes, the ambient field's specific intensity, the strength and density of its scatterers if any, and most importantly attenuation. We propose two approaches with detailed formulations: linear array methods and more general methods for 2D station networks. We propose to use a "flattening" data preprocessing procedure, which speeds up EGF convergence but also preserves amplitudes.

OBJECTIVES

The objectives of this research are to develop methods for extracting attenuation from ambient noise, to develop methods for practical applications using the Tibetan Plateau as a test bed, and to develop preliminary surface wave attenuation maps of the Tibetan Plateau.

RESEARCH ACCOMPLISHED

1. Theoretical Formulations for Extracting Attenuation from Ambient Noise

Weaver (2011) provides a theoretical derivation that, even in the case of incompletely diffuse noise field, cross-correlation can permit us to robustly recover more than just travel times, but also ray arrival amplitudes, the ambient field's specific intensity, the strength and density of its scatterers if any, and most importantly attenuation. A full examination of the amplitude X of a correlation waveform between stations *i* and *j* shows that it takes the form

$$X_{ij} = 2 s_i s_j B_i(\hat{n}_{i\to j}) \sqrt{2\pi c / (\omega_o \mid x_i - x_j \mid)}\ \exp(-\alpha \mid x_i - x_j \mid) \qquad (1)$$

where a is the average attenuation between stations *i* and *j*; w_o is the frequency; c is wavespeed, and s_i and s_j are site effects at the two stations.

B_i is the ambient intensity in the direction from *i* towards *j* evaluated at station *i*. An important and useful result for this research is that the ray amplitude *X* depends only on *B* in that direction as an asymptotically valid approximation (at the next order, the differences with respect to direction are of order 1% or less).

1) In the Case of a Linear Array

For a linear array, along a direction $\hat{n}$ of several seismic stations, the amplitudes X_{ij} of cross correlation arrivals for j > i should be

$$X_{i<j} = 2 s_i s_j B_i(\hat{n}_{i\to j}) \sqrt{2\pi c / (\omega_o \mid x_i - x_j \mid)}\ \exp(-\int_{x_i}^{x_j} \alpha\, dx). \qquad (2)$$

Formulation I-1: Path average. Equation (2) indicates that amplitude X from station i (near one end of the array) to all stations j in one direction (to the other end of the array) depends only on the intensity at station i along the same strike direction. Thus the slope of the logarithm of the geometrically corrected amplitude, X*sqrt(distance), as a function of distance would give an estimate of the average attenuation (coefficient **a**) along the linear array.

Formulation I-2: Inversion for a linear array. The system in eqn (2) can be linearized by taking logarithm as in traditional earthquake-based attenuation studies (e.g., Yang et al., 2004). This system is overdetermined and can be solved with a reasonable number of stations. Taking N to be the number of stations along this array, we have at most N(N-1)/2 such ray-amplitudes in one direction. Using one parameter per station to describe the local attenuation, there are up to 3N unknowns (the site factor, the B value along direction $\hat{n}$, and using one local attenuation factor at each station). Correlations from the direction $-\hat{n}$ can provide up to N(N-1)/2 additional amplitudes and N additional unknowns B. Thus if amplitudes along both directions are available, one needs only 5 to 7 stations along this line to solve all unknowns. This is a very general approach without *a priori* constraints on the noise intensity.

Formulation I-3: Assuming no internal scattering. The noise intensity cannot be arbitrary. If we assume the ambient noise sources are from the far field (the oceans as many studies have pointed out for the seismic bands we are interested in) and further assume that scattering is not important, it can be shown that the noise intensity B decays like exp(-2*a*distance), where a is the same medium attenuation coefficient we try to extract. Thus in this formulation, we need only two Bs (one at either end of the linear array).

2) The Case of a 2D Station Network

Formulation II-1: An expansion of the linear array approach. In general, we have a network of stations whose distribution is irregular throughout the study region. However, we may often be able to identify 3 or more stations that roughly lie on the same great circle path. In this case, we can use amplitude ratios to eliminate the unknown intensity B along that direction. Similar ideas are commonly used in earthquake studies to measure phase velocity between two stations (the "two-station" method) or derive surface attenuation using amplitude ratios between two stations along the great circle with the earthquake (e.g., Yang et al., 2004).

Consider 3 stations (station 1, 2, 3) on the same great circle, the ratios of the *geometrically-corrected* amplitudes $X_{13}/X_{12}=s_3/s_2 \exp(-a_2x_2)$, $X_{31}/X_{32}= s_1/s_2 \exp(-a_1x_1)$, where s_i is the site factor for station i, x_1 and x_2 are distance between stations 1 and 2 and stations 2 and 3, respectively, and a_1 and a_2 are average attenuation coefficients between stations 1 and 2 and stations 2 and 3. If we assume no internal scattering, such that intensity B decays like exp(-2a*distance) as discussed above, we can use two other amplitude ratios: $X_{23}/X_{12}=s_3/s_1 \exp(-a_1x_1-a_2x_2)$, and $X_{21}/X_{32}=s_1/s_3 \exp(-a_1x_1-a_2x_2)$. The logarithm of such an amplitude ratio is linear to distance. Once enough amplitude ratios are measured along paths of different azimuths and locations to provide sufficient coverage, it is straightforward to discretize the region and construct a tomographic inversion for the attenuation coefficients for the entire region.

Formulation II-2: The most general approach. The linear array approach relies on identifying a linear array of sufficient length. How might one use sets of seismic stations that are not aligned along a linear array? How quickly ought one permit the diffuse intensity B implicit in the above formulation to vary in direction and from place to place? The diffuse intensity B, in particular how it is permitted to vary in space and direction, cannot be arbitrary. The noise field ought to obey a Radiative Transfer Equation (RTE) (e.g., Turner and Weaver 1994), which involves noise intensity, noise sources, scattering strength, and attenuation. In this project, we will explore this situation in theory and in practice.

2. Numerical Simulations

1) Simulation of Noise Wave Field with an Azimuthally Varying Noise Source

We have carried out numerical simulations to test our proposed approaches. Waves are simulated in a discrete mesh representing a square two-dimensional domain using finite differencing (e.g., Weaver, 1994 and 2001). The domain is shown in Figure 1 where the dark annulus represents the positions of the Gaussian noise sources with azimuthally varying noise strength, and the discrete dots indicate six receiver stations in a linear array. The interior has a uniform attenuation a=0.0078 nepers/mesh spacing with no internal scattering and nominal wave speed of unity.

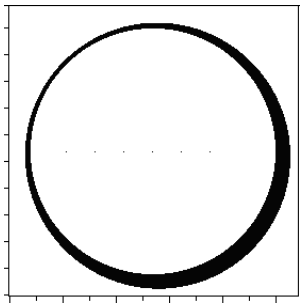


Figure 1. **Sketch of the 271x271 mesh on which diffuse wave field was simulated. Gaussian noise sources were distributed on an annulus of diameter 230 units whose thickness in the figure represents the source intensity $(3 + \cos(q+p/4))^2$. The locations of the six receiver stations (numbered 1 through 6 from left to right with inter-station spacing of 27 units) are indicated by the dots.**

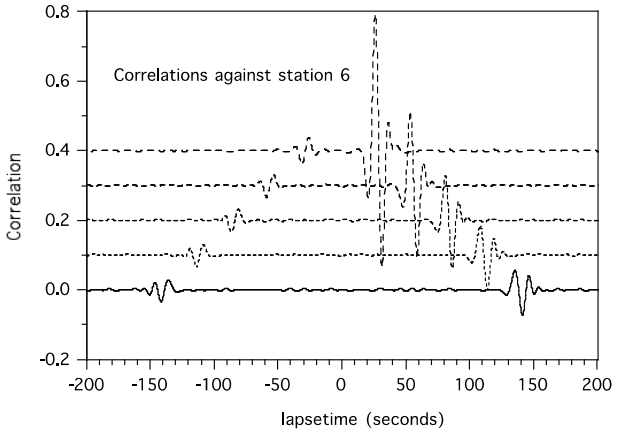


Figure 2. Stack of correlation waveforms between station 6 (the rightmost in Figure 1) and the five others (from top to bottom are 6-5, …, 6-1, respectively). Temporal asymmetry indicates that the on-strike noise intensities in the two directions are not equal. Amplitude decay is evident at positive lapse time (in direction from left to right, i.e., 6->5, …, 6->1) due to geometric and intrinsic attenuation. See text for an explanation of roughly constant amplitudes at negative lapse time.

The set up is equivalent in seismic scale as follows: one time unit of the simulation of one second, seismic speed of ~3 km/sec, mesh spacings of 3 km, source annulus diameter of 700 km, and the station separations of 81 km. The simulation is run for 2^25 time steps of dt = 0.3 sec each, thus a scaled duration of four months. The received signal at each of the six stations is correlated with that at each of the others and filtered into a band centered on a period of 10 sec. At this frequency, the station separation is 2.7 wavelengths. The specified attenuation corresponds to a seismic Q of 43 (Small Q are convenient to observe the effect of attenuation for these preliminary runs). A typical stack is shown in Figure 2.

2) Extraction of Attenuation along a Linear Array

Following Formulation I-1, the average attenuation along the linear array can be retrieved from the fitting of the log of the geometrically-corrected amplitudes vs distance (Figure 3, left). The results agree with the input model (0.0078 nepers/unit spacing or per 3 km) quite well. The vertical offsets of different fitted lines are due to different noise intensity at different originating stations. The intensity B should diminish like exp(-2 a *distance), in the absence of scattering, which is confirmed by examining the amplitude decay of the adjacent pairs (Figure 3, right).

3) Tests on 2D array from Simulated Data

We used the similar set up as above, but simulated data are recorded at a 2D array (10x10 or a total of 100 stations). As before, the Gaussian noise sources are distributed on an annulus with azimuthally varying strength. However, the attenuation of the medium is not uniform: it has four different values at the four quadrants of the array. The data duration is about four month with sampling interval of 1s and Green's functions are filtered at 10 s. Following Formulation II-1, we identify linear arrays within an azimuth of 10 degrees for each station. We then form amplitude ratios for stations along each linear array. We obtain a total of about 5600 independent amplitude ratios. These amplitude ratios are then used to invert for 2D attenuation maps and site factors. The inversion with 4 cells (as in the input model) recovers perfectly the input model (Figure 4, left) and the inversion with 36 cells recovers quite well the input model except cells at the corner which are not constrained by the amplitude ratios (Figure 4, right).

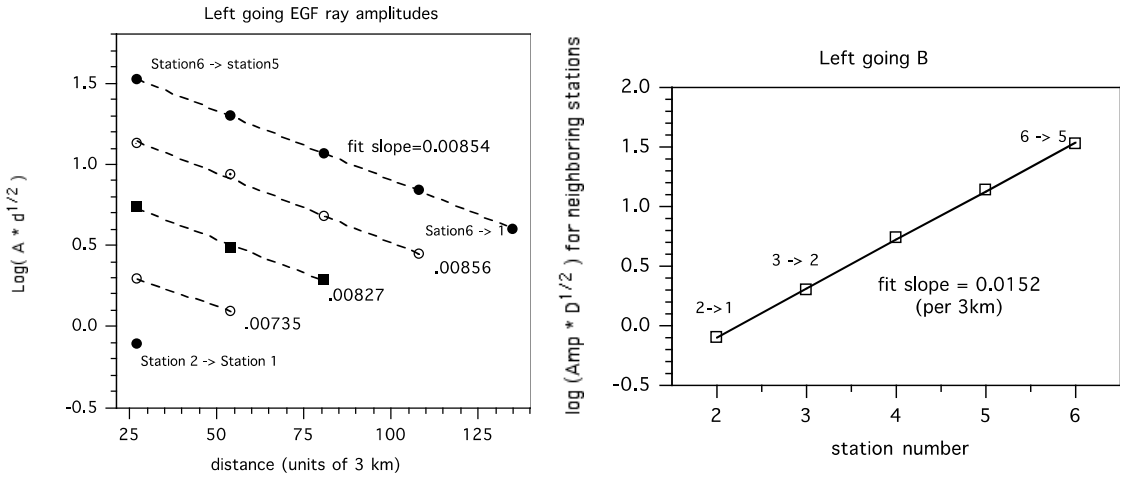


Figure 3. (Left) Amplitudes of the left-going rays in our simulations (corrected by geometrical spreading). Dashed lines are linear fits (in nepers/3km) (the input value is 0.0078 nepers /3 km). (Right) The left-most data points of the figure on the left, i.e., the offsets between the lines, corresponding to the left going intensities B at stations two through six, are seen to diminish with distance from the right to left like exp(- 2 a * distance), as predicted.

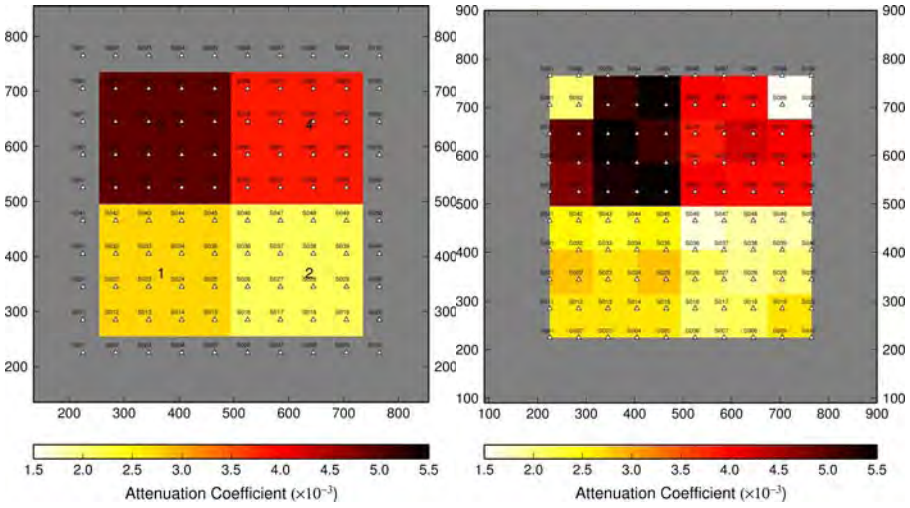


Figure 4. Extraction of attenuation from 2D array with simulated data. The input model has four different values at the four quadrants, respectively. The noise source varies in strength azimuthally. (Left) The input Qs are fully recovered using 4 cell parameterization. (Right) The input Qs are reasonably recovered in a 36 cell inversion, except at the four corners, which are not constrained by the method.

3. A New Procedure for Data Pre-Processing

To reduce the influence of earthquake signals and instrument irregularities and to enhance the strength and bandwidth of the ambient noise correlations, studies using ambient noise correlations have commonly applied some types of data pre-processing that includes temporal normalization and spectral whitening before the correlations (e.g., Bensen et al., 2007). However, such severe nonlinear preprocessing will almost always cause problems in amplitude retrieval, particularly when the ambient noise is not uniform (Larose et al., 2007; Cupillard and Capdeville, 2010).

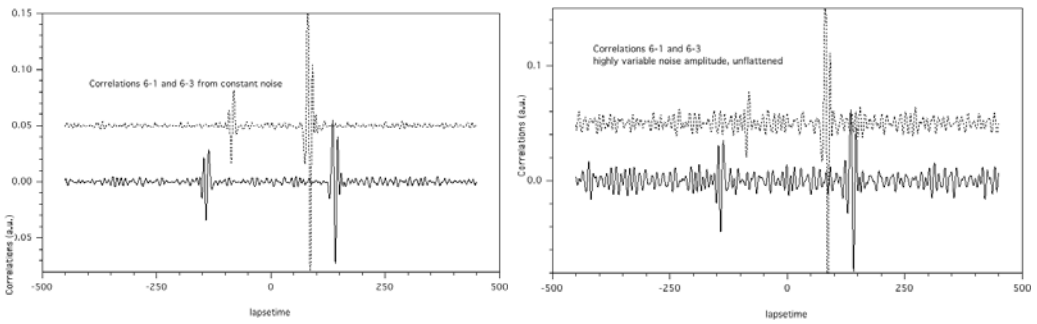


Figure 5. The temporal "flattening" procedure preserves relative amplitudes while speeding up convergence. (Left) The correlations are generated by flattening the raw noise data. (Right) The correlations are generated using the raw data.

We tests on our simulated data above show that if we apply one-bit normalization, we don't recover the attenuation correctly. In order to retain rapid convergence amidst time-varying noise intensity, we suggest a different procedure. If noise intensity is varying slowly in time, on a scale of the propagation time across the array (within 30 min or so), it should suffice to do narrow-band temporal "flattening", in which every station's band-limited signal is normalized by a running average of the *total* band-limited array energy. Thus each station is treated equally, and relative amplitudes are preserved. Furthermore, one day of high ocean noise will not dominate a month's averaging.

To demonstrate the procedure, we generate new numerical simulations using the same setup as above but increasing the noise intensity by a factor of 16 for $1/16^{th}$ of the time. Correlations are generated using the raw data and the flattened data, respectively (Figure 5). We see that the relative amplitudes of the arrivals (at positive lapse time) are nearly the same for the two cases, suggesting the attenuation is preserved in the flattening. However, the SNR based on raw signals is degraded, but the SNR based on temporally flattened signals is significantly better. In fact, the correlations from the flattening are completely identical to our previous case with constant noise (in time). Essentially, the temporal flattening equalizes the variable noise source, leading to faster convergence with all noise information being used, and in the meantime, preserves relative signal amplitudes between stations.

4. Tests on Real Data

We have tested the "flattening" procedure described above using the HiClimb data (Figure 6). All the traces are first band-pass filtered around 10 s (from 8 to 12 s). For each station, we then remove automatically all transient spikes (either artificial or from earthquakes) by muting a 20 min time window from the spike. A flattening procedure is then applied to the non-muted segments: each amplitude point within a 2-hour running window of the non-muted segments of each trace is normalized by the global rms value of all the traces within that 2-hour running window.

We see clear surface-wave signals with a group velocity of about 3.2 km/s (Figure 6B). The signals are observable at positive and negative lapse times, but generally are not symmetric, indicating anisotropic ambient noise field. Comparison with the usual one-bit processing shows good agreement in arrival times but notable difference in amplitudes (Figure 6C). The similar SNRs in the correlations suggest that our flattening procedure can produce convergence of the EGFs comparable to one-bit processing. Measurements of amplitudes show clear decay beyond geometric spreading. This set of measurements and the method Formulation I-1 give a reasonable attenuation coefficient of 0.00065+/-0.00025 (1s) per km (for 10 s Rayleigh wave) with an average of 162.

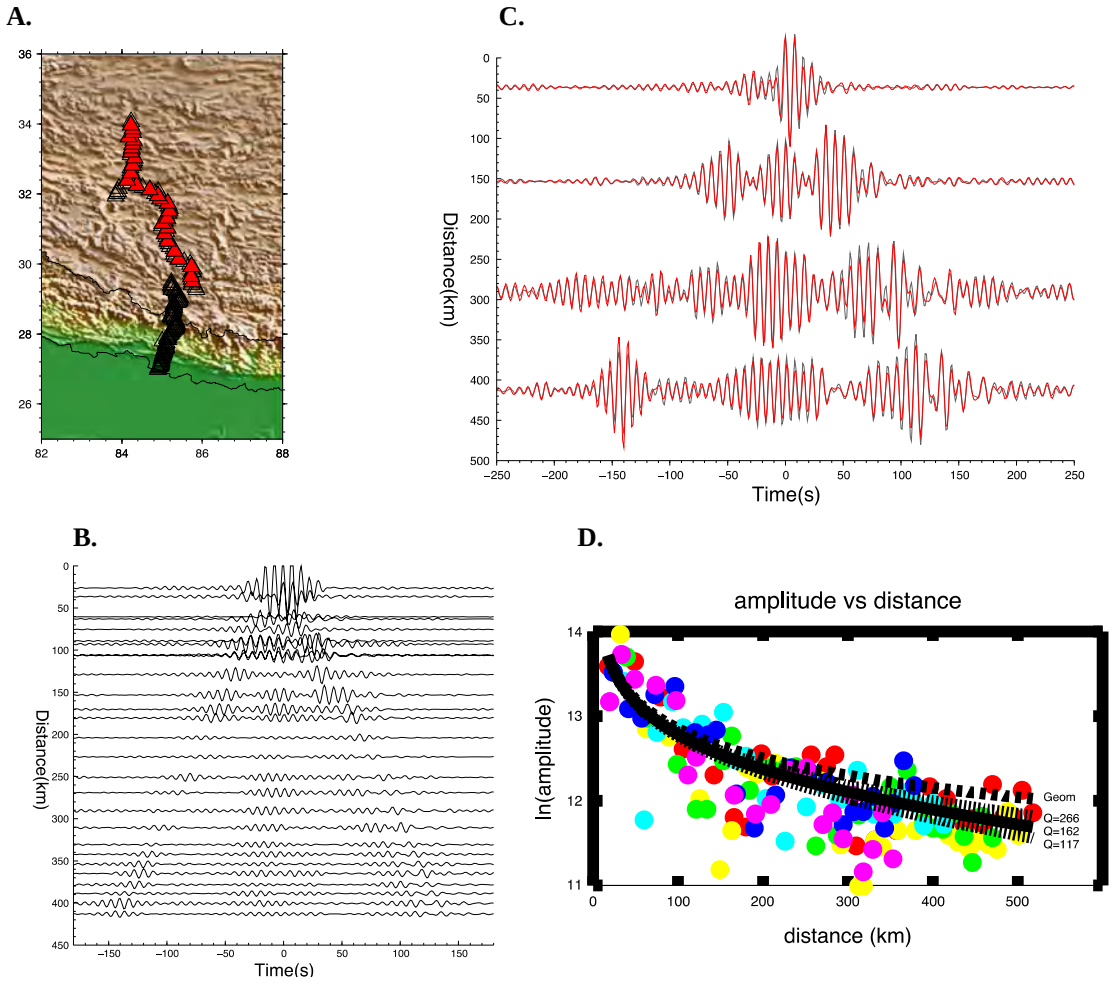


Figure 6. Tests on EGF amplitudes with a subset of HiClimb stations. A) Station map (red is used). B) Example of cross-correlations with the "flattening" procedure. Shown are traces between station H1150 in the south and other stations to the north. C) Overlays of EGFs from one-bit preprocessing (dark traces) and flattening (red traces). The station pairs are between station H1150 and stations H1190, H1340, H1490, H1620 with increasing distance to the north, respectively. The amplitudes at different distances have been equalized but the relative amplitudes between one-bit and flattening are kept the same. D) Amplitudes of Rayleigh waves from the EGFs from 6 southern-most stations (H1030 to H1220 in different colors) to their northern stations. Lines indicate geometrical spreading and fitted Q value and confidence estimates. The amplitude is in natural logarithm.

5. Rayleigh Wave Attenuation Tomography in China Mainland

The project will focus on extraction of attenuation from noise methods. However, as an important effort to verify the noise results, we will also compare directly with earthquake-based studies. We have recently performed an unprecedentedly high resolution Rayleigh wave attenuation tomography in China Mainland at the periods of 10 s and 20 s. We use over 200 earthquakes recorded by some 800 stations of China National Seismic Network and China Regional Seismic Network (Figure 7, Left). We adapted a phase matching technique to a process semi-automatic process, which allowed us to obtain a large quantity of high-quality Rayleigh wave amplitude measurements. After an initial data process that includes grouping and clustering stations to generate station pairs of similar azimuths, calculating the amplitude ratios in each group, and rejecting data with large residuals, we extracted more than 60000 paths of amplitude ratios. Figure 7 (right) shows the attenuation map for 20 s Rayleigh wave. The image reveals low attenuation in the main basins and the stable blocks and high attenuation in the orogens in the Western China.

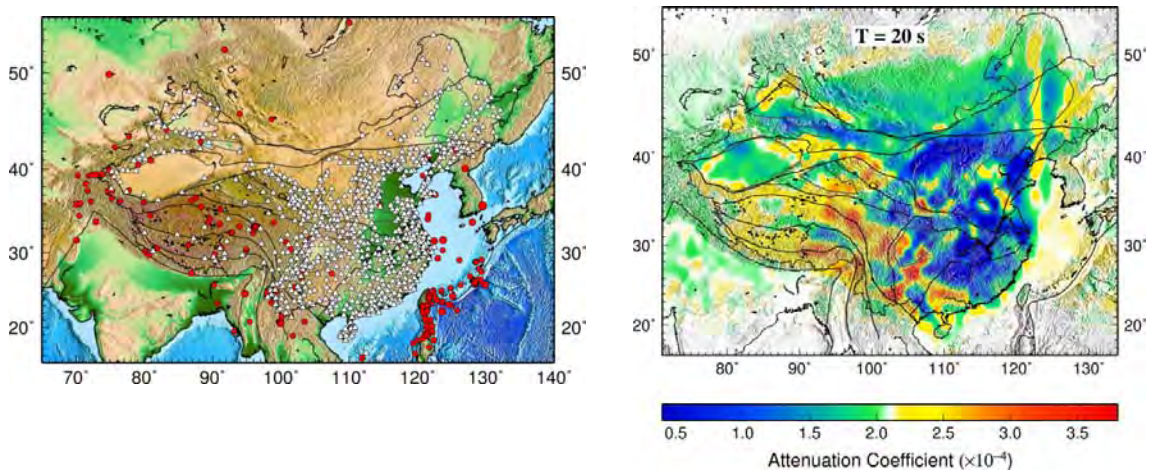


Figure 7. New Rayleigh wave attenuation study of China using earthquake data. (Left) Distributions of earthquakes (red dots) and stations (white triangles) used. The events are Mw 4.8 or greater over a period of 1.5 years (Jan. 2010 to June 2011). (Right) Rayleigh wave attenuation map at 20 s based on earthquake data.

CONCLUSIONS AND RECOMMENDATIONS

We are still at early stage of this project and the topic is a frontier research problem. In this report, we outline a few key aspects of our comprehensive approach that includes basic theory, detailed formulation of different approaches, preliminary results from numerical simulations, data pre-processing consideration, tests on real data, and a new earthquake-based attenuation map of China. These results all look very promising.

REFERENCES

Bensen, G., M. Ritzwoller, M. Barmin, A. L. Levshin, F. Lin, M. P. Moschetti, N. M. Shapiro, and Y. Yang (2007). Processing seismic ambient noise data to obtain reliable broad-band surface wave dispersion measurements, *Geophys. J. Int*. **169**(3), 1239–1260.

Cupillard, P. and Y. Capdeville (2010). On the amplitude of surface waves obtained by noise correlation and the capability to recover the attenuation: a numerical approach, *Geophys. J. Int*., doi: 10.1111/j.1365-246X.2010.04586.x.

Larose, E., P. Roux, and M. Campillo (2007). Reconstruction of Rayleigh-Lamb dispersion spectrum based on noise obtained from an air-jet forcing, *J. Acoust. Soc. Am*. **122**, 3437–3444.

Turner, J.A. and R. L. Weaver (1994). Radiative rransfer of ultrasound, *J. Acoust. Soc. Am*. **96**, 3654.

Weaver, R.L. (1994). Anderson Localization in the time domain: Numerical studies of waves in two-dimensional disordered media, *Phys Rev B.* **49**, 5881–5895.

Weaver, R.L. (2011), Towards Green's function retrieval from imperfectly partitioned ambient wave fields: travel times, attenuations, specific intensities, and scattering strengths, *From Waves in Complex Systems to Dynamics of Generalized Continua --Tributes to Professor Yih-Hsing Pao on his 80th Birthday*, Kolumban Hutter, Tsung-Tsong Wu, and Yi-Chung Shu eds, World Scientific, in press.

Yang, X., S. R. Taylor, and H. J. Patton (2004). The 20-s Rayleigh wave attenuation tomography for central and southeastern Asia, *J. Geophys. Res*. **109**, B12304, doi:10.1029/2004JB003193.

JOINT INVERSION OF CRUSTAL AND UPPERMOST MANTLE STRUCTURE IN WESTERN CHINA

Xiaodong Song[1], Zhen Xu[1], Lupei Zhu[2], and Yuming Zhou[2]

University of Illinois at Urbana-Champaign[1] and Saint Louis University[2]

Sponsored by the Air Force Research Laboratory

Award No. FA9453-10-C-0216
Proposal No. BAA10-55

ABSTRACT

The objective of this research is to develop joint-inversion methods involving P travel times (including secondary P), receiver functions, and surface wave dispersion measurements from ambient noise correlation and to apply them to the western China region to obtain 3D models of P and S structures of the crust and upper mantle.

This is the last year of the 3-year project. Our joint inversion methods involve obtaining crustal a P model and Pn station delays, which are then used with surface wave dispersion and receiver functions at each station to invert jointly for S structure, the Moho depth, and Vp/Vs ratios in the crust. Our main accomplishments include the following three areas. (1) We successfully implemented a search-based algorithm (neighborhood algorithm) for joint inversion of surface wave dispersion data, receiver function, and Pn delay time. The implementation uses parallel programming with MPI calls, making massive data processing possible. (2) We tested joint inversion methods on HiClimb data, which improves resolution of crust and the Mohorovičić discontinuity (Moho) and shows features of mid-crustal low velocity and Moho variations. (3) We are systematically carrying out the joint inversions. We constructed new dispersion maps using a combination of both ambient noise data with multi-fold increase of dispersion measurements. We implemented parallel algorithm for speeding up computation of correlation Green's functions by using multi-processors at the same time. We are systematically processing receiver functions in western China using a semi-automatic procedure. We are systematically picking new Pn arrival times to construct a new Pn tomographic inversion in Western China.

OBJECTIVES

The objective of this research is to develop joint-inversion methods involving P travel times, receiver functions, and surface-wave dispersion measurements from ambient noise correlation and to apply them to the western China region to obtain 3D models of P and S structures of the crust and upper mantle.

RESEARCH ACCOMPLISHED

Our joint inversion in this project involves surface wave dispersion, receiver functions, and P data. Below we describe research accomplishments for each major component.

1) Development of Joint Inversion Methods

The combination of receiver functions and surface-wave dispersions is well-known, bridging some resolution gaps associated with either dataset (e.g., Julia et al. 2000). Adding well-constrained P information helps the joint inversion of receiver function and surface-wave dispersion to find the right S model when the Vp/Vs ratio is not known (Song et al., 2010, 2011). One type of P information is the Pn station delay time, which provides a constraint on Moho depth and average crustal velocity.

We have implemented the joint inversion method that includes surface wave dispersion data, receiver functions, and Pn station delay time, which has been described in some detail previously (Song et al., 2011). A feature of this joint inversion is that all the individual components (surface wave dispersion, receiver function, and Pn delay time) are quantified with respect to the same station of interest. The implementation uses a global search approach and includes the following key elements. (1) We use a fast global search method, neighborhood algorithm (NA) (Sambridge, 1999). Using a global parameter search approach, compared with the more traditional linearized iterative inversion approach, has two key advantages: (a) We have more control on parameterization, for example, to include Pn data, we need to define a Moho; and (b) we are able to explore parameter space more fully and to quantity the resolution and uncertainty of the solution more easily. (2) Our parameterization includes the Moho, the depth of which is allowed to vary. It can include variable crustal layers as well. Regions between layers are parameterized as smooth functions (linear or splines) to reduce the number of search parameters. (3) The implementation uses parallel programming with MPI calls, which greatly speeds up the model search with multi-processor or parallel machines.

2) Dispersion Measurements and Dispersion Maps

We have continued to systematically add dispersion measurements for the construction of dispersion maps, from ambient noise correlations as well as traditional earthquake data (Song et al., 2010). The stations include the Chinese national backbone stations and open permanent and temporary stations from early 1990s with a total of over 500 stations. Earthquake data include events greater than magnitude 5.0 from 2000 to 2007. We made a key improvement in the computation of ambient noise inter-station Green functions, which is essential because of the tremendous amount of continuous data involved (Song et al., 2011). Using the LINUX POSIX message queue (mq) capabilities, the method distributes tasks to multi-processors and executes them simultaneously. Our current total dataset has dispersion measurements for period from 8 s to 120 s and a maximum of ~35000 measurements for group velocity and ~22500 measurements for phase velocity at the period of 20 s.

3) Receiver Functions

We have continued to systematically process receiver functions of stations in Western China (Figure 1). We have developed a semi-automatic procedure to generate receiver functions. Because of large number of stations and large amount of data, such a procedure is essential for productivity. The procedure includes interactive review and selection of good quality raw data using a graphic interface, picking and alignment of P waveforms using waveform cross-correlation and a graphic interface, automatic calculations of receiver functions and stackings according to ray parameters and azimuths, and interactive selections of good quality receiver functions using a graphic interface.

4) Pn Tomography

We have also been working systematically on Pn waves. Our data come from three sources: 1) Chinese bulletin data, 2) international bulletin data (ISC), and 3) hand-picked data at temporary and permanent stations. Distribution of permanent stations in western China (even including regional and provincial networks in China) is quite sparse. However, there have been a number of PASSCAL experiments in Western China. These stations are usually in remote areas where permanent stations are lacking, providing complimentary ray coverage.

We design an inter-active scheme to pick Pn arrival times semi-automatically. It involves inspecting original seismograms (vertical component, filtered at 0.2 to 3 Hz), discarding noisy traces, zooming in Pn arrivals, picking each trace by hand, plotting travel-time curves and reduced travel-time curves, and double-checking picks if there are obvious anomalies. We have examined about 200 shallow events (depth less than 40 km) with magnitude greater than 5.5 over 15 years (1995-2009) in the region from 25 to 56 deg north and 68 to 108 deg east. We require epicentral distances to be from 2 to 12 degrees and at least 10 Pn picks for each event. We picked over 1800 Pn arrivals from 81 events.

We impose the following data selection criteria. (1) Earthquakes whose depth is over 45 km are discarded. (2) The apparent velocity of rays is limited between 7.0 and 9.0 km/s. (3) To ensure robust constraint on the station delays, we keep the stations with at least 5 Pn picks and keep the earthquakes with at least 5 Pn records. (4) We use an earthquake-grouping technique (Liang et al., 2004) to locate earthquake clusters, then choose the earthquake with the largest number of Pn picks in a cluster and exclude all the other earthquakes in the same cluster. After the data selection, we obtain 54,849 rays from 398 stations and 6,220 earthquakes.

For Pn tomography, we follow the basic approach of parameterizing the Pn residual into mantle perturbation, the earthquake term, and the station term (e.g., Hearn, 1996; Liang et al., 2004; Liang and Song, 2006). For the initial model of inversion, we choose average crustal velocity of 6.3 km/s, average Pn velocity of 8.06 km/s, and average Moho depth of 51 km (Liang and Song, 2006). We divide the study region into 2-D grids with the size of 1° × 1°.

The inversion results of Pn velocities and station delays are shown in Figure 2. The Pn velocity map (Figure 2A) shows a number of significant features consistent with the geology of the region and previous studies, including high Pn velocity anomalies in four major basins (Sichuan, Tarim, Qaidam, and Junggar basin), high uppermost mantle velocities in the southern Tibetan Plateau (TP), low Pn velocities in northern TP, and a striking low velocity belt extending from west to east beneath northern TP to the eastern and southeastern margins of the plateau, observed previously by Liang and Song (2006). The station delays vary greatly in the study region (Figure 2B), suggesting large changes in crust thickness, as we expect.

5) Tests of Joint Inversion with Hi-Climb Data

We tested our joint inversion algorithm on the dense Hi-Climb array. In these tests, we have used the receiver functions and the Rayleigh wave dispersion but have not included Pn station delays yet.

Figure 3 shows results from the joint inversion, in comparison with those from surface waves and receiver functions separately. Our results demonstrate that the joint inversion method has application to a variety of different crustal structures, in particular it does not depend on whether the Moho is sharp or not (Fig. 3D). A pronounced low-velocity zone at depth of around 25 km in the mid-crust exists in most of the Tibetan Plateau. However, it seems that the low-velocity feature is not continuous; the thickness and velocity reduction varies at different locations. Under the Himalaya block near Yarlung-Zangbo suture, the low-velocity zone can be over 25 km thick with velocity reduction of more than 10% while under Lhasa block both thickness and velocity reduction decrease significantly while the amplitude of low velocity picks up again under Qiangtang block.

Crustal thickness varies from about 50 km in the southern part of the profile under Ganga foreland in Indian plate to about 75 km under south Lhasa block and gradually decreases to less than 65 km under Qiangtang block. The location of Moho discontinuity under each individual station is shown by crosses or circles, where crosses indicate the stations with clear shear velocity jump while circles mark the place where the shear velocity jump is smaller than 0.15 km/s across the Moho discontinuity. Most circles and large Moho variations locate from 27.5°N to 29°N, where the topography changes drastically from the low land to the highly elevated plateau over a relatively short distance and from 31.5° N to 33°N in northern Lhasa block near Bangong-Nujiang suture. The complex Moho discontinuity coincides with scattered Ps delay time measurements. Particularly, the northern segment of complex Moho is consistent with the region where Moho Ps conversion is weak (Nabelek, et al., 2009, white dashed line in Figure 3) and a disrupted Moho is identified from Gaussian beam migration (Nowack, et al., 2010).

CONCLUSIONS AND RECOMMENDATIONS

We successfully developed and implemented a search-based algorithm (NA) for joint inversion of surface wave dispersion data, receiver function, and Pn delay time using parallel programming. We obtained unprecedented data sets for surface wave dispersion, receiver functions, and Pn tomography, needed for the joint inversion. We tested the joint inversion method with the Hi-Climb data, which improves resolution of crust and the Moho. The method is effective in capturing the main features of a variety of different structures and data behaviors.

REFERENCES

Hearn, T. M. (1996) Anisotropic Pn tomography in the western United States, *J. Geophys. Res*. **101**, 8403–8414.

Julia, J., C.J. Ammon, R.B. Herrmann, and A.M. Correig (2000). Joint inversion of receiver functions and surface-wave dispersion observations, *Geophys. J. Int*. **143**, 99–112.

Liang, C.T., X.D. Song, and J.L. Huang (2004). Tomographic inversion of Pn travel times in China, *J. Geophys. Res*. **109**, B11304.

Liang, C.T. and X.D. Song (2006). A low velocity belt beneath northern and eastern Tibetan Plateau from Pn tomography, *Geophys. Res. Lett*. **33**, L22306, 2006.

Nabelek, J., Hetenyi, G., Vergne, J., et al. (2009). Underplating in the Himalaya-Tibet collision zone revealed by the Hi-CLIMB experiment. *Science* **325**, 1371–1374.

Nowack, R. L., Chen, W.P., and Tseng, T.L. (2010). Application of Gaussian beam migration to multi-scale imaging of the lithosphere beneath the Hi-CLIMB array in Tibet, *Bull. Seismol. Soc. Am*. **100**, 1743–1754.

Sambridge, M. (1999). Geophysical inversion with a Neighborhood Algorithm -I. Searching a parameter space. *Geophys. J. Int.***138**, 479–494.

Song, X.D., Z.J. Xu, L.P. Zhu, Y.M. Zhou (2010). Joint inversion of crustal and uppermost mantle structure in western China, in *Proceedings of the 2010 Monitoring Research Review: Ground-Based Nuclear Explosion Monitoring Technologies*, LA-UR-10-05578, Vol. 1, pp. 224–231.

Song, X.D., Z.J. Xu, L.P. Zhu, Y.M. Zhou (2011). Joint inversion of crustal and uppermost mantle structure in western China, in *Proceedings of the 2011 Monitoring Research Review: Ground-Based Nuclear Explosion Monitoring Technologies*, LA-UR-11-04823, Vol. 1, pp. 198–205.

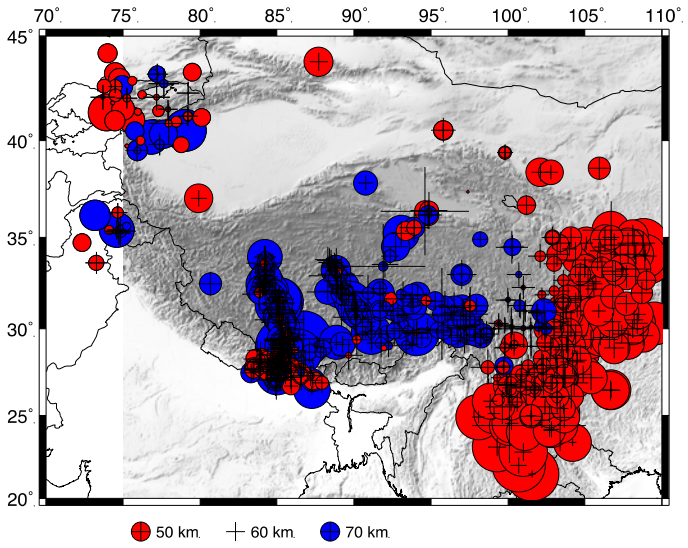


Figure 1. Stations in western China for which receiver functions have been obtained. Crustal thickness is plotted at each station.

A. B.

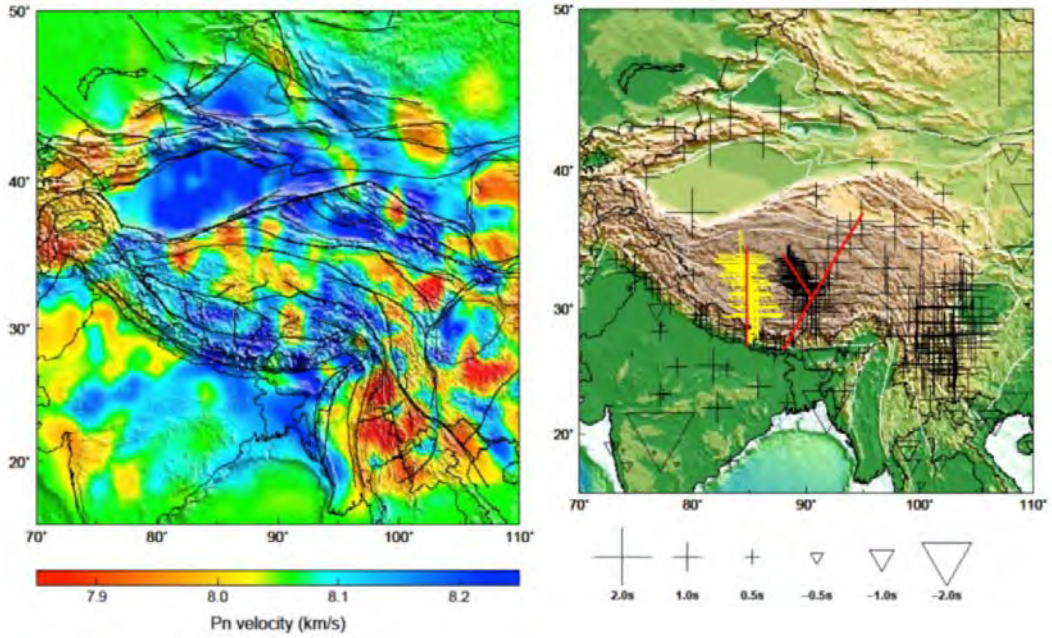


Figure 2. Results of preliminary Pn tomography in western China. (A) Pn velocity map. (B) Station delays. The number of stations is around 400, including bulletin stations and PASSCAL stations.

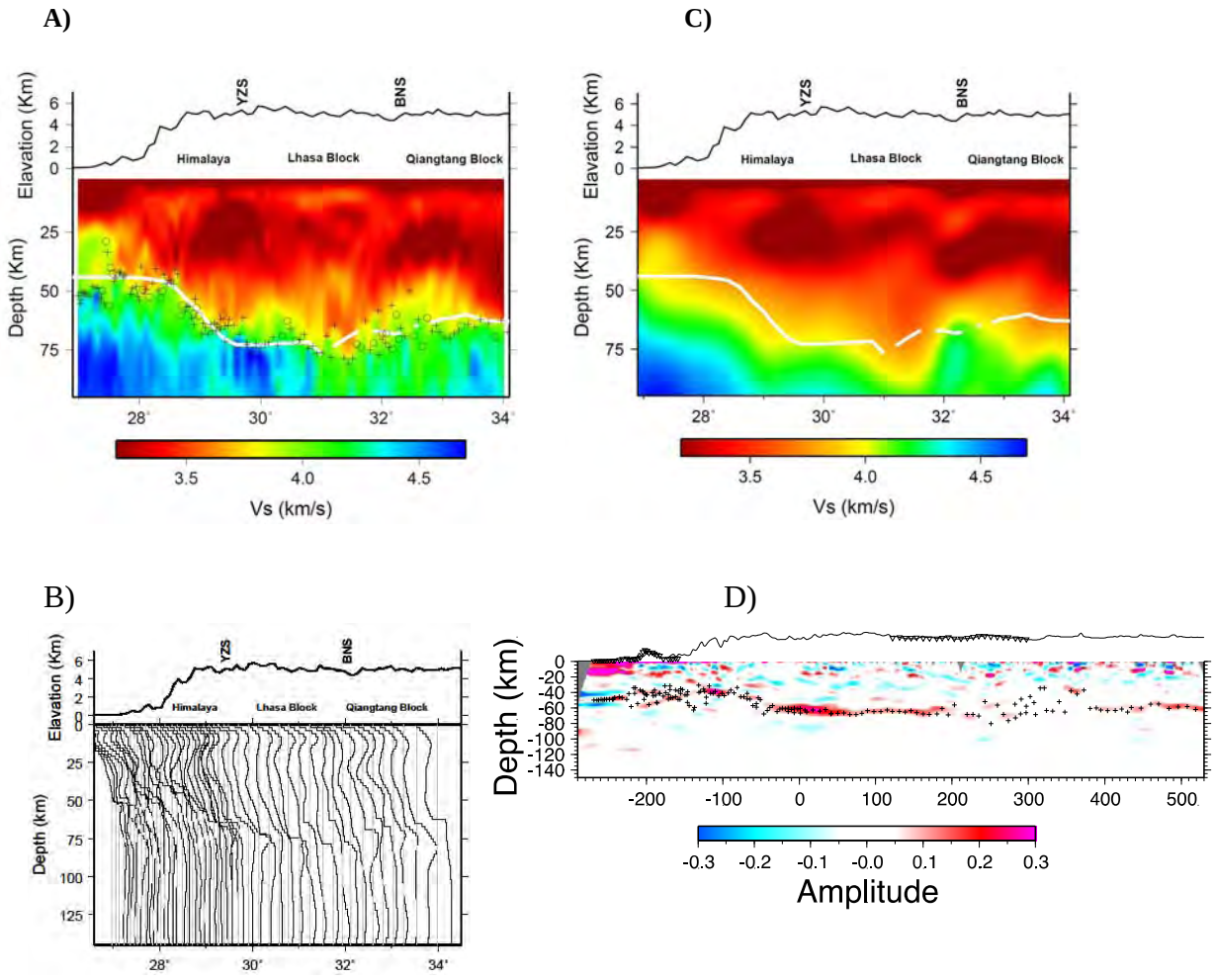


Figure 3. Results of joint inversion with Hi-CLIMB data (A, B). Crosses and circles indicate the Moho depth under the stations. Crosses indicate a strong Moho discontinuity while circles mark a gradual Moho velocity transition. Shown in comparison are results from surface wave dispersions only (C) and from common conversion point stacking of the receiver functions only (D). The thick white line is the approximated Moho location from the receiver function study by Nabelek et al. (2009) using the same Hi-CLIMB stations.

3D VARIATIONS IN SEISMIC WAVESPEED AND MASS DENSITY IN THE CRUST AND UPPER MANTLE OF SE ASIA FROM JOINT INVERSION OF SEISMIC AND GRAVITY DATA

Robert D. van der Hilst[1], Haijiang Zhang[1,2], Monica Maceira[3], Charlotte A. Rowe[3], Huajian Yao[2]

Massachusetts Institute of Technology[1], University of Science and Technology of China[2], and
Los Alamos National Laboratory[3]

Sponsored by the National Nuclear Security Administration

Award Nos. DE-NA0001523 and DE-AC52-06NA25396
Proposal No. BAA12-17

ABSTRACT

We bring together a team having extensive experience with tomography and joint inversion to determine 3D variations in seismic velocity (δVp, δVs) and mass density (δρ) in the SE Asian crust and shallow mantle from joint inversions of seismic and gravity data. We propose several methodological advances. First, we will combine our double difference and global (travel time) tomography codes to improve constraints on wavespeed variations in the shallow mantle through inversion of regional and teleseismic P and S time picks. Second, we will implement a method for surface wave inversion that bypasses the need for phase velocity maps and which facilitates joint inversion with travel times (NB the implementation uses asymptotic theory but extension to finite frequency theory is straightforward). Third, we will use sensitivity kernels to relate observed Rayleigh wave phase and group speeds to variations in Vs and Vp and ρ. Fourth, knowing the sensitivities of (i) S travel times and Rayleigh wave dispersion to δVs, of (ii) P times and Rayleigh wave dispersion to δVp, and of (iii) gravity data and Rayleigh wave dispersion to δρ, we formulate an explicit joint inversion of seismic and gravity data for δVp, δVs, and δρ. Through careful design of the misfit function we aim, within the limits of the data, to enforce realistic relationships between these three parameters (with scaling relationships) and maximize structure coherence of the 3D wavespeed and density variations (through crossgradient minimization). In order to account for spatial variations in data coverage, the models will be represented by means of irregular grids and multi-resolution wavelets. The wavespeed models will be validated using ground truth events and waveforms from regional earthquakes.

The high-resolution, seamless 3D models of δVp, δVs, and δρ produced by this joint inversion will aid the location and characterization of local and regional seismic events and improve monitoring capabilities. Our strong track record of research and delivery of 3D models and tomography codes and the fact that we already have most of the data that we need puts in an excellent position to achieve the ambitious goals of the research proposed here.

OBJECTIVES

The National Nuclear Security Administration (NNSA) and the Air Force Research Laboratory (AFRL) have decided to move toward 3D modeling to improve the knowledge of spatial variations in compressional (P) and shear (S) velocity as well as the accuracy of locating small (mb < 4) seismic events, both of which lead to improved capabilities for nuclear explosion monitoring (NEM). For seismically active areas with good ground truth event coverage, models with limited intrinsic accuracy can be corrected through interpolation from nearby 'ground truth' events (with, for instance, the kriging method) and, therefore, large events (for which there is much data) can be located well even with structural models of relatively poor resolution. However, this approach may not be adequate for smaller earthquakes (with fewer observations) and/or for aseismic regions (with few – or no – ground truth events). To improve monitoring capability in such regions we must develop better earth models than are currently available. This study aims at improving seismic monitoring technology through the development of advanced multivariate inversion techniques and the generation of comprehensive and accurate 3D models of the seismic structure of the crust and upper mantle that are consistent with and validated against independent geophysical datasets. The main objectives of this study are to (i) develop an advanced joint inversion method and (ii) to produce well calibrated, seamless Vp and Vs models of SE Asia from a large set of body wave travel time, surface wave dispersion, and gravity data.

RESEARCH ACCOMPLISHED

This project is just recently started and so far our efforts have been focused on the design of this project. In this paper, we report our research plan and theoretical framework for this project.

1. Data

1.1 Data for Travel-Time Tomography

The P and S wave arrival times (from local, regional, and global stations) come from four sources: (1) Phase readings from about 1200 national and provincial stations of the Chinese Seismograph Network (CSN) during the period 1967-2004 (Figure 1); (2) arrival times picked from ~170 stations of regional (temporary) arrays in Tibet and SW China (Figure 2); (3) EHB (Engdahl et al., 1998) data reprocessed from the International Seismological Centre (ISC) bulletins (1960-2007); and (4) travel times from active source profiles in China. The data under (1), (2), and (3) has been used in the Vp inversions by Li and Van der Hilst (2010), but the S picks in (1) and (3) have not yet been used for the type of detailed regional study envisioned here.

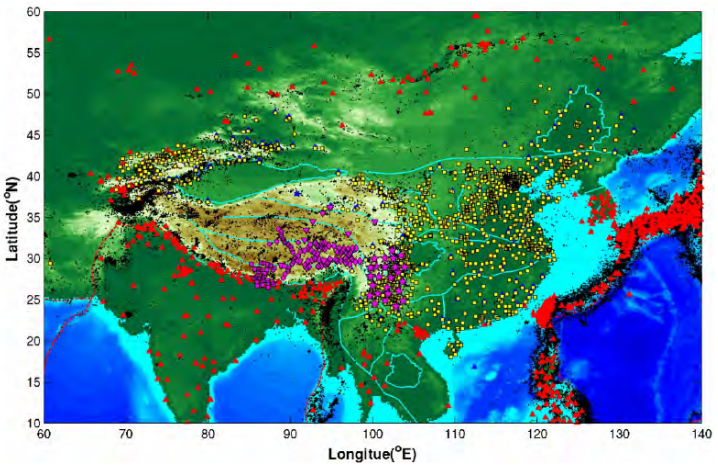


Figure 1. Distribution of regional stations and earthquakes (black dots) that contributed travel time data used in inversions. Red triangles depict ~1300 stations of the EHB in East Asia; yellow squares are ~1000 stations from Chinese Seismograph Network (CSN); Magenta samples represent stations of seismic arrays in the Tibetan plateau. From east to west: stars – MIT CIGMR array (2003-2004); diamonds - Lehigh-CIGMR array (2003-2004); inverse triangles - Sino-American array (1991-1993); dots - INDEPTH-II (1994) and INDEPTH-III (1998-1999); squares - Himalayan Nepal Tibet array (2001-2003). After Li and Van der Hilst (2010).

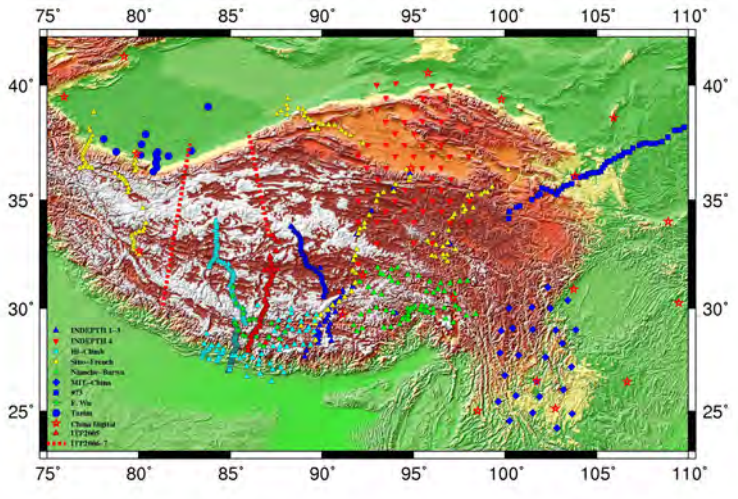


Figure 2. The distribution of seismograph stations on the Tibetan Plateau and surrounding regions.

Combining global, regional, and local seismic network data from various sources requires careful processing in order to avoid internal inconsistencies. Fortunately, the travel time picks from sources 1 and 2 have already been integrated and processed along with data from source 3 (i.e., the existing EHB data) using a non-linear process of earthquake relocation and phase re-identification (Engdahl et al., 1998), and they are ready for use for the study proposed here.

1.2 Data for surface-wave inversion

In the past decade, the number of (broad-band) stations in SE Asia, in particular in and around Tibet, has increased dramatically (Figure 2), and this has greatly enhanced the lateral resolution for tomographic studies in this region. Through our own extensive surface wave studies in this area we already have access to dispersion measurements from many of these stations, and as part of this project we will make an effort to augment this data with data from various other studies.

We consider both earthquake and noise-based dispersion measurements. For earthquake-based measurements it is difficult to obtain short period dispersion due to strong crustal scattering; a typical period range for this type of data is 30 - 150 s (Figure 3), and at these periods surface wave dispersion constrains structure in the upper mantle. To help constrain shallower structure we include inter-station dispersion measured from empirical Green's functions, which are estimated from ambient noise cross-correlation (e.g., Campillo and Paul, 2003; Yao et al., 2006, 2008, 2010; Zheng et al., 2008; Yang et al., 2010). This type of measurement is most effective within the period band 5 - 40 s and becomes less reliable at longer periods (Yao et al., 2010). Because of the short periods, dispersion data from ambient noise can constrain crustal structure (Figure 2). In combination, these data sets allow for high resolution surface tomography of both the crust and upper mantle (to about 250 km).

As a result of almost a decade of collaborative research with various groups in China, PI Van der Hilst and his group at MIT have already collected a large volume of dispersion measurements from hundreds of (permanent) provincial network and transportable array stations in China. Moreover, Dr. Yingjie Yang (University of Colorado, Boulder) has kindly agreed to share his inter-station dispersion measurements of over 100,000 paths from ambient noise in China for our new study. The existing data consists of (1) phase velocity measurements from classical two-station analysis (Yao et al., 2010; Yi et al., 2010) and single-station source-receiver propagation (Lebedev & Van der Hilst, 2008) – Figure 3 shows the Rayleigh wave phase velocity distribution in China at periods 20, 35, 50, and 120s from two-station analysis of teleseismic surface waves, and (2) ambient-noise-based dispersion measurements, including inter-station phase velocity dispersion data by Yao et al. (2010) and Yang et al. (2010). In addition, we will use the automatic dispersion analysis software developed at MIT by Dr. Huajian Yao to measure more earthquake-based phase and group velocity dispersion curves, in particular, from the many transportable arrays deployed in China in the past five years.

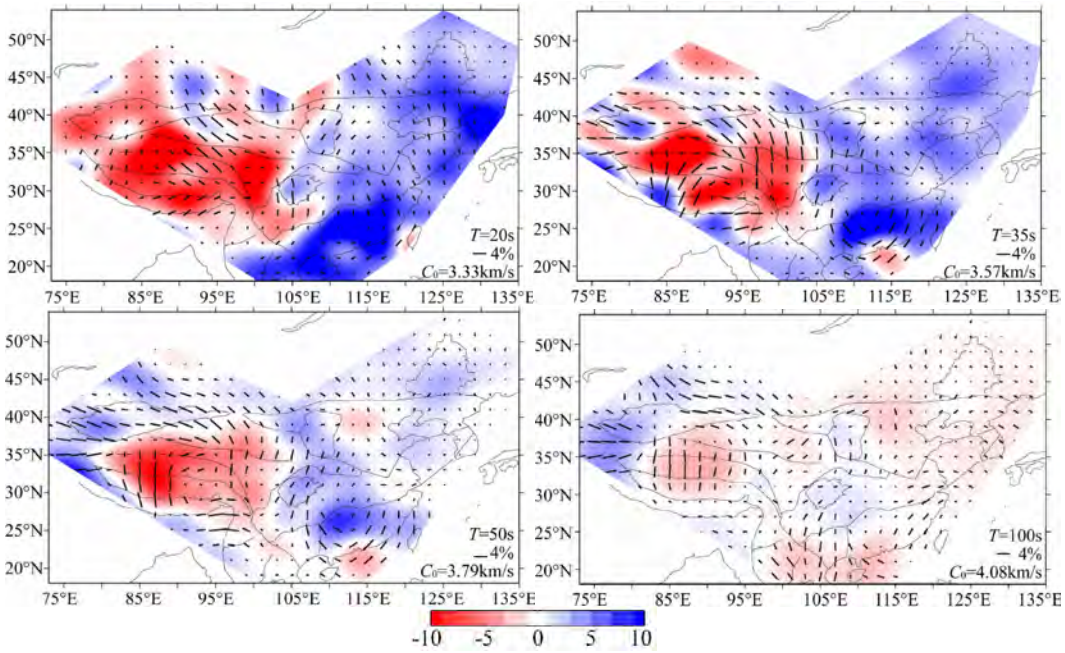


Figure 3. Azimuthal anisotropic phase velocity maps at periods 20, 35, 50, and 100s, from inter-station phase velocity measurements (From Yi et al., 2010). The background image shows the perturbation of phase velocities (%) with respect to the mean value; black bars show the pattern of azimuthal anisotropy.

1.3 Data for gravity inversion

Gravity data will be extracted from the global gravity model derived from the Gravity Recovery and Climate Experiment (GRACE) satellite mission. A detailed description of the satellite data and the computation of the gravity field are given by Tapley et al. (2005). The new gravity field is more accurate than previous data and reveals previously unobservable tectonic features. Figure 4 shows the free-air gravity anomalies for the proposed study region. Red colors represent gravity highs such as the Himalayas and Tibetan Plateau region where uplift arises from plate collision. Gravity lows, that is, mass deficits, are represented in blue. The large basins in the area (e.g., Tarim, Junggar, Qaidam) have thick sediment sections that produce substantial regional gravity variations (up to several hundred milliGals).

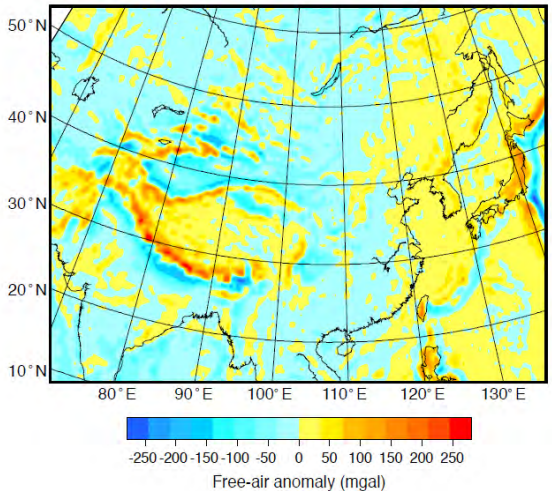


Figure 4. Free-air gravity observations for the proposed region of study. These anomalies have been extracted from the global gravity model derived from the GRACE satellite mission. Blue colors represent gravity lows meaning a mass deficit. Red colors are gravity highs.

2. Joint Inversion of Body Wave, Surface Wave, and Gravity Data

The results by Maceira and Ammon (2009) demonstrate that joint inversion of surface wave and gravity data not only offers a simple and elegant compromise between fitting both data sets, but that it also improves the Vs model. In turn, this will enhance earthquake location and characterization and, hence, the capability for Nuclear Explosion Monitoring. We plan to develop a comprehensive inversion scheme of seismic body wave travel times, seismic surface wave (phase and group) dispersion, and Bouguer gravity anomalies. In contrast to Maceira and Ammon (2009), who inferred Vs profiles from group velocity maps, we will adopt the one-stage surface wave inversion to facilitate joint inversion with body wave travel times, in which the surface wave dispersion data are directly used to invert for Vp, Vs and density.

2.1 Joint Inversion Framework

For the proposed joint inversion system, the P travel times are sensitive to Vp perturbations δα, that S travel times are sensitive to Vs perturbations δβ, that gravity data to mass density perturbation δρ, and that Rayleigh wave dispersion is sensitive to δα, δβ and δρ. With sensitivity kernels G computed from (3D) starting model, and updated in iterative schemes, we can formulate an explicit relationship between seismic and gravity data and δα, δβ, and δρ:

$$\mathbf{Gm} = \begin{bmatrix} \mathbf{G}_{\alpha}^{T_p} & 0 & 0 \\ 0 & \mathbf{G}_{\beta}^{T_s} & 0 \\ \mathbf{G}_{\alpha}^{S} & \mathbf{G}_{\beta}^{S} & \mathbf{G}_{\rho}^{S} \\ 0 & 0 & \mathbf{G}_{\rho}^{grav} \end{bmatrix} \begin{bmatrix} \delta\boldsymbol{\alpha} \\ \delta\boldsymbol{\beta} \\ \delta\boldsymbol{\rho} \end{bmatrix} = \begin{bmatrix} \mathbf{d}^{T_p} \\ \mathbf{d}^{T_s} \\ \mathbf{d}^{S} \\ \mathbf{d}^{grav} \end{bmatrix} = \mathbf{d}. \quad (1)$$

Hereinafter, this system will be written as **Gm**=**d**. For simplicity, the perturbations to seismic event hypocenters and origin times are not shown, but they will be included in the inversion.

We use the iterative LSQR algorithm to minimize an objective function that combines a measure of data misfit and regularization terms. In its simplest forma we consider the misfit

$$\varepsilon = \left\|\mathbf{Gm} - \mathbf{d}\right\|^2 + \lambda_1 \left\|\mathbf{m}\right\|^2 + \lambda_2 \left\|\mathbf{Lm}\right\|^2. \quad (2)$$

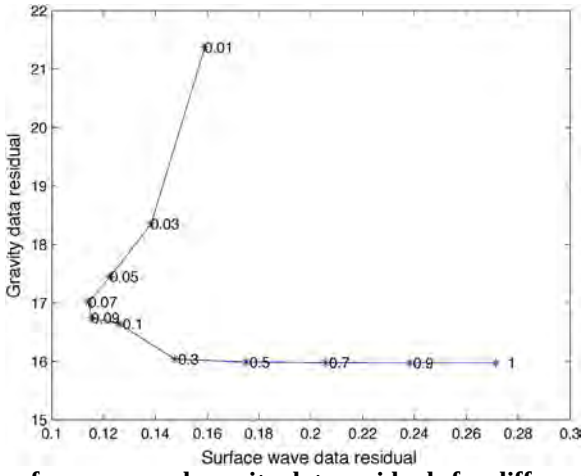


Figure 5. Trade-off curve of surface wave and gravity data residuals for different weightings (after Zhang et al., 2009).

As before, **m** represents the model vector (that is, **δα**, **δβ**, **δρ** in each grid cell as well as hypocenter perturbation terms) and **G** is the sensitivity matrix (for seismic travel time, surface wave, and gravity data). Data vector **d** represents the travel-time residuals, seismic surface wave dispersion measurement residuals, and gravity anomalies. The second and third terms represent traditional Tikhonov regularization: the second term represents "norm damping" and favors a result that is close to the reference model. The third term reduces the difference between adjacent cells, which produces smooth models: L is a first order differential operator, and λ_1 and λ_2 are the weights

of Tikhonov regularization. The misfit function (2) can be modified in order to impose bounds on parameter ranges (using scaling arguments) and to favor structure coherence between parameters (through cross gradient minimization, see below).

Joint inversion of seismic travel times, surface wave dispersion, and gravity data represents a multiple-objective optimiza-tion problem. Because it is unlikely that the different "objectives" (data types) would be optimized by the same parameter choices, some trade-off between the objectives is needed. Figure 5 shows an example of finding the relative weightings between the gravity and surface wave data through a trade-off analysis of surface wave data residual and gravity data residual. As a result, the final model optimally fits both the surface wave and the gravity data. Figure 6 shows the comparison of the Vs model obtained from the joint inversion of surface wave and gravity data with that obtained using all three data types. The latter model fits the three data sets well and shows better definition of the velocity anomaly associated with the transition from the Basin and Range to the west to the Colorado Plateau to the east.

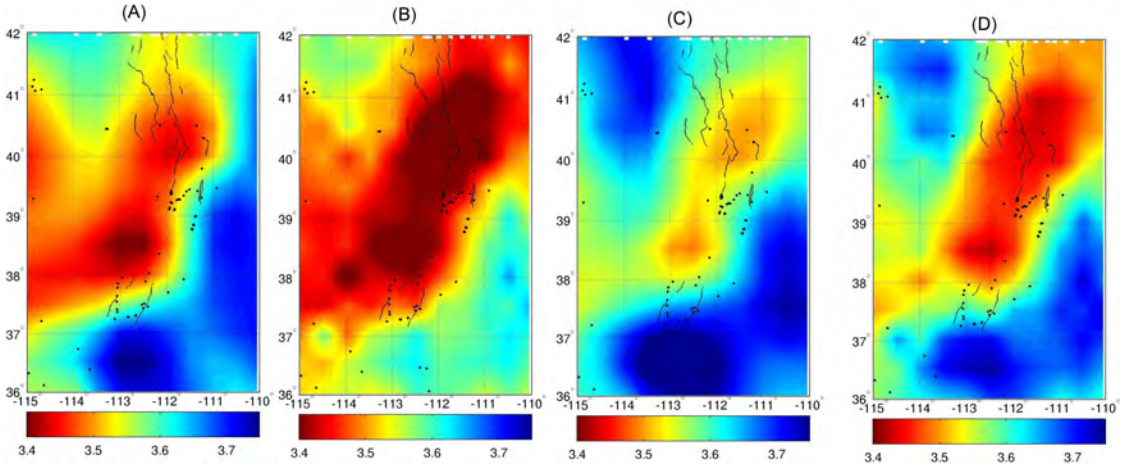


Figure 6. Vs model of an area in Utah at a depth of 17 km obtained from (A) surface wave data, (B) surface and gravity data, (C) surface and travel time data, and (D) surface, gravity, and travel time data.

2.2 Cross-gradient constraint

Explicit scaling between gravity and seismic data assumes (spatially) coincident changes in model structure. This needs not be the case, however, so we wish to relax this requirement. In order to favor solutions in which the variations of the model parameters coincide only as long as the data allow it, we can use a cross-gradient operator Φ_m to measure the structural similarity between models (Zhang and Morgan, 1996; Gallardo and Meju, 2007):

$$\phi_m = \sum_{i=1}^{N} \left(\nabla m_1^i \times \nabla m_2^i \right) \qquad (3)$$

The null values of this cross-gradient operator define either full colinearity or the absence of gradients within one or both models. The latter permits accurate recovery of models in situations where one model parameter changes and the other may not. The homogeneous physical property B has zero gradient; hence Φ_m is minimized and the required gradient in physical property A remains unaffected. It is only when both data sets require non-vanishing gradients that the structure penalty function steps in to enforce colinearity of the gradients. A consequence of using an unnormalized operator is that the colinearity of larger gradients will be more actively enforced than smaller gradients during the inversion.

With this type of linkage the deficiencies in spatial resolution associated with each data set can be partially overcome. The cross-gradient approach has been applied in local earthquake tomography for joint inverting for Vp and Vs, in which the Vp and Vs models are constrained using the cross-gradient constraint (Tryggyason and Linde, 2006). In our study, we propose to explore the cross-gradient constraint among Vp, Vs, and density models using the synthetic and real data sets; cross-gradient minimization can be included in the misfit function (10).

2.3 Solving the Joint Inversion System in the Wavelet Domain

One way to deal with uneven data distribution is to use an irregular inversion grid adapted to the sampling density of ray paths, e.g. at the local scale (Zhang and Thurber, 2005) and at the global scale (Kárason and Van der Hilst, 2001; Burdick et al., 2008). Alternatively, we can consider a wavelet representation (e.g. Chiao and Liang, 2003). The advantage of the latter is that it implicitly solves for the model parameters at multiple scales due to the inherent multi-resolution wavelet representation of model parameters and Fréchet derivatives. We will test and compare the two ways of dealing with uneven data distribution.

Multigrid methods are now fairly common, but wavelet representations are not routinely used. A wavelet transform provides a compact and natural multiresolution representation of scalar fields (such as the models considered here) thanks to orthogonal or bi-orthogonal basis functions built by translating (localization property) and dilating (scaling property) a mother wavelet and a scaling function. These functions are the basis of functional spaces generally denoted V_i for the scaling functions φ_i and W_i for the wavelet functions ψ_i in the frame of a wavelet multiresolution analysis (Mallat, 1998). The wavelet function spans the difference between any two adjacent scaling subspaces V_i and V_{i-1}. Scaling function and wavelet function are each associated with a filter, known as low-pass filter H and high-pass filter G. Therefore, the wavelet transform of any dimensional signal can be realized through a fast multilevel decomposition using these two filters H and G (similar to sub-band filtering in signal processing). Inverse wavelet transforms proceed from coarser to the finer scales.

When a 3D velocity (or slowness, as in seismic tomography) model that is represented on a (fine) regular grid is decomposed by wavelet transform, each level *i* corresponds to a grid increment. The starting point is the slowness model on the finest grid of the multiresolution representation. Generally, the resolution of each grid decreases by a factor of 2 and the mesh spacing is set accordingly when the level *i* increases. The wavelet transform applies a cascade of orthogonal restrictions of the slowness model over different approximation grids. The restrictions of the slowness model on a coarse grid are encoded by the scaling coefficients. These coefficients are the components of the model represented by the scaling functions. At each step, the increment of information lost during the restriction on the coarser grid is encoded by the wavelet coefficients before proceeding to the next grid. At the last iteration of the orthogonal transform, we end up with the wavelet coefficients on each grid plus the scaling coefficients on the coarser grid.

For a linearized inverse problem **Gm=d** (as in Section 2.1) we can apply the wavelet transform **W** to the model vector **m** as follows:

$$\mathbf{GW^{-1}Wm=d} \tag{4}$$

If the chosen wavelet basis is orthogonal such that $\mathbf{W^{-1}} = \mathbf{W}^{T}$, then the new linearized system can be written as $\mathbf{GW^{T}Wm = GW^{T}C=d}$, where **C** denotes the wavelet coefficients of the velocity or slowness model. $\mathbf{GW^{T}}$ represents the wavelet transform of one row of the Frechet derivative matrix. In the case of seismic tomography in 2D, a row of the sensitivity matrix has $n_1 \times n_2$ model parameters where the number of horizontal grid points is n_1 and the number of vertical grid points is n_2; it contains the contribution of one ray to the Frechet derivatives. After transformation, the model parameters are solved in the wavelet domain and partial derivatives are with respect to scale and wavelet coefficients.

Solving the model parameters in the wavelet domain naturally characterizes them at multiple scales. Recall that wavelet coefficients at different levels are related to different scales or resolutions. In areas where no data or fewer data (e.g. ray paths) illuminate the medium, partial derivatives of the data with respect to the wavelet coefficients at the finer scales will be zero or close to zero. By contrast, the partial derivatives of the data with respect to the wavelet coefficients at the coarser scales will be non-zero. Hence, only the coarse-scale wavelet coefficients of the model will be non-zero (or greater than a prescribed threshold) after inversion, which will automatically lead to a smooth representation of the true model.

We will test different wavelet families, and appropriate parameter settings will be chosen based on data fits, convergence behavior, and model appearance.

2.4 Model Resolution and Uncertainty Estimation in the Wavelet Domain

With iterative solvers, such as LSQR, it is difficult to construct model resolution and covariance matrices. In addition to checkerboard test, we propose to calculate the model resolution matrix by estimating singular values and vectors for large matrices based on the Lanczos bi-diagonalization with partial re-orthogonalization (BPRO)

(Larsen, 1998; Zhang and Thurber, 2007). This algorithm is accurate and efficient, even for very large sensitivity matrices. The memory space required by BPRO is proportional to the square of the number of singular values and vectors requested. When there are far more observations than model parameters, Zhang and Thurber (2007) show it is more efficient to estimate singular values and vectors for $\mathbf{A}^T\mathbf{A}$ under the condition that the problem is regularized by damping and/or smoothing. With BPRO it is also straightforward to construct the covariance matrix. This allows formal uncertainty analysis for large geophysical inverse problems, although we note that the solution from the regularized system is biased by the applied regularization.

If model parameters are solved in the wavelet domain, we can also apply BPRO to the wavelet transformed derivative matrix $\mathbf{GW}^T$ and its singular value decomposition $\mathbf{USV}^T$. Because $\mathbf{W}$ is an orthogonal matrix, the singular value decomposition of the original matrix $\mathbf{G}$ can be represented as $\mathbf{G}=\mathbf{USV}^T\mathbf{W}=\mathbf{USV'}$, where $\mathbf{V'}=\mathbf{V}^T\mathbf{W}$. Considering that many wavelet coefficients will be zero or close to zero in the region where few data are available, the wavelet transformed Frechet derivative matrix is highly sparse and therefore BPRO may be faster compared to the original matrix. Solving the model parameters in the wavelet domain gives an opportunity to estimate the model resolution matrix with different scales or grid intervals. We can hierarchically represent the model parameters at different levels. If we suppress wavelet coefficients (and the corresponding transformed partial derivatives) at certain levels, the recovered model will be represented at a coarser grid lacking the detailed grid nodes corresponding to those wavelet coefficients. For example, if we just represent the model at one level and zero-out all the wavelet coefficients but leave all the scale coefficients untouched, then the model resolution matrix gives the model resolution at a twice greater grid interval.

3. Generation of an Updated Catalog and Validation of Velocity Models

Our proposed Asian tomography study will generate new 3-D Vp and Vs models, along with an updated catalog of earthquake locations. We propose to validate the final velocity models in several different ways. First, the Vp and Vs models from travel time tomography will be compared to other studies for consistency and differences.

Second, we will validate the models by using travel times from GT events including explosions at several test sites such as Lop Nor, China (e.g. Fisk, 2002; Waldhauser et al., 2004) and Balapan, Kazakhstan (Thurber et al., 1993) and some assembled events from available sources (e.g. Bondár et al., 2004).Validation of the models developed in this work will take place at LANL, where travel-time calculations and event location errors will be estimated for the >500 highest quality (GT <5) events in the LANL database. Most of these events are nuclear explosions, although a few are large chemical blasts and some unusually well-located earthquakes. This work will be followed by relocation of all events in the LANL data holdings, and we will compare the results to other 1D, 2.5D and 3D models available to us. Of greatest interest will be the performance of the model within the newly-developed global, 3D, tessellated parameterization (e.g., Ballard et al., 2009) and comparison of its performance to the recently developed SALSA3D model.

Third, we will calculate synthetic seismograms for selected events with well-constrained source mechanisms using the discrete wavenumber method and the spectral element method (SEM) and compare them to the broadband seismograms. Q models will also be added when calculating synthetic seismograms to see whether the fitting is better. Our approach is to build on the existing tools that we have developed but to use 3D waveform modeling to help assess the model. The SEM provides higher accuracy than other methods when wavefields are sufficiently spatially smooth and it is particularly suited to modeling seismic wave propagation over large distances within complex structures (Komatitsch and Tromp, 1999). The main limitation to application of the mentioned methodologies for 3D modeling is the significant computational costs. To overcome the computational challenges associated with this type of problem, we will be making use of LANL high-performance computing resources.

CONCLUSIONS AND RECOMMENDATIONS

We plan to develop joint inversin methods with a series of methodological advances and, eventually, conduct an explicit joint interpretation of the seismic and gravity data that are available to us. First, we will combine our double difference and global (travel time) tomography codes in order to improve constraints on δVp and δVs in the shallow mantle through inversion of regional and teleseismic P and S time picks. Second, we will implement a method for surface wave inversion that bypasses the need for phase or group velocity maps and which facilitates joint inversion with travel time. Third, we will use sensitivity kernels to relate observed Rayleigh wave phase and group speeds not only to variations in Vs but also in Vp and ρ. Fourth, knowing the sensitivities of (i) S travel times and Rayleigh wave dispersion to δVs, of (ii) P travel times and Rayleigh wave dispersion to δVp, and of (iii) gravity data and

Rayleigh wave dispersion to δρ, we can formulate an explicit joint inversion of seismic and gravity data for δVp, δVs, and δρ. Our joint inversion methods will also take advantage of the recently developed cross-gradient constraint to maximize structure coherence of the 3D wavespeed and density variations and the wavelet-based seismic tomography method.

REFERENCES

Ballard, S., Hipp, J.R., and Young, C.J. (2009). Efficient and Accurate Calculation of Ray Theory Seismic Travel Time through Variable Resolution 3D Earth Models, *Seismol. Res. Lett*. **80**, 989–999.

Bondár, I., Engdahl, E.R, Yang, X., Ghalib, H.A.A., Hofstetter, A., Kirichenko, V., Wagner, R., Gupta, I., Ekström, G., Bergman, E., Israelsson, H., and McLaughlin, K. (2004). Collection of a reference event set for regional and teleseismic location calibration, *Bull. Seismol. Soc. Am.* **94**, 1528–1545.

Burdick, S., Li, C., Martynov, V., Cox, T., Eakins, J., Astiz, L, Vernon, F.L., Pavlis, G.L., and Van der Hilst, R.D. (2008). Multi-scale travel time tomography with *USArray* data, *Seismol. Res. Lett*. **79**, 384392.

Campillo, M and A. Paul (2003). Long-range correlations in the diffuse seismic coda, *Science*, **299**, 547–549.

Chiao, L.-Y. and Liang, W.-T. (2003). Multiresolution parameterization for geophysical inverse problems, *Geophysics* **68**, 199–209.

Engdahl, E.R., Van der Hilst, R.D., and Buland, R.P. (1998). Global teleseismic earthquake relocation from improved travel times and procedures for depth determination, *Bull. Seismol. Soc. Am.* **88**, 722–743.

Fisk, M.D. (2002). Accurate locations of nuclear explosions at the Lop Nor test site using alignment of seismograms and IKONOS satellite imagery, *Bull. Seismol. Soc. Am.* **92**, 2911–2925.

Gallardo L.A. and Meju, M.A. (2007). Joint two-dimensional cross-gradient imaging of magnetotelluric and seismic traveltime data for structural and lithological classification, *Geophys. J. Int*. **169**, 1261–1272.

Kárason, H. and Van der Hilst, R. D. (2001). Tomographic imaging of the lowermost mantle with differential times of refracted and diffracted core phases (PKP, Pdiff), *J. Geophys. Res.* **106**,6569–6587.

Komatitsch, D. and Tromp, J. (1999). Introduction to the spectral element method for three-dimensional seismic wave propagation, *Geophys. J. Int.* **139**, 806–822.

Larsen, R. M. (1998). Lanczos bidiagonalization with partial reorthogonalization, Department of Computer Science, Aarhus University, Technical Report, DAIMI PB-357, September 1998.

Lebedev, S. and Van der Hilst, R. D. (2008). Global upper-mantle tomography with the automated multi-mode surface and *S* waveforms, *Geophys. J. Int*. **173**, 505–518.

Li, C., and Van der Hilst, R.D. (2010). High-resolution *P*-wave tomography of upper mantle beneath East Asia, *J. Geophys. Res* **115**, doi:10.1029/2009JB006882.

Mallat, S. (1998). *A wavelet tour of signal processing*, Academic Press, San Diego, 577pp.

Maceira, M. and Ammon, C. J. (2009). Joint inversion of surface wave velocity and gravity observations and its application to central Asian basins shear velocity structure, *J. Geophys. Res.*, **114**, B02314, doi:10.1029/2007JB005157.

Tapley, B., Ries, J., Bettadpur, S., Chambers, D., Cheng, M., Condi, F., Gunter, B., Kang, Z., Nagel, P., Pastor, R., Pekker, T., Poole, S., and Wang, F. (2005). GGM02—An improved Earth gravity field model from GRACE, *J. Geod.* **79**, 467–478, doi:10.1007/s00190-005-0480-z.

Thurber, C.H., Quin, H.R., and Richards, P.G. (1993). Accurate locations of nuclear explosions in Balapan, Kazakhstan, 1987 to 1989, *Geophys. Res. Lett.* **20**:399–402.

Tryggvason, A. and Linde, N. (2006). Local earthquake (LE) tomography with joint inversion for P- and S-wave velocities using structural constraints, *Geophys. Res. Lett.* **33**, L07303, doi:10.1029/2005GL025485.

Waldhauser, F., Schaff, D. P., Richards, G., and Kim, W.-Y. (2004). Lop Nor revisited: Underground nuclear explosion locations, 1976-1996, from double-difference analysis of regional and teleseismic data, *Bull. Seismol. Soc. Am.* **94**, 1879–1889.

Yang, Y, Zheng, Y., and Ritzwoller, M.H. (2010). Rayleigh wave phase velocity maps in Tibet and the surrounding regions from ambient seismic noise tomography, *Geochem., Geophys., Geosys.* **11**, Q08010.

Yao, H., Beghein, C., and Van der Hilst, R.D. (2008). Surface-wave array tomography in SE Tibet from ambient seismic noise and two-station analysis: II – Crustal and upper mantle structure. *Geophys. J. Int.* **173** (1), 205–219, doi: 10.1111/j.1365-246X.2007.03696.x.

Yao, H., Van der Hilst, R.D., and de Hoop, M.V. (2006). Surface-wave array tomography in SE ibet from ambient seismic noise and two-station analysis: I - Phase velocity maps, *Geophys. J. Int.* **166**, 732–744, doi: 10.1111/j.1365-246X.2006.03028.x.

Yao, H., Van der Hilst, R.D., and Montagner, J-P. (2010). Heterogeneity and anisotropy of the lithosphere of SE Tibet from surface wave array analysis, *Geophys. J. Res.*, doi:10.1029/2009JB007142.

Yi, G.X., Yao, H.J., Zhu, J.S., Van der Hilst, R.D (2010). Lithospheric deformation of continental China from Rayleigh wave azimuthal anisotropy, *Chinese J. Geophys*. (in Chinese) **53**, 256–268.

Zhang, H., Maceira, M., Toksoz, M. N.,Burlacu, R., Rowe, C., and Yang, Y. (2009). Joint geophysical imaging of the Utah area using seismic body waves, surface waves and gravity data, Eos Trans, AGU, Fall Meet. Suppl., Abstract.

Zhang, J. and Morgan, F.D. (1996). Joint seismic and electrical tomography, *Proc. EEGS Symposium on Applications of Geophysics to Engineering and Environmental Problems*, 391–396.

Zhang, H., and Thurber, C. (2005). Adaptive-mesh seismic tomography based on tetrahedral and Voronoi diagrams: Application to Parkfield, California, *J. Geophys. Res.* **110**, B04303, doi:10.1029/2004JB003186.

Zhang, H. and Thurber, C.H. (2007). Estimating the model resolution matrix for large-seismic tomography problems based on Lanczos bidiagonalization with partial reorthogonalization, *Geophys. J. Int.* **170**: 337–345.

Zheng, S., Sun, X., Song, X., Yang, Y., and Ritzwoller, M. H. (2008). Surface wave tomography of China from ambient seismic noise correlation, *Geochem. Geophys. Geosyst.* **9**, Q05020, doi:10.1029/2008GC001981.

JOINT INVERSION OF MULTIPLE SEISMIC DATA FOR THREE-DIMENSIONAL VELOCITY STRUCTURE BENEATH SOUTHERN AND EASTERN ASIA

Suzan van der Lee[1], Sung Joon Chang[2], Michael Witek[1], Tae Seob Kang[3], Mei Feng[4]

Northwestern University[1], University of East Anglia[2], Pukyong National University[3], and Chinese Academy of Geological Sciences[4]

Sponsored by the Air Force Research Laboratory

Award No FA9453-11-C-0231

ABSTRACT

The 3D *S*-velocity structure for the crust and mantle along the Tethyan margin has been modeled through the joint inversion of multiple seismic data such as teleseismic *S*-arrival times, regional waveform fits, fundamental-mode group velocities, and independent Moho constraints (Chang et al., 2010). We now aim to construct a 3-D *S*-velocity model for the crust and mantle beneath eastern Asia using the same joint inversion method, augmented with ambient seismic noise data, gravity data, and converted body wave data. We aim to model the 3D crust and mantle *P*-velocity structure using a scaled version of the 3D *S*-velocity model as a reference model relative to which we invert teleseismic and regional *P* delay times.

Our 3-D *P*-velocity model derived this way for the Tethyan margin (EAPV11) is more uniformly resolved with better depth resolution, including velocity anomalies for aseismic regions with few stations, than is typically obtained from traditional teleseismic delay time inversions. EAPV11 is also able to predict delay times for ground truth (GT25) events, which were not used in the inversion. This implies that although scaling *S* velocities to *P* velocities may be uncertain, the scaled velocities contribute to the accurate prediction of delay times at regional distances. Our planned *S* and *P* velocity models for eastern Asia will be validated using the methods of Flanagan et al. (2007) for regional delay time prediction and Komatitsch et al. (2002) for regional *S* and Rayleigh wave train prediction.

OBJECTIVES

Our primary objective is to construct a high-resolution 3-D model for the *S*-velocity of the mantle and beneath eastern Asia. The model is to have

1) high-resolution crustal structure of Korean peninsula, constrained by gravity data and ambient seismic noise data,

2) consistently good resolution from the surface to the lower mantle obtained from multiple data sets with different resolving powers,

3) topography of seismic discontinuities such as the Moho, which is essential for travel time prediction and seismic phase discrimination, and

4) uncertainties for each data set taken into account to weight individual data sets in the joint inversion according to data quality.

RESEARCH ACCOMPLISHED

We finalized a manuscript on the *P* velocity structure, and its validation, of the mantle along the Tethys Belt (Chang et al., 2012). The *P* velocity model (Fig. 1) is the result of inverting teleseismic *P* arrival times relative to a reference model that was converted to *P* velocity from an *S* velocity model, derived from the joint inversion of teleseismic *S*-arrival times, regional waveform fits, fundamental-mode group velocities, and independent Moho constraints (Chang et al., 2010).

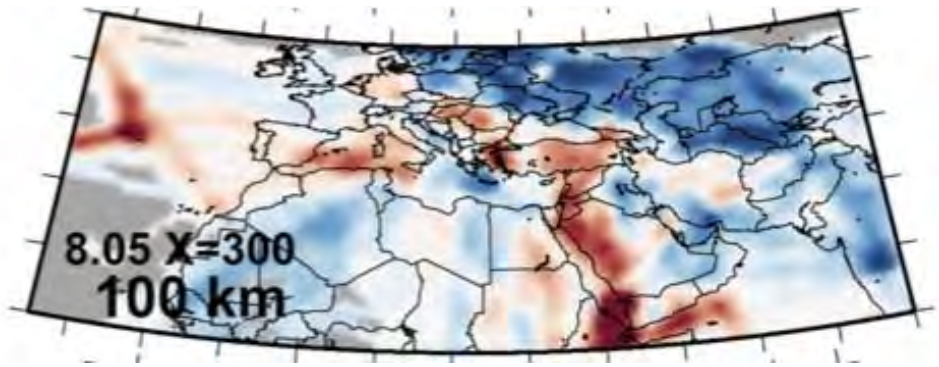


Figure 1. *P* velocity structure at a depth of 100 km beneath the western Tethys Belt. In this project we aim to expand this imaging eastwards to east Asia.

In this project we aim to model the *P* velocity of east Asia similarly, and with enhanced resolution for the crustal structures. A major first step in this process is to model the *S* velocity of east Asia, using the same types of *S* data as in Chang et al. (2010), enhanced with constraints from the dispersion of ambient noise and relative to a three-dimensional starting model in those regions where data access is problematic.

A rough version of the larger study region is provided in Fig. 2. Feng et al.'s (2010) *S* velocity model for this region is based on data from 283 permanent and temporary broadband stations deployed in and around China before 2006. The permanent networks include New China Digital Seismograph Network, the Broadband Array in Taiwan, GEOSCOPE, Global Seismographic Network, and the Kazakhstan Network, among others. The temporary networks/arrays include experiments deployed upon the Tibetan Plateau, in North China, and in NE China, among others. Not all of the Chinese data utilized are publicly accessible. Therefore, we will use this *S* velocity model as a starting model in our inversion. This starting model shows reasonable detail in the crust, owing to the inclusion of

group velocity dispersion curves, and significant, resolved heterogeneity in the mantle (Fig. 3). Feng et al. (2010) converted this seismic velocity model to mantle temperatures to study the strength and thickness of the Chinese lithosphere. The velocity structure of Figure 3 also shows that the lithosphere of the North China Craton thins eastwardly, but the Yangtze Craton, Tibetan Plateau, and Tarim Basin, show stronger and thicker lithosphere (see Feng et al., 2010). Also beyond China, the mantle wedge beneath Japan is distinct from other structures in the model.

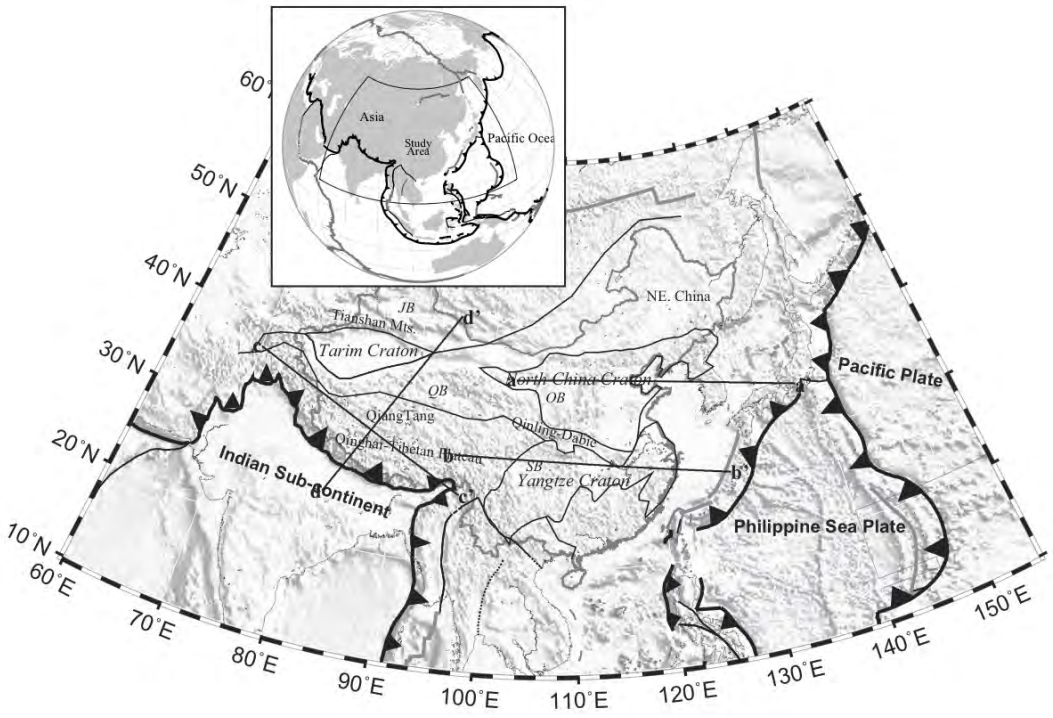


Figure 2. Map of larger study region (from Feng et al. (2010)). Profile aa' (Fig. 3) runs through the North China Craton, the Korean peninsula, and ends near the triple junction of the Eurasian, Pacific, and Philippine Sea plates.

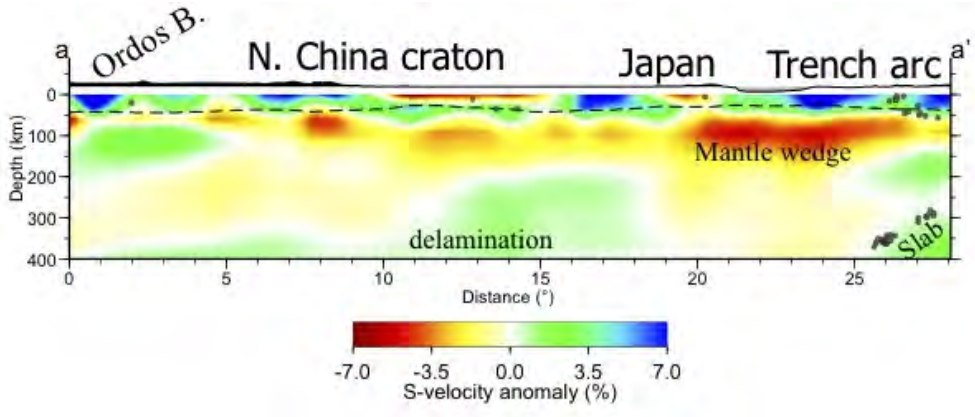


Figure 3. Cross section through the *S* velocity model of Feng et al. (2010) along line aa' of Figure 2. This model shows an eastwards thinning lithosphere beneath the North China Craton and a distinct mantle wedge east of Korean Peninsula (beneath the "n" of the "Japan" label).

Data that will be inverted relative to this starting model will be collected from the stations and events illustrated in Figure 4. The types of data we will collect and analyze are teleseismic *S*-arrival times, regional waveform fits, fundamental-mode group velocities, independent Moho constraints (from receiver function studies, for example Chang and Baag (2007)), and ambient noise dispersion.

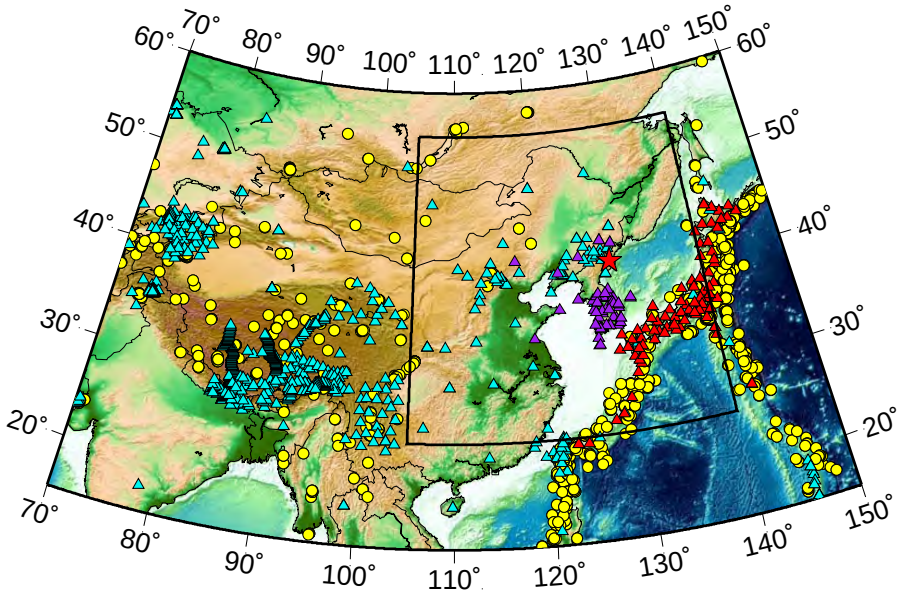


Figure 4. Map of stations which are available for this study and event distribution. Stations from IRIS, Korea, and Japan are indicated by cyan, purple, and red triangles, respectively. Events with magnitude more than or equal to Ms 5.0 from 1998 to 2010 (< 70 km depth) are represented as yellow circles.

We are currently collecting data from F-net (Japan), KIGAM, and KMA (Korea) and preparing to estimate ambient noise dispersion in these data for periods of 5 s and more. These data are essential for improving the resolution of crustal structure in eastern Asia. Inclusion of data from open stations in northeastern China will further optimize regional and azimuthal coverage, including for regions in the Korean Peninsula without accessible data (Figure 5).

The only data type in our collection that is sensitive to lower-mantle structure are the teleseismic arrival times. Resolution of the lower mantle can, however, be improved by consistently better resolving structure of the upper mantle (Chang et al, 2010), because of their shared sensitivity for upper mantle structure. By including dispersion estimates from ambient noise, we anticipate to further improve resolution, from the crust to the lower mantle.

We do not invert solely for *S* velocity anomalies, but also for lateral variations in depths of important seismic discontinuities, specifically the Moho and the 410 and 660-km discontinuities. Having accurate estimates for the depths and lateral variations therein, is essential for travel time predictions and seismic phase discrimination. Ultimately, we will solve the following system of equations in the joint inversion for an *S* velocity model:

$$\begin{bmatrix} w_{ta}A_S^{ta} & w_{ta}A_m^{ta} & 0 & 0 & w_{ta}A_{ta,e} & w_{ta}A_{ta,o} \\ w_{rw}A_S^{rw} & w_{rw}A_m^{rw} & 0 & 0 & 0 & 0 \\ w_U A_S^U & w_U A_m^U & 0 & 0 & 0 & 0 \\ 0 & w_{ic}A_m^{ic} & 0 & 0 & 0 & 0 \\ w_G A_S^G & w_G A_m^G & 0 & 0 & 0 & 0 \\ w_{410}A_S^{P410s} & 0 & w_{410}A_{410}^{P410s} & 0 & 0 & 0 \\ w_{660}A_S^{P660s} & 0 & 0 & w_{660}A_{660}^{P660s} & 0 & 0 \\ w_1 I & w_1 I & 0 & 0 & 0 & 0 \\ w_2 F_h & w_2 F_h & 0 & 0 & 0 & 0 \\ w_3 F_v & 0 & 0 & 0 & 0 & 0 \end{bmatrix} \begin{bmatrix} \Delta V_S \\ \Delta d_{moho} \\ \Delta d_{410} \\ \Delta d_{660} \\ \Delta x_e \\ \Delta e \end{bmatrix} = \begin{bmatrix} w_{ta}d^{ta} \\ w_{rw}d^{rw} \\ w_U d^U \\ w_{ic}d^{ic} \\ w_G d^G \\ w_{410}d^{P410s} \\ w_{660}d^{P660s} \\ 0 \\ 0 \\ 0 \end{bmatrix}$$

where A_b^a is a matrix of partial derivatives of a with respect to b. Superscripts *ta*, *rw*, *U*, *ic*, *G*, *P410s*, and *P660s* represent teleseismic arrival times, regional waveform fits, Rayleigh-wave group velocities including ambient noise cross-correlation, independent Moho constraints, gravity data, P410s-P and P660s-P phases, respectively. The corresponding data vectors are d^a. Furthermore, ΔV_S, Δd_{moho}, Δd_{410}, Δd_{660}, Δx_e, and Δe are anomalous *S* velocity, depths to Moho, 410, and 660 km discontinuities, event mislocations, and origin time errors, which constitute model parameters. I is the identity matrix for damping operator; F_h and F_v are horizontal and vertical flattening operators, respectively. Weights w are applied to each data set and operator and are used to weight individual data sets according to data quality.

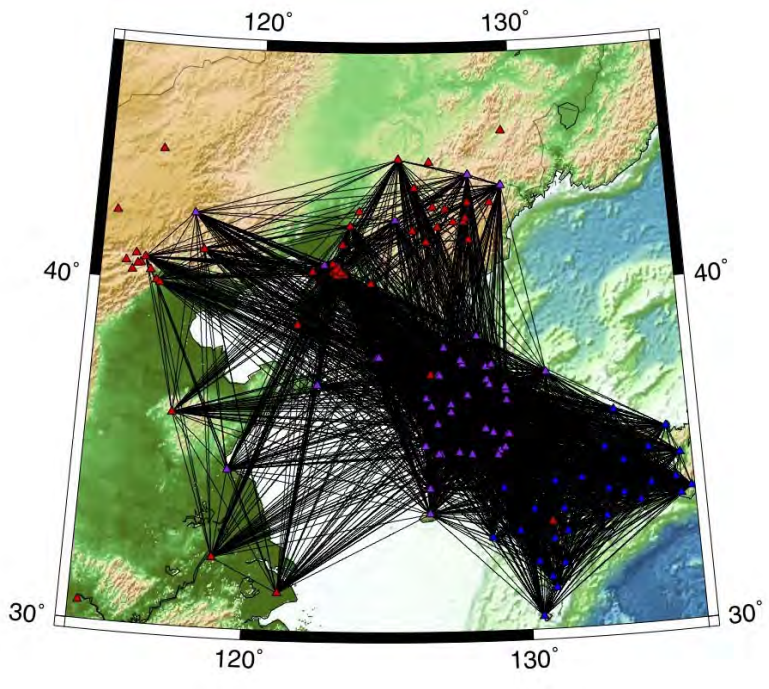


Figure 5. Great-circle paths for ambient noise cross-correlation to measure short-period group velocity data. Stations are the same as in Figure 4.

CONCLUSIONS AND RECOMMENDATIONS

None yet.

REFERENCES

Chang, S.-J., S. van der Lee, M. P. Flanagan, H. Bedle, F. Marone, E. M. Matzel, M. E. Pasyanos, A. J. Rodgers, B. Romanowicz, and C. Schmid (2010). Joint inversion for 3-dimensional S-velocity mantle structure along the Tethyan margin, *J. Geophys. Res.* **115**, B08309, 22 pp., doi:10.1029/2009JB007204.

Chang, S.-J., S. van der Lee, and M. P. Flanagan (2012). A new P-velocity model for the Tethyan margin from a scaled S-velocity model and the inversion of P and PKP delay times, submitted to *PEPI.*

Chang, S.-J. and C.-E. Baag (2007). Moho depth and crustal Vp/Vs variation in southern Korea from teleseismic receiver functions: Implication for tectonic affinity between the Korean Peninsula and China, *Bull. Seismol. Soc. Am*. **97**, 1621–1631.

Feng, M., S. van der Lee, M. An, and Y. Zhao (2010). Lithospheric thickness, thinning, subduction, and interaction with the asthenosphere beneath China from the joint inversion of seismic S-wave train fits and Rayleigh-wave dispersion curves, *Lithos* **120**, 116–130, doi:10.1016/j.lithos.2009.11.017.

ANALYSIS AND SIMULATION OF NEAR-FIELD GROUND MOTION FROM THE SOURCE PHYSICS EXPERIMENT

Oleg Y. Vorobiev, Heming Xu, Ilya N. Lomov, Eric Herbold, Tarabay H. Antoun, and Lew A. Glenn

Lawrence Livermore National Laboratory

Sponsored by the National Nuclear Security Administration

Award No. DE-AC52-07NA26594/NST11-NCNS-TM-EXP-PD15

ABSTRACT

The Source Physics Experiment (SPE-N) at the Nevada National Security Site (NNSS) is a series of chemical explosions under a variety of emplacement conditions. The goal of the SPE-N is to improve our physical understanding of explosively generated seismic waves, particularly S-waves, through modeling and simulation. Two SPE-N explosions (SPE-1, SPE-2) have been conducted in the Climax Stock (i.e., granite). The shots were recorded by an array of over 150 instruments, including both near-field wave motion measurements as well as far-field seismic measurements. The relationship between the peak velocities for SPE-1 and SPE-2 and scaled distance are quite consistent. It is also evident that the borehole records from SPE-1 and SPE-2 show significant vertical motions at the source depths relative to the total amplitudes testifying that the outgoing waved emitted by the two SPE tests are neither spherical and the roles assumed by the onsite heterogeneities such as fractures and faults are crucial in interpreting the observations.

This paper focuses on analysis of the measurements and modeling of the near-field data. Three-dimensional numerical simulations of SPE tests were performed with explicit representation of joints and faults. The focus of this work aims to understand the role of fractures and heterogeneities (such as joints and faults) resulting in wave anisotropy observed both underground, on the surface and transverse motion. A parametric study is presented that shows the sensitivities of calculated waveforms to the modeling parameters at various distances. The effect of damage in repeated explosions was also considered.

OBJECTIVES

The SPE-N at the NNSS is planned as a series of chemical explosions under a variety of emplacement conditions. The SPE-N goal is to improve our physical understanding and ability to model how explosions generate seismic waves, particularly S-waves.

RESEARCH ACCOMPLISHED

Analysis of SPE-1 and S-PE2 Data

We have analyzed the near-field measurement data from two consecutive experiments (SPE-1 and SPE-2). Due to uncertainty in possible gauge rotation used in the experiments our analysis will focus on quantities invariant to the orientation of the gauges such as total velocity magnitude and vertical velocities at depths of 150ft and 180ft.
Figure 1 shows the peak total velocity amplitudes obtained from the borehole records for SPE-1 (triangles) and SPE-2 (circles). The locations of the boreholes are given in (Antoun et al., 2011). The peak amplitudes from the historical nuclear explosions at Degelen, HardHat, Hoggar, PileDriver and Shoal are displayed with the small black symbols. It is seen that the relationships between the peak velocities for SPE-1 and SPE-2 and scaled distance are quite consistent in this scale range and are in agreement with those measurements from the hard rock nuclear explosions (small black symbols).

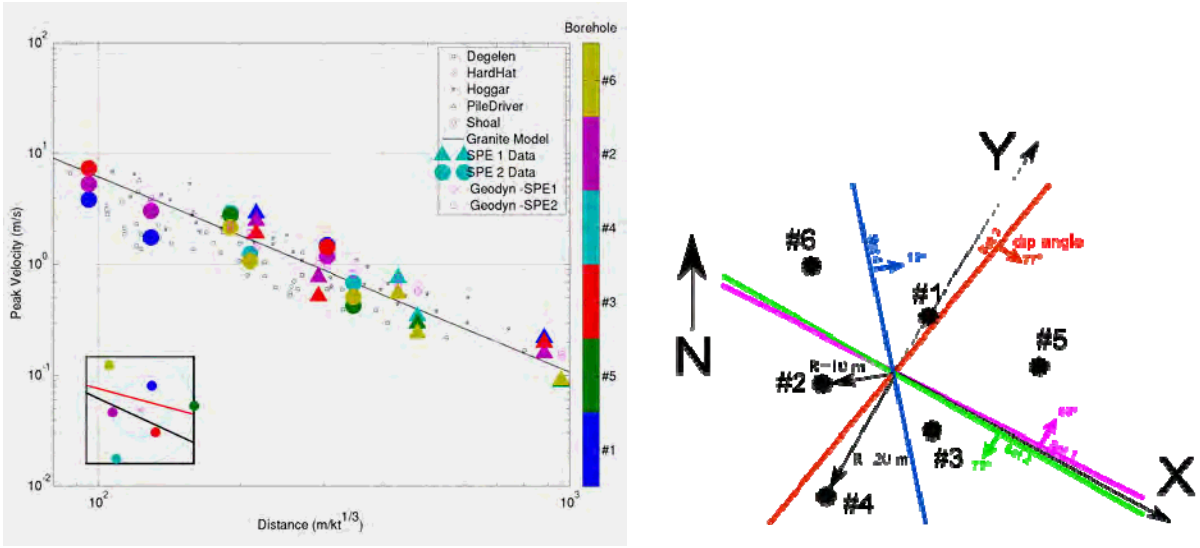


Figure 1. Peak total velocity amplitudes versus scaled distance for SPE-1 (triangle) and SPE-2 (circle). The peak velocities from the hardrock nuclear explosions are indicated by the small symbols. The continuum modeling results are displayed for SPE-1 (small red circle) and SPE-2(small red square). The line is the regression model for the nuclear explosions in granite. The inset shows the location of the 6 borehole locations and the locations of the two faults at 150ft. Joint set locations as well as the coordinate systems used in GEODYN-L is shown on the right

Although the peak velocity magnitudes for SPE-1 and SPE-2 decay at a similar rate compared to the historical explosions and show comparable azimuthal variations, detailed studies on the borehole records show that SPE-1 and SPE-2 explosions are not purely spherical. Figure 2 shows the comparison of the vertical motion with the total velocities for SPE-1 (left) and for SPE-2 (right). The solid lines represent the total velocity amplitude and the dashed lines display vertical velocities (upward positive).

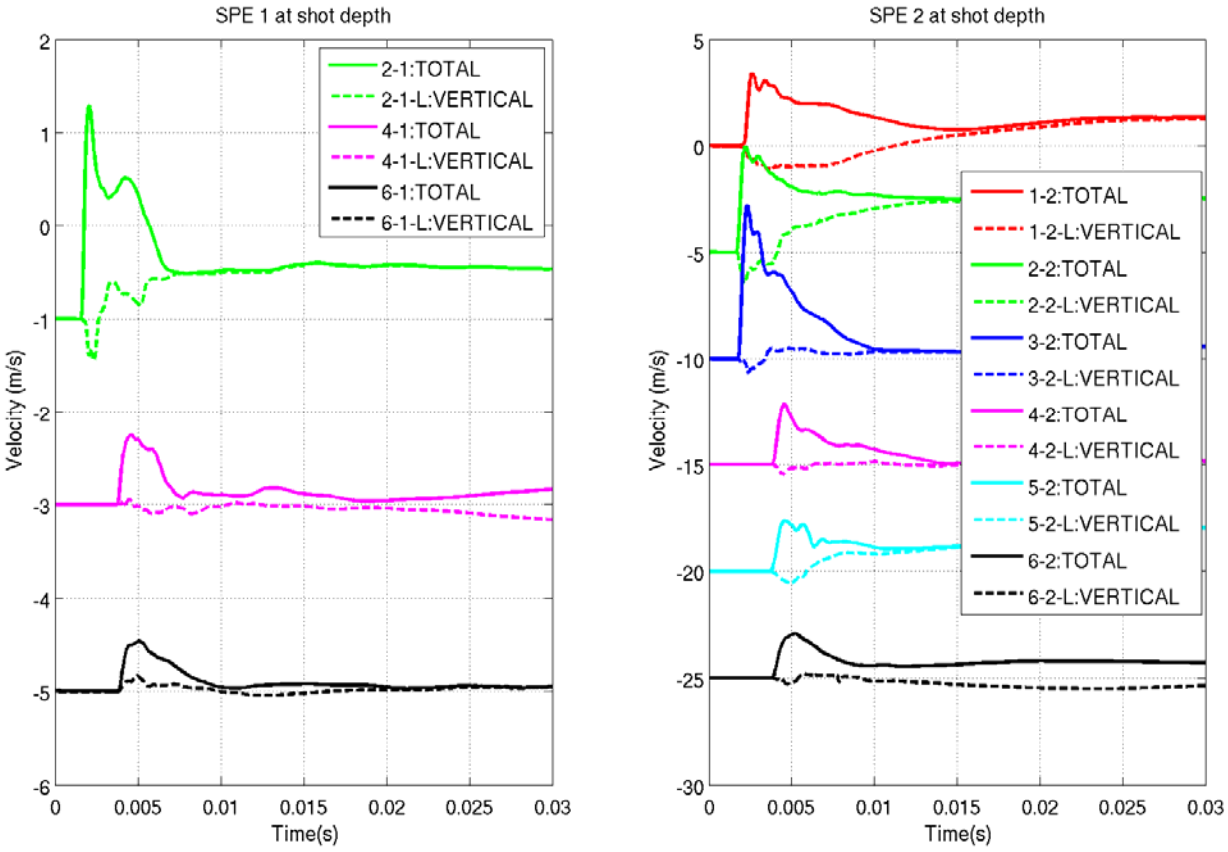


Figure 2. Vertical motions (dashed lines) at the shot levels of SPE-1 (left) and SPE-2 (right) in comparison with the total amplitudes at the gages. Each colored line-pair is offset vertically for visual clarity.

There are only 3 gauges with complete 3-component records for SPE-1 (left) at the shot depth while 6 gauges for SPE-2 (right). The gage locations are shown in the inset of Figure 1. It is evident at borehole 2 (green, 10m distance), where the vertical motions are significant relative to the total amplitudes for both SPE-1 and SPE-2. The vertical motions are also clear in borehole 1 and 3 records for SPE-2 at the shot depth. At a larger distance (boreholes 4-6, 20m) the vertical motion decays with distance as expected and the relative amplitudes are still significant. All these vertical motion observations confirm that the wave fields generated by SPE-1 and SPE-2 are not spherical. For example, shear waves are certainly generated in the vicinity of the source region and might be related to the onsite heterogeneities such as fractures, joints and faults as observed in the borehole logs.

Continuum Simulations and Material Modeling

An Eulerian hydrocode, GEODYN (Antoun et al, 2001), and a Lagrangian hydrocode, GEODYN-L (Vorobiev, 2011) were used to calculate spherical wave propagation both in 2D and 3D. The (ensemble) constitutive model employed was derived by calibrating to match peak velocities and displacements for a number of underground nuclear explosions of different magnitude in granitic rock conducted both in the US and abroad as seen in Figure 1 (Antoun et al, 2001). Figure 3 shows comparison between the Lagrangian and Eulerian calculations for SPE-2 using the ensemble model where the radial velocity history at 20 m range is plotted. The differences between these results are within a few percent and are explained by the mesh resolution around the source (for example, longer rise time for the Lagrangian results can be explained by transitioning between the meshes used for the spherical source and the region occupied by the granite) and artificial viscosity (extra oscillations after the shock observed in both 2D and 3D Lagrangian calculations).

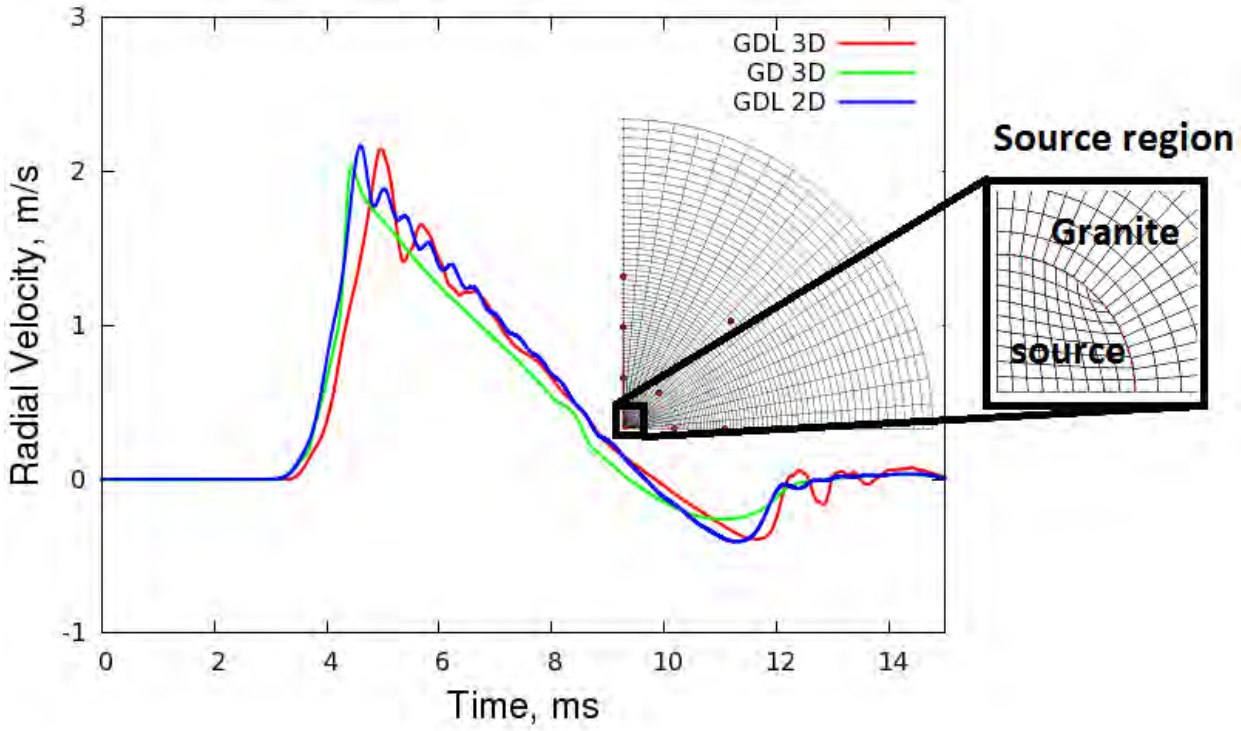


Figure 3. Comparison between 3D GEODYN calculations, 2D axisymmetric GEODYN-L and 3D GEODYN-L calculations for a spherical explosion in granite. The ensemble model was used in both codes, the yield corresponded to SPE-2 event. 2D mesh used in GEODYN-L is shown on the right with 9 cells used across the source region.

The ensemble model is an isotropic plasticity model designed for large-scale simulations. It does not use small-scale test data for calibration and assumes that any joints in the granite formation are distributed uniformly resulting in an isotropic material response. Since the model is isotropic, it cannot explain the observed variability in the data, deviations from a spherical shape and the generation of significant shear (transverse) waves from explosions. The wave motion data from SPE on the other hand exhibit significant non-radial motions, even at the 10m range, the closest gage location to the explosive source. Logging data from the instrumentation bore holes, as well as from the SPE charge emplacement hole indicate that the granite is highly fractured, with an average joint spacing of about 1ft. In addition, the logging data shows that the joints are not randomly orientated; instead four joint sets have been identified; each of which exhibiting a distinct orientation with relatively little variability.

Granite Model for Small Samples and its Extension to Large Scale

The model developed in (Vorobiev et al 2007; Vorobiev, 2008) was used to describe the constitutive behavior of the intact granite. It describes the effects of bulking, porous compaction, shear enhanced compaction, and pressure dependent yield on the material response. The yield strength function is chosen in the form

$$Y = Y_{HB} F(\beta)\left[\delta + (1-\delta)\left(\frac{P_c - \max(P_0, P^*)}{P_c - P_0}\right)^r\right] R(\dot{\varepsilon}), Y_{HB} = Y_c\left[\sqrt{s + \frac{m^2}{36} + \frac{mP^*}{Y_c}} - \frac{m}{6}\right], \qquad (1)$$

$$0 < \delta = \frac{\varepsilon_p}{\varepsilon_{p0} + \varepsilon_p} < 1, \; r > 1, P^* = P / R(\dot{\varepsilon}),$$

where β is the Lode angle, Y_c is the unconfined compressive strength, δ is a function of plastic strain describing material hardening, P_c and P_0 are history dependent variables describing a cap surface that governs porous compaction and Y_{HB} is the ultimate compressive strength. The coefficients *s* and *m* depend on the quality of the

rock as expressed by the Geological Strength Index (GSI), a rock quality index widely used by the geotechnical engineering community:

$$s = \exp\left(\frac{GSI - 100}{9}\right), \quad m = m_i \exp\left(\frac{GSI - 100}{28}\right) \qquad (2)$$

For the intact material, s=1 and the value m_i can be found from static laboratory tests on intact samples.

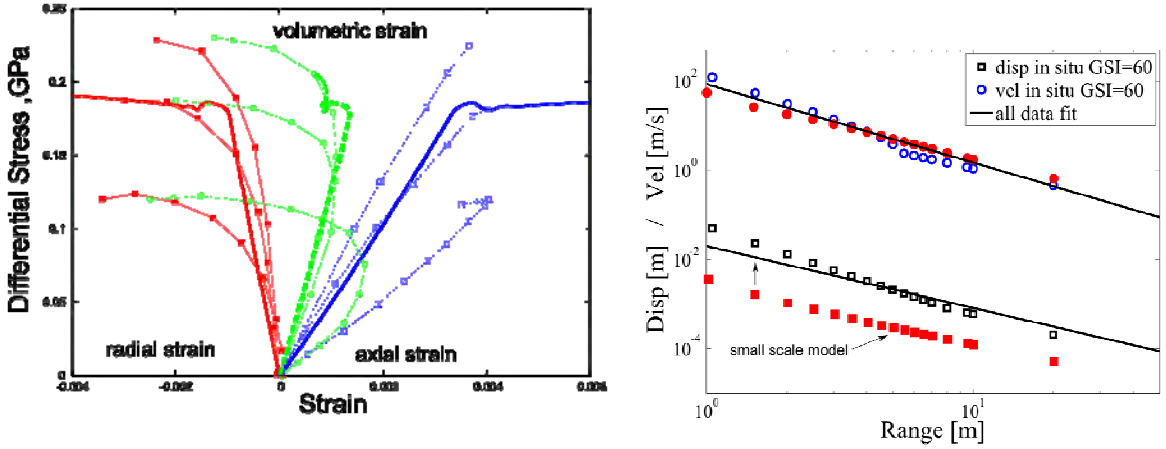


Figure 4. (a) Comparison of model fits to unconfined compressive strength test for intact granite samples from the SPE test bed. Bold lines are simulation results, and thinner lines with markers are experimental data (Broome and Pfeifle, 2011). (b) Peak displacement and velocity attenuations calculated in 1D spherical explosion using the small scale model (solid squares and circles) versus the nuclear data fit. Open squares and circles show an *in situ* model calculations

The model was calibrated to match intact granite data from the literature, as well as the unconfined compressive tests performed on the granite samples collected at the SPE-1 site (see Figure 4(a)). The model can be scaled to field scale by changing the GSI index, introducing extra porosity associated with the joints and modifying the porous compaction law. Figure 4 (b) shows, that while the small scale model does not reproduce the wave attenuation data for large scale explosions, such as SPE-1, it can be tuned to match the data by changing the GSI index, which describes the quality of rock mass. In this case, a GSI=60 was needed to match the measured displacement, which appropriately corresponds to a blocky rock with fair-to-poor surface conditions. In the mesoscale simulations described below, we used the model for intact granite, because the joints are included explicitly in the simulations.

The model account for poroelasticity in porous rocks which can be attributed to the elastic closing of the microcracks. Details of the model describing the poroelasticity implementation can be found in (Vorobiev, 2008).The initial bulk modulus is related to the reference porosity, Φ, the poroelasticity parameters, a, and the solid bulk modulus K_s , as

$$K_0 = K_s(1-\Phi)(1-a)^2, \quad K_s = -J_s \frac{\partial P_s}{\partial J_s} \qquad (3)$$

It is known from experimental observations that the joint normal closure is a non-linear function of the applied normal stress resembling a hyperbola (Bandis et al., 1983). Therefore the normal modulus of the joint, E_j , can be expressed as

$$E_j = E_{j0} \frac{u_0^{\,2}}{(u_0 - u_{max})^2}, \qquad (4)$$

where u_0 is the aperture of the joint and u_{max} is the maximum joint closure for all times. Joint special density and their initial elastic normal and shear moduli, E_{j0} and G_{j0} will define how much the bulk modulus of jointed rock material should be reduced, and thus will define the poroelasticity parameter *a*. In continuum approach we assume that the joints are distributed uniformly and material remains isotropic. Fossum (1985) derived the formula for the

average bulk modulus in a randomly jointed elastic media with compliant joints which could be used to estimate poroelasticity parameter,a, if joint density as well as joint elastic moduli are known.

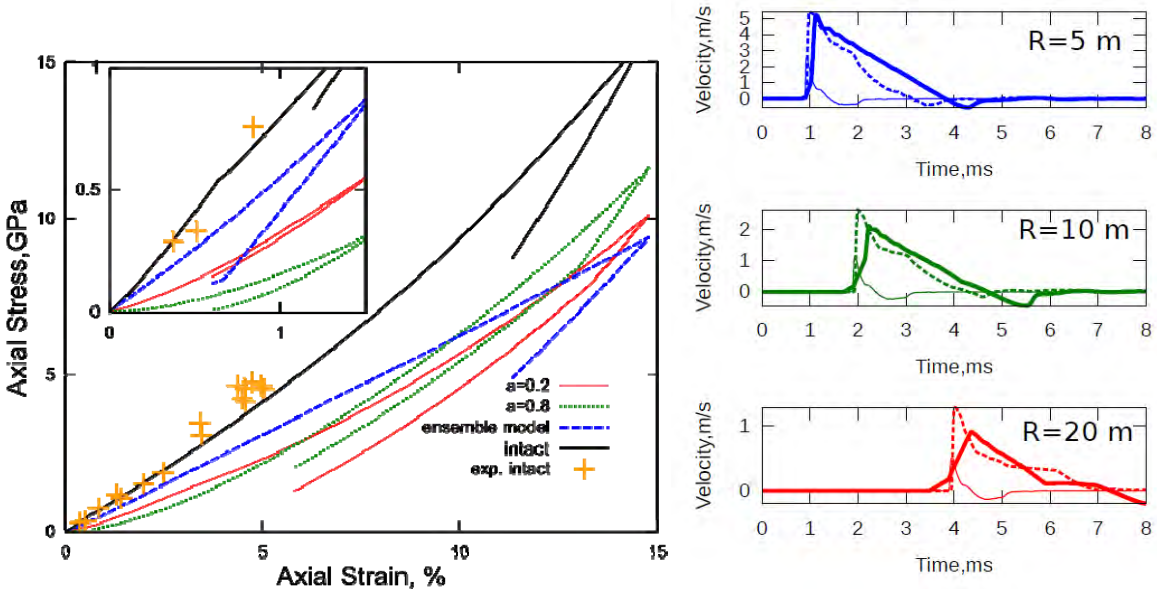


Figure 5. (a) Effect of poroelasticity parameter,a, on the stress-strain response for the insitu model. Intact model results (bold solid line) as well as the experimental data for granite samples (marker points) from the area are shown (b) Radial velocities calculated for SPE-1 test using various models: bold- ensemble model developed to fit nuclear data, thin lines-model built based on the intact samples collected from the site, dashed – continuum model built using guidance from the large scale simulations

Figure 5shows response of various granite models in a uniaxial strain compression. The intact model was calibrated using lab-scale measurements for small granite sample from the area (shown with points). To represent increased poroelasticity caused by the joints parameter, a, was increased to 0.2, also GSI scaling was applied to reduce the yield surface as described above. For the top layer, we assumed that the joint density was higher and therefore increased the poroelasticity parameter to 0.8. In the ensemble model, shown for comparison in Figure 5, a linear elastic response is assumed in the same pressure range.

Under high confinement, the cracks and joints are closed and effect of poroelasticity is reduced. Since the poroelasticity is caused by cracks and joints, *in-situ* rock mass, containing many joints should have an increased effect. Mesoscale modeling of a jointed rock (Vorobiev, 2008) showed that some features of the mechanical response of joints such as, strongly nonlinear stress-strain response in the stress range of 1-10 MPa and hysteresis in loading-unloading cyclic loading, are inherited by the rock mass. If joints are distributed nonuniformely, this may cause elastic anisotropy, because the poroelasticity associated wit the joints will work differently in various directions.

Thus, the joints present in the rock formation can cause both degradation of the effective strength as well as the reduction in the elastic wave speeds. The former is modeled using GSI strength scaling and the later is modeled by increasing the poroelasticity parameter, a. The poroelasticity will mostly effect the wave propagation in a far range where the normal stresses are not big enough to close the joints.

The extended intact granite model described above presents an alternative to the ensemble model for in-situ applications. Figure 5 (b) shows comparison between the ensemble model (bold curves) and the current model (dashed lines- GSI scaled model, thin lines- the intact granite model) for a spherical explosion. The yield was equivalent to SPE-1 explosion. It is seen from Figure 5 (b), that GSI scaled model can produce waveforms much different from the intact granite model and similar to the ensemble model.

Discrete Modeling and Joint Effects

GEODYN-L, a Lagrangian massively parallel hydrocode (Vorobiev, 2011) was used to investigate the effects of joints by modeling them as contact interfaces. In the discrete simulations, the geologic medium is represented as an assembly of intact rock blocks separated by joints and fractures. As it was shown above, the intact rock was modeled

using a constitutive model that accounts for the salient features of the response of geologic materials, and calibrated for granite using laboratory data, including data from core samples obtained from the SPE test bed. The joints were modeled as frictional interfaces with their own constitutive relations, which include governing equations for both frictional sliding along the joint surface as well as compressibility, or compliance, normal to the joint surface. The computational resources required in this case are formidable because of the large number of joints and the 3D character of the problem. Preliminary analysis done on smaller problems showed that the joint orientation and persistence play a big role in formation and attenuation of the waves.

The jointed rock formation shown in Figure 6 was is composed of parallelepiped blocks. The size of the region was 40x40x40 m centered around the source. Each block was subdiscretized by a number of elements with contacts set at the exterior faces. The properties of the contacts were varied randomly from highly frictional to weak contact (with low frictional coefficient, corresponding to the wet joint described above). This approach allowed us to describe a joint system with three main joint directions. These directions were identified from the experimental characterization of the joints at different locations.

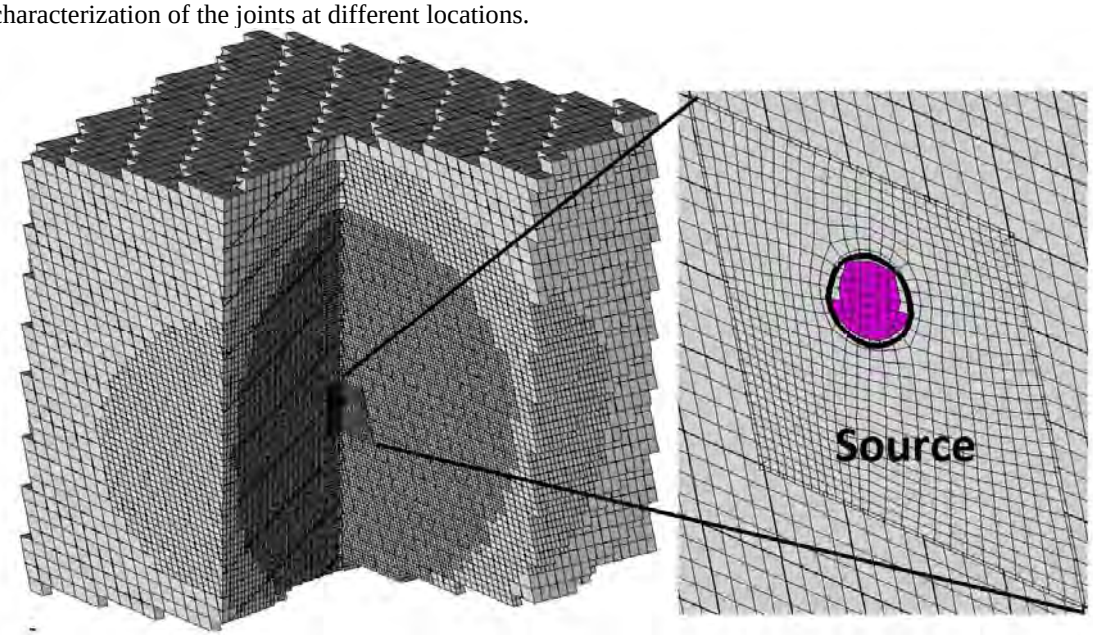


Figure 6. Computational mesh used for 3D calibration study, the source block was meshed separately (shown on the left)

By decreasing the joint persistency an anisotropic wave turns into a symmetric wave, which would be generated in an isotropic media. Figure 7 shows effect of joint persistency on the shape of the wave generated by the explosion. The radial velocity at a range of 10 m in two different azimuthal directions are shown on plot D. The plastic slip on the joints is shown on plot C. Figure 8 shows that in the case of the persistent joints more energy is flowing in the northern direction (to the left) rather than in the southern one due to wave interaction with joint Set 3 dipped at 77 degrees in south-east direction as it is shown in Figure 1. That may explain higher vertical velocity observed at the surface on the northern side. Joint stiffness is important to overall impedance of the granite mass. Figure 9 shows that the calculated arrival times could be significantly delayed if the initial joint normal stiffness is reduced by an order of magnitude. Reducing the aperture at the same initial stiffness makes the joints more non-linear. It is interesting to note that peak velocities remain the same in this case even though the time of arrival is substantially reduced. Resolving a sub millimeter aperture could be problematic with mesh resolution ~1 m in some areas. We apply an advanced semi-implicit contact algorithm described in (Vorobiev, 2011) to reduce time step control by the joints. We see that the joints can make the waveform much wider but at the same time softening the joints effects the arrival time.

Discrete calculations produce some vertical velocities at the level of the explosion, which are 10-20 times smaller than the total velocities which is at least twice smaller than observed in the experiment (shown in Figure 2)

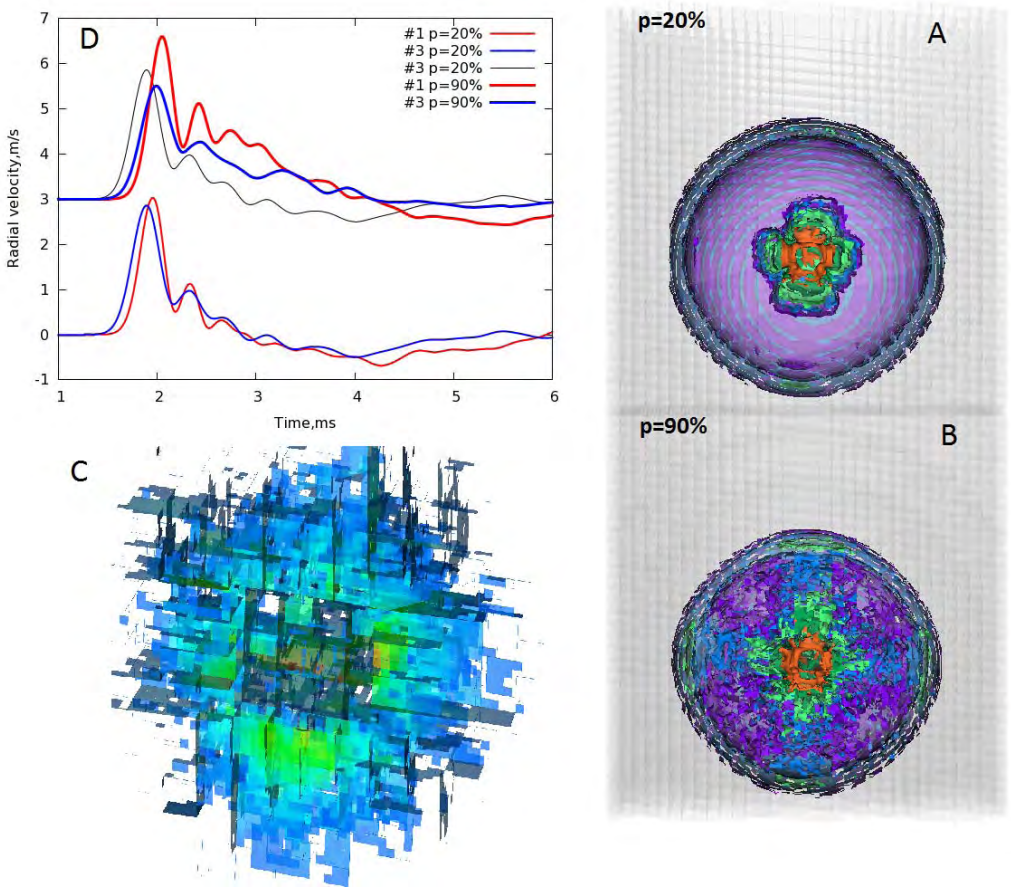


Figure 7. Effect of the joint persistency: Pressure contours (5-50 MPa) calculated for joints with different persistency (A-20%, B-90%) at time 2.6 ms, C- shear slip 0-10 mm calculated at the joint planes around the source, D- Radial velocities calculated at gauge locations #1 and #3 at the rage 10 m in different azimuthal directions.

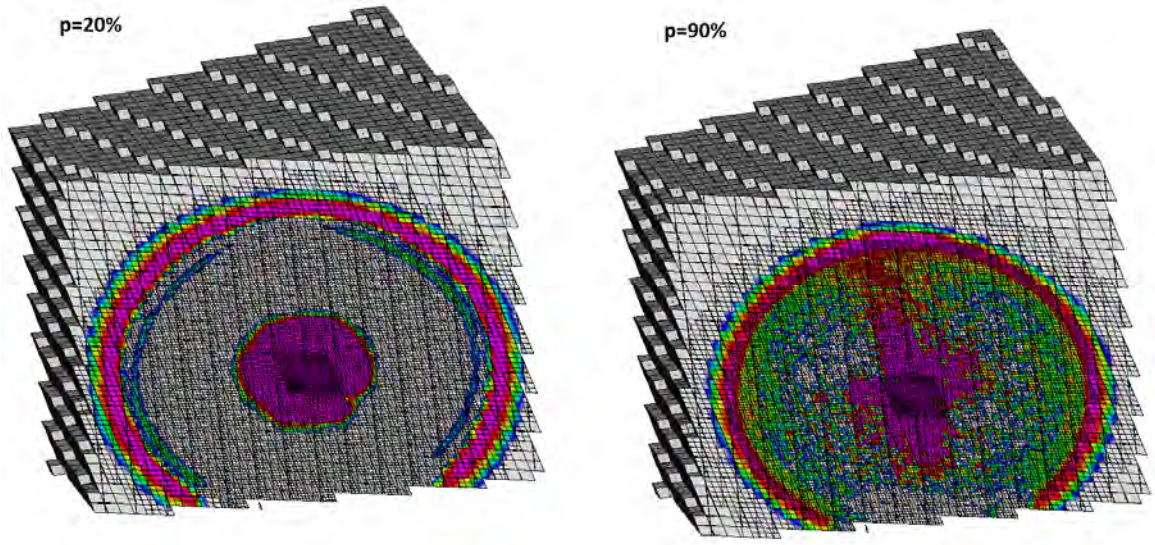


Figure 8. Cross sectional view in the eastern direction on the pressure contours (0-0.008 GPa) generated in jointed rock with different persistency (20% on the left and 90% on the right).

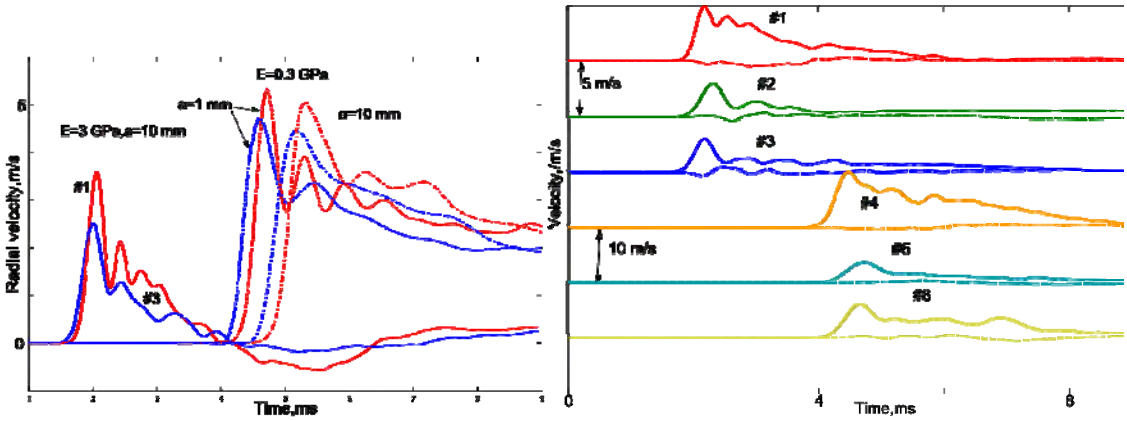


Figure 9. (a)Effect of the joint initial stiffness and aperture on the wave forms and the arrival time at 10 m range: bold lines –stiffer contacts 10 GPa, thin lines- softer contacts (b) Calculated total velocity (bold lines) and vertical velocities in discrete simulations.

Effects of Damage and Porous Compaction in Repeated Explosions

Results reported in this section are entirely based on numerical simulations for SPE-3 preshot predictions. A detailed account of these simulations is in preparation for documentation in an SPE-3 preshot predictions report.

Using the ensemble model, we perform numerical simulations for the upcoming SPE-3 explosion, which will have the same yield as SPE-2. SPE-3 will detonate at the same location as SPE-2 and the scenario suggests that the damages around the cavity induced by SPE-2 affect the outgoing waves generated by SPE-3. In the numerical implementation we first performed the calculation for the first explosion (SPE-2) and retained the nonlinear damage parameters at the end of the calculation. This damage serves as the initial condition for the second explosion simulation (SPE-3). The preliminary results of the induced damages are shown in Figure 10. In these calculations the two faults are modeled with pure slip condition. The left plot shows the damage region calculated in the first explosion (SPE-2) and the right one shows the damage calculated in the second explosion (SPE-3) displayed in a vertical cross section. It is seen that the nonlinear region calculated using the above continuum ensemble model extends slightly by the repetitive explosion. The weak top layer is 20m and the nonlinear damage is not shown here. Similar as in the SPE-2 calculations the calculations for SPE-3 are also dominated by the outgoing spherical waves and have insignificant nonspherical components. An example of the waveform comparison of the radial components calculated for SPE-2 (green) and SPE-3 (red) at depth 150ft in borehole #4 is shown in Figure 10 (b). The comparison shows that the peak velocity is slightly reduced in SPE-3 due to the damage sustained by SPE-2 and the pulse width is narrowed, indicating the peak displacement is consequently reduced. It is again noted that ensemble model used in the predictions is calibrated to the big yield events thus the porosity–related effects such as compacting and bulking, would not be significant, as expected. In such small yield events as SPE sequences the effects of the porosity compacting and bulking might be significant and their effects are being investigated by developing an adequate model and calibrating against the future SPE-3 observations.

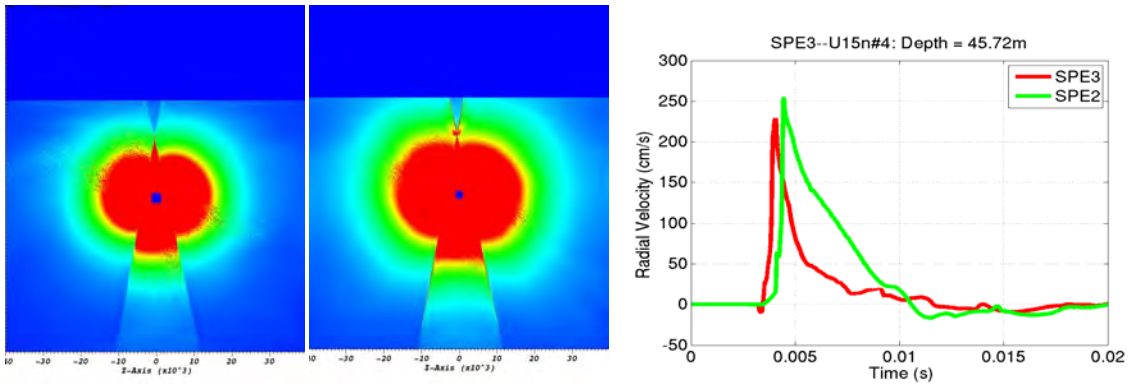


Figure 10. (a) Plastic strain generated in SPE-2 (on the left) (0-0.1%) was used as the initial condition for SPE-3 (in the middle) (b) Comparison of the waveforms predicted for SPE-2 and SPE-3 at 150ft in borehole #4 using the ensemble model (on the right)

CONCLUSIONS AND RECOMMENDATIONS

We have performed analyses of the SPE-1 and SPE-2 borehole records and observed that the vertical motions are evident at the shot depths, indicating the nonspherical characteristics of the two explosions. The simulations of SPE events have been performed to understand those characteristics using both an Eulerian and a Lagrangian hydrocodes (GEODYN and GEODYN-L). Both codes agree well with each other for the same material model.

We have used both an ensemble model, calibrated to match records from past nuclear events, as well as a new granite model calibrated for granite samples from the site, where SPE tests were conducted. The new model contains scalable parameters, which allow us to apply it both to small and the large scales. Once scaled, it produces results similar to ones obtained with the ensemble model. In contrast to the ensemble model, the new model includes new features such as effects of poroelasticity and water saturation.
We have conducted discrete modeling of the SPE events with various joints properties to investigate the effects of joints on the wave anisotropy. The parametric studies show that persistent joints sets can introduce anisotropy in the wave generation and cause tangential motions.

Preliminary simulations of repeated events (SPE-2 and SPE-3) with ensemble granite model showed that, the second explosion (SPE3) produces shorter pulses and has earlier arrival time. These response features are not surprising, especially in light of the fact that the ensemble granite model does not account for softening effects, which are of lesser importance in single explosion simulations than they may be in multiple explosion simulations. If damage-induced softening is a dominant mechanism in the SPE-3 response, the waveforms would be expected to exhibit lower peak amplitude and longer duration with a resultant increase in peak displacements, as well as slower wave speeds. Such a response, if observed, would point the way to future model improvements that account for the effect of damage and property degradation in a manner consistent with SPE near-field. More simulations are performed underway where the damage is considered along with compaction both at the joints and in the granite.

REFERENCES

Antoun, T.H., Lomov, I.N., and Glenn, L.A. (2001). Development and Application of a Strength and Damage Model for Rock under Dynamic Loading, *Proceedings of the 38th U.S. Rock Mechanics Symposium, Rock Mechanics in the National Interest*, Edited by D. Elsworth, J. Tinucci, and K. Heasley, A.A. Balkema Publishers, Lisse, The Netherlands, 369–374.

Antoun, T.H, H. Xu, O. Vorobiev, and I. Lomov (2011). Initial near field predictions of the first two source physics experiments (SPE), LLNL-TR-508474.

Bandis, S.C., Lumsden, A.C.,Barton, N.R. (1983). Fundamentals of Rock Joint Deformation. *Int. J. Rock.Mech.Min. Sci. Geomech*. Abstr. **20**(6), 249–268.

Broome, S., and T. Pfeifle (2011). Phase 1 Mechanical Testing Results on Core from Borehole U-15n, Nevada National Security Site, in Support of NCNS Source Physics Experiment, Technical Memo 6914, Sandia National Laboratories, June 8.

Fossum, A.F. (1985). Effective Elastic Properties for a Randomly Jointed Rock Mass. *Int. J. Rock. Mech. Min. Sci. Geomech*. Abstr. **226**, 467–470.

Vorobiev, O. (2008). Generic strength model for dry jointed rock masses. *Int. J. Plas.* **24**(12), 2221–2247.

Vorobiev, O. Y., Liu, B. T., Lomov, I. N., and Antoun, T. H. (2007). Simulation of penetration into porous geologic media. *International Journal of Impact Engineering*, **34**(4), 721–731.

Vorobiev, O. (2011). Simple Common Plane Contact Algorithm, *Int. J. Num. Meth.Eng.*, 243–268.

CRUSTAL VELOCITY HETEROGENEITY AND ASSESSMENT OF REGIONAL EXPLOSION DISCRIMINANTS IN NORTH-CENTRAL WYOMING: RESULTS FROM THE BIGHORNS ARCH SEISMIC EXPERIMENT (BASE)

Lindsay L. Worthington[1], Kate C. Miller[1], Hans E. Hartse[2], W. Scott Phillips[2], Steven H. Harder[3], Anne F. Sheehan[3]

Texas A&M University[1], Los Alamos National Laboratory[2], University of Texas at El Paso[3], and University of Colorado[4]

Sponsored by the Air Force Research Laboratory, the National Science Foundation, and the National Nuclear Safety Administration

Award Nos. FA9453-10-C-0214, DE-AC52-06NA25396, NSF-EAR-0843835, NSF-EAR-0843657, and NSF-EAR-0843889
Proposal No. BAA10-31

ABSTRACT

We used data from 21 seismic shots deployed as part of the Bighorn Arch Seismic Experiment (BASE) to determine P-wave velocity structure and assess regional explosion discriminants in north-central Wyoming. BASE is a multi-scale, hybrid active/passive seismic experiment designed to determine crust and mantle structure below the Bighorn Mountains. Additionally, this region experiences a spectrum of manmade and natural events, from regional earthquakes and teleseisms to mine blasts and single fire shots, making the region a compelling natural laboratory in which investigate implications for regional discrimination.

The active source component of BASE was conducted in July-August 2010 and consisted of ~1800 portable "Texan" seismometers with 4.5 Hz geophones deployed at 100-500 m spacing along two profiles: one crossing the Bighorn Arch from east to west and one traveling along-strike from north to south. The instruments recorded 21 seismic shots ranging in size from 500–2000 lbs. Additionally, four shots were recorded on a grid of passive-mode Texans that were deployed at 1 km spacing. This data coverage will enable future 3-dimensional modeling of the velocity structure in the region.

The north-south profile lies on the western flank of the arch and crosses its southern extension. The velocity model from the profile shows little structural variation. Rather, crustal velocities on this profile are laterally continuous in the upper crust, with mantle velocities (>7.8 km/s) at ~50 km depth below surface elevation. The east-west profile is sub-parallel to the direction of contraction across the mountains. Low velocities (~2.8-4.2 km/s) in the foreland basins on either side of the arch within the upper ~5-10 km correlate with known basin geometries. Low-velocity zones (~5.2 km/s) within the upper 20 km of the crust locally coincide with known and predicted large-scale fault zones. These zones provide targets for kinematic modeling and reconstruction efforts. The vertical velocity gradient increases on both profiles at ~20 km depth, which we interpret as a mid-crustal transition associated with compositional changes within the crust. Above this mid-crustal transition, the east-west profile shows thickening of the upper crust under the arch culmination.

Crustal thickness across the arch, constrained by PmP and Pn phase arrivals on the E-W profile, varies between ~45 km and ~50 km. The modeled Moho topography shows no major offsets and only minor deflections directly below the arch. The absence of large scale offsets of the Moho and the evidence for upper crustal thickening favors arch formation by crustal detachment, consistent with structural modeling suggesting listric thrusting on a west-dipping master fault that flattens at ~30 km depth. Integration with passive source results from BASE, including receiver function analysis and 3D tomography will further constrain upper mantle structure and three-dimensional Moho topography in the region. The detailed velocity models can also be used to investigate the degree of spatial sampling of the seismic wavefield needed to characterize 3D wave propagation effects.

Using the single-charge explosions from the BASE experiment, about 65 coal-mining explosions from the Powder River Basin, about 10 mining explosions from the Bighorn Basin, and around 40 earthquakes we tested seismic discriminants using USARRAY broadband data and data recorded at station RSSD. In total, we used about 20 stations that had recorded events at local to near-regional distances. An amplitude ratio of Pg (6–12 Hz) versus Lg (6–12 Hz) mostly separated the earthquakes from the explosions. Lg spectral ratios also separated the explosions from the earthquakes, but not as well as the Pg/Lg ratio. A few earthquakes from the geothermal regions of Yellowstone Park are lacking high frequencies, and depending on the discriminant, can appear explosion-like. We continue to test discriminants which may separate the delay-fired mining explosions from the single-charge explosions.

OBJECTIVES

The primary objective for this work is ultimately to quantify the degree of regionalization and instrumentation necessary for successful discrimination in a tectonically complex region. This result will provide a basis for assessing regional discrimination performance in areas with comparatively sparse data sets. During a May-December 2010 field season, we collected a large and diverse seismic data set in north-central Wyoming. The work we present here can be divided into two studies:

1. An analysis of two active-source wide-angle reflection and refraction profiles across the Bighorn Mountains and the Bighorn and Powder River Basins (Figure 1). We have developed compressional wave velocity models through a series of tomographic inversions.
2. A preliminary event identification study using earthquakes, single-charge chemical explosion from the active-source profiles, and mining explosions recorded at local to near-regional distances (Figure 2).

The work for this contract is integrated with the Bighorns Arch Seismic Experiment (BASE), a project sponsored by the National Science Foundation EarthScope program. The focus of BASE is imaging the deep structure of basement-cored arches in order to understand the mechanisms of the formation of the Rocky Mountains. Other BASE science goals are focused on the nature of faults at depth in the crust and deep crustal rheology. In addition to producing velocity models of the crust and upper mantle, the seismic imaging experiment will determine whether faults at depth remain discrete or if they diffuse into a broader zone of ductile deformation.

RESEARCH ACCOMPLISHED

Active Source Experiment

Data

The active source component of BASE consisted of two profiles. BASE01 extended ~300 km west to east (Figure 1), crossing the Bighorn Basin, the Bighorn Arch and the Powder River Basin. Data for this profile was recorded by ~1300 Reftek RT125 (Texan) seismographs with vertical-component 4.5 Hz geophones deployed at 500 m spacing within the basins. For a 100 km-long section in the mountains, receiver interval spacing along the profile was decreased to 100 m in order to improve imaging of near-vertical incidence arrivals. BASE02 traveled north to south (Figure 1), sub-parallel to the arch, for ~250 km on the western flank of the Bighorn Mountains. This profile included ~500 Texans deployed at 500 m spacing. Data from 21 single-fired shots, ranging in size between 500-2000 lbs, were recorded by the Texans across both profiles, contributing to three-dimensional coverage across the region. For this paper, we restrict our analysis to a two-dimensional inversion scheme, using data from 15 inline shots along BASE01 (Figures 2-4) and 6 inline shots along BASE02 (Figures 5-6). The dominant energy in the shots ranged between 8-20 Hz.

For interpretation, the active source record sections were filtered between 2-18 Hz. Figures 2-4 show representative shot gathers from the western and central portions of the BASE01 profile with interpreted arrivals for several phases. SP 103 (Figure 2) is located at the western end of the profile. Refracted waves traveling through the basin sediments and the crust (Pg; blue) are the first arrivals at offsets up to ~150 km. Refractions from the base of the crust (Pn; magenta) arrive first at offets >~150 km. We also observe reflected energy from the crust-mantle boundary (PmP; red). SP111 (Figure 3) is located within the Bighorn Arch. The dense instrument spacing of 100 m across within the Arch allowed for interpretation of near-vertical incidence Moho reflections (PmP; red). SP 114 (Figure 4) is located ~20 km east of the Bighorn Arch. Here, we observe the PmP phase (red) at near-vertical offsets. The darker section in the middle of each record section denotes the portion of the profile in which we decreased instrument spacing from 500 m within the arch- bounding basins to 100 m across the Bighorn Arch. The lower portion of Figures 2-4 shows sample ray paths through the velocity model associated with the travel time data. Data from 15 seismic shots across the BASE01 profile contribute > 9000 travel time picks to the inversion.

Some difficulty in the correct identification of secondary phases within the shot gathers arises for two primary reasons: complicated velocity structure within the lower crust and local, shallow structure such as near-surface faults or basin edges. To assist in the process of phase identification, we conducted a series of forward modeling tests. These models were constructed using velocities from initial first-arrival models. We raytraced through these starting models using both the shortest path method utilized by van Avendonk et al. (2004) and the MacRay software program (Luetgert, 1992). After raytracing through the models, we compared the resulting calculated and observed

travel time curves to the data gathers. An important element in this analysis was making sure that our picks for these secondary phases were consistent across multiple data gathers. We adjusted our travel time picks where appropriate based on these comparisons.

Figures 5 and 6 show representative shot gathers from the southern and northern parts of the BASE02 profile with interpreted arrivals for crustal refractions (Pg) and Moho reflections (PmP). SP 201 (Figure 5) is located at the southern extent of the profile; SP208 (Figure 6) is the northern most shotpoint. The lower portion of Figures 5-6 shows sample ray paths through the velocity model associated with the travel time data. Data from six seismic shots across the BASE02 profile contribute ~3000 travel time picks.

Methods

Figures 7 and 8 show the current 2D velocity model across the BASE01 and BASE02 profiles. By using both first-arriving and later phases from the travel time data in a joint inversion, we can simultaneously constrain seismic velocities and layer boundaries. The resulting seismic velocity models are constructed through a series of linearized tomographic inversions of travel time data following the general method of van Avendonk et al. (2004): for each iteration, we trace rays in the current velocity model using the shortest path method and ray-bending (Moser et al., 1992; van Avendonk et al., 2001) to develop a set of calculated raypaths and travel times. Subsequently, we invert for an update to the current velocity model using the difference between picked and calculated travel times. In each inversion, we tune the strength of smoothness constraints. The updated velocity model becomes the starting model for the next iteration of ray-tracing and inversion until a normalized data misfit, χ^2, of ~1 is achieved (van Avendonk et al., 2004).

The root-mean-square error for the current BASE01 model is 150 ms, with a χ^2 error of 1.4. The bottom part of the Figure 7 shows total ray coverage across the model. Dense ray coverage in upper 10 km of model constrains basin structure and upper crustal velocities. Modeled Moho reflections (PmP) and refractions (Pn) arrivals constrain lower crustal velocity and Moho depth beneath the Bighorn Arch and at ~80-125 km offset on either side of the Arch.

Figure 9 compares travel time curves for our data picks (solid) with the calculated arrivals for crustal refractions (top) and for the secondary arrivals, PmP and Pn (bottom), through the model for the east-west profile (BASE01).

The BASE02 model (Figure 8) has a root-mean-square error of 225 ms and a χ^2 of 2.3. Modeling across this line is currently in progress. We are continuing modeling along this profile to better fit PmP arrivals. This further modeling will likely result in a shallower Moho than what is shown here, especially in the southern portion of the line. Crustal velocities are laterally continuous in the upper crust (Figure 8).

Results

The BASE01 velocity model includes three layers: basins, crust, and mantle. In the lower crust, the vertical velocity gradient increases slightly at ~25 km depth below the Bighorn Basin. Above this mid-crustal transition, the profile shows thickening of the upper crust from west to east under the arch culmination. Velocities within the lower crust generally increase from west to east. The modeled Moho is relatively flat across the eastern 200 km of the profile, ranging between ~39-37 km depth. There is a slight upward deflection of ~2 km below the arch. The Moho appears to dip slightly eastward beneath the Powder River Basin, reaching a maximum depth of ~46 km (see Figure 7).

Low velocities (~2.8-4.2 km/s) in the basins on either side of the arch within the upper ~5-10 km correlate with known basin geometries. Top of Tensleep Formation (white line) approximates the top of basement (Blackstone, 1993). The lower crust shows low-velocity zones (~5.2 km/s) within the upper 20 km that may partially coincide with known and predicted large-scale fault zones. These zones will provide targets for future kinematic modeling and reconstruction efforts.

Discrimination Study

Data

For our discrimination study, station and source locations are shown in Figure 10. We used data from about 20 broadband US-array stations, and station RSSD located on the edge of the Black Hills. We selected earthquakes based on event time-of-day from a region slightly broader than the BASE profile lines. Origin times are from National Earthquake Information Center (NEIC) bulletins, the Reviewed Event Bulletin (REB), and the Array Network Facility (ANF) bulletin (http://anf.ucsd.edu/). We assumed night time events (between 7 pm and 7 am local

time) are earthquakes. We selected day time earthquakes from areas where a mix of night and day events occur, assuming these were areas of natural seismicity. In total, we selected about 40 earthquakes recorded from early 2009 to mid-2010. Magnitudes were not reported for many of the smaller earthquakes, but for events with reported magnitudes, sizes ranged from near 1.5 to near 4.0. Event-station distances range from a few km to nearly 500 km.

There are hundreds of coal mining explosions east of the Bighorn Mountains in the Powder River Basin (PRB). We selected about 50 PRB coal mining explosions where (1) we had obtained ground truth information from mine operators and (2) the events were also listed in seismic bulletins. Based on day-time event locations, we identified mining regions in the Bighorn Basin where bentonite and limestone quarrying is active, and we selected about 12 of these explosions for our discrimination analysis. Of course, we also used the ground truth events from the BASE single-charge explosions.

Methods

We measured Pg and Lg RMS amplitudes on vertical displacement seismograms over several frequency bands between 0.5 Hz and 16 Hz. See Hartse et al. (1997) for a basic description of our measurement methodology. Prior to phase amplitude measurement, when no P-arrival was reported at a given station, we picked first-P on the seismogram whenever possible. For seismograms where unfavorable S/N obscured first-P, we did not make amplitude measurements. Our amplitude measurement windows ranged from 5.9 to 5.0 km/s for Pg and 3.6 to 3.0 km/s for Lg.

Following measurements of all event types, we estimated linear amplitude-distance correction parameters using earthquake data at each station, and then applied the corrections to all event types where signal amplitude exceeded pre-event noise amplitude by at least 1.75. We then experimented with Pg and Lg spectral ratios and Pg/Lg phase ratios at each station, averaging results from all stations to generate final discrimination plots.

Results

Promising discrimination results are shown in Figures 11 and 12. The high-frequency Pg/Lg ratio (Figure 11) separates the explosions from the earthquakes. The most interesting event appears as an earthquake at the top of Figure 12, the Lg spectral ratio plot. This earthquake plots above the explosions and is almost devoid of high frequencies. This event is from Yellowstone Park, probably with a shallow focus from a geyser basin.

CONCLUSIONS AND RECOMMENDATIONS

One important question we can derive from our current results is how crustal structure changes across the broader region of northern Wyoming. Previous investigations of crustal structure in the area include the Deep Probe seismic profile immediately to the west of our study area (Snelson et al., 1998) (Figure 1). Using a combination of gravity data, well log data and seismic data from three lithospheric shots, Snelson et al. (1998) calculated a crustal velocity model that features Moho depths of > 50 km and a 20 km-thick high-velocity (>7 km/s) layer at the base of the crust. Our velocity model does not extend as far west as Cody, but does give us velocity control east of Cody in the Bighorn Basin. Our current model predicts a Moho depth <40 km within the Bighorn Basin. Addtionally, our model does not include a high-velocity 7.xx layer in the lower crust. However, current results from receiver function analysis as part of the passive component of BASE correspond well with the Moho depths presented here. These results also show that crustal thickness increases fairly rapidly between the Bighorn Basin and Cody (Yeck et al., 2011).

We have investigated the apparent discrepancy between the BASE and Deep Probe models by comparing travel time data from the Deep Probe experiment to the Bighorns data. First arrivals on Deep Probe shotpoint 49 show a distinct change in slope of the first arriving phases at offsets >180 km, indicating a change in velocity from 6.7 km/s to 7.1 km/s in the lower crust (Figure 13). The travel-time curve from Bighorns shotpoint 114 displays no such feature, indicating that the crust maintains an apparent velocity between 6.7-6.8 km/s in the lower crust (Figure 13). The emerging discrepancy between the Deep Probe results and the current Bighorns model leads to some important questions regarding the regional structure of the lower crust in northern Wyoming. Namely, how does the 7.xx layer pinch out beneath the Bighorn Basin, directly east of the Deep Probe model?

Future seismic and gravity modeling across BASE01, including further integration with passive seismic results, will be targeted towards addressing this apparent discrepancy. We are currently constructing a gravity model that will connect the BASE01 profile to the Deep Probe study area. The gravity modeling will be specifically targeted to

investigate changes within the lower crustal structure across the Bighorn Basin and into the Arch. We are also working to integrate our velocity models with results from receiver function analysis. Depth to Moho derived from common-conversion point stacking using short-period data across the profile is consistent with the results from inversion of the active source data.

For event identification, we can separate explosions from earthquakes, but we have not found a reliable method to separate the single-charge BASE explosions from the relatively uncontained, delay-fired mining explosions. We have begun experimenting with techniques to detect and measure Rg amplitudes, and we are beginning to experiment with coda amplitudes as possible discriminants that can separate single-charge from mining explosions. We also plan to apply magnitude and distance corrections (MDAC) to our discrimination data set, but first we must estimate moment magnitudes and derive appropriate attenuation models.

ACKNOWLEDGEMENTS

We thank the National Science Foundation, IRIS, the PASSCAL instrument center, Bighorns National Forest, Bureau of Land Management, and private landowners for their support. We gratefully acknowledge the efforts of our logistics team including Galen Kaip, Victor Avila, Michelle Kuhn and Melissa Dozier for their efforts in the field. We also thank all the student volunteers from across the country that helped deploy seismometers.

Seismic instruments were provided through the USArray Flexible Array, a pool of instruments available through the National Science Foundation EarthScope program that is housed at the PASSCAL Instrument Center of the Incorporated Research Institutions for Seismology (IRIS) at the New Mexico Institute for Mining and Technology. Data will be archived and available through the IRIS Data Management Center.

REFERENCES

Blackstone, D.L. (199) Precambrian basement map of Wyoming: Outcrop and structural configuration, in: Schmidt, C.J., Chase, R., and Erslev, E.A., eds., Laramide basement deformation in the Rocky Mountain foreland of the western United States, *Geol. Soc. Am. Special Paper* **280,** 335–337.

Hartse, H.E., S.R. Taylor, W.S. Phillips, and G.E. Randall (1997). A preliminary study of regional seismic discrimination in central Asia with emphasis on western China, *Bull. Seismol. Soc. Am.* **87**, 551–568.

Luetgert, J.H. (1992). MacRay: Interactive two-dimensional seismic raytracing for the Macintosh, *U.S. Geological Survey Open-File Report* 92-356, 1–2

Moser, T. J., G. Nolet, and R. Snieder (1992). Ray bending revisited, *Bull. Seismol. Soc. Am.* **82**(1), 259–288.

Snelson, C.M., et al. (1998). Crustal and uppermost mantle structure along the Deep Probe seismic profile, *Rocky Mountain Geology* **33**(2), 181–198

Van Avendonk, H. J. A., A. J. Harding, J. A. Orcutt, and W. S. Holbrook (2001). Hybrid shortest path and ray bending method for traveltime and raypath calculations, *Geophysics*, **66**(2), 648-653.

Van Avendonk, H. J. A., Shillington, D. J., Holbrook, W. S., and Hornbach M. J. (2004). Inferring crustal structure in the Aleutian arc from a sparse wide-angle seismic data set, *Geochem. Geophys. Geosyst.* **5**, doi:10.1029/2003GC000664.

Yeck, W.L., Sheehan, A.F., Schulte-Pelkum, V., Yang, Z., Anderson, M.L., Erslev, E.A. (2011). Bighorn Arch Seismic Experiment (BASE) crustal thickness: results from two layer teleseismic receiver function H-K stacking, Abstract S51C-2239 presented at 2011 Fall Meeting, AGU, San Francisco, CA, 5-9 Dec.

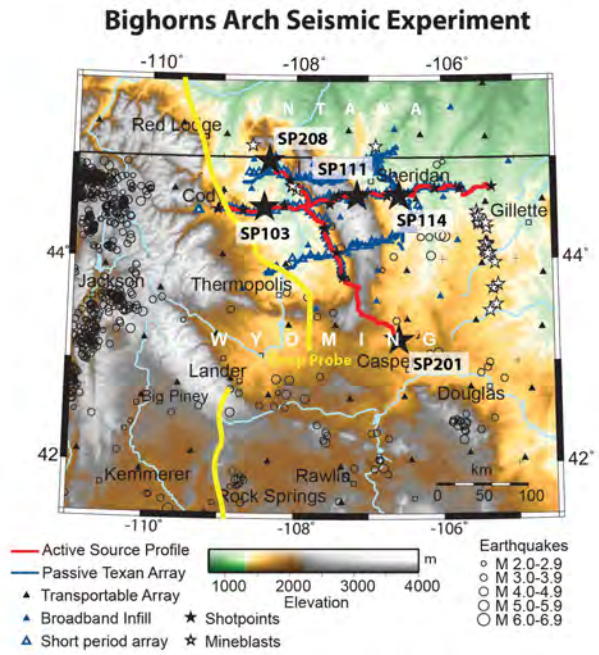


Figure 1. Topographic map of north-central Wyoming showing the experiment geometry for the Bighorn Arch Seismic Experiment (BASE). Active source profiles in red. Single-fire shots (black stars) of 250 to 2000 lbs of emulsion blasting agent were fired into ~1800 Texans deployed along two profiles at intervals of 100 m to 1000 m.

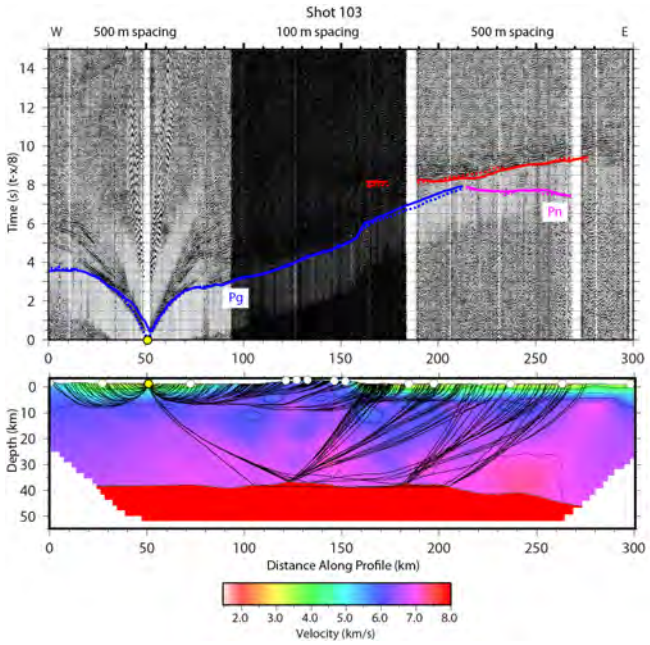


Figure 2. Shot record section shot point 103, in the Bighorn Basin. Solid lines mark arrivals for crustal refractions (blue), Moho reflections (red) and Moho refractions (magenta). Dashed lines are calculated travel times through the model, corresponding rays shown in bottom part of figure.

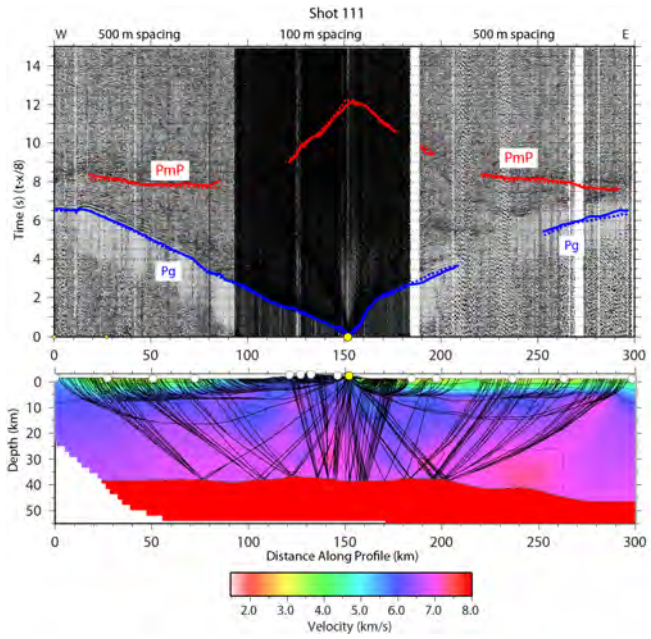


Figure 3. Shot record section shot point 111, in the Bighorn Arch. Solid lines mark arrivals for crustal refractions (blue) and Moho reflections (red). Dashed lines are calculated travel times through the model, corresponding rays shown in bottom part of figure.

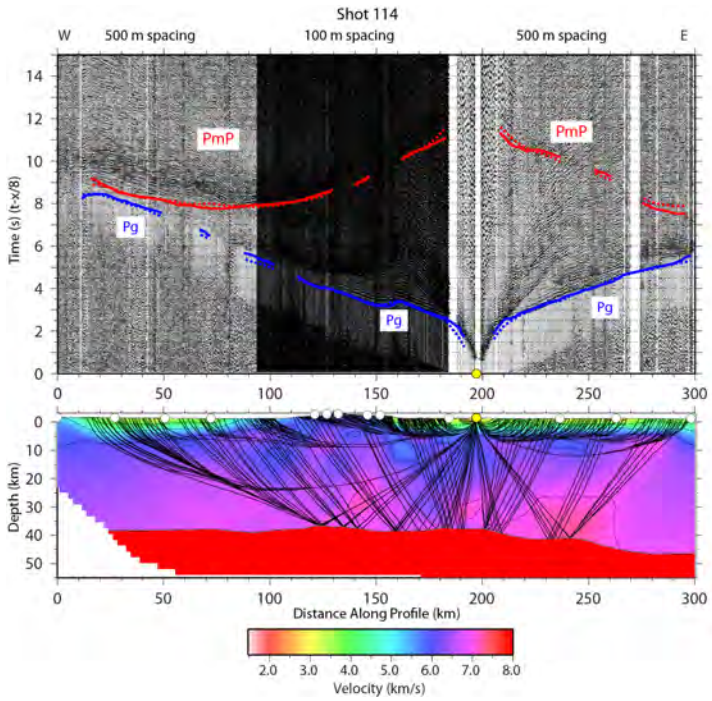


Figure 4. Shot record section shot point 114, in the Powder River Basin on BASE01. Solid lines are arrivals for crustal refractions (blue) and Moho reflections (red). Dashed lines are calculated travel times through the model, corresponding raypaths are shown in the bottom portion of the figure.

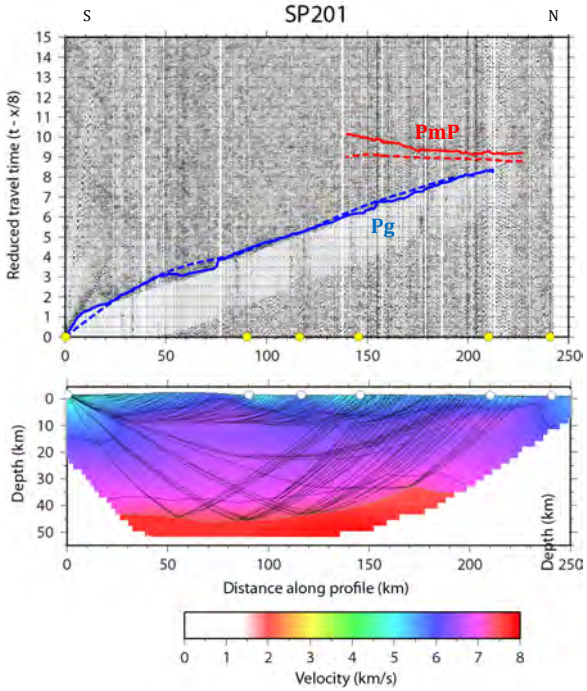


Figure 5. Shot record section shot point 201, the southernmost shot on the N-S profile, BASE02. Solid lines are arrivals for crustal refractions (blue) and Moho reflections (red). Dashed lines are calculated travel times through the model, corresponding raypaths are shown in the bottom portion of the figure.

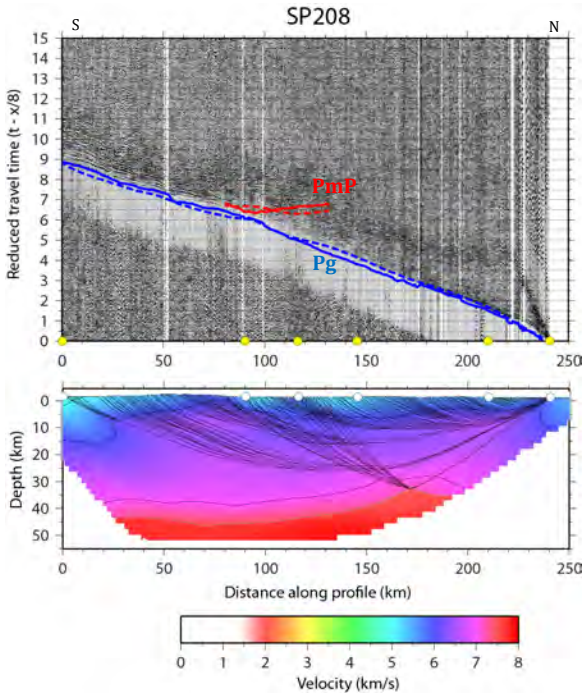


Figure 6. Shot record section shot point 208, the northernmost shot on the N-S profile, BASE02. Solid lines are arrivals for crustal refractions (blue) and Moho reflections (red). Dashed lines are calculated travel times through the model, corresponding raypaths are shown in the bottom portion of the figure.

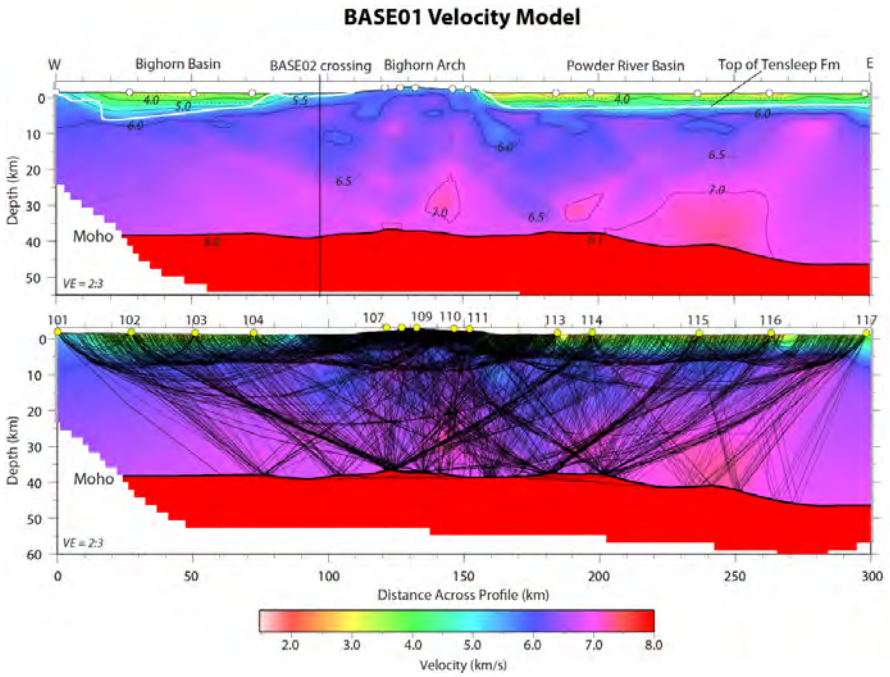


Figure 7. Velocity model along BASE01, the east-west profile; shown with calculated raypaths (bottom). Shotpoint locations are white circles. Contour interval = 0.5 km/s.

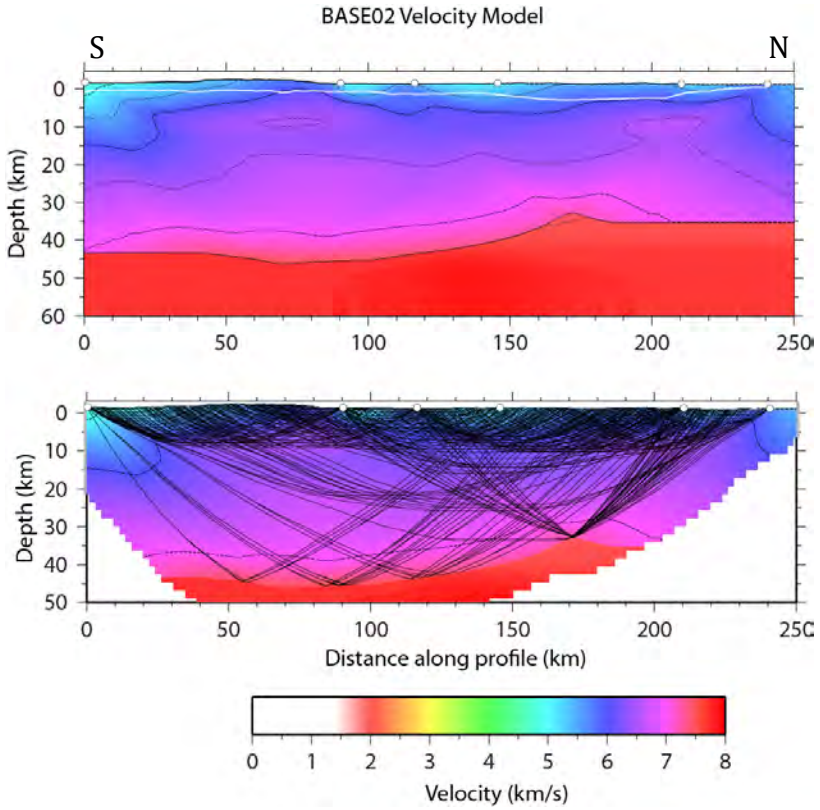


Figure 8. Velocity model along BASE02, the north-south profile (top); shown with calculated raypaths (bottom). Shotpoint locations are white circles. Contour interval = 1.0 km/s.

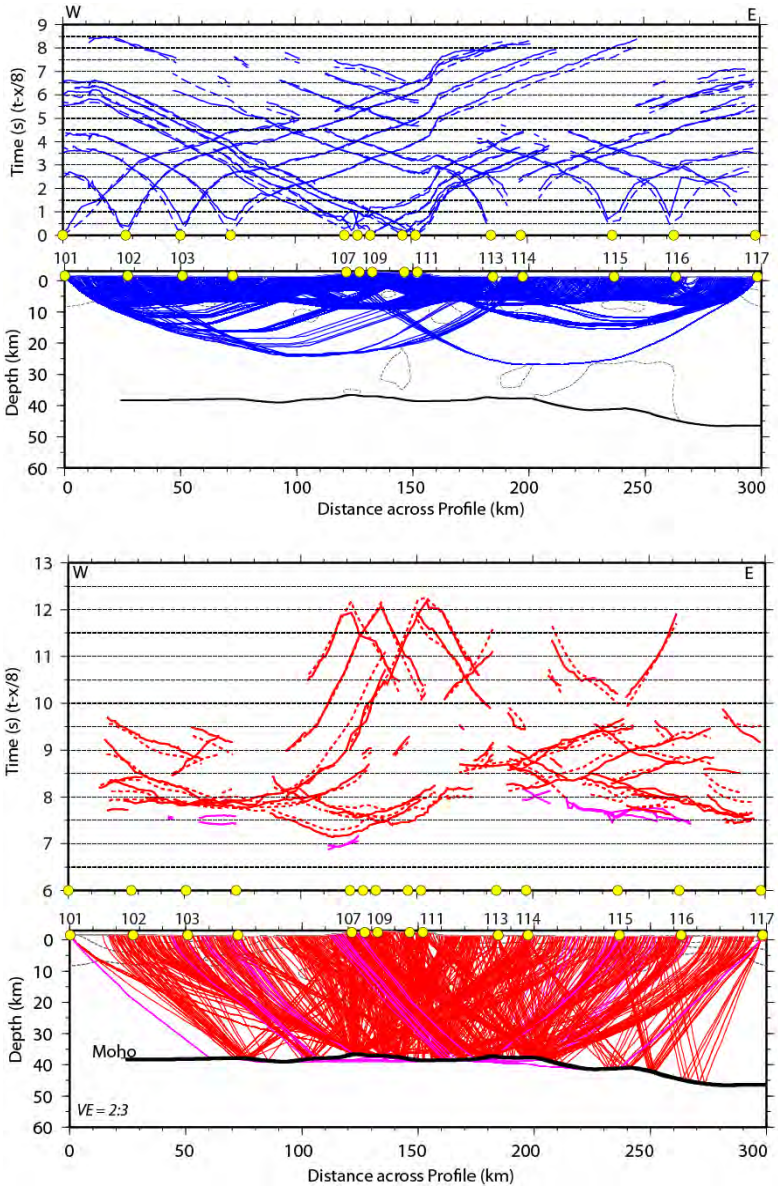


Figure 9. Top: Picked (solid) and calculated (dashed) travel time curves for BASE 01 for crustal refractions (Pg). Bottom: Picked (solid) and calculated (dashed) travel time curves for BASE 01 for Moho reflections (PmP) and Moho refractions (Pn).

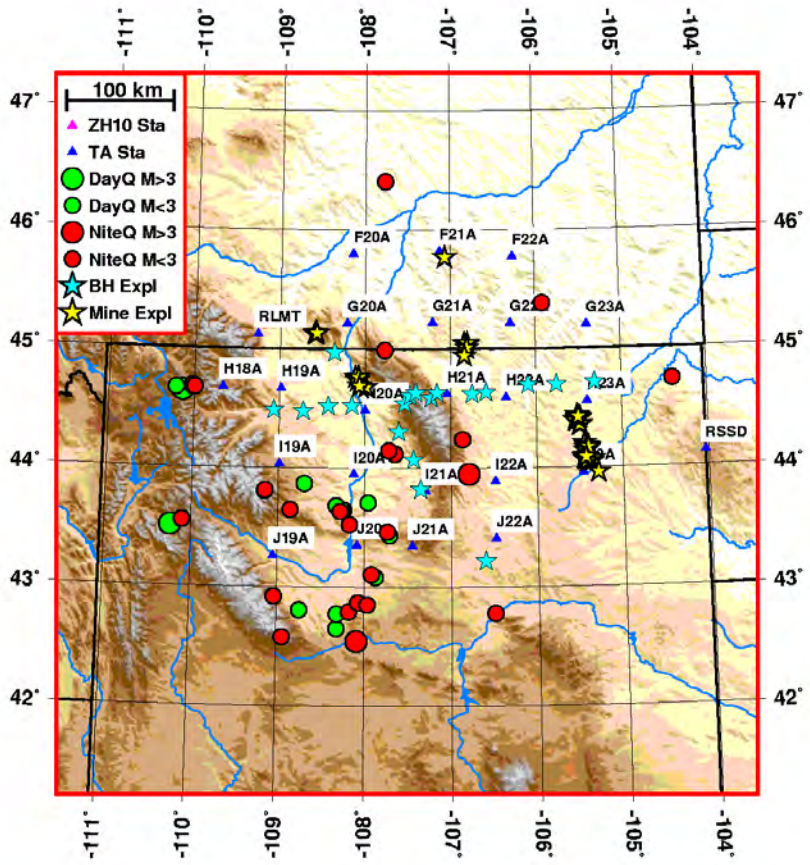


Figure 10. Discrimination study map showing stations and events.

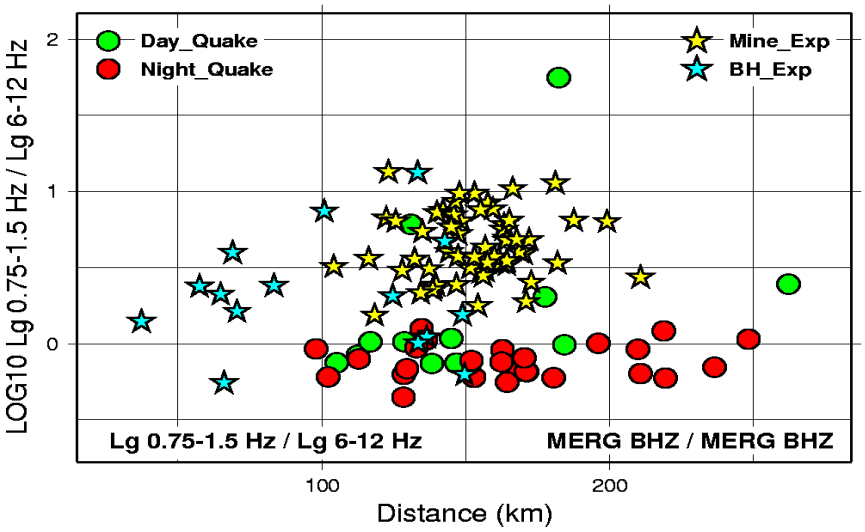


Figure 11. High-frequency Pg/Lg discrimination plot. Ratios have been averaged over all stations, and a linear distance correction has been applied at each station prior to averaging. No magnitude and distance corrections (MDAC) have been applied because we currently lack moment magnitude values for each event, and we lack detailed attenuation models for the region.

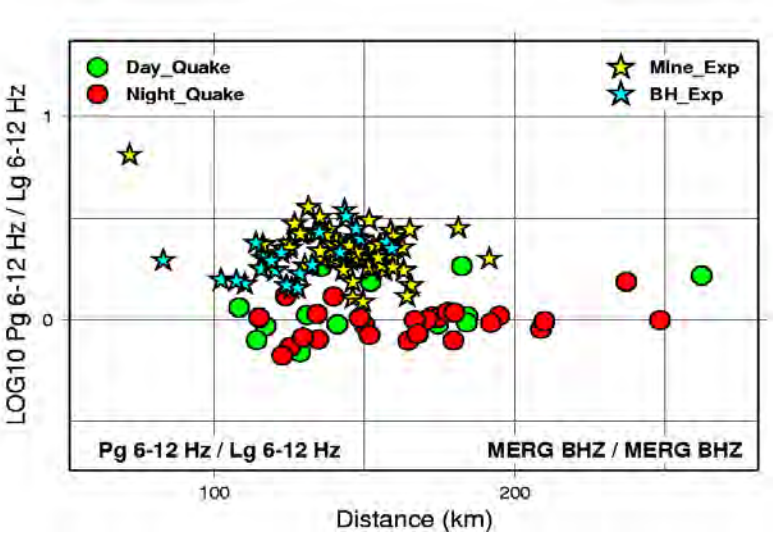


Figure 12. Lg spectral ratio discrimination plot. The earthquake plotting above the explosions is from the geyser region of Yellowstone Park and appears to lack high frequencies.

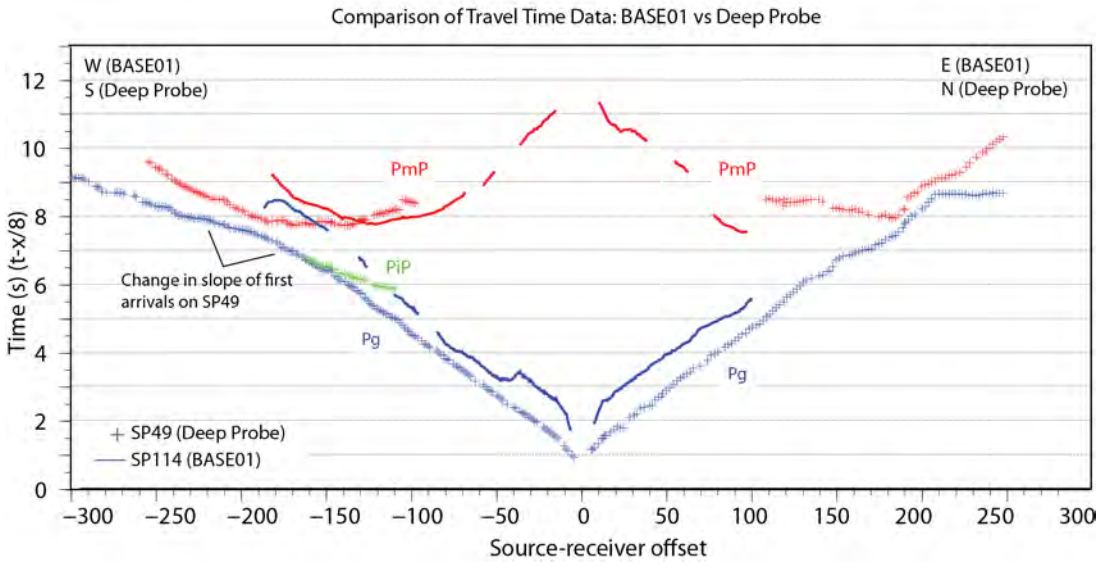


Figure 13. Comparison of travel time curves from BASE01 shotpoint 114 and the adjacent Deep Probe experiment shotpoint 49 (Snelson et al., 1998) through the Bighorn Basin. BASE01 profile is oriented east-west; Deep Probe profile is oriented north-south (see Figure 1). Pg = crustal refractions; PiP = 7.xx reflections; PmP = Moho reflections.

Seismic Event Detection and Location

ANALYST EVALUATION OF MODEL-BASED BAYESIAN SEISMIC MONITORING AT THE CTBTO

Nimar S. Arora[1], Jeffrey Given[2], Elena Tomuta[2], Stuart Russell[1,3], Spiro Spiliopoulos[2]

Bayesian Logic, Inc.[1], the Comprehensive Nuclear-Test-Ban Treaty Organiztion[2], and
the University of California at Berkeley[3]

Sponsored by the Comprehensive Nuclear-Test-Ban Treaty Organization

ABSTRACT

NET-VISA (NETwork processing Vertically Integrated Seismic Analysis) is a generative probabilistic model of global-scale seismology and an inference algorithm which deduces the seismic bulletin with the highest posterior probability given all the seismic detections (aka arrivals or triggers) and misdetections observed by a network of stations. It has been developed to potentially succeed the current automatic association tool – GA (Global Association). Early testing has already demonstrated that this probabilistic approach to treaty monitoring is able to find weak seismic events that were either mislocated or missed entirely by GA. In this research, we provide analyst verification of these early results.

Our general approach is to run GA and NET-VISA in parallel, on the same set of detections, all the way through to analyst evaluation and to compare the quality of the final products. Currently, the final GA bulletin SEL3 is the basis for the analyst-produced bulletin LEB. In parallel, we are now producing a new NET-VISA bulletin named VISA which is the basis for an analyst-produced bulletin LEB_VISA. We have compared the two LEB bulletins in terms of the number of events that they contain and the number that satisfy the REB (Reviewed Event Bulletin) criteria. We restrict our comparison to only the events that the analysts created from the underlying automatic bulletin, i.e., no manually added events were considered. This restriction together with the fact that the same analyst worked on any given time interval in either bulletins helps ensure that we are not measuring analyst skill.

Our experiments indicate that NET-VISA finds roughly 20% more events than GA. Of the events found by both NET-VISA and GA, NET-VISA associates on average two additional stations per event. With more associated stations and with a probabilistic model which accounts for misdetections and detection amplitudes, the locations determined by NET-VISA tend to be much closer to the final event locations after analyst review than those found by GA.

OBJECTIVES

The purpose of this study is to evaluate NET-VISA for routine operational use at the International Data Centre of the CTBTO. Towards this end, IDC analysts were asked to review an event list produced by NET-VISA in addition to the normal GA event list for each time slot allotted to them over a period of one week. We report here the subjective feedback of the analysts as well as the empirical analysis of the resulting analyst-reviewed bulletins.

This work builds on an earlier evaluation of NET-VISA (Le Bras et al., 2011) that compared the event in the NET-VISA event list directly with the events in the automatically-generated Third Standard Event List (SEL3) and the analyst-reviewed Late Event Bulletin (LEB).

RESEARCH ACCOMPLISHED

Background

NET-VISA (Arora, 2012, Arora and Russell, 2012) is designed to address the network processing problem in seismology, i.e. it deduces the set of seismic events given the set of detections on a network of stations. The general approach is to build a generative probabilistic model of global-scale seismology and to use this model to infer the set of seismic events which have highest posterior probability given the observed detections and misdetections.

Our approach differs in various aspects from the analysis currently in operations at the IDC, which processes the data in stages. In the IDC processing pipeline, detected signals from a single station are examined first to determine an initial phase label (e.g. Pn, P, Lg). Next, the detections from the entire network are clustered together to form events based on consistency in their arrival time, azimuth, slowness, amplitude, and phase label. During this stage, the phase labels may be modified according to limited transformation rules. The locations of these events are computed using the time, azimuth, and slowness of the associated detections and the assigned phase labels. Further attributes of the event like magnitude are then computed from the amplitude measurements. Finally, other global measures as well as other detection attributes like SNR are examined using simple heuristics to determine event quality, and then a decision is made to either keep the event or discard it.

In contrast, our approach incorporates all aspects of this pipeline into a single vertically integrated generative model. The inference in our approach uses all the attributes of the detections – time, azimuth, slowness, amplitude, signal-to-noise ratio—as well as all the misdetections to identify the events. The phase labels can be freely modified in order to associate detections with an event. Finally, the decision to keep or discard an event is based solely on the probability of the world where the event exists and the alternate world without the event.

The generative model consists of multiple subcomponents that are combined together by the independence and conditional independence assumptions in the model. The various subcomponents are:

- A distribution of possible event locations that is learned from the historical distribution of seismicity plus a uniform distribution to allow for explosions anywhere on the earth.
- The Gutenberg-Richter distribution of event magnitude.
- A station- and phase-specific detection probability that depends entirely on the event magnitude, depth, and distance to station. The probability model (logistic regression with local input features) is calibrated from historical data that record which events were detected by which stations.
- For each detection, the following predictive distributions over attributes of the detection:
    - A distribution for the measured arrival time given the predicted arrival time for the true phase from the event location to the station. NET-VISA currently uses the 1-D model iasp91 with station-specific corrections, i.e., the same model as the CTBTO. The uncertainty captures both the travel time uncertainty as well as the pick error. This is modeled as a Laplacian distribution.
    - A distribution for the measured amplitude given the event magnitude and distance – i.e., an attenuation model. The log amplitude is assumed to decay linearly with distance after an initial exponential drop off, with Gaussian error.
    - A multinomial distribution for the measured phase label given the true phase label, again estimated from historical data.

    - Distributions for the measured azimuth and slowness given the true azimuth and slowness for the event also follow a Laplacian distribution.

- Two types of false detections are modeled:
    - Independently generated false detections for each station are modeled by a time-homogeneous Poisson distribution. Each such detection has its amplitude drawn from an empirically estimated distribution (a mixture of Gaussians), its phase label from an empirically estimated multinomial distribution, and its azimuth and slowness from uniform distributions.
    - Coda false detections are randomly triggered by both true and false detections depending on the amplitude of the prior detection. The attributes of the coda detection are strongly correlated with the corresponding attributes of the prior detection.

The inference algorithm operates by a sequence of global and local moves which iteratively improve the deduced world, where a world is a complete specification of the set of events, their associated detections, as well as the independent and coda false detections. The initial world has no events, and all detections are marked as false. The following moves are then executed to improve the world:

- A *birth move* that adds a number of events. These events are created by inverting individual detections such that the proposed event is well supported by the other arrivals.
- An *improve detection move* that finds the best event and phase for each detection or marks it as false (independent or coda).
- An *improve event move* that changes the event location, time, and magnitude to the best possible given the currently associated set of detections and misdetections.
- Finally, a *death move* that kills unsupported events.

Analyst Evaluation

Procedure

The analyst evaluation of NET-VISA was designed to mimic the current procedures at the CTBTO for the review of the SEL3 bulletin, which is the final GA (Le Bras et al., 1994a,b) product. A new bulletin named VISA was produced by the NET-VISA software running 6 hours behind real time, similar to SEL3, and using the same automatic seismic detections as are available to SEL3. (Note that only seismic detections were used for the VISA bulletin in contrast to SEL3 which also includes infrasound and hydroacoustic detections.) The analysts were asked to review the VISA bulletin using the usual ARS (Analyst Review Station) software and to save the results in a new LEB_VISA bulletin. In the interest of time, the analysts were not asked to manually add any events to LEB_VISA, as is normally done for SEL3 using a tool called Scanner. In the opinion of the analysts, the manually added events are entirely due to the skill of the analysts and reflect nothing of the underlying automatic bulletin. It was thus decided to compare the LEB_VISA events with only the automatic events in the LEB bulletin.

In the normal procedure, the LEB bulletin that is produced by an associate analyst is reviewed by a lead analyst. To avoid this additional overhead for the LEB_VISA bulletin, only lead analysts were asked to review it. Finally, in order to rule out analyst skill from affecting the results, the analyst assigned to work on a time block for LEB_VISA was asked to work on the identical time block for LEB.

Empirical Analysis

A total of 27 hours of VISA events were reviewed by the analysts during the two week period from June 11 to June 25, 2012. In these 27 hours, the LEB bulletin had 101 automatic events and the LEB_VISA bulletin had 119 automatic events. The magnitude distribution of these automatic events is shown in Figure 1. The magnitude distribution shows that half of the additional events found by NET-VISA are weak regional events. The rest of the additional events are spread out evenly between low and high magnitudes.

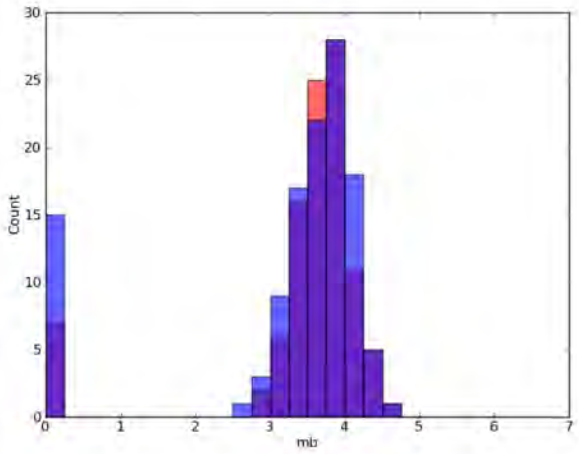


Figure 1. **The body-wave magnitude distribution of automatic LEB events, in red, and LEB_VISA events, in light blue. The overlapping counts are shown in dark blue. A magnitude of zero is reported for an event which has only regional phases, and body-wave magnitude cannot be computed.**

NET-VISA and GA had 92 common events. Of the nine GA events not in NET-VISA, five met the REB criteria. On the other hand, of the 27 NET-VISA events not in GA, 15 met the REB criteria. These 27 events included 25 that the analysts manually added in LEB (a total of 44 events were manually added in LEB). 2 NET-VISA events were missed even by the analysts (of these two one was a four-station regional event and the other a three-station magnitude 2.9 event, neither met the REB criteria).

For the common events, NET-VISA associated on average 2.2 more time-defining phases that were also retained by the analysts than GA. These additional phases translated into 1.8 additional stations, on average, with time-defining phases. The distribution for the number of additional phases associated by NET-VISA is shown in Figure 2 and the number of additional stations in Figure 3.

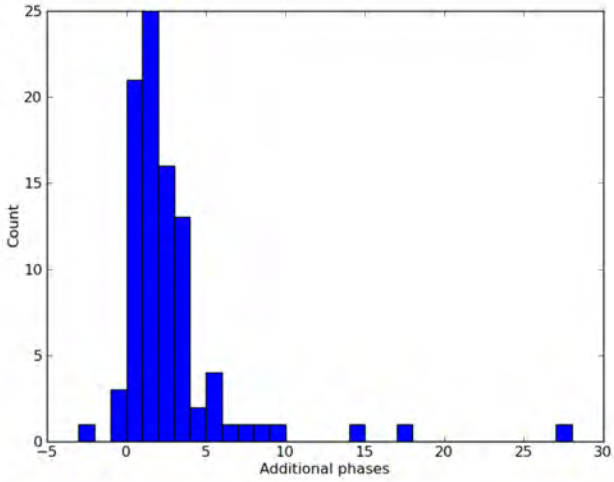


Figure 2. **The distribution of the number of additional time-defining phases found by NET-VISA versus GA.**

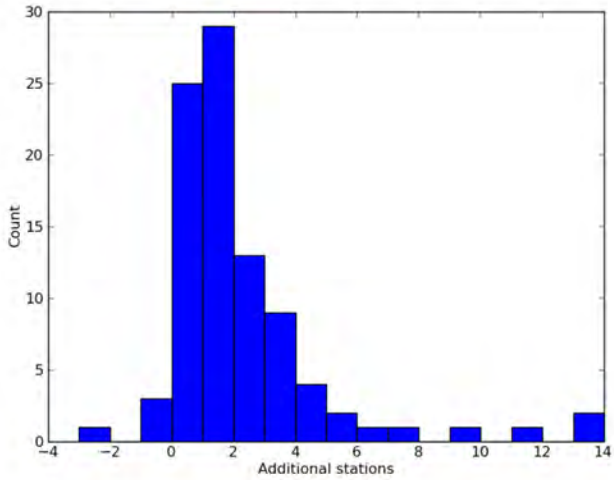


Figure 3. The distribution of the number of additional stations with time-defining phases associated by NET-VISA versus GA.

The locations of the GA events tended to move considerably more than NET-VISA locations after analyst review. Again restricting ourselves to the common events found by both GA and NET-VISA we found that GA locations changed on average 297 km versus 152 km for NET-VISA locations. The median location change for GA and NET-VISA was 82.5 km and 75.3 km respectively. The statistics of these location errors are displayed in Figure 4. The actual errors in location are displayed in Figure 5.

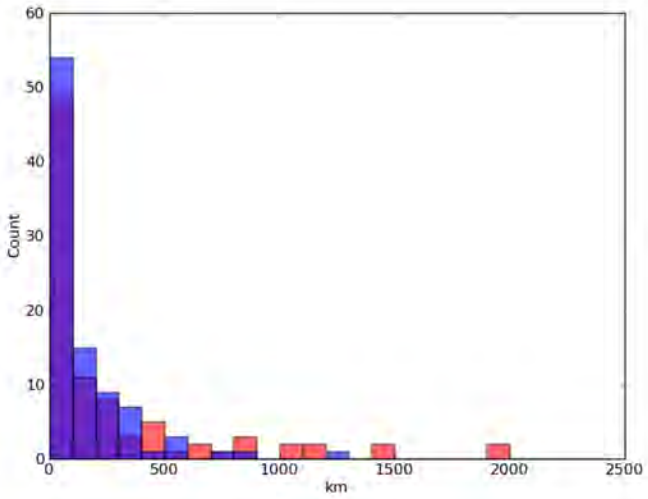


Figure 4. The distribution of the change in the GA location after analyst review (in red) versus the distribution for NET-VISA (in light blue, overlapping counts are shown in dark blue).

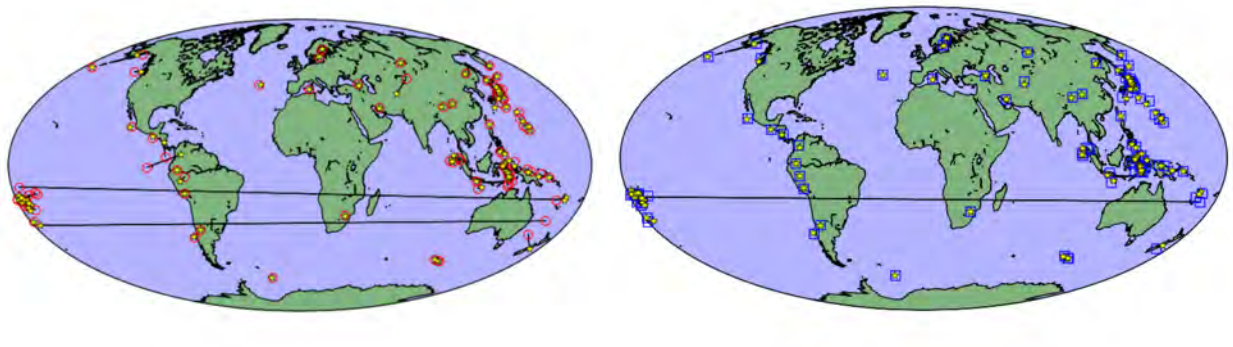


Figure 5. The changes in location of GA events (left figure, red circles) to the corresponding LEB events (yellow stars) and the changes in location of NET-VISA events (right figure, blue squares) to the corresponding LEB_VISA events (yellow stars). Straight lines (and not great circle lines) are drawn between corresponding events.

However, the improvement in NET-VISA locations is not entirely due to the additional phases and stations. In Figure 6, we plot the distribution in location errors for events with an identical number of stations with time-defining phases. For these events, the GA location changed on average 360.4 km and the VISA location by 226.4 km. The median location change for GA and NET-VISA was 157.9 km and 114.0 km respectively.

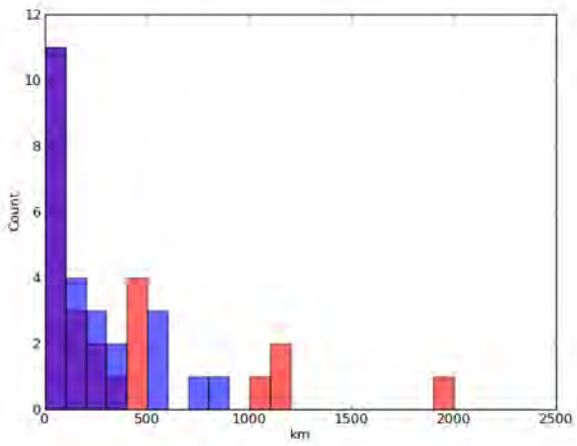


Figure 6. For events with an identical number of stations with time-defining phases, the distribution of the change in the GA location after analyst review (in red) versus the distribution for NET-VISA (in light blue, overlapping counts are shown in dark blue).

In Figure 7, we plot the distribution of depth errors for the common GA and NET-VISA events. The average of the absolute GA depth error was 70.3 km while NET-VISA had an error of 84.3 km. The median depth error was 0.0 km and 8.1 km for GA and NET-VISA respectively. This difference appears to be due to the fact that NET-VISA has no *depth prior*. Currently, the depth of each event in NET-VISA is assumed to be uniformly distributed. GA, on the other hand, has *depth cells* in regions of known deep seismicity.

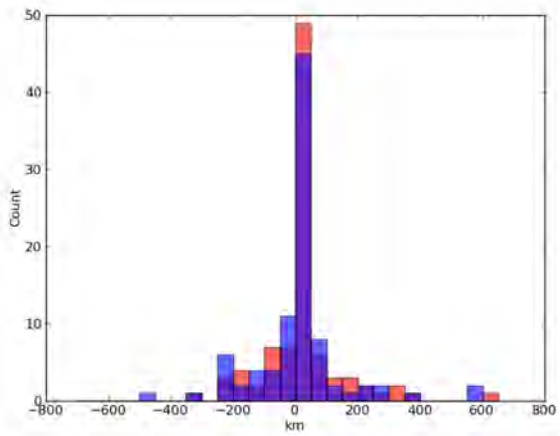


Figure 7. The distribution of the errors in the GA depth (in red) versus the distribution for NET-VISA (in light blue, overlapping counts are shown in dark blue). A positive error represents a higher value for the automatic event versus the reviewed event.

The number of false events found by GA and NET-VISA were comparable at 46 and 50 respectively. The magnitude distribution of these false events is displayed in Figure 8 and the locations of these events are displayed in Figure 9. The magnitude distribution shows that the NET-VISA false events are mostly in the 2 to 3 range (2 is the minimum magnitude that NET-VISA can report for an event, these are typically regional events). GA seems to have many more false events in the 3 to 4 range than NET-VISA.

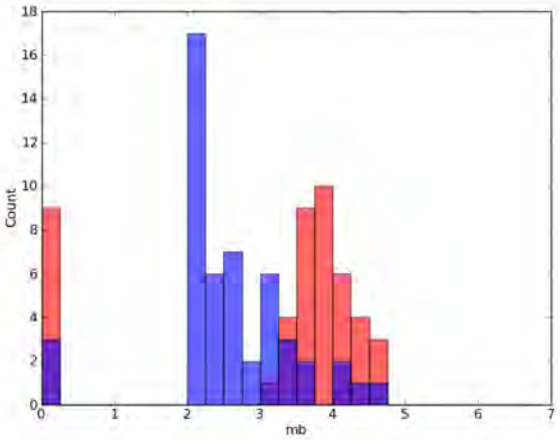


Figure 8. The distribution of the magnitudes of false events reported by GA (red) and NET-VISA (light blue). Overlapping counts are shown in dark blue.

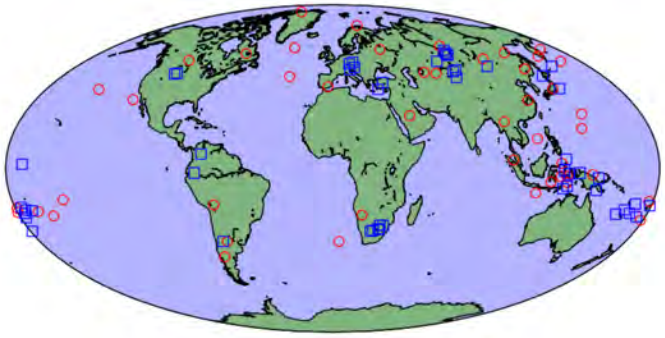


Figure 9. The locations of false events reported by GA (red circles) and NET-VISA (blue squares).

Subjective Feedback

The most common analyst feedback was regarding the usage of the so-called "depth phases." These are phases like Lg, which constrain events to be close to the surface, or pP which provide strong depth information. The analysts felt that because NET-VISA used these phases very early on in its processing, it severely biased the NET-VISA location and sometimes led to inferior or missed events.

The other frequent complaint was that NET-VISA seemed to mark all non-noise phase values of time, slowness, and azimuth as time-defining while analysts had specific policies regarding this. The analysts were thus forced to mark many of the attributes not time-defining before they could *locate* the event.

Some of the analysts were a bit puzzled by the *event definition criteria* used by NET-VISA. For example NET-VISA would sometimes create a very weak event with exactly one station, but with multiple phases – Pn, Sn, Lg. This was often because there was no data available in nearby stations to prove or disprove the existence of the event.

A more subtle issue was noticed by an analyst who rejected an S phase with slowness 7 for an event which already had a P phase with slowness 9 at the same station. The analyst pointed out that the S phase was normally expected to have a higher slowness than the P phase even with the usual measurement error.

Notwithstanding the above issues, the analyst had in general a very positive impression of NET-VISA. They noticed that many of the phases which they had to manually add were automatically associated. It was also immediately obvious to the analysts that NET-VISA found many more events which heretofore had to be built manually using Scanner. This earned NET-VISA the epithet "GA plus Scanner."

CONCLUSIONS AND RECOMMENDATIONS

The VISA bulletin is clearly an improvement over the current SEL3 bulletin as demonstrated by the number of events located (20% additional events), the location of the events, and the number of associated phases (2.2 additional phases and 1.8 additional stations). These improvements had previously been hypothesized by matching VISA and LEB events. However, with the analyst feedback there is now concrete evidence of this improvement.

The evaluation by the analysts has identified a number of potential improvements to NET-VISA.

- Depth phase travel times should be *tempered* to not influence the location very early on in the inference.
- Depth prior needs to be added to the model to better estimate the depth of events in regions of known deep seismicity.
- Phase attributes should be modeled as correlated to each other rather than independently generated.
- A careful analysis needs to be made of the small number of GA and Scanner events which NET-VISA is still missing to see if the birth proposer needs any improvement.

- A final round of post-processing needs to be done on the NET-VISA bulletin so that it has time-defining attributes marked as expected by analysts.

ACKNOWLEDGEMENTS

We are thankful to Dr. Lassina Zerbo, IDC Director, for allowing us to publish this research and for his continued support of the development of the NET-VISA software. The research in this paper could not have been possible without the diligence of the various lead analysts Tajan, Ali Kasmi, Ezekiel Jonathan, Jane Gore, Marcela Villarroel and Kirill Sitnikov who produced the LEB_VISA bulletin and provided detailed feedback.

REFERENCES

Arora, N. S., S. Russell (2012). A model of seismic coda arrivals to suppress spurious events, *European Geophysical Union* (EGU2012-6763*).*

Arora, N. S. (2012). Model-Based Bayesian Seismic Monitoring. University of California, Berkeley. Technical Report No. UCB/EECS-2012-125.

Le Bras, R., H. Swanger, T. Sereno, G. Beall, and R. Jenkins (1994a). Global association. Technical Report ADA304805, Science Applications International Corp, San Diego, CA.

Le Bras, R., H. Swanger, T. Sereno, G. Beall, R. Jenkins, and W. Nagy (1994b). Global association: Design document and user's manual. Technical Report SAIC-94/1142, Science Applications International Corp, San Diego, CA.

Le Bras, R., S. Russell, N. Arora, and V. Miljanovic. Machine Learning at the CTBTO (2011). Testing and Evaluation of the False Events Identification (FEI) and Vertically Integrated Seismic Association (VISA) Projects, in *Proceedings of the 2011 Monitoring Research Review: Ground-Based Nuclear Explosion Monitoring Technologies*, LA-UR-11-04823, Vol 1, pp. 313–321.

DISCLAIMER

The views expressed in this paper are those of the authors and do not necessarily reflect the views of the CTBTO Preparatory Commission.

VALIDATING A GLOBAL 3D P-VELOCITY MODEL OF THE EARTH'S CRUST AND MANTLE FOR IMPROVED EVENT LOCATION

Michael L. Begnaud[1], Sanford Ballard[2], Christopher J. Young[2], James R. Hipp[2], André V. Encarnacao[2], W. Scott Phillips[1], Eric P. Chael[2], and Charlotte A. Rowe[1]

Los Alamos National Laboratory[1] and Sandia National Laboratories[2]

Sponsored by the National Nuclear Security Administration

Award Nos. DE-AC52-06NA25396/LA12-Signal Propagation-NDD02[1]
and DE-AC04-94AL85000/SL12-SignalPropagation-NDD02[2]

ABSTRACT

We are developing a global 3D P wave velocity model of the Earth's crust and mantle using seismic tomography to assess improvement to seismic event locations obtained using high quality 3D Earth models in lieu of 1D and 2/2.5D models. In this paper, we present the most recent version of our model, SALSA3D (SAndia LoS Alamos 3D) version 1.9, and demonstrate its ability to reduce mislocations for a large set of realizations derived from a carefully chosen set of globally-distributed ground truth (GT) events.

Our model is derived from the latest version of the Ground Truth (GT) catalog of P and Pn travel-time picks assembled by Los Alamos National Laboratory. For the current version of the model, we employ more robust data quality control measures than previously used, as well as additional global GT data sources. To prevent over-weighting due to ray path redundancy and to reduce the computational burden, we cluster rays into representative rays. Reduction in the total number of ray paths is ~50%. The model is represented using the triangular tessellation system described by Ballard et al. (2009), which incorporates variable resolution in both the geographic and radial dimensions. For our starting model, we use a simplified layer crustal model derived from the NNSA Unified model (Pasyanos et al., 2004; Steck et al., 2004) in Eurasia and Crust 2.0 model everywhere else, overlying a uniform *ak135* mantle. Sufficient damping is used to reduce velocity adjustments so that ray path changes between iterations are small.

We obtain proper model smoothness by using progressive grid refinement, refining the grid only in areas where the data warrant such a refinement. In previous versions of SALSA3D, we based this refinement on velocity changes from previous model iterations. For the current version, we utilize the diagonal of the model resolution matrix to control where grid refinement occurs, resulting in more consistent and continuous areas of refinement than before. In addition to the changes in grid refinement, we also employ a more robust convergence criterion between successive grid refinements, allowing a better fit to first broader model features, then progressively to finer ones. Our approach produces a smooth, multi-resolution model with node density appropriate to both ray coverage and the velocity gradients required by the data. This scheme is computationally expensive, so we use a distributed computing framework based on the Java Parallel Processing Framework, providing us with ~400 processors.

We compare the travel-time prediction and location capabilities of SALSA3D to standard 1D and 2/2.5D models via location tests on a global event set with GT of 5 km or better. These events generally possess hundreds of Pn and P picks from which we generate different realizations of station distributions, yielding a range of azimuthal coverage and ratios of teleseismic to regional arrivals, with which we test the robustness and quality of relocation. For the current version of the model, we test using the full 3D covariance matrix to calculate path-dependent travel time uncertainty rather than standard 1D, distance-dependent uncertainty. The SALSA3D model reduces mislocation over the standard 1D *ak135* model regardless of Pn to P ratio, with the improvement being most pronounced at higher azimuthal gaps. SALSA3D also reduces mislocation compared to the combined RSTT/*ak135* model (2.5D – RSTT for regional phases), with SALSA3D and RSTT performing about the same when using only Pn arrivals in location tests.

OBJECTIVES

The evolving U.S. monitoring needs require accurate location of ever-smaller seismic events. Given the limited station coverage of a typical global monitoring network, such as the International Monitoring System (IMS), it is likely that such events will be detected by very few stations, providing poor network geometry. For locating such events, it is essential to have extremely high fidelity travel-time predictions, particularly at regional distances where lateral heterogeneity can be significant. Accurately accounting for lateral heterogeneity implies using 3D models of the Earth to calculate travel times, but relatively few of the available 3D Earth models are appropriate for high fidelity travel-time prediction, and it is unclear whether any of those that are appropriate actually improve event locations. Rowe et al. (2009) demonstrated that when 3D models are used to predict travel times in a manner inconsistent with how the models were developed, the resulting values tend to have higher residuals than those produced when using standard 1D velocity models. This is not surprising in itself, but does indicate problems utilizing contributed models that have vastly different assumptions and/or ray tracing methodologies. It is crucial that a seismic location algorithm used with a 3D model also use the same ray tracer as during model development. Thus, we are developing our own global 3D P-wave velocity model of the Earth's crust and mantle—SALSA3D using seismic tomography based on a carefully assembled data set of P-phase travel times collected by LANL over the past decade. An important difference between our effort and previous efforts is that our model was produced specifically for improving event location; the model also provides potentially valuable information about the structure of the Earth, but this is not our focus. Hence, all decisions about data processing and tomography were made with this goal in mind.

In this paper, we present the most recent SALSA3D, version 1.9, and we demonstrate its ability to reduce mislocations for a large set of realizations derived from a carefully chosen set of distributed GT events.

RESEARCH ACCOMPLISHED

Data Set

The data used for the tomographic inversion were collected by LANL over the past decade and include events categorized with a GT level of 25 km or better (Bondár et al., 2004). Arrivals for these events were merged from various sources to produce a single set of arrivals for each event with redundancies removed, maximizing the available arrivals (Begnaud, 2005). For SALSA3D 1.9, we employ more rigorous data quality control, removing data outliers using data similarity within event clusters. Regional Pn and teleseismic P arrivals were then extracted from this "cleaned" data set for use in the tomography, resulting in ~122K events, ~13K stations, and almost 13 million individual ray paths (Figure 1). Unique data sets include USArray data and the Deep Seismic Soundings in the former Soviet Union (e.g., Li and Mooney, 1998).

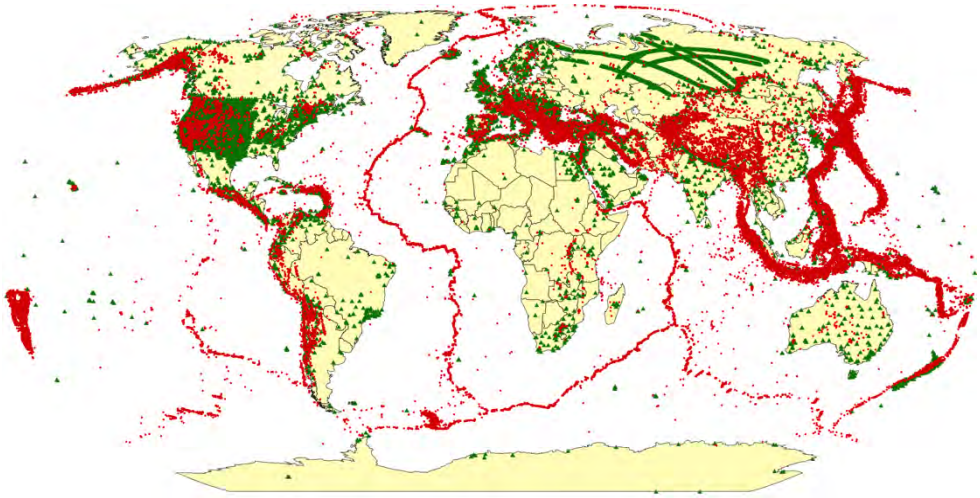


Figure 1. Stations (green triangles) and events (red points) used as the raw data for global tomography inversion. These data were collected by LANL over the past decade and are all categorized with a ground truth level of 25 km or better. Recent additions to this data set include the mid-western portion of USArray as well as several PASSCAL deployments in Asia.

Summary rays were produced from the ~13 million rays to remove redundant ray paths, search for data outliers, and reduce the computational load of ray tracing required during tomographic inversion. Each unique station/GT level combination was clustered separately, preserving GT levels and their relative weighting (lower GT levels are weighted more heavily), giving ~7 million summary rays.

Tomographic Inversion

We use the LSQR algorithm of Paige and Saunders (1982) to invert the data to find the P wave velocity distribution in the mantle which optimally reduces the misfit between observed and predicted travel times for P and Pn phase arrivals. Our starting model for the inversion consists of the NNSA Unified Model for Eurasia (Pasyanos et al., 2004; Steck et al., 2004) with the Crust 2.0 model elsewhere (Laske and Masters, 1997; Laske *et al.*, 2000) modified by combining their six layers into four by merging the three sedimentary layers into one. The crust is damped heavily in the inversion so it is essentially fixed.

The full iterative inversion is run three separate times, relocating the GT>5 events with the SALSA3D model after each full inversion (including grid refinement below). After each relocation step (which we call outer tomography iterations), the tomographic inversion is restarted using the original starting model and the updated locations. This has the effect of improving the locations for events having poorer GT levels (e.g., GT25) whose original locations were based on the *ak135* model (Kennett et al., 1995). This shifting of locations tends to occur mostly along subduction zones, where the locations migrate up-slab as the use of *ak135* model along with the commonly one-sided station distribution has pushed locations farther off-shore. New for version 1.9 is testing of subsequent tomography runs using updated measurement and model error estimates based on the spread of residuals after updated locations.

For the inner tomographic iterations, we retrace rays in each iteration using the pseudo-bending algorithm (Um and Thurber, 1987; Zhao and Lei, 2004; Ballard *et al.*, 2009). During early iterations, the mantle is moderately damped to discourage the inversion from progressing too rapidly but then damping is relaxed in later iterations. Convergence of the inversion is achieved when successive iterations result in overall residual changes of $\leq 0.25\%$. Regularization is not required during the inversion since it is accomplished by refining the grid several times during the inversion (Simmons et al., 2009).

Adaptive Grid Refinement

P wave velocity in our model is stored on a 3D grid of nodes having variable resolution in both geographic and radial dimensions. Our basic starting point is a two-dimensional, multi-level triangular tessellation of a unit sphere (Wang and Dahlen, 1995; Ballard et al., 2009). We assign a tessellation with 8° triangles to the lower mantle, a tessellation with 4° triangles to the transition zone and upper mantle, and a third tessellation with variable resolution to all crustal layers. The crustal tessellation (not shown) has 2° triangles in oceanic regions, 1° triangles in most continental regions, and 0.5° triangles in the United States where the additional resolution is warranted due to the dense station coverage afforded by the USArray. The two tessellations in the mantle are refined, in both the geographical and radial dimensions, during the progress of the tomographic inversion.

Grid refinement was originally accomplished based on a minimum change in the slowness values during tomographic iterations. We now are able to solve for the full 3D resolution matrix (Hipp et al., these Proceedings) and have applied the resolution matrix for a coarse grid to drive the grid refinement steps. By using the diagonal of the resolution matrix, we are able to take advantage of data coverage. Figure 2 is an example of the final grid in the upper mantle.

Velocity Model

The final SALSA3D 1.9 model is shown in Figures 3 and 4. Although it is not our primary goal to resolve detailed tectonic features, many present themselves. Clearly visible in the figures are subduction zones, mid-ocean ridges, slower velocities in western North America, including the Yellowstone hot spot, faster velocities in eastern North America associated with the craton, the Red Sea rift, detailed variations in Europe and the Middle East, and faster velocities in northern Russia and into Tibet and India. These features are consistent with previous 3D models (e.g., Li et al., 2006) in most areas. The full 3D model resolution matrix indicates that the best laterally-resolved areas correspond to natural areas of higher seismicity, of course, typically in the western United States, Europe, and into most of Asia. Resolution at depth is best in the upper portion of the lower mantle, due to the large number of teleseismic raypaths in our dataset that bottom near this depth.

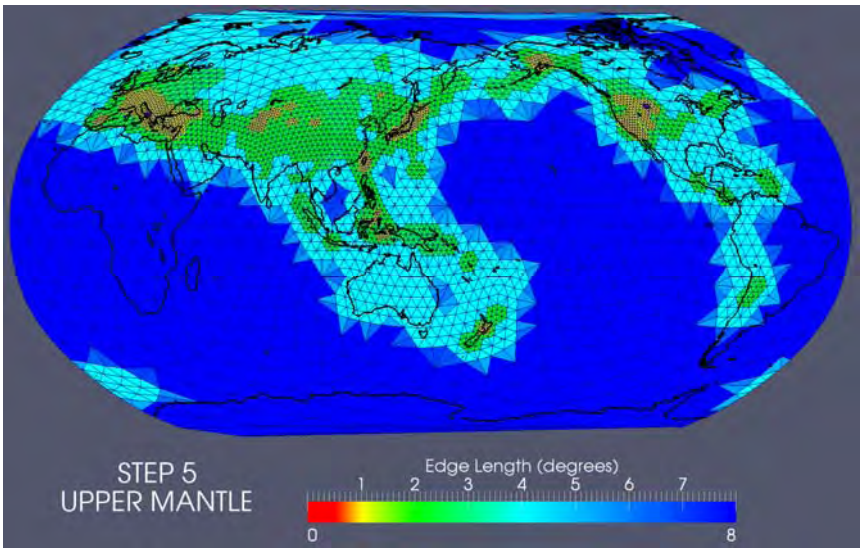


Figure 2. Example of the final SALSA3D grid in the upper mantle after the grid-refinement process using the diagonal of the full 3D resolution matrix. Grid color is relative to approximate edge length.

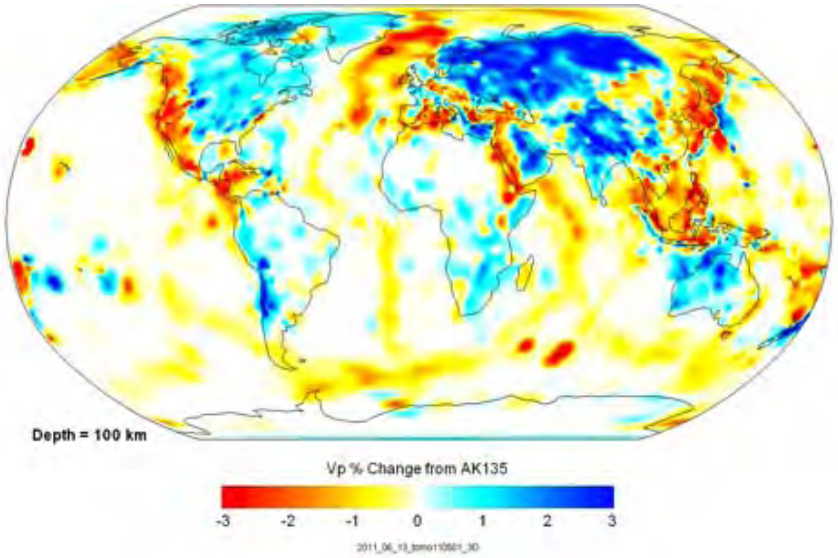


Figure 3. Depth slice through the SALSA3D 1.9 model at 100 km demonstrating the Vp velocity structures produced. Colors are percent change from the *ak135* model. Clearly visible are tectonic features such as mid-ocean ridges, subduction zones, and large cratons.

Reduction of Travel-Time Residuals

When validating a new velocity model, the first step is usually to test the reduction in travel-time residuals, typically with distance. We plotted the median residual with distance (bias) along with the L1 norm spread or the median absolute difference from the median (MAD1) (Figure 5).

For the starting model (*ak135* model, CRUST2.0, DOE Unified), the offset is significant, especially for regional distances (~<25°), as well as the spread. For teleseismic distances, the starting model still shows an observable offset, although greatly reduced over regional distances. When using the SALSA3D model, the offset is significantly reduced, most noticeably for regional distances, although some offset is still observed for triplication distances (~18-25°). The residual offset is almost zero for teleseismic distances when using SALSA3D. The spread of the residuals for SALSA3D is displaying a significant reduction compared to the starting model. We associate this reduction in global spread versus distance actually to travel time offset reductions within specific tectonic regions, while real residual spread is more likely due to pick error which cannot be corrected using a different model. The

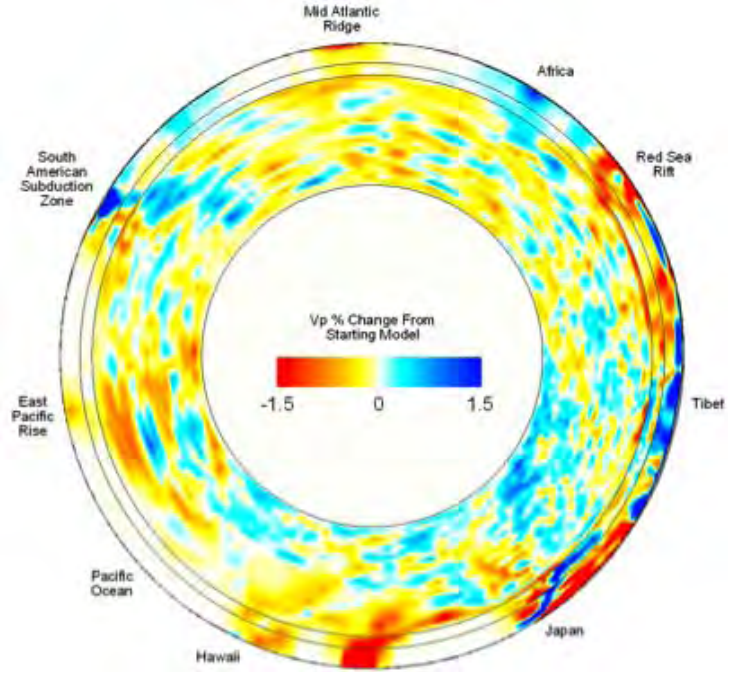


Figure 4. Cross-section through the SALSA3D 1.9 model in a pseudo-great circle pattern to highlight structures- Colors represent percent change from the starting model (in this view, mostly the *ak135* model). Of particular prominence are the delineation of the Japanese subduction zone, the thicker, faster Tibetan area, and other subduction zones, rifts, and mid-ocean ridges.

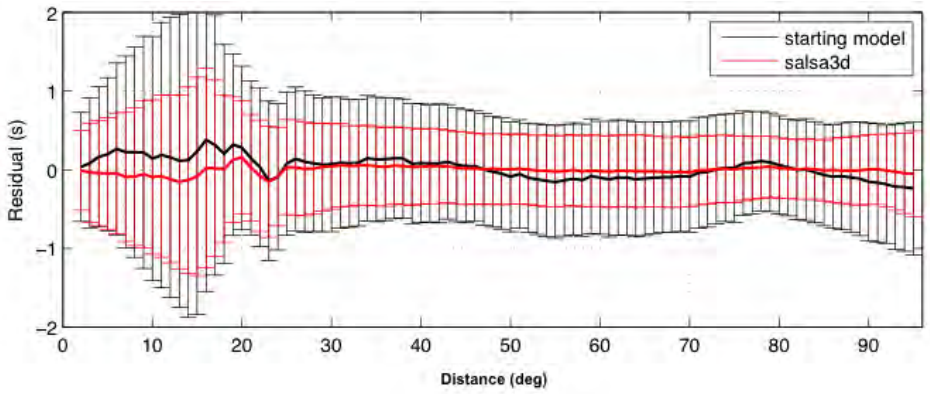


Figure 5. Travel-time residuals with distance (top) showing the median residual (solid line) and L1 spread (error bars) for residuals binned in 1° bins. Data are those used in the tomography model. The starting model displays significant residual offset, especially for regional data, while the SALSA3D reduces this to almost zero, with a corresponding reduction in residual spread.

SALSA3D model reduces residual offset in tectonic regions and, thus, is manifested in global residuals versus distance as a reduction in overall residual spread.

Reduction in Event Mislocation

For monitoring purposes, the assessment of any new velocity model is based on the degree to which it reduces mislocation of seismic events with well-constrained locations. We compare location results to the standard *ak135* model, as well as the recently developed Regional Seismic Travel Time (RSTT) model (Myers et al., 2010). The RSTT model is designed for regional phases (e.g., Pn) and is combined with *ak135* when using teleseismic arrivals. If the SALSA3D model does not exhibit location improvement over *ak135* and RSTT, then it does not support the level of effort required to develop and implement 3D models for location in the context of nuclear explosion monitoring.

Model/Prediction Uncertainty

To run relocation tests, an uncertainty model must first be determined for SALSA3D. For standard location procedures, a simple residual spread with distance is used to estimate the prediction or model uncertainty for any arrival. The problem with this simple-minded assumption is that it does not account for aseismic areas or areas that do not predict travel times well. To perform location tests with SALSA3D, however, we needed a standard prediction uncertainty model as a function of distance to use with the location code. Comparison of the spread with distance is a validation test to compare SALSA3D to other models and should show a reduction in spread with distance.

When comparing these distance-dependent or prediction uncertainty curves, we follow these guidelines to ensure a fair comparison:

1. The distance-dependent uncertainty values should be created **using the same data for each model**. Comparing curves developed with different validation data is inconsistent.
2. Since most travel times (i.e., origin times) were determined using a 1D model such as *ak135*, **all travel times should be baselined to the models that are being compared**. The baselining is accomplished by adjusting origin times using average residuals per event. This is done so travel times are determined relative to the specific model being compared.
3. If possible, the data used for the uncertainty curves should not be used in the tomography models. For best results, the uncertainty curve with distance should be based on similar data that will eventually be used in practice with the model and uncertainty.

To follow guideline (3), a SALSA3D model (version 1.7) was determined with ~5% of the raw arrival data removed (within the boundaries of the RSTT model for consistency). Summary ray production and relocation steps continued normally following data removal. After tomography, the segregated events were relocated through the alternative SALSA3D model and the removed arrival data were grouped into 1° distance bins to evaluate uncertainty (Figure 6). We use the same segregated arrivals to evaluate both *ak135* and RSTT uncertainty; however, these data were not necessarily removed from the RSTT model determination, violating guideline (1) above. This could not be rectified for this analysis as the RSTT model was developed with a different data set base. The origin times were baselined to each model used. One disadvantage of using residual spread with distance as a proxy for uncertainty is that the residual spread consists of both pick errors and model errors. To isolate only the model errors, an estimate of pick error was removed.

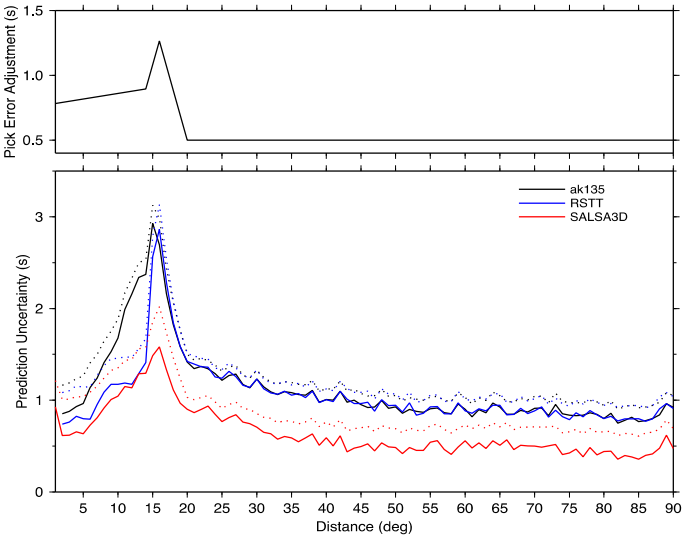


Figure 6. Distance-dependent uncertainty using ~5% of the original SALSA3D data set left out of the 3D model (version 1.7). These data were not necessarily left out of the RSTT model, however, due to a different data set base. Dashed lines are raw uncertainty with solid lines being uncertainty after an estimate of pick error was removed.

The adjusted uncertainty values for regional Pn distances (< 15°) show a significant reduction in uncertainty for SALSA3D over *ak135* and to a lesser degree over RSTT. The uncertainty associated with triplication distances (~15-20°) is reduced for the SALSA3D model. For teleseismic distances (> 20°), the SALSA3D uncertainty has decreased by almost 0.5 s.

Location Validation Tests

The paramount model validation is testing for improved location accuracy and precision or reduced mislocation. To compare location results between models, **it is best to use the same validation events among models**, if possible, that were left out of the tomographic inversions. By using similar validation events, any concerns over inconsistency of the events themselves are eliminated, as well as circularity issues. Comparisons are then strictly affected only by model differences.

To be consistent with RSTT, we created another SALSA3D model and left out the validation events used in the validation of the RSTT model (Myers et al., 2010) in the Eurasia and in North America (Figure 7). These events were chosen from GT0-5 events to maximize both coverage as well as the number of available P and Pn phases for location tests.



Figure 7. RSTT and SALSA3D validation events in North America (left) and Eurasia (right).

To test improvements in location using the SALSA3D model and compare with other models, a set of origins and associated arrivals is needed for location testing. Since we are interested in the combination of P and Pn arrivals and how different combinations affect the resulting location, we generate a grid of random combinations of P and Pn arrivals from **existing arrivals** of the validation events, using the LANL Location Database. The various combinations simulate different network configurations arising from a variety of possible event magnitudes, usually in non-optimal configurations.

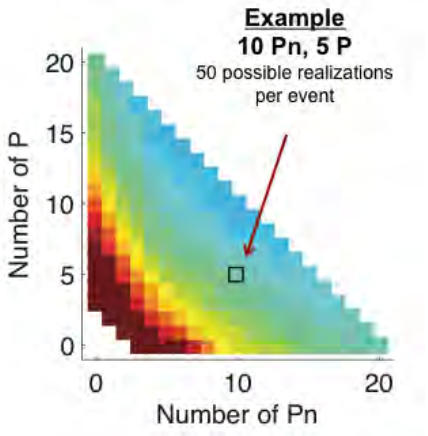


Figure 8. Example of random realizations of phases, generating selections of origins for different network configurations and event magnitudes. Each grid position is a target number of P and Pn phases.

A target set of P and Pn arrivals is determined from a total of 3 to 20 phases, and all of the available arrivals for an event are assigned a random number, then sorted by that random number. For the target number N phases, the first N phases are chosen from the sorted set. The process is repeated 50 times for each event in each target number of phases (Figure 8). **We use 50 realizations per event as it provides a large number of origins and a valid statistical base. Using too few realizations per event can result in erratic looking mislocation grids that also show significant variations with different realization sets.**

The random realization "events" were relocated using *ak135*, RSTT/*ak135*, and SALSA3D. No arrivals were eliminated during relocations unless the model was undefined for that particular ray path. The uncertainty-with-distance values from Figure 6 were used to estimate model uncertainty during relocation. The median values for each grid of target phases were determined for each

grid position (Figure 9). For origin realizations with very few arrivals (<~10), the SALSA3D model exhibits significant mislocation reduction over the other models.

Perhaps an easier method of comparing the mislocation results is to difference the plots and look at relative values from one model compared to another (Figure 10). When very few arrivals are used, the differences between SALSA3D and *ak135* are on the order of tens of kilometers improvement (numbers listed on grid positions in (Figure 10)). Other validation tests were completed (azimuthal gap, coverage ellipse percentages, etc.), demonstrating similar results to the mislocation grids (not shown).

CONCLUSIONS AND RECOMMENDATIONS

We have presented the latest version (1.9) of SALSA3D, the Sandia-Los Alamos global tomography 3D P-velocity model of the crust and mantle. Our model is multi-resolution, with the resolution determined as part of the tomographic inversion. Additional nodes are added where ray coverage is high and the full 3D resolution matrix suggests sufficient resolution; other areas maintain the starting grid sampling. SALSA3D successfully images many well-established features within the Earth, such as subducting slabs and hot spots, and is generally consistent with other recent global and regional models.

More important than illumination of structural features is the fact that SALSA3D provides unambiguous improvement in travel-time prediction and in event location compared to *ak135* and, to a lesser extent, RSTT/*ak135*. Event location improvement is evaluated by re-locating a set of well-characterized events in Europe and Asia. By forming many different random realizations of these events, we can evaluate relocation improvement for a large number of different scenarios. SALSA3D improves locations to a lesser extent when the number of stations is large, but as the number of available phases becomes smaller, the 3D model performs significantly better. Further, because our model is developed to fit both P and Pn data, it performs well with regional data, teleseismic data, or a combination of the two, eliminating the requirement of using multiple models based on path length.

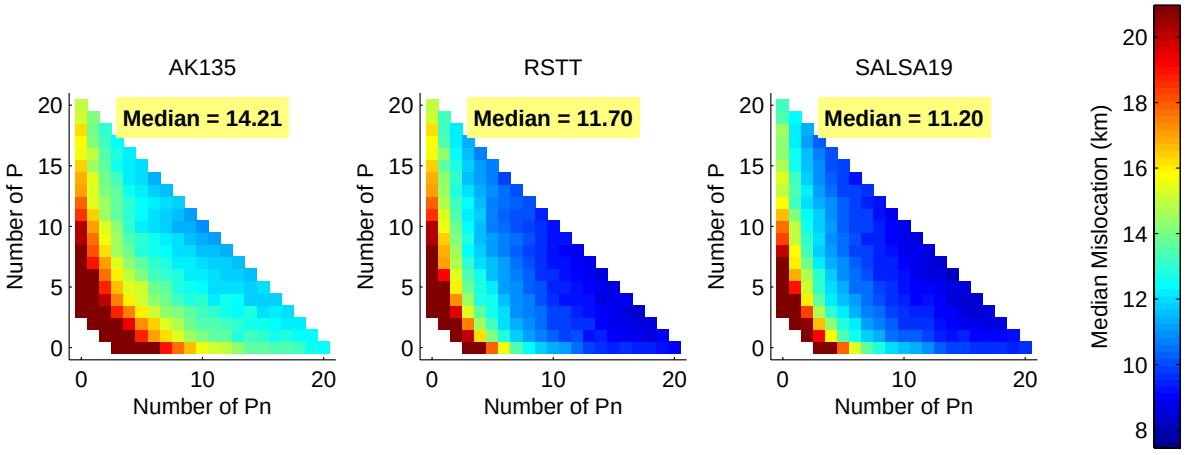


Figure 9. Median mislocation values for each grid position of target phases and for each model tested (*ak135*, RSTT/*ak135*, SALSA3D). The SALSA3D model displays an overall reduction in mislocation over ak135 and a slight reduction over RSTT/ak135.

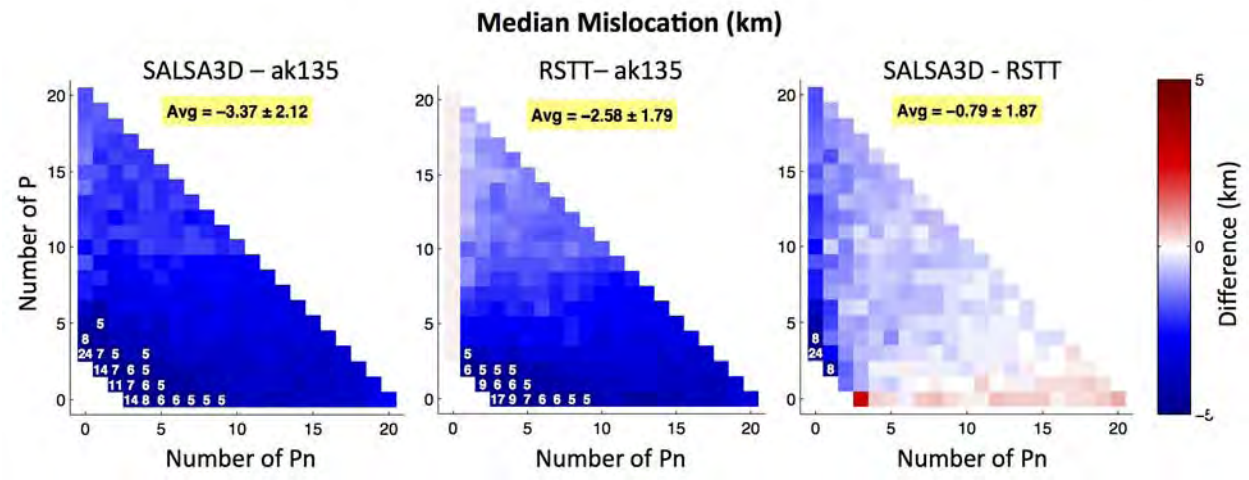


Figure 10. Mislocation differences (km) between the three models tested. The median values in each of the grid positions in Figure 9 have been differenced. Any grid position with a difference of 5 km or more has the integer value plotted on the grid position. At small numbers of phases, SALSA3D shows a significantly reduced mislocation compared to *ak135*.

REFERENCES

Ballard, S., J. R. Hipp, and C. J. Young (2009). Efficient and accurate calculation of ray theory seismic travel time through variable resolution 3D earth models, *Seis. Res. Lett.* **80**, 6, 989–998, doi:10.1785/gssrl.80.6.989.

Begnaud, M. L. (2005). Using a dedicated location database to enhance the gathering of ground truth information, Los Alamos National Laboratory LA-UR-04-5992, 22 pp.

Bondár, I., S. C. Myers, E. R. Engdahl, and E. A. Bergman (2004). Epicentre accuracy based on seismic network criteria, *Geophys. J. Int.* **156**, 483–496.

Kennett, B. L. N., E. R. Engdahl, and R. Buland (1995). Constraints on seismic velocities in the Earth from travel times, *Geophys. J. Int.* **122**, 108–124.

Laske, G., G. Masters, and C. Reif (2000). CRUST 2.0: A New Global Crustal Model at 2x2 Degrees, http://igppweb.ucsd.edu/~gabi/crust2.html.

Laske, G., and T. G. Masters (1997). A global digital map of sediment thickness, Abstract F483 presented at Fall Meeting, American Geophysical Union, San Francisco, California,

Li, C., R. D. van der Hilst, and M. N. Toksöz (2006). Constraining P-wave velocity variations in the upper mantle beneath Southeast Asia, *Phys. Earth Planet. Inter.* **154**, 180–195.

Li, S., and W. D. Mooney (1998). Crustal structure of China from deep seismic sounding profiles, in *Proc. of the 7th international symposium on Deep seismic profiling of the continents,* Asilomar, CA, United States, Tectonophysics 288, 105–113.

Myers, S. C., M. L. Begnaud, S. Ballard, M. E. Pasyanos, W. S. Phillips, A. L. Ramirez, M. S. Antolik, K. D. Hutchenson, G. S. Wagner, J. J. Dwyer, C. A. Rowe, and D. R. Russell (2010). A crust and upper mantle model of Eurasia and North Africa for Pn travel time calculation, *Bull. Seismol. Soc. Am.* **100**, 2, 640–656.

Paige, C. C., and M. A. Saunders (1982). LSQR: An algorithm for sparse linear equations and sparse least squares, *ACM Trans. Math. Softw.* **8**, 1, 43–71.

Pasyanos, M. E., W. Walter, R., M. P. Flanagan, P. Goldstein, and J. Bhattacharyya (2004). Building and testing an a priori geophysical model for western Eurasia and North Africa, *Pageoph* **161**, 235–281.

Rowe, C., S. Ballard, M. Begnaud, C. Young, L. Steck, and J. Hipp (2009). Validating 3D geophysical models for use in global travel-time calculation for improved event locations, in *Proceedings of the 2009 Monitorning Research Review: Ground-Based Nuclear Explosion Monitoring Technologies,* LA-UR-09-05276, Vol. 1, pp. 408–415.

Simmons, N. A., S. C. Myers, and A. L. Ramirez (2009). Multi-resolution seismic tomography based on a recursive tessellation hierarchy, in *Proceeding of the 2009 Monitoring Research Review: Ground-Based Nuclear Explosion Monitoring Technologies,* LA-UR-09-05276, Vol. 1, pp. 211–220.

Steck, L. K., C. A. Rowe, M. L. Begnaud, W. S. Phillips, V. L. Gee, and A. A. Velasco (2004). Advancing seismic event location through difference constraints and three-dimensional models, in *Proceedings of the 26th Seismic Research Review - Trends in Nuclear Explosion Monitoring,*LA-UR-04-5801, Vol. 1, pp. 346–355.

Um, J., and C. Thurber (1987). A fast algorithm for 2 point ray tracing, *Bull. Seismol. Soc. Am.* **77**, 972–986.

Wang, Z., and F. A. Dahlen (1995). Spherical-spline parameterization of three-dimensional Earth models, *Geophys. Res. Lett.* **22**, 3099–3102.

Zhao, D., and J. Lei (2004). Seismic ray path variations in a 3D global velocity model, *Phys. Earth Planet. Inter.* **141**, 153–166.

FROM CRATON TO RIFT: EMPIRICALLY BASED GROUND TRUTH CRITERIA FOR REGIONAL NETWORKS

Richard A. Brazier[1], Karen B. Boomer[2], John P. O' Donnell[1] Andrew A. Nyblade[1],
Stephen C. Myers[3], Jennifer Kokoska[2], and Soniya R. Liu[1]

The Pennsylvania State University[1], Bucknell University[2],
and Lawrence Livermore National Laboratory[3]

Sponsored by the Air Force Research Laboratory and the National Nuclear Security Administration

Award Nos. FA9453-10-C-0211[1,2] and DE-AC52-07NA27344[3]
Proposal No. BAA10-42

ABSTRACT

Extending the approaches of Bondár et al. (2004), Bondár and McLaughlin (2009), and Boomer et al. (2010), region-specific empirically based ground truth (EBGT) criteria used to estimate the epicentral location accuracy of seismic events have been developed for a variety of geological settings. Boomer et al. (2010) outline the development of local criteria for the simple crustal structure of the Archean Kaapvaal Craton in southern Africa. Continuing the development of criteria for regions of varying geological complexity, we now have criteria for the Main Ethiopian Rift, the Tibetan Plateau and preliminary criteria for the central Asian region in the vicinity of the Kyrgyz seismic network (KNET). In each case, the local crustal structure is well known and hand-picked arrival times of GT0 ground truth reference events (explosions and mine tremors) were available, facilitating the establishment of the location accuracy criteria through the stochastic forward-modelling of travel times for epicentral locations.

In the geologically very complex region of the Main Ethiopian Rift, we use the 2003 Ethiopia-Afar Geoscientific Lithospheric Experiment (EAGLE; Maguire et al., 2003) data to obtain criteria. Four of the 25 large refraction line shots were used as reference events to develop the criteria while nine of the remaining shots were used for verification purposes. In the vicinity of the Main Ethiopian Rift, a seismic event is required to be recorded on at least eight stations within the local Pg/Pn crossover distance and yield a network quality metric (Bondár and McLaughlin, 2009) of less than 0.43 in order to be classified as *EBGT5*$_{95\%}$ (GT5 with 95% confidence). The criteria were subsequently used to identify 10 new GT5 events recorded on the Ethiopian Broadband Seismic Experiment network.

The crust and upper mantle structure of the Tibetan Plateau is arguably more complicated than the Kaapvaal Craton, yet less complicated than the Main Ethiopian Rift. Four of the larger shots from the International Deep Profiling of Tibet and the Himalaya (INDEPTH III) refraction line were used to develop local criteria, subsequently validated using three additional shots. The criteria for the Tibetan Plateau are similar to the Main Ethiopian Rift criteria, yet slightly less restrictive as the network quality metric needs to be less than 0.45. We include a compiled list of 28 new GT5 events recorded on the INDEPTH III network.

Meanwhile, criteria are being developed for the central Asian region between the northern Tien Shan Mountains and Kazakh Platform spanned by the Kyrgyz seismic network (KNET). When considered in conjunction with criteria developed previously for the Kaapvaal Craton in southern Africa, it is apparent that increasing restrictions on the network quality metric mirror increases in the complexity of geologic structure from craton to plateau to rift.

OBJECTIVES

Determining accurate seismic locations with representative uncertainty estimates is of fundamental importance to ground-based nuclear explosion monitoring, including the assignment of accurate ground truth (GT) levels. The monitoring community relies on seismic network coverage criteria for classifying events at the GT5 level, which specifies the absolute location error as being less than 5 km. Bondár et al. (2004) developed the $GTX_{C\%}$ criteria for characterizing location accuracy, where X is the epicenter accuracy in kilometers at a C confidence level. Regional-network locations are currently validated at the $GT20_{90\%}$ level, which does not satisfy the $GT5_{95\%}$ validation requirement for inclusion in the NNSA Knowledge Base.

Our recent work testing the existing global GT criteria against GT0 mine events recorded on a sparse regional network in southern Africa shows that the global GT criteria (Bondár et al., 2004; Bondár and McLaughlin, 2009) presently employed by the community may be overly restrictive for certain tectonic settings, at least for regions with relatively homogeneous crustal and upper mantle structure (Boomer et al., 2010). Consequently, it is very probable that there exist many events recorded by regional networks that could satisfy regional $GT5_{95\%}$ criteria, but which presently do not qualify for inclusion within GT5 catalogs on the basis that they fail to meet the more stringent constraints of the global criteria. This potentially includes events in strategically important areas.

The objective of this project is to develop new criteria for acquiring location ground truth from regional networks that account for both the complexities in regional Earth structure and the fact that, through careful phase picking, high quality travel time measurements can be obtained. In particular, empirically based ground truth criteria (EBGT) have been developed for the Main Ethiopian Rift and the Tibetan Plateau, both of which are regions of contrasting and considerable geological complexity compared to southern Africa. Having established the region-specific criteria, we subsequently apply the criteria to datasets from Ethiopia and Tibet in order to identify new GT5 events.

The EBGT5 criteria for these two regions, when combined with the criteria already obtained for the Kaapvaal Craton, will enable us to compare regionally-developed criteria against the existing global criteria for a range of tectonic settings (i.e., stable craton, plateau within a collisional zone and an active rift). We anticipate that as the level of heterogeneity in the geologic structure increases, at some point the regional EBGT criteria will converge on the global criteria.

Future work will include both expanding the suite of tectonic-specific criteria and assessing whether generic criteria can be feasibly applied to geologically similar regions (e.g., datasets from eastern Turkey, the Arabian Peninsula and Kyrgyzstan are available) with the goal of identifying new GT5 events. In addition, we will use a correlation method between observed and synthetic seismograms to improve the precision of the arrival time measurements, thus further improving the location accuracy of the events we anticipate adding to the GT5 catalog.

RESEARCH ACCOMPLISHED

The deliverables to date include the development of EBGT5 criteria for the Main Ethiopian Rift and the Tibetan Plateau.

Geological Background and Data Sources

The Main Ethiopia Rift is geologically very complex, with crustal and upper mantle studies from several seismic investigations revealing heterogeneity in structure both across and along the rift. We are using the data set from the 2003 Ethiopia-Afar Geoscientific Lithospheric Experiment (EAGLE; Maguire et al., 2003) to obtain EBGT5 criteria for the rift. The data set includes a combined active-passive source seismic experiment, where 25 large shots were well recorded across the refraction profiles as well as by a local/regional network of 80 broadband stations (see Figure 1). Hand-picked arrival times for these shots were provided by Keranen et al. (2004), while station and path dependent velocity models were adapted from EAGLE seismic refraction and receiver function studies (Maguire et al., 2006; Dugda et al., 2005). In addition, Keir et al. (2006) carried out a seismicity study of the rift using the broadband stations, listing over 2000 local events, while the Ethiopian Broadband Seismic Experiment recorded over 400 local and regional events on 25 broadband seismic stations between 1999 and 2001 (Brazier et al., 2008).

The Tibetan Plateau resulted from a continent-continent collision between the Indian and Eurasian plates, creating an uplifted region (5 km of topography in places) 550-1200 km wide with crustal thickening of up to ~70 km. The crust and upper mantle structure of the plateau is arguably much more complicated than that in the vicinity of the Kaapvaal Craton, and includes a number of prominent suture zones. The International Deep Profiling of Tibet and the Himalaya (INDEPTH III) project involved a 400 km long active-passive seismic project that recorded more than 50 shots (Table 1). The largest shots had charge sizes ranging from 180 to 1160 kg, which we used to develop local criteria (Figure 2).

At the conclusion of the active-source experiment, many broadband stations remained in place to record naturally occurring seismic events. This facilitated a seismicity study during which Langin et al. (2003) compiled a catalogue of 267 local and regional events, many of which have magnitudes larger than 3. The events were located using a 1D velocity model of the crust and upper mantle derived from the refraction profiles.

Development of existing *GT* criteria

Bondár et al. (2004) explore the use of network coverage as a metric for assessing location accuracy. In their work, network coverage was quantified by measuring not only the primary but also the secondary azimuthal gap. By restricting the primary gap to less than 110° and the secondary gap to less than 120° (160° for local networks), selection criteria (see Table 1) were developed for classifying an event location as being accurate to within 5 km (or 20 km, regionally) with 95% (or 90%) confidence ($GT5_{95\%}$ and $GT20_{90\%}$, respectively). However, because the criteria are based on the global average Pg/Pn crossover distance of 250 km, they may be unrepresentative of local velocity structure, which can potentially lead to phase identification errors.

In 2009, Bondár and McLaughlin modified the selection criteria using a 150 km Pg/Pb crossover to relocate over 90 GT0 reference events, in part to address the concern over phase identification errors (Table 1). A new network quality metric, ΔU, was introduced as a means of assessing the uniformity of station azimuthal coverage. This metric is similar to the Kolmogorov-Smirnov statistical test that can determine whether stations are uniformly radially distributed around a particular epicenter. Bondár and McLaughlin found that networks with values of ΔU less than 0.35 tend to provide GT5 candidates. As with the 2004 selection criteria, these modified criteria were developed using events recorded on a large number of local and regional recording stations with travel times reported in bulletins.

Using a local Pg/Pn crossover distance of 215 km, Boomer et al. (2010) developed EBGT criteria for the Kaapvaal Craton. Events with a primary azimuthal gap exceeding 202° yielded epicentral mislocations in excess of 40 km, considered to be obvious outliers. Due to the regional homogeneous crustal structure, the secondary gap as an additional constraint was rendered redundant. Unlike the regions used to develop the 2004 and 2009 criteria, the Kaapvaal Craton criteria were developed on a sparse network, with some of the larger mine-related events (e.g., GT0 events) recorded on 16 or fewer stations.

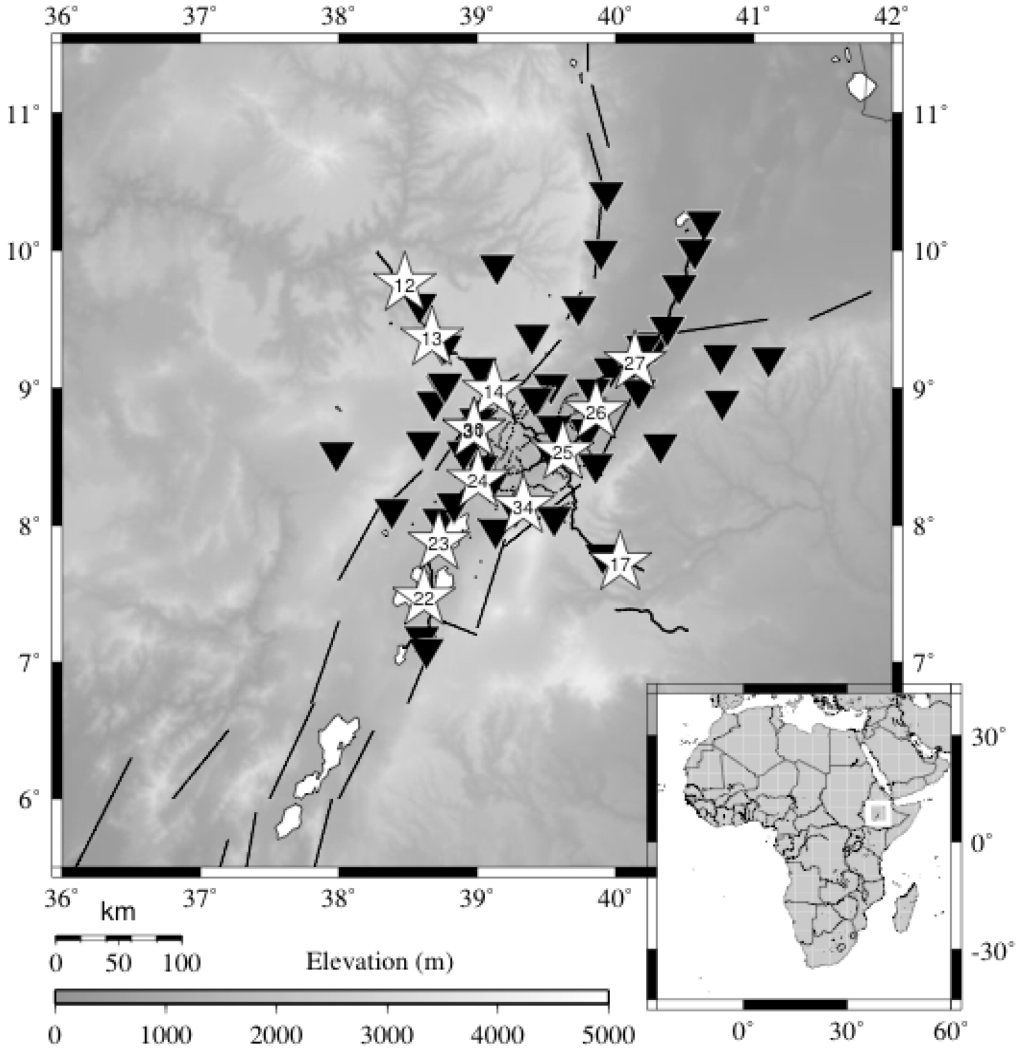


Figure 1. Station locations (inverted black triangles; small circles for the wide-angle profiles) for the 2001-2003 Ethiopia-Afar Geoscientific Lithospheric experiment (EAGLE) network. The stars show the locations of the four ground truth reference shots (shots 14, 24, 26 and 31) and nine verification shots (12, 13, 17, 22, 23, 25, 27, 30 and 34) used to develop and validate empirically based region-specific ground truth criteria for the Main Ethiopian Rift.

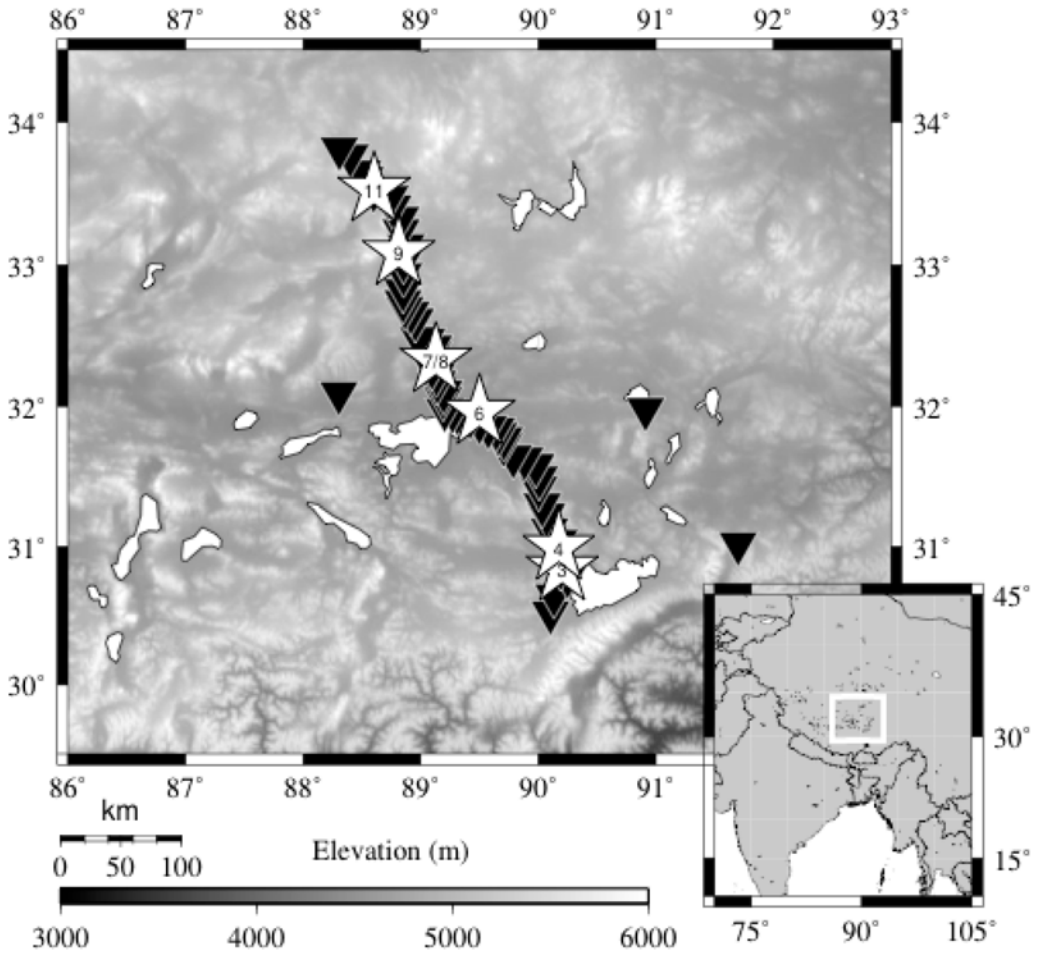


Figure 2. Station locations (inverted black triangles) for the 1997-1999 International Deep Profiling of Tibet and the Himalaya (INDEPTH) network. The stars show the locations of the four ground truth reference shots (shots 6, 7, 8 and 9) and three verification shots (shots 3, 4 and 11) used to develop and validate empirically based region-specific ground truth criteria for the Tibetan Plateau.

.

Table 1: Existing epicentral location accuracy criteria

Network	Distance Range (degrees)	Primary Azimuthal Gap	Secondary Azimuthal Gap	Number of stations within specified distance			GT level
				Between Pg/Pn crossover and 1000km	< Pg/Pn Crossover	minimal distance	
Local[a]	0°-2.5°	110°	160°		10	1 within 30km	$GT5_{95\%}$
Near Regional[a]	2.5°-10°		120°	10			$GT20_{90\%}$
Teleseismic[a]	28°-91°		120°				$GT25_{90\%}$
Kaapvaal EBGT[b]	0°-1.9°	202°			8	1 within 79 km	$GT3_{95\%}$
Network	**Distance Range (degrees)**	**Network Quality Metric ΔU**		**Between Pg/Pb or Pg/Pn crossover and 1000km**	**< Pg/Pn (< Pg/Pb) Crossover**	**< 10km**	**GT level**
Local[c]	0°-1.35°	< 0.35			5	1 within 10 km	$GT5_{95\%}$
Ethiopia EBGT[d]	0°-1.6°	< 0.43			8		$GT5_{95\%}$
Tibet EBGT[d]	0°-1.5°	< 0.45			8	1 within 65 km	$GT5_{95\%}$

Notes: [a]Bondár et al. 2004
[b]Boomer et al. 2010
[c]Bondár and McLaughlin, 2009
[d] This report

The re-sampling method often used in developing selection criteria (e.g. Bondár et al., 2004; Yang et al. 2004; Bondár and McLaughlin, 2009) is bootstrapping in which $k \leq n$ arrival times are sampled with replacement from the set of n available arrival times. Sampling with replacement is used to ensure independent samples, and, particularly when there are a large number of possible elements (e.g., arrival times), a large number of realizations can easily be achieved. The EBGT Kaapvaal Craton criteria were developed using a similar statistical re-sampling technique, the jackknife method. This approach considers all possible subsets of the $k \leq n$ arrival times, permitting the determination of criteria based on the number of recording stations.

Empirically Based Ground Truth Criteria for the Tibetan plateau

We have developed EBGT criteria for the Tibetan Plateau using data from shot points (SP) 6, 7, 8 and 9 which were recorded on up to 49 stations - 46 in the refraction profile and three cross profile (Figure 2). Hand-picked arrival times and station dependent velocity models were obtained and adapted from Zhao et al. (2001), respectively. The number of arrival times recorded per shot varied between a minimum of 18 and a maximum of 38, permitting the use of the bootstrap resampling method. Three bootstrap samples, each based on 10,000 realizations of n = 7, 8 or 9 arrival times, were analyzed. Networks are quantified based on a maximum and minimum epicentral distance, and the network quality metric, ΔU.

The maximum shot-station separation used in developing the criteria was ~160 km, which is well within the local Pg/Pn crossover distance. Thus, we cannot claim that the criteria are valid for epicentral distances extending to the Pg/Pn crossover distance. Rigorously, the criteria require the maximum epicentral distance to not exceed ~160 km and the minimum epicentral distance to be less than 65 km. Although the minimum epicentral distance constraint is unnecessary for constraining the epicentral location, relocations without a station within 65 km fail to constrain the depth. The empirical cumulative distribution function and scatterplot in Figure 3 demonstrate that the estimated mislocation error is less than 5km, with 95% confidence, when ΔU < 0.45 for events recorded on eight stations.

Under the same circumstances, the depth mislocation error is less than 8 km, and origin time error less than 0.8 seconds.

Three of the remaining shots in the Tibet dataset with charge sizes greater than 180 kg were used to successfully validate the criteria. Based on the criteria in Table 1, 23 and five new $GT5_{95\%}$ events have been extracted and relocated from the Langin et al. (2003) and ISC catalogues, respectively (see Table 2).

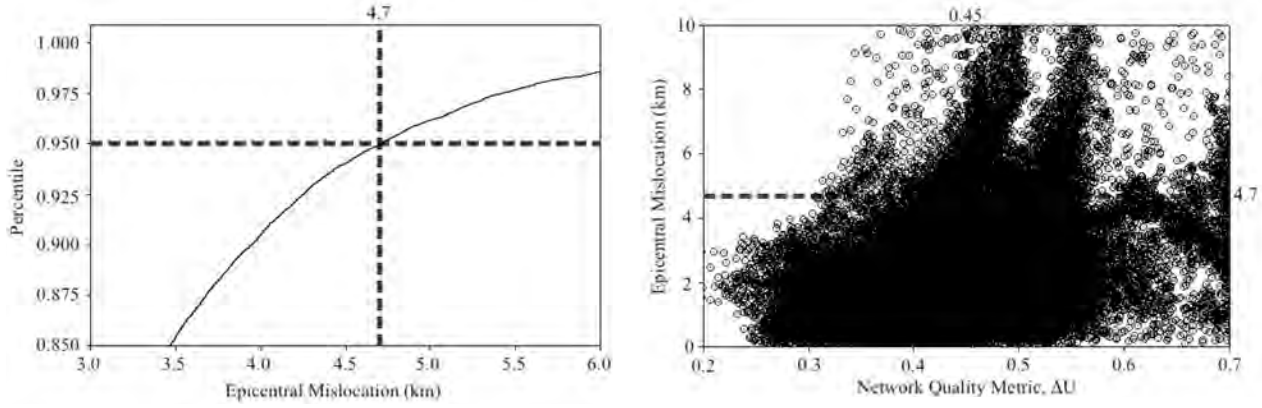


Figure 3. (Left) Empirical Cumulative Distribution Function demonstrates that the 95th percentile of epicentral mislocation is less than 5 km. (Right) The scatterplot of epicentral mislocation versus ΔU shows that a mislocation of less than 5 km corresponds to ΔU < 0.45 with 95% confidence.

Table 2: INDEPTH III events meeting the Tibetan plateau $EBGT5_{95\%}$ criteria

Date	Time	Lat	Lon	Depth	N	Dist	Gap	Mag	ΔU
10/06/1998	00:53:54	33.16	88.54	5	36	31.5	190	4.4	0.34
10/11/1998	21:11:01	33.20	88.57	11	36	25.4	188	4.3	0.40
10/11/1998	22:00:00	33.20	88.58	5	37	24.0	185	3.9	0.34
10/13/1998	04:59:29	33.15	88.51	8	38	34.7	157	4.5	0.35
03/18/1999	16:50:25	33.04	89.02	7	27	15.3	142	2.9	0.29
08/23/1998	14:04:15	32.19	89.49	31	44	30.2	147	2.8	0.29
09/04/1998	14:09:17	32.04	89.77	14	30	25.6	126	2.7	0.26
09/05/1998	07:26:17	32.19	89.76	5	33	40.9	136	2.6	0.28
09/13/1998	08:37:52	32.51	90.01	14	44	89.4	157	3.6	0.30
10/01/1998	20:07:45	32.09	89.54	5	39	19.4	120	2.9	0.23
10/17/1998	04:57:15	31.91	89.79	4	40	16.0	118	3.3	0.21
10/24/1998	10:26:28	31.83	89.69	6	28	4.6	174	2.8	0.29
11/08/1998	21:17:15	32.17	89.09	5	38	5.4	124	2.7	0.30
11/11/1998	21:11:28	32.23	89.54	5	36	36.6	130	3.1	0.25
11/13/1998	01:07:33	32.21	89.66	5	40	39.1	134	2.9	0.26
11/16/1998	20:52:35	32.31	89.61	14	39	45.8	138	2.9	0.26
11/19/1998	09:50:59	31.88	89.80	4	35	16.0	124	2.8	0.21
11/30/1998	02:58:57	32.21	89.92	6	31	52.1	143	2.7	0.31
12/23/1998	05:53:23	32.67	89.04	10	35	10.4	138	3.2	0.28
01/02/1999	10:19:16	32.19	89.20	5	37	5.8	114	3.2	0.26
01/03/1999	19:30:47	32.29	89.82	12	35	58.6	140	3.0	0.34
01/13/1999	14:43:09	32.29	89.56	9	37	41.1	129	3.1	0.20
02/05/1999	01:58:09	31.88	89.89	5	36	24.6	116	3.1	0.23
02/23/1999	23:39:43	32.29	89.90	24	36	60.7	148	2.9	0.32

Date	Time	Lat	Lon	Depth	N	Dist	Gap	Mag	ΔU
03/04/1999	17:25:31	32.07	89.26	5	39	6.9	109	3.5	0.25
03/24/1999	09:54:42	32.20	89.60	8	36	40.6	134	2.8	0.31
04/03/1999	21:10:09	32.09	89.56	11	33	25.3	121	2.7	0.26
05/17/1999	14:54:46	32.35	89.74	5	30	57.9	148	2.9	0.30

Empirically Based Ground Truth Criteria for the Main Ethiopian Rift

$EBGT5_{95\%}$ criteria have been developed for the Main Ethiopian Rift using four explosions (SP14, SP24, SP26, SP31) located centrally in the EAGLE array Figure 1. The shots were recorded on up to 32 EAGLE broadband stations and over 600 stations in the refraction lines within the Pg/Pn crossover distance. Three bootstrap samples for each shot, based on 10,000 realizations of n = 7, 8 or 9 arrival times from the refraction line stations only, were used to develop these criteria. Networks were quantified based on maximum epicentral distance and the network quality metric, ΔU.

The criteria obtained require that the maximum epicentral distance be 1.6 degrees or less, which is the local Pg/Pn crossover distance, and that ΔU < 0.43 (Table 1). Although all of the relocations have a minimum epicentral distance of 100 km or less, a minimum epicentral distance does not emerge from the data as a necessary criterion for a $GT5_{95\%}$ event. However, it may be that in the case of the Ethiopian Rift a required epicentral distance simply exceeds 100 km. Meanwhile, although a portion of the relocations failed to constrain event depths, these were eliminated under the network quality metric criterion.

The empirical cumulative distribution function and scatterplot in Figure 4 demonstrate that the estimated mislocation error is less than 5 km, with 95% confidence, when ΔU < 0.43. In addition, the depth mislocation error is less than 11 km, and origin time error less than 1.8 seconds under the same constraint. We verified the criteria using data from the four shots recorded on refraction line stations (that were not part of the broadband stations used in developing the criteria) along with data from nine other shots recorded on non-broadband stations.

Using the criteria, we have identified 10 events from the Ethiopian Broadband Seismic Network (Table 3) and 196 events from the EAGLE dataset that could potentially meet the $EBGT5_{95\%}$. The EAGLE candidate events are currently being tested and relocated.

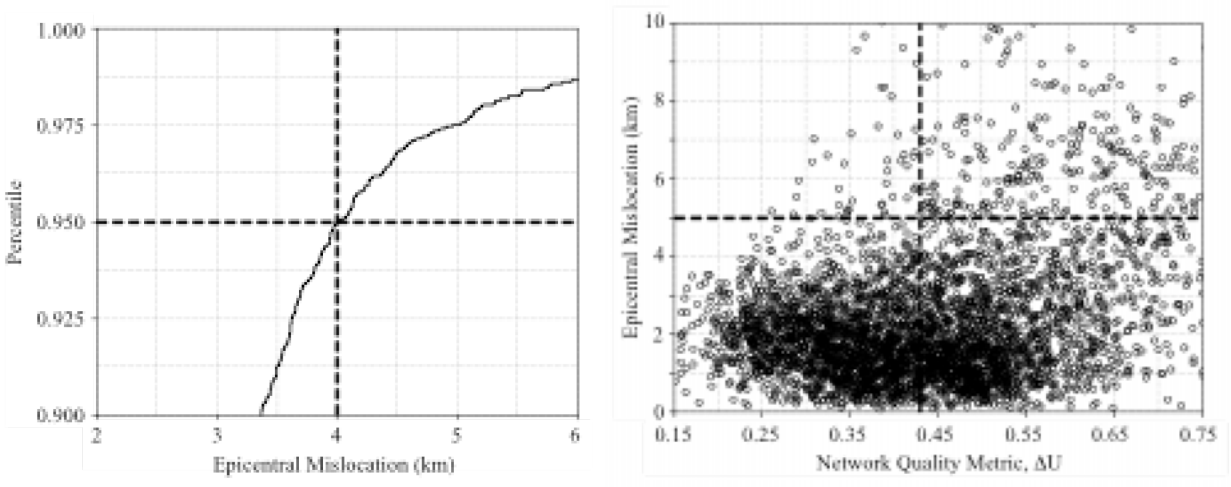


Figure 4. Ethiopian local $EBGT5_{95\%}$ criteria are based on the cumulative distribution function for epicentral mislocation (95^{th} percentile = 4 km) and a network quality metric value of ΔU < 0.43.

Table 3. Ethiopia Broadband Seismic Experiment events meeting the Ethiopia EBGT5$_{95\%}$ criteria

Date	Time	Lat.	Lon.	Dep.	N	Dist.	Gap	RMS	Mag	ΔU
5/12/2001	2:06:42	9.4984	39.7118	0.03	8	28	62	0.3295	2.8	0.13
5/23/2001	1:16:10	9.4611	39.4401	1.72	10	25	95	0.39	3.6	0.18
6/15/2001	0:19:24	8.3794	38.6859	35.92	7	44	136	3.6028	2.5	0.38
11/2/2001	23:04:25	9.4785	39.6956	5.75	8	28	82	0.2433	2.2	0.33
11/11/2001	21:05:23	9.5617	39.5127	0	9	12	73	5.1336	2.2	0.17
11/11/2001	22:32:43	9.462	39.6982	11.18	8	30	84	0.3925	3.1	0.14
11/11/2001	22:38:03	9.4443	39.7032	0.05	8	32	84	0.5243	3.8	0.13
11/11/2001	23:35:45	9.4705	39.716	0.1	7	31	83	0.7221	2.2	0.12
11/27/2001	21:35:37	9.4986	39.6886	17.36	9	26	66	0.7404	2.5	0.2
12/13/2001	2:14:40	9.4639	39.6881	1.89	8	29	85	0.4401	3.1	0.14

A basic premise of recent work in developing GT criteria is that network geometry influences event location, with greater coverage yielding more accurate locations. Developed criteria have a stated range of epicentral distances and a measure of azimuthal coverage, either in terms of azimuthal gap or the network quality metric. We are interested in describing network geometry in terms of both azimuthal coverage as well as the distribution of epicentral distances. This is an important aspect of developing local and regional criteria in areas with heterogeneous crustal structures; in an extreme case, a network could satisfy existing criteria by having adequate azimuthal coverage yet have all stations at the same epicentral distance (with the exception of one station within the stated minimal distance). Such a configuration may lead to unrepresentative arrival times for the region.

In addition, metrics based primarily on azimuthal coverage suffer when there is more than one station with the same azimuth, yet with different epicentral distances. This is especially problematic when analyzing data along a refraction line. In developing the local Tibet EBGT criteria, one event was recorded close to the center of the refraction line. Despite being recorded on almost all stations on the refraction line, many had the same azimuth. As a result, only 18 stations had unique azimuths. We are interested in spatial metrics that describe the two dimensional coverage of a network within the Pg/Pn crossover distance; early work using the bootstrap samples from Ethiopia have considered the sum of nearest neighbors and the area of the polygon formed by the network. Both measures capture the dispersion of network stations in ways that metrics based on azimuthal uniformity do not.

Figure 5 shows boxplots for the sum of nearest neighbors in a network, for bootstrap samples which meet EBGT5 criteria, those that do not, and for arrays generated to represent complete spatial randomness (CSR). Larger values of this metric indicate more disperse networks. Using the lowest 0.05 percentile from the CSR distribution to representing the most compact networks ($\Sigma NN<4$), 77% of the GT5 networks and 90% of the networks with GT > 5 km are more clustered than we would expect under CSR. While the physical placement of stations is not a spatial point process (e.g. physical constraints limit areas in which stations can be placed), this preliminary result suggests spatial methods may be able to discriminate between networks that are or are not likely to meet GT5 criteria.

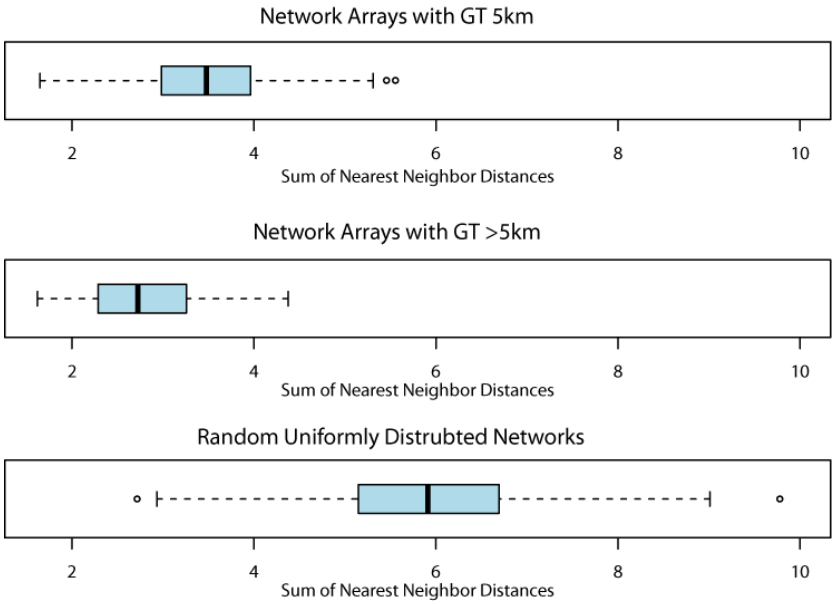


Figure 5. Early developments using a spatial metric to characterize networks indicate some ability to discriminate between networks that do and do not meet GT5 criteria.

To what degree are region-specific EBGT transferable to other regions?
As the complexity of geologic structure increases from craton to plateau to rift our criteria show increasing restrictions in the network quality metric. This motivates the question of whether, and if so to what degree, the regiona-specific EBGT criteria determined are transferrable to other regions. While assessing or comparing geological complexity across different regions is of course fraught with difficulty due to the fact that all regions are ultimately geologically unique, first order approximations may nonetheless be viable. A single calibration shot recorded on the Eastern Turkey Seismic Network (ETSE), providing a test case, is currently being analyzed.

Meanwhile, the Kaapvaal EBGT3$_{95\%}$ can potentially be applied other cratons. In particular, 61 from the Tanzanian Craton and 97 from the Saudi Arabian Network qualify as candidates for validation and relocation.

Comparison of Local Criteria
The local criteria for southern Africa, the Ethiopian Rift and the Tibetan plateau show that increasing geological complexity corresponds to increasingly restrictive criteria. Comparing the network quality metric, we have found that $\Delta U < 0.55$ corresponds to the local EBGT5$_{95\%}$ criteria in the Kaapvaal Craton. In Tibet and in the more complex Ethiopian Main Rift, values of the network quality metric of $\Delta U < 0.45$ and $\Delta U < 0.43$, respectively, correspond to local EBGT5$_{95\%}$ criteria. As the network quality metric ranges from 0 (uniform azimuthal coverage) to 1 (stations with the same azimuth), we observe that more uniform coverage is required in more complex regions. In addition, depth and origin time mislocation increase with geological complexity (Table 4).

Table 4. Comparison of local ground-truth criteria

Network	Distance Range (degrees)	Network Quality Metric ΔU	< Pg/Pn (< Pg/Pb) Crossover	Minimal Distance	Depth Mislocation	Origin time Mislocation	GT level
Local[c]	0°-1.35°	< 0.35	5	1 within 10 km			*GT*5$_{95\%}$
Kaapvaal EBGT[b]	0°-1.9°	< 0.55+	8		5.7km		*GT*3$_{95\%}$
Tibet EBGT[d]	0°-1.5°	< 0.45	8	1 within 65 km	8km	0.8s	*GT*5$_{95\%}$
Ethiopia EBGT[d]	0°-1.6°	< 0.43	8		11km	1.8s	*GT*5$_{95\%}$

CONCLUSIONS AND RECOMENDATIONS

We have developed $EBGT5_{95\%}$ criteria for the Main Ethiopia Rift and the Tibetan plateau. There are ten events from the Ethiopia Broadband Seismic Experiment meeting the appropriate criteria and an additional 196 potential events currently being relocated from the EAGLE dataset. 28 events from Tibet have been confirmed as $GT5_{95\%}$, relocated and are ready to be added to the NNSA knowledge database. Data from Kyrgystan and Eastern Turkey are being collated ready for determination of potential Ground Truth events.

The transferability of criteria to other regions is being assessed with the hope that 97 events recorded on the Saudi Arabian Plateau can be relocated and included in the database also. As criteria for regions with varying geological complexity are being developed, it is apparent that the azimuthal uniformity constraint needs to become more stringent as the geological complexity increases. In addition, it also appears than constraining depth and origin time becomes more difficult as geological complexity increases.

ACKNOWLEDGEMENTS

We thank K. Keranen for her assistance with EAGLE shot information, J. Mechie for INDEPTH III shot information, E. Sandvol for ETSE shot data and the Incorporated Research Institutions for Seismology Data Management Center (IRIS) for data access.

REFERENCES

Bondár, I., S. C. Myers, E. R. Engdahl and E. A. Bergman (2004). Epicenter accuracy based on seismic network criteria, *Geophys. J. Int.* **156**: 483–496.

Bondár, I, and K. L. McLaughlin (2009). A new ground truth data set for seismic studies, *Geophys. Res. Lett.* **80**, 465–472.

Boomer, K., R. Brazier, and A. Nyblade (2010). Empirically-based ground truth criteria for seismic events located using regional networks with application to southern Africa, *Bull. Seismol. Soc. Am.* **100**, 8–21.

Brazier R. A., Q. Miao, A. A. Nyblade, A. Ayele, and C. A. Langston (2008). Local magnitude scale for the Ethiopian Plateau, *Bull. Seismol. Soc. Am.* **98**, 2341–2348, doi: 10.1785/0120070266.

Dugda, M. T., A. A. Nyblade, J. Julia, C. A. Langston, C. J. Ammon, and S. Simiyu (2005). Crustal structure in Ethiopia and Kenya from receiver function analysis: Implications for rift development in eastern Africa, *J. Geophys. Res.*, **110,** B01303.

Keir, D., G.W. Stuart, A. Jackson and A. Ayele (2006). Local Earthquake Magnitude Scale and Seismicity rate for Ethiopia, *Bull. Seismol. Soc. Am.* **96,** 2221–2230.

Keranen K., S. Klemperer,R. Gloaguen, L. Asfaw, A. Ayele, C. Ebinger, T. Furman, S. Harder, G. Keller, G. Mackenzie, P. Maguire, and G. Stuart (2004). Three-dimensional seismic imaging of a protoridge axis in the Main Ethiopian Rift, *Geology (Boulder),* **32,** 949–952.

Wetenschapen, Proceedings Series A, 63: 38–47.

Langin, W.R., L.D. Brown, and E. A., Sandvol (2003). Seismicity of central Tibet from Project INDEPTH III seismic recordings, *Bull. Seismol. Soc. Am.* **93,** 2146–2159.

Maguire, P.K.H, and 15 other authors (2003). Geophysical project in Ethiopia studies continental breakup, *Eos, Trans. AGU* **84**, 337–343.

Maguire, P K H, Keller, G R; Klemperer, S L, Mackenzie, G D, Keranen, K; Harder, S, O'Reilly, B, Thybo, H, Asfaw, Laike M, Khan, M A, Amha, M. (2006). Crustal structure of the northern Main Ethiopian Rift from the EAGLE controlled-source survey: A snapshot of incipient lithospheric break-up, *Geological Society Special Publications* **259**, 269–291.

Yang, X., I. Bondár, J. Bhattacharyya, M. Ritzwoller, N. Shapiro, M. Antolik, G. Ekström, H. Israelsson, and K. McLaughlin (2004). Validation of regional and teleseismic travel-time models by re-locating ground-truth events, *Bull. Seismol. Soc. Am.* **94**, 897–919.

Zhao W., J. Mechie, L. Brown,J.Guo, S. Haines, T. Hearn, S. Klemperer, Y. Ma, R. Meissner, K. Nelson, J. Ni, P. Pananont, R. Rapine, A. Ross, and J. Saul (2001). Crustal Structure of central Tibet as derived from project INDEPTH wide-angle seismic data. *Geophys. J. Int.* **145**, 486–498.

REFINEMENT AND TESTING OF THE PROBABILISTIC EVENT DETECTION, ASSOCIATION, AND LOCATION ALGORITHM

Timothy J. Draelos[1], Sanford Ballard[1], Christopher J. Young[1], and Ronald A. Brogan[2]

Sandia National Laboratories[1] and ENSCO, Inc.[2]

Sponsored by the National Nuclear Security Administration

Award No. DE-AC04-94AL85000/SL12-SignalAnalysis-NDD02

ABSTRACT

We present results of testing of the latest version of our Probabilistic Event Detection, Association, and Location algorithm (PEDAL). As before, in our method, the Earth is discretized into a dense 3D grid of 383,753 nodes, extended to 4D by the addition of a time dimension. Given a set of seismic observations (arrival time, horizontal slowness, and azimuth), a 'fitness' value is calculated at each grid node, assuming that each observation was generated by a refracted P wave. The node with peak fitness value is accepted as a hypothetical seismic event location, subject to some peak criteria and minimal fitness value. Once we have identified the peak, we solve for the corresponding origin time and then associate individual arrivals with the event, considering many different phases.

In the new method, we have made several improvements: 1) we incorporate a prior probability of signal detection for each station; 2) we do association in two stages, P first, then later phases; 3) after the P phase association, we calculate an m_b and perform association with secondary phases based on magnitude, depth, and distance from event to station; 4) we use the SNL-LANL Salsa3D model to predict travel times for grid nodes that do not have sufficient data to define predictions empirically. We tested the new version on a two-day period of time that has been processed by the IDC and that have also been carefully examined by an analyst to identify all legitimate events. A sophisticated bulletin review algorithm is used to compare PEDAL results to both the automatically-generated IDC SEL3 event list, a product of the Global Associator (GA) software, and the analyst-reviewed LEB. We show that our latest version of PEDAL significantly improves our processing results.

OBJECTIVES

Inferring possible nuclear events from the set of signals recorded on a global network of stations, i.e., "association", is perhaps the most formidable routine data processing task for a nuclear explosion monitoring system. Even after decades of algorithm development and tuning, false event rates from automated event association systems are typically about 50%, and about 10% additional legitimate events are missed (time-consuming human analysis is required to achieve excellent results). This is because the problem is ill-posed:

- Neither the locations nor number of sources are known.
- The distribution and numbers of sensors is not optimal.
- Characteristics of signals change with source location and distance. Consequently, signals recorded at one station for different events may be more similar to each other whereas signals from the same event recorded at different stations may be less similar to each other.

The objective of this work is the refinement of the Probabilistic Event Detection, Association, and Location algorithm (PEDAL), developed to address the identification of seismic events from a stream of monitoring station observations (detections and corresponding feature measurements). Generalized Association, the current seismic event association technology in use by the Comprehensive Nuclear-Test-Ban Treaty Organization (CTBTO) for their International Data Center (IDC), is almost 15 years old (Le Bras et al. 1994), predating some important innovations in computer software and hardware. While the quality of the IDC automatically produced bulletin (SEL3) has improved over the past decade, there is still significant room for improvement, suggesting that a new approach is warranted.

PEDAL exploits modern computational resources and many years of historical data (observables) for known sources to address the automated association problem in a new manner. A set of observables readily available from IDC database tables, such as arrival time, slowness, azimuth, and their uncertainties (deltim, delslo, and delaz) from all monitoring stations over a window of time (e.g., 33 minutes) can be combined in elemental and differential form to create a global map representing all source events occurring in the specified time window. Improved travel time predictions via Salsa3D (Begnaud et al., 2012) and a priori probabilities of stations detecting events are used in the new PEDAL method. Estimation of event magnitude is used with prior probabilities of stations detecting primary and secondary phases from events at various depths in the association step. Finally, we utilize a bulletin comparison tool to evaluate the performance of PEDAL on a contiguous set of multiday events. These improvements to PEDAL are of great importance because accurately locating a seismic event in 3D space (latitude, longitude, and depth) is a key step in identifying nuclear explosions.

RESEARCH ACCOMPLISHED

Introduction

PEDAL provides a new approach to the problem of associating isolated seismic observations from a network of stations into a list of hypothesized seismic events consistent with those observations. In our method, the Earth is discretized into a dense 3D grid of nodes that spans the globe from the surface down to the maximum depth at which earthquakes are likely to occur. The grid is extended to 4D by the addition of a time dimension. Given a set of seismic observations within a specified time window, a network ‘fitness’ value is calculated at each grid node by summing the station-specific conditional fitnesses. Assuming that each observation was generated by a refracted P wave, these fitness values are proportional to the conditional probabilities that each observation was generated by a seismic event at the grid node. The node with the highest fitness value is accepted as a hypothetical seismic event location, subject to some minimal fitness value, and all seismic arrivals that are consistent with that event are associated with it. First, P phases are associated from which event magnitude is estimated. Then, the assumption that the arrival was a direct P arrival is relaxed and many different phases are considered based on event magnitude, depth, and distance from an arrival’s station. Once an arrival is associated with an event, it is removed from further consideration. While there are still unassociated arrivals, the search is repeated to find other hypothetical seismic events until no more seismic events are identified that satisfy the minimum fitness criteria.

The PEDAL Process

The input to PEDAL is a set of detections, called the arrival batch, within a 33-minute time interval (23 minutes to account for the travel time of a first-P phase between an event and a station as far away as possible plus a fixed PEDAL time step, which is 10 minutes for the purposes of this paper). The output of PEDAL is a bulletin of events with location and magnitude information and associated phases caused by these events. Depending on the origin time of an event, it will reside in one of the following time windows and be given a corresponding label. Refer to Figure 1 for the following discussion.

1. *Preliminary Origins* – This time window includes origins that have been detected by virtue of peak spatial fitness, but are preliminary because their origin times are greater than t-23 minutes or their sets of associated arrivals do not pass the trusted origin criteria given below. Preliminary origins will be labeled as such, but their associated arrivals will be returned to the arrival list when PEDAL is finished with processing the current time interval so that this origin can be detected again in the next time interval, potentially with a richer set of arrivals contributing to its detection.

2. *Trusted Origins* – This time window includes origins that are considered trusted because its set of arrivals passes the trusted origin criteria, but their origin times are such that additional arrivals of secondary phases associated with them could exist in the future (next time interval). Note that trusted origins cannot have any more first-P arrivals associated with them.

3. *Completed Origins* – This time window includes origins that are considered complete and final because all possible arrivals that could be associated with these origins have been seen by virtue of their origin times and the travel time of the latest arriving expected secondary phases (T_{Smax}).

For our testing, PEDAL operates on IDCX arrivals in the 33-minute Spatial Fitness and Association Arrival Window, from 148 primary and secondary IMS seismic stations. For the spatial fitness calculation, all detections are assumed to be first-P. Following identification of the location of a hypothetical event (i.e. a fitness peak), the origin time is computed using first-P predictions and arrivals in the Spatial Fitness and Association Arrival Window. At this point, association of all arrivals is performed on the hypothetical event. All associated arrivals are removed from the arrival list and a search for new hypothetical events is repeated until no more seismic events are identified that satisfy the minimum fitness criteria.

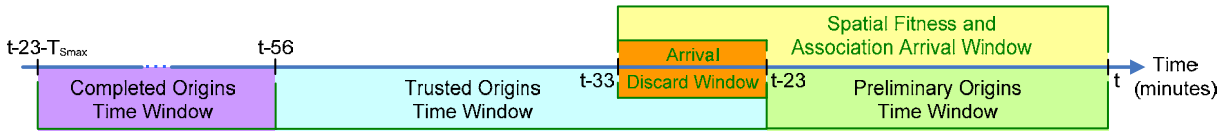


Figure 1. PEDAL time windows.

As we discussed above, once all hypothetical events have been identified for the current time window, a final association step is performed based on arrival time fitness alone. Each remaining unassociated arrival is fitted with each hypothetical origin and the arrival is associated with the origin that results in the highest fitness, assuming a minimal fitness threshold. At this point, we are ready to move on to the next time interval. First, however, we must add to the final event bulletin events that satisfy the following criteria.

Trusted Origin Criteria: Test each hypothetical origin against the following criteria, in order:

- *Has at least one of its associated arrivals in the Discard Window*. This indicates that the event cannot have additional P arrivals. If there is not at least one associated arrival in the Discard Window, then the detected origin is discarded. This event will likely get formed again in the next processing interval.
- *Has at least two associated arrivals* (as a result of the previous step, at least one of them will be in the Discard Window). This test insures that all events must have more than one associated arrival. If so, then add the origin to the permanent set of origins.

Arrivals associated with origins that do not satisfy the criteria are placed back into the input arrival batch to be processed in the next time interval or permanently stored as unassociated arrivals, depending on the arrival times. The entire iterative PEDAL process is depicted in a flowchart in Figure 2.

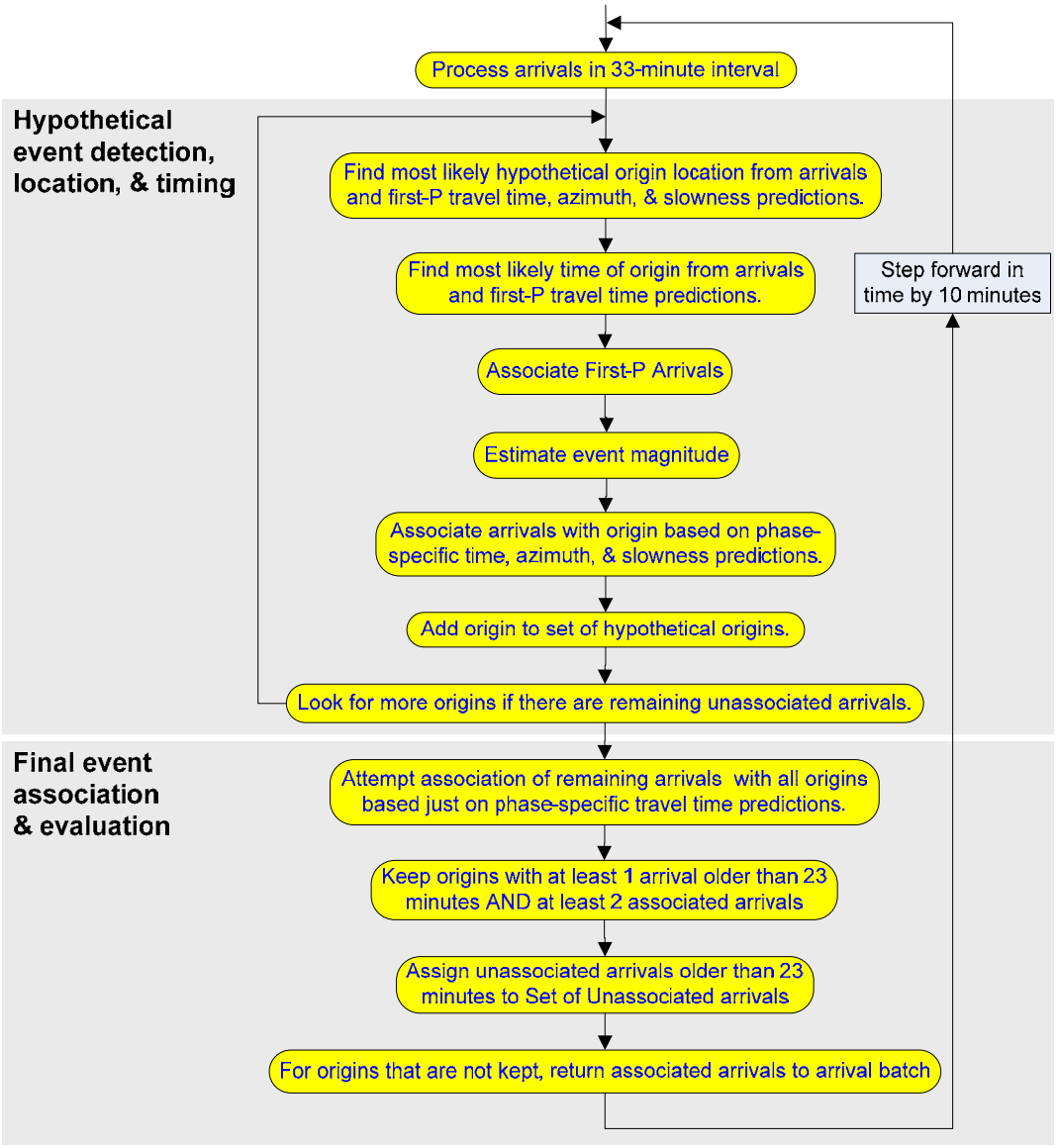


Figure 2. PEDAL flowchart.

PEDAL Fitness Formulas

PEDAL uses the notion of fitness in three ways to determine the best match with a set of arrivals:

- Spatial Fitness for the detection of events in 3-dimensional space,
- Temporal Fitness for the determination of origin time, and
- Association Fitness for association of an arrival phase with an origin.

Given each arrival A_i from station S_i that includes observations (attributes) of arrival time (T_i.), azimuth (az_i), horizontal slowness (sh_i), and their corresponding measurement uncertainties $deltim_i$, $delaz_i$, and $delslo_i$., the location of the Earth grid node ω, event origin time T_o, and phase label of the arrival are determined from the largest fitness values.

Hypothetical events are located by identifying the largest "fitness" value calculated for each of the nodes in the PEDAL Earth grid. Consider an arbitrary grid node ω and event origin time T_o and a single arrival A_i, from station S_i.The conditional probability that A_i was generated by a seismic event, E_{ω,T_0}, which occurred at (ω, T_0), is given by

$$F(A_i \mid E_\omega) = \exp\left[-\frac{(T_i - T_0 - p_{t,i,\omega})^2}{\varepsilon_{t,i,\omega}^2 + deltim_i^2} - \frac{(az_i - p_{az,i,\omega})^2}{\varepsilon_{az,i,\omega}^2 + delaz_i^2} - \frac{(sh_i - p_{sh,i,\omega})^2}{\varepsilon_{sh,i,\omega}^2 + delslo_i^2} \right] \quad (1)$$

where $p_{t,i,\omega}$, $p_{az,i,\omega}$ and $p_{sh,i,\omega}$ are the expected travel time, azimuth and horizontal slowness for an event at ω, and $\varepsilon_{t,i,\omega}$, $\varepsilon_{az,i,\omega}$, and $\varepsilon_{sh,i,\omega}$, are tolerance values. Figure 3 shows the implied Gaussian distribution associated with each attribute, which are used to calculate likelihoods. The overall likelihood is a product of the likelihoods for travel time, azimuth, and slowness, so the value is controlled by the smallest individual attribute value.

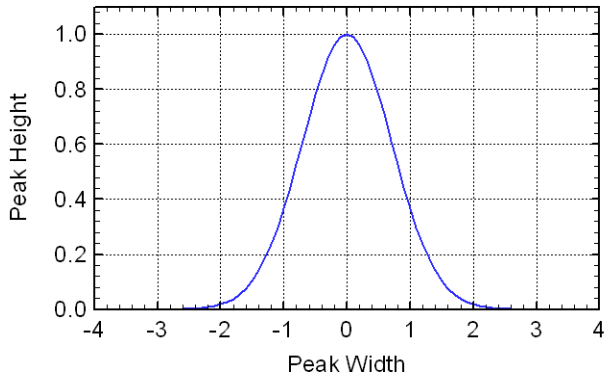


Figure 3. General Gaussian attribute distribution with σ = 1.

Spatial Fitness using Pairs of Arrivals

For computational efficiency, PEDAL uses pairs of arrivals to compute the spatial fitness values at each grid node. With this formulation, it is only necessary to search for a peak in 3D space (latitude, longitude, depth) rather than 4D space (latitude, longitude, depth, time). For all events E_ω, the differential time ($T_i - T_j$) observed at two stations S_i and S_j is independent of event origin time. So the joint fitness of any two arrivals, i and j, is

$$F(A_i \cap A_j \mid E_\omega) = \mathrm{P}(\mathrm{d}_{s_i} \mid E_\omega) \times \mathrm{P}(\mathrm{d}_{s_j} \mid E_\omega) \times \exp\left[\begin{array}{l} -\dfrac{\left((T_i - T_j) - (p_{t,s_i,\omega} - p_{t,s_j,\omega})\right)^2}{\varepsilon_{t,s_i,\omega}^2 + \varepsilon_{t,s_j,\omega}^2 + deltim_i^2 + deltim_j^2} \\ -\left(\dfrac{az_i - p_{az,s_i,\omega}}{\varepsilon_{az,s_i,\omega} + delaz_i} \right)^2 - \left(\dfrac{az_j - p_{az,s_j,\omega}}{\varepsilon_{az,s_j,\omega} + delaz_j} \right)^2 \\ -\left(\dfrac{sh_i - p_{sh,s_i,\omega}}{\varepsilon_{sh,s_i,\omega} + delslo_i} \right)^2 - \left(\dfrac{sh_j - p_{sh,s_j,\omega}}{\varepsilon_{sh,s_j,\omega} + delslo_j} \right)^2 \end{array} \right]. \quad (2)$$

Note that we have added in conditional probability of detection terms for each station. Also, our tolerance values (variances) in the denominators of the exponential terms are a combination of terms for uncertainty of the predicted (modeled) values as well as the uncertainty associated with each measurement. Now we sum the conditional fitnesses of all pairs of arrivals in a specified time interval (33 minutes = 23 minutes for first-P travel time + 10 minute time step)

$$F_\omega = \sum_{i=1}^{NA-1} \sum_{j=i+1}^{NA} F(A_i \cap A_j \mid E_\omega) \quad (3)$$

and search 3D grid space for the point with the highest F_W. We sum the fitnesses rather than multiplying them because we are treating all arrivals as first P. In almost any typical time window there will be arrivals that violate this assumption (i.e. noise detections and/or secondary phase detections) and hence will have very low fitness scores. Such low fitness scores would effectively zero out a peak were a product used, but there is no such problem if a summation is used instead. Note that if there are arrivals from more than one event in the time interval (not uncommon for a global monitoring system), then there will be multiple peaks in the 3D grid space as illustrated in Figure 4. Our goal at this stage is to find the overall highest peak, i.e. the event with the most arrivals.

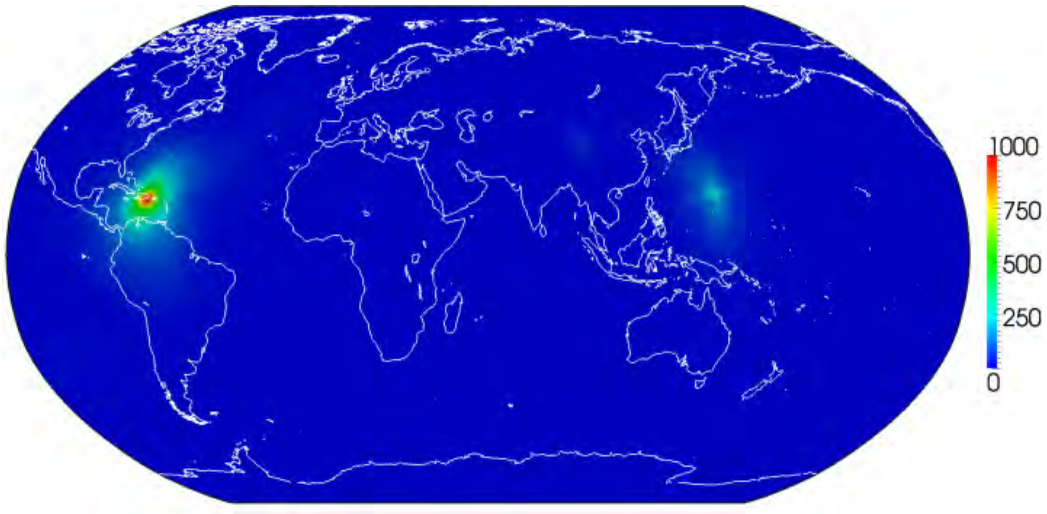


Figure 4. Spatial fitness map representing the spatial fitness value of each grid node. The peaks indicate locations of likely origins (spatial fitness is unitless—refer to Equations 2 and 3).

Temporal Fitness

Once the overall peak has been found, the next step in PEDAL is to search the time axis for an origin time, T_0, with maximum temporal fitness.

$$F_{\mathrm{W},\mathrm{T}_0} = \sum_{i=1}^{NA} \mathrm{P}(\mathrm{d}_{\mathrm{s}_i} \mid E_{\mathrm{W}}) \times \exp\left[-\frac{\left((T_i - T_0) - p_{t,s_i,\mathrm{W}}\right)^2}{\varepsilon^2_{t,s_i,\mathrm{W}} + deltim_i^2} - \left(\frac{az_i - p_{az,s_i,\mathrm{W}}}{\varepsilon_{az,s_i,\mathrm{W}} + delaz_i^2} \right)^2 - \left(\frac{sh_i - p_{sh,s_i,\mathrm{W}}}{\varepsilon_{sh,s_i,\mathrm{W}} + delslo_i^2} \right)^2 \right] \quad (4)$$

Depth phases from an event produce an additional peak in the temporal fitness curve, so we use the first large peak as the location of origin time. Thus, we have identified both the spatial and temporal position of an event in our time interval.

Association Fitness

After an event, $O_{\mathrm{W},To}$, is detected, located, and its origin time established, the arrivals that this event generated are identified and associated with the event. Given a detected event at location W and origin time T_o, we associate arrivals with $O_{\mathrm{W},To}$ using phase-specific predictions and tolerance values.

$$F_{ph,\mathrm{W},\mathrm{T}_0} = \mathrm{P}(ph_i \mid \mathrm{m}_\mathrm{b}, \mathrm{depth}, \Delta_{\mathrm{s}_i,\mathrm{W}}) \times \sum_{i=1}^{NA} \exp\left[-\frac{\left((T_i - T_0) - p_{t,\mathrm{s}_i,\mathrm{W},ph}\right)^2}{\varepsilon^2_{t,\mathrm{s}_i,\mathrm{W},ph} + deltim_i^2} - \left(\frac{az_i - p_{az,\mathrm{s}_i,\mathrm{W},ph}}{\varepsilon_{az,\mathrm{s}_i,\mathrm{W},ph} + delaz_i^2} \right)^2 - \left(\frac{sh_i - p_{sh,\mathrm{s}_i,\mathrm{W},ph}}{\varepsilon_{sh,\mathrm{s}_i,\mathrm{W},ph} + delslo_i^2} \right)^2 \right] \quad (5)$$

For each unassociated arrival in the current time window, we find the phase, *ph*, for which F_{ph,W,T_0} is greatest. If F_{ph,W,T_0} is greater than an established threshold, then we associate the arrival with O_{W,T_0} and remove the arrival from the window. Once all the appropriate arrivals have been associated with the current event, we recalculate the fitness for the 3D grid with the remaining arrivals and look for another peak. The process of identifying events and associating arrivals based on travel time, azimuth, and slowness continues until there are less than two arrivals in the window or the peak spatial fitness is less than an established threshold.

At this point, one final association step is performed, based solely on travel time, in an attempt to sweep up any remaining arrivals that can be associated with our events. For each unassociated arrival, the fitness value is computed for each detected event and, assuming the highest fitness value is greater than an established threshold, the arrival is associated with the event having the highest fitness.

$$F_{ph,\mathrm{W},T_O} = \sum_{i=1}^{NA} \exp\left[-\frac{\left((T_i - T_O) - p_{t,i,\mathrm{W},ph}\right)^2}{\varepsilon^2_{t,i,\mathrm{W},ph}} \right] \tag{6}$$

Data Structures

Several data structures are utilized during PEDAL operation to identify event locations and origin times and label phases with detected events.

- **Predictions** – PEDAL uses predictions of travel time, horizontal slowness, azimuth, and respective uncertainties in its fitness formulas. For spatial fitness, prediction of the most likely first-P phase originating at each grid node and traveling to each station is first modeled with Salsa3D for travel time and AK135 for slowness and azimuth and then adjusted (where possible) with statistics gathered from historical data. The prediction values are computed in advance and used by PEDAL during operation. Predictions of other phases used in association are computed in real time because they are only needed for the later phase association step, which happens much less frequently and doesn't have the same performance requirement.
- **Probability of Event Detection** – The probability of detecting a first-P Phase from an event at each station is used in the spatial and temporal fitness calculations as a way to identify "hot stations".
- **Magnitude Table** – the Veith-Clawson magnitude formula is used to estimate the magnitude of an event once first-P phases have been associated,
- $$m_b = \frac{1}{NP} \sum_{i=1}^{NP} \left(\log_{10}\left[-\frac{amp_i}{period_i} \right] + Attenuation(dist_i, depth_i) \right) \tag{7}$$

  where the amplitude, period, distance from station to event, and depth of the event from all NP associated first-P phases are used.
- **Probability of Phase Detection** – Historical data is used to establish the probability of each station detecting each phase from an event within 10˚ distance bands, three different depth ranges (depth < 100 km, 100 < depth ≤ 350 km, and depth > 350 km), and three different magnitude ranges (m_b < 4.2, 4.2 < m_b ≤ 5.6, and m_b > 5.6).

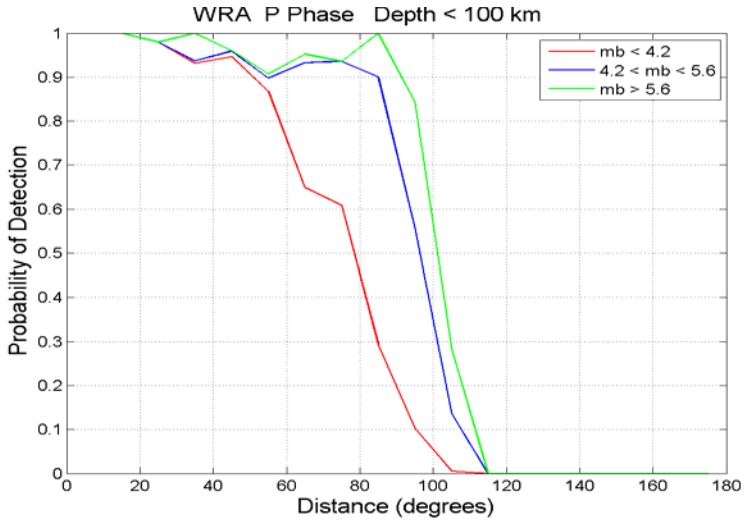


Figure 5. The probability of station WRA detecting a P phase.

Computational Issues

The calculation of the spatial fitness value for each of the 383,753 grid nodes is the most expensive operation in PEDAL. However, each grid node's calculation is independent of all the others, so the problem is fully parallelizable. Each node uses the same set of arrivals in its computation to compute spatial fitness, which is an $O(n^2)$ calculation in the number of arrivals. For $n = 500$, the calculation involves evaluation of the exponential function 47 billion times. Recall that PEDAL performs the spatial fitness calculation in three dimensions followed be a temporal fitness calculation in one dimension. Calculation of fitness in four dimensions over a 70 minute window with 0.1 second time steps would require the evaluation of the exponential function 2 quadrillion times, hence our preference for considering pairs of arrivals. Figure 6 shows the extreme difference in computational cost between sequential and parallel processing of the spatial fitness function, where Graphics Processing Units (GPUs) were used to perform the task. Of course many desktop computers can perform parallel processing as well and have some advantages over GPUs because of their increased memory capacity and utilization.

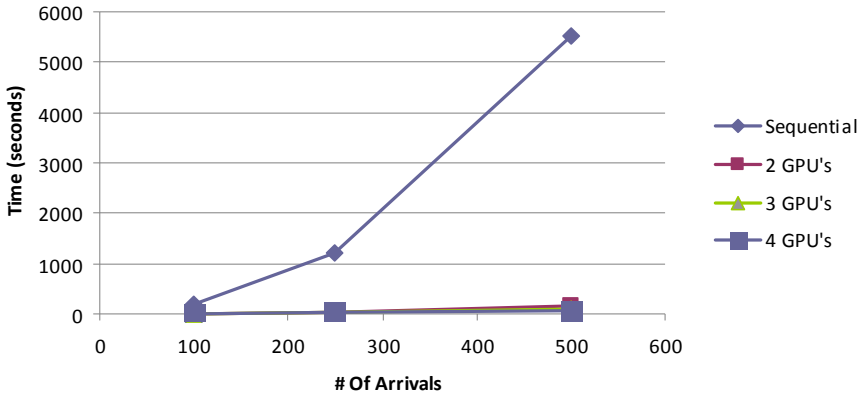


Figure 6. Sequential processing vs. Parallel processing of PEDAL spatial fitness calculation.

Results

Our lastest version of PEDAL was evaluated on a two-day window of IDCX arrivals from May 4-5, 2010. The LEB tables within that time frame were augmented with 25 additional valid events via expert analyst review to create a very high quality and complete ground truth review bulletin. The results are shown in Figures 7 and 8. The maps show PEDAL and SEL3 results with respect to the augmented LEB bulletin.

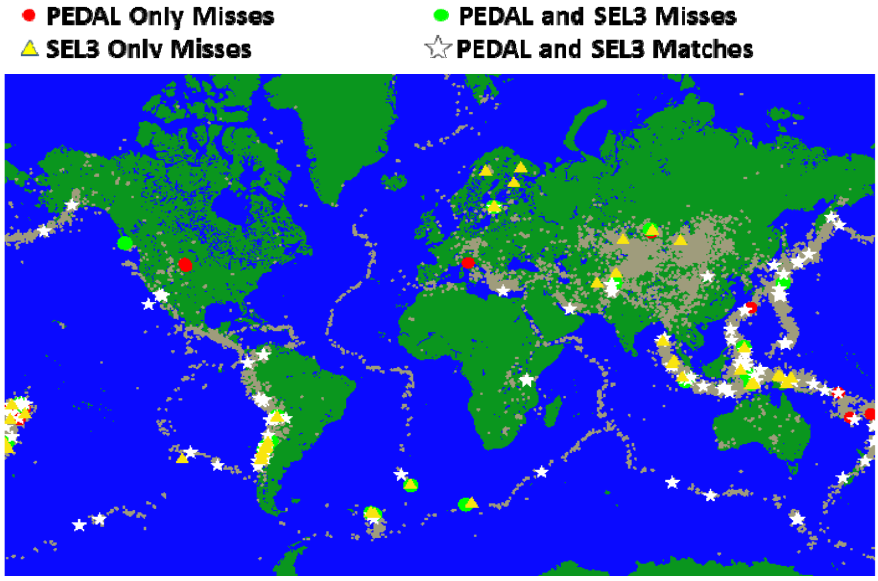


Figure 7. Events Missed by PEDAL and GA.

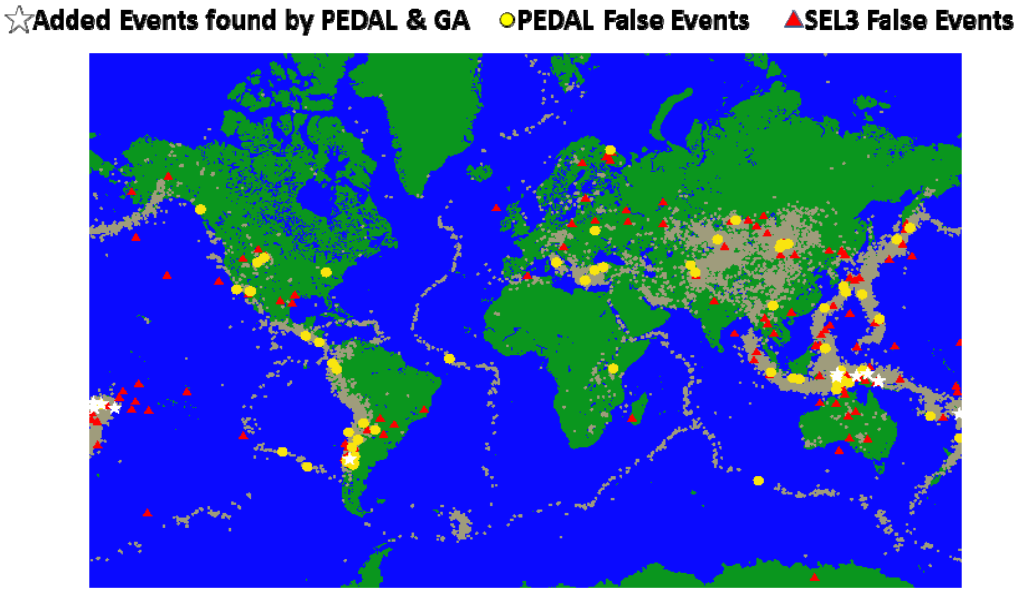


Figure 8. False Events Detected by PEDAL and GA.

Bulletin Comparison

Analyzing the output of PEDAL, an event bulletin, is challenging. We use an event commonality metric (Figure 9, Table 1) to compare a bulletin generated by an automated system, either PEDAL or GA, to a reference bulletin (LEB plus events added by our expert analyst review). The Event Commonality Score (ECS) between an automated event E_{AUTO} and the reference event E_{REF} is a function of the location and association differences of the events. The higher the ECS, the better the match between two events.

ECS = Location Difference Factor + False Association Factor + Missed Association Factor

Location Difference Factor = $\exp(-(d / A)^2)$,

where d = distance in km between two events and A = distance scaling factor (e.g., 1500 km).

False Association Factor = a_s / a_{AUTO}

a_s = # shared associations between the events

a_{AUTO} = total # associations in E_{AUTO}

Missed Association Factor = ta_s / ta_{REF}

ta_s = # shared time-defining associations

ta_{REF} = # time-defining associations in E_{REF}

Event Types

Each event in the automated bulletin (B_{AUTO}) is assigned a category based on its commonality with events in the Reference Bulletin (B_{REF}).

- Valid: best PEDAL event with ECS > 0.4
- Split: additional PEDAL events sharing arrivals with the same reference event
- Merged: automated events having ECS > 0.4 with multiple reference events
- False: ECS < 0.4
- Events that share no associations with B_{REF} have ECS = 0
- Missed: Events in B_{REF} with no match in B_{AUTO}

Table 1. Event commonality statistics for two-day test interval, PEDAL vs. GA.

	PEDAL		GA	
Event Type	**# Events via ECS**	**# Events via Analyst Review**	**# Events via ECS**	**# Events via Analyst Review**
Valid	137	179	137	160
Split	29		14	
False/Split	19		17	
False	112		108	
Average ECS	0.38		0.44	
Missed	19	29	18	42

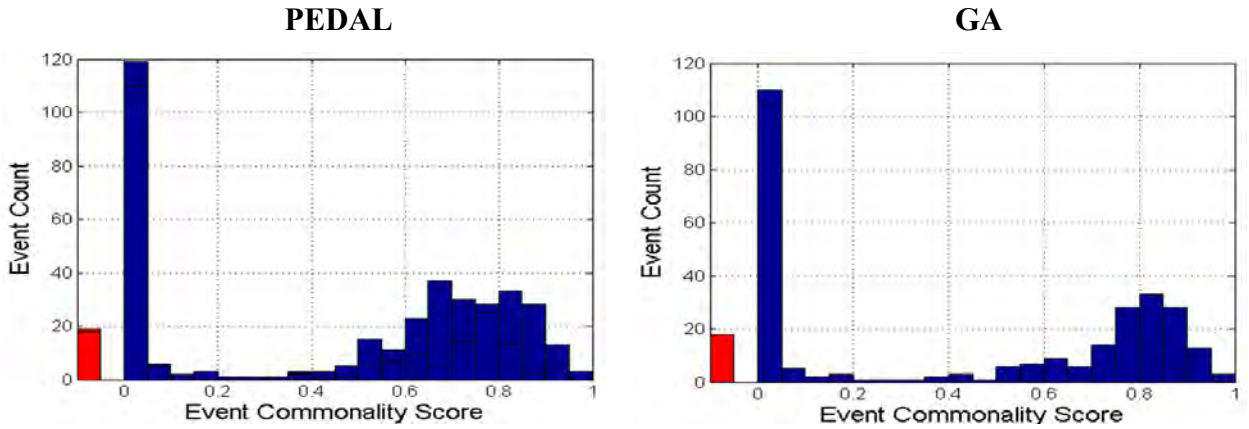


Figure 9. Event commonality scores for two-day test interval, PEDAL vs. GA.

CONCLUSIONS AND RECOMMENDATIONS

PEDAL continues to show promise in detecting events and associating phases as compared to GA. Improvements include the use of prior probability of event and phase detection at each station and the use of the SNL-LANL Salsa3D model to predict travel times. Testing on a two-day period of IDCX arrivals shows performance superior to GA in many ways. The focus of future work is integration of waveform correlation with PEDAL, improvement of a bulletin comparison metric, optimizing PEDAL parameters, and evaluation on a 30-day period of time.

REFERENCES

Le Bras, R., H. Swanger, T. Sereno, G. Beall, R. Jenkins, W. Nagy, and A. Henson (1994). Global Association Final Report, SAIC Technical Report SAIC-94/1155.

Begnaud, M., S. Ballard, C. Young, J. Hipp, A. Encarnacao, W. Phillips, E. Chael, and C. Rowe1 (2012). Validating a global 3D P-velocity model of the Earth's crust and mantle for improved event location, these Proceedings.

MODEL-BASED CORRECTIONS TO OBSERVED BACK AZIMUTH AND SLOWNESS OBSERVATIONS FROM A DIPPING MOHOROVICIC DISCONTINUITY

Megan P. Flanagan, Stephen C. Myers, and Nathan A. Simmons

Lawrence Livermore National Laboratory

Sponsored by the National Nuclear Security Administration

DE-AC52-07NA27344/LL12-SignalAnalysis-NDD02

ABSTRACT

Back azimuth and slowness anomalies observed at seismic arrays can be used to constrain local and distant structural and propagation effects in the Earth. Observations of large systematic deviations in both azimuth and slowness measured for several *P* phases (i.e., *Pg, Pn, P, PKP*) recorded at several IMS arrays show a characteristic sinusoidal pattern when plotted as a function of theoretical back azimuth. These deviations are often interpreted as the affect of the wavefield being systematically bent by refraction from a dipping velocity structure beneath the array, most likely a dipping Mohorovičić discontinuity (Moho).

We develop a model-based technique that simultaneously fits back azimuth and slowness observations with a ray-based prediction that incorporates a dipping layer defined by its strike and dip. Because the azimuth and slowness deviations both vary as a function of true azimuth, fitting both residuals jointly will give a more consistent calibration for the array. The technique is used to fit over 9900 observations at CMAR from a global distribution of well-located seismic events.

Under the assumption that the dipping layer is the Moho with mantle velocity 8.04 km/sec and crustal velocity 6.2 km/sec, we estimate that Moho strike and dip under the CMAR array are 192.6° and 18.3°, respectively. When the trend of the Moho is removed from the back azimuth and slowness residuals, both the sinuous trend and variations with predicted slowness are mitigated. While a dipping interface model does not account for all of the discrepancy between observed and predicted back azimuth and slowness anomalies, and additional calibration whether empirical or model-based should be pursued, this technique is a good first step in the calibration procedure for arrays exhibiting sinusoidal residual trends.

OBJECTIVES

The goal of this project is to test the robustness of a ray-based prediction of azimuth and slowness anomalies to fit a dipping Moho geometry beneath an array. To date the modeling of such anomalies has been simplified to removing a sinusoidal-fit function from the back azimuth and slowness residuals separately. This approach does not properly account for the effect of variable slowness at a given back azimuth. Here we present a more complete model approach that simultaneously fits back azimuth and slowness observations with a ray-based prediction that incorporates a dipping Moho. Because the azimuth and slowness deviations both vary as a function of true azimuth, fitting both residuals jointly will give a more consistent calibration for the array.

RESEARCH ACCOMPLISHED

Seismic array data provide an advantage over single station data for monitoring purposes because they allow for the additional measurement of the vector velocity of an incident wave front. Specifically, the back azimuth and slowness may be determined as the seismic wavefronts sweep across the array of sensors. The back azimuth and slowness parameters are commonly used to distinguish between different seismic phases, associate arrivals to an event, and can even provide needed constraints on event location when an event is recorded at just one or two stations. Since their inception, seismic arrays have been used for both monitoring as well as numerous studies of Earth structure (see Rost and Thomas [2002] for an excellent review). However, to use arrays effectively they need to be calibrated to account for local structural effects (e.g., Ringdal and Husebye, 1982; Ram and Yadav, 1984; Koch and Kradolfer, 1997; Tibuleac and Herrin, 2001; Bondar et al. 1999; Lindquist et al., 2007; Tibuleac and Stoujkova, 2009).

For Earth models with spherically symmetric velocity structure, the great-circle path from the event to the station is used to predict back azimuth, and theoretical ray parameter is used to predict slowness. Empirically, back azimuth and slowness measurements are often observed to deviate significantly from theoretical predictions, and most notably they can show a sinusoidal azimuthal dependence. Such a pattern suggests that the ray paths have been systematically bent by refraction from a dipping velocity structure beneath the array, and the Moho is a likely candidate (Figure 1). The functional relationship between the Moho strike ϕ and dip δ angles and the sinusoidal pattern of back azimuth and slowness residuals was derived by Niazi (1966) and subsequently used in several array calibration studies (e.g., Otsuka, 1966a, 1966b; Greenfield and Sheppard, 1969; Havskov and Kanesewich, 1978; Koch and Kraundoffer, 1997; Tibuleac and Herrin, 1997; Schweitzer, 2001; Lindquist et al., 2007; Tibuleac and Stroujkova, 2009).

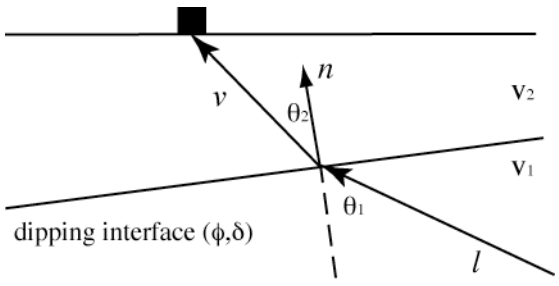


Figure 1. Geometry of the incident and refracted wavefronts with respect to a dipping interface with a specified orientation (defined by ϕ, δ). Note that the illustration is simplified to 2 dimensions, whereas the actual problem is 3 dimensional. *l* is the directional vector of the incident beam (determined by theoretical back azimuth and slowness), *v* is the directional vector of the refracted beam, *n* is the normal vector to the dipping-Moho plane (using ϕ and δ), θ_1 is the angle of incidence, and θ_2 is the angle of refraction. We use the iasp91 *P*-wave velocities, 8.04 and 6.2 km/sec respectively, for v_1 and v_2, below and above the Moho.

The discrepancies (hereafter called errors) of back azimuth and slowness can be attributed to deviations in the assumption of spherically symmetric velocity structure (model error) and measurement error. In this paper we address model error, even though measurement error is also significant. Studies based on the approach of Niazi (1966) address back azimuth and slowness model errors. For array stations with uncommonly large errors, back azimuth and slowness errors often exhibit a discernable trend when plotted as a function of theoretical back azimuth. Empirical approaches may correct for these trends if the calibration data set provides outstanding geographic coverage with minimal measurement error. However, a model-based approach may better exploit the data trend by allowing trend extrapolation for data sets with limited geographic coverage. Using a model-based first step in the calibration procedure will also improve subsequent empirical calibration because back azimuth and slowness residuals (following a model-based correction) will better adhere to the zero-mean assumption that is implicit in empirical calibration methods such as kriging.

To date the modeling has been simplified to removing a sinusoidal-fit function from the back azimuth and slowness residuals. This approach does not properly account for the effect of variable slowness at a given back azimuth. Here we present a more complete model approach to a dipping layer correction that simultaneously fits back azimuth and slowness observations with a ray-based prediction that incorporates a dipping layer defined by its strike and dip. In this method the free parameters would be the strike ϕ and dip δ angles of the Moho plane in contrast to the phase and amplitude of cosine waves that are fit to back azimuth and slowness residuals separately. Because the azimuth and slowness deviations both vary as a function of true azimuth, fitting both residuals jointly will give a more consistent calibration.

We examine the effect of a dipping Moho discontinuity on the angle of incidence and the observed azimuth of a seismic wave, and what follows is an overview of the geometry and derivation of the equations governing the azimuthal dependence of both observed azimuth and slowness parameters, some examples of the ray-based forward predictions, and finally some examples of fitting data.

Azimuth and Slowness Measurements

We use back azimuth and slowness measurements made from *P* phases (i.e., *Pg*, *Pn*, *P*, *PKP*) recorded at several IMS arrays between the years 1995 and 2009. These measurements are provided by the USNDC and are produced from well-located events with epicenter error of 25 km or less (GT25) and $m_b > 4.5$. The back azimuth and slowness are estimated using a standard frequency-wavenumber algorithm (e.g., Capon, 1969; Kvaerna and Doornbos, 1986). We include only those measurements having uncertainties of less than 15° for back azimuth and 1.5 sec/° for slowness, and we further restrict the slowness to be less than 13.5 sec/° as such horizontally travelling waves with high slowness cause instabilities in the optimization code. The global distribution of events provides good back-azimuthal coverage at several arrays allowing us to discern patterns in the azimuth and slowness residuals.

The back azimuth and slowness measurements are next compared with theoretical predictions made using the iasp91 velocity model and residuals are formed. Examples of these residuals are shown in Figure 2 for the CMAR (Chiang Mai, Thailand) and ILAR (Eilelson, Alaska) arrays. Both the back azimuth and slowness residuals show the characteristic sinusoidal shape indicative of a dipping layer beneath the array. Note the effect of slowness (incoming ray inclination) on the magnitude of the azimuth deflection. The effect of the dipping interface is strongest for rays that approach the interface with a small slowness (i.e., at a steep angle).

We observe this pattern in the residual distribution at a number of IMS arrays and report results here for only CMAR and ILAR as there are calibration studies for both of these arrays, by Tibuleac and Stroujkova (2009) and Lindquist et al. (2007), which use the Niazi (1966) approach to determine Moho dip and strike and thus provide a direct comparison with our results.

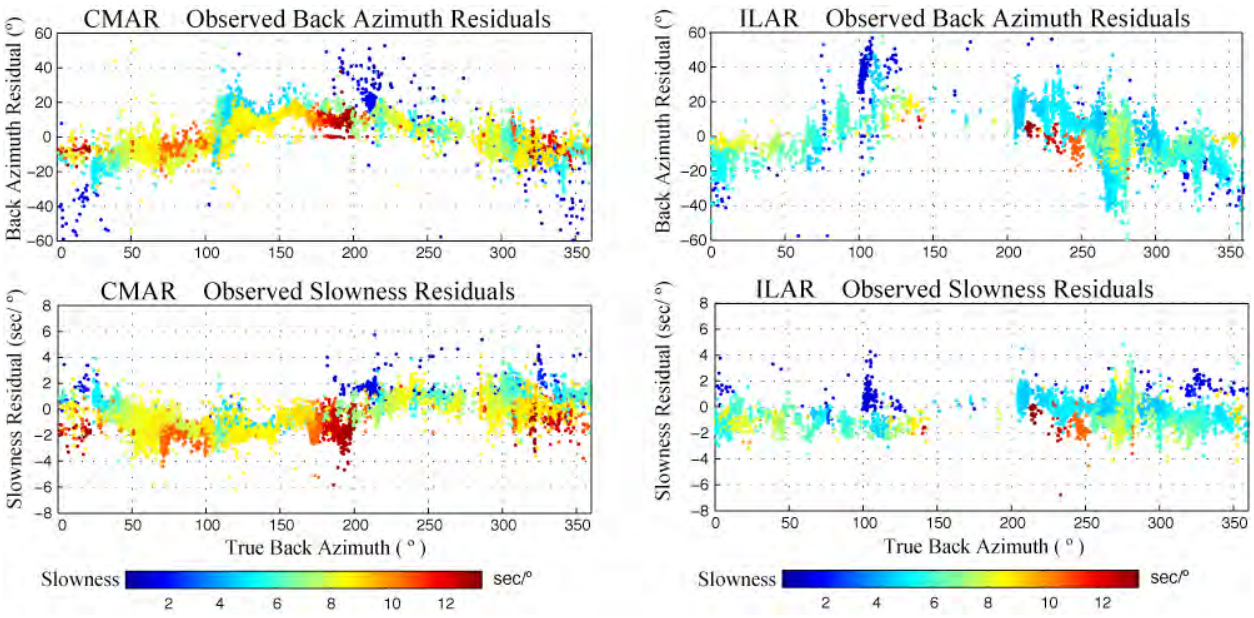


Figure 2. Back azimuth and slowness residuals plotted against true back azimuth for stations CMAR (left) and ILAR (right). Color indicates theoretical slowness of the incident wavefront (in sec/°) based on the iasp91 velocity model and essentially represents the epicentral range. The sinuous trend of the residuals and the affect of slowness on the azimuth residual are both consistent with a dipping interface beneath the array.

Dipping Layer Determination

Niazi (1966) attributed systematic back azimuth and slowness deviations to dipping geologic interfaces under the array, and he derived equations to compute these deviations for a dipping interface. Both back azimuth and slowness residuals have an *asymmetric* cosine shape and their values should be close to zero for rays coming along strike and maximum (absolute value) for rays coming up- or down-dip. This is indicated by the 360° periodicity and 90° phase shift between slowness and back azimuth anomalies (Figure 2). The extent of the azimuth bias varies with the angle of incidence, dip of the Moho, and velocity ratio. The pattern of azimuth perturbation can constrain the dip if the velocity contrast is known, or vice versa, but the pattern is not unique when both dip angle and velocity contrast are varied. Typically one determines the strike from a cosine fit to azimuth residuals then uses that strike to find the dip angle from a cosine fit to the slowness residuals.

The strike is found from the crossover points of the back azimuth residuals and the dip is found from the amplitude of the slowness residuals. The strike of the dipping Moho is the point with the largest azimuth residual following the first zero crossing of the cosine fitting curve. According to Niazi (1966), if the azimuths are read clockwise the direction of the dip is given by the point of transition of the back azimuth residuals from negative to positive values. Both Tibuleac and Stroujkova (2009) and Lindquist et al. (2007) used this approach to determine the Moho orientation beneath CMAR and ILAR respectively.

As the refraction of the seismic wavefront follows Snell's law, the effect of a dipping interface on an incident seismic ray may be more directly computed using vector arithmetic and Snell's law (*http://en.wikipedia.org/wiki/Snell's_law*) allowing us to solve for the Moho strike ϕ and dip δ angles by simultaneously fitting both the back azimuth and slowness residuals using:

$$v = \left(\frac{V_2}{V_1}\right) l + \left(\frac{V_2}{V_1}\ COS\Theta_1 + COS\Theta_2\right) n \qquad [1]$$

and

$$COS\Theta_1 = n \cdot (l) \quad , \quad COS\Theta_2 = \sqrt{1 - \left(\frac{V_2}{V_1}\right)^2 (1 - COS^2\Theta_1)}$$

where *l* is the directional vector of the incident ray (determined by theoretical back azimuth and slowness), *v* is the directional vector of the refracted ray, *n* is the normal vector to the dipping-Moho plane (using ϕ and δ), θ_1= angle of incidence, and θ_2= angle of refraction. We use the iasp91 *P*-wave velocities below and above the Moho, 8.04 and 6.2 km/sec respectively, for v_1 and v_2.

We have written a MATLAB™ code based on equation [1] to invert back azimuth and slowness residual data for the strike and dip of an interface using a multi-variable optimization technique. The forward model may be written in the generalized form:

$$(\Delta\alpha_i, \Delta\mu_i) = f(\phi, \delta, \alpha_i, \mu_i, v_1, v_2) \qquad [2]$$

Where $\Delta\alpha_i$ and $\Delta\mu_i$ are differential back azimuth and slowness residuals for the i^{th} data point (i.e., the measured data). The function *f* describes how an incoming plane wave with an expected back azimuth of α_i and slowness μ_i, based on the known source receiver configuration, interacts with an oriented plane with specified velocities above and below the boundary (v_1 and v_2 respectively). The goal is therefore to find the optimal orientation of the plane that satisfies equation [2] (i.e., to determine ϕ and δ).

We chose to utilize a pre-existing algorithm from the MATLAB Optimization Toolbox™ called *lsqcurvefit* which is a nonlinear curve-fitting routing that is designed to solve multivariant systems in a least squares sense. In our specific case, the *lsqcurvefit* algorithm searches for the strike and dip of the plane by minimizing:

$$\sum_{i=1}^{n} \{f(\phi, \delta, \alpha_i, \mu_i, v_1, v_2) - (\Delta\alpha_i, \Delta\mu_i)\}^2 \qquad [3]$$

where the summation is over all *n* slowness/azimuth residual data points. The MATLAB™ function utilizes the *trust-region-reflective optimization* algorithm, based on the interior-reflective Newton method developed in Coleman and Li (1994, 1996), to simultaneously search for the optimal strike and dip of the proposed orientation of a plane defining the Moho.

Results

We applied this optimization technique to determine the best-fitting strike and dip of a Moho interface beneath the CMAR array and compare the results using the same data set with Niazi's technique. The azimuth residuals for 9903 *P* phases recorded at CMAR are shown in Figure 3 (top, left) and are fit by an asymmetric cosine curve of the form 1.04 - 14.2*cos(Z – 188.4°) where Z is the true back azimuth computed from iasp91. The curve fit is done using the *fminsearch* function in MATLAB™, and as described by Niazi (1966) strike of the dipping Moho is the point with the largest azimuth residual following the first zero crossing of the cosine fitting curve, which in this case is 188.4°. The lower left plot in Figure 3 shows the azimuth residuals distribution after the cosine function has been removed.

Using our optimization method we find that the best fitting Moho at CMAR has strike 192.6° and dip 18.3°. The predicted azimuth residuals from this Moho model are shown in Figure 3 (top, right), and when these values are removed from the observed values the resulting distribution is shown in Figure 3 (lower, right). The major sinuous trend in the residuals is removed, and the correlation between error and theoretical slowness is also mitigated. This shows the importance of using a dipping interface model, which simultaneously fits azimuth and slowness data, in contrast to simply fitting the azimuth trend with a sinusoid. First, a simple sinusoidal curve fit does not account for the strong dependence on slowness. Second, the effect of a dipping interface is not a pure sinusoid. The deviation from a sinusoid becomes stronger as dip angle and slowness increase.

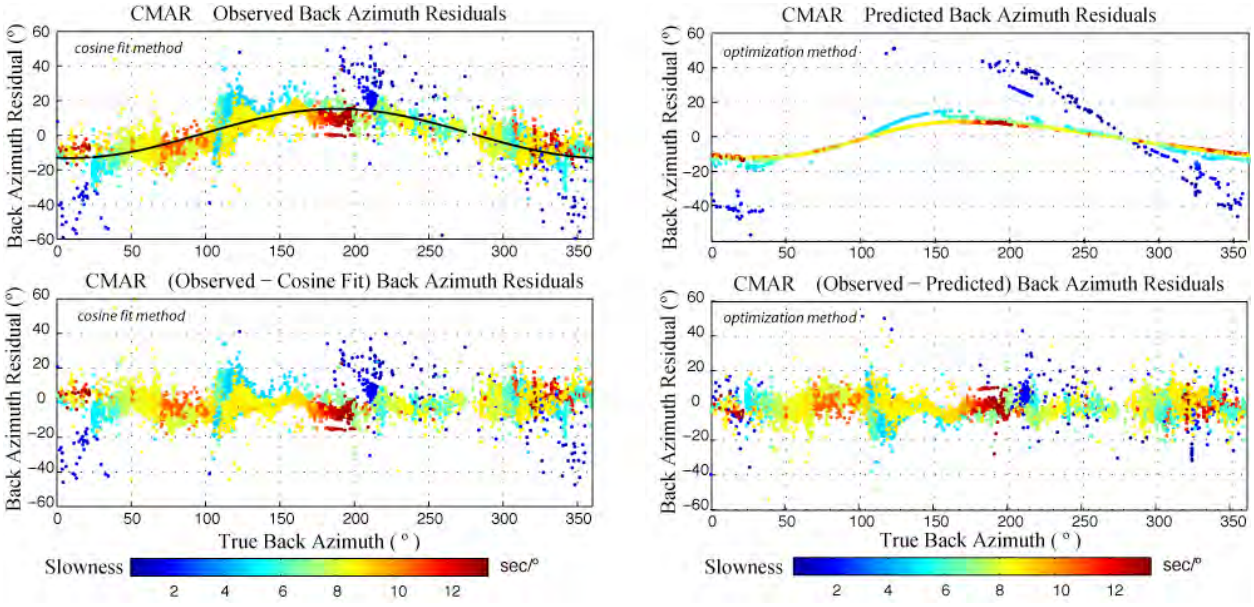


Figure 3. Corrected azimuth residuals at CMAR using the two methods. (Left, top) Azimuth residuals at CMAR with the cosine fit shown by the black line which has the form 1.04 – 14.2* cos(Z- 188.4) and yields a Moho strike estimate of 188.4°. The fit is then subtracted from the residuals to give the corrected distribution (Left, bottom). (Right, top) Azimuth residuals predicted for CMAR from a dipping Moho model, with strike 192.6° and dip 18.3°, obtained from our optimization code which inverts both the azimuth and slowness data for CMAR in Figure 2 simultaneously. (Right, bottom) Azimuth residuals after fitting a dipping interface; both the sinuous trend and variations with predicted slowness are mitigated. See Table 1 for goodness-of-fit statistics.

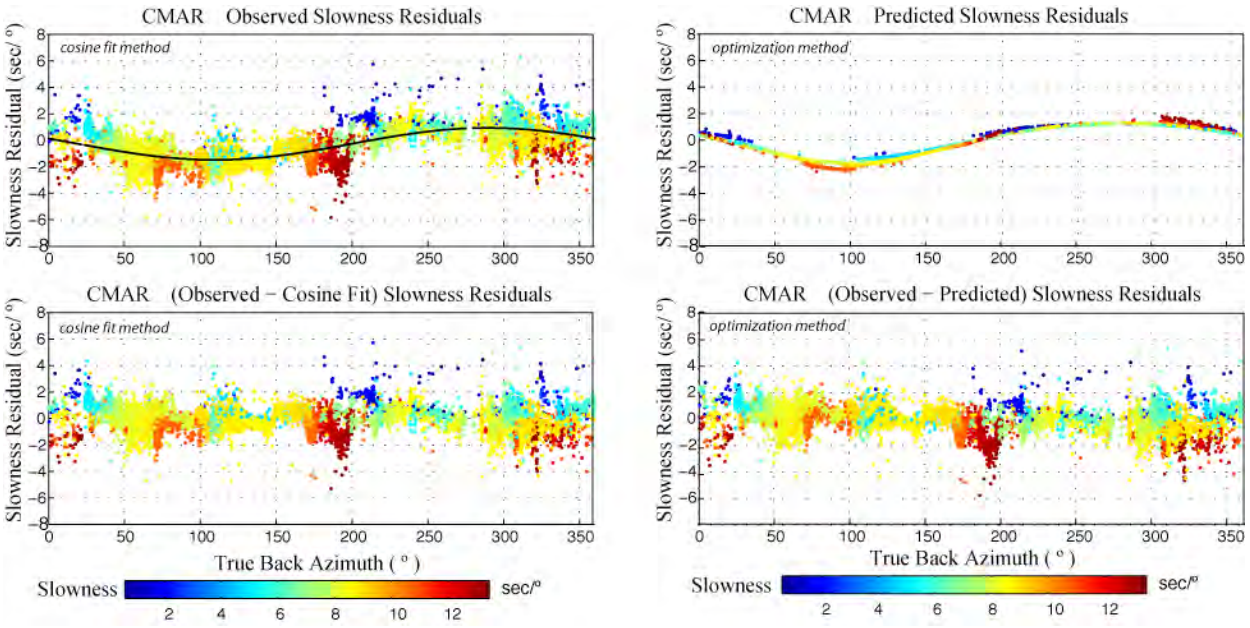


Figure 4. Corrected slowness residuals at CMAR using the two methods. (Left, top) Slowness residuals for CMAR with the cosine fit shown by the black line which has the form 0.27 + 1.2*cos(Z+70.4) and yields a Moho dip estimate of dip 13.1° or 16.8°. The fit is then subtracted from the residuals to give the corrected distribution (Left, bottom). (Right, top) Slowness residuals predicted for CMAR from a dipping Moho model, with strike 192.6° and dip 18.3°, obtained from our optimization. (Right, bottom) Slowness residuals after fitting a dipping interface; both the sinuous trend and variations with predicted slowness are mitigated. See Table 2 for goodness-of-fit statistics.

Slowness residuals for CMAR are shown in Figure 4 (top, left). Slowness is not as strongly affected by incoming ray angle as azimuth for the CMAR case, but the change in slowness can become strongly dependent on incident angle if the interface dips steeply. Using the Niazi method, the Moho dip is found by forward prediction using the strike=188.4° and the median incident angle (determined from the median slowness) for this data set. We find a Moho dip of 13.1° or 16.8° depending on whether we minimize the fit to the azimuth residuals or the slowness residuals respectively. Since this method does not account for the effects of varying incidence angle (or slowness), it cannot provide corrections for the full suite of observed azimuths and slownesses as they are coupled. Our optimization method shows significant variance and SMAD reduction (SMADR) over the Niazi method for both azimuth and slowness although it is particularly good for azimuth as one may expect due to the strong dependency on incident angle (see Table 1 and Table 2).

The predicted slowness residuals obtained from our optimization code are shown in Figure 4 (top, right), and the slowness residuals after removing the predicted values are shown in Figure 4 (bottom, right) . There is a dependence of the slowness residual on theoretical slowness (incoming ray inclination), but this effect is not as great as the effect on azimuth residual (Figure 3). This observation is reflected in the statistics listed in Table 1 and Table 2 where the SMAR values show our optimization method is significantly better for azimuth and moderately better for slowness.

Tibuleac and Stroujkova (2009) also estimated the parameters of a dipping Moho under CMAR (strike=197.7° or 213.5° and dip=18.4° or 15.5° using the forward-modeling method of Niazi; the results are for two different methods) using the forward-modeling method of Niazi (1966). Our resulting Moho strike and dip estimates are in very good agreement with these previously published values.

Table 1. Summary Statistics for Azimuth Residuals at CMAR

	Observed	Cosine fit Corrected	Optimization Corrected
Mean (°)	0.988	0.987	-0.745
Median (°)	0.649	2.720	-0.842
rms (°)	0.102	0.082	0.062
SMAD (°)	12.795	12.46	4.924
Variance (°)	121.38	78.92	44.82
SMADR		2.57%	61.51%
Variance Reduction		34.98%	63.07%

Table 2. Summary Statistics for Slowness Residuals at CMAR

	Observed	Cosine fit Corrected	Optimization Corrected
Mean (sec/°)	-0.492	-0.492	0.100
Median (sec/°)	-0.646	-0.801	-0.016
rms (sec/°)	0.012	0.009	0.008
SMAD (sec/°)	1.406	0.991	0.692
Variance(sec/°	1.618	0.876	0.813
SMADR		29.49%	50.82%
Variance Reduction		45.84%	49.74%

CONCLUSIONS AND RECOMMENDATIONS

We have developed a new method for modeling the strike and dip of the Moho beneath a seismic array by simultaneously fitting the sinusoidal pattern of azimuth and slowness deviations from a one-dimensional velocity model. The new method is tested at CMAR for over 9900 observations, and we determine the Moho beneath this array to have a strike angle of 192.6° and a dip angle of 18.3° which are in good agreement with previous estimates made by Tibuleac and Stroujkova (2009). When the dipping Moho predictions are removed from the azimuth and slowness residuals, both the sinuous trend and variations with predicted slowness are mitigated. While a single dipping interface model does not account for all of the discrepancy between observed and predicted back azimuth and slowness anomalies, this technique is a good first step in the calibration procedure for arrays exhibiting sinusoidal residual trends. Additional modeling with multiple dipping interfaces included within the outlined optimization scheme should be pursued.

ACKNOWLEDGEMENTS

Thanks to Ileana for helpful discussions and making available her MATLAB™ script to fit the Moho dip angle using the Niazi method. We are also grateful to Stan Ruppert for helpful comments on this paper.

REFERENCES

Bondar, I., R. G. North, and G. Beall (1999). Teleseismic slowness-azimuth station corrections for the International Monitoring System Network, *Bull. Seismol. Soc. Am.* **89,** 989–1003.

Capon, J. (1969). High-resolution frequency-wavenumber spectrum analysis, *Proc. IEEE* **57,** 1408–1418.

Coleman, T.F. and Y. Li (1994). On the Convergence of Reflective Newton Methods for Large-Scale Nonlinear Minimization Subject to Bounds, *Math. Program.*, **67** (2), 189-224, 1994.

Coleman, T.F. and Y. Li, (1996). An Interior, Trust Region Approach for Nonlinear Minimization Subject to Bounds, *SIAM J. Optim.* **6**, 418–445.

Greenfield, R. J. and R. M. Sheppard (1969). The Moho depth variations under the LASA and their effect on $dT/d\Delta$ measurements, *Bull. Seismol. Soc.Am.* **59**, 409–420.

Havskov, J. and E. R. Kanesewich (1978). Determination of the dip and strike of the Moho from array analysis, *Bull. Seismol. Soc. Am.,* **68**, 1415–1419.

Koch, K. and U. Kradolfer (1997). Investigation of azimuth residuals observed at stations of the GSETT-3 alpha network, *Bull.Seismol. Soc. Am.* **87,** 1576–1597.

Kvaerna, T. and D. J. Doornbos (1986). "An Integrated Approach to Slowness Analysis With Arrays and Three-component Stations", Semiannual Technical Summary, 1 October 1985 - 31 March 1986, NORSAR sci. Rep. 1-86/87, Kjeller Norway.

Lindquist, K. G., I. M. Tibuleac, and R. A. Hansen (2007). A semiautomatic calibration method applied to a small-aperture Alaskan seismic array, *Bull. Seismol. Soc. Am.* **97,** 100–113, doi: 10.1785/0120040119.

Niazi, M. (1966). Corrections to apparent azimuths and travel-time residuals for a dipping Mohorovicic discontinuity, *Bull. Seismol. Soc. Am.* **56,** 491–509.

Otsuka, M. (1966a). Azimuth and slowness anomalies of seismic waves measured on the Central California Seismographic Array, part I: Observations, *Bull. Seismol. Soc. Am.* **56,** 223–239.

Otsuka, M. (1966b). Azimuth and slowness anomalies of seismic waves measured on the Central California seismographic array, Part II: Interpretation, *Bull. Seismol. Soc. Am.* **56,** 655–675.

Ram, A. and L. Yadav (1984). Structural corrections for slowness and azimuth of seismic signals arriving at Gauribidanur array, *Bull. Seismol. Soc. Am.* **74,** 97–105.

Ringdal, F. and E. S. Husebye (1982). Application of arrays in detection, location and identif cation of seismic events, *Bull. Seismol. Soc. Am.* **72,** S201–S224.

Rost, S. and C. Thomas (2002). Array seismology: methods and applications, *Rev.Geophys.* **40,** 2-1–2-27.

Schweitzer, J. (2001). Slowness Corrections – One way to improve IDC products, *Pure Appl. Geophys.*, **158**, 375-396.

Tibuleac, I. M. and E. T. Herrin (1997). Calibration studies at TXAR, *Seismol. Res. Lett.* **68,** 353–365.

Tibuleac, I. M. and E. T. Herrin (2001). Detection and location capability at NVAR for events on the Nevada Test Site, *Seismol. Res. Lett.***72,** 97–107.

Tibuleac, I. M. and A. Stroujkova (2009). Calibrating the Chiang Mai seismic array (CMAR) for improved event location, *Seismol. Res. Lett.* **80,** 579–590, doi: 10-1785/gssrl.80.4.579.

OPTICAL MEMS-BASED SEISMOMETER

Dominique Fourguette[1], Volkan Ötügen[2], Liane M. Larocque[1], Ulas A. Ayaz[2], and Greg A. Ritter[1]

Michigan Aerospace Corporation[1] and Southern Methodist University[2]

Sponsored by the National Nuclear Security Administration

Award No. DE-FG02-08ER85099 Phase II

ABSTRACT

Low-yield man-made seismic activity is difficult to detect and most often occurs in remote areas where seismic detection is weak. The whispering gallery mode based seismometer is an optical Micro-Electro-Mechanical System-based (MEMS) instrument. The final version of this seismometer will be a three-axis instrument, compact, low power dissipation and capable of unattended operation.

The seismometer design exploits morphology-dependent optical resonance shifts in small dielectric spheres (<1 mm in diameter). These optical resonances, called whispering gallery modes (WGM), are extremely narrow, making the transducer highly sensitive to force ($< 10^{-9}$ Newtons). The MEMS sensing element in this seismometer has demonstrated an optical Q-factor of 10^7. As a result, the instrument is capable of measuring accelerations as low as 10 nano-g.

The prototype was tested in the Earth Sciences Department at the Southern Methodist University (SMU). The results show a good agreement with the data from a Guralp CMG-3T seismometer.

OBJECTIVES

Michigan Aerospace Corporation, in collaboration with Southern Methodist University, is developing a compact Whispering Gallery Seismometer. The sensing principle of the seismometer exploits the morphology-dependent optical resonance shifts of dielectric spheres to detect ground motion. These optical resonances are extremely narrow, making the transducer highly sensitive to ground motion. The small dielectric spheres are easily packaged into a small instrument capable of measuring accelerations as low as 10 nano-g.

The optical MEMS sensing element, typically a microsphere (with diameters in the range 200 to 1000 μm), is weakly coupled to an optical fiber, as shown in Figure 1a. The optical fiber, which carries light from a tunable laser, serves as an input/output port for the microsphere. When the microsphere comes into contact with an exposed section of the fiber core, light is coupled into the outer layer of the sphere, (Figure 1b). When the sphere is compressed (as shown in Figure 1c), the wavelength of the resonances shifts. Its resonances are observed as sharp dips in the transmission spectrum as depicted in Figure 1d.

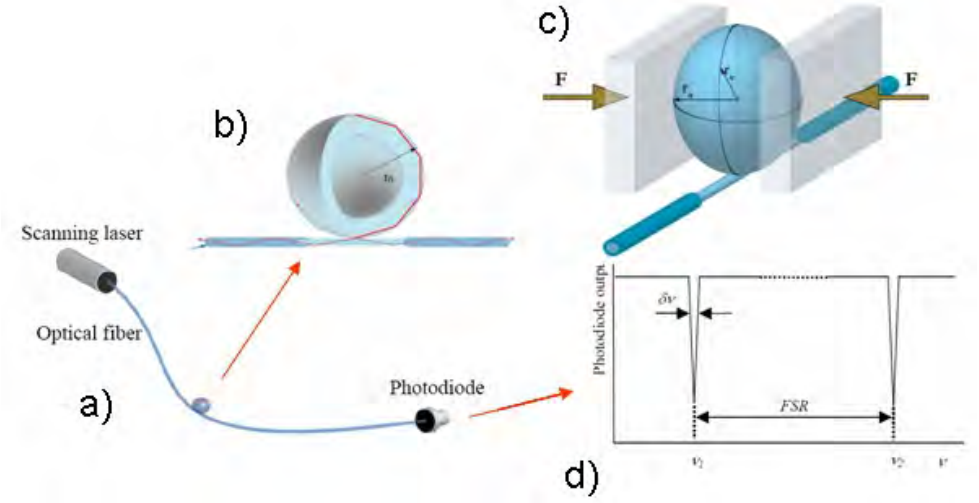


Figure 1. Principle of the WGM pressure-induced wavelength shift $\delta\nu$.

These optical resonances, also known as the "whispering gallery modes" (WGM), are extremely narrow and hence are highly sensitive to any morphological change in the microsphere.

The Phase II objectives include the fabrication of the dielectric microspheres, engineering model fabrication and preliminary tests, and instrument fabrication.

Objective 1:
The first objective of this effort was the experimental investigation of WGM characteristics of different-sized spheres (ranging from ~ 200 μm and 1 mm) and the fabrication of the microspheres. The candidate material used for the spheres is PDMS (commercially known as Sylgard 184).

Objective 2:
The second objective was the fabrication of the engineering model to demonstrate the seismometer principle.

Objective 3:
The third objective entails the fabrication of the seismometer prototype.

RESEARCH ACCOMPLISHED

Prior to testing, the seismometer was calibrated (Figure 2) to assess the sensitivity and the natural resonance frequency. The data were acquired and processed with LabVIEW™. The resonance is near 40 Hz (the seismometer is undamped).

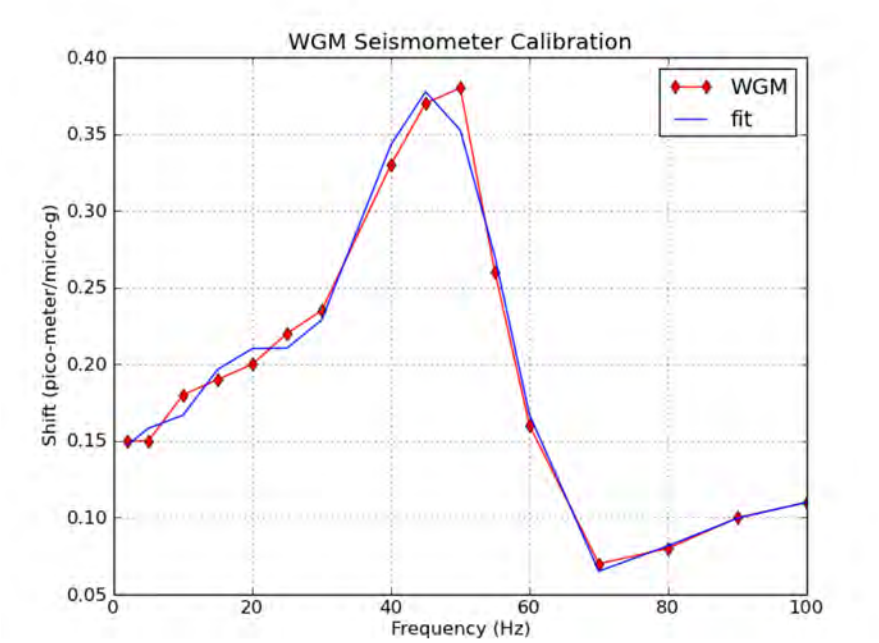


Figure 2. Seismometer calibration.

After preliminary tests were completed, the instrument was then sent to SMU for additional tests to compare the prototype results with the current state of the art technology. These tests were performed jointly by our partners at SMU's Micro-Sensor Laboratory and the SMU Geology Department.

Figure 3 compares seismic data taken by the CMG-3T seismometer with that of WGM Seismometer sensor taken on March 21, 2012, GMT 20:18 hrs in the Earth Sciences Laboratory at SMU. The sensors were placed adjacent to one another on a pier that is isolated from the building and anchored to bedrock below the building foundation. The top plot shows the WGM shifts (in pico-meters). The CMG-3T seismometer acceleration output for the vertical, East/West horizontal and North/South horizontal planes are shown in the subsequent traces. (Note that the CMG-3T seismometer output is in velocity. Therefore, in the seismometer traces in Figure 3, these velocity outputs have been converted to acceleration for comparison with the WGM Seismometer output).

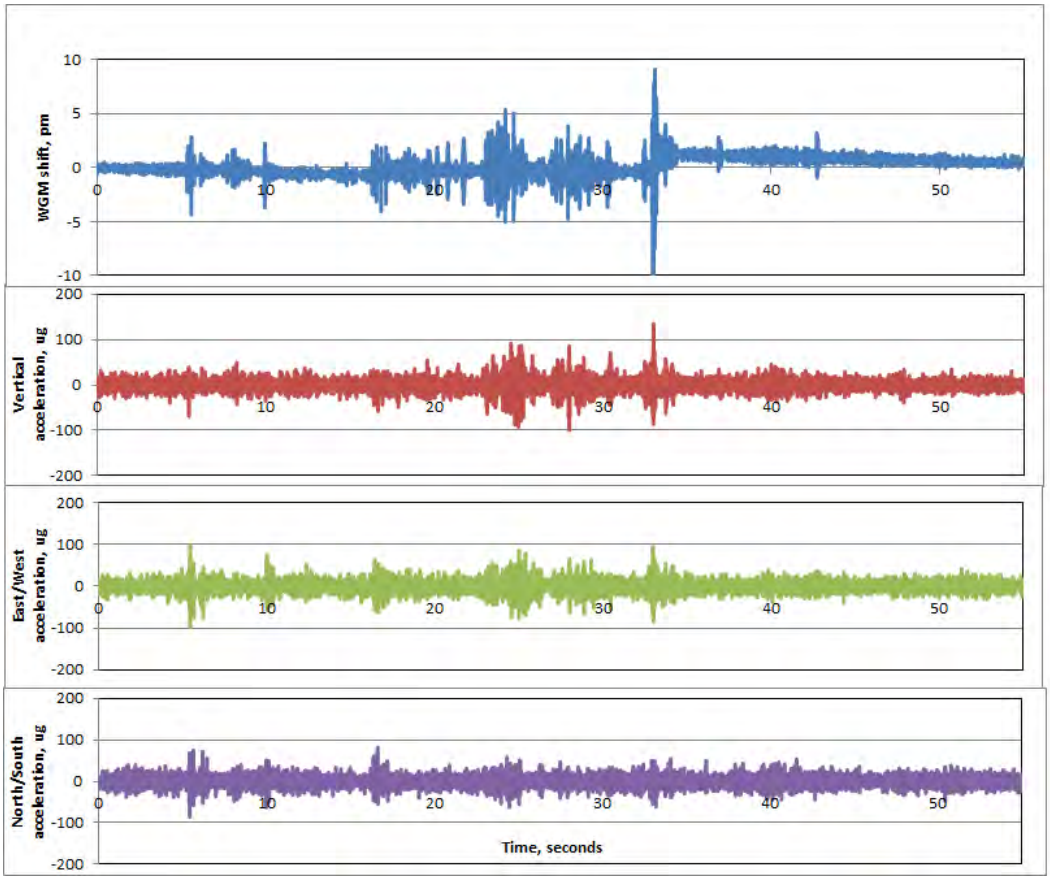


Figure 3. Seismic data taken by CMG3T seismometer with that of WGM Seismometer sensor taken on March 21, 2012, GMT 20:18 hrs in the Earth Sciences Laboratory at SMU.

Figure 3 shows a shift of 10 picometers for 100 μg acceleration. The minimum measurable shift at this time is 0.1 picometers, therefore the minimum acceleration measurable with the present seismometer is ~10 μg. This value can be lowered to the nano-g range by refining the measurement of the minimum shift and using mechanical amplification to generate a larger proof mass displacement.

Figure 4 displays the FFT for the WGM seismometer output and the vertical output of the CMG3T seismometer. The WGM seismometer exhibits a low frequency component caused by drift (observable at ~32 s into the data set) and a loss of sensitivity at 15 Hz and harmonic. This behavior could be an artifact of the design or assembly. The power spectral density of the two seismometers is displayed in Figure 5; a good agreement exists between the peaks.

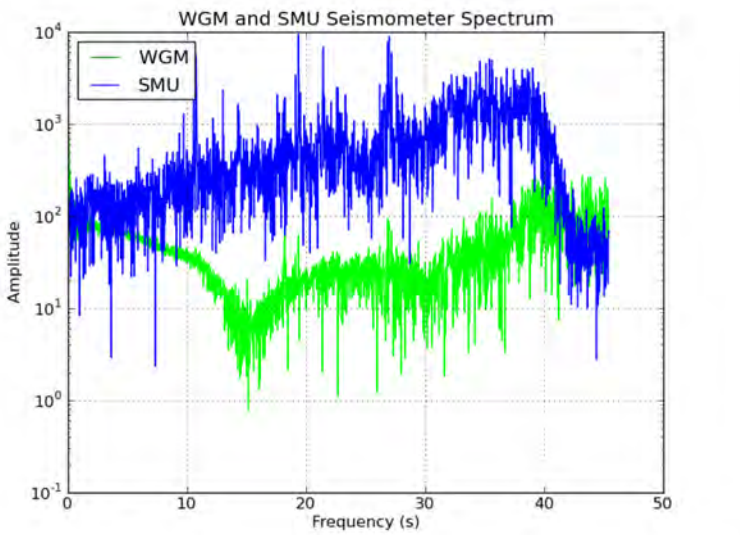


Figure 4. FFT of the WGM and SMU seismometers.

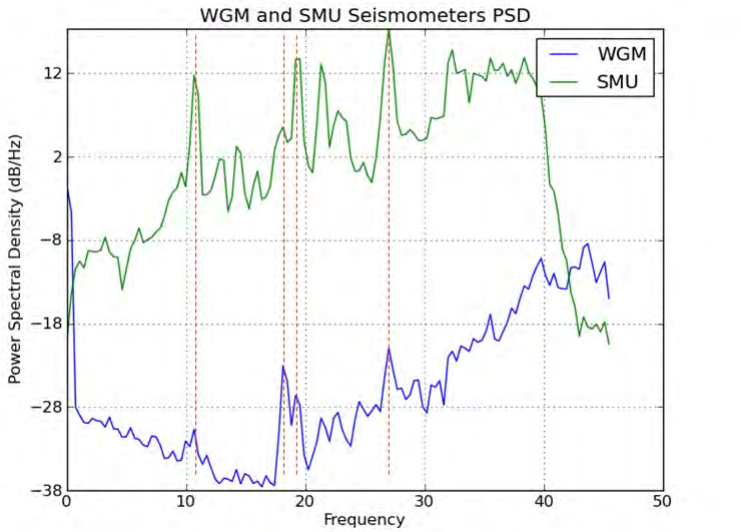


Figure 5. Power spectral density plots for the WGM and SMU seismometers.

CONCLUSIONS AND RECOMMENDATION

This Phase II effort included the design, fabrication, assembly and tests of the WGM seismometer. The following results and conclusions were drawn from this effort:

- WGM technology was proven to be an excellent sensing technique for this application
- The preliminary mechanical prototype developed during this Phase II demonstrated a sub-micro-g sensitivity.
- The data processing used to obtain the wavelength shifts is powerful yet simple enough to be handled by a low power dissipation FPGA.
- While the electronics developed for this project was not used in the testing, the possibility of low dissipation electronics was demonstrated.
- A mechanical assembly equipped with a lever action will provide mechanical amplification to 10 nano-g sensitivity.

REFERENCES

Benner, R.E.and S. C Hill (1988). Morphology-dependent Resonances, in *Optical effects Associated with Small Particles*, P.W. Barber and R.K. Chang, Eds., *Advanced Series in Applied Physics*, World Scientific.

Guan, G., S. Arnold and M.V. Ötügen, (2006). Temperature measurements using a micro-optical sensor based on whispering gallery modes, *AIAA Journal* **44** (10), 2385–2389.

A NEW NETWORK MODELING TOOL FOR THE GROUND-BASED NUCLEAR EXPLOSION MONITORING COMMUNITY

Stephen L. Heck[1], Benjamin R. Hamlet[1], Eric P. Chael[1], Christopher J. Young[1], William R. Walter[2], Dale N. Anderson[3]

Sandia National Laboratories[1], Lawrence Livermore National Laboroatory[2], and Los Alamos National Laboroatory[3]

Sponsored by the U.S. Department of State

Award No. DOS SIAA-11-AVC/NMA-1

ABSTRACT

Network simulations have long been used to assess the performance of monitoring networks to detect events of interest for a variety of purposes, such as determining where additional stations are needed to reduce monitoring thresholds and studying network resilience to station outages. Since the early 1990s, the standard tool for such simulations has been the SAIC-developed NetSim package. With carefully chosen parameters for the network, sources, and paths through the Earth, NetSim can produce useful simulations; however, the package has several significant shortcomings: an older coding language (FORTRAN), a strong emphasis on seismic monitoring with limited support for other waveform technologies, limited documentation, and a limited default parameter set with known errors. Thus, we are developing NetMOD (Network Monitoring for Optimal Detection), a new Java-based open-release software package designed to assess the performance of ground-based waveform sensor networks. As designed, NetMOD will have several clear advantages: 1) it is coded in a modern object-oriented language that is inherently multi-platform, 2) it will take advantage of modern computing performance (e.g. multi-core processors), 3) it can easily incorporate ground-based monitoring technologies other than seismic, and 4) it will include a new, well documented and well-validated default parameter set including information for all the IMS stations corresponding to technologies implemented in each software release.

NetMOD is designed to be extendable through the use of plugins, so new phenomenological models can be added as separate plugin modules. Development of the Seismic Detection Plugin is being pursued first. Seismic location and infrasound and hydroacoustic detection plugins are planned to follow. By making NetMOD an open-release package, we hope that it can provide a common tool that the monitoring community can use to produce assessments of monitoring networks and to verify assessments made by other parties.

OBJECTIVES

The nuclear explosion monitoring system run by the Comprehensive Nuclear-Test-Ban Treaty Organization (CTBTO), consists of the International Monitoring system (IMS) global network of sensors and the International Data Centre (IDC) in Vienna, Austria, where the IMS data is processed to detect nuclear events. The sensors span four technologies – seismic, hydroacoustic, infrasound, and radionuclide – but hereafter we will discuss only the waveform technologies (i.e. radionuclide monitoring is not included). This is consistent with the way the technologies are used at the IDC, where the waveform data are processed together and quite differently from the radionuclide data.

The CTBTO uses modeling of the waveform technologies for a variety of purposes, such as assessing the overall IMS+IDC monitoring performance, prioritizing IMS station deployment and repair, and assessing the difference between the current and the fully built IMS network. Currently the CTBTO uses a new version of NetSim, a software tool that was originally developed in the late 1980s and early 1990s. Though the new version has some important new innovations (as we discuss below), the software still has significant limitations: it is antiquated, poorly documented, does not take advantage of modern computing technology (e.g., multiple cores), has only a rudimentary user interface, and is not easy to extend to cover new simulations. Further, the large and complex set of Earth model parameter files included in the package has been shown by the CTBTO to have significant problems. For these reasons, the U.S. Department of State has provided funding to a team from Sandia National Laboratories (SNL), Lawrence Livermore National Laboratory (LLNL), and Los Alamos National Laboratory (LANL) to develop a new open-release software tool (NetMOD), as well as a new parameter set baseline, to meet the CTBTO needs.

REVIEW OF NETWORK MODELING SOFTWARE

The most obvious way to assess the effectiveness of a nuclear explosion monitoring system is to analyze the output of the system itself, i.e. the event bulletin. When the IDC first began processing data, this was not possible because there were not enough detected events to perform robust estimates, but now with nearly a decade of archived operational IDC results available, direct analysis can be done. However, this empirical approach has significant inherent limitations. First, it can only be used to assess system effectiveness for areas where archived events have taken place, and these areas are very limited, e.g., most seismic events occur along the tectonic plate boundaries. For actual nuclear events, the IMS+IDC sampling is much worse, consisting only of the North Korean test site (all other testing pre-dates the CTBTO event archive, which began in 1999). Given that a nuclear test can in theory be set off nearly anywhere on the Earth, this limited sampling is a fundamental problem. A second difficulty is that the configuration of sensors in the IMS has changed over the operational history of the CTBTO, so results from 5 years ago cannot be directly compared with current results. For these reasons, for many areas of the Earth of interest, analysis of empirical results can tell us very little if anything about the effectiveness of the current IMS+IDC (to say nothing of projected future versions) for detecting and locating nuclear tests.

Previous work on monitoring system assessment has tended to treat the three ground-based waveform monitoring technologies separately. For seismic, the state-of-the-art assessment tool is NetSim (Sereno et al., 1990), which can be used to estimate detection or location performance. NetSim models the generation of the signal at the source, attenuation of the signal during signal propagation, the noise environment at the station, and the gain boost provided if the station is an array. All of these factors can have frequency dependence, and assessments can be based on multiple phase types. The calculations can be very high quality, with properly chosen parameters, but as discussed above, the software is difficult to use and equally hard to modify (to our knowledge, few users have made any attempt to alter the code).

NetSim also seems to be the only widely used tool for estimating infrasound performance, though it was not originally designed for that purpose. Clauter & Blandford (1998) showed how the software could be used with infrasound-specific parameter files to incorporate attenuation and wind-dependent noise information appropriate for infrasound monitoring. The important effects of wind variations (seasonal and daily) on signal propagation, however, were not captured, severely limiting the quality of the simulations. More recently, the modified version of NetSim that the CTBTO uses includes a new true infrasound simulation feature that does account for such wind variations using the HWM93 model (Hedlin et al., 1996).

The tool of choice for estimating hydroacoustic monitoring performance is HydroCAM, (e.g. Pulli & Upton, 2003). To accurately simulate hydroacoustic monitoring, it is essential to accurately predict signal propagation through the ocean basins using: 1) accurate models of bathymetry to properly model blockage and 2) accurate models of

seasonal variations in the depth of the SOFAR channel. HydroCAM accounts for these factors. However, it is complicated to run and it is not openly available, so HydroCAM is not widely used for simulations. A considerably simplified hydroacoustic simulation is included in the modified version of NetSim that the CTBTO uses. This version does account for blockage, but not for reflections or diffractions.

In summary, there are existing software tools to simulate the various ground-based monitoring technologies, some of which can produce very high-quality simulations. However, there is no single package available that 1) models all three waveform technologies, 2) produces high quality simulations, 3) has a well-designed, user-friendly GUI, 4) is easily extensible to add new types of simulations, 5) takes advantage of modern computing resources, 6) that can be openly released. For these reasons, we have undertaken the development of the NetMOD tool.

RESEARCH ACCOMPLISHED

NetMOD Simulation Algorithms

The need for a new simulation tool is driven primarily by inadequacies in the implementation of simulation algorithms, not in the algorithms themselves. Thus the simulation methods used in NetMOD will be taken from the well-vetted models from literature and/or existing simulation tools. For example, for seismic detection NetMOD will initially perform the same calculations as NetSim (see Sereno et al., 1990 for details). Once the first version of the NetMOD tool has been developed and released, improved simulation algorithms could be developed and implemented, as needed.

NetMOD Design and Implementation

NetMOD is implemented in Java, which allows it to run on a variety of operating systems without modification. The implementation takes advantage of modern computing resources such as multiple-cores, an in-memory relational database for storing and querying results, and an easy-to-use graphical user interface.

NetMOD is designed to be highly configurable by utilizing a plugin-based architecture. This software design pattern provides flexibility by allowing the addition or removal of new software features via plugins without affecting other functionality. For example, a seismic detection model and an infrasound detection model would be developed as separate plugins. The presence of the seismic plugin would have no effect on how the infrasound plugin works and vice-versa. Furthermore, the NetMOD code is implemented such that the results for the seismic and infrasound simulations can be combined to produce a multi-phenomenology simulation. The following picture depicts how NetMOD is structured. Again the key idea is that plugins do not interact directly with each other.

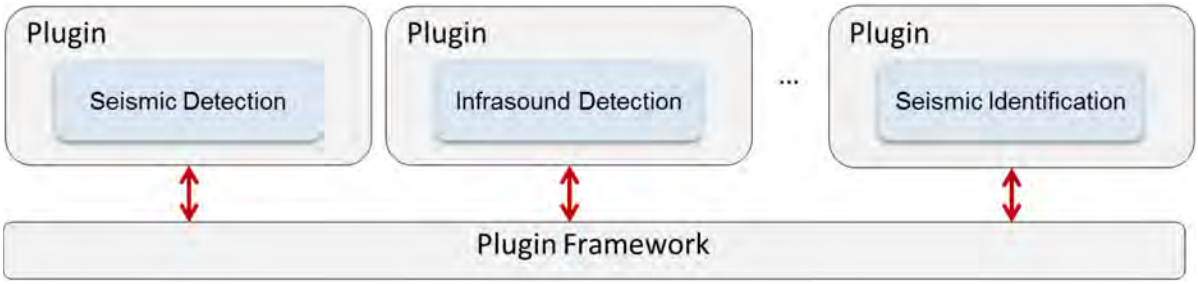


Figure 1. Each phenomenological model is implemented as a "plugin" that can be easily added or removed from the NetMOD software.

It is also worth noting that because of this extremely flexible plugin architecture, there is potential that NetMOD could be adapted for use beyond the ground-based waveform technology monitoring community.

Graphical User Interface

The NetMOD Graphical User Interface is designed to give users the ability to easily set up simulations, navigate the results and answer many "what-if" questions in an effortless manner. Notable features of the GUI include

1) The ability to create and modify the simulation configuration – As anyone who has run NetSim knows, setting up a simulation run is by far the most difficult part and can take many days or even weeks due to the large numbers of parameter files that must be created and reviewed. NetSim provides no GUI to help the user with this process. The NetMOD GUI provides a tabbed display that guides the user through the various major portions of setting up a simulation.
2) An integrated map for displaying configuration and results – Simulation outputs are fundamentally geographic in nature, as are many of the input parameters. Thus NetMOD includes an integrated map for both parameter set up and simulation analysis.
3) A comparison tool for quickly assessing the differences between two simulations – Often simulations are calculated to ask specific questions about the effect of making a small change in the network, e.g. leaving out a station or adding a station. The differences in overall network performance, however, can be subtle. NetMOD provides a tool that calculates and displays the differences directly, making analysis much easier.
4) The ability to drill down into the results in order to track how the simulation input affects the output – Network simulations are very complex calculations, involving numerous intermediate calculations and hundreds of input parameters. Trying to understand why a particular result was calculated is sometimes desirable, particularly when there is any question about the validity of a simulation. The NetMOD drill down function (introspection) provides an easy way to quickly find out why a particular result was obtained.

As an example of the GUI, the following figures are screen shots from NetMOD. The first figure shows the tab layout for viewing/setting the simulation configuration. In particular this is the station configuration tab for a seismic simulation. The station configuration tab allows the users to set the station specific properties for the simulation such as the list of stations to use, the site response parameters for specific seismic phases and the station's ambient noise. Also displayed is the ambient noise file that was specified for station ARCES. Other configuration areas (such as network simulation parameters, source media parameters, propagation path parameters, etc.) have their own tabs with features similar to that of the station tab.

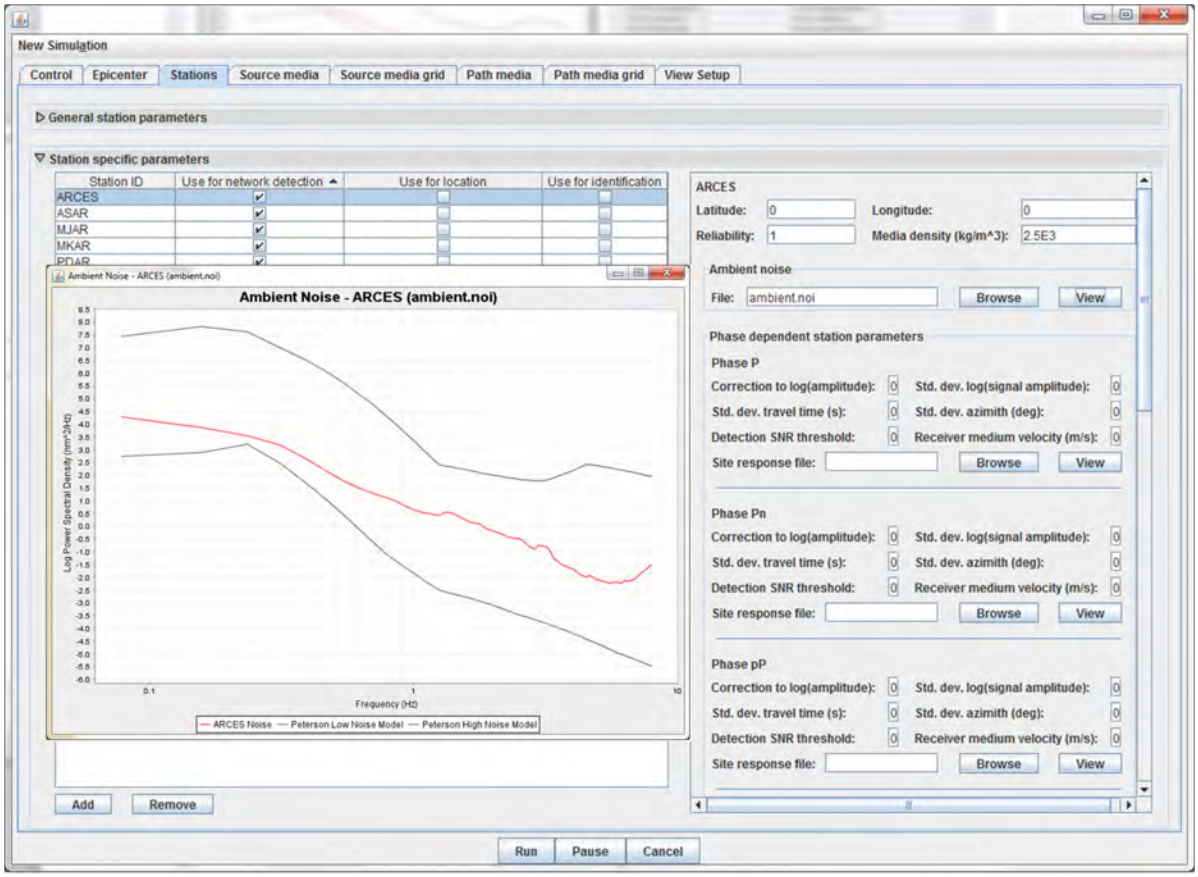


Figure 2. An example of the NetMOD simulation configuration for a seismic simulation.

As mentioned earlier, NetMOD includes an integrated map. The following figure shows the station and event epicenter configuration for a hypothetical seismic detection simulation. Stations are denoted by green triangles while the event locations are denoted by stars. The locations for stations and events can be easily changed through the appropriate tabs in the GUI.

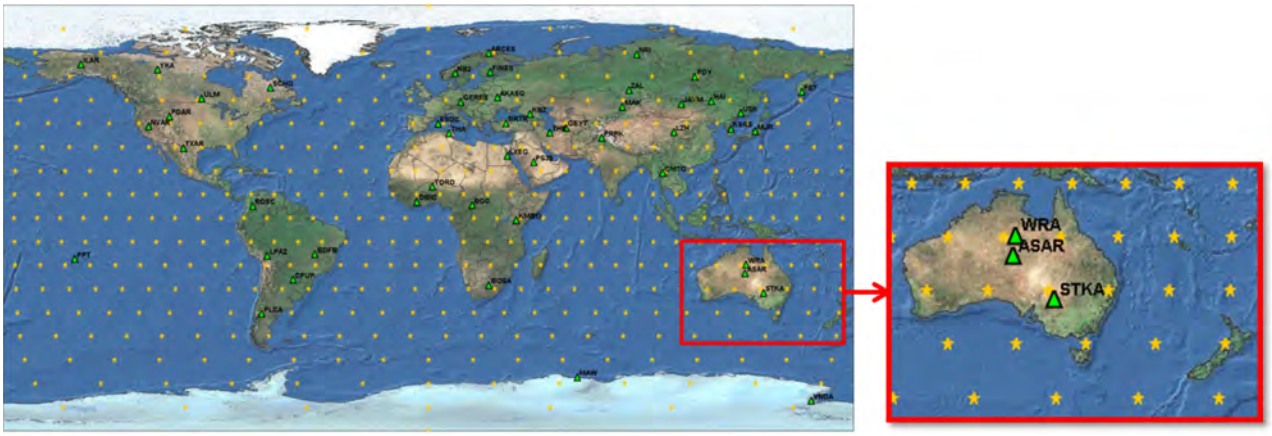


Figure 3. The NetMOD map. The stations are represented by triangles and the event epicenters by stars.

After a simulation is run, a colored overlay is generated to quickly convey the results. The following figure shows the results of a hypothetical seismic detection simulation for the IMS primary network. The colored overlay in Figure 4 indicates varying probability of detecting a seismic event with red indicating a better detection probability. This is an interactive map, allowing the user to zoom, select objects, measure distances, add other overlays for reference, etc.

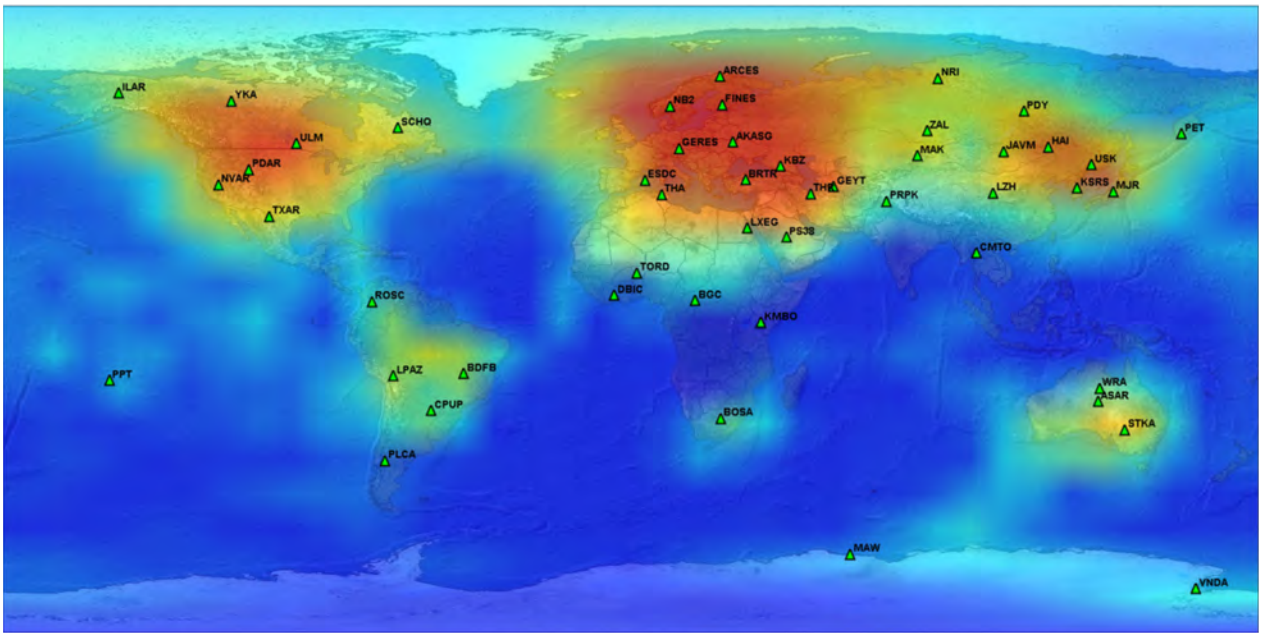


Figure 4. The NetMOD map showing the results of a hypothetical seismic detection simulation. Red indicates a better probability of event detection.

As helpful as the NetMOD GUI is, in some cases a user may want to run simulations for a set of small variations to an existing configuration – e.g. leaving out network stations one at a time to assess importance – in which case using

the GUI is slow and cumbersome. For this reason, NetMOD also includes a batch mode where a set of simulations can be scripted to run without the use of the GUI.

Configuration Files

For someone not wanting to use the GUI, the format of the various parameter files is important. In NetSim, many of the parameter files are just collections of numbers with no fields labeled, so the user must constantly refer back to the NetSim User's Manual to figure out what to modify, a very cumbersome process. To improve the situation, NetMOD uses the setpar/getpar file format developed by Robert Clayton of Caltech and widely used by the seismological research community. This format is much better suited for editing with text-editors. Comments can be embedded directly in the configuration files to document the configuration format and values. NetMOD can also convert NetSim-style configuration files into the new setpar/getpar format so that existing simulations won't need to be re-created.

Listing 1 shows an example of the format for storing simulation information. Notice that comments are preceded with a pound sign '#', support for basic mathematical operations allows variables to be derived from other variables, and the ability to represent tabular data.

```
#comments can be embedded to describe variables and structure

#basic variable declarations

one=1
two=2
three=3 ten=10

#support for basic mathematical operations on variables
sixty=bc $(one)*$(two)*$(three)*$(ten)


#Tables are convenient for storing matrix data
#!BeginTable Table1
col1 | col2 | col3 |
@row1 1 2 3 #rows in a table can be named
@row2 2 3 4
@row3 3 4 5
@row4 4 5 6
@row5 5 6 7

#!EndTable
```

Listing 1: An example of the file format that NetMOD uses for its project files.

Current Development Status

Development of the NetMOD software is ongoing. The initial version of the plugin-framework is in place and work is now focused on implementing the seismic detection plugin as the basis for the first open release version. Next in priority will be adding plugins for infrasound detection and hydroacoustic detection. Further out will be plugins for location and event screening.

In parallel with the software development, we are developing a new baseline parameter set for the IMS primary network that will be included with the software release. This will include improved station noise models, source models, and attenuation models (both regional and teleseismic).

CONCLUSIONS AND RECOMMENDATIONS

NetMOD has been designed to become the new standard in waveform sensor network simulation for the ground-based monitoring community. It will provide simulation quality as good or better than the existing available packages, with a vastly improved user interface, and with a much improved plugin-based architecture that should allow it to be adapted to the needs of the monitoring community for many years to come.

REFERENCES

Clauter, D.A. and R.R. Blandford (1998). Capability modeling of the proposed Internation Montoring System 60-station infrasonic network, proceedings of the infrasound workshop for CTBT monitoring, Santa Fe, NM, 1997, LANL report number LA-UR-98-56.

Hedlin, A.E., E.L. Fleming, A.H. Manson, F.J. Schmidlin, S.K. Avery, R.R. Clark, S.J. Franke, G.J. Fraser, T. Tsuda, F. Vial, and R.A. Vincent (1996). Empricial wind model for the upper middle and lower atmostpher, *J. Atmos. Terr. Phys*. **53** (13), 1421–1447.

Pulli, J & Z. Upton (2003). Hydroacoustic studies using HydroCAM – station-centric integration of models and observations, BBN Technical Memorandum W-2003, 9 pp.

Sereno, T.J., S.R. Bratt, and G. Yee (1990). NetSim: a computer program for simulating detection and location capability of regional seismic networks, SAIC Annual Technical Report SAIC90/1163.

IMPROVEMENT OF GT CLASSIFICATION OF SOVIET PNEs

Kevin G. Mackey and Kazuya Fujita

Michigan State University

Sponsored by the U.S. Department of State

Award No. SAQMMA11M2465

ABSTRACT

The monitoring/verification community generally utilizes PNE (Peaceful Nuclear Explosion) locations from Sultanov et al. (1999) as known Ground-Truth (GT) events. In reality, 43 of the 122 locations were determined seismically and are erroneous by up to 40 km. We seek to determine GT0-1 values for those seismically located events in Russia, Ukraine, Kazakhstan, and Turkmenistan, and to reconfirm or validate the locations of other Soviet PNEs thought to be GT0-1. The PNE locations in question are widely distributed, thus GT0-1 locations are very useful to the monitoring community as calibration events. Some PNEs currently categorized as GT0 or GT1 also have larger errors, up to 25 km. Locations will be determined using an integrated approach encompassing published open literature, analysis of satellite imagery and regional seismic data, perhaps supplemented by GPS determinations from visits to selected sites.

Our initial research in this project has been successful. We have determined a GT0 location for the PNE 'Taiga', which took place on 23 March 1971 and was the simultaneous detonation of three 15 kt devices for the purpose of a canal building experiment. The correct location is at 61.305^{o}N, 56.600^{o}E and is approximately 24km southeast of the location listed by Sultanov et al. (1999). Spacing between the devices was 165m. The excavation crater for Taiga is clearly visible on Google Earth satellite imagery as a north-south trending oblong lake approximately 600 m by 300 m in size.

Two PNEs were conducted on the territory of Ukraine, neither of which is listed as GT0-1 by Sultanov et al. (1999). The first PNE, 'Fakel', took place 9 July, 1972, and was a 3.8 kt detonation designed to extinguish a natural gas well fire. The PNE was located just north of the settlement of Pershotravneve, and approximately three km west of the village of Khrestyshche in northern Ukraine. The location was determined in the field following discussions with officials and geologists from the gas company that operates the wells in the area. We note that there is no clear expression of the PNE, and the site has been redeveloped with a large compressor station a few hundred meters to the south. The correct coordinates for the PNE Fakel are 49.552^{o}N, 35.471^{o}E, which is approximately 28 km south of the location given in Sultanov et al. (1999).

The second PNE in Ukraine was 'Cleavage'. Cleavage was a small 0.3 kt explosion that took place on 16 September, 1979 in the Younokommunist coal mine in eastern Ukraine. The location of Cleavage was determined by a site visit to the mine and a discussion with mines chief engineer. The coordinates for the PNE Cleavage are 48.214^{o}N, 38.284^{o}E. The location is approximately 2 km northwest from that given in Sultanov et al. (1999).

We have conducted literature searches on several other PNEs, are have generally confirmed the GT0-1 locations published by Sultanov et al. (1999) for the Azgir sequence. We have also uncovered film clips of several PNE detonations.

OBJECTIVES

The objective of this project is to determine GT0-1 locations for the PNEs that occurred in the Soviet Union. The main emphasis is on improving locations for those having only seismically determined locations as listed in Sultanov et al. (1999). We also hope to reconfirm or validate the locations of other Soviet PNEs thought to be GT0-1.

RESEARCH ACCOMPLISHED

Our research has identified GT-1 or better locations of both PNEs (Cleavage and Fakel) to have occurred on the territory of Ukraine, PNE Taiga in Russia, and confirmed the locations as given by Sultanov et al. (1999) for most of the Azgir PNE sequence in Kazakhstan. In addition, on-line video clips for three PNE detonations have been found to be available on Youtube. All Soviet PNEs are shown in Figure 1. Events discussed in this paper are labeled, as are other PNE sequences in Yakutia (Fujita et al., in press) and Mangyshlak (Mackey et al., these Proceedings) for which we have determined or verified GT0-1 locations.

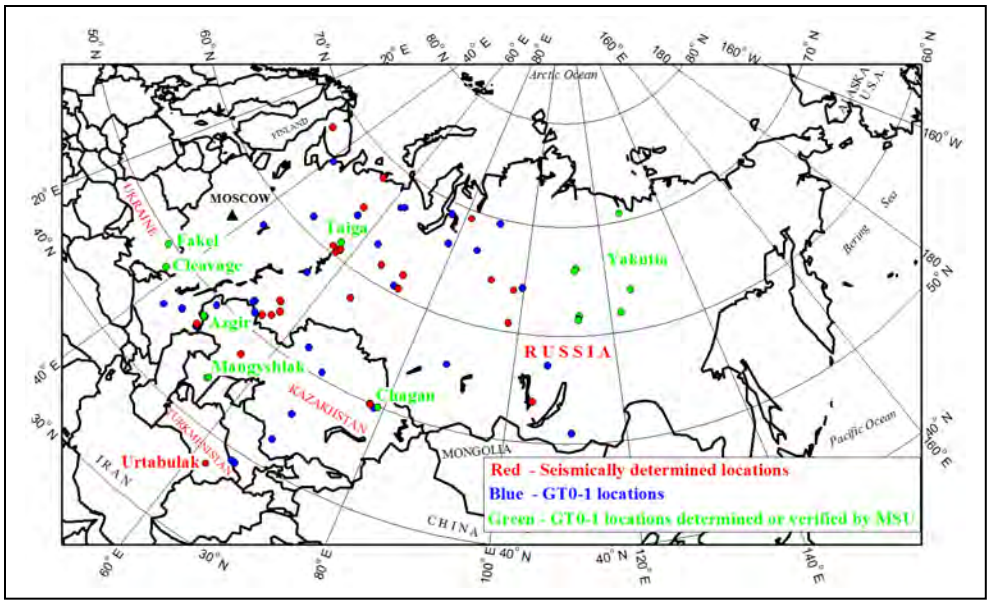


Figure 1. PNEs of the Soviet Union. Green events represent GT0-1 locations determined as a part of this or studies conducted at Michigan State University. See Fujita et al., (in press) for Yakutia events and Mackey et al. (these Proceedings) for Mangyshlak events. Red and blue represent events as published by Sultanov et al. (1999) as having unknown GT quality or GT0-1 quality respectively.

Taiga

The PNE 'Taiga' took place on 23 March, 1971, and was the simultaneous detonation of three 15 kt devices for the purpose of a canal building experiment. Sultanov et al. (1999) lists a location for Taiga in an isolated forest region with no apparent crater or nearby surface expression that would be expected from large excavation explosions. Ramzaev et al. (2011) and Ramzaev et al. (2012) have recently conducted radiological surveys of the Taiga PNE site. Both publications include maps and photos of the PNE site and an approximate location of the experiment. The excavation crater for Taiga is clearly visible on Google Earth satellite imagery as a north-south trending oblong lake approximately 600 m by 300 m in size (Figure 2).

From Google Earth imagery, the center of the lake is at 61.306°N, 56.599°E, which corresponds to the central of the three thermonuclear explosive devices. The other two devices were emplaced 165m north and 165m south of this point, based on notations in Sultanov et al. (1999). This location for Taiga, which we consider to meet GT0-1 criteria, is approximately 24 km southeast of the seismically determined location listed by Sultanov et al. (1999). A short Soviet era documentary film of the Taiga PNE was produced and is available on Youtube at http://www.youtube.com/watch?v=DV9OsftqDxw in Russian. The film shows preparation work for the experiment, the detonation, and after effects.



Figure 2. Excavation crater of the Taiga PNE experiment. Three 15 kt explosions were detonated simultaneously to form this lake. Image from Google Earth.

Fakel

The PNE 'Fakel' took place on 9 July, 1972, and was a 3.8 kt detonation designed to extinguish a natural gas well fire. The PNE was located just north of the settlement of Pershotravneve, and approximately three km west of the village of Khrestyshche in northern Ukraine (Figure 3). The location was determined in the field following discussions with officials and geologists from the gas company that operates the wells in the area. A sketched map provided indicated that the PNE took place about mid-way between well numbers 258 and 181 (about 100m from each) and about 200m west of well number 303. We located well numbers 258 and 303 in the field. The number tag for well 181 was missing, but given its proximity to the other wells and the match to the sketch map provided we are confident in its identification. Figure 4 shows a ground view of well 258 with the PNE site behind. We note that there is no clear expression of the PNE, and the site has been redeveloped with new gas wells and a large compressor station a few hundred meters to the south. The immediate vicinity of the Fakel site is not farmed, though we are unsure if this is significant. We are also unsure if the location determined represents the surface point above the detonation, or the surface location of the borehole into which the bomb was emplaced. For general but independent verification of the site, we asked people in the nearby (~1 km distant) settlement of Pershotravneve the location of the explosion, and we were told it took place just north of the east end of the new compressor station. The coordinates for the PNE Fakel are 49.552^{o}N, 35.471^{o}E, which is approximately 28 km south of the location given in Sultanov et al. (1999).

Various locally published newspaper articles and internet articles in Russian indicate that there was some level of radiation release following the detonation. In addition, the gas company geologists we spoke to questioned us as to whether we had dosimeters or other equipment for measuring radiation with us because there can or could be some contamination at the site. Collectively, this seems to suggest that the site should be formally surveyed.

Fakel was recorded by seismic stations in Ukraine. We obtained several scans of seismograms of the explosion from the Crimean seismic network, several hundred km to the south (Figure 5).



Figure 3. Left – Overview of the site of PNE Fakel in north-central Ukraine. Right – The location of Fakel as determined using referenced Gas wells. Image from Google Earth.



Figure 4. Left – Site of the PNE Fakel looking south. The compressor station is located in the background. Right – Gas well #258 used as a reference in locating Fakel. The PNE was approximately 100 m to the left (north) from this location. Photos by K. Mackey.

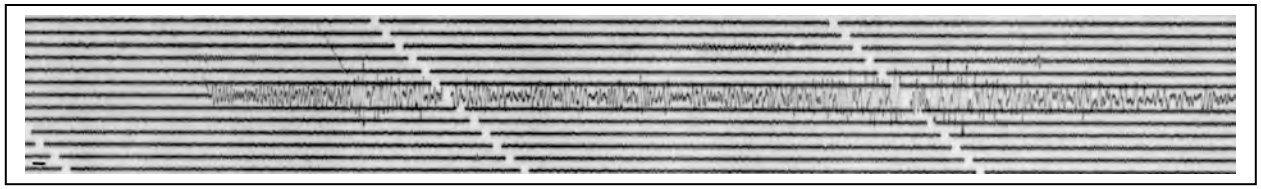


Figure 5. Scanned seismogram of Fakel as recorded at seismic station Alushta, several hundred km south on the Crimean peninsula. This and other scanned seismograms are of sufficiently good quality that they are candidates for digitization and other studies.

Cleavage

Cleavage was a small 0.3 kt explosion that took place on 16 September, 1979, in the Yunokommunarsk coal mine, about 5 km east of Yenakijeve in eastern Ukraine (Figure 6). The location of Cleavage was determined by a site visit to the mine and a discussion with mine's chief engineer. The explosion took place about 600m south of the mine's shaft house and approximately below the southeastern edge of the mine's tailings pile at the surface (Figure 7). The coordinates for the PNE Cleavage are 48.214°N, 38.284°E, approximately 2 km northwest from those given in Sultanov et al. (1999). The mine is no longer in possession of most information regarding the explosion, though the depth is confirmed as being between the 826 and 936 m levels, consistent with the 903 m reported by Sultanov et al. (1999).

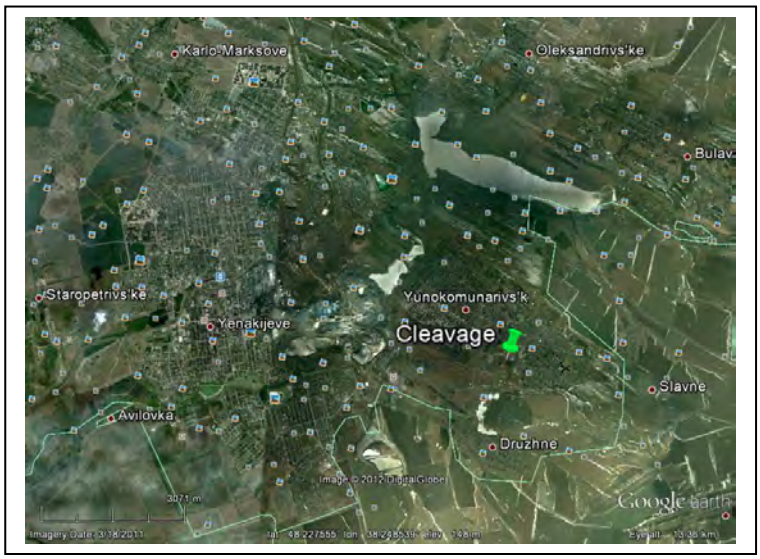


Figure 6. Location of the PNE Cleavage in eastern Ukraine, about 5 km east of Yenakijeve. Image from Google Earth.



Figure 7. Left – Location of the PNE Cleavage showing the relation to the mine shaft house and tailings dump. Image from Google Earth. Right – On-site photo of the mine tailing dump. The explosion took place at depth just to the left of the tailings. Photo by K. Mackey.

Cleavage was not well recorded and there is no seismically determined epicenter. It was recorded at weakly NORSAR but not recognized as a nuclear explosion due to its small size until after the collapse of the Soviet Union when more information became available (Ringdal and Richards, 1992). From our discussions at the mine,

seismographs were in-place and operating in other nearby coal mines when the explosion occurred. The explosion was preferentially recorded by stations to the east, while weakly visible on stations to the west. The reason for this is unclear, and it is also unclear if any of the mine seismograms still exist or if they are obtainable.

The mine is currently closed though being kept dewatered. Mining and government officials are unsure if or how radioactive contaminants may migrate if the mine is allowed to flood.

Azgir Sequence

The Azgir sequence consisted of 17 PNEs in western Kazakhstan between 1966 and 1979 (Figure 8; Table 1). Some of the PNEs consisted of 2 or 3 devices in the same hole detonated simultaneously. All Azgir PNEs are listed as GT0-1 by Sultanov et al. (1999). Careful examination of Google Earth satellite imagery revealed that in close proximity to each of the Azgir A-4 through A-11explosions is an area of disturbed ground with a circular fenced area between about 40 to 80 m in diameter (Figure 9), which we interpret to be the borehole locations. Azgir A-9 is an exception in that a circular lake is present. We also note that relocating these PNEs to the circular structures, the distribution of events becomes constrained to a systematic grid pattern of detonation locations, with many events lining up with each other. From this, we are confident that we can consider Azgir A-4 through A-11 to be GT-0 locations. This also verifies the GT0-1 location quality of Sultanov et al. (1999) for these events. Only Azgir A-5 was moved slightly more at 1.12 km.

The Azgir A-1 and A-2-X and A-3-X sequences are slightly more problematic as similar ring structures are not visible, though all Sultanov et al. (1999) locations are in near proximity to areas of disturbed ground. The Azgir A-1 and A-2-X sites have multiple areas of disturbed ground that could represent borehole locations. However, a fairly detailed map of the Azgir test site is available at http://wikimapia.org/6013134/Nuclear-test-site-Azgir that constrains the specific areas of disturbance and PNE location to within tens of meters. Both the Azgir A-1 and A-2-X sites differ from the Sultanov et al. (1999) locations by about 250 m. The Azgir test site map also verifies the correct identification of disturbed ground locations chosen for the Azgir A-4 through A-11 sites.

The Azgir A-3-X sequence can be relocated to a small area of disturbed ground about 250 m west of the Sultanov et al. (1999) location that places it exactly on a linear trend that connects the Azgir A-4, A-8, and A-10 explosions. At this location, there appears to be two small dome structures that we speculate may be associated with the two PNEs conducted at the Azgir A-3 site. However, we note that the Azgir test site map identifies two regions for Azgir A-3-X, with the second being about 500 m southeast of the first that we identified above. The nature of the two sites remains unknown, though the Sultanov et al. (1999) location is approximately midway between the two.

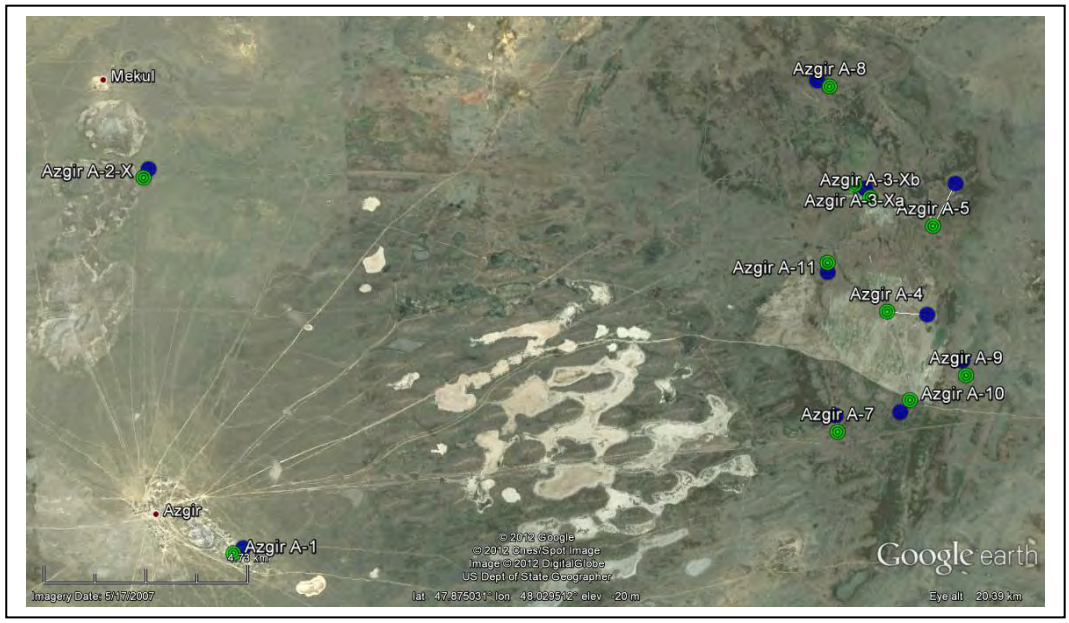


Figure 8. The Azgir test site. Blue points represent locations from Sultanov et al. (1999) and green this paper. See Table 1 for coordinates. Image from Google Earth.

Table 1. Coordinates of the PNEs detonated at the Azgir test site.

#	PNE Name	Date MM/DD/YYYY	Coordinates – This Paper	Coordinates – Sultanov et al. (1999)	Difference in km
1	**Azgir A-1**	04/22/1966	47.828°N 47.932°E	47.829°N 47.935°E	0.25
2	**Azgir A-2-1**	07/01/1968	47.907°N 47.910°E	47.909°N 47.912°E	0.23
3	**Azgir A-3-1**	12/22/1971	47.898°N 48.130°E a 47.895°N 48.134°E b	47.897°N 48.133°E	0.26 a 0.24 b
4	**Azgir A-2-2**	04/25/1975	47.907°N 47.910°E	47.909°N 47.912°E	0.23
5	**Azgir A-3-2**	03/29/1976	47.898°N 48.130°E a 47.895°N 48.134°E b	47.897°N 48.133°E	0.26 a 0.24 b
6	**Azgir A-4**	07/29/1976	47.871°N 48.138°E	47.870°N 48.133°E	0.93
7	**Azgir A-5**	09/30/1977	47.888°N 48.153°E	47.897°N 48.161°E	1.12
8	**Azgir A-2-3**	10/14/1977	47.907°N 47.910°E	47.909°N 47.912°E	0.23
9	**Azgir A-2-4**	10/30/1977	47.907°N 47.910°E	47.909°N 47.912°E	0.23
10	**Azgir A-2-5**	09/12/1978	47.907°N 47.910°E	47.909°N 47.912°E	0.23
11	**Azgir A-7**	10/17/1978	47.847°N 48.120°E	47.850°N 48.120°E	0.38
12	**Azgir A-2-6**	11/30/1978	47.907°N 47.910°E	47.909°N 47.912°E	0.23
13	**Azgir A-9**	12/17/1978	47.857°N 48.161°E	47.860°N 48.160°E	0.35
14	**Azgir A-2-7**	01/10/1979	47.907°N 47.910°E	47.909°N 47.912°E	0.23
15	**Azgir A-8**	01/17/1979	47.919°N 48.124°E	47.920°N 48.120°E	0.32
16	**Azgir A-11**	07/14/1979	47.882°N 48.120°E	47.880°N 48.120°E	0.22
17	**Azgir A-10**	10/24/1979	47.852°N 48.143°E	47.850°N 48.140°E	0.36



Figure 9. Google Earth images of the Azgir 10 and 11 sites showing the typical ring or presumed fence that we interpret as enclosing the borehole locations for the Azgir tests.

An area of disturbance that appears similar in character to the PNE detonation sites is also visible at coordinates 47.864°N x 48.114°E. This location falls on the geographical grid of detonation locations. As apparent on figure 9, a rectangular structure is clear at the center of the Azgir-11 ring, and visible to a lesser extent in the Azgir-10 ring. An identical structure is also present on the ground at 47.853°N x 48.135°E. It is not clear to us what either site represents, but we can speculate they may be sites of unused boreholes or experiments that did not occur.

Urtabulak

The Urtabulak PNE took place on 30 September, 1966 in Turkmenistan for the purpose of extinguishing a gas well fire. Although we have not yet established an improved location for the event, we note that a short Soviet era documentary film of the PNE was produced and is available on Youtube at http://www.youtube.com/watch?v=ord-AyaFLaA in Russian. The film shows the gas fire, preparation work for the experiment, the detonation, and after effects.

Chagan

Chagan was the first official PNE to occur in the Soviet Union, taking place 01/15/1965. This explosion took place at the test site in Kazakhstan and was intended to produce a crater. The crater was subsequently flooded and is now called Atomic Lake. The crater is clearly visible on Google Earth imagery and is at the coordinates published in Sultanov et al. (1999; Figure 10). The Chagan PNE is also the subject of a short Soviet documentary film that is available at http://www.youtube.com/watch?v=ZAoSUIASET0 in Russian.



Figure 10. Google Earth image of the crater formed from the Chagan PNE. The blue point represents the coordinates as published in Sultanov et al. (1999).

CONCLUSIONS AND RECOMMENDATIONS

The explosions of the Soviet PNE program represent a large dataset of GT events that are useful to the nuclear explosion monitoring community as well as the seismologists in general. This project is establishing GT0-1 locations for PNEs that previously had less accurate locations as well as verifying the quality of already established GT0-1 events.

ACKNOWLEDGEMENTS

We would like thank Konstantine Chalii for assistance in accessing PNE sites in Ukraine, the administrations of the Yunokommunarsk coal mine and Khrestyshche gas field for discussions and information on their respective PNE sites. We would also like to thank B. Pustovitenko for assistance in obtaining scans of seismograms from the Crimean seismic network of the Fakel PNE.

REFERENCES

Fujita, K., K. G. Mackey, and H. E. Hartse (in press). Ground truth determinations on Yakutian PNEs, *Bull. Seismol. Soc. Am*.

Mackey, K., H. Hartse, D. Burk, K. Fujita, and M. Pasyanos (2012). Seismic and geophysical characterization of northern Asia, these Proceedings.

Ramzaev, V., V. Repin, A. Medvedev, E. Khramtsov, M. Timofeeva, and V. Yakolev (2011). Radiological investigations at the "Taiga" nuclear explosion site: Site description and in situ measurements, *J. Environ. Radioac.* **102** (7), 672–680. doi:10.1016/j.jenvrad.2011.04.003

Ramzaev, V., V. Repin, A. Medvedev, E. Khramtsov, M. Timofeeva, and V. Yakolev (2012). Radiological investigations at the "Taiga" nuclear explosion site, part II: man-made γ-ray emitting radionuclides in the ground and the resultant kerma rate in air, *J. Environ. Radioac.* **109** (7), 1–12. doi:10.1016/j.jenvrad.2011.12.009

Ringdal, F. and P. G. Richards (1992). The Ukrainian event of 16 September 1979, *in* NORSAR Scientific Report No. 1-92/93, Semiannual Technical Summary 1 April – 30 September 1992, p. 120–124.

Sultanov, D. D., J. R. Murphy, and K. D. Rubinstein (1999). A seismic source summary for Soviet peaceful nuclear explosions, *Bull. Seismol. Soc. Am.* **89**, 640–647.

PROGRESS IN SIGNAL-BASED BAYESIAN MONITORING

David A. Moore[1], Kevin M. Mayeda[1], Steve M. Myers[2], Min Joon Seo[1], and Stuart J. Russell[1]

University of California at Berkeley[1] and Lawrence Livermore National Laboratory[2]

Sponsored by the Defense Threat Reduction Agency and the Comprehensive Nuclear-Test-Ban Treaty Organization

Award Nos. HDTRA1-11-1-0026 and 2011-2000

ABSTRACT

Localization tools such as the CTBTO's GA (Global Association) system work by analyzing detections of arriving phases; these detections constitute a discretized, thresholded summary of information from the underlying seismic waveforms. By contrast, our SIG-VISA (SIGnal-based Vertically Integrated Seismic Analysis) system operates directly at the level of the raw waveforms or envelopes, applying Bayesian inference to a generative probabilistic model of seismic traces to search for the event bulletin having the highest posterior probability given the observed signals. The signal-based approach has the potential for improved sensitivity and localization performance compared to purely detection-based methods.

The SIG-VISA generative envelope model views the observed signal envelope as the composition of a background noise process plus a set of arriving phase envelopes; in its simplest form, each phase envelope consists of a parameterized template perturbed by an autoregressive process. We build station-specific models for the template shape parameters, including amplitude and coda decay rates across multiple frequency bands, as well as the parameters of the noise and signal perturbation processes. The signal-based model leads to increased sensitivity compared to a purely detection-based model, since by comparing the observation likelihoods under the signal and noise models we can extract statistical evidence from sub-threshold arrivals (or their absence) which would otherwise be ignored. This capability is especially valuable for faintly detected (low-magnitude and/or teleseismic) events.

A further advance of SIG-VISA is the incorporation of *nonparametric* modeling using Gaussian processes (GPs), a class of statistical models closely related to the kriging method in geophysics. GPs provide a probabilistic framework for predicting the attributes of future events based on past events in similar or nearby locations. SIG-VISA makes use of GP models for the template shape parameters, improving localization performance relative to simpler parametric models of the types used in previous systems (e.g., NET-VISA). Moreover, we provide preliminary results from a nonparametric model for the template perturbations that captures the phenomenon of correlated waveforms from nearby events; this allows a waveform matching effect to fall out naturally from the probabilistic inference.

OBJECTIVES

Our objective is to realize dramatic improvements in sensitivity, accuracy, and robustness of global monitoring systems for nuclear tests through a novel Bayesian approach to whole-network data analysis.

The project is developing a new mathematical and computational approach to the analysis of the sensor data collected from global monitoring systems. The approach involves the application of rigorous Bayesian statistical analysis to the entire monitoring problem and requires the development of a complete, vertically integrated, empirically validated, generative statistical model of event occurrence, signal propagation, and sensing, as well as efficient and provably correct inference algorithms for extracting the most likely event history and/or a posterior distribution over event histories from the measured sensor data. At a fundamental level, we hope to gain a much deeper and more accurate understanding of the limits of detectability than is given by a classical per-station SNR analysis.

We expect to realize the following benefits: (1) Substantially more accurate and sensitive detection and localization of events, particularly at lower magnitudes. (2) A monitoring software architecture that allows straightforward incorporation of multiple sensor modalities (including new modalities as they arise) and new and improved physics-based models such as source models and phase velocity and attenuation models. (3) Extensibility to other monitoring problems arising in treaty verification.

RESEARCH ACCOMPLISHED

This report presents a fully specified generative model for seismic waveform envelopes observed across a network, implemented in a prototype version of the SIG-VISA system. We describe the components of the model, demonstrate the process of learning model parameters, and demonstrate localization of events using data from the CTBTO's International Data Centre (IDC).

Background: Signal-based Bayesian monitoring

Seismic monitoring can be described in the language of statistics as an *inference* problem: given as input the waveform data recorded by a network of monitoring stations over a period of time, the goal is to infer an event bulletin, i.e., a list of seismic events hypothesized to have occurred during that period, identified by their locations and estimated magnitudes. This is sometimes referred to as an *inverse* problem, since it requires reasoning backwards from the observations to the events that produced them. Bayesian statistics provides a rigorous mathematical framework for the solution of inverse problems, and has been well-established throughout the sciences including seismology (Duijndam, 1988a,b), having been applied successfully in areas including tomography (Taylor et al., 2001; Simmons et al., 2010b) and event localization (Myers et al., 2007, 2009). Recently, the NET-VISA system (Russell et al., 2009, 2010; Arora et al., 2011a,b) has demonstrated what is to our knowledge the first complete Bayesian monitoring system, yielding more accurate locations and fewer missed events when compared to traditional systems such as IDC's Global Association (GA) system.

A Bayesian approach to inference involves two components: a *prior probability distribution* $\Pr(X = x)$ over a set of hypotheses X, and a *likelihood* or *conditional probability model* $\Pr(Y = y \mid X = x)$ which gives the probability of observing the evidence y under the given hypothesis x. The prior and the likelihood together comprise a *generative model* specifying a complete joint distribution over hypotheses and observations, as well as any additional latent variables introduced by the model. In seismic monitoring, the hypotheses are the event bulletins, the evidence consists of the raw waveforms recorded by the network, and the conditional probability model (sometimes called the *forward* model) describes how signals propagate through the earth and how they are detected by sensors, as well as the ways in which noise signals arise. The *posterior probability distribution* allows us to reason backwards from the evidence (observed waveforms) to hypotheses (event bulletins), and is given by *Bayes' rule*:

$$Pr(X \mid Y = y) = \alpha \, Pr(Y = y \mid X) \Pr(x)$$

where α is a normalizing constant. To the extent that the prior and conditional distributions correctly describe knowledge of seismicity, propagation, and so on, the posterior distribution represents an optimal inference from the available data. Computing the posterior distribution (or a point estimate of it, e.g., the single most probable hypothesis) is generally nontrivial and often requires sophisticated search or sampling algorithms.

As a simplifying assumption, current seismic monitoring systems generally include a concept of *detections*; standard practice is to declare a detection when the average amplitude in a short time window increases above a predefined multiple of average amplitude in a long time window (a.k.a. short-term average/long-term average, STA/LTA). The

set of detections thus functions as an intermediate representation of the raw waveforms recorded throughout the network, yielding a simpler inference problem at the cost of throwing away potentially valuable information. By contrast, the signal-based approach developed in SIG-VISA models the waveform traces directly, reducing information loss and yielding a number of potential advantages:

- Detection-based systems face a tradeoff in setting the detection threshold: too low and the system is swamped with false detections, too high and it could miss genuine events. Modeling the signal directly eliminates the need for such a threshold and allows SIG-VISA to incorporate arrivals of all strengths as statistical evidence; thus, a large number of very weak (sub-threshold) arrivals might have the same inferential power as a smaller number of stronger arrivals. Roughly speaking, signal-based Bayesian monitoring improves over detection-based methods in much the same way that array stations improve over single seismometers, by aggregating signals recorded at multiple sensors to increase SNR.
- When signals from two events overlap at a station, a detection-based system might record only a single large detection incompatible with the locations and magnitudes of both events. By contrast, the signal-based approach simply models the observed waveform signal and has the ability to assign a fraction of the received energy at each moment to each event, in proportions determined by the inference process.
- Finally, signal-based approaches have the ability to take into account more detailed information regarding the shape and characteristics of the observed waveforms. This can involve modeling high-level characteristics such as the decay rate of the seismic coda, which can in some cases be predicted quite accurately from an event's location (Mayeda et al., 2003), as well as lower-level details including the fluctuations of the waveform itself, which are known to be correlated for events in nearby locations; folding this information into the probabilistic model allows the inference process to achieve some of the benefits of waveform matching algorithms (Thorbjanrardottir et al., 1987; Harris, 1991; Withers et al., 1999, Waldhauser and Ellsworth, 2000; Schaff and Richards, 2004).

In this paper we focus primarily on modeling the shape and characteristics of observed signal envelopes, describing a generative probabilistic model for signal envelopes that includes a location-dependent template model learned from historical data, as well an extension to this model that implements an additional location-specific component, modeling shorter-term fluctuations determined by path effects.

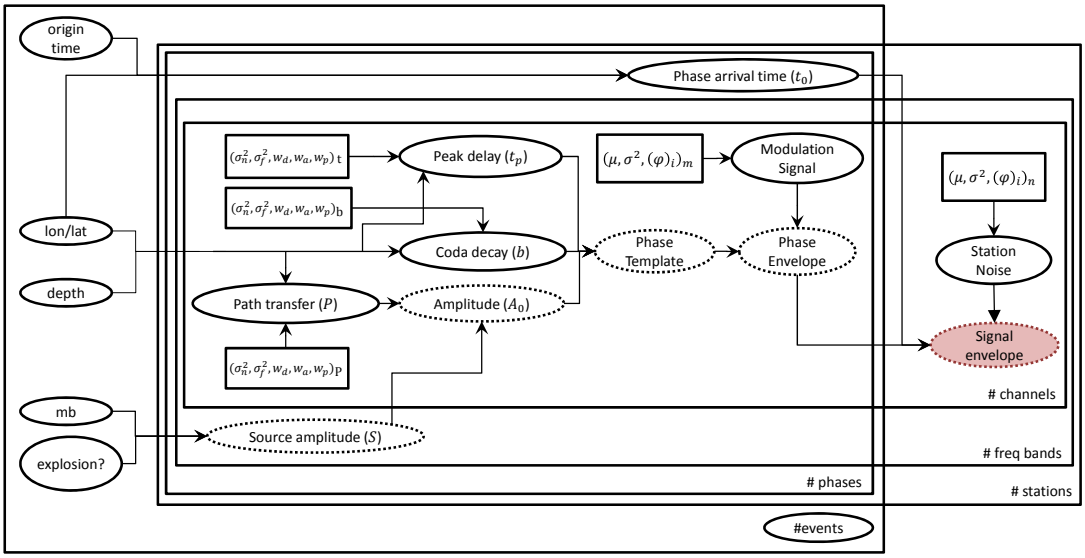


Figure 1. The SIG-VISA generative envelope model. The graph shows dependence relationships among variables in the model, beginning with the event attributes on the left and ending on the right with the observed signal envelopes, in all channels and frequency bands at all stations in the network. The model specifies a conditional probability distribution for each variable given its parents; variables shown with dotted borders are deterministic functions of their parents. Parameters for the Gaussian and autoregressive process components are indicated in square boxes. The "plate" notation is standard for graphical models and should be interpreted as creating a number of independent copies of each variable, e.g., each event has an origin time sampled independently of the other events.

The SIG-VISA Model

The prototype SIG-VISA implementation takes as input the waveforms observed by a network of three-component stations (an extension to array stations is planned as future work). Rather than modeling the raw waveforms directly, we instead model their envelopes within a range of narrow frequency bands, from 0.1-0.2Hz up to 6-8Hz. The envelope representation removes phase information while retaining the level of energy arriving over time; using multiple frequency bands allows us to more accurately model frequency-dependent characteristics of the signal such as the coda decay rate (Mayeda et al, 2003) and spectral content.

Figure 1 shows a graphical view of the SIG-VISA generative model. The model can be understood intuitively as telling a generative story, i.e., a series of steps to generate a sample observation:

1. First, the number of events in the world is sampled from a prior distribution.
2. Characteristics of each event are then sampled independently from prior distributions, including origin time, location, depth, body wave magnitude, and whether the event is a natural event or an explosion. Note that the "explosion" attribute is not intended to be a determinative feature of the system output, but is used internally to allow the model to fit events whose source spectra are not consistent with the predicted spectrum of a natural event.
3. Each event generates a P and S arrival at each site. (Other phase types are supported by the modeling framework but are not currently implemented.) The arrival time of each phase depends on the origin time of the event as well as the event's location relative to the station.
4. Each arriving phase generates a phase envelope, which is taken to be the product of a parameterized template with a stochastic modulation signal. The template captures the general pattern of arriving energy and subsequent decay, while the modulation signal corresponds to shorter-term, less predictable fluctuations (though these fluctuations can sometimes be predicted due to waveform correlations between nearby events, as described below).
5. Finally, the observed envelope for each channel in each frequency band at each station is modeled as the sum of all the arriving phase envelopes, plus a background noise process. Figure 2 shows an example.

The first three steps are essentially the same in both the SIG-VISA and NET-VISA models; Arora et al. (2011a,b) provide details on the event prior distributions and phase arrival time model. Here we focus on the later steps of the process, including the template model and its parameterization as well as models for the modulation signal and station noise processes.

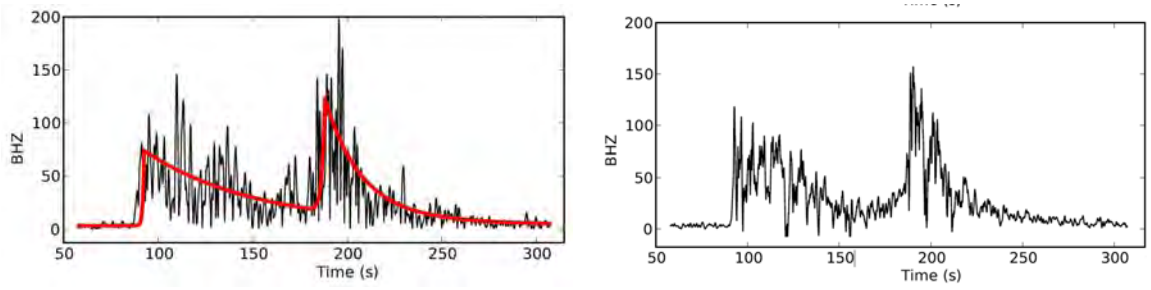


Figure 2. (a) An observed envelope at a station (IDC evid 5305385 at AFI, 2-3Hz), showing the P and S arrivals and subsequent coda decays. The red line indicates the template fit. (b) A synthetic envelope generated from the template and an autoregressive modulation process.

Template Model

The Bayesian framework allows wide flexibility in the choice and parameterization of a template model. Currently we model each phase envelope using a simple paired-exponential template (cf. Huseby et al, 1998) with three parameters: the peak delay t_p(in seconds, the time from the first particle motiont_0 until the envelope reaches its peak), the amplitude/peak height A_0, and the decay rate b. The decaying portion of the paired-exponential template models the seismic coda, and corresponds to a special case (with γ=0 fixed) of the coda decay model introduced by Aki (1969) and used in subsequent coda-modeling work, by, e.g., Mayeda et al. (2003):

$$A(f,d,a,t) = A_0\,(f,d,a) \cdot (t - (t_0 + t_p))^{\gamma} \cdot \exp\,(b(f,d,a) \cdot (t - (t_0 + t_p)))$$

This expression indicates that the template parameters A_0 and b are dependent on the frequency band f as well as the station-event distance d and azimuth a (our model also allows t_p to depend on $f, d, and\ a$, but in practice we have not found any significant empirical relationship between these quantities) . The time in seconds elapsed from the template peak is given by $t - (t_0 + t_p)$. The template amplitude $A_0\ (f, d, a) = S(f) \cdot P(f, d, a)$ is a function of the source amplitude *S*, as well as a path-dependent amplitude correction term *P* that encapsulates the site response, transfer function, and geometrical spreading/attenuation terms used by Mayeda et al. (2003). Models for the source amplitude and path correction terms are described in the sections that follow.

Source Spectra

The source amplitude *S* is computed deterministically as a function of frequency using a source spectrum model. Since natural events and explosions have different spectral signatures, we use different models for the two event types; the inference algorithm considers both hypotheses for each event. For explosion spectra we plan to implement the Mueller–Murphy model (Mueller and Murphy, 1971), whereas for events hypothesized to be natural we currently use a version of the Brune source model (Brune, 1970):

$$S(f) = \frac{FM_0}{\left(1+\frac{f}{f_0}\right)^2}$$

$$f_0 = K\beta^3 \sqrt{\frac{16\Delta\sigma}{7M_0}}$$

where f_0 is a corner frequency calculated following Myers et al (1998), assuming a stress drop ($\Delta\sigma$) of 10 bars for shallow events, S wave velocity of 4.5m/s, and with the constant K set to 1.5 for P waves and 0.33 for S waves. The constant *F* is not set a priori, but is instead learned empirically as part of the path-specific correction *P(f,d,a)* described below. Finally, the seismic moment M_0 is estimated from the IDC body wave magnitude (m_b) using the following relationships:

$$M_w = 1.46 m_b\ 0 - 2.42 \qquad \text{(Sipkin, 2003)}$$

$$M_0 = \exp\left(1.5 Mw + 9.1\right) \qquad \text{(Kanamori, 1977; Hanks and Kanamori, 1979)}$$

Nonparametric Models of Template Parameters

Since SIG-VISA's templates are defined by three parameters, training the template model involves learning models for each of those parameters conditioned on the event properties (note that in the case of the amplitude A_0 this reduces to learning the path-specific corrections $P(f, d, a)$). In particular, we learn these models using Gaussian process regression (Rasmussen and Williams, 2006), also known as kriging. Since GP regression is a fully probabilistic technique — i.e., it computes a Bayesian posterior distribution on the regression function — it delivers a fully quantified estimate of uncertainty along with each prediction. Thus a GP regression model can produce highly confident predictions in areas where historical data are abundant, while still providing its best guess (and admitting its uncertainty) in areas where no data are available.

The extent to which a training example in a particular location influences the predictions in a different location is determined by the *covariance kernel* of the Gaussian process. The kernel currently used by SIG-VISA represents event locations using cylindrical coordinates centered at the station location; that is, $x = (x_d, x_a, x_p)$ where x_d is the station-to-event distance, x_a is the station-to-event azimuth, and x_p is the event depth. The functional form of the kernel is given by:

$$k\left(x^{(1)}, x^{(2)}\right) = \sigma_f^2 \cdot \exp\left(-\left(\frac{\sqrt[3]{x_d^{(1)}} - \sqrt[3]{x_d^{(2)}}}{w_d} \right)^2 - \left(\frac{d_a\left(x_a^{(1)}, x_a^{(2)}\right)}{w_a} \right)^2 - \left(\frac{\sqrt[3]{x_p^{(1)}} - \sqrt[3]{x_p^{(2)}}}{w_p} \right)^2 \right) + \sigma_n^2 \cdot \delta\left(x^{(1)}, x^{(2)}\right)$$

where $\sigma_f, \sigma_n, w_d, w_a, w_p$ are hyperparameters specifying the regression function variance, iid noise variance, and correlation length-scales for distance, azimuth, and depth respectively. Note that the distances and depths are transformed by a cube root; this serves to emphasize the effect of small changes in those coordinates at regional distances and shallow depths, and correspondingly to de-emphasize them for teleseismic or deep events. The azimuth-comparison function d_a computes the difference in degrees between $x_a^{(1)}$and $x_a^{(2)}$, and then scales the result by (the cube root of) the mean distance of the two events, $\sqrt[3]{\frac{x_d^{(1)} + x_d^{(2)}}{2}}$. This gives greater weight to differences in azimuth between teleseismic events, corresponding to the greater physical distances between such events.

We construct the training sets for the GP models using the iterative process described in the section on "Learning" below. Given a training set, the GP hyperparameters are learned via maximum likelihood on the training set and then used to train the full GP model (Rasmussen and Williams, 2006). Figure 3 evaluates the effectiveness of this process, showing that the nonparametric, location-sensitive models output by the GP often perform significantly better than a simple linear trend based on distance from the station, both when predicting the coda decay rate as well as when predicting the observed amplitude of an arrival. Figure 4 shows the relationship between coda decay rates and station-to-event distance and azimuth at a single station; note that despite the lack of clear linear trends in the data with respect to distance or azimuth individually, GP regression was able to perform well at this station. This suggests that the regression is successfully learning the properties of events in specific regions. By way of illustration, Figure 6 shows the predicted coda decay rates, and the uncertainty in those predictions, for locations around the world. Note that the GP regression predictions are most confident in areas where the most training data are available, as one would expect.

Modulation and Noise Models

The simplest form of the SIG-VISA model takes both the template modulation and station noise processes to be autoregressive (AR) processes (Box et al., 1994), parameterized by a mean μ, white noise variance σ^2, and a set of n weights (φ_i), where n is the order of the AR process (a more sophisticated modulation model is described below). The use of an AR model allows these signals to exhibit relatively smooth and coherent fluctuations over time, as opposed to, e.g., an iid Gaussian noise model which would be much more "jumpy" and would introduce a strong dependence on the signal sampling rate. The parameters of the modulation process are learned from historical data at each station for each channel and frequency band, while the AR station noise models are re-learned for every hour of incoming data, to account for potential changes in background noise levels over time. When a signal can be fully observed, as is the case with the station noise process in the absence of any arriving phases, then learning the AR parameters for a process of a given order is straightforward using the Yule–Walker equations. We search for the process order that maximizes the log-likelihood of the data under five-fold cross-validation; in our experiments the optimal order tends to be relatively constant around 17 (with signals sampled at 40Hz) across a range of stations and time periods.

Learning the Model

Although we have discussed straightforward methods for learning both the template parameter models and the modulation signal model (GP regression and the Yule–Walker equations respectively), we are generally not so lucky as to be able observe or train models for these quantities directly. Instead, the envelope that we observe is merely the product of an unknown modulation process with an unknown template, leaving us with some uncertainty about the contributions of each component. To learn models for these unobserved variables, we apply "hard" expectation-maximization (Dempster et al., 1977): beginning with an initial guess for a set of AR parameters describing the modulation process, we find the most likely template for every phase arrival in our training set (that is, we run an optimization algorithm to find the set of template parameters that maximizes the probability of the observed signal under the assumed modulation model parameters). We then use these templates to re-estimate the modulation process parameters, by dividing the observed envelope by the optimized template to extract the modulation signal (which we cut off at some threshold above the noise floor to reduce the potential impact of station noise on the extracted signal), then using the Yule–Walker equations to directly learn a new set of modulation parameters. We also use these templates as a training set for learning the template parameter models. By iterating these steps,
SIG-VISA converges to increasingly accurate estimates of modulation signal parameters as well as the template parameters.

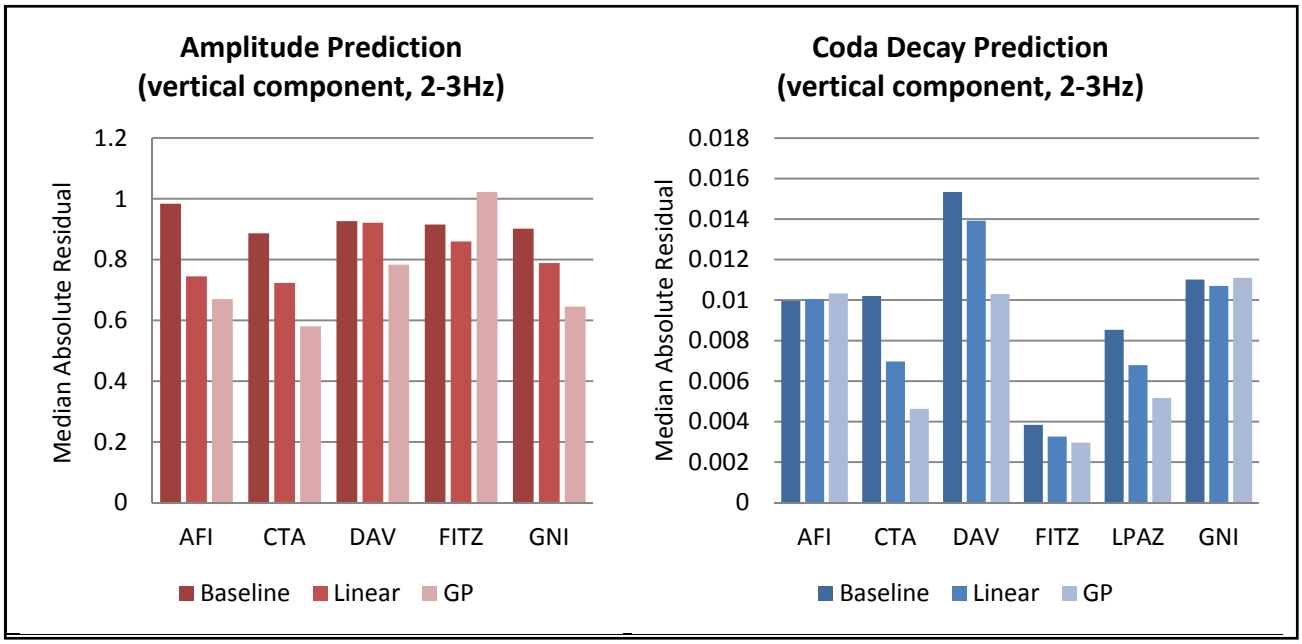


Figure 3. A comparison of models for P wave coda amplitude and decay rates at several IDC stations. Each result is a five-fold cross validation The linear model performs separate linear regressions against the event distance for regional and teleseismic (>2000km distance from station) events, while the baseline always predicts the mean value observed at the station.

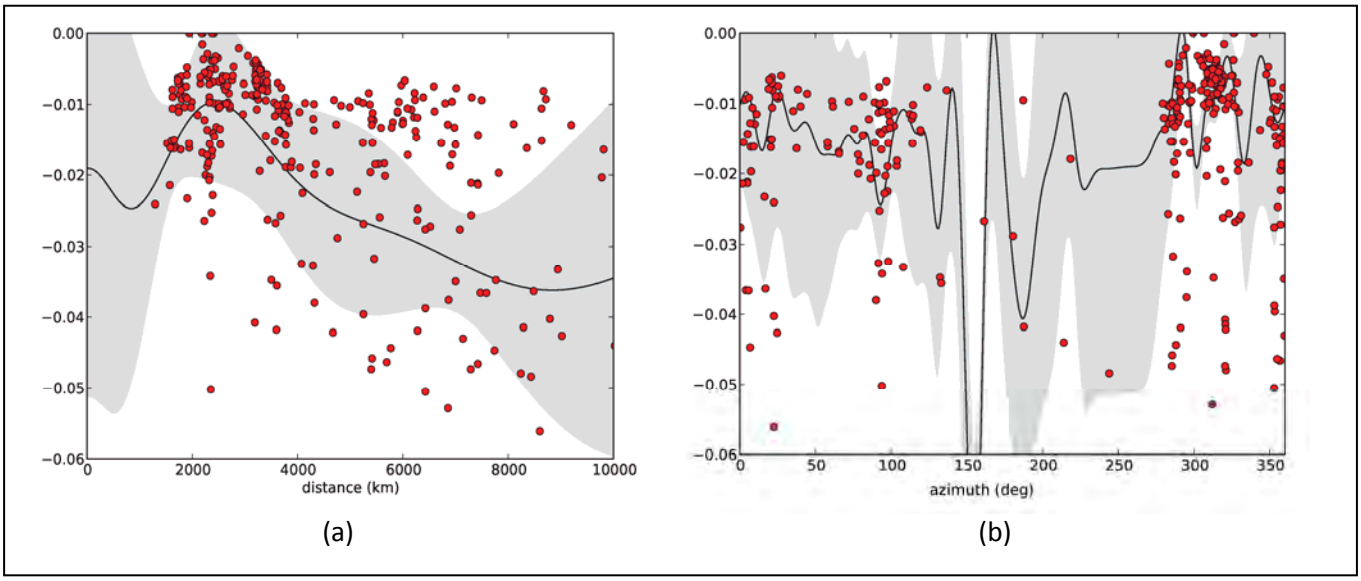


Figure 4. P coda decay rates at site CTA. (a) Gaussian process predictions for events at a range of distances, with station-to-event azimuth and event depth fixed at 0 (note that many of the points far away from the regression line have very different azimuths or depths). (b) Gaussian process predictions for a range of station-to-event azimuths, assuming depth 0 and a distance of 2700km. The shaded area illustrates one standard deviation from the mean (thus about 68% of the probability mass).

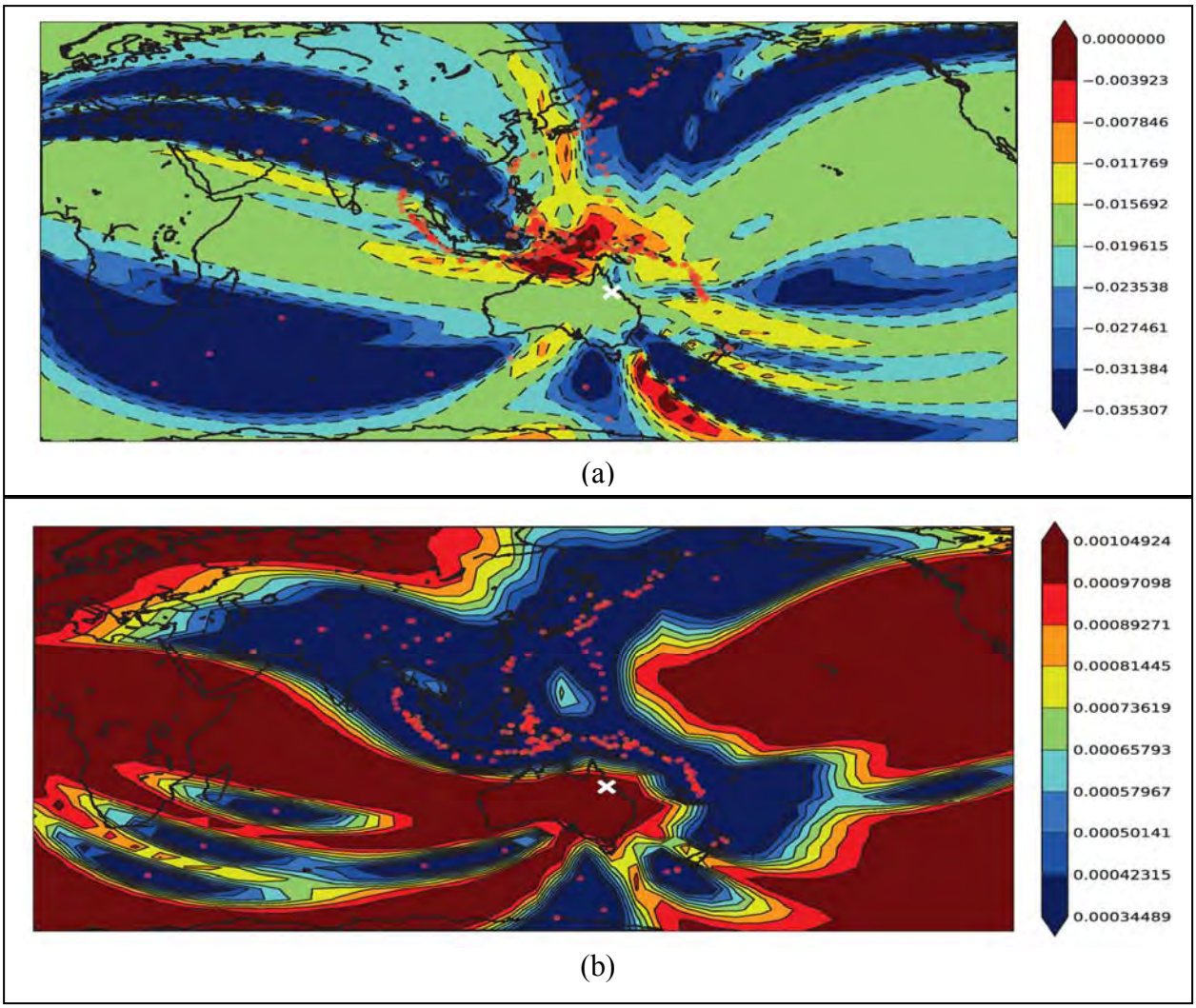


Figure 5. (a) Predicted P wave coda decay for surface events detected at site CTA (site location is labeled with a white 'x'). (b) Variance of P wave coda decay. Both maps show the 313 events from the training set plotted in red.

Inference and Event Localization

Although we have focused primarily on the task of building a generative model, performing efficient inference within such a model is one of the major challenges in signal-based Bayesian monitoring. We plan to take on this challenge directly in future work. Our current prototype implementation uses a grid search over event locations, integrating out the template parameters using Monte Carlo sampling and evaluating the likelihood of the sampled envelopes relative to the observed envelope under the autoregressive noise and modulation models, to compute the density for a single event location using evidence from a small number of stations. An example is shown in Figure 6.

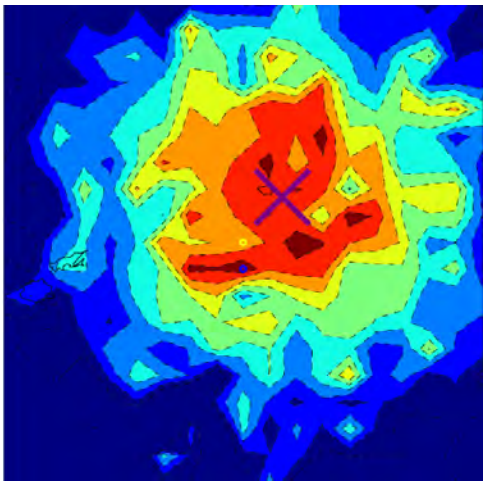


Figure 6. Posterior location density for IDC evid 5373954 using waveforms from sites AFI and URZ. The posterior mode is marked by a blue circle, the LEB location is labeled with a yellow circle, and the purple X indicates the location of station AFI. The width of the plot is 20 degrees, and the distance between the posterior mode and LEB location is approximately 1.2 degrees.

Waveform Matching via the Modulation Model

An interesting extension to the basic SIG-VISA system described above involves replacing the randomly sampled modulation signal with a signal conditioned on the event location. This addition models the established tendency of nearby events to produce highly correlated waveforms due to path-specific scattering, which has been exploited by waveform matching techniques (Thorbjanrardottir et al., 1987; Harris, 1991; Withers et al., 1999, Slinkard et al., 2011). Including such a constraint in our model causes waveform matching behavior to emerge naturally from the probabilistic inference process. Such behavior is especially valuable for a monitoring system dealing with aftershock sequences consisting of a large number of events occurring within a small area. More generally, waveform matching improves localization and helps in avoiding association errors, thus improving overall monitoring performance.

To obtain the desired functionality, we need a generative model for the modulated signal that produces similar modulations when two events are nearby. In an ideal world, events in the *same* location with the *same* source mechanism would produce *identical* modulated signals at a given station; hence, one could consider learning a deterministic spatial model of modulations. Absent any information about the source mechanism, we should still allow for variations in modulation even from events in the same location. One simple mechanism which implements this functionality is to model the modulation signal as an autoregressive process as above, but with a spatial prior distribution over the AR process parameters (e.g., a Gaussian process learned from historical data, similar to the use of GP regression for template parameters described above) instead of assuming a single constant set of parameters for all events observed at a station. Since the parameters of an AR process determine its spectral characteristics, this technique allows the model to learn the general spectral properties of events occurring in different locations. Figure 7(a) shows the power spectral density of three event arrivals, two from nearby locations and one further away, suggesting that such spectral properties have the potential to distinguish event locations. The spectra from the two "close" events (18km apart) are strikingly similar. By way of demonstration, Figure 7(b) plots the posterior location density for IDC event id 4689462, based on the waveform detected at a single station (MK31) and using a GP regression model trained on the parameters of an order-5 AR model for the raw waveforms. (In our preliminary experiments we have not yet had the chance to test this approach for modeling the modulation signal in the context of the template model described above, but expect those experiments to yield similar results.) Note that the figure shows a likelihood peak within the same cluster of events as the true event location.

A second mechanism we are considering is to model the modulation signal as a random linear combination of Fourier or wavelet basis functions, now with a spatial prior distribution (e.g., a Gaussian process) on the basis coefficients. Since this approach models the modulation signal as a deterministic function of the regression outputs (as opposed to the autoregressive approach of the previous paragraph, which introduces additional randomness in the sample path of the AR process), we believe it has the potential to yield sharper location estimates, though our experiments are still in the preliminary stages. Figure 8 shows a pair of synthetic signals generated using this approach.

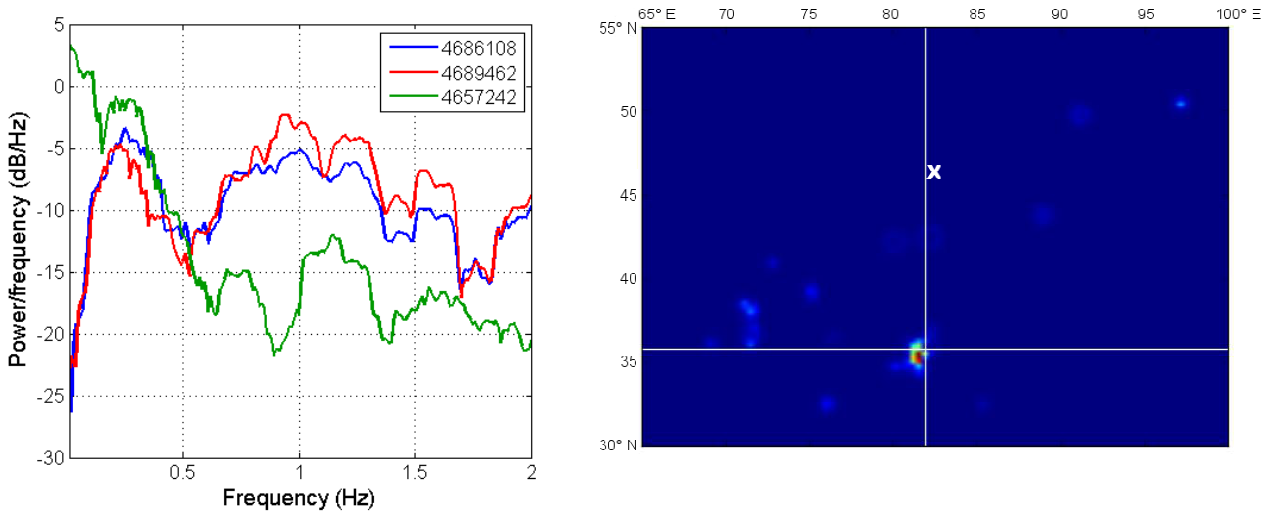


Figure 7. (a) Power spectral densities of raw waveforms (40s after Pn arrival) recorded by the vertical component of IDC station MK31 from the Makanchi array. The events with IDC evids 4689462 and 4686108 are located at distance 18km from each other, and their waveforms have a normalized cross-correlation peak of 0.59. Event 46572742, which is included for contrast, is at a distance of approximately 70km and has a cross-correlation peak of approximately 0.07 vs each of the other two events. (b) Posterior location density for IDC evid 4689462, under a GP regression model for the AR coefficients trained on raw waveforms from 99 other event arrivals during a two-week time period at MK31 (the station location is market with a purple X). The intersection of the two white lines is the true event location.

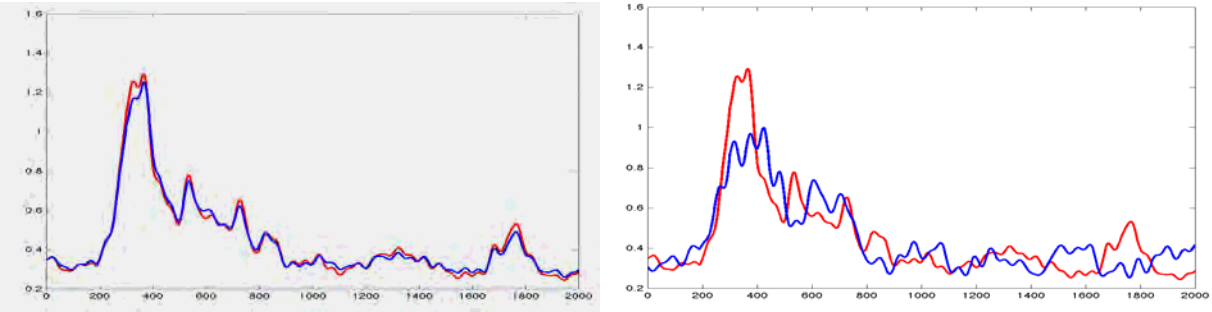


Figure 8. Illustration of a deterministic location-based prior for a synthetic Fourier basis envelope model. (a) A reference envelope (red) and a sampled envelope (blue) from the Gaussian-process generative model for a nearby event location. (b) The same reference envelope (red) and a sampled envelope (blue) from a distant event location. Here, "nearby" and "distant" are relative to the Gaussian process correlation distance.

CONCLUSIONS AND RECOMMENDATIONS

Our work builds upon recent successes in Bayesian monitoring and aims to continue the progress by extending a generative probability model to waveform envelopes. Here we have described such a model, which is implemented in a prototype system. Areas for future work include refinement of the model and an extension to array stations, more complete incorporation of a waveform matching component, and progress towards efficient inference techniques.

ACKNOWLEDGEMENTS

We gratefully acknowledge the support of DTRA for this work; as well as the CTBTO for providing data as well as access to their vDEC system where several of these experiments were performed. We also thank Megan Slinkard and Regina Eckert of Sandia National Labs for sharing with us their data on correlated arrival waveforms.

REFERENCES

Aki, K. (1969). Analysis of the seismic coda of local earthquakes as scattered waves. *J. Geophys. Res*. **74**, 615–631.

Arora, N. S., S. J. Russell, P. Kidwell, and E. Sudderth (2011a). Global seismic monitoring as probabilistic inference. In *Advances in Neural Information Processing Systems 23*, MIT Press.

Arora, N. S., S. J. Russell, P. Kidwell, and E. Sudderth (2011b). Global seismic monitoring: A Bayesian approach. In *Proc. AAAI-11*, San Francisco.

Box, G., G. Jenkins, and G. Reinsel (1994). *Time Series Analysis: Forecasting and Control*. Prentice-Hall.

Brune, J. (1970). Tectonic stress and the spectra of seismic shear waves from earthquakes. *J. Geophys. Res.* **75**, 4997–5009.

Dempster, A.P., N. M. Laird, and D. B. Rubin (1977). Maximum likelihood from incomplete data via the EM algorithm. *Journal of the Royal Statistical Society, Series B (Methodological)*, 39(1), 1–38.

Duijndam, A. (1988a). Bayesian estimation in seismic inversion—Part I: Principles. *Geophys. Prosp*. **36**, 878–898.

Duijndam, A. (1988b). Bayesian estimation in seismic inversion—Part II: Uncertainty analysis. *Geophys. Prosp*., **36**, 899–918.

Hanks, T., and H. Kanamori (1979). A moment magnitude scale. *J. Geophys. Res.* **84**, 2348–2350.

Harris, D.B (1991). A wave-form correlation method for identifying quarry explosions. *Bull. Seismol. Soc. Am*. **81**, 2395–2418.

Huseby, E.S., Ruud, B.O., and Dainty, A.M. (1998). Robust and reliable epicenter determinations: Envelope processing of local network data. *Bull. Seismol. Soc. Am*. **81**(1), 284–190.

Kanamori, H. (1977). The energy release in great earthquakes. *J. Geophys. Res.* **82**, 2981–2987.

Mayeda, K., A. Hofstetter, J. L.O'Boyle, W. R. Walter (2003). Stable and transportable regional magnitudes based on coda-derived moment-rate spectra. *Bull. Seismol. Soc. Am.* **93**, 224–239.

Myers S.C., S.L. Beck, G. Zandt, and T.C. Wallace (1998). Lithospheric-scale structure across the Bolivian Andes from tomographic images of velocity and attenuation for P and S waves, *J. Geophys. Res*. **103**, 21,233–21,252.

Myers, S. C., G. Johannesson, and W. Hanley (2007). A Bayesian hierarchical method for multiple-event seismic location. *Geophys. J. Int.* **171**, 1049–1063.

Myers, S. C., G. Johannesson, and W. Hanley (2009). Incorporation of probabilistic seismic phase labels into a Bayesian multiple-event seismic locator. *Geophys. J. Int*. **177**, 193–204.

Rasmussen, C. and C. Williams (2006). *Gaussian Processes for Machine Learning*. MIT Press.

Russell, S., Vaidya, S., and Le Bras, R. (2010). Machine Learning for Comprehensive Nuclear-Test-Ban Treaty Monitoring. *CTBTO Spectrum* **14**, 32–35.

Russell, S., Arora, N., Jordan, M., and Sudderth, E. (2009). Vertically Integrated Seismological Analysis I: Modeling. *Eos Transactions of the American Geophysical Union*, **90**(52), Abstract S33D-08.

Schaff D.P., and P.G. Richards (2004). Lg-wave cross correlation and double-difference location: Application to the 1999 Xiuyan, China, sequence, *Bull. Seismol. Soc. Am*. **94**, 867–879.

Slinkard, Megan E., Dorthe B. Carr, Stephen L. Heck, and Christopher J. Young (2011). Towards an automated waveform correlation detector system, in *Proceedings of the 2011 Monitoring Research Review*: *Ground-Based Nuclear Explosion Monitoring Technologies*, LA-UR-11-04823, Vol. 1, pp. 392–399.

Sipkin, S.A. (2003). A correction to body-wave magnitude m_b based on moment magnitude M_W. *Seismol. Res. Lett*. **74**(6), 739–742.

Thorbjarnardottir, B. S. and J. C. Pechmann (1987). Constraints on relative earthquake locations from cross-correlation of waveforms. *Bull. Seismol. Soc. Am*. **77**, 1626–1634.

Waldhauser, F. and W. L. Ellsworth (2000). A double-difference earthquake location algorithm: Method and application to the Northern Hayward Fault, California. *Bull. Seismol. Soc. Am.* **90**(6), 1353–1368.

Withers, M., R. Aster, and C. Young (1999). An automated local and regional seismic event detection and location system using waveform correlation. *Bull. Seism. Soc. Am*. **89**, 657–669.

EXTENSION OF THE *BAYESLOC* MULTIPLE-EVENT LOCATION ALGORITHM TO INCLUDE DIFFERENTIAL TRAVEL-TIME MEASUREMENTS

Stephen C. Myers and Garder Johannesson

Lawrence Livermore National Laboratory

Sponsored by the National Nuclear Security Administration

Award No. DE-AC52-07NA27344/LL12-Signal_Analysis-NDD02

ABSTRACT

We add differential- arrival-time measurements that are derived from waveform cross correlation to the *Bayesloc* multiple-event location algorithm. *Bayesloc* is a formulation of joint probability over event locations, travel-time corrections, phase labels, and arrival-time measurement errors. The *Bayesloc* formulation is hierarchical with distinct statistical models for each component of the multiple-event system, including prior constraints for any of the parameters. Bayes' Theorem enables calculation of the joint probability for hypothesized configurations of *Bayesloc* parameters, which facilitates the use of the Markov-Chain Monte Carlo (MCMC) method to draw samples from the joint probability function. The marginal posteriori distribution for each parameter, or covariance between parameters, is inferred from MCMC samples. Differential-time data are assumed to be based on waveform cross correlation, which results in a time difference between arrivals of similar phase for two events at a common station. We base the uncertainty of differential-time picks on correlation coefficient, whereas absolute arrival-time precision—as described in previous work—is formulated as a function of phase type, the station, and the individual event. This allows the precision of differential- and absolute-time data to be distinctly different and for the uncertainty of the two types of data to map properly through the *Bayesloc* probability function.

We have developed a synthetic data set based on the Nevada National Security Site (formerly known as the Nevada Test Site) explosions. In the synthetic data set arrival times are computed using a predefined, 1-dimensional velocity model plus an error term. The error term has an uncorrelated, random component with a standard deviation of a few tenths of a second, which is meant to represent pick error. The error term also has a correlated component, whereby error is correlated for common event/phase pairs for a given station. The correlated error has a standard deviation of a few hundredths of a second, which is meant to represent differential-time data based on waveform cross correlation. We first note that the new *Bayesloc* algorithm unambiguously and accurately estimates measurement uncertainty for the two data types. Second, if locations are determined using the absolute-time data, then the uncorrelated error of a few tenths of a second results in location errors of approximately 1 kilometer. If differential-time data are used alone, then the absolute-event location is very poorly constrained, and prior information for at least one location is needed to determine a meaningful result. However, if differential- and absolute-arrival-time data are used together, then anomalously large arrival-time errors (the tails of the absolute-time error distribution) are determined to be phase misidentifications and the absolute-location error is reduced to approximately 0.3 kilometers. Relative location uncertainty is estimated based on the covariance of location parameters for all events. For this data set, relative location errors are approximately one hundred meters.

OBJECTIVES

The objective of this project is to introduce differential-time arrival data into the *Bayesloc* algorithm. We refer to the version that allows differential-time data as *Bayesloc3*. *Bayesloc3* maintains the ability to operate solely on absolute-time data, but *Bayesloc3* is meant for use with mixed differential- and absolute-time data sets. Input of differential-time data alone is allowed, but this is practical when constraints for one or more event location are available. We hypothesize that the precise constraints on relative event locations from differential-time data will improve absolute-location accuracy compared to locations constrained by absolute-time data alone. The primary objective of the work presented here is to test this hypothesis using a synthetic data set.

RESEARCH ACCOMPLISHED

Background

Precise measurement of the time difference between two seismic signals can be made by cross correlation of waveforms (e.g., Poupinet et al., 1984; Deichmann and Garcia-Fernandez, 1992). Differential-time measurements based on waveform cross correlation can be used to precisely constrain relative event locations (Shearer, 1997; Waldhauser and Ellsworth, 2000; Zhang and Thurber, 2003; Schaff et al., 2004; Richards et al., 2006). Menke and Schaff (2004) demonstrate that absolute-event locations can be constrained in studies with exceptional, local network coverage, but the network geometry needed to constrain absolute-event location using differential-time picks is unprecedented in explosion monitoring. Constraints on one or more event locations in the multiple-event set are routinely used to place relative event locations in an absolute location context. However, there is considerable benefit to determining the most accurate set of locations possible using seismic data alone.

With the goal of determining both accurate and precise locations, Myers et al. (2011a) introduced differential-arrival-time measurements into the *Bayesloc* multiple-event location formulation. We start with a brief review of the *Bayesloc* method. For a complete description of the *Bayesloc* joint probability model the reader is referred to Myers et al. (2007, 2009).

Bayesloc

Bayesloc is a formulation of the joint probability function that spans hypocenters, travel-time corrections, pick precision, and phase labels. *Bayesloc1*, which is open source, is tailored for application to event clusters (e.g., aftershock sequences), with travel-time correction and pick precision formulations that were designed for robustness (Myers et al., 2007, 2009). *Bayesloc2* extended the travel-time correction model to include event terms, which enabled application to data sets that cover arbitrarily large geographic areas (Myers et al., 2011b). *Bayesloc2* also includes parallelization of the MCMC procedure at the event sampling level, which was needed in order to simultaneously relocate a global data set with tens of thousands of events and millions of arrivals. In all versions of *Bayesloc*, phase labels are probabilistic, and at no point is one phase label chosen. Possible labels include all phases under consideration and the possibility that the label is erroneous. *Bayesloc* allows prior constraints on any aspect of the multiple-event system, enabling direct utilization of previous work that statistically characterizes the accuracy of event hypocenters, picks (e.g., Bondár et al. 2004; Bondár and McLaughlin 2009), and travel-time prediction uncertainty. The use of prior information helps to mitigate regional location bias, and reduce uncertainties for all *Bayesloc* parameters.

The *Bayesloc* joint probability model is hierarchical with three primary components:

1) Travel-Time Model. The conditional distribution of the corrected travel times (T) given travel-time predictions (F) and collection of travel-time correction parameters (τ);

$$p(T \mid F, \tau) \qquad (1)$$

2) Arrival Data Model. The conditional distribution of the arrival-time data (a) and the differential- arrival-time data (d) given the origin times (o), the corrected travel times (T), phase configurations (W, V), and a collection of arrival data error parameters (σ, ρ);

$$p(a \mid o, T, W, \sigma)\, p(d \mid o, T, V, \rho) \qquad (2)$$

3) Prior Model. Prior distributions for hypocenter parameters, arrival data error parameters, travel-time correction parameters, and phase configurations;

$$p(x,o)\, p(\tau)\, p(\sigma)\, p(\rho)\, p(W \mid w)\, p(V \mid v) \qquad (3)$$

Note that we assume that absolute arrival-times and errors (a, σ) are independent from the differential arrival-times and errors (d, ρ). Similarly, we assume independence between the phase labels for the two data sources (W and V).

Using Bayes' theorem, these three physically related probability models are brought together into a joint posterior distribution

$$p(o,x,T,W,V,\sigma,\rho,\tau \mid a,w) = \\ p(a \mid o,T,W,\sigma)\,p(d \mid o,T,V,\rho)\,p(T \mid F(x),\tau)\,p(W \mid w)\,p(V \mid v)\,p(x,o)\,p(\sigma)\,p(\rho)\,p(\tau)/\,p(a)\,p(d) \quad (4)$$

where $p(a)$ and $p(d)$ are the marginal distribution over absolute-time and differential-time data, respectively. Equation 4 allows us to easily combine the 3 components of the hierarchical model to calculate the conditional probability for locations, travel times, and phase-name configurations given a set of arrival data.

We refer the reader to Myers et al. (2007, 2009, and 2011) for details on each component of the Bayesloc statistical model, particularly the formulation of travel-time corrections. Because the different types of arrival-time data are the primary topic here, we provide the formulation of the probability model for absolute- and differential-time data.

For a phase (w), and event (i), and a station (j), absolute-arrival errors are assumed to be Gaussian distributed with a mean of $A_{wij} = o_i + T_{wij}$, and variance

$$Var(a_{ijk} - A_{wij}) = 1/\kappa_{wij}, \text{ where } \kappa_{wij} = \kappa_w \kappa_i \kappa_j \kappa_{wi} \kappa_{wj} \quad (5)$$

Each of the precision parameters, κ, are treated as random variables that are distributed Gamma (see Myers et al., 2007). Larger data sets with many events can enable resolution of each precision parameter. Utilization of only the phase, station, and event parameters is recommended for smaller data sets with fewer events.

The differential-time measurement errors are formulated similarly to absolute-time data. We first note that the expected differential- arrival-time is

$$D_{wii^*j} = (o_i - o_{i^*}) + (T_{wij} - T_{wi^*j}), \quad (6)$$

where the asterisk specifies a second event. Given the expected differential- arrival-times, we assume that the differential- arrival-time residuals are distributed Gaussian with mean zero and a relatively simple mode for the variance,

$$Var(d_{ii^*jk} - D_{vii^*j}) = 1/\phi_{vii^*j}, \text{ where } \phi_{vii^*j} = \phi_v \exp(\theta C_{ii^*jk}) \quad (7)$$

C_{ii^*jk} is the correlation coefficient for the two waveforms associated with the differential- arrival-time d_{ii^*jk}. ϕ_v and θ are unknown parameters to be estimated. The statistical model for the variance can be easily extended to accommodate other information related to the precision of the differential- arrival-data.

Markov Chain Monte Carlo for Posterior Inference

Markov Chain Monte Carlo (MCMC) sampling is used to generate realizations from the joint posterior distribution of all multiple-event model parameters. MCMC sampling is well established as a method of parameter estimation and uncertainty quantification (e.g., Gelman et al., 2004). The sampler used in *Bayesloc1* and *Bayesloc2* is described in Myers et al. (2007 and 2009). Inclusion of differential-time data into *Bayesloc3* is a relatively straightforward addition to the statistical model; precise resolution of relative locations results in the need to jointly sample event locations that are constrained by differential-time data. Without joint sampling, the sampling process is inefficient, requiring many times more trials to adequately sample the posteriori distribution. Likewise, differential-time data provide strong constraints on the slowness component of the travel-time adjustment model, requiring joint sampling of locations and slowness corrections. Joint (correlated) sampling of epicenters and travel-time corrections is a large change to the Metropolis-Hastings and Gibbs sampling routines (respectively) that were used in previous versions of *Bayesloc*.

Synthetic Test

We generated a synthetic data set to test the utility of jointly analyzing differential- time and absolute-time data. The synthetic data set is based on 5 historic explosion events at the Nevada National Security Site (NNSS; formerly the Nevada Test Site). Arrival times are computed by adding the travel time between event and station locations to the event origin times. Locations and origins times are from Springer et al. (2002) and origins times are based on the *ak135* model (Kennett et al., 1995). Differential-times are then computed by subtracting absolute-arrival times for

arrivals with a common station and phase. Gaussian noise was added to each arrival based on the data type (absolute or differential) and the phase (See Table 1). In order to isolate the effects of differential-time data, travel-time biases, which would simulate travel-time prediction errors, were not introduced; all synthetic data errors are Gaussian and zero mean.

Events were simultaneously relocated using two data configurations: 1) absolute-time data alone, and 2) absolute- and differential-time data. It is well known that using differential-time data alone will result in precise relative locations and very poor constraints on absolute location, so we do not repeat that experiment here. Priors on event locations and data precision were not used. Figure 1 shows epicenters and epicenter-probability ellipses for the two test cases. Epicenters are computed by averaging MCMC samples, and elliptical probability regions are computed based on the variance/covariance of the MCMC samples.

Table1. Synthetic (true) and estimated standard deviation for arrival time error. Estimates are based on *Bayesloc3* simultaneous analysis of the multiple-event system. See text for discussion.

Phase	Absolute-Time Error True (Sec)	Absolute-Time Error Estimated (Sec)	Differential-Time Error True (Sec)	Differential-Time Error Estimated (Sec)
Pn	0.25	0.28	0.01	0.010
Pg	0.50	0.40	0.02	0.018
Lg	1.0	0.93	0.04	0.038

Epicenter results are shown in Figure 1, and hypocenter error and uncertainty estimates are listed in Tables 2 through 5. When absolute-time data are used to determine locations, the mean epicenter error is 1.05 km, and the average area of the 0.95 probability region is 44.6 km^2. The high level of accuracy and small probability regions are the result of small standard deviations for data errors. The magnitudes of data and epicenter errors in this synthetic test are consistent with those reported by Myers et al., (2007) for a real NNSS data set (Walter et al., 2004). Including differential- time data dramatically reduces mean epicenter error to 0.28 km and the average area of the 0.95 probability region is reduced to 4.7 km^2. In one instance for the absolute-time data set the ground-truth location is just outside of the probability ellipse, but this result is not statistically significant for the 5-event sample. Ground-truth locations are inside the 0.95 probability ellipses for all of the instances based on the absolute and differential-time data. This result is remarkable considering the dramatic reduction in ellipse area (Table 3).

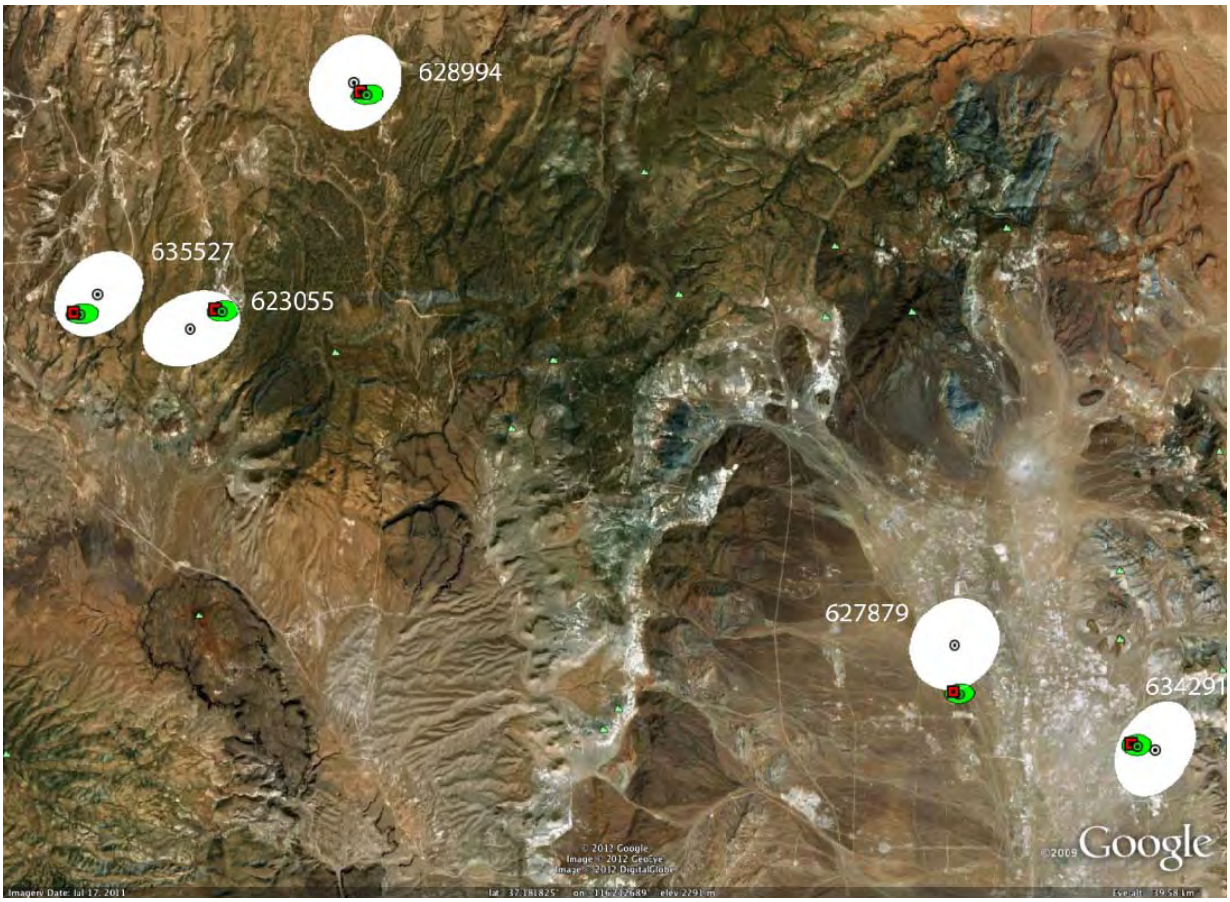


Figure 1. Synthetic test of epicenter probability regions constrained by an absolute-time data set and a data set consisting of absolute- and differential-times. The synthetic test is based on 5 NNSS (formerly NTS) explosion events. The map shown here is a GoogleEarth image of the NNSS that is approximately 45 km by 30 km in dimension. Ground truth locations (red squares). Epicenters (points) and probability regions determined using absolute-time data (white). Epicenters (points) and probability regions determined using absolute- and differential-time data (green). Event ID is shown for cross-reference with Tables 2 through 5.

Event depth and origin time errors are listed in Tables 4 and 5, respectively. Because the synthetic data do not include travel-time prediction error, depth and origin time can be resolved due to the slight difference in the sensitivity of event depth to travel times for the Pn, Pg, and Lg phases. Similar to the epicenter results, depth and origin time error are significantly smaller on average when absolute- and differential-time data are used together. This result is not likely to be repeated for real data, where travel-time prediction errors (biases) become large, but the test demonstrates that event depth could be constrained without surface-reflected phases (e.g., pP, sP) if travel-time prediction errors are reduced.

Table 2. Epicenter error for locations based on absolute-time data and based on absolute and differential-time data.

Event ID (EvID)	Epicenter Error Absolute-Time Data (km)	Epicenter Error Absolute- and Differential-Time Data (km)
623055	1.14	0.24
627879	1.68	0.25
628994	0.39	0.42
634291	0.90	0.24
635527	1.05	0.24

Table 3. Area of 0.95 probability regions for locations based on absolute-time data and based on absolute and differential-time data. Validation of probability regions is tested by determining whether or not the ground-true epicenter is inside of the 0.95 probability region.

EvID	Absolute-Time Data		Absolute- and Differential-Time Data	
	Ellipse Area (km^2)	Ellipse contains GT? (Boolean)	Ellipse Area (km^2)	Ellipse contains GT? (Boolean)
623055	23.2	true	5.8	true
627879	46.4	false	3.3	true
628994	52.1	true	6.2	true
634291	62.1	true	2.3	true
635527	39.4	true	6.0	true

Bayesloc3 estimates for arrival-time measurement uncertainty are listed in Table 1, alongside the synthetic (true) values. The uncertainty estimates listed in Table 1 are based on the absolute- and differential-time data set. Validation of uncertainty estimates for an absolute-time data set can be found in Myers et al. (2007; 2009). The results demonstrate that the standard deviation of absolute- and differential-time measurements can be independently resolved, due to the unique sensitivity of the event locations to the two types of data. Further, the estimates of data uncertainty are in good agreement with synthetic values. Although we note that resolution of measurement errors will be complicated for real data, this demonstration shows that measurement errors for the two types of data can be resolved and the *Bayesloc3* code is functioning properly.

Table 4. Event depth error for locations based on absolute-time data and based on absolute- and differential-time data.

EvID	Depth Error Absolute-Time Data (km)	Depth Error Absolute- and Differential-Time Data (km)
623055	1.40	-0.03
627879	0.27	-0.07
628994	0.00	-0.04
634291	0.60	-0.09
635527	0.74	0.02

Table 5. Event time error for locations based on absolute-time data and based on absolute- and differential-time data.

EvID	Time Error Absolute-Time Data (km)	Time Error Absolute- and Differential-Time Data (km)
623055	0.213	-0.007
627879	-0.123	-0.014
628994	0.077	-0.010
634291	-0.09	-0.015
635527	0.06	-0.004

We have identified two reasons that joint use of differential- and absolute-time data improves absolute-event locations over the use of absolute-time data alone. First, the spatial probability distribution of an event location is significantly reduced by the constraint imposed by precise relative position with respect to neighboring events. In other words, the marginal probability function of each event location becomes conditional on the relative location with other events. This is the primary cause of improved location accuracy and reduced probability area for the test case. Second, precise differential- time measurement provide constraints on the time difference between absolute-time data, which results higher probability identification of absolute-time outliers. Identification of absolute-time outliers reduces the estimate of absolute-time variance, which in turn reduces location probability area.

CONCLUSIONS AND RECOMMENDATIONS

Bayesloc3 enables the simultaneous use of absolute- and differential-arrival times in a multiple-event location algorithm. A demonstration using a synthetic data set with realistic measurement errors suggests that a combined absolute- and differential-time data set can significantly improve location accuracy over events constrained using absolute-time data alone. The addition of differential-time data significantly reduces the size of absolute-location probability regions (not just relative location). Further, absolute-time and differential-time measurement errors are assessed independently, and the variances of both error processes are accurately estimated in the *Bayesloc3* relocation procedure. This approach can lead to improved event location accuracy, quantification of measurement errors, and identification of data outliers. Absolute- and differential-time data should be used together whenever possible.

REFERENCES

Bondár, I., S.C. Myers, E.R. Engdahl, E.A. Bergman (2004). Epicenter accuracy based on seismic network criteria, *Geophys. Jou. Int*. **156**, 483–496.

Bondár, I. and K.L. McLaughlin (2009). A new ground truth data set for seismic studies, *Seismol. Res. Lett*. **80**, 3.

Deichmann, N., and M. Garcia-Fernandez (1992). Rupture geometry from high-precision relative hypocenter locations of microearthquake clusters, *Geophys. J. Int*., **110**, 501–517.

Gelman, A., Carlin, J.B., Stern, H.S., and Rubin, D.B. (2004) Bayesian Data Analysis (2nd ed.). Boca Raton, Florida: Hapman and Hall/CRC.

Kennett, B.J.N., E.R. Engdahl and R. Buland (1995). Constraints on seismic velocities in the Earth from travel times, *Geophys. J. Int* **122**, 108–124.

Myers, S.C., G. Johannesson, and W. Hanley (2007). A Bayesian hierarchical method for multiple-event seismic location, *Geophys. J. Int*. **171**, 1049–1063.

Myers, S.C., G. Johannesson, and W. Hanley (2009). Incorporation of probabilistic seismic phase labels into a Bayesian multiple-event seismic locator, *Geophys. J. Int*. **177**, 193–204.

Myers, S.C., G. Johannesson, D.A. Dodge, and N.A. Simmons (2011a). Combining analyst and waveform-correlation-based arrival time measurements in the Bayesloc multiple-event location algorithm, in *Proceedings of the 2011 Monitoring Research Review: Ground-Based Nuclear Explosion Monitoring Technologies*, Vol. 1, pp. 336–341.

Myers, S.C., G. Johannesson, and N.A. Simmons (2011b). Global-scale P-wave tomography optimized for prediction of teleseismic and regional travel times for Middle East events: 1. Data set Development, *Jour, Geophys. Res*. **116**, B04304, doi:10.1029/2010JB007967.

Poupinet, G., W. L. Ellsworth, and J. Fre´chet (1984). Monitoring velocity variations in the crust using earthquake doublets: An application to the Calaveras fault, California, *J. Geophys. Res*. **89**: 5719–5731.

Richards, P.G., F. Waldhauser, D. Schaff and W-Y Kim (2006). The applicability of modern methods of earthquake location, Pure Appl. Geophys. 163, 2–3, 351–372.

Schaff, D., G.H.R. Bokelmann, W.L. Ellsworth, E. Zanzerkia, F. Waldhauser and G.C. Beroza (2004). Optimizing correlation techniques for improved earthquake location, *Bull. Seismol. Soc. Am.* **94**, 705–721.

Shearer, P. (1997). Improving local earthquake locations using the L1 norm and waveform cross correlation: Application to the Whittier Narrows, California, aftershock sequence, *J. Geophys. Res.* **102**, 8269–8283.

Springer, D.L., G.A Pawloski, J.L. Ricca, R.F. Rohrer, and D.K. Smith (2002). Seismic source summary for all U.S. below-surface nuclear explosions, *Bull. Seismol. Soc. Am*. **92**, 1806–1840.

Waldhauser, F. and Ellsworth, W.L. (2000). A double-difference earthquake location algorithm: method and application to the north Hayward fault, California. *Bull. Seismol. Soc. Am*. **90**, 1353–1368.

Walter, W.R., K.D. Smith, J.L O'Boyle, T.F. Hauk, F. Ryall, S. Ruppert, S.C. Myers, R. Abbot, and D.A. Dodge (2004). An assembled western United States dataset for regional seismic analysis. Lawrence Livermore National Laboratory technical report, UCRL-TR-206630, 17 pp.

Zhang, H. and C.H. Thurber (2003). Double-difference tomography: The method and its application to the Hayward fault, California, *Bull. Seismol. Soc. Am.* **93**, 1875–1889.

SOURCE AND PATH CALIBRATION IN REGIONS OF POOR CRUSTAL PROPAGATION USING TEMPORARY, LARGE-APERTURE, HIGH-RESOLUTION SEISMIC ARRAYS

John L. Nábělek[1], Jochen Braunmiller[1], Evan Riddle[1], Patrick W. Monigle[1], and W. Scott Phillips[2]

Oregon State University[1] and Los Alamos National Laboratory[2]

Sponsored by the Air Force Research Laboratory and the National Nuclear Security Administration

Award Nos. FA8718-09-C-004[1] and DE-AC52-06NA25396[2]
Proposal No. BAA09-28

ABSTRACT

Broadband seismic data acquired during the Hi-CLIMB experiment are used to study seismic events and path propagation in the Nepal Himalaya and the south-central Tibetan Plateau. The 2002–2005 experiment consisted of 233 stations along a dense 800 km linear north-south array extending from the Himalayan foreland into the central Tibetan Plateau. The main array was flanked by a 350 km x 350 km sub-array in southern Tibet and central and eastern Nepal. The dataset provides an opportunity to obtain seismic event locations for ground truth evaluation, to determine source parameters, and to study distance evolution of seismic coda for yield estimation in low Q regions.

The Hi-CLIMB experiment revealed intense and distributed seismicity in the south-central Tibetan Plateau. The unique dataset provides an opportunity to jointly invert for 3D upper mantle-crustal velocity structure and refined seismic event locations from local and near-regional P and S waves. The Hi-CLIMB seismic event database, which contains over 22,500 events from June 2004 to August 2005, is based on automated arrival time picks from vertical component data consisting primarily of P and relatively few S waves. To increase the number of S picks and to obtain accurate picks at distances larger than 1°-2°, we implemented an automatic S-wave picker that utilizes signal attributes from three-component seismic data. Data are rotated into the ray-coordinate system based on known event location and velocity model. S arrivals are picked when rectilinearity, directivity relative to incoming P wave, ratio of transverse to overall energy and the transverse amplitude reach a data-dependent threshold. We adjusted picking parameters and thresholds to optimize automatic picks relative to manual picks from events distributed throughout south-central Tibet. For shallow events, S_g can be picked accurately to the S_g/S_n crossover distance of about 3° while S_n arrivals are absent. Deep events beneath the southern Tibetan Plateau and the High Himalayas produce clear S arrivals that can be picked to 5°-6° distance. In an initial step, we applied the S-picker to 584 $M_L(P) \geq 2.7$ events that occurred within 2° from the closest station and had at least 60 picks (P and S combined) in our original database resulting in about 20,000 quality S picks.

Initial tomography efforts using tomoDD are focused on inverting synthetic data to evaluate the resolving power of the P- and S-wave dataset for 3D crust and upper mantle structure in the south-central Tibetan Plateau considering the actual station and event distribution. Before applying tomoDD to actual data, we will update event locations, discussed in our previous MRR presentations, using the additional S picks and invert for an average 1D crust-upper mantle model using these 584 best-constrained events close to the network and with a large number of picks. We will apply the S picker to the entire Hi-CLIMB seismic event database and relocate all events with added S picks and in the new average 1D model. The 1D model will be used as starting point for joint 3D P- and S-tomography and location inversion using well-located events that provide good ray coverage. The 3D tomography effort is aimed at complementing and expanding on the existing receiver function image of the collision zone. Results will be presented at the research review.

OBJECTIVES

The Hi-CLIMB array provides a unique broadband seismic dataset across the Himalayan-Tibetan collision zone that allows source and path calibration in a low Q and highly scattering region. Results from the project will enhance the monitoring community's capability to estimate magnitude and yield in regions of poor crustal propagation. Main objectives are to obtain ground-truth seismic event hypocenters, independent magnitude and depth estimates from waveform modeling, and estimates of distance evolution of seismic coda. For this report, efforts focused on adding S-arrivals to the existing arrival time database to further improve seismic event locations and to perform 3-D tomography inversions to resolve the P-wave and S-wave structure.

RESEARCH ACCOMPLISHED

Data

The Hi-CLIMB broadband seismic experiment (Nábělek et al., 2009) in Nepal and south-central Tibet occupied 233 sites and consisted of a densely spaced 800 km long north-south array with additional lateral deployments in Nepal and southern Tibet (Figure 1). The linear array, which extended from the Ganges foreland into the Tibetan Plateau, has provided a detailed image of the geometry of the India-Eurasia collision zone from receiver function analysis (Nábělek et al., 2009) and is ideally suited to study distance evolution of seismic waves and seismic coda. The lateral deployments, with about 30-40 km station spacing, significantly improve seismic event location capabilities and allow high-resolution 3-D wave speed and attenuation tomography.

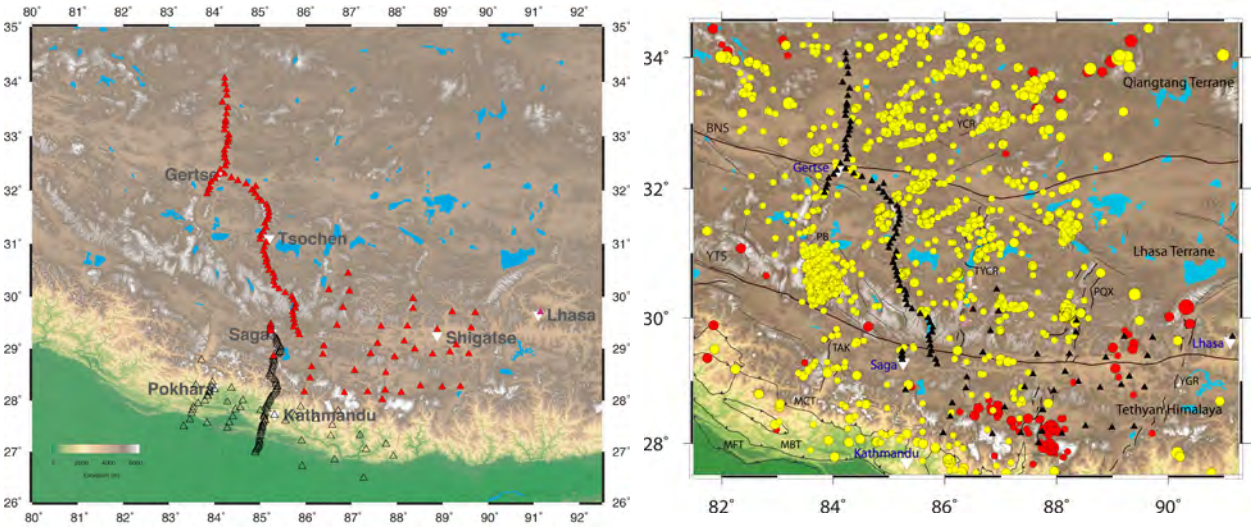


Figure 1. Left shows map of Hi-CLIMB seismic network (phase-2: red triangles, phase-1: open triangles) and permanent GSN station Lhasa. Right shows map of 7,900+ well-located events with at least 25 P and S picks that occurred during the Hi-CLIMB phase-2 deployment from June 2004 to August 2005. Yellow circles are crustal and red circles are near-Moho events (z≥65km), respectively. Black triangles are phase-2 stations. PB is the Payang Basin, PQX the Pumqu-Xianza Rift, and YTS the Yarlung-Tsangpo Suture. Red events outside the network, e.g. in the Qiangtang terrane north of the Banggong Nujiang Suture (BNS), reflect poorly determined focal depth and not deep seismicity.

The Hi-CLIMB experiment revealed intense seismicity in the south-central Tibetan Plateau. The database for the June 2004 to August 2005 period contains over 22,500 seismic events (about 50 events per day). Figure 1 (right) shows a subset of over 7,900 events with 25 or more P and S picks corresponding to well-located events, which are distributed throughout the study area. For a more detailed description of the event database including an evaluation for location accuracy, event magnitude $M_L(P)$, and GT5 ground truth events see Nábělek et al. (2011). A detailed analysis of low-angle normal faulting in the Pumqu-Xianza Rift has been published in Monigle et al. (2012).

Polarization S-Picker

We had used the Antelope software developed by Boulder Real Time Technologies for automatic detection and arrival time picking and for event association and location. The arrival picks were obtained through STA/LTA analysis on vertical component seismic data. Our arrival time database does contain a significant number of S-wave picks. However, due to picking from vertical component data, the quality of the S picks overall is relatively low and degrades rapidly with epicenter distance (Figure 3 in Nábělek et al., 2011) such that we could use S arrivals for locations only to 2° epicenter distance.

We implemented a new automatic S-wave picker in order to increase the number of S picks and to obtain accurate picks at distances larger than 1°-2°. Additional accurate S picks are particularly important to further improve seismic event locations and to perform 3D inversions for S-wave velocity, which combined with P-wave tomography, provides critical information regarding composition and physical state of crust and upper mantle.

The new S picker uses signal attributes from three-component seismograms. The S-wave onset is determined from shear wave energy and polarization analysis. The picker has been adapted from an implementation by Diehl et al. (2009) with the polarization analysis following Cichowicz (1993). The first step is to rotate the ZNE data into the LQT ray-coordinate system to separate P-wave (L-component) from S-wave energy; the T-component includes SH and the Q-component SV energy, respectively. For rotation, we used the 'known' event location and velocity model, since the events had already been identified and located with picks, primarily P phases, from the Antelope STA/LTA algorithm.

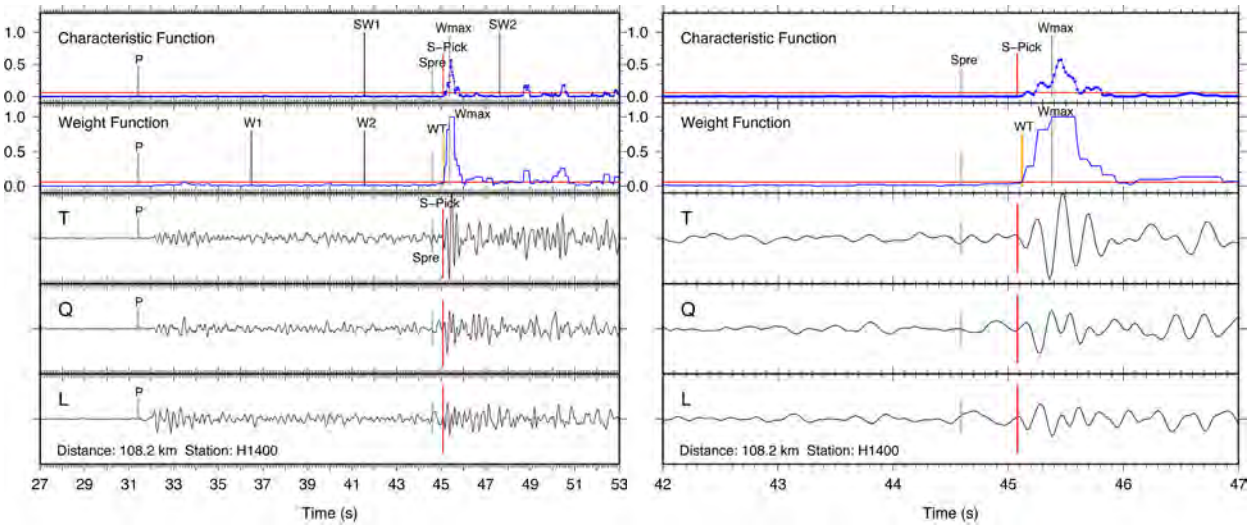


Figure 2. Left shows an example of the automatic picking process for station H1400 at epicenter distance of 108 km from the 3 July 2005 M_L(P)=3.0 earthquake at 31.55°N and 85.62°E. Shown are (top to bottom panel): *Characteristic function* CF(t), *weight function* W(t), and rotated seismograms (T, Q, and L). The red horizontal lines are the thresholds for CF(t) and W(t), respectively. The P-wave pick (P) and predicted S pick (Spre) are shown in gray, the actual pick is shown as red vertical line (S-Pick), orange shows the coarse preliminary pick WT from W(t). The traces are filtered with a Wood-Anderson filter followed by a high-pass filter with corner at 0.5 Hz. See text for details. Right, close up around the S arrival.

An S phase is picked when rectilinearity, directivity relative to the incoming P wave, as well as ratio of transverse to overall energy and the transverse amplitude reach a data-dependent threshold. The procedure is illustrated in Figure 2 with the bottom three traces showing the LQT-rotated seismograms including the P-phase pick and the predicted (gray) and picked (red) S-phase arrivals. The predicted S-arrival time is for the initial 'known' event location and the *tib3p* velocity model (Figure 2 in Nábělek et al., 2011). The top panel shows the *characteristic function* CF(t) (see below) and the time window from SW1 to SW2 within which the S pick has to occur; the window is centered on the predicted S-arrival time and its length depends on epicenter distance. The second panel

shows the *weight function* W(t), which is simply the square of the ratio of the maximum amplitude on either the T or Q component within a short picking interval relative to the overall maximum amplitude on either component; W(t) reaches its maximum Wmax when the picking interval includes the overall maximum amplitude.

A coarse pick at time WT (orange vertical line) is obtained when W(t) (blue line) exceeds a threshold (thin red line) determined from the mean and standard deviation of the *weight function* W(t) in the window W1 to W2. The window end, W2, coincides with the earliest possible S-arrival time, SW1, and the window begin W1 is at the mid-point between the P arrival and W2. This window is chosen to exclude direct P energy, to precede the S arrival, and to be of sufficient length to characterize the T and Q component 'noise' level. The theshold is set high and we expect the S arrival to closely precede WT.

For the final pick, we use the *characteristic function* CF(t), which is the product of rectilinearity (R(t)), directivity (D(t)), ratio of T and Q energy relative to total three-component energy (H(t)), and W(t); see Diehl et al. (2009) for definitions of these functions. However, our choice of the *weight function* and the picking algorithm are substantially different from the original Diehl et al. (2009) procedures. CF(t) thus incorporates S wave signal strength attributes, H(t) and W(t), as well as polarization attributes, R(t), D(t) and H(t). For a pick, CF(t) (blue) has to exceed a threshold (red horizontal line), defined from mean and standard deviation of CF(t) between times SW1 and WT. In order to avoid spurious maxima in CF(t) prior to the actual S arrival, the algorithm works backwards in time along the CF(t) starting at Wmax. A pick is declared when CF(t) reaches a mimimum after it has dropped below the threshold, i.e., prior in time to where CF(t) reaches the threshold, and stays below the threshold. The example shown in Figure 2 shows a case where CF(t) had reached a local minimum. To avoid local minima, the algorithm, for several samples, continues its search backwards in time to be able to 'climb' over preceding maxima and to find the instance where CF(t) reaches a minimum after dropping below the threshold and stays below it.

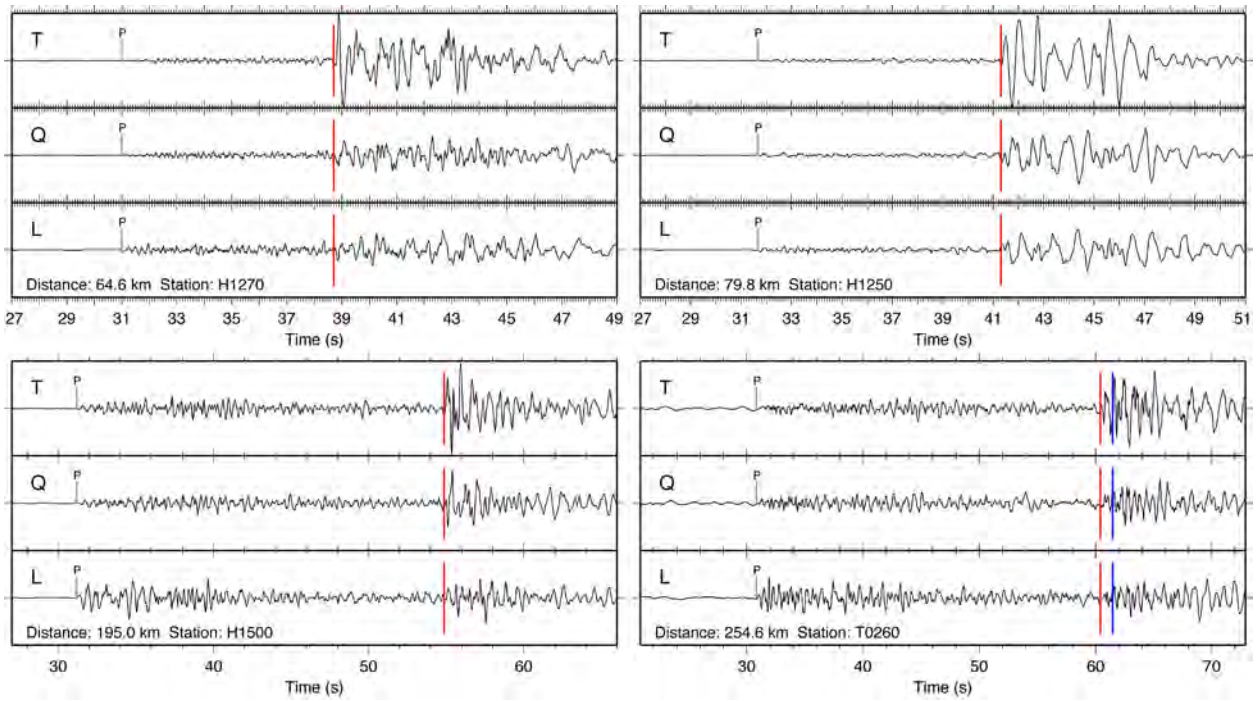


Figure 3. Examples of S-phase picks with increasing distance, from 65 to 255 km, for same event as in Figure 2. Red are automatic S picks using the new picker, blue, in lower right, shows an S pick from Antelope STA/LTA analysis on vertical component data, which is about 1.0 s late relative to the S arrival and the new S pick.

Figure 3 shows additional examples of S picks as a function of epicenter distance, which increases from 65 to 255 km, for the upper-crustal event used in Figure 2. All arrivals are crustal S_g phases considering the 70 km thick crust of the Lhasa block. The picks are very good. For this event, we obtained 34 S-phase picks with the new

polarization S picker compared with 5 S-phase picks from the Antelope STA/LTA analysis. The bottom right panel of Figure 3 shows the STA/LTA pick in blue, which is about 1.0 s late relative to the S arrival and the new S pick. For the set of common stations, the STA/LTA picks are 0.7 s later than our new S picks. It is no surprise that the STA/LTA based picks are usually late considering the higher noise level in the P coda that precedes the actual S arrival.

We have adjusted the picking parameters and thresholds multiple times to optimize automatic picking results for our data based on visual inspection of the algorithm's performance and on comparison with manual picks from events distributed throughout south-central Tibet. No pick will be declared when the thresholds for W(T) or CF(t) are large or when CF(t) oscillates around its threshold.

We also applied the new automatic S picker to 50 shallow seisimc events in the Pumqu-Xianxa Rift (near 30°N and 88°W) to test its perfromance relative to manual picks (Monigle et al., 2012) and to STA/LTA based picks (Figure 4). The manual picks were generally read from un-rotated horizontal seismograms. For the actual locations in Monigle et al. (2012), we reduced the weight of individual picks linearly from one to zero between 2° and 3° distance based on the observed increase in difficulty of accurately picking arrivals in that distance range and beyond. As with all manual data, this reference dataset is not perfect and subjective (for some stations another analyst could make different picks).

Figure 4 shows the difference between the new automatic S picks and the manual S picks in red as a function of epicenter distance. For comparison, we show the difference between STA/LTA derived S picks and manual S picks in blue. For the shallow events, the three methods picked S_g arrivals to the S_g/S_n crossover distance of about 3° while S_n arrivals are basically absent. Overall, results from the polarization S picker are more consistent with the manual picks than the STA/LTA derived picks, which are considerably late even at relatively short distances. The solid red and blue lines in Figure 4 show moving window averages of the differences and illustrate that up to about 200-250 km distance, the new automatic picks and the manual picks are in agreement and, on average, differ by 0.5 s or less.

Besides improving pick quality, the polarization S picker also led to a significant increase in number of successful S picks. For the Pumqu-Xianxa Rift dataset, the STA/LTA picker had found 419 S arrivals, while the polarization picker found 612. Even more important, at shorter distances, as shown in Figure 4 (right), where pick quality is high, the number of S picks almost doubled from 115 to 206. Also note the strong difference at distances shorther than about 100 km, critical for accurate hypocenter locations, where the polarization picker detected many more S arrivals than the STA/LTA algorithm and where, on average, polarization and manual arrival times are identical.

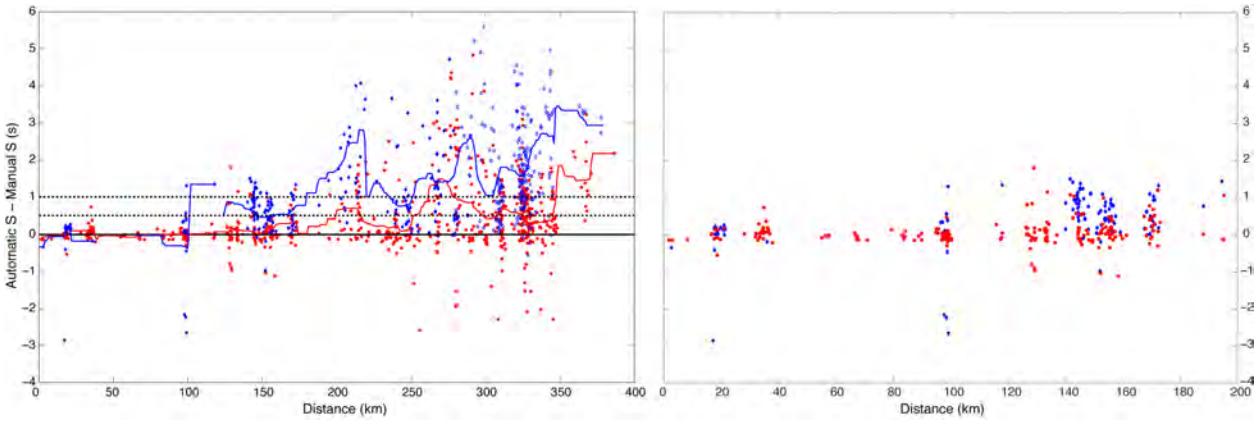


Figure 4. S pick comparison between polarization S picker (red) and STA/LTA based picks (blue) for dataset of 50 manually picked events from the Pumqu-Xianza Rift (Monigle et al., 2012) as function of epicenter distance. Picks are shown relative to their manual S picks. Left, solid lines are moving window averages, horizontal lines are for 0, 0.5, and 1.0 s differences. Right. Close up of left. Number of picks: 206 from polarization picker and 115 from STA/LTA picker.

Next, we applied the polarization S picker to 584 $M_L(P) \geq 2.7$ events that occurred within 2° from the closest station and had at least 60 picks (P and S combined) in our original database. These are stronger events with already well-constrained epicenter locations and with strong signals that are well-recorded across the entire Hi-CLIMB array. We do not expect their locations to change significantly when changing and adding S picks. For the 561 shallow events (here set as $z \leq 40$ km), S_g can be picked reliably to the S_g/S_n crossover distance of about 3° while S_n arrivals are either absent or very weak such that they could not be picked reliably. In contrast, deep events ($z > 40$ km) beneath the southern Tibetan Plateau and the High Himalayas produce clear S arrivals that can be picked to 5°-6° distance. Application of the S picker resulted in about 20,000 S picks doubling the number of picks compared to STA/LTA-based picks and, at short distances of $\Delta < 1°$, quintupling the number to over 1,000. Relocation including the new S picks are shown in Figure 5 (yellow and orange). As expected for events based on many phase picks, locations remained largely unaffected (the median difference is 0.6 km) except for events at the periphery of the network, which generally moved slightly towards the network. Similarly depth, on average, changed by less than one km, even though, on average, over 22 more S picks were available per event.

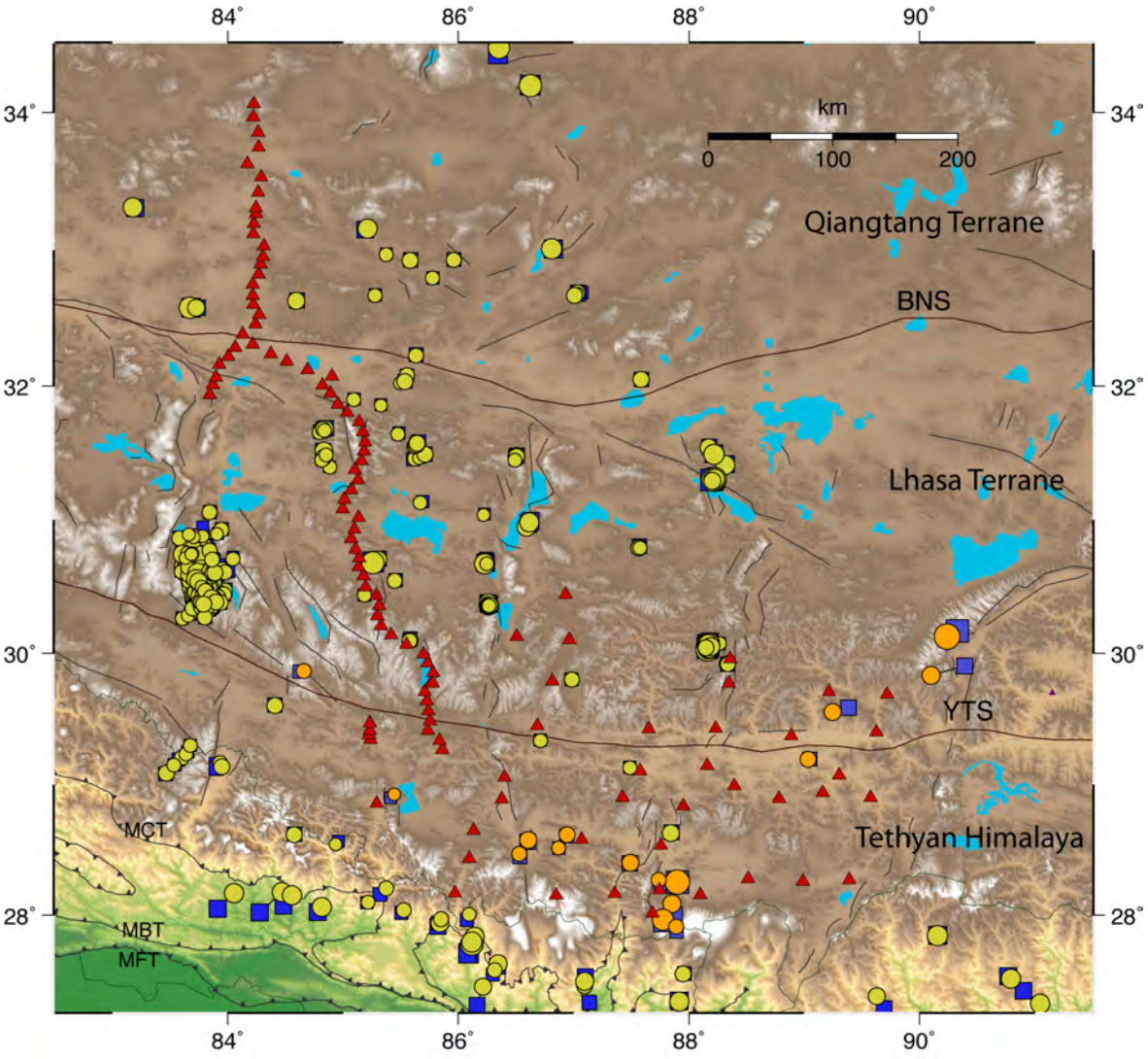


Figure 5. Map of 584 seismic events to which the polarization S picker was applied. Locations incorporating the new S picks are shown in yellow for crustal and orange for near-Moho events (z≥65km). Blue are previous locations with S picks from STA/LTA analysis; these locations generally include fewer S phases. All events, based on at least 60 P and S picks, are well constrained and adding or changing the S picks did not change locations significantly. The median location difference is 0.6 km. Events in the outskirts of the network, however, were generally pulled slightly towards the network.

We are using the new locations and additional S picks of these 584 best-constrained events close to the network and with a large number of P and S picks to check and possibly update the existing 1D velocity model *tib3p*, either by inverting for a single new average 1D model or by obtaining regionalized 1D models. At the same time, we are in the process of applying the polarization S picker to the entire Hi-CLIMB seismic event database, which we will then relocate with the added S picks and the new average 1D model(s).

3D Tomography Using P and S Waves

Resolving 3D P and S wave velocity and compositional structure of the south-central Tibetan Plateau is the focus of a tomography effort aimed at complementing and expanding on the existing receiver function image of the collision zone (Nábělek et al., 2009). We are using the tomoDD double-difference tomography code (Zhang and Thurber, 2003) and have begun with synthetic data inversions to evaluate how well the existing P and S wave dataset can resolve 3D crust and upper mantle structure considering the actual station and event distribution.

Figure 6 shows sample ray paths for a sub-Moho (left) and for a shallow upper-crustal (right) earthquake assuming an even 2D station distribution, akin to the lateral Hi-CLIMB network east of 86°E (Figure 1). A combination of deep events, with relatively steep up going rays in the crust, and of shallow events, with crustal paths sampling mainly the upper crust, would provide the best ray coverage and could resolve the crust and upper mantle velocity distribution beneath the lateral array (Figure 7). However, the seismic event distribution is not uniform with deep events confined to the southern Tibetan Plateau and the High Himalayas (Figure 1) such that sampling is uneven.

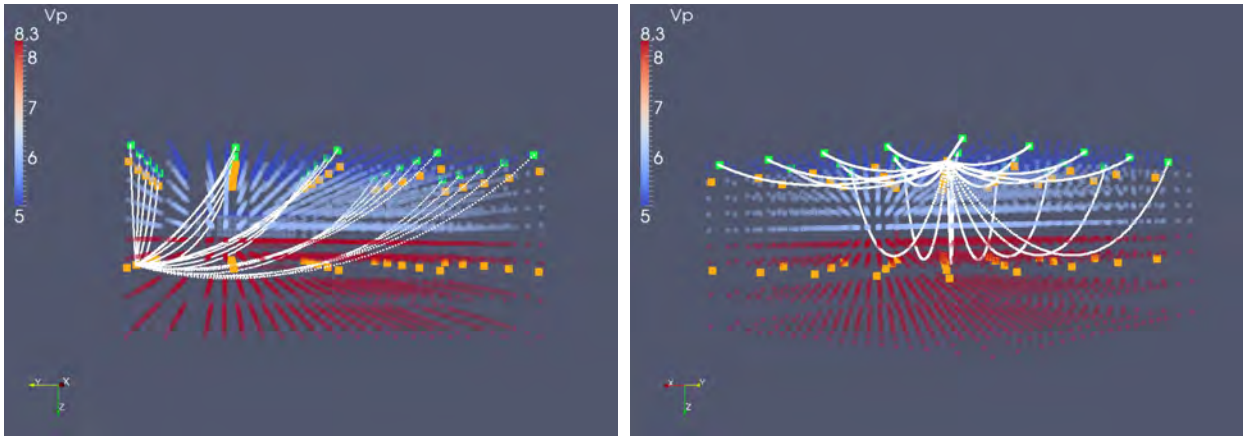


Figure 6. Sample ray paths (white lines) for two seismic events to stations (green squares). Stations and events (orange squares) for this test are evenly distributed, model dimensions are 2°x2° horizontal and 100 km vertical. Red nodes (50 km and deeper) have mantle P-wave speeds and blue nodes crustal P-wave speeds. Left shows ray paths for a deep, sub-Moho event. Cross-sectional view. Right are ray paths for a shallow, upper-crustal event illustrating shallow ray penetration at P_g distances with lower crust and mantle penetration only for relatively distant stations at P_n range. Cross-sectional view with model corner towards viewer.

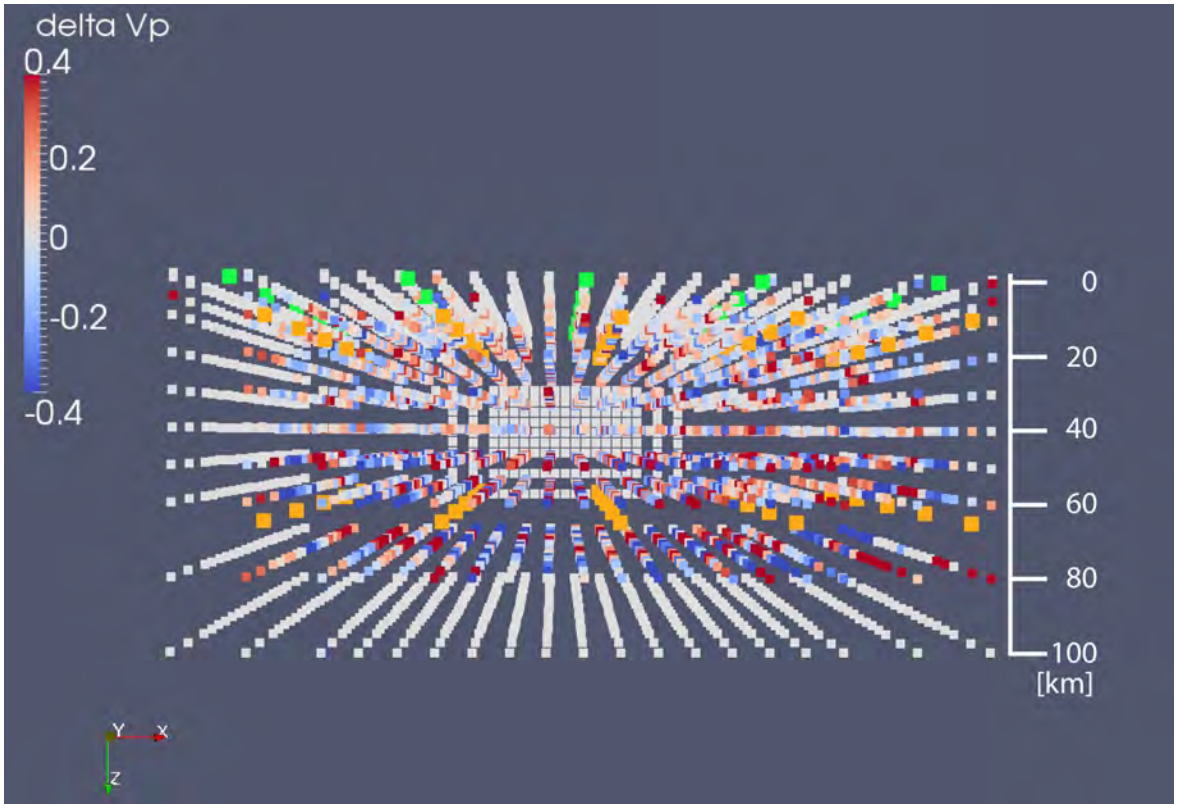


Figure 7. Resolved variation of P wavespeed (in km/s) relative to the starting model (Figure 6) assuming perfect ray coverage from 25 evenly distributed sub-Moho (orange squares) and 25 evenly distributed shallow events (orange squares) recorded at 25 evenly distributed stations (green squares) after adding Gaussian noise with σ=0.25 s to synthetic arrival times. As expected, velocity perturbations are random and their values are larger in the faster mantle than in the slower crust. Cross-sectional view looking straight into the 3D model.

The 1D model(s) from relocating the best-constrained 584 events (see above) will be used as starting point for joint 3D P- and S-tomography and location inversion using well-located events that provide good ray coverage. Initial results will be presented at the research review.

CONCLUSIONS AND RECOMMENDATIONS

The Hi-CLIMB seismic network covered the otherwise sparsely instrumented Nepal Himalaya and south-central Tibetan Plateau regions. The dataset provides a unique opportunity to determine ground truth event locations, regional velocity models, earthquake source parameters, and seismic attenuation in a region of poor crustal propagation. During the last reporting period, our focus was on the implementation of an automatic S-phase picker, which uses polarization characteristics specifically geared towards detecting shear wave signals and performs superior to a standard STA/LTA detector in terms of number of detections and pick accuracy. After optimizing picking parameters and threshold settings to our dataset, we applied the polarization S picker to 584 larger well-located events resulting in a doubling of S picks. Based on comparison with manual picks, the new automatic S picks are of higher quality and are accurate over a wider distance range than the STA/LTA-based picks. We are currently applying the polarization S picker to the entire Hi-CLIMB dataset and will first use the resulting S picks to improve the S-velocity model used for location before relocating all 22,500 seismic events in the Hi-CLIMB study area previously identified for the June 2004 to August 2005 period and checking for GT5-candidate events. Further improvements in event location and characterization through tomographic imaging and attenuation analysis are currently under way. The location, velocity model, and attenuation results will contribute to SLBM tomographic efforts, allow evaluation of depth for crustal models, and enhance model accuracy throughout central and southern Asia and, in general, will contribute to the National Nuclear Security Administration Knowledge Base.

REFERENCES

Cichowicz, A. (1993). An automatic S-phase picker, *Bull. Seismol. Soc. Am.* **83**, 180–189.

Diehl, T., N. Deichmann, E. Kissling, and S. Husen (2009). Automatic S-wave picker for local earthquake tomography, *Bull. Seismol. Soc. Am.* **99**, 1906–1920, doi: 10.1785/0120080019.

Monigle, P. W., J. Nábělek, J. Braunmiller, and N. S. Carpenter (2012). Evidence for low-angle normal faulting in the Pumqu-Xianza Rift, Tibet, *Geophys. J. Int.* doi: 10.1111/j.1365-246X.2012.05581.x.

Nábělek, J., G. Hetényi, J. Vergne, S. Sapkota, B. Kafle, M. Jiang, H. Su, J. Chen, B.-S. Huang, and the Hi-CLIMB Team (2009). Underplating in the Himalaya-Tibet collision zone revealed by the Hi-CLIMB experiment, *Science* **325**, 1371, doi: 10.1126/science.1167719.

Nábělek, J. L., J. Braunmiller, P. W. Monigle, N. S. Carpenter, and W. Scott Phillips (2011). Source and path calibration in regions of poor crustal propagation using temporary, large-aperture, high-resolution seismic arrays, in *Proceedings of the 2011 Monitoring Research Review: Ground-Based Nuclear Explosion Monitoring Technologies*, LA-UR-11-04823, Vol. 1, pp. 352–363.

Zhang, H. and C. H. Thurber (2003). Double-difference tomography: The method and its application to the Hayward Fault, California, *Bull. Seismol. Soc. Am.* **93**, 1875–1889.

EXPLOITING AMBIENT NOISE FOR SOURCE CHARACTERIZATION OF REGIONAL SEISMIC EVENTS

Michael H. Ritzwoller, Anatoli L. Levshin, and Mikhail P. Barmin

University of Colorado at Boulder

Sponsored by the National Nuclear Security Administration

Award No. DE-AC52-09NA29326
Proposal No. BAA09-52

ABSTRACT

The purpose of this research is to develop and test novel methods to characterize regional seismic events by exploiting Empirical Green's Functions (EGFs) that are produced from ambient noise. Elastic EGFs between pairs of seismic stations are determined by cross-correlating long ambient noise time-series recorded at the two stations. The EGFs principally contain Rayleigh and Love wave energy and our focus is placed on utilizing these signals between periods of 5- and 15-seconds (sec). Epicentral location based on the envelope functions of the Rayleigh wave EGFs has been described by Barmin et al. (2011) and epicentral location based on the joint interpretation of observations of Rayleigh and Love wave group travel times has been described by Levshin et al. (2012). During the past year we have extended the method to incorporate phase travel times and to redefine the method to be based on phase and group velocity maps derived from ambient noise data rather than observations obtained directly on the EGFs. These refinements stabilize the location procedure and now allow us to estimate hypocentral depth and the source mechanism of regional events.

OBJECTIVES

The purpose of this research is to improve seismic event location accuracy and event characterization by exploiting EGFs that emerge by cross-correlating long time sequences of ambient noise observed at pairs of seismic stations. Because ambient noise EGFs are dominated by surface waves, the method uses surface wave energy for location purposes. The method of epicentral location, as well as proof-of-concept applications to a set of seismic events in the western US, have been described by Ritzwoller et al. (2009) and more recently and completely by Barmin et al. (2011) and Levshin et al. (2012). During the past year, we have extended the method to incorporate phase travel times and to redefine the method to be based on phase and group velocity maps derived from ambient noise data (or a 3-D model based on ambient noise) rather than observations obtained directly on the EGFs. The use of group and phase time residuals for estimating source mechanism and depth was investigated using USArray Transportable Array (TA) data and reveals encouraging results.

RESEARCH ACCOMPLISHED

Introduction

The purpose of this work is to investigate how ambient noise can be used to improve regional to local scale event characterization. Ambient noise cross-correlations provide new information about crustal structure revealed dominantly through Rayleigh and Love waves. The cross-correlations themselves, group or phase velocity maps determined from them, or 3-D crustal and uppermost mantle models determined from them can be exploited to improve estimates of epicentral location and, in principle, also focal mechanism and hypocentral depth for seismic sources larger than magnitude 3.0-3.5.

Barmin et al. (2011), referred to hereafter as Paper I, presented a new approach to the epicentral location of shallow seismic events based on use of the Empirical Green's Functions (EGFs) obtained from ambient seismic noise. The vertical component of the ambient noise in the period range from 7 to 15 sec, which is dominated by the fundamental Rayleigh wave, was used to compute the EGFs. It was demonstrated that this approach has several features that make it a useful addition to existing location methods. First, the method is based on surface waves, which are usually not applied in most location algorithms. Second, it does not require knowledge of Earth structure and is, therefore, unbiased by uncertainties in the knowledge of structure near the epicenter. Third, it works well for weak seismic events even if the detection of body wave phases is problematic. Fourth, the EGFs computed during a temporary deployment of a base network (such as the USArray Transportable Array [TA] or PASSCAL deployments) may be applied to events that occur earlier or later using permanent remote stations even if the temporary stations are absent.

The method presented in Paper I has several limitations. In particular, it is based on the assumption that the event source mechanism and depth are unknown and does not attempt to estimate them. Time shifts in the surface waves caused by the source mechanism, therefore, can bias the epicentral location. Paper I shows that this degradation is worst for source depths between about 2 and 5 km if the source mechanism is different from pure strike-slip, thrust or normal faulting. In this case, the method described in Paper I will deliver a biased estimate of the epicentral location.

Levshin et al. (2012), hereafter referred to as Paper II, addressed this limitation by introducing Love waves into the location method. Love waves possess different sensitivity to the source mechanism than Rayleigh waves and, in fact, Love wave source phase times are quantitatively less sensitive to the source mechanism (Levshin et al., 1999). Love waves are, however, in many cases more difficult to observe than Rayleigh waves due to higher noise levels on horizontal components. Epicentral estimates based on Love waves, therefore, on average have a larger variance than those based on Rayleigh waves. Thus, the joint application of Rayleigh and Love waves to estimate epicentral locations may be preferable to the locations based on either wave type alone, as it strikes a balance between bias and variance.

The procedure presented in Paper II differs from that in Paper I in another way in addition to introducing Love waves. The direct comparison of envelope functions of the earthquake and ambient noise EGFs is replaced with comparing theoretical group velocity curves (computed, for example, from the EGFs, existing group velocity maps or a 3-D model) with the measured group velocity curves obtained from the event records. Using curves from existing group (or phase) velocity maps computed from ambient noise tomography or from curves predicted from a 3-D model that originated by inverting ambient noise dispersion maps, in particular, makes the algorithm more flexible and opens the possibility to estimate other source parameters such as hypocentral depth and the moment tensor.

Here we, first, summarize some of the principal results from Paper II, illustrating the effect of introducing Love waves with Rayleigh waves in a joint inversion for epicentral location. Second, we present some early results that demonstrate the feasibility of obtaining improved estimates of focal mechanism and depth based on using a 3-D model constructed from ambient noise.

Joint Application of Rayleigh and Love Wave EGFs to Locate Several Events in the Western USA

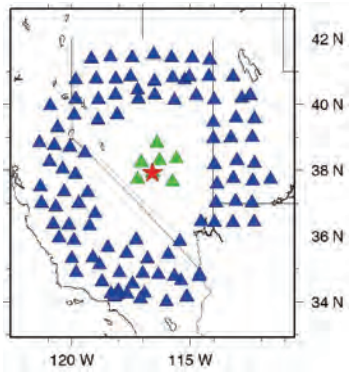


Figure 1. The network of base (green triangles) and remote (blue triangles) stations used in the synthetic location experiment from Paper II.

To clarify the capabilities of the methods described in Papers I and II we present examples of epicentral location using simulated seismograms for a set of theoretical earthquakes with different source mechanisms and depths located in central Nevada. Figure 1 presents the locations of the base and remote stations used in the simulation. Synthetic seismograms and Green's functions (replacing the ambient noise EGFs) are computed for each theoretical earthquake and the location procedures in Papers I and II is applied. Examples of misfit surfaces using Rayleigh and Love waves, respectively, are presented in Figure 2a, and 2b for the red focal mechanism shown in Figure 3 at 5 km depth. This earthquake type and depth are chosen because they provide large Rayleigh wave group time shifts, which results in a large epicentral bias using Rayleigh waves alone as can be seen in Figure 2a.

In Figure 2a, the Rayleigh wave location is biased by about 2.0 km. In contrast, for this event there is very low bias using Love waves alone, as Figure 2 b illustrates. Weighting Love waves and Rayleigh waves equally in the location algorithm, reduces the bias appreciably, although bias does remain at about 1.0 km, as seen in Figure 2c. However, if the wave types are weighted inversely by minimum misfit, which is very low for Love waves and considerably larger for Rayleigh waves, then the resulting joint location is again essentially unbiased, as Figure 2d shows.

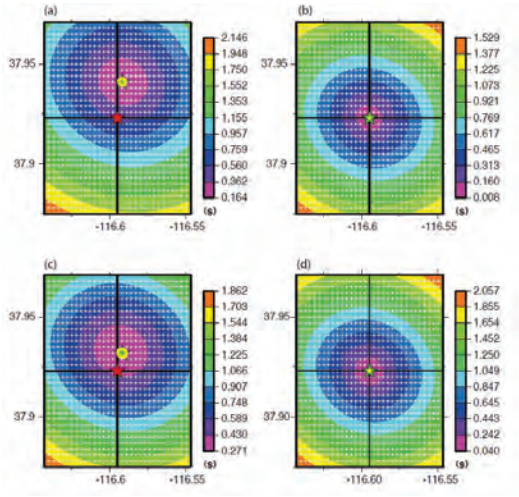


Figure 2. Simulated misfit for the virtual source whose location is shown in Figure 1 at 5 kilometer (km) depth and with red source mechanism shown in Figure 3. Grid spacing is about 300 m. (a) Rayleigh wave location. (b) Love wave location. (c) Joint location where Rayleigh and Love waves are weighted equally. (d) Joint location where Love and Rayleigh waves are weighted by their minimum misfits.

We repeat this procedure systematically to estimate location bias for the four different mechanisms (red, green, light blue, dark blue) shown in Figure 3 that occur at depths ranging from 1 to 25 km and with different data (Rayleigh, Love, joint) applied in the location procedure. Estimated bias using Rayleigh waves alone is shown in Figure 3a, using Love waves alone is shown in Figure 3b, using equally weighted Rayleigh and Love waves jointly is shown in Figure 3c, and using Rayleigh and Love waves jointly but weighted by minimum misfit is shown in Figure 3d. Figure 3a is similar to a result presented in Paper I, illustrating that location bias for Rayleigh waves can be large, up to several kilometers, for certain types of events that occur between depths of 2 and 5 km. (This figure differs slightly from the comparable figure in Paper I in which large epicentral shifts more than 3 km from the input location were not considered and Paper I, therefore, slightly underestimated the level of bias.) Figure 3b illustrates that locations based on Love waves suffer a much smaller bias, with expected values less than about 400 m. Jointly interpreting equally weighted Rayleigh and Love waves reduces the Rayleigh wave bias substantially, but residual bias at an expected level of about 1 km would remain for events between 2 and 5 km depth as Figure 3c shows. Finally, the location bias based on the joint location that differentially weights Rayleigh and Love waves inversely by misfit illustrates that the resulting bias is very low (Figure 3d).

Bias is even lower than for Love waves alone because the effect of including the Rayleigh wave is to cancel part of the Love wave bias. It is tempting to conclude from these synthetic experiments that differentially weighting Rayleigh and Love waves based on minimum misfit would produce a largely unbiased estimator. This is true for noise-free data, but for real data the signal-to-noise ratio (SNR) of Love waves is typically lower than of Rayleigh waves and the minimum Love wave misfit is not much lower than the Rayleigh wave misfit even in the best cases. In fact, on average, Love wave misfit is higher than for Rayleigh waves. In practice, it is difficult with real data to identify the events for which the Rayleigh wave location would be biased. Although misfit is an excellent guide for synthetic data, for real data it is at best imperfect. For this reason, in presenting results with real data below we will only show joint locations that weight Rayleigh and Love waves equally. However, a better scheme may be found for particular applications.

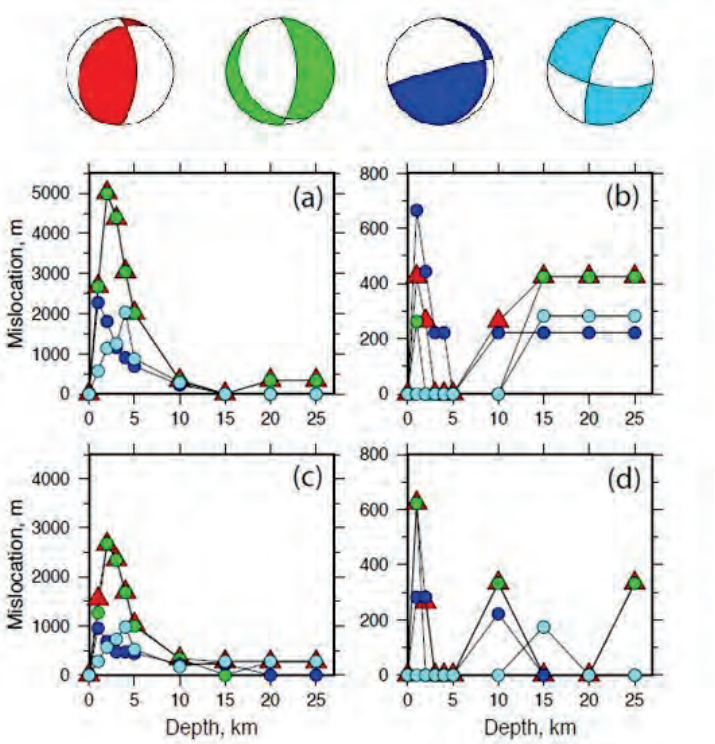


Figure 3. Summary of the mislocations found in the synthetic experiment as a function of the source depth for the four source mechanisms shown at top: red, green, dark blue, light blue. In (a) Rayleigh waves are used alone, in (b) Love waves are used alone, and in (c) Rayleigh and Love waves are used jointly and weighted identically. In (d) Rayleigh and Love waves are used jointly and weighted inversely by the minimum misfit for each wave type (with weights 0.95 and 0.05, correspondingly).

To test the ability of joint use of Rayleigh and Love wave EGFs to locate earthquakes and mining events, we selected ground-truth events with magnitudes in the 3 sec or 4 sec range whose epicenters and depths are well known, in particular with epicenters known to 500 m or better. Such events are strikingly rare in the western US. These include the Crandall Canyon Mine collapse in Utah on August 6, 2007 (Pechmann et al., 2007), whose location using Rayleigh wave EGFs was described in Paper I, two ground-truth events in California and Utah, the Wells earthquake in Western Nevada, and the sequence of its aftershocks (Mendoza & Hartzell, 2009).

Results of locations are summarized in Table 1. The deviations of our locations from references are mostly less than 1.5 km for any combination of Rayleigh or Love waves. It is necessary to take into account that the accuracy of reference locations is mostly not better than 1 km and in the case of Wells events may be worse. The distances between locations using Rayleigh and Love EGFs vary between 0 and 2.3 km and on average are less than 1.1 km. Error ellipses for the 95% confidence level obtained for Rayleigh (*R)*, Love (*L)*, and joint (*RL)* locations cover the reference locations and mostly overlap each other as Figures 4 and 5 illustrate. The size of the error ellipses for Love wave locations is comparable or slightly larger than for Rayleigh waves. Ellipses for joint Rayleigh and Love wave locations are mostly the smallest among the three types of location procedures.

Table 1. Locations using Rayleigh (R) waves, Love waves (L), and both waves (RL).

Event	Ref-R, (km)	Ref-L (km)	Ref-RL (km)	RMS_Q (sec Q)	Ellipse (km Q)
Earthquake, CA	0.7	1.9	0.7	1.2 R	2.5 RL
Mine collapse, UT	0.4	0.7	0.7	1.4 R	1.4 RL
Earthquake, UT	1.3	0.0	0.4	0.9 R	1.7 RL
Wells Event, NV	0.6	1.1	0.6	0.7 R	1.1 R
aftershock#1	0.7	0.7	0.7	0.7 R	0.9 RL
aftershock#2	0.4	0.6	0.4	1.0 R	1.4 R
aftershock#3	1.1	0.7	0.7	0.7 R	0.8 RL
aftershock#4	0.0	1.0	0.7	0.8 L	1.0 RL
aftershock#5	1.2	1.4	1.2	0.8 L	1.0 RL
aftershock#6	0.4	1.2	0.7	0.6 R	1.1 RL

"Ref-R" is the distance between the reference (GT) location and the Rayleigh wave location. "Ref-L" is the same but for Love waves. "Ref-RL" is the same but using both types of waves. "Misfit" is the minimum value (sec) of the misfit functionals F_R, F_L, and F_{RL}. "Ellipse" is the length (km) of the semi-major axis of the 95% confidence ellipse. Epicentral grid spacing is 500m for earthquakes and 200m for the Utah mine collapse. "Q" specifies which method produces the best result: Rayleigh wave location (R), Love wave location (L), or joint location using both wave types weighted equally (RL).

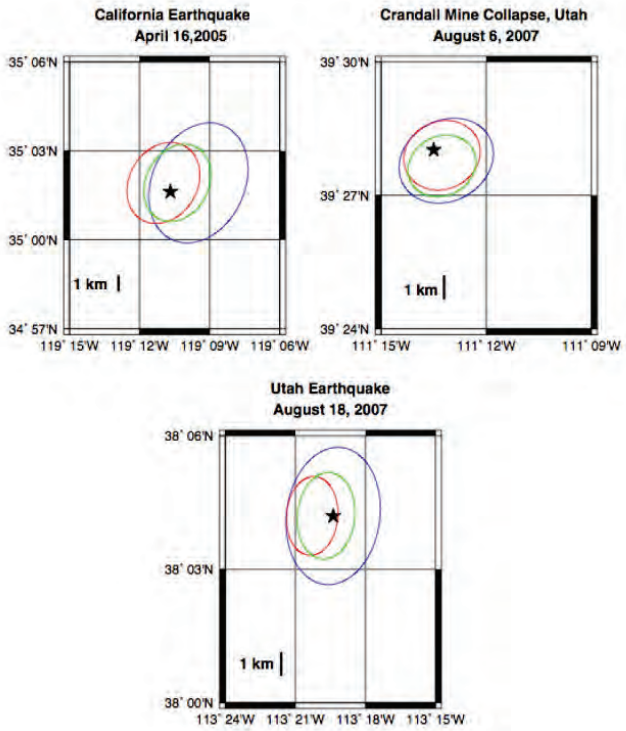


Figure 4. Locations of reference events (stars, Table 1) in California and Utah compared with locations from the methods described herein. Ellipses correspond to the 95% confidence level where the location results from the Rayleigh estimator (red ellipse), the Love estimator (blue ellipse), and the joint estimator where Rayleigh and Love waves are equally weighted (green ellipse).

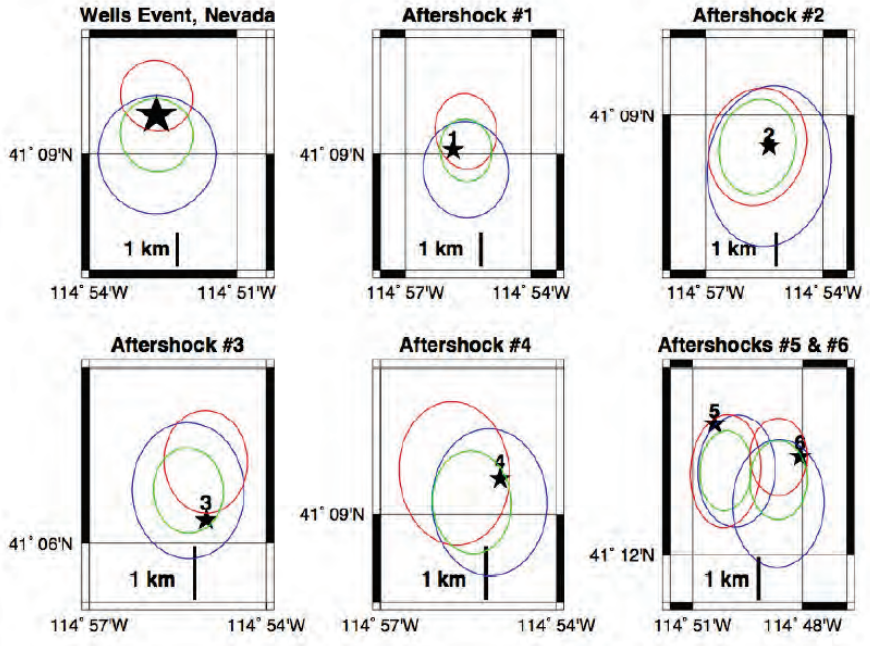


Figure 5. Same as Figure 4, but for the location of the large Wells earthquake on February 21, 2008, and its six aftershocks.

Source Characterization based on Travel Times from a 3-D Model Estimated from Ambient Noise

The methods described above and in Papers I and II are designed to estimate epicentral location based either on comparison of the envelopes of the event waveform with ambient noise empirical Green's functions or on group times measured from ambient noise EGFs and event waveforms. There are two primary shortcomings of the method. First, the method only provides information about epicenter and not focal mechanism, moment, or hypocenteral depth. Second, there is data other than group times that can be used to constrain other aspects of the source and, in fact, group times are a difficult observable compared with phase times. The other data includes both Rayleigh and Love wave phase travel times for the fundamental mode as well as the spectral amplitudes of the Rayleigh and Love waves.

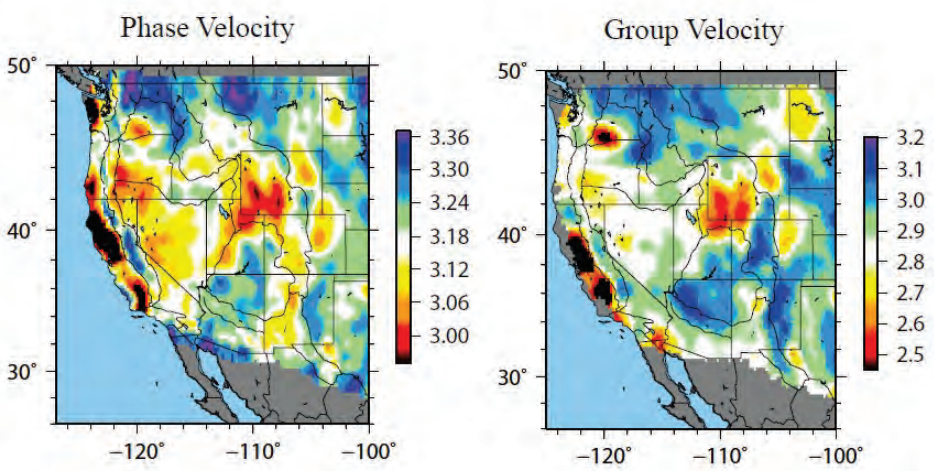


Figure 6. Rayleigh wave phase and group velocity maps at 10 sec period predicted from the 3-D model of Shen et al. (2012).

Ambient noise tomography provides ideal information to construct maps of phase and group speeds across extended regions and 3-D models of Vs in the crust and uppermost mantle. The US is the best region for this application because of the USArray Transportable Array (e.g., Figure 6), but countries on other continents increasingly have been developing extended seismic networks of hundreds to thousands of broadband seismometers that can be used to produce similar models (e.g., China, Europe). Increasingly accurate azimuthally anisotropic maps are also becoming available as seen in Figure 7.

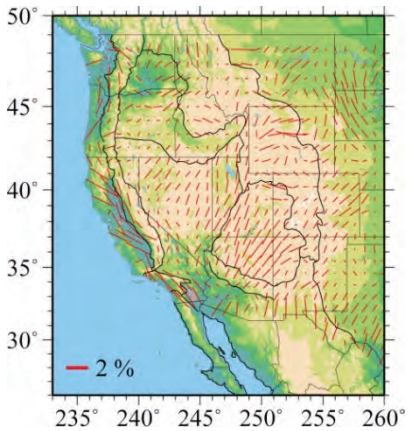


Figure 7. The map of 2ψ-anisotropy for Rayleigh wave phase velocity in percent at 10 sec period.

The quality of source characterization will depend in large part on the ability to predict observables without bias using an earth model. 1-D models notoriously produce biased location estimates as the number of observing stations decreases and as open azimuth increases. Misfit information using a 1-D model following one of the Wells aftershocks in northeastern Nevada is shown in Figure 8.

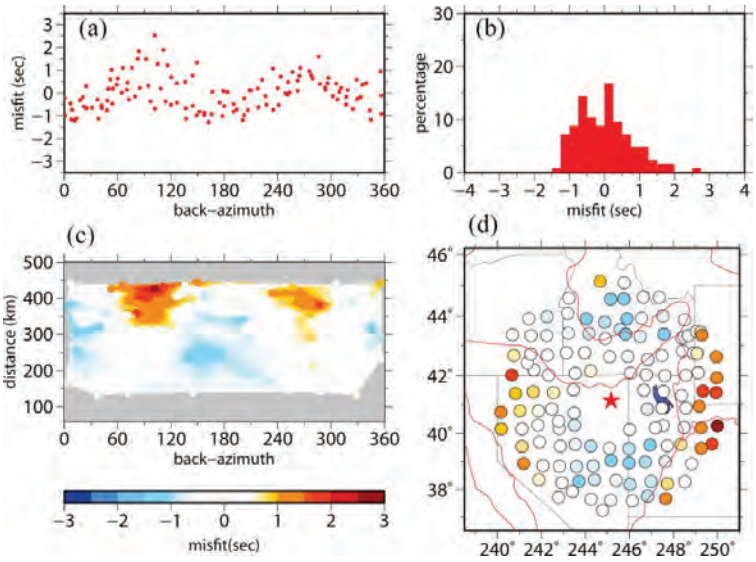


Figure 8. Summary of misfit to observations of phase travel time at 12 sec period observed after the Wells aftershock #4 (Feb 28 2008, M=3.9) using an average 1-D model for the region after correcting for source mechanism. (a) Misfit at individual stations plotted as a function of azimuth (N=0°, E=90°, etc.). (b) Histogram of misfit (RMS misfit = 0.92 sec). (c) Color-coded misfit plotted as a function of back-azimuth and distance. (d) Color-codes misfit plotted at station locations.

In contrast, an accurate 3-D model allows phase travel times to be fit much more accurately, as Figure 9 illustrates. This will allow better epicentral location estimates based on phase travel times as well as provide better estimates of focal mechanism. The inclusion of azimuthal anisotropy actually provides a significant component of the misfit improvement shown in Figure 9.

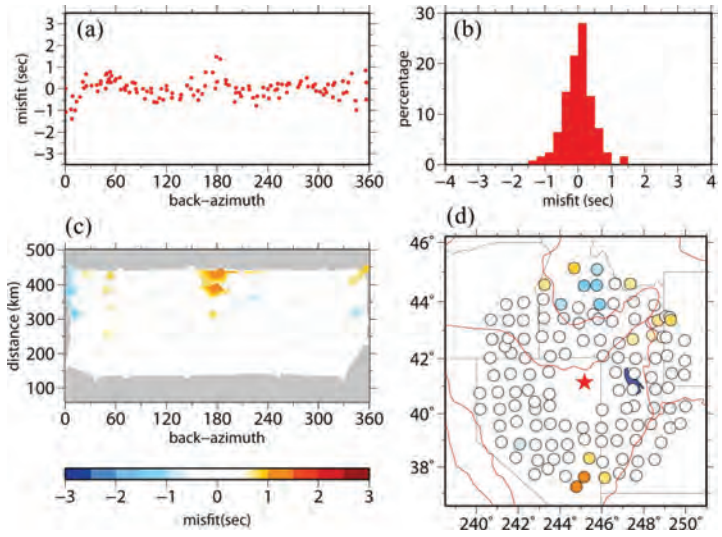


Figure 9. Same as Figure 8, but computed from the 3-D isotropic model of Shen et al. (2012) with the azimuthal anisotropy from Lin et al. (2011). RMS misfit = 0.44s.

The region surrounding Wells, Nevada in the Basin and Range province is actually relatively homogeneous compared with most seismogenic regions. A better estimate of the advantage in fitting Rayleigh wave phase travel times using the 3-D model compared to a 1-D model is presented in Figure 10 for an earthquake near Dillon Montana in 2007 where the observing stations (USArray Transportable Array) were mainly to the west of the epicenter.

We have also estimated the ability of the 1-D and 3-D models to locate the Dillon, MT earthquake from 2007. We do this by using random selections of 5-station subsets of the TA network. Fixing the focal mechanism and depth estimated with the 3-D model using the full observing network (>100 stations) and using the epicenter determined from the full network based on the 3-D model as a reference, we randomly generated 5-station subsets of the full network and located the epicenter based on Rayleigh wave travel times alone at 12 sec period. Using the 1-D model we found that there was an rms error in the epicentral location of about 7.0 km with a 3.9 km bias. With the 3-D model, in contrast, we found that the rms error in the epicenter reduced to about 2.0 km with a 0.5 km bias. Thus, with a small number of stations and a far from ideal observing geometry, the 3-D model produced nearly unbiased epicentral location with an uncertainty of about 2 km, an improvement of more than a factor of three relative to the 1-D model in random error and a factor of eight in systematic error.

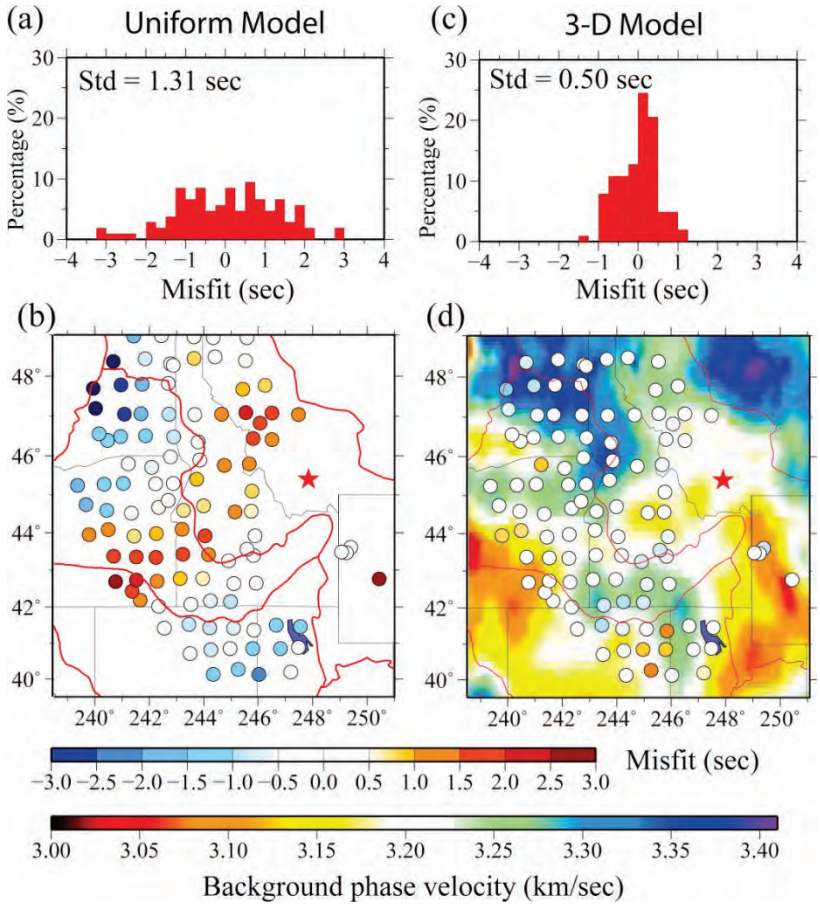


Figure 10. Comparison of misfit to Rayleigh wave phase travel time measurements at 12 sec period using (a and b) a laterally uniform model taken from the 3-D model of Shen et al. (2012) at the epicentral location, and (c and d) the 3-D model of Shen et al. (2012). Earthquake (red star in (b) and (d)): 2007/05/08 15:46:49 45.394N 112.130W, M=4.5, Dillon Montana. In (b) and (d), misfit between +/-3 sec is color-coded in circles at each TA station (operating mostly to the west of the event) and model phase velocity is shown in the background.

Further applications are needed to definitively quantify the expected improvement in source characterization from a 3-D model based on ambient noise tomography. The use of Love waves and a broader period band (e.g., 8-14 sec rather than just 12 sec) should improve location capabilities beyond the examples that we present here. Based on phase travel times alone (perhaps augmented with group travel times), however, depth cannot be well estimated. To estimate depth spectral amplitudes need to be measured. Examples of observed spectral amplitudes corrected for geometrical spreading and average attenuation at 8 sec and 14 sec period for the Wells earthquake #4 are shown in Figure 11a. The scatter at 8 sec period is larger than at 14 sec period even though the amplitude at 8 sec is higher. This is because of interference from microseismic noise for this small earthquake. The expected amplitudes predicted from the focal mechanism estimated using the phase travel time data at 10 km depth are plotted over the observations. The ratio of spectral amplitudes at 14 sec and 8 period provides a constraint on event depth. Figure 11b presents a histogram of the ratio of the amplitudes at 14 sec and 8 sec period taken from Figure 11a. The mean and mode of the distribution of the amplitude ratio are about that expected for an event at 10 km depth. Events at depths of 6 km and 14 km predict amplitude ratios that are either too small or too large, respectively, compared with the observations. The spectral amplitude ratio method is a promising technique to constrain event depths, but further work is on-going to improve measured spectra and to correct them for propagation effects such as attenuation, site response, and focusing/defocusing.

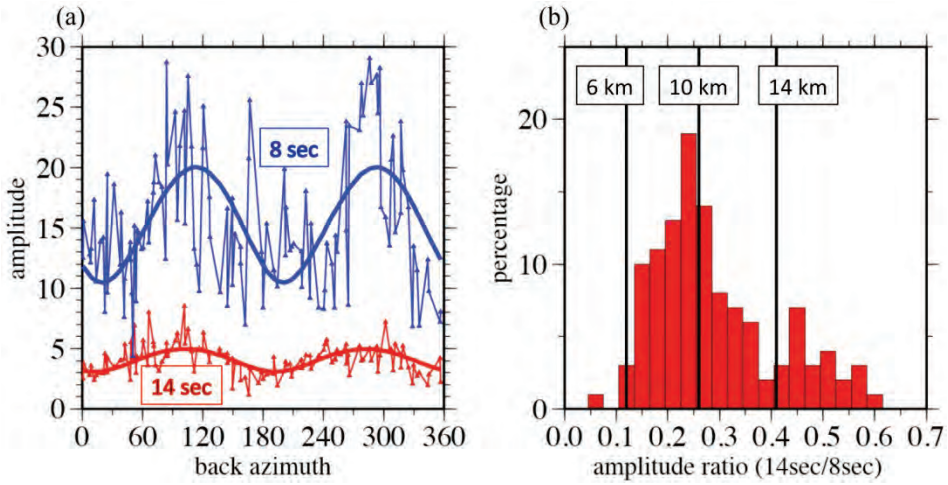


Figure 11. Example of the use of the ratio of Rayleigh wave amplitudes at different periods to estimate event depth for the Wells aftershock #4 (M=3.9). (a) Measured Rayleigh wave amplitudes as a function of azimuth corrected for geometrical spreading and average attenuation at 8 sec period (blue triangles) and 14 sec period (red triangles) observed at USArray TA stations at epicentral distances from 150 km and 450 km. Predicted curves are drawn with bold lines using a hypocentral depth of 10 km and the focal mechanism determined from phase travel times. (b) Histogram of the ratio of observed amplitudes in (a) at each azimuth. Black vertical lines indicate the expected value of the spectral ratios at 14 sec and 8 sec period for the event at different depths. A depth of 10 km agrees best with the obervations in (a).

CONCLUSIONS AND RECOMMENDATIONS

The method to locate the epicenter of regional seismic events based on the envelope of Empirical Green's Functions determined from ambient seismic noise that has been described by Barmin et al. (2011) and Levshin et al. (2012) has several features that make it a useful addition to existing location methods. Love wave EGFs are less sensitive to unknown source parameters (moment tensor, depth) than Rayleigh EGFs, and may provide smaller bias in location for source depths between 1 and 7 km. The advantage of using Love waves to locate seismic events is mitigated by the fact the Love wave EGFs typically have a lower SNR than Rayleigh waves. We demonstrate that the combined use of both types of waves provides locations with the smallest error ellipses. The next step in development of the method is based on using regional 3-D models obtained by tomographic inversion of ambient noise EGFs (e.g., Shen et al., 2012). Phase and group travel times predicted by these models are compared with observed travel times to estimate both epicentral location and focal mechanism. The results presented here illustrate that this technique can be used to improve location and focal mechanism for small crustal events. Depth can be constrained by measuring ratios of the amplitudes of Rayleigh waves at different periods, such as 14 sec and 8 sec periods used here.

ACKNOWLEDGEMENTS

For this research, the facilities of the IRIS Data Management System, and specifically the IRIS Data Management Center, were used to access the waveform and metadata required in this study. The IRIS DMS is funded by the National Science Foundation and specifically the GEO Directorate through the Instrumentation and Facilities Program of the National Science Foundation under Cooperative Agreement EAR-0552316. We are grateful to Dr. C. Mendoza and Dr. M.P. Moschetti for their help in data analysis and Dr. F.C. Lin and Mr. W. Shen for providing us with Rayleigh wave phase and group velocity maps for the Western USA.

REFERENCES

Barmin, M.P., A.L. Levshin, Y. Yang, and M.H. Ritzwoller (2011). Epicentral location based on Rayleigh wave Empirical Green's Functions from ambient seismic noise, *Geophys. J. Int.* **184**, 869–884, doi: 10.1111/j.1365-246X.2010.04879.x.

Levshin, A.L., M.H. Ritzwoller, and J.S. Resovsky (1999). Source effects on surface wave group travel times and group velocity maps, *Phys. Earth Planet. Inter*. **115**, 293–312.

Levshin, A.L., M.P. Barmin, M.P. Moschetti, C. Mendoza, and M.H. Ritzwoller (2012). Refinements to the method of epicentral location based on surface waves from ambient seismic noise: Introducing Love waves, *Geophys. J. Int*., (in press).

Lin, F. M.H. Ritzwoller, Y. Yang, M.P. Moschetti, and M.J. Fouch (2011). Complex and variable crustal and uppermost mantle seismic anisotropy in the western United States, *Nature Geoscience*, DOI:10.1038/NGEO1036.

Mendoz, C. and S. Hartzell (2009). Source analysis using regional empirical Green's functions: The 2008 Wells, Nevada, earthquake, *Geophys. Res. Lett*. **36**, L11302, doi:10.1029/2009GL038073.

Pechmann, J. C., W.I. Arabasz, K.L. Pankow, R. Burlacu, and M.K. McCarter (2007). Seismological report on the 6 Aug 2007 Crandall Canyon Mine Collapse in Utah, *Seismol. Res. Lett*. **79** (5), 620–636.

Ritzwoller, M.H., M.P. Barmin, A.L. Levshin, and Y. Yang (2009). Epicentral location of regional seismic events based on empirical Green functions from ambient noise**,** in *Proceedings of the 31th Monitoring Research Review: Ground-Based Nuclear Explosion Monitoring Technologies*, LA-UR-09-05726, Vol. 1, pp. 389–398.

Shen, W., M.H. Ritzwoller, V. Schulte-Pelkum, F.-C. Lin (2012). A 3-D model of the crust and uppermost mantle beneath the central and western US by joint inversion of receiver functions and surface wave dispersion, *J. Geophys. Res.*, submitted.

A UNIFIED APPROACH TO JOINT REGIONAL/TELESEISMIC CALIBRATION AND EVENT LOCATION WITH A 3D EARTH MODEL

William L. Rodi[1], Delaine T. Reiter[2], Stephen C. Myers[3], and Nathan A. Simmons[3]

Massachusetts Institute of Technology[1], Weston Geophysical Corporation[2], and
Lawrence Livermore National Laboratory[3]

Sponsored by the National Nuclear Security Administration

Award Nos. DE-AC52-08NA28539[1, 2] and DE-AC52-07NA27344[3]
Proposal No. BAA08-19

ABSTRACT

This project addresses the problem of locating seismic events with combined data sets of regional and teleseismic arrival times, using a unified 3D Earth model to predict travel times for both types of data. Inherent to this problem is the joint tomographic calibration of the Earth model using regional and teleseismic ground-truth data. The goal of the unified approach is to remove the inconsistencies that result when travel-time prediction is performed with a mixture of separately calibrated regional and global models and empirical corrections, which can degrade event location performance. The primary focus of the project has been the computational challenges involved in implementing a unified location/calibration capability. A major challenge is presented by the large, nonlinear inverse problem involved in travel-time calibration. A unified calibration of travel times for routinely observed regional and teleseismic phases entails tomographic inversion with millions of arrival-time data and 3D Earth models parameterized with millions of grid nodes. This challenge is intensified by the difficulties of raytracing in 3D Earth models. Full 3D raytracing methods are computationally intensive and many such methods are designed for first arrivals and not easily adapted to reflected phases and other secondary arrivals. Three-dimensional travel-time modeling also poses challenges for routine event location with a large network of monitoring stations.

Our project has pursued an approximate technique for travel-time modeling as an efficient and versatile alternative to full 3D raytracing. The technique is based on linearization with respect to the velocity structure, whereby the travel time in a 3D model is approximated by integrating its slowness function along the raypath computed in a 1D reference model. While travel-time linearization has been popular in modeling teleseismic travel times, it has been generally avoided for regional travel-time modeling owing to the strong lateral variations in the Earth's crust and upper mantle structure. In this project we have developed two enhancements to travel-time linearization that significantly improve its accuracy: a ray warping technique that corrects for lateral variations in the thickness of the crust and layers within the crust, and the minimization of times over multiple reference rays. We have conducted numerical experiments, comparing linearized travel times to highly accurate times calculated with a raybending method, that show that our enhanced linearization technique achieves accuracies well within 0.5 s at teleseismic and near regional distances (up to 10° or so). The accuracy at far regional distances is not as good but still within 1 s for a large majority of the paths we tested. We have incorporated this approximate approach to 3D travel-time modeling into our travel-time tomography algorithm and are applying it to regional and teleseismic arrival-time data from southern Asia.

OBJECTIVE

This project is investigating the problem of locating seismic events with combined data sets of regional and teleseismic arrival times, using a single 3D velocity model to predict consistent travel times for all phases. Implicit in this approach is the joint calibration of the 3D model via tomographic inversion of regional and teleseismic ground-truth data. The feasibility and value of the unified 3D modeling approach has been demonstrated recently by Myers et al. (2011), Simmons et al. (2011) and Ballard et al. (2010), among others. Our efforts in this project have focused on developing computational methods that improve the efficiency and practicality of joint regional/teleseismic location and calibration. The remainder of this paper describes our progress in developing two key components of the unified model approach: 3D travel-time calculation and joint regional/teleseismic tomography.

RESEARCH ACCOMPLISHED

A New Approach to Travel-Time Linearization

A number of numerical methods are available for raytracing and travel-time calculation in 3D Earth models, such as two-point raybending (e.g., Um and Thurber, 1987), the finite-difference eikonal method (e.g., Podvin and Lecomte, 1991), and fast marching (Rawlinson and Sambridge, 2004). Given the computational intensity of these full 3D methods, many applications, such as global tomography with teleseismic data, have used approximate travel times calculated with linearization around a 1D reference model. We will describe this approach as it is conventionally applied and then describe modifications we have developed to improve its accuracy for regional travel-time calculation.

Standard Travel-Time Linearization

We consider the calculation of a travel time T_{3D} between a source point $\mathbf{r}_0$ and receiver point $\mathbf{r}_1$ through a 3D velocity function $v_{3D}(\mathbf{r})$, where $\mathbf{r}$ denotes the position vector in the Earth. Geometrical ray theory implies that T_{3D} is obtained by integrating the slowness function, $1/v_{3D}(\mathbf{r})$, along the geometrical ray connecting $\mathbf{r}_0$ and $\mathbf{r}_1$. Letting η be a dimensionless variable ranging from zero to one, the geometrical ray can be represented as a trajectory $\mathbf{r} = \mathbf{r}^*(\eta)$ such that

$$\mathbf{r}^*(0) = \mathbf{r}_0 \quad (1)$$
$$\mathbf{r}^*(1) = \mathbf{r}_1. \quad (2)$$

The travel time is then given by

$$T_{3D} = \int_0^1 \frac{1}{v_{3D}(\mathbf{r}^*(\eta))} \left|\frac{d\mathbf{r}^*}{d\eta}\right| d\eta \quad (3)$$

where $|d\mathbf{r}^*/d\eta|d\eta$ is the differential distance along the ray. We write (3) more concisely as

$$T_{3D} = \int_{\mathbf{r}_0}^{\mathbf{r}_1} \frac{1}{v_{3D}(\mathbf{r}^*)} |d\mathbf{r}^*|. \quad (4)$$

Fermat's Principle states that T_{3D} is stationary with respect to perturbations to the ray trajectory. An approximation to the travel time through the 3D model is thus given by

$$\tilde{T}_{3D} = \int_{\mathbf{r}_0}^{\mathbf{r}_1} \frac{1}{v_{3D}(\tilde{\mathbf{r}})} |d\tilde{\mathbf{r}}| \quad (5)$$

where $\tilde{\mathbf{r}}$ is an approximate ray connecting $\mathbf{r}_0$ and $\mathbf{r}_1$. The accuracy of the approximation is determined by the proximity of $\tilde{\mathbf{r}}$ to $\mathbf{r}^*$.

The standard approach to linearization applies Eq. (5) with $\tilde{\mathbf{r}}$ taken as the geometrical ray in a reference velocity function, $v_{ref}(\mathbf{r})$. Denoting this ray as $\mathbf{r}^*_{ref}$, (5) becomes

$$\tilde{T}_{3D} = \int_{\mathbf{r}_0}^{\mathbf{r}_1} \frac{1}{v_{3D}(\mathbf{r}^*_{ref})} |d\mathbf{r}^*_{ref}|. \quad (6)$$

In this case $\tilde{T}_{3D}$ is a linearization of T_{3D} around v_{ref}, which is apparent if we rewrite (6) as

$$\tilde{T}_{3D} = T_{ref} + \int_{\mathbf{r}_0}^{\mathbf{r}_1} \left[\frac{1}{v_{3D}(\mathbf{r}^*_{ref})} - \frac{1}{v_{ref}(\mathbf{r}^*_{ref})} \right] |d\mathbf{r}^*_{ref}| \qquad (7)$$

where T_{ref} is the travel time through v_{ref}:

$$T_{ref} = \int_{\mathbf{r}_0}^{\mathbf{r}_1} \frac{1}{v_{ref}(\mathbf{r}^*_{ref})} |d\mathbf{r}^*_{ref}|. \qquad (8)$$

Linearization becomes advantageous when the computation of $\mathbf{r}^*_{ref}$ is more efficient than the computation of $\mathbf{r}^*$, as when v_{ref} is a 1D velocity model.

In previous years of the project we performed numerical experiments to assess the accuracy of travel-time linearization using an early version of the 3D P-wave velocity model LLNL-G3D, derived by Lawrence Livermore National Laboratory (LLNL) with global P-wave travel-time tomography (Myers et al., 2011; Simmons et al., 2011). We have repeated the accuracy tests with a newer version of LLNL-G3D (version 2.3), which is an update of the published model. The newer model presents some additional challenges to travel-time modeling compared to the earlier model we used (version 1.0), having stronger 3D velocity variations in the deeper mantle and topography on the 410-km and 660-km discontinuities. Moreover, version 2.3, unlike version 1.0, builds the Earth's ellipticity as a function of depth into the model parameterization.

Our latest accuracy tests considered travel times between four station locations and a 3D grid of event locations. The epicenter grid covered the box 10° – 55° N, 20° – 100° E at 1° spacing, a larger grid than we used previously. The vertical grid is the same as before, containing five event depths between the surface and 120 km. The four stations, each at zero depth, were located near the corners of the event epicenter grid. LLNL computed highly accurate travel times through LLNL-G3D for the resulting 74,520 paths using its raybending algorithm, based on methods due to Zhao et al. (1992) and Zhao and Lei (2004). The left panel of Figure 1 shows the raybending calculations for events at 15 km depth, displayed as differences from travel times through the global 1D model AK135 (Kennett et al., 1995). We see that LLNL-G3D produces significant travel-time anomalies, reaching -6 s at regional distances.

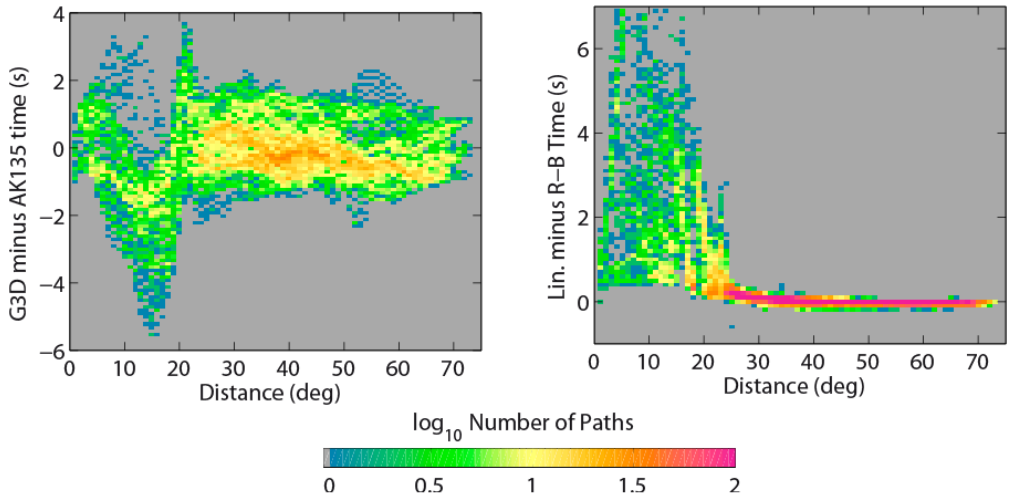


Figure 1. ***Left:*** **Travel-time anomalies predicted by model LLNL-G3D relative to model AK135. The anomalies are displayed for 14,904 paths connecting a grid of events at 15-km depth to four stations near the grid corners. The travel times through LLNL-G3D were calculated with the raybending method. The anomalies are displayed as a histogram binned with respect to time (with 0.1 s increment) and epicentral distance (1° increment).** ***Right:*** **Discrepancy between the same raybending calculations and travel times through LLNL-G3D calculated with the linearization method, using AK135 as the reference model. The traveltime scale on the right has been clipped at +7 s.**

The raybending calculations through LLNL-G3D were used as a benchmark to evaluate the accuracy of travel times calculated with the linearization method, as embodied in Equation (6), taking the reference model to be AK135. The right panel of Figure 1 shows the discrepancy between the raybending and linearized times for the events at 15 km. These results, and those for the other event depths (not shown here), indicate that the errors in linearized times at

teleseismic distances are generally less than 0.2 s. At regional distances, however, the errors can be several seconds or more (greater than 20 s for some paths).

Ray Warping

A major contributor to the large errors in linearized travel-tine calculations at regional distances is the difference between the AK135 Moho depth (35 km) and that of LLNL-G3D, which varies in this region from about 10 km under the Indian Ocean to 75 km beneath the Himalayan Mountains. Because of this, the mantle leg of a first-arriving Pn rays in LLNL-G3D may be partly contained in the AK135 crust, or the crustal leg in the AK135 mantle. Figure 2 illustrates this problem.

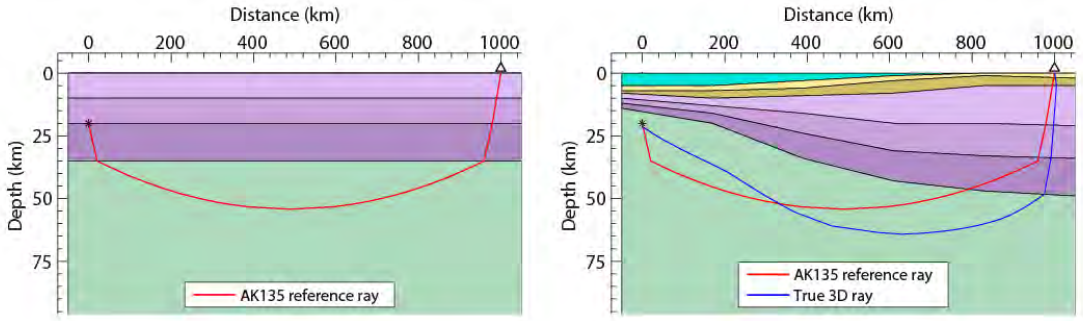


Figure 2. Schematic illustration of the travel-time linearization method. The travel time to be calculated is from an event at 20 km depth to a station at distance 1000 km. *Left:* The reference ray traced in the AK135 model (red line) is shown in relation to the AK135 model layers. *Right:* The AK135 reference ray is compared to the true ray in the 3D model (blue line), both rays shown in relation to the 3D model layers. Near the event, the crustal leg of the AK135 ray is in the mantle of the 3D model; under the station, a portion of the mantle leg of the AK135 ray is in the crust of the 3D model.

To address the problem, we have been investigating a modification of the travel-time linearization method in which the approximation to the geometrical ray in the 3D velocity model is given the form

$$\tilde{\mathbf{r}} = W(\mathbf{r}^*_{\mathrm{ref}}) \qquad (9)$$

where W is a specified warping transformation. The ray $\mathbf{r}^*_{\mathrm{ref}}$, as before, is a geometrical ray calculated in v_{ref} but now with modified endpoints given by

$$\mathbf{r}^*_{\mathrm{ref}}(0) = W^{-1}(\mathbf{r}_0) \equiv \mathbf{r}'_0 \qquad (10)$$

$$\mathbf{r}^*_{\mathrm{ref}}(1) = W^{-1}(\mathbf{r}_1) \equiv \mathbf{r}'_1 \qquad (11)$$

where W^{-1} is the inverse transformation of W. This ensures that $\tilde{\mathbf{r}}$ has the correct endpoints, $\mathbf{r}_0$ and $\mathbf{r}_1$. Substituting Equation (9) into (5) yields $\tilde{T}_{3\mathrm{D}}$ as an integral along the warped reference ray:

$$\tilde{T}_{3\mathrm{D}} = \int_{\mathbf{r}_0}^{\mathbf{r}_1} \frac{1}{v_{3\mathrm{D}}\left(W(\mathbf{r}^*_{\mathrm{ref}})\right)} |\, \mathbf{J}(\mathbf{r}^*_{\mathrm{ref}}) \cdot d\mathbf{r}^*_{\mathrm{ref}}| \qquad (12)$$

where $\mathbf{J}$ denotes the Jacobian tensor of W, such that for any point $\mathbf{r}$,

$$dW(\mathbf{r}) = \mathbf{J}(\mathbf{r}) \cdot d\mathbf{r}. \qquad (13)$$

Equation (12) can be evaluated as an integral along the reference ray itself, as in conventional linearization, by writing it alternatively as

$$\tilde{T}_{3\mathrm{D}} = \int_{\mathbf{r}_0}^{\mathbf{r}_1} \frac{\gamma(\mathbf{r}^*_{\mathrm{ref}})}{v_{3\mathrm{D}}\left(W(\mathbf{r}^*_{\mathrm{ref}})\right)} |\, d\mathbf{r}^*_{\mathrm{ref}}| \qquad (14)$$

where the "distortion" factor γ is given by

$$\gamma(\mathbf{r}) = \mathbf{J}(\mathbf{r}) \cdot \mathbf{n}(\mathbf{r}), \qquad (15)$$

where $\mathbf{n}(\mathbf{r})$ is the unit vector tangent to the ray at any point $\mathbf{r}$ on the ray.

The objective in the warping technique is to choose W so that it transforms a geometrical ray in the reference model into a good approximation of the geometrical ray in the 3D model, as illustrated in Figure 3. This goal is compatible with making $v_{\mathrm{ref}}\left(W^{-1}(\mathbf{r})\right)$ a good approximation to $v_{3\mathrm{D}}(\mathbf{r})$. We have attempted to accomplish this with a warping transformation that moves points vertically in such a way that velocity discontinuities in the 1D reference model are mapped into the corresponding discontinuities of the 3D model. Thus, for example, $W(\mathbf{r})$ will be at the Moho discontinuity of the 3D model when **r** is at the Moho of the reference model, ensuring that Pn rays in the reference model traverse the upper mantle of the 3D model. A vertical warping function can also account for the ellipticity of the Earth as a function of depth, offering an alternative formulation of travel-time ellipticity corrections, *vis-à-vis* Dziewonski and Gilbert (1976), and providing a convenient way to handle elliptical 3D Earth models, such as LLNL-G3D.

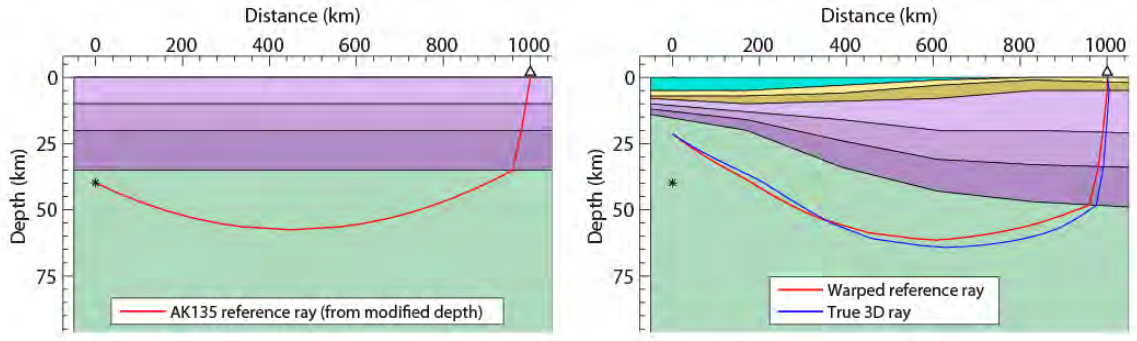


Figure 3. Schematic illustration of travel-time linearization with ray warping, applied to the same situation as in Figure 2. *Left:* A reference ray (red line) is traced through AK135 from a *modified* source depth of 39.8 km. *Right:* The AK135 reference ray is warped vertically so that it emanates from the true source depth of 20 km. The warped reference ray and the true 3D ray (blue line) are shown in relation to the 3D model layers.

Model LLNL-G3D contains seven crustal layers: water (lake or ocean) overlying three sediment layers overlying three hard rock layers. The layers are laterally variable in thickness and, except for water, in velocity. Where a layer does not exist (e.g., water and soft sediments over most of the land masses) the layer thickness is set to zero. LLNL-G3D also includes the Moho discontinuity and mantle discontinuities at approximately 410 km and 660 km, all with laterally varying depth. In the mantle, velocity varies both vertically and laterally between discontinuities. LLNL-G3D terminates with a constant radius (except for ellipticity) core-mantle boundary. All told, the LLNL-G3D model has ten laterally varying velocity discontinuities, counting the Earth's surface.

To implement a vertical warping transformation for use with LLNL-G3D, we modified the AK135 model (the reference model) so that it had the same ten interfaces as LLNL-G3D, adding thin (1 meter) water and sedimentary layers to the AK135 crust and splitting the lower crust into two 10-km layers. The warping transformation mapped the depths of the resulting AK135 interfaces into the geographically variable depths of the corresponding LLNL-G3D interfaces. The vertical warping between interfaces was defined by linear interpolation.

Figure 4 compares the errors in linearized travel-time calculations obtained without the use of ray warping (left panel) and with the warping transformation described above (right). We see that ray warping greatly reduces the errors in linearized times at regional distances. The discrepancies from raybending are now well below 0.5 s for almost all paths shorter than 10° and for a large majority of paths shorter than 15°. The errors at teleseismic distance remain small. However, ray warping does not reduce the errors at epicentral distances between about 14° and 24° to acceptable levels. This distance range corresponds to AK135 rays that turn in or near the mantle transition zone.

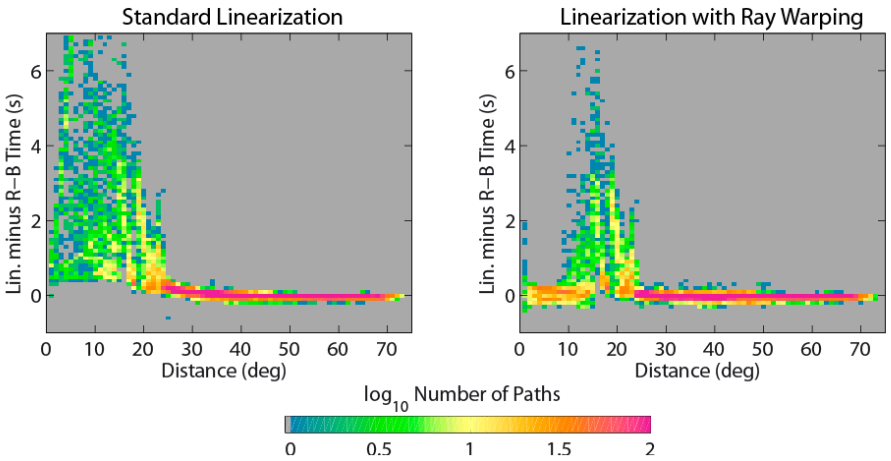


Figure 4. Discrepancy between travel times calculated through model LLNL-G3D with travel-time linearization and with raybending, for the same 14,904 paths considered in Figure 1 (event grid at 15-km depth). The linearized times were calculated either with the standard method (left) or with ray warping (right). Note that the left panel repeats the right panel of Figure 1.

Multiple Reference Rays

The linearized travel times shown in Figure 4 were obtained by integrating the 3D model slowness along the ray corresponding to the first arrival in the reference model. However, when more than one refracted ray arrives at a given epicentral distance (i.e. at triplications), it is possible that integration along a later arriving reference ray yields a faster time through the 3D model. This may in part explain why linearized times, even with ray warping, are less accurate at far regional distances. To test this hypothesis, we extended our linearization technique to compute linearized times with respect to a suite of geometrical rays in the reference model, taking the earliest such time to be the linearized approximation to the first-arrival travel time in the 3D model.

Figure 5 shows the travel-time errors resulting with this multiple-ray technique. The upper left panel uses only the first-arrival reference ray and thus repeats the right panel of Figure 4. In each other panel, the linearized travel-time was minimized over multiple reference rays, for paths having such, but with the number of rays limited to at most two, three, or five. We see that most of the benefit is realized when up to three rays are considered, in which case the errors in linearized times at far regional distances are mostly 1.0 s or less. Figure 6 displays the multiple-ray calculations for three rays as a function of event epicenter, with one panel for each of the four corner stations.

Thus far we have shown travel-time calculations only for events at a depth of 15 km, one of the five depths in our event grid. The results for two deeper event depths, 40 and 75 km, are quite similar to those for 15 km. The other two depths we considered, 0 and 120 km, showed some differences, however. Figure 7 shows the travel-time discrepancies for these depths, where the linearized calculations were done with ray warping and multiple rays (with a 3-ray maximum). The accuracy of linearized times is surprisingly good for surface events (z=0, left panel) considering that many of these are at the ocean surface or atop a thick sedimentary column. For the deep events (right panel) the enhanced errors associated with rays in and near the mantle transition zone affect shorter regional distances.

Joint Regional/Teleseismic Tomography

Over the course of the project we have developed an algorithm for joint regional/teleseismic travel-time tomography, building on the regional tomography algorithm of Reiter and Rodi (2009). The core algorithm solves the linearized tomography problem, i.e. with travel-time sensitivities fixed or, equivalently, using travel-time linearization for forward modeling. The algorithm finds simultaneous least-squares solutions for nodal velocities on a 3D model grid, using geostatistical constraints for regularization, and first-order corrections to event hypocenters and origin times, constrained by prior estimates of location uncertainty. The solutions are calculated with a conjugate gradients scheme, avoiding matrix inversion. To solve the nonlinear inverse problem, the linearized tomography algorithm must be iterated with intervening steps of raytracing and event relocation.

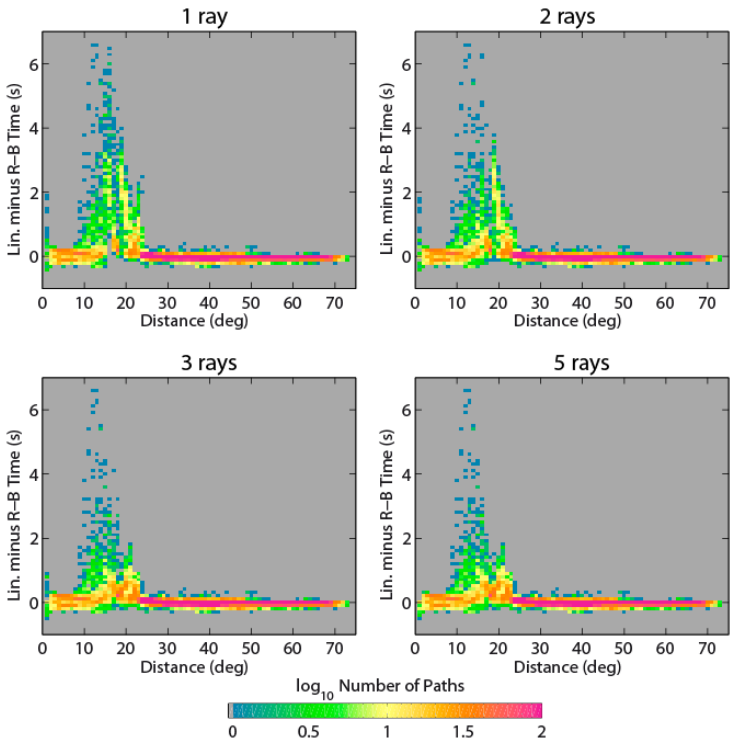


Figure 5. Travel-time discrepancies resulting from four versions of the linearization method. Each version used ray warping and travel-time minimization among multiple rays. The maximum number of rays allowed was varied and is labeled above each panel. Note that the upper left panel repeats the right panel of Figure 4.

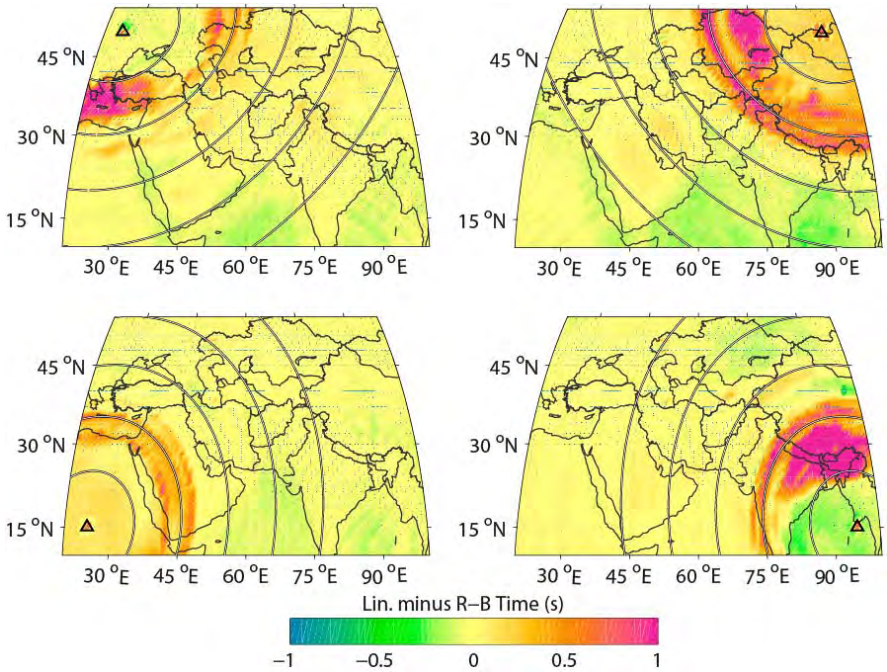


Figure 6. The travel-time discrepancies in the bottom-left panel of Figure 5, which are a result of linearization using ray warping and multiple rays (3-ray maximum), are displayed as a function of event epicenter, with a separate panel for each of the corner stations (marked as triangles). The color scale is clipped at ±1 s.

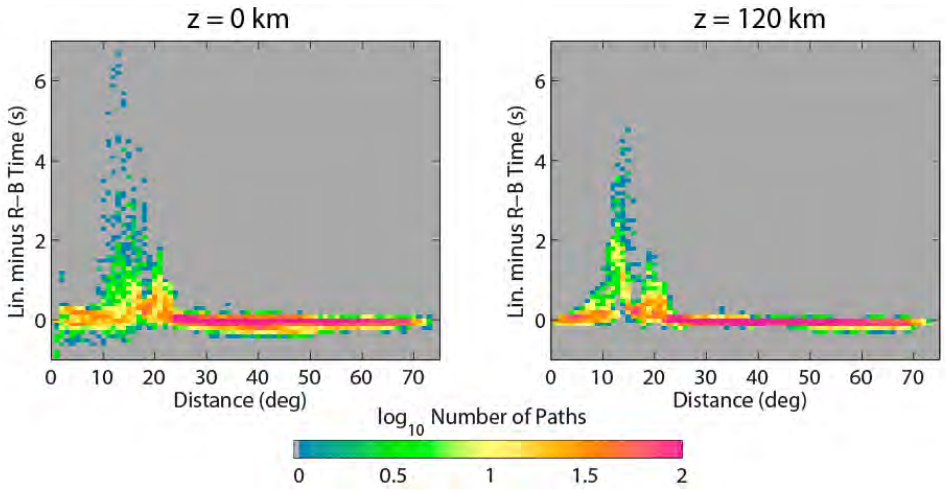


Figure 7. The travel-time discrepancies resulting from linearization using ray warping and multiple rays (3-ray maximum) are shown for event grids at two other event depths, as labeled.

We have incorporated our newest travel-time linearization technique into the tomography algorithm and are applying it to regional and teleseismic arrival times for paths in southern Asia, extracted from an updated version of the EHB database (Engdahl et al., 1998) containing event through 2006. The geographic extent of our model grid is the same as that used by Reiter and Rodi (2009) in their crust/upper mantle tomography: 0 – 60° N, 30 – 120° E. We are using local, regional and teleseismic P-wave arrivals from event-station paths fully contained within this model region, the longest paths being just under 90° in epicentral distance. We restrict the data set to include only events shallower than 200 km and which satisfy criteria established by Reiter and Rodi (2009) for well-determined locations. The tomographic data set, after rejecting a small number of outliers, comprises 601,509 arrival-time picks, of which 60% are teleseismic P, 40% Pn, and less than 0.5% Pg or Pb. We truncated our inversion model grid at a depth of 1500 km since less that 5% of the data sense the velocity structure below this depth. The lateral spacing of our model grid is 1° in both latitude and longitude while the depth spacing is about 25 km in the upper mantle and transition zone and 50 km below 660 km. The prior model for our inversion consists of the 3D model Crust2.0 (Bassin et al., 2000), including its variable Moho depth, atop the AK135 mantle profile.

We are performing our joint regional/teleseismic tomography using travel-time linearization around AK135 as the forward model for both regional and teleseismic travel times. This departs from our original approach of using 3D raytracing (with the Podvin-Leconte method) to model regional times. Fixing the reference model for linearization to AK135 for all data would suggest, since we do not vary the depths of velocity interfaces in the inversion, that the tomography problem is completely linear and does not require iteration of linearized tomography. However, the multiple-ray feature of our linearization method introduces a degree of nonlinearity. Moreover, travel-time sensitivities will change if nonlinear event relocation is performed after the velocity model is changed.

To date we have performed one linearized tomography step to obtain a first update of the Crust2/AK135 prior model. A vertical slice of the resulting velocity model is shown in Figure 8. The slice is displayed only to a depth of 1000 km, below which the velocity variations are quite small. The shallower portion of the velocity model (<300 km) contains features very similar to the crust/upper mantle model of Reiter and Rodi (2009) (model JWM). At greater depths, though, extending into the lower mantle, our joint inversion model contains low velocity anomalies not present in JWM, which are needed to fit the teleseismic travel times.

Figure 9 shows histograms of travel-time residuals produced by the prior and joint regional/teleseismic inversion models. In the case of the inversion model (red line), the residuals are reduced by both changes in velocity from the prior model and changes in event hypocenters and origin times from their prior (EHB) values. The location perturbations were constrained by an assumed prior location accuracy, which we took to be 10 km in epicenter and depth and 2 s in original time (at 95% confidence). To assess how much of the residual reduction is due to velocity vs. location changes, the green lines show the residual histograms resulting when only the event locations are allowed to vary. It is clear that most of the residual reduction is attributable to the velocity inversion model, especially for the teleseismic data.

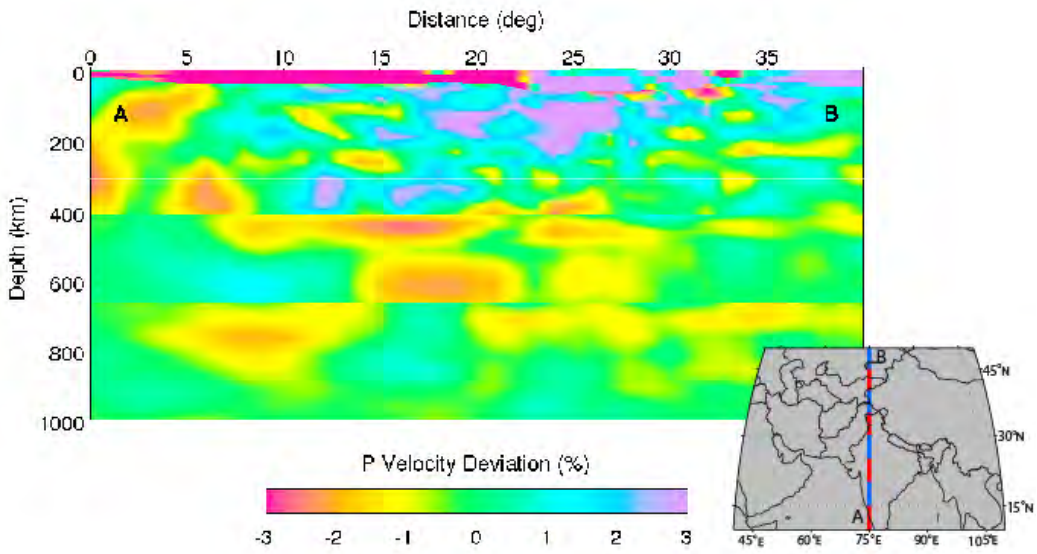


Figure 8. A vertical slice through the inversion model obtained with linearized joint regional/ teleseismic P-wave travel-time tomography, shown in terms of its velocity deviation from the Crust2/AK135 prior model.

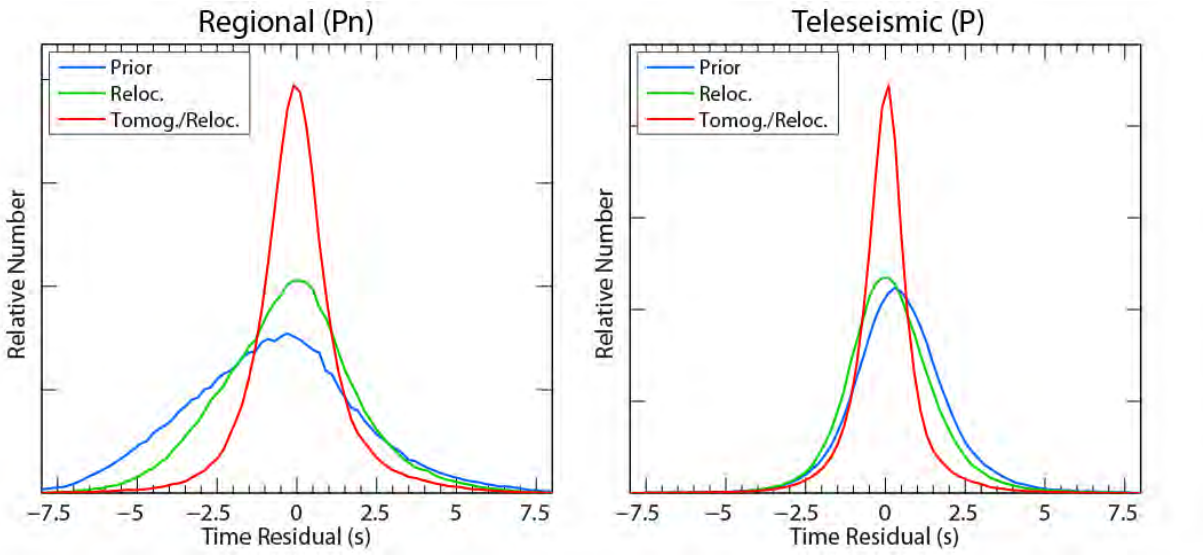


Figure 9. Histograms of regional (left) and teleseismic (right) travel-time residuals for the Crust2/AK135 prior model (blue line) and joint regional/teleseismic inversion model (red line). The inversion model residuals are also reduced by event location perturbations which the inversion solves for simultaneously with the velocity model. The residual histogram resulting from location perturbations only (with the velocity fixed to Crust2/AK135) is shown as the green line.

CONCLUSIONS AND RECOMMENDATIONS

In this project we have developed numerical techniques that promise to significantly enhance the practicality of joint regional/teleseismic location and calibration with a unified 3D Earth model. In particular, our enhancements to the travel-time linearization method for calculating travel times in 3D models, commonly used for teleseismic modeling, extend the applicability of the method to much of the regional distance range, providing an efficient alternative to full 3D raytracing. While there are still situations where linearization is not adequate, we are pursuing its use as the forward model in a joint regional/teleseismic travel-time tomography algorithm, which we are applying to a large

data set of regional and teleseismic arrival times from southern Asia. Although this tomography application is still in progress, we anticipate it will result in a velocity model for the crust and mantle in this region having improved travel-time prediction capability compared to previous models, consistent between regional and teleseismic phases. We plan to demonstrate this with event location validation tests.

REFERENCES

Ballard, S., M. A. Begnaud, C. J. Young, J. R. Hipp, M. Chang, A. V. Encarnacao, C. A. Rowe, W. S. Phillips, and L. K. Steck (2010). A global 3D P-velocity model of the Earth's crust and mantle for improved event location – SALSA3D, *Proceedings of the 2010 Monitoring Research Review: Ground-Based Nuclear Explosion Monitoring Technologies,* LA-UR-11-05578, Vol. 1, pp. 31–39.

Bassin, C., G. Laske, and G. Masters (2000). The current limits of resolution for surface wave tomography in North America, *Eos Trans. AGU* **81**, F897.

Dziewonski, A. M. and F. Gilbert (1976). The effect of small, aspherical perturbations on travel times and a re-examination of the corrections for ellipticity, *Geophys. J. R. Astr. Soc*. **44**, 7–17.

Engdahl E.R., R. van der Hilst, and R. Buland (1998). Global teleseismic earthquake relocation with improved travel times and procedures for depth determination, *Bull. Seismol. Soc. Am.* **88**, 722–743.

Kennett, B. L. N., E. R. Engdahl, and R. Buland (1995). Constraints on the velocity structure in the Earth from travel times, *Geophys. J. Int.* **122**, 108–124.

Myers, S. C., G. Johannesson, and N. A. Simmons (2011). Global-scale P wave tomography optimized for prediction of teleseismic and regional travel times for Middle East events: 1. Data set development, *J. Geophys. Res*. **116**, B04304, doi:10.1029/2010JB007967.

Podvin, P. and I. Lecomte (1991). Finite difference computation of traveltimes in very contrasted velocity models: a massively parallel approach and its associated tools, *Geophys. J. Int*. **105**, 271–284.

Rawlinson, N. and M. Sambridge (2004). Wave front evolution in strongly heterogeneous layered media using the fast marching method, *Geophys. J. Int.* **156**, 631–647.

Reiter, D. T. and W. L. Rodi (2009). Validated 3D velocity models in Asia from joint regional body- and surface-wave tomography. *Final Report*, Weston Geophysical Corp., AFRL-RV-HA-TR-2009-1009.

Simmons, N. A., S. C. Myers, and G. Johannesson (2011). Global-scale P wave tomography optimized for prediction of teleseismic and regional travel times for Middle East events: 2. Tomographic inversion, *J. Geophys. Res*. **116**, B04305, doi:10.1029/2010JB007969.

Um, J. and C. H. Thurber (1987). A fast algorithm for two-point seismic ray tracing, *Bull. Seismol. Soc. Am*. **77**, 972–986.

Zhao, D., A. Hasegawa, and S. Horiuchi (1992). Tomographic imaging of P and S wave velocity structure beneath Northeastern Japan, *J. Geophys. Res*. **97**, 19909–19928.

Zhao, D. and J. Lei (2004). Seismic ray path variations in a 3D global velocity model, *Phys. Earth. Planet. Int*. **141**, 153–166.

SEISMIC SIGNAL ANALYSIS FOR EVENT DETECTION AND CATEGORIZATION

Charlotte A. Rowe, Richard J. Stead, Michael L. Begnaud, and Emily A. Morton

Los Alamos National Laboratory

Sponsored by the National Nuclear Security Administration

Award No. DE-AC52-06NA25396/LA12-Signal_Analysis-NDD02

ABSTRACT

We explore a variety of signal analysis techniques with the goal of automatically detecting, categorizing, and picking phases on waveforms under a variety of source type and signal-to-noise (SNR) scenarios. These techniques will ultimately be incorporated into an automated system whose implementation will improve the consistency of our signal analysis operations and the quantitative consistency of autopicking approaches. Moreover, with the application of orthogonal and independent approaches in a synchronous and complementary fashion, we will be able to determine the uncertainties not only of our phase picks (and automated locations) but also of our detections and event categorization decisions.

Detection can proceed in a variety of ways, which are dependent upon the history of the system as well as the nature of incoming data. In cases where no a priori knowledge exists among waveforms, such approaches as waveform template cross-correlation or subspace detection based on templates are not possible, and typically such tools as STA/LTA are employed. We explore the application of these threshold methods not only to waveforms themselves but also to derived parameters such as signal kurtosis and time-varying polarization, as well as spectral functions. These will be compared to an exploration of changes in the subnet subspace dimensionality and sensitivity of that dimensionality to the time-varying contributions of the basis vectors.

Categorization and identification tools include the unsupervised dendrogram clustering and probability function accept/reject criteria, as well as new experiments using self-organizing maps (SOM). We demonstrate a variety of methods applied to waveforms from our East Asia database, including a large catalog obtained for the Korean Peninsula from the Korean Meteorological Agency (KMA) and Korean Institute of Geoscience and Mineral Resourcas (KIGAM). These provide a dense network of seismometers and accelerometers across South Korea, with a large collection of small and moderate-sized events on which to test our methods.

OBJECTIVES

Three important applications of automated or semi-automated signal analysis techniques are 1) real-time or retroactive event detection in a continuous digital data stream; 2) automatic event categorization of detected signals, based on a priori information regarding existing event types and 3) improvement of event location and characterization by improving analytical consistency for derived parameters.

Automatic detection methods can be roughly divided into two categories: those which search for signals by comparing to known templates, and those which seek to declare an event based on some quantifiable change to background signal characteristics, where previous example waveforms do not exist. Our goal is to continue exploring technologies that will aid in signal analysis automation both for the 'previous known events' and the 'new data stream – no examples' scenarios. Ultimately the objective is to develop a real-time system that applies multiple techniques in an ongoing basis, to best ascertain the features of incoming signals of interest and whether detailed human review is needed. As thresholds are lowered and networks expand, the volume of data to be analyzed is increasing at a fast pace. The more robust tools available for partially automating the process, the more cost-effective and reliable our monitoring systems will be.

RESEARCH ACCOMPLISHED

Use of pre-existing / *a priori* data

Among the template-based methods are included the broadly used scanning cross-correlation approach and the scanning subspace detection. For both of these methods, it is necessary to identify templates which represent a signal of interest, against which the larger waveform catalog can be compared. In most observatories, a large collection of waveforms is readily available from which templates can be chosen for this purpose; in general, the point of automating an event recognition tool is to eliminate from the human review process events that have been seen before and are recognizable by the computer. Classic targets include active mines, highly productive earthquake swarm sources (either tectonic or volcanic/geothermal) and to some extent, aftershock sequences. In cases of repeating sources, the waveforms, if sufficiently similar, can be aligned and stacked to produce a stack template, whose signal-to-noise (S/N) has been correspondingly improved, and against which the continuous signals are more successfully correlated. Most seismically active regions exhibit a fraction of their seismicity in the form of repeating events, but this varies substantially depending on the region. High numbers of repeating events generally are restricted to smaller magnitudes, whose waveforms are more difficult to detect at significant distances from the source region. As the monitoring community moves toward smaller thresholds, the ability to identify and categorize automatically the portion of repeating events in a catalog is even more important. Not only are smaller events more numerous overall, but the proportion of repeating events increases as thresholds are lower. Automated means of detecting and identifying such events will play and increasingly important role in reducing the workload for human analysts.

Scanning cross-correlation detection of waveforms using templates ('matched filter') has been successful for many researchers (e.g., Stankova et al., 2008; Bisrat et al., 2012) and can be performed either in a single-channel or multi-channel fashion. We show in Figure 1 an example of seismic swarm activity and single-channel detections using as a template a stack of manually identified repeating events.

It is generally accepted that one of the primary drawbacks of cross-correlation scanning is the low tolerance for minor differences between template and waveform. One is generally required to either accept a low correlation threshold, which may result in numerous false positive detections, or multiple nearly identical events whose cross-correlation fails to meet a high threshold due to minor source variations or noise, will be missed. One way to circumvent this problem, particularly in cases where a range of similar but not identical waveforms are known to arise from a single limited source region (a mine, for instance), is to use instead the method of subspace detection.

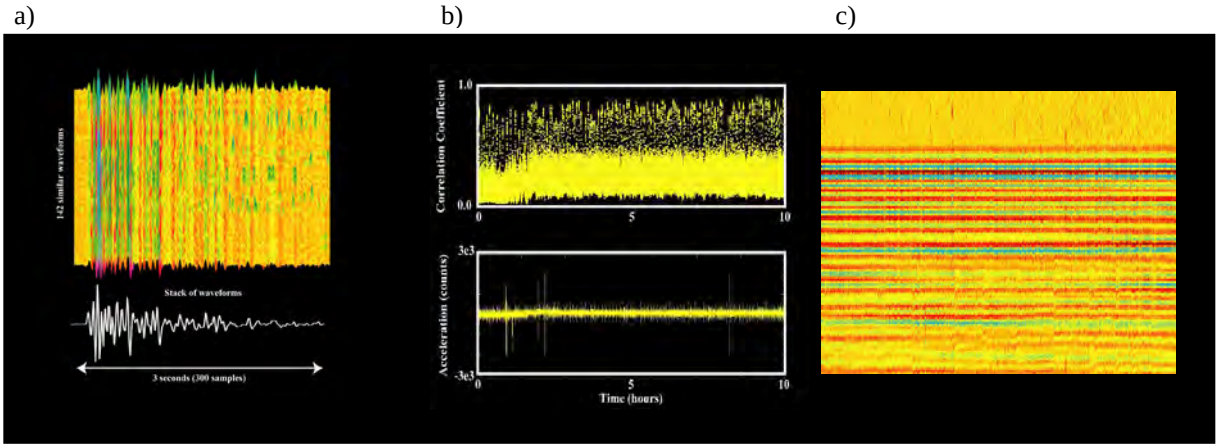


Figure 1. Example of scanning correlation detection for a single channel. a) We have taken 142 members of a cluster and stacked to form the template, boosting by nearly 12 times the S/N. b) Ten hours of data are shown in the bottom panel, with the corresponding cross-correlation coefficient for each sliding window position as the template is scanned through the continuous data. c) The resulting 782 detections, aligned for visual comparison.

This technique does not perform waveform analysis per se, but rather treats a suite of N similar seismograms as a matrix composed of N vectors. Following singular value decomposition, the M eigenvectors associated with the most significant eigenvalues can be viewed as defining the M-dimensional subspace which contains any possible linear combination of the input template waveforms. A projection of any new waveform onto this subspace matrix yields a (normalized) coefficient that is a measure of the ability of the subspace to reproduce the test signal. Thus the need for identical signals is eliminated and more tolerance of variation is permitted, without accepting completely unrelated waveforms. As with correlation templates, however, the subspace method depends for its success on the careful selection of representative templates whose characteristics successfully span the space of signals arising from a source area of interest. In Figure 2 we illustrate six of sixteen similar templates selected from an episode of swarm activity at Mount St. Helens in 2004.

We applied the correlation scanning method to the continuous data stream using three templates from the selected sixteen, and we compare these results to a subspace analysis of the same data set. In Figure 3 we show the discrete correlation coefficients for a scan using each of three templates from the sixteen.

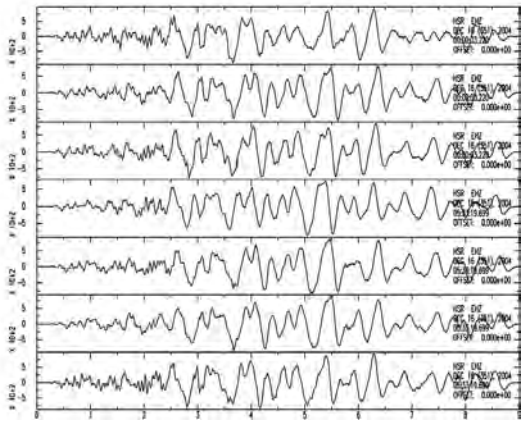


Figure 2. Six of sixteen templates identified during a swarm at Mount St. Helens in 2004. These templates were used both for cross-correlation analysis and subspace detection, to compare the two methods on a well-defined data set.

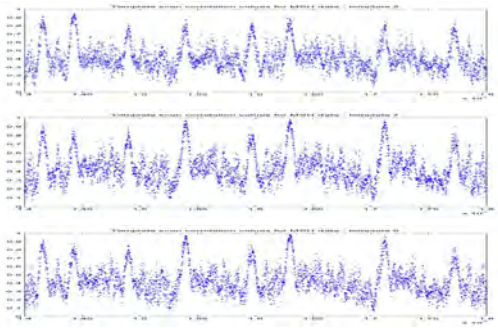


Figure 3. Waveform correlation results for each of three selected templates, across the continuous waveform illustrated at the bottom. Because of minor differences in the templates, we see minor differences in the correlation values, although the overall behavior is similar

We can see that the template correlation scans all succeeded in picking up the events observable in the waveform, with slight variations as might be expected. We can also observe that the noise level is high – possibly due to spectral similarity between the background tremor and the discrete events – and thus for any of these individual templates, selection of a threshold could be problematic. Some event detections appear at or below some of the noise on the function, thus we are faced with a choice whether to tolerate false alarms or missed events. In early waveform correlation analyses, some researchers have advocated selecting a threshold based on some combined correlation function, such as a mean or median for several stations. It is tempting to consider this approach for our example application, but given the similar noise levels and signal levels on the different functions, the mean or median would not differ significantly from any of the individual functions. If, however, we view the functions as probabilities, then one can argue that the correct treatment at any step is a multiplicative combination, rather than linear, in much the same way that probabilities of isolated events are calculated in this fashion. If you toss a pair of dice, your odds of getting snake eyes is not ((1/6) + (1/6))/2, but is rather 2 × (1/6) × (1/6). Hence, to illustrate, we perform a point-by-point multiplication of the correlation coefficients in the three example functions of Figure 3. Because correlation coefficients vary between zero and one, intuition tells us that peaks should remain near one, whereas smaller values will be severely attenuated. The results (Figure 4) bear this out, and demonstrate that a combinational correlation approach can yield similar results to the subspace detection.

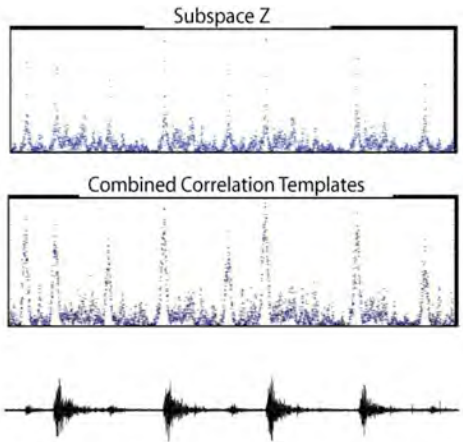


Figure 4. Top: Results of subspace detection applied to St. Helens continuous swarm data. Center: Results of three-vector correlation multiplication on the same data set, using three of the same templates comprising the subspace detector. Bottom: Waveform on which the analysis was performed.

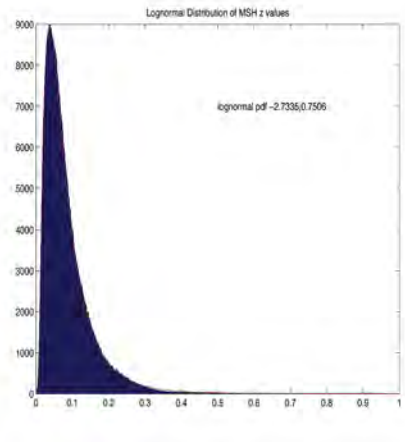


Figure 5. Fitting a PDF to the ongoing detector projection values provides a means of automatically determining optimal threshold for declaring an event with a given level of confidence.

Subsequent to running the detector, a decision is needed regarding the final threshold for an automated system to declare an event. In an analysis of subspace detections on low-frequency events within subduction zone tremor, Maceira et al. (2010) determined the probability of an event by fitting a probability distribution function to the collection of projection values for the subspace. In their case they used a beta function, and found that for their data a probability of missing an event of less than 2% could be achieved with a threshold of about 0.76. In the case of the MSH swarm in our example, the data are best fit with a lognormal PDF (Figure 5), and it was not possible to achieve a good fit with the beta distribution. This suggests that each data set is unique and in fact the distribution could vary on a daily basis depending on noise, as well as varying for any given station or network.

Application to the Korean Peninsula

We routinely download segmented waveforms from the Korean Meteorological Administration (KMA) and Korean Institute of Geoscience and Mineral Resources (KIGAM), both of whom operate seismic monitoring networks throughout South Korea.

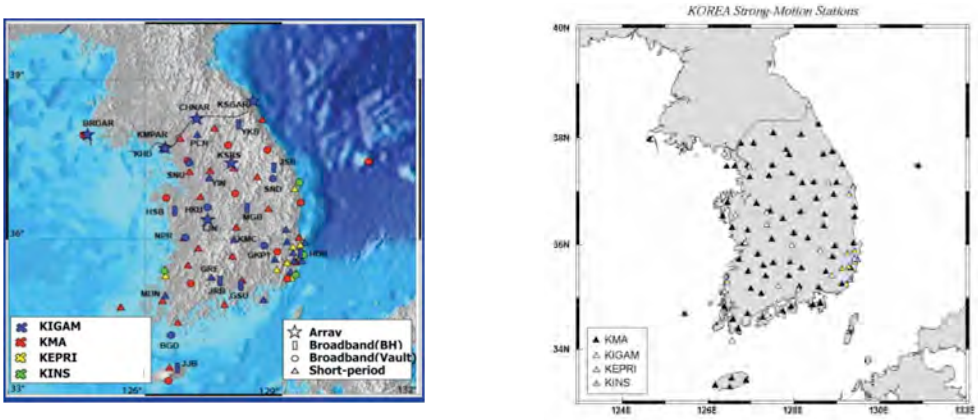


Figure 6. Seismic network coverage on the Korean Peninsula is dense, thanks to the combined seismometer and accelerometer networks of KIGAM, KMA and other agencies.

Preliminary event origins and associated waveforms are available for download from the websites of both these agencies, although phase arrival information is not. We are using a combination of dendrogram-based correlation clustering (e.g., Rowe et al., 2002) and correlation scanning detection (Stankova et al., 2008) to identify repeating sources within these catalogs and provide correlation-guided phase picking, towards a goal of high-precision event locations for crustal tomography.

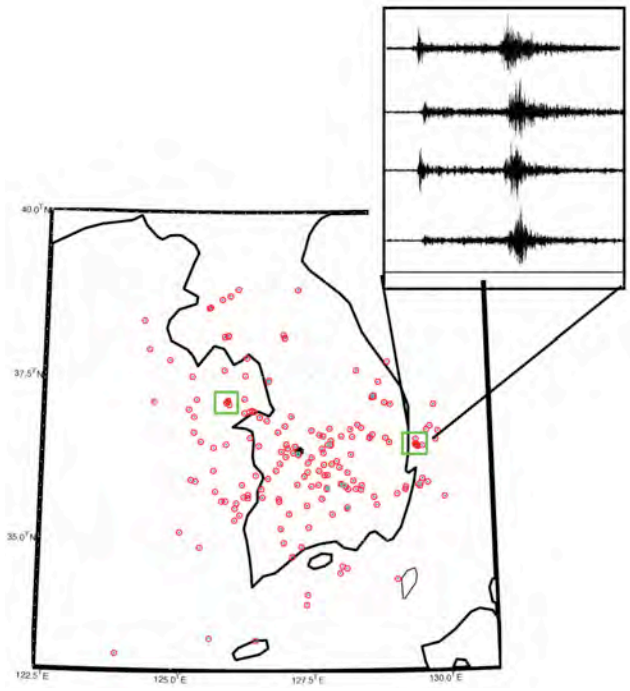


Figure 7. Epicenters of downloaded events, with example waveforms for one identified cluster.

Figure 7 shows preliminary (published) epicenters for approximately ten years of earthquake data obtained from KMA and KIGAM, shown as red crosses. Two of the identified clusters are delineated by green boxes. We provide an example of four similar waveforms for station TEJ (shown as a black X) from one cluster, identified through correlation scanning. Events are small, ranging between magnitude 2 and 4, and the correlation scanning and clustering are only of limited use, as the seismicity is diffuse so repeating events are a very small part of the catalog.

From the perspective of cross-correlation efforts, the diffuse nature of the seismicity is disappointing, as little benefit is realized in terms of enhanced automatic event identification and phase picking improvement. On the other hand, the diffuse nature of the sources is a benefit for our goal of tomographic inversion for a 3D crustal model, as numerous crossing raypaths will be realized with the dense seismic networks. These events yield good P-wave arrivals for about twenty seismic stations on average.

Unsupervised Detections

The above methods are predicated on the existence of templates from previous analysis, to use in the detector. In situations where a new data stream begins, a blind event detection method will be needed. A host of tools exist for this purpose, ranging from short-term-average / long-term-average (STA/LTA) approaches to spectral fingerprinting (e.g., Joswig, 1990) to running polarization (Maceira et al., 2010). We have explored a few innovative approaches that show promise, which we anticipate inmplementing in parallel with a trained (template-based) recognition system.

Seismic waveforms exhibit a variety of characteristics, several of which can be expected to differ when a signal of interest occurs. Visually the most obvious of these is the amplitude of the waveform, and the standard STA/LTA method is successful in detecting events of interest under good recording conditions. During periods of high noise, however, or for subtle signals, or when events occur in close succession such that the detector is saturated, STA/LTA will fail to detect; alternatively, it is vulnerable to dropouts, spikes and other nonseismic sources.

Two of the approaches we are currently investigating for real-time signal detection include running signal kurtosis, and time-varying subspace dimension.

Signal Kurtosis

There are various descriptions for the statistic known as 'kurtosis,' but the general agreement among them is that it represents the degree of peakedness of a distribution, and the 'heaviness' of its tail. This applies only to a symmetric (skewness=0) distribution. A familiar distribution with zero excess kurtosis (mesokurtic) is the normal distribution. Because we assume that seismic background noise is possessed of a normal distribution, whereas event signals are not, it is reasonable to expect an analysis of kurtosis to distinguish anomalies in the baseline signal at a seismic station. Galiana-Merino (2008) applied a kurtosis-based autopicking approach in combination with wavelet decomposition to demonstrate success in reproducing the quality of human analyst picks for previously identified seismic events, one of the technologies we are currently exploring, but at a more basic level we have implemented the kurtosis measure to test its utility as part of an event detector.

In Figure 8 we illustrate a running kurtosis function for four days of continuous data recorded at one channel (MK01) at the Makanchi array (MKAR). This particular test was run using a 5000-sample (50 s) window of data for each kurtosis assessment, with 100-sample window overlap. The signal kurtosis appears to be a good tool for highlighting event arrivals, even when buried within the coda of another event.

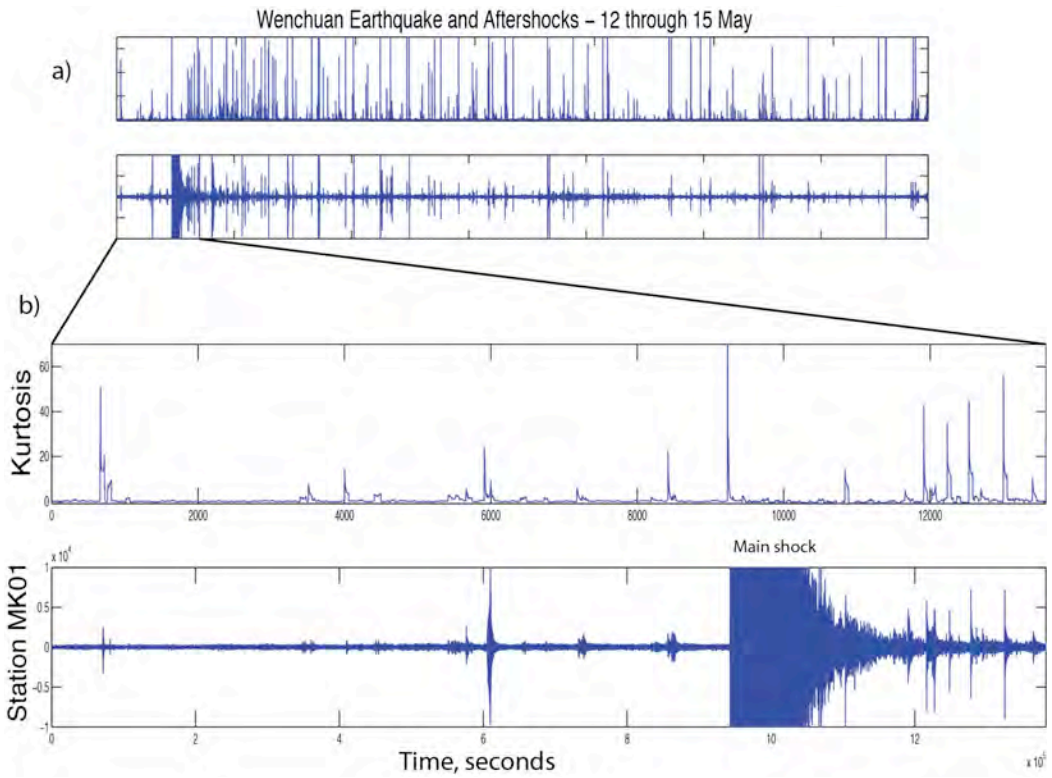


Figure 8. a) Four days of data recorded at station MK01 including main shock and aftershocks for the 2008 Wenchuan earthquake. Top: Kurtosis function using 50-s window moving in 1-s steps. Bottom: Seismogram. b) Close-up of first ten hours of these data, showing the ability of the kurtosis function to distinguish overlapping events. Top and bottom panels as in a).

We speculate that good performance could be obtained by pairing an event auto-detector, such as STA/LTA, or an Akaike Information Criterion (AIC) auto-regressive picker, with the time-dependent kurtosis function. The lower pair of panels shows a close-up of the first ten hours of the time series, beginning 6.3 hours before the mainshock (labelled). Peaks in the kurtosis function correspond with onset of foreshocks, mainshock and multiple overlapping aftershocks. A STA/LTA thresholding detector operating on the seismogram directly might saturate and fail to identify onsets for many of the rapid-fire aftershocks, whereas such a detector operating on the kurtosis function should exhibit superior sensitivity. We have not yet explored the false alarm rate for this example; the kurtosis clearly provides spikes for subtle events prior to the mainshock, some of which are clearly earthquakes barely above the noise level, but positive identification of others we have yet to determine.

Subspace Dimension

We continue exploration of the subspace method for event detection. The application has been well described and developed for comparing templates of seismic waveforms to identify an event from a known source region (i.e., Harris et al., 2006; Maceira et al., 2010) but we wish to explore the subspace approach for detecting seismic events in previously unanalyzed data streams. Of course, this means that the use of an *a priori* subspace detector, built on manually selected waveforms, is not possible. Instead, we explore a technique developed for real-time analysis of anomaly diagnosis in computer networks. Researchers have found that even in networks with hundreds of individual flows, abrupt changes in traffic can be captured in a relatively small number of dimensions using a subspace approach. Our preliminary inspection will be followed in the future with a more detailed analysis applying the GROUSE algorithm developed by Balzano et al. (2010, 2011). Their method analyzes incremental gradient descent on a Grassmannian manifold of subspaces. In a nutshell, this method tracks an *n*-dimensional subspace that changes over time.

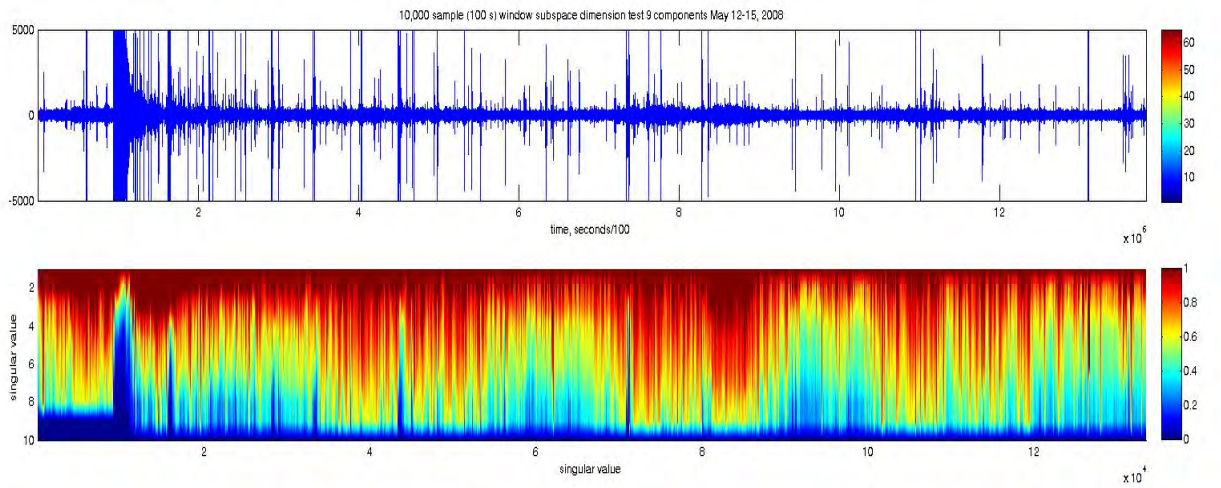


Figure 9. Four days of seismic data during and after the May, 2008 Wenchuan earthquake (top) and running function of sorted singular values for the Makanchi Array (Z component only) sensors. Note the marked change in relative amplitudes of singular values during discrete earthquake events. The lower dimensionality at the beginning of the plot corresponds to missing data from one channel for part of the first day.

In routine application of subspace techniques to seismic data, a collection of waveform templates is aligned in a matrix, on which a singular value decomposition (SVD) is performed to ascertain the dimensionality of the subspace that spans the collection of templates, to some predetermined threshold. The theory is that by selecting the *n* most significant singular values, we can describe any of the contributing waveforms by some linear combination of the eigenvectors associated with our subset of singular values – thus the eigenvectors span a significant subspace of the full template space. The choice of how many eigenvectors to include depends on a function of the sorted singular values and the completeness with which the user wishes to characterize the family of template events.

We anticipate that for a static collection of seismic stations, or an array, the space that defines routine, background noise might be representable by a subspace with dimensionality near the total input number of channels, but dominated by a vector representing any coherent noise, and that its dimension is relatively stable in the absence of anomalous transient signals. Much like the abrupt change seen in computer network traffic load, which significantly perturbs the dimensionality of the background subspace, we expect a change to the seismic network subspace, and its characteristic dimensionality, in the presence of a discrete, transient signal. As a preliminary test, we perform a running SVD analysis of synchronous waveforms for the Makanchi Array. The time series we inspect is a time period including the Wenchuan 2008 mainshock and aftershocks to which we applied the kurtosis test, above. Figure 9 depicts the sorted singular values for each 10000-sample matrix windowed in the analysis. The time window moves in 100-sample steps through the continuous data files. The sorted SVDs for each time step are normalized and presented side-by-side as a surface. A change in dimension should result in a change in the shape of the surface, in that the number of significant singular values and their relative magnitudes will change.

We note that overall, the dimensionality of the significant subspace appears to decrease (the lower-numbered singular values dominate) when an event occurs, whereas the dimension increases during background noise. This is consistent with the introduction of a significant transient signal that briefly dominates the waveforms for the array. Future work will include experimentation with the characteristics of the eigenvectors themselves, and whether they can provide us with a means of de-noising the data for improved detection capability. Application of the method in conjunction with beam-forming methods and polarization analysis may yield important tools for automated analysis.

CONCLUSIONS AND RECOMMENDATIONS

We note that the features of time series (seismograms, acoustic signals, other time-varying recorded functions) are typically under-utilized in efforts to detect and characterize anomalous signals of interest. Observatories are often invested in systems that rely solely on one or two signal features (amplitude, perhaps frequency) for detecting anomalies of interest, and often solely reliant upon correlation of only raw or filtered seismograms for categorizing events in the presence of previously identified signals. We assert that exploration of all aspects of signal features should be undertaken so that complementary tools may be employed, providing not only combined strengths of each method (mitigating weaknesses) but also a means of assessing the confidence with which events are detected, identified and categorized through agreement of independent methods. Such features as spectral signature, signal polarization, kurtosis, subspace dimensionality may provide important measures themselves, or may produce meaningful functions on which other methods (such as STA/LTA) can operate under circumstances when the raw data are not optimal for threshold detectors.

REFERENCES

Balzano, L., R. Nowack and B. Recht (2010). Online tracking of subspaces from highly incomplete information. arXiv:1006.4046v2 [cs.IT]

Balzano, L., B. Recht and R. Nowack (2011). High-dimensional matched subspace detection when data are missing. arXiv:1002.0852v2 [cs.IT].

Bisrat, S., H.R. DeShon and C.Rowe (2012). Microseismic Swarm Activity in the New Madrid Seismic Zone. *Bull. Seismol. Soc. Am*. **102**, 1167–1178.

Galiana-Merino, J.J., J.L. Rosa-Herranz, and S. Parolai (2008). Seismic P-phase picking using a kurtosis-based criterion in the stationary wavelet domain. IEEE Trans. *Geosci. Rem. Sensing* **46**, 3815–3825.

Harris, D.B. (2006). *Subspace Detectors: Theory*. Lawrence Livermore National Laboratory Technical Report UCRL-TR-222758.

Joswig, M. (1990). Pattern recognition for earthquake detection, *Bull. Seismol. Soc. Am.* **80**, 170–186.

Maciera, M., C.A. Rowe, G. Beroza and D. Anderson (2010). Identification of low-frequency earthquakes in non-volcanic tremor validated with the subspace detector method. *Geophys. Res. Lett*. **37**, L06303, doi:10.1029/2009GL041876.

Rowe, C.A., R.C. Aster, B.Borchers and C.J. Young (2002). An automatic, adaptive algorithm for refining phase picks in large seismic data sets, *Bull. Seismol. Soc. Am.* **92**, 1660–1674.

Stankova, J., S. Bilek, C. Rowe and R. Aster (2008). Characteristics of the October 2005 microearthquake swarm and reactivation of seismic swarms over decade-scale time periods near Socorro, New Mexico. *Bull. Seismol. Soc. Am.* **98**, 93–105.

GLOBAL P-WAVE TOMOGRAPHY FOR IMPROVED TRAVEL-TIME PREDICTIONS AND EVENT LOCATIONS

Nathan A. Simmons, Stephen C. Myers, Gardar Johannesson, and Eric M. Matzel

Lawrence Livermore National Laboratory

Sponsored by the National Nuclear Security Administration

Award No. DE-AC52-07NA27344/LL12-SignalPropagation-NDD02

ABSTRACT

We have developed a global-scale P-wave velocity model (LLNL-G3Dv3) designed to accurately predict seismic travel times at regional and teleseismic distances simultaneously. The model provides a new image of Earth's deep interior, but the underlying practical purpose of the model is to provide enhanced seismic event location capabilities. Previous versions of LLNL-G3D provide substantial improvements in event location accuracy due to a more explicit Earth representation from the surface to the core and 3-D ray tracing. The latest model is based on ~2.8 million *P* and *Pn* arrivals that are re-processed using our global multi-event locator known as Bayesloc. We construct LLNL-G3Dv3 within a spherical tessellation based framework, allowing for explicit representation of undulating and discontinuous layers including the crust and transition zone layers. Using a multi-scale inversion technique, regional trends as well as fine details are captured where the data allow. LLNL-G3Dv3 exhibits large-scale structures including cratons and superplumes as well as numerous complex details in the upper mantle, including the transition zone. Particularly, the model reveals new details of a vast network of subducted slabs trapped within the transition beneath much of Eurasia, including beneath the Tibetan Plateau. We demonstrate the impact of Bayesloc multiple-event location on the resulting tomographic images through comparison with images produced without the benefit of multiple-event constraints (single-event locations). We find that the multiple-event locations allow for better reconciliation of the large set of direct P phases recorded at 0-97° distance and yield a smoother and more continuous tomographic model than the single-event locations, even when an iterative inversion/relocation technique is employed. We demonstrate that travel time predictions can differ by seconds at regional distances and up to a second at teleseismic distances, depending on the initial locations of the input data. Therefore, accurate locations of the tomographic input data are crucial for developing a model with the ability to accurately locate future events. Event location validation tests with our preferred model (LLNL-G3Dv3) yield epicenter mislocation improvements of 60% using only regional arrivals, 30% improvement using only teleseismic arrivals, and a gradation of improvement between 30% and 60% when regional and teleseismic data are used together. These tests demonstrate the value of global 3-D tomography for predicting future event locations.

OBJECTIVES

The overall objective of this project is to generate a global-scale 3-D image of the Earth's crust and mantle that is capable of accurately predicting regional and teleseismic travel times. Achieving this objective will allow for accurate seismic event location determination for events occurring anywhere on the globe. The sub-objectives outlined in this report include: 1) the design of a global model of P-wave velocity structure that predicts P and Pn travel times globally, and 2) demonstrating the importance of multiple-event locations for the input data prior to tomographic inversion.

RESEARCH ACCOMPLISHED

We develop a new global P-wave tomography model called LLNL-G3Dv3 by leveraging several imaging techniques outlined in previous Monitoring Research Review proceedings (Simmons et al. 2009, 2010a, 2011a) and journal articles (Myers et al. 2011; Simmons et al. 2011b). The model also leverages starting models including the global joint seismic-geodynamic model called GyPSuM (Simmons et al. 2010b) and the Regional Seismic Travel Time (RSTT) model (Myers et al. 2010). We invert travel times for a global distribution of events with locations determined via the Bayesloc multiple-event location technique (Myers et al. 2007, 2009, 2011), modified in the current study to account for regional travel time curve trends. We compare our location procedures and model results to a global model obtained without the benefit of multiple-event location prior to tomographic inversion. Predicted travel times are found to be substantially different depending on the initial locations of events used to develop the image.

Dataset and Multiple-event Clustering Technique

Travel-time data were gathered from the Lawrence Livermore National Laboratory (LLNL) database (see Ruppert et al., 2005), which is a massive compilation of data from a variety of sources. Those include the EHB bulletin (Engdahl et al., 1998) provided by the International Seismological Centre (ISC), the National Earthquake Information Center (NEIC) bulletin, and a variety of regional bulletins. Additional data are derived from seismic deployments for Peaceful Nuclear Explosions (PNE's), large refraction surveys, the USARRAY Transportable Array (TA) and temporary PASSCAL deployments around the world. A large number of the travel time measurements were made by staff at LLNL. Currently, the full travel-time data consists of ~13.4 million measurements from ~118,000 seismic events.

Given the redundancy of very large tomography data sets, many studies choose to combine the information by forming summary rays through simple averaging or a more sophisticated process. Instead of forming summary rays, we chose to select specific events to be simultaneously relocated with Bayesloc. Therefore, we designed an event selection strategy to find seismic events with the highest probability to be accurately located using the Bayesloc procedures and events that provide the greatest number of P and Pn data for tomography. The selected events include all available Ground Truth 5 (GT5, ground truth information of accuracy 5 km) or better based on the Bondár et al. (2004) criteria. In addition, we selected events with the most:

1) teleseismic P travel-time measurements,
2) even azimuthal coverage of the teleseismic networks
3) regional Pn travel-time measurements, and
4) local Pg measurements provided that Pn or P measurements exist for the event.

Sampling was achieved by rank-ordering events based on the four criteria. The first event in the list was selected and other events within 1° were removed from consideration for that criterion. Event sampling with the above selection criteria was repeated for events in 6 depth bins: 0-35 km, 35-75 km, 75-150 km, 150-300 km, 300-450 km and 450-700 km depth range.

Through this selection process, we reduced the number of considered events to 13,069 of the global seismic events with the most measurements and the best network geometry. The selected events provided ~3.4

million travel time measurements for a suite of teleseismic, regional, and depth phases (Table 1) recorded at 7,370 seismic stations worldwide.

Table 1: Travel time arrivals for input into Bayesloc multiple-event location

Phase	Number Input to Bayesloc	Number Used in tomography
P	2,662,081	2,553,180
Pn	286,297	266,882
pP	182,890	
Sn	80,912	
sP	78,696	
PcP	62,458	
Pg	30,911	
Lg	22,162	
Total	3,406,407	2,820,062

The 13,069 events were located using the Bayesloc multiple-event location technique (Myers et al. 2007, 2009), previously applied to a global dataset (Myers et al. 2011). Bayesloc is a formulation of the multiple-event location system that includes travel-time corrections, arrival-time measurement (pick) precision, and stochastic phase labels. The hierarchical Bayesian formulation allows for prior constraints on any aspect of the multiple-event system, and a Markov-chain Monte Carlo method is used to draw samples from the joint distribution of multiple-event location parameters.

The Bayesloc travel-time correction formulation includes a correction to the travel time curve for each phase, which accounts for regional travel-time error trends. To the travel-time curve corrections, Bayesloc adds station and event terms with a zero-mean prior constraint to account for small, path-dependent errors. Myers et al. (2011) relocated a set of global events, but limited regional-distance travel-time data to the Middle East. Therefore, one adjustment for each regional-phase travel-time curve was sufficient. In this study we include regional-phase data from all parts of the globe, which necessitates spatially variable corrections to regional-phase travel-time curves. Varying regional travel-time curve corrections are achieved by forming a cluster of neighboring events around each event and simultaneously relocating the cluster (see Figure 1 for cluster examples). In addition to allowing for region-specific travel-time curve corrections, simultaneous relocation of event clusters maintains the ability to propagate prior constraints from GT0-GT5 through the data set and provides robust estimates of pick precision and phase labels.

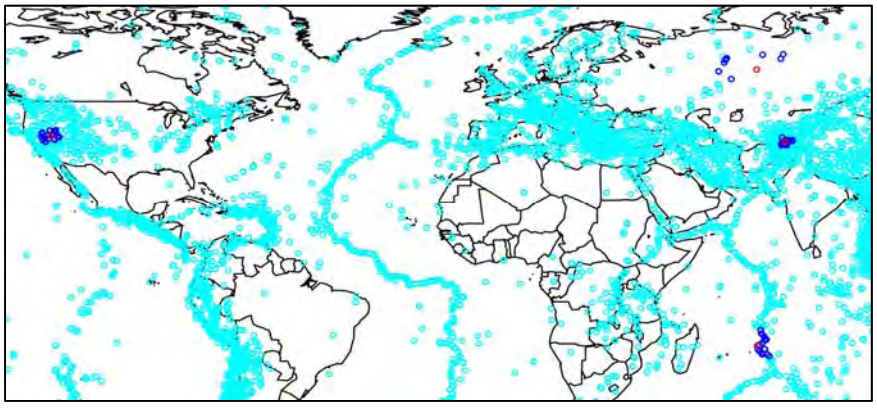


Figure 1. Examples of event clusters formed during the Bayesloc multiple-event relocation process. Red circles are the 4 example target events and dark blue circles are events that are members of each cluster. Light blue circles mark events not used to form any of the example clusters.

Bayesloc multiple-event processing results in median epicenter shifts of 6.8 km, depth shifts of 5.5 km, and origin time shifts of -0.67 seconds compared to single-event locations (Figure 2). Figure 2 shows that epicenter shifts are not random, but rather regionally dependent. The largest shifts are observed at subduction zones, where events tend to move trenchward, which is consist with the observations and reasoning of Creager and Boyed (1992). Many events in the Former Soviet Union are explosions with known locations and hence display small epicenter shifts, as the locations are constrained by priors. After Bayesloc processing we remove events if the 90% epicenter probability region for that event exceeds 1000 km2 in area. Events are also removed if the depth uncertainty exceeds 18 km or if the origin time uncertainty exceeds 1 second. Individual travel-time picks are removed if the phase label is not determined with probability greater than 0.95 or if arrival-time uncertainty is greater than 1 second. Based on these criteria, the number of events is reduced to 12,571 (3.8% reduction) and the number of P and Pn picks is reduced from 2,948,378 to 2,820,062 (4.3% reduction). Relocation using Bayesloc and removal of a relatively modest percentage of untrusted data results in a reduction in travel-time residuals (with respect to ak135) from 1.59 seconds to 1.26 seconds, which equates to a 37% reduction in variance.

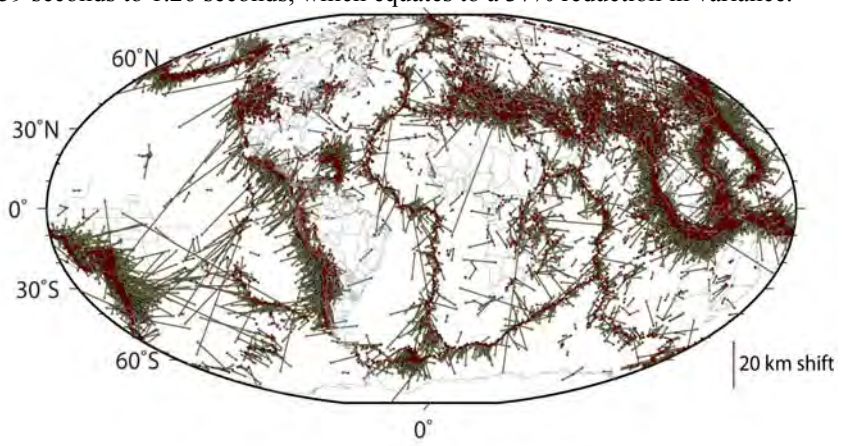


Figure 2. Bayesloc multiple-event relocation vectors. The red circles mark the epicenter locations determined one event at a time (single-event locations). Arrows illustrate the epicenter shifts due to multiple-event relocation using the clustering technique described in the text.

The LLNL-G3Dv3 Model and Location Validation

The LLNL-G3Dv3 model is parameterized with nodes defined by triangular tessellations of spherical surface. Spherical tessellation grids have been employed in numerous global geophysical studies primarily for generating evenly spaced points and avoiding polar distortions created by latitude-longitude grids (e.g., Wang and Dahlen, 1995). Spherical tessellation grids are conveniently extensible to any resolution level and hierarchies of different resolution grids are intrinsic. Within the spherical tessellation framework, we represent undulating and discontinuous layers by placing nodes at arbitrary radii. The maximum lateral resolution considered is ~1° spacing laterally, and 57 layers from the surface to the core (giving ~1.6 million points). We exploit the hierarchical nature of the tessellation grid through our multi-resolution inversion approach called Progressive Multi-level Tessellation Inversion (PMTI) developed in Simmons et al. (2011).

The effort to generate complex global-scale tomography models is motivated by the fact that accurate model-based travel-time prediction necessitates 3-D ray tracing given significant ray path discrepancies between 1-D and 3-D ray paths. Deviations in the ray paths from the 1-D assumption are particularly large where high degrees of velocity variability exist, such as in the shallow upper mantle where regional rays travel. Thus, we adapted a 3-D ray tracing approach based on the Zhao et al. (1992) methodology. Our particular adaptation of the 3-D ray tracing methodology is described in Simmons et al. (2011).

The PMTI imaging technique yields multi-resolution images without developing irregular grids and also provides intrinsic regularization similar to a regionally variable smoothing operator. The only regularization required to generate reasonable images is a single damping term. We identify the appropriate damping level with basic L-curve analysis (Figure 3). The optimum model (providing a balance of image roughness and data misfit) fits the ~2.8 million P-wave arrivals with an overall standard deviation of 0.96 seconds. This equates to 64% variance reduction relative to the initial event locations and travel-time residuals with respect to the ak135 model.

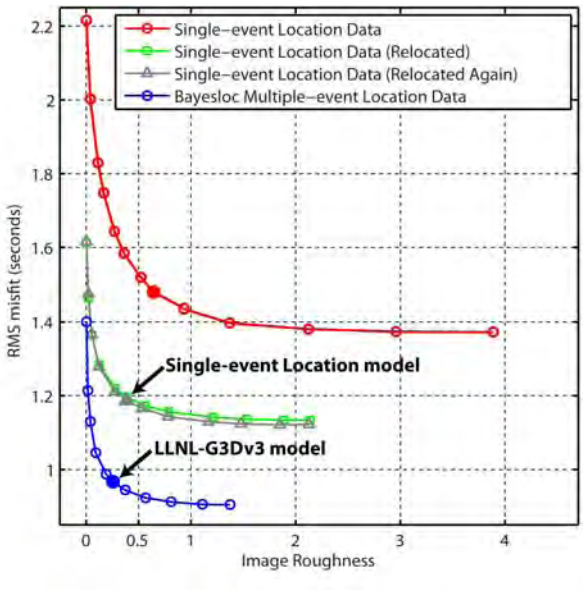


Figure 3. Roughness versus data misfit for a spectrum of damping weights. The multiple-event locations allow for higher degrees of data fit relative to single-event locations, even when an iterative tomography/inversion procedure is employed.

Long-wavelength features in the shallow upper mantle are depicted where P-wave coverage is limited, such as beneath ocean basins (Figure 4). As noted in Simmons et al. (2010), joint inversion of multiple data types that include seismic and geodynamic constraints is a powerful way to estimate heterogeneities where single types of data may provide only limited constraints. Specifically to this modeling effort, it is extremely difficult to resolve reasonable images of P-wave velocity heterogeneity associated with mid-ocean ridges and entire cratons without inversions including surface-reflected multiples and/or surface waves. Since our starting model is based on the joint seismic-geodynamic model (GyPSuM), many of the shallow regions with considerable data gaps are filled in with reasonable estimates of velocity heterogeneity. Thus large portions of the velocity anomalies attributed to cratonic roots and linear mid-ocean ridge structures are also seen as dominant structures in the LLNL-G3Dv3 model.

Although many of the long-wavelength shallow upper mantle structures are largely seen in the starting model, details in the upper mantle P-wave velocity structure are better resolved in several regions; particularly where data are abundant such as beneath the North American continent and most of Eurasia. Complex velocity structures are clearly evident along tectonic margins, where active seismicity yields numerous data providing powerful constraints. However, we note that complexities in the shallow upper mantle are also found well within the stable continental interiors of North America and Eurasia, where considerable regional travel-time data exist as well. These mostly stable cratonic/platform regions are clearly less complex than tectonically active regions and are generally imaged as long-wavelength features. However, stable continental regions may be more complex than generally recognized, due to a lack of resolution.

Like many previous global P-wave tomography studies, we image tabular subducted slabs in the upper mantle along most of the world's active (or recently active) convergent margins and ancient slabs in the

lower mantle. We also detect large high-velocity structures within the transition zone beneath much of Eurasia, which are likely subducted slabs deflected horizontally near the 660-km discontinuity and trapped within the transition zone. These trapped slab structures beneath the Eurasian continental interior tend to have sharper velocity gradients along the edges and are more expansive in the LLNL-G3Dv3 model than most other global P-wave models.

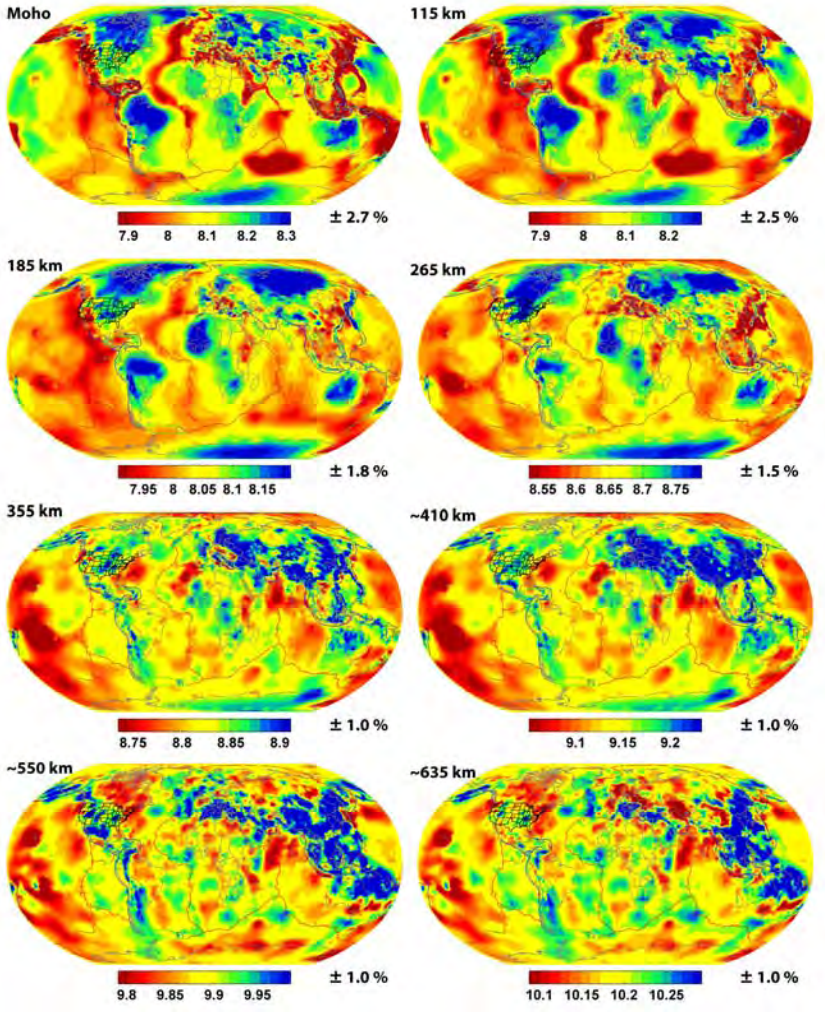


Figure 4. The LLNL-G3Dv3 model P-wave velocity structure in the upper mantle.

Along the western Pacific margin, the fast anomalies in the transition zone have long been identified as subducted Pacific lithosphere deflected near the base of the upper mantle. However, we also detect a broad fast anomaly above and within the transition zone beneath western China. The anomaly extends from India to Mongolia and lies directly beneath the Tibetan Plateau (see Figure 4). This broad fast anomaly is possibly a large remnant slab subducted resulting from the convergence of India with Eurasia and thus the closing of the Tethys Oceans. It has proven difficult to identify enough subducted lithosphere in the Tethys region from tomographic images to account for the expected volume of slabs subducted since the Mesozoic Era (Hafkenscheid et al., 2006). It is apparent that a substantial quantity of lithosphere has sunken into the lower mantle deep beneath present-day India, contributing to the estimated volumetric budget of subducted material. However, our model indicates that a large volume of the subducted material may be trapped in the transition zone beneath most of western China (Figure 4).

Preliminary location validation tests were performed with a globally distributed set of 116 explosions with known locations, as well as earthquakes with locations constrained by a local network. Validation events were excluded from the tomographic inversion to prevent circularity. Test data sets for each event consisted of a specified number of randomly selected P and Pn arrivals. Ten random realizations were drawn for each test set, unless fewer then ten unique permutations were possible. Each data realization was used to relocate the events using LLNL-G3Dv3 travel-time predictions, and summary statistics were computed for each data category (number of P and Pn data). Relative to the ak135 model, epicenter mislocation errors are generally reduced by ~60% when only regional phases are used, and ~30% when only teleseismic phases are considered (Figure 5). A comprehensive validation study is currently underway and will be the subject of an upcoming report.

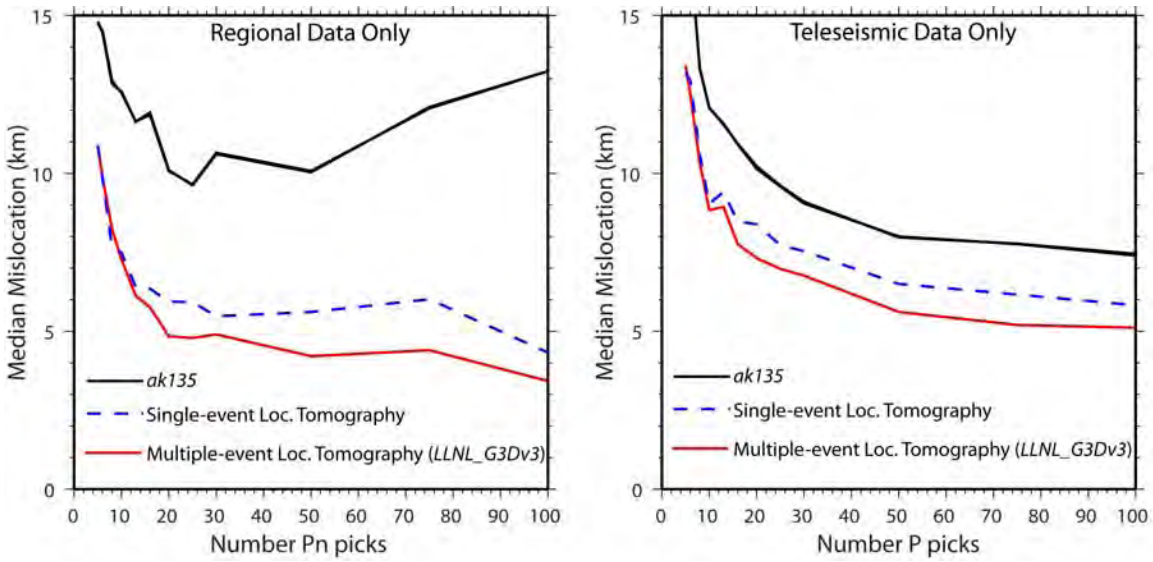


Figure 5. Median mislocations for the 116 well-known test events. Independent tests were performed with 3 models: ak135, the Single-event location model, and the Multiple-event location model (LLNL-G3Dv3).

Single-event Locations versus Multiple-event Locations

Knowledge of the location of past seismic events used to develop tomography models is a classical problem, and is of particular importance when designing a model that allows for accurate prediction of future event locations. To test the importance of the multiple-event locations used to develop LLNL-G3Dv3, we developed an alternative model using the common approach of iterative tomography/relocation beginning with event locations determined without the aid of multiple-event constraints. We refer to these alternative event locations as *single-event locations* (or 'SELs') since individual events are located independent of the others (a typical global tomography approach). For clarity of further discussion, we will refer to the multiple-event locations as 'MELs'.

Identical to the procedures described in previous sections, we constructed a roughness versus misfit trade-off curve to estimate the appropriate damping weights (Figure 3). It is immediately evident that the same level of fit obtained using the MELs is impossible to achieve with the SELs. This observation holds even when the damping term is set to zero in the tomographic inversion. With a damping weight that balances misfit and image roughness, the root-mean-squared (RMS) misfit of the SELs data is 1.47 seconds compared to 0.96 seconds using the MELs. It should also be noted that the image produced using the SELs data is more than 2 times rougher, suggesting that a much more complex model is required to explain the data when these event locations are assumed.

After generating a tomographic model with the SELs data, we relocated the events in single-event mode using the newly generated tomographic model. We find that the new SELs tend to move in the direction of the MELs. To demonstrate this behavior, we computed the parallel and normal components of SELs

relocation vectors relative to the MELs relocation vectors and mapped out the occurrences (Figure 6). If all of the relocated SELs were co-located with the MELs, all events would plot at (1, 0). We find that the mode of the occurrences is at 0.70 in the direction of the MELs and -0.10 normal to the MELs. It is evident from this analysis that the SELs tend to move in direction of the MELs, but there exists a substantial spread in the distribution. With these adjusted SELs, the data fit substantially improves (Figure 3). However, the MELs still provide a better fit to the data, with a less complicated tomographic model.

It may be expected that performing the iterative tomography/relocation procedure multiple times would allow the SELs to eventually converge to the MELs. However, we find no clear indications that we can determine the same event locations with this approach (Figure 6). We also find that a 2nd tomography/relocation cycle does not allow for significant improvement in data fit (Figure 3).

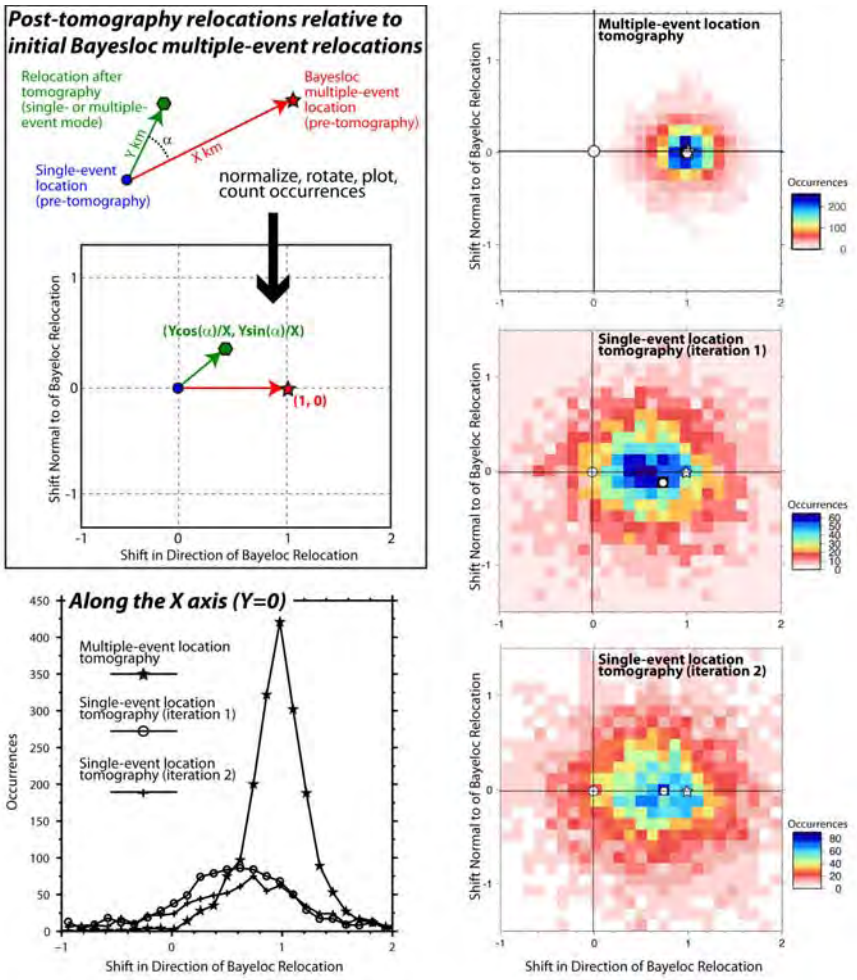


Figure 6. Epicenter relocations after tomography compared to initial (pre-tomography) Bayesloc multiple-event locations. Multiple-event locations tend to be stable after tomography, whereas single-event locations tend to shift in the direction of the multiple-event locations (but never converge).

The tomographic image produced with the relocated single-event locations (referred to as the 'SEL model') differs from the LLNL-G3Dv3 model produced with multiple-event locations (MELs). The differences between the tomographic models often appear localized and subtle, but this is not always the case. For example, the Cocos slab and the deeper Farallon anomaly appear to be a single continuous structure beneath the northern edge of the Caribbean plate in the LLNL-G3Dv3 model (Figure 7). The SEL model depicts a very different configuration. Namely, the Cocos plate appears faster and broader in the shallow mantle and is disconnected from the ancient Farallon remnant in the transition zone and lower mantle.

Although it is not known which model most closely resembles the actual Earth, it is clear that the SEL and LLNL-G3Dv3 models are distinctly different.

For the purposes of this study, one of our primary concerns is how each of the models predicts travel times. Therefore, we computed direct P-wave travel times for each of the 3-D models (SEL and LLNL-G3Dv3 models) to understand how the velocity differences translate to travel-time prediction differences. An example travel-time grid is shown in Figure 8.

The two 3-D velocity models often produce fairly similar travel-time residual patterns overall; however, there are marked differences in the predicted travel times. Specifically, we find that the differences in travel times predicted by the two 3-D models can be 2 seconds or more at regional/intermediate distances (compared to ~4 seconds relative to ak135) and 1 second or more at teleseismic distances (compared to ~2 seconds relative to ak135). Thus, the differences between the LLNL-G3Dv3 and SEL model travel times often exceed 50% of the difference relative to the ak135 model. These residual travel-time patterns and intensities are important for location determinations; the fact that the patterns are different suggests that each 3-D model will predict different locations for future seismic events. This assertion is confirmed via location validation tests that show a systematic degradation in location performance using the SEL model (Figure 5).

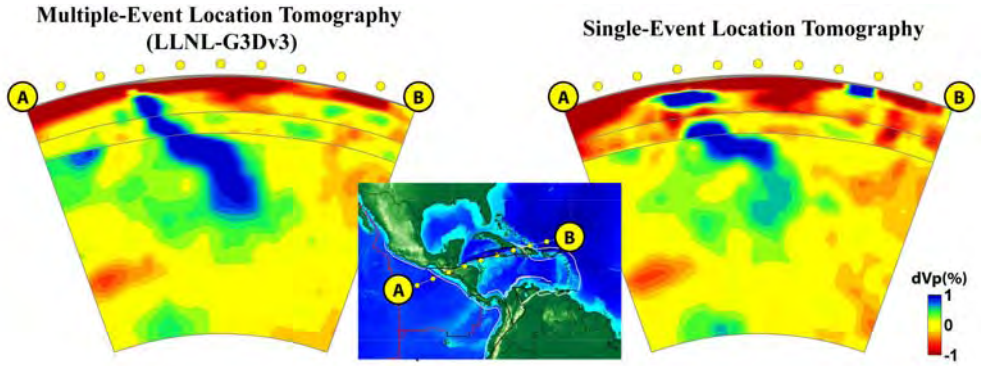


Figure 7. Image of the Cocos slab beneath Central America comparing Single- and Multiple-Event location tomography.

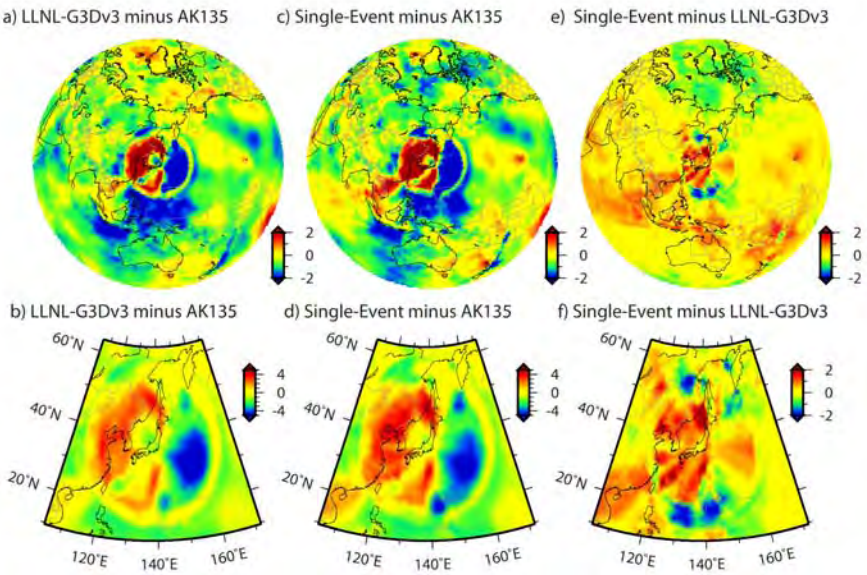


Figure 8. Travel-time residual patterns for times predicted with LLNL-G3Dv3 and the Single-Event Location model for events up to 90° from station MAJO in Matsushiro, Japan.

CONCLUSIONS AND RECOMMENDATIONS

We have constructed a new global P-wave tomography model called LLNL-G3Dv3 using ~2.8 million P and Pn travel times and events located with the Bayesloc multiple-event locator, modified for regional travel-time curve adjustments. Travel times predicted from the model provide substantial improvement in location accuracy based on some preliminary location validation tests (30-60% mislocation reduction). Comparison of our multiple-event location approach to an iterative tomography/location approach demonstrates that the optimal event locations for the input data may not be realized from the classical iterative approach. We also confirm that the multiple-event locations produce a model that more accurately predicts the locations of 116 explosions and well-constrained earthquakes. We recommend developing future global tomographic images with seismic events that are accurately located with a multiple-event location algorithm such as Bayesloc, prior to tomographic inversion.

REFERENCES

Bondár, I., S. C. Myers, E. R. Engdahl, and E. A. Bergman (2004). Epicenter accuracy based on seismic network criteria, *Geophys. J. Int.* **156**, 483–496, doi:10.1111/j.1365-246X.2004.02070.x.

Creager, K. C. and T. M. Boyed (1992). Effects of earthquake mislocation on estimates of velocity structure, *Phys. Earth Planet. Inter*. **75**, 63–76, doi:10.1016/0031-9201(92)90118-F.

Engdahl, E. R., R. van der Hilst, and R. Buland (1998). Global teleseismic earthquake relocation with improved travel times and procedures for depth determination, *Bull. Seismol. Soc. Am*. **88** (3), 722–743.

Hafkenscheid, E., M. J. R. Wortel, and W. Spakman (2006). Subduction history of the Tethyan region derived from seismic tomography and tectonic reconstructions, *J. Geophys. Res.* **111**, B08401, doi: 10.1029/2005JB003791.

Myers, S. C., G. Johannesson, and W. Hanley (2007). A Bayesian hierarchical method for multiple-event seismic location, *Geophys. J. Int*. **171**, 1049–1063.

Myers, S. C., G. Johannesson, and W. Hanley (2009). Incorporation of probabilistic seismic phase labels into a Bayesian multiple-event seismic locator, *Geophys. J. Int*. **177**, 193–204.

Myers, S. C., M. L. Begnaud, S. Ballard, M. E. Pasyanos, W. S. Phillips, A. L. Ramirez, M. S. Antolik, K. D. Hutchenson, J. J. Dwyer, C. A. Rowe, and G. S. Wagner (2010a). A crust and upper-mantle model of Eurasia and North Africa for P_n travel-time calculation, *Bull. Seismol. Soc. Am*. **100** (2), 640–656.

Myers, S. C., G. Johannesson, and N. A. Simmons (2011). Global-scale P-wave tomography optimized for prediction of teleseismic and regional travel times for Middle East events: 1. Data set development, *J. Geophys. Res*. **116**, B04304, doi:10.1029/2010JB007967.

Ruppert, S., D., Dodge, A. Elliott, M. Ganzberger, T. Hauk, and E. Matzel (2005). Enhancing seismic calibration research through software automation and scientific information management, in *Proceedings of the 27th Seismic Research Review: Ground-Based Nuclear Explosion Monitoring Technologies,* LA-UR-05-6407, Vol. 2, pp. 937–945.

Simmons, N. A., S. C. Myers, and A. Ramirez (2009). Multi-resolution seismic tomography based on a recursive tessellation hierarchy, in *Proceedings of the 2009 Monitoring Research Review: Ground-Based Nuclear Explosion Monitoring Technologies*, LA-UR-09-05276, Vol. 1, pp. 211-220.

Simmons, N. A., S. C. Myers, and G. Johannesson (2010a). Global-scale P-wave tomography designed for accurate prediction of regional and teleseismic travel times for Middle East events, in *Proceedings of the 2010 Monitoring Research Review: Ground-Based Nuclear Explosion Monitoring Technologies*, LA-UR-10-05578, Vol. 1, pp. 211–220.

Simmons, N. A., A. M. Forte, L. Boschi, and S. P. Grand (2010b). GyPSuM: A joint tomographic model of mantle density and seismic wave speeds, *J. Geophys. Res*., 115, B12310, doi:10.1029/2010JB007631.

Simmons, N. A. and S. C. Myers (2011a). The updated LLNL-G3D global P-wave velocity model and its performance in seismic event location, in *Proceedings of the 2011 Monitoring Research Review: Ground-Based Nuclear Explosion Monitoring Technologies*, LA-UR-11-04823, Vol. 1, pp 188-197.

Simmons, N. A., S. C. Myers, and G. Johannesson (2011b). Global-scale P-wave tomography optimized for prediction of teleseismic and regional travel times for Middle East events: 2. Tomographic inversion, *J. Geophys. Res*., 116, B04305, doi:10.1029/2010JB007969.

Wang, Z. and F. A. Dahlen (1995). Spherical-spline parameterization of three-dimensional Earth models, *Geophys. Res. Lett*. **22** (22), 3099–3102.

Zhao, D., A. Hasegawa, and S. Horiuchi (1992). Tomographic imaging of P and S wave velocity structure beneath northeastern Japan, *J. Geophys. Res*. **97**, 19909–19928.

DEVELOPMENT OF MINE EXPLOSION GROUND TRUTH SMART SENSORS

Steven R. Taylor[1], Phillip E. Harben[1], Steve P. Jarpe[2], David B. Harris[3]

Rocky Mountain Geophysics[1], Jarpe Data Solutions[2], and Deschutes Signal Processing[3]

Sponsored by the National Nuclear Security Administration

Award No. DE-SC0004230 Phase II

ABSTRACT

Accurate seismo-acoustic source location is one of the fundamental aspects of nuclear explosion monitoring. Critical to improved location is the compilation of ground truth data sets for which origin time and location are accurately known. Substantial effort by the National Laboratories and other seismic monitoring groups have been undertaken to acquire and develop ground truth catalogs that form the basis of location efforts. In Phase I, we have demonstrated the feasibility of constructing an inexpensive, compact deployable Ground Truth Monitoring System (GTMS) for obtaining calibration ground truth information (timing, location, magnitude) autonomously from mining regions. The standoff distance is to be less than 5 km and accuracies of 0.1 second in origin time, 1 km in epicentral location and 0.3 magnitude units without any human intervention are operational goals of the system. Information is to be transmitted for mine explosions that exceed magnitude 2.5.

In our first year of Phase II, the prototype GTMS_V1.0 was developed and deployed in the Morenci Copper Mine in eastern Arizona in March 2012. GTMS_V1.0 employs a 24 bit digitizer, a three-component geophone sensor, and a pressure sensor. A 32-bit Atmel AVR microprocessor is used for data buffering and processing. It has the capability for high performance computations, is low cost, low-power consumption and has 32 Mb RAM. A circuit board was designed that interfaces to external components such as the 24-bit Analog-to-Digital Converter (ADC), the GPS, serial and flash memory. The AV32 microprocessor is configured to be turned on for short time periods to process detected events using a fully interrupt-based software framework allowing low-power operation. Intermittent GPS operation also saves on power and is only activated during event triggers. Nederland SM-6 4.5 Hz long coil transport three-component geophones are used which appear to be well suited for the GTMS. We have found that the geophones can be operated in close proximity to large mine explosions (e.g., > 200,000 lbs) without clipping. Additionally, the SM-6 geophones have reasonably good low-frequency response so that Rg waves are faithfully recorded. Also in March, a remote site was located approximately 6 km to the north of the mine at our Dead Skunk site (DSK) in the Clifton Ranger district of the Apache National Forest. The DSK site consists of a RefTek 130 digital recorder and marine battery in a weatherproof box. External to the box is a 100 Watt solar panel, a GPS receiver, a microphone and buried SM-6 geophones. Low-bandwidth ORBCOMM satellite is being prepared for GTMS_V2.0 for inexpensive two-way communication between the GTMS and the Ground Truth Processing Center (GTPC).

Most of our processing software work to date has focused on detection algorithms specific to large mining explosions. In this sense, detection is not necessarily a problem, but it is important to minimize the number of false detections in order to conserve power. Processing software is being developed to have the fewest mathematical operations and is focused around 3C Bayesian algorithms to combine detection and picking with location. A GTMS may be deployed in a mining region where just one particular mine may be targeted. Other noise sources can create large signals that can be filtered out using polarization detectors. Also, our work has shown that polarization detectors can be used for reasonably accurate *P* and *S* wave arrival time picks. For the GTMS we use a Bayesian approach because the location of the target mine will be known *a priori*. *A priori* information can be used to reduce false detections and greatly aid with location accuracy and uncertainty estimation.

OBJECTIVES

Accurate seismo-acoustic source location is one of the fundamental aspects of nuclear explosion monitoring. Critical to improved location is the compilation of ground truth data sets for which origin time and location are accurately known. Substantial effort by the National Laboratories and other seismic monitoring groups have been undertaken to acquire and develop ground truth catalogs that form the basis of location efforts (e.g., Sweeney, 1998; Bergmann et al., 2009; Waldhauser and Richards, 2004). In particular, more GT1 (Ground Truth 1 km) events are required to improve three-dimensional velocity models that are currently under development. Mine seismicity can form the basis of accurate ground truth datasets. Although the location of mining explosions can often be accurately determined using array methods (e.g., Harris, 1991) and from overhead observations (e.g., MacCarthy et al., 2008), accurate origin time estimation can be difficult. Occasionally, mine operators will share shot time, location, explosion size and even shot configuration, but this is rarely done, especially in foreign countries. Additionally, shot times provided by mine operators are often inaccurate. An inexpensive, ground truth event detector that could be mailed to a contact, placed in close proximity (< 5 km) to mining regions or earthquake aftershock regions that automatically transmits background-truth parameters, would greatly aid in development of ground truth datasets that could be used to improve nuclear explosion monitoring capabilities.

We are developing an inexpensive, compact, lightweight smart sensor unit (or units) that could be used in the development of ground truth datasets for the purpose of improving nuclear explosion monitoring capabilities. The units must be easy to deploy, be able to operate autonomously for a significant period of time (> 6 months) and inexpensive enough to be discarded after useful operations have expired (although this may not be part of our business plan). Key parameters to be automatically determined are event origin time (within 0.1 sec), location (within 1 km) and size (within 0.3 magnitude units) without any human intervention. The key parameter ground truth information from explosions greater than magnitude 2.5 will be transmitted to a recording and transmitting site. Because we have identified a limited bandwidth, inexpensive two-way satellite communication (ORBCOMM), we have devised the concept of an accompanying Ground-Truth Processing Center that would enable calibration and ground-truth accuracy to improve over the duration of a deployment.

We have developed the concept for a Ground Truth Monitoring System (GTMS; Figure 1) that will be supported by a Ground Truth Processing Center (GTPS; Figure 2). The sensors consist of a three-component (3C) short-period geophones and an acoustic sensor. The signals are digitized and processed by a Digital Signal Processor (DSP) where signal picks are made, back azimuths are calculated and locations are made using a Single Station Bayesian Locator (SSBL). The GTPS is used to analyze waveforms in order to improve local calibration for improved accuracy over the deployment period. This will be possible because of the OBCOMM two-way communication system that we are proposing for the GTMS so that some waveform data can be transmitted to the GTPC for analysis. Calibration can be improved and transmitted back to the GTMS along with any necessary software patches. This way we can offer calibration as a service providing the ground truth information to contracting organizations. Through collaboration with U.S. nuclear explosion monitoring agencies, employees at the GTPC would handle the mine discovery, development of mine contacts, GTMS shipping, telemetry, data processing and package recovery. The GTPC also can be used to refurbish GTMC units that have been returned for subsequent deployments if it appears that this is a cost-effective approach. Figure 3 shows a high-level block diagram of our signal processing system prototype.

RESEARCH ACCOMPLISHED

The current configuration of the GTMS_V1.0 is illustrated in the left-hand portion of Figure 1. A 32-bit Atmel AVR microprocessor is used for data buffering and processing. It has the capability for high performance computations, is low-cost and low-power consumption and has a large amount of memory. GTMS_V1.0 employs a 24 bit digitizer, a three-component geophone sensor, and a pressure sensor (Figure 4). A circuit board was designed that interfaces to external components such as the 24-bit ADC, the GPS, serial and flash memory. The AV32 microprocessor is configured to be turned on for short time periods to process detected events (using a simple STA/LTA) using a fully interrupt-based software framework allowing low-power operation. Intermittent GPS operation also saves on power and is only activated during event triggers. To meet the objectives of long term operation and small size, while simultaneously allowing the use of advanced processing algorithms, the DSP is turned off most of the time, and is only turned on when an event of interest occurs.

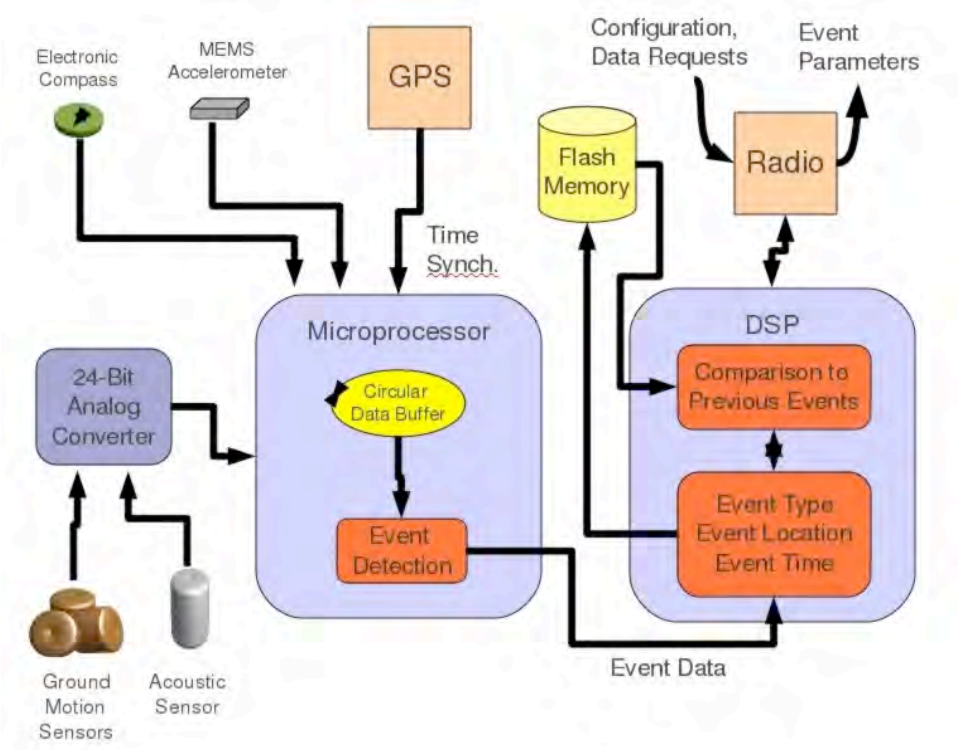


Figure 1. Schematic block diagram of our Ground Truth Monitoring System showing possible configuration of the major and the major paths of communication.

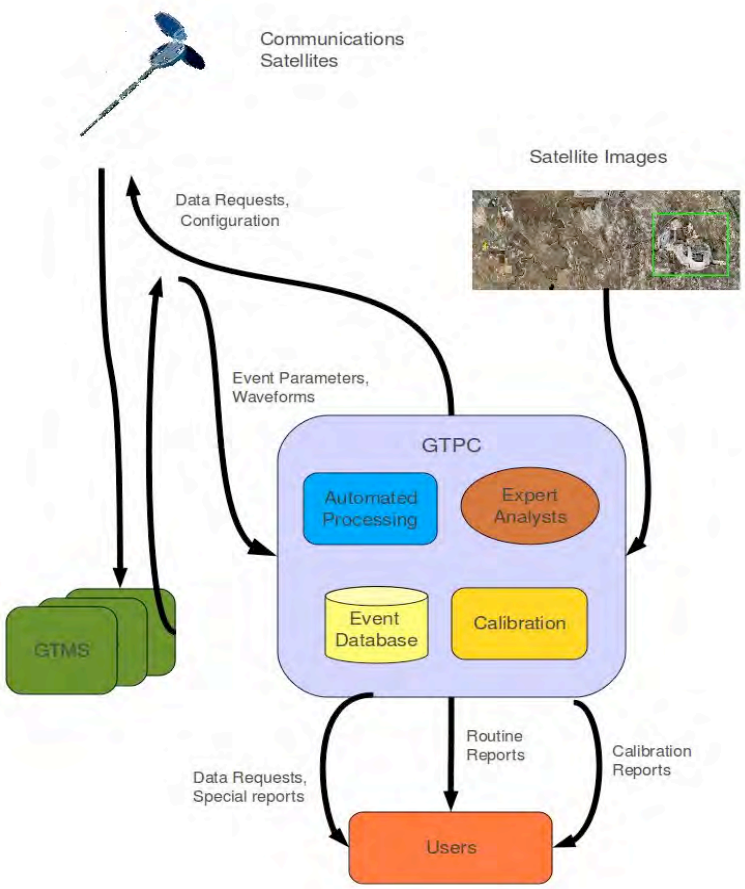


Figure 2. Schematic block diagram of our Ground Truth Processing Center.

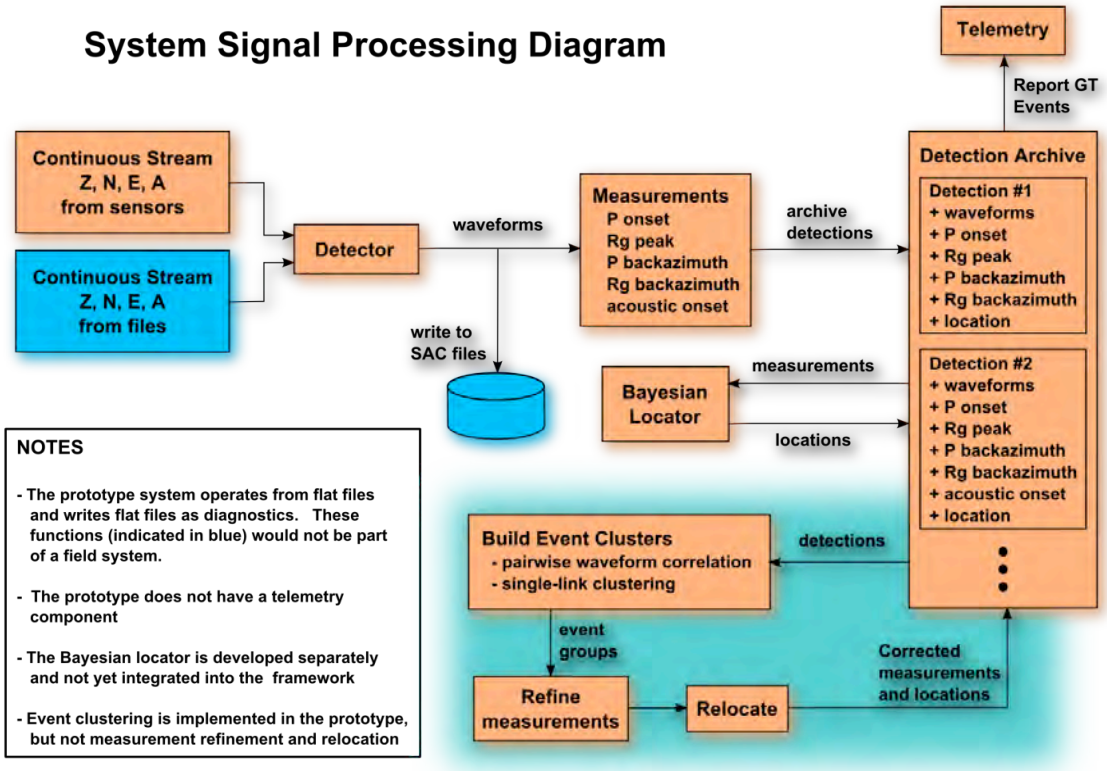


Figure 3. High-level block diagram of a signal processing system prototype under development as part of the Ground Truth Monitoring System.

Nederland SM-6 4.5 Hz long coil transport three-component geophones are used which appear to be well suited for the GTMS. The 4.5 Hz Nederland SM-6 long coil travel geophones appear to be an excellent choice for the GTMS because they do not clip even at close range of the large mine explosions. We purchased two three-component packages, one already packaged with emplacement spikes and one with separate sensors for which we built custom-made box. A custom made steel plate was constructed with a leveling bubble and with attachments for both the SM-6 geophones as well as the Kinemetrics Episensor FBA. We have found that the geophones can be operated in close proximity to large mine explosions (e.g., > 200,000 lbs) without clipping. Additionally, the SM-6 geophones have reasonably good low-frequency response so that Rg waves are faithfully recorded. Therefore, it appears that the micro electro-machanical system (MEMS) backup shown in Figure 1 will not be necessary for the GTMS. Figure 4 shows the GTMS_V1.0 electronics package and enclosure. Figure 5 shows GTMS_V2.0 board that is currently being prepared for deployment.

GTMS_V1.0 is currently operating at the Morenci Copper Mine in eastern Arizona. The Morenci mine is owned by Freeport-McMoRan Copper & Gold, Inc. Through a series of letters and correspondences, arrangements were made to deploy a prototype GTMS in the mine and a RefTek recording system in National Forest Service (NFS) approximately 5 km north of the mine (Figure 6). Figures 7 and 8 show the GTMS_V1.0 at the SPJ site in the Morenci Mine. Note that the unit is compact and the external geophones only need orientation and leveling. In future versions, the geophones will be included within the single package. A simple on/off switch is used to begin recording and on-board processing. The solar panel is optional and not planned to be required for six months autonomous operation for the final product. The SPJ site overlooks the Garfield pit and is in an excellent location to provide ground truth information on the Morenci shots. At this point the GTMS_V1.0 is providing ground truth for development of processing algorithms for data collected at the DSK site. The Morenci Mine is kindly providing information regarding their shot locations and configuration.



Figure 4. GTMS_V1.0 electronics and enclosure.

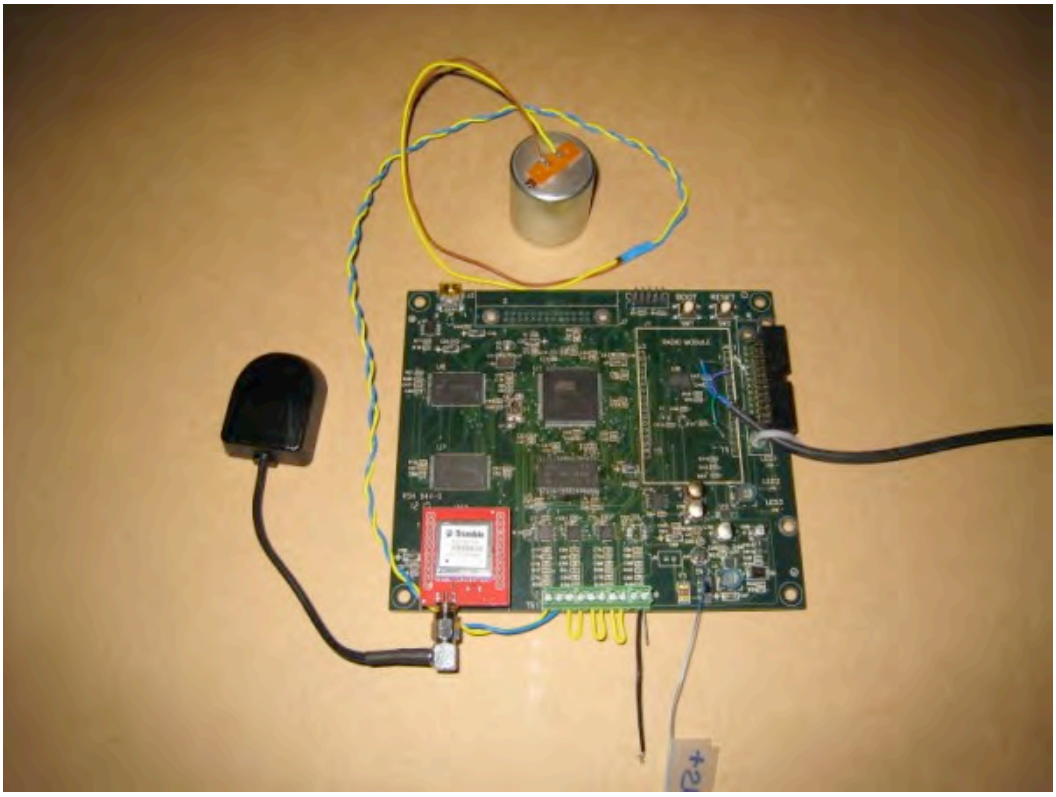


Figure 5. GTMS_V2.0 electronics showing additional elements of V2.0 relative to V1.0 shown in Figure 4.

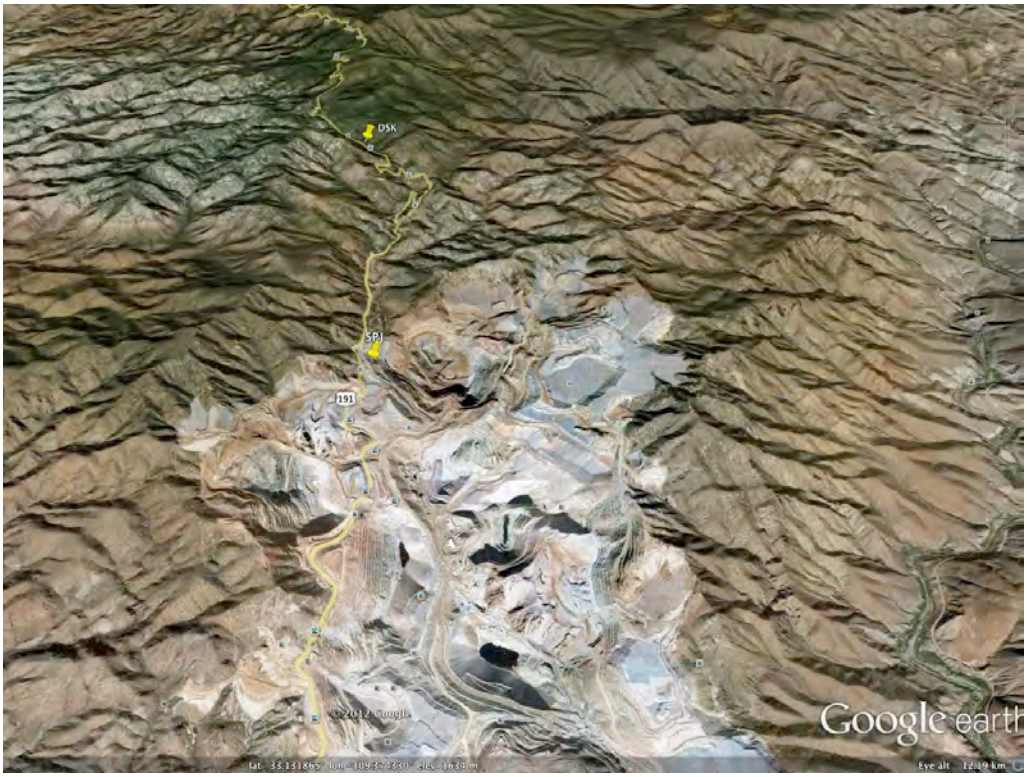


Figure 6. Google Earth image showing DSK and SPJ sites as yellow thumbtacks.



Figure 7. Steve Jarpe flips the "on" switch for the GTMS_V1.0 at SPJ site.



Figure 8. Steve Jarpe at SPJ site and the GTMS_V1.0.

On Board Processing

The next major undertaking is to develop algorithms to measure the key parameters (origin time, location and size) to be transmitted. This is a formidable task and the algorithms need to be simple yet robust in order to operate on onboard computers having limited processing capability. We consider methods that can be used to adaptively improve parameter estimates over the period of deployment and Bayesian methods to simplify calculations by reducing the size of the solution space and to provide realistic uncertainty estimates (e.g., Fagan et al., 2009; Modrak et al., 2010). For location and origin time, the obvious tools at our disposal for single-station operation revolve around *P*-acoustic or *P-Rg* wave arrival times, three-component back azimuth (from body and surface waves), surface wave dispersion measurements, correlation and coda wave measurements. The key prior piece of information is an epicentral region that encompasses the mine to be monitored. This can be performed by examination of satellite photos of the mine at the GTPC (Figure 2) prior to deployment. The prototype system (Figure 3) runs an STA/LTA to define a *P* detection, sets about making *P* and *Rg* timing and back azimuth measurements, then archives the detection and moves on. At the end of five days it cross-correlates and clusters all detections. Events in a cluster then can be processed further to refine back azimuths and onsets. The results on clusters could be more reliable than the individual measurements, as well as help reject noise burst triggers.

As an example we have developed a horizontal polarization detector and applied it to a small explosion at a distance of 6.1 km filtered between 6 and 15 Hz. To estimate the back azimuth (ϕ) from the station to the source, a grid search is performed between 0 and 180° to find the maximum variance of the radial component. At each back azimuth, the variance of the radial component is computed using a 0.5 second window moved down the N and E seismograms with a shift window length of 0.1 seconds. For each time window, the N, E are rotated through angles of 0 to 180° and the radial variance is computed for each angle. The maximum radial variance gives the estimated back azimuth for each time window. The *P* wave train arrives at about 3 seconds, the shear waves at 10 seconds and an acoustic to seismic converted phase at 17 seconds. At this point, the maximum radial variance is referenced to the observed back azimuth, and is controlled by the signal amplitude, as well as the degree of polarization. The ratio R_s given by the maximum to minimum radial variance is treated as a random variable and is a

measure of the degree of horizontal polarization at an observed back azimuth. R_s is conditioned on a prior back azimuth and is closely related to the commonly used rectilinearity parameter that is related to the ratio of the principal component eigenvalues of the N, E covariance matrix. The rectilinearity (ρ) is simply computed using $1-\sigma_n^2/\sigma_R^2$. Because seismologists are familiar with the meaning of rectilinearity it acts as a specified input parameter and is tied to the non-centrality parameter, λ, used in χ^2 tests discussed below. R_s is the test statistic measuring the degree of polarization at the observed back azimuth. Under a signal hypothesis to be defined below, R_s is assumed to have χ^2 distribution having $2TB$-1 degrees of freedom (*dof*), where T is the window length of each time segment (s) and B is the filter bandwidth (Hz). In particular, under the null hypothesis of a signal, a non-central χ^2 distribution is assumed

$$R_s \sim \chi^2\left(2TB-1,\lambda\right) \tag{1}$$

where the non-centrality parameter is related to the rectilinearity. The rectilinearity parameter is not actually used as a test statistic because of its complicated analytical form.

At this point, the signal is defined as a horizontally polarized phase corresponding to the observed back azimuth. Note that the under the single null hypothesis, the noise distribution (represented by a central χ^2 distribution) is never actually used although it could be for a binary hypothesis test involving likelihood ratios.

The joint probability function of the horizontal polarization R_s and the observed back azimuth for each time window is factored into two independent functions given by

$$\Phi\left(R_s,\hat{\phi}\right)=\Phi_R\left(R_s\mid\hat{\phi}\right)\Phi_p\left(\hat{\phi}\right) \tag{2}$$

where as discussed above, Φ_R is represented by a non-central χ^2 under a signal hypothesis. Φ_p represents a prior on the back azimuth that can be used to filter out polarized signals from unexpected back azimuths (say if a certain region is to be monitored).

The null hypothesis for signal detection is H_0: P wave from back azimuth ϕ_0 where ϕ_0 is a prior on the back azimuth. Note that the null hypothesis can be easily modified for shear-wave detection or a Rayleigh wave (e.g., Rg) by incorporating the Hilbert transformed vertical component. Under H_0 the probability of detection (aka p-value) is given by the cumulative distribution function (CDF)

$$p_d = P\left(H_0\mid R_s,\phi_0\right)=\int_0^{R_s}\int_{\phi_0-\Delta\phi}^{\phi_0+\Delta\phi}\Phi\left(R_s,\phi_0\right)d\phi_0 dR_s \tag{3}$$

It can be assumed that the observed back azimuth is either normally or uniformly distributed around a prior back azimuth that might be used to detect polarized signals from a given azimuth range.

Figure 9 shows the detection probability using using λ = 50 (ρ = 0.98) and a Gaussian prior on the back azimuth of ϕ_0 = 99° and σ_ϕ = 5° showing a case that might be used for automatically detecting *P* waves from large, highly polarized events (e.g., explosions) emanating from a given region.

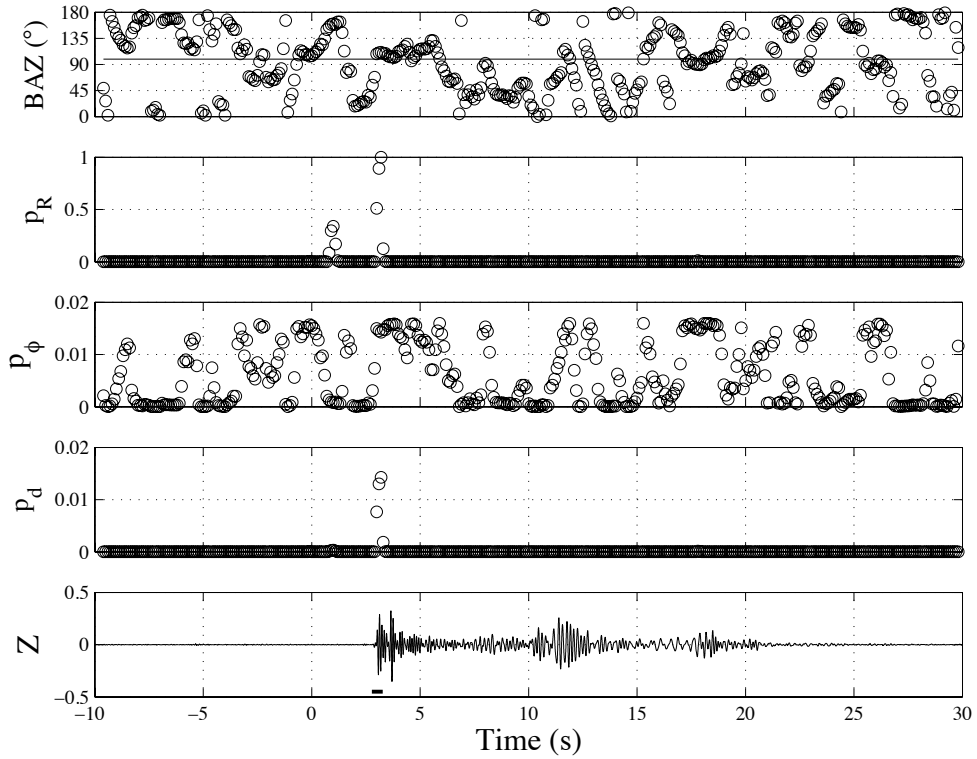


Figure 9. Back azimuth estimate and true back azimuth as horizontal line. P_R is detection *p*-value for each time window under null hypothesis of horizontally polarized signal with ρ = 0.98 having a no prior on back azimuth. $P_,$ is same as P_R but with a prior on the back azimuth. P_d is combined detection probability that is the product of $P_,$ and P_R (see text for details).

We have also been investigating more general Bayesian polarization detectors that involve a binary hypothesis approach on all three components. Polarization detectors have been described widely in the seismological literature, but generally are derived under simple assumptions such as a deterministic polarization vector and noise which is uncorrelated among the channels in the three-component set. The innovations reported here include:

1) A probabilistic description of the polarization vector and using the Kent distribution as a prior. The Kent distribution allows different uncertainties to be assigned to the azimuth and angle of incidence.
2) Proper formulation of the problem as a Generalized Likelihood Ratio Test (GLRT) in which unknown parameters are estimated with maximum likelihood estimators, in the process of forming the detection statistic.
3) Generalization of the detection statistic to account for the polarization structure of ambient noise. When the Bayesian prior on the polarization vector is removed (i.e., the polarization vector is considered to be deterministic, but unknown), the polarization vector is found as the principal eigenvector in a generalized eigenvalue problem, making it a generalization of classical principle components detectors.
4) A detector formulation, drawn from conventional power detectors, that uses two windows, one to estimate the covariance of the background noise and a second to serve as the signal detection window.
5) Efficient gradient search for the polarization vector when the vector is subject to a Bayesian prior. The algorithm performs searches along geodesics of the constraint manifold (the unit sphere) for polarization vectors.

CONCLUSIONS AND RECOMMENDATIONS

We are developing a Ground Truth Mine Monitoring System that will be used to improve location capabilities of U.S. nuclear explosion seismic monitoring systems. Most of our work to date has been development and deployment of the GTMS and we are currently preparing datasets upon which to develop our processing algorithms.

ACKNOWLEDGEMENTS

We wish to thank Robert Chelini, David Ball, William Seibert and David Rhoades of the Morenci Mine for all of their extensive efforts to make this deployment possible. We also wish to thank Forest Service Ranger Mike Bailey of the Clifton Ranger District for issuing the Special Use Permit and for occasionally checking on the DSK site.

REFERENCES

Bergmann, E.A., E.R. Engdahl, M.H. Ritzwoller and S.C. Myers (2009). Crustal structure from in-country and ground-truth data, in *Proceedings of the 2009 Monitoring Research Review: Ground-Based Nuclear Explosion Monitoring Technologies,* LA-UR-09-05276, Vol. 1, pp. 22–31.

Fagan, D.K., S.R. Taylor, F.R. Schult, and D.N. Anderson (2009). Using ancillary information to improve hypocenter estimation: Bayesian Single Event Location (BSEL), *Pure Appl. Geophys.* **166**, 521–545.

Harris, D.B. (1991). A waveform correlation method for identifying quarry explosions, *Bull. Seismol. Soc. Am.* **81**, 2395–2418.

Modrak, R.T., S.J. Arrowsmith, and D.N. Anderson (2010). A Bayesian framework for infrasound location, *Geophys. J. Int.*, doi: 10.1111/j.1365-246X.2010.04499.x.

Sweeney, J. (1998). Criteria for selecting accurate event locations from NEIC and ISC bulletins, *Lawrence Livermore National Laboratory*, UCRL-JC-130655.

Waldhauser, F. and P.G. Richards (2004). Reference events for regional seismic phases at IMS stations in China, *Bull. Seismol. Soc. Am.* **94**, 2265–2279.

Seismic Identification and Source Characterization

INVESTIGATION OF AN UNUSUALLY SHALLOW EARTHQUAKE SEQUENCE IN MOGUL, NV FROM A DISCRIMINATION PERSPECTIVE

Glenn P. Biasi, David von Seggern, John G. Anderson, and Ileana M. Tibuleac,

University of Nevada Reno

Sponsored by the Air Force Research Laboratory

Award No. FA9453-11-1-0236
Proposal No. BAA11-51

ABSTRACT

Very shallow earthquakes are rare. As a consequence, their source parameter scaling and their local and regional propagation characteristics are not well understood. Thus, distinction between very shallow (1-4 km deep) earthquakes and underground nuclear explosions remains an important issue in discrimination research. The primary objective of this study is a detailed investigation of a sequence of shallow earthquakes that occurred during 2008 west of Reno, Nevada, in Mogul. This sequence consisted of over 2000 earthquakes with M_L of 1.0 or greater, concentrated in depth between 1 and 4 km and ranging in magnitude up to M_w 5.0 (the "main shock"). We are investigating, compared to earthquakes at typical depths, uncharacteristically high amplitude near-field ground motions and uncharacteristically rapid attenuation with distance of the main shock, which could affect magnitude estimates and discrimination metrics. For our investigations, we use a unique broadband and strong-motion database recorded at portable and permanent stations, located as close as 1 km from the epicenter of the main shock. We have organized our study in four tasks: First, we have completed building a detailed database. In addition to available public domain information on very shallow event discrimination analysis, the database includes near-field and seismic network recordings of all the M_L>1.0 Mogul, Nevada earthquakes located by the Nevada Seismological Laboratory; mining explosions (M_L>2.0) and crustal earthquakes (M_L>2.5) in the Reno-Carson City, NV, area; the waveforms from the 1993 Rock Valley sequence (depth < 4 km, m_b≤4.3); and waveforms from the 2007 Crandall Canyon mine collapse (M_L 3.9). In preparation for the second task, we have relocated the Mogul earthquakes with HYPODD, incorporating time-domain *P*-phase cross-correlations. Location shifts as large as several hundred meters were observed, when compared to the original catalog hypocenters. The main shock has been relocated at 2.8 km below the surface when using HYPODD.

We report progress on the second task, which consists of analysis of the stress drop and radiated energy of the main shock, principal foreshocks, and principal aftershocks as well investigations of the source scaling of the Mogul sequence. We find a relatively low median stress drop of 0.82 MPa (8.2 bars) for M_L≥3 earthquakes. The main shock stress drop of 4.5 MPa was the largest. A new direct estimate of source region shear-wave velocity significantly improves moment calculations. No depth dependence is found in earthquake moment or stress drop. Investigation of peak ground accelerations indicates that the main shock is not remarkably different in its attenuation characteristics from other Mogul events. We will attempt to understand the origin and nature of the near-source attenuation and its effect on magnitude estimates and energy content-related discriminant performance. We will compare our results to other very shallow earthquake sequences, induced seismicity and nuclear explosions results.

OBJECTIVES

The objective of our study is to investigate the effectiveness of discrimination algorithms when applied to an unusually shallow (1-4 km deep) sequence of well-documented earthquakes, which occurred 2008 in western Nevada. In addition, we are investigating source parameters, scaling and local and regional propagation characteristics of these earthquakes in comparison to other relevant shallow events.

RESEARCH ACCOMPLISHED

An important aspect of nuclear explosion monitoring is event identification. Because earthquakes less than 4 km deep are rare, and their characteristics are poorly known, it is difficult to rule them out as suspect events. The earthquake sequence that occurred in 2008 west of Reno, Nevada, beneath the community of Mogul (Anderson et al., 2009; Tibuleac et al., 2011a) was unusual for several reasons relevant to nuclear monitoring. First, events in this swarm were exceptionally shallow, with the bulk of the seismic activity taking place at depths of 1-4 km. Only few other sequences occurring above the 5 km deep upper limit of the "seismogenic zone" have been observed, principally in California (Fletcher et al., 1987; Frankel *et al*., 1986, Prejean and Ellsworth, 2001) and Nevada (Smith et al., 2006). Second, the protracted swarm-like activity prior to the main shock provided time to instrument the epicentral area with temporary broadband and strong-motion stations, in advance of the largest events. These stations complemented the Nevada and California permanent seismic monitoring stations, and the high-quality broadband stations of the EarthScope Transportable Array network deployed in Nevada in 2008. Third, the main shock (M_w 5.0) had exceptional source and attenuation characteristics (Anderson et al., 2009).

We have organized our study in four tasks, as follows:

Task 1. Build a database, including well-located earthquakes and explosions and acquire available public domain information on very shallow event discrimination analysis. The database will be used, as appropriate, and unless similar studies have not been already performed, in Tasks 2, 3 and 4;

Task 2. a). Analyze the stress drop and radiated energy of the main shock and principal fore- and aftershocks; b) Investigate the source scaling of the Mogul sequence;

Task 3. Investigate the effect of source depth on P and S spectra and spectral ratios, signal complexity, and m_b-M_s discrimination;

Task 4. Understand the origin and nature of the exceptional near-source attenuation and its effect on magnitude estimates and energy content-related discriminant performance.

Work on Task 1 has been completed. A well-located shallow earthquake and explosion database is available, also including available public domain information on very shallow event discrimination analysis. The database includes: 1) 2000 earthquakes with $M_L \geq 1.0$, more than 600 earthquakes with $M_L \geq 1.5$; 283 earthquakes with $M_L \geq 2.0$; 88 earthquakes with $M_L \geq 2.5$; 38 earthquakes with $M_L \geq 3.0$ and three events with $M_L \geq 4.0$, all with near-field recordings. Fewer than 1% of earthquakes in the relocated Mogul sequence ($M_L > 1.0$) are located from 5 to 6 km depth. Regional and teleseismic records of the largest Mogul events from Incorporated Research Institutions for Seismology (IRIS) and the Air Force Research Laboratory are in the database. A sorted mining explosion database (more than 50 events with $M_L>1.5$) in the Reno-Carson City, NV, area is available. The explosions occurred within 100 km of the Mogul main shock. Records of nuclear explosion waveforms at LLNL stations are in the database. The waveforms from events belonging to the 1993 Rock Valley sequence (depth < 3 km) and the available IRIS and NN data (including Southern Great Basin Seismic Network records), for the largest event M_w 3.7 (m_b 4.3) in this sequence are also added to the database. High quality waveforms from crustal earthquakes ($M_L \geq 2.4$) occurred in the project area, recorded at the Nevada Seismic Network and at IRIS stations from 1984 to 2011, an earthquake sequence occurred south of Reno (main shock M_L 3.0, 12 km deep, on 11/28/2010, 09:47:38) and events (depth 2-17 km) from the 2011 Hawthorne earthquake sequence (main shock M_L 4.6, 15 km depth, on 04/16/2011, 17:45:37) are also archived. Sorted records of the Crandall Canyon mine collapse (0.6 km depth, M_L 3.9) and of USGS-located events ($M_L > 2.5$) within 100 km of the mine are available for further analysis. A collection of crustal earthquakes ($M_L > 2.5$), composed of events that occurred within 20 km of regional stations in Nevada and that can provide reversed path information is sorted and prepared for analysis.

Here we report progress on Task 2, which consists of stress drop and radiated energy analysis of the main shock, principal foreshocks and principal aftershocks, and investigations of source scaling of the Mogul sequence. We report results of the first of three related methods we use to estimate source parameters for $M_L \geq 3$ Mogul events: 1) Spectral M_w estimates; 2) Estimates of stress drop and radiated energy using empirical Green's Functions and 3) Estimates of stress drop and radiated energy using measurements of coda envelopes at different frequencies (Mayeda and Walter, 1996).

Adequate source parameter analysis is possible when the earthquake hypocenter location and the velocity model in the source area are well resolved. Thus, hypocentral location corrections are estimated and new, improved seismic velocity models are used for event location, as discussed below. We use the location code HYPODD (Waldhauser and Ellsworth, 2000) in an effort to reduce the errors of depth estimation for the main shock (4/26/2008, 06:40:10.6 UTC) and for other events of the Mogul sequence. The depth of the main shock from various available sources is shown in Table 1. Several velocity models are used in HYPODD to compare results (Tables 1 and 2). The *pickema2* velocity model is the standard location model for the Nevada Seismological Laboratory (NSL) seismic catalog, with comparably high (5.85 km/s) P-wave velocity near the surface. Two other models are used, one developed by Dr. Ken Smith (KS, personal communication) and a model developed by Tibuleac *et al.*, (2011b; named NOISE, because it uses ambient seismic noise to estimate shear velocity). All depth estimates are referenced to the mean elevation of the seismic stations used, which is 1.4 km above sea-level. The new HYPODD epicenter locations using the three models listed in Table 2 are all approximately one km east of the NSL catalog location. The HYPODD result using the KS model is preferred because the mean error of hypocentral parameters is lower than when using other seismic models. The results using the NOISE and KS models are very similar, and either is preferable to the *pickema2* model results. Standard errors of 1 - 10 m are estimated in the three dimensions of the hypocenter space and most of the events have a HYPODD standard error of ~3 m. Final event locations are shown in Figure 1.

The fine precision of the hypocenters from HYPODD, however, applies to relative positioning only. The absolute accuracy is affected by the seismic velocity model. However, using three different models, one of which (*pickema2*) is different from the other two for shallow depths, affects the hypocenter parameters by only one to two hundred meters. The main shock location is controlled by the four closest stations, all of which have P-wave travel times of less than 0.65 seconds from the origin. As a result, we believe no reasonable model change could move the hypocenter by more than 1 km, probably much less, in any of the three spatial dimensions. Thus, we estimate that evidence for GT1 accuracy for the main shock, with a depth of approximately 2.8 km below the surface, can be developed. A similar expectation follows for the larger fore- and aftershocks because locations are estimated using cross-correlations in HYPODD.

The seismic moment depends on the cube of the shear-wave velocity, so this parameter is especially important for moment and magnitude scaling evaluations. A supplementary confirmation of the KS and NOISE models accuracy for shear-wave velocity at seismogenic depths in the Mogul source area is obtained from observed *S*-phase arrival times to station SKYF for $M_L > 3.0$ earthquakes. The strong-motion station *SKYF* is located such that the Mogul events form a linear source array (Figure 1, upper plot). Epicentral distance and elapsed time t_S (S-arrival time minus origin time) were computed using HYPODD relocated events. A linear fit, $t_S = 0.348r + 0.38$ sec, and a shear-wave velocity of 2.87 km/sec were estimated by least-squares (Figure 2, left upper plot). Residuals to the linear fit, (Figure 2, lower left plot), show no systematic dependence of depth. A source-region *P*-wave velocity of 5.13 km/sec (*P* elapsed time $t_P = 0.195r + 0.008$) (Figure 2, right upper plot) was estimated using the same method. This direct estimate of *Vp* is similar, within errors, to that of the Herrmann velocity model (Table 2), and is slower than the KS and NOISE models. The source-region shear-wave velocity estimated with this method was used to develop estimates of seismic moment, M_o for the M_L>=3.0 Mogul earthquakes.

Using the new hypocentral locations, we analyze the $M_L \geq 3$ Mogul events using waveforms recorded at digital three-component stations, with the goal to estimate M_w. A modified version of the Matlab code *kappaAH* (Biasi and Anderson, 2007) is used to estimate earthquake spectral parameters. *KappaAH* is a macro suite that uses hand-marked *S*-phase times to window time series and to compute spectra for each component of each station recording the earthquake. Noise spectra are calculated from before the *P* arrival in the time series. Both inputs and results are managed in an integral *CSS-3.0*-based database. The multi-taper spectral estimation method is selected for this analysis. Spectra are fit to a modified Brune model spectral shape that incorporates attenuation through a single linear (in frequency) parameter, *kappa* (Anderson and Humphrey, 1991). *KappaAH* uses the trial corner frequency and least squares method of Anderson and Humphrey (1991) to estimate three parameters per spectrum,

the low frequency spectral level, the corner frequency f_0, and *kappa*. Seismic moments, stress drops, and source radii are computed from these measured values. The spectra from *kappaAH* are retained and used directly for computations involving multiple spectra such as site responses and frequency-dependent attenuation estimates.

Parametric results from spectral measurements for strong-motion stations less than 25 km in distance are shown in Figure 3. Event average parameters are estimated from horizontal component accelerometers with 5:1 signal to noise ratios over 70% of the spectral fitting band. M_o is estimated from a log-average of the individual spectra of each earthquake. We find that event averaged stress drops (Figure 3a) are low for the Mogul sequence, with a median of only 0.82 MPa (8.2 bars) and only 3 events have stress drops over 2 MPa. Moment release shows no clear dependence on event depth (Figure 3b). The rate of spectral decay with frequency (*kappa*) shows no systematic trend with seismic moment (Figure 3c). At the short station-event distances considered here, smaller values of *kappa* would be associated with richer high frequencies at the source. We consider the dependence of stress drop on depth (Figure 3d) to test for variations with lithostatic stress. No clear dependence is observed. Thus, event parameters seem not to depend on being foreshocks or aftershocks, being deep or shallow, large or small. Our estimates of M_w (Table 3) are compared with M_L in Figure 4. M_w tends to be larger by 0.1 to 0.3 units than the seismic network M_L. With the specific *Vs* at the source of 2.87 km/s the M_w = 5.1 value for the main shock estimated using stations within 25 km of the main shock is now very close to regional estimates (Table 1).

The Mogul main shock exhibited unusual attenuation properties (Anderson et al., 2009; Tibuleac et al., 2011a). The observed near-field peak accelerations were above average for an M_w 5.0 earthquake, up to two standard deviations above the median at station MOGL. We investigate in Figure 5 the degree to which these amplitude anomalies are a general property of the Mogul sequence. Based on a comparison of the main shock peak ground acceleration (*PGA*) to the *PGA* of several $M_L \geq 3$ foreshocks, we find that the rapid amplitude decay with distance is a common feature of the Mogul earthquakes (Figure 5). A decrease in *PGA* by a factor of ~20 from the epicentral area to ~10 km away is observed for each of the three smaller events considered. We note that accelerations less than 1 cm/s^2 recorded on strong motion accelerographs have a low signal-to-noise ratio, resulting in a greater spread among measurements beyond 10 km for the M_L 3 example events. For example, the M_L 3.1 event (Figure 5) was not recorded above noise levels at the Carson City accelerographs beyond 40 km. The apparent increase in *PGA* beyond 40 km in Figure 5 above the data trend at shorter distance may be explained by low attenuation of the shear-waves in the Sierra Nevada batholith or possibly by basin amplification in the Carson City area.

CONCLUSIONS AND RECOMMENDATIONS

We are currently in the second phase of a research program in which we aim to investigate the effectiveness of discrimination algorithms when applied to an unusually shallow (1-4 km deep) sequence of well-documented earthquakes that occurred in 2008 in Mogul, near Reno, Nevada. We have built a detailed shallow event database, including the Mogul earthquakes and other relevant earthquake sequences and explosions. Double-difference event relocations have been completed and confirm that the $M_L \geq 3$ events of the Mogul sequence are shallower than 4 km, with a main shock at 2.8 km below the surface. Relocation precision is such that the larger events of the sequence are expected to satisfy location criteria for GT1 qualification. We have confirmed that the high amplitude near-field ground motions and rapid attenuation with distance seen in the Mogul main shock are also seen in principal fore- and aftershocks. We are investigating how these qualities could affect magnitude estimates and the discrimination metrics.

Stress drops for the Mogul $M_L \geq 3$ earthquakes are remarkably low, with a median of 0.82 MPa. Stress drop and moment do not correlate with hypocentral depth. The main shock stress drop, estimated at 4.5 MPa, is the largest of the entire sequence. The moment magnitude of the main shock from nearby strong-motion recordings, after new corrections for source zone shear wave velocity and precision depth, compares favorably with regional estimates that use 20 second and longer period surface waves. With basic parametric and earthquake location data in hand, we are positioned to apply discrimination methods to the Mogul sequence and other relevant shallow events to address questions about the origin and nature of the near-source attenuation and its effect on discriminant performance.

REFERENCES

Anderson J. G. and J. R. Humphreys (1991). A least-squares method for objective determination of earthquake source parameters, *Seismol. Res. Lett.* **62**, 201–209.

Anderson, J. G., I. M. Tibuleac, R. Anooshehpoor, G. Biasi, K. Smith, and D. von Seggern (2009). Exceptional ground motions recorded during the 26 April 2008 M_w 5.0 earthquake in Mogul, Nevada, *Bull. Seismol. Soc. Am.* **99**, 3475–3486, doi: 10.1785/0120080352.

Biasi, G. P. and J. G. Anderson (2007). Measurement of the parameter kappa, and reevaluation of kappa for small to moderate earthquakes at seismic stations in the vicinity of Yucca Mountain, Nevada, Final Technical Report TR-07-007, Nevada System of Higher Education (NSHE), University of Nevada, Las Vegas (UNLV), 232 pp, doi 10.2172/920643.

Fletcher, J., L. Haar, T. Hanks, L. Baker, F. Vernon, J. Berger, and J. Brune (1987). The digital array at Anza, California: processing and initial interpretation of source parameters, *J. Geophys. Res.* **92**, 369–382.

Frankel, A., J. Fletcher, F. Vernon, L. Harr, J. Berger, T. Hanks, and J. N. Brune (1986). Rupture characteristics and tomographic source imaging of $M_L \approx 3$ earthquakes near Anza, southern California: *J. Geophys. Res.* **91**, 12633–12650.

Mayeda, K. and W. R. Walter (1996). Moment, energy, stress drop, and source spectra of western U.S. earthquakes, *J. Geophys. Res*. **101**, 11195–11208.

Smith, K., G. Shields and J. N. Brune (2006). A sequence of very shallow earthquakes in the Rock Valley fault zone, southern Nevada Test Site in geologic and geophysical characterization studies of Yucca Mountain, Nevada, Chapter L, 1–11.

Tibuleac, I. M., G. P. Biasi, D. von Seggern, J. G. Anderson, and D. Molisee (2011a). Investigation of an unusually shallow earthquake sequence in Mogul, NV from a discrimination perspective, in *Proceedings of the 2011 Monitoring Research Review: Ground-Based Nuclear Explosion Monitoring Technologies*, LA-UR-11-04823, Vol. 1, pp. 592–600.

Tibuleac, I. M., D. H. von Seggern, J. G. Anderson, and J. N. Louie (2011b). Computing Green's functions from ambient noise recorded by narrow-band seismometers, accelerometers, and analog seismometers, doi: 10.1785/gssrl.82.5.661 *Seismol. Res. Lett.* **82**, 661–675.

Waldhauser, F. and W. L. Ellsworth (2000). A double-difference earthquake location algorithm: Method and application to the northern Hayward fault, California, *Bull. Seismol. Soc. Am.* **90**: 1353–1368.

Table 1. Main shock depth from available sources.

Source	Origin time	Lat (deg)	Lon (deg)	Depth (km)	Earth model
NSL original catalog	2008/04/26, 06:40:10.6	39.5247	-119.9180	2.6	pickema2
Berkeley	2008/04/26, 06:40:14.0	39.4687	-120.0587	3.5	
Herrmann	2008/04/26, 06:40:10	39.52	-199.93	1.0	herrmann
NSL HYPODD	2008/04/26, 06:40:10.6	39.5238	-119.9186	2.63	pickema2
NSL HYPODD-KS	2008/04/26, 06:40:10.59	39.5244	-119.9175	2.76	KS
NSL HYPODD-NOISE	2008/04/26, 06:40:10.6	39.5244	-119.9172	2.76	NOISE
IRIS	2008/04/26 06, 06:40:12.6	39.45	-119.95	5	

Table 2. Seismic velocity model parameters. The P/S velocity ratio was set to 1.73 (Poisson solid).

KS		**pickema2**		**herrmann**		**NOISE**	
Top of the layer (km)	P velocity (km/s)	Top of the layer (km)	P velocity (km/s)	Top of the layer (km)	P velocity (km/s)	Top of the layer (km)	P velocity (km/s)
0.0	3.5	0	5.9	0	3.4	0	2.9
1.0	4.5	7	6.00	1.9	5.5	1	3.8
2.0	5.5	22.1	6.7	8	6.3	2	5.8
4.0	6.0	28.1	7.9	21	6.4	4	6.40
7.0	6.4			40	7.9	6	6.9
12.0	6.6					8	7.2
18.0	6.8					18	7.8
						30	8.0

Table 3 The M_L (notation M_L local magnitude estimated at the Nevada Seismological Laboratory), M_o is the seismic moment, and M_w (moment magnitude) for Mogul events with $M_L \geq 3.0$.

Date Time (UT)	**Ml**	**log10(Mo)**	**Mw**	**f0 (Hz)**
3/8/08 10:07	3.3	14.178	3.4	2.53
3/24/08 19:16	3.1	13.971	3.2	1.76
3/27/08 3:42	3.2	14.121	3.3	1.50
4/15/08 14:59	3.4	14.486	3.6	2.30
4/15/08 21:26	3.2	14.044	3.3	1.74
4/15/08 21:32	3.4	14.768	3.8	1.36
4/15/08 21:33	3.6	14.450	3.6	1.97
4/21/08 19:14	3.1	13.989	3.3	2.14
4/24/08 22:47	4.0	15.137	4.0	1.34
4/24/08 22:55	4.1	15.687	4.4	0.97
4/25/08 1:00	3.3	14.163	3.4	2.76
4/25/08 17:30	3.3	14.227	3.4	2.04
4/26/08 1:13	3.7	14.838	3.8	1.40
4/26/08 6:39	3.9	14.701	3.7	1.35
4/26/08 6:40	4.7	16.709	5.1	0.61
4/26/08 6:43	3.4	14.485	3.6	2.13
4/26/08 7:29	3.5	14.537	3.6	2.73
4/26/08 9:11	3.4	14.552	3.6	2.18
4/26/08 14:35	3.1	13.950	3.2	2.53
4/26/08 14:47	3.1	14.027	3.3	3.07
4/26/08 15:20	3.5	14.464	3.6	2.00
4/27/08 17:49	3.3	14.268	3.4	2.16
4/27/08 18:31	3.0	14.265	3.4	2.48
4/28/08 11:33	4.3	15.306	4.1	1.43
4/28/08 12:12	3.0	14.094	3.3	2.13
4/29/08 5:51	3.2	13.885	3.2	3.17

Date Time (UT)	Ml	log10(Mo)	Mw	f0 (Hz)
4/29/08 6:01	3.2	14.278	3.5	2.14
4/29/08 16:14	3.1	14.414	3.5	1.65
5/8/08 5:55	3.8	14.960	3.9	1.67
5/15/08 13:44	3.4	14.510	3.6	2.20
5/31/08 9:09	3.0	14.026	3.3	1.99
6/8/08 10:13	3.2	14.312	3.5	1.46
6/8/08 17:53	3.6	14.920	3.9	1.34
6/8/08 17:55	3.9	15.383	4.2	1.24
6/10/08 0:18	3.2	13.974	3.2	2.24
6/17/08 14:01	3.1	14.009	3.3	3.52
11/13/08 7:42	3.1	14.035	3.3	2.51

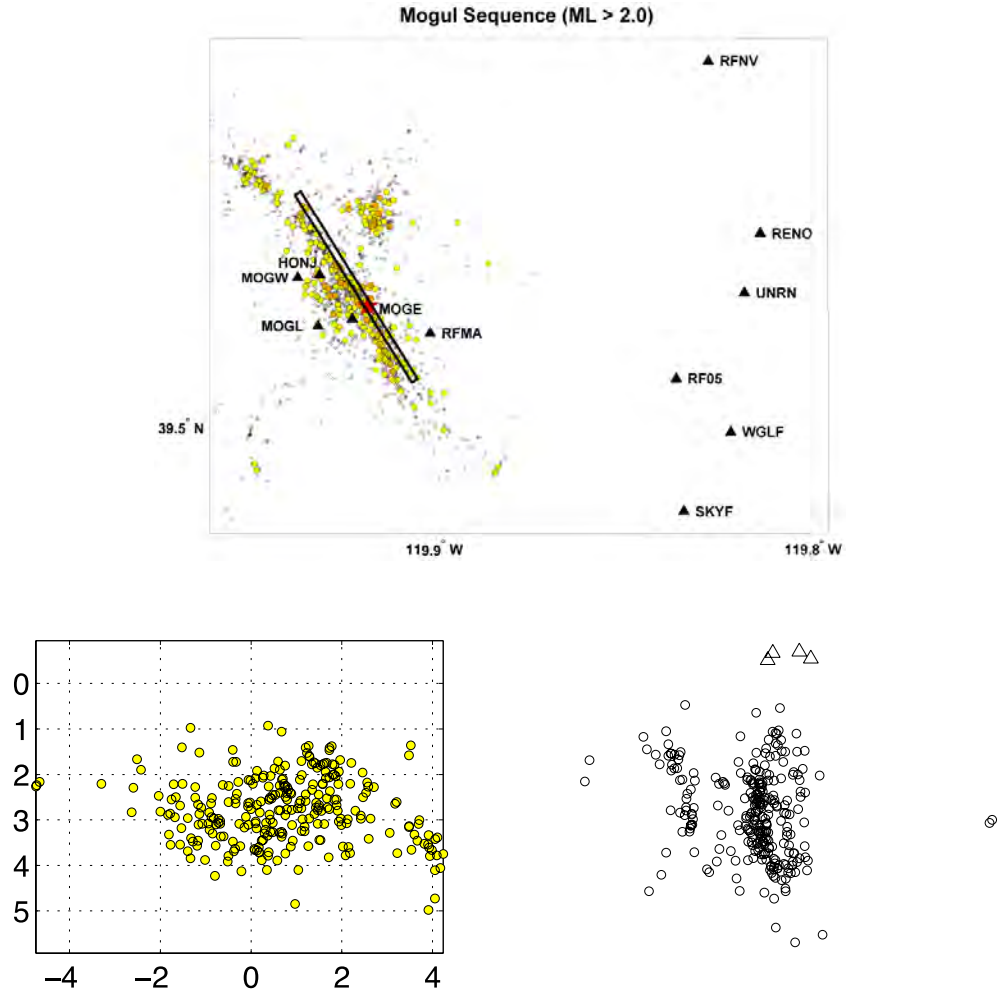


Figure 1. The upper plot shows a map of relocated Mogul earthquakes with M_L≥2.0, and locations of permanent and temporary stations within 10 km of the epicenter. Orange circles indicate M_L≥3.0 events. The lower left plot shows the event distribution in the fault plane along the strike and the black rectangle is the approximate fault zone. The lower right plot shows a cross section of the relocated Mogul earthquakes with M_L≥2.0 in a plane perpendicular to the fault strike.

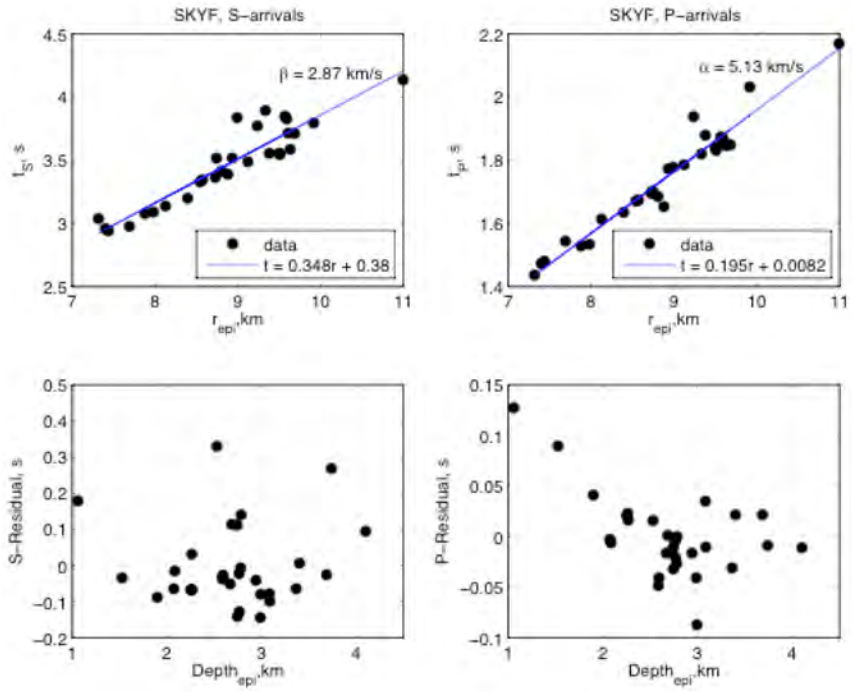


Figure 2. (Top-left) Shear-wave transit times (observed arrival time – origin time) t_S plotted versus epicentral distance (km) provide a direct estimate of the shear-wave velocity of the source area. (Bottom-left) S-time residuals show no systematic variation with hypocentral depth indicating that the source area velocity gradient is small. (Top-right) A source area *P*-wave velocity of 5.13 km/sec is estimated from differences in *P*-wave transit times to station *SKYF*. (Bottom-right) Residuals to the linear fit plotted versus depth show no systematic trend for sources below two km depth.

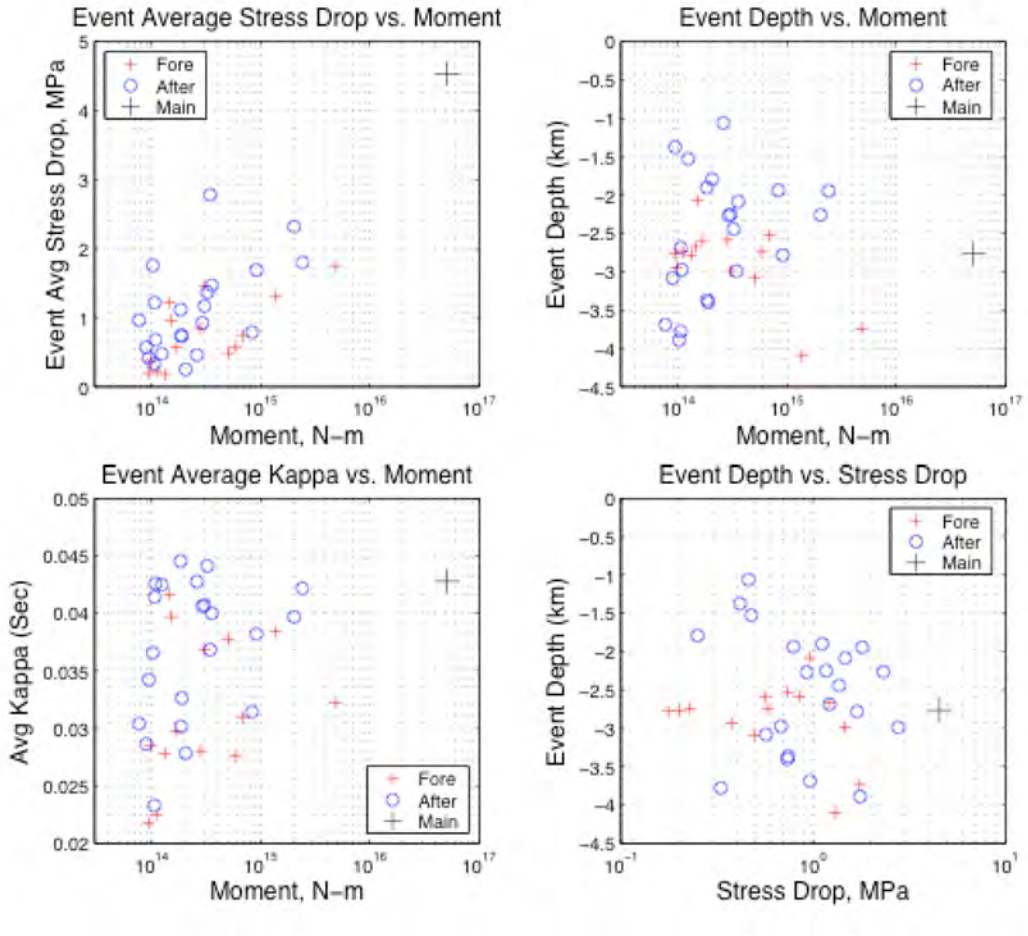


Figure 3: Event averaged earthquake parameters for $M_L \geq 3.0$ Mogul earthquakes. Only horizontal component measurements at strong-motion stations within 25 km of the sequence are included in event averages. (a) Stress drop as a function of seismic moment (M_o). Stress drops are generally low, with a median of 0.82 MPa. Foreshocks ("Fore") and aftershocks ("After") are not distinguished by stress drop. (b) Event depth as a function of M_o. (c) Event averaged spectral slope parameter *kappa* as a function of M_o. Foreshocks and aftershocks have similar gross high-frequency spectral content. (d) Event depth as a function of stress drop has no apparent trend.

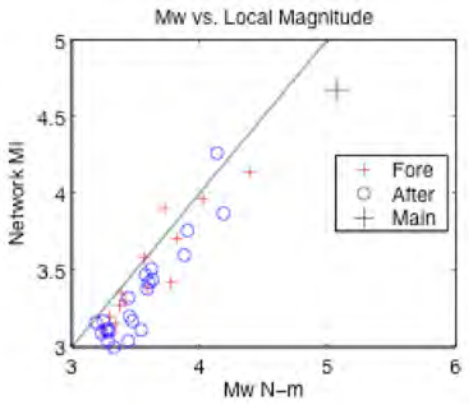


Figure 4. Preliminary results show *Mw* as a function of M_L (notation Ml) for earthquakes in Table 3. Foreshocks and aftershocks are similar in degree of correlation and average offset. The black line indicates equality between M_L and M_w

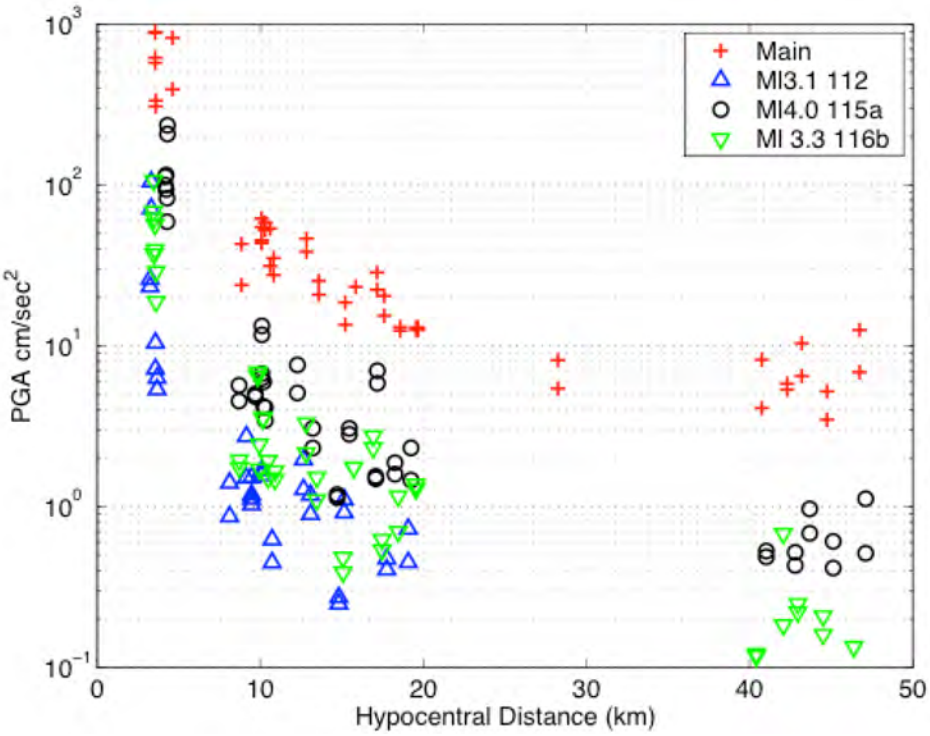


Figure 5. Peak ground acceleration vs. hypocentral distance for strong-motion recordings of the Mogul main shock ("Main") and three M_L ≥3 foreshocks. The numbers in the legend box after magnitude are the Julian day in 2008 of the event plotted, with "115a" referring to the first M_L ≥3 event on that day and "116b" being the second event on day 116.

ESTIMATING YIELD USING SHORT-PERIOD SURFACE WAVES

Jessie Bonner and David Russell

Weston Geophysical Corporation

Sponsored by the Air Force Research Laboratory

Award No. FA8718-09-C-0051

ABSTRACT

Yield estimation of small explosions is a significant challenge for the nuclear explosion monitoring community. To meet this challenge, we are examining the feasibility of using short-period surface wave magnitudes, called M_{Rg}, to estimate explosion yields at local distances. We have modified the Russell (2006) M_s formula, which was derived for periods of 8-25 s for distances beyond 50 km, for application at local distances and 1 s period. We have studied short-period surface wave attenuation in diverse lithologies in order to incorporate an attenuation term in the magnitude scale that is suitable for *Rg*. We have also incorporated multiple excitation corrections for *Rg* based on the near source seismic velocities, which greatly affect the source region amplitudes for *Rg*. We have derived a new Butterworth filter configuration for filtering *Rg* near 1 s period at distances between 2-50 km. We have applied the M_{Rg} formula to synthetic seismograms from explosions to determine the effect of depth and distance on the magnitude estimation. We also estimated M_{Rg} for 39 small ($37 \leq Y \leq 12{,}270$ kg TNT equivalent) and shallow (<120 m) explosions detonated in the United States in lithologies ranging from alluvium to granite. Regressions of the magnitudes with yield in all these environments result in the equation $M_{Rg} = \log(Y) - 3.03$ for chemical explosions with $Y < 12{,}270$ kg. An F factor with 95% confidence was determined to be 2.25, suggesting the lower and upper bounds on the yield estimates are Y/2.25 and Y*2.25, respectively. We also applied the relationship M_{Rg}:yield relationship to nuclear explosions detonated at the Degelen and Shagan, Kazakhstan, test sites. A majority of the estimated yields based on *Rg* magnitudes were within 20% of the true yield and had smaller F factor than the US chemical explosions.

OBJECTIVES

Chemical and nuclear explosions with yields of a kiloton (kt) or less represent a difficult problem for the nuclear explosion monitoring community. These events must be detected, located, and identified even when these small explosions are recorded on relatively few stations. An important task for event identification is yield estimation. The objective of our research is to develop a new methodology for yield estimation based on magnitudes of short-period, fundamental mode Rayleigh waves (*Rg*) recorded at local-to-near-regional distances.

RESEARCH ACCOMPLISHED

During the past year, we have developed a new formula for short-period (~1 s) surface wave magnitudes. This new formula, called M_{Rg}, was developed using the methods of Russell (2006) and can thus be tied back to regional and teleseismic surface wave magnitudes at intermediate periods (8 to 25 s). Attenuation coefficients for short-period surface waves have been derived from diverse tectonic settings to help calibrate the new M_{Rg} formula. Finally, we demonstrate the utility of the formula at estimating magnitudes for small explosions, and then attempt to correlate the magnitudes to yield with uncertainty estimates.

Formula Development

Russell (2006) developed the M_s(VMAX) magnitude formula that could effectively measure surface-wave magnitudes at local, regional and teleseismic distances, at variable periods, T, between 8 and 25 s. During the past year, we have modified the original Russell (2006) formula for application to T=1 s *Rg*. The changes include a decrease in the filter order, new filter constraints to determine f_c, a new attenuation correction based on observed *Rg* data in diverse geologies, and choices for the excitation correction based on near-source medium properties and *Rg* velocities.

Filter Order. The first modification to the Russell (2006) formula for M_{Rg} is to consider a 2nd order Butterworth filter rather than 3rd order. This decision was based on multiple comparisons of filtered *Rg* waveforms using both filters, and preferring 2nd order filtering in the identification and processing of the waveforms. The constant (C=0.43) in the original Russell (2006) formula is changed to C=0.46 as a result of employing a 2nd order filter, due to the constant being dependent on the Butterworth gain term b_n, which is a function of the Butterworth filter order (Russell, 2006).

Filter Definition. To estimate the time-domain amplitude of *Rg*, we filter the time series with a 2nd order, zero-phase Butterworth bandpass filter with corner frequencies $1/T - fc$, $1/T + fc$ where

$$f_c \le \frac{0.1}{T\sqrt{\Delta}}, \qquad (1)$$

where Δ is the epicentral distance in degrees. The constant, 0.1, in Equation 1 is based on the dispersive properties of short-period Rayleigh waves , which exhibit strong dispersion in the 1 second range. For 8-25 s Rayleigh waves (e.g., Russell, 2006), the constant was 0.6. We note that Zeiler and Velasco (2009) used a constant of 0.2 in a study to estimate short-period M_s magnitudes for explosions in Arizona. The constant has units of degrees$^{1/2}$ (Russell, 2006).

Attenuation Correction. We estimated the *Rg* attenuation coefficient, γ, for explosion datasets in the southern Basin and Range (igneous rocks), Colorado Plateau (sedimentary), central Alaska (metamorphic), New England (granite), Albuquerque Basin (alluvium), Yucca Flat (alluvium), and Wyoming (sedimentary). The period-dependent attenuation coefficients for all datasets are shown in Figure 1. The results show that for most of the explosion datasets, intrinsic attenuation of *Rg* results in an average γ=0.05±0.03 /km at T=1 s based on available data at distances less than 50 km. We note that this value will not be sufficient in an area of strong *Rg* scattering similar to the faults in the Albuquerque Basin. This is not a significant problem given that identifiable *Rg* will likely not propagate to stations beyond such fault zones.

Figure 1 also shows the period-dependent attenuation correction from the Russell (2006) M_s(VMAX) surface wave magnitude formula. For the M_s(VMAX) formula, the attenuation correction is of the form:

$$B_{att}\left(\frac{To}{T}\right)^{p}\Delta, \qquad (2)$$

where B_{att} and p (Equation 2) were 0.0031 and 1.8, respectively for T=8-25 s surface waves. We find that to better match the *Rg* attenuation coefficients at T=0.1 to 2 s, the exponent (p) value should be increased to 2.19 which corresponds to a γ = 0.05 /km at T=1 s. We initially used this value in the development of $\mathbf{M_{Rg}}$, but noted that for our small chemical explosion dataset, if *Rg* was observed beyond ~25 km, it was usually in a region with smaller attenuation coefficients (e.g., New England granites or Wyoming sedimentary rocks). As a result, the $\mathbf{M_{Rg}}$ at distances greater than 20 km would be overcorrected for attenuation using a γ = 0.05 /km. Thus we decided to weight the attenuation correction in $\mathbf{M_{Rg}}$ to a lower gamma estimate and chose one standard deviation from the mean, which corresponds to γ = 0.02 /km (or a p-value of 1.96). Returning to Equation 2, the attenuation term for our proposed $\mathbf{M_{Rg}}$ formula is:

$$0.0031\ (20)^{1.96}\ \Delta\ , \text{ or } 1.1\Delta. \qquad (3)$$

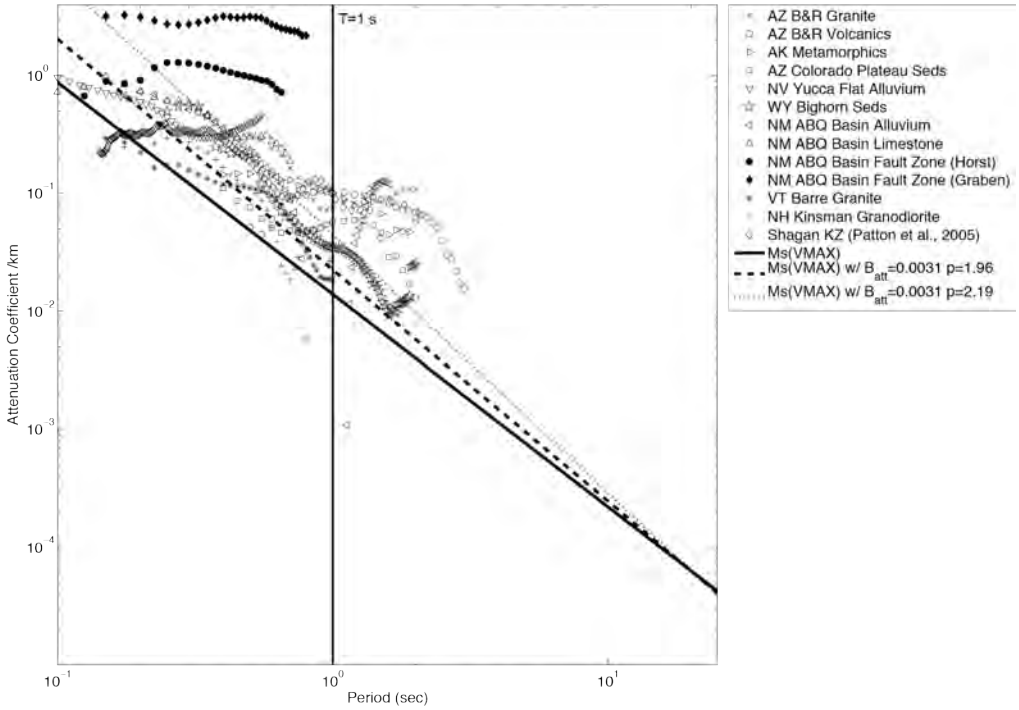


Figure 1. *Rg* attenuation coefficients as a function of period for diverse lithologies in the United States as well as data for Kazakhstan from Patton et al. (2005). Also shown are the period-dependent attenuation terms (B_{att}=0.0031 p=1.8) for the Russell (2006) formula as well as the proposed terms (B_{att}=0.0031 p=1.96 and B_{att}=0.0031 p=2.19) for *Rg* based on the measured attenuation coefficients.

***Rg* Excitation Correction.** M_s(VMAX) included a source excitation correction of -0.66 log $\left(\frac{20}{T}\right)$ in the estimation of surface wave magnitudes at T=8-25 s. The correction seeks to reduce short-period Rayleigh-wave amplitudes, which are enhanced for shallow sources—particularly explosions—in order to approximate a magnitude that would be measured for the same event near the reference period of 20 seconds. Figure 2 shows the theoretical magnitude correction required to extend the excitation correction to T=1 s *Rg* for five different crustal models. The theoretical magnitude corrections are based on explosion synthetics at 1 km for a source at 0.01 km depth. The corrections are referenced to T=20 s. Also shown is the excitation correction from Russell (2006), which matches the theoretical magnitude correction for most models in the 8-25 s range.

Figure 2 suggests that a single excitation correction may not provide optimal results for estimating T=1 s *Rg* magnitudes. The magnitude corrections range from -0.6 m.u for the global average AK135 model (Kennett et al., 1995) to -1.4 m.u. for a western United States (WUS) crustal model (Herrmann et al., 2011). If the upper km of the WUS model is replaced with velocities representing dry alluvium, the resulting excitation correction increases to approximately -2.6. The nulls in the spectrum for the alluvium model show the sensitivity of the synthetics to the low velocities. The Russell (2006) correction term is -0.9 at T = 1 s which is similar to the theoretical correction based on velocity models for the Korean Peninsula (Cho et al., 2007) and the central United States (Herrmann et al., 2011).

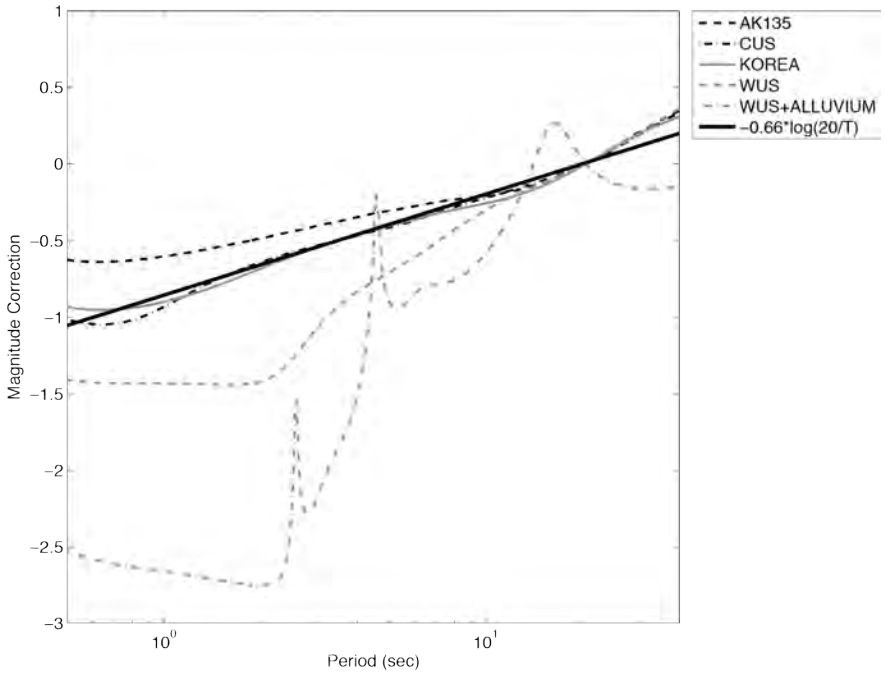


Figure 2. Excitation corrections for M_s to periods as low as 0.5 s for five different crustal models compared to the excitation correction used in Russell (2006).

The velocities of the layer where the explosion is synthesized primarily controls the amount of the of the magnitude correction. For example, the V_p and V_s for the upper layer of the western United States model are 3.4 km/s and 2 km/s, respectively. Conversely, for the AK135 model, the V_p and V_s are 5.8 km/s and 3.46 km/s, respectively. For the WUS+dry alluvium model, the V_p and V_s for the upper layer are 2.0 and 0.8 km/sec, respectively. Based on these results, we propose to use the following excitation correction, *E(T)*, for T=1 s *Rg* in the $\mathbf{M_{Rg}}$ formula:

$$E(T) = \begin{cases} -2.5 & U_{Rg} \leq 0.8 \text{ km/sec} \\ -1.5 & U_{Rg} \leq 2 \text{ km/sec} \\ -1 & U_{Rg} > 2 \text{ km/sec} \end{cases} \quad (4)$$

where U_{Rg} is the measured group velocity of T=1 sec *Rg* near the test site. The choice of *Rg* group velocity is based on the assumption that it is always expected to be slightly smaller than the upper crustal shear wave velocities and can be measured assuming an origin time estimate for the event. As more data are analyzed from diverse settings, we plan to continue to improve upon these excitation corrections. This highlights the importance of emplacement properties on the generation of *Rg* and provides for a larger magnitude correction, relative to T=20 s, for alluvium and "soft" rock test sites than "hard" rock test sites.

Final $\mathbf{M_{Rg}}$ Formula. Based on the above changes to the Russell (2006) formula, we introduce:

$$M_{Rg} = \log(a_{Rg}) + 0.5 \log(\sin \Delta) - \log(f_c) + 1.1\Delta + E(T) - 0.46 \quad (5)$$

where Δ is distance in degrees between 0.02° and 0.45° (2 and 50 km). The current distance limitations are constrained by the data that are discussed in this paper. Waveforms are corrected for instrument response and converted to displacement (in nanometers) and filtered between 1-f_c, 1+f_c using a zero-phase, 2nd order Butterworth bandpass filter f_c is determine by Equation 1. Zero-to-Peak amplitudes of *Rg* (a_{Rg}) are measured, and the time of the peak amplitude recorded and converted to group velocity (U_{Rg}) in order to estimate an excitation correction, E(T), defined in Equation 4. The processing can be completed automatically using pre-selected group velocity windows for *Rg* or manually by an analyst picking the peak amplitudes for *Rg*.

Application of the M_{Rg} Formula

We have applied the M_{Rg} formula to several explosion datasets recorded at local distances. Figure 3a shows the Butterworth-filtered waveforms (1-f_c, 1+f_c) for a 101.4 kg (TNT equivalent) explosion detonated in Barre granite and recorded from 2 to 24 km. The filtered waveforms highlight the T=1 sec *Rg*. Group velocities of the peak amplitude of the filtered signals are between 2.2 and 2.8 km/sec and increase with distance (Figure 3b). The mean U_{Rg} is 2.6 km/sec thus the processing automatically choses an excitation correction of E(T)=-1 for U_{Rg} > 2.0 km/sec, which is typical of "hard" rock emplacement media. The M_{Rg} estimates using Equation 5 are shown in Figure 3c. The network average M_{Rg}, which is estimated after discarding ±5% of high and low estimates in the population, is -1.05 with of ± one standard deviation of 0.07 m.u. To ensure that we are not biasing these results by using "Texan" 4.5 Hz geophone data, we calculated the magnitude using 15 instrument-corrected 1 Hz seismometers and obtained M_{Rg} = -1.06±0.10.

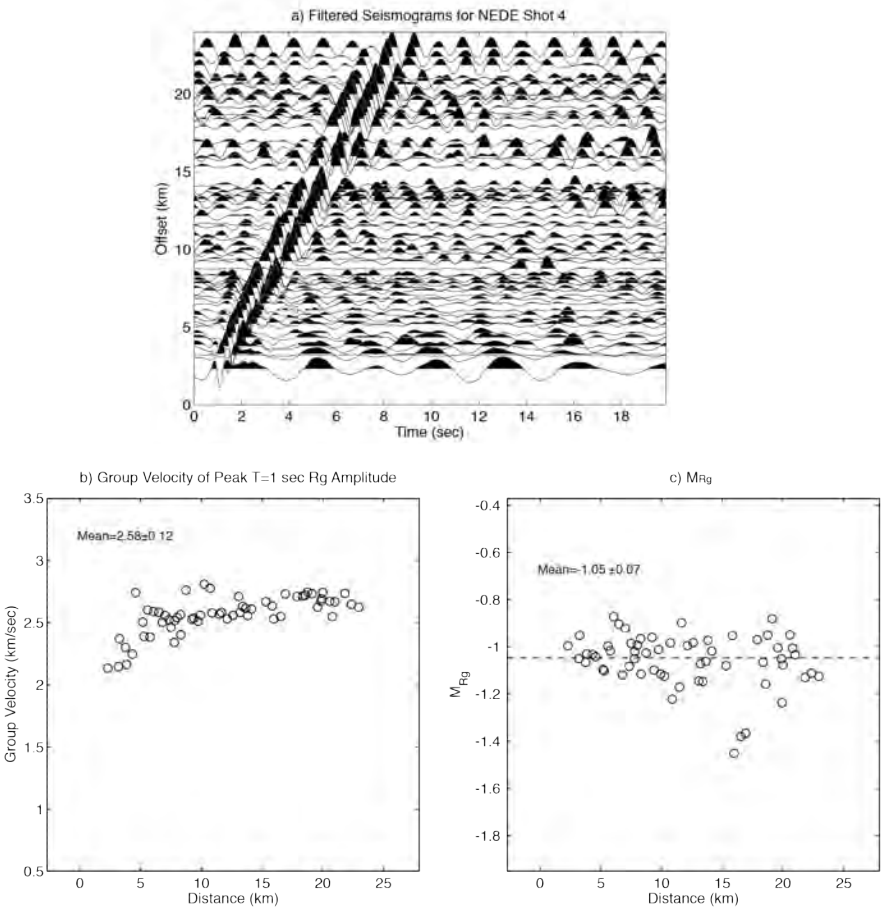


Figure 3. Processing example showing a) filtered waveforms b) group velocity estimates for *Rg*, and then c) magnitude estimates for a 101.4 kg (TNT equivalent) explosion conducted in Barre granite (Vermont, USA).

When we originally used 2.2Δ as the attenuation correction instead of 1.1Δ, the results showed a distance trend with many smaller magnitude estimates than the mean (M_{Rg} = -0.95) in the first few kilometers followed by mainly larger magnitudes at distances beyond 10 km. This trend has been removed as a result of using the 1.1Δ term and the magnitude scatter was decreased.

We have estimated M_{Rg} for 39 explosions recorded at distances between 2 and 50 km. The explosions were part of multiple experiments, including the Arizona Source Phenomenology Experiment (SPE-A), Bighorn Active Seismic Experiment (BASE), the DO Experiment, the Fracture Decouple Experiment (FDE), the Frozen Rock Experiment (FRE), HUMBLE REDWOOD (HR) I and II, and the New England Damage Experiment (NEDE). The explosion yields for the 40 events range from 37 kg to 12,270 kg TNT equivalent. All of the explosions were detonated below ground; however, the explosions include both fully- and partially-confined shots. All of the explosions were conducted at depths less than 120 m thus should not have significant depth effects for M_{Rg}.

Yield-M_{Rg} Relationship

Figures 4 and 5 compare the estimated M_{Rg} to yield. In Figure 4a,b, the results for each experiment are plotted as a different color or symbol. To show the effect of the excitation correction, we include results (Figure 4a) for M_{Rg} with three possible excitation corrections (-1, -1.5, -2.5) as defined in Equation 4, and we present the M_{Rg} results (Figure 4b) with using a single correction (-1) for all events. The use of multiple excitation corrections provides a significantly tighter yield-magnitude cloud than the use of a single correction. The observed magnitudes in Figure 4b do confirm the theoretical results shown in Figure 2 that the slower velocity rocks (alluvium, sedimentary) excite larger amplitude T=1 s *Rg* than a similar yield explosion in faster media (e.g., granite). More data are needed in alluvium to further validate these results, as the three HUMBLE REDWOOD events we have analyzed have only a few stations that are far enough from the highly scattering basin-bounding fault zone to provide an accurate estimate of source size.

We regressed log yield (Y) versus M_{Rg} in Figure 5 to determine the relationship:

$$M_{Rg} = \log_{10}(Y) - 3.03 \qquad \text{(Chemical)} \qquad (6a)$$

for $37 \leq Y \leq 12270$ kg (TNT equivalent). The slope from the analysis was 0.99, thus essentially representing a slope of unity between M_{Rg} and log Y. Slopes for historical M_s-log yield relationships typically fall somewhere between 0.75 to 1.2 (Murphy,1977; Bache, 1982; Evernden and Marsh, 1987). Slopes of 1 have been reported by Stevens and Murphy (2001) for the Shagan Test Site in Kazakhstan and Bache (1982) for multiple datasets. The 95% confidence intervals were also determined for the data and plotted in Figure 5. As an example, for any future event recorded in similar media that had an estimated M_{Rg} = 0, we could say with 95% confidence the event had a yield between 501 and 2512 kg (TNT-equivalent) with Equation 6 predicting a yield of 1072 kg (2362 lbs).

Another way of determining approximate confidence bounds on yields of explosions is to estimate F factors. For 95% confidence interval, the F factor is defined as:

$$F = 10^{\frac{1.96\,\sigma}{\alpha}}, \qquad (7)$$

where σ is the standard deviation of the magnitudes about the regression line with slope (α) = 1. The regression in Figure 5 has σ = 0.18 resulting in an F= 2.25. The confidence bounds on the yield are defined as:

$$Y_{lower} = Y/F$$
$$Y_{upper} = Y*F \qquad (8)$$

which for the yield estimate of 1072 kg would result in Y_{lower}=476 kg and Y_{upper}=2412 kg.

The yield-M_{Rg} relationship (Equation 6) was developed for a series of chemical explosions. The source function for the chemical explosion is equivalent to that of a nuclear explosion with twice the yield (Denny et al., 1995). Thus for nuclear explosions, Equation 6 would be modified to solve for yield by adding 0.3 to the constant. Also, for convenience, we subtract 6 to the formula to convert kilograms into kilotons:

$$\log_{10}(Y)\ (kt) = M_s - 2.67 \qquad \text{(Nuclear)} \qquad (6b)$$

Thus for a 1 kiloton nuclear explosion, we would expect an M_{Rg}=2.67. This is higher than most historical yield-M_s relationships would predict. The offset between the yield-M_{Rg} formula and the nearest yield- M_s formula (e.g., Stevens and Murphy, 2001) is 0.6 units. Recent papers, such as Patton and Taylor (2008), have shown the strong dependence of nuclear explosions on "spall" effects, or tensile failure at 20 seconds, especially in larger explosions at Shagan River. This effect may be significantly diminished for 1 sec measurements of chemical and nuclear explosions, which can explain the offset between the M_{Rg} formula and standard yield-M_s formulas. This hypothesis is clearly demonstrated in the next section, at least for Degelen and Shagan River nuclear explosions.

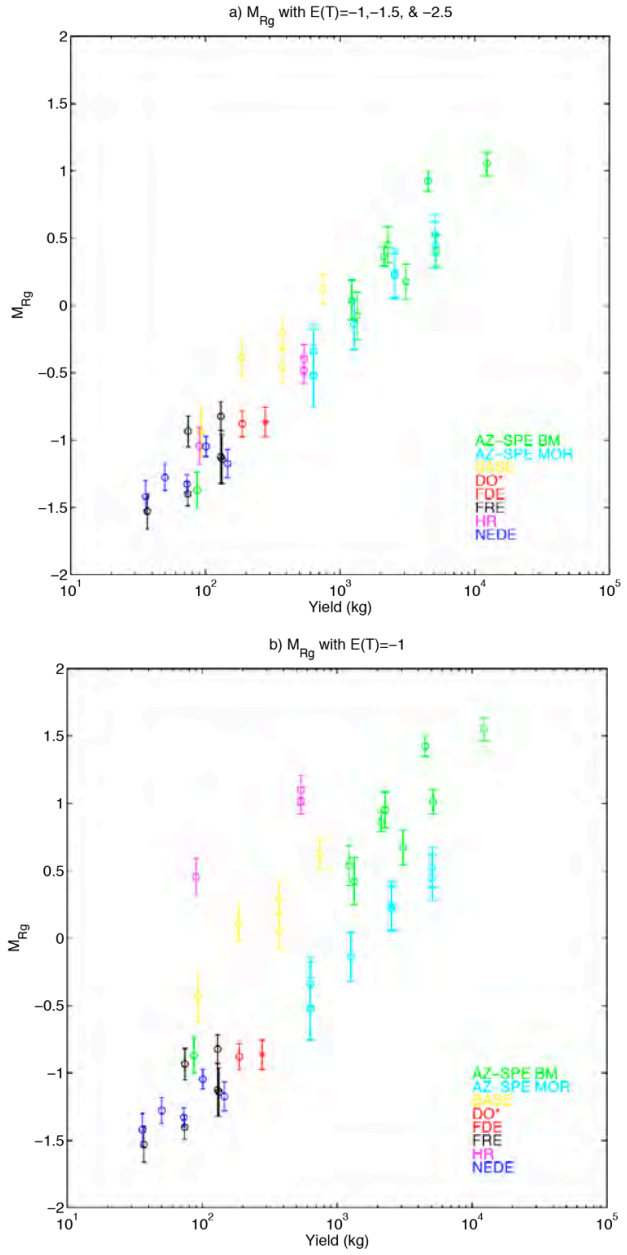


Figure 4. Final M_{Rg} estimates (error bars show ±1σ) for 39 small explosions in different lithologies. The results are plotted against the TNT-equivalent yields for the explosions. a) Results using three excitation corrections (-1, -1.5, -2.5) as defined by Equation 11. b) Results using a single excitation correction (-1) for all events.

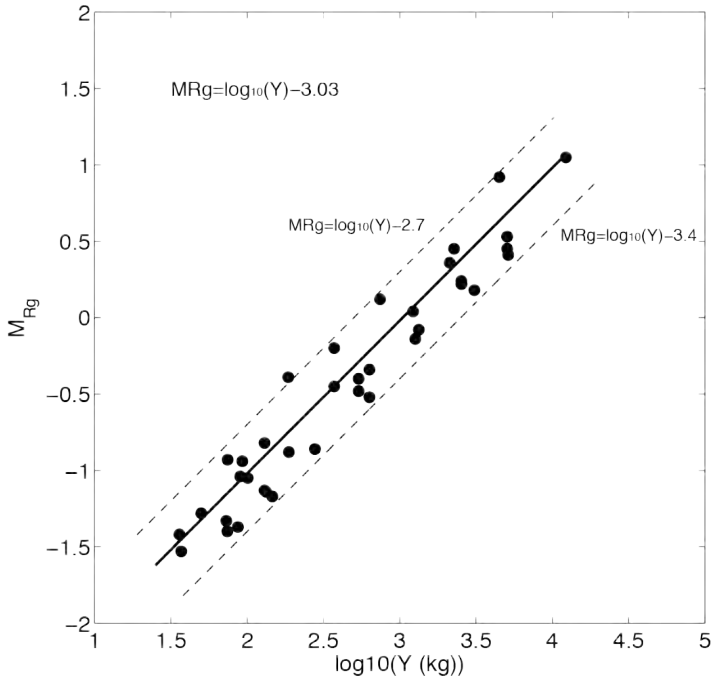


Figure 5. A yield-M_{Rg} relationship based on regression results for chemical explosions. The data points are shown as circles, the best fit regression line is solid, and the dashed line describe the 95% confidence intervals.

Formula Validation

We have also tested the new yield-M_{Rg} formula on additional datasets that were not included in the development processes. The test included estimating magnitudes for 8 Degelen, Kazakhstan, Test Site (DTS) and 10 Shagan, Kazakhstan, Test Site (STS) nuclear explosions and recorded at local distances by the Institute for Dynamics of the Geosphere (IDG). The datasets are described in Stevens et al. (2007) and has excellent examples of *Rg* recorded at local distances. The test sites both have *Rg* velocity > 2 km/sec resulting in a choice for the excitation correction, E(T)=-1. The M_{Rg} estimates for all 18 events were converted to yield using Equation 6b.

The comparison of the true and estimated yields is shown in Figure 6. Because of the small number of stations recording these events (typically 4-6 stations), we did not trim the mean for these results. For the STS dataset only, we have extended the M_{Rg} estimation to 100 km and estimated the magnitudes for the 10 explosions (Table 5), which were converted to a yield estimate using Equation 9. We note slightly higher variance in the interstation magnitude at this extended distance range; however, the magnitude estimates continue to provide robust yield estimates.

The highest percentage error between the estimated and true yield is 64%, which suggests a smaller F factor for DTS that what was determined for the chemical explosions used to derive Equation 6. For 12 of the 18 events, the estimated yield percentage error is 20% or less, which is similar to Adushkin's (2001) yield estimates for Shagan River Test Site nuclear explosions using *Rg* with stations corrections. Considering that these DTS nuclear explosions have yields that are orders of magnitude larger and significantly greater depths than the events used to develop Equation 6, these results are very promising.

CONCLUSIONS AND RECOMMENDATIONS

We have developed a new yield estimation method based on the magnitudes obtained from 1 s fundamental mode Rayleigh waves (*Rg*). The method was developed using local recordings of *Rg* from numerous chemical explosions in the United States, and has been successfully applied to nuclear explosions at the Shagan and Degelen test sites to distances up to 100 km. In the remainder of this study, we plan to continue validation of the formula on additional

datasets, including possible local recordings of nuclear explosions at the Nevada National Security Site (formerly the Nevada Test Site) (Abbot, 2011). The applicability of the method may be limited to local distances; however, it is important to have the ability to estimate a robust yield from *Rg* should it be observed from nuclear and chemical explosions. An advantage of this method is that it only requires an empirical estimate of source rock type using observed group velocities to calculate M_{Rg}.

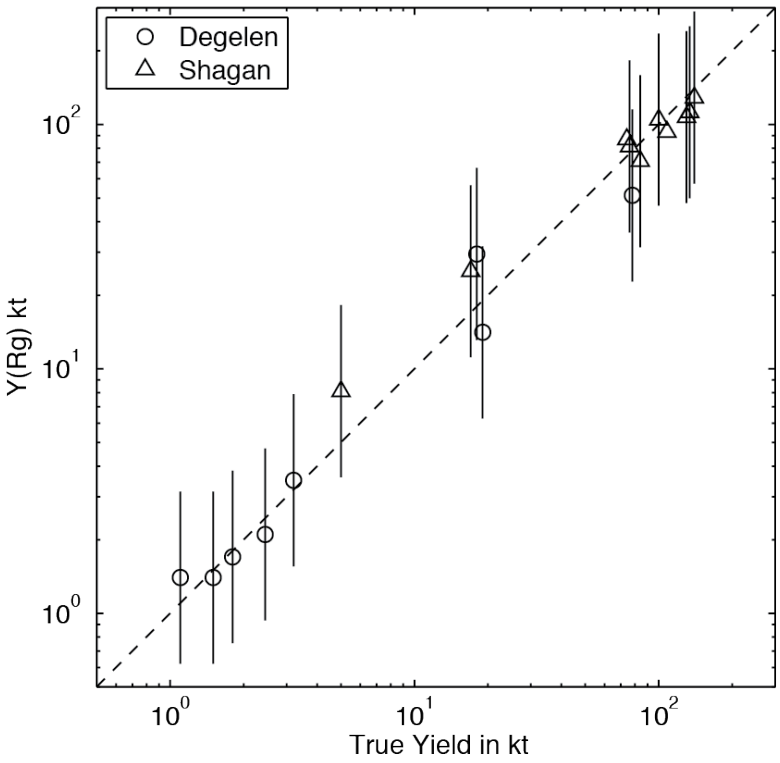


Figure 6. Estimated yields from M_{Rg} (Y[*Rg*]) in kt versus true yields for 8 Degelen and 10 Shagan nuclear explosions. The dashed line represents a 1:1 relationship. The vertical error bars represent an F factor of 2.25, which is based on the US chemical explosion datasets used to develop the yield-M_{Rg} relationship. When only the Shagan and Degelen nuclear explosions are considered, the F factor is estimated as 1.6.

ACKNOWLEDGEMENTS

Data used in this project is derived from numerous small-scale explosion experiments conducted by various organizations. Most of the datasets used in this project, which are older than 2 years from the publication date, can be found at the Incorporated Research Institutions in Seismology (IRIS) Data Management Center (DMC). We thank Drs. Steve Harder, Kate Miller, and Anne Sheehan for their assistance in obtaining the BASE data. We thank Jeff Stevens and Eli Baker for access to the Degelen and Shagan nuclear explosion data. Most of the datasets used in this study would not have been collected without the excellent planning and execution of Mark Leidig. We thank Bob Herrmann for his excellent Computer Programs in Seismology code as well as assistance on the excitation corrections. We also wish to express our thanks to Howard Patton for many fruitful discussions regarding short-period surface waves over the years. We thank James Lewkowicz of Weston Geophysical for his enduring and patient support of this and many other projects.

REFERENCES

Abbott, R.E. (2012). Progress report on a project to digitize data from hundreds of Nevada underground nuclear tests recorded by the Sandia seismic network. Abs. Seism. Soc. Am. Meeting 2012, San Diego

Adushkin, V. V. (2001). Yield estimation for Semipalatinsk underground nuclear explosions using seismic surface wave observations at near-regional distances, *Pure Appl. Geophys*. **158**, 2217–2226.

Bache, T. (1982). Estimating the yield of underground nuclear explosions, *Bull. Seism. Soc. Am.*, **72**, S131–S168.

Bonner, J. L., D. Russell, D. Harkrider, D. Reiter, and R. Herrmann (2006). Development of a Time-Domain, Variable-Period Surface Wave Magnitude Measurement Procedure for Application at Regional and Teleseismic Distances, Part II: Application and M_s—m_b Performance. *Bull. Seism. Soc. Am.* 96, 678–696.

Denny, M., P. Goldstein, K. Mayeda, and W. Walter (1995). Seismic results from DOE's Non-Proliferation Experiment: a comparison of chemical and nuclear explosions, in Monitoring a Comprehensive Test Ban Treaty, NATO ASI Series, Kluwer Academic, Hingham, Massachusetts.

Evernden, J.F. and G.E. Marsh (1987). Yield of US and Soviet nuclear tests. *Physics Today*, **4**. Pp. 37–34.

Herrmann, R. B. and B. J. Mitchell (1975). Statistical analysis and interpretation of surface wave anelastic attenuation data for the stable interior of North America, *Bull. Seism. Soc. Am.* **65**, 1115–1128.

Herrmann, R.B., H. Benz, and C.J. Ammon (2011). Monitoring the earthquake source process in North America. *Bull. Seismol. Soc. Am*. **101**, 2609–2625.

Kennett, B.L.N. Engdahl, E.R. & Buland R. (1995). Constraints on seismic velocities in the Earth from travel times, *Geophys J Int*, **122**, 108–124

Murphy, J.R. (1977). Seismic source functions and magnitude determinations for underground nuclear explosions. *Bull. Seism. Soc. Am*. **67**, 135–158.

Nuttli, O.W. (1986). Yield estimates of Nevada Test Site explosions obtained from seismic Lg waves, *J. Geophys. Res.* **91**, 2137–2151.

Patton, H., J. Bonner, and I. Gupta (2005). *Rg* Excitation by Underground Explosions: Insights from Source Modeling the 1997 Kazahkstan Depth of Burial Experiments. *Geophys. J. Int.* doi:10.1111/j.1365-246X.2005.02752.x

Patton, H. J., and S. R. Taylor (2008). Effects of shock-induced tensile failure on *mb* - *Ms* discrimination: Contrasts between historic nuclear explosions and the North Korean test of 9 October 2006, *Geophys. Res. Lett.* **35**, L14301, doi:10.1029/2008GL034211.

Russell, D.R. (2006). Development of a time-domain, variable-period surface wave magnitude measurement procedure for application at regional and teleseismic distances. Part I—Theory. *Bull. Seismol. Soc. Am.* **96**, 665–677.

Stevens, J. L. and J. R. Murphy (2001). Yield estimation from surface wave amplitudes. *Pure and Applied Geophys*. 158, 2227-2251, DOI: 10.1007/PL00001147.

Stevens, J. L., G. Eli Baker, and Heming Xu (2007). The physical basis of the explosion source and generation of regional seismic phases. Final Report. SAIC. AFRL-RV-HA-TR-2007-1139, 156 p.

Vaněk, J., A. Zatopek, V. Karnik, Y.V. Riznichenko, E.F. Saverensky, S.L. Solov'ev, and N.V. Shebalin (1962). Standardization of magnitude scales. *Bull. (Izvest.) Acad. Sci. U.S.S.R., Geophys. Ser.*, **2**, 108.

Zeiler, C. and A. A. Velasco (2009). Developing local to near-regional explosion and earthquake discriminants. *Bull. Seismol. Soc. Am* **99**, 24–35.

A SYNTHETIC STUDY OF SURFACE WAVE MAGNITUDES

Jessie Bonner[1], Robert Herrmann[2], and David Russell[1]

Weston Geophysical Corporation[1] and St. Louis University[2]

Sponsored by the Air Force Research Laboratory

Award No. FA8718-09-C-0012
Proposal No. BAA09-75

ABSTRACT

We continue to investigate the M_s(VMAX) surface wave estimation procedure (Russell, 2006; Bonner et al., 2006) using synthetic simulations. The main objective of these simulations is to determine the possible sources of bias between M_s(VMAX) and historic narrow band methods for estimating M_s at periods (T) near 20 s. The simulations also allow quantification of the effects of radiation pattern and focal mechanisms, explosion emplacement media, and various attenuation models on the surface wave magnitudes. We have studied synthetics generated using the global AK135 model as well as regional velocity and attenuation models for the central United States (CUS), Italy, Korea, and the western United States (WUS). The synthetics were calculated at distances ranging from 500-6000 km. The attenuation correction used in M_s(VMAX) is based on the low CUS attenuation and thus matches closely with the attenuation model used in the CUS model. Explosion synthetics generated using the CUS model show little, if any, variation in M_s(VMAX) estimates with distance. Because the attenuation in the WUS is higher, the M_s(VMAX) estimates show a distance trend, with 0.1 magnitude unit (m.u.) larger magnitudes estimated at regional distances that at teleseismic distances. M_s(VMAX) shows no significant distance trends for synthetic earthquakes and explosions using the Korean model, whereas the largest distance trends in M_s(VMAX) estimates are observed for the global AK135 and regional Italian models. For earthquakes, the synthetics allow us to determine the source of the scatter in the surface wave magnitude estimates. Improper attenuation models may account for as little as 0.1 m.u. scatter at 500-6000 km distances; however, radiation pattern effects can produce significantly larger variance in the estimates (e.g., > 0.2 m.u). We typically observe that M_s(VMAX) is 0.1-0.2 m.u. larger than historic M_s measurement near T=20 s, which we attribute to two different effects. First, the historic M_s narrow band measurements are based on band pass filtered data that does not incorporate a filter correction for the amplitude reduction associated with the narrow-band filters. Second, surface wave amplitudes from some earthquake focal mechanisms can be significantly reduced near T=20 s, while M_s(VMAX) is designed to seek larger amplitudes on either side of a spectral hole. For example, a 10 km deep strike slip has a significant spectral hole near T=16 s that reduces historic M_s measurements by 0.7 m.u. when compared to M_s(VMAX).

OBJECTIVES

The objective of our current research focus is to quantify the performance of M_s(VMAX) (Russell, 2006; Bonner et al., 2006) using synthetic seismograms. Recent questions have been posed regarding a possible offset or bias between M_s(VMAX) estimates, which are made between 8-25 s period (T), and historic narrow band M_s measurements, typically made near T=20 s, and whether inadequate attenuation correction could lead to significant magnitude errors. To answer these questions, we have completed a synthetic study that quantifies M_s(VMAX) estimates for a variety of different velocity and attenuation models at regional to teleseismic distances. The results are compared to the historical M_s estimates in the 17-23 s period band.

RESEARCH ACCOMPLISHED

Formulas

We provide a brief overview of the two magnitude formulas tested in this paper. First, Russell (2006) developed a magnitude formula that could effectively measure surface-wave magnitudes at local, regional and teleseismic distances, at variable periods, T, between 8 and 25 s. The magnitude equation is:

$$M_{s(b)} = \log(a_b) + \frac{1}{2}\log\left(\sin\left(\Delta\right)\right) + 0.0031\left(\frac{20}{T}\right)^{1.8}\Delta - 0.66\log\left(\frac{20}{T}\right) - \log\left(f_c\right) - \mathrm{C}, \quad (1)$$

where a_b is the amplitude of the Butterworth-filtered surface waves (zero-to-peak in nanometers), Δ is the distance in degrees, and f_c is the filter frequency of 3rd order, zero phase Butterworth filters with corner frequencies of $1/T$-f_c, $1/T$+f_c, respectively, and C=0.43. Because the equation finds the maximum amplitude at variable periods, it is often referred to as M_s(VMAX).

For $8 \le T \le 25$, the equation is corrected to T=20 s, accounting for frequency-dependent source effects, attenuation, and dispersion. The second term of Equation 1, 0.5 log(sin(Δ)), is a correction for the geometrical spreading; the third term, $0.0031(20/T)^{1.8}\Delta$, is a period-dependent attenuation correction; and the fourth term, 0.66log(20/T), is a period-dependent excitation correction. The constant, C, is determined to be 0.43 to scale the equation at T=20 s to von Seggern's formula (1977), which is scaled to Vaněk et al. (1962) at Δ=50 degrees.

For the "historic" magnitude formula, we used:

$$M_s = 1\log10(\mathrm{A/T}) + \log10(\Delta) + 1.12 \quad (2)$$

where A is the peak-to-trough trace amplitude in nanometers and Δ is the epicentral distance in degrees. This equation represents the Prague formula (Vaněk et al., 1962) scaled to Δ=50 degrees (Yacoub, 1988). In order to measure the amplitudes at each period of interest and simplify time domain processing of data, we construct a 2nd-order Butterworth bandpass filter that emulates the Gaussian filters originally designed by Yacoub (1983) for pseudo-spectral magnitude estimation (Figure 1). Following Herrmann (1973), Yacoub (1983) utilized a narrow band Gaussian filter of the form

$$H = exp\left[-16\pi\left(\frac{\omega-\omega_0}{\omega_0}\right)^2\right]. \quad (3)$$

A zero phase Butterworth filter can be designed with the same maximum time domain amplitude as the Gaussian, using the method outlined in Russell (2006). For the Gaussian and Butterworth filter, the maximum time domain amplitudes are respectively, $A/(2T)$, $A \cdot 2\pi b_n f_c$, where A is the frequency domain amplitude at period T, b_n is the Butterworth gain for an n^{th} order filter (Russell, 2006), and f_c is the one-sided bandwidth of the Butterworth filter. Equating the maximum time domain amplitudes and solving for f_c gives

$$f_c = \frac{1}{4\pi b_n T}. \quad (4)$$

For a Butterworth filter of order n, using f_c as defined above will give an equivalent maximum time domain amplitude as the Gaussian filter defined by Yacoub (1983).

The filters are combed through the data at periods between T=17-23 s allowing 7 magnitudes to be estimated using Equation 2. The maximum magnitude is selected as the final magnitude for comparison with M_s(VMAX) after we add 0.3 m.u. to the constant in Equation 2 to effectively render it a zero-to-peak measurement. We refer to this method as the historic magnitude or M_s estimate in this paper.

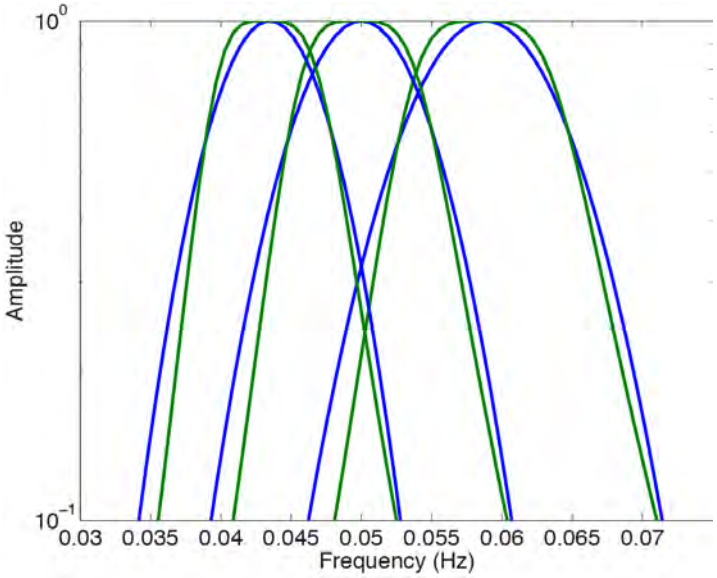


Figure 1. Comparison of the Gaussian filters (blue) suggested by Yacoub (1983) at T=17s, 20s, and 23 s used for filtering surface waves for magnitude estimation and an emulated 2nd order Butterworth version used in our study. Both the Gaussian and Butterworth filters have the same maximum time domain amplitudes.

Models

We chose five different velocity and attenuation models for the comparison of the magnitude formulae using synthetics. The models include the global average AK135 model (Kennett et al., 1995; tak135sph.mod), central and western United States crustal models (Herrmann and Mitchell, 1975; Herrmann et al., 2011; CUS.mod, WUS.mod), a Korean Peninsula model (Cho et al., 2007; t6.invSNU.CUVEL.mod), and a model for the central Italian Apennines (Herrmann et al., 2011; nnCIA.mod). Examples of the layered shear wave velocity are shown in Figure 2a.

The other aspect of the study is to propagate the motions from the source regions to large distances. The CUS and WUS model Q values are based on work at St. Louis University by Mitchell and Herrmann, and perform quite well in defining the fundamental surface wave propagation observed from current permanent and temporary broadband stations in North America. The AK135 model has Q_{kappa} and Q_{mu} values which were converted to Q_P and Q_s. The Q values for the Korea and Central Italy models have not been thoroughly tested because of the short distance of observations. The period-dependent attenuation coefficients for each model are shown in Figure 2b. We note that the way the scripts are set up to run these programs, any velocity and Q map could easily be tested in a similar manner.

The M_s(VMAX) formula uses an attenuation correction of the form:

$$B_{att}\left(\frac{To}{T}\right)^{p}\Delta, \tag{5}$$

where p describes the power law decay for the attenuation coefficient with frequency, and B_{att} is a magnitude correction defined by:

$$B_{att}(T) = \log(e)\,\kappa\,\gamma_0 \tag{6}$$

where κ is a degree to km conversion (111.2 km/deg) and γ_0 represents the attenuation coefficient in /km at the reference period (T_o) = 20 s. We note that For the Russell (2006) M_s(VMAX) formula, the B_{att} and p were based on central United States attenuation values (e.g., Q_{20}=800; Herrmann and Mitchell, 1975) and determined to be 0.0031

and 1.8, respectively for T=8-25 s surface waves. This results in a similarity between the Russell (2006) and CUS attenuation coefficients shown in Figure 2.

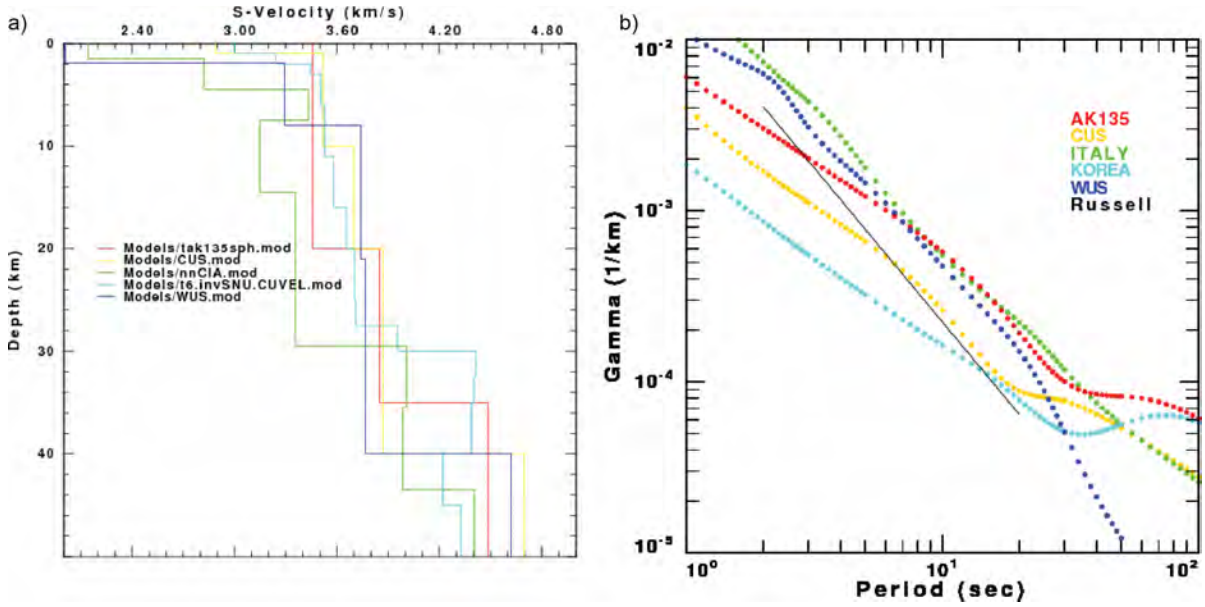


Figure 2. Velocity and attenuation models used in the synthetic study. a) Shear wave velocity profiles for five different models including AK135 (tak135sph.mod), central United States (CUS.mod), central Italian Apennines (nnCIA.mod), the Korean Peninsula (t6.invSNU.CUVEL.mod), and the western United States (WUS.mod). The period-dependent attenuation coefficients for each model as well as the period-dependent attenuation correction term for the Russell (2006) M_s(VMAX) formula are also shown.

We selected these models as a representative set of crustal structures, some of which are relevant to areas of monitoring interest. The CUS model is applicable to stable cratons, the WUS model to regions with lower velocities in the upper 6 km, and the Central Apennines model for central Italy which has even lower upper crustal velocities. The Korean Peninsula model was selected due to monitoring interest, while the AK135 continental model is a standard reference model for travel times.

Explosion Synthetics

For the first comparison of the two magnitude formulas, we synthesized a shallow explosion (M_w=5.0) in each velocity/attenuation model. We used modal summation (Herrmann, 2004) to generate the vertical-component synthetics at stations placed every 500 km starting at 500 km and ending at 6000 km. The synthetics at each station were then analyzed and an M_s(VMAX) and M_s estimated. Plots were produced for each model that have four subplots. The first panel represents the M_s(VMAX) selected for each distance based on the period of maximum amplitude (red dot) and the M_s(VMAX) computed for each period (red curves). The second panel is the M_s(VMAX) as a function of distance (red dots) and historic M_s vs. distance (blue dots). The third panel shows a set of plots to test the assumption that the M_s(VMAX) processing effectively results in pseudo-spectral amplitudes (black dots) based on time-domain measurements, and that these amplitudes are equivalent to actual spectral amplitudes (red line). The final panel shows the historic M_s period as a function of distance and will be a number between 17 and 23 s.

Figure 3 shows the magnitude results the CUS model, which as mentioned previously, has a similar attenuation structure to what was incorporated into the Russell (2006) M_s(VMAX). Figure 3a shows that the M_s(VMAX) spectra are essentially flat between 8-25 s and overlay each other. One of the objectives of the M_s(VMAX) formula development was to apply excitation corrections that attempted to flatten the spectra for an explosions. These results suggest that the excitation and attenuation corrections for M_s(VMAX) are well suited for earth structures similar to

the stable cratonic features of the central United States. As shown in Figure 3c, the explosion spectra at short distances have increased short period amplitudes that will bias the magnitude estimate high if not corrected for using an excitation correction, which would degrade M_s:m_b performance.

The M_s(VMAX) is distance independent as shown in Figure 3b for the CUS model; however, we note that the M_s has smaller magnitudes than M_s(VMAX) at regional distances. There are two reasons for these differences. First, the filter combs emulated from Yacoub (1983) are too narrow and introduce error into the estimation of magnitudes, whereas M_s(VMAX) has a –log(f_c) correction to correct for this problem. We derived a correction to M_s (see Appendix) and restricted the analysis of both magnitudes to T=20 s, and thus were able to show that this corrects for the narrow band error, resulting in very close magnitudes for both formulas. The second reason for differences in the two magnitude estimates is related to the actual Rayleigh-wave excitation spectra between T=8-25 s. At shorter distances, M_s(VMAX) migrates to shorter periods for the final estimate (see Figure 3a), whereas the M_s is restricted to 17-23 s, is actually pegged at T=17 s, and would prefer to migrate to lower periods with larger amplitudes. One of the primary objectives of the M_s(VMAX) development was to use these shorter periods at regional distances, which lowers the detection capabilities to smaller magnitudes (Bonner et al., 2006). At teleseismic distances, both formulas are using T~17 s amplitudes to produce the magnitude estimates thus resulting in similar results.

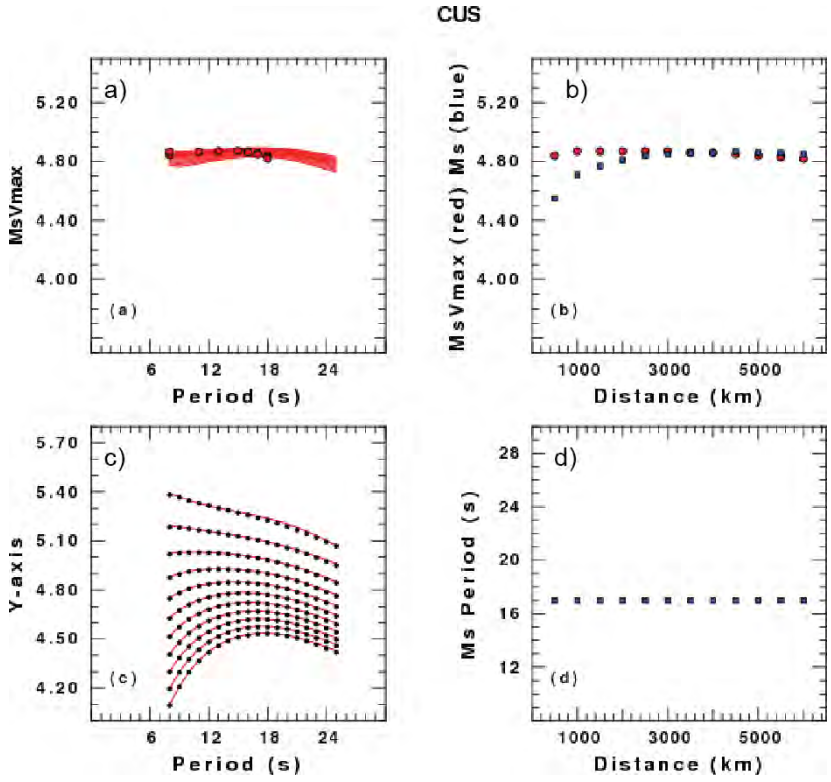


Figure 3. M_s and M_s(VMAX) processing results for the CUS model. a) M_s(VMAX) selected for each distance based on the period of maximum amplitude (black dot) and the M_s(VMAX) computed for each period (red curves). b) M_s(VMAX) as a function of distance (red dots) and historic M_s vs. distance (blue dots). c) Ms(vmax) pseudo-spectral amplitudes (black dots) derived from the peak amplitude in the filtered time series compared to actual spectral amplitudes (red line). d) historic M_s period as a function of distance.

Results for the western United States (WUS) model are shown in Figure 4. With this analysis, we begin to see the effects of an attenuation model that differs from the Herrmann and Mitchell (1975) attenuation incorporated into M_s(VMAX). Figure 4a shows that the M_s(VMAX) magnitude "spectra" do not overlay each other and are not all flattened as was the case for the CUS model. The magnitude "spectra" at regional distances show a slight increase in magnitudes at the shorter periods, which has been noted on analyses of NTS explosions at WUS stations at regional

distances (Figure 5). With the attenuation model differences, the M_s(VMAX) period of maximum amplitude migrates from 8 s at 500 km to 24 s at 6000 km, which reduces the scatter in the final magnitude estimates to less than 0.15 magnitude unit (m.u.). The M_s(VMAX) estimates are distance dependent with larger magnitudes at regional distances. Notice also how the bias between M_s(VMAX) and M_s increases at regional distances, which is problematic if only regional data are used for smaller magnitude explosions. These results suggest the possible need to regionalize the M_s(VMAX) formula for attenuation.

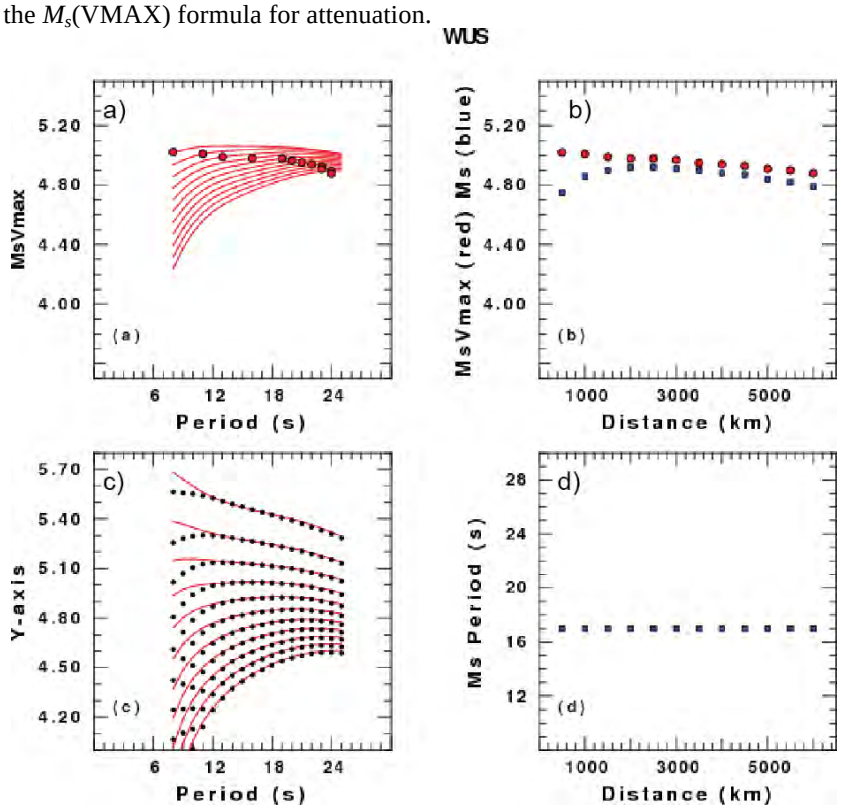


Figure 4. M_s and M_s(VMAX) processing results for the WUS model.

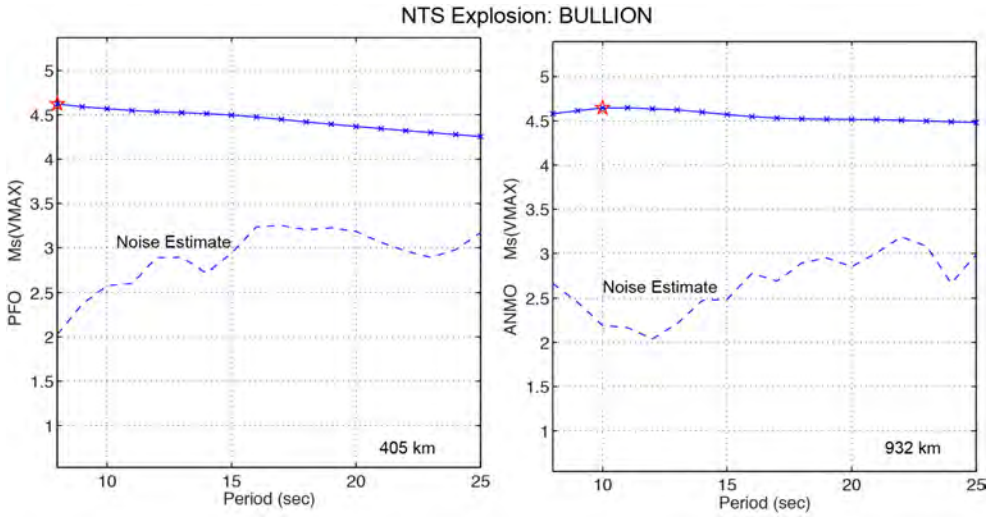


Figure 5. M_s(VMAX) processing for two stations (Pinon Flats-left; ANMO-right) that recorded the Nevada Test Site explosion BULLION. The M_s(VMAX) results suggest slightly larger magnitudes at shorter periods that synthetic results (Figure 4a) suggest is a result of the differences between the real earth attenuation and the M_s(VMAX) attenuation correction.

For example, based on the WUS model, a regionalized Q for the WUS would include a B_{att} and p of 0.0070 and 1.7, respectively, for T=8-25 s. Using the regionalized Q, the standard deviation in the final magnitudes would be reduced from 0.05 m.u. to 0.02 m.u.

Figure 6 shows the processing results for the final three models. The results show that both M_s(VMAX) and M_s have significant distance dependencies for the AK135 and Italian models. The Q values for the latter model have not been thoroughly tested. In all three models, we see a bias between M_s(VMAX) and M_s that averages ~0.1 m.u. (Figure 7) and is larger at regional distances and smaller at teleseismic distances. We note that for the Korean Peninsula model, we observe that the M_s(VMAX) magnitude "spectra" overlay one another but are not flattened. This suggests that the excitation correction could be improved for this region to better flatten the spectra. However, even with this problem, the M_s(VMAX) estimates are approximately distance-independent, whereas M_s has some distance dependence.

Earthquake Synthetics

For the second comparison of the two magnitude formulas, we synthesized earthquakes (M_w=5.0) at depths of 1, 10, 20, 30, 40, and 50 km. We considered normal (Strike 40/Dip 45/ Rake -90) and strike slip (30/90/0) fault focal mechanisms. We again used modal synthetics to synthesize fundamental-mode Rayleigh waves at distances between 500 and 6000 km; however, we varied the source-to-station azimuth from 0 to 352 as a function of distance. For example, station 1 was located at 500 km and 0 degrees azimuth, station 2 was at 1000 km at 32 degrees azimuth, station 3 was at 1500 km and 64 degrees, and this patterned continued until the final station was located at 6000 km and 352 degrees.

Figure 8 shows the results for a normal fault source generated and propagated through the CUS model at source depths ranging from 1 to 30 km. Some of the interesting features include:

- For the 1 km depth event, the scatter in the magnitudes caused by the radiation pattern is very large, with magnitudes ranging from 4.4 to 5.2. The magnitude scatter is much less for the deeper events.

- An odd effect is observed for the 10 km depth in which the M_s(VMAX) and M_s are approximately mirror images of each other. This is caused by the shape of the Rayleigh wave spectra due to a spectral hole near T=20 s for some azimuths.

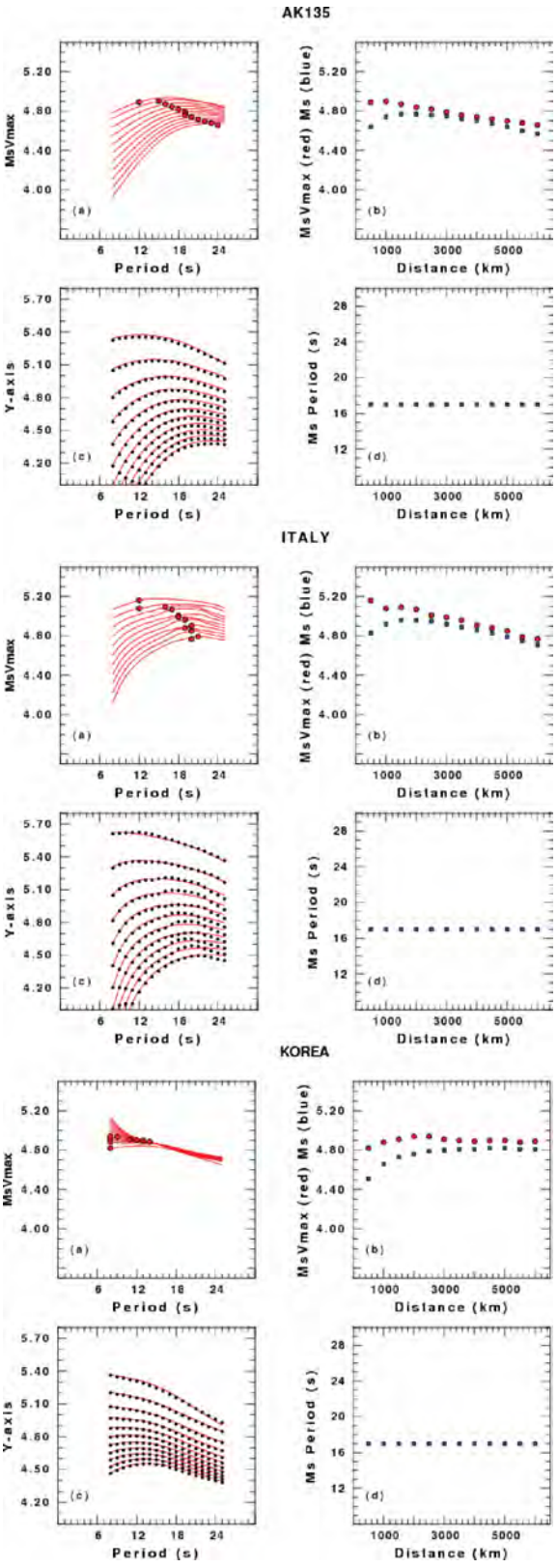


Figure 6. Processing results for the AK135, Italian, and CUS models.

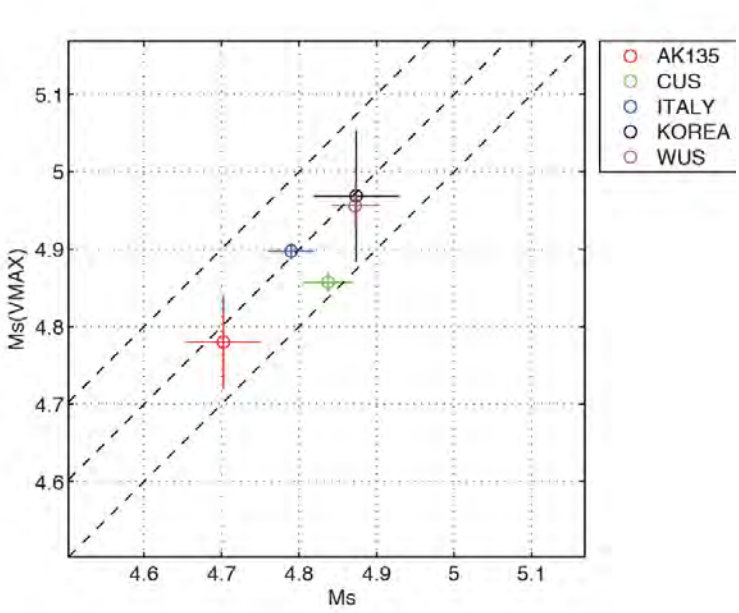


Figure 7. Bias between averaged M_s(VMAX) and M_s for explosion synthetics at distances between 500 and 6000 km for five different models. For most of the models, we observe that M_s(VMAX) is ~ 0.1 m.u. larger than the historic M_s estimates.

- When the radiation pattern effects are removed, we see a similar small distance dependent bias between M_s(VMAX) and M_s that was observed for explosions, which we believe is due to filter and excitation effects for the CUS model, while for other models, the differences can also be attributed to attenuation model mismatch.

Figure 9 shows an example where the bias between M_s(VMAX) and M_s can be significantly larger than 0.1 m.u. In this case, a 10 km deep strike slip event creates a very large spectral hole near T=16 s. M_s(VMAX) straddles this hole and choses peak amplitudes either at T=8-10 s or T=25 s period, while M_s tries to move as far away from the hole as possible at T=23 s period. The result is a 0.4 m.u. difference in the two magnitude estimates, with M_s(VMAX) providing an estimate that is much closer to the seismic moment used to generate the synthetics.

CONCLUSIONS AND RECOMMENDATIONS

We have learned several important features about M_s(VMAX) from this synthetic study. These include:

- For explosions, M_s(VMAX) is biased high by ~0.1 m.u. when compared to a historic M_s for most of the models studied in this research. For earthquakes, the bias can be significantly larger depending on depth and focal mechanism. We hypothesize that in most cases, the M_s(VMAX) provides an estimate that is closer to the true moment of the event.
- The M_s(VMAX) measurement procedure does correctly estimate the Rayleigh-wave spectra, however, the extrapolation of that spectral amplitude back to a 1 km distance for explosions could be improved with regionalized attenuation models and excitation corrections.
- Regionalized Q models will not significantly reduce the scatter for the earthquake magnitude estimates, as most of it is due to radiation pattern effects. We are investigating other methods to reduce this scatter, which include using both the Rayleigh and Love waves in a combined magnitude.
- In most cases, we see only a small distance dependent bias between M_s(VMAX) and M_s, thus, we recommend using a simple bias correction of 0.1 m.u. since we believe that we have isolated the cause in terms of Q effects, filter effects, and excitation.

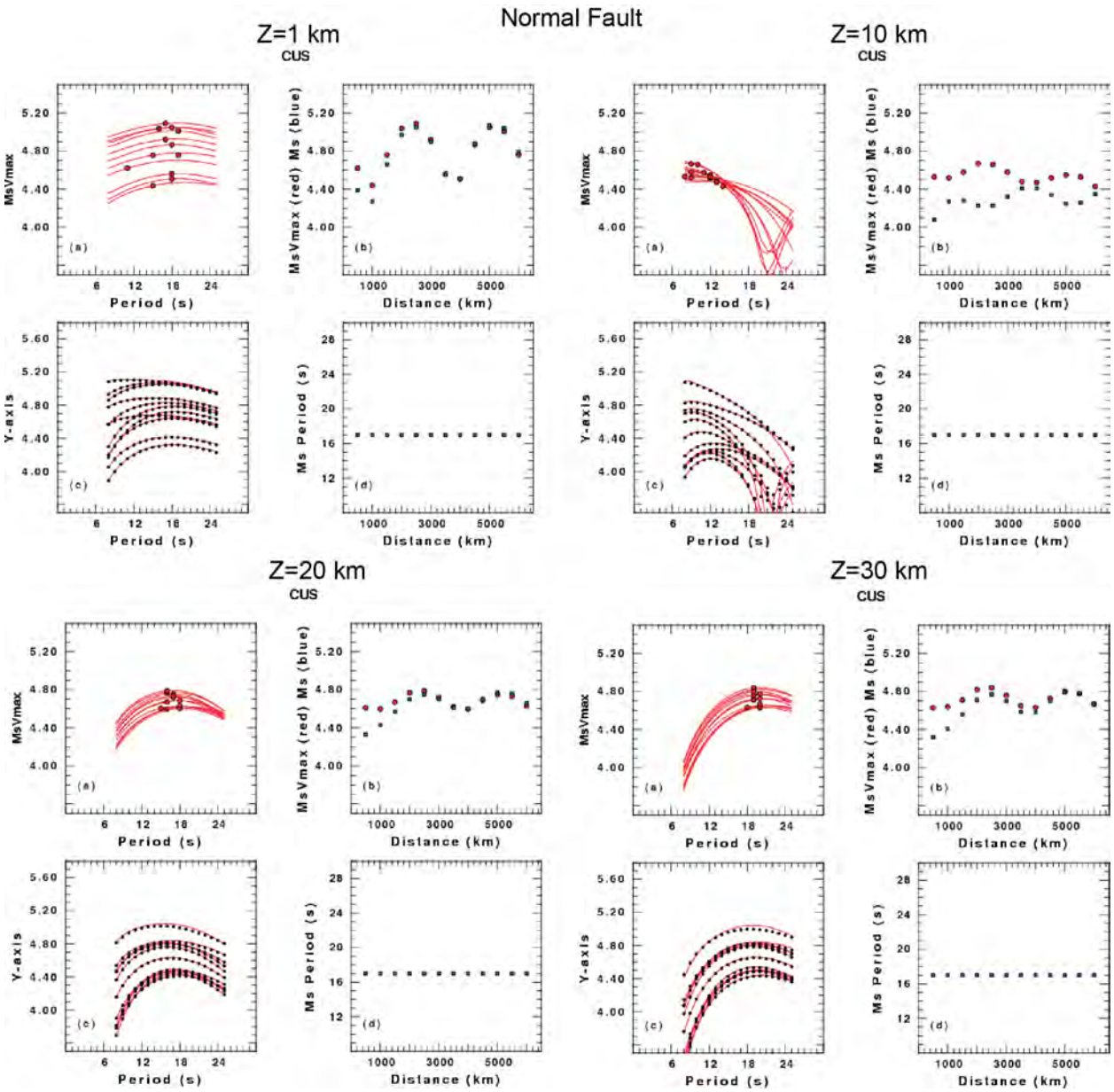


Figure 8. M_s and M_s(VMAX) processing results for a normal fault earthquake in the CUS model at depths of 1 km, 10 km, 20 km, and 30 km.

REFERENCES

Bonner, J. L., D. Russell, D. Harkrider, D. Reiter, and R. Herrmann, (2006). Development of a Time-Domain, Variable-Period Surface Wave Magnitude Measurement Procedure for Application at Regional and Teleseismic Distances, Part II: Application and M_s—m_b Performance. *Bull. Seismol. Soc. Am.* **96**, 678–696.

Cho, K. H., R. B. Herrmann, C. J. Ammon, and K. Lee (2007). Imaging the upper crust of the Korean peninsula by surface-wave tomography, *Bull. Seismol. Soc. Am.* **97**, 198-207.

Herrmann, R.B. (1973). Some aspects of band-pass filtering of surface waves. *Bull. Seismol. Soc. Am.* **63**, 663–671.

Herrmann, R. B., and B. J. Mitchell (1975). Statistical analysis and interpretation of surface wave anelastic attenuation data for the stable interior of North America, *Bull. Seismol. Soc. Am.* **65**, 1115–1128.

Herrmann, R. B. (2004). *Computer Programs in Seismology*. St. Louis University.

Herrmann, R.B., H. Benz, and C.J. Ammon (2011). Monitoring the earthquake source process in North America. *Bull. Seismol. Soc. Am*. **101**, 2609–2625.

Kennett, B.L.N. Engdahl, E.R. & Buland R., (1995). Constraints on seismic velocities in the Earth from travel times, *Geophys J Int*, **122**, 108–124

Russell, D.R., (2006). Development of a time-domain, variable-period surface wave magnitude measurement procedure for application at regional and teleseismic distances. Part I—Theory. *Bull. Seismol. Soc. Am*. **96**, 665–677.

von Seggern, D., (1977). Amplitude distance relation for 20-Second Rayleigh waves. *Bull. Seismol. Soc. Am.* **67**, 405–411.

Vaněk, J., A. Zatopek, V. Karnik, Y.V. Riznichenko, E.F. Saverensky, S.L. Solov'ev, and N.V. Shebalin, (1962). Standardization of magnitude scales. *Bull. (Izvest.) Acad. Sci. U.S.S.R., Geophys. Ser.* **2**, 108.

Yacoub, N. K. (1983). "Instantaneous Amplitudes": a new method to measure seismic magnitude, *Bull. Seismol. Soc. Am.* **73**, 1345–1355.

Yacoub, N.K. (1988). Maximum spectral energy for seismic magnitude estimation. Part I: Rayleigh-wave magnitude.

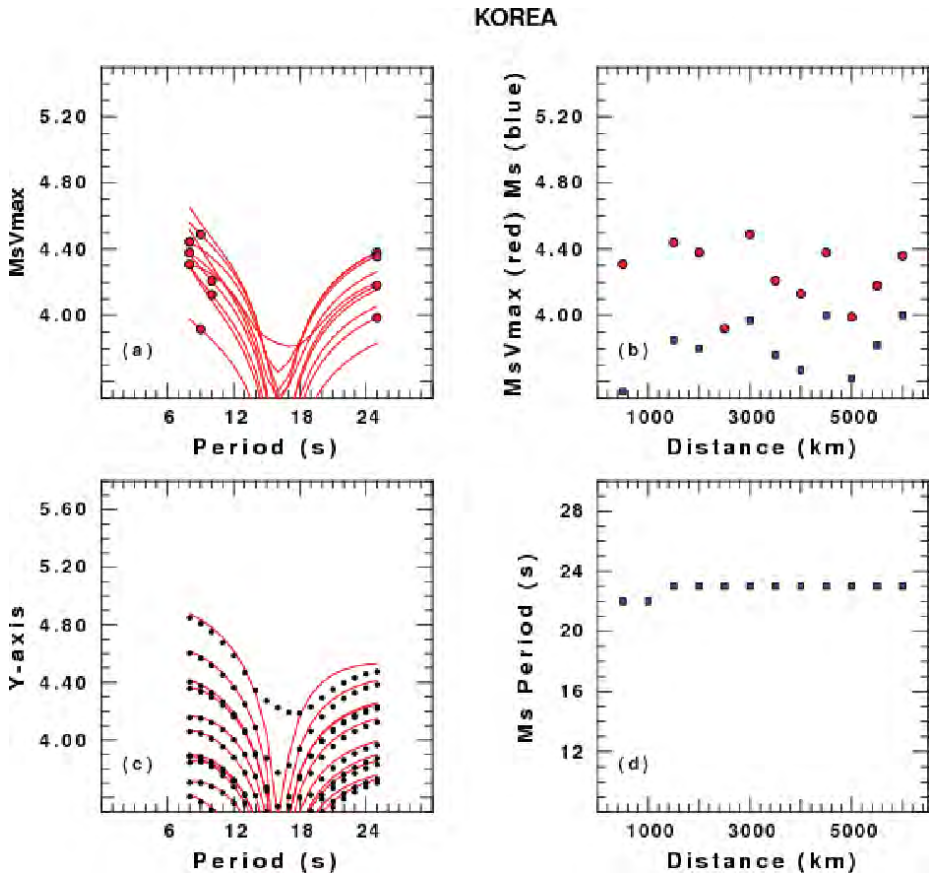


Figure 9. M_s and M_s(VMAX) processing results for a strike-slip fault earthquake in the Korean Peninsula model at depths of 10 km.

APPENDIX: Correction in narrow band historic M_s formula

Yacoub's (1988) fundamental method is to calculate a spectral amplitude in the frequency domain using a Gaussian filter of the form $exp[-c(\omega-\omega_0)^2]$, FFT it back to the time domain, and insert the maximum envelope amplitude into a standard magnitude formula such as von Seggern (1977). The problem with this direct approach to utilizing the spectral magnitude is that it does not modify the standard magnitude formula to account for the Gaussian filter, in that it has no correction for the filter value "*c*" in the standard magnitude formula. Newer results using equivalent Butterworth filters in M_s(VMAX) correct for the filter width in the final magnitude formula by the term $\log(f_c)$, where f_c the one-sided width of the Butterworth filter. That this can cause significant errors can be easily seen by putting a very large value of *"c"* in the Gaussian, which would result in a vanishing small time domain maximum. The actual error is a complicated term, but it can be analytically calculated for typical crustal structures as shown below.

Following (Russell, 2006), a dispersed surface wave can be mapped from the frequency to time domain using

$$a = A/\sqrt{\pi\alpha} \tag{A1}$$

Where *A* is the frequency domain amplitude, *a* is the time domain amplitude and

$$\alpha = \frac{x}{4\pi}\frac{T^2}{U^2}\frac{dU}{dT} \tag{A2}$$

x=epicentral distance (km), *T*=period of interest (sec), *U*= group velocity at period *T* (km/sec), and *dU/dT*=derivative of group velocity with respect to period, evaluated at period *T* (km/sec^2). If the same signal is filtered with a sufficiently narrow Gaussian bandpass filter of the form $exp[-c(\omega-\omega_0)^2]$, it can be mapped from the frequency to time domain using

$$a_f = A/\sqrt{\pi c} \tag{A3}$$

"Sufficiently" means that $c > \alpha$, that is, the Gaussian filter is narrower than the earth's dispersion filter coefficient α in (A2), thus (A3) controls the process. To transform the unfiltered time domain amplitude in (A1) to the filtered amplitude in (A3), equate frequency domain amplitudes *A* for

$$a_f = \sqrt{\alpha/c}\, a \tag{A4}$$

Substituting into (A4) the expanded value for α in (A2) gives

$$a_f = \sqrt{\frac{x}{4\pi c}\frac{T^2}{U^2}\frac{dU}{dT}}\, a \tag{A5}$$

In Yacoub (1988), he references his earlier paper (Yacoub, 1983) for the exact form of the exponential filter he is using, which follows Herrmann (1973):

$$H = exp\left[-c'\left(\frac{\omega-\omega_0}{\omega_0}\right)^2\right] \tag{A6}$$

where c' is now normalized to ω_0^2, and therefore $c = c'/\omega_0^2 = c'T^2/(4\pi^2)$. Substitute into (A5) and rearrange for

$$a_f = \sqrt{\frac{\pi}{c'U^2}\frac{dU}{dT}}\, x\, a \tag{A7}$$

Herrmann (1973) recommends a value of $c' = 16\pi = 50.27$, which Yacoub (1983, 1988) uses. Notice in this case that the width of the Gaussian filter is inversely proportional to the square of the period *T*, but not to the distance *x*. In the derivation for *Ms*(VMAX) (Russell, 2006) the equivalent Butterworth filter used has a bandwidth inversely proportional to both period and distance, i.e., $f_c \propto 1/(xT)$, where the constant of proportionality is calculated to

ensure that the filter bandwidth is always less than the earth dispersion bandwidth. Substituting $c' = 16\pi$ into (A7) gives

$$a_f = \frac{1}{4U}\sqrt{\frac{dU}{dT}x}\,a \tag{A8}$$

For a typical continental crust (Russell, 2006), at T=20 sec let U=2.9 km/sec, and dU/dT= 0.02 km/sec^2 in (A8) for

$$a_f = (0.0122\sqrt{x})\,a \tag{A9}$$

Equation (A9) can now be used to determine the effect of using filtered amplitudes in standard magnitude dispersion curves. Notice that in (A9), at a distance of x=6730 km, $a_f = a$, which means that beyond this point the Gaussian filter has a filter bandwidth greater than the earth dispersion filter and no longer controls the maximum amplitude. Equation (A9) no longer applies for distances beyond this point, for the particular crustal and period values used. However, for distances less than 6730 km, an error will be introduced into standard magnitude formulas due to not correcting for the bandwidth in the formula, as will be shown below.
Yacoub (1988) takes the filtered amplitudes and directly inserts them into a time domain magnitude formula of the form:

$$M_s = \log\left(\frac{a}{T}\right) + F(x,T) \tag{A10}$$

The reason to use this general formula is to show that the error does not depend on the explicit form of the magnitude formula, as long as the measured amplitude enters only into the first log term. Substituting the filtered amplitude (A9) into (A10) gives:

$$M_s = \log\left(0.0122\sqrt{x}\frac{a}{T}\right) + F(x,T) \quad = \quad \log\left(\frac{a}{T}\right) + F(x,T) + \frac{1}{2}\log(x) - 1.914 \tag{A11}$$

Thus, for the period and crustal parameters used, there is an error introduced of

$$Error = \frac{1}{2}\log(x) - 1.914 \tag{A12}$$

Notice that in (A12), closer epicentral distances mean larger errors. Notice also that the error is independent of the particular event magnitude. Figure A1 shows the error as a function of distance, for Gaussian filters, 20 sec periods, and a typical continental crust. Yacoub (1988) noted that he found an average decrease in his spectral amplitudes of 0.17 magnitude units for all station distances used in his NTS teleseismic study, which is consistent with these results. Subtracting Equation (A12) from the historical magnitude formula will correct it for the width of the Gaussian filter.

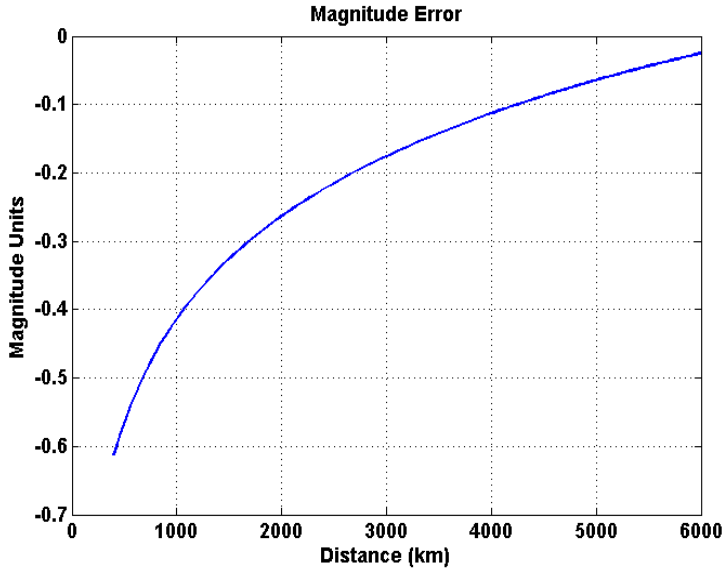


Figure A1. Magnitude errors as a function of distance due to Gaussian filter methods.

REFINEMENT OF REGIONAL DISTANCE SEISMIC MOMENT TENSOR AND UNCERTAINTY ANALYSIS FOR SOURCE-TYPE IDENTIFICATION

Douglas S. Dreger[1], A. Chiang[1], S. R. Ford[2], and W. R. Walter[2]

Berkeley Seismological Laboratory[1] and Lawrence Livermore National Laboratory[2]

Sponsored by the Air Force Research Laboratory

Award No. FA9453-10-C-0263
Proposal No. BAA10-76

ABSTRACT

Previous efforts (Dreger et al., 2008; Ford et al., 2010; Ford et al., 2009a, b; Ford et al., 2008) demonstrated that regional distance moment tensor analysis can discriminate explosions from naturally occurring earthquakes and mine collapses. In this project, as an effort to refine procedures for implementation we develop a more complete understanding of uncertainties, and define robust methods for their characterization. In Ford et al., 2008 it was found that populations of explosions, earthquakes and collapses separated well on a Hudson (1989) diagram enabling source-type discrimination. We have published a paper combining regional waveform and teleseismic P-wave polarity data to better constrain the source-type sensitivity for the 2009 North Korean nuclear test (Ford et al., 2012). This approach removes the isotropic-CLVD tradeoff, and results in unique discrimination of the event as an explosion. A question the current research addresses is whether source-type populations remain separated in other regions of the world, as is the case for NTS and western US seismicity. We have compiled a database of naturally occurring, and induced seismicity to examine the distribution of non-double-couple seismic moment tensors in a Hudson source-type diagram to be used as an a priori constraint on the complementary probability distribution of an explosion. In addition, we have computed full moment tensor solutions on 877 events in the Berkeley Seismological Laboratory catalog.

The results show that the explosion and large negative CLVD region, typical for explosions, is a low probability region for natural, and even induced seismicity. We have evaluated the significance of full moment tensor solutions for the Berkeley catalog with respect to deviatoric moment tensor solutions using the F-test. These results indicate that only 20 of the events have statistical significance above 90%, and that the vast majority of events (97.7%) are best characterized as deviatoric without a volumetric term. Of the 20 events with F-test statistical significance above 90% only 7 have statistical significance above 98%. These events occur in the Long Valley Caldera and the Geysers geothermal field where events with large positive volumetric components have been well constrained. We are continuing to investigate the velocity model dependence of vanishing free-surface traction effects on seismic moment tensor inversion of shallow sources. Our synthetic data tests indicate that biases for shallow sources are small and can be understood in a systematic manner. We will present the frequency dependence of vanishing traction for a very shallow (10m depth) explosion recorded at several km distance. Scalar moment and moment tensor element biases, and the ability to uniquely discriminate the event as an explosion will be evaluated. Finally, we are working toward extending the regional seismic moment tensor database for nuclear explosions and natural seismicity for Kazakhstan.

OBJECTIVES

In this project we build on our earlier results (Dreger et al., 2008; Ford et al., 2010; Ford et al., 2009 a,b; Ford et al., 2008) to investigate whether source-type populations (explosion, collapse, earthquakes) that were found to separate for the Western US remain separated for other regions of the world. We expand the database of studied events to include natural and man-made seismicity from the Korean Peninsula, Kazakhstan, Middle East, and European Arctic. In each region we apply regional distance seismic moment tensor analysis, investigating aleatoric and epistemic (velocity model and network configuration) uncertainties. This regional characterization and the resulting moment tensor database are necessary steps in order to form a regional moment tensor decision basis for source-type identification and discrimination.

RESEARCH ACCOMPLISHED

Introduction

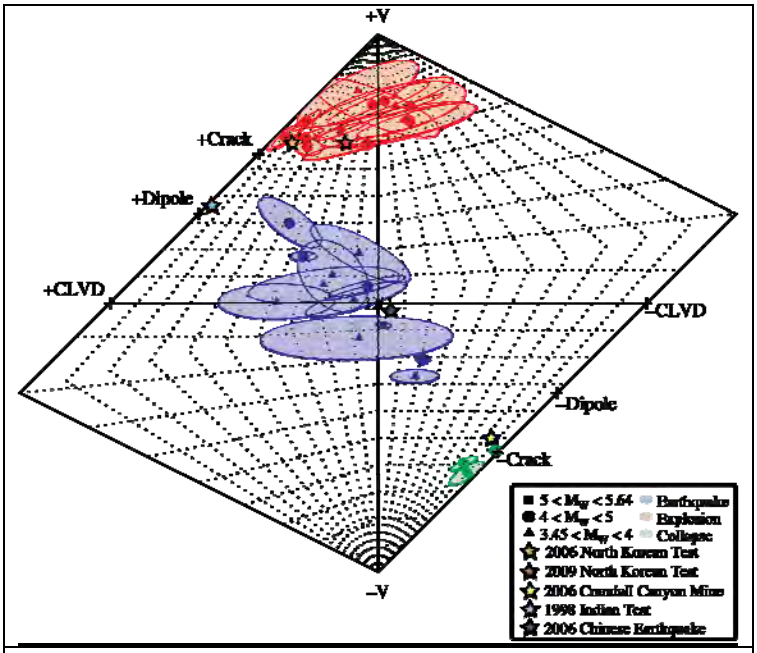


Figure 1. Compilation of regional moment tensor results for western US earthquakes, nuclear explosions, mining collapses, and the North Korean and Indian nuclear explosions. Modified from Ford et al. (2009a).

Ford et al. (2009a) calculated seismic moment tensors for 17 nuclear test explosions, 12 earthquakes, and 3 collapses in the vicinity of the Nevada Test Site in the Western US. They found that the relative amount of isotropic and deviatoric moment provided a good discriminant between the explosions, earthquakes and collapses (Figure 1). As shown in Figure 1, the different source type populations separate, enabling seismic moment tensor based discrimination. Importantly, the populations of explosions and cavity collapses separate dramatically whereas in traditional mb:MS and regional phase P/S ratio discriminants this separation is less clear (e.g., have inconsistent results (Walter et al., 2007)). Previously we have reported on methods (NSS, Ford et al., 2010) to capture solution dependence on station configuration, data bandwidth, and signal-to-noise ratio (SNR).

In this report we present efforts to move regional distance moment tensor analysis towards a more structured decision basis. One such effort has been the augmentation of earthquake and explosion catalogs to obtain better constraints on the distributions of the two populations of seismic events. Another effort has been to test a P-value decision basis utilizing the two moment tensor source type parameters -T=-2ε (deviation from a double-couple), and κ (strength of the volumetric component) (e.g., Hudson et al., 1989).

We have begun our analysis of seismic events in the Kazakhstan region, identifying several events for preliminary moment tensor analysis, and velocity model calibration work. Figure 2 shows a map of the region and regional broadband stations. The region around the Semipalatinsk test site is relatively well covered by modern instrumentation. We will model recent events in this region to verify, and calibrate seismic velocity structure to improve sparse network moment tensor capabilities. We are also investigating

the level of bias in isotropic and non-dc moment tensor solutions due to the sparse recording geometry and the assumed velocity models.

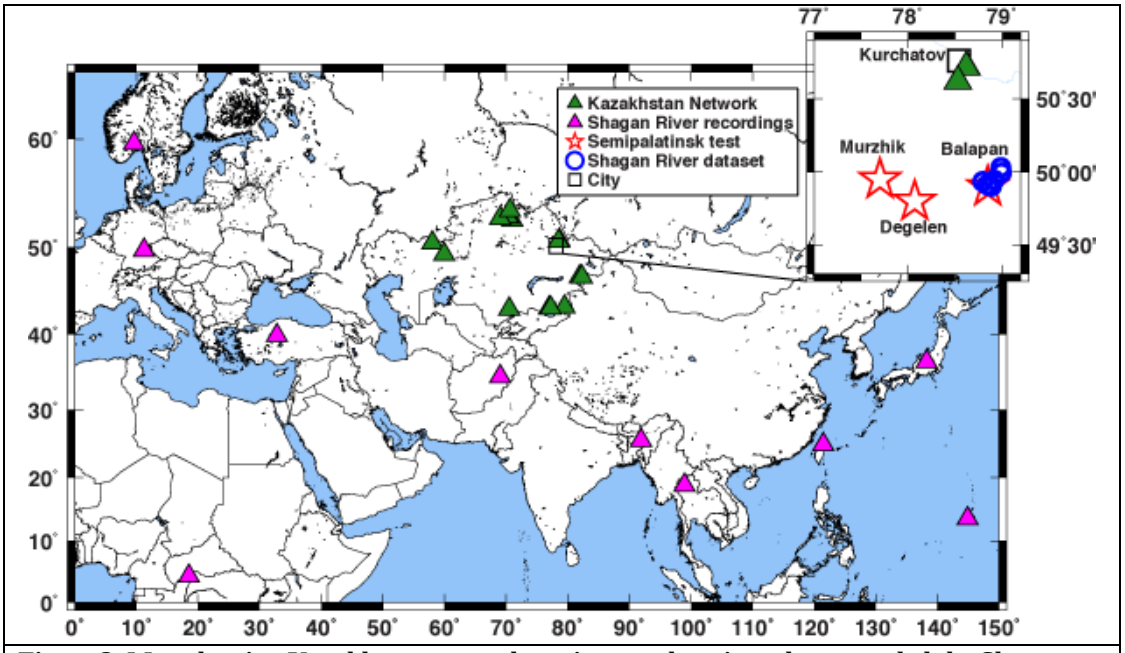


Figure 2. Map showing Kazakhstan network stations, and stations that recorded the Shagan River tests. The Semipalatinsk tests are shown as red stars, and the Shagan River tests are data that will be investigated.

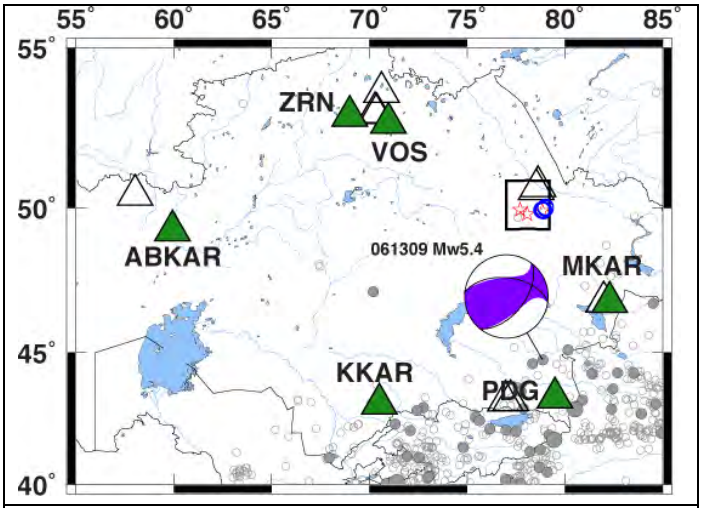


Figure 3. Regional map showing the locations of the Semipalatinsk test (red stars), natural seismicity (gray circles), broadband stations with high quality waveform data (green triangles), and the GCMT moment tensor solution.

Figure 3 shows a regional map and the location of a Mw 5.4 event that we are analyzing. Although there are problems with the data at some stations due to saturation or other system problems there are high quality broadband records at a sufficient number of stations to recover the seismic moment tensor solution. The focal mechanism shown in Figure 3 is from the GCMT catalog, and is used as a reference.

A suite of possible velocity models have been compiled and tested, however it was found that additional waveform modeling was needed to better constrain the structure for the purpose of computing long-period seismic moment tensors.

Using Green's functions computed for the refined velocity model moment tensor solutions for a June 13, 2009, Mw 5.4 event were computed using two stations PDG and VOS located 161 and 1063 km from the event, respectively. We are in the process of improving the velocity structure for paths to stations KKAR and ABKAR.

Figure 4 shows the moment tensor results. The velocity data have been first instrument corrected, integrated to displacement, and then bandpass filtered between 0.02 to 0.05 Hz using an acausal, 4-pole Butterworth filter. Using data from two stations, PDG and VOS, a solution is found that is consistent with the GCMT solution (Figure 3) in terms of the focal parameters and scalar seismic moment. As Figure 4 shows the solution is dominantly double-couple in nature. When the full moment tensor solution is solved for a negligible isotropic component is found that does not appreciably improve the fit, and the solution remains dominantly double-couple with a small –CLVD. This is an important result showing that a false isotropic bias is not introduced due to the very sparse station coverage and imprecise velocity model.

This one sparse network example is very promising, however there is additional work that is needed to further refine velocity structure in the region, obtain verifiable solutions for more earthquakes, and to extend the analysis to the large distances, and more sparse network configurations for the analysis of the Semipalatinsk tests. We will present this modeling on our MRR poster.

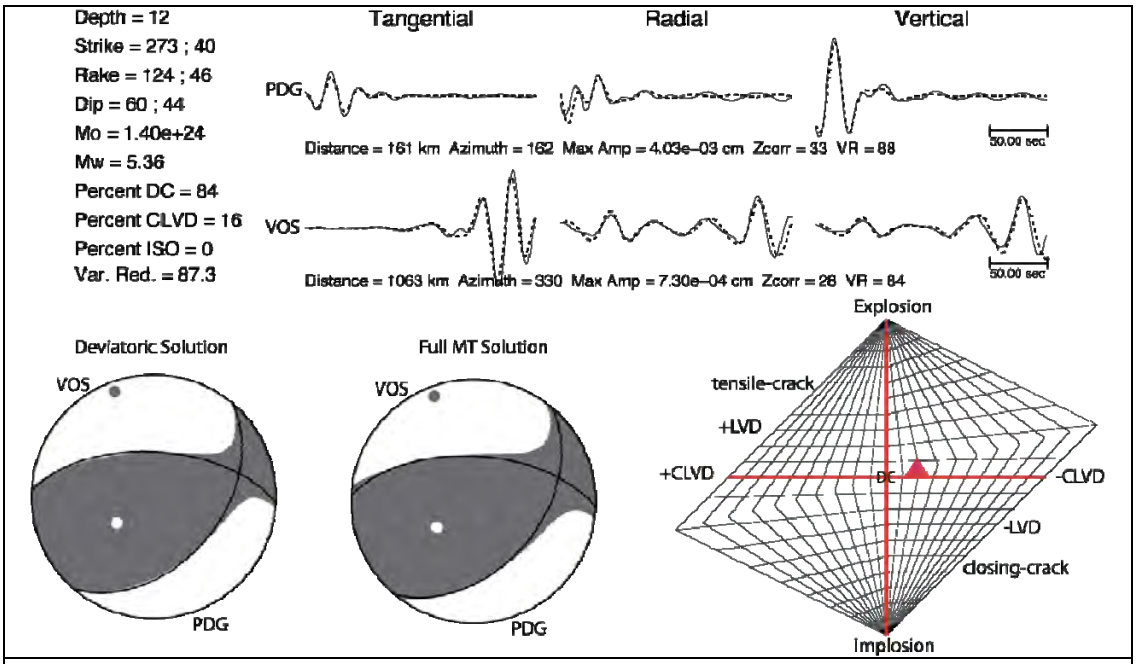


Figure 4. Moment tensor solution for the June 13, 2009 event. The deviatoric solution obtained from the two stations, VOS and PDG is very similar to the GCMT catalog solution. The full moment tensor solution results in a small isotropic component and the source type diagram shows the solution is dominantly double-couple.

Moment Tensor Analysis of the 1988 Joint Verification Experiment

We have applied the techniques from Ford et al. (2009 a, 2010, 2012) to the September 14, 1988, Joint Verification Experiment test at Semipalatinsk. Four intermediate period stations, BAY and KKL (part of the JVE deployement; Priestly et al., 1990), BRVK (a former Soviet STsR-SS station), and WMQ (China Digital Seismic Network, CDSN) were used in the analysis. The distances range from 255 to 953 km. Green's functions were computed with velocity models calibrated by Walter and Ammon (1993) assuming a source depth of 1 km. The three-component waveforms from each station were instrument corrected and bandpass filtered to maximize signal to noise given the bandwidth characteristics of each instrument. BAY and KKL were filtered between 0.05 to 0.08 Hz with a causal Butterworth filter. BRVK was filtered between 0.033 to 0.08 Hz with an acausal Butterworth, and WMQ was filtered between 0.02 to 0.05 Hz with an acausal Butterworth filter. Figure 5 shows the moment tensor results indicating a predominantly explosive moment tensor with a deviatoric component comprised of a near-vertically oriented CLVD in tension. This secondary CLVD is consistent with the model of Patton and Taylor (2008).

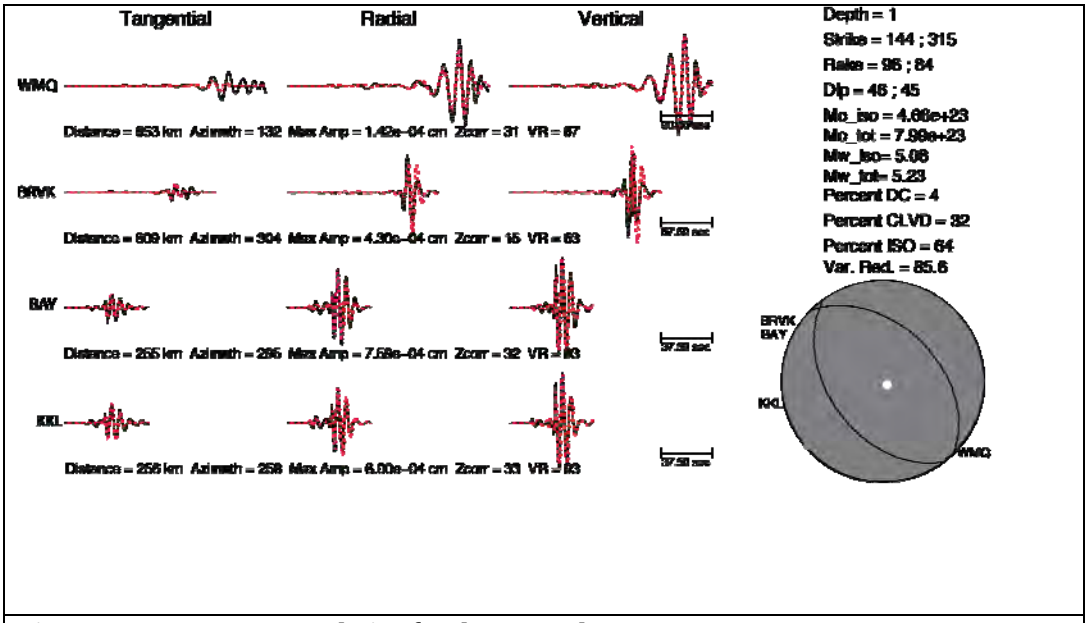


Figure 5. Moment tensor solution for the September 14, 1988, JVE.

A best fitting pure double-couple solution fits the data at 76.7%, whereas the best deviatoric moment tensor fits at 82.0% and the full moment tensor solution shown in Figure (5) fits at 85.6%. The NSS shown in Figure 6 is consistent with distributions obtained for NTS explosions (Ford et al., 2010) and the 2009 DPRK test (Ford et al., 2012). The P-wave focal mechanisms for the best full moment tensor and deviatoric moment tensor are compared to observed first-motion polarities from the regional stations and the Adirondack Array (Battis and Cipar, 1991). The positive polarity of all P first motions are in conflict with the deviatoric solution. In Figure 7 we show the waveform NSS results (Figure 6) filtered by the first motions. For this composite waveform, first motion NSS the variance reduction distribution for each data set were normalized to their maximum values, and then in Figure 7 the product of the two is plotted. The combined intermediate period waveforms and first motions uniquely discriminate this event as an explosion. This is the same behavior that was found for the 2009 DPRK test (Ford et al., 2012).

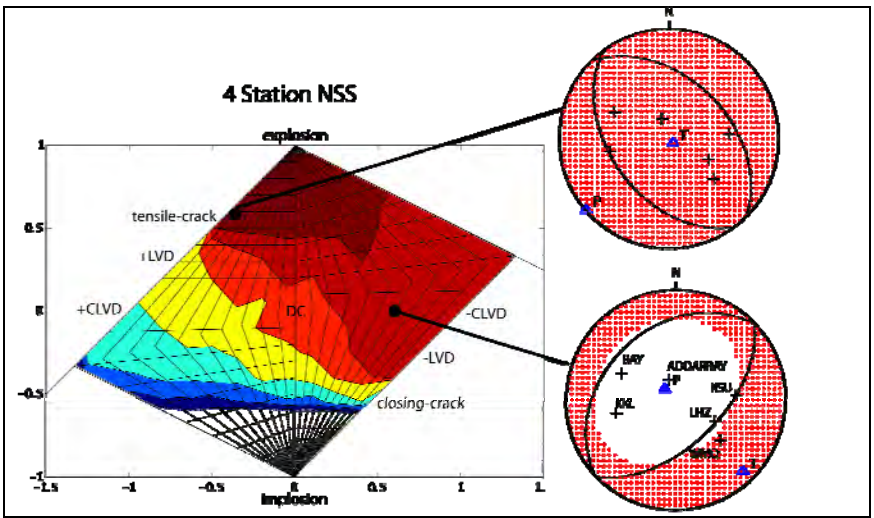


Figure 6. NSS formed from 20 million moment tensors. The shading from blue to dark red is 50, 60, 70, 80, 90, 95 and 98% of the best fitting solution.

The best fitting full moment tensor solution results in a K=2.6, where K is defined following Patton and Taylor (2011). This value indicates a strong tectonic release consisting of a vertical CLVD in tension resulting from tensile damage above the shot point. The large value for K is consistent with other Semipalatinsk explosions, some of which have K large enough where the tensile CLVD results in reversed

polarity Rayleigh waves
(e.g., Patton and Taylor, 2008).

At the MRR we will present solutions for different subsets of data to evaluate how robust discrimination is under very sparse conditions, as well as an analysis of other Shagan River tests.

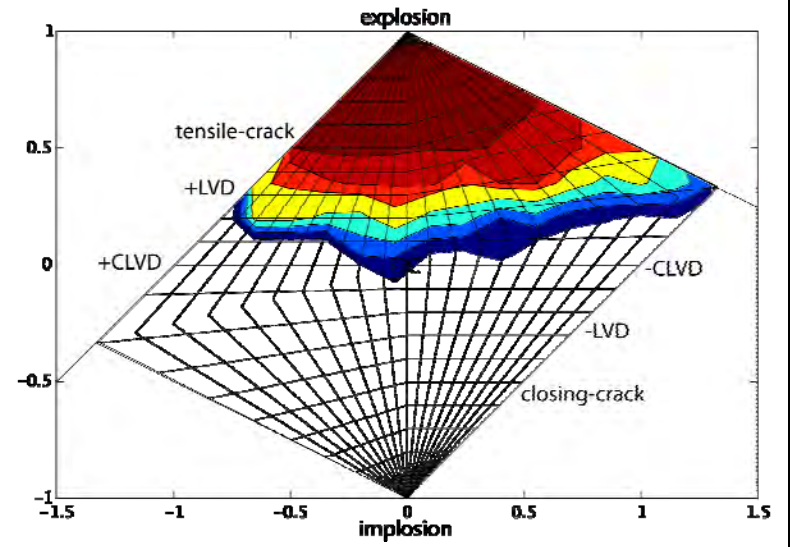


Figure 7. The NSS shown in Figure 6 for the 1988 JVE at Shagan River is modulated (or filtered) by P-wave first motion observations. The explosion source is uniquely discriminated.

Full MT Analysis of the Berkeley Moment Tensor Catalog

We have compiled a database of naturally occurring, and induced seismicity to examine the distribution of non-double-couple seismic moment tensors in a Hudson source-type diagram to be used as an a priori constraint on the complementary probability distribution of an explosion as was reported last year (Dreger et al., 2011). In addition, we have computed full moment tensor solutions for 877 events in the Berkeley Seismological Laboratory (BSL) catalog (Figure 8a). These solutions have all been reviewed and are of the highest quality. Figures 8b and 8c shows the distributions on the x-axis (deviatoric axis) and y-axis (volumetric axis). The mean is T=-0.00544 and κ=0.03499 essentially a double-couple, and the data is normally distributed. The results show that the explosion and large positive CLVD area of the source-type diagram, typical for explosions, is a low probability region for natural, and as shown at the 2011 MRR (Dreger et al., 2011) even for induced seismicity. For the BSL catalog we have evaluated the significance of improved fit of full moment tensor solutions compared to deviatoric moment tensor solutions using the F-test. These results indicate that only 20 of the events have statistical significance above 90%, and that the vast majority of events (97.7%) are best characterized as deviatoric without a volumetric term. Of the 20 events with F-test statistical significance above 90% only 7 have statistical significance above 98%. These events occur in the Long Valley Caldera and the Geysers geothermal field where events with large positive volumetric components have been well constrained (e.g., Dreger et al., 2000; Ross et al., 1999).

The P-value is a statistical significance test to evaluate observations against a null hypothesis (Anderson et al., 2007). Here our analysis makes use of the two source type parameters T, and κ (Hudson et al., 1989). Our null hypothesis is that observations of T and κ are consistent with an explosion.

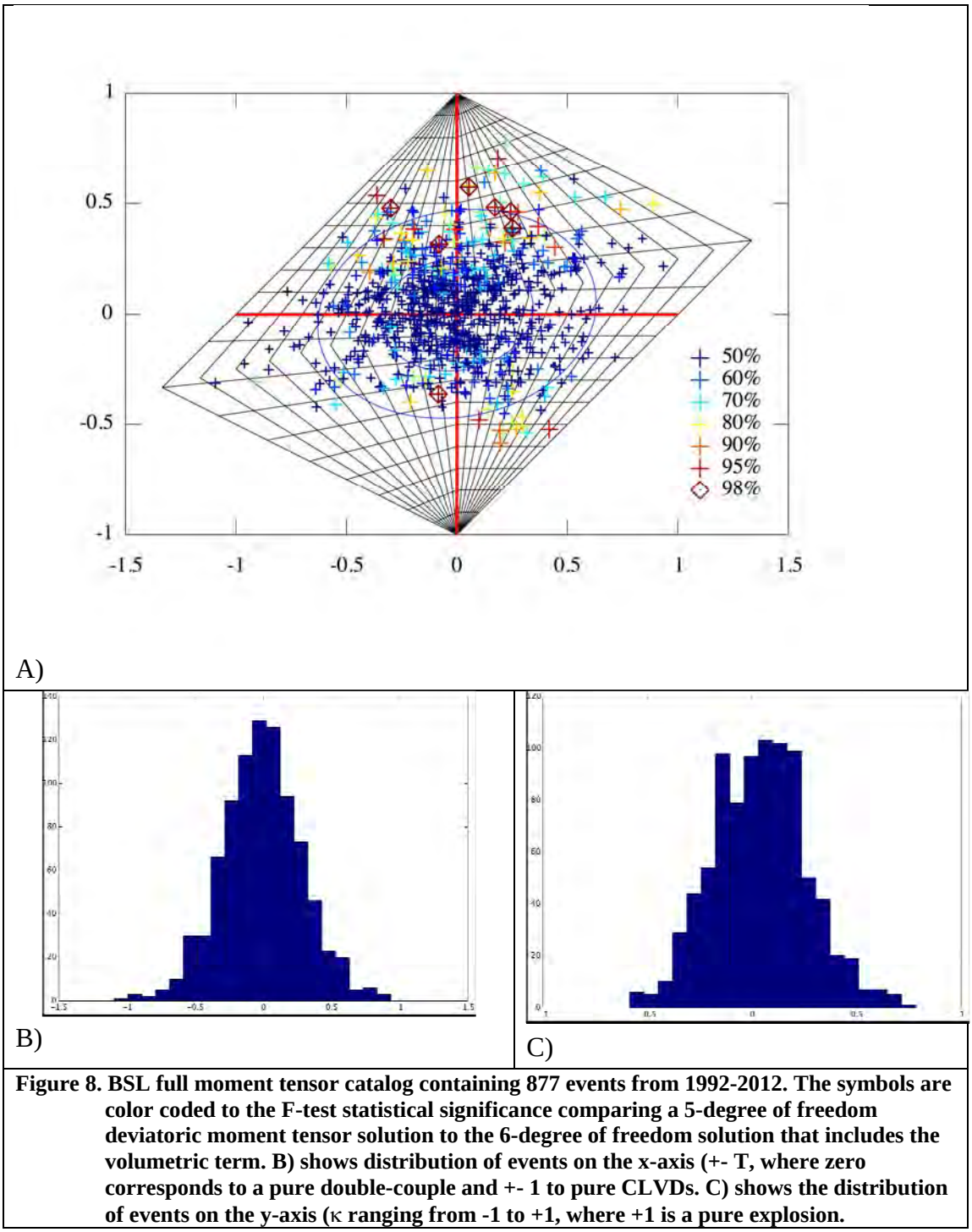


Figure 8. BSL full moment tensor catalog containing 877 events from 1992-2012. The symbols are color coded to the F-test statistical significance comparing a 5-degree of freedom deviatoric moment tensor solution to the 6-degree of freedom solution that includes the volumetric term. B) shows distribution of events on the x-axis (+- T, where zero corresponds to a pure double-couple and +- 1 to pure CLVDs. C) shows the distribution of events on the y-axis (κ ranging from -1 to +1, where +1 is a pure explosion.

To construct our test we make use of the distribution of T and κ for NTS nuclear explosions from Ford et al. (2009 a). We also determine the distribution of T and κ for a population of earthquakes. For this initial effort we use the Berkeley Seismological Laboratory (BSL) moment tensor catalog (Figure 8a). In future work we will incorporate additional T and κ data for earthquakes from other suitably well determined catalogs. These catalogs can be regionally defined taking unique aspects of background natural seismicity into account. There are two components to the test. One is a test for evidence rejecting an earthquake null hypothesis, and the other is evidence rejecting an explosion null hypothesis. These tests are combined by

considering the product of the P distribution for the explosion null hypothesis and the complement of the P distribution for the earthquake null hypothesis. Thus the test is for evidence of an event not being an explosion, and being consistent with the earthquake distribution. This P distribution is shown in Figure 9. Small values of P reject the explosion null hypothesis, whereas large values reject the earthquake null hypothesis and are consistent with an explosion null hypothesis.

As Figure 9 shows only a few earthquakes plot in the region of relatively high P-value for explosion evidence, and only 6 for P-value>0.5. Thus 6 out of 877 (0.68%) test potentially high as an explosion, however only two of these have F-test significance that would indicate that the isotropic component is resolved. These two events occurred in the Geysers geothermal field where events with isotropic components have been previously observed (e.g., Ross et al., 1999), and our own studies of moment tensors in the region indicate the presence of statistically significant positive isotropic components. There are other Geysers and Long Valley events that have relatively large isotropic components (the other red plusses) however they plot significantly outside the explosion P-value region.

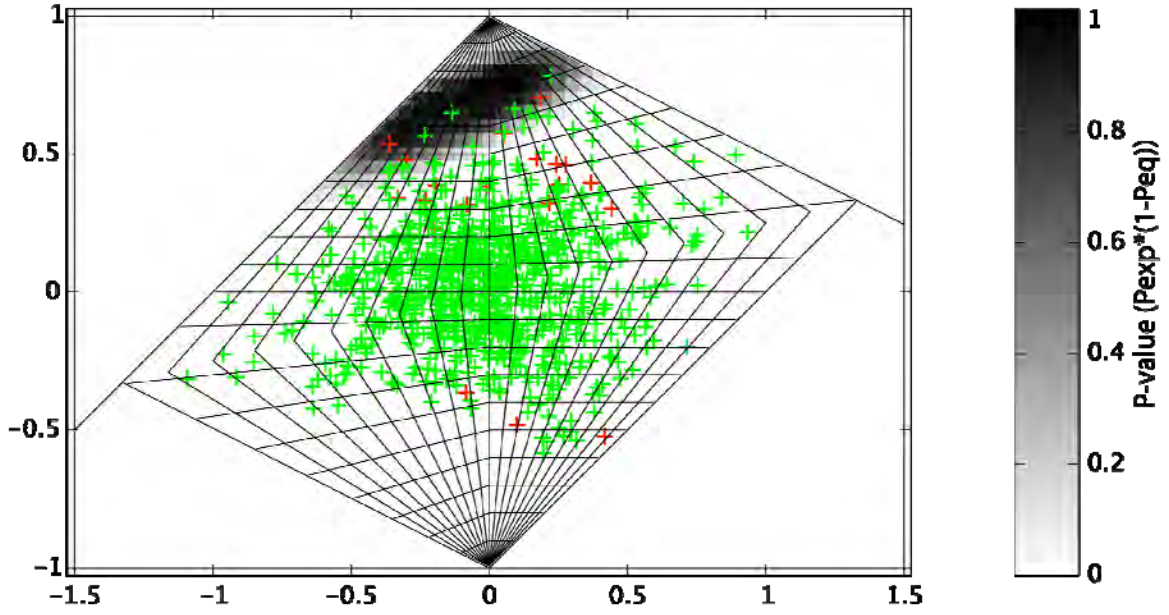
Figure 9b compares the explosion dataset to the composite P-value test. The green plusses are the NTS events used to determine the source type distributions for the P-value analysis, and the colored squares are test events that include the 1988 JVE (Figure 5), 1998 India, 2006 and 2006 DPRK nuclear tests, and a fifth shallow industrial explosion. All of the events discriminate except for the 1998 India test. It is notable, however that the India explosion when tested as an earthquake also falls outside that P-value distribution indicating that this event is classified as inconsistent with both earthquake and explosion hypotheses, thus flagging it for further analysis.

CONCLUSIONS AND RECOMMENDATIONS

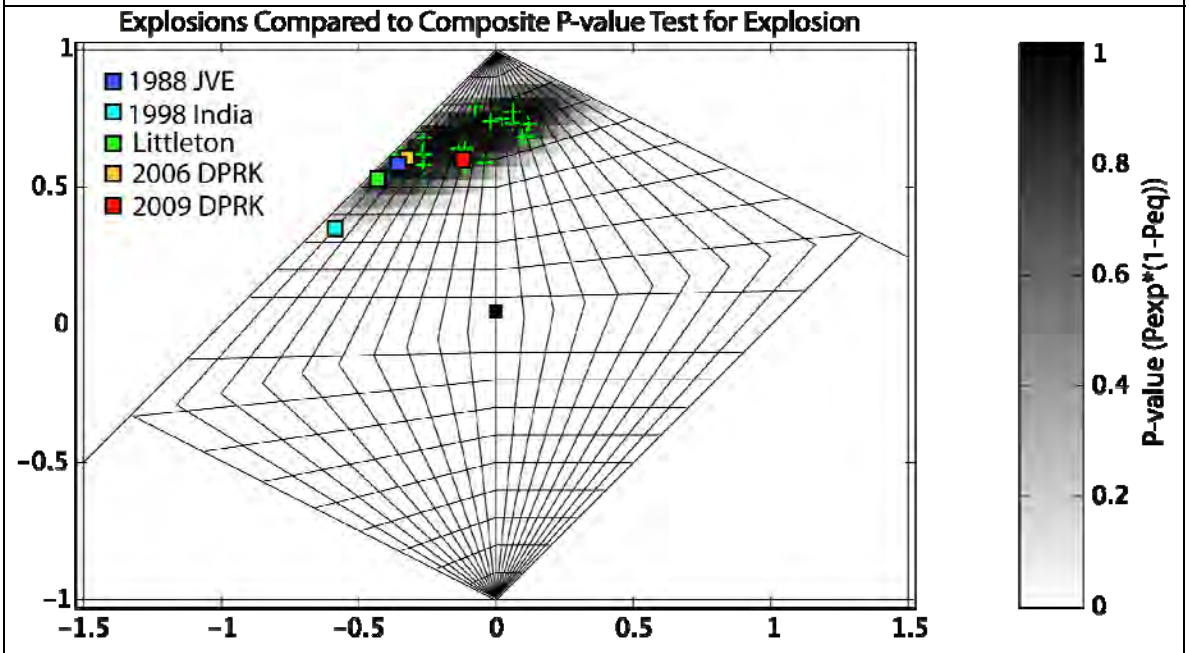
We have begun to expand the database of full moment tensor solutions for earthquakes and explosions. The applications in Kazakhstan show that with suitably well-calibrated velocity structure it is possible to obtain robust estimates of moment tensors for both earthquakes and explosions, where in the former little false isotropic bias is introduced. Effort needs to be focused on expanding earthquake and reference explosion moment tensor catalogs for different regions.

We have shown that under sparse monitoring conditions at regional distances with intermediate period complete wavefields in combination with the use of robust estimates of first motion polarity that the tradeoff between explosion source models and the negative CLVD, particularly a CLVD with a vertically oriented major vector dipole in compression, is eliminated leading to unique discrimination of events as explosions. More effort is needed to determine optimal fitting parameters and functions when combining intermediate period waveform and first motion data.

We have shown that preliminary treatment of the seismic moment tensor based discrimination problem using a P-value formulism results in discrimination of test events. Efforts need to be directed to study natural seismicity that might locate close to distributions of source-type parameters for explosions (e.g., the Geysers and Long Valley regions, as well as geothermal and volcanic environments elsewhere). While the 1998 India test fails to discriminate as an explosion in this initial attempt it also fails the earthquake null hypothesis and is therefore classified as indeterminate requiring further scrutiny. Finally this initial effort to characterize the discrimination problem in terms of P-value makes use of the Hudson et al. (1989) source-type space, and other representations such as Tape and Tape (2012a,b) may be more suitable.



A)



B)

Figure 9. A) The BSL full moment tensor catalog (red plusses for F-test significance greater than 95%) is compared to the composite P-value for explosion evidence and the complement of earthquake evidence. B) NTS explosions (green plusses), and test explosions (1988 JVE, 1998 India, 2006 and 2009 DPRK, nuclear tests, and a shallow conventional explosion; colored squares) are compared to the composite P-value test.

ACKNOWLEDGEMENTS

We thank Bruce Julian for scripts to make the source-type plots, and Václav Vavryčuk for MatLab code to plot full moment tensors and compare first motions.

REFERENCES

Anderson, D. N., D. K. Fagan, M. A. Tinker, G. D. Kraft, and K. D. Hutchenson (2007). A Mathematical Statistics Formulation of the Teleseismic Explosion Identification Problem with Multiple Discriminants, *Bull. Seismol. Soc. Am*. **97**, (5), 1730–1741.

Battis, J. C. and J. J. Cipar (1991). Seismic Recordings in the Northeastern United States of the Shagan River Nuclear Test of 14 September 1988, Geophysics Directorate of Phillips Laboratory, Air Force Systems Command, PL-TR-91-2001, 38pp.

Dreger, D. S., H. Tkalcic, and M. Johnston (2000). Dilational processes accompanying earthquakes in the Long Valley Caldera, *Science*, **288**, 122–125.

Dreger, D. S., S. R. Ford, and W. R. Walter (2008). Source Analysis of the Crandall Canyon, Utah, Mine Collapse, *Science,* **321**, 217.

Dreger, D. S., S. R. Ford, W. R. Walter, A. Chiang, and O. S. Boyd (2011). Refinement of regional distance seismic moment tensor and uncertainty analysis for source-type identification, in *Procedings of the 2011 Monitoring Research Review: Ground-Based Nuclear Explosion Monitoring Technologies*, LA-UR-11-04823, Vol. 1, pp. 446–455.

Ford, S., D. Dreger, and W. Walter (2008). Source Characterization of the August 6, 2007 Crandall Canyon Mine Seismic Event in Central Utah, *Seismol. Res. Lett*. **79**, 637–644.

Ford, S. R., D. S. Dreger, and W. R. Walter (2009a). Identifying isotropic events using a regional moment tensor inversion, *J. Geophys. Res*. **114**, B01306, doi:10.1029/2008JB005743.

Ford, S. R., D. S. Dreger, and W. R. Walter, (2009b). Source Analysis of the Memorial Day Explosion, Kimchaek, North Korea, *Geophys. Res. Lett*. **36** (21), Citation L21304.

Ford, S. R., D. S. Dreger, and W. R. Walter (2010). Network sensitivity solutions for regional moment tensor inversions, *Bull. Seismol. Soc. Am*. **100**, 1962–1970.

Ford., S. R., W. R. Walter, and D. S. Dreger (2012). Event discrimination using regional moment tensors with teleseismic-P constraints, *Bull. Seismol. Soc Am*. **102**, 867-872, doi:10.1785/0120110227.

Hudson, J. A., R. G. Pearce, R. G., and R. M. Rogers (1989). Source type plot for inversion of the moment tensor, *J. Geophys. Res*. **9**, (B1), 765–774.

Patton, H. J. and S. R. Taylor (2008). Effects of shock-induced tensile failure on m_b-M_s discrimination: Contrasts between historic nuclear explosions and the North Korean test of 9 October 2006, *Geophys. Res. Lett.* **35**, L14301, doi:10.1029/2008GL034211.

Patton, H. and S. R. Taylor (2011), The apparent explosion moment: Inferences of volumetric moment due to source medium damage by underground nuclear explosions, *J. Geophys. Res.* **116**, doi: 10.1029/2010JB007937.

Priestly, K. F., W. R. Walter, V. Martynov, and M. V. Rozhkov (1990). Regional Seismic Recordings of the Soviet Nuclear Explosion of the Joint Verification Experiment, *Geophys. Res. Lett*. **17** (2), 179–182.

Ross, A., G. R. Foulger, and B. R. Julian (1999), Source processes of industrially-induced earthquakes at The Geysers geothermal area, California, *Geophysics* **64**, 1877–1889.

Tape, W. and C. Tape (2012a). A Geometric Setting for Moment Tensors, *Geophys. J. Int*. **190**, 476–498.

Tape, W., and C. Tape (2012b). A Geometric Comparision of Source-Type Plots for Moment Tensors, *Geophys. J. Int*. **190**, 499–510.

Walter, W. R., and C. J. Ammon (1993). Complete Regional Seismic Waveform Inversion for Crust and Upper Mantle Structure: The September 14, 1988 JVE Explosion, Kazakhstan, Eurasia, UCRL-JC-112844.

Walter, W., E. Matzel, M. Pasyanos, D. Harris, R. Gok, and S. Ford (2007). Empirical Observations of Earthquake-Explosion Discrimination Using P/S Ratios and Implications for the Sources of Explosion S-Waves, in *Proceedings of the 30th Monitoring Research Review: Ground-Based Nuclear ExplosionMonitoring Technologies*, LA-UR-07-5613, Vol. 1, 684-693,

AN EMPIRICALLY-BASED PARAMETRIC EXPLOSION SPECTRAL MODEL

Sean R. Ford, William R. Walter, Stanley D. Ruppert, Eric M. Matzel, Teresa F. Hauk, and Rengin Gök

Lawrence Livermore National Laboratory

Sponsored by the National Nuclear Security Administration

Award No. DE-AC52-07NA27344/LL12-Parametrics-NDD02

ABSTRACT

We propose a parametric model of the nuclear explosion far-field seismic source spectrum for the regional phases Pn, Pg, and Lg that is a generalized version of the Brune spectrum,

$$S(f) = S_0 \Big/ \sqrt{1 + \left(f^2 / f_c^2 \right)^{\psi}}$$

a three-parameter model that describes the long-period level S_0, corner-frequency f_c, and spectral slope ψ at frequencies greater than f_c. The relationships for S_0 and f_c of the Pn and Pg spectra are derived from the Denny and Johnson (1991) empirical relations, which account for emplacement material strength. The Pn spectra are modified by the ratio of body-wave speeds and cubed ratio of body-wave speeds in order to obtain f_c and S_0, respectively, for the Lg spectral model. Explosions in competent media are fit well by a spectrum with ψ equal to two, a behavior similar to earthquakes, but explosion spectra in weak material are fit better if ψ is allowed to increase with gas porosity (GP), so that $\psi = 2 \times 10^{1.2GP}$, where GP is in volume fraction. The success of the regional P/S high-frequency spectral ratio discriminant is due to the difference between the observed 1-to-1 ratio of P-to-S corner frequencies for earthquakes and the lower S than P corner frequency for explosions. The model presented here predicts even greater performance of the discriminant for explosions in weak material where the high-frequency spectral slope of the explosions is increased relative to both that of explosions in competent material and the similar slope in earthquakes.

OBJECTIVES

We develop an empirical explosion parametric far-field source spectral model, based on all available digital data recorded for explosions at the Nevada National Security Site (NNSS) (formerly the Nevada Test Site [NTS]). The model describes nuclear explosion P- and S-wave source spectra for a variety of geologic and containment conditions. This approach follows the simple earthquake parametric spectral model based on Brune (1970), which is used for the MDAC (Magnitude and Distance Amplitude Correction) approach (Walter and Taylor, 2001) to improve earthquake/explosion discrimination. In regions without prior explosions, this parametric model could be combined with earthquake-derived path corrections to predict explosion regional phase amplitudes, improve discriminants such as P/S ratios, and support identification procedures (e.g., Event Categorization Matrix) that explicitly need to use explosion discriminant probability density functions.

Depth and near-source material properties can affect seismic estimates of explosion yield, and prior work at the NNSS has found that explosions in weak materials have lower corner frequencies and steeper spectral fall-offs for P-waves than is predicted by the standard Mueller and Murphy (1971, hereafter referred to as MM71) model. As part of this research, we hope to quantify these effects as a function of frequency and wave type. Additionally, many of the most effective regional discriminants (high-frequency P/S ratios) make use of S-waves, as do S-wave coda yield estimation techniques, yet there remain many questions about how to predict explosion S-wave amplitudes. The development of a combined P- and S-wave spectral model consistent with observed regional P-and S-wave data is an objective of this work.

RESEARCH ACCOMPLISHED

Introduction

In previous work that looked at low to high frequency ratios of regional phase (e.g., Pn, Pg, Lg) amplitudes to separate explosions from earthquakes at the NNSS (the former NTS), Walter et al. (1995) noted that the results showed a strong dependence on the source media properties. Nuclear tests in weak and/or high gas porosity media tended to have higher values and discriminate better from earthquakes than explosions in stronger and/or lower gas porosity media. These observations required an explosion spectral model where not only are the long-period level and corner-frequency dependent on source media as described in Denny and Johnson (1991, hereafter referred to as DJ91), but also the roll-off at high-frequency required some dependency on medium strength as suggested by Denny and Goodman (1990).

Data and Methods

We employ the NNSS explosion dataset of Walter et al. (2004), specifically the raw spectra of that dataset. Waveforms are de-meaned, de-trended and instrument corrected to acceleration. The signal is windowed with a 5% cosine taper that starts before the pick, where the time before the pick is 5% of the total time window. The Fourier transform is calculated and displacement spectra are obtained via double integration in the frequency domain. Finally, the resultant amplitude spectra are interpolated and smoothed to obtain a sampling period of 0.05 $\log_{10}$ Hz. Examples of regional phase spectra are given in Figure 1.

Spectra of each seismic phase for each explosion are calculated from the recordings of stations of the Livermore NTS Network, ELK (Elko, NV), KNB (Kanab, UT), LAC (Landers, CA), and MNV (Mina, NV). These spectra are then corrected for geometrical spreading and regional, frequency-dependent attenuation of the form $Q = Q_0 f^{\gamma}$, where Q_0 is Q at 1 Hz and γ is the power-law dependence on frequency, f. The attenuation and spreading model parameters for each seismic phase are given in Table 1.

Table 1. NNSS regional attenuation and geometric spreading parameters.

Phase	η	r_0 (km)	Q_0	γ
Pn	1.1	0.001	210	0.65
Pg	0.5	100	190	0.45
Lg	0.5	100	200	0.54

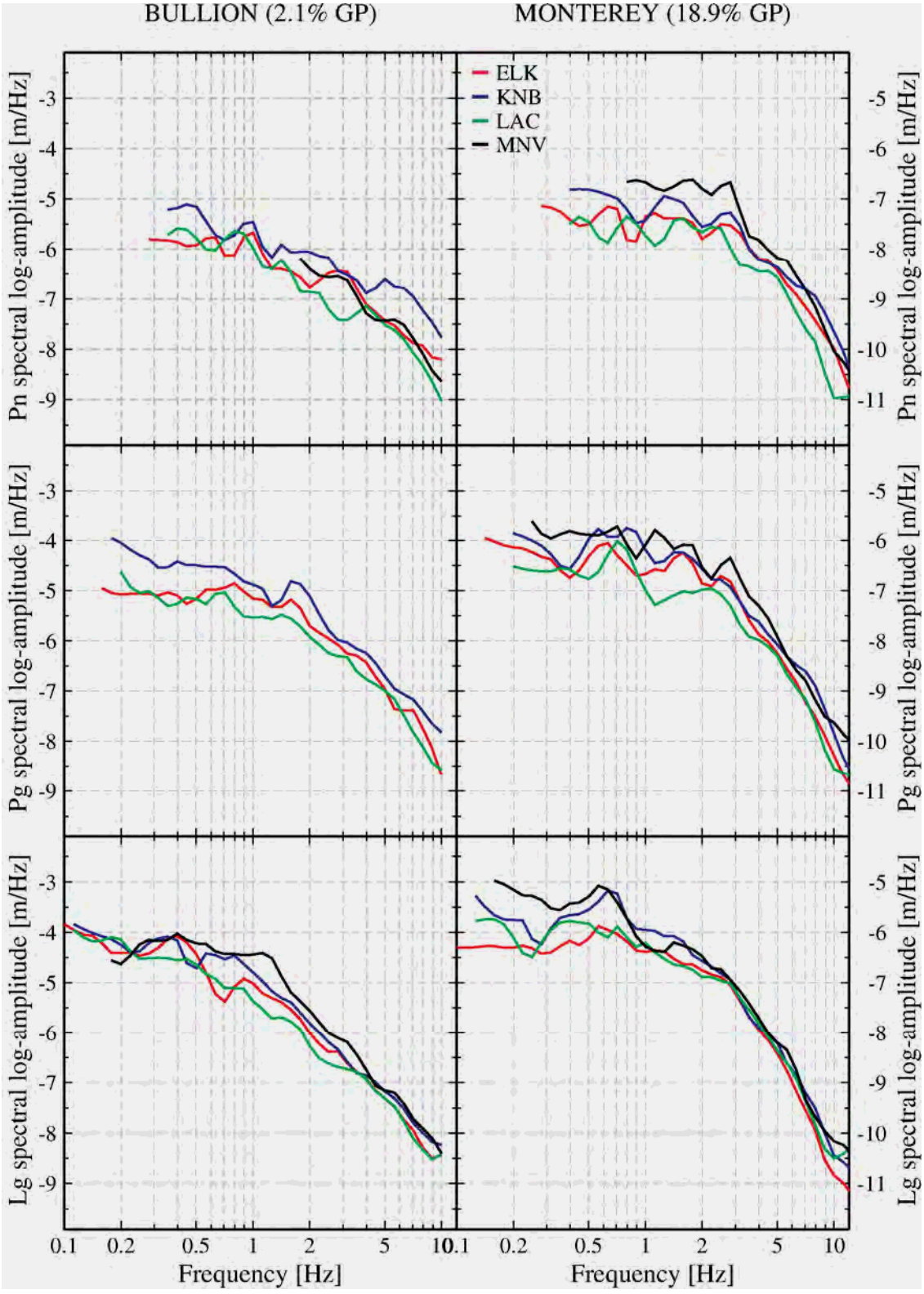


Figure 1. Raw spectral amplitudes of a low-GP (BULLION) and a high-GP (MONTEREY) explosion at the NNSS.

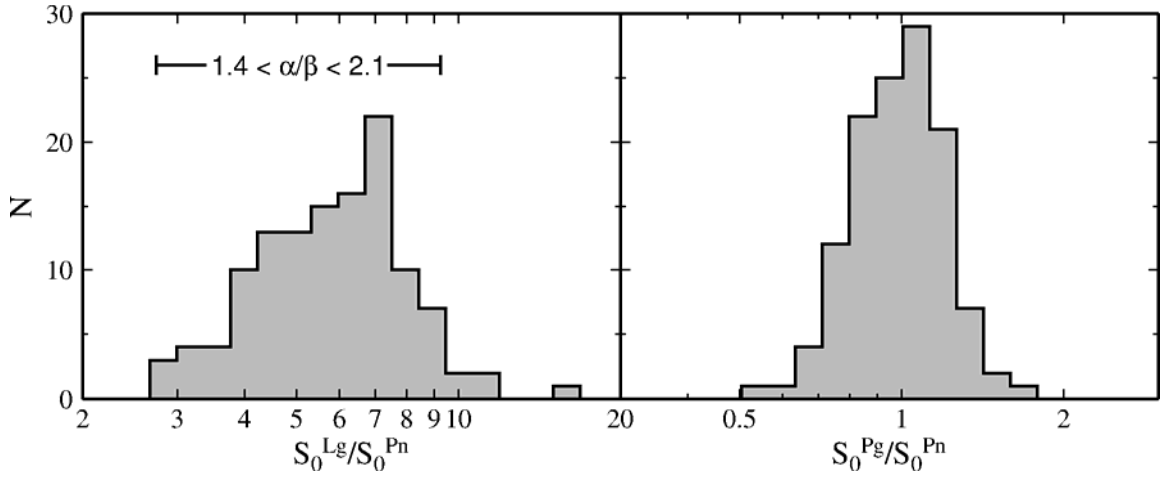


Figure 2. Comparison of measured long-period spectral levels (S_0) for regional phases at the NNSS. The range of Lg/Pn ratios is consistent with the cubed ratio of wavespeeds.

We require three of the four stations listed above to have recorded an event with a signal-to-noise ratio greater than two. We also inspect each spectra for non-stationary noise at high frequency (typically >9 Hz) due to multi-band recording problems and restrict spectral fitting to bands unaffected by problems. The spectra are jointly fit with a simple parametric form given by

$$S(f) = S_0 \Big/ \sqrt{1+\left(f^2 / f_c^2\right)^{\psi}}\,, \tag{1}$$

in a nonlinear least-squares inversion that also provides standard error for each parameter estimate. Equation (1) describes the simplest behavior expected for seismic spectra. It has a constant level at low frequencies (S_0), which is proportional to static displacement, and falls off at high frequencies with a slope of ψ beyond a corner frequency f_c. This parametric model exhibits a trade-off between increased f_c and ψ, so we fixed f_c with the value given by the DJ91 relations, which was only a slight improvement in fit over the value provided by the MM71 relations. As shown in Figure 1, the Lg corner frequency f_c^{Lg} is reduced relative to Pn. Fisk (2007) analyzed NNSS regional spectra with low GP and found that the ratio of P-to-S corner frequency is approximately equal to the ratio of P-to-S wavespeeds (α/β). When fitting Lg spectra with equation (1) we fix f_c using the DJ91-predicted f_c divided by α/β.

Results

The long-period level of the Lg explosion spectrum is on average greater than Pn. For earthquakes the ratio of these long-period levels is approximately equal to the ratio of S-to-P radiation multiplied by the cubed ratio of wavespeeds, or $S_0^{Lg}/S_0^{Pn} = (R_S/R_P)(\alpha/\beta)^3$, where R_S/R_P is the S-to-P radiation ratio. The ratio of the long-period levels calculated for the explosions is given in Figure 2 and are on average the cubed ratios of typical wavespeeds at NNSS, so that S_0^{Lg} is equal to the DJ91-defined S_0^{Pn} multiplied by the cubed ratio of P-to-S wavespeed of the emplacement medium, $S_0^{Lg} = (\alpha/\beta)^3 S_0^{Pn}$. In other words, the long-period S-to-P ratio is the same as earthquakes except that for explosions we assume the S radiation is equal to the P radiation. For earthquakes the ratio of the azimuthally average S/P radiation pattern is about 1.36 (0.60/0.44).

As hinted at by the raw spectra in Figure 1, we hypothesize that there is a correlation between gas porosity (GP, in volume fraction) and spectral fall-off ψ. We fit a model of the form $\psi = 2\times10^{kGP}$ to the data given in Figure 3 where the best-fit $k = 1.2$. At low GP this model approximates the behavior of Brune earthquake spectrum where $\psi = 2$, but ψ increases with increasing GP.

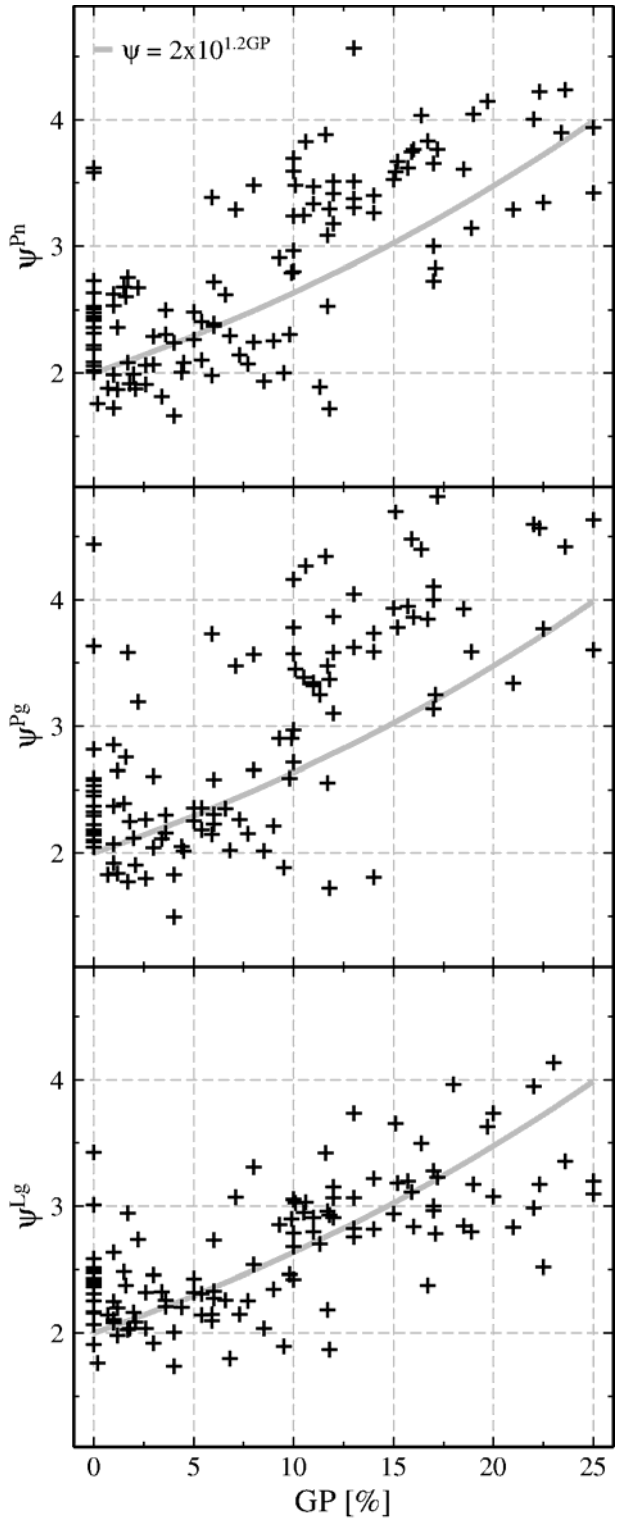


Figure 3. High-frequency spectral roll-off (ψ) versus medium gas porosity (GP). The function used to approximate the GP-dependence is given by the gray line.

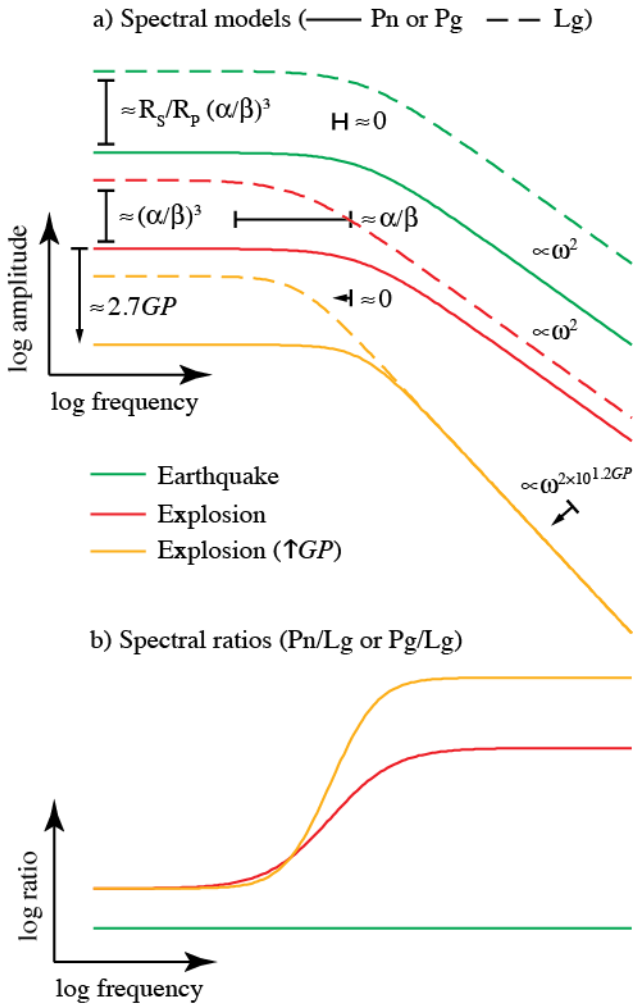


Figure 4. a) Pn and Lg spectral models for an earthquake (green), explosion (red), and an explosion in weak emplacement material (high GP, orange). The earthquake model is the classic Aki-Brune spectrum with frequency squared high-frequency fall-off and long-period difference between the S and P sources equal to the ratio of the radiation pattern coefficient multiplied by the Vp/Vs ratio cubed. The corner frequencies are identical as supported by observation and not a theoretically-predicted Vp/Vs ratio. The explosion model is the classic Aki-Brune earthquake model where the ratio in radiation pattern coefficients is one. The long-period level and corner-frequency are from the Denny & Johnson empirical model. The model for an explosion in weak emplacement material is the same as the explosion model with the addition of increased high-frequency roll-off proportional to GP. A decrease in the long-period level and increase in the corner-frequency are predicted by the Denny & Johnson relations as the material properties change with increased GP.
b) Spectral ratios of Pn/Lg for the three models presented in a).

Discussion

The parametric spectral model is shown in Figure 4a where all the parameters in Equation (1) are described. The earthquake model is described more fully in Walter and Taylor (2001) and Taylor et al. (2002), but we note that counter to some theories that predict earthquake corner frequencies should be proportional to the ratio of P/S velocity, the observed ratio of P-to-S corner frequencies is approximately one. The ratio should vary between one and the ratio of the wave velocities depending upon the rupture time compared to the total source dimension. A

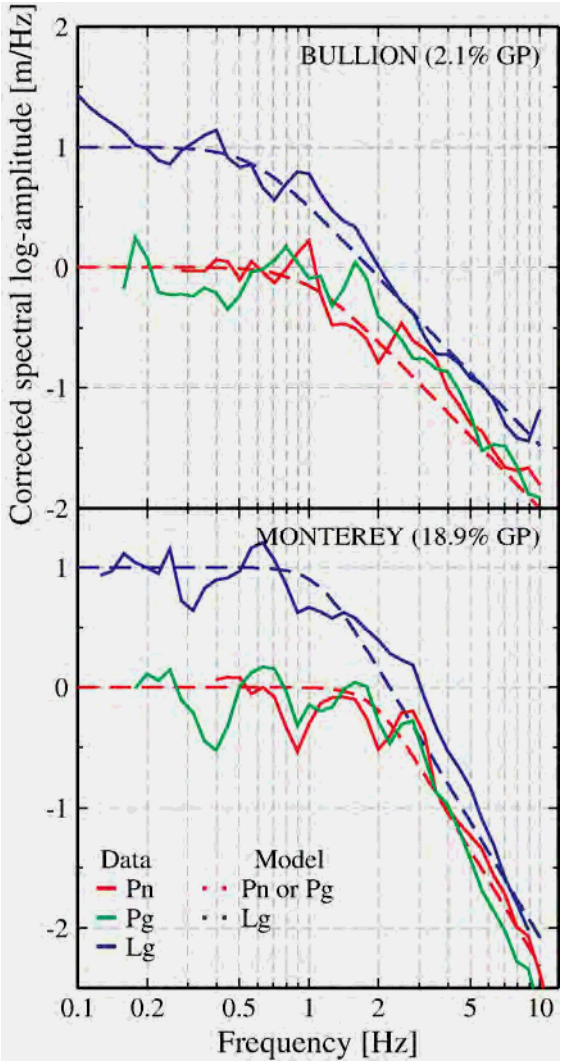


Figure 5. Model fit (dashed line) to corrected spectra (solid line) from Figure 1 where the median amplitude of all stations is plotted. The Pn and Pg models are the same and are given by the red dashed line.

value of one is consistent with rupture times that are short compared to overall fault dimension (Walter and Brune, 1993). The long-period level and corner frequency of the explosion P-wave model are given by DJ91. The explosion Lg model starts with the reduction in corner frequency equal to the wavespeed ratio and an increase in amplitude similar to the earthquake model, but where the P-to-S radiation ratio is one. This relationship would argue that explosion-generated Lg energy is created near the source and scales with the P energy (e.g., Fisk, 2006). DJ91 incorporate GP into their models, so the long-period level is already given and is approximately equal to the explosion model in competent material (GP = 0) decreased by a factor of ~3×GP (given in volume fraction). The corner frequency is approximately the same, but the spectral fall-off is now also a function of GP ($\psi = 2\times10^{1.2GP}$). The ratio of the P-to-S long-period level ratio does not change with GP and is the same as for an explosion in competent material.

Figure 4b shows the Pn (or Pg) to Lg spectral ratio for the earthquake, explosion, and explosion in weak material (high GP) models. The decrease in explosion Lg corner frequency relative to an earthquake is responsible for the success of high-frequency P-to-S spectral discriminants. There is some discriminatory power at low-frequencies, but this is only equal to the ratio of the earthquake S-to-P radiation, which on average is small. The models are compared with corrected spectra in Figure 5, where fairly good agreement is obtained.

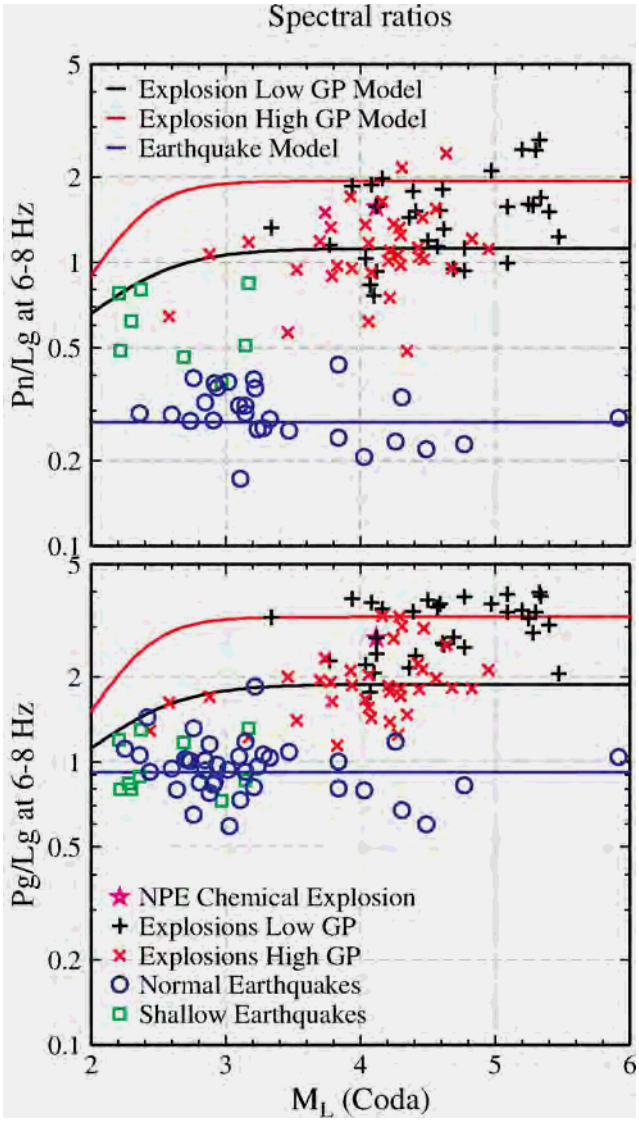


Figure 6. Regional P/S spectral ratios from Walter et al. (1995) and model fits.

We revisit the phase and spectral ratios given in Walter et al. (1995) where the effect of GP on ratios was quantified via low-strength, high-GP populations. In order to compare with the ratio versus magnitude observations given in Walter et al. (1995) we convert the magnitude to corner frequency from the relations given in Al-Eqabi et al. (2001). Figure 6 shows the model comparison to the spectral ratios and Figure 7 shows the comparison to the phase ratios. The models presented here are successful at explaining the difference between explosion and earthquake ratios, and the difference in high- and low-GP Lg phase ratios. However, the models predict a larger difference between high- and low-GP spectral ratios than is present in the observations.

CONCLUSIONS AND RECOMMENDATIONS

Our preliminary analysis of regional phase spectra of NNSS explosions shows that a simple spectral model with variable fall-off dependent on GP is appropriate and can be used to predict spectral and phase ratios.

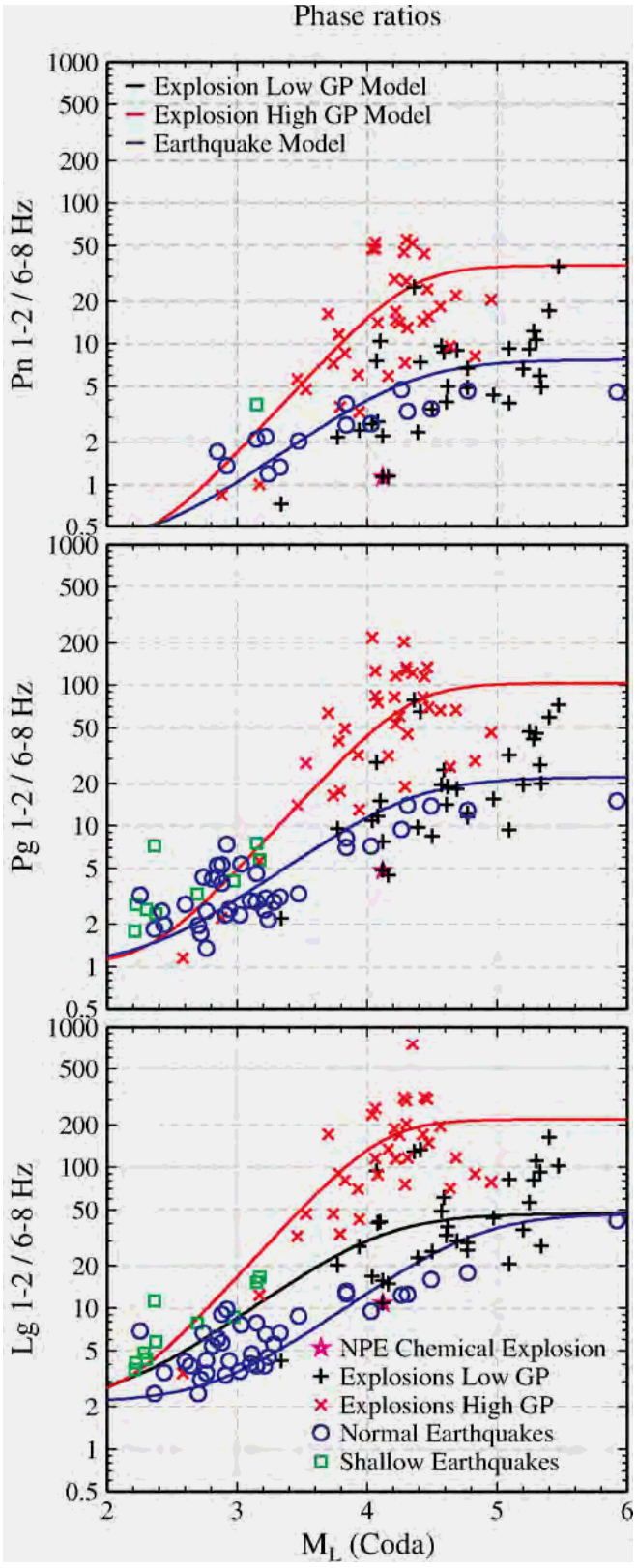


Figure 7. Regional low-/high-frequency phase ratios from Walter et al. (1995) and model fits.

REFERENCES

Al-Eqabi, G. I., K. D. Koper, and M. E. Wysession (2001). Source characterization of Nevada Test Site Explosions and western earthquakes using Lg waves: Implications for regional source discrimination, *Bull. Seismol. Soc. Am.* **91** (1), 140–153.

Brune, J. N. (1970). Tectonic stress and the spectra of seismic shear waves from earthquakes, *J. Geophys. Res.* **75**, 4997–5009.

Denny, M. D. and D. M. Goodman (1990). A case study of the seismic source function; SALMON and STERLING reevaluated, *J. Geophys. Res.* **95**, 19705–19723.

Denny, M. D. and L. R. Johnson (1991). The explosion seismic source function: Models and scaling laws reviewed, in *Explosion Source Phenomenology*, eds. Taylor S. R. et al., *AGU Monograph* **65**, 1–24.

Fisk, M.D. (2006). Source spectral modeling of regional P/S discriminants at nuclear test sites in China and the Former Soviet Union, *Bull. Seismol. Soc. Am.* **96**, 2348–2367.

Fisk, M. D. (2007). Corner frequency scaling of regional seismic phases for underground nuclear explosions at the Nevada Test Site, *Bull. Seismol. Soc. Am.* **97**, 977–988.

Mueller, C. S. and J. R. Murphy (1971). Seismic characteristics of underground nuclear detonations, Part I: Seismic spectrum scaling, *Bull. Seismol. Soc. Am.* **61**, 1675–1692.

Taylor, S. R., A. A. Velasco, H. E. Hartse, W. S. Phillips, and W. R. Walter (2002). Amplitude corrections for regional seismic discriminants, *Pure Appl. Geophys.* **159**, 623–650.

Walter, W. R, K. D. Smith, J. L. O'Boyle, T. F. Hauk, F. Ryall, S. D. Ruppert, S. C. Myers, R. Abbot, and D. A. Dodge (2004). An assembled western United States dataset for regional seismic analysis, *Lawrence Livermore National Laboratory* document, UCRL-TR-206630.

Walter, W. R. and S. R. Taylor (2001). A revised magnitude and distance amplitude correction (MDAC2) procedure for regional seismic discriminants, *Lawrence Livermore National Laboratory* document, UCRL-ID-146882.

Walter, W. R., K. M. Mayeda, and H. J. Patton (1995). Phase and spectral ratio discrimination between NTS earthquakes and explosions, Part 1: Empirical observations, *Bull. Seimol. Soc. Am.* **85**, 1050–1067.

Walter, W. R. and J. N. Brune (1993). Spectra of seismic radiation from a tensile crack, *J. Geophys. Res.* **98** (B3), 4449–4459.

REGIONAL EVENT IDENTIFICATION RESEARCH IN CENTRAL ASIA

Hans E. Hartse, George E. Randall, Dale N. Anderson, W. Scott Phillips, and Stephen J. Arrowsmith

Los Alamos National Laboratory

Sponsored by the National Nuclear Security Administration

Award No. DE-AC52-06NA25396/LA12-Source Physics-NDD02

ABSTRACT

Recent event identification efforts at Los Alamos National Laboratory (LANL) have focused on two event types: mining explosions and sub-crustal earthquakes. For nuclear explosion monitoring both of these event types can be problematic. On far-local to regional discrimination plots mining events can have characteristics similar to single-charge explosions, but can also sometimes appear similar to earthquakes. Sub-crustal earthquakes are known to sometimes have explosion-like characteristics due to their high-frequency P-waves and relatively weak S-waves. Both types of events can become mixed into populations of crustal-depth earthquakes used for calibrating magnitude and distance correction (MDAC) parameters. Unintentional use of contaminated calibration data can eventually reach the final event identification decision process – the Event Categorization Matrix (ECM). Hence, our goal has been to find discriminants that will identify mining explosions and sub-crustal earthquakes, such that the ECM process can be expanded to include the event categories of mining explosion and sub-crustal earthquake recorded at regional (rather than teleseismic) distances.

The challenge of developing discriminants for mining explosions and sub-crustal earthquakes is to first establish ground-truth (GT) event types for mining detonations, crustal earthquakes, and sub-crustal earthquakes. We have chosen two adjacent areas of central Asia to build event-type GT. Our mining event efforts have identified over 20 mines and more than 1,000 mining explosions from around the former Soviet nuclear test site (KTS) in eastern Kazakhstan. Using the Kazakh National Data Centre (KNDC) bulletin from 2002 to 2009 and waveforms recorded at station KURK and array MKAR, we combined time-of-day event analysis, waveform cross correlations, seismic-event location methods, and image analysis to identify active mines. We have learned that mining explosions do not occur during hours 21, 22, and 23 GMT (3, 4, and 5 AM local time) in this area, and we therefore classed events from these early-morning hours as GT crustal earthquakes. Sub-crustal earthquakes occur in the Hindu Kush region of central Asia where the Indian Subcontinent is colliding with Asia. Many smaller events from this area are not recorded at sufficient signal-to-noise levels for picking of teleseismic depth phases. Hence, many Hindu Kush earthquakes may be sub-crustal but are reported as shallow. To build a GT event data set in this region we required at least 4 reported depth phases for both sub-crustal and crustal earthquakes.

Our preliminary measurements and discriminant tests for mining events versus crustal earthquakes in eastern Kazakhstan indicate several options for separating event types. First, a strong correlation coefficient ($>\sim 0.4$) using a known mine-related waveform as a template is the best indicator of a mining explosion. Other options where template waves are not available are Pg/Lg ratios where $F > 6$ Hz, cepstral analysis (good for some mines depending on shooting styles), and either the presence of the Rg phase or a Lg-coda (enhanced by Rg presence) to direct Lg-wave ratio. For the Hindu Kush we find a Pg spectral ratio (which is essentially a P-coda spectral ratio for the deep earthquakes) separates crustal from sub-crustal earthquakes. We will be applying the MDAC procedure to improve the phase-ratio discriminants we describe, above, and for future efforts we will exploring how to combine all discriminants into the ECM process.

OBJECTIVES

Our primary objective is to develop mining explosion and sub-crustal earthquake discriminants suitable for incorporation into the Event Categorization Matrix (ECM) procedure (Anderson et al., 2007). That is, we seek to find and apply seismic event discriminants that will reliably identify deep, sub-crustal earthquakes (depths between about 50 and 300 km) and routine delay-fired mining explosions. We focus on smaller events recorded at far-local to mid-regional event-station distances (between about 100 km and 700 km). Our primary study areas are eastern Kazakhstan (for mining events) and the India-Asia collision zone (for sub-crustal earthquakes). To date, we have worked to confidently build ground truth event-type data sets, and using these data sets (crustal earthquakes, mining explosions, and sub-crustal earthquakes), we have started testing discriminants. Our techniques for building event-type ground truth data sets and our preliminary discrimination results are presented below.

RESEARCH ACCOMPLISHED

Kazakh Mining Ground-truth

We have been expanding our seismic ground-truth data collection efforts for central Asia by identifying mines and mining explosions. Working with Kazakh National Data Centre (KNDC) bulletins (2002–2009), we combine time-of-day event analysis, waveform cross correlations, seismic-event location methods, and image analysis, to identify active mines in the area between the International Monitoring System (IMS) array MKAR and the Global Seismic Network (GSN) station KURK. Most of the events within this area occur during daytime (Figure 1), are usually small (often recorded at only 1 or 2 stations or arrays), and therefore tend to be poorly located. Our goal is to tie similar events to specific mine sites, and thereby establish ground-truth location and event-type information.

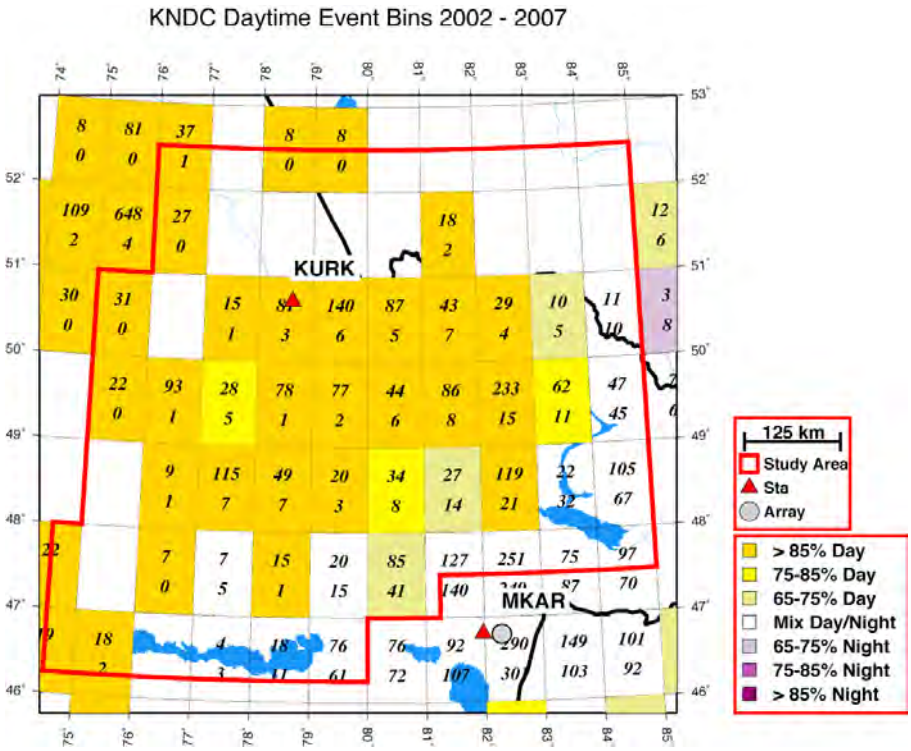


Figure 1. Time-of-day seismicity for eastern Kazakhstan and surrounding regions. The primary event information source is the KNDC web-published bulletin. Gold and yellow regions are dominated by daytime mining explosions. Within each bin, the upper number is the daytime event count and the lower number is the nighttime event count. We focused on the area within the red box between array MKAR and station KURK, which includes the former Soviet nuclear test site (KTS).

Using KNDC locations as a guide, we assembled about 2,500 three-component, event-segmented waveforms from MKAR array-element MK31 and station KURK. After bandpass filtering between 1.5 and 5.5 Hz, we cross-correlated the first 20 seconds of each component's (vertical, east, and north) record with every other record from the same component. After stacking and normalizing the individual component correlations into three-component correlations, we assembled similar-event clusters based on peak correlation coefficients exceeding 0.4. From the relative timing offsets within a given cluster's correlation peaks, we time-shifted, aligned, and stacked the individual event waveforms at stations MK31 and KURK. These waveform sums become the reference waves of each event cluster. Figure 2 shows the stacked BHZ wave and several aligned individual waves at station MK31 for explosions at the Kara-Zhyra coal mine located about 50 km north of KTS.

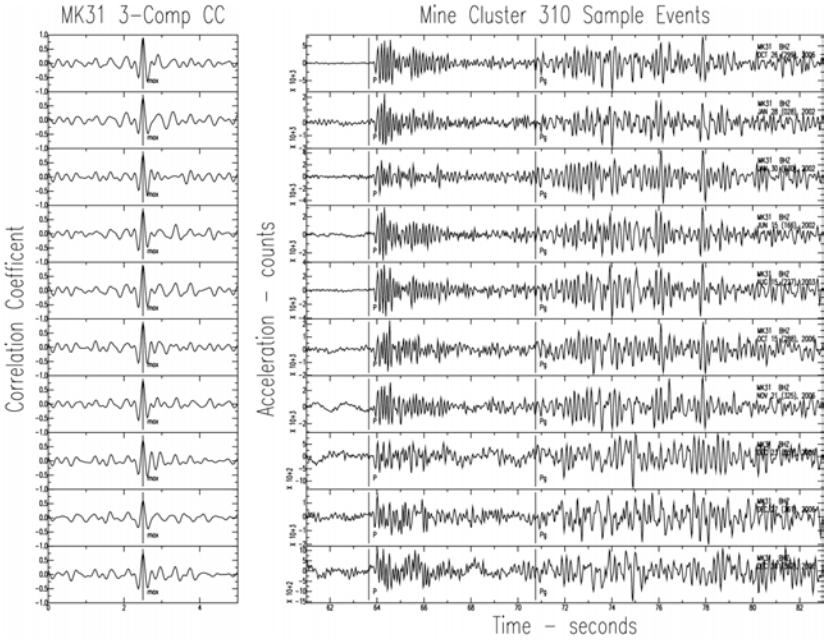


Figure 2. Event cluster (Kara-Zhyra coal mine) waveform stack (top trace) and individual, vertical-component, time-aligned P-waves at MK31. The three-component cross-correlation results are shown at left, with autocorrelation at top left. Note improved S/N ratio on the stacked wave for Pn (first break).

In all, we found 23 clusters, each with 5 or more events from probable mines, totaling about 1,000 individual events. Event-station distances for the clusters are between about 75 and 550 km, and most event magnitudes are between about 1.0 and 3.5 mb. Although nearly all mining events occur during local day-time (about hour 2 GMT to hour 14 GMT), we did find two clusters where events occur predominantly at local midnight. From previous studies (MacCarthy et al., 2008, Hartse et al., 2007) we had assumed unclustered, night events were earthquakes, but for our current study we now assume only events occurring during hours 21–23 GMT (3–5 AM local time) are earthquakes.

Figure 3 shows events we selected for our Kazakhstan mining event discrimination study. These are events recorded at station KURK (operated under the II and KZ network codes). They include about 250 events from the three mine locations (identified by time-of-day and cross correlation as described above), 9 presumed earthquakes (that is, reported events from non-mining hours or any event within 350 km of KURK with mb larger than 4.0), and several single-charge chemical explosions from around KTS, including (1) the 1997 DOB experiments (Glenn and Myers, 1997), (2) the Omega test series of tunnel explosions (Knowles, 2006), and (3) other hole-closing explosions (NNC RK, 1998).

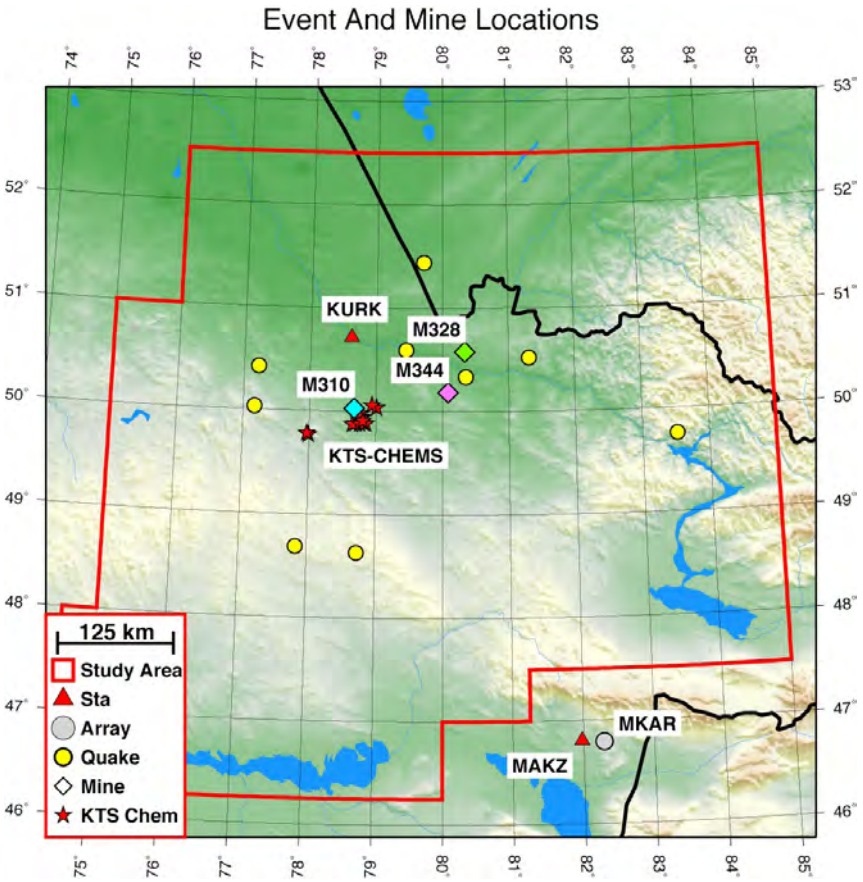


Figure 3. Eastern Kazakhstan area showing mine locations (diamonds), single-charge chemical explosions (stars), and probable earthquakes (yellow circles). About 250 events are tied to the mines. Earthquake locations are from seismic bulletins. The KTS explosions are from published reports.

Sub-crustal Earthquake Ground-truth

Sub-crustal earthquakes are known to sometimes have explosion-like characteristics, attributable to their impulsive, high-frequency P-waves and relatively weak S-waves. Figure 4 shows sample waveforms of a crustal earthquake, a sub-crustal earthquake, and a nuclear explosion in the 1-2 Hz and 6-8 Hz bands, all recorded at seismic station MAKZ. In the 6-8 Hz band, where P, S, and Lg amplitudes are often measured to form discrimination plots, the sub-crustal earthquake and the explosion are lacking S- and Lg-waves. Further, both of these events have similar impulsive P-waves. Thus, on standard high-frequency P/S or P/Lg discrimination plots, sub-crustal earthquakes sometimes merge into explosion populations.

For event identification purposes, a constrained estimate of earthquake depth at mid-crustal or deeper levels is all that is necessary to eliminate an event as a possible explosion. Unfortunately, standard methods of seismic location are routinely unsuccessful at constraining event depth unless either (1) a number of clear depth phases (near source reflections) are observed, or (2) at least one seismic station reporting phase arrival times is at an epicentral distance no greater than about 2 times the true event depth. Depth phases are extremely difficult to observe for small events as the reflections are often smaller than the direct (first arrival) phase and are either below the noise floor or lost in the reverberant coda of the direct arrival.

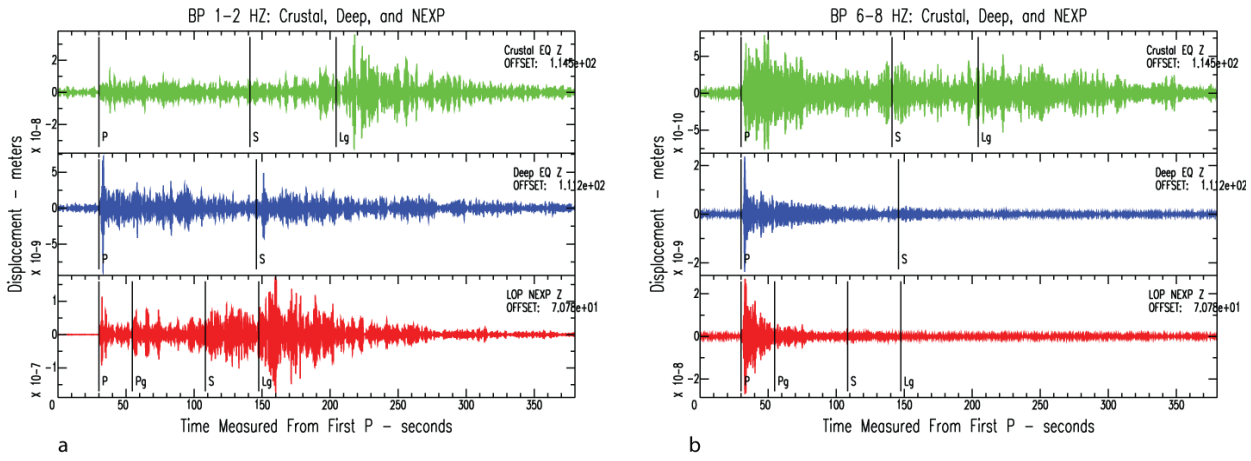


Figure 4. Examples of a crustal earthquake (green), a sub-crustal earthquake (blue), and a nuclear explosion (red) from western China recorded at station MAKZ in Kazakhstan. Vertical component seismograms with a 1 to 2 Hz bandpass filter (a), and bandpass filter between 6 and 8 Hz (b). Note the lack of S and Lg for the deep earthquake and the nuclear explosion.

The Hindu Kush region produces many earthquakes with depths ranging from a few km down to near 300 km. Figure 5a shows events from this collision zone held in our research database. From just over a three-year time span nearly 1500 events were reported between station NIL and array KKAR. Within the collision zone, we believe many of these events may have been deep, but because depth phases are lacking, they were reported at shallow depths. For finding discriminants that separate shallow from deep earthquakes, we must use a data set where we have confidence in depth. Thus, we selected events for our discrimination study that had 4 or more depth phases reported with the event location (Figure 5b).

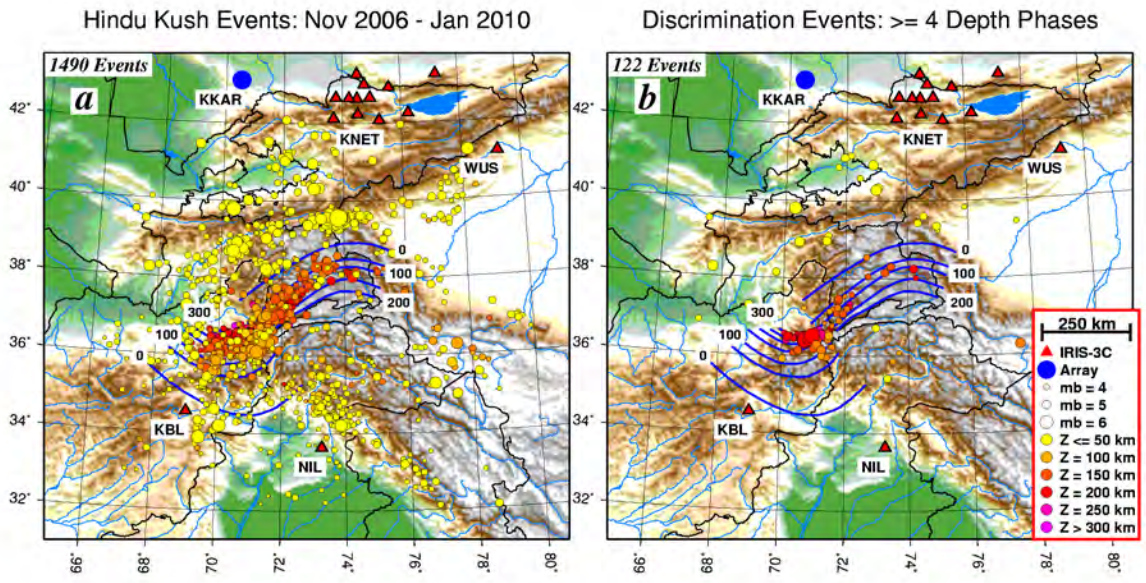


Figure 5. Earthquakes of the Hindu Kush region. Blue contours and labels represent depth in km of subducting slabs. In (a) all events in LANL research database are plotted. We believe many depths associated with these reported locations are wrong. (b) Only those events used for our preliminary discrimination analysis. That is, events with 4 or more distinct teleseismic depth phases, such as pP and sS.

Discrimination Results – Mining Explosions

Most events in our Kazakhstan data set are within or only slightly beyond the crossover distance at KURK (Figure 3). Thus, we measured vertical-component Pg and Lg body wave amplitudes as root mean square (RMS) displacement in meters, and also measured pre-phase and pre-event noise windows. Hartse et al. (1997) describes the measurement methods we followed. We formed Pg/Lg amplitude ratios and corrected the ratios for a distance trend prior to forming final ratio-versus-magnitude discrimination plots. We used only earthquake ratios to find the distance trends.

Figure 6a shows discrimination results from station KURK, comparing earthquakes, the KTS single-charge explosions, and the explosions from the three mines shown in Figure 3. Most KTS hole-closing and some tunnel explosions at KTS were shallow and not contained. However, we are confident that at least two DOB explosions were contained (larger red stars). These explosions vary in size from about 2 tons up to 100 tons. In Figure 6a only two uncontained explosions are within or near the earthquake population. The contained, and the majority of the uncontained explosions, separate from the earthquakes. Thus, Figure 6a shows that small, single-charge explosions can be separated from earthquakes using a high-frequency P/S (or P/Lg) ratio at local to near-regional distances, even when containment is not complete. Most mining explosions also separate from the earthquakes on the P/S plot. Events from mines 344 and 310 separate from the earthquakes more completely than explosions from mine 328.

To test for evidence of multi-hole, delay-fired shooting, we applied the method of Arrowsmith et al. (2007) to derive a cepstral estimate for each earthquake and mining explosion. We obtained the cepstral results using the array elements at MKAR. In Figure 6, mining explosions with larger cepstral numbers (indicating a greater likelihood of delayed shooting), are shown with heavy borders around the diamond symbols. At Mine 310 it therefore appears that delayed shooting is more common than at the other mines, but Mine 344 also has several events where delayed shooting apparently has occurred.

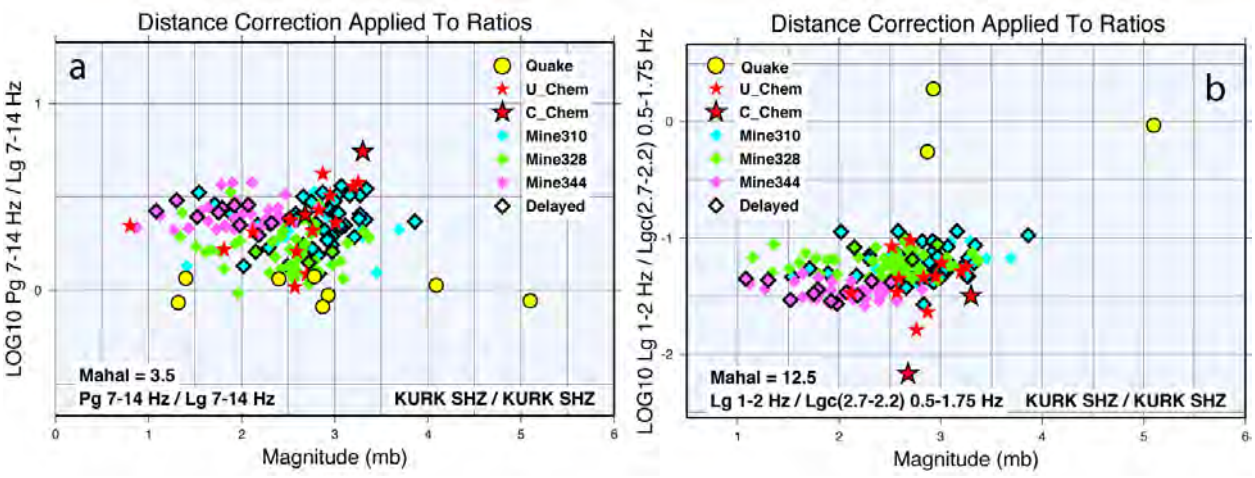


Figure 6. Pg(7–14 Hz)/Lg(7–14 Hz) ratio versus magnitude for all explosions and earthquakes (a). Mining explosions where cepstral processing results suggest delay-fired shooting are shown by heavy black borders on diamonds. Lg(1–2 Hz)/LgCoda(0.75–1.75 Hz) ratio versus magnitude (b). We measured the amplitude of the Lg coda over a velocity window between 2.7 and 2.2 km/s, which captured the Rg phase of the explosions.

From past experience with Kazakhstan events, we were aware of a strong Rg arrival for both mining and single-charge explosions relative to the direct Lg phase. This suggests that, within the appropriate group-velocity window, an Lg coda amplitude could be measured and placed into a ratio with direct Lg to form an earthquake-explosion discriminant. We determined that an Lg coda velocity window between 2.7 and 2.2 km/s captures the Rg arrival for these local to near-regional events, and we then measured RMS amplitudes in the 0.5–1.75 Hz band. Our Lg/Lgcoda discrimination plot is shown in Figure 6b. The "delayed" mining explosions have the same ratios as the mining

explosions with small cepstral numbers. The earthquakes have no Rg, and true Lg coda was therefore measured. Because most earthquakes were small and at distances greater than 200 km from KURK, only three had coda amplitudes that remained above background noise. But those three earthquakes are clearly separated from the explosions. One contained, single-charge explosion had a small direct-Lg amplitude and a large Rg arrival, resulting in separation from the mining events (lowest red star on Figure 6b). The second contained, single-charge explosion and two other single-charge explosions are at the bottom of the mining event population. This suggests a possible discriminant for separating contained and uncontained explosions, but further information regarding the emplacement and containment of the single-charge events is necessary before conclusions can be reached.

Scanning continuous data using waveform templates that are representative of a given mine can be used for event identification when a large correlation coefficient (or other measure of waveform similarity) is found. In November, 2009, the CTBTO declared an explosion at the Kara-Zhyra coal mine in Kazakhstan as a "Non-Proliferation Experiment" event (now known as NPE 2009). Mikhailova and Sinyova (2010) provide ground truth details for this event. Upon reading their report, we realized the Kara-Zhyra coal mine is our mine 310. Thus, we used our MK31 waveform template to scan continuous data from mid-November to mid-December in an attempt to detect the NPE event. Figure 7 shows maximum correlation coefficients per 15-minute data window we scanned. Over this one month period we detected the NPE 2009 event with a correlation coefficient near 0.5 and 7 other events. All eight events are listed in KNDC bulletins and all have locations near the Kara-Zhyra mine. Figure 8 compares our template waveforms to the detected NPE 2009 waveforms.

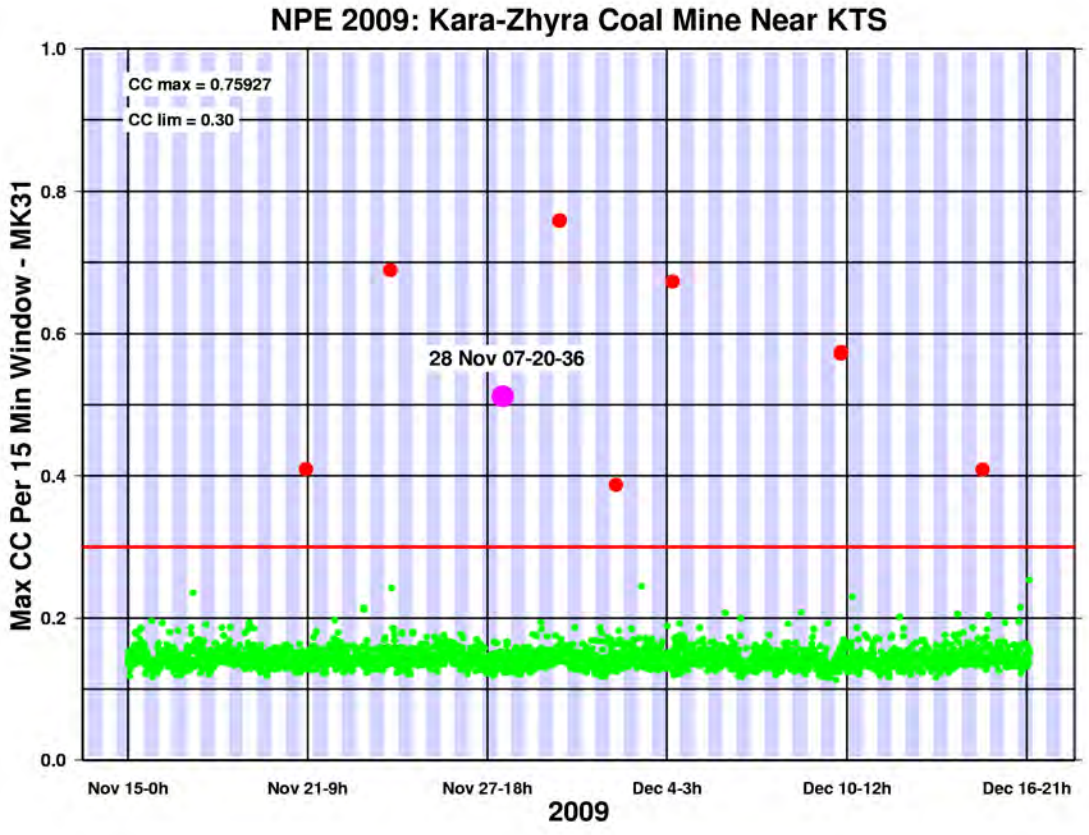


Figure 7. Correlation scanning results for the Kara-Zhyra coal mine during late 2009. We detected 8 coal mine explosions (red dots), including the November 28 07h 20m 36s NPE 2009 explosion (magenta). Green dots represent correlation coefficients below 0.3.

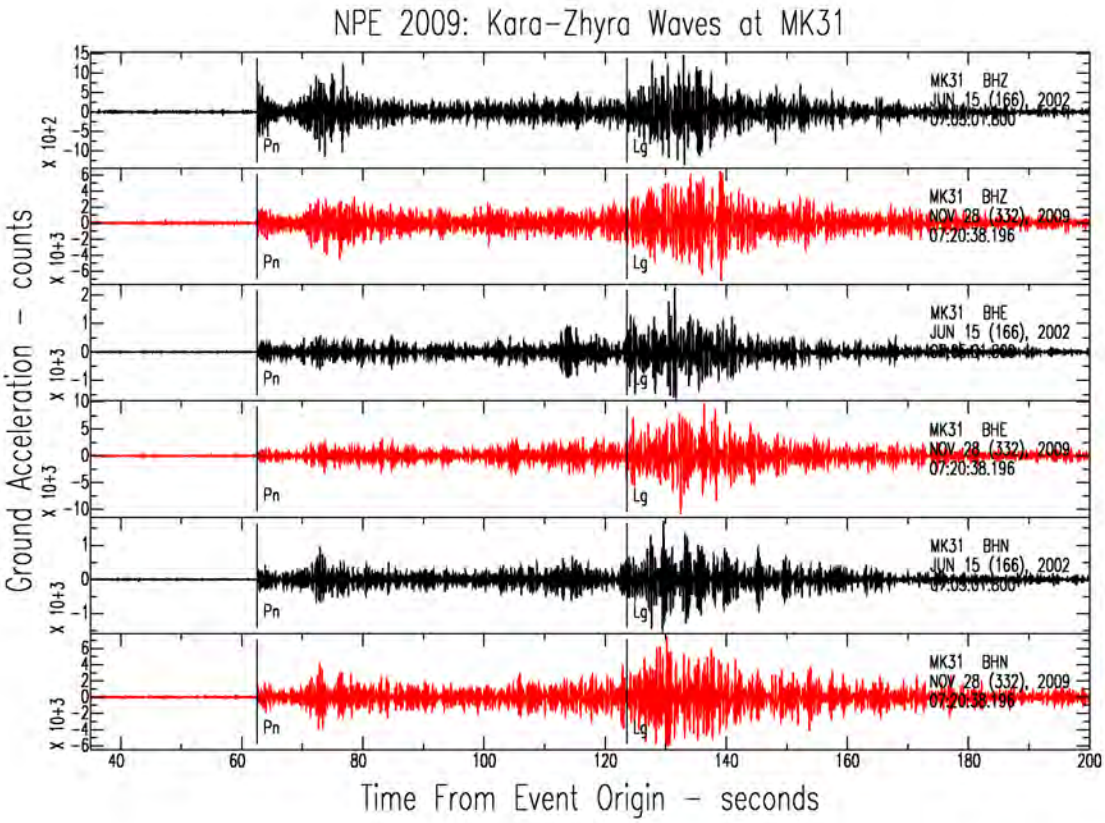


Figure 8. Kara-Zhyra coal mine waveform templates (black), and the detected NPE 2009 waveforms (red).

Discrimination Results – Deep Earthquakes

Referring back to Figure 4 (regional waveforms of crustal and sub-crustal earthquakes), we have experimented with several discriminants that use P (or Pn) amplitudes and Pg amplitudes (or P-coda where Pg is not present). For sub-crustal earthquakes we are assuming the first-P will be impulsive, but P-coda will decay smoothly and there will be an absence of a distinct Pg phase. Further, for crustal earthquakes, we assume Pg will be richer in frequencies near 1 Hz and deficient in higher frequencies because of greater attenuation over a relatively long path within the crust.

Figure 9 shows two discriminants with potential for separating crustal and sub-crustal earthquakes. They are derived from RMS amplitude measurements made at station KK31 (KKAR array). Events and stations are shown in Figure 5b. Event-station distances vary from between 250 km and about 900 km. Figure 9a shows ratio-versus-magnitude (top) and ratio-versus-distance (bottom) for a Pg spectral ratio. A ratio-distance trend (derived using crustal earthquakes) has been removed from all ratios. In this case, for sub-crustal earthquakes we have measured a P-window segment where Pg would exist if the event had been at crustal depths. We believe this discriminant shows promise due to attenuation at the 6-12 Hz band for the shallow earthquakes with exclusively crustal paths. Figure 9b shows the same plots as 9a, but for a Pn/Pg ratio at the 0.75-1.5 Hz band. We believe this discriminant shows promise because the "Pg" measurement for sub-crustal earthquakes is actually a P-coda measurement where coda decay has reduced the amplitude relative to the impulsive first-P. For this discriminant, the crustal earthquakes have roughly the same amplitudes for Pn and for Pg. These are preliminary results and we intend to test further by applying MDAC corrections to see if separation between crustal and sub-crustal earthquakes can be increased. After MDAC experimentation, we will process and categorize all earthquakes shown in Figure 5a.

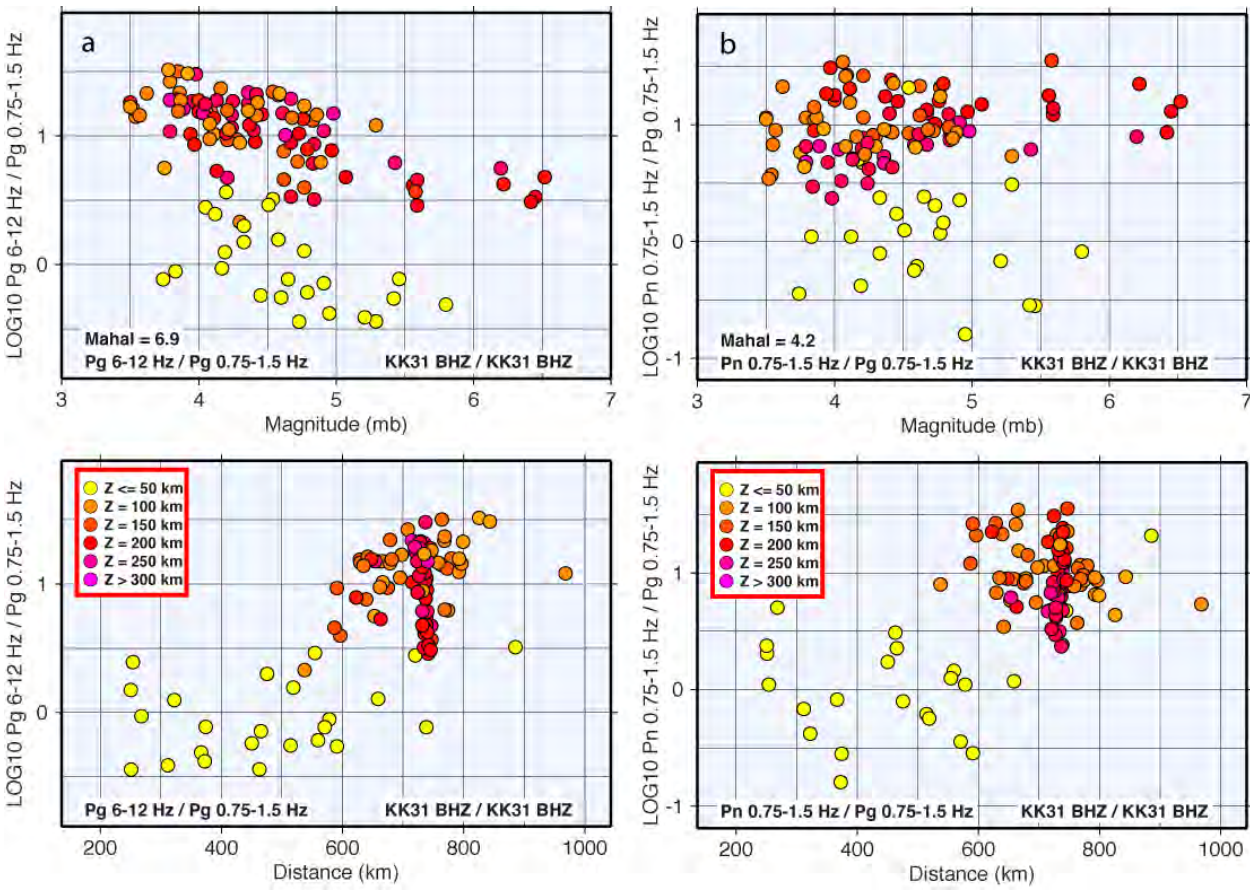


Figure 9. (a) Discrimination plots of Pg spectral ratio (6-12 Hz / 0.75-1.5 Hz) from RMS amplitude measurements (in displacement) made at KK31. Only events with 4 or more teleseismic depth phases were used to make this figure. A distance trend derived from the crustal earthquakes has been removed from all ratios. As the deep events have no true Pg phase, this plot is comparing a phase ratio for the crustal events to a P-coda ratio for the deep events. (b) Discrimination plots of first-P amplitude in ratio with a "Pg" amplitude (see text, above).

CONCLUSIONS AND RECOMMENDATIONS

We have an ongoing program to identify mining seismicity clusters and establish ground-truth mining event information from waveform correlations. For our eastern Kazakhstan study area, we have tied over 1,000 events to 23 distinct mining-event clusters. Event time-of-day analysis shows that mining explosions occur during all hours of the day in eastern Kazakhstan, except during the early morning hours (hours 21–23 GMT). We have identified 9 earthquakes near KTS by assuming that early morning events are earthquakes. We have also assembled KURK waves from contained and uncontained single-charge chemical explosions detonated during experiments from the late 1990s at KTS. Using the earthquakes, single-charge explosions, and mining explosions from three mines near KTS, we have tested several discriminants. We find that (1) the high frequency (7-14 Hz) Pg/Lg ratio separates earthquakes from contained and partially contained single-charge explosions, and this discriminant separates most mining explosions from the earthquakes; (2) apparent delay-firing of mining events does not seem to influence the Pg/Lg discriminant performance; and (3) Lg/Lg-coda ratios that exploit the presence of the Rg phase may be useful for separating mining explosions from earthquakes and, possibly, contained explosions from uncontained explosions. We will continue to investigate discriminant measurement and correction methods in an attempt to improve performance in separating mining events from earthquakes and single-charge, contained explosions.

We developed a small ground truth data set for crustal and sub-crustal earthquakes from the Hindu-Kush region. These events are recorded at near- to mid-regional distances. We found promising discriminants for separating crustal earthquakes from sub-crustal earthquakes. These are the Pg spectral ratio and a Pn/Pg (1 Hz) phase ratio. We intend to develop additional ground truth data for both deep and crustal events in the Hindu-Kush region, experiment with other discriminants, and apply MDAC processing to the earthquake measurements to see if improvement can be obtained in identifying sub-crustal earthquakes.

ACKNOWLEDGEMENTS

We thank the entire LANL Ground-Based Nuclear Explosion Monitoring Research and Development team for supporting efforts that make this work possible, and we especially thank Richard Stead, Julio Aguilar-Chang, and Diane Baker for their database assembly and maintenance efforts. We thank the IRIS DMC for rapidly filling data requests. We used data from operators and host institutions affiliated with the II, IU, and KZ networks.

REFERENCES

Anderson, D.N., D.K. Fagan, M.A. Tinker, G.D. Kraft, and K.D Hutchenson (2007). A mathematical statistics formulation of the teleseismic explosion identification problem with multiple discriminants, *Bull. Seismol. Soc. Am.* **97**, 1730–1741.

Arrowsmith, S. J., M. A. Hedlin, M. D. Arrowsmith, and B. W. Stump (2007). Identification of delay-fired explosions using seismic array: application to the PDAR array in Wyoming, USA, *Bull. Seismol. Soc. Am.* **97,** 989–1001.

Glenn, L. A. and S. C. Myers (1997). *Depth of burial experiments at Balapan,* LLNL report UCRL-JC-128313, 7 pp.

Hartse, H. E., S. R. Taylor, W. S. Phillips, and G. E. Randall (1997). A preliminary study of regional seismic discrimination in central Asia with emphasis on western China, *Bull. Seismol. Soc. Am.* **87,** 551–568.

Hartse, H., G. Randall, X. Yang, and C. Rowe (2007). Regional event identification research in Asia*,* in *Proceedings of the 29th Monitoring Research Review: Ground-Based Nuclear Explosion Monitoring Technologies,* LA-UR-07-5613, Vol. 1, pp. 582–591.

Knowles, C. P. (2006). *The Omega test series,* Defense Threat Reduction Agency technical report DTRA 01-99-D-0047.

MacCarthy, J. K., H. E. Hartse, M. Greene, and C. Rowe (2008). Using waveform cross-correlation and satellite imagery to identify repeating mine blasts in eastern Kazakhstan, *Seismol. Res. Lett.* **79** (3), 393–399.

Mikhailova, N.N. and Sinyova, Z.I. (2010). New ground truth events in central Asia, PDF file from: www.ctbto.org 14 pp.

NNC RK (1998). *Report on seismic monitoring of test hole closures at Balapan,* Institute of Geophysical Research of the National Nuclear Center, Republic of Kazakhstan (no authors listed), 62 pp.

HYDRODYNAMIC ANALYSIS OF THE EFFECT OF A NON-UNIFORM WEATHERED LAYER ON FREE SURFACE ACCELERATION SIGNALS

Earl. E. Knight, Esteban Rougier, Alek Zubelewicz, Aviva J. Sussman, David Coblentz, David W. Steedman, Wendee M. Brunish, and Christopher R. Bradley.

Los Alamos National Laboratory

Sponsored by the National Nuclear Security Administration

Award No. DE-AC52-06NA25946 / NST11-NCNS-TM-EXP-PD15

ABSTRACT

The Source Physics Experiment (SPE-N) was designed to provide a carefully controlled seismic and strong motion data set from buried explosions at the Nevada National Security Site (NNSS). To date, two experiments have been conducted: SPE-1 (May 2011) and SPE-2 (October 2011). The focus of this paper is on the analysis of SPE-2, which consisted of a 1000 kg high explosive stemmed for coupling at 45 meters below the surface. The experiment was heavily instrumented with a free-field and free-surface accelerometers, as well as infrasound sensors and an extensive seismic monitoring network.

The approach presented here uniquely combines two major factors into the free-surface acceleration analysis: the site topography and a 3D geologic characterization of the non-uniform weathered layer. The site topography was obtained though digital elevation models, wave speed variation with depth data provided from Sandia National Laboratories, combined with borehole core sample analysis allowed for the development of a first order 3D non uniform weathered layer model that will be refined via gravity modeling from Los Alamos National Laboratory.

In addition, we developed a unique continuum-based-visco-plastic strain-rate-dependent material model. Despite notable successes in the development of fracture models for geological materials, the prediction of the behavior and fracture of rock formations remains a significant challenge. Several constitutive models have been proposed, most of which use rate insensitive plasticity. In addition, it is frequently assumed that macro-damages can be treated as non-interacting micro-cracks randomly distributed in an otherwise homogeneous material. Since the crack opening strain is collected from the individual micro-cracks, these descriptions are suitable for predicting the material's responses at the early stage of the damage process. Often, the cracks are characterized in terms of the crack surface area, while their orientations are defined in terms of stresses. Fracture processes are built into the constitutive description by either degrading the material's strength or shear modulus. In this description, the fracture processes are monitored in terms of stress tractions at the dominant load chains acting on the crack opening displacements. As in many other cases, the fracture plane is co-rotational with principal stresses and, therefore, this model produces fracture that is stress-co-rotational, thus isotropic. This model was developed because, even though our analysis depicts the trends seen at the free surface gages, a more comprehensive material model is needed in order to better describe the wave propagation through pre-damaged or weathered media.

Provided in this paper are the qualitative analysis of the results obtained from hydrodynamic calculations for the free-surface gages. The readings obtained from the experiments initially suggested that there were apparent anomalies in the arrival times for some of the free surface gauges. However, for SPE-2, numerical results demonstrate that the inclusion of a non-uniform weathered layer and the local topography are mandatory when examining any of the free surface effects.

Objectives

The National Center for Nuclear Security (NCNS) has chosen the Nevada National Security Site (NNSS) as the test location for the Source Physics Experiment (SPE-N) program. The primary purpose of the SPE-N program is to improve strong ground motion prediction capabilities (ranging from coupled to decoupled scenarios) as well as seismic wave generation and propagation detection thresholds. Verification and validation of the program's developed models will then allow analysts to detect and discriminate between "low yield" nuclear explosions, conventional explosion tests, and seismic energy from earthquakes. NNSS was chosen as the test-bed for it provides an ideal natural laboratory and more importantly, the geology at the NNSS is well-characterized.

One of our main goals within the SPE-N framework is to develop hydrodynamic simulation capabilities that will provide a physical basis for modeling aspects of explosion phenomena that are of interest to LANL's mission. Inherent in this goal is the development of an approach that accounts for all physical processes that cause shear wave generation. As such, the important components of our hydrodynamic approach include 1) utilizing three-dimensional fully-coupled strong motion hydrodynamic codes that provide a way to explicitly model near source finite displacement as well as surface damages; 2) developing material models that will allow us to realistically treat the microcrack releases that dominate near-source energy as well as fracture processes; 3) coupling the strong motion codes to higher order spectral element codes with variable gridding to accurately model the effect of surface topography; and 4) coupling our hydrodynamic calculations to seismic source models that utilize Compensated Linear Vector Dipole (CLVD) models in order to unequivocally separate source-generated shear waves from scattering-generated shear waves.

Research Accomplished

The SPE-N is designed to provide a carefully controlled seismic and strong motion data set from buried explosions at the NNSS. To date, two planned experiments have been conducted. This paper focuses on surface acceleration signal analysis from the second experiment, which was conducted in October, 2011.

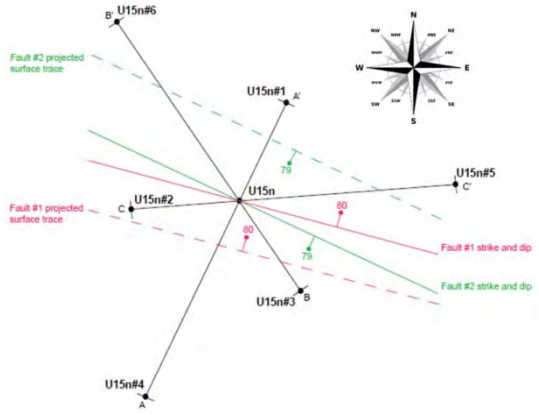


Figure 1. Top view of the general setup of the SPE2 experiment.

SPE-2 was placed in the U15n borehole in Area 15 of the NNSS. It consisted of a cylindrical 2572-lb (1167-kg) heavy ANFO explosive (1000-kg TNT equivalent) charge placed in a 36-in (0.91-m) borehole at the 150-ft (45.72-m) depth. In addition to the six monitoring boreholes used to place free-field accelerometers (Figure 1) Sandia National Laboratories (SNL) deployed several surface accelerometer gauges (Figure 2). Two notable faults were seen in the U15n borehole photo logs and in the extracted cores. Because there was no surface expression of the faults, they were projected to the surface as shown in Figure 1 using a constant strike and dip angle. In contrast to recent analysis efforts that have primarily concentrated on the effect of faults and joints to understand free-field accelerometer readings, this effort seeks to understand the effect of topography and a non-uniform weathered layer on free-surface readings.

Review of SPE-2 Surface Accelerometer Data (Arrival Times)

Six gauges were installed for the SPE-2 shot; four at 15-meter range (A6, A7, A10, and A11), and two at 30-meter range (A5 and A12) – see Figure 2. Post-shot evaluation of the accelerometer data revealed significant variation in the arrival times for gauges at the same range (Figure 3; Steedman, 2012). Specifically, arrival times for gauges

A7 and A10 (15 meters range) are about 1 ms faster than for gauges A6 and A11 (which are at the same range, 15 meters). Furthermore, the initial arrival time at A12 (30 meters range) is earlier that A11 (which is at a closer range, 15 meters).

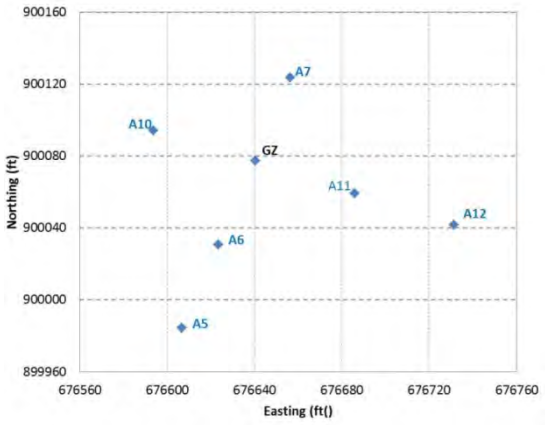


Figure 2. Location of the Free Surface Accelerometers for SPE-2.

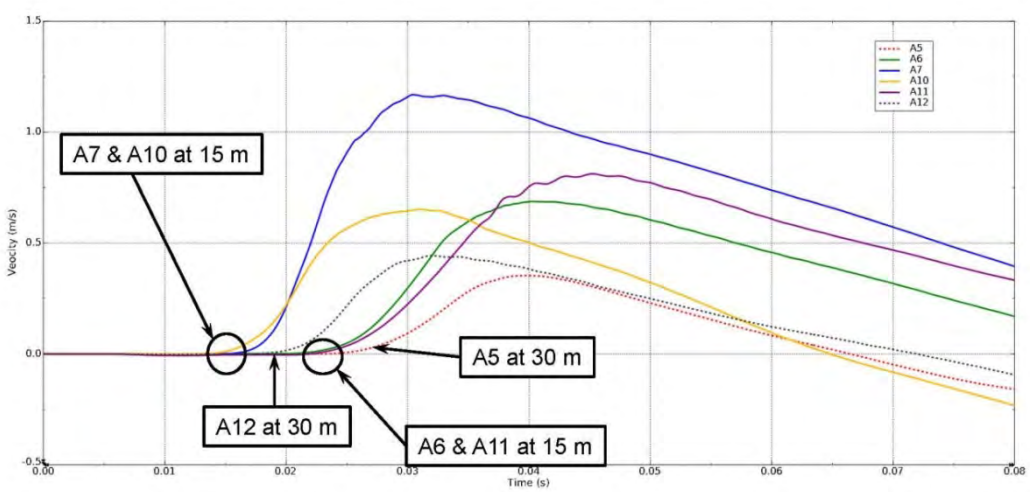


Figure 3. Arrival Times and Peak Velocities for the Gauges shown in Figure 2.

Apparent Velocity in the Near-Surface Due to Weathered Layer Geometry

Variations in the arrival times from the surface accelerometer data motivated the computation of apparent velocity across the SPE test bed. The apparent velocity contours (Figure 4) were computed from the arrival times and gauge slant range distances. The apparent velocity shows a definitive trend decreasing to the southeast and suggests a southeast dipping interface between the weathered layer and the intact granite at the SPE site.

Description of the SPE Weathered Layer

Although the Climax Stock area was selected as the site of the first set of SPE tests because its granite lithology provides a relatively "homogenous" medium, there are a number of geologic features that have a profound impact on the shock propagation at the SPE site (Townsend et al., 2012). For this investigation, two geologic features have been incorporated into LANL's Geologic Framework Model (GFM): the geometry of the interface between the near-surface weathered granite and the underlying intact granite and the topography near the shot borehole.

Description of the SPE Weathered Layer (continued)

The depth of weathering was not well documented in the early geologic studies at the Climax Stock. Shellum and Fisher (1996) noted that the extent of highly weathered granite at Climax stock varies from about 12 to 18 m (40 to 60 ft) deep in the low-lying areas of the stock, and may only be 1 to 6 m (3 to 20 ft) deep in the hilly portions of the

area. Well hole logs of the emplacement hole (U15n) at the SPE site indicate the depth of the weathered layer to be about 15.2 m (50 ft.) or at an elevation of about 1510m (above sea level).

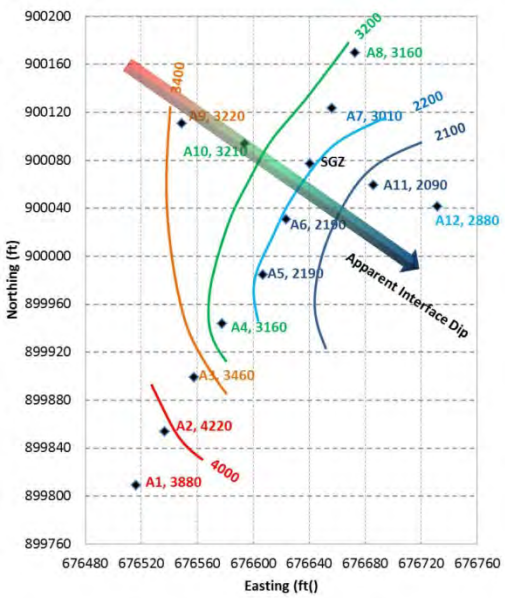


Figure 4. Apparent Velocity Contours for the SPE Site.

In an attempt to resolve the spatial variability of the weathered layer at the SPE site, SNL conducted a seismic tomographic survey in April 2010 (Abbott, see Acknowledgements). Variations in the seismic velocities along two profiles bisecting the SPE site along with the interpreted base of the weathered layer are shown in Figure 5.

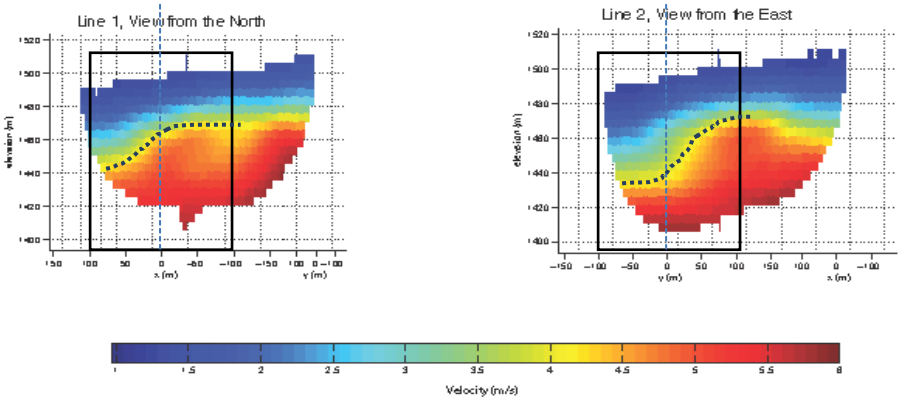


Figure 5. Seismic tomography profiles (Abbott, see Acknowledgements) bisecting the SPE site. The dashed line designates the location of the shot point along the profiles. Dashed lines designate the interpreted interface between the weathered and intact granite. The black box defines the spatial extent of the GAMUT model shown in Figure 6.

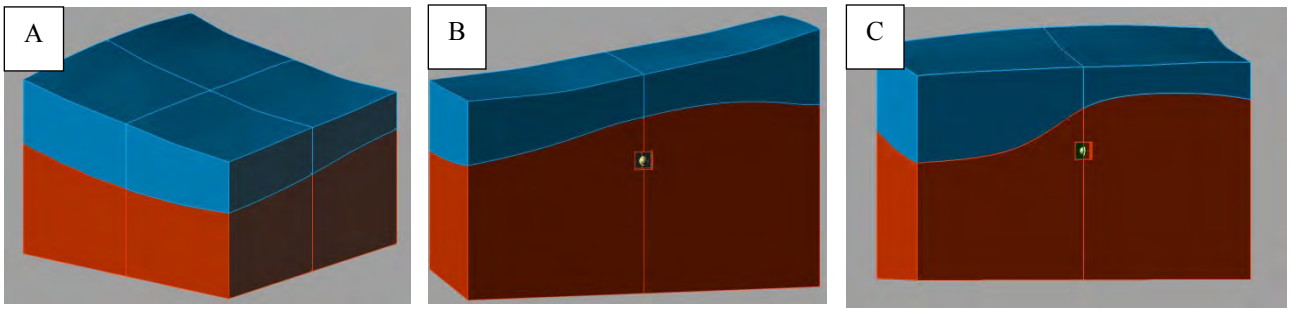


Figure 6. A) View to the NW of the SPE GFM model showing the weathered layer (blue) and intact granite (red) to a depth of 1400m above sea level. B) View to the north (EW profile) and C) View to the West (NS profile) showing the details of the weathered interface (which can be compared with the seismic profiles shown in Figure 4). The GFM model extends +/- 100m about the shot point. For reference, the spheres shown in B) and C) indicate the shot point depth. The topographic surface was based on a 10-m DEM.

Spatial variation of the weathered surface is shown in Figure 7, which illustrates the geometry of the top of the intact granite at the SPE site. The elevation of the weathered layer thickness at the center of the model (corresponding to the emplacement hole U15n) is 1500m, the thickness of the weathered layer increases considerably to the southeast, where it is at an elevation of 1467 m at (x = 100m, y = -100m) and the weathered layer has a thickness of about 40m.

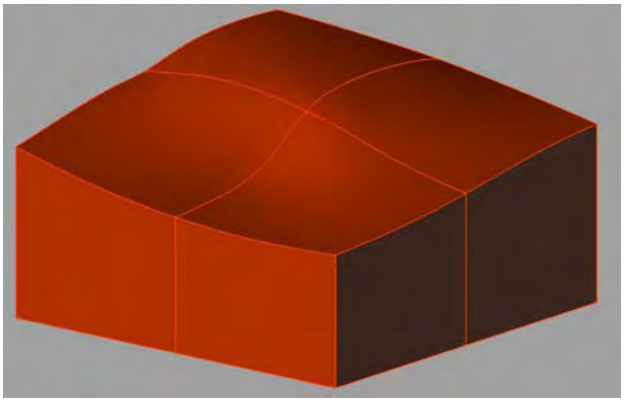


Figure 7. View to the NW of the surface of the intact granite (base of the weathered layer) at the SPE site. The lines bisect the shot point location (U15n).

Computational Geometry and Mesh

The volumetric elements of the GFM were meshed using SNL's meshing tool Cubit, resulting in a mesh consisting of 3984k elements. The mesh is refined near the shot borehole in order to provide accurate surface data collection at the 15/30m points. Figure 8 (left) shows the mesh of the View to the West (NS profile) showing the details of the weathered interface while Figure 8 (right) shows the mesh of the spatial variation between the intact granite and weathered granite layer.

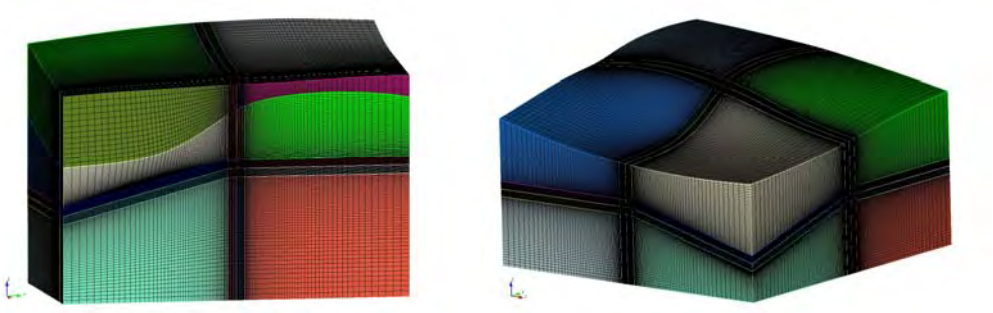


Figure 8. Mesh depictions for NS profile of view to the west and view to the NW.

A wing view of the intact granite and weathered granite layer along with a depicted charge (Figure 9) shows the profound difference in layer elevation over the 200m by 200m analysis block.



Figure 9. Wing view of the granite/weathered granite layer with charge depiction.

Material Properties

Material properties for NTS intact climax stock granite were taken from LLNL (Antoun et al., 2001) and SNL (Fossum, 2004; Broome and Pfeifle, 2011) studies. Weathered granite properties were estimated based on the p-wave speed and Poisson ratio provided by SNL's study of U15-n core data. The set of parameters employed in the simulations is shown in Table 1, where K is the bulk modulus, τ_{max} is the maximum shear stress and σ_{tens} is the tensile strength.

Table 1: Granite Material Properties Parameters

Granite	ρ **(kg/m^3)**	K **(GPa)**	ν	τ_{max} **(GPa)**	σ_{tens} **(MPa)**	α (m/s)
Intact	**2630**	**35.0**	**0.226**	**1.5**	**25.0**	**4700**
Weathered	**2580**	**1.7**	**0.330**	**0.6**	**0.1**	**1000**

EOS and Material Models

The calculations were conducted utilizing CASH, (Campbell-Shashkov) (Dey and Bos, 2001), which is a lagrangian strong motion code used to simulate the explosive source propagation. The calculation utilized the Tillotson EOS and a three invariant strength model with damage for the granite. The shear strength material model utilized also includes a damage model. The damage model relaxes the yield surface as a function of the equivalent plastic shear strain. At the beginning of the simulation the damage parameter is set to zero everywhere. As the simulation progresses and the material starts to yield in shear, the equivalent plastic shear strain increases. Complete damage was obtained when the equivalent plastic shear strain reached a value of 0.0125.

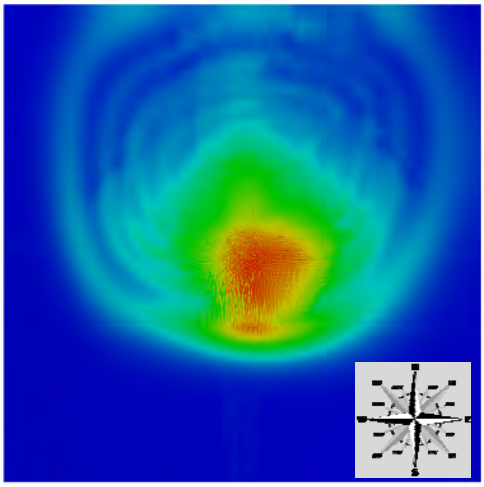


Figure 10. Top view of the wave propagation at 40 ms.

Computational Results

The results presented in this section correspond to the full 3D model shown in Figure 8. The model contained approximately 4 million elements, incorporated gravity effects, and was run on 128 processors (in LANL's LOBO cluster).

A snapshot of the velocity map at 40 ms is shown in Figure 10. As it was expected, the presence of the non-uniform weathered layer introduced quite strong asymmetries to the results obtained from the 3D simulations. The snapshot shows that the p-wave propagates much faster where the weathered layer is thinner. Two cross sections of the model (see Figure 11) were also made in order to further demonstrate the influence of the weathered layer in the wave propagation results.

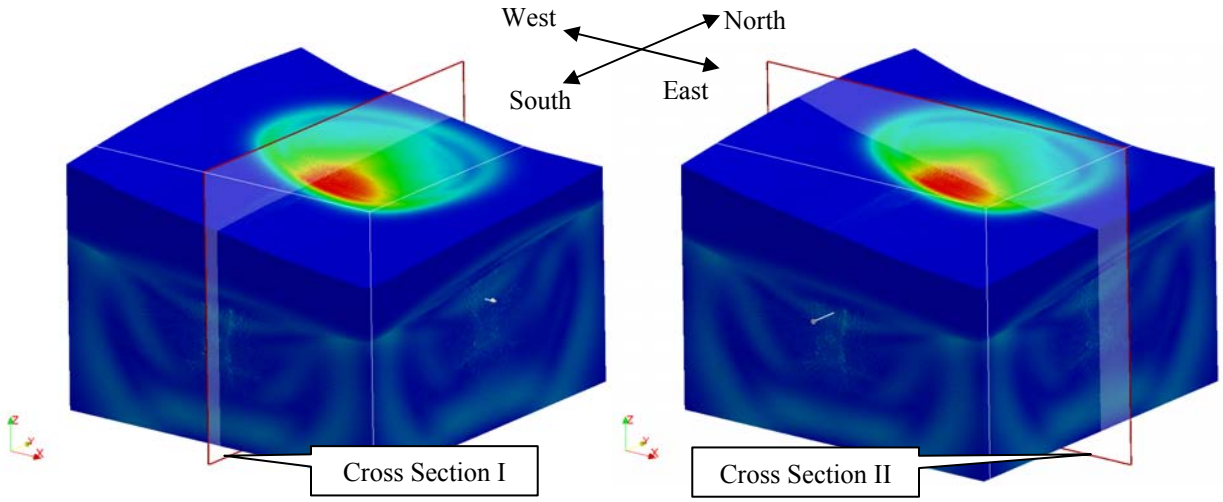


Figure 11. Schematics of the cross section I and II used for the analysis.

The more pronounced effects of the weathered layer scattering are seen in Figure 12 and 13. In the region where the weathered layer is thinner, the p-wave reaches the surface much sooner than in the rest of the model. From the figures it can be observed that the main difference in arrival times are encountered in the North-South direction, while only small differences in arrival times are being seen in the East-West direction.

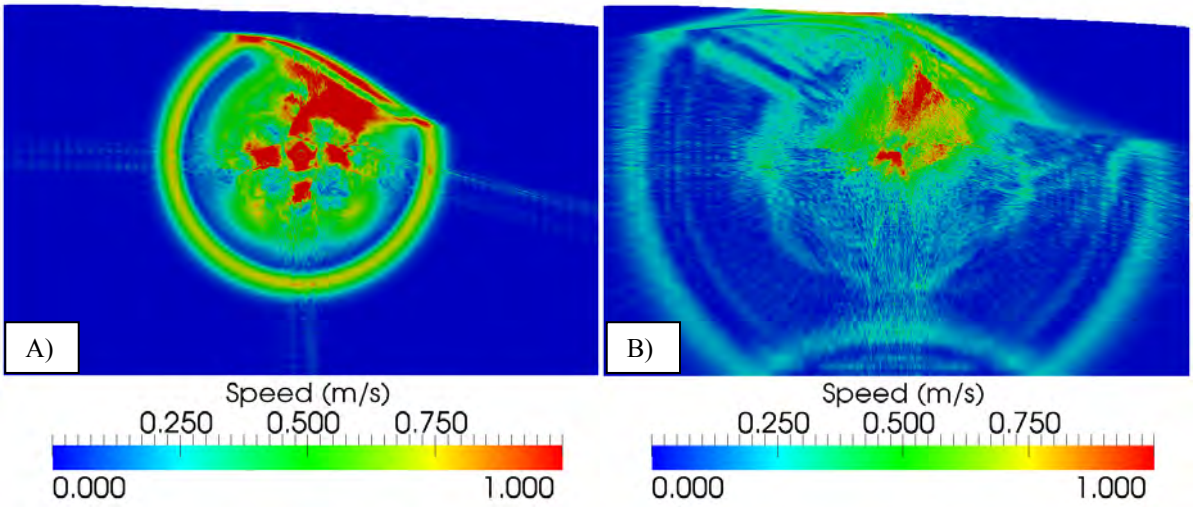


Figure 12. Cross section I: view of the wave propagation looking West. A) 10 ms; B) 20 ms.

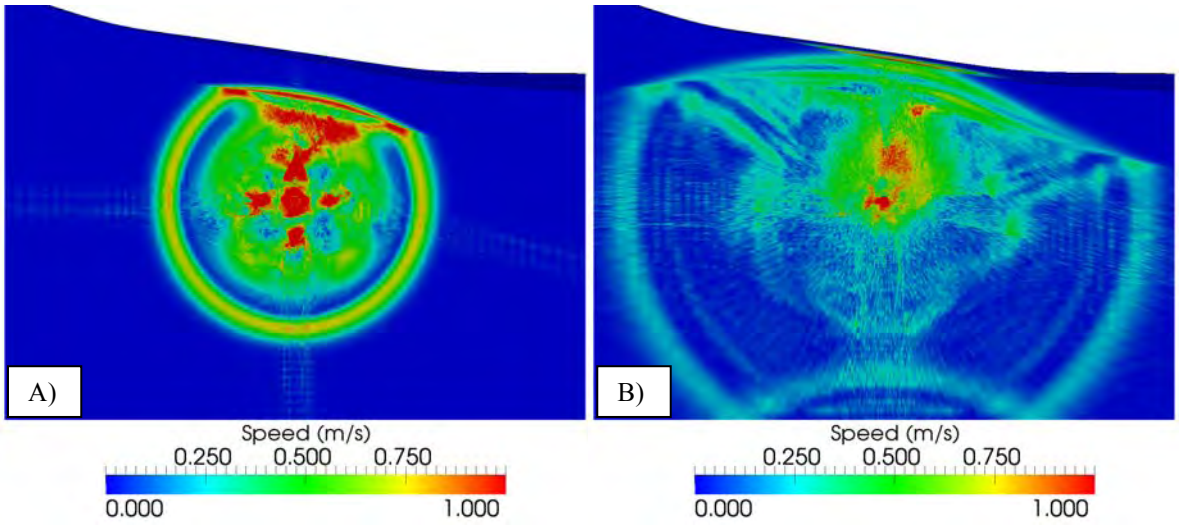


Figure 13. Cross section II: view of the wave propagation looking South. A) 10 ms; B) 20 ms.

The simulated vertical velocity histories for all six SNL gages are shown in Figure 14. To better understand these results it is necessary to look at the trends of individual gages vs. actual SNL observations.

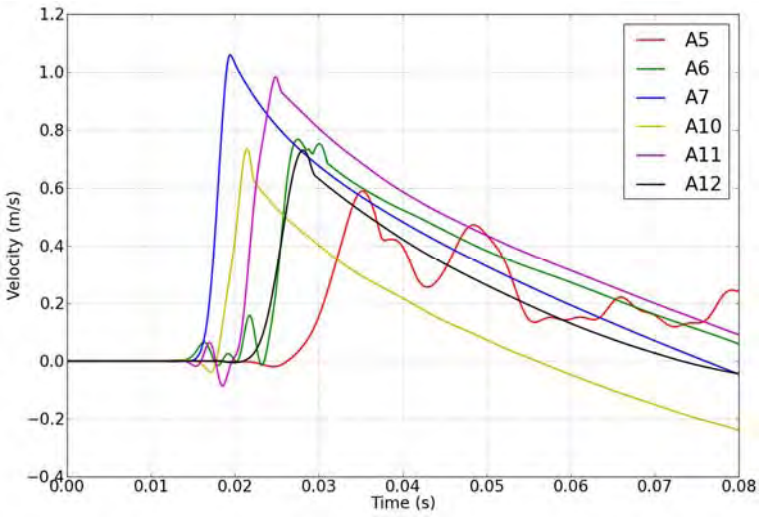


Figure 14. Vertical velocity histories for free surface gages A5, A6, A7, A10 A11 and A12.

The arrival times for gages A5, A7 and A10 are in good agreement with the observations (see Figure 3). As expected, the peak velocity for gage A5, which is located at 30m range is much lower that the values obtained for the 15m range gages (A7 and A10). However, even though gages A7 and A10 are both at the same 15m range, the inclusion of a non-uniform weathered layer in the model properly discriminates the differences in the peak velocity for those two gages.

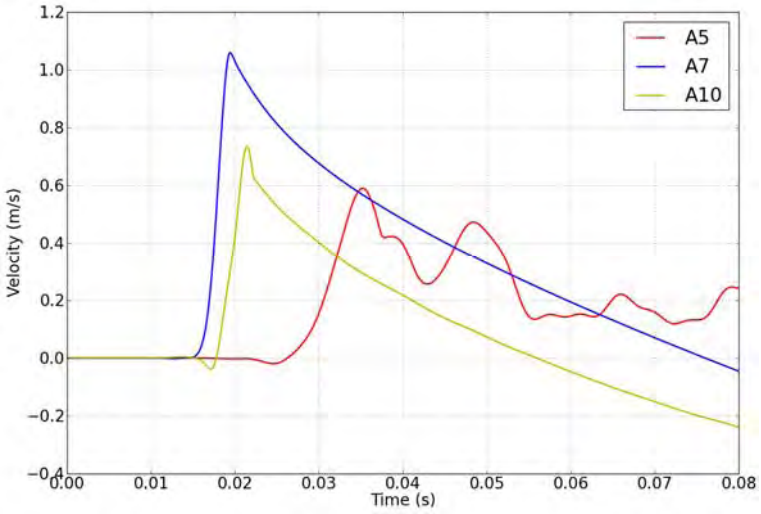


Figure 15. Vertical velocity histories for free surface gages A5, A7 and A10.

Further investigation of the 30m gages (A5 and A12) shows that the simulation results properly account for the different arrival times seen in SNL's observations. However, there is a consistent over prediction of the velocity peaks for both gages.

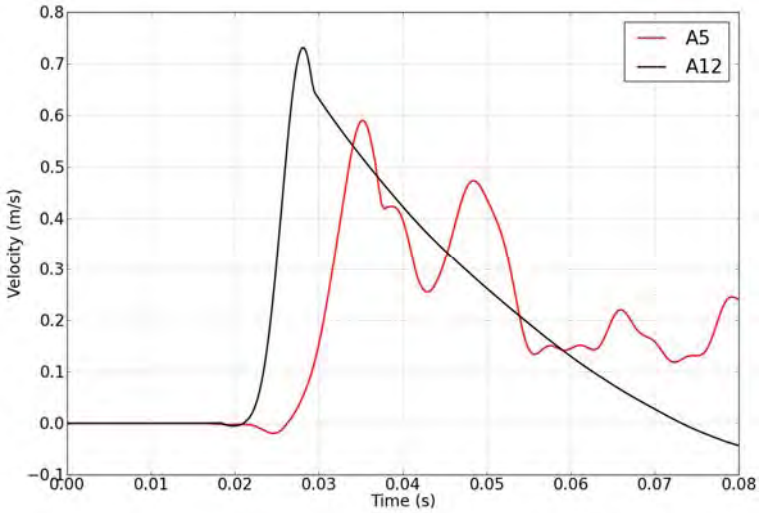


Figure 16. Vertical velocity histories for free surface gages A5 and A12.

Additionally, for all four 15m gages the simulation properly accounts for arrival time differences for the North-West vs. South-East gages locations, i.e., A7 and A10 arrive earlier than A6 and A11 (see Figure 17). However, as with the 30m gages we are seeing an over-prediction of the peak velocities for gages A6 and A11.

Given the results, it is clear that incorporation of a non-uniform weather layer is required for evaluating the free surface accelerometer gages. The first order 3D non-uniform weather layer model utilized in this study reproduces the general trends observed in the velocity history graphs from SNL's 15m and 30m gage packages. In order to improve the match between the predicted and observed velocity data, we plan to refine the geometry of the non-uniform weather layer when further data is obtained from LANL gravity modeling. We note, however, that despite our success in matching the trends, it is clear that a more comprehensive material model is required to improve our modeling of wave propagation through pre-damaged or weathered media. Specifically, we anticipate a decrease in the peak velocities for the two 15m (A6 and A11) and two 30m gages (A5 and A12) where the wave travels through a thicker layer of weathered material. To address this aspect, efforts are under way within LANL's Geodynamics team to develop a novel continuum-based visco-plastic strain-rate-dependent material model.

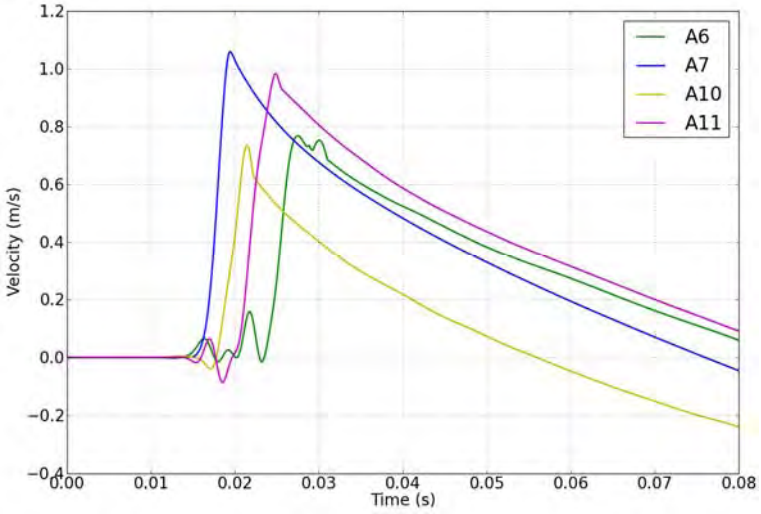


Figure 17. Vertical velocity histories for free surface gages A6, A7, A10 and A11.

AZ_Frac Material Model

Key features of this new model will be the ability to describe continuum fracture processes (crack opening and closure, energy dissipation, etc.) while also handling general anisotropic material characteristics. Characterization

analysis on the weathered layer has shown that there exists a preferential set of discontinuities that are oriented with a relatively high angle (80º in the vertical direction).

In the proposed development, we utilize an earlier approach (Zubelewicz and Bazant, 1987) and construct the model within the framework of a tensor representation theory. The rates of the homogeneous visco-elastic deformation and the growth of micro-damages are described in terms of symmetric second order flow tensors which include shear (deviatoric strain) and dilatation (volumetric strain) contributions. The fracture is embedded into an isotropic elastic material and is degrading the responses at the plane of the dominant fracture. A full description of the model along with verification and validation results can be found in LANL report LA-UR-12-21536 (Zubelewicz et. al., 2012). The model has built-in anisotropy due to the material's directional properties (A) and includes anisotropy which results from the fracture process (AF). Also, we capture the directionality present in a weathered geomaterial. The later phenomenon is treated as weather induced anisotropy (WA). In our mechanisms-based approach we included the fracture processes in three directions coupled with the directions of principle stresses. The three damages are linked together and, therefore, are suitable for the reconstruction of the Mode I, II and III fractures. In this manner, rubble produced in shock compression reduces the strengths in tension and shear. These phenomena are very important when describing the material's behavior and failure under shock loading. For our approach, a previously fractured material regains a loading bearing capacity upon recompression (FR). Furthermore, the model is developed in the framework of visco-plasticity and, as such, enables a smooth elastic-plastic transition, while adding to the dissipation associated with friction (energy damping). Lastly, the model has built-in an energy based equation of state (EOS) which in our case works only on the elastic component of the volumetric change of the material.

CONCLUSIONS AND RECOMMENDATIONS

Provided in this paper was the qualitative analysis of the results obtained from 3D hydrodynamic calculations for the SPE-2 free-surface gages. The readings obtained from the experiments initially suggested that there were apparent anomalies in the arrival times for some of the free surface gauges. However, numerical results demonstrate that the inclusion of a non-uniform weathered layer and the local topography are mandatory when examining any of the free surface effects.

Based on the results discussed above we recommend continued study to:

1. Refine GFM upon arrival of LANL's gravity data.
2. Incorporate further geologic features, such as faults, joints, etc.
3. Account for saturation effects.

ACKNOWLEDGEMENTS

The authors would like to thank the National Nuclear Security Administration and the National Center for Nuclear Security for sponsoring this research effort. Large field activities like the Source Physics Experiment require the cooperation of individuals from many organizations. Thanks to our colleagues and collaborators for their support and the advice provided during this project. Finally, we thank R. Abbott for information gleaned from personal communications.

REFERENCES

Antoun, T. H., I. N. Lomov and L. A. Glenn (2001). Development and application of a strength and damage model for rock under dynamic loading, in *Proceedings of the 38th U.S. Rock Mechanics Symposium, Rock Mechanics in the National Interest*, D. Elsworth, J. Tinucci and K. Heasley (eds.), A. A. Balkema Publishers, Lisse, The Netherlands, 369–374

Broome, S. and T. Pfeifle (2011). Phase 1 mechanical testing results on core from borehole U-15n, Nevada National Security Site, in support of NCNS Source Physics Experiment, Sandia National Laboratory Memorandum dated 8 June 2011.

Dey, T. N. and Bos, R. J. (2001). *CASH Code*, LA-CC-01-53.

Fossum A. F. and R. M. Brannon (2004). THE SANDIA GEOMODEL: Theory and User's Guide. Sandia National Laboratories.

Steedman, D.W. (2012). Los Alamos National Laboratory. SPE-2 Surface Accelerometer Analysis.

Shellum, C. and P. Fisher (1996). Springfield Research Facility. Written communication to G. Baladi, Defense Special Weapons Agency. Subject: *Mechanical Properties for Climax Granitic Rock, NTS*. October 4, 1996.

Townsend, M., L. B. Prothro, and C. Obi (2012). Geology of the Source Physics Experiment Site, Climax Stock, Nevada, National Security Site, DOE/NV/25946-1448, 707pp.

Zubelewicz, A. and Bažant, Z. P. (1987). Interface element modeling of fracture in aggregate composites, *J. Eng. Mech.,* **113**(11), 1619–1630.

Zubelewicz, A., Rougier, E., Knight, E.E. Bradley, C., and Steedman, D. (2012) AZ_Frac Material Model: Code Implementation - Progress Report, May 15, 2012, LA-UR-12-21536.

EFFECTS OF 3D SURFACE TOPOGRAPHY ON REGIONAL AND TELESEISMIC SIGNALS FROM UNDERGROUND EXPLOSIONS

Thorne Lay[1], Megan Avants[1], Xiao-bi Xie[1], and Arthur J. Rodgers[2]

University of California Santa Cruz[1] and Lawrence Livermore National Laboratory[2]

Sponsored by the Air Force Research Laboratory

Award Nos. FA9453-11-C-0234[1] and DE-AC52-07NA27344[2]
Proposal No. BAA11-09

ABSTRACT

Recent underground nuclear tests conducted by North Korea have reaffirmed the importance of near-source rough surface topography for the generation of complex seismic signals observed at regional and teleseismic distances. Complex reflections from the irregular 3D surface scatter into both horizontally and vertically propagating wave fields, producing directionally dependent focusing and defocusing of *P* and *S* wave fields, conversion of *P*-to-*Rg* high frequency energy, and generating complex signal codas, complicating robust event discrimination and precise estimation of burial depth (and hence yield). Quantifying these effects requires numerical methods capable of accurately accounting for the 3D interactions with a rough surface. We are applying two distinct finite difference methods with which we have extensive experience to quantitatively determine the effects of near-source rough topography on seismic waves from shallow underground nuclear explosions, using high-resolution topography models for the North Korea test site and exploring the effects of precise emplacement location relative to the topography. Preliminary work indicates that the very complexity of the wave field that complicates waveform interpretation holds the key to event quantification if the topographic effects are accurately modeled. High-resolution near-source models are being coupled to regional and teleseismic propagators using two methods; representation theorem and embedded slowness array calculations, and comparisons will be made with available recordings from regional arrays and broadband stations and teleseismic IMS arrays. The representation theorem approach has been developed and the LLNL finite difference code WPP has been updated to output strains (from which to compute stresses), as well as displacements, on an integration surface, simplifying the calculation of far-field P wave motions. The goal of this research program is to develop fundamental understanding of the effects of surface topography and guidelines for how resulting waveform complexity can be exploited for precise emplacement location determination, improved yield estimation, and understanding of regional discriminant behavior. We have conducted analysis of regional Lg signals for the 2006 and 2009 North Korean tests. Vertical component broadband seismograms from nine stations were used for the 25 May 2009 event and eight of the same stations for the 9 October 2006 event. An additional 599 broadband seismograms from 82 regional events were used to calibrate the network Lg-magnitudes. The 2009 event is found to have m_b(Lg) = 4.53. The regional Pn velocity is estimated as 8.0 km/s, indicative of stable continental lithosphere, and using a fully-coupled magnitude-yield relation, the yield for the 2009 event is estimated as approximately 2.35 kt.

OBJECTIVES

Seismic waves recorded at regional and teleseismic distances are routinely analyzed to locate, identify and measure the yield of underground nuclear explosions amidst a background of naturally occurring earthquakes. These applications require understanding of elastic wave propagation effects on the seismic waveforms and it is recognized, although incompletely quantified, that the effects of surface topography can be very important for all three applications. Very precise location estimation within a tunneled mountainous terrain is needed to evaluate the effective burial depth beneath any overlying topography. The precision required exceeds that of standard arrival-time location methods, motivating use of complete waveform information, but the roughness of the free surface complicates the nature of depth-phase arrivals (*pP*, *pPn*) in both regional and teleseismic waveforms. Overburden thickness estimates directly influence yield estimation due to predictable effects of confining pressure relative to scaled depth of burial calibration (e.g., Murphy et al., 2010). Enhanced high-frequency S-wave excitation from near-source scattering (*pS*) has strong directionality in radiation, and reduces the discrimination capabilities of regional phases for these events. The relatively strong surface wave excitation may also be influenced by the stress state at the shot point and the topographic environment.

The primary objective of this project involves modeling the effects of 3D rough surface topography on regional and teleseismic signals from shallow underground nuclear explosions. We are performing preliminary 3D work on North Korea, building on the results of Rodgers et al. (2010), and the work on 2D free-surface scattering by He et al. (2008). The overall objectives include:

(1) Verification of the Lawrence Livermore National Laboratory (LLNL) and University of California, Santa Cruz (UCSC) 3D finite difference codes using the North Korea surface topography model with various degrees of smoothing. This is important for recognizing the stability and reproducibility of results for different formulations of the numerical solution for a rough free surface.

(2) For both WPP and the UCSC code, implement both the 2D and 3D finite-difference simulation and local slowness analysis (FDSA) methods of Xie et al. (2005) and Xie et al. (2007) along with connection to teleseismic propagators using the representation theorem. For WPP the FDSA method is directly useful, as the solution produces the displacement field directly, and we will process embedded arrays to separate energy with varying slowness and slant-stack to generate specific teleseismic *P* wave synthetics. For the representation theorem, stress vectors and displacements are computed over a bounding surface in the lower portion of the finite-difference grid and integrated to provide a far-field response using appropriate teleseismic point-force and point-couple Green functions.

(3) Implement connection to regional phases synthetics for both WPP and the UCSC code. FDSA is already configured for the UCSC finite difference code for regional phases, and we can couple this to either mode or frequency-wavenumber propagators. This effort is essential to go from near-field complete wave fields which are informative, but not directly observed, to isolated regional distances where signals are observed.

(4) Using both codes, extend the modeling of sensitivity to surface roughness, position of the source relative to the scattering topography, and observability of the effects at regional and teleseismic distances. Consider several near-source topographic environments to understand S wave generation, Rg-to-P scattering, and pP effects.

(5) By comparison of synthetics and data, we will seek to refine the location and depth of events. The analysis of sensitivity to position above will be exploited to determine which aspects of the complex wave field provide information about the source position, depth beneath the surface, and explosion yield. The best data for comparison is certainly the regional broadband recordings for North Korea, along with stacked signals from IMS arrays at teleseismic distances.

RESEARCH ACCOMPLISHED

We performed a series of numerical simulations of shallow explosions to investigate the effect of surface topography on ground motions with particular emphasis on scattering and the generation of shear waves. Seismic wave simulations were performed with the WPP anelastic finite difference code developed at LLNL (Petersson, 2010). This code uses an algorithm based on a second-order node-centered finite difference scheme (Nilsson et al., 2007; Petersson and Sjogreen, 2010) including free-surface topography using a curvilinear grid (Appelo and Petersson, 2008). Simulations represented a Cartesian domain 30 km x 30 km x 15 km with a grid spacing of 25 m. We used material properties representative of seismically fast granitic rock (5190 m/s, 3000 m/s and 2500 kg/m^3 for the P- and S-wave wavespeeds and density, respectively). The second order WPP method requires 15 points per wavelength for numerical accuracy, so the calculations were accurate to frequency up to 8 Hz. The calculations were run out to about 12 seconds after the origin time and required nearly one billion (1x10^9) grid points. No anelastic attenuation was included in these calculations in order to isolate elastic scattering effects.

Surface topography was generated by the Fourier method with random phase (Frankel and Clayton, 1986). The correlation structure was chosen to be a von Karman function with an isotropic correlation length of 2000 m. The mean elevation of the topography was set to 1000 m and the standard deviation was varied from 50 m to 300 m. Topographic variations were kept limited to a threshold of plus or minus three standard deviations, so that topography varied by ±150 m to ±900 m, for standard deviations of 50 and 300 m, respectively. Figure 1a shows the topography for one realization. The source was placed at the center of the domain at a depth of 500 m below the surface. Three-component ground motion time-series were output along profiles (every 15° in azimuth) radiating from the source from 5-30 km, with 1 km spacing. Figure 1a also shows the points on the surface where ground motion time-series were recorded.

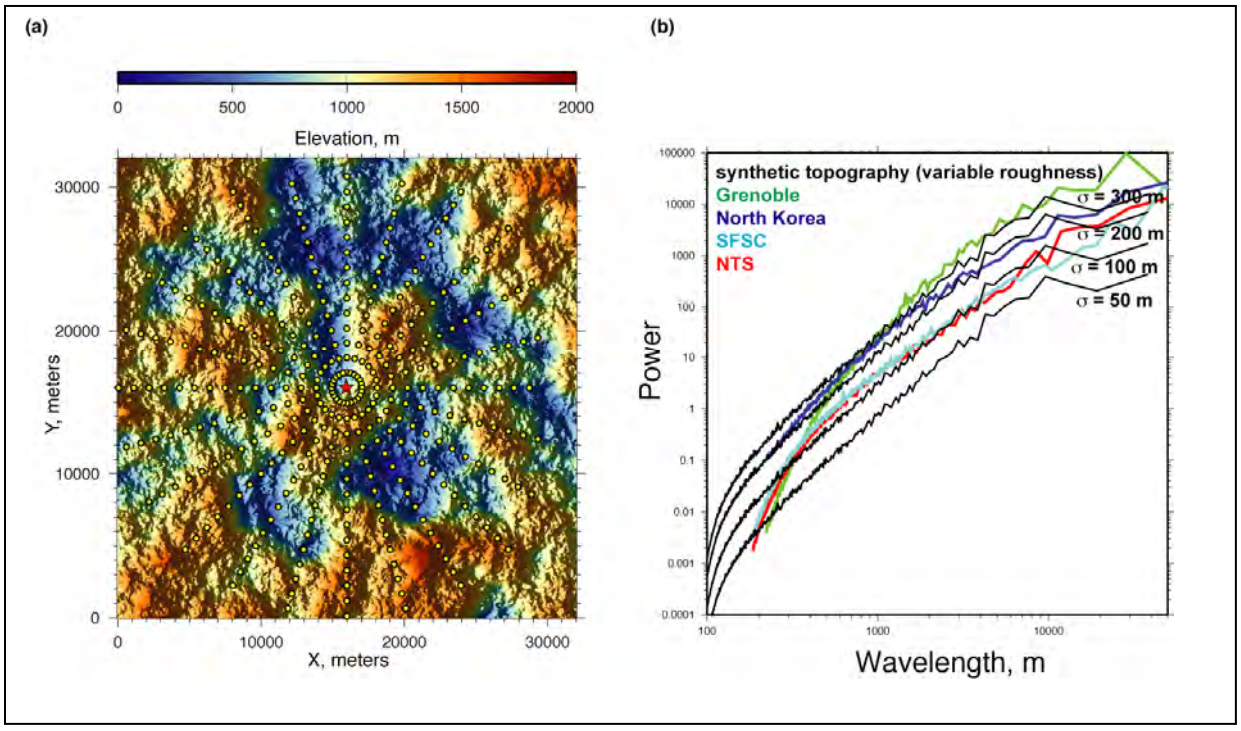


Figure 1. (a, left) Computational domain showing randomly generated surface topography (color scale), source (star) and marker points where ground motions were output (yellow triangles). (b) Power spectra of surface topography as a function of wavelength for (black) the random topography generated with the von Karman autocorrelation function (correlation length of 2000 m and standard deviations of 50, 100, 200 & 300 m). Also shown are the power spectra of actual topography for four regions: Grenoble Basin (green); North Korean nuclear test site (blue); Nevada Test site (red); and San Francisco Bay Area (cyan).

Surface topography is represented in WPP with a curvilinear mesh. The actual topography is read into the code and spatially filtered based on the gird spacing at the surface and wave propagation parameters so that no short wavelength waves will be introduced by interaction with the surface. For sufficiently small grid spacing and/or smooth topography the curvilinear mesh honors the topography. We used a von Karman autocorrelation function to generate the random topography and this has power at short wavelengths. Some of the topographic power is reduced after WPP spatially filters the surface in order to render it on the computational mesh; however, for the fast wavespeeds and fine mesh (25 m) this has only a modest effect on the surface roughness for wavelengths less than 500 m (on the order of the wavelength of highest frequencies resolved on the mesh).

The correlation structure of the topography was chosen because it matches closely that of actual topography. Figure 1b shows the topographic power versus wavelength for four regions (colored lines) of comparable domain size to our simulations: Grenoble, France (in the French Alpes, studied by Chaljub et al., 2010); North Korea (studied in Rodgers et al., 2010); San Francisco Bay, Santa Clara Valley and East Bay Hill; and the Nevada National Security Site (formerly the Nevada Test Site), southern Nevada. Note that in the range of wavelengths from 500–20000 m the actual topographies have a very similar slope, but are offset by different roughnesses or multiplicative factors. By trial and error we found that these topographic correlation structures can be well matched by a von Karman autocorrelation function with correlation length of 2000 m. The synthetic topographies were generated by the Fourier method and their powers are shown with black with the range of topographic roughness: 50, 100, 200 and 300 m. These match the correlation structure of a range of actual topographies and indicates that the assumed correlation structure for the free surface is representative of regions of the Earth with rough topography.

Simulations of ground motions for shallow explosions in a homogeneous half-space show that free surface topography very strongly alters the wavefield. Figure 2 shows the vertical component ground motions in record section format for two of the topographic realizations with different roughnesses: 50 m for (a) and 200 m for (b). The motions at all 24 locations at the same distance from the event along each of the radial lines are plotted in gray and the mean response (stack of all traces at a given distance) is shown in red. In this plot the seismograms are scaled by the square-root of distance so that the surface wave (Rg) should have constant amplitude, reflecting only geometric spreading. Note that the variability in the P-wave amplitudes and waveforms is quite small, however the variability between individual traces increases with time in the window between P and Rg, due to P-to-S scattering. Furthermore, note that the amplitude of scattered energy is proportional to the topographic roughness.

In order to quantify the effect of topographic scattering on high-frequency ground motions near explosions we windowed the phases and measured the Fourier amplitude spectra of each phase. Figure 3a shows the response at 10 km range for a single azimuth for the flat case (which corresponds to a half-space response) and the topographic case with a roughness of 100 m. The response varies with azimuth for the topographic case, but not for the flat case. Note that the P, P-coda and Rg phases are windowed and indicated by the different colors. The Fourier amplitude spectra are computed for each window and shown in Figure 3b. Note that the P spectra for the flat case is broadband, representing the source spectrum, while the Rg spectrum for the flat case is peaked due to the excitation eigenfunction of the fundamental mode Rayleigh wave. The P-coda has no energy for the flat case. For the topographic case the P spectra is broadly similar to that of the flat case, with some modulation due to scattering. The P-coda spectrum for the topographic case is non-zero and tracks the P spectrum with amplitude about a factor of three less than the P spectrum. The Rg spectrum for the topographic case has the same peak frequency as the flat case (1-2 Hz), but does not decay rapidly as it does for the flat case. Energy in the Rg window for the topographic cases roughly tracks with the P spectrum and is up to a factor of ten greater than that for the flat case.

The individual spectra for the P, P-coda and Rg windows show substantial path-specific variability. However, if the spectra for traces recorded at 10 km range and each topographic roughness are grouped together ensemble behavior emerges. Figure 3c shows the average spectra for the flat and four topographic roughnesses. Remarkably, the P spectra are not impacted by the different roughnesses, but the P-coda and Rg spectra show a strong dependence on topographic roughness. As the surface roughens, the P-coda spectra are uniformly increased, approaching the P spectra and mimicking the source spectrum. The Rg spectra for the topographic cases maintain the peak frequency of 1-2 Hz characteristic of the flat (half-space) solution, but as the topography roughens the Rg window contains more and more higher frequency energy.

These results indicate that scattering of P-to-Rg by surface topography is efficient at generating high frequency energy in the S-wave window. How this energy propagates to long range is a question we hope to investigate. Key

to our investigations will be to evaluate the vector slowness of energy in the Rg window near the source (< 10 km). We will investigate the composition of this energy (P- or S-wave), whether it is trapped in the crust or escapes to the

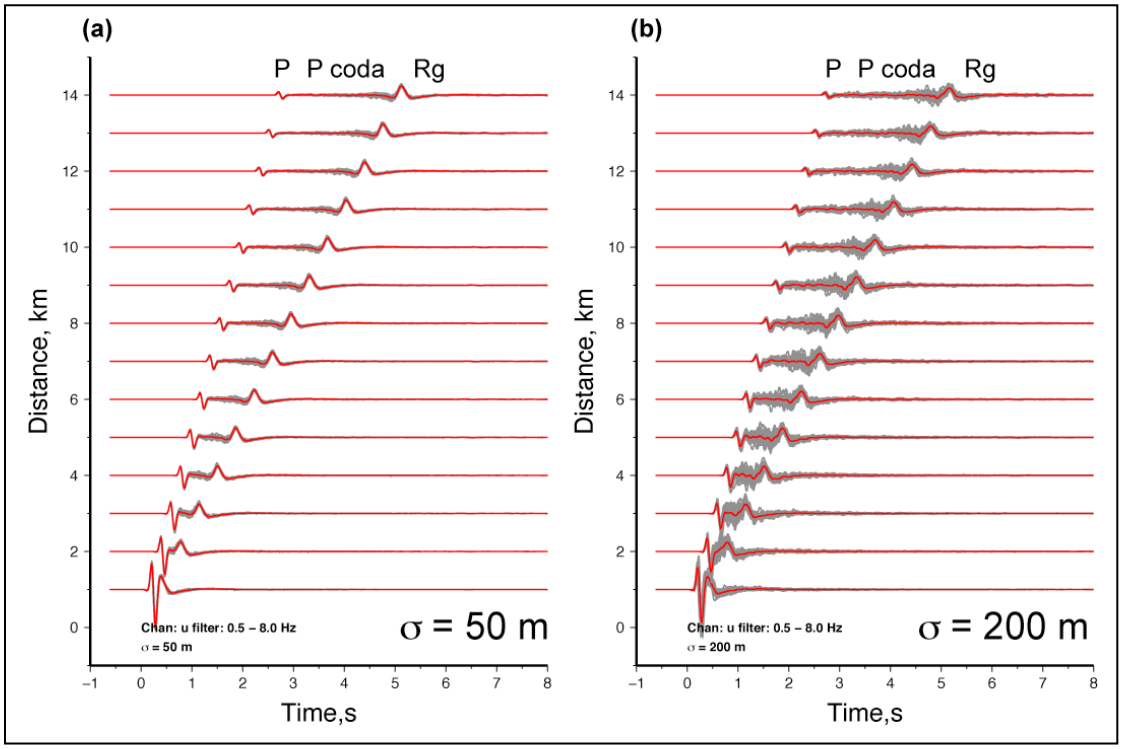


Figure 2. Record section of vertical component ground motions for two realizations of surface topography with different topographic roughness of (a) 50 m and (b) 200 m. The individual traces at each marker point from the domain map (Figure 1a) are shown in gray and the mean response at each distance is shown in red.

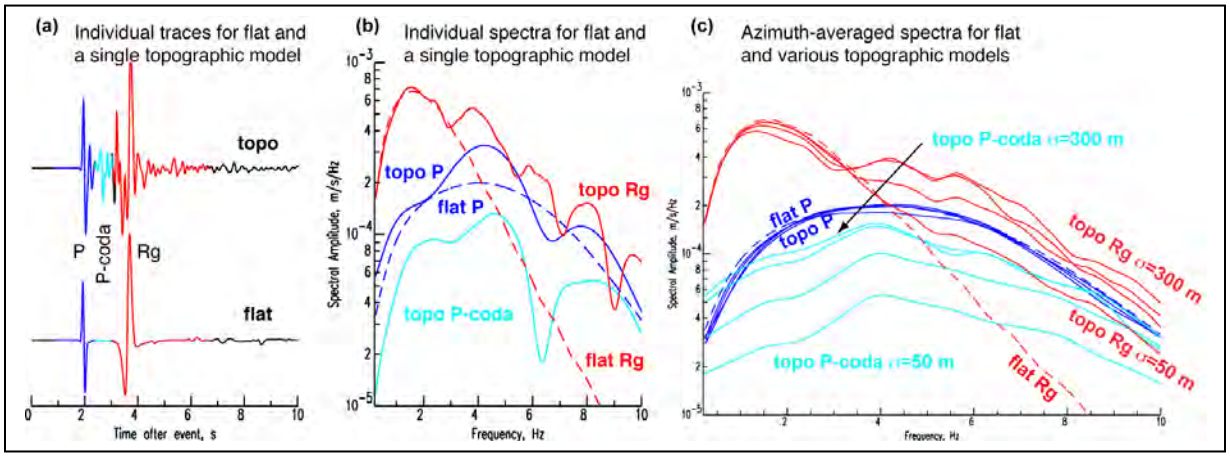


Figure 3. (a) Vertical component traces at 10 km for a single topographic (top) and the flat (bottom) case. The P, P-coda and Rg windows are indicated by the blue, cyan and red colors, respectively. (b) The Fourier amplitude spectra for a single topographic (solid) and the flat (dashed) case using the windowed traces shown in (a) and using the same color scheme. (c) Average spectra at 10 km for all azimuths for various topographic roughnesses (solid) and the flat case (dashed).

mantle and with what horizontal slowness. Note that we observe substantial energy on the transverse component in these simulations as was shown in Rodgers et al. (2010). The generation and fate of this energy will also be investigated.

The near-source computations can be performed with the 3D finite-difference algorithm as shown above; however, connection to observations requires prediction of far-field waveforms or spectral measures at both regional and remote locations. This requires coupling of the finite-difference calculations to long-range propagators in one form or another, and we are using two approaches; wavefield decomposition into energy partitioned by wave slowness and representation theorem coupling to far-field Green functions. In our initial work, coupling from the WPP grid to far-field is being performed by integration over a deep horizontal surface within the WPP grid, far enough removed from the absorbing boundary condition domain that the down-going signals are accurately retained. The representation theorem involves integration of the displacements and tractions acting on a surface enclosing the source domain contracted with corresponding point couple and point source Green function responses, respectively.

Figure 4 illustrates computation of the necessary displacement and stress component terms on a deep horizontal surface of the WPP grid below a surface vertical point-force calculation. WPP directly computes displacements, and we initially used the 3D displacement field to compute the necessary traction-vector components. As with any

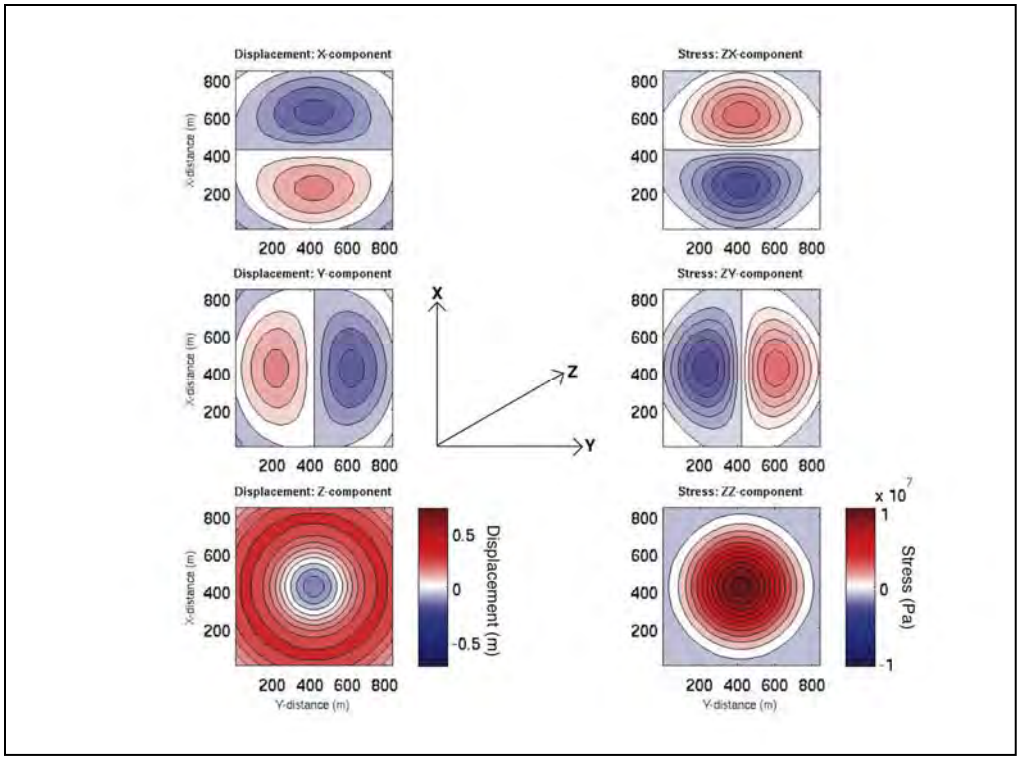


Figure 4. A snapshot of the movie of displacement and stress components on a horizontal plane near the bottom of the 3-D WPP computational domain. Shown in the left column from top to bottom are the x-, y-, and z-components of displacement recorded at each grid point across the plane. The right column contains the x-, y-, and z-components of stress acting on this plane. The seismic source for this example is a point force acting straight down (into the plane of the figure) on the surface of the 3-D computational domain, and is located directly above the center of each plot as shown. The grid origin is in the lower left corner. The z-components of displacement and stress are most intuitive—the initial positive displacement (red) in the z-direction is expanding across the plane, and the stress magnitude is greatest near the center of the grid which is where the z-component of displacement has transitioned from from positive (downward) to negative (upward).

surface integral technique, the main considerations include smoothness of the fields over the surface, accuracy of the integration and suppression of integral truncation effects. During this year's research WPP was modified by LLNL

to output strain calculations directly so that we could eliminate the step of writing out multiple grid layers of displacement time histories for computing stresses using difference operators. We have compared the predictions of stress terms from the strains directly and from our earlier difference calculations and found excellent agreement, so the new output capabilities will greatly facilitate applications of the representation theorem to WPP calculations. With six output time series indicated in Figure 4, we predict a far-field response using travel time variations across the integration surface along with radiation pattern terms for single force and couple terms activated by the stress and displacement fields, respectively. The integrated contribution from each stress vector term and each displacement term (with the latter being time-differentiated due to the spatial derivative of the Green function operator that weights them), is then summed to make the far-field synthetic waveform. Much of the effort this year has addressed stabilizing the integration to the intrinsic truncation of the edges of the integration surface and dealing with suppression of near-source energy such as down-going S wave energy from the source (for double-couple sources), which can produce strong arrivals that sweep across the integration surface that are not of interest. Currently this is being done with simple ray theory (geometric spreading, with a constant ray parameter calculation of the receiver function using a propagator matrix), and we are exploring sensitivity to the very small variations of ray slowness across the grid and the subtle effects of embedding the Cartesian grid into a spherical model.

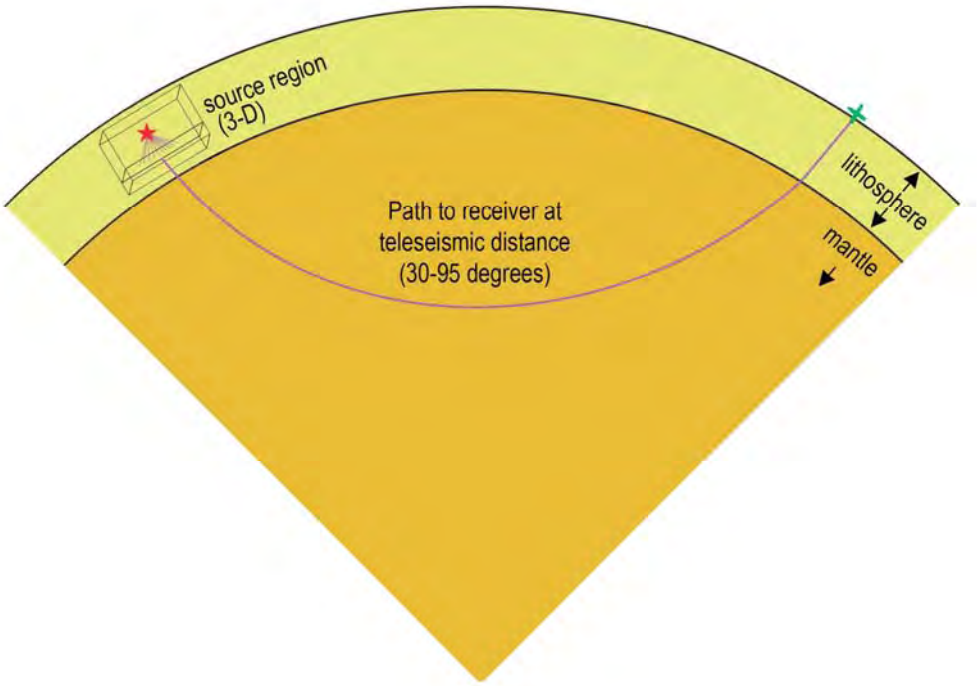


Figure 5. Teleseismic propagation of the stress and displacement wave excitation on the lower surface of the near-field finite-difference grid to the far-field. We are using ray theory to make the far field synthetic seismograms from the surface integrated responses.

As part of our analysis of the North Korean test site effects, we have been examining the regional phases for the underground tests and exploring their implications for the explosion yields. We have just published a paper (Zhao et al., 2012), in which we have describe analysis of the regional Lg signals for the 2006 and 2009 North Korean tests. Vertical component broadband seismograms from nine stations (Figure 6) were used for the 25 May 2009 event and eight of the same stations were used for the 9 October 2006 event (Zhao et al., 2008). An additional 599 broadband seismograms from 82 regional events were used to calibrate the network Lg-magnitudes. The 2009 event is found to have $m_b(Lg)$ = 4.53. The regional Pn velocity is estimated as 8.0 km/s, indicative of stable continental lithosphere, and using a fully-coupled magnitude-yield relation, the yield for the 2009 event is estimated as approximately
2.35 kt. The regional Q model has strong path variations, complicating separation of source and path effects on the

Lg signals (Figure 7). Our expectation is that the regional Pn and teleseismic P signals will provide the best control on the topographic contributions.

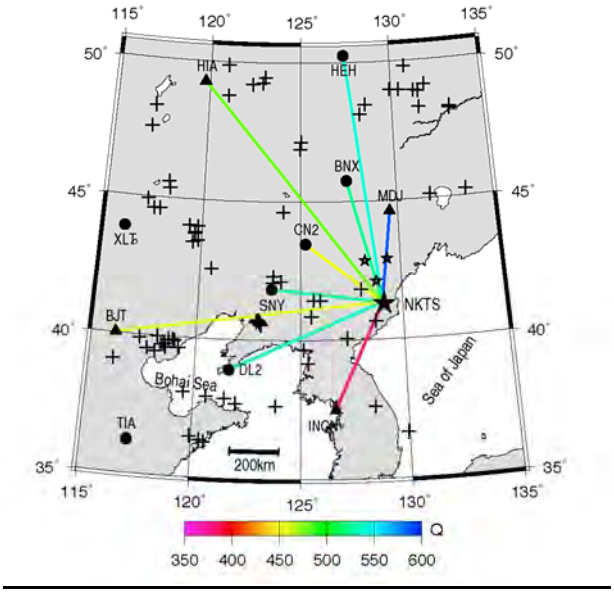


Figure 6. Map showing the locations of the North Korea test site (solid star labeled by NKTS) and CNDSN (solid circles) and GSN (triangles) stations used in this study. Also illustrated in the figure are epicenters of earthquakes (crosses) which occurred between December 1995 and May 2009 and three small chemical explosions (hollow stars) with known yields. The colors on great circle ray paths from the NKTS to individual stations denote the average path Q extracted from the Lg wave Q model. The Q values vary between 379 and 589. (From Zhao et al., 2012).

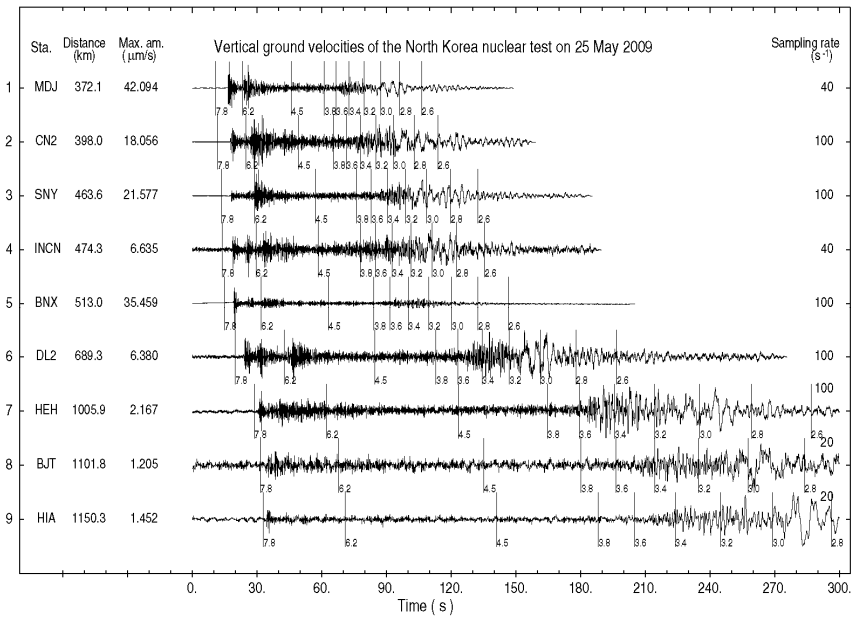


Figure 7. Vertical ground velocities observed from the May 25, 2009 North Korea nuclear explosion. The traces are ordered according to their epicentral distances. The station names and peak amplitudes in μm/s are listed on the left side, and the corresponding sampling rates are listed on the right side.

Vertical bars and numbers on the traces indicate apparent group velocities. (From Zhao et al., 2012).

CONCLUSIONS AND RECOMMENDATIONS

At this phase of work on this project, we have established the strong impact of surface scattering on the near-source wavefield using realistic realization of free-surface topography. Modulation and enhancement of short-period signals and generation of scattered coda can be significant, and these effects can impact far-field measurements. Progress has been made on connecting the near-source finite-difference environments to the far-field using the Representation Theorem. We are beginning comparisons with the effects of slowness analysis from and embedded three-dimensional grid of displacement calculations; as this provides an independent approach to capturing the finite-frequency contributions to the far-field displacements. We have performed analysis of the large regional data set for eastern China, including good quality Lg observations for the 2006 and 2009 North Korean tests. The $m_b(Lg)$ value for the 2009 event is 4.53.

REFERENCES

Appelo, D., and N. A. Petersson (2008). A stable finite difference method for the elastic wave equation on complex geometries with free surfaces, *Comm. Comput. Phys*. **5**, 84–107.

Chaljub, E., P. Moczo, S. Tsuno, P.-Y. Bard, J. Kristek, M. Käser, M. Stupazzini, and M. Kristekova (2010). Quantitative Comparison of Four Numerical Predictions of 3D Ground Motion in the Grenoble Valley, France, *Bull. Seismol. Soc. Am*. **100**, 1427–1455, doi: 10.1785/0120090052.

Frankel, A., and R. Clayton (1986). Finite Difference Simulations of Seismic Scattering: Implications for the Propagation of Short-Period Seismic Waves in the Crust and Models of Crustal Heterogeneity, *J. Geophys. Res*. **91** (B6), 6465–6489.

He, Y., X.-B. Xie, and T. Lay (2008). Explosion-Source Energy Partitioning and *Lg*-Wave Excitation: Contributions of Free-Surface Scattering, *Bull. Seismol. Soc. Am*. **98**, 778–792.

Murphy, J. R., B. C. Kohl, J. L. Stevens, T. J. Bennett, and H. G. Israelsson (2010). Exploitation of the IMS and other data for a comprehensive advanced analysis of the North Korean nuclear tests, SAIC Final Technical Report. DOS Contract No. SAWMMA09C0250.

Nilsson, S., N.A. Petersson, B. Sjogreen, H.-O. Kreiss (2007). Stable difference approximations for the elastic wave equation in second order formulation, *SIAM J. Numer. Anal*. **45,** 1902–1936.

Petersson, N. A. (2010). https://computation.llnl.gov/casc/serpentine/software.html (website).

Petersson, N. A., and B. Sjögreen (2010). Stable grid refinement and singular source discretiztion for seismic wave simulations, LLNL-JRNL-419382, *Communications in Computational Physics*.

Rodgers, A. J., N. A. Petersson, and B. Sjogreen (2010). Efficient generation of shear waves from shallow explosions by topographic scattering near the North Korean nuclear test site, *J. Geophys. Res*., doi:10.1029/2010JB007707, LLNL-JRNL-433892.

Xie, X. B., Z. Ge, and T. Lay (2005). Investigating explosion source energy partitioning and Lg-wave excitation using a finite-difference plus slowness analysis method, *Bull. Seismol. Soc. Am*. **95,** 2412–2427.

Xie, X. B., T. Lay, R. S. Wu, and Y. He (2007). Near source energy partitioning for regional waves in 2d and 3d models, effects from random free surface scattering, in *Proceedings of the 29th Monitoring Research Review: Ground-based Nuclear Explosion Monitoring Technologies*, LA-UR-07-5613, Vol. 1, pp. 322–332.

Zhao, L.-F., X.-B. Xie, W.-M. Wang, and Z.-X. Yao (2012). Yield estimation of the 25 May 2009 North Korean Nuclear explosion, *Bull. Seism. Soc. Am*. **102**, 467–478, doi:10.1785/0120110163.

Zhao, L. F., X. B. Xie, W. M. Wang, and Z. X. Yao (2008). Regional seismic characteristics of the 9 October 2006 North Korean nuclear test, *Bull. Seism. Soc. Am.* **98,** 2,571–2,589, doi: 10.1785/0120080128.

ANISOTROPY OF THE BARRE GRANITE IN THE VICINITY OF THE NEDE

Randolph J. Martin[1], Peter Boyd[1], Anastasia Stroujkova[2], Mark Leidig[2],
James F. Lewkowicz[2], and Jessie L. Bonner[2]

New England Research Inc. [1] and Weston Geophysical Corporation[2]

Sponsored by the Air Force Research Laboratory

Award No. FA9453-10-C-0257
Proposal No. BAA10-19

ABSTRACT

Weston Geophysical Corporation and New England Research, Inc. conducted the New England Damage Experiment (NEDE) in July 2008. The experiment included the detonation of five small (60 to 120 kg) chemical explosions in relatively unfractured, homogeneous Barre granite in Vermont, USA. The emplacement granite was characterized before and after the experiment using laboratory scale measurements on borehole cores. During the past year, we have quantified the damage from the explosions on micro, meso, and macroscales and examined the seismic wave generation and propagation at near-source, local, and regional distances. Site characterization indicates that although the Barre granite is massive with a low fracture density, it is transversely isotropic. The anisotropy is largely due to a planar array of microcracks commonly referred to as the "rift".

The post shot macro-and microscale damage of each core was studied. Five distinct zones were identified ranging from highly pulverized/granulated rock through intact with high angle fractures parallel to the rift. The shape of damaged zones is non-spherical and appears to be influenced by the orientation of the rift. Microscale damage is concentrated in the horizontal plane at the emplacement depth and a vertical ellipsoid through the working point.

In light of the effects of anisotropy on the damage observed in the vicinity of the test shots, a more extensive study was undertaken to quantify the anisotropic properties of intact and microcrack damaged rock. The elastic coefficients, the linear compressibilities and the strength and failure criterion as a function of orientation have been measured. For elastic behavior, transverse isotropy was assumed. Oriented samples were prepared parallel, normal and 45^o to the rift. The constitutive relation in matrix notation is

$$\sigma_i = C_{ij}\,\varepsilon_j \qquad (i, j = 1, 2, 3, \ldots 6)$$

where σ is stress, ε is strain, and C is stiffness. For a transversely isotropic rock, five independent elastic constants need to be determined. C_{11}, C_{12}, C_{33}, C_{44}, and C_{13} were computed from the measured acoustic wave velocities as a function of confining pressure. The linear compressibilities were measured using strain gages on the same specimens. The stiffnesses and the linear compressibilities increase with confining pressure. The linear compressibilities vary by nearly 20% as a function of orientation at low pressures. The difference decreases with increasing pressure. The greatest compressibility is normal to the rift and the minimum is parallel to the rift. The elastic coefficients computed from the velocity data exhibit a similar behavior.

OBJECTIVES

Shear wave generation from explosions continues to be an important problem for the nuclear explosion monitoring community. Damage from the explosion may also play an important role in shaping the seismic waves from an explosion including the generation of shear waves. Most recently, Patton and Taylor (2011) have demonstrated the importance of considering the moment from the damage separate from the explosion moment. Other proposed mechanisms of explosion-generated *S* waves involve processes related to the damage and deformations caused by the explosions. Nonlinear effects in the immediate vicinity of the explosion cause rock damage that can effectively generate shear-waves provided that asymmetries exist in the damage pattern (Ashby and Sammis, 1990). Sammis (2003) has suggested that movement along pre-existing cracks can also produce large amplitude *S* waves. Bykovtsev (2007) has postulated that radial crack generation from explosions should generate *S* waves with distinct radiation patterns.

RESEARCH ACCOMPLISHED

Weston Geophysical Corporation (WGC) and New England Research, Inc. (NER) conducted the New England Damage Experiment (NEDE) in July 2008. The experiment included the detonation of five small (60 to 120 kg) chemical explosions in relatively unfractured, homogeneous Barre granite. The emplacement granite was characterized before and after the experiment using borehole cores and acoustic imaging. The explosions were designed with variable velocities of detonations (VOD) to fracture the rock differently. The site characterization and description of the explosions are presented in Martin et al. (2011). The analysis seismic data collected on these shots are presented in Stroujkova et al., in press.

A prominent feature of Barre Granite is the rift, a nearly vertical planar feature that strikes at N30E at the test site. The rift is a set of pervasive, similarly oriented, open and partially healed, inter- and intra-granular microcracks (Nasseri and Mohanty, 2008). Visible fractures were observed on quarry faces with spacing on the order of 4 to 5 m. The fractures are typically clean, planar features, which often represent sheeting joints that follow the topography (Richter, 1987). The homogeneity was verified with a ground penetrating radar (GPR) study of the site and a borehole geophysical logging program using an oriented acoustic televiewer, an optical televiewer, and a caliper. In addition, detailed observations on two preshot coreholes verify the low fracture density. The site is above the water table; no water infiltrated the emplacement holes for the explosives.

To quantify the damage to the granite resulting from the explosions, the physical properties of the granite were measured from cores recovered from holes drilled before the detonations. Two control holes were cored adjacent to the emplacement holes for Shots #2 and #5. There was complete core recovery from the pre-shot coreholes. The *P* and *S* wave velocities were measured on each core as a function of depth and azimuth at ambient conditions. Time of flight velocity measurements were performed normal to the core axis along the core in a bench top apparatus. At each point, the core was rotated between the transducers. The velocity varied with azimuth. For example at one depth, the velocity increases from a minimum value of 3.84 km/sec to a maximum value of 4.56 km/sec as the core was rotated 90° from the minimum value. These results indicate that there is a pronounced anisotropy in the granite and it is controlled by the orientation of the rift. The two preshot cores, as well as the post shot cores, were evaluated using this method. Similar results were obtained on both preshot cores (Martin et al., 2011)

In order to quantify the radial and vertical extent of the damage due to a small chemical explosion, Shot #4 a 122.7 kg ANFO detonation, was selected for detailed study. Five coreholes were drilled along the trend of the rift, from the working point to a range of 7.01 m. The coreholes were drilled deeper than the emplacement level (12.8-13.7 m) to a maximum depth of 23 m. After evaluation of the data from these cores, three additional coreholes were drilled perpendicular to strike of the rift. The large scale and microscale damage were studied on each core. Figure 1 presents a schematic interpretation of this analysis. The shapes of the boundaries between damage regions are complex. However, the most well defined region encompasses the microscale damage determined using ultrasonic measurements (Martin et al., 2011). Note that the macroscale fracturing extends below the explosive charge only in close proximity to the working point and it extends laterally beyond the farthest borehole parallel to the rift. Five distinct zones based on the degree of rock damage are shown in Figure 1. The data indicate a non-spherical damage surface.

The distinct damage zones are:

- ***Damage Region I*:** Highly pulverized/granulated with zone. Microscale damage is extreme**.**
- ***Damage Region II*:** Significant disaggregation with numerous high angle fractures with strikes parallel to the rift. Extreme microscale damage in intact core pieces. Damage extends above and below explosive emplacement level.
- ***Damage Region III***: Generally intact with microscale damage greatest nearer to shot point. High-angle fractures parallel to the rift present only above the emplacement level.
- ***Damage Region IV*:** Generally intact with few high angle fractures striking parallel to the rift. Microscale damage observed close to the working point.
- ***Damage Region V*:** Mostly intact with few randomly oriented fractures. Large scale fracturing extends to the surface at the Black Powder and ANFO/Emulsion shots. Microscale damage is not present.
- ***Core Disking*:** Core disking was encountered in three coreholes. In all cases it is located within or very near the explosives column level.

One of the five core holes that were to be drilled along the trend of the rift was inadvertently drilled off axis (CH #9). Analysis of the data from this core suggested that the damage zone was not axisymmetric, but rather elliptical with the major axis parallel to the strike of the rift. To better define the geometry of the damage zones, three additional vertical core holes were drilled normal to the strike of the rift. The locations are shown in Figures 2a, 2b and 3. Velocity analysis on these cores resulted in a distribution of microcrack damage normal to the rift as shown in Figure 2b. The shape of the microcrack damage boundary is similar to the geometry of the microcrack damage measured parallel to the rift (Figure 2a). However, the lateral extent of the damage is significantly less. An elliptical plan view of the damage zones was inferred from these data; the contours of damage are shown in Figure 3. The strike of the major axis of the ellipse is parallel to the strike of the rift. Symmetry was assumed and the elliptical pattern was drawn for a 360^0 rotation around the working point.

The observation that the damage zone was not axisymmetric through the working point or spherical in cross section, raises an obvious question. What controls the damage that was observed? The most obvious controlling parameter is the rift. The regions of similar damage parallel to the rift, extend further than the damage normal to the rift for both micro and macroscale damage. The initial anisotropy of the granite, especially in the near surface, plays a significant role in the distribution of damage for each detonation.

The orientation of most of the fractures described in the damage analysis was parallel to the rift. In light of this, a confined compression experiment was conducted to evaluate the influence of the rift on the deformation and failure on the sample. A right circular cylinder was prepared for a confined compression experiment with the axis of the sample parallel to the rift. The sample was instrumented with three strain gages to measure the axial strain, the transverse strain parallel to the rift, and the transverse strain normal to the rift. In addition, compressional and shear wave velocities were measured with a propagation direction parallel to the axis of the sample. The shear wave polarizations were oriented parallel and normal to the rift. The data for this experiment, at a confining pressure of 10 MPa, are shown in Figures 4 and 5. The stress difference is plotted as a function of strain in Figure 4. The axial strain data show that the sample compacted nearly linearly up to a failure stress of 279 MPa. In contrast, the radial strain deviated from linearity at a stress difference of approximately 125 MPa. The change in slope indicates that the sample is dilating. Numerous studies on the deformation of granites have shown that the non-linearity is due to the opening of microcracks parallel to the loading axis (Brace et al.,1966; Kranz, 1979; Ashby and Sammis, 1990). After the initiation of dilatancy, the transverse strain normal to the rift increases more rapidly than the strain parallel to the rift. As the specimen approaches failure above 225 MPa, the strain normal to the rift at failure is nearly three-fold greater than that parallel to the rift.

The shear wave velocity data with polarizations parallel and normal to the rift are shown as a function of stress difference in Figure 5. The velocities for both polarizations increased to a stress of approximately 125 MPa. Note that this is where the sample began to deviate from linearity in the stress-strain data. Between 125 and 225 MPa, the velocities remained relatively constant or increased slightly. Above 225 MPa, the velocities began to decrease. The rate of decrease for the polarization normal to the rift exceeded that of the polarization parallel to the rift. These data are consistent with the strain observations. The initiation and growth of microcracks produce a decrease in wave velocity. The attenuations (Q^{-1}) were computed for each polarization using a spectral ratio technique. Q began to decrease noticeably beyond a differential stress of 225 MPa. The relative attenuation for the vibration direction

normal to the rift increased two-fold compared to the attenuation parallel to the rift. These observations are consistent with the stress strain data shown in Figure 4. Finally, the sample was removed from the pressure vessel and examined. The orientation of the fracture was in the plane of the rift. These data reinforce the observation that the failure observed *in situ*, especially in the high stress regimes, is influenced by the rift.

The next step is to quantify the effect of the rift on the elastic properties. The elastic properties were computed using linear compressibility measurements with simultaneous compressional and shear wave velocities on oriented cores. The data reported here are the initial tests on the intact sections of core. Additional tests are underway on samples recovered from the damage zones subsequent to the shots. A specimen from preshot CH #1 at a depth of 15.4 m is shown in Figure 6. Strain is plotted as a function of pressure for strains measured perpendicular to the rift, parallel to the rift and perpendicular to the hardway, but parallel to the rift (see Figure 7). Two pressurization cycles were conducted. The first cycle shows pronounced hysteresis; subsequent cycles continue to load and unload over the same path with less hysteresis. This behavior is characteristic of most data collected on rocks during hydrostatic loading. Strains for each orientation are nonlinear; at pressures below 30 MPa, the effect is most pronounced. At this pressure, strains measured perpendicular to the rift were as much as a factor of two greater than measured parallel to the rift. This observation is consistent for the closure of microcracks oriented parallel to the rift. The data also indicate that the material is strongly anisotropic, but is not precisely transversely isotropic. For this case, the two strains parallel to the rift should be the same. However, for simplicity in obtaining elastic constants that can be used for modeling, we will assume that the difference between the strains parallel to the rift is small and that the granite can be characterized as transversely isotropic.

In order to use the anisotropy data in a forward modeling calculation, the elastic constants of the granite are required. For an isotropic material, there are two independent elastic constants. For a transversely isotropic material, five independent elastic constants are required. The constitutive relation for stress and strain in matrix notation is

$$\boldsymbol{\sigma_i = C_{ij}\,\varepsilon_j} \qquad (i, j = 1, 2, 3, \ldots 6)$$

where $\boldsymbol{\sigma}$ is stress, $\boldsymbol{\varepsilon}$ is strain, and $\mathbf{C}$ is stiffness. The stiffnesses are computed from the compressional and shear wave velocities on three oriented cores of the granite. The three samples were prepared with core axes normal to the rift, parallel to the rift, and at 45^{o} to the rift. For each core, one compressional and two orthogonally polarized shear wave velocities were measured as a function of pressure. The velocities used to calculate the elastic stiffness coefficients are plotted as a function of pressure in Figure 8. The *P* velocity parallel to the rift is greater than the *P* velocity normal to the rift. The *P* velocity at 45^{o} is intermediate. For the shear velocities, the *S* velocity with a vibration direction in the plane of the rift is greater than the *S* velocity with a vibration direction normal to the plane of the rift. All of the velocities increase with pressure due to the closure of pre-existing microcracks. The greatest increase is observed for the *P* velocity propagating normal to the rift.

The elastic stiffnesses are next computed from the velocity data. Using the notation of Lo et al. (1986), the relationships between the stiffnesses and the velocities are

$$C_{11} = \rho V_{P11}^2 \quad (1)$$

$$C_{12} = C_{11} - 2\rho V_{SH1}^2 \quad (2)$$

$$C_{33} = \rho V_{P33}^2 \quad (3)$$

$$C_{44} = \rho V_{S3}^2 \quad (4)$$

and

$$C_{13} = -C_{44} + \sqrt{4\rho^2 V_{P45}^4 - 2\rho V_{P45}^2 (C_{11} + C_{33} + 2C_{44}) + (C_{11} + C_{44})(C_{33} + C_{44})} \quad (5)$$

where C_{11}, C_{12}, C_{13}, C_{33}, and C_{44} are the stiffnesses, ρ is the density of the rock, and V_{P11} , V_{P45}, V_{P33}, V_{SH1}, and V_{S3} are P and S wave velocities measured in different directions. V_{P11} is a compressional wave measured normal to the rift, V_{P33} is the compressional wave measured in the plane of the rift, and V_{P45} is the compressional wave velocity measured at 45 degrees to the rift. V_{SH1} and V_{SH3} are shear waves. V_{SH3} is a shear wave propagating normal to the rift with a vibration direction in the plane of the rift. V_{SH1} is a shear wave propagating in the plane of the rift with a vibration direction normal to the rift.

Using these data and Equations 1, 2, 3, 4, and 5 above with a density of 2.63 g cm^{-3}, the elastic stiffnesses were computed. These data are shown as a function of pressure in Figure 9. All the stiffness coefficients increase with pressure.

From the elastic stiffnesses, the dynamic bulk modulus, two dynamic Young's moduli, and three dynamic Poisson's ratios were computed. Using the notation of King (1969), the more intuitive elastic constants are computed from the stiffnesses and the determinate of coefficients, **D** (Nye, 1957).

$$E_v = \frac{D}{C_{11}^2 - C_{12}^2} \quad (6)$$

$$E_h = \frac{D}{C_{11}C_{33} - C_{13}^2} \quad (7)$$

$$v_1 = \frac{C_{12}C_{33} - C_{13}^2}{C_{11}C_{33} - C_{13}^2} \quad (8)$$

$$v_2 = \frac{C_{13}(C_{11} - C_{12})}{C_{11}C_{33} - C_{13}^2} \quad (9)$$

$$v_3 = \frac{C_{13}}{(C_{11} + C_{12})} \quad (10)$$

$$K = \frac{C_{33}(C_{11} + C_{12}) - 2C_{13}^2}{C_{11} + 2C_{33} + C_{12} - 4C_{13}} \quad (11)$$

E_v is the dynamic Young's modulus perpendicular to the rift, E_h is the dynamic Young's modulus parallel to the rift. v_1 is a dynamic Poisson's ratio for loading parallel to the rift with the transverse strain measured normal to the rift. v_2 is a dynamic Poisson's ratio for compression normal to the rift and transverse strain measured in the plane of the rift. Similarly, the dynamic Poisson's ratio, v_3, is for compression parallel to the rift with transverse strain in the plane of the rift. Three elastic constants computed from the stiffnesses are shown in Figure 10. The Young's moduli increase with increasing confining pressure. The elastic modulus in the plane of the rift is greater than that measured normal to the rift. At higher pressures the Young's moduli for each orientation asymptotically approach the same value of approximately 84 GPa. These data indicate that the pre-existing cracks that control the rift are closing with pressure. The bulk modulus increases with increasing pressure and approaches a value of 52 GPa at pressure of 70 MPa.

The computed Poisson's ratios are shown in Figure 11. These data exhibit weak pressure dependence. The Poisson's ratio v_1 is increases from 0.31 to 0.34 as the pressure is increased to 70 MPa. The Poisson's ratios v_2 and $v_3$are 0.11 and 0.16 at low pressure and asompytically approach 0.17 at a pressure of 70 MPa.

CONCLUSIONS AND RECOMENDATIONS

Although the site at the quarry in Barre, Vermont was selected as homogenous, isotropic granite, the rock is strongly anisotropic especially at low pressures. The anisotropy of the granite is approximately 20% for the elastic properties. The anisotropy plays a strong role in the character of the damage observed in the post shot core. A more quantitative approach was to consider the granite as a transversely isotropic rock and develop an elastic tensor at each pressure. Additional measurements are now underway on specimens with varying degrees of microcrack damage. These data will be essential in monitoring the wave propagation through the site, in the vicinity of the source.

The blast induced fractures in the source region were most commonly parallel to the rift. To test the influence of the rift on the fracturing process, a series of confined compression experiments were carried out. For samples with their loading axis parallel to the rift, the fracture plane was in the rift. These are consistent with the observations of the damage in the source region.

The shapes of the damage zones are not spherical and there is little damage below the working point. Detailed analysis of bore holes drilled parallel and normal to the rift outward from the working point in the vicinity of a 122 kg shot showed that the damage zones for the anisotropic Barre granite, were elliptical in plan view. The damage at all scales had the greatest lateral extent parallel to the rift. These observations suggest that the shape and extent of the damage is controlled by the rock properties. These results may play an important role in the generation of shears waves in the source region and need to be incorporated into models for the near and far field seismic response.

Next year, we will concentrate on the failure of the granite for realistic loading and unloading paths coupled with the influence of the rift on the fracture characteristics. Since much of the damage occurs during unloading after the shock front loads the sample in uniaxial strain, uniaxial strain experiments will be conducted on cores prepared parallel and normal to the rift. The samples will be loaded in uniaxial compression to a peak stress and then unloaded over different unloading paths that represent the fall off in stress in the source region. Understanding of this behavior will be important in understanding at what stress levels fracturing occurs and the nature of the failure. In close proximity of the source we expect that the samples will fail in compression. As the range increases, the fracture mode transitions to extension with no compressional failure. The variation in fracture morphology will be observed. These data will be integrated into the interpretation of the observed damage in the source as shown in Figure 1. In addition, fracture strength as a function of confining pressure will be measured for samples cored parallel to the rift and cored normal rift. We expect that these data will show different behaviors and may have significant impact on the energy partitioning in the source region.

REFERENCES

Ashby, M.F. and C. G. Sammis (1990). The Damage Mechanics of Brittle Solids in Compression, *PAGEOPH*, **133** (3), 489–521.

Brace, W.F., B. W. Paulding, and C. H. Scholz,. (1966) Dilatancy in the fracture of brittle rocks, *J. Geophys. Res*. **71**, 3939-3953.

Bykovtsev, A.S. (2007). Mathematical description of the explosion source with a system of cracks, Abs. *Seism. Res. Letts.*

King, M.S. (1969). Static and dynamic moduli of rocks under pressure, in Somerton, W. H., Ed., Rock mechanics: Theory and practice; in *Proceedings of the 11th Symposium on Rock Mechanics*, University of Calif., Berkeley, 329, 351.

Kranz, R. L. (1979). Crack growth and development during creep in Westerly granite, *Int. J. Roch Mech Min Sci.* **16**, 23–36.

Lo, Tien-when, Karl B. Coyner, amd M. Nafi Toksoz (1986). Experimental determination of the elastic anisotropy of Berea sandstane, Chicopee shale, and the Chelmsford granite, *Geophysics* **51** (1), 164–171.

Martin, R., P. Boyd, A. Stroujkova, M. Leidig, J. Lewkowicz, and J. Bonner (2011). Correlating near-source rock damage from single-hole explosions to seismic waves, in *Proceedings of the 2011 Monitoring Research Review: Ground-Based Nuclear Explosion Monitoring Technologies,* LA-UR-11-04823, Vol. 1, pp. 484–494.

Nasseri, M.H.B. and B. Mohanty (2008). Fracture toughness anisotropy in granitic rocks, *Int. J. Rock Mech. Mining Sci*. **45**, 167–193.

Nye, J. R. (1957). *Physical properties of crystals: Their representation by tensors and matrices*. Oxford: Oxford University Press.

Patton, H. J. and S. R. Taylor. (2011). The apparent explosion moment: Inferences of volumetric moment due to source medium damage by underground nuclear explosions, *J. Geophys. Res*. **116**, B03310, doi:10.1029/2010JB007937.

Richter, D. A. (1987). Barre granite quarries, Barre, Vermont, *Geological Society of America Centennial Field Guide*. Northeastern Section.

Sammis, C. (2003). Scaling laws for secondary seismic radiation generated by fracture damage in *Proceedings of the 25th Seismic Research Review:Building the Knowledge Base,* LA-UR-03-6029. Vol. 1, pp. 450–455.

Stroujkova, Anastasia, Jessie L. Bonner, Mark Leidig, Peter Boyd, and Randolph J. Martin (2012). Seismic Studies of Explosion with Different Velocities of Detonation in Barre Granite, *BSSA* (in press).

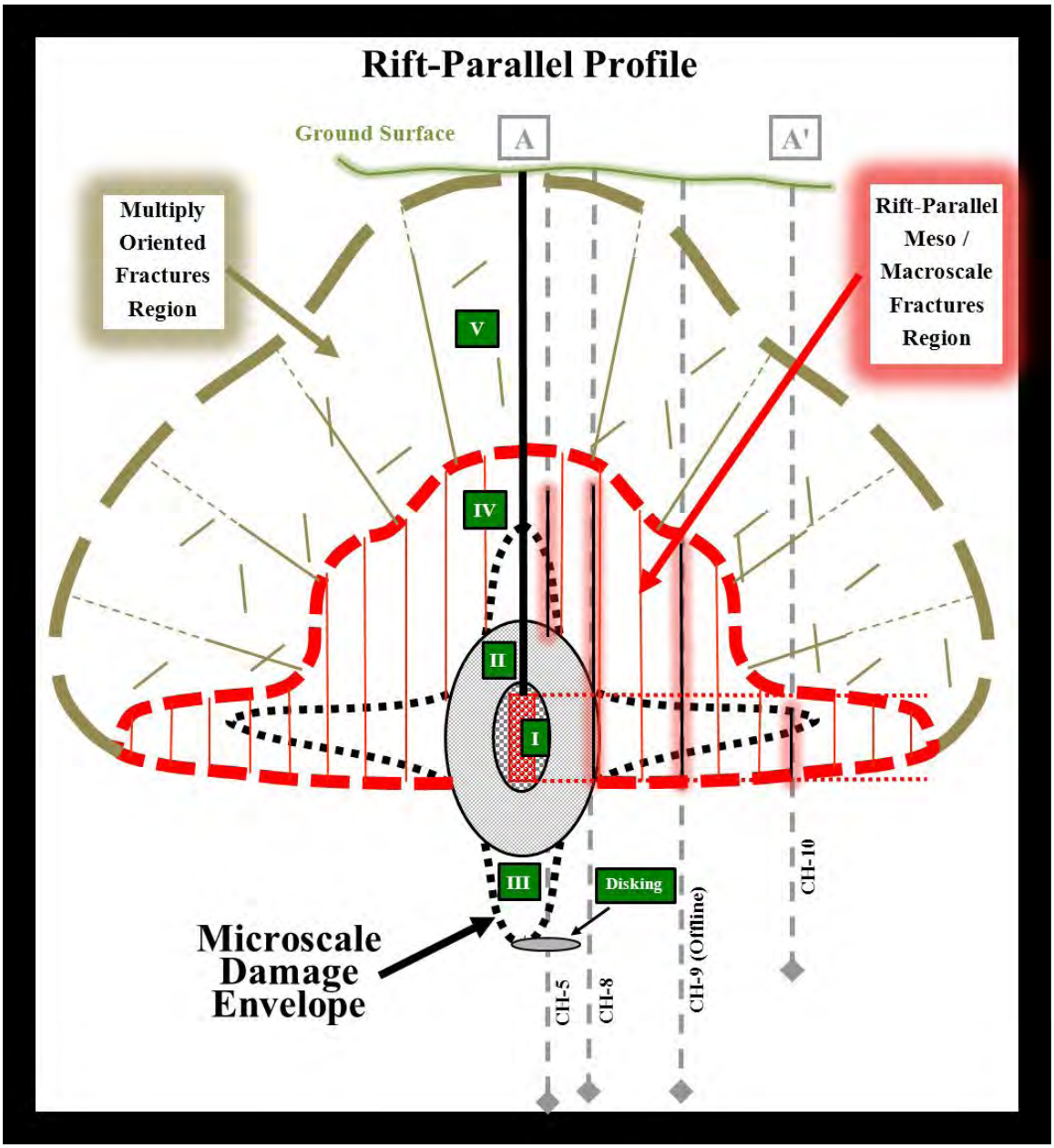


Figure 1. Schematic cross section for a 122.7 kg ANFO shot in Barre, VT (Shot #4) showing the distribution of damage at all scales along a cross section parallel to the rift. Distinct damage regions are identified.

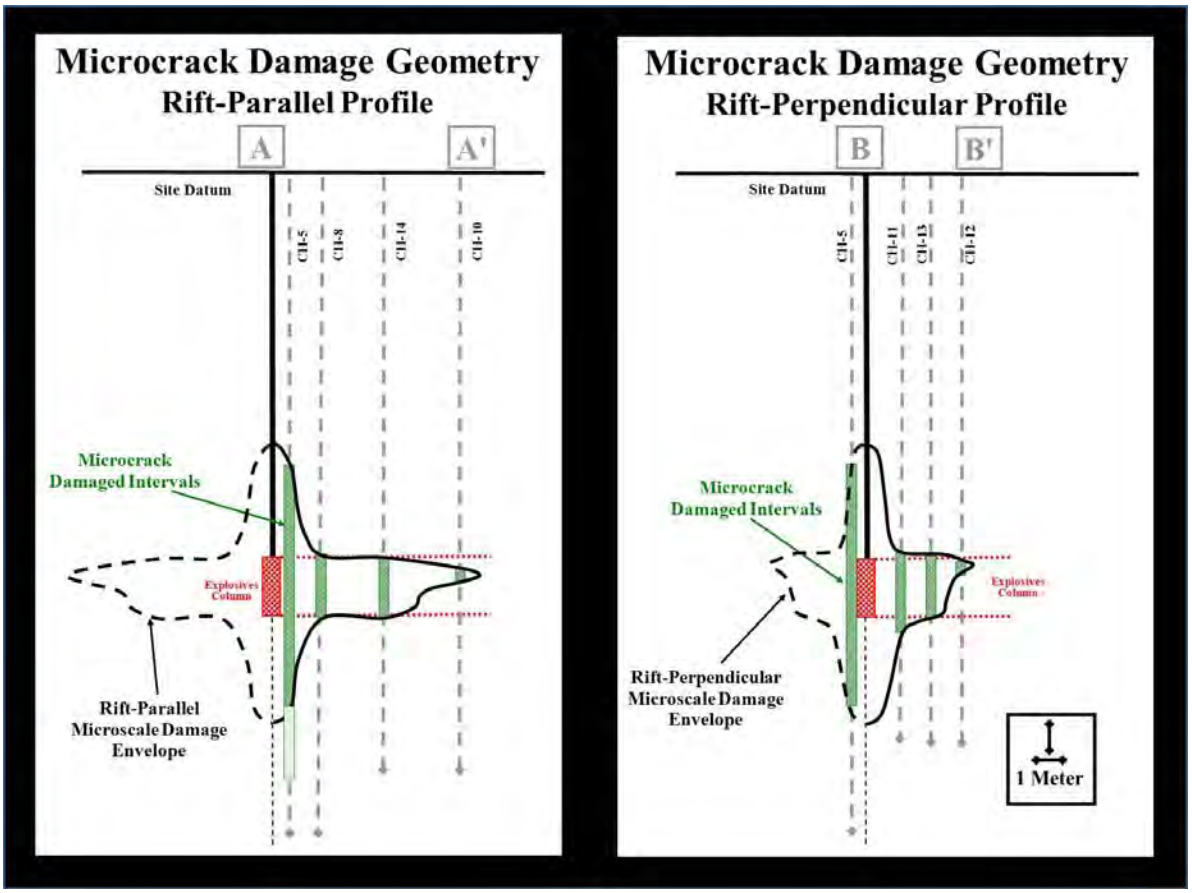


Figure 2a and 2b. Microcrack damage profiles for a 122.7 kg ANFO shot in Barre, VT. The cross section in the plane of the rift is on the left. The cross section perpendicular to the rift is on the right. The relative location of the coreholes and their depth are shown for each projection. The charge was emplaced at a depth of 12.8-13.7 m.

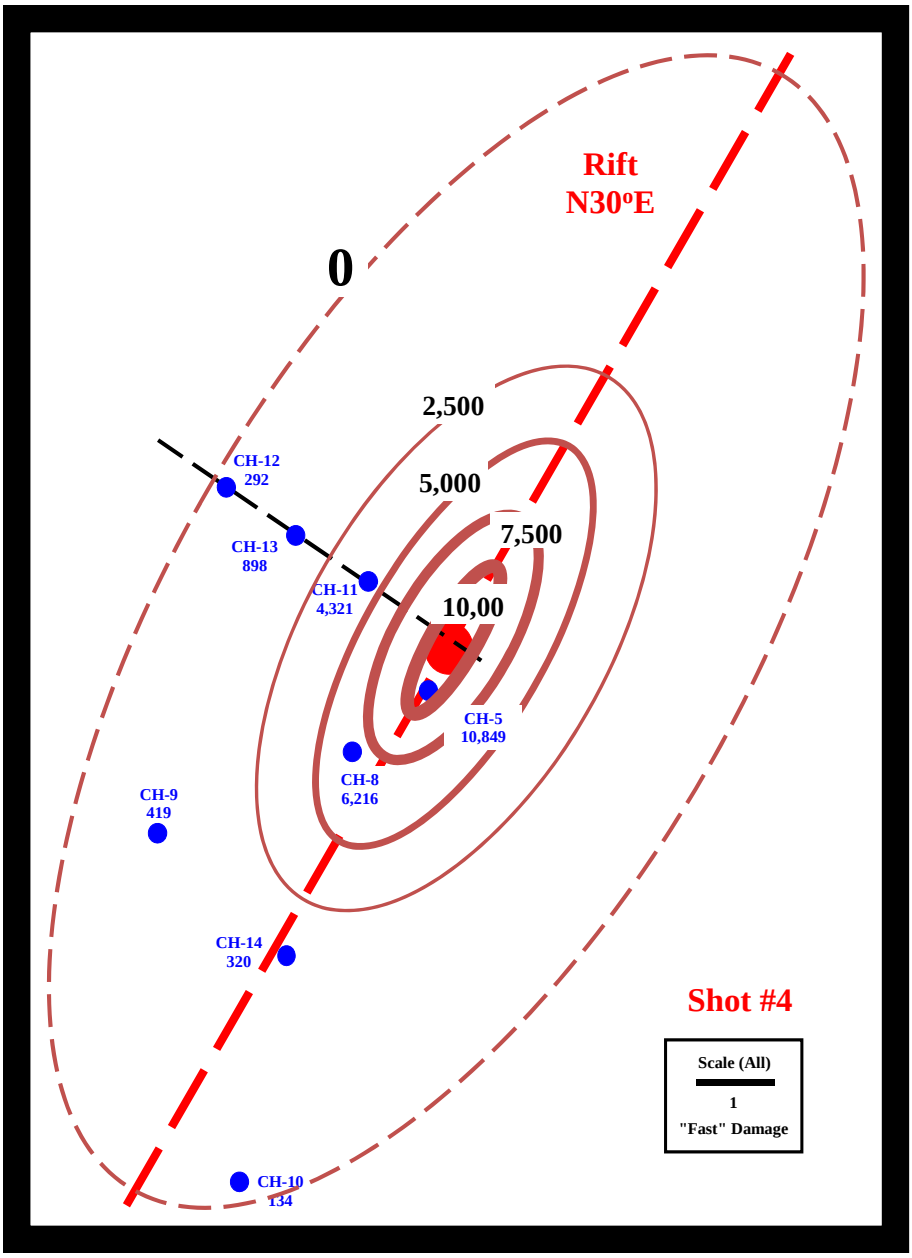


Figure 3. Plan view of the damage contours for a 122.7 kg ANFO shot in Barre, VT. The locations of the vertical coreholes are shown. Core recovery was limited to the SW quadrant. Symmetry was assumed along the plane of the rift to develop representation of the iso- damage levels.

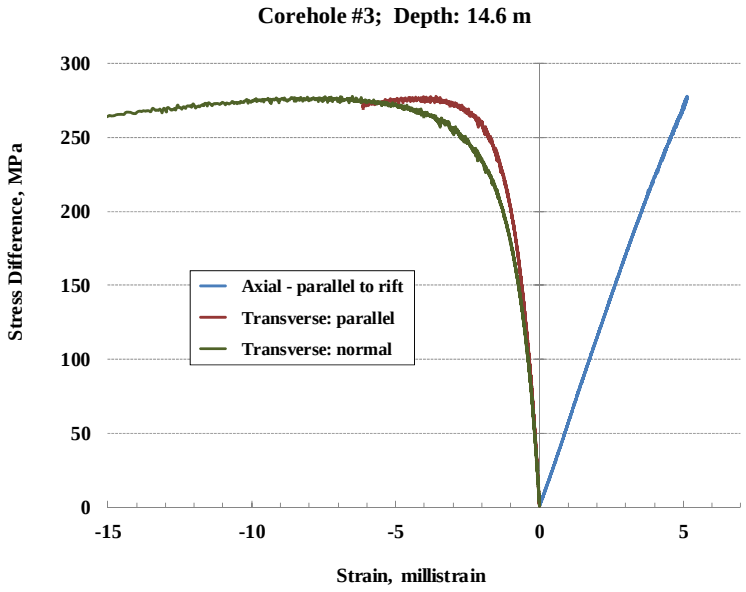


Figure 4. Data for a confined compression test on a sample of Barre granite. The axis of the core was in the plane of the rift. Strain gages were positioned parallel to the axis of the rift (axial), normal to the axis of rift (transverse normal), and parallel to the rift (transverse parallel). Stress difference is plotted as a function of strain. The test was performed at a confining pressure of 10 MPa.

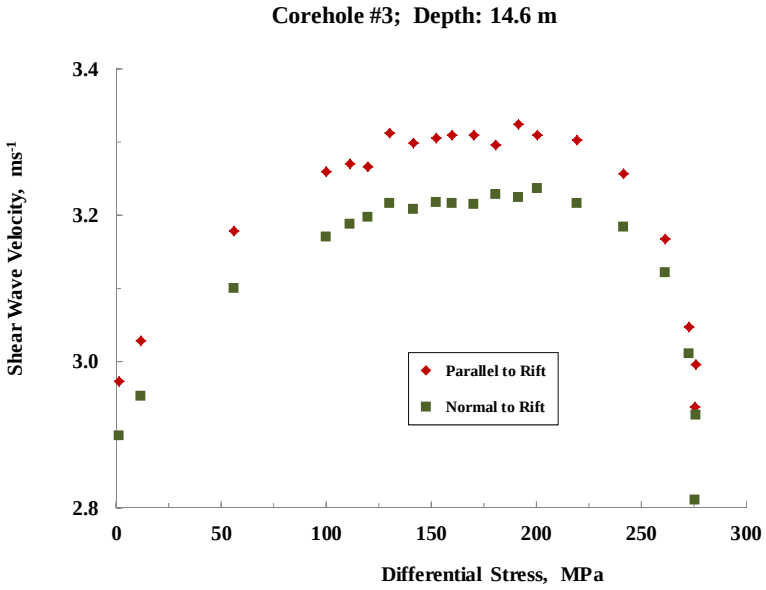


Figure 5. Polarized shear wave velocities are plotted as a function of differential stress for the confined compression experiment shown in Figure 4. Propagation is parallel to the rift with shear vibration directions parallel and normal to the rift.

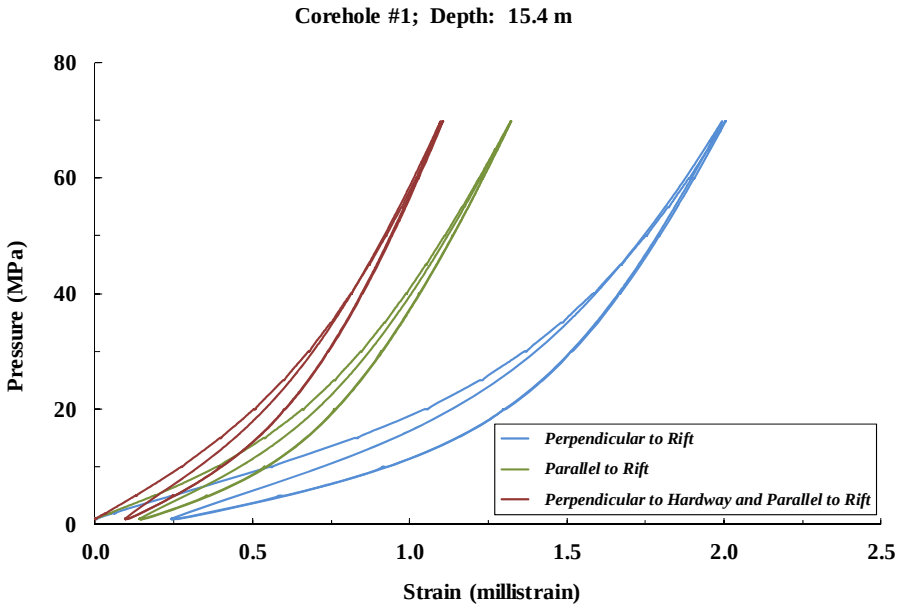


Figure 6. Strains are measured in the principal strain directions for a sample of Barre granite. Gages were positioned perpendicular to the rift, parallel to the rift, and parallel to the rift – perpendicular to the hardway. Pressure is plotted as a function of strain, Two cycles were performed to a pressure of 70 MPa.

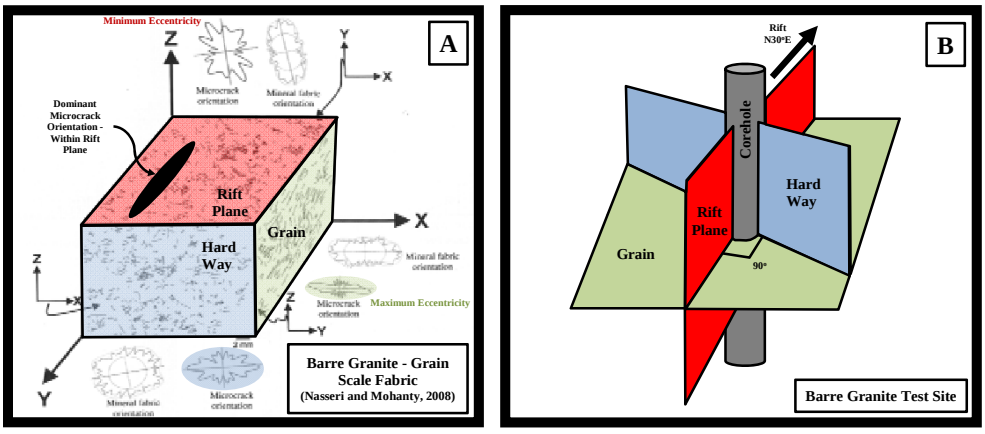


Figure 7. The pervasive rift microfabric is due to an oriented planar array of microcracks. A: Microscopic analysis interpretation by Nasseri and Mohanty (2008). B: Granite planar orientations in the Barre granite.

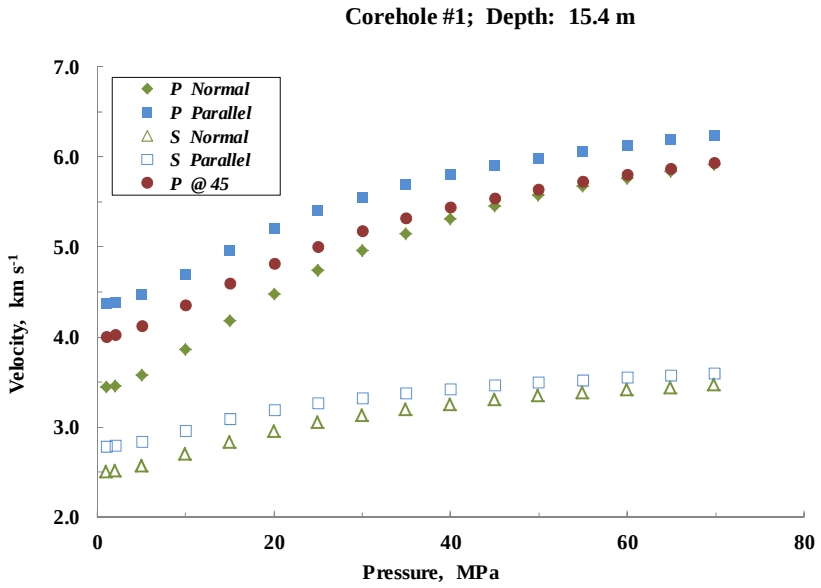


Figure 8. Compressional and shear wave velocities are plotted as a function of pressure. Three oriented samples were tested to obtain these data. *P* waves were propagated normal, parallel and at 45° to the rift in Barre granite. *S* waves were propagated normal to the rift with a vibration direction in the plane of the rift and parallel to the rift with a vibration direction normal to the rift.

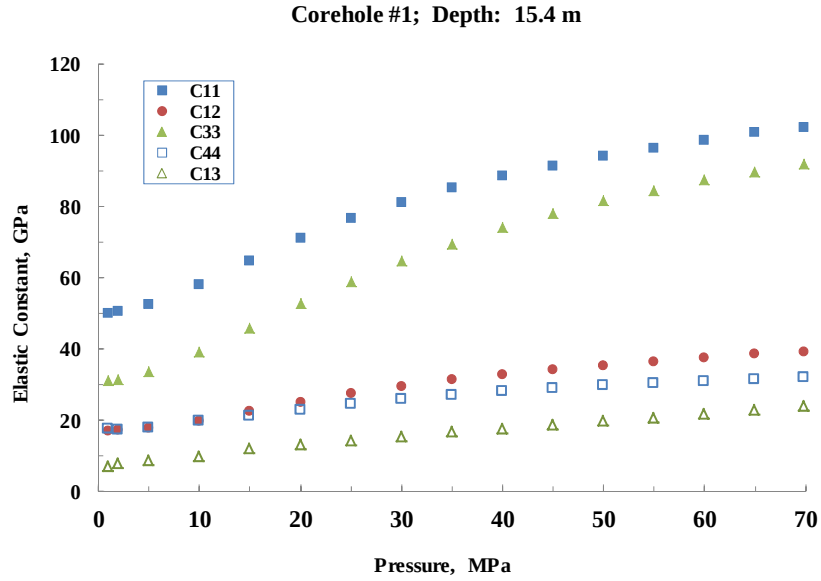


Figure 9. Five elastic stiffnesses for a transversely isotropic sample of Barre granite are plotted as a function of pressure. These coefficients were computed using the velocity data presented in Figure 8.

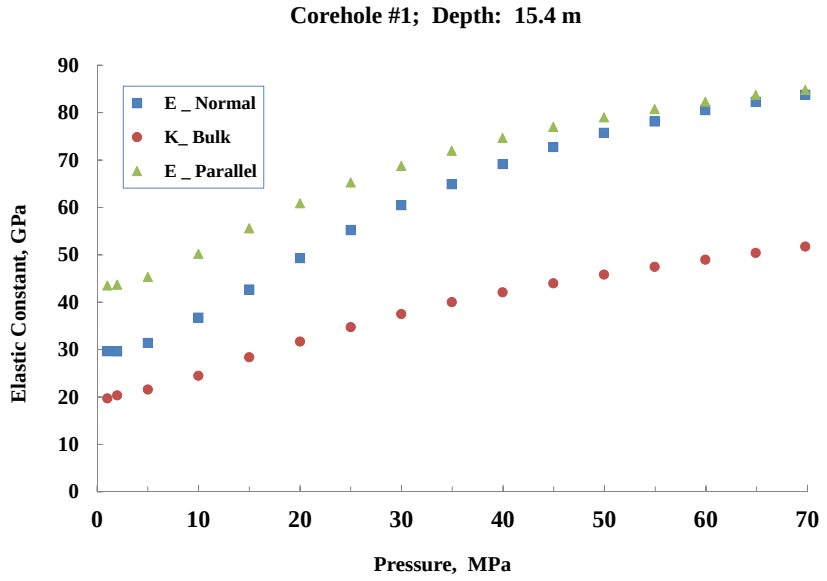


Figure 10. Young's moduli parallel and normal to the rift and the bulk modulus are plotted as a function of pressure. These values were computed from the stiffnesses presented in Figure 9.

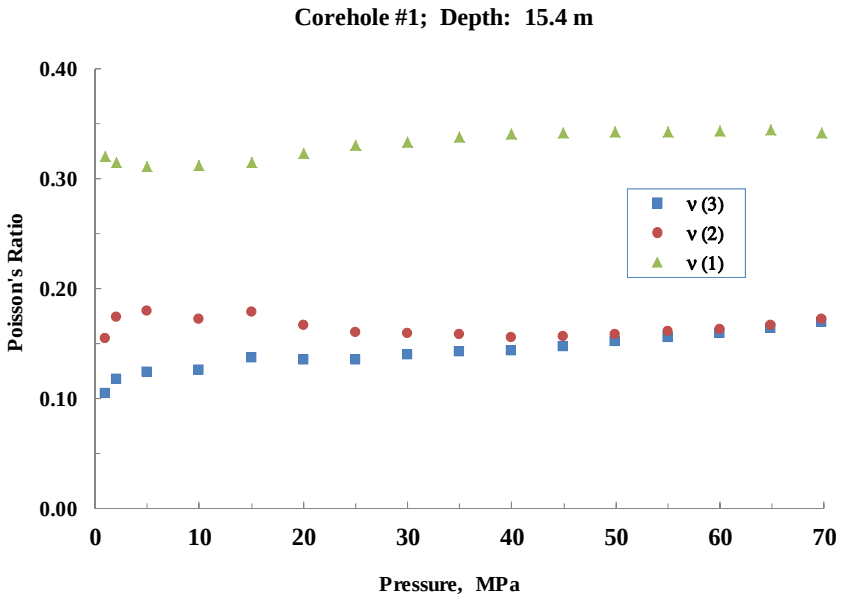


Figure 11. Poisson's ratios for the transversely isotropic Barre granite are plotted as a function of pressure. ν_1 is the Poisson's ratio for the compression parallel to the rift and the transverse strain normal to the rift. ν_2 is the Poisson's ratio for compression normal to the rift and transverse strain measured in the plane of the rift. ν_3 is the Poisson's ratio for compression parallel to the rift and transverse strain measured in the plane of the rift.

ABSOLUTE AMPLITUDE VS EXPLOSION YIELD SCALING FOR *P* AND *S*-CODAS: ON THE PATH TO REMOVING TEST SITE BIAS AND CONSTRAINING SOURCE PHENOMENOLOGY

Kevin M. Mayeda[1] and Seung-Hoon Yoo[2]

Weston Geophysical Corporation[1] and UC Berkeley, Seismological Laboratory[2]

Sponsored by the Air Force Research Laboratory

Award No. FA9453-10-C-0210
Proposal No. BAA10-64

ABSTRACT

The regional coda calibration methodology has evolved over the past decade but is rooted in the coda's stability relative to its direct wave counterparts. The coda's unique properties are universal and make it attractive in monitoring scenarios with sparse station coverage, lateral structural variations, and limited *a priori* knowledge of the regional tectonics. It was applied to earthquake data in the Western United States by Mayeda et al. (1996) and subsequently applied globally, providing unprecedented stability in source spectral estimates and moment magnitude. Regional m_b's for yield and discrimination have been calculated based on the *P*-based phases such as *Pn* (e.g., Denny et al., 1987) and *Pg* (e.g., Mayeda, unpublished manuscript for the Korean Peninsula; Tibuleac et al., 2001) as well as L_g (e.g., Nuttli, 1986). However, Mayeda (1993) and others have shown that these local and regional measures have significant scatter associated with them, and thus significant numbers of station recordings would be required to reduce the inherent data scatter. One additional issue facing regional *S*-based magnitudes, such as $m_b(L_g)$ and $m_b(L_g$-coda), is that there is a bias for earthquakes relative to explosions. We show that *P*-coda m_b's do not have this bias and are a factor of 2-to-3 times smaller in data standard deviation. We show recent evidence of stable *P*-coda envelopes for the Wells, NV earthquake recorded by the U.S. Transportable Array that is a factor of 3 less scattered than direct *Pg*. We then report on *Pg*-coda attenuation relationships that could be easily replicated in new regions of monitoring interest.

OBJECTIVES

Stable source estimates from local and regional coda are now the basis of estimating moment magnitude (M_w) for events that are too small to be waveform modeled. In turn, these coda-derived M_w's are used as input into the MDAC discrimination algorithm outlined by *Walter and Taylor* (2001) to reduce variance in high frequency amplitude ratios. In addition to providing stable M_w's, the high-frequency L_g and S_n-codas correlate very well with explosion yield at Nevada, Novaya Zemlya, Lop Nor, and Semipalatinsk test sites. Slopes of coda-derived amplitude vs. yield relationships are remarkably consistent and transportable between test sites; however, we observe an intercept bias, which could be related to test site variations in near-source material properties, but is also sensitive to scaling assumptions applied during calibration. Before we can reliably extend the coda-yield methodology to the broad area, we must better understand the physical basis of the bias so that we have predictive capability in whatever region we are monitoring. The coda methodology of Mayeda et al. (2003) that we use is predicated on knowing the seismic moments of earthquakes that serve to set absolute spectral levels. Previously, we applied a Green's function spectral flattening method that relied on small earthquakes to derive site and transfer function parameters. That methodology has been widely applied to estimate M_w. Subsequently, we found that the flattening method lead to progressively higher error at high frequencies (> ~2 Hz) that had little effect on M_w, but was important for high precision yield estimation. For Asia test site studies, we shifted to a reference event method that relied only on calibration events of known moment. Thus, corrections for the high frequencies are sensitive to assumptions on the apparent stress-drop scaling of those calibration events. A new approach introduced by Mayeda et al. (2007) provides unprecedented stability in estimates of apparent stress drop scaling and corner frequency. We propose to use this new method to re-calibrate NTS, which appears to be biased high relative to all other test sites. Recalibration will bring NTS closer to Asia test sites, a prerequisite to understanding the physical basis of the *Lg*-coda test site bias. Further, by comparing with test site biases of source spectra from other regional phases using the same calibration procedure, namely direct L_g and *P*-coda, we will narrow the list of potential bias mechanisms. Once the physical basis for the bias is identified and quantified, we will be able to derive amplitude-yield curves for broad regions including the Middle East, central Asia, and the Korean peninsula, extending traditional teleseismic m_b-based yield estimation to small events that are only recorded regionally.

Stability of *P*-coda for Explosions:

We first compare the inter-station scatter between RMS P_g at 2-3-Hz at two regional stations, ELK and MNV, with those using P_g-coda (Figure 1). Station ELK is roughly 400 km from NTS and provides roughly 45 seconds of *P*-coda to measure whereas station KNB is roughly 240 km and the coda measurement lengths are approximately 30 seconds. We see that the use of the *P*-coda provides a factor of two lower data scatter which is significant for regions where station coverage is sparse. In addition, it is expected that the data variance for direct P_g will be even larger for earthquakes because of source radiation pattern and possible directivity, whereas coda measurements has been shown to be nearly free of these effects (e.g., Mayeda and Malagnini, 2010).

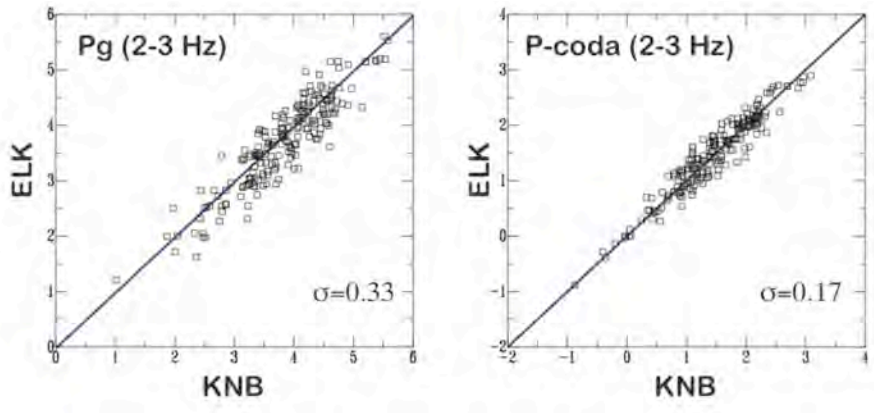


Figure 1. Interstation scatter for direct P_g (2-3-Hz) (left) is roughly a factor of two larger than its corresponding *P*-coda for nuclear explosions at NTS.

Stability of *P*-coda for Earthquakes:

For the case of earthquakes, we wanted to test the effect of source radiation pattern and source directivity, as both of these effects will likely only increase the data scatter. We consider the 2008 M_w 5.9 Wells, Nevada mainshock and compare narrowband P_g at 1.5-2.0-Hz with its corresponding coda. Because the U.S. Transportable Array was deployed during the mainshock, large amounts of broadband data were available for this sequence. We consider site-normalized narrowband (1.5-2.0-Hz) vertical component envelopes from 31 stations ranging between 385-420 km in epicentral distance where we normalized each of the envelopes to the coda level at 200 seconds from the origin time. Figure 2a shows the narrowband envelopes along with the group velocity windows that were used for both mean P_g amplitude (red) (6.8-5.7 km/s) and mean P_g-coda amplitude (red) (5.6-4.0 km/s). We see that the mean P_g amplitudes have a data standard deviation of 0.48 whereas the P_g-coda has variance of 0.15, very comparable to that found for explosions from NTS in Figure 1.

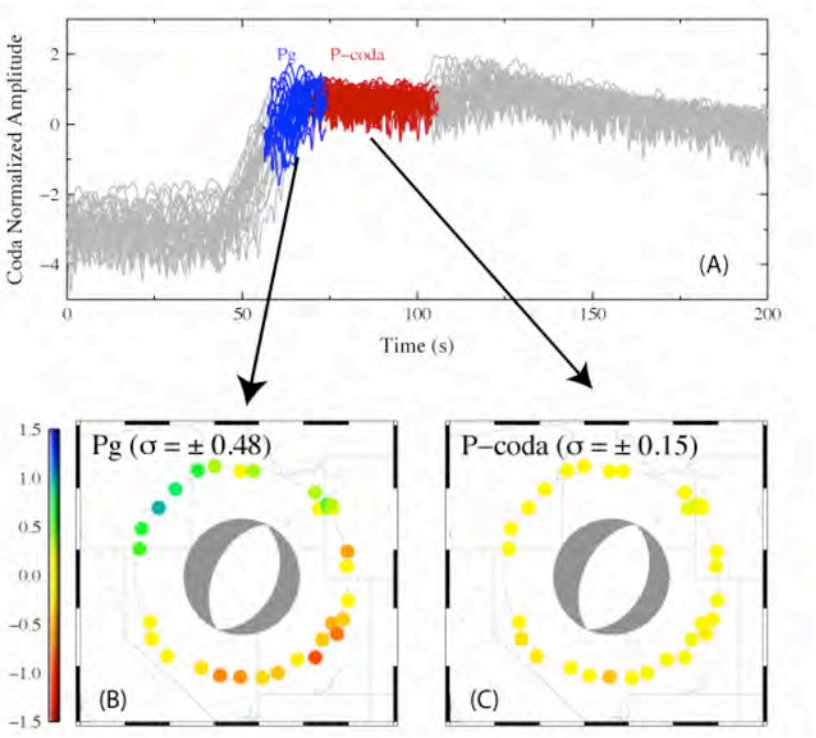


Figure 2. (A) Site-normalized narrow band envelopes (1.5-2.0-Hz) for the Wells, NV mainshock along with P_g (blue) and P_g-coda (red) group velocity windows. (B) Map of P_g amplitude data scatter is roughly 3 times larger than the corresponding P_g-coda amplitude in (C).

Novaya Zemlya m_b(P_n-coda)

As a further test we looked at regional P_n-coda for explosions and earthquakes for the following array and three-component stations: NORSAR, SPITS, ARCESS, KEV, APA. We used explosion and earthquake data in and around the island of Novaya Zemlya (NZ). Figure 3 (left) shows examples of narrowband P_n-coda envelopes for explosions recorded for a sub-array at NORSAR and Figure 3 (right) shows m_b(*P*-coda) (y-axis) relative to the maximum likelihood m_b(ML) (x-axis) for selected explosions and earthquakes following the same procedure outlined previously for the NTS example.

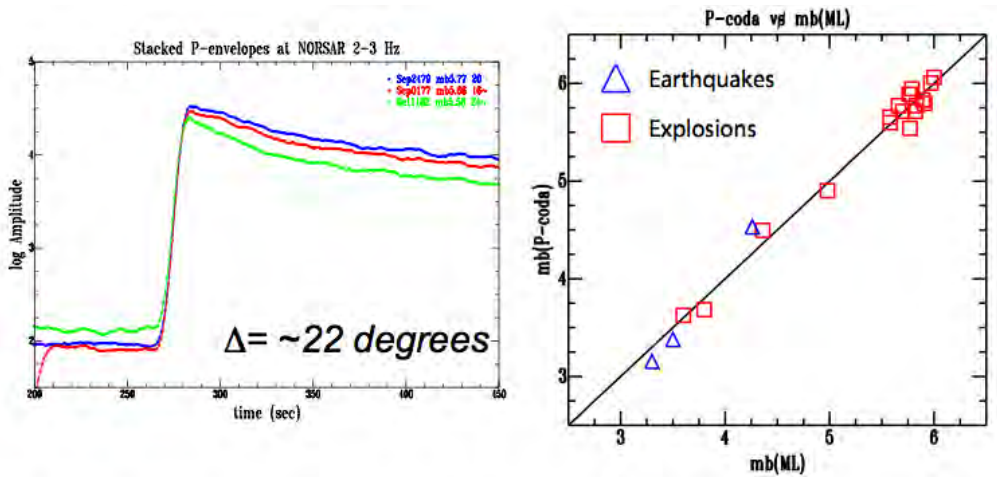


Figure 3. We show P_n-coda envelopes (left) for selected NZ explosions recorded at NORSAR. The relative m_b is shown (right) for both explosions and earthquakes where we plot m_b(*P*-coda) (y-axis) relative to the maximum likelihood m_b, m_b(ML). Again, we note that there is no bias for the earthquakes, in contrast to *S*-based magnitudes.

We see from Figure 3 that the earthquakes (blue triangles) are in good agreement with the maximum likelihood estimate of m_b. Again, this is in sharp contrast to $m_b(L_g)$ and $m_b(L_g$-coda) which over predict the magnitude for earthquakes by nearly 1 magnitude unit (*e.g., H. Patton*, pers comm., 2001). Our findings strongly suggest that at regional distances the *P*-coda can be used as a surrogate for teleseismic m_b for both earthquakes and explosions based on the findings at NZ and NTS.

***P*-coda Findings**

a. For NTS explosions, m_b(*P*-coda) is a factor of 2 times more stable than regional $m_b(P_n)$ and $m_b(P_g)$ and can be tied to the teleseismic $m_b(P)$. This was validated by comparing interstation scatter between stations ELK (~400 km) and KNB (~240 km) where *P*-coda window lengths are ~45 and 30 seconds, respectively.

b. For earthquakes, we find that P_g-coda is 3 times more stable than regional P_g (Figure 2) because the earthquakes have a radiation pattern and possibly source directivity that adds to the data variance whereas the coda is unaffected.

c. Unlike shear-based magnitudes such as $m_b(L_g)$ and $m_b(L_g$-coda), m_b(*P*-coda) at NZ and NTS exhibit no bias between earthquake and explosion m_b's when compared to the teleseismic $m_b(P)$ for both test sites. This means that a regional Ms:m_b can be constructed using the m_b(*P*-coda) for events that are too small to be seen at far-regional and near-teleseismic distances. This will provide a seamless tie to its teleseismic counterpart.

d. *P*-coda amplitude at 2-3-Hz scales with yield with a slope comparable to teleseismic *P* in sharp contrast to L_g and L_g-coda. This is significant because the F-value is both a function of the data scatter, s, as well as the amplitude-yield slope. (Steeper slopes provide better sensitivity to yield than shallow slopes.)

RESEARCH ACCOMPLISHED:

For this past year we have tested path corrections for P-coda and looked at azimuthal variations on P-coda amplitudes (e.g., Figures 2 and 4). For example, to demonstrate how we will perform our path corrections we show a brief example from the Western United States where we formed narrow band envelopes for stations ranging between ~100 km to 500 km from the Wells, NV mainshock (Figure 4). Red traces in A and C represent *Pg*-coda between 5.6 and 4.0 km/sec group velocity and the corresponding blue diamonds are the mean coda amplitude. Figures B and D show the distance dependence of the *Pg*-coda (blue diamonds) relative to the direct *Pg* (red squares). We note that the *Pg*-coda has a very stable decay, regardless of azimuth and that it behaves very similarly to the direct *Pg*, but with significantly less scatter. This is noteworthy because this event exhibited strong source directivity (e.g., Dreger et al., 2009).

We feel confident that we can derive frequency-dependent empirical path corrections for the *Pg*-coda as shown in Figure 4 for most regions of interest.

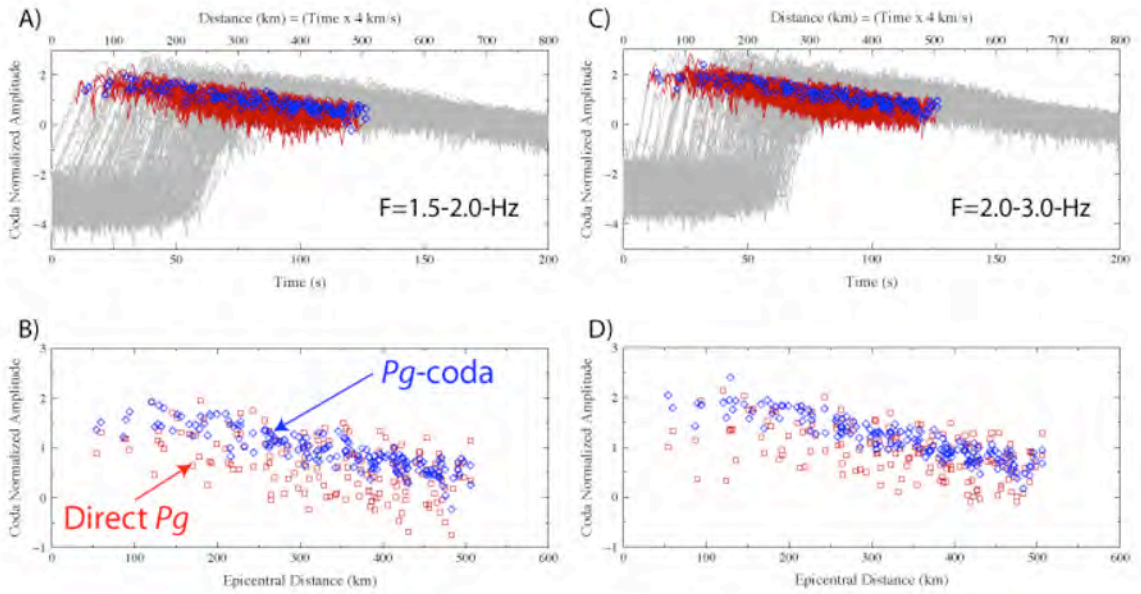


Figure 4. A) Narrow band *Pg*-coda envelopes (red lines) and mean amplitude values (blue diamonds) at 1.5-2.0-Hz and corresponding dependence upon distance in (B) for both coda (blue diamonds) and direct *Pg* (red squares). The same is shown for the 2.0-3.0-Hz band in figure C and D. We can generate path terms for the AI data using the same approach using the large amounts of data already at Weston Geophysical.

CONCLUSIONS AND RECOMMENDATIONS:

Our approach involves building a stable source spectrum from narrow band *P*-coda envelope amplitudes using source spectral models. This approach is identical to the *S*-coda method outlined by Mayeda et al. (2003) and can be applied to *P*-coda but we can use both the Mueller-Murphy explosion source model for potential calibration shots in regions of interest and also a *P*-wave earthquake model by varying the existing parameters of the Brune (1970) source model. We plan to develop both of these approaches on NTS data since we have both types of events and use these results as a basis for transporting the methods to areas of interest. This will provide an excellent set of tests since we can calibrate for the scenario when we only have earthquakes in a given area or if we have a calibration explosion. For the case of calibrating earthquake source spectra we will leverage existing coda calibrations for moment-magnitude estimates from moderate-to-large events, as well as apparent stress scaling results from a currently funded BAA. Having *a priori* knowledge of the apparent stress scaling and its absolute values is a necessary step in accurately calibrating the source spectra. We can leverage these parameters that are already in use by MDAC. If we have absolute source spectral amplitude for regional *P*-coda, then we can compare these directly to yield by transporting the same relationships from known test sites. From the previous examples, we have high confidence that the regional m_b(*P*-coda) calibration methodology can be successfully transported to earthquakes in other regions of interest. Deriving *P*-coda envelope functions that are a function of distance will be straightforward due to the high seismicity rate and extensive data holdings.

REFERENCES

Brune, J. N. (1970). Tectonic stress and spectra of seismic shear waves from earthquakes, *J. Geophys. Res.* **75**, 4997–5009.

Denny, M. D., Taylor, S.R., and Vergino, E.S., (1987). Investigation of mb and Ms formulas for the western United States and their impact on the Ms/mb discriminant, *Bull. Seismol. Soc. Am.* **77** (3), 987–995.

Dreger, D.S., S. R. Ford, and I. Ryder (2009). Finite-source study of the Wells, Nevada Earthquake, submitted to Nevada Bureau of Mines and Geology, Special Publication.

Mayeda, K., (1993). $m_b(L_g coda)$: A stable single station estimator of magnitude. *Bull. Seismol. Soc. Am.* **83**, 851–861.

Mayeda, K. and W.R. Walter (1996). Moment, energy, stress drop, and source spectra of western U.S. earthquakes, *J. Geophys. Res.***101**, 11195–11208.

Mayeda, K., Hofstetter A., O'Boyle J. L., Walter, W. R., (2003). Stable and transportable regional magnitudes based on coda-derived moment-rate spectra. *Bull. Seismol. Soc. A.*, **93**, 224–239.

Mayeda, K., L. Malagnini, W.R. Walter (2007). A new spectral ratio method using narrow band coda envelopes: Evidence for non-self-similarity in the Hector Mine sequence, *Geophys. Res. Lett.*, doi:10.1029/2007GL030041.

Mayeda, K., and L. Malagnini (2010). Source radiation invariant property of local and near-regional shear-wave coda: Application to source scaling for the Mw 5.9 Wells, Nevada sequence, *Geophys. Res. Lett.*, **37**, L07306, doi:10.1029/2009GL042148.

Nuttli, O. W. (1986). Yield estimates of Nevada Test Site explosions obtained from seismic Lg waves, *J. Geophys. Res.*, **91**, 2137-2151.

Tibuleac, I. M, E.T. Herrin and Petru Negraru (2001). Calibration Studies at NVAR, *Seis. Res. Lett.* **72**, 754.

LOCAL MICRO-CALIBRATION FOR GROUND-TRUTH SOURCE SPECTRAL DATABASE IN BROAD REGIONS OF MONITORING INTEREST

Kevin M. Mayeda[1] , Seung-Hoon Yoo[2], William R. Walter[3], Luca Malagnini[4]

Weston Geophysical Corporation[1], UC Berkeley, Seismological Laboratory[2], Lawrence Livermore National Laboratory[3], and Istituto Nazionale di Geofisca e Vulcanogia[4]

Sponsored by the Air Force Research Laboratory

Award Nos. FA9453-11-C-0237 and DE-AC52-07NA27344,
Proposal No. BAA11-59

ABSTRACT

Identifying Underground Nuclear Explosions (UNEs) and discriminating them from natural earthquakes is a critical issue for the verification of the Comprehensive Nuclear-Test-Ban Treaty (CTBT). The earthquake source is a shear dislocation on a fault plane, which generates both P- and S-wave at the source. On the other hand, the nuclear explosion source is an isotropic volumetric expansion, which theoretically generates only P-waves. However, significant S-wave generation is commonly observed from explosion sources and the mechanism remains controversial. A number of explanations (e.g., phase interaction and conversion at the free-surface or any other near source boundary, Rg generation by a compensated linear vector dipole source (CLVD), scattering due to topography, spallation, rock damage, etc) have been proposed but a unifying model does not yet exist. To enhance the identification and discrimination capability of explosions, a more comprehensive understanding of explosion sources including primary and secondary processes are essential.

OBJECTIVES

Over the past decade, the PI's have developed an empirically-based regional shear wave coda methodology that provides unprecedented amplitude stability for events at local and regional distances. In sufficiently small regions, small-scale so-called, 1-D "micro" coda calibrations provide very low variance estimates of the source spectra. Just as the collection and cataloguing of ground-truth locations have been useful in seismic location/tomography studies over the past decade, there is a growing need to have a collection of ground-truth broadband source spectra to provide constraints on current calibration projects related to regional yield estimation, attenuation, seismic discrimination, and coda source calibration for the broad areas. Though long-period waveform modeling is now commonplace and provides stable M_w estimates for moderate-to-large magnitude events, this only provides GT source information on the long-period (< ~0.2-Hz) part of the seismic spectrum. For smaller sources, the accurate knowledge of the broadband spectra (0.05<f<10 Hz) is necessary and we plan to provide local (so-called "micro-calibration") ground-truth source spectra for sub-regions that are tied to local and regionally derived Mw estimates. Our goal will be to catalog many source spectra for use in a myriad of explosion monitoring endeavors that have direct application to monitoring goals.

We analyze seismic coda waves from near-source explosion data to better understand the generation and properties of the scattered P and S wavefields. These well-instrumented experiments (tamped single fired with a variety of explosives, ripple fired) provide us with excellent data to document the characteristic spectral shape and relative partitioning between P- and S-waves. We report on two cases (experiments). In the first case, we examine tamped single-fired explosions, which were conducted in the Barre granite during the 2008 New England Damage Experiment (NEDE). The experiment included the detonation of five small (135 to 270 lbs) chemical explosions in relatively unfractured, homogeneous Barre granite in Vermont. To examine a hypothesis that different damage would lead to possible variations in S-wave generation, the explosions (black powder, ANFO, Composition B) were designed with variable velocities of detonations (VOD) ranging from 0.5 to 8 km/sec. In the second case, we analyze five explosions (a delay-fired production blast and four single-fired shots) using ANFO explosive at a Massachusetts quarry. For the production shot, the total explosives used was 20,377 lbs with the typical delay between the holes in each row being 16 msec and the delays between rows being 106 msec. The four single-fired shots were detonated with different amount of explosive ranging from 132 to 788 lbs.

The five shots in each experiment are closely located within several ten meters in radius. We assume that all shots in each experiment share common path effects and apply the coda ratio method (Mayeda et al., 2007). The coda ratio method is a well vetted technique that has been widely used in the explosion monitoring community for accurate source spectral estimation using sparse station deployments and for use in magnitude, discrimination, and explosion yield estimation, with variances that are typically 3-to-4 times smaller than direct wave methods. The coda ratio methodology is similar in every respect to the traditional direct wave spectral ratio methods which takes advantage of co-located earthquakes to remove common path and site effects, the so-called Green's function events. The significant difference however comes from the fact that the coda envelopes are very stable and not sensitive to either the source radiation pattern or source directivity and represent a convolution over the entire source process.

We measure coda amplitudes for 3-components and narrow frequency bands (1/2 octave bandwidth with 1/8 octave overlapping) with central frequencies ranging between 2 to 80 Hz (NEDE) and 42 Hz (a Massachusetts quarry experiment). We form the average spectral ratios ratio between the high and low yield explosions over stations and components. A total of 19 short-period stations (2.8-30 km) are averaged for NEDE and 7 broadband stations (1.3-4.5 km) and 10 short-period stations (0.5-5.3 km) are averaged for the Massachusetts quarry experiment (Figure 1). Then, we perform grid-search using the MM71 explosion source model (Mueller and Murphy, 1971) to get the theoretical source spectra.

We perform time-domain full moment tensor inversion for selected high yield explosions. Independent seismic moment estimates are needed to convert the dimensionless coda amplitudes to an absolute physical unit. This is also very important to get a stable estimate of source spectrum by constraining the long period coda ratio in the source model search. Using the derived theoretical source spectra and independent seismic moment, we calibrate all measured coda amplitudes to source spectra for other explosions (e.g., Mayeda and Walter, 1996) (Figure 2).

RESEARCH ACCOMPLISHED

From NEDE source spectra, we found the source spectrum for the black powder shot (slow burning explosive) falls off rapidly at high frequency compared to the source spectra of ANFO and Composition B. However, the black powder shot produced spectral amplitudes comparable to the same yield of ANFO shot below 5 Hz. Composition B (fast burning explosive) explosions effectively radiate more high frequency energy, however they are deficient in low frequency S-wave energy. The Composition B shot produced significantly smaller spectral amplitudes than the black powder shot below 5 Hz. We also found that there is a factor of ~2 difference in seismic moment for similar yield shots between the NEDE and the Massachusetts quarry data due to the venting effect. In the source spectrum of the ripple-fired shot (see PROD in Figure 2), we clearly see the modulation peaks at theoretical modulation frequencies based on the delay times.

CONCLUSIONS AND RECOMMENDATIONS

For this year we have computed source spectra for a series of local explosion datasets to test and validate the method. For the upcoming year we plan on applying the methodology to other data sets in the Weston Geophysical database from the Middle East region to begin building at GT source spectral database. The following lists our planned tasks for this project.

Define Micro Calibration Sequences & Envelope Formation and Initial Processing: Using the combined data sets, the PI's will define roughly 30 earthquake sequences that provide good spatial sampling of the Middle East region. We expect to define roughly 30 sequences that will satisfy the requirement of having a good range in event sizes and adequate numbers of local and near-regional stations. Start routine envelope formation and data quality checking.

Sequence-Specific Source Scaling: After defining the micro-calibration data sets, the PI's will divide the coda processing duties and start calibration for source scaling for each particular sequence using the

method outlined in Mayeda et al. (2007). It should be pointed out that all three PI's are experienced in coda processing.

Formation of Coda-Derived Source Spectra: Upon completion of the source scaling for each sequence, coda-derived source spectra will be computed and averaged over all available stations. Averaged source spectra will be QA'd and checked against existing independent M_w estimates.

Deliveries and Final Reports: Deliveries and final reports will be made for use in related projects such as MDAC, Q tomography, broad area 2-D coda calibration, and explosion yield estimation.

REFERENCES

Mayeda, K., and W. R. Walter (1996). Moment, energy, stress drop, and source spectra of western United States earthquakes from regional coda envelopes, *J. Geophys. Res.* **101**, 11,195–11,208.

Mayeda, K., L. Malagnini, and W. R. Walter (2007). A new spectral ratio method using narrow band coda envelopes: Evidence for non-self- similarity in the Hector Mine sequence, *Geophys. Res. Lett*. **34**, L11303, doi 10.1029/2007GL030041.

Mueller, C. S., and J. R. Murphy (1971). Seismic characteristics of underground nuclear detonations, Part I: seismic spectrum scaling, *Bull. Seismol. Soc. Am*. **61**, 1675–1692.

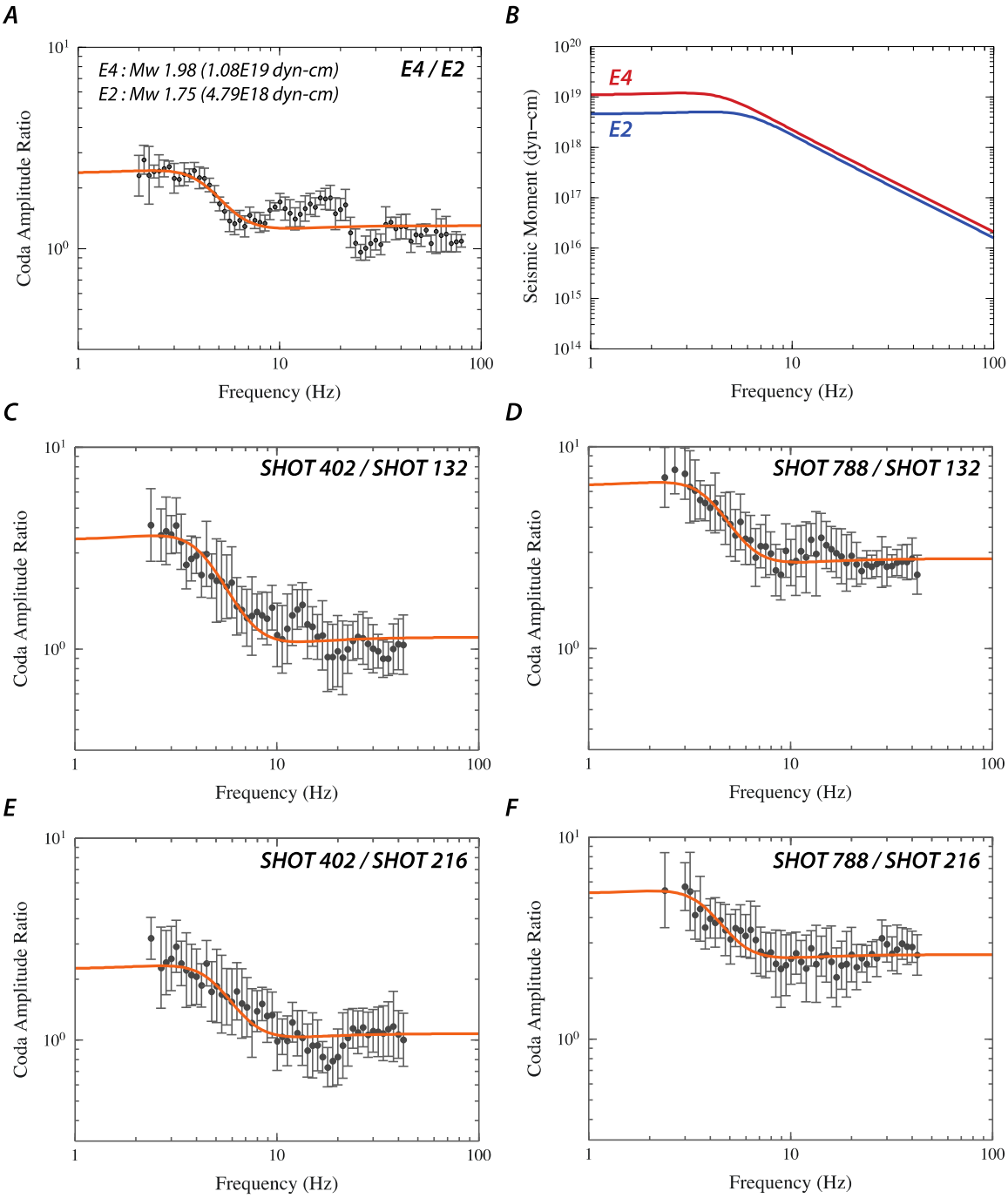


Figure 1. A and B: Coda spectral ratio between E4 and E2 (NEDE) and the corresponding theoretical source spectra. We formed the averaged spectral ratio between the high and low yield explosions over stations and components, then grid-searched using the MM71 explosion source model constraining the low frequency level by seismic moment ratio from the time domain moment tensor inversion. C–F: Examples of the Littleton quarry shots. We see that the corner frequencies of high-yield explosions (shot 401 and shot 788) are consistently defined, regardless of which of the small yield shots were used.

.

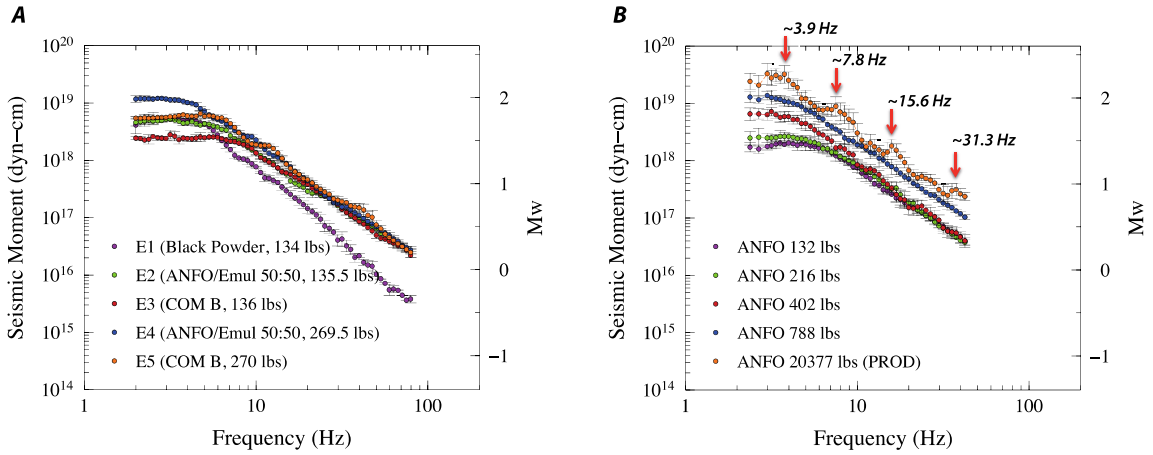


Figure 2. A: Coda-derived averaged moment-rate source spectra for 5 explosions in the NEDE experiment which can be used to estimate explosive yield from as few as one station. Note the error bars are roughly the size of the symbols. B: Coda-derived averaged moment-rate source spectra for 5 explosions in the Littleton quarry experiments which can be used to estimate explosive yield from as few as one station. Note that the production shot shows the characteristic spectral peaks related to the ripple-fire delays.

IMPROVED HIGH FREQUENCY DISCRIMINATION: A NEW APPROACH TO CORRECT FOR REGIONAL SOURCE SCALING VARIATIONS

Kevin M. Mayeda[1] , Seung-Hoon Yoo[2], William R. Walter[3], Rengin M. Gök[3], Luca Malagnini[4]

Weston Geophysical Corporation[1], UC Berkeley, Seismological Laboratory[2], Lawrence Livermore National Laboratory[3], and Istituto Nazionale di Geofisca e Vulcanogia[4]

Sponsored by the Air Force Research Laboratory

Award No. FA8718-09-C-0014 and DE-AC52-07NA27344
Proposal No. BAA09-74

ABSTRACT

The Magnitude and Distance Amplitude Correction (MDAC) methodology of Walter and Taylor (2001) corrects ratios of regional phase amplitudes for source, path, and site effects and has proven effective for event identification. This has been an ongoing project where we have looked at over 20+ M>6.0 sequences globally, including regions that are tectonically very distinct. The MDAC formulation includes a term that describes the earthquake source scaling as the apparent stress variation with magnitude. In almost all regions we find evidence for non-self similar source scaling. The behavior of earthquake source scaling has been the topic of significant debate in the earthquake source community mainly because current methods require substantial path, site, and source radiation pattern corrections that ultimately yield large variance of the apparent stress. The coda ratio methodology of Mayeda et al. (2007) provides unprecedented estimates for corner frequency and apparent stress drop, roughly 3 times less variance than conventional methods using a minimal number of stations and events. Within broad regions it is likely that apparent stress varies with location due to lateral variations in regional stress field, rheology, and degree of tectonic activity. Currently MDAC assumes a single linear apparent stress scaling with moment for a given region, but if we have *a priori* information on lateral variations in apparent stress, then we can use this to lower the amplitude ratio scatter and increase the discrimination capability. The coda ratio methodology has been applied to a variety of tectonic regions and we find clear distinctions between each of them. In this paper, we describe the methodology again and show recent results taken from earthquake sequences in 4 distinct regions of the United States.

OBJECTIVES

Conventional direct wave methods of estimating apparent and static stress drop have significant errors, so large in fact that the earthquake source community is divided roughly 50-50 on whether or not self-similarity even holds, a fundamental assumption in many earthquake source models that have been used for roughly 4 decades (e.g., Aki, 1967; Brune, 1970). One such method involves frequency-dependent path, site, and radiation pattern corrections to get at the source spectra. More often than not, these approaches result in corrections that are so large, the resulting estimates on radiated energy and corner frequency are questionable (see reviews by Abercrombie et al., 2004; Ide and Beroza, 2001). One attempt to alleviate some of the problems is to take source ratios of closely spaced events of different magnitude. These can be either a time-domain deconvolution to extract the source-time function (e.g., Hough, 1997) or source spectral ratios (e.g., Izutani and Kanamori, 2001). Figure 1 shows a typical *S*-wave source ratio result from Izutani (2005) for the 2004 M_w 6.7 Niigata, Japan earthquake and selected co-located aftershocks. In spite of a plethora of seismic stations that surround the source region, the scatter on the ratio is huge and estimating corner frequency and apparent stress will have large errors.

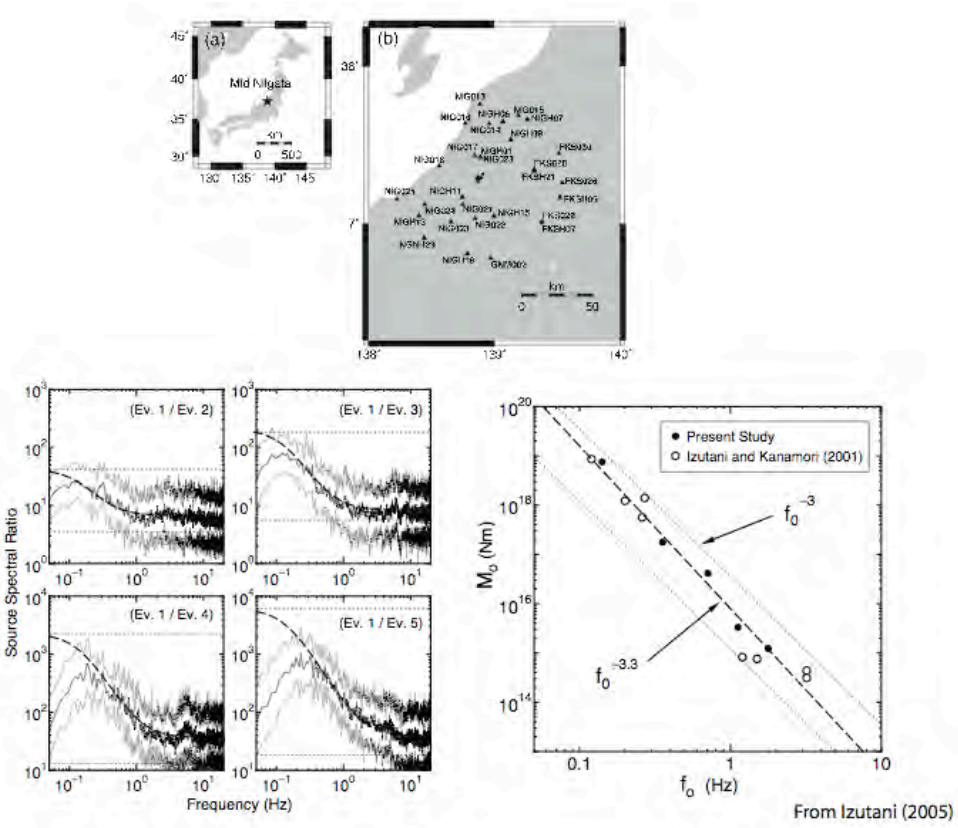


Figure 1. From Izutani (2005) showing direct *S*-wave spectral ratios (lower left) for the 2004 Niigata earthquake in Japan (Ev. 1) relative to four other smaller aftershocks (Ev. 2,3,4,5). Dashed line shows average ratio and dark lines represent +/- 1 σ from the stations shown in above map. Moment versus corner frequency exhibits non-constant scaling ($f^{-3.3}$) however no error estimates are shown, but are presumably large.

In addition to seismic hazard prediction and fundamental research on faulting dynamics, an *a priori* knowledge of apparent stress drop can have a profound influence on high-frequency seismic discrimination. The MDAC

methodology of Walter and Taylor (2001) removes source, path, and site effects from regional phase amplitudes ratios used for regional seismic discrimination. MDAC works by correcting observed amplitudes at each frequency by subtracting the predicted earthquake amplitudes based on the distance and magnitude of the source. This requires an independent estimate of the seismic moment, which is usually obtained from regional coda envelopes. Implicit in the MDAC formulation is a term that describes the earthquake source spectra in terms of its apparent stress (e.g., Wyss, 1970). For a given region we usually use either a fixed average apparent stress, or a linear apparent stress relation that increases with seismic moment. We search for the choice that best reduces the earthquake scatter.

To date, in regions of monitoring interest, the apparent stress scaling has been obtained usually through a grid-search or by geophysical analogy (see Equation 3). What is found in almost all regions is that apparent stress appears to increase with magnitude, indicating a non-self similar source scaling. The estimation of earthquake source scaling in general, has been the topic of large debate in the earthquake source community mainly because current methods require substantial path, site, and source radiation pattern corrections that ultimately yield large variance in apparent stress. A new, state-of-the-art methodology has been developed by Mayeda et al. (2007) which provides unprecedented estimates in static and apparent stress drop, roughly 3 times less variance than conventional methods using a minimal number of stations and events. For broad areas, there is every reason to believe that lateral variations in source scaling exist due to lateral variations in regional stress field, rheology, and degree of tectonic activity.

Methodology

Assuming the simple single corner frequency source model (Aki, 1967; Brune, 1970) used in MDAC, the ratio of the moment-rate functions for two events (1 and 2) is given by,

$$\frac{\dot{M}_1(\omega)}{\dot{M}_2(\omega)} = \frac{M_{0_1}\left[1+\left(\omega/\omega_{c_2}\right)^2\right]^{p/2}}{M_{0_2}\left[1+\left(\omega/\omega_{c_1}\right)^2\right]^{p/2}} \qquad (1)$$

where M_0 is the seismic moment and ω_c is the angular corner frequency ($2\pi f_c$) and p is the high frequency decay rate. At the low frequency limit the source ratio shown in equation 1 is proportional to the ratio of the seismic moments $\left[M_{0_1}/M_{0_2}\right]$, whereas at the high frequency limit, equation 1 is asymptotic to $\left[M_{0_1}/M_{0_2}\right]^{\left(1-\frac{p}{3}\right)}$ under self-similarity. If we follow the usual Brune (1970) omega-square model and set p=2, the exponent of the high-frequency ratio becomes 1/3. However, it has been proposed by Kanamori and Rivera (2004) that the scaling between moment and corner frequency could take on the form,

$$M_o \sim \omega_c^{-(3+\varepsilon)} \qquad (2)$$

where ε represents the deviation from self-similarity and is usually thought to be a small positive number. For example, Walter et al. (1995) found ε to be close to 0.5 for the Hector Mine mainshock and its aftershocks using independent spectral methods. For the current study we use the source spectrum portion of the MDAC methodology of Walter and Taylor (2001), which allows for the variation of the corner frequency that does not have to be self-similar. For example,

$$\omega_c = \left(\frac{k\sigma_a}{M_0}\right)^{1/3} \text{ and } \sigma_a = \sigma_a'\left(\frac{M_0}{M_0'}\right)^{\psi} \text{ and } \psi = \frac{\varepsilon}{\varepsilon + 3} \qquad (3)$$

where σ_a is the apparent stress (Wyss, 1970), σ_a' and M_0' are the apparent stress and seismic moment of the reference event, and ψ is a scaling parameter. For constant apparent stress, ψ = 0 and ε =0, however, Mayeda and Walter (1996) found ψ=0.25 for moderate to large earthquakes in the western United States. By using the corner frequency defined in (3) into Equation 1, we can apply a grid search to find the parameters that best fit the spectral ratio data.

Finally, in addition to Oklahoma, Wells and Parkfield sequences that were completed this past year, we show example spectral ratios from the *Mw* 5.65, 2011 Virginia earthquake in Figure 2.

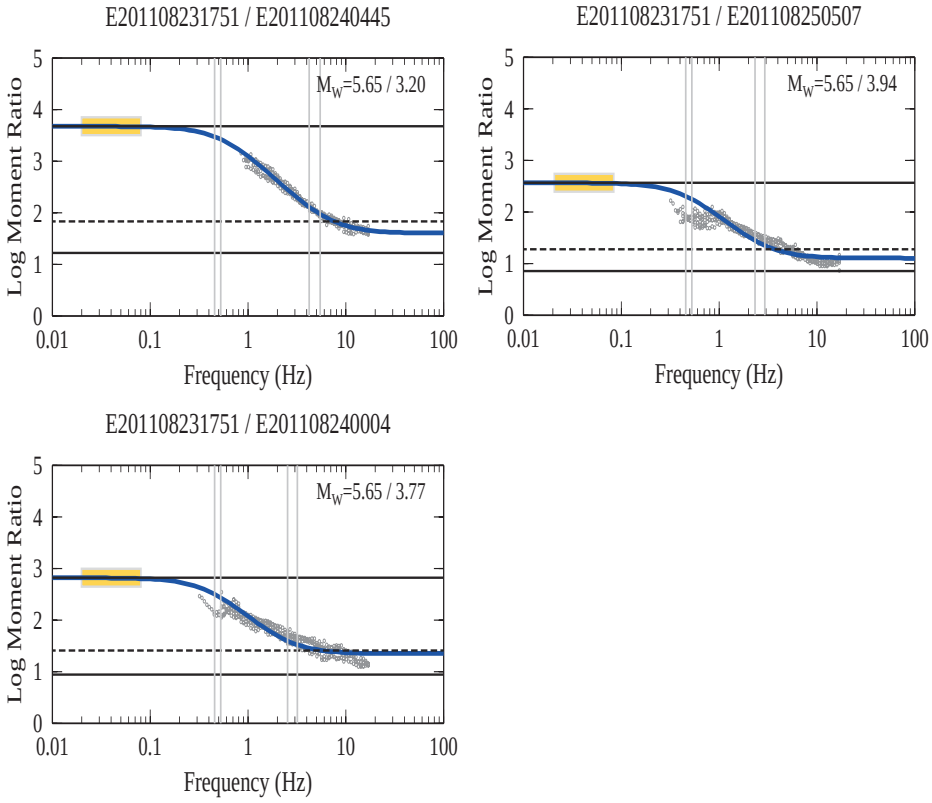


Figure 2. Spectral ratio fits for Virginia sequence where top horizontal solid line represents the theoretical low-frequency limit based upon the two events' moment estimates, the bottom solid line represents the theoretical high-frequency limit assuming self-similarity, and dashed line is when *p*=1.5 in equation 1. Estimates of f_c and ± 1 standard deviation error bars (vertical lines) for the Virginia mainshock and 3 aftershocks.

Research and Work Completed During this Past Year

This past year we compared earthquakes of comparable size that come from distinct tectonic provinces within the United States: Parkfield, CA; Wells, Nevada; Oklahoma; Mineral, Virginia. A summary of their respective corner frequency versus seismic moment is shown in Figure 3 using spectral ratios such as those shown in Figure 2. As expected we see distinctive differences, with the Virginia sequence exhibiting the highest stress drops.

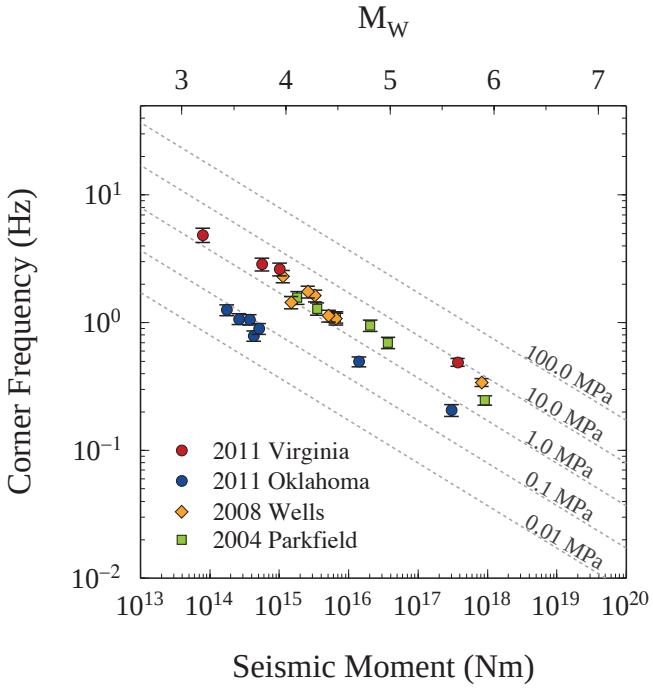


Figure 3. Results of corner frequency versus seismic moment for all four U.S. sequences all show an increase in stress drop and apparent stress. A dramatic difference in apparent stress is observed which appears to be dependent upon the source region. The Mineral, VA mainshock has a stress drop of roughly 9 MPa and characterized by a compact source, as evidenced by the regional *P*-waves. In contrast, the Oklahoma mainshock has a stress drop of roughly 0.5 MPa and a much longer, more complicated source. We also compare Wells, NV and Parkfield, CA sequences and note that Wells is also comparable to Virginia.

CONCLUSIONS AND RECOMMENDATIONS:

We have completed a journal article that compares over 20 sequences globally and will begin focusing on sequences specific to the Middle East region in the upcoming year. A summary of our results for this past year is as follows:

1) The Mineral, VA mainshock is characterized by a short duration of roughly 2-3 seconds and corresponding high stress drop of roughly 9 MPa.
2) In contrast, the Oklahoma mainshock has a more extended duration of about 5 seconds and complicated rupture and a stress drop of only 0.5 MPa.
3) Comparison to two other comparably sized events (Wells, NV and Parkfield, CA) show interesting regional variations in stress drop.
4) Globally, coda-derived estimates of stress drop and apparent stress increase with increasing seismic moment from Mw 3.7 up to ~Mw 5.5, then become self-similar for larger events.

Again, we highlight the advantages of the methodology below:

- The coda is not sensitive to lateral variations in structure and effectively homogenizes its energy over a broad area
- Directivity and source radiation pattern will not affect the coda envelope amplitude measurement due to azimuthal averaging
- Unlike direct wave methods that require large amounts of data to average, the coda method can use a minimal number of events and stations.

- The methodology does not require path and site corrections.
- Large amounts of data have already been archived by LLNL and Weston in the regions of monitoring interest and coda envelope shape and velocity parameters have already been derived for all the regions.

REFERENCES:

Abercrombie, R.E., and J.R. Rice (2005). Can observations of earthquake scaling constrain slip weakening?, *Geophys. J. Int.* **162**, 406–424.

Aki, K. (1967). Scaling law of seismic spectrum. *J. Geophys. Res.* **72**, 1217–1231.

Brune, J. N. (1970). Tectonic stress and spectra of seismic shear waves from earthquakes, *J. Geophys. Res.* **75**, 4997–5009.

Hough, S.E. (1997). Empirical Green's function analysis: Taking the next step, *J. Geophys. Res.* **102**, 5369–5384.

Ide, S. and G. C. Beroza (2001). Does apparent stress vary with earthquake size?, *Geophys. Res. Lett.* **28**, 3349–3352.

Izutani Y. and Kanamori, H. (2001). Scale-dependence of seismic energy-to-moment ratio for strike-slip earthquakes in Japan, *Geophys. Res. Lett.* **28** (20), 4007–4010.

Izutani, Y. (2005). Radiated energy from the mid Niigata, Japan, earthquake of October 23, 2004 and its aftershocks, *Geophys. Res. Lett.* **32**, L21313, doi:10.1029/2005GL024116.

Kanamori H. and L. Rivera (2004). Static and dynamic scaling relations for earthquake and their implications for rupture speed and stress drop, *Bull. Seismol. Soc. Am*. **94**, 314–319.

Mayeda, K. and W.R. Walter (1996). Moment, energy, stress drop, and source spectra of western U.S. earthquakes, 11195-11208, **101**, *J. Geophys. Res.* **101**, 11195–11208.

Mayeda, K., L. Malagnini, and W.R. Walter (2007). A new spectral ratio method using narrow band coda envelopes: Evidence for non-self-similarity in the Hector Mine sequence, *Geophys. Res. Lett.* doi:10.1029/2007GL030041, 2007.

Walter, W.R., K. Mayeda, and H. Patton (1995). Phase and spectral ratio discrimination between NTS earthquakes and explosions, Part I: Empirical Observations, *Bull. Seismol. Soc. Am.* **85**, 1050–1067.

Walter, W. R. and S. R. Taylor (2001). A revised magnitude and distance amplitude correction (MDAC2) procedure for regional seismic discriminants: theory and testing at NTS, Lawrence Livermore National Laboratory Report, UCRL-ID-146882,

http://www.llnl.gov/tid/lof/documents/pdf/240563.pdf

Wyss, M. (1970). Stress estimates of South American shallow and deep earthquakes, *J. Geophys. Res.* **75**, 1529-1544.

INTEGRATING WORK IN SEISMIC ATTENUATION, CODA DECAY, AND SOURCE MODELS FOR EVENT IDENTIFICATION AND CHARACTERIZATION

Michael E. Pasyanos[1], William R. Walter[1], Eric M. Matzel[1], Rengin Gök[1], Sean R. Ford[1], Heming Xu[1], and Kevin M. Mayeda[2]

Lawrence Livermore National Laboratory[1] and University of California, Berkeley[2]

Sponsored by the National Nuclear Security Administration

Award No. DE-AC52-07NA27344/LL12-Source Physics-NDD02

ABSTRACT

For the past number of years, Lawrence Livermore National Laboratory has been developing a wide variety of research products for use in nuclear explosion monitoring. These include coda calibration for magnitude determination, attenuation models for amplitude prediction, velocity models like RSTT and LLNL-G3D for predicting travel times, as well as earthquake and explosion source models. Here, we present on work we have done integrating all of these products in the creation and modeling of regional waveform envelopes across a broad frequency band. By specifying the noise levels, along with arrival times, source amplitudes, propagation (geometrical spreading and attenuation) effects and coda decay parameters for the regional phases (Pn, Pg, Sn, Lg), we can construct envelope templates, which can be compared to the observed envelopes. This represents an effort to use more of the waveform than parametric information, such as travel times or magnitudes, but not attempting the difficult task of trying to fit the whole waveform, swing-for-swing, at high frequencies. This method has applications for event identification, depth determination, magnitude estimation, and more sophisticated analysis, such as estimating the yield and depth-of-burial of explosions. We will first report on the progress we are making on many of the individual constitutive products, such as the high-resolution attenuation tomography of the crust and upper mantle that we are developing for Eurasia. For earthquakes, we use the MDAC source model while, for explosions, we explore the Mueller-Murphy model and proposed extensions of the model for S-waves, and explosion source spectral models based on modifications to the Denny-Johnson model. We will then illustrate how we are utilizing the methodology to characterize events in the Korean Peninsula and at the Nevada National Security Site (NNSS, formerly known as the Nevada Test Site).

OBJECTIVES

Our objective is to integrate work in seismic attenuation, coda decay, and source models in order to improve out ability to identify events as either earthquakes or explosions, and then further characterize their source attributes, such as depth and seismic yield. Improvements to many of these individual elements has allowed us to develop a new method of fitting significantly more of the waveform with envelopes over a broad frequency band, with potential payoff in event identification and source characterization.

RESEARCH ACCOMPLISHED

In the past year, we have accomplished a number of research goals: improved regional attenuation maps in Eurasia, demonstration of event discrimination (calibrated high-frequency P/S discriminants) over broad regions, and the development of a new method of using regional waveform envelopes for event identification and source characterization, shown here for events in the Korean Peninsula and at the NNSS. We will also discuss how the attenuation models are used in capability analysis, including extensions of the method to coda phases.

Seismic Attenuation

LLNL has developed a four-phase amplitude tomography which allows us to determine a set of attenuation, site, and source corrections for the primary regional phases of Pn, Pg, Sn, and Lg. Our basic methodology, employed in Pasyanos et al. (2009a) for Lg, uses an MDAC source model (Walter and Taylor, 2001), which more explicitly defines the source expression in terms of an earthquake source model formulated in terms of the seismic moment. We applied the technique to simultaneously invert amplitudes of Pn, Pg, Sn and Lg in the Middle East to produce P-wave and S-wave attenuation models of the crust and upper mantle for the region (Pasyanos et al., 2009b).

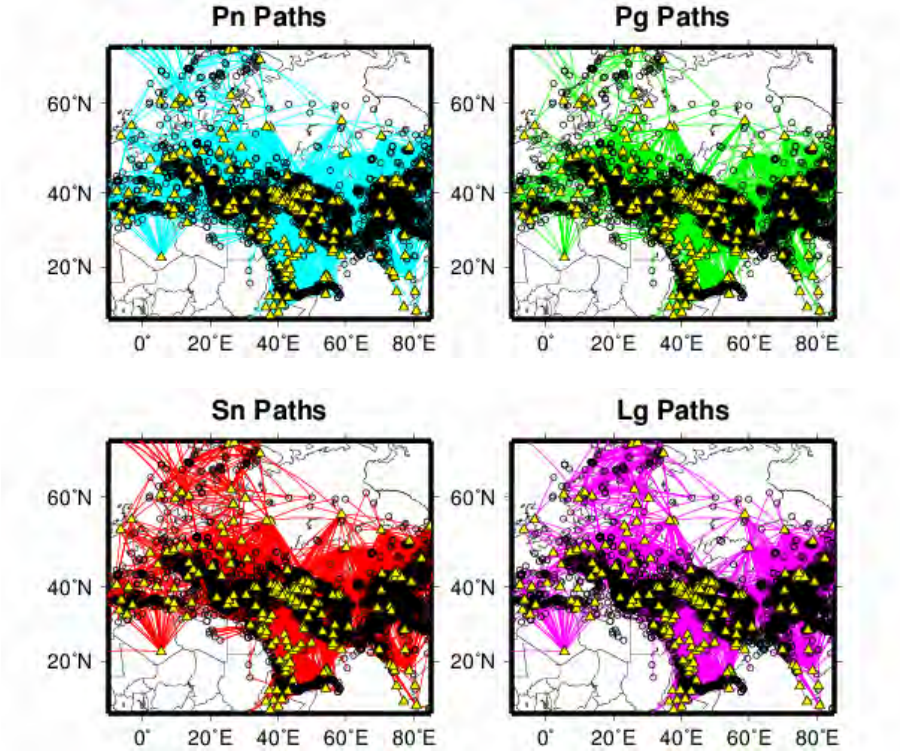


Figure 1. Path map of Pn, Pg, Sn, and Lg attenuation measurements for western and central Eurasia in the 1-2 Hz passband.

We have extended the region into Europe to cover all of western Eurasia and portions of North Africa, as shown by the path maps in Figure 1. The attenuation is modeled as P-wave and S-wave attenuation layers for the crust, and a similar set for the upper mantle. Inverting all of the phases simultaneously allows us to determine consistent

attenuation, site, and source terms for all phases, and eliminates non-physical inconsistencies among them. Attenuation results are shown in Figure 2.

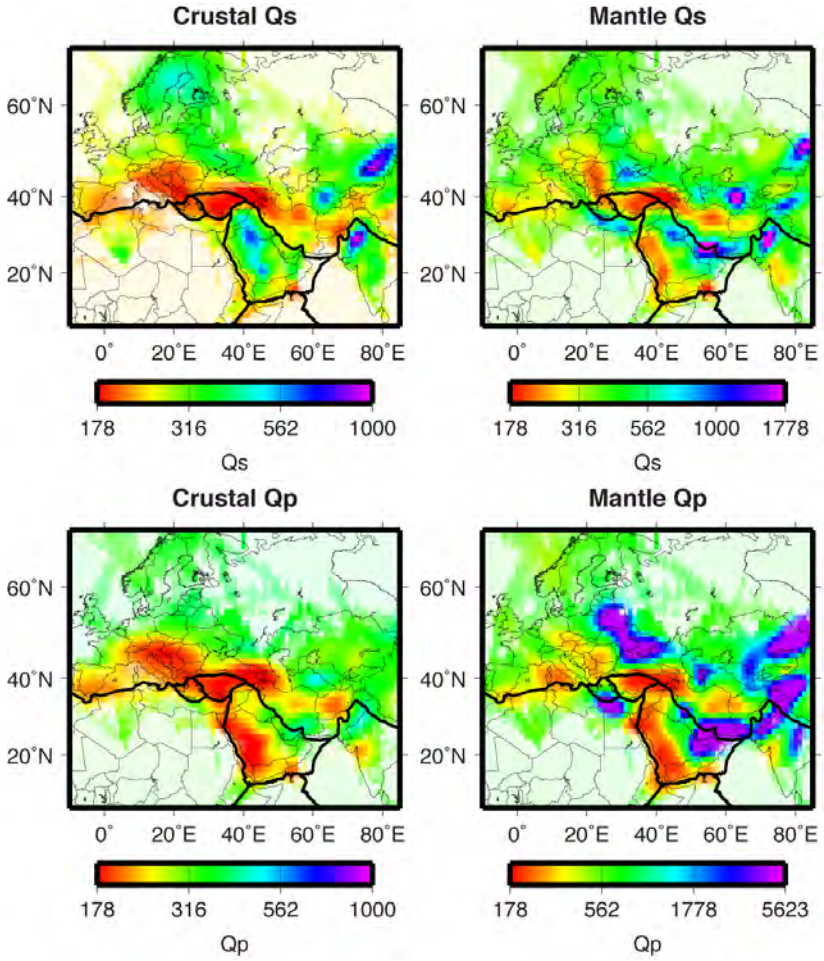


Figure 2. Attenuation of crustal Qs, mantle Qs, crustal Qp, and mantle Qp of western and central Eurasia in the 1-2 Hz passband.

It has been demonstrated that applying corrections with the attenuation models can significantly improve earthquake-explosion discrimination using high-frequency regional P/S amplitude ratios (Pasyanos and Walter, 2009). P/S discriminants are expressed as the ratio between the P-wave amplitude (A^P) and the S-wave amplitude (A^S) and, because of the large variations, are usually plotted on a log scale. To correct the phase ratio for path and source effects, we adjust the individual amplitudes assuming an earthquake source. We then form our discriminant using the ratio of the corrected amplitudes:

$$\text{discriminant} = \log\left[\frac{(A^P / A_0^P)}{(A^S / A_0^S)}\right] = \log\left[\frac{A^P}{A^S}\right] - \log\left[\frac{A_0^P}{A_0^S}\right] \qquad (1)$$

where A_0 are the amplitude predictions for an earthquake of that phase and size. As a result, the corrected discriminant should now have a value around 0 (P/S ratio of 1) for earthquakes. We input a best estimate of the earthquake size by using a moment magnitude, if available, or otherwise estimating Mw using other magnitude estimates.

We have tested the use of the 2-D attenuation model for discrimination over broad regions by using data from the historical Borovoye dataset (Kim and Ekstrom, 1996; Baker et al., 2009) which has recorded dozens of events from the Semipalatinsk Test Site, as well as Peaceful Nuclear Explosions (PNEs) from the broader region.

Figure 3 shows an example of the good separation that is achieved between earthquakes and explosions with Pn/Sn in the 4-6 Hz passband using corrections from the attenuation model. Only a known overburied PNE does not separate well from the earthquakes at this frequency (Pasyanos et al., 2012a) and the explosion-like presumed earthquakes are coming from a known mine region (Hans Hartse, see Acknowledgements). The improvements using 1-D and 2-D corrections are quantified in the right panel, which shows increasing Mahalanobis distance and reduced equiprobable points at all frequency bands using the 2-D model. The overall discrimination performance and improvements using the 2-D model are most significant at 2-4 Hz.

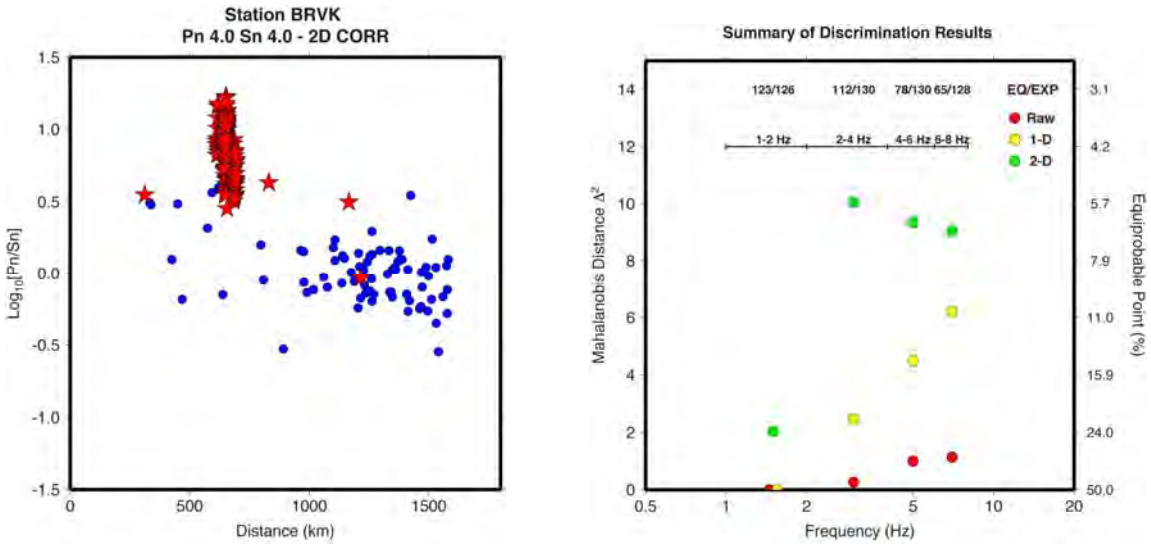


Figure 3. The left figure shows corrected Pn/Sn ratios of earthquakes (blue circles) and explosions (red stars) recorded at station Borovoye. Explosions included nuclear tests from the Semipalatinsk Test Site as well as PNEs from the broader region. The right figure shows a comparison of discrimination performance (in both Mahalanobis distance and equiprobable point) at various frequencies using raw ratios, 1-D corrected ratios, and 2-D corrected ratios. Figure from Pasyanos et al. (2012a).

Coda Shape

To create model amplitude envelopes, we will be employing the Coda Wave Method (Mayeda and Walter, 1996; Mayeda et al., 2003). With this technique, the analytic expression that we used to fit the observed narrowband envelopes at the center frequency f as a function of distance r (in kilometers) for times greater than the direct S-wave arrival is

$$A_C(f,r,r) = S(f) \cdot U(r,f) \cdot P(f) \cdot T(r,f) \cdot H\left(t - \frac{r}{v(r)}\right)^{-\gamma(r)} \cdot exp\left[b(r) \cdot \left(t - \frac{r}{v(r)}\right)\right] \quad (2)$$

where S(f) is the source amplitude, U(r,f) is the propagation (geometrical spreading and attenuation), P(f) is the site response, T(f) is the direct phase-to-coda transfer function. H is the Heaviside step function, t is the time in seconds from the origin, r is the epicentral distance in km, v(r) is the velocity of the peak arrival in km/sec, and γ(r) and b(r) are coda shape parameters, which can be complicated functions of frequency and distance.

Calibration of coda in the Middle East and other areas is complicated by the fact that the dominant S-wave phase varies depending on tectonic region, distance, and frequency. This past year, we have been improving coda calibrations in the Middle East, including lateral variability in the attenuation and coda decay parameters across the region.

Source Models

For earthquake source spectra, we make use of the MDAC source model (Walter and Taylor, 2001), that is a more generalized form (encompassing P, S-waves and variable apparent stress) of the well-known and widely used Brune

(1970) model. The minimum input parameter would be a seismic moment Mo, although, if available, additional source parameters such as apparent stress could be input to provide a more accurate source term. For explosions, we explore the use of several models. First, we will make use of the Mueller-Murphy model (Mueller and Murphy, 1971) for P-waves, which produce a source model for a specified depth, yield, and choice of emplacement media (e.g., granite, salt, tuff, or shale). For explosion S-waves, we make use of the Fisk conjecture which posits that "S-wave corner frequency is reduced by the ratio of near-source shear and compressional velocities" (Fisk, 2006). The S-wave corner frequency, low frequency level and high frequency falloff remain areas of active research.

Ford et al. (2012) developed a parametric model of the nuclear explosion seismic source spectrum derived from regional phases, using data from the Nevada and Semipalatinsk Test Sites. Source spectra are fit with a generalized version of the Brune spectrum, which uses a three-parameter model (long-period level, corner-frequency, and spectral slope at high-frequencies). The parameters are then correlated with near-source geology and containment conditions. We will be testing the model of Ford et al. (2012) and other explosion source spectral models based on modifications to the Denny-Johnson model (Denny and Johnson, 1991).

Regional Amplitude Envelopes

We consider a less empirical, more physics-based method of fitting the complete regional amplitude envelope. The full regional waveform envelope in a given frequency band can be described as the sum of the noise and all of the regional phase envelope amplitudes or:

$$A_{total} = A_{noise} + A_{Pn} + A_{Pg} + A_{Sn} + A_{Lg} \qquad (3)$$

where A_{noise} is the noise level in that frequency band, and A_{Pn} and A_{Sn} are zero at local distances where these phases are non-geometric. The regional phase terms (A_{Pn}, A_{Pg}, A_{Sn}, A_{Lg}) include the direct phase and coda can be described as:

$$A = A_{direct} \cdot H(t - t_a) \cdot (t - t_a)^{-\gamma(r)} \cdot \exp\left(b \cdot (t - t_a)\right) \qquad (4)$$

where A_{direct} is the direct phase amplitude. This is the same form as equation (2) above, but with direct amplitudes (which include source, propagation, and site terms) replacing the first four terms used earlier. The only term not directly incorporated in the direct phase amplitudes is the transfer term T(f), which we will be considering more later. We have also replaced r/v(r) with the arrival time t_a.

Conceptually, this is shown in Figure 4, where the envelopes will have a sawtooth pattern from the arrival and decay of local and regional phases. The amplitude of the direct phase may be sensitive to factors such as radiation pattern, directivity, path propagation, and multipathing. The direct phase, however, only represents a relatively short segment of the overall envelopes, and are only important for setting the overall coda levels, which are not sensitive to these same factors.

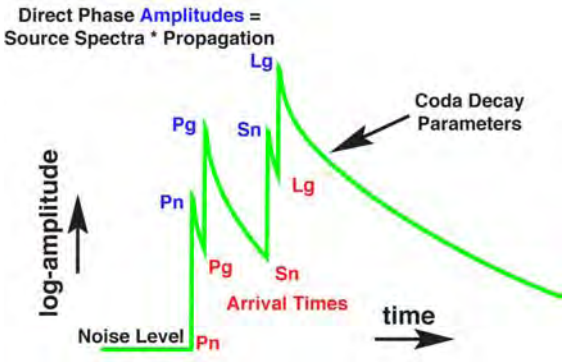


Figure 4. Illustration of expected envelope shapes for regional events. The plot shows logarithmic velocity variation as a function of time and the sawtooth pattern comes from the arrival and decay of prominent regional phases. Figure from Pasyanos et al. (2012a).

Changes in moment and corner frequency (for earthquakes) and changes in the yield, depth, or material properties (for explosions) will change the source spectra, which will result in differences to the synthetic coda envelopes, as illustrated in Figure 5. The top panels show the effect of changes to seismic yield on the moment spectra and the 2-3 Hz envelopes. The bottom panels show the effect of changes to depth of burial. Notice the increase in amplitudes for the intermediate depth (500 m) in this particular frequency band; this would not happen at higher and lower passbands.

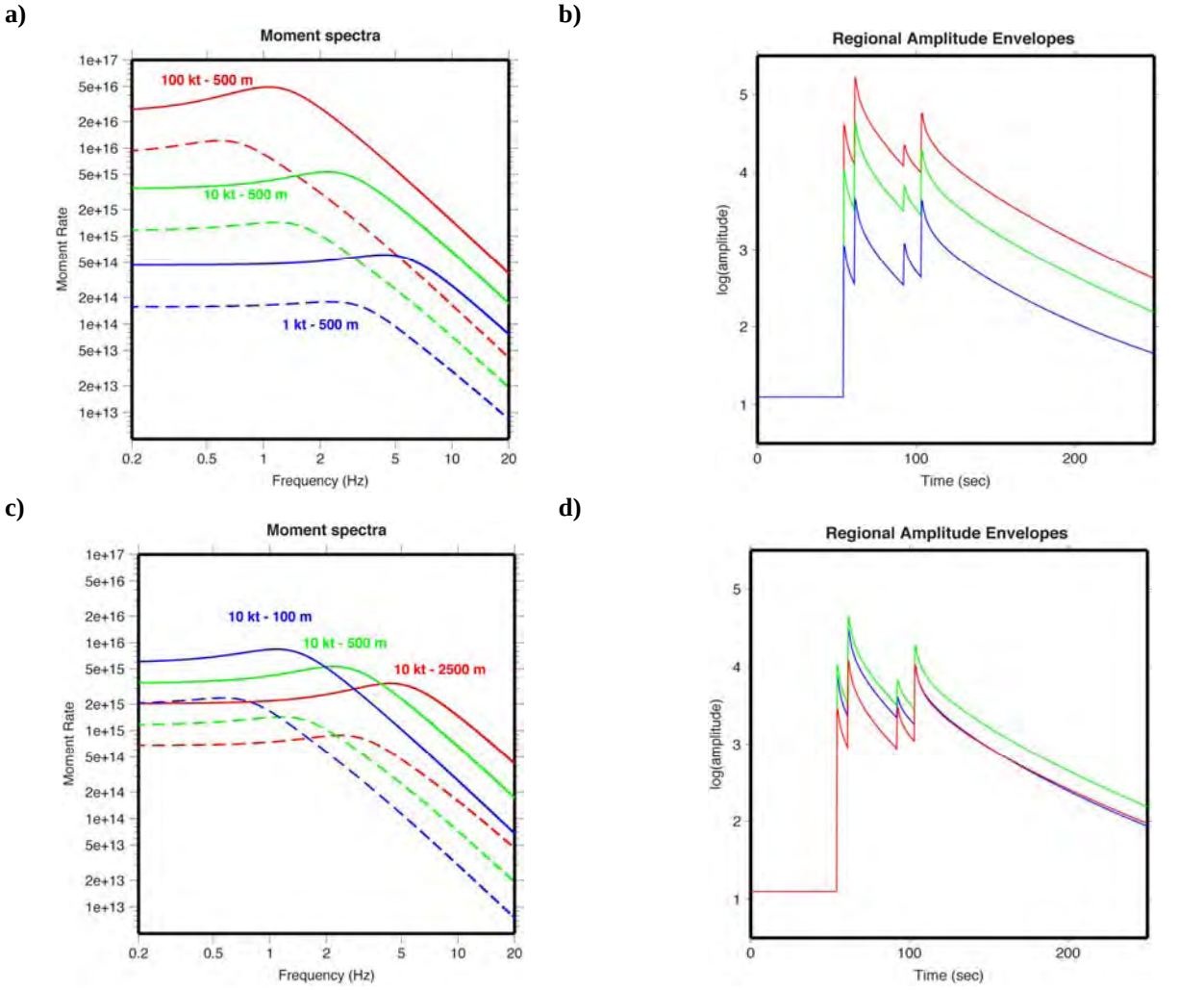


Figure 5. A comparison of moment spectra and regional amplitude envelopes from explosion sources of varying yield (a, b) and varying depth (c, d). In the moment spectra plots (a, c), the solid lines indicate P-wave spectra and dashed lines indicate S-wave spectra. Regional amplitude envelopes are shown for the 2-3 Hz passband. The color of the envelopes in panels b and d refer to the corresponding sources indicated in panels a and c. Figure from Pasyanos et al. (2012b).

This sensitivity of the envelopes to source parameters allows us to estimate these parameters by minimizing misfit. We perform a grid search of 2006 and 2009 DPRK tests for variable yield and depth of burial (DOB) assuming the same source type and material. We perform a search ranging from 0.01 to 100 ktons in yield and from 10 to 1000 m in depth at every first significant digit of 1, 2, and 5. We used both station MDJ and TJN using the 1-1.5, 2-3, 4-6, and 6-8 Hz frequency bands. Misfits were calculated using log-amplitudes, which emphasizes reducing the misfit of the coda relative to the higher-amplitude direct phases. Results are shown in Figure 6, along with a standard depth of burial estimated for Kazakhstan (Israelsson, 1994). For the 2006 event, a minimum misfit is found at a yield of 500 tons (200-800 tons) and a DOB of 100 m (20-300 m). For the 2009 event, the minimum occurs at a yield = 2

ktons (1-5 ktons) and DOB = 200 m (70-600 m). These are consistent with the analysis reported by the Director of National Intelligence (DNI). The yield estimate depends on the particular explosion model used and other authors have found different estimates (Figure 6).

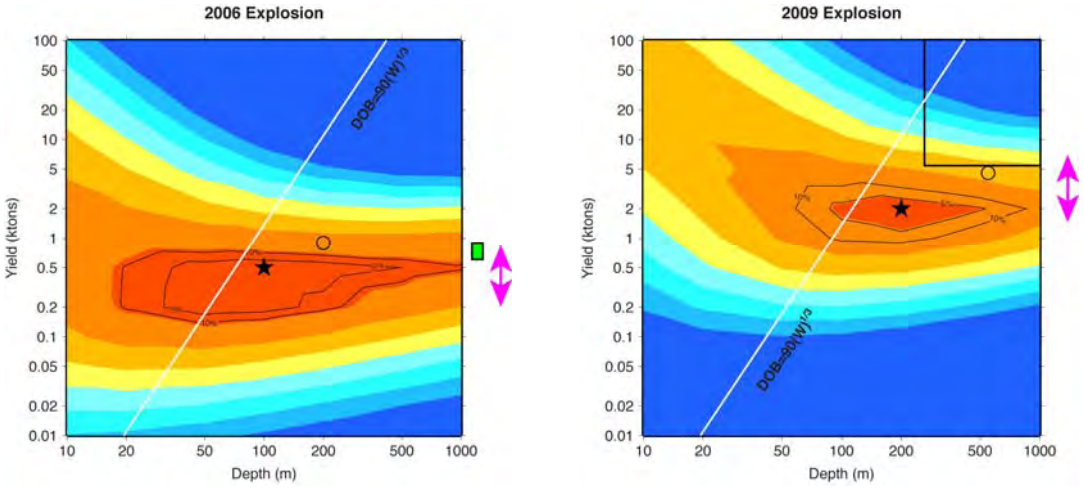


Figure 6. Misfit of the 2006 and 2009 events as a function of depth of burial and explosive yield assuming the Mueller-Murphy model, granite shot point and the Fisk conjecture. The minimum RMS is indicated with the star. Contours of 5% and 10% above the minimum are drawn. The line shows a standard depth of burial of 90 $(W)^{1/3}$ (Israelsson, 1994). Other symbols on figures represent estimates from other studies (not discussed here). Figure from Pasyanos et al. (2012b)

While we cannot independently confirm the validity of these values for the DPRK tests, the methodology has also been tested on explosions at the Nevada Test Site (NTS), where the true depth and yield were reported. Figure 7 shows the RMS misfit of the Atrisco event recorded at station ELK (Elko, Nevada). The minimum misfit (indicated by the star) occurs at a depth of 500 m and a yield of 100 ktons, which compares favorably to the depth of 640 m and yield of 138 ktons reported in Springer et al. (2002).

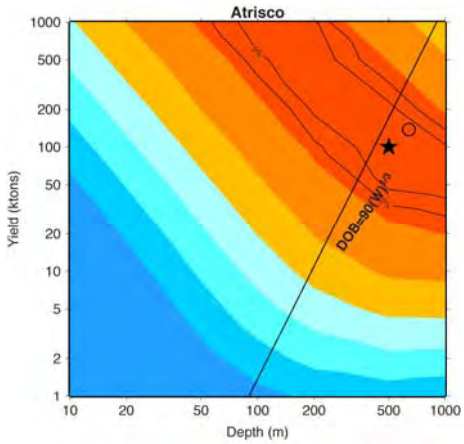


Figure 7. Misfit of the Atrisco event as a function of depth of burial and explosive yield assuming the M-M model, granite shot point and Fisk conjecture. The minimum RMS is indicated with the star. The line shows a standard depth of burial of 90 $(W)^{1/3}$ (Israelsson, 1994). The circle indicates the true yield and depth values from the report of Springer et al. (2002). Figure from Pasyanos et al. (2012b)

Capability Analysis

We can use our regional attenuation models, along with associated earthquake and explosion source models, to predict expected signal-to-noise at a station for a given combination of phase, frequency, path, magnitude, etc.

Figure 8 shows an example of maps with predicted signal-to-noise of an Mw 4.0 earthquake recorded at station UOSS in Sharjah, UAE using an average noise level for the station. The panel to the left shows the signal-to-noise ratio (SNR) for Sn in the 2-4 Hz passband, while the panel to the right shows 2-4 Hz Lg. Plotted on top are observed SNR from events with magnitudes around 4.0. There is some variation in the observations due to changes in the background noise level and the individual event magnitudes sometimes being slightly higher or lower than magnitude 4.0.

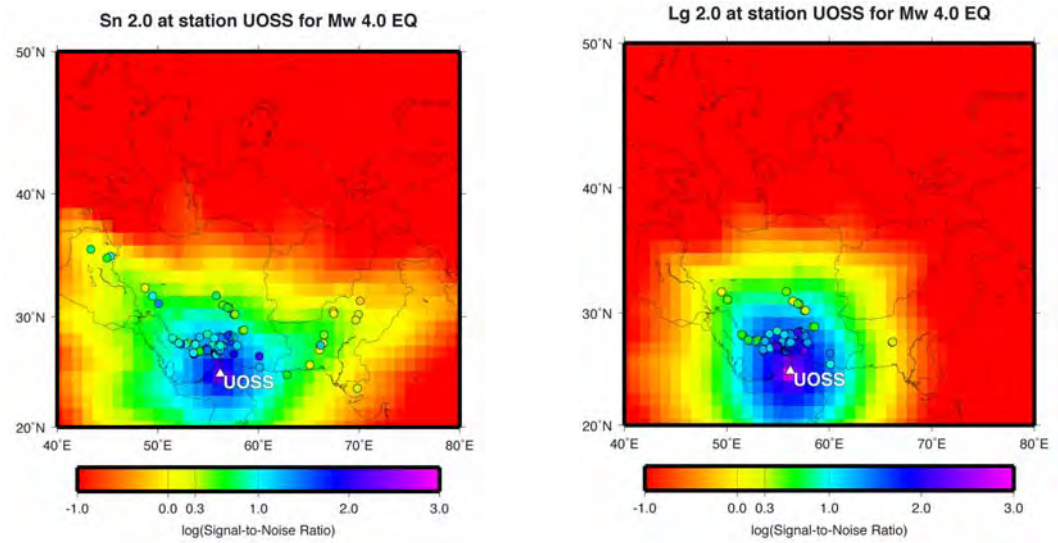


Figure 8. Expected signal-to-noise of an Mw 4.0 earthquake recorded at station UOSS in Sharjah, UAE for 2-4 Hz Sn and Lg. Colored symbols show observed SNR from events.

While magnitudes can be estimated from direct phase amplitudes, measuring them on coda provides stability to the magnitude estimate. Figure 9 show a comparison of estimated signal-to-noise for both the direct *Sn* and *Sn*-coda, in the same 2-4 Hz passband. The coda figure shows the smaller area in which a reliable magnitude estimate can be made. Here we use 60 seconds of coda, which results in an interstation standard deviation of 0.10 magnitude units (e.g., Figure 13 from Mayeda et al., 2003). Longer coda windows would have lower uncertainties, while shorter windows would have higher uncertainties.

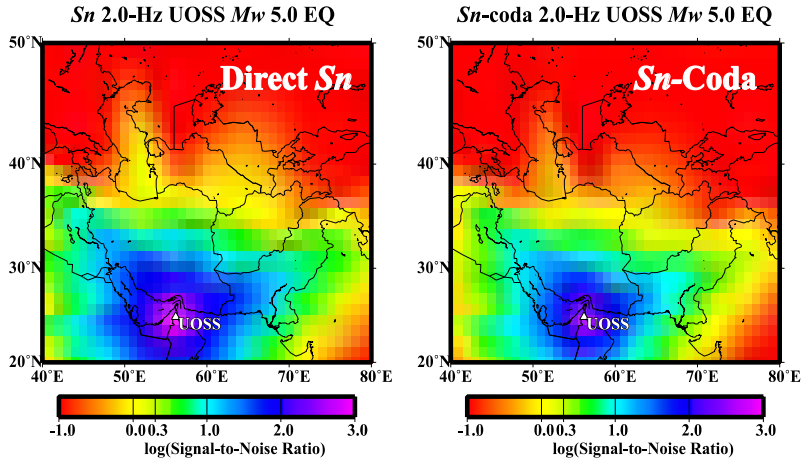


Figure 9. A comparison of estimated signal-to-noise ratios for Sn and Sn-coda in the 2-4-Hz passband from Mw 5.0 event recorded at station UOSS. The panel to the left shows the SNR of the direct phase, while the panel to the right shows the SNR of Sn-coda that has decayed 60 seconds from the direct phase.

CONCLUSIONS AND RECOMMENDATIONS

For many years, we have been building, developing, and improving all of the components that can allow us to construct the envelopes of regional phases out to observing stations from arbitrary events. These components include earthquake and explosion source models, travel time models for predicting arrivals, attenuation models that can account for the propagation, and coda decay parameters that predict the falloff that accounts for the envelope shape. Here, we integrate all of this work to allow us to estimate magnitude (or explosive yield), identify events as earthquakes or explosions, and assist in station and network capability assessments. While we will continue to improve the constitutive source, velocity, attenuation, and coda models, the integrated approach can be used now in explosion monitoring applications.

ACKNOWLEDGMENTS

We thank Stan Ruppert, Terri Hauk, Doug Dodge, and Mike Ganzberger for maintaining the LLNL Seismic Research Database and development of tools. We thank Gene Ichinose for the regional moment magnitudes used in the coda calibration. And many thanks to Hans Hartse, LANL, for valuable information gleaned from personal communications.

REFERENCES

Baker, D., W.-Y. Kim, H. Patton, G. Randall, and P. Richards (2009). Improvements to a major digital archive of seismic waveforms from nuclear explosions: The Borovoye seismogram archive, in *Proceedings of the 2009 Monitoring Research Review: Ground-Based Nuclear Explosion Monitoring Technologies*, LA-UR-09-05276, Vol. 1, pp. 12–21.

Brune, J., (1970). Tectonic stress and the spectra from seismic shear waves earthquakes, *J. Geophys. Res*. **75**, 4997-5009.

Denny, M.D. and L.R. Johnson (1991). The explosion seismic source function: Models and scaling laws reviewed, in *Explosion Source Phenomenology*, *AGU Monograph,* **65,** ed. S. Taylor et al., 1–24.

Fisk, M.D. (2006). Source spectral modeling of regional P/S discriminants at nuclear test sites in China and the Former Soviet Union, *Bull. Seismol. Soc. Am*. **96**, 2348–2367.

Ford, S., W.R. Walter, S.D. Rupppert, E.M. Matzel, T.F. Hauk, and R. Gok (2012). An empirically-based parametric explosion spectral model, these Proceedings.

Israelsson, H. (1994). Analysis of historical seismograms – root mean square Lg magnitudes, yields, and depth of explosions at the Semipalatinsk Test Range, *Geophys. J. Int.* **117**, 591–609.

Kim, W.-Y. and G. Ekstrom (1996). Instrument responses of digital seismographs at Borovoye, Kazakhstan, by inversion of transient calibration pulses, *Bull. Seismol. Soc. Am*. **86**, 191–203.

Mayeda, K., A. Hofstetter, J.L. O'Boyle, and W.R. Walter (2003). Stable and transportable regional magnitudes based on coda-derived moment-rate spectra. *Bull. Seismol. Soc. Am*. **93**, 224–239.

Mayeda, K. and W.R. Walter (1996). Moment, energy, stress drop, and source spectra of western U.S. earthquakes, *J. Geophys. Res.* **101**, 11195–11208.

Mueller R.A. and J.R. Murphy (1971). Seismic characteristics of underground nuclear detonations: Part I. seismic spectrum scaling, *Bull. Seismol. Soc. Am.* **61**, 1675–1692.

Pasyanos, M.E. and W.R. Walter (2009). Improvements to regional explosion identification using attenuation models of the lithosphere, *Geophys. Res. Lett.,* doi:10.1029/2009GL038505.

Pasyanos, M.E., E.M. Matzel, W.R. Walter, and A.J. Rodgers (2009a). Broad-band Lg attenuation modeling of the Middle East, *Geophys. J. Int.* **177**, 1166–1176, doi:10.1111/j.1365-246X.2009.04128.x

Pasyanos, M.E., W.R. Walter, and E.M. Matzel (2009b). A simultaneous multi-phase approach to determine P-wave and S-wave attenuation of the crust and upper mantle, *Bull. Seismol. Soc. Am*, **99** (6), 3314–3325, doi:10.1785/0120090061.

Pasyanos, M.E., W.R. Walter, and K.M. Mayeda (2012). Exploiting regional amplitude envelopes: a case study for earthquakes and explosions in the Korean Peninsula, *Bull. Seismol. Soc. Am*., in press.

Pasyanos, M.E., S.R. Ford, and W.R. Walter (2012). Testing event discrimination over broad regions using the historical Borovoye Observatory explosion dataset, submitted to *Pure Appl. Geophys*.

Walter, W.R. and S.R. Taylor (2001). A revised magnitude and distance amplitude correction (MDAC2) procedure for regional seismic discriminants: theory and testing at NTS, Lawrence Livermore National Laboratory, UCRL-ID-146882, http://www.llnl.gov/tid/lof/documents/pdf/240563.pdf

SEISMIC STUDIES OF SOURCE PHYSICS EXPERIMENTS CONDUCTED AT THE NEVADA NATIONAL SECURITY SITE USING CLOSE-IN (< 2 KM) WAVEFORMS

Howard J. Patton, Carene Larmat, Esteban Rougier, Charlotte A. Rowe, and Xiaoning Yang

Los Alamos National Laboratory

Sponsored by the National Nuclear Security Administration

Award No. DE-AC52-06NA25946/NST11-NCNS-TM-EXP-PD15

ABSTRACT

This paper reports on studies investigating source and propagation effects of seismic waves emitted by small chemical explosions conducted in the granites of Climax Stock on the Nevada National Security Site (formerly the Nevada Test Site) as part of the Source Physics Experiments (SPE). To date, two such explosions (SPE-1 and SPE-2) have been executed with chemical yields of 100 and 1000 kg and burial depths of 55 and 46 m, respectively. A third experiment conducted in the summer of 2012 is not reported on in this paper. As many as four follow-on experiments in this SPE series are planned in subsequent years. All experiments are designed to be detonated in the same emplacement hole and recorded by the same free-field, free-surface, close-in, and local networks of ground- motion sensors, including some infrasound sensors. The focus of this paper is on the analysis and modeling of waveforms recorded close-in on five linear geophone lines emanating on a spread of azimuths from ground zero with distances ranging from 100 to 2000 m and station spacing of 100 m. In general, the vertical-component geophone (4.5 Hz free period) recordings show strong arrivals of *P*-wave energy and high-frequency *Rg* waves (four installations spaced 400 m apart have three components of motion also). Our studies have exploited mainly these arrivals to investigate and characterize: (1) the shallow Earth structures of Climax Stock using *P*-wave move-out times and *Rg* dispersion measurements, (2) azimuthal variations in geometrical spreading and attenuation of *Rg* waves, (3) source spectra based on moment tensor inversions of recorded waveforms and synthetic waveforms computed by coupling hydrodynamic simulations of the explosions with wave propagation codes, and (4) sources of material damage radiating seismic waves.

There are two significant features, one structural and the other source-related, that play a major role in the source and propagation effects of close-in seismic waves recorded on Climax Stock. The structural feature is a weathered layer of varying thickness and low wave speeds overlying intact granite of much higher wave speeds extending to depths as great as the seismic energy penetrates. The source-related feature is associated with excellent energy coupling of both down-going seismic waves recorded in the farfield and up-going shock waves which interacted with the free surface and resulted in an unanticipated strong spallation signature. Spallation is a visible sign of material damage and a facilitator of damage occurring in the sub-surface. A theme in all of our results for all four topics of study is the importance of these features in controlling the source and propagation effects we have uncovered. These results include: a contrast in *P*-wave speeds between weathered and intact granite on the order of a factor of 3 to 4, strong differences in apparent decay rates of *Rg* waves depending on direction of propagation, anomalous peaking in source spectra related to non-linear behavior in the weathered layer near the free surface, and persistent phase shifts in *Rg* waves that could be related to the effects of superposition of waves radiated from the explosion source at depth and damage sources near the free surface related to spallation.

OBJECTIVES

A key scientific objective of the Source Physics Experiment (SPE) is to gain a better understanding of *S* wave generation by underground explosions. Quoting from the 2010 SPE Project Execution Plan (PEP) authored by National Securities Technology (NSTec) LLC, "The SPE Program will provide ground truth data to create and improve strong ground motion and seismic *S*-wave generation and propagation models. These validated, improved seismic models and simulations will enhance the U. S. ability to detect and discriminate 'low-yield' nuclear explosions amid the clutter of conventional explosions and small earthquake signals."

RESEARCH ACCOMPLISHED

The focus of this paper is on the analysis and modeling of waveforms recorded on five linear geophone lines numbered 1-5 clockwise from north with distances ranging from 100 to 2000 m and station spacing of 100 m (Figure 1). Ground zero is hole U-15n on Climax Stock. To date, two chemical explosions have been executed with yields of 100 and 1000 kg and burial depths of 55 and 46 m, respectively. The vertical-component geophone (4.5 Hz free period) recordings show strong arrivals of *P*-wave energy and high-frequency *Rg* waves. Our studies have exploited these arrivals to investigate: (1) the shallow earth structures of Climax Stock using *P*-wave move-out times and *Rg* dispersion measurements, (2) azimuthal variations in geometrical spreading and attenuation of *Rg* waves, (3) source spectra based on moment tensor inversions of recorded waveforms and synthetic waveforms computed by coupling hydrodynamic simulations of the explosions with wave propagation codes, and (4) sources of material damage radiating seismic waves.



Figure 1. Deployment of geophone lines on Climax Stock and neighboring geologies.

Climax Stock earth structure studies

We have evaluated first arrivals using the record sections for each of the five lines, and observe complexities that are likely due to dipping interfaces and the irregular topography impacting three of the five lines. The second explosion (SPE-2) consisted of 1 ton of explosives, detonated at 46 m depth. This shot provided good signal-to-noise for first break identification (*P*) even at the distal receivers, up to 2000 m from the source (Figure 2). In our preliminary evaluation we treat the site as a simple 1D structure with assumed flat-lying layers. A time-distance plot of first breaks (Figure 3) yields a starting *P*-wave model for Line 2 (northeast trending line in Figure 1).

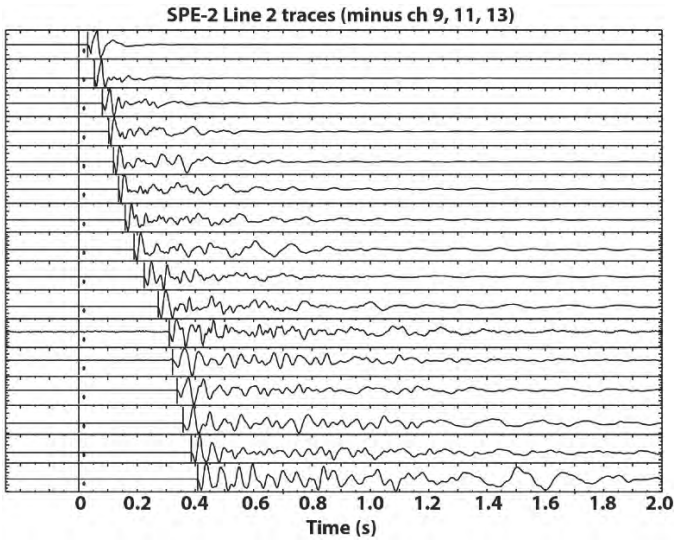


Figure 2. Seismic Line 2 arrivals for explosion SPE-2. Receiver distances range 100 to 2000 m from the source.

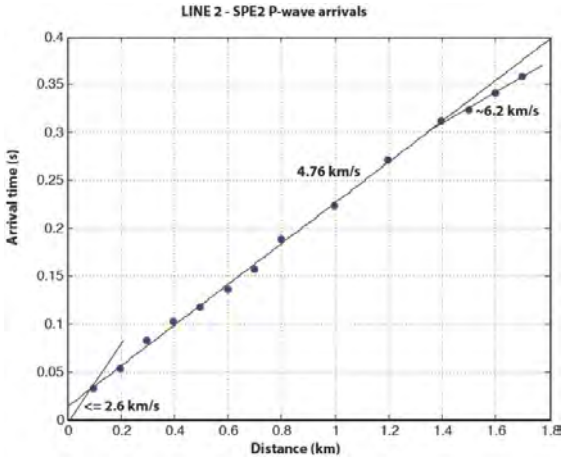


Figure 3. First-arrival time-distance plot for Line 2, SPE-2. The greatest portion of the data is consistent with a velocity of 4.76 km/s, with a faster, deeper rock mass appearing on the final three stations. The non-zero intercept of the 4.76 km/s layer indicates the presence of a shallow, slow layer whose velocity cannot exceed 2.6 km/s, but could be less.

P-wave velocities of 4.76 km/s are exhibited for the bulk of the data, with a suggestion of higher velocity at depth. The 4.76 km/s does not intercept the origin, indicating the presence of a very thin, very slow surface layer. Receiver spacing does not allow resolution for this layer, but it cannot possess a velocity greater than 2.62 km/s, nor thickness more than ~26 m, based on a standard seismic refraction head-wave cross-over analysis method (Dobrin, 1976). These numbers assume a planar, horizontal interface; without reversing the profile (detonating a source on the opposite end), we must assume that the velocities and depths are apparent velocities, although some consistency among the five radially-arranged seismic profile lines regarding the 4.76 km/s horizon suggests that interface dips may not be extreme.

We examine the phase velocity for *Rg* using two distinct techniques. First, in the time domain, by using several narrowband-filtered realizations of the seismograms, we measure the phase velocity in each frequency band to generate a dispersion function. Shown in Figure 4 is an example for Line 2 filtered at 5-6 Hz for shot SPE-1. We also constructed the phase dispersion curve in the frequency domain. In this approach, we calculate phase spectra, and plot the spectra after performing phase unwrapping to eliminate discontinuities. We show in Figure 5 the spectra for Line 2 using data for SPE-1. Note the increasing slope with shot offset.

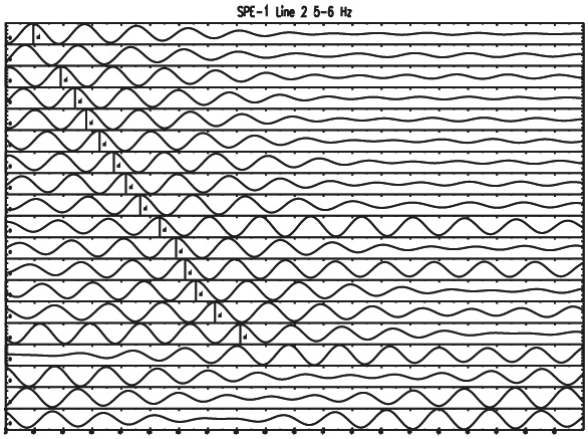


Figure 4. *Rg* phase measurement at 5-6 Hz, filtered using 4-pole, 2-pass Butterworth filter. Structural complexity and topography impact the surface wave dispersion measurements at all frequencies, but quasi-linear behavior can be found between about 3 Hz and 9 Hz.

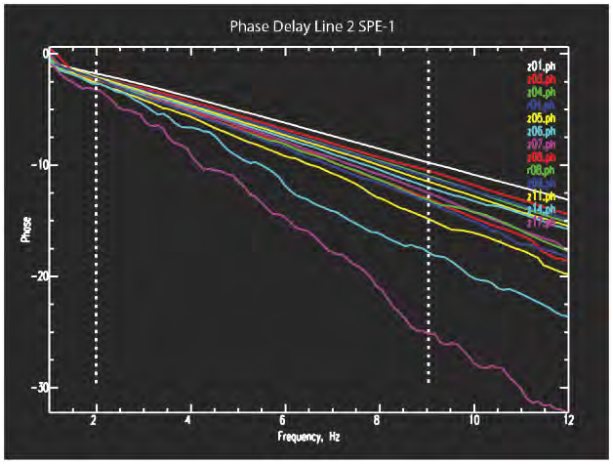


Figure 5. Phase delay spectra for Line 2, shot SPE-1.

Useful frequencies for this analysis lie between 2 and 9 Hz. Following phase unwrapping, we collect the phase and offset information across the array at each frequency of interest (in this analysis we use 32 frequency samples) and perform a linear inversion at each selected frequency to estimate phase velocity across the array. These individual phase velocities then combine to produce an *Rg* dispersion curve. We iteratively adjust the *P*-wave model obtained in the refraction analysis to find a model *Rg* phase dispersion curve that fits the observed values from our time- and frequency-domain *Rg* investigation. We used MODESB, a computer

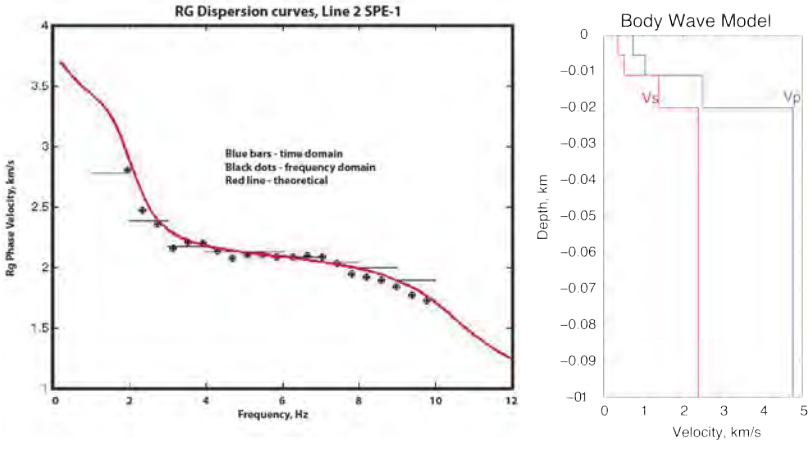


Figure 6. (a) *Rg* dispersion from frequency- (dots) and time-domain (horizontal bars) analysis. Model predicts red curve. (b) Best-fit velocity model from refraction and dispersion curve data.

program by K. Nakanishi, to adjust Poisson ratio, one-dimensional (1-D) *P*-wave velocity profile, and material density in each of the layers of the input model. For the *P*-wave model we are constrained by the well-defined 4.75-4.76 km/s beneath the shallowest (weathered) material, and by the maximum permitted thickness and velocity of the poorly defined surface material. Using a standard time-distance crossover method, we define our deepest, ~6 km/s layer, as residing at ~450 m depth. After generating a suite of theoretical *Rg* phase curves, we obtained a best-fit result with both the time-domain and frequency-domain measurements shown in Figure 6a. The resulting model, to a depth of 100 m, is shown in Figure 6b. Minor adjustments to the thickness of the surface layer and significant slow-down of its preliminary velocity were required to fit the *Rg* observations; however, the observed *P*-wave parameters are not violated. In the major granitic layer we find an unusually high Poisson ratio of around 0.33, which needs further investigation.

Rg wave propagation in 2-D media on Climax Stock

High-frequency (4 to 8 Hz) *Rg* waves exhibit weaker amplitude decay on Line 1 compared to Line 2 (Figure 7). Moreover, amplitudes show a peak of a factor of four times greater than the general trend on Line 1 for stations on a Paleozoic outcrop located 800 to 1200 m from ground zero. Clearly *Rg* spreading and attenuation are not very uniform on Climax Stock. We decided to conduct 2-D modeling with the Spectral Element Method (SEM) to investigate what structural features might be responsible. SEM solves the wave equation in its integral form on customized meshes adapted to realistic earth models using a high order finite-element method with exponential convergence for smooth solutions while maintaining the geometric flexibility of finite elements (Komatitsch and Tromp, 2002). We used the 2D SEM code SEM2DPACK developed by Ampuero (2002). The volume of propagation considered is a 2-D cross-section of dimension 2.1km by 600m. Meshes were designed to sustain frequencies up to 15 Hz according to the rules of sampling and stability. Un-deformed hexahedral elements have a size of 30m by 30m, which allows velocities as low as 600 m/s for waves at 15 Hz. The time step chosen has to be < $3x10^{-4}$s to sustain velocities up to 6.5 km/s.

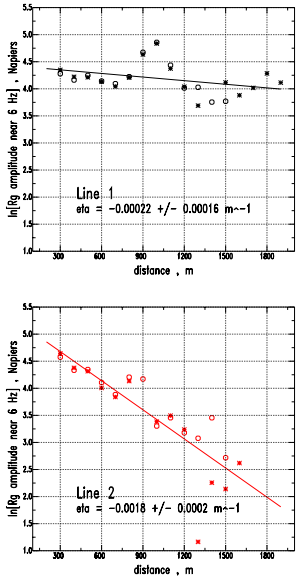


Figure 7. Observed *Rg* amplitude decay on Lines 1 and 2.

Topographic effects were tested because the elevation increases by over 100 m on Line 1, and Line 2 is on relatively level ground. Previous studies have shown how irregular topography on the free surface and on sub-surface interfaces can lead to strong body to surface wave conversion (Bard and Bouchon, 1980; Kawase and Aki, 1989).

An effect due to surface topography was rejected by the modeling results shown in Figure 8. Two models with homogeneous velocity properties were considered, the first with a flat free surface and the second with topography. We find that increasing elevation retards *Rg* arrivals and decreases their amplitude too much.

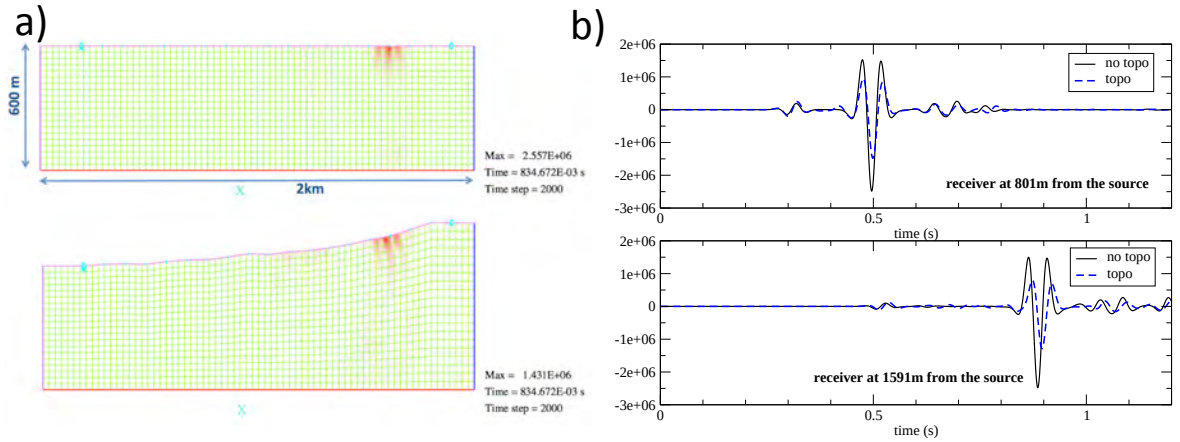


Figure 8. (a) Two models under consideration. b) Signals generated at two stations for the models (top: station at 800m from the source; bottom: station at about 1600m from the source). The black trace is for the model without topography, and the blue dashed trace is for the model with topography.

The presence of a weathered layer on Climax Stock has been discussed in the previous sub-section. A series of modeling exercises were performed with two layers to get some insight into the effect of such a low wave speed surficial layer on the *Rg* waves. We found that amplitude, polarity, and arrival times depend strongly on the properties of this layer. The *Rg* onset becomes very complex with the emergence of multiples as the velocity contrast between the weathered layer and bedrock approaches 30%. Another finding is that the arrival time of *Rg* is extremely sensitive to the average thickness of the layer, which is constrained at ~30 m for Line 1.

Our first modeling exercise rules out the effect of the free surface alone but the hypothesis of an irregular sub-surface interface remains to be tested. A "best" model for the profile on Line 1 is shown on Figure 9. Dr. Maggie Townsend of NSTec interpreted the geologic setting and suggested a thicker weathered layer under the stations deployed on a patch of Paleozoic rocks where high *Rg* amplitudes are observed (Figure 7). Results of modeling *P* wave travel times and *Rg* dispersion constrains wave speeds for the different layers, and 2-D forward modeling helped constrain the average thickness of the weathered layer.

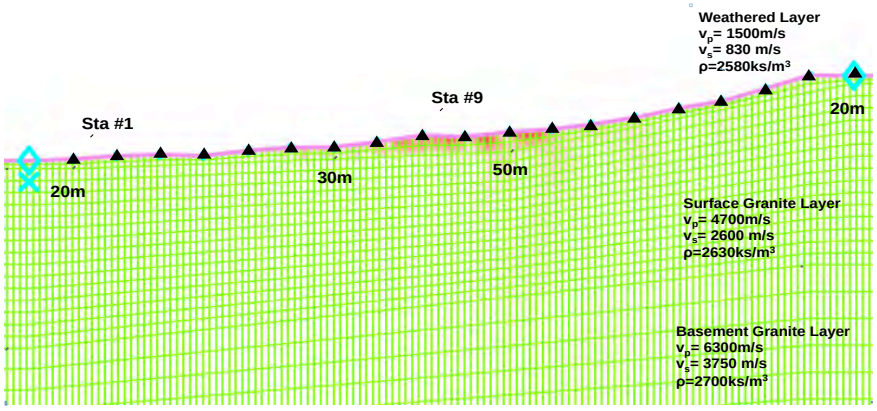


Figure 9. Model profile for north-trending Line 1. Thickness of weathered layer is greatest (35 - 50 m) under stations 8 – 11 sitting on Paleozoic rocks. The basement granite interface lies at ~450 m depth. Source point is at cyan X on left edge of profile.

We measured amplitude decay off synthetics for this model and obtained an average attenuation coefficient η along the whole profile of 1.6×10^{-4} m^{-1} for 6 Hz *Rg* waves measured on the vertical component (filled circles in Figure 10a). This value is close to the measured η (2.2×10^{-4}; Figure 7) and is an order of magnitude less than the attenuation measured on Line 2 ($\eta = 1.8 \times 10^{-3}$ m^{-1}). Synthetic radial component *Rg* waves (open circles) showed more scatter, and the amplitude decay is very uncertain. The decay of vertical component *Rg* waves is compared with the decay for a model with a constant thickness weathered layer in Figure 10b. It can be seen that, while the average fall-off of amplitude is similar, there is more variability for the model in Figure 9. Enhancement of amplitudes for stations 8 – 12 is caused by a thicker weathered layer, where the profile crosses the Paleozoic outcrop.

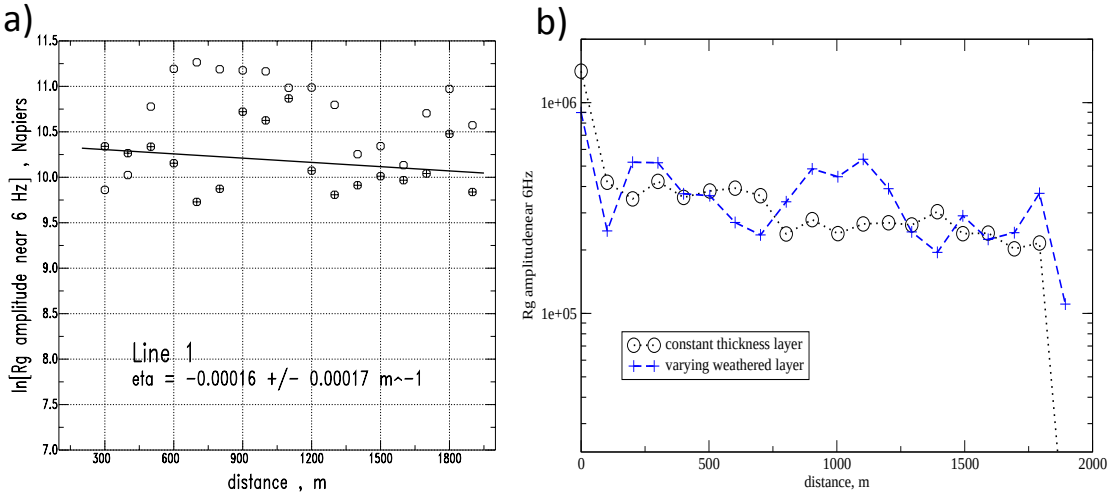


Figure 10. (a) 6 Hz *Rg* amplitude decay for the model in Figure 9 measured on the vertical (filled circles) and radial (open circles) components. (b) Comparison of *Rg* decay for two models: a model like that shown in Figure 9 except with uniform thickness weathered layer and the varying layer thickness model in Figure 9.

SPE Source Functions from Moment Tensor Inversions of Hydrodynamic and Recorded Signals

To characterize source functions of SPE explosions, we conducted moment-tensor inversions for SPE-1, the 100-kg explosion at 55-m depth, using both synthetic and observed close-in data. We used a frequency-domain inversion method in which independent time histories of the six moment-tensor components are recovered. As a result, the method resolves not only the strength of moment-tensor components, but their time histories as well.

To calculate synthetic seismograms, we first conduct hydrodynamic modeling of the explosion to simulate the nonlinear phenomenology that occurs in the source region. The simulation includes explosive detonation, material inelastic deformation, damage and spallation. Particle motion and stress signals from the simulation are then coupled to a seismic calculation code and propagated to seismic distances of a few kilometers. We assumed an axisymmetric problem in our simulation. We used synthetic seismograms at 1.0, 1.5 and 2.0 km distances at the free surface in our inversion. These distances are comparable to distances spanned by the linear geophone arrays deployed for the SPE. We used seismograms recorded by these linear arrays in the observed-data moment-tensor inversion. Figure 11 plots the inverted moment-tensor time histories and the spectra of diagonal components of the simulated SPE-1. The moment-tensor time histories show that the inverted source is largely isotropic. The three diagonal components have similar waveforms as well as similar amplitudes. The source signal is consistent with the theoretical signal predicted by an explosion source model, e.g., the Mueller-Murphy explosion model (Mueller and Murphy, 1971).

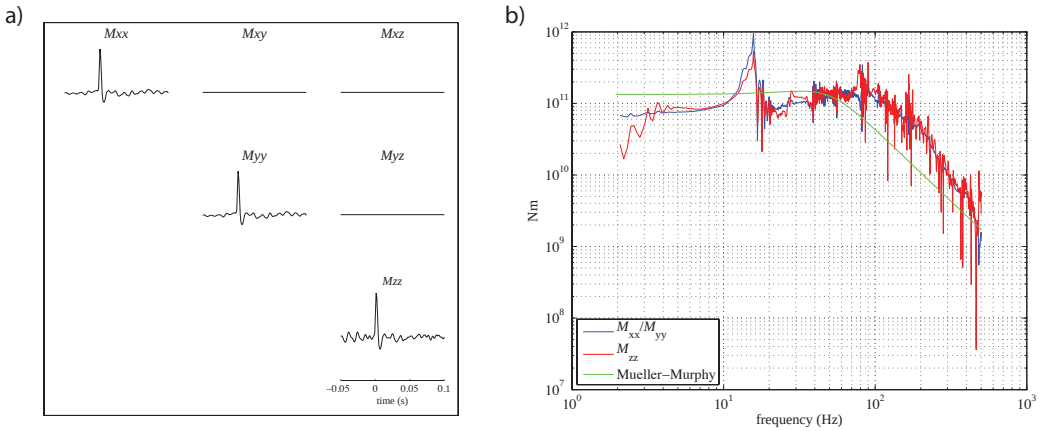


Figure 11. a): Inverted moment-tensor time histories for the simulations. b): Spectra of diagonal moment-tensor components and the spectrum of a Mueller-Murphy source model. The model was calculated with material properties used in the simulation and the Denny & Johnson (1991) cavity-radius scaling relationship. Due to the symmetry of the problem, the M_{xx} and M_{yy} spectra are identical.

As the moment-tensor time histories imply, the spectra of the three diagonal moment-tensor components are similar. When we compare the spectra with the spectrum of a Mueller-Murphy model calculated using the SPE-1 source size and depth, and SPE site material properties, we see some similarities and some differences. The long-period level of the simulated SPE-1 spectra is about a factor of 1.6 lower than that of the Mueller-Murphy model. The corner frequency is a factor of 3.6 higher. The rates of the high-frequency spectral roll-off, between 40 and 500 Hz for the Mueller-Murphy model and between 90 and 210 Hz for SPE-1, are similar. SPE-1 spectrum beyond 210 Hz is not reliable due to the finite cell size of the hydrodynamic simulation mesh. The difference in the long-period level might be due to uncertainties of parameters used in the simulation and in calculating the Mueller-Murphy model. The difference in the corner frequency is more puzzling. The corner frequency is controlled largely by the elastic radius of the source. In the Mueller-Murphy model, the elastic radius was derived from empirical data. We will also show later that the Mueller-Murphy corner frequency fits the observed SPE-1 spectrum pretty well. Apparently more analysis is required to resolve the issue.

Aside from the spectral characteristics mentioned above, the simulated SPE-1 spectra also have a prominent peak between 10 and 20 Hz, which is not predicted by any theoretical explosion source models. After some testing, we decided that this spectral peak comes from signals generated by material failure, or spall, in the top weathered layer of the velocity model, which are trapped in the layer. The peak disappears if we remove the layer from the model.

In addition to the synthetic inversion, we also conducted preliminary moment-tensor inversion using observed SPE-1 data from the five linear geophone arrays. In our inversion, we did not constrain the moment tensor to be isotropic or axisymmetric. Figure 12 shows the inverted SPE-1 moment-tensor time histories and the spectra of the diagonal components. Similar to the simulated SPE-1, the observed SPE-1 moment tensor is dominated by its isotropic component with similar waveforms and amplitudes for the diagonal moment-tensor components. There is some energy on the off-diagonal components as well, particularly on M_{xy}. Because SPE-1 is a small explosion, it is unlikely that the off-diagonal energy is caused by tectonic release. It is possible that the energy might be the result of local stress-field perturbation. Another possibility is that the effective explosion source itself is not symmetric due to source-region geology.

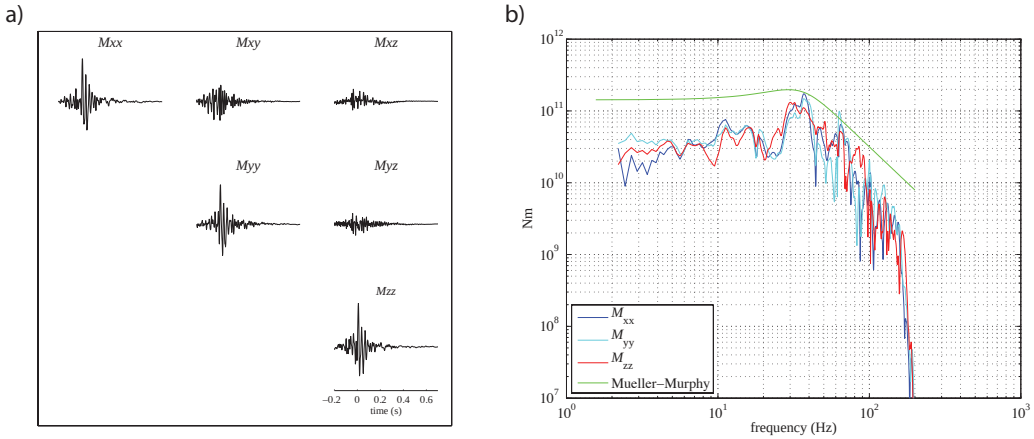


Figure 12. a) Inverted SPE-1 moment-tensor time histories. b) Spectra of diagonal moment-tensor components and the spectrum of a Mueller-Murphy source model. The model was calculated using the source-region material properties derived from the seismic data and the Denny and Johnson (1991) cavity-radius scaling relationship.

The source spectrum also shows that the inverted moment tensor is largely isotropic. Besides some fluctuations, the spectra of the three diagonal moment-tensor components are similar. The long-period level of the spectra is about a factor of 3.5 lower than that of the Mueller-Murphy model. One of the reasons for the discrepancy could be that the attenuation of the model we used in calculating the Green's functions for the inversion is not strong enough. We tentatively determined the medium attenuation by analyzing the decay of *P* and *Rg* amplitudes. More rigorous modeling and inversion is required to develop a reliable attenuation model. Nevertheless, the SPE-1 spectra compares well with the Mueller-Murphy model in terms of corner frequency and high-frequency roll-off.

The observed SPE-1 source spectra show spectral modulations between 9 and 50 Hz with spectral enhancements between 10 and 20 Hz, and between 25 and 40 Hz. Compare these features with the spectral peak observed in the simulated SPE-1 spectrum (Figure 11). The comparison suggests that the amplitude enhancements in the observed SPE-1 spectrum might also be the result of material damage and the trapping of energy in low-velocity layers. If so, the phenomenon demonstrates the importance of secondary source effects, such as material damage and spall, in shaping the source spectrum. It also demonstrates the need for better accounting of depth finiteness of the source because moment tensor inversions of explosion sources always assume a point source with centroid at the depth of burial.

Analysis of *Rg* Waves to Quantify Damage Source Mechanisms

Observed *Rg* waves for Climax Stock path segments of geophone lines in Figure 1 are phase shifted when compared to synthetics calibrated for those segments (Figure 13; see sub-section on Climax Stock earth models). In order to compare with the recorded data traces for SPE-1, the synthetics for a pure explosion source with a burial depth of 55 m were passed through a seismometer system response for the GS11D geophone instrument. Observed and synthetic traces were then band-pass filtered using a Butterworth filter with corners at 3 and 6 Hz, three poles, and two passes (phase-free). The filtered signals have a nominal frequency of ~5.3 Hz. The dotted line shows the phase move-out for a speed of 2200 m/s predicted by the velocity model used to compute the synthetics (see phase velocity curve in Figure 6a). This speed matches the observed *Rg* move-out as it should because the velocity model was derived from *Rg* dispersion curves measured on these lines. The fact that observed *Rg* waves lead the synthetics for all stations on both lines suggests a source effect. This feature is referred to as "phase advance" in the recorded

signals, and the phase advance time in seconds is a negative number given at the right edge above the traces. The mean phase advance time for waveforms recorded on 27 stations (10 each on Lines 1 and 2, 3 on Line 4, and 4 on Line 5) is −14 ± 2 ms (milliseconds, standard deviation of the mean). For the best calibrated lines (1 and 2), the mean phase advance time is −17 ± 2 ms. For a 5.3-Hz *Rg* wave, this time represents about one tenth of a cycle or a phase angle of 36°.

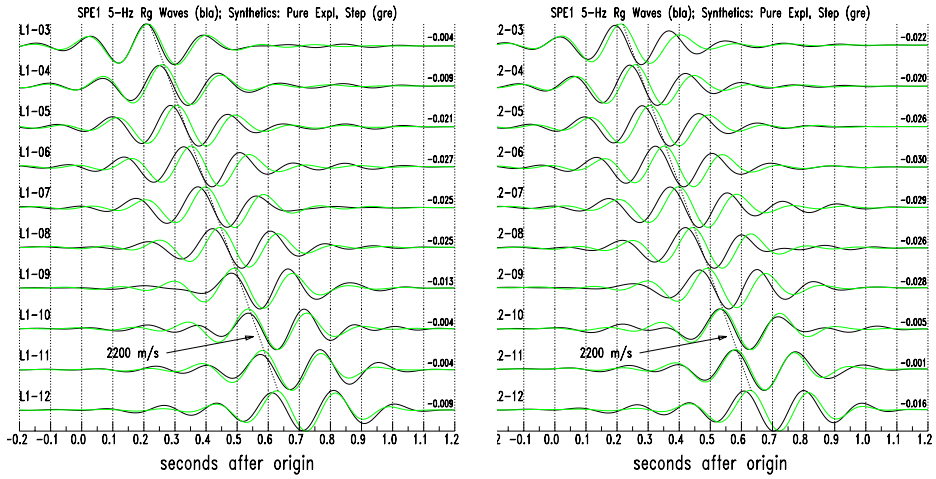


Figure 13. Filtered *Rg* waves for the best-calibrated geophone Lines 1 (left) and 2 (right) recorded on stations 3 – 12, SPE-1. Observed traces are black, synthetics for a pure explosion source are green.

Filtered data traces for SPE-1 and -2 are compared in Figure 14. They are filtered as in Figure 13, and their amplitudes have been normalized for plotting purposes. Because the geophone stations occupy the same sites and the tests were conducted in the same hole, propagation and local station-site effects are identical. Phase shifts in the signals must have their origin in source effects. Indeed, the phasing differences detected here is an excellent example of high-precision seismic interferometry for studying details of the source. The filtered signals for each test are very similar, but there is a small, yet consistent time delay between the signals. Phase delay times at the right edge of each record section were determined from cross-correlation analysis, as they were in Figure 13. The mean delay time of SPE-2 signals with respect to SPE-1 is 6 ± 0.5 ms for Line 1 and 6 ± 0.4 ms for Line 2, about 1/3 the size of the mean phase advance times in Figure 13. *Rg* signals for SPE-2 also lead the synthetics for a pure explosion source, but it would appear that the phase advance time is 1/3 smaller than the time estimated for SPE-1 signals. However, the explosion source function also affects phasing as discussed next.

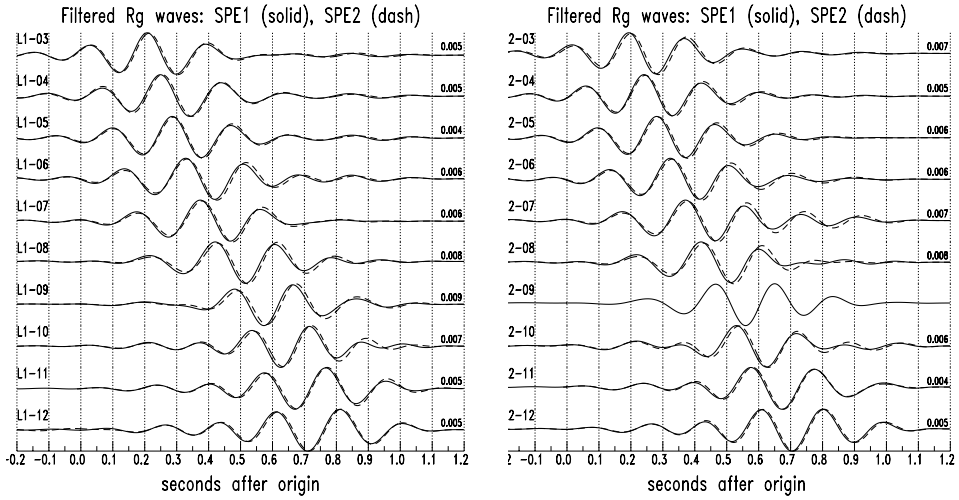


Figure 14. Filtered observed *Rg* waves for Lines 1 (left) and 2 (right).

The synthetics in Figure 13 were computed for an explosion with a step-function in time moment release. A step function corresponds to an impulse for the seismic moment-rate release. An instantaneous release of moment is unrealistic, and various models for moment release by underground explosions have been developed over the years. Synthetics for a step function are compared with those predicted by the Mueller-Murphy model (MM71) for yields of 0.0002 kt (SPE-1) and 0.002 kt (SPE-2). It can be seen that a model allowing for finite duration moment release (such as MM71) introduces phase delay; the greater the yield, the more delay. Thus the estimated phase advance times based on synthetics for a step function must be regarded as lower bounds because synthetics for a more realistic source function will have more delay. Interestingly, the observed delay between SPE-1 and SPE-2 signals in Figure 14 (6 ms) is not too different from the prediction of delay for MM71 synthetics (15 – 7 = 8 ms).

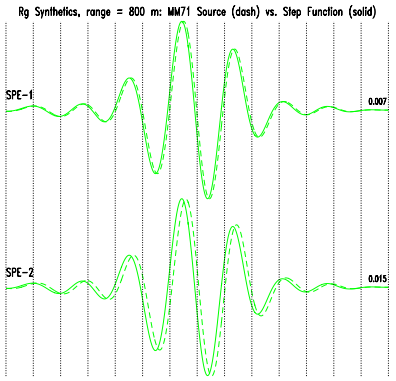


Figure 15. Filtered *Rg* synthetics for a distance of 800 m for a step function (solid) and a MM71 source function for moment release (dash).

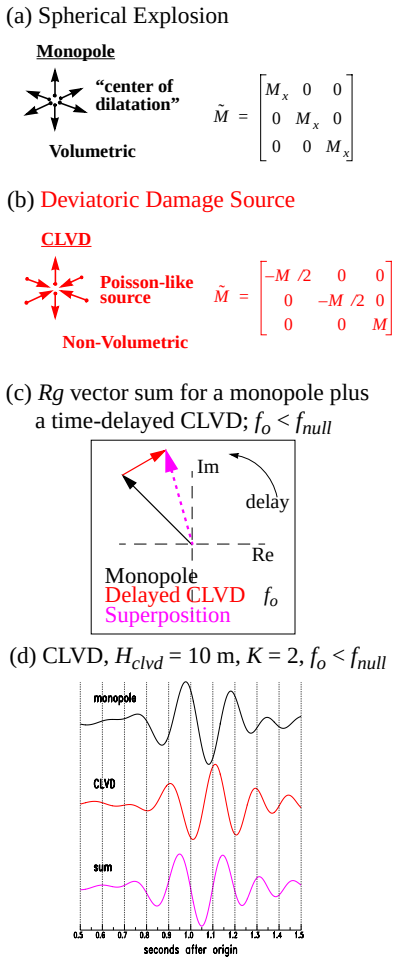


Figure 16. (a) Monopole and (b) CLVD sources and their respective moment tensors. (c) Vector representation of *Rg* superposition for explosion and damage sources. (d) Waveform realization of (c) showing phase advance in sum waveform relative to the monopole waveform.

A model to explain phase advance of *Rg* waves is provided in Figure 16. A pure explosion is represented by a "monopole" source with three orthogonal, outward-directed, dipole body forces of equal strength M_x, acting at the centroid of the source, the explosion's depth of burial (top graphic). Source medium damage is represented by an additional force system, and the model proposed by Patton and Taylor (2008; 2011) is for damage after the shock waves have interacted with the free surface and have established a tensile regime in the source medium, as oppose to "prompt" damage caused by shock waves under compression before encountering the free surface. This model has a vertical axis of symmetry and consists of volumetric and deviatoric components. Our concern is with the deviatoric component: a volume-compensated linear vector dipole, or CLVD, with a vertical axis in extension as shown in red in Figure 16b. M is the strength of the vertical dipole body force. For frequencies f_o below a critical frequency called the "null frequency" f_{null} (because *Rg* waves with this frequency are not excited), the inward-directed dipole forces of the CLVD dominate excitation, and *Rg*'s polarity is exactly opposite to *Rg* excited by a monopole source. In the Figure 16c, *Rg* waves are represented on the complex plane by a vector. The length of the vector is a measure of the *Rg* source amplitude; its phase angle, measured counter-clockwise from the real axis (Re), is the phase delay due to the source. The black and red vectors represent *Rg* waves excited by the monopole and CLVD. The red vector would point exactly in the opposite direction (180°) from the black except for the fact that the CLVD source is delayed in time because shock waves must travel to the free surface and reflect off in tension before this source excites *Rg* waves. Thus the red vector is rotated counter-clockwise because of the time delay. For example, the observed vertical travel time for SPE-1 is ~22 ms. If the damage centroid is located on the free surface, this travel time delay corresponds to a phase delay of 0.11 circles for 5 Hz *Rg* waves (0.022/0.2) or about 40°. (Note: the rotation angle of the red vector in the graphic is larger, more like 75°.) Linear superposition of waves from monopole and damage sources is depicted with vectors adding tip to tail, and the resultant vector (magenta) rotates clockwise. Thus seismic radiation from damage introduces a phase advance into *Rg* waves compared to what they would be if the source were just a pure explosion. The last graphic shows a waveform realization of this effect for synthetics where the centroid depths of the CLVD and monopole are 10 and 55 m, while their vertical dipole forces differ by a factor of two (e.g., $M = M_x/2$ or a damage index K = 2 [Patton and Taylor, 2011]).

Synthetics for a source model including damage are compared with observed waveforms for the SPE-1 recorded on Line 2 in Figure 17. Processing of waveforms is the same as it is in Figure 13. The model parameters are: 55 m depth of burial, 5 m damage centroid depth, K = 1.5, and a MM71 source function for yield of 0.0002 kt. Compare the fit in this figure with that in Figure 13 on the right. As in Figure 13, the phase time of the recorded trace with respect to the synthetic is provided on the right edge for each station (positive for delay, negative for advance). The mean time difference and standard deviation of the mean for SPE-1 is +6 ± 3 ms. For SPE-2 (not shown), is +2 ± 3 ms. Including damage into the source model brings the synthetics into better phase alignment with the recorded signals. Clearly, the effects of damage radiation can account for the observed phase shifts.

A future SPE test, SPE-4, is planned for a burial depth of 110 m and the same yield as SPE-1. With a depth twice as great as SPE-1 and scaled depth of ~1900 m/kt$^{1/3}$, *Rg* waves from damage should be suppressed compared to SPE-1. Seismic interferometry of signals from SPE-1 and -4 should detect differences in phase arrivals as large as 15 – 20 ms, and will provide a test for the model presented herein.

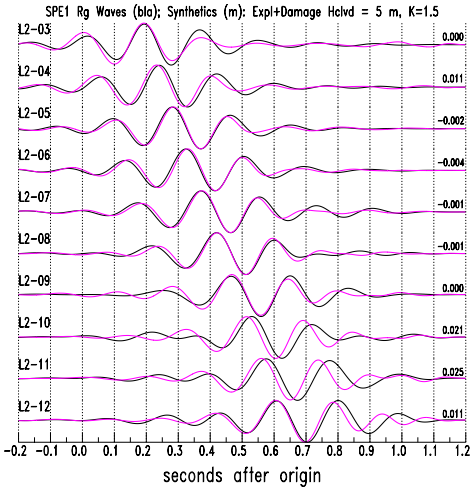


Figure 17. Filtered *Rg* waves for Line 2 (observed black, synthetic magenta).

CONCLUSIONS AND RECOMMENDATIONS

One of the goals of the SPE is to provide essential ground motion data under well-controlled experimental conditions in order to gain a better understanding of *S* wave generation by underground explosions. To this end, we are encouraged by the seismic data collected on the first two experiments. Due to the interrelated purposes of the experimental designs, it is critical that the complete series of experiments as planned (SPE-1 through -7) be conducted in order to achieve the stated scientific goals of the program and to benefit the nuclear monitoring regime.

ACKNOWLEDGEMENTS

We thank the teams at NSTec, Sandia Laboratories, and University of Nevada, Reno, who were involved in seismic field deployment, data collection, and seismic and meta data distribution, all which are essential before conducting studies such as the one reported herein.

REFERENCES

Ampuero, J.-P. (2002). Étude physique et numérique de la nucléation des séismes." Ph.D. thesis, Université de Paris 7, Denis Diderot, Paris.

Bard, P.Y. and M. Bouchon (1980). The seismic response of sediment-filled valleys. 2. The case of incident *P* waves and *S* waves, *Bull. Seismol. Soc. Am*. **70,** 1921–1941.

Denny, M. D. and L. R. Johnson (1991). The explosion seismic source function - models and scaling laws reviewed, in *Explosion Source Phenomenology*, edited by S. R. Taylor, H. J. Patton, and P. G. Richards, pp. 1–24, American Geophysical Union.

Dobrin, M. B. (1976). *Introduction to Geophysical Prospecting* (3rd Edition), McGraw-Hill, New York, NY, 630 pp.

Kawase, H. and K. Aki (1989). A study on the response of a soft basin for incident *S* waves, *P* waves, and Rayleigh waves with special reference to the long duration observed in Mexico City, *Bull. Seismol. Soc. Am*. **79,** 1361–1382.

Komatitsch, D. and J. Tromp (2002). Spectral-element simulations of global seismic wave propagation: II. Three dimensional models, oceans, rotation and self-gravitation, *Geophys. J. Int*. **150,** 303–318.

Mueller, R. A. and J. R. Murphy (1971). Seismic characteristics of underground nuclear detonations, Part 1. Seismic spectrum scaling, *Bull. Seismol. Soc. Am*. **6,** 1675–1692.

Patton, H. J. and S. R. Taylor (2008). Effects of shock-induced tensile failure on m_b-M_s discrimination: Contrasts between historic nuclear explosions and the North Korean test of 9 October 2006, *Geophys. Res. Lett*. **35,** L14301, doi: 10.1029/2008GL034211.

Patton, H. J. and S. R. Taylor (2011). The apparent explosion moment: Inferences of volumetric moment due to source medium damage by underground explosions, *J. Geophys. Res.* **116,** B03310, doi:10.1029/2010JB007937.

ANALYTICAL EXPLOSION MODELS INCLUDING SOURCE MEDIUM DAMAGE: IMPLICATIONS FOR TELESEISMIC *P* WAVES AND REGIONAL PHASE EXCITATION

Howard J. Patton[1], George E. Randall[1], and Steven R. Taylor[2]

Los Alamos National Laboratory[1] and Rocky Mountain Geophysics[2]

Sponsored by the National Nuclear Security Administration

Award No. DE-AC52-06NA25396 / LA12-SourcePhysics-NDD02

ABSTRACT

This paper reports on accomplishments this past year directed at further advancing analytical explosion source models and investigating the impact of these models on seismic wave generation. Past studies performed by the Los Alamos National Laboratory (LANL) and Rocky Mountain Geophysics (RMG) have shown the considerable impact of models incorporating elasto-dynamic descriptions of material damage on the amplitude of long-period Rayleigh waves. Recent work has shown that systematic changes in long-period radiation from damage and coupling as a function of yield (W) can account for commonly observed M_s-log[W] scaling exponents greater than 1.0, when in fact M_s scales as ~0.8·log[W] for pure explosions conducted under cube-root containment practice and in media with uniform coupling (Patton, 2012). We are extending our studies to investigate the conditions under which damage could affect the performance of m_b-M_s discrimination through effects on m_b, just as it does on M_s (Patton and Taylor, 2008). Preliminary results of these studies are reported on in this paper. On another research front, LANL is commencing the development of depth-distributed source models to study the importance of "late-time" damage for the generation of *S* waves. Late-time damage refers to damage occurring after a tensile regime has been set up in the source medium as a result of shock-wave interactions with the free surface. We have written code for computing synthetic seismograms out to 15 Hz using the reflectivity method for a distribution of point sources in depth above the explosion monopole. Each point source is a time-delayed, volume-compensated linear vector dipole (CLVD) with appropriate source-time functions and source strengths. Spectral analysis is carried out on time windows corresponding to *Pn*, *Pg*, *Sn*, *Lg*, *LR*, and *Rg* in layered Earth structures for Pahute Mesa and the Basin and Range. A 10-m sampling of the point sources computed with a reflectivity code using double-precision accuracy and multi-taper Fourier transforms provide reasonable spectral results, although testing of the code is still in progress in order to identify possible artifacts at high frequencies. Spectral ratios of regional phases are computed to investigate frequency and yield dependencies. Ultimately, our goal is to build enough physics into these models in order to lay a physical basis for key features in spectral ratio observations for explosions in weak- and hard-rock environments.

OBJECTIVES

The objective is to develop new analytical explosion source models based on seismic moment tensor theory for further improvement and advancement of regional seismic discrimination and yield estimation technologies. Such technologies rely heavily upon the source information contained in high-frequency shear (*S*) waves. The use of coda waves following regional *S* phases to estimate explosion yield is one example of an emerging technology offering great promise for improved nuclear monitoring. Unfortunately, an understanding of how *S* waves are generated by underground explosions is quite limited. A widening gulf between theory and practice undermines our confidence to monitor broad areas at small yields. The new models will provide a physical basis for explosion-generated *S* waves and theoretical insights for advancing yield estimation and discrimination capabilities, thereby closing the gulf between theory and practice.

RESEARCH ACCOMPLISHED

This project builds upon spherical explosion (monopole) source models developed in the 1970s. An important feature of those models is the theory relating seismic amplitudes of *P* waves directly to yield, depth of burial, and material properties of the source medium. The theory draws upon empirical yield scaling behaviors of key model constructs, such as the elastic radius. The analytical nature of these models facilitated their use because they were easy to implement, and as such, widely applied to study the explosion source. Their application continues to this day, but with the recognition that a spherical point source is inadequate to explain *S*-wave generation.

The model under development consists of a monopole explosion source with linear superposition of tectonic and material damage sources. Material damage occurs as a sudden change in the source medium's elastic moduli. To date, much of our research has focused on long-period applications where all source components are safely assumed to be coincident in time and space (e.g., a point source is still valid) and share the same source-time histories. The current project addresses high-frequency applications where those assumptions are no longer valid. As pointed out by Patton and Gupta (2010), a distributed source in depth can have significant consequences for regional phase generation, especially if *Rg* near-field scattering is involved. In this regard, a distributed explosion source is sometimes not considered by studies investigating mechanisms of *S* wave generation. In our view, the nature and relative importance of various mechanisms cannot be resolved until a complete description of the seismic energy release by a distributed explosion source is developed. Our progress to date developing a new analytical model for such energy release is reported on in the second half of this section.

The first half of this section presents preliminary results investigating the effects of source medium damage on the amplitudes of teleseismic *P* waves used to measure m_b.

Effects of Source Medium Damage on m_b

One aspect of our study is estimating the effect of the depth phases *pP* and *sP* on m_b for the combined explosion and damage source model. Referring to Figure 1, is it possible that the destructive interference between the *pP* wave from the monopole and the direct *P* wave from the CLVD explains the so-called *P*-wave paradox of Douglas (1991) and Lay (1991)? Further, can this interference affect the m_b from explosions?

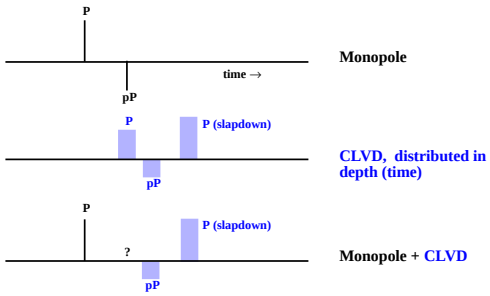


Figure 1. Schematic far-field spike-o-grams for a compound source, monopole + CLVD, where the damage source is represented by a CLVD. Note: relative amplitudes are ad hoc.

We have prepared a synthetic seismogram code to perform these calculations for a half space following the technique of Kennett (1983). The advantage of using this technique is that the up-going and down-going energy can be separated; this is important when the effect of the CLVD from rock damage is included. Using Kennett's notation, the basic equation for this synthesis of *P* wave motions u_P is given by

$$u_P = T_d^{r0}\tilde{R}T_u^{0s}\Sigma_u^s + T_d^{rs}\Sigma_d^s \qquad (1)$$

The 1st term gives the *pP* arrival and the second term the direct *P* arrival at receiver *r* located below source *s*. Reading from right to left, the six factors are the down-going waves from the source *s*, the transmission matrix for the down-going waves to the buried receiver *r*, plus (+) the up-going waves from the source, the up-going transmission from the source to the free surface, the free surface reflection coefficient, and finally the down-going transmission from the free surface to the buried receiver.

The relative strength between the monopole and the CLVD is governed by a damage index *K* (Patton and Taylor, 2011; PT11). For an identity matrix explosion moment tensor, the CLVD moment tensor is

$$\frac{2(K-1)}{K+2}\begin{bmatrix} -1/2 & 0 & 0 \\ 0 & -1/2 & 0 \\ 0 & 0 & 1 \end{bmatrix} \qquad (2)$$

The CLVD is initiated when the *pP* from the monopole passes ½ DOB of the monopole. Currently, there is no source time function for either source and the signals are passed through a World Wide Standard Seismographic Network (WWSSN) Short Period (SP) instrument. For all of the cases described below, the free-surface reflection coefficient was set to 0.3 although the dependence upon this term will be investigated in the future.

Automated measurements were made to compute *a*, *b*, and *c* amplitudes, as well as the *Tox* zero crossing time of Stewart (1988) to follow Blacknest Seismological Centre m_b measurement procedures. The left portion of Figure 2 shows teleseismic *P* waves and measurements used in m_b calculations for two cases of *K*=1 (monopole) and *K*=3 with *Vp* = 5100 m/s and a monopole depth of 550 meters. The right portion of Figure 2 shows the dependency of m_b

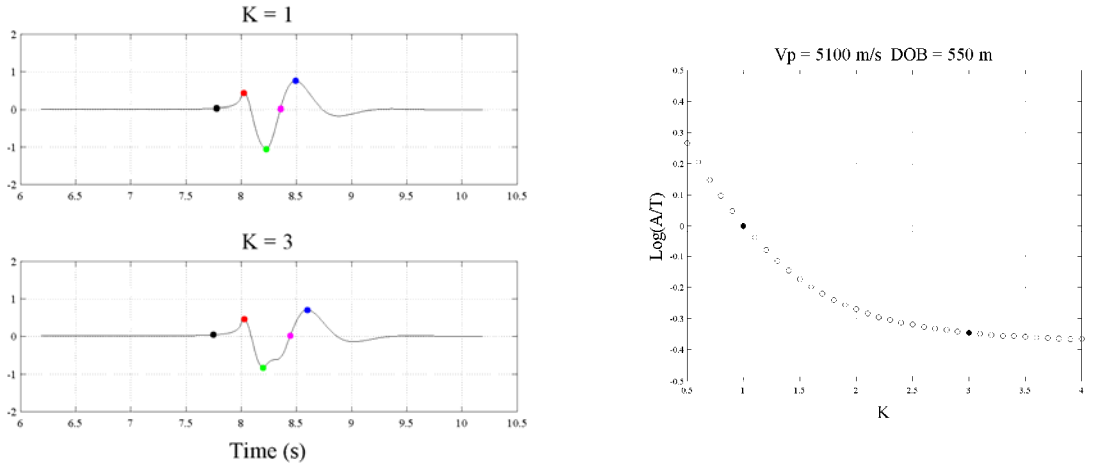


Figure 2. Teleseismic *P* –wave simulations and measurements for Vp = 5100 m/s and DOB = 550 meters through a WWSSN SP instrument. Color code for dots: black – *P* wave arrival; red – a amplitude; green – b amplitude; magenta – 2nd zero crossing used for period measurement. blue – c amplitude.

which is represented as log[*A*/*T*] as a function of *K*. Everything is normalized to *K* value of 1, and the two black circles represent the points at which the seismograms were calculated. The amplitude *A* is measured from ½A_{bc} where the *b* and *c* amplitudes and times are given by the green and blue dots, respectively. The period *T* is measured from the time difference between the *P* wave arrival time (black dot) and second zero crossing of the baseline (magenta dot). We still need to implement the strict definition of the period measurement described in Stewart (1988) to include twice the time between the *b* and *c* amplitudes (T_{bc}). *Tox* is used when there is an inflection in the *b*-*c* swing (e.g. see *K*=3 seismogram in Figure 2). Although the amplitudes do not vary much as a function of *K*, the period does producing a reduction in m_b of –0.35 magnitude units. The decrease in m_b in this case is mainly caused by the period increase due to partial destructive interference of the *pP* from the monopole and the direct *P* from the CLVD leaving mainly the *pP* from the CLVD. There is also some amplitude reduction from the destructive interference, but the m_b reduction comes mainly from the increased period.

Figure 3 is the same as Figure 2 except *Vp* has been increased to 5500 m/s and DOB reduced to 275 meters. In this case, the m_b increases with *K*. The reason for the increase in m_b in this case is that the *P* wave from the monopole and the CLVD constructively interfere in the WWSSN SP pass band.

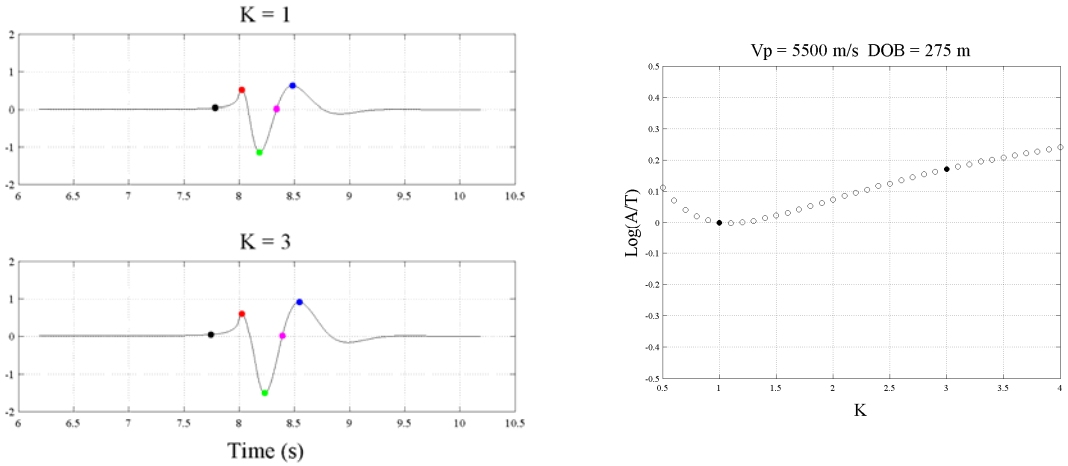


Figure 3. Same as Figure 2 but for Vp = 5500 m/s and DOB = 275 meters.

Figure 4 is a two-dimensional plot showing the difference in m_b between the compound source and the monopole as a function of *Vp* and monopole DOB for a *K* value of 3. In general, shallow DOB and high *Vp* favor constructive interference resulting in an increase in m_b. For lower velocity and increased burial depth, a reduction in m_b is observed mainly due to the increase in period caused by the interference of the *pP* from the monopole and the direct *P* wave from the CLVD. In the future, we will be investigating the effect of the free surface reflection coefficient, the centroid depth of the CLVD relative to the monopole, and the effect of source time functions for the monopole and CLVD.

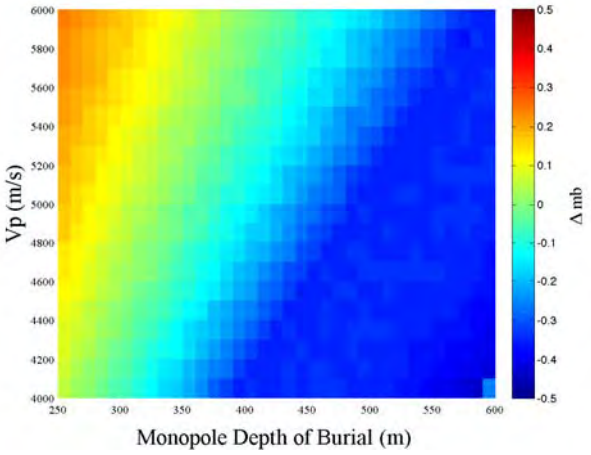


Figure 4. Variation of m_b as a function of *Vp* and DOB.

A Depth-Distributed Analytical Explosion Source Model with Damage

The model consists of a point explosive monopole plus a depth-distributed line source for damage without lateral extent. *M* is defined to be the isotropic moment of the explosive monopole, and its moment rate time function could be set to any number of existing models. At this preliminary stage, the function is a zero-width impulse. The damage source is made up of depth-discretized CLVDs, which extend from the free surface to a significant fraction of the DOB. The fraction can be a variable in the model; at this preliminary stage, it is set to 2/3. CLVDs with a positive value moment have a vertical axis of symmetry in extension; a negative moment value designates a vertical axis in compression.

The damage source has two phenomenological "modes": a tensile failure mode identified with spallation and a deeper-seated mixed tensile-shear failures mode. For model building purposes, the modes are distinguished only by their deformation time histories and the depth range over which they act. For spallation, permanent deformation is negligible: surface strata detach, go ballistic, and return to their original position upon slapdown. A doublet is used for its far-field time function and the source strength is assumed to equal M_{spall}. Mixed-mode damage occurs at depth and has permanent deformation. The moment rate function is an impulse, as it is for the monopole, and its moment M_{damage} is specified by the index *K* (PT11). The depth split is arbitrary: spallation extends from the free surface to 1/2 DOB, and mixed-mode damage between 1/2 and 2/3 DOB. Future work will develop a generalized moment time function for both modes, which varies continuously (e.g., seamlessly) with depth.

The focus of this model is *S* wave generation due to "late-time" damage as oppose to "prompt" damage occurring under compressive stresses due to out-going shock waves emitted by the explosion. Late-time damage occurs after the shock waves have interacted with the free surface, and rarefactions have established a tensile regime in the source medium. As such, the damage source is delayed by the time it takes for the shock wave to propagate from the burial depth to the free surface and back down to the centroid depth of a damage element. This time is computed using elastic *P* wave speeds and a vertical take-off angle.

We plan to investigate hard- and weak-rock emplacements for test sites wherever observations exist in order to test and validate the model. As such, it is necessary to define a coupling function, which varies only with depth coordinate *z* and can have very different character from one test site to the next. For example, an NTS coupling function shows stronger variation for burial depths corresponding to yields of 1–200 kt (e.g., from the surface to 700 m depth) than a coupling curve for Semipalatinsk due to the great differences in water table depth at the two sites. We define a coupling function $C(z)$ such that the far-field explosion moment M_I equals $M \cdot C(h)$, where h is the DOB. This is a simplification because coupling as applied here is the same for all seismic phases where in reality it could vary from phase to phase. Nevertheless, it is adequate to first order. If N_{spall} is the number of discrete source elements of spallation damage, then for the i^{th} element at a centroid depth z_i

$$M_{spall} = \sum_{i}^{N_{spall}} m_i^s \cdot C(z_i) \qquad (3)$$

m_i^s is the intrinsic source strength of the i^{th} element, and it is clear from this equation that M_{spall} is the net far-field source strength. Likewise for the mixed-mode damage source,

$$M_{damage} = \sum_{i}^{N_{damage}} m_i^d \cdot C(z_i) \qquad (4)$$

Initially, m_i^s and m_i^d are assumed to be constant for each element, i.e., $m_i^s = \bar{m}^s$, $m_i^d = \bar{m}^d$. We can solve for $\bar{m}^d$ using equation (6) of PT11 and equation (4) above

$$\bar{m}^d = M_I \cdot \frac{2(K-1)}{(K+2)\sum_i C_i} \qquad (5)$$

$C_i = C(z_i)$ and the summation is over N_{damage} elements. Similarly for $\bar{m}^s$

$$\bar{m}^s = M_I \cdot \frac{2(K-1)}{(K+2)\sum_i C_i}, \qquad (6)$$

for summation over N_{spall} elements. Since ΣC_i in equations 5 and 6 are not equal, $\bar{m}^s \neq \bar{m}^d$. Let $G_h^{monopole}$ be the regional waveform response for a layered medium due to a monopole with depth h and impulsive moment release, and $G_{z_i}^{clvd}(\Delta t_i)$ be the response due to a CLVD with depth z_i and also impulsive moment release but delayed in time with respect to the monopole by Δt_i. The net response for the depth-distributed model under development is

$$u = M_I G_h^{monopole} + \bar{m}^s \sum_{i}^{N_{spall}} \left[C_i \cdot \frac{dG_{z_i}^{clvd}(\Delta t_i)}{dt} \right] + \bar{m}^d \sum_{i}^{N_{damage}} \left[C_i \cdot G_{z_i}^{clvd}(\Delta t_i) \right] \qquad (7)$$

It is understood that u is for a particular component of motion in displacement or velocity depending on the manner in which the Green's function responses are computed.

Seismic responses for a distributed source in a Pahute Mesa layered earth model are examined here for illustration purposes. The wave speed-density model and coupling function are plotted in Figure 5. Poisson ratio was set to 0.3 in the upper 1500 m. The depth dependence of coupling is a sigmoid function developed by PT11 with a full coupling asymptote below a depth of ~1000 m. The shallow-depth asymptote was obtained by taking the log mean of the Rayleigh- and *P*-wave coupling curves in Figure 5 of Patton (2012). We adopted the containment model, $h = 120W^{1/3}$, and computed responses for yields of 8, 27, 64, and 125 kt with a reflectivity code using double-precision accuracy. The coupling factors for the corresponding burial depths of 240, 360, 480, and 600 m equal 0.113, 0.118, 0.154, and 0.364, respectively. Suitability of this coupling curve is a subject of continuing study. A 10-m depth sampling for discrete source elements gave satisfactory results out to 15 Hz. The propagation model includes Q appropriate for the Basin and Range. This results in strong high-frequency spectral falloffs on regional phases for the 500 km distance at which the synthetics were computed. Such falloffs probably resulted in leakage at the highest frequencies when computing spectral ratios discussed below; as such, the ratios were truncated at 8 Hz. We are investigating the use of multi-taper Fourier transforms.

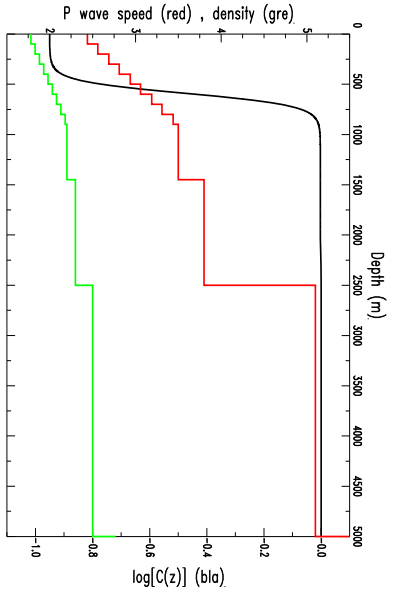


Figure 5. Pahute Mesa wave speed, density, and coupling profiles.

Synthetic vertical-component waveforms for a 125 kt shot are plotted in Figure 6. A breakdown into spall, deep-seated damage, and monopole contributions to the net response is provided for broadband, low- and high-frequency pass bands. Several features of note are: (1) energetic *Pg* waves from the spall source, even at high frequencies, (2) robust *Rg* waves from all three sources in the mid-frequency band (0.2 – 2 Hz, noted by their presence on the broadband traces and absence on the filtered traces), (3) lower *LR* signal amplitudes on the net response compared to the pure monopole due to destructive interference between monopole and damage signals, and (4) very small *Lg* waves in general. It is important remember that these responses are seen through a very strong attenuating medium where Q of shear waves equals 85 in the top kilometer, ~170 over the next 14 km, and ~100 in the lower 16 km of the crust (Patton and Taylor, 1984). Also recall that the moment-rate functions for all sources are not realistic at this stage in the development. Our future work will address the source function issue and will use observed waveforms of Pahute Mesa explosions to tune the relative source strengths. *K* values for the deep-seated damage source have already been quantified for their dependence on yield (PT11).

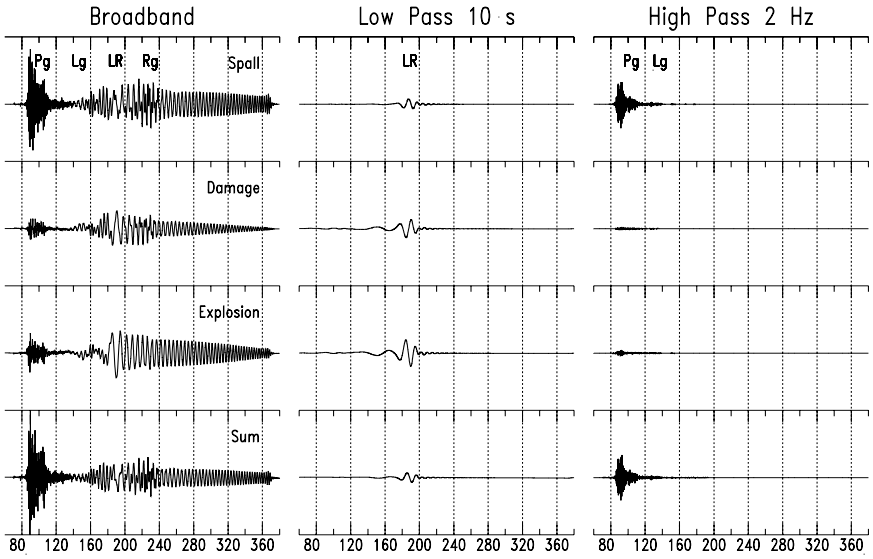


Figure 6. Full regional waveforms for a depth-distributed source described in the text. "Sum" is the net response of explosion monopole plus spall and deep-seated damage sources. Amplitude scales are common on plots. *LR* refers to longer period Rayleigh waves. Damage index *K* = 2.

Even though we are still in the preliminary stages of model development, it is beneficial to examine the behavior of discriminants. Figure 7 shows *Pg*/*Lg* spectral ratios for two cases, one for a yield of 125 kt and the other for 8 kt. For each case the ratio is computed for an ideal point-source monopole and for the distributed source model (referred to as "net" in the figure). Since source functions are not realistic yet, these results should be viewed as a comparison of the discriminant behavior due to effective Green's function responses for distributed and point-source explosion models. Comparisons are provided in the bottom graph showing the spectral ratios of *Pg*/*Lg* ratios taken between the distributed and monopole sources for all four yields. It can be seen that *Pg*/*Lg* ratios are more energetic at high frequencies for the distributed source. This is due to the additional *Pg* waves generated by the spall source. Also interesting to note is that the more distributed in depth the source becomes (e.g., the greater the yield), the lower in frequency that ratios significantly depart from the point-source model, as seen by the shift of peaks to lower frequency as yield increases. This makes sense because the source obviously becomes more compact as yield decreases and the monopole approaches the free surface.

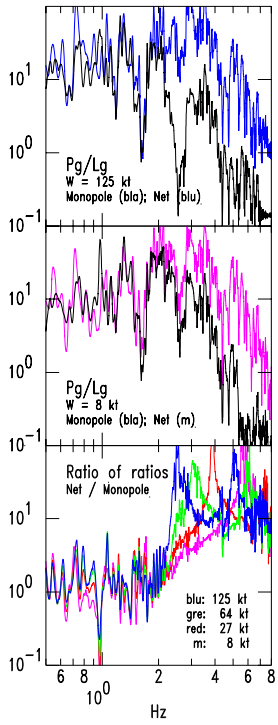


Figure 7. *Pg*/*Lg* spectral ratios for 125 and 8 kt, and the ratio of ratios for a distributed source and point-source monopole.

Fisk (2007) measured *Pg*/*Lg* ratios for NTS explosions. The ratios for Pahute Mesa are among the most uniform in their behavior of all testing areas. The measured ratios differ in their frequency dependence and amplitudes from the ratios for a distributed source in Figure 7. Of course, this can be attributed to any number of factors including source function and attenuation (Fisk makes a correction for attenuation). The amplitudes compare much better at high frequencies (8 Hz) than they do at low frequencies (< 1 Hz). Differential attenuation between *Pg* and *Lg* can explain a factor of three in amplitude, but that falls far short (the low frequency asymptotes differ by a factor of roughly 100). Such as large amplitude discrepancy is our highest priority to resolve, and future studies will identify if one or both phases are responsible and if the cause is related to the Green's function responses or to a source effect.

CONCLUSIONS AND RECOMMENDATIONS

Seismic radiation from source medium damage has been shown to have significant effects on M_s which actually improves the performance of m_b:M_s discrimination (Patton and Taylor, 2008). We are now studying the effects of damage radiation on teleseismic m_b. Our preliminary results suggest that the effects can be important. In the near future, we will be quantifying the conditions under which they enhance and/or degrade the performance of this discriminant. LANL has embarked upon a project to develop depth-distributed source models to study the impact of "late-time" damage for the generation of *S* waves. A preliminary model was exercised by computing *Pg*/*Lg* spectral ratios, and the results provide a comparison of the discriminant behavior due to Green's function responses for distributed and point-source explosion models. The ratios for a distributed source bear little resemblance to observed ratios for Pahute Mesa explosions. An outstanding difference is the amplitude of ratios at low frequency. Future studies will resolve if this amplitude discrepancy is caused by the Green's function responses for a distributed source or to source effects.

REFERENCES

Douglas, A. (1991). Broad band estimates of the seismic source function of Nevada explosions from far-field observations of *P*-waves, in *Explosion Source Phenomenology*, *Geophys. Monograph* **65**, S. R. Taylor, H. J. Patton and P.G. Richards, eds., 127–140.

Fisk, M. D. (2007). Corner frequency scaling of regional seismic phases for underground nuclear explosions at the Nevada Test Site, *Bull. Seismol. Soc. Am.* **97**, 977–988, doi 10.1785/0120060186.

Kennett, B.L.N. (1983). *Seismic Wave Propagation in Stratified Media*, Cambridge University Press, Cambridge, UK, 342pp.

Lay, T. (1991). The teleseismic manifestation of *pP*: Problems and paradoxes, in *Explosion Source Phenomenology*, *Geophys. Monograph* 65, S.R. Taylor, H.J. Patton and P.G. Richards, eds., 109–125.

Patton, H. J. (2012). Modeling M_s-yield scaling of Nevada Test Site nuclear explosions for constraints on volumetric moment due to source-medium damage, *Bull. Seismol. Soc. Am.* **102**, August issue, doi 10.1785/0120110302.

Patton, H. J. and S. R. Taylor (1984). Q structure of the Basin and Range from surface waves, *J. Geophys. Res*. **89,** 6929–6940.

Patton, H. J. and I. N. Gupta (2010). Comment on "An upper bound on *Rg* to *Lg* scattering using model energy conservation" by Jeffry L. Stevens, Heming Xu, and G. Eli Baker, *Bull. Seismol. Soc. Am.* **100,** 408–415, doi 10.1785/0120090109.

Patton, H. J. and S. R. Taylor (2008). Effects of shock-induced tensile failure in $m_b - M_s$ discrimination: Contrasts between historic nuclear explosions and the North Korean test of 9 October 2006, *Geophys. Res. Lett.* **35**, L14301, doi 10.1029/2008GL034211.

Patton, H. J. and S. R. Taylor (2011). The apparent explosion moment: inferences of volumetric moment due to source medium damage by underground nuclear explosions, *J. Geophys. Res.* **116**, B03310, doi 10.1029/2010JB007937.

Stewart, R.C. (1988). *P*-Wave seismograms from underground explosions at the Shagan River Test Site recorded at four arrays, AWRE Report No. O 4/88, HMSO.

MODEL BUILDING FOR AMPLITUDE PREDICTION

W.Scott Phillips[1], Xiaoning (David) Yang[1], Richard J. Stead[1], Michael L. Begnaud[1], Hans E. Hartse[1], Dale N. Anderson[1], Mark C. Fisk[2], and Kevin M. Mayeda[3]

Los Alamos National Laboratory[1], ATK[2], and Weston Geophysical[3]

Sponsored by the National Nuclear Security Administration

Award No. DE-AC52-06NA25396/LA12-Signal_Propagation-NDD02[1]

ABSTRACT

We develop models that predict regional direct and coda wave amplitudes over broad areas to improve high-frequency event identification, including Mw estimation via coda analysis, as well as regional yield estimation. Path effects on Mw and yield estimates are highly variable and we need no further motivation for their investigation. Path effects on high frequency discriminant ratios are more subtle, but experience has taught us that discriminant scatter can be reduced for broad area earthquake and explosion populations, and reductions are especially important in intermediate band ranges (2 - 5 Hz), which are more readily observed than the higher bands that we know perform well (5 - 10 Hz).

Our largest gains in prediction power are made by allowing attenuation to vary laterally for crust and upper mantle phases, and resulting patterns correlate well with regional geological features. In general, high attenuation is associated with active tectonic deformation, and low attenuation with inactive and shield areas, as observed by many previous authors. Resolution is calculated to approach 0.5 degrees for Lg in areas of high coverage such as the western US, which may approach the natural limit for this phase as it is on the order of the crustal thickness.

Recent developments in this effort have included improved spreading models for the Pn phase, the least predictable of the regional phases. We also detail amplitude processing steps that precede tomographic inversion, namely analysis of relative site response between channels, and between closely spaced stations, including array elements, and similar analysis applied to event clusters. These steps allow data to be stacked and reduced in number. Third, we present results from analysis of USArray Lg that demonstrate the use of high quality source spectra as constraints on absolute levels, particularly between frequency bands, in the tomography. Inversions were run with differing source and path parameterizations. We observe power law Q to fit very well, relative to individual band Q, and Brune model sources with varying moment and corner frequency to fit well relative to individual band source terms, although less well than the power law Q. The source constraints are critical to accurately model edge regions, and can be used to validate the amplitude prediction models using cross validation techniques.

OBJECTIVES

We develop models that will allow the prediction of absolute spectral levels of regional phases and coda, for purposes of event identification and yield estimation. Models can be constrained and validated using independently measured spectra that are based on relative amplitude (spectral ratio) techniques and regional moment tensor studies. The independent source information also allows the extension of models into poorly covered regions, as they serve as virtual, (although temporary) stations. Models reduce scatter in discriminant populations, and will allow the isolation of near-source effects on explosion spectra, and the evaluation of test site biases, thus enable transportable, regional phase yield estimation.

RESEARCH ACCOMPLISHED

Attenuation models are critical for magnitude and yield work (e.g., Nuttli, 1973) and benefit event identification studies through the reduction of discriminant scatter for distributions of earthquakes across large areas. Phillips et al. (1998) showed that 2-D path correction for 0.5 - 8 Hz Pn, Pg, Sn and Lg phases reduced discriminant scatter in earthquake populations in China, especially for lower and intermediate bands (0.5 - 5 Hz). The effect in intermediate bands (2 - 5 Hz) is of particular importance as discrimination performance degrades toward low frequency (Walter et al., 1995; Taylor 1996). Discrimination is known to perform well in high bands (> 5 Hz), but signal-to-noise considerations limit the range at which those bands are observed. Thus, intermediate band discrimination is of importance in extending discrimination to smaller events and larger distances. Figure 1 shows results of a broad area, 2 - 4 Hz, Pg/Lg discrimination study that included over 10,000 central and East Asia events. 2-D corrections reduce scatter in both earthquake and explosion populations. We compute the operational burden for this discriminant over a range of bands as shown in Figure 2. This demonstrates that employing 2-D path corrections in discrimination procedures should reduce analyst workloads.

Q model results for multi-phase, multi-band inversions have been shown in these proceedings in past years, so here we describe basic procedures used to process amplitude data prior to inversion. Codes employ “par” file input and are designed to be used by researchers who are not the primary author. Although coda and direct phase codes are distinct at this time, procedures following amplitude measurement will be standardized between the two. The codes begin with database site, event and waveform information that allows us to cut regional phase data, correct for instrument effects, set magnitude distance cutoffs, and position amplitude windows for measurement. The process is easily repeatable if parameters are to be changed, or when new waveforms, instrument responses, or phase picks become available.

We also study noise patterns in order to identify large, unaccounted for changes in instrument response and gain. Figure 3 shows an example for station KURK. For 1287 Asia stations, each with its own set of channels, we identified 2334 suspicious intervals using this technique. Amplitudes from those time intervals are left out of the processing until the data can be verified manually.

Quality control begins with pre-event and pre-phase S/N cutoffs that vary with phase and can be increased when analyst picks are not present. We use multiple windows to obtain best possible noise estimates. Pre-phase windows longer than the standard 5 seconds improve stability. Basic quality control is applied by fitting 1-D Q and site terms to groups of stations using mb-based source correction (SPAC, Taylor and Hartse 1998). Picked phases are emphasized, followed by phases with picked first P. Order-of-magnitude residual cuts remove data flyers that satisfy our S/N cuts, generally high frequency noise and coda measurements at long distances. Figure 4 shows a high -frequency example for the USArray. We developed this technique for use with coda waves, as described in Phillips et al., 2008.

Many channels are generally available for each station, and we solve for relative site effects between channels, as a function of phase and band, using common events. Significant variations between channels are often observed. Figure 5 shows results for various channels at BJT, illustrating two groups of non-time-overlapping sets of channels that appear to behave similarly. Figure 5 also shows dramatic differences between surface and borehole channels deployed at LZH. After analysis, we can combine amplitude data from channels that are well constrained relative to one another. We can also specify that site terms are the same, based on the direct measurement just described, in which case similarity is enforced for all phases and bands, or based on independent information, generally for non-overlapping channels, that includes noise observations, similarity of tomographic site terms, and knowledge of deployment details. Finally, residual analysis allows us to observe non-compliant behavior and lead to data down weighting or removal. Figure 6 shows the drift of an STS-1 instrument (channel BHZ00) at station HIA. We only keep the central interval for this channel, based on a cutoff of 0.1 $\log_{10}$ units.

Similar techniques can be applied to array elements, and to clusters of nearby stations, in which case we apply relative distance corrections using 1-D Q models. Again, we combine amplitude measurements from nearby stations and arrays for which relative site effects are well resolved. Using a cluster size of 60 km, this procedure decreases the effective number of non-array stations by over 50% in our Asia study area, the large reduction mostly due to a number of dense PASSCAL deployments.

We then apply relative techniques to event clusters, which allows us to further reduce the number of amplitudes in the data set. At this stage, source parameters from independent study (Mayeda et al, 2007; Fisk and Taylor, 2007; Fisk and Phillips, these Proceedings) can be introduced to verify results.

Tomographic procedures can then be applied to the reduced data set to obtain Q models, site parameters and source terms. The Q and site models can be used to correct amplitude data to obtain source spectra for future events, on which we can base event identification, and magnitude and yield estimation. We test multiple ways of inverting for these models. Simple, single phase and band inversions to multi-phase/multi-band simultaneous inversions are supported by the same code. Various options for regularizing and constraining parameters are also offered. Our preferred method is a multi-phase, multi-band simultaneous inversion that employs high quality, source parameter constraints for well-studied events (see previous MRR Proceedings). In this case, site terms are allowed to float freely and will end up with absolute levels that reflect the source constraints (Malagnini et al., 2006). We also lightly regularize apparent stress to stabilize poorly constrained corner frequencies for small events. Best fits to data are obtained by parameterizing source and Q as functions of frequency, but very little is lost by inverting for power law Q parameters ($Q = Q_0 f ^\eta$) or by using an omega-square source model. Figures 7-9 show results for a USArray Lg data set that show images for the two Q parameterizations, as well as residual fits for the four combinations of Q and source parameterizations.

CONCLUSIONS AND RECOMMENDATIONS

Interest in amplitude prediction has grown in the past decade, in both the monitoring as well as the general seismology community. Here, we recommend a number of ideas and techniques that have helped us, especially with monitoring applications. We emphasize that models are needed for magnitude and yield estimation as well as for event identification, and the absolute nature of the former requires attention to the following:

Use high quality, absolute source constraints. Regional moments and high quality, absolute spectral estimates from coda and direct wave spectral ratio studies are available for model building (Mayeda et al., 2007, Fisk and Taylor, 2007). These spectra can be used to validate amplitude prediction models using "leave-N-out" type techniques. Resolution in less dense and edge regions of networks, which often correspond to denied areas, can be greatly improved. Coda data sets have the same resolution issues as direct waves, and we recommend the same constraints be applied to both data types. In particular, coda results that have not been obtained using high quality spectral constraints should not be used to constrain direct wave amplitude models.

Allow Pn and Pg, as well as Sn and Lg site effects to be independent. Site terms collect unmodeled amplitude variations, which include varying portions of the focal sphere that focus into each phase, particle motion effects at the recording site, and small excursions from assumed spreading models at short distances. We observe crust and mantle phase site terms to be correlated, but offset from each other. Tests show that inversion for correlated site terms with a freely varying offset are effective. Tests also show that constraining crustal and mantle phase site terms the same reduces fit to data and degrades tomographic image quality.

Account for site terms that vary by channel. Many seismic stations employ multiple channels that can be deployed very differently. For example, borehole channels are found alongside standard vault deployments across the CDSN. Effects that this has on amplitudes are very easy to quantify using common event studies (Figures 5 and 6).

Use positivity constraints on Q. The Pn phase maintains its amplitude very well over regional distances and this causes Q to be non-physically high, or negative. Inversion for log(1/Q) is simple and, although non-linear, converges quickly. Truncating Q where results are extreme is poor practice, especially when Q is negative, as the model wants to add energy into the phase in those regions, and the Q of surrounding areas will have been modified to compensate. Further, regularizing (applying smoothing constraints to) log(1/Q) is more effective than regularizing 1/Q.

Explore non-power law spreading models for Pn. Power law spreading models are too steep for Pn, producing the effects described above. Yang et al., 2007, and Yang, 2011, describe frequency dependent spreading models based on empirical fits to spherical earth synthetics, and modifications based on fit to data, respectively. These models

produce reasonable Q values. We see variance reduction of > 10% when comparing these models to power law spreading in inversions that employ positivity constraints on Q. Conversely, little improvement is noted for the Yang models when positivity constraints are not employed, but this is unsatisfactory as non-physical Q is often obtained.

Employ the $Q_0 f ^ \eta$ model for Q. The empirically observed power law model for Q works remarkably well, and lends stability to multi-band inversions. When we see deviations from this model, noise is generally the culprit. We do not rule out other behaviors, but we recommend that studies that demonstrate such behavior be validated by independent analysis.

Extend and densify list of frequency bands. Figure 2 shows that 2-D models best improve Pg/Lg discrimination for bands 2.5 - 5 Hz and 3 - 6 Hz. These happen to be non-standard bands. We use the following list of bands to develop direct phase amplitude models: 0.25 - 0.5, 0.375 - 0.75, 0.5 - 1, 0.75 - 1.5, 1 - 2, 1.25 - 2.5, 1.5 - 3, 2 - 4, 2.5 - 5, 3 - 6, 4 - 6, 4 - 8, 6 - 8, 8 - 10, 6 - 12, and 8 - 16 Hz.

Prove new ideas against data. Models such as the coupled-path model (Pasyanos et al., 2009) may improve fit to data by better accounting for event-side, crustal path lengths for mantle phases; however, they may also degrade fit by requiring crustal portions of mantle paths to experience the same attenuation as crustal phases, which we know will work poorly when crustal phase attenuation is dominated by non-intrinsic mechanisms. Quantitative understanding of these effects, and bounding regions where they can be confidently applied, will benefit amplitude prediction efforts.

ACKNOWLEDGEMENTS

This study relied on IRIS and PASSCAL waveform collections, and we greatly appreciate help from IRIS DMC personnel. Graphics were made with GMT software.

REFERENCES

Fisk, M. and S. R. Taylor, (2007). Robust magnitude and path corrections for regional seismic phases in Eurasia by constrained inversion and enhanced kriging techniques, in *Proceedings of the 29th Monitoring Research Review: Ground-Based Nuclear Explosion Monitoring Technologies*, LA-UR-07-5613, Vol. 1, pp. 24–33.

Fisk, M and W. S. Phillips (2012). Constraining source terms, regional attenuation model, geometric spreading, and site effects for Eurasia, in *Proceedings of the 2012 Monitoring Research Review: Ground-Based Nuclear Explosion Monitoring Technologies*, these Proceedings.

Malagnini, L., P. Bodin, K. Mayeda, and A. Akinci (2006). Unbiased moment-rate spectra and absolute site effects in the Kachachh Basin, India, from the analysis of the aftershocks of the 2001 Mw 7.6 Bhuj earthquake, *Bull. Seismol. Soc. Am.* **96**, doi:10.1785/0120050089.

Mayeda, K., L. Malagnini, and W. R. Walter (2007). A new spectral ratio method using narrow band coda envelopes: Evidence for non-self-similarity in the Hector Mine sequence, *Geophys. Res. Lett.*, doi:10.1029/2007GL030041.

Nuttli O. W. (1973). Seismic wave attenuation and magnitude relations for eastern North America, *J. Geophys. Res.* **78**, 876–885.

Pasyanos, M.E., W.R. Walter, and E.M. Matzel (2009). A simultaneous multiphase approach to determine P-wave and S-wave attenuation of the crust and upper mantle, *Bull. Seismol. Soc. Am.* **99**, 3314–3325.

Phillips, W. S., G. E. Randall, and S. R. Taylor (1998). Path correction using interpolated amplitude residuals: An example from central China, *Geophys. Res. Lett.* **25**, 2729–2732.

Phillips, W. S., H. E. Hartse, S. R. Taylor, A. A. Velasco, and G.E. Randall (2001). Application of regional phase amplitude tomography to seismic verification, *PAGEOPH*, **158**, 1189–1206.

Phillips, W. S., R. J. Stead, G. E. Randall, H. E. Hartse, and K. Mayeda (2008). Source effects from broad area network calibration of regional distance coda waves, in Advances in Geophysics, 50, *Scattering of Short Period Waves in the Heterogeneous Earth*, H. Sato and M.C. Fehler, Eds., 319–351.

Taylor, S. R. (1996). Analysis of high frequency Pg/Lg ratios from NTS explosions and western US earthquakes, *Bull. Seismol. Soc. Am.* **86**, 1042–1053.

Taylor, S.R. and H.E. Hartse (1998), A procedure for estimation of source and propagation amplitude corrections for regional seismic discriminants, *J. Geophys. Res.* **103**, 2781-2789.

Walter, W.R., K.M. Mayeda, and H.J. Patton (1995). Phase and spectral ratio discrimination between NTS earthquakes and explosions: 1. Empirical observations, *Bull. Seismol. Soc. Am.* **85**, 1050–1067.

Walter, W. R. and S. R. Taylor (2002). A revised magnitude and distance amplitude correction (MDAC2) procedure for regional seismic discriminants: theory and testing at NTS, Lawrence Livermore National Laboratory, UCRL-ID-146882, pp. 13.

Yang, X., T. Lay, X.-B. Xie, and M. S. Thorne (2007). Geometric spreading of Pn and Sn in a spherical Earth model, *Bull. Seism. Soc. Am.* **97** (6), 2053–2065.

Yang, X. (2011). A Pn spreading model constrained with observed amplitudes in Asia, *Bull. Seismol. Soc. Am*. **101**, 2201–2211.

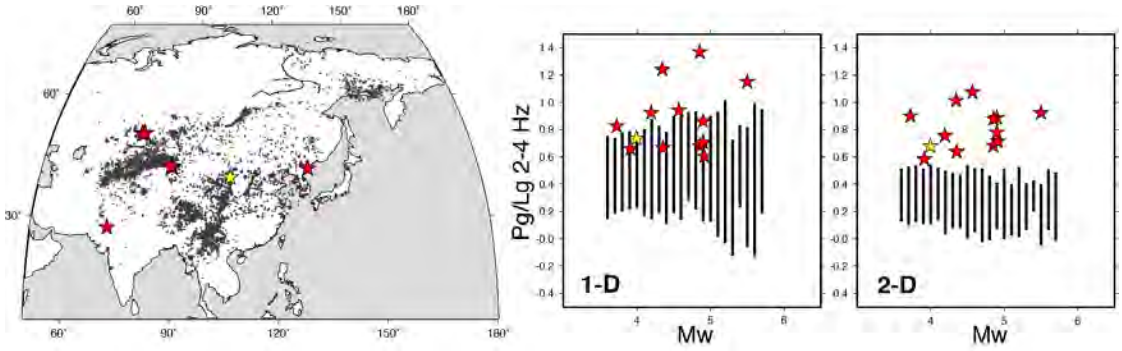


Figure 1. Broad area, network discrimination across central and east Asia. The map shows earthquakes (dots), nuclear explosions (red stars) and a chemical explosion (yellow star) included in the 2-4 Hz Pg/Lg examples shown on the right. The 1-D model uses laterally flat Q for each frequency band. When Q is allowed to vary on a 2-D grid, populations of both earthquakes and explosions shrink around their means. Earthquake discriminants are shown as vertical bars representing 1-sigma variation. From Phillips et al. (2009).

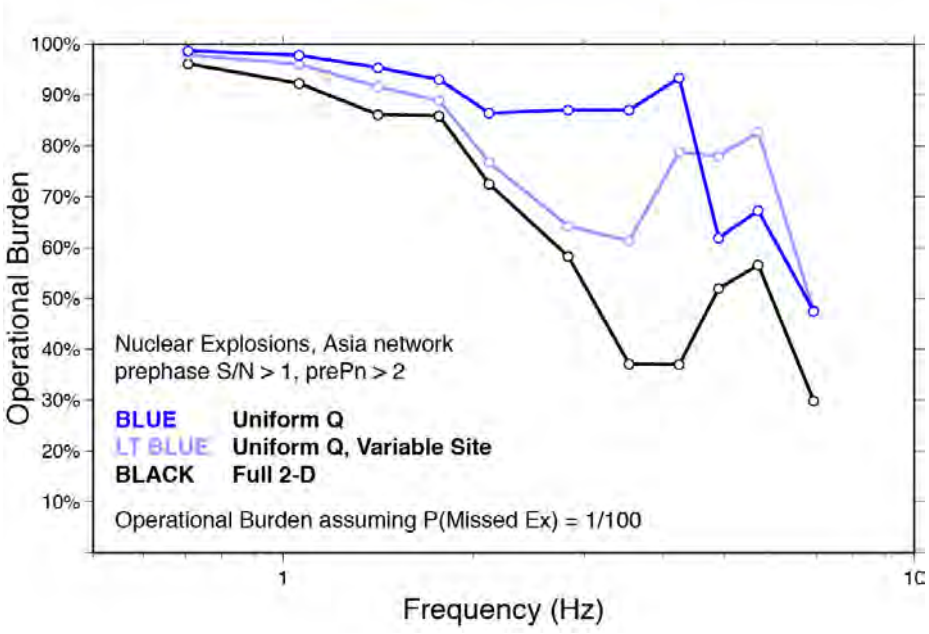


Figure 2. Estimate of operational burden versus frequency for Pg/Lg discrimination, assuming probability of a missed explosion of 1%. Operational burden is the fraction of events for which we cannot rule out an explosion, requiring further examination by an analyst. The plot shows that operational burden can be decreased using 2-D regional phase attenuation models, and that the bands of greatest improvement are 2.5-5 Hz and 3-6 Hz. From Phillips et al. (2009).

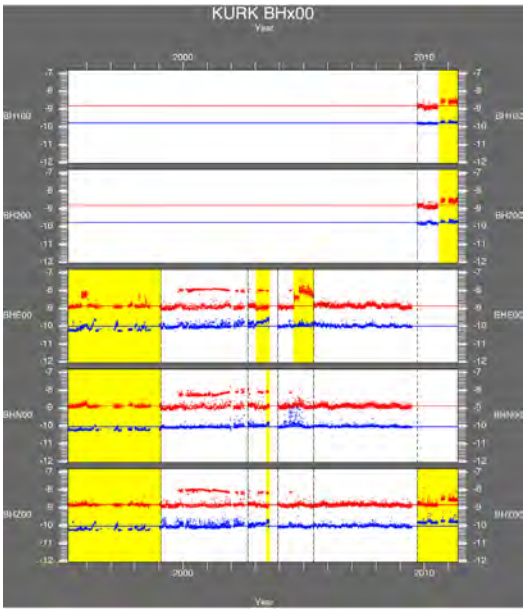


Figure 3. Nighttime noise versus time for bands 1-2 Hz (red) and 4-8 Hz (blue), for five channels of station KURK. Noise amplitude units are $\log_{10}$ displacement (m). 1-2 Hz amplitudes are shifted up one $\log_{10}$ unit for display purposes. Vertical dashed lines mark known instrument response changes (sensor table on and off times). Yellow regions have been marked as "suspicious" and will not be used in amplitude studies without further review.

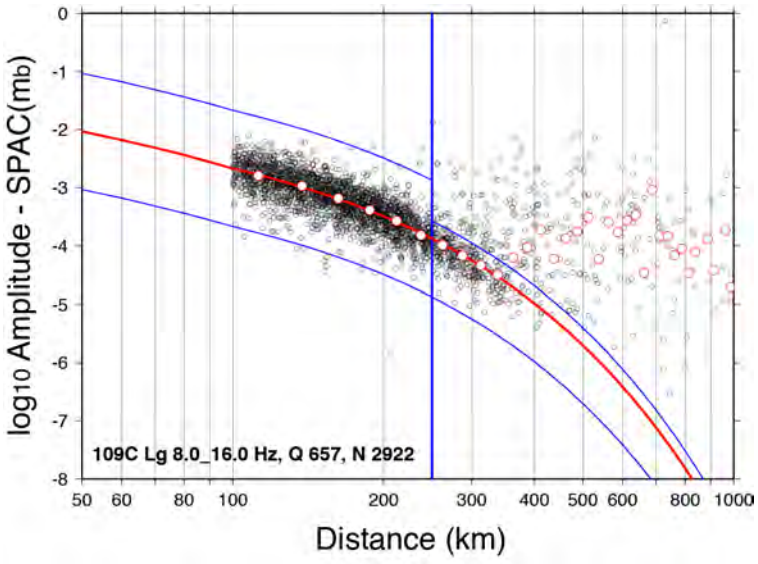


Figure 4. A USArray example showing quality control of amplitude data. Amplitudes are corrected for source size using USGS magnitudes and a magnitude-based scaling model (SPAC, Taylor and Hartse, 1998) for a group of southern California stations. We choose a cutoff distance manually (vertical blue bar), and fit a Q-plus-site-term model to data below that distance. Site corrected results are plotted versus distance as shown (black circles), along with distance-binned median levels (red circles) and the model fit (red curve). Selection criteria are indicated by the blue curves, which allow an order of magnitude deviation from the model, except for high amplitudes above the cutoff distance, for which we only allow 0.3 deviation from the model. High source-corrected amplitudes at long distances are noise or coda measurements that slip through our signal-to-noise filters, mixed with good data from high Q paths that we hope to sample with measurements from closer stations.

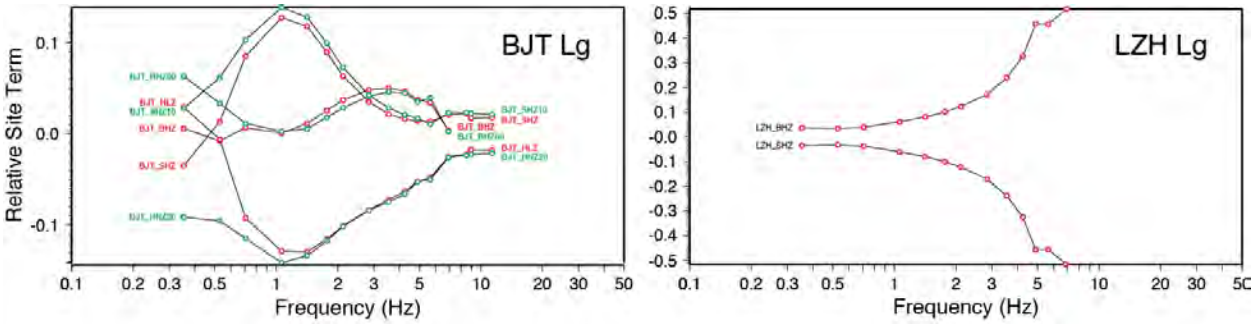


Figure 5. Relative Lg site effects between channels for stations BJT and LZH. The BJT behavior approaches a factor of two at 1 Hz, and site terms for channels from two time periods (green vs. red dots) follow similar patterns with frequency. Results for station LZH are more extreme as the SHZ channel is in a borehole while the BHZ channel sits on soft sediments near the surface. Note different site term axes for the two plots.

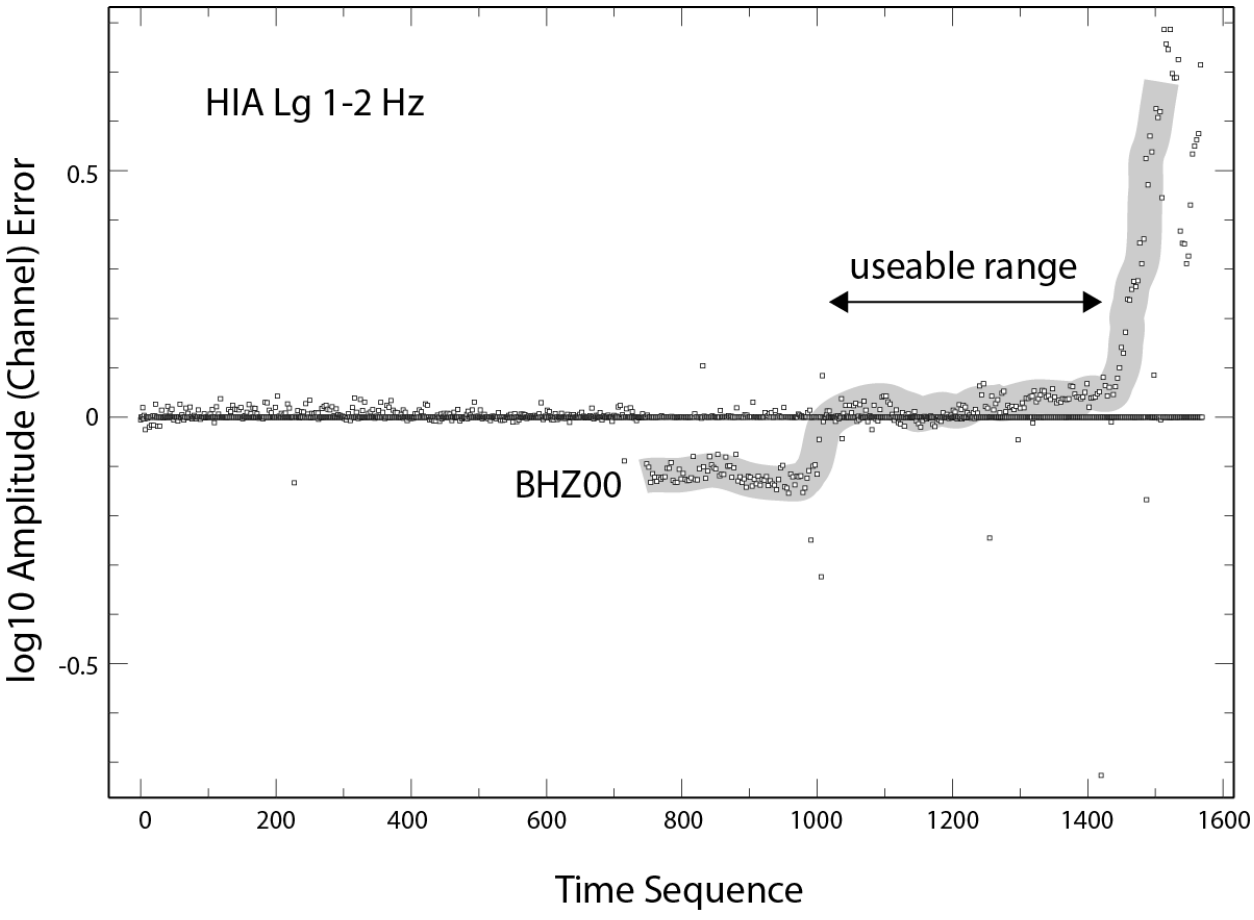


Figure 6. Channel difference residuals can be analyzed to assign error to the most likely channel(s) for each event, which shows the drift with time of the STS-1 instrument on the BHZ00 channel at HIA. We can select intervals of relative consistency for analysis using such plots.

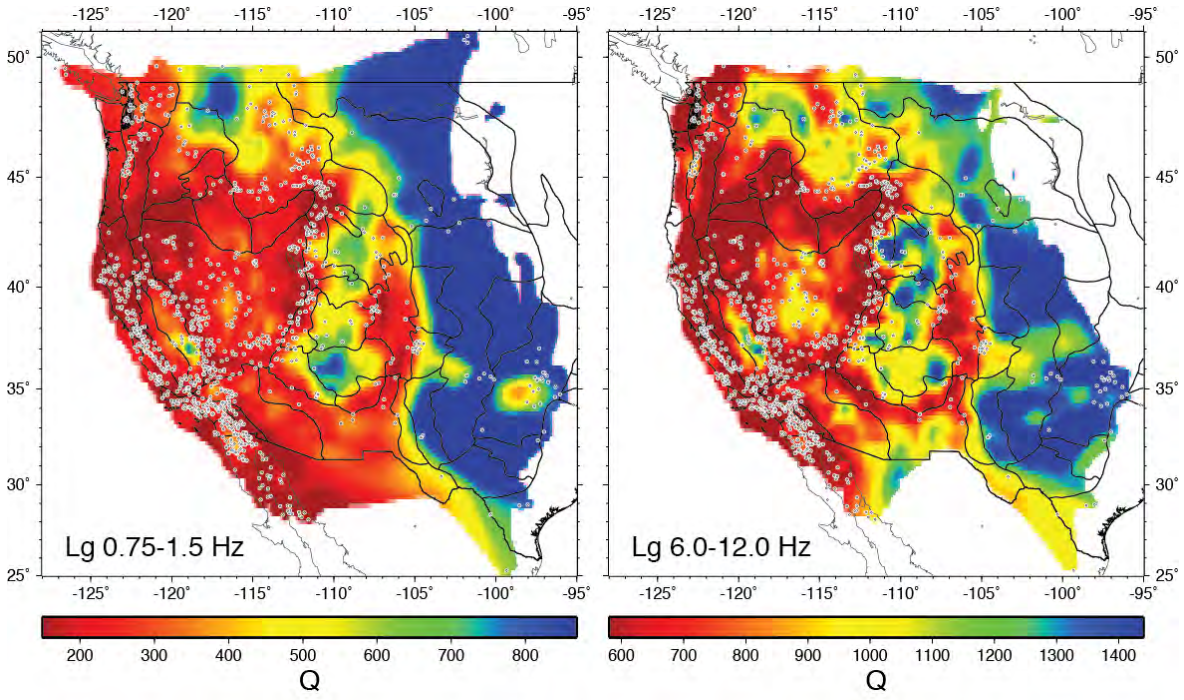


Figure 7. Q for two frequency bands. Results for the 0.75-1.5 Hz band are shown on the left and for the 6-12 Hz band on the right. Color bars differ, we see roughly twice the Q variation at low frequency that we see at high frequency. Geophysical provinces are outlined and events used in the inversions are represented by small dots.

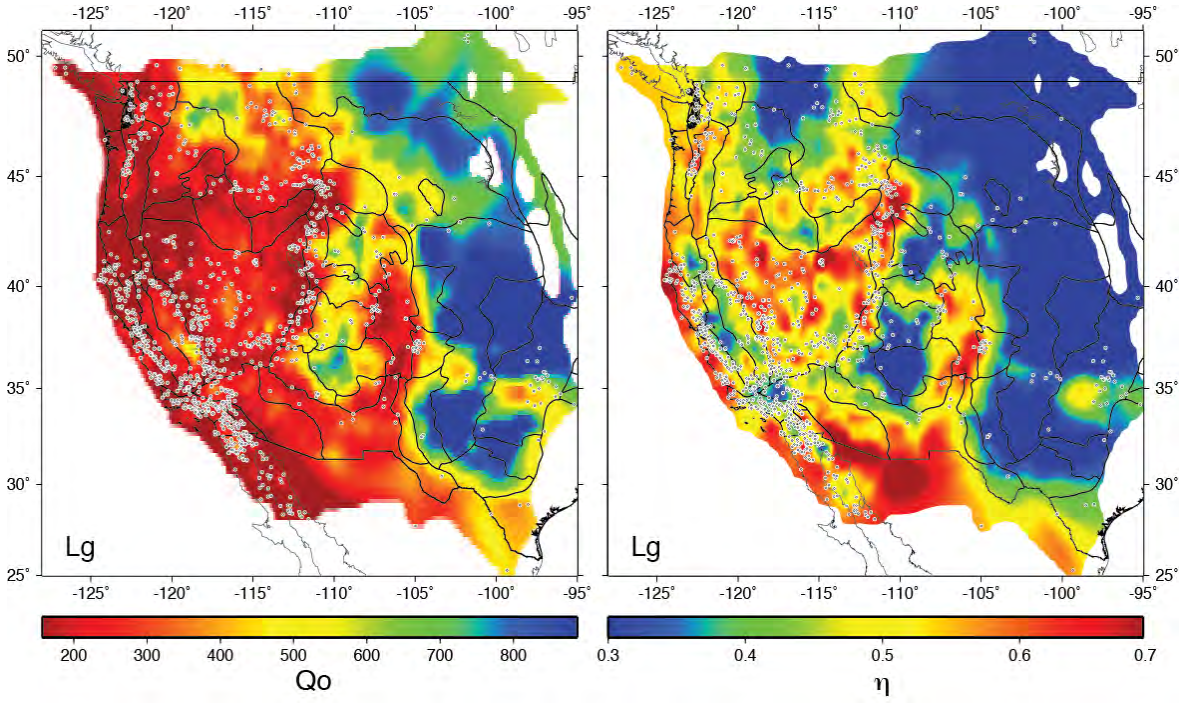


Figure 8. Frequency dependent attenuation. 1-Hz Q (Qo) is shown on the left and the frequency dependent η parameter is shown on the right. Geophysical provinces are outlined and events used in the inversions are represented by small dots. Qo and η are known to vary inversely. We observe that pattern here, and emphasize it with the color scheme.

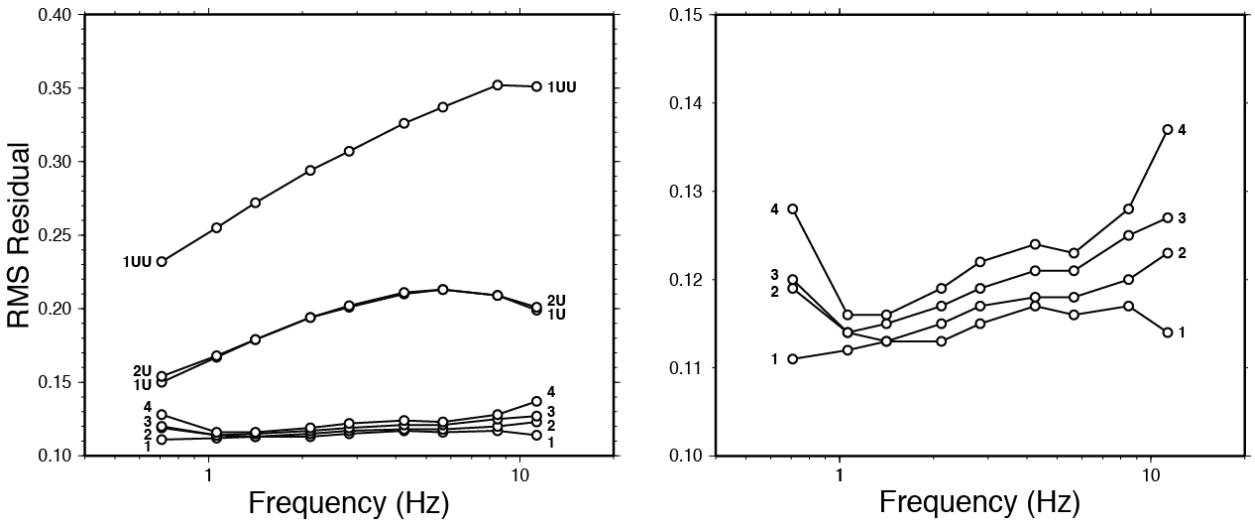


Figure 9. RMS $\log_{10}$ amplitude residuals versus frequency for various inversions. The left shows an expanded view that includes uniform model results. Inversions 1-4 are 2-D inversions, "U" indicates various uniform Q results, and "UU" indicates the uniform Q plus uniform site result. Results shown in Figures 7 and 8 are for inversions 1 and 4, respectively. We see little degradation in fit to data when switching from frequency band source and Q terms, to omega-square and power law Q parameterizations.

ANALYSIS AND MODELING OF SHEAR WAVES GENERATED BY EXPLOSIONS AT THE SAN ANDREAS FAULT OBSERVATORY AT DEPTH

Fred F. Pollitz, William L. Ellsworth, and Justin L. Rubinstein

US Geological Survey, Menlo Park, CA

Sponsored by the National Nuclear Security Administration

Award No. DE-AI52-09NA29328
Proposal No. BAA09-69

ABSTRACT

Using a deep deployment of an 80-element, 3-component borehole seismic array stretching from 1.5 to 2.3 kilometer (km) depth at the San Andreas Fault Observatory at Depth (SAFOD), we examine recordings of chemical explosions to better understand the generation of shear waves by explosive sources. The well is near-vertical at 1.5km and gradually transitions to a dip of 38 degrees at the deepest recording location. The chemical shots are high velocity chemical shots buried between 10-30 m and fired electrically, of size ~36 kg. The shotpoints are offset from the wellhead by 1 to 2 km. Previous analysis of zero-offset recordings (Pollitz et al., 2012) gave a velocity structure ranging from 1500 m/s (meters per second) in the upper 50 meters to 5000 m/s at the bottom of the well, as well as attenuation structure. The larger-offset recordings analyzed here have a strong, impulsive P arrival polarized as a longitudinal wave, and S waves composed of dominantly converted P to SV at the internal discontinuities and, to a lesser extent, the upward P to downgoing S converted wave pS.

We compute synthetic waveforms using the Direct Radial Integration method of Friederich and Dalkolmo (1995), which handles a layered transversely isotropic medium with anelasticity. We use a hybrid 1D structure consisting of the local Bleibinhaus et al. (2007) structure determined from an active-source experiment combined with the near-well structure determined from the zero-offset shots. Using forward modeling on this velocity structure, both observed P and S wave energy are identified with the traveltimes expected for direct and/or reflected phases as well as the moveout associated with the local velocity structure around the receiver array. For larger-offset shots, S-wave energy is polarized primarily along the radial and propagation direction, consistent with converted P to SV energy. The longer-offset shots analyzed here have more distinct and energetic S arrivals than seen for the zero-offset shots, likely because of greater P to S conversions along the longer propagation paths. Forward modeling using the synthetics enables a reasonable match to observed arrival times and moveouts of major body-wave packets and suggest an additional vertical-dipole source, which represents damage.

Seismic data from the Hole-Ryberg Line, a 46 km long refraction line, further illuminates sources of S wave energy. Three-component recordings obtained from a line of 100 kg chemical shots detonated along the line reveal substantial SV and SH energy, tending to increase with distance from the source. The line crosses several geologic boundaries with substantial lateral variations in seismic velocity (e.g. McPhee et al., 2004). The generated S energy is interpreted to arise from P to S conversions at subhorizontal discontinuities, and the generated SH energy from P to S conversions at near-vertical discontinuities and/or scatterers away from the vertical plane containing the direct raypath.

OBJECTIVES

The principal objective of the work being undertaken is to better characterize and understand the generation of S waves from explosive sources. The amplitudes of *S* waves are commonly used as a discriminant between explosion- and earthquake-generated sources, in that explosion sources primarily produce P waves. Thus, characterizing how S waves are generated by explosive sources is critical to improving explosion discrimination criteria. In this project, we focus on *S* waves generated in the near-source region (up to several km laterally and 2.5 km in depth).

RESEARCH ACCOMPLISHED

Downhole Observations

The 80-level P/GSI Main Hole Array (Paulsson Geophysical Services, Inc.) of 3-component borehole instruments (15 m spacing) was deployed between the surface and 2.3 km depth in the SAFOD Main Hole (Zoback et al., 2010) in May 2005 (Chavarria et al., 2007). More than three terabytes of continuous, high sample rate data were collected, including 14 explosions at PASO array stations (Figure 1). Each shot consisted of 36 kg of Pentolite (detonation velocity
7.8 km/s) emplaced in a vertical borehole between 20 m and 30 m depth. We focus on shots conducted at PASO stations on the southwest side of the San Andreas fault in order to avoid the substantial lateral variability in velocity structure across the SAF. Record sections for 3-component velocity recorded from shots at PIGH, BURN, and FLIP are shown in Figures 2, 3, and 4. The seismograms are resolved onto three borehole-oriented components: Axial=locally downhole; Dip=component in the vertical plane locally passing through the borehole and perpendicular to it. Strike=horizontal component locally perpendicular to the borehole. For all shots, the recordings exhibit strong P waves on the longitudinal component (primarily the axial component for the PIGH shot; primarily the strike component for the BURN and FLIP shots). Wave packets arriving with the expected S-wave moveout are seen for all shots, particularly PIGH.

Methods for Computing Synthetic Seismograms

Synthetic seismograms are generated using the Direct Green's Function (DGF) method of Friederich and Dalkolmo (1995). This method synthesizes the seismic wavefield for a spherically layered structure of seismic velocities V_p and V_s, density ρ, and attenuation factors Q_p and Q_s in the $l-\omega$ domain, where l denotes spherical harmonic degree. It is the spherical equivalent of the frequency-wavenumber method employed for flat-layered structures (e.g., Zhu and Rivera, 2002). It has been validated against analytic solutions, including those for elastic wave propagation in a full space for both isotropic and shear sources (eq. 4.29 of Aki and Richards [1980]) and in a half-space, e.g., Lamb's Problem (Kuhn, 1985), as well as the independent numerical solutions AXITRA (Bouchon, 1981) and $f-k$ method (Zhu and Rivera, 2002).

The DGF method is applied to buried sources in the layered structure given in Figure 5. The velocity structure is a hybrid of a regional 2D velocity structure determined on a profile passing close to the SAFOD well (Bleibinhaus et al., 2007) and a 1D velocity structure determined for the local SAFOD well using near-zero offset shots (Pollitz et al., 2012). The velocity structure in the upper 2.0 km is modified from a 1D model extracted from the Bleibinhaus et al. (2007) model near PIGH, while the velocity structure below 2.0 km is the local SAFOD structure. A velocity discontinuity at 0.5 km depth, not present in the Bleibinhaus et al. (2007) model, is introduced in order to partially account for waves observed to arrive mid-way between expected direct P and direct S, which are tentatively interpreted as P to S conversions at internal discontinuities. The attenuation structure is based on forward modeling trials aimed at accounting for the amplitude decay with distance and frequency content of our observations. The V_s structure is based on the V_p structure and the V_p/V_s ratio determined by regional tomography (Zhang et al., 2009), and the density structure is based on empirical $V_p-\rho$ relationships (Gardner et al., 1984; Brocher, 2006). The Q_s values are not estimated from the data but are chosen such that the quality factor for bulk modulus is twice that for shear modulus.

For a x − y − z coordinate system (where x, y, and z denote distance in the due East, North, and Up directions, respectively) and a point source located at $r_0 = (x_0, y_0, z_0)$, we consider a moment tensor density M(r) given by

$$\mathbf{M} = M_{\text{expl}} \begin{pmatrix} 1 & 0 & 0 \\ 0 & 1 & 0 \\ 0 & 0 & 1 \end{pmatrix} H(t)\delta(\mathbf{r}, \mathbf{r}_0) + M_{\text{d}} \begin{pmatrix} 0 & 0 & 0 \\ 0 & 0 & 0 \\ 0 & 0 & 1 \end{pmatrix} H(t)\delta(\mathbf{r}, \mathbf{r}_0)$$

where H(t) is the step function, δ(r,r0) is the Dirac delta function, and Mexpl and Md are the moments associated with explosion and vertical-dipole source components, respectively. This is simply the sum of two volumetric sources: a monopole explosion and a vertical dipole source representing damage (Mosse, 1981; Patton and Taylor, 2011), and it is equivalent to the sum of an explosive source and CLVD source. Although a delayed implosion likely accompanies the chemical explosions because of collapse of a cavity surrounding the source (Pollitz et al., 2012), we do not attempt to model the implosive components here.

Simulation of Explosive Sources and Their Fit to Downhole Observations

Synthetic record sections using an explosive source and corresponding to the various shots are shown in Figures 6, 7, and 8. The inclination of the borehole is 5° from vertical at 1500 m and is progressively steeper at greater depth, up to 55° at 2.3 km depth with a dip towards the northeast. Thus the axial-component velocity is dominated by vertical velocity in the upper part of the record section and includes progressively greater northeastward component with greater depth. Prominent arrivals include direct P and pS but also converted P to SV waves at internal discontinuities. The velocity discontinuity at 0.5 km depth (Figure 1) is partially effective in matching the wave packet labeled P0.5S, which we interpret as an S wave converted from downgoing P at this discontinuity. The very slow moveout at the deeper receivers (those at >2 km depth) is matched by the synthetics since the velocity model has a low-velocity zone between 2.0 and 2.5 km depth, i.e., in the lower half of the borehole array. The strong velocity discontinuity at 2.0 km depth gives rise to another converted S wave, best seen in the PIGH record and there labelled P2.0S.

Simulation of Vertical-Dipole Sources

CLVD-equivalent source components are often inferred from far-field modeling of nuclear explosions (Dreger and Woods, 2002; Patton and Taylor, 2011). Inference of vertical-dipole source components here is tentative and based on matching the temporal spread of wave packets arriving relatively late with the S wave moveout. For example, the synthetic PIGH shot record section using a purely explosive source (Figure 6) predicts only a pS arrival, which coincides with an observed arrival on the dip component (Figure 2) but does not capture observed S wave arrivals in the ~0.10 – 0.15 s before the pS wave (Figure 2). We performed trial-and-error modeling designed to broaden the temporal spread of late-arriving S energy, which likely represents a combination of direct S, direct S multiples from shallow discontinuities, and pS. For the PIGH record, the synthetics calculated using a model of the source using a ratio Md/Mexpl=0.7 (Figure 9) produces a better match to these S wave arrivals than those calculated using a purely explosive source Md/Mexpl=0 (Figure 6).

S wave energy arriving about 0.15 s before the time expected for pS is also seen on the BURN record section (Figure 3). Forward modeling of combined explosive and vertical-dipole sources as described above confirms that a vertical-dipole source produces additional S-wave energy preceding pS. However, in general, it is difficult to replicate the full extent of observed S wave energy arriving between the time of P0.5S (i.e., the P to S conversion at the 0.5 km deep discontinuity) and pS. This and the greater observed broadness of the observed P0.5S wavetrain -- relative to the synthetic P0.5S wavetrains -- suggests that both P-wave and S-wave multiples from very shallow discontinuities contribute to the broadness of a number of major observed seismic phases. Such multiples were previously modeled for the near-zero offset shots using a velocity model with a strong low-velocity zone in the upper 50 m (Pollitz et al., 2012).

Observations along the Hole-Ryberg Line

A refraction survey was conducted along a 46 km long refraction line (Figure 10) in November 2003 for purposes of regional velocity characterization in preparation for the SAFOD experiment Hole et al., 2006). Sixty-three shots were detonated along the line with a shot size of 100 kg at nominal 1 km spacing along the line (and 25 kg within a denser portion near the SAF). These shots were recorded by an array of surface seismometers, used by Hole et al. (2006) and Bleibinhaus et al. (2007) to estimate local velocity structure, as well as the 32-level 3C SAFOD Pilot

Hole array (Oye and Ellsworth, 2005). Sensors are placed at 40 m intervals between 856 and 2096 m below ground level. Recordings on the Pilot Hole array are useful for constraining the properties of the wavefield at distances up to ~20 km from the explosive source.

Shot gathers at level 10 of the receiver array (1.74 km below ground level) from shots to the northeast and southwest of the Pilot Hole are shown in Figures 11 and 12, respectively. All shot gathers exhibit clear P-wave arrivals on the vertical and radial components. The shot gather on the southwest side exhibits large-amplitude later arrivals traveling at the S wave speed on the vertical and transverse components, corresponding to SV and SH waves, respectively. The SV arrivals are likely associated with P to S conversions at subhorizontal discontinuities at depths between the surface and 1.74 km depth, while the SH arrivals are likely associated with P to S conversions at subvertical discontinuities or isolated scatterers located away from the vertical plane containing the source and receiver. The large size of these shots may make them capable of producing significant secondary source components (e.g., vertical-dipole source components) as found for recordings of nuclear tests (Patton and Taylor, 2011). The precise origins of the S wave energy may be clarified by future 2D and 3D forward modeling of the seismic wavefield through velocity structures available for the region (Hole et al., 2006; Bleibinhaus et al., 2007; Zhang et al., 2009). These velocity structures involve several subhorizontal and vertical discontinuities (e.g., at the SAF) and are likely to account for at least part of the generated S wave energy.

Discussion

All borehole records exhibit considerable wave energy arriving about mid-way between the direct P and direct S arrivals (Figures 2, 3, and 4). These wave packets arrive with the S wave moveout and are likely incident as downgoing S from the top of the receiver array ~ 1.5 km depth at a minimum. If the velocity structure varied only with depth, then these observations would demand P to S conversions at horizontal discontinuities between the surface and 1.5 km depth. Our velocity model accommodates this with a discontinuity at 0.5 km depth (Figure 5). However, the waves observed on the transverse component are much stronger than predicted, i.e., the strike component for the PIGH shot (Figure 2) or the axial component for the BURN and FLIP shots (Figures 3 and 4). This suggests that some of the converted P to S waves must be on sub-vertical discontinuities and/or other scatterers located off the direct source-receiver path.

While a single 1D velocity model enables approximate matches of synthetics to the arrival times and moveouts of several observed seismic phases, it is deficient in several details. The amplitude of synthetic pS is always greater than that of observed pS, which is present in the observed PIGH section (Figure 2) but barely discernable in the BURN and FLIP sections (Figures 2 and 3). It is possible that observed pS is weaker than predicted because of secondary shear in a small volume above the source, as was inferred to be the case for a small-offset shot that produced a substantial observed pS wave (Pollitz et al., 2012). The moveouts of all identified seismic phases for the synthetic FLIP section (Figure 8) are flatter than observed (Figure 4). This is likely because of the strong lateral velocity gradient near the SAFOD well, becoming slower as the deeper borehole approaches the SAF (Hole et al., 2006; Bleibinhaus et al., 2007; Zhang et al., 2009). Thus all propagating waves are likely sampling progressively lower-velocity material on the paths to the deeper borehole stations, resulting in a steeper moveout than predicted by the 1D model, which does not account for such lateral variations.

CONCLUSIONS AND RECOMMENDATIONS

Downhole recordings of near-surface chemical explosions at offsets of a few kilometers from the SAFOD Main Hole richly document the seismic wavefield at near-field distances. These recordings are generated by near-surface explosions at several PASO stations. Wave packets observed in the borehole from these near-surface shots arrive as SV waves, based on their moveout and polarization. Most of the observed S-wave energy arrives at times between direct P and direct S and is interpreted as P to S conversions at internal discontinuities. Forward waveform modeling of the shots detonated at PASO stations 1 to 2 km from the SAFOD wellhead reveals that for these small explosions the effective source may be described, to first order, as the seismic response to an explosive point source. Wave packets arriving at the time of direct S may require the superposition of an explosive point source and a vertical-dipole source. This complements the inferences based on waveform fitting of near-zero offset shots, which provided evidence of additional secondary source components (e.g., delayed implosion). Such secondary sources would probably support failure of a weak upper crustal rock in response to large local shear and isotropic stresses imparted by the chemical explosion (Sammis, 2002). A 1D (vertically-varying) seismic velocity model accounts approximately for arrival times and moveouts of major seismic phases. However, many details of the observed

wavefields demand 2D or 3D seismic wavefield modeling in order to explain them. Continuing work will focus on: (1) applying 2D and 3D seismic wave-propagation codes to a 3D velocity model of the SAFOD region, and (2) more in-depth analysis of the Pilot Hole recordings of the Hole-Ryberg line in order to better understand the origin of observed S wave energy.

ACKNOWLEDGEMENTS

Data has been provided by Paulsson Geophysical Services Inc. SAFOD is a part of Earthscope, a program funded by the National Science Foundation and carried out in cooperation with the U.S. Geological Survey, the International Continental Scientific Drilling Program, Stanford University, NASA, and other agencies.

REFERENCES

Aki, K. and Richards, P. G. (1980). *Quantitative Seismology*, volume 1. W.H. Freeman and Company, San Francisco.

Bleibinhaus, F., Hole, J. A., Ryberg, T., and Fuis, G. S. (2007). Structure of the California Coast Ranges and San Andreas Fault at SAFOD from seismic waveform inversion and reflection imaging, *J. Geophys. Res*. **112**, B06315, doi:10.1029/2006JB004611.

Bouchon, M. (1981). A simple method to calculate greens functions for elastic layered media, *Bull. Seismol. Soc. Am*. **71**, 959–971.

Brocher, T. M. (2006). Empirical relations between elastic wavespeeds and density in the Earth's crust. *Bull. Seismol. Soc. Am* **95**, 2081–2092.

Chavarria, J. A., Goertz, A., Karrenbach, M., Paulsson, B., Milligan, P., Soutyrine, V., Hardin, A., Dushman, D., and LaFlame, L. (2007). The use of VSP techniques for fault zone characterization: An example from the San Andreas Fault. The Leading Edge, June: 770–776.

Dreger, D. and Woods, B. (2002). Regional distance seismic moment tensors of nuclear explosions. *Tectonophysics*, **356**, 139–156.

Friederich, W. and Dalkolmo, J. (1995). Complete synthetic seismograms for a spherically symmetric earth by a numerical computation of the greens function in the frequency domain, *Geophys. J. Int*. **122**, 537–550.

Gardner, G. H. F., Gardner, L. W., and Gregory, A. R. (1984). Formation velocity and density - The diagnostic basics for stratigraphic traps. *Geophysics* **39**:770–780.

Hole, J. A., Ryberg, T., Fuis, G. S., Bleibinhaus, F., and Sharma, A. K. (2006). Structure of the San Andreas Fault Zone at SAFOD from a seismic refraction survey, *Geophys. Res. Lett*. **33**(7), L07312, doi:10.1029/2005GL025194.

Kuhn, M. J. (1985). A numerical study of Lamb's Problem. *Geophys. Prospect.* **33**, 1103–1137.

McPhee, D., Jachens, R. C., and Wentworth, C. M. (2004). Crustal structure across the San Andreas Fault at the SAFOD site from potential field and geologic studies. *Geophys. Res. Lett*. **31**, L12S03.

Mosse, R. P. (1981). Review of seismic source models for underground nuclear explosions. *Bull. Seismol. Soc. Am*. **71**, 1249–1268.

Oye, V. and Ellsworth, W. L. (2005). Orientation of Three-Component Geophones in the San Andreas Fault Observatory at Depth Pilot Hole, Parkfield, California, *Bull. Seismol. Soc. Am* **95**, 751–758.

Patton, H. and Taylor, S. (2011). The apparent explosion moment: Inferences of volumetric moment due to source medium damage by underground nuclear explosions. *J. Geophys. Res*. **116**, B03310.

Pollitz, F.F., J.L. Rubinstein, and W.L. Ellsworth (2012). Source characterization of near-surface explosions at SAFOD, *Bull. Seismol. Soc. Am*, in press.

Sammis, C. G. (2002). Generation of high-frequency P and S wave energy by rock fracture during a buried explosion: its effect on P/S discriminants at low magnitude, in *Proceedings of the 2010 Monitoring Research Review: Ground-Based Nuclear Explosion Monitoring Technologies*, LA-UR-02-5048, Vol. I, pp. 542–551.

Zhang, H., Thurber, C., and Bedrosian, P. (2009). Joint inversion for Vp, Vs, and Vp/Vs at SAFOD, Parkfield, California. *Geochem. Geophys. Geosyst*. **10**, Q11002, doi:10.1029/2009GC002709.

Zhu, L. and Rivera, L. A. (2002). A note on the dynamic and static displacements from a point source in multilayered media. *Geophys. J. Int.* **148**, 619–627.

Zoback, M. D., Hickman, S., and Ellsworth, W. (2010). Scientific drilling into the San Andreas fault zone, *EOS Trans. AGU* **91**(22):197–199.

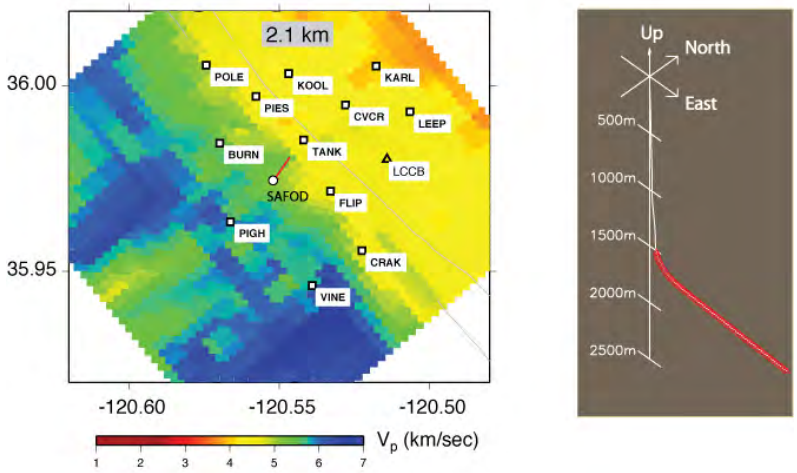


Figure 1. Locations of PASO array stations (squares) and an HRSN station (triangle) for which shots were conducted at recorded at the PGSI downhole seismic array, highlighted in red in the right panel. Superimposed is the V_p structure at 2.1 km depth extracted from Zhang et al. (2009).

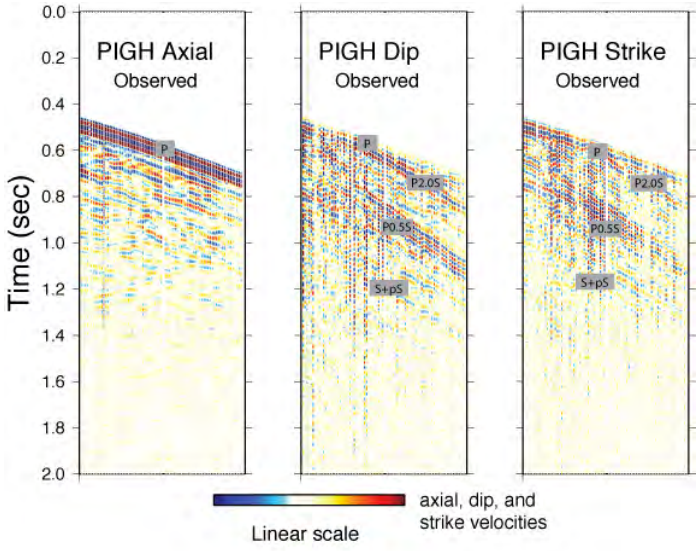


Figure 2. Observed three-component waveforms from the downhole array for a chemical shot located at PASO station PIGH. Seismograms are low-pass filtered at 0.023 s (43.5 Hz).

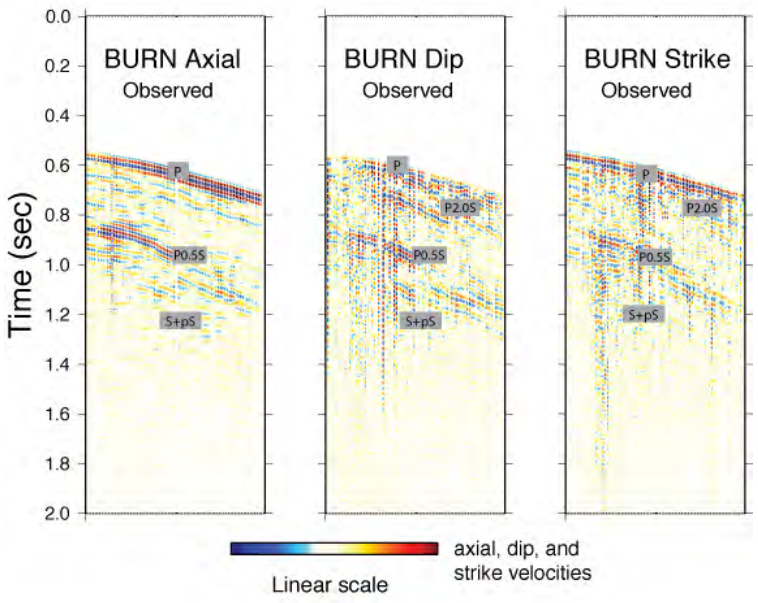


Figure 3. Observed three-component waveforms from the downhole array for a chemical shot located at BURN.

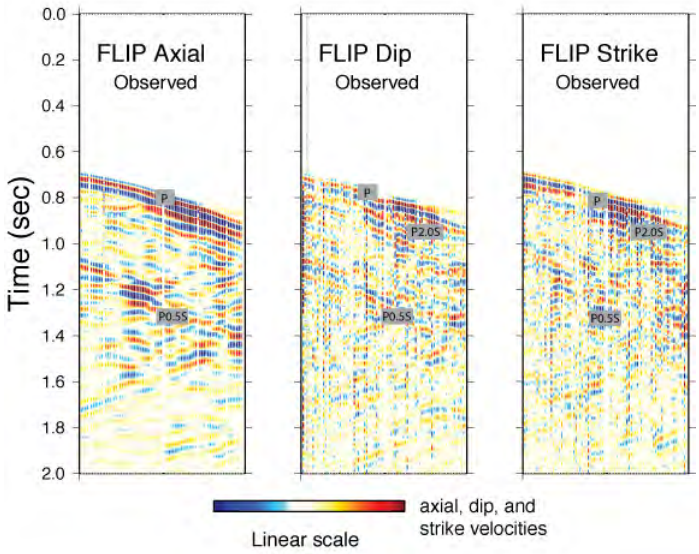


Figure 4. Observed three-component waveforms from the downhole array for a chemical shot located at FLIP. The deep reflections observed in this record likely represent reflections off the San Andreas fault.

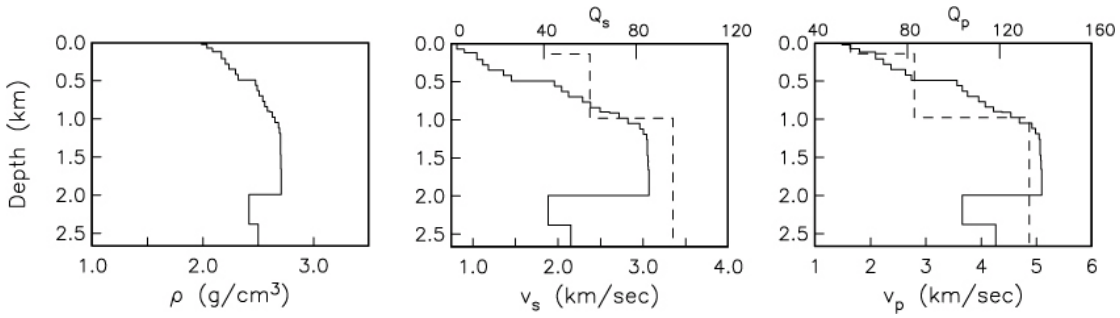


Figure 5. Layered structure of P and S velocities V_p and V_s, density ρ, and P and S-wave quality factors Q_p and Q_s (dashed lines) as a function of depth.

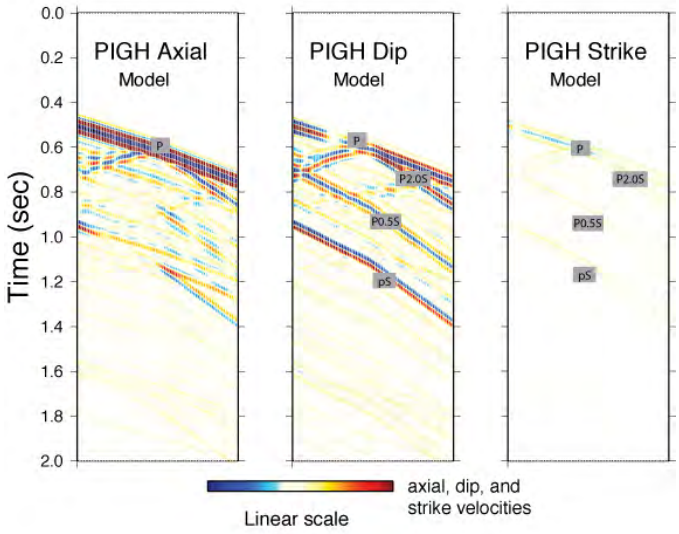


Figure 6. Synthetic wavefield for a shot recorded at the SAFOD downhole array for a shot at PASO station PIGH, using a purely explosive source. P0.5S and P2.0S denote converted P to S waves at strong discontinuities in velocity structure at 0.5 and 2.0 km depth, respectively (Figure 5).

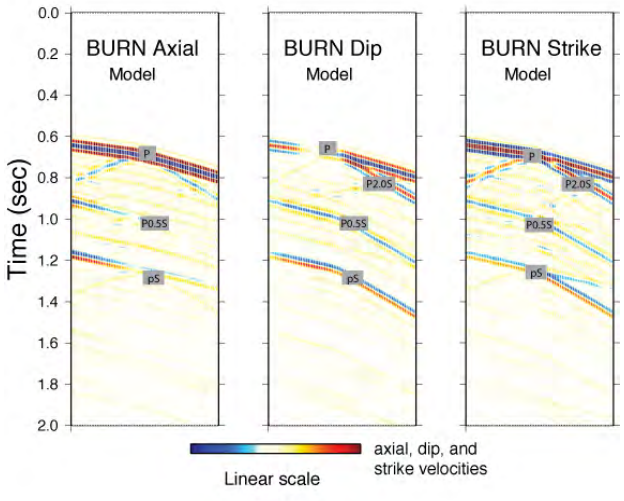


Figure 7. Synthetic wavefield for a shot recorded at the SAFOD downhole array for a shot at PASO station BURN, using a purely explosive source.

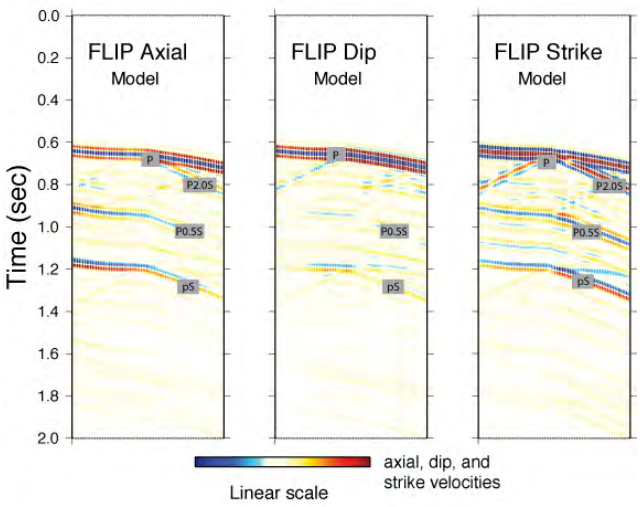


Figure 8. Synthetic wavefield for a shot recorded at the SAFOD downhole array for a shot at PASO station FLIP, using a purely explosive source.

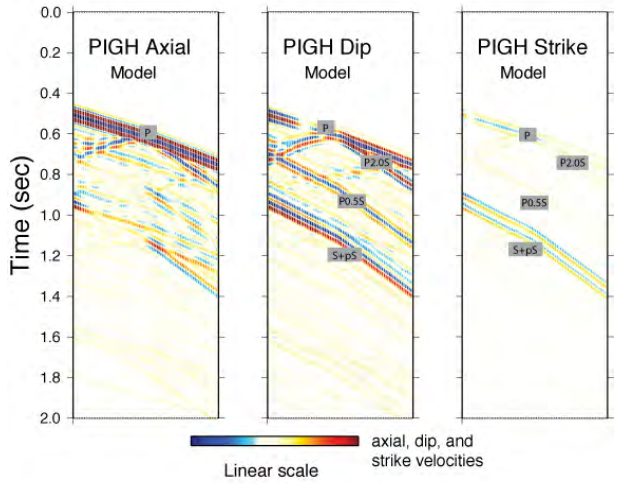


Figure 9. Synthetic wavefield for a shot recorded at the SAFOD downhole array for a shot at PASO station PIGH, using a combined explosive and vertical-dipole source with Md/Mexpl=0.7.

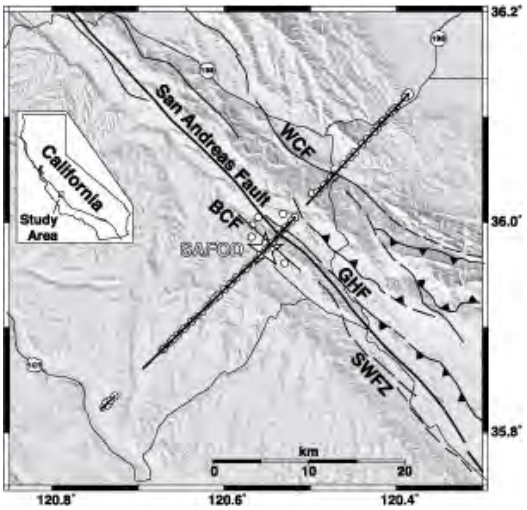


Figure 10. 2003 seismic survey crossing the SAFOD wellhead (Hole-Ryberg Line) superimposed on shaded-relief topography. Shots are shown with white circles. Major faults are BCF, Buzzard Canyon; GHF, Gold Hill; SWFZ, Southwest Fracture Zone; WCF, Waltham Canyon). Modified from Figure 1 of Hole et al. (2006).

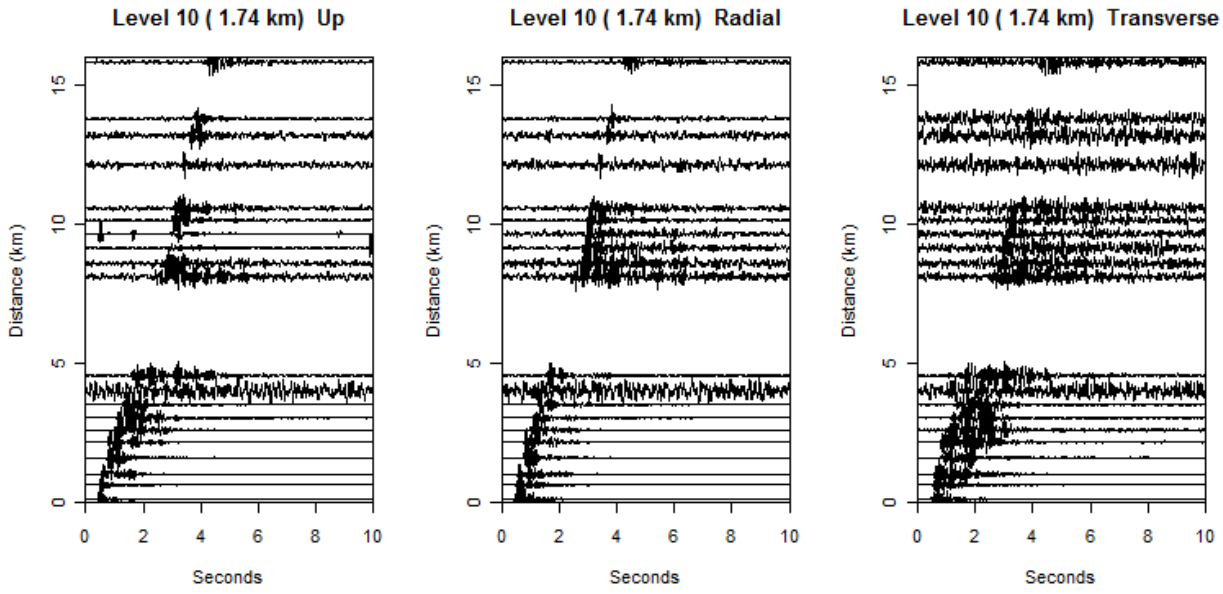


Figure 11. Shot gather at downhole array level 10 (1.74 km) from shots northeast of the Pilot Hole.

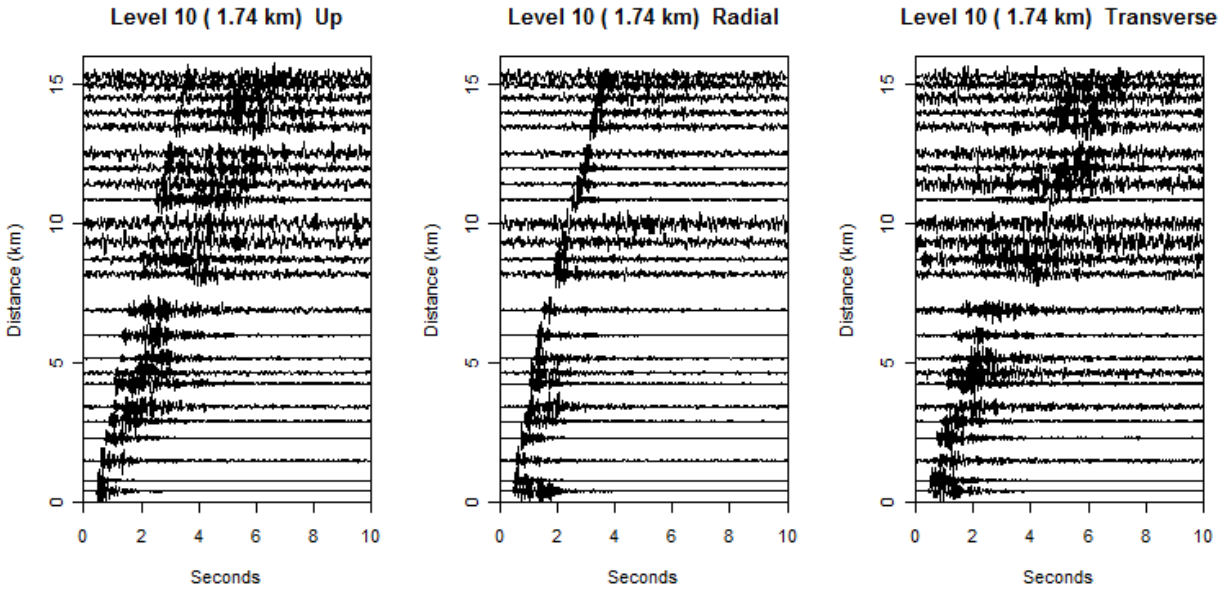


Figure 12. Shot gather at downhole array level 10 (1.74 km) from shots southwest of the Pilot Hole.

PROGRESS ON SEISMIC GROUND MOTION SIMULATIONS FOR NUCLEAR EXPLOSION MONITORING USING HYDRODYNAMIC AND ANELASTIC MODELING

Arthur J. Rodgers, Heming Xu, N. Anders Petersson, Bjorn Sjogreen, Ilya Lomov, and Oleg Y. Vorobiev

Lawrence Livermore National Laboratory

Sponsored by the National Nuclear Security Administration

Award No. DE-AC52-07NA27344/LL12-Source_Physics-NDD02

ABSTRACT

This paper describes progress in LLNL's seismic ground motion simulation capabilities for nuclear explosion monitoring. We developed capabilities to model seismic ground motions in detailed three-dimensional (3D) models using both hydrodynamic and linear anelastic wave propagation codes. For hydrodynamic modeling we use GEODYN, an Eulerian finite volume code with an extensive non-linear material model parameterization. For linear anelastic modeling we use WPP, a Cartesian finite difference code for modeling the seismic response to arbitrary forcing (e.g., explosions, earthquakes, body forces). Both GEODYN and WPP were developed at LLNL. In the last year we demonstrated that GEODYN reproduces explosion P-wave source spectra of the widely accepted model of Mueller and Murphy (1971) for underground nuclear explosions in granite. We also showed that chemical explosions in granite have seismic moments greater than nuclear explosions of the same yield by a factor of two (Xu et al., 2011). Furthermore we showed that GEODYN can accurately model elastic waves, including surface waves, for Lamb's problem and for shallow explosion sources. In order to model explosions at distances where seismic observations are typically made we developed a hybrid GEODYN-to-WPP one-way coupling methodology (Xu et al., 2012). In this approach motions are computed with GEODYN including the non-linear response of the near-source region, saved in the elastic region just beyond the region of permanent deformation and passed to WPP. We show with verification examples that GEODYN motions can be accurately and efficiency propagated to the far-field with WPP. Algorithms were implemented to use either two- or three-dimensional (2D or 3D, respectively) GEODYN calculations. The 2D GEODYN calculations are axisymmetric and much easier to perform than fully 3D calculations. These advancements allow modeling of ground motions using more complete physics of the near-source response to explosive loading. In another study reported in this volume this methodology was used for source-to-sensor simulation of observed motions form the Source Physics Experiment (Pitarka et al., 2012).

OBJECTIVES

Understanding the excitation of seismic energy emerging from underground explosions is key to nuclear monitoring (e.g. yield estimation, source-type discrimination). The non-linear response of earth materials to high-energy loading from buried explosions strongly impacts the amplitude and frequency content of energy observed at distant seismic stations (e.g. Rodean, 1981). Thus source parameters are closely related to the rheological properties of the shooting medium, especially material strength and emplacement depth. Advances in numerical methods, improved three-dimensional (3D) earth models and the inexorable escalation of computational power continue to make full waveform simulations of the mechanical motions excited by explosion and earthquakes more accessible.

The objective of this research is to develop capabilities to simulate the excitation and propagation of seismic motions to advance nuclear explosion monitoring. Using hydrodynamic simulations that account for the non-linear response of the emplacement region we can model near-source motions from explosions. Using linear anelastic wave propagation solvers we can model earthquake and explosion motions. In order to model explosion motions out to distances where seismic measurements are typically made we pass hydrodynamic motions to a linear anelastic propagation code for efficient computation of the response of earth materials to explosion loading. These capabilities, combined with modern massively parallel computers, enable ever more accurate and detailed numerical simulations of seismic motions from explosions. Results of these simulations can improve understanding of the amplitude and frequency content of seismic energy from explosions and be related to explosion source phenomenology, yield estimation and source-type discrimination.

RESEARCH ACCOMPLISHED

In the last year we completed two journal article manuscripts that document recent advances in our modeling capabilities. The first study investigates near-field motions for buried explosions in granite (Xu et al., 2011). The second study demonstrates and validates a method for coupling motions computed with a hydrodynamics code to a linear anelastic (seismic) code (Xu et al., 2012). The results of these efforts are described in detail below, but first we briefly describe the two computer programs we use to model seismic motions as these underpin our simulation efforts.

Computer Codes for Seismic Simulations

For near-source motions we use GEODYN, a parallel Eulerian finite volume code developed at LLNL (Lomov et al., 2003). This code incorporates many important features for modeling shock waves in geologic materials, including non-linear material constitutive properties (e.g., compressional and tensile failure, yielding, porous compaction and dilation, material strength hardening and softening as well as scale and rate-dependence; see Rubin et al., 2000; Vorobiev et al., 2007; Vorobiev, 2008), topography, gravity, and material heterogeneities. Importantly it uses adaptive mesh refinement to accurately represent the discontinuous expanding shock wave front and model the material response under rapid loading. GEODYN can be run in one-dimension (radially symmetric), two-dimensions (2D, axially symmetric) or three-dimensions (3D). Several studies have used GEODYN to model explosion loading (e.g., Antoun et al., 1999, 2001) including the Source Physics Experiment (Pitarka et al., these Proceedings).

For the seismic (linear anelastic) solver we use WPP, a parallel Cartesian Eulerian finite difference code also developed at LLNL (Nilsson et al., 2007; Petersson and Sjögreen, 2012). WPP has several desirable features including mesh refinement to increase the grid spacing as seismic wavespeeds increase with depth, free-surface topography, attenuation and absorbing boundary conditions (Appelo and Petersson, 2008; Petersson and Sjögreen, 2009, 2010, 2012). WPP has been successfully used for modeling moderate and scenario earthquake ground motions in the San Francisco Bay area (Aagaard et al., 2008, 2010) and the effects of surface topography on explosion generated ground motions (Rodgers et al., 2010). Note that WPP is an open-source computer code accessible to all (Petersson, 2012; Petersson and Sjogreen, 2011).

Simulations of Buried Explosions in Granite

Hydrodynamic simulations are used to model near-source motions. Recorded peak free-field motions from explosions in granite are an important data set for numerical code and model validation. Figure 1 shows the one-dimensional (1D) GEODYN simulation responses (radial component peak velocity and displacement) for whole-space models compared to measurements from historical nuclear explosions in granite. The simulation

predictions are seen to be in good agreement with the average behavior from historical data. Using the same constitutive model we extend the calculations to a two-dimensional (2D) axisymmetric domain including the free surface.

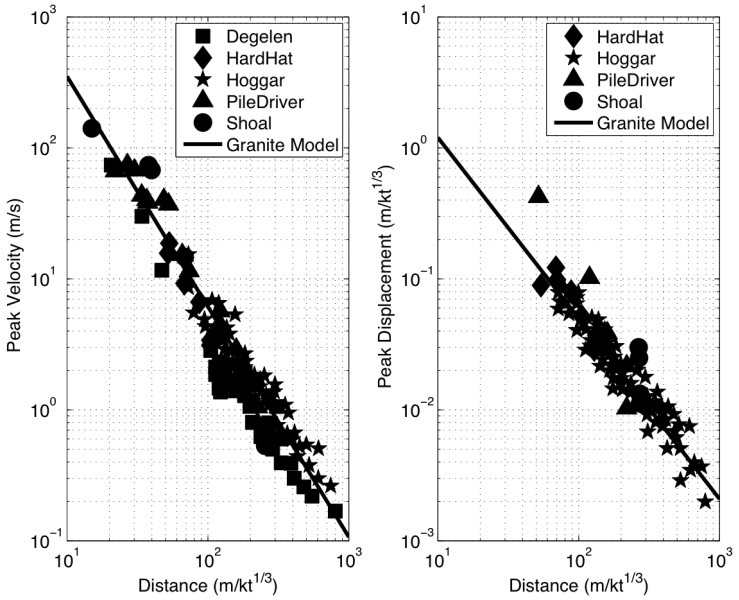


Figure 1. Comparison of the observed peak radial velocities (left, symbols) and displacement (right, symbols) from historical nuclear tests in granite versus scaled range with predictions from GEODYN simulations for the granite model (solid line).

In this study we considered explosive yields in units of TNT mass-energy equivalent in the range 0.5 to 5 kiloton (kt). All explosions are fully tamped, that is explosives are in contact with hard rock material and emplaced at normal depth-of-burial for containment. The source spectra are derived from the simulated motions by calculating reduced velocity potentials (RVP) (Haskell, 1967; Rodean, 1971). The waveforms are taken from the near-field region at the shot depth where motions are elastic (permanent plastic deformations are less than 1%). Note that reduced displacement or velocity potentials (RDP and RVP, respectively) are defined in the context of elastic motions for an isotropic disturbance in a uniform whole-space (Haskell, 1967; Rodean, 1971). The presence of the free surface above the explosion results in a reflected tensile wave and we carefully windowed the waveforms to minimize interference by these waves (Murphy, 1991). The source spectra are approximated by taking the Fourier transform of the RVP's and converting to displacement spectra. Simulated source spectra are compared to the Mueller and Murphy (1971, MM71) source model (Stevens and Day, 1985) at several yields assuming normal scaled depth-of-burial (SDOB) of 122 m/kt$^{1/3}$ following standard containment practice (U.S. Congress Office of Technology Assessment, 1989). The results for nuclear explosions with yields of 0.5, 1, 2, 3, 4 and 5 kt and at normal SDOB are shown in Figure 2a. Solid lines represent the source spectra from GEODYN calculations with the granite model and dashed lines represent the empirical MM71 model for each yield. The simulations predict the source spectra quite well with good agreement of the corner frequency and low frequency level, although the low frequency levels from the simulations are slightly higher than that predicted by the MM71 model. At higher frequency the roll-off slope is quite consistent between the simulated and MM71 spectra. The simulations show complexity above the corner frequency, probably due to windowing and/or interferences from the free surface. Interestingly, the source spectra from the simulated RVP's do not show overshoot as predicted by the MM71 model.

Figure 2b shows the inferred seismic moments, M_0, from the simulation RVP's (triangles) and MM71 model (circles) and the seismic moment corresponding to the overshoot spectral level from the MM71 model (squares). It is seen that the seismic moments inferred from simulations are slightly higher (less than 50%) than the MM71 model predictions and lie closer to the moments corresponding to the overshoot levels. Small adjustments in the material model could bring these predictions in better agreement and time-domain modeling of actual explosion motions could better guide material adjustments. Note that the seismic moment–yield slopes are in excellent agreement between the MM71 model and the GEODYN calculations with the granite model for these nuclear explosions at

normal SDOB. The close agreement of the source spectra for explosions in granite between the MM71 model and the calculations using the reduced velocity potentials implies that it is appropriate to infer seismic source characteristics from the hydrodynamic simulations of explosions. Such good agreement between simulations and the MM71 empirical model implies that this methodology should be applicable to other materials provided adequate calibrations are used to define the rheological model.

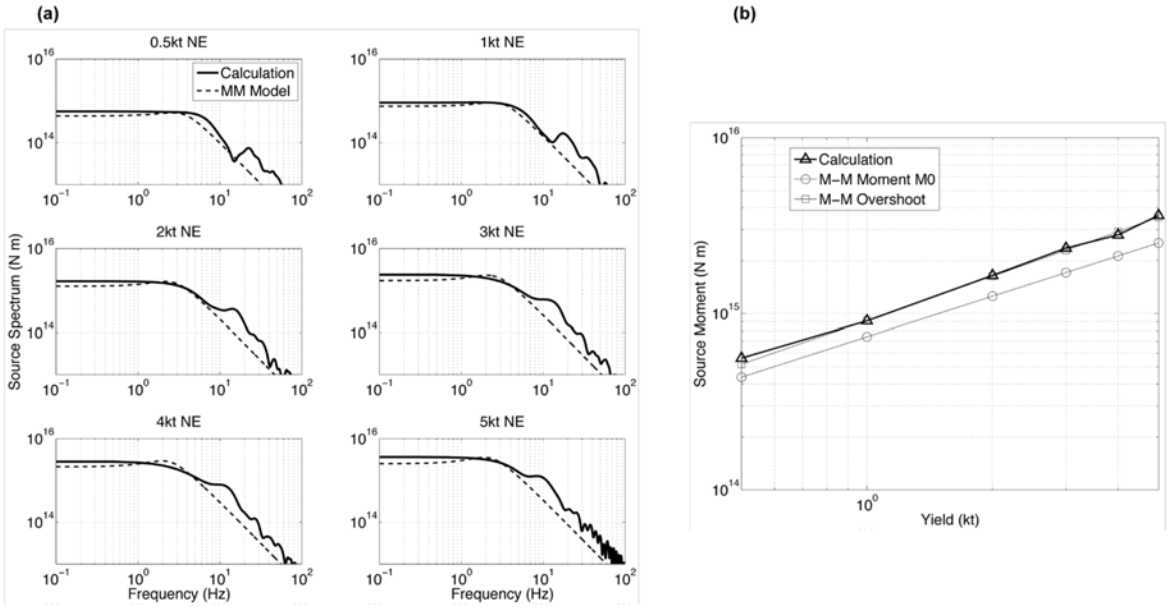


Figure 2. (a): Comparison of the derived source spectra (solid lines) with the Mueller and Murphy (1971) model (dashed lines) for normally buried nuclear explosions at 0.5, 1, 2, 3, 4, 5 kt. (b): Scaling of source moment with yield for GEODYN calculations (triangles), MM71 (circles), and seismic moment from the MM71 models using the overshoot spectral levels (squares).

Differences between Chemical and Nuclear Explosions in Granite

The differences between seismic energy emerging from nuclear and chemical (high-explosive) explosions are important for interpreting data from nuclear tests and conventional calibration experiments. The fundamental differences between the two explosion types include the initial energy density and the rate of energy released during the explosion (Goldstein and Jarpe, 1994). Reports based on the 1993 Non-Proliferation Experiment (NPE) and nearby NTS nuclear explosions indicate that the chemical source spectral amplitude is enhanced relative to that of nearby nuclear explosions by about a factor of two (Denny, 1994; Glenn and Goldstein, 1994; Goldstein and Jarpe, 1994). In this study we examine the differences in the source spectra from a 1 kt nuclear explosion and 1 kt (TNT energy equivalent) heavy ANFO explosion in granite. The nuclear explosion source representation is an instantaneous energy deposition while the chemical explosion is simulated as a finite detonation with the JWL equations (Lee et al, 1973) as a spherical charge ignited at the center. The resulting time-domain velocity time-histories and source spectra are shown in Figure 3a. The source strengths for 1 kt nuclear and chemical explosions are denoted by solid and dashed lines, respectively. In the time-domain the chemical explosion motions are higher amplitude and longer duration than the nuclear explosions. In the frequency domain the chemical explosion has a higher low frequency level by about a factor of two and a lower corner frequency than the nuclear explosion. These differences are due to the differences of the energy release rate and not the material properties, which are identical in the two simulations.

Modeling Explosion Motions with Elastic Green's Functions

The motions computed with GEODYN include non-linear material effects such as cavity creation, damage and permanent deformations. We would like to know if computed near-field motions can be represented by a point explosion in an equivalent elastic medium (half-space with v_P=5.6 km/s, density, ρ= 2.6 g/cc, attenuation quality

factor Q_P =200). We used a wavenumber integration code to compute elastic Green's functions for a buried explosion. These were convolved with the source time-function of the RVP of a normally buried 1 kt nuclear explosion (Figure 3b, top left) and compared to the motions computed with GEODYN. For points below the shot the direct P-waves are well-modeled by the elastic response (Figure 3b). For points along the surface the response is more complicated. Figure 3c (top row) shows the comparison of the elastic response (with source-time function from the RVP) for points along the surface at 210 m and 300 m assuming a point explosion at the DOB. The elastic response predicts larger and smaller motions on the vertical and radial component, respectively, compared to the GEODYN responses. The effect of spall above the explosion has been modeled as a compensated linear vector dipole (CLVD). We added the response of a CLVD located half-way between the source and the surface with half the moment and the same source-time history. This improves the fit to the vertical components, but degrades the fit to the radial components (Figure 3c, middle row). Subtracting a CLVD with half the moment greatly degrades the fit to the vertical components, while improving the fit to the radial components (Figure 3c, bottom row). This exercise indicates that more complicated spatial and/or temporal distribution of sources must be considered in order to represent the effects of non-linear material response near an underground explosion.

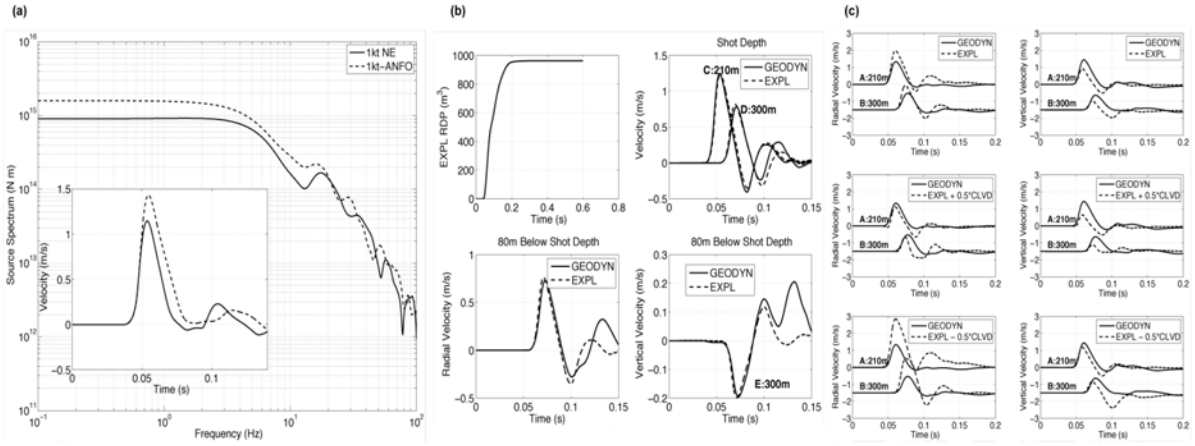


Figure 3. (a): Comparison of source spectra from 1kt nuclear and 1kt (by weight) chemical explosion. The inset shows the waveforms in time domain. Note that the chemical explosion (dashed line) results in a stronger source than a nuclear explosion (solid line) of the same yield. (b): Top left: reduced displacement potential for a 1kt nuclear explosion. Top right: comparison of the radial velocity GEODYN and elastic solution using the Green's function and the derived source function at radial distances of 210m (C) and 300m (D) at the shot depth. Bottom: comparison of the GEODYN calculation and solutions using the Green's function and the derived source function on radial and vertical components at radial distances of 300m (E) at a depth of 80m below the shot point. (c): Comparison of the GEODYN and elastic solutions at distances of 210m (A) and 300m (B) at the surface. Top: the source is a simple explosion source. Middle: composite source is an explosion plus a vertically oriented CLVD with half the explosion moment. Bottom: composite source is an explosion minus a CLVD with half the explosion moment.

Coupled Hydrodynamic-to-Linear Elastic Motions

While hydrodynamic simulations include more complex (and hopefully accurate) physics of material response, hydrodynamic wave propagation is inherently more computationally expensive than linear anelastic simulations. Fortunately the non-linear response of Earth material decays quickly away from an explosion and linear anelastic physics can accurately represent the wave motion. In order to efficiently model wave motions from the non-linear near-source region to the far-field linear anelastic region we developed a one-way hydrodynamic-to-elastic coupling methodology (Xu et al., 2012). In this approach we save motion time-histories in the elastic region computed with GEODYN on a dense grid of points. Motions (vector velocities) are interpolated on to the faces of a three-dimensional cube, filtered to remove unresolvable high frequencies and introduced in WPP where they propagate as elastic waves.

A key factor in this approach is that GEODYN must be able to accurately propagate elastic motions because the motions must be recorded outside the non-linear near-source region before being saved and passed to WPP. Because we are interested in sources near the free-surface (shallow explosions) it is essential that GEODYN be able to accurately model surface waves. We have verified that GEODYN can propagate elastic waves by computing the response for Lamb's problem (a vertical point force on an elastic half-space), which has an analytic solution. Figure 4a shows the computed response compared to the analytic solution and good agreement is evident. The agreement of the exact and numerical solutions at the surface locations (top two plots) is excellent for body waves, but there is some slight mismatch for Rayleigh waves in phase and amplitude. Since GEODYN relies on an Eulerian scheme, the free surface is not a clear interface between rock and air, and wave motion results in mixed cells of air and solid earth. The surface wave is very sensitive to the treatment of the free surface boundary. In this case, the imperfect implementation of the free surface might result in some energy leakage into the air above the free surface. Nonetheless the agreement between the responses computed with GEODYN and the analytic solutions is very good.

In order to verify the coupling approach, we considered a shallow (10 m) explosion source in a purely elastic medium (granite equivalent) and computed the solution in four different ways. We computed the response analytically, using the RVP convolved with an elastic Green's function (described above), running GEODYN out to long range and using the GEODYN-to-WPP coupling approach. Figure 4b shows the four solutions and differences between the computed and analytic solutions (dashed lines).

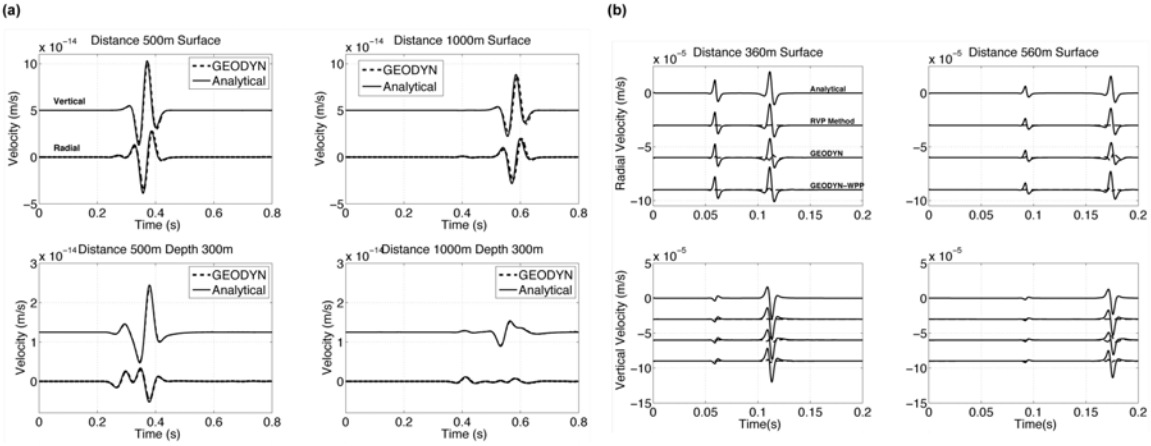


Figure 4. (a): Computed and analytic solutions for Lamb's problem. The top and bottom traces represent vertical and radial component velocities, respectively with GEODYN (dashed) and analytical (solid) solutions at two surface locations and two deep locations. (b): Computed and analytic solutions for a shallow dilatational source. The top and bottom traces represent vertical and radial component velocities, respectively. Each panel shows the analytical solution (solid, top trace), semi-analytical solution using the numerically derived reduced velocity potential (solid, 2nd trace), direct GEODYN calculation (solid, 3rd trace) and the GEODYN-to-WPP solutions coupled as driving boundary conditions (solid, bottom trace). The dashed lines with each trace represent the deviation of the solution from the analytical solution (top).

It is evident that a buried explosion source (Figure 4b) excites stronger body waves (relative to the Rayleigh waves) than Lamb's problem (compare with Figure 4a). Again we see there is an excellent agreement between the GEODYN numerical solution (third solid trace) and analytical solution (top trace) for body waves and some slight mismatch for Rayleigh waves at the same location, presumably due to free-surface boundary condition effects as in Lamb's problem (discussed above). In addition, for this type of volume source the reduced velocity potential (Murphy, 1991; Xu et al., 2011) is conveniently derived in the linear elastic region from the GEODYN calculation then convolved with elastic Green's functions for a point source. These semi-analytical solutions are plotted as second traces and are also in good agreement with the analytical solutions. Note that the difference between the RVP solutions and the analytical solutions is quite small as indicated by the dashed line. This serves an additional check that GEODYN yields accurate spherical waves for calculating the RVP. Finally, we use the coupling strategy described above to propagate GEODYN's solutions through the elastic region using WPP (4th trace in Figure 4b). The grid spacing in WPP is 0.5m and the resolution is about 40 points-per-wavelength for better accuracy. It is seen that the body waves calculated by the coupling method match well the analytical solutions and Rayleigh waves are

in phase with the analytical solutions but the amplitudes show some differences from the analytical solutions at both locations. Note that the errors (differences between the computed and analytic solutions) are largest for the GEODYN calculation to the far-field. Again this is likely attributable to the imperfect free surface implementation for elastic motions in the hydrodynamic numerical scheme.

As another verification exercise of the hydrodynamic-to-elastic coupling methodology we considered a shallowly buried explosion with a fully non-linear material model. The test case is a 1 kt trinitrotoluene (TNT) equivalent chemical explosion at a depth of 10 m. The material used is non-linear weathered granite (with a porosity of 1.4%) in a half-space overlain by air. The material model was built to fit the laboratory tri-axial experiments (Chitty and Danna, 2010) with bulking and compacting and has lower P and S wave speeds of 3800 m/s and 2166 m/s, respectively. No gravity is included in this hydrodynamic calculation. The chemical explosion source is represented by the JWL equation (Lee et al., 1973). As above we calculate non-linear wave propagation due to the explosion source with GEODYN, including cratering of the surface. The focus of this test case is to further illustrate that the coupling strategy functions with the complex waves generated by a nonlinear model as well as in the linear elastic cases above, and the details of the nonlinear model should not be essential to the validation. We computed the response in two ways: firstly we performed a very expensive 2D GEODYN calculation to propagate the solution to a distance of 500 m at the surface; secondly we use the coupling strategy to propagate the GEODYN solutions beyond the elastic radius (about 60 m) to distance with WPP.

Figure 5a shows the resulting density distribution in which the shaded region denotes the solid granite region. Figure 5b shows the nonlinear deformation in which the shaded region denotes the plastic strains greater than 0.03% (darker locations correspond to higher plastic strains) at 3 s after the explosion. Initially the surface is at depth=0 m. The near-surface explosion vaporizes and ejects the surface material and produces a shallow depression to form a crater of depth 30 m and radius of 20 m along the surface (the approximate volume of the crater is about 12000 cubic meters). Note that the incurred non-linear deformation region is not spherically symmetric. It rather extends to about 50 m horizontally and vertically even further (shorter than the elastic radius ~200 m for normally buried 1kt explosions in granite (Perret and Bass, 1975). As described above, the numerical GEODYN solutions are saved at the locations beyond the non-linear deformation region starting from the dashed line at a radial distance of 64 m to about 100 m, and from the surface to a depth of 60 m. The location of the monitoring surface is usually selected to be close to the nonlinear region boundary to save the storage cost although the results would not vary if a larger monitoring surface were used according to the uniqueness theorem. For this particular seismic calculation the GEODYN solutions in the elastic region are resampled by interpolation in time and space, and then low-pass filtered below 30 Hz, resulting in a minimum grid resolution of 42 points-per-wavelength for high accuracy. Higher frequencies are resolvable by using a finer mesh with the elastic code.

Figure 5c shows the comparison of the direct 2D GEODYN solutions (thick dashed line) and the WPP solutions (solid) at an offset of 500 m on the free surface and at a depth of 100 m for the 1 kt chemical blast. The top line is the vertical component and the bottom radial component in each plot. The thin dashed lines indicate the difference of the GEODYN and GEODYN-to-WPP solutions above. The agreement of the two solutions at the surface and depth is excellent for both the body waves and Rayleigh waves. The differences at late times are probably due to the imperfect outflow boundary conditions for the small volume used in these simulations. The excellent agreement in such nonlinear complex source calculations involving cratering further demonstrates that the coupling scheme is adequately implemented and complex motions due to the underground explosions are appropriately propagated to distant locations where the seismic measurements are obtained to characterize the explosion sources.

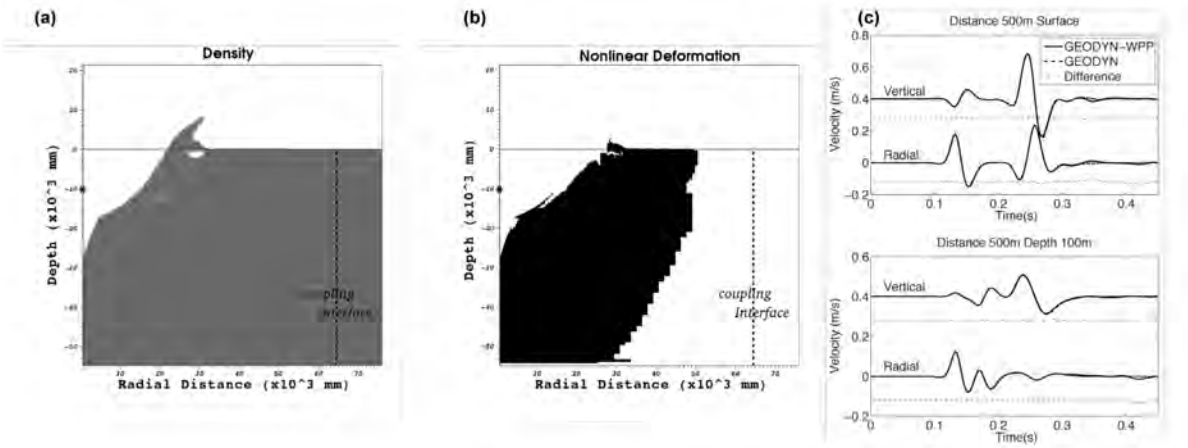


Figure 5. Explosion-induced crater formation (a) density distribution (grey region is solid) and (b) nonlinear deformation (plastic strain >0.03%, the dark region) at 3 s after explosion. The free surface is initially at depth=0. The explosion is centered at a depth of 10 m (star). In (a) and (b) the dashed line coupling interface. (c) Comparison of the direct GEODYN solutions (thick dashed line) and WPP solutions (solid) coupled with GEODYN solutions at a surface location (top) and 100 m deep location (bottom). The top is the vertical component and bottom the radial component in each plot. The thin dash lines denote the difference of the two solutions above. All solutions are low-pass filtered at 30 Hz. The agreement of the two solutions is excellent.

CONCLUSIONS AND RECOMMENDATIONS

In this study seismic source spectra of underground nuclear explosions are inferred from velocity time-histories computed with hydrodynamic simulations with a well-calibrated non-linear material model for granite. Source spectra computed with hydrodynamic simulations are in good agreement with those predicated by the MM71 empirical model. For calculations in two dimensions the waves reflected from the free surface arrive soon after the direct P-wave. Caution was taken to reduce the interference effects. The scaling of seismic moment with yield is found to be consistent with previous results. Computed source moments are higher by about a factor of two for chemical explosions than for the nuclear explosions of the same yield due to the difference in energy release rate. The relative difference is in good agreement with the observations at the NTS site (Denny, 1994; Goldstein and Jarpe, 1994). The relative energy transfer efficiency might correlate with the emplacement material properties such as material inhomogeneities and porosity, and the enhancement of the chemical explosion source is likely be different for porous materials (e.g., Rodgers et al., 2011).

We attempt to quantify the contributions from the damage around the source and near the free surface for normally buried explosions in the near field. It is noted that damage can be a significant factor affecting radiated seismic waves (e.g., Patton and Taylor, 2011). We use the derived source functions from a 1 kt nuclear explosion convolved with elastic Green's functions to obtain the response at nearby receivers at and below the surface. The comparison between the non-linear calculation and elastic response from an isotropic explosion source shows that the primary waves at steep (downward) takeoff angles are well approximated with the volumetric source (which certainly contains the contribution of damage just around the explosion source) but at shallower angles the primary waves are complicated by near-surface damage. This is consistent with the shape of the damage zone. In the calculations with composite elastic sources, a simple addition/subtraction of a CLVD with half the explosion moment cannot match the primary near-field surface motions on both the vertical and radial components simultaneously. It is possible that an equivalent CLVD source has a different time history and/or cannot be approximated by a point source half way between the free surface and shot point. Further investigation of the equivalent elastic source for seismic radiation in the near-field is required.

We demonstrated that GEODYN, our hydrodynamic code can accurately simulate elastic motions with a free surface, so that simulated motions can be confidently propagated from the non-linear region near the source to the

elastic region. We verified GEODYN's elastic wave propagation capabilities by reproducing the analytic solutions to Lamb's problem (Figure 4a) and several solutions for a shallow dilatational source (Figure 4b). The accuracy of the coupling scheme from GEODYN-to-WPP is validated by comparing the solutions computed directly by GEODYN (that is computationally intensive) and the WPP coupled solutions with the GEODYN motions as time-dependent boundary conditions in linear elastic medium (Figure 5). The agreement of the direct GEODYN solutions and GEODYN-to-WPP coupled solutions at distance also checks the accuracy of GEODYN calculations. In summary, the above results demonstrate that the hydrodynamic code GEODYN is accurate and the coupling scheme from the nonlinear hydrodynamic calculations to linear elastic calculations is properly implemented.

Recent advances in numerical modeling allow improved understanding of the generation and propagation of explosion-generated seismic motions. These methods can be used to model the non-linear processes that occur very near the source. Computed motions can be analyzed to evaluate the impact of non-linear processes on the amplitudes and frequency content of seismic waves observed in the far-field. This line of research can improve understanding of explosion source physics for improved nuclear explosion monitoring.

ACKNOWLEDGEMENTS

We are grateful for access to high-performance computing resources operated by Livermore Computing. WPP was developed in part under LLNL Laboratory Directed Research and Development.

REFERENCES

Aagaard, B., T. Brocher, D. Dreger, A. Frankel, R. Graves, S. Harmsen, S. Larsen, K.McCandless, S. Nilsson, N. A. Petersson**,** A. Rodgers**,** B. Sjogreen and M. L. Zoback (2008). Ground motion modeling of the 1906 San Francisco earthquake II: Ground motion estimates for the 1906 earthquake and scenario events, *Bull. Seismol. Soc. Am.* **98,** 1012–1046, doi: 10.1785/0120060410.

Aagaard, B. T., R. W. Graves, A. Rodgers, T. M. Brocher, R. W. Simpson, D. Dreger, N. A. Petersson, S. C. Larsen and S. Ma (2010). Ground motion modeling of Hayward fault scenario earthquakes II: Simulation of long period and broadband ground motions, *Bull. Seismol. Soc. Am.* **100**, 2945–2977.

Appelo, D. and N.A. Petersson (2008). A stable finite difference method for the elastic wave equation on complex geometries with free surfaces, *Comm. Comput. Phys*., **5**, 84-107.

Antoun, T. H., O. Y. Vorobiev, I. N. Lomov, L. A. Glenn (1999). Simulations of an underground explosion in granite, *Proceedings of the 11th American Physical Society Topical Conference on Shock Compression of Condensed Matter*, Snowbird, UT June 27-July 2, 1999.

Antoun, T. H., I. N. Lomov and L. A. Glenn (2001). Development and application of a strength and damage model for rock under dynamic loading, *Proceedings of the 38th U.S. Rock Mechanics Symposium, Rock Mechanics in the National Interest*, D. Elsworth, J. Tinucci and K. Heasley (eds.), A. A. Balkema Publishers, Lisse, The Netherlands, 369–374.

Chitty, D and Dana, D., 2010. A unified methodology for estimation of rock mass properties and associated uncertainties to support characterization of inaccessible sites, DTRA report ARA-T3-LR-1.18-05

Denny, M. (1994). Introduction and Highlights, 1-1, *Proceeding of Symposium on the Non-Proliferation Experiment*, Rockville, Maryland

Glenn, L and P. Goldstein (1994). The influence of material models on chemical or nuclear-explosion source functions, 4-68, *Proceeding of Symposium on the Non-Proliferation Experiment*, Rockville, Maryland

Goldstein, P. and S. Jarpe (1994). Comparison of chemical and nuclear-explosion source spectra from close-in, local and regional seismic data, 6-98, *Proceeding of Symposium on the Non-Proliferation Experiment*, Rockville, Maryland.

Haskell, N. A. (1967). Analytic approximation for the elastic radiation from a contained underground explosion, *J. Geophys. Res*. **66**, 2937.

Lee, E., M. Finger and W. Collins (1973). JWL equations of station coefficients for high explosives, LLNL report UCID-16189

Lomov. I. N., T. H. Antoun, J. Wagoner and J. Rambo (2003). Three-dimensional simulation of the Baneberr nuclear event, *Proceedings of the 13th American Physical Society Topical Conference on Shock Compression of Condensed Matter*, Portland, OR July 20-25, 2003.

Mueller, R. and J. Murphy (1971). Seismic characteristics of underground nuclear detonations Part 1: Seismic source scaling, *Bull. Seismol. Soc. Am*. **61**, 1675–1692.

Murphy, J. (1981). P wave coupling of underground explosions in various geologic media, in *Identification of Seismic source – Earthquake or Explosion*, E. S. Husebye and S. Mykkelveit (eds.), p. 201–205.

Murphy, J.R (1991). Free-field seismic observations from underground nuclear explosions, *Explosion Source Phenomenology*, 25–33, Eds. S. R Taylor, H. J. Patton and P.G Richards, Geophysical Monograph, 65.

Nilsson, S., N.A. Petersson, B. Sjogreen, H.-O. Kreiss (2007). Stable difference approximations for the elastic wave equation in second order formulation, *SIAM J. Numer. Anal*. **45**, 1902–1936.

Patton, H. J. and S. R. Taylor (2011). The apparent explosion moment: Inferences of volumetric moment due to source medium damage by underground nuclear explosions, *J. Geophys. Res.* **116**, B03310, doi:10.1029/2010JB007937

Perret, W. R. and Bass, R. C. (1975). Free-field ground motion induced by underground explosions, Sandia National Laboratory Report No. SAND74-0252.

Petersson,N. A. (2012). WPP software website, https://computation.llnl.gov/casc/serpentine/software.html

Petersson, N. A., and B. Sjögreen (2009). An energy absorbing far-field boundary condition for the elastic wave Equation**,** *Comm. Comput. Phys*. **6**, 483–508.

Petersson, N.A., and B. Sjögreen (2010). Stable grid refinement and singular source discretization for seismic wave simulations, *Comm. Comput. Phys.* **8**(5), pp. 1074–1110.

Petersson, N. A., and B. Sjögreen (2011). User's guide to WPP version 2.1, Lawrence Livermore National Laboratory technical report, LLNL-SM-487431.

Petersson, N. A. and B. Sjögreen (2012). Stable and efficient modeling of anelastic attenuation in seismic wave simulations, *Comm. Comput. Phys Comm.* **12**(1), 193–225.

Pitarka, A., R. Mellors, A. Rodgers, S. Ford, P. Harben, J. Wagoner, W. Walter, M. Pasyanos, N. A. Petersson, O. Vorobiev and H. Xu (2012). Analysis and Simulation of far-field seismic data form the Source Physics Experiment, these Proceedings.

Rodean, H. (1971). *Nuclear-Explosion Seismology*, U.S. Atomic Energy Commission, Oak Ridge, TN.

Rodean, H (1981). Inelastic prcesses in seismic wave generation by underground explosions, in *Identification of Seismic source – Earthquake or Explosion*, E. S. Husebye and S. Mykkelveit (Eds.), 97–189.

Rodgers, A., N. A. Petersson, and B. Sjögreen (2010). Efficient generation of shear waves from shallow explosions by topographic scattering near the North Korean nuclear test site, *J. Geophys. Res.* **115**, B11309, doi:10.1029/2010JB007707.

Rodgers, A. J., H. Xu, I. N. Lomov, N. A. Petersson, B. Sjogreen, O. Y. Vorobiev and V. Chipman (2011).Improving ground motion simulation capabilities for underground explosion monitoring: coupling hydrodynamic-to-seismic solvers and studies of emplacement conditions, in *Proceeding of the 2011Monitoring Research Review*: *Ground-Based Nuclear Explosion Monitoring Technologies*, LA-UR-11-04823, Vol. .1, pp. 363–371.

Rubin, M. B., O. Vorobiev and L. A. Glenn (2000). Mechanical and numerical modeling of a porous elastic viscoelastic material with tensile failure, *Int. J. Solids and Structure* **37**, 1841–1871.

Stevens, J.L and Day, S. M. (1985). The physical basis of mb:Ms and variable frequency magnitude methods for earthquake/explosion discrimination, *J. Geophys. Res*. **90**, 3009–3020.

Vorobiev O.Yu, Liu B.T, Lomov I.N, Tarabay T.H (2007) Simulation of penetration into porous geologic media, *Int. J. of Impact Eng.* **34**, 721–731.

Vorobiev, O. (2008). Generic strength model for dry jointed rock masses, *Int. J. of Plasticity*, 24, 2221-2247.

U.S. Congress, Office of Technology Assessment (1989). *The Containment of Underground Nuclear Explosions,* OTA-ISC-414, U.S. Government Printing Office, Washington, DC.

Xu, H., A. J. Rodgers, I. N. Lomov, O. Y. Vorobiev (2011). Seismic source characteristics of nuclear and chemical explosions in granite from hydrodynamic simulations, submitted to *Pure App. Geophys.*, December 2011.

Xu, H., A. J. Rodgers, I. N. Lomov, N. A. Petersson, B. Sjogreen and O. Y. Vorobiev (2012). Simulation of explosion ground motions using a hydrodynamic-to-elastic coupling approach in three-dimensions, submitted *Bull. Seismol. Soc. Am.*, May 2012.

SIMULATING THE RESPONSE OF A FAULTED TEST SITE WITH A FULLY COUPLED EULER-LAGRANGE HYDROCODE

David W. Steedman, David Coblentz, Chris R. Bradley, and Aviva J. Sussman

Los Alamos National Laboratory

Sponsored by the National Nuclear Security Administration

Award No. DE-AC52-06NA25946 / NST11-NCNS-TM-EXP-PD15

ABSTRACT

The second shot of the Source Physics Experiment (SPE-2) was conducted in granite with two high-angle faults that intersect the test shaft. This geologic scenario was incorporated into LANL's Geologic Framework Model (GFM) and used to model the ground shock created by a buried high explosive. The GFM incorporates available geological and geophysical data into a volumetric framework that provides a mesh-able model for numerical simulation. Using a fully coupled Euler-Lagrange (CEL) code we model the high-deformation source region as Eulerian in full physical interaction with the Lagrange domain containing a complex user constitutive model that considers a non-linear equation of state compaction model along with three-invariant yield and failure. Shell structures are used to explicitly model the local faults, and Lagrange contact provides for the interaction between the faults and the adjoining rock masses. We present the computed effects of the main identified faults on the ground response, which compare favorably in both magnitude and trend with light detection and ranging (LIDAR) data collected prior to and following SPE-2.

OBJECTIVE

The objective of this research was to use high fidelity calculations to help to identify the phenomenology of a buried high explosive event. The test bed for the Source Physics Experiment (SPE-N) is located the in granitic rock of the Climax stock, in northern Yucca Flat at the Nevada National Security Site (NNSS). A volumetric GFM was constructed to match the known geologic setting at the SPE site. The GFM was used for numerical simulation of the second event in the SPE test series (SPE-2) using a fully coupled Euler-Lagrange code and included detailed geologic information including explicit modeling of observed faults at the test bed. The character and magnitude of the computed response was compared to test data. In particular, the surface expression of computed displacement was compared to LIDAR survey data. Those data were taken both before and after the event to determine permanent surface displacement.

RESEARCH ACCOMPLISHED

The second event in the Source Physics Experiment series (SPE-2) was simulated numerically using a fully coupled Euler-Lagrange (CEL) finite element code. Results of the simulation are compared to relevant data collected from the event.

The CEL code allows a single numerical tool to be applied for the modeling of the complex nature of an explosive event in a geologic framework model that incorporates the relevant geologic detail. An Eulerian region is used to model the high-deformation explosive source region that uses JWL explosive equation of state material for the region of the charge container. Further out from the explosive source a Lagrangian region is used to model the shock propagation through the surrounding geology, which includes both weathered and intact granite, as well as the faults identified during the drilling of the emplacement- and instrument-holes.

A GFM of the SPE site was constructed using the GAMUT (Geologic Assessment Methodology for Subsurface Structures) approach. Although the Climax Stock area was selected as the site of the first set of SPE tests because its granite lithology provides a relatively “homogenous” medium, there are a number of geologic features that have a profound impact on the shock propagation at the SPE site (Townsend et al., 2012). Two geologic features have been incorporated into the GFM for this study: the geometry of the interface been the near-surface weathered granite and the underlying intact granite and two faults identified during the drill of the emplacement hole. The depth of weathering was not well documented in the early geologic studies at the Climax Stock. Shellum and Fisher (1996) noted that the extent of highly weathered granite at Climax stock varies from about 12 to 18 m (40 to 60 ft) deep in the low-lying areas of the stock, and may only be 1 to 6 m (3 to 20 ft) deep in the hilly portions of the area. For the purpose of this study, we have assumed a uniform thickness weathered layer of 15.24 meters (50 ft) in depth, which is consistent with the weathered layer thickness observed in the emplacement hole (Townsend et al., 2012).

Rock and fault material constitutive models combining a yield model with an equation of state are used for the geologic units. The explicit modeling of the faults and the blocks allow for realistic sliding and interaction. Figure 1 displays the Geologic Framework Model (GFM) developed for SPE-2.

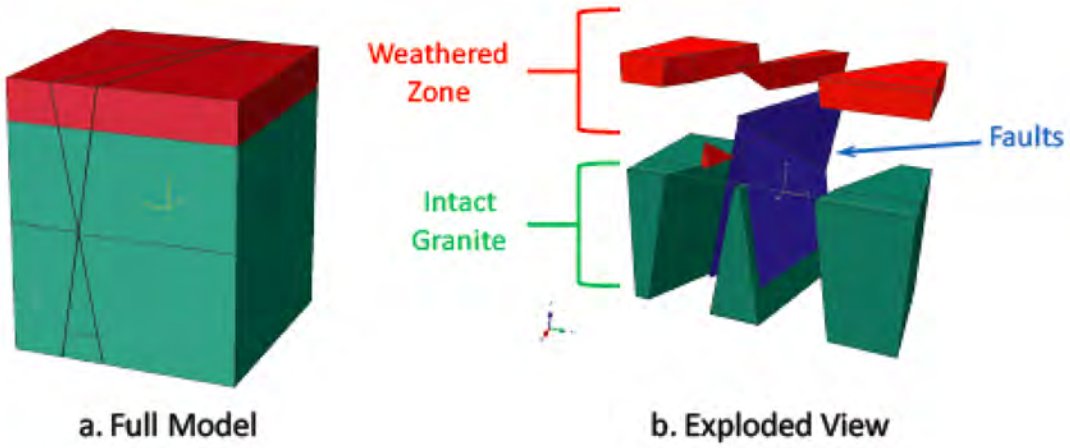


Figure 1. GFM model of SPE-2 for CEL simulation.

The CEL code allows for automatic interaction between the two computation regimes. The expanding explosive source pressure boundary develops full contact with the surrounding rock cavity. This results in full pressure and kinematic load transfer on an element-by-element, time-step by time-step basis. This avoids the shortcomings of mapping between two separate codes that can be compromised by either 1) incomplete environment transfer or 2) temporal and spatial inaccuracies.

Figures 2 and 3 are snapshots in time (at 8 ms and 17 ms, respectively), of displacement contours on a vertical slice through the model. The slice intersects the surface at A-A' identified in Figure 4 and passes through the charge center at depth. These figures clearly show the effect of the faults on the shock propagation. The faults are thick (on the order of 0.3 m) and are filled with gouge material that forms an impedance mismatch with the surrounding rock. In the simulation this causes the shock in the central region to reflect off of the intersection between the two faults (seen in Figure 2), thus mitigating the strength of the direct vertically propagating shock entering the central block above the charge. Meanwhile, refracted waves travel up the outside of the fault surfaces (seen in Figure 3), causing excess motion in those regions.

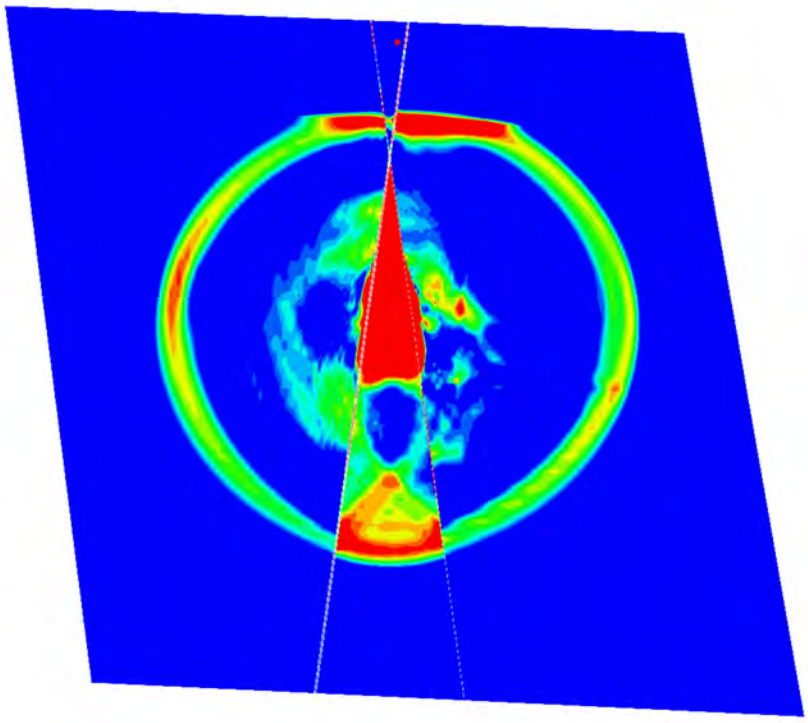


Figure 2. Displacement contours on a slice through the model at 8 ms.

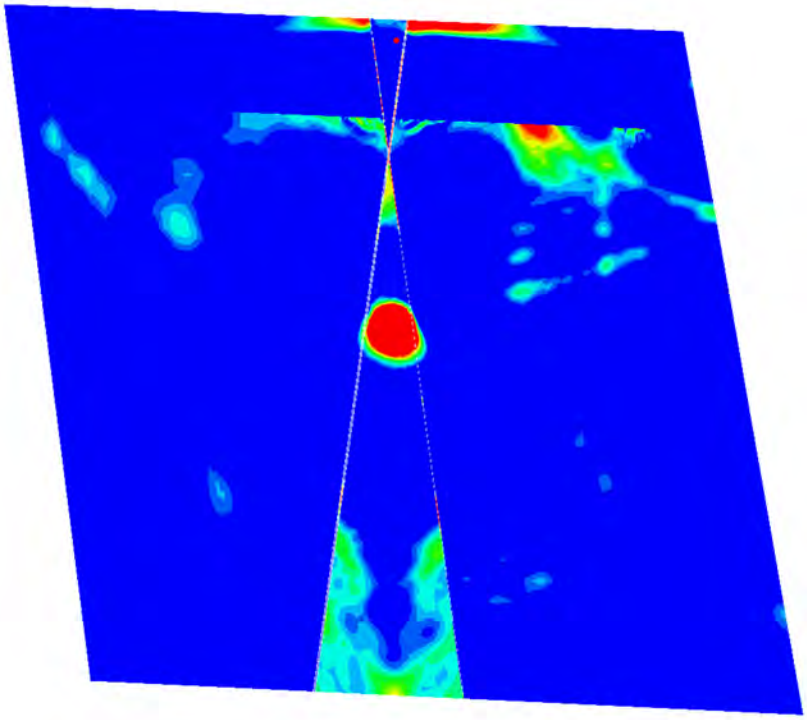


Figure 3. Displacement contours on a slice through the model at 17 ms.

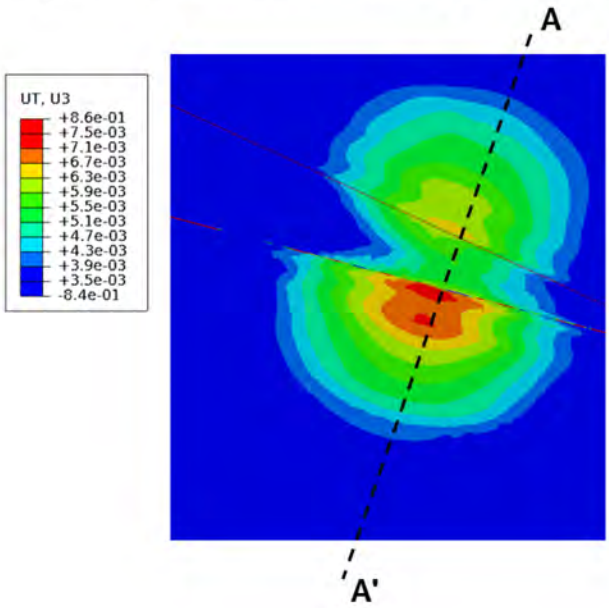


Figure 4. Final computed surface displacements (view looking down onto the ground surface at the SPE site).

This effect is manifest in the final computed displacements shown in Figure 4. In this figure we see a high region just on the outside of the southernmost fault.

A LIDAR–based evaluation of the pre- to post-shot surface elevation of the SPE test bed was conducted for the SPE-2 event. The permanent displacement caused by the event is shown in Figure 5. Qualitatively, the observed

displacement results are quite similar to the computed displacement (Figure 4). We note that there is a shift to the south in the computed displacement relative to the observed displacement.

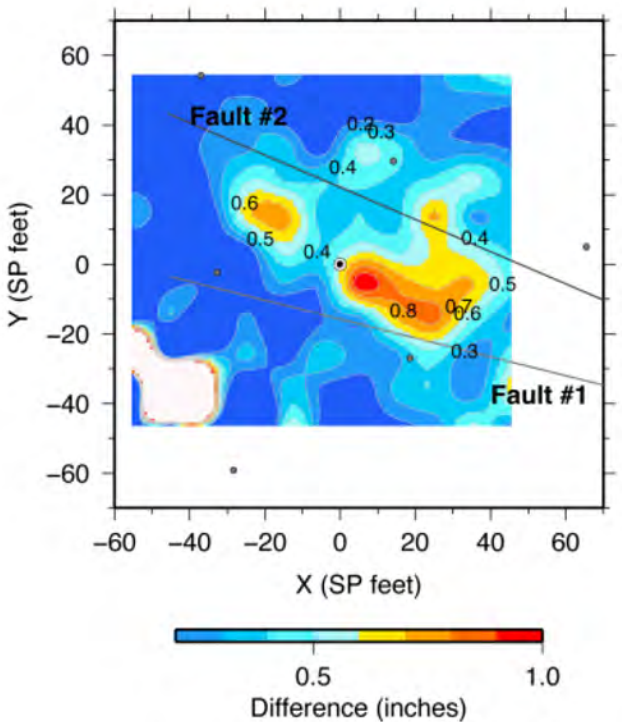


Figure 5. Permanent surface displacement from the LIDAR survey.

We recall that the faults were actually only measured in a borehole at about the 100-ft depth and the lines shown in these figures for the two faults are only projections to the surface of those single point measurements. Consequently the faults located in the simulation may not be accurate. We submit that if the phenomenology identified in the simulations is correct so that the uplifted region is on the outside of the fault block, then the proper alignment of the fault can be identified by the location of the uplift region seen in the LIDAR results as shown in Figure 6.

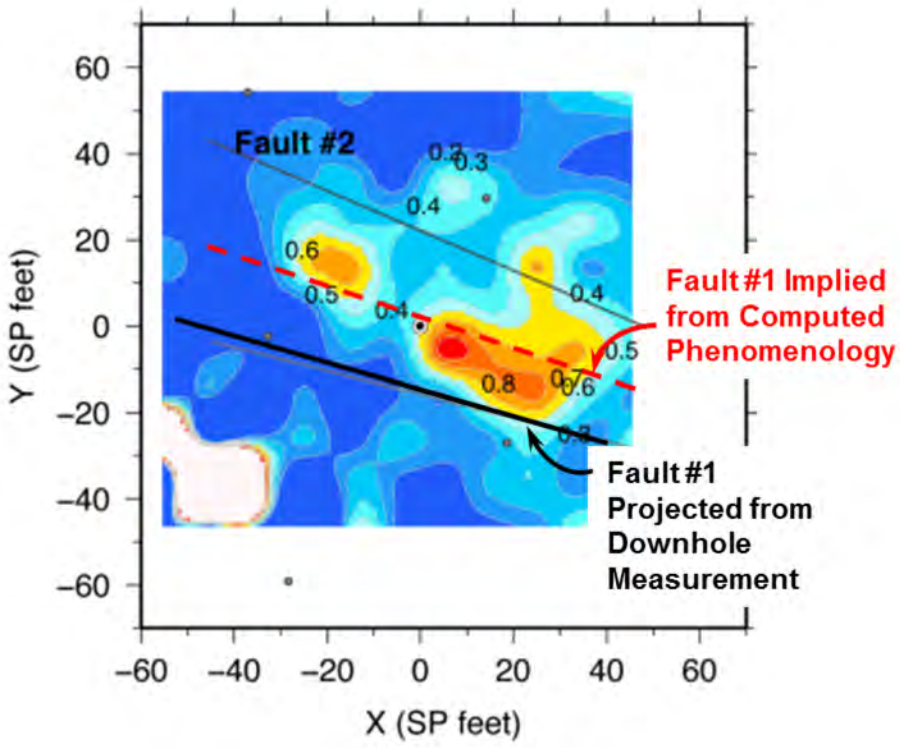


Figure 6. Possible actual location of Fault#1 based on computed phenomenology compared to LIDAR measurements.

CONCLUSIONS AND RECOMMENDATIONS

Explicit modeling of faults in the SPE test bed leads to response that is similar to the measured displacements. If the computed phenomenology is correct it is likely that the single point projection for the faults is not accurate. We recommend additional site characterization to identify the actual location of the faults. This will lead to better future modeling, and could confirm the phenomenology identified from simulations already accomplished.

In addition to the two major faults, borehole logs indicate three major joints sets that pervade the test bed area. We plan to use the general contact capability of our code and will model the geologic units as a compilation of discrete blocks. This will not be a “discrete element” calculation and thus will not have the shortcomings, such as block lack of deformability and constitutive response that characterize such modeling. The blocks will be separate Lagrange “parts” with full compliant contact between adjacent blocks. The Lagrange constitutive response will include a tensile damage and failure model developed from laboratory data on the local materials.

ACKNOWLEDGEMENTS

We thank Maggie Townsend (NS Tech) for valuable conversations and insights into the geology of the SPE site.

REFERENCES

Shellum, C. and P. Fisher, Springfield Research Facility (1996). Written communication to G. Baladi, Defense Special Weapons Agency. Subject: *Mechanical Properties for Climax Granitic Rock, NTS*. October 4, 1996.

Townsend, M., L. B. Prothro, and C. Obi (2012). Geology of the Source Physics Experiment Site, Climax Stock, Nevada, National Security Site, DOE/NV/25946-1448, 707pp.

SEISMIC WAVE GENERATION AND PROPAGATION FROM COMPLEX 3D EXPLOSION SOURCES

Jeffry L. Stevens and Michael O'Brien

Science Applications International Corporation

Sponsored by Air Force Research Laboratory

Award No. FA9453-11-C-0232
Proposal No. BAA11-39

ABSTRACT

We are investigating generation of complex seismic waves by explosions in media with realistic 3D heterogeneity, including topography. We are using available information on subsurface heterogeneity from nuclear test sites to develop 3D models that have the characteristics of the emplacement media for actual nuclear tests. We then run calculations in these structures and compare results with near field, regional and teleseismic data. Since we will never have complete information on the subsurface structure, we do not expect exact matches of the data, but if the heterogeneous characteristics of the media are correct, we expect the characteristics of the calculated data and the variations in the calculated data to be similar to those of the observed data. We particularly want to understand why shear waves are generated by all underground nuclear explosions.

Three dimensional calculations are required to simulate horizontal variation in strength and material properties as well as non-isotropic tectonic release. The extra degree of freedom provided in three dimensions makes generation of shear waves much easier than with the restriction to axisymmetric geometry. A three dimensional explosion source can be represented by a full moment tensor source plus dipoles in any direction. The dipoles are equivalent to point forces and do not have a moment tensor representation. This type of source is not generally considered in explosion modeling, and while it must vanish in the long period limit, it can be significant at frequencies of importance to nuclear monitoring.

We have developed a 3D nonlinear finite element code designed for calculation of explosions in 3D heterogeneous media with well-tested material models and including gravity; and implemented interface codes using the representation theorem that propagate the numerical solution from the source region to regional and teleseismic distances. We performed calculations in the presence of topography and lateral elastic and nonlinear heterogeneities in order to look at the effect these variations cause on explosion-generated seismic waves. Topography is implemented by gradually distributing offsets of the grid from top to bottom and heterogeneities are implemented by setting different material properties from the background properties in different areas.

The variation in overburden pressure with depth is very important in nonlinear calculations because strength is pressure dependent and so material becomes much weaker at shallow depths. Because of this we need to bring the grid into gravitational equilibrium before running an explosion calculation. This is done by starting with an approximate solution for overburden pressure in the grid and then running an initial calculation without the explosion. While this can be accomplished relatively easily for a plane-layered structure, bringing the grid to gravitational equilibrium in a structure with significant topography has proven to be difficult. We have experimented with several approximate solutions, but none have been good enough to allow the equilibrium runs to be completed without taking considerable time.

We performed two 3D nonlinear calculations of the Non-Proliferation Experiment (NPE) using material models previously used for modeling this event with a two-dimensional axisymmetric calculation. We ran the calculation with 3D topography, using the actual topography of the site, and ran a calculation with flat topography for comparison. As other researchers have looked at scattering effects due to topography, we are particularly trying to model the differences in waveforms due to nonlinear effects together with topography. Although there are some noticeable effects such as generation of SH by surface topography, the differences between waveforms at most locations with and without topography are small.

We performed a 3D calculation of the Shoal underground nuclear explosion including tectonic prestress. This event had strong heterogeneity in near field waveforms and is in a region under primarily extensional tectonic stress. Including prestress in the calculation causes variations in the late time near-field waveforms similar to those observed in Shoal.

OBJECTIVES

The objective of this project is to investigate generation of complex seismic waves by explosions in media with realistic 3D heterogeneity, including topography. This is being accomplished using a recently completed 3D finite element code designed for explosion calculations, together with a method based on the exact representation theorem for propagating complex 3D calculations to the local, regional and teleseismic distances at which they are observed.

RESEARCH ACCOMPLISHED

Background and Motivation

This project follows a previous project on 3D numerical modeling and wave propagation. In that project, we did the following:

1. Developed a 3D nonlinear finite element code designed for calculation of explosions in 3D heterogeneous media with well-tested material models and including gravity;
2. Implemented interface codes using the representation theorem that propagate the numerical solution from the source region to regional and teleseismic distances;
3. Used the code to evaluate the effect of near source heterogeneity including non-linear material property variations, elastic variability and topography.

The reason that 3D calculations are important for understanding shear wave generation is that symmetry constraints imposed by 1D and 2D calculations act to suppress shear waves. Imposition of 2D axisymmetry requires that the motion generated by the explosion be identical in all horizontal directions through propagation of the shock wave, nonlinear deformation of the surrounding material, and rebound to a final state. Since the motion is never identical in all directions, shear waves will always be generated, and in fact shear waves are observed from all underground explosions. In this project we are attempting to develop realistic representative models for 3D near-source heterogeneity, followed by 3D explosion calculations in these models. We have also performed calculations for two specific events: the Non-Proliferation Experiment (NPE) and the Shoal underground nuclear test. For the Shoal explosion we included tectonic prestress corresponding to the expected stress state for that location in Nevada.

The CRAM3D Code

CRAM 3D is an explicit three-dimensional Lagrangian finite element code designed to run on multiple processors (Stevens and Xu, 2010; Stevens et al, 2011). For an explosion simulation, the cavity is placed near the center of the grid and is enclosed by a spider grid which facilitates applying the pressure boundary condition and rezoning elements (Figure 1). The well-tested nonlinear material models from CRAM 2D have been implemented in CRAM 3D. The code includes gravity and so includes the important effects that result from variation of overburden pressure with depth. Gravitational equilibrium is established by running an initial calculation with no source, followed by a second calculation including the explosion source. We have also recently implemented the capability to include tectonic prestress in the calculations.

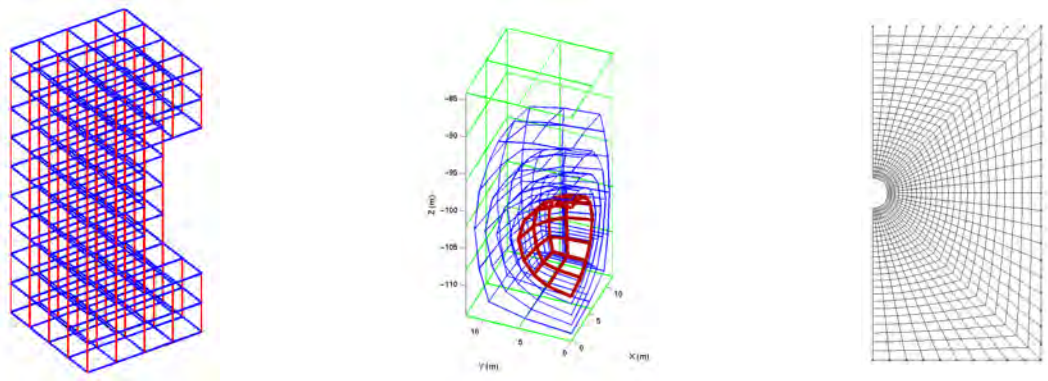


Figure 1. The CRAM 3D finite element outer grid (left) is rectangular. The inner grid (center) is shaped to match the shape of the explosion shock wave. CRAM2D uses a similar axisymmetric spider grid (right) in the region around the explosion.

Propagation with the Elastodynamic Representation Theorem

The representation theorem allows us to perform arbitrarily complex nonlinear calculations in the source region, and then propagate them with an appropriate Green's function. The representation theorem is exact. That is, no matter how complex the 3D motion is on the source region boundary, it will be correctly propagated by the representation theorem. The only exception is that it will not calculate the interaction of backscattered waves reflected from outside the source region with complexities of the source region.

In the three-dimensional numerical finite difference calculations, we save displacements and stresses due to the seismic source on a monitoring surface on the boundary of a rectangle (5 planar surfaces, excluding the upper surface), and calculate Green's functions from each point on the monitoring surface to the receiver and so the synthetic seismogram at the receiver point *X* outside of the monitoring surface is obtained by integrating over the monitoring surface s_M

$$u_i = \iint_{S_M} \left\{ G_j^i(\xi; X) * T_j^M(\xi) - u_j^M(\xi) * S_{jk}^i(\xi; X) n_k \right\} dA \qquad (1)$$

in the frequency domain, where $G_j^i(\xi; X)$ and $S_{jk}^i(\xi; X)$ are the Green's function and the stress tensor on the monitoring surface due to a unit impulsive force at *X* in direction *i*, T_j^M is the traction on the monitoring surface due to the seismic source, *u* is the displacement on the monitoring surface, and *n* is the normal to the monitoring surface. The operator * denotes convolution and the summation convention is assumed.

We use a plane-layered Green's function outside the source region. The Green's functions for the complete seismograms are derived from an algorithm based on the work of Luco and Apsel (1983) and Apsel and Luco (1983). The technique used for surface waves is similar to the method of Bache et al. (1982). The Green's functions for body waves are generated by a procedure similar to that described by Bache and Harkrider (1976) using a saddle point approximation to calculate a far-field plane wave for a given takeoff angle from a source in a plane-layered medium. Although the full waveform Green's functions generate the complete waveform, the other Green's functions can provide additional insight into the source and waveform generation.

Incorporation of Tectonic Prestress

The effect of tectonic prestress on explosion-generated surface waves has been discussed in many prior studies (e.g., Archambeau, 1972; Rygg, 1979; Toksoz and Kehrer, 1972). In most of these studies tectonic release was modeled as superposition of a tectonic source modeled as a double couple, multipole or moment tensor source, plus a point explosion source. The size of the tectonic source was determined by comparison with the observed Love waves and Rayleigh wave radiation pattern. Day et al. (1987) first attempted to perform numerical modeling of tectonic release through an axisymmetric calculation of the explosion Piledriver. Murphy et al. (2011) performed similar calculations for the North Korean explosions. To the best of our knowledge no one has previously performed numerical calculations for a three-dimensional stress field.

The first step in performing a calculation of tectonic release is to determine the stress state of the earth. While the stress state varies between regions, considerable work has also been done on this subject (e.g., Zoback, 2010). In general the vertical stress is equal to the overburden weight of the material above at any given point. The horizontal stresses may be larger or smaller than this value up to the point where failure due to frictional sliding relieves the stress. In most of the world tectonic stresses are applied continuously, and so the prestress is in general close to equilibrium with frictional sliding. The ratio of maximum to minimum principal stress, both reduced by pore pressure, is given by $\left[\mu + \left(\mu^2 + 1 \right)^{\frac{1}{2}} \right]^2$ where μ is the coefficient of friction. For a typical coefficient of friction of 0.6, this ratio is 3.1, so the difference between principal stresses can be substantial and the effect on seismic waves potentially large. In our calculations, we use the normal overburden calculation

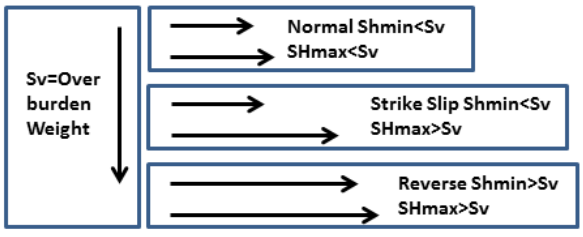


Figure 2. Stress regimes vary by region. Horizontal stresses may be substantially larger or smaller than the vertical stress.

to determine the vertical stress, and then modify the horizontal stresses to some fraction of the frictional limit. This is the initial stable state of the calculation prior to introduction of the explosion. Note that although the vertical stress is still equivalent to the overburden weight, the pressure is not, and it may be either increased or reduced by the tectonic stresses. Since material strength increases with pressure, this also can substantially affect the seismic source. In general, normal faulting regimes will amplify seismic signals, while reverse faulting regimes will decrease seismic signals; strike-slip regimes could do either (Figure 2).

Incorporation of Topography

CRAM3D incorporates topography by gradually distributing offsets of the grid from top to bottom so that change in cell dimensions is gradual rather than abrupt at the surface. The main difficulty in implementing topography is establishing gravitational equilibrium. The variation in overburden pressure with depth is very important in nonlinear calculations because strength is pressure dependent and so material becomes much weaker at shallow depths. Because of this we need to bring the grid into gravitational equilibrium before running an explosion calculation. As mentioned above, this is done by starting with an approximate solution for overburden pressure in the grid and then running an initial calculation without the explosion. While this can be accomplished relatively easily for a plane-layered structure, bringing the grid to gravitational equilibrium in a structure with significant topography has proven to be difficult. While the calculation will eventually come to equilibrium, adding topography is the equivalent of dropping a mountain onto the free surface, and so it takes quite a long time to come to equilibrium. We have experimented with several approximate solutions (e.g., Liu and Zoback, 1992), but have not as yet found a solution that allows the equilibrium run to be completed without taking considerable time. The calculated displacements caused by topography close to the NPE calculation are shown in Figure 3.

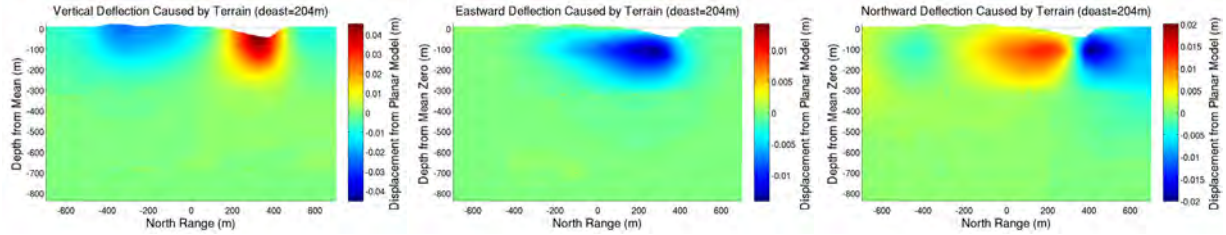


Figure 3. From left to right, vertical, eastward and northward displacements caused by topography along a slice 240 meters from the NPE shot point.

Calculation of the NPE

As our first calculation of a historical event with 3D heterogeneity, we model the Non-Proliferation Experiment (NPE), including the surface topography. The NPE was a chemical explosion with yield equivalent to one kiloton of TNT. The explosive is 1.315 kilotons of a 50/50 ANFO/emulsion mix in a cylindrical cavity centered at 389 m depth, 7.7 m in radius (horizontally) and 5.2m in height (vertically). We previously modeled this event in a two-dimensional axisymmetric calculation (Stevens et al, 2004), and initially used the same material properties, which were derived from Rimer et al (1994) for the 3D calculation. The material geology at the NPE site is based on that of the nearby Misty Echo event and consists of four layers. Layers 1 and 4 are non-porous, and layers 2 and 3 have porosities of 3% and 0.5% respectively. Comparison of the initial calculations with recordings from this event showed that calculated arrival times were early relative to the data, so porous moduli in the material were reduced so that P-velocities were more consistent with the observed arrival times, similar to material velocities used by Kamm and Bos (1995).

Figure 4 shows the actual topography near the NPE (National Elevation Dataset 1/3 Arc-Second http://seamless.usgs.gov/ned13.php). For this calculation, we modeled the area within 650 meters of the explosion. Even that relatively small area has substantial topography, with elevation differences of up to 140 meters. The strongest topographic changes are along a canyon to the north and a ridge to the south. The calculation area is tapered at the edges to bring it to a constant elevation at and outside the monitoring surface that is used to propagate the calculation as described above.

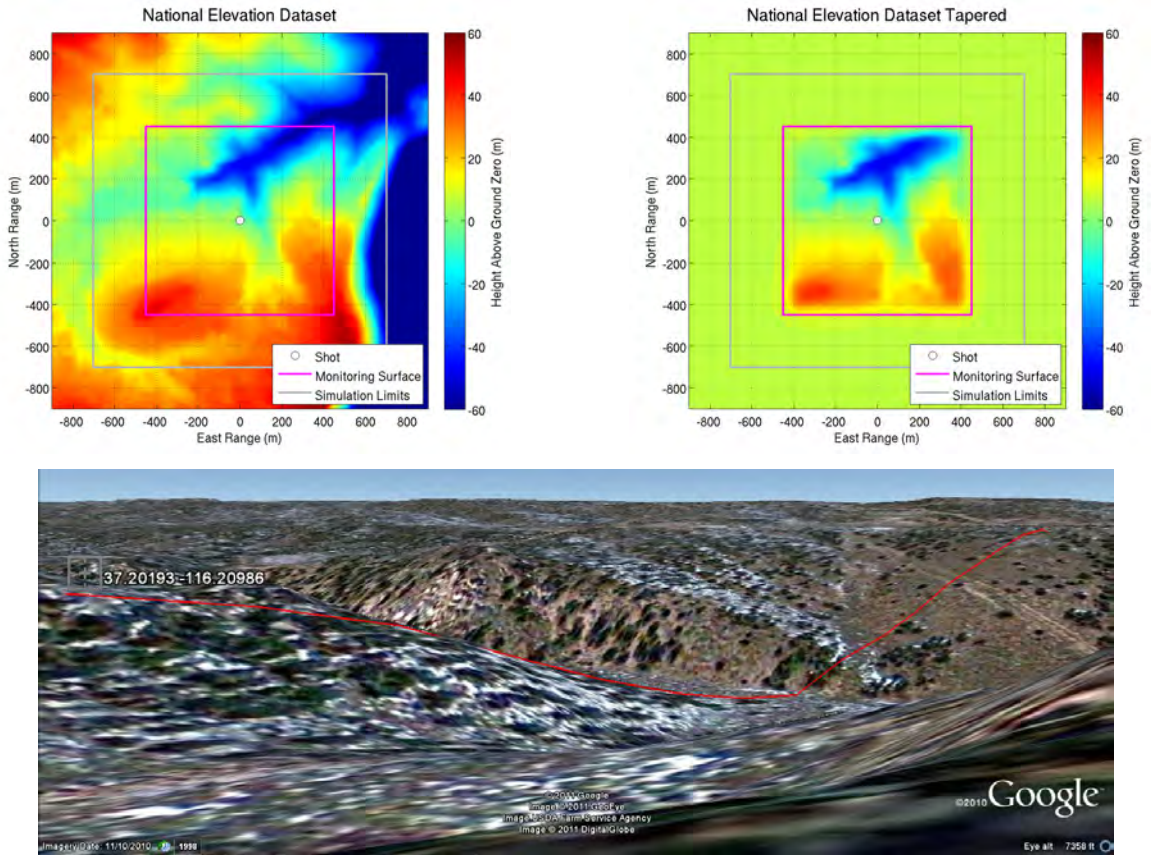


Figure 4. Topography around the area of the NPE calculation (top left) and the topography on the CRAM grid surface (top right). Lower figure shows a line due north from directly above the explosion to the edge of the grid.

Figure 5 (left) shows the pressure field output from the calculation with topography at several times. The upgoing shock wave interacts with the surface in a complicated way causing distortion of the reflected waves. Figure 5 (right) shows the region of nonlinear deformation and tensile cracking. Nonlinear deformation near the explosion is approximately spherical, but elongated and slightly offset vertically. The region of cracking is confined to near the free surface. This explosion is deeply overburied, so there is less asymmetry than in a normally buried explosion.

Figure 6 shows the calculated and observed velocity waveforms at three points on the free surface. Spall is indicated by a linear trending velocity with a slope of g, and is readily apparent in the ground zero waveform and also visible in the more distant surface stations. The match between calculated and observed waveforms is quite good.

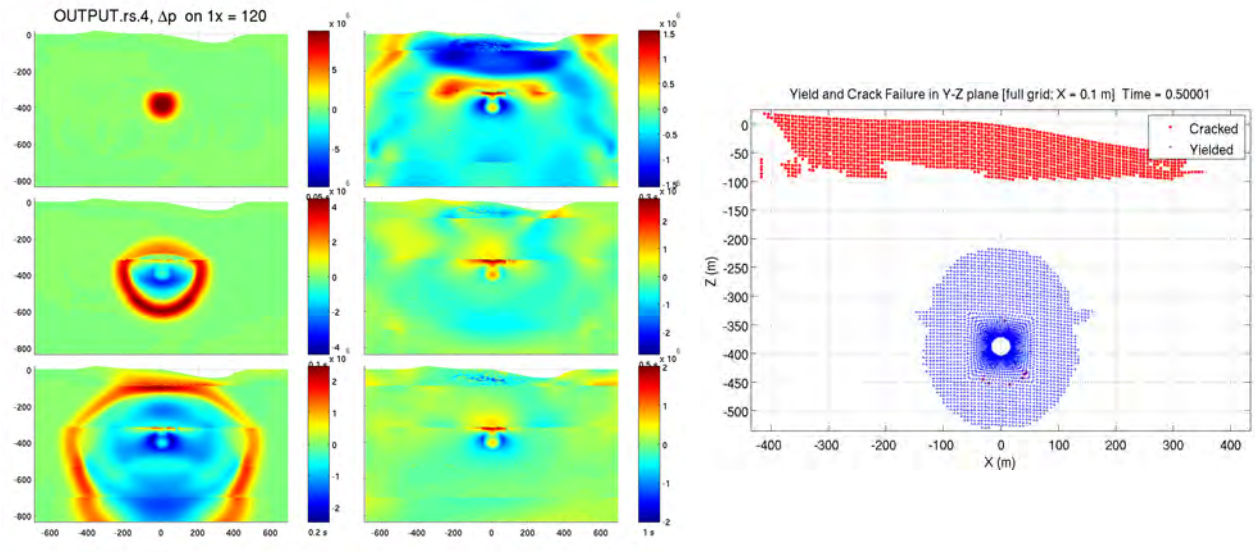


Figure 5. Left: Pressure field along a vertical slice 120 meters from the origin at 6 times: 0.05, 0.1, 0.2, 0.3, 0.5 and 1.0 seconds. Note the strong interactions between the shock wave and both the free surface topographic features and material layer boundaries. Right: final nonlinear deformation along a cross section through the source showing regions of yielding and tensile cracking.

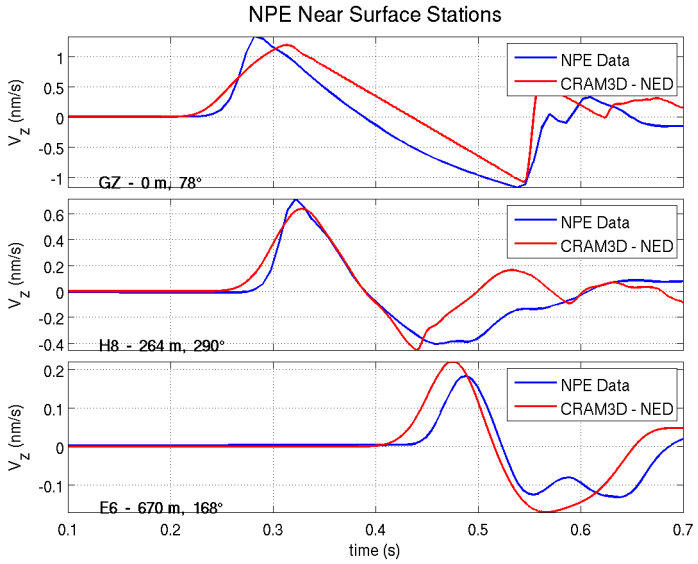


Figure 6. Comparison of calculated and observed waveforms from the NPE on the surface at three locations: ground zero, immediately above the explosion, and at distances of 264 and 670 meters. Note the distinct spall phase that decreases in duration with distance in both the data and the calculation.

In order to assess the effect of topography distinct from other mechanisms that might affect waveforms, we also ran a calculation with flat topography. In general the results are not very different. With topography there is some tangential motion not present in the flat calculation and small differences in waveforms, but the differences are not significant in most cases. Figure 7 shows a comparison of near field observed and calculated waveforms at shot depth. In a uniform medium only the radial component would be nonzero. However, the free surface interaction causes a large arrival on the vertical component at about 0.7 seconds. Neither the flat nor topographic calculation predicts significant tangential motion at this location. Although there is motion on the tangential component, the

clear P arrival and strong resemblance to the vertical component suggests that the motion is mostly off-axis vertical or radial motion rather than true tangential motion.

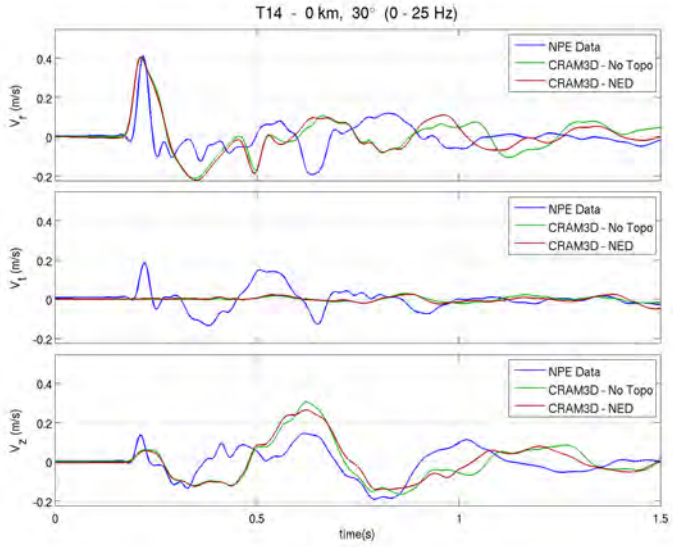


Figure 7. Shot level calculated and observed waveforms at a distance of 500 meters. Observed tangential motion is most likely off-axis radial and/or vertical motion. Blue line: NPE data, Green line: calculated velocity without topography, Red line: calculated velocity with topography.

We used the representation theorem to calculate waveforms for comparison with observations at a number of locations. We used an earth model derived by merging the local NPE model of Rimer et al (1994), and the regional 3D model of Myers et al (2007). The Q structure used in the calculation is based on Swanger's Law, Q=β/10 where β is shear velocity. The calculated and observed waveforms at ELK are shown in Figure 8. The waveforms are generally similar, and the relative P and S amplitudes are quite good. Arrival times are earlier in the observations than the calculation, indicating that the structure used is somewhat slower than the actual earth structure between the NPE and ELK.

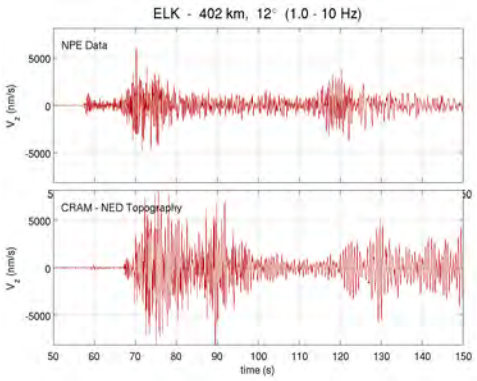


Figure 8. Observed (top) and calculated (bottom) waveforms from the NPE at station ELK at a distance of 400 km.

Calculation of Shoal

Shoal was a 12.5 kiloton nuclear explosion detonated near Fallon, Nevada (Weart, 1965). There were three near-field shot level recording stations located in three directions each at about 590 meters from the shot (Figure 9). The minimum principal stress Shmin in this part of Nevada is in extension. It is unclear from regional tectonics whether the maximum horizontal stress SHmax is less than or greater than the vertical stress Sv. For the purpose of

this calculation, we made SHmax 20% larger than Sv, and made Shmin 95% of the critical stress corresponding to frictional sliding with a coefficient of friction of 0.6. The stress state in the upper kilometer is shown in Figure 10.

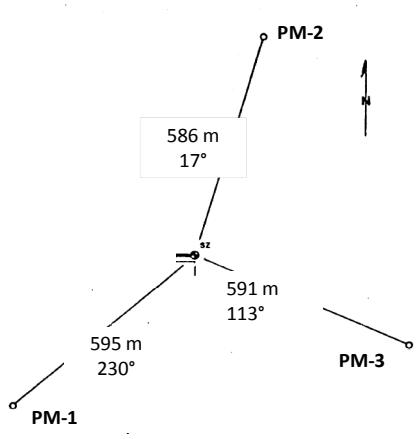


Figure 9. Location of the Shoal explosion and the three near-field shot level recording stations

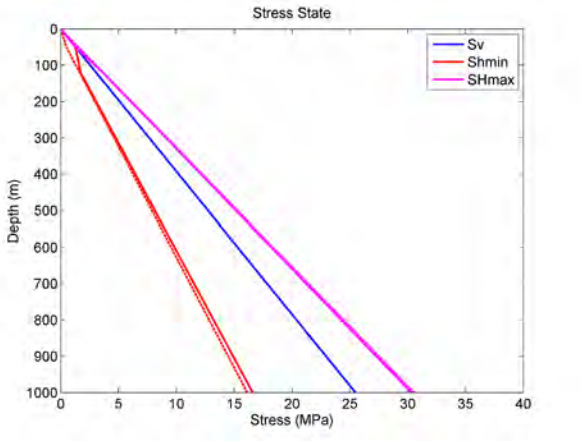


Figure 10. Vertical and horizontal stresses used in the calculation shown vs. depth. Dashed lines indicate the critical stress limited by balance against friction.

Figure 11 shows the waveforms observed at the three stations compared with calculated waveforms at the same depth in the directions of minimum and maximum horizontal stress. One of the surprising aspects of the data from this event is the strong directionality of the shot-level seismic waveforms, in particular the fact that the final displacements were so different at the three stations. We see a similar effect in our calculations. The late time displacement is amplified in the direction of minimum principal stress compared to the other directions. PM-3, the station with the largest displacement, is in the direction of the regional tectonic minimum principal stress, so prestress is very likely a strong contributor to the differences in the observed displacements.

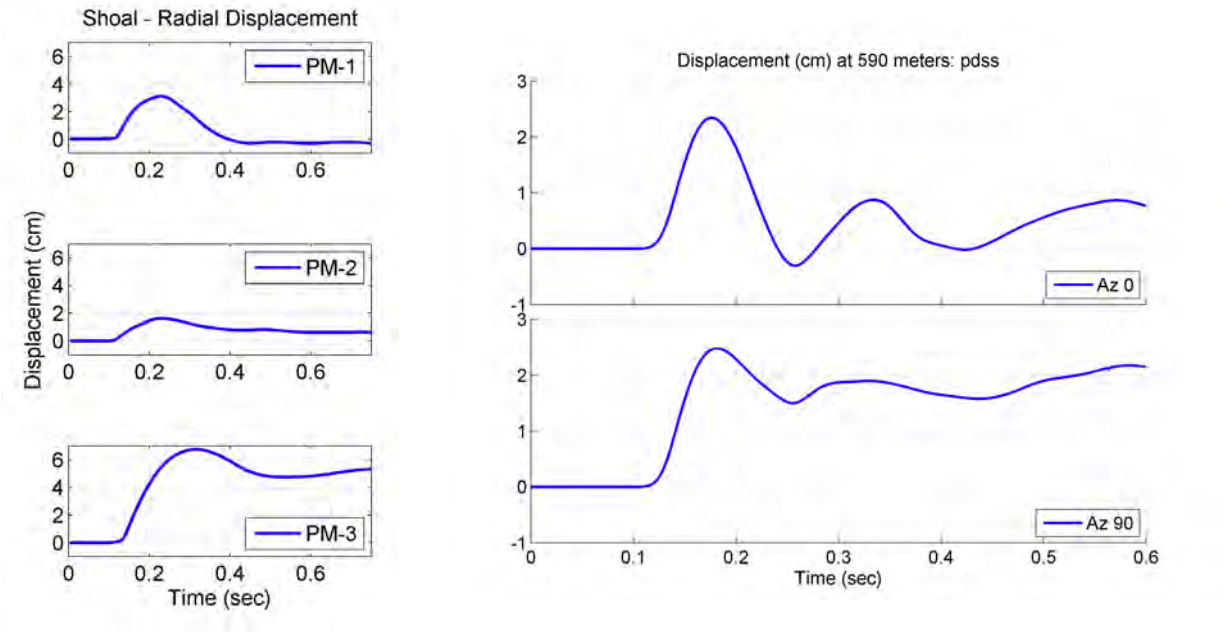


Figure 11. Left: observed displacement waveforms at the three shot-level Shoal recording stations. Right: calculations with prestress in the directions of maximum (Az=0) and minimum (Az=90) horizontal stress. Both data and calculations show enhanced late time displacements in the direction of minimum principal stress.

General 3D Structural Variability

We can calculate explosions in 3D heterogeneous media and propagate the results of those calculations, and would like to ensure that the subsurface heterogeneity is consistent with the real earth so that the calculations are relevant to nuclear monitoring. There are two obvious common types of heterogeneity: 1) variability in elastic properties (moduli and density) and 2) variability in strength. Measurement of granite properties near SHOAL, for example, show density ranging from 2.4-2.7 gm/cm^3, compressional velocity ranging from 5.27-5.7 km/sec and shear velocity ranging from 2.89-3.11 km/s. This is enough difference to cause distortion in the wavefront as it passes through the granite media.

Variability in strength is likely to be the stronger effect. Almost all rock is cracked and jointed, and although the cracks and joints are under substantial overburden pressure, they are still much weaker than the intact rock, and the rock as a whole will be weaker if it contains a higher density of cracks and joints. In our previous work on modeling of near field data in Degelen granite (Stevens et al, 2003), we found that rock strength could be modeled fairly well by several nonlinear models, but that the strength varied substantially, with the rock near a few explosions exhibiting much higher strength than other explosions. We are attempting to model nonlinear variability using a variable strength model based on a distribution of cracks and joints in the rock, with crack size and density based on nuclear test site observations and measurements. Figure 12, for example, shows the pre-shot fracture density measured in drift walls prior to 3 Degelen explosions (details are given in Rimer et al, 1998). The amount of variability in fracture density implies a corresponding variability in rock strength.

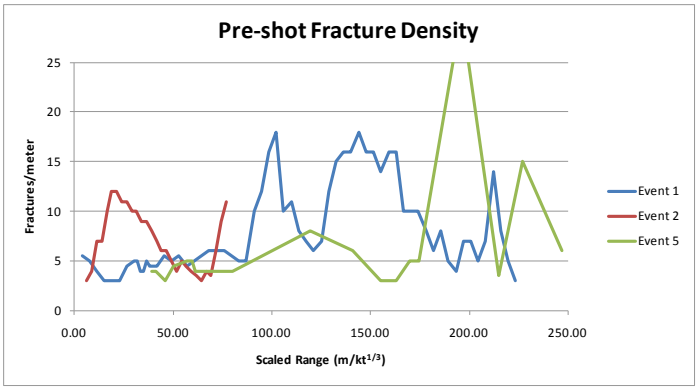


Figure 12. Preshot fracture density measurements prior to 3 Degelen explosions (from Rimer et al, 1998)

CONCLUSIONS AND RECOMMENDATIONS

We are working to understand the effects of 3D structural variations on seismic waves from underground explosions, using a 3D nonlinear finite element program to run calculations with 3D heterogeneity. We have implemented the capability to include tectonic prestress as well as material property and strength variations. We have run two specific calculations: for the NPE and for Shoal. The Shoal calculation including prestress shows a distinct variability in near field waveforms with azimuth, similar to observations from this event. We have implemented calculations with topography and used it in the NPE calculation. We have experimented with several ways to initialize the calculation with topography to gravitational equilibrium, but a more efficient solution is still needed. We are working to develop models for the calculations that are consistent with actual subsurface variability at test sites.

ACKNOWLEDGEMENTS

We thank Steve Myers of Lawrence Livermore National Laboratories for providing the 3D earth model and topography for the NPE site.

REFERENCES

Apsel, R. J. and J. E. Luco (1983), On the Green's Functions for a layered half-space, Part II, *Bull. Seismol. Soc. Am.* **73**, 931–951.

Archambeau, C. B. (1972). The theory of stress wave radiation from explosions in prestressed media, *Geophys. J.* **29**, 329–366.

Bache, T. C. and D. G. Harkrider (1976). The body waves due to a general seismic source in a layered earth model, *Bull. Seismol. Soc. Am.* **66**, 1805–1819.

Bache, T. C., S. M. Day, and H. J. Swanger (1982), Rayleigh wave synthetic seismograms from multi-dimensional simulations of underground explosions," *Bull. Seismol. Soc. Am.* **72**, 15–28.

Day, S. M., J. T. Cherry, N. Rimer, and J. L. Stevens (1987). Nonlinear model of tectonic release from underground explosions, *Bull. Seismol. Soc. Am* **77**, 996–1016.

Kamm, J. R. and R. J. Bos (1995). Comparison of chemical and nuclear explosions: numerical simulations of the non-proliferation experiment, Los Alamos National Laboratory report LA-12942-MS.

Liu, L., and M. D. Zoback (1992). The effect of topography on the state of stress in the crust: application to the site of the Cajon Pass Scientific Drilling Project, *J. Geophys. Res*. **97**(B4), 5095–5108, doi:10.1029/91JB01355**.**

Luco, J. E. and R. J. Apsel (1983). On the Green's Functions for a layered half-space, Part I, *Bull. Seismol. Soc. Am*. **73**, 909–929.

Murphy, J. R., J. L. Stevens, B. C. Kohl, T. J. Bennett, and B. W. Barker (2011). Supplemental analyses of the seismic characteristics of the 2006 and 2009 North Korean nuclear tests, in *Proceedings of the 2011 Monitoring Research Review: Ground-Based Nuclear Explosion Monitoring Technologies*, LA-UR-11-04823, Vol. 1, pp. 513–523.

Myers, Stephen C., Jeffery L. Wagoner, and Shawn C. Larsen (2007). Numerical experiments investigating the source of explosion S-waves, in *Proceedings of the 29th Annual Monitoring Research Review: Ground-Based Nuclear Explosion Monitoring Technologies*, LA-UR-07-5613, Vol. 1, pp. 175–184.

Rimer, N., W. Proffer, E. Halda and R. Nilson (1994). Containment related phenomenology from Chemical Kiloton," Maxwell Laboratories technical report to Defense Nuclear Agency, SSS-DTR-94-14405.

Rimer, N., K. Lie, J. L. Stevens, J. R. Murphy, and G. G. Kocharyan (1998). A micro-mechanical damage model for estimating seismic source characteristics of underground explosions in hardrock, Maxwell Technologies Technical Report submitted to Defense Special Weapons Agency, MFD-DTR-98-15985, January.

Rygg, E. (1979). Anomalous surface waves from underground explosions, *Bull. Seismol. Soc. Am*. **69**, 1995–2002.

Stevens, J. L., N. Rimer, H. Xu, G. E. Baker and S. M. Day (2003). Near field and regional modeling of explosions at the Degelen Test Site, SAIC final report to DTRA, SAIC-02/2050, January.

Stevens, J. L., G. E. Baker, H. Xu, T. J. Bennett, N. Rimer and S. M. Day (2004). The physical basis of Lg generation by explosion sources, SAIC Final Report submitted to the National Nuclear Security Administration under contract DE-FC03-02SF22676, December.

Stevens, Jeffry L. and Heming Xu (2010). Wave propagation from complex 3D sources using the representation theorem, in *Proceedings of the 2010 Monitoring Research Review: Ground-Based Nuclear Explosion Monitoring Technologies*, LA-UR-10-05578, Vol. 1, pp. 519–528.

Stevens, Jeffry L., Heming Xu, Michael O'Brien, Walter Nagy and Norton Rimer (2011). Wave propagation from complex 3D sources using the representation theorem, SAIC final report SAIC-11/3003 submitted to Air Force Research Laboratory, AFRL-RV-HA-TR-2011-1019, March.

Toksoz, N. and H. Kehrer (1972). Tectonic strain release by explosions and its effect on discrimination, *Geophys. J. R. Astr. Soc*. **31**, 141–161.

Weart, Wendell D. (1965). VELA UNIFORM, Project SHOAL, Project 1.1, Free Field Earth Motion and Spalling Measurements in Granite, Sandia Corporation final report VUF-2001 to the Advanced Research Projects Agency, February.

Zoback, M. D. (2010). *Reservoir Mechanics*, Cambridge University Press, 449 pages.

TOPOGRAPHIC SCATTERING AT LOCAL DISTANCES: INSIGHTS FROM MODELING OF SPE-ARIZONA DATA

Anastasia Stroujkova and Jessie L. Bonner

Weston Geophysical Corporation

Sponsored by the National Nuclear Security Administration

Award No. DE-AC52-08NA28655
Proposal No. BAA08-97

ABSTRACT

Ten single-fired explosions ranging in size from 1700 to 13,600 lbs. of a mixture of Ammonium Nitrate Fuel Oil (ANFO) and emulsion explosives were conducted in a southeastern Arizona copper mine as a part of Source Phenomenology Experiment (SPE-A). The main objective of the experiment was to quantify the differences in seismic source phenomenology for various types of explosions that affect local and regional seismograms. In this study we concentrated on two single-hole 1700 lbs explosions: an unconfined free-face explosion (B1) and a fully confined overburied explosion (B6). A moment tensor analysis by Zhou et al. (2005) has shown that Shot B1 was best modeled using a combination of a vertical dipole and a smaller isotropic component. Conversely, Shot B6 was well represented by an isotropic source with a smaller vertical dipole component.

At local distances we observed high *P/Rg* ratios compared to the amplitudes predicted using the flat layer model. In order to determine the effect of topography on *Rg* propagation and scattering we performed numerical modeling of the observed seismic traces using the software package WPP developed by Lawrence Livermore National Laboratory (e.g., Nilsson et al., 2007). To study the effect of scattering on different frequencies we used the source wavelets with center frequencies of 2 Hz, 4 Hz and 8 Hz and repeated all simulations for both flat and rough surface topography. An isotropic source ($M_{xx}=M_{yy}=M_{zz}=1$) was used for the majority of calculations. To study the effect of the source isotropy we performed a modeling experiment using a vertical dipole source ($M_{xx}=M_{yy}=0$, $M_{zz}=1$).

The results of the numerical simulations indicated that:

1) For the isotropic source at lower frequencies (0.5–4 Hz) the ratios between the *P* and *Rg* amplitudes are significantly higher for the observed data than for the synthetics. The scattering due to topography at these frequencies cannot explain significant *Rg* amplitude reduction.
2) At higher frequencies (6–8 Hz) the topographic scattering becomes important. The peak amplitude *P/Rg* ratios for the observed data significantly exceed the ratio for the synthetic data with flat free surface. Adding the surface topography produces more realistic seismograms with *P/Rg* ratios approximately matching the observed ratios in the order of magnitude.
3) Using a vertical dipole source can account for lower *Rg* amplitudes and explain high observed *P/Rg* ratios in the frequency range between 2–6 Hz. It can also explain the differences in the amplitude ratios between the free-face shot (modeled as a dipole) and the double-depth shot (modeled as an isotropic source).

These results show that the topographic scattering is an effective mechanism of *Rg*-to-*P* scattering at higher frequencies (above 6 Hz). Other mechanisms (e.g., scattering due to lateral velocity perturbations and variations in layer thickness) may be significant at lower frequencies to explain the *Rg* amplitude reduction compared to *P*-wave amplitude. Adding a vertical dipole source component may explain lower *Rg* amplitudes, particularly at low frequencies (below 4 Hz). Above 4 Hz the combined effect of the focal mechanism and the topography produces higher than observed amplitude decay rate with distance. It is possible that the vertical dipole component (e.g., due to spall) could be important at low frequencies, while at higher frequencies the source radiation is dominated by the isotropic component.

OBJECTIVES

Ten explosions with different yields were conducted at Morenci copper mine in Arizona as a part of the Source Phenomenology Experiments (SPE-A). The main purpose of the experiment was to study the explosion source characteristics as a function of the yield, depths of burial, and confinement conditions in variable lithologies. In addition, the differences between the single-fired test explosions and the delay-fired mining explosions were investigated. We performed numerical modeling of the observed seismic traces using the software package called WPP developed by LLNL (e.g., Nilsson et al., 2007). The objective of the modeling was to determine the effect of topography on *Rg* propagation and attenuation.

RESEARCH ACCOMPLISHED

The testing area is situated in Precambrian granite (Stump et al., 2005), with a shallow weathered layer (12–14 ft thick) with very low velocities (~1,200–2,000 ft/s). A second layer with velocities between 6,500 and 8,000 ft/s (40–50 ft thick) overlays faster velocities ranging from 10,000–15,000 ft/s. The explosive sources are buried below the weathered surface layer in the intermediate velocity granite. Figure 1 shows there is significant topography (1440 m at MR00 to 2068 m at MR04) along the source-to-station profile.

Table 1. Velocity model used for numerical simulations (from Stump et al., 2005)

Layer	H (km)	*P* (km/s)	*S* (km/s)	ρ (g/cm^3)
1	0.154	4.55	2.62	1.97
2	3.38	5.21	3.01	2.22
3	Half space	6.07	3.51	2.55

WPP Modeling

To simulate seismic waves generated by the explosions, we used Version 2.0 of the WPP software package. WPP solves the 3D wave equation using a second order numerical scheme. The current version of the software allows imposing the free surface boundary on a curved topography by creating a curvilinear mesh. It is also possible to make a computational mesh finer near the surface.

To perform the calculations we used the two-layer velocity model (Table 1) given in Stump et al. (2005). To parameterize the surface topography we used a global digital elevation model, created from images collected by the Japanese Advanced Spaceborne Thermal Emission and Reflection Radiometer (ASTER). The spatial resolution of the elevation model is 30 m. The topography read by WPP is spatially filtered based on the spacing of the computational grid. This filtering, however, should have a limited effect on the wavelengths of interest (on the order of 200 m for the lowest wavelength resolved by the computations).

In this study we concentrate on Shots B1 (free-face) and B6 (twice depth) (Table 2). Zhou et al. (2005) calculated the moment tensors for the SPE-A shots (Table 2). The resulting moment tensors for all explosions have horizontal components (M_{xx} and M_{yy}) that are similar in amplitude and shape, and an enhanced vertical component M_{zz}. This source anisotropy is related to the free surface and is more pronounced for shallow Shot B1. Figure 2 demonstrates the differences in the estimated time-dependent moment tensors between the free-face and twice depth shots. In order to match the amplitudes between the synthetics and the observed data we used the moment tensor components estimated by Zhou et al (2005) as $M_0=(M_{xx}+M_{yy}+M_{zz})/3$.

Table 2. Summary of the shots used in this report

Shot	Yield, lbs	Centroid Depth, m	sDOB, m/kt$^{1/3}$	Moment tensor (Zhou et al., 2005) x10^{13} N·m					
				M_{xx}	M_{xy}	M_{xz}	M_{yy}	M_{yz}	M_{zz}
B1 - Single Hole Free-Face	1,700	13	102	0.0497	0.0148	0.0550	0.0340	0.0425	0.1973
B6 - Single Hole 2x Depth	1,700	33	255	0.2802	0.0343	0.1025	0.2441	0.1111	0.4748

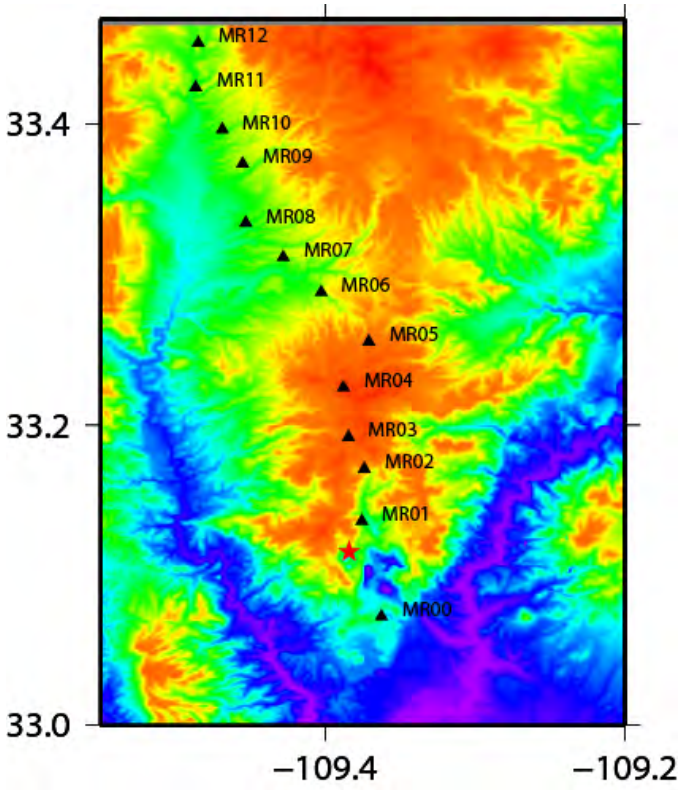


Figure 1. Station map showing topography from ASTER digital elevation model. Red star shows the test site.

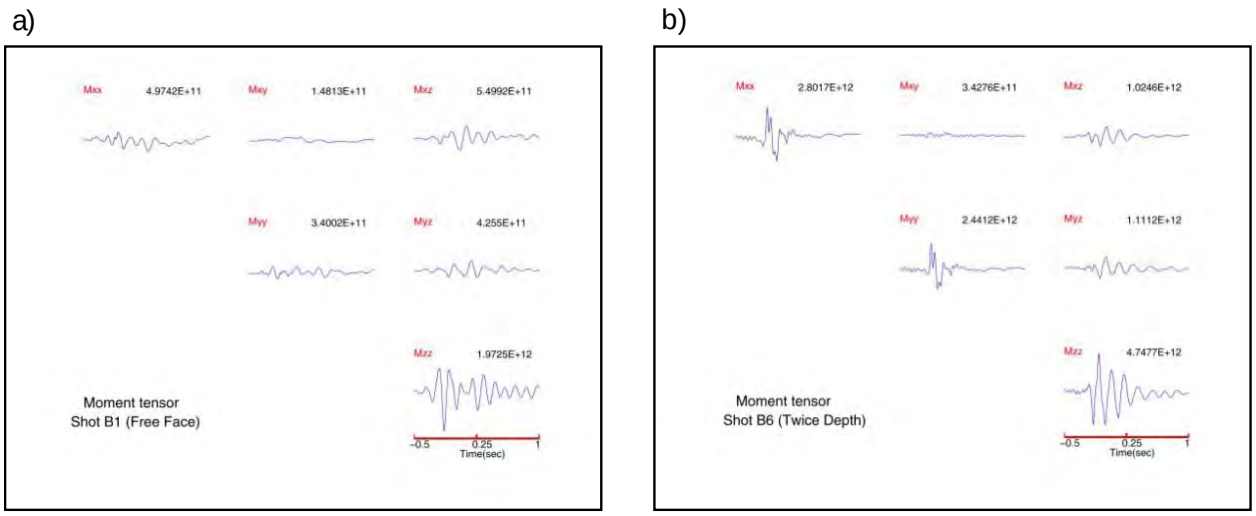


Figure 2. Time dependent moment tensor from Zhou et al. (2005): a) Shot B1, b) Shot B6.

The number of grid points per shortest wavelength of interest is an important parameter defining the solution error. Since shear waves have the lowest velocities, the shortest wavelength is given by:

$$\lambda_{min} = \frac{V_s^{min}}{f^{max}} \quad (1)$$

where V_s^{min} is the minimum shear velocity, and f^{max} is the largest significant frequency in the source time function. The number of grid points per wavelength (P) is given by:

$$P = \frac{V_s^{min}}{hf^{max}} \quad (2)$$

According to the Petersson and Sjogreen (2010), WPP gives reasonably accurate solution for $P \geq 15$, however this value can be made smaller in cases where there are significant uncertainties in material properties.

Table 3 summarizes the model parameters used in the simulations. We used the integral of the Ricker wavelet (denoted *RickerInt* wavelet in Peterson and Sjogreen, 2010) with f_0=2*Hz*, f_0=4*Hz*, and f_0=8*Hz* as the source time function (STF). According to the Peterson and Sjogreen (2010), the highest significant frequency for this wavelet is defined as $f_{max} \sim 2.5 f_0 = 5Hz$ for the 2*Hz* wavelet, f_{max}= 10*Hz* for the 4Hz wavelet, and f_{max}= 20*Hz* for the 8*Hz* wavelet. The slowest *S*-wave velocity for the model was 2620 m/s. Due to the computational limitations we had to reduce the computational domain and computed the synthetics for the stations MR00-MR07 only. The size of the computational domain was 28 km by 18 km (Figure 2). The spacing between the grid nodes depended on the wavelet frequency. Unfortunately the computational grid becomes prohibitively large for grid size of less than 30 m. We used the 3D grid with between 30 and 40 m spacing between the nodes in each direction with a mesh refinement in two upper layers to reduce the grid size to 15-20 m. Using Equation 2 and the parameter values from Table 1, we estimate the values of P for each run also provided in Table 3 (column 8). In some cases the value of P was lower than the recommended value of 15. In these cases we filter the synthetic traces below the frequency (f_{15}) recommended for the smaller computational error.

Table 3. Simulation parameters used in this study

Model	Topography	Source wavelet[2]	f_{max}, Hz	$M_{xx}/M_{yy}/M_{zz}$	V_s^{min}, m/s	h, m	P	f_{15}, Hz[4]
3 layers[1]	-	RI 2Hz	5	1/1/1	2620	40	13	4.4
3 layers	+	RI 2Hz	5	1/1/1	2620	40	13	4.4
3 layers	-	RI 4Hz	10	1/1/1	2620	40/20[3]	13	5.9
3 layers	+	RI 4Hz	10	1/1/1	2620	40/20	13	5.9
3 layers	-	RI 8Hz	20	1/1/1	2620	30/15	8.7	11.6
3 layers	+	RI 8Hz	20	1/1/1	2620	30/15	8.7	11.6
3 layers	-	RI 4Hz	10	0/0/1	2620	40/20	13	5.9
3 layers	+	RI 4Hz	10	0/0/1	2620	40/20	13	5.9

[1] 3 layer model from Table 1.
[2] *RickerInt* (RI) wavelet with different central frequencies was used in all computations
[3] The second number (if shown) represents the grid size at the surface in the upper layer due to grid refinement
[4] f_{15} is the highest frequency which can be resolved with the parameter P of at least 15

Figure 3 shows the snapshots of the vertical components of ground velocity for the 4 *Hz* wavelet. The snapshots computed using the topography (Figure 3b) clearly show the effects of the topographic scattering. The effect of the source anisotropy is demonstrated in Figure 3c, which shows the results computed for the vertical dipole. The *P*-wave amplitudes for the dipole source appear to be higher than for the isotropic source (compare Figure 3a and 3c) due to the reduction in the *Rg* amplitudes.

Figure 4 shows a comparison between the data and the synthetics for Station MR05. The seismograms in each panel show the observed data and the synthetics with the flat and the topographic/rough surface filtered in the same frequency band. An isotropic source was used to model Shot B6 (Figure 4a, b and c), and a vertical dipole was used to model Shot B1 (Figure 4d). At lower frequencies (Figure 4a, b) *Rg* amplitudes significantly exceed *P* amplitudes for both flat and rough surface synthetics. The differences between *P* and *Rg* for the recorded data are not as dramatic. At higher frequencies (Figure 4c) *Rg* amplitude is significantly degraded by topographic scattering. Notice that the vertical dipole source (Figure 4d) produces lower *Rg* amplitude than the isotropic source (Figure 4b), resulting in higher *P/Rg* ratio. Thus, the *Rg* amplitude reduction may be achieved by either scattering/attenuation, or by changing the moment tensor of the source.

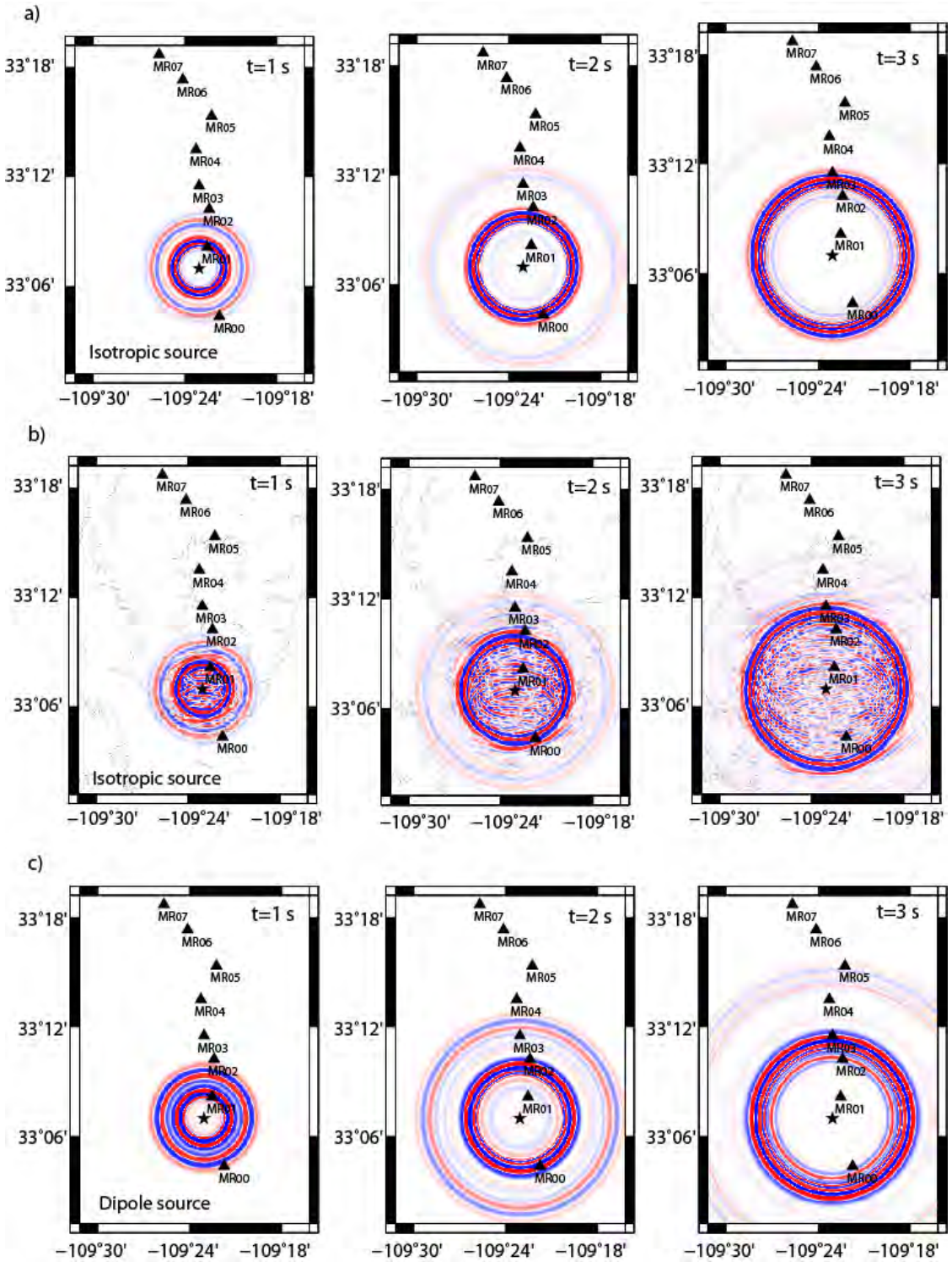


Figure 3. Snapshots of the vertical component of the displacement at the surface using 4 *Hz RickerInt* wavelet: a) isotropic source, flat free surface; b) isotropic source, free surface with topography; c) vertical dipole source, flat free surface. The snapshots are shown for 1s, 2s and 3s from the origin time.

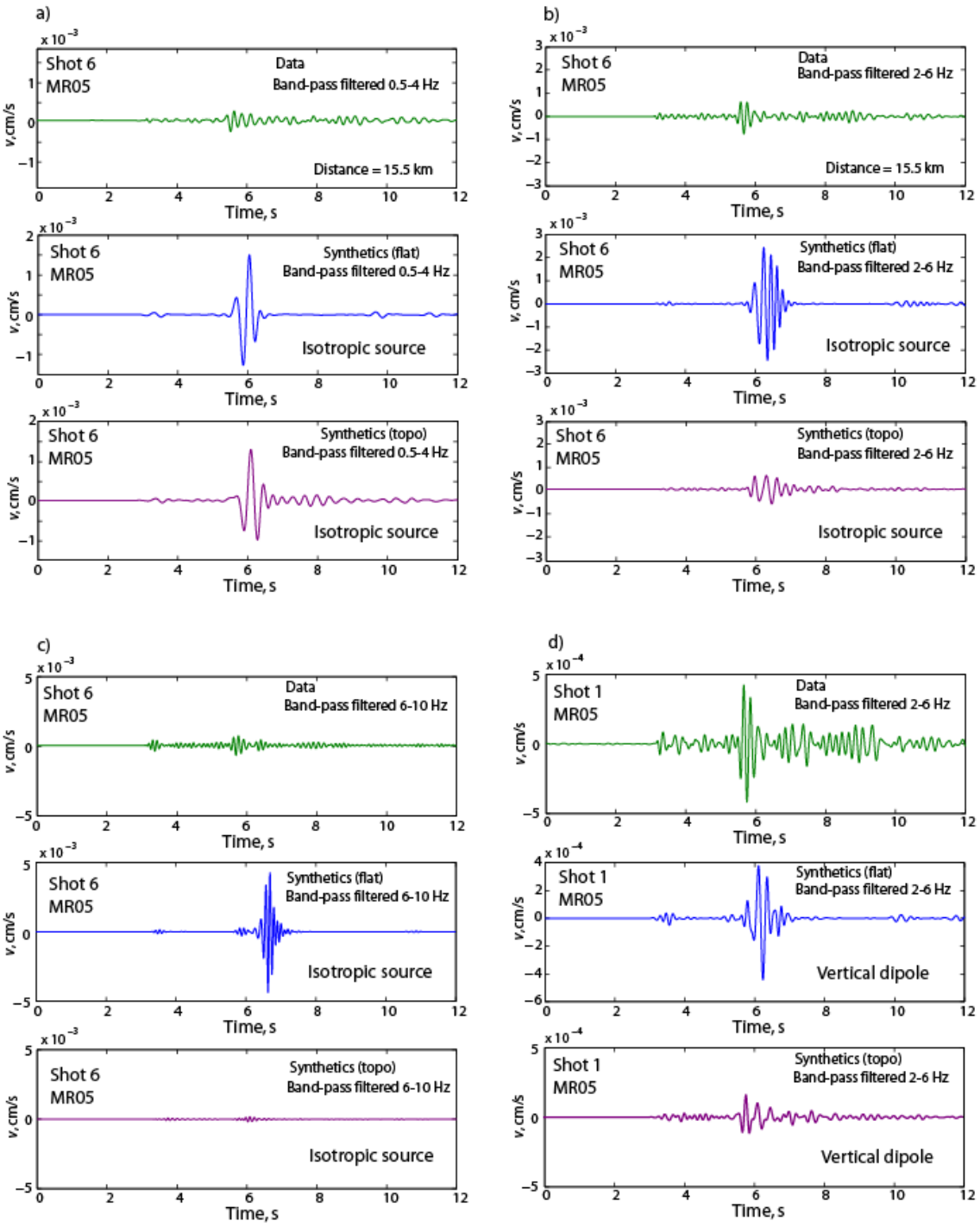


Figure 4. Velocity seismograms for Station MR05 for the data (green), flat synthetics (blue), and the synthetics with topography (purple). a) data and the synthetics (2 *Hz RickerInt* STF, isotropic) filtered between 0.5 – 4 *Hz*, b) data and the synthetics (4 *Hz RickerInt* STF, isotropic) filtered between 2 – 6 Hz, b) data and the synthetics (8Hz *RickerInt* STF, isotropic) filtered between 6 – 10 *Hz*, and d) data and the synthetics (4*Hz RickerInt* STF, vertical dipole) filtered between 2 – 6 *Hz.*

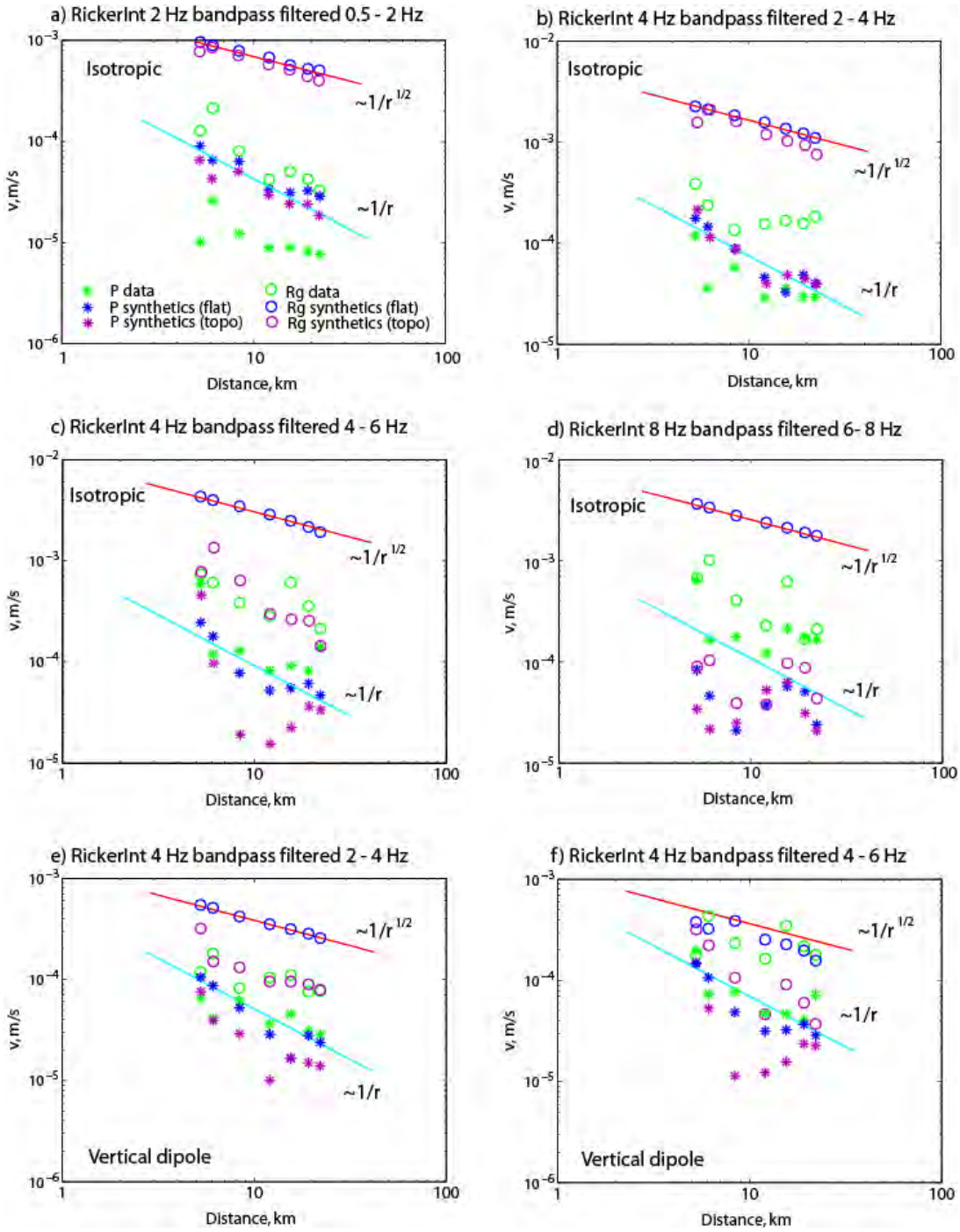


Figure 5. Amplitude reduction with range for the data (green), flat synthetics (blue), and the synthetics with topography (purple). The cyan and red lines shows the theoretical decay rate proportional to *1/r* and *1/r* $^{1/2}$ appropriate for the body and surface waves respectively: a) Shot 6 data and the synthetics (2 *Hz RickerInt* STF, isotropic) filtered between 0.5 – 2 *Hz*; b) Shot 6 data and the synthetics (4 *Hz RickerInt* STF, isotropic) filtered between 2 – 4 *Hz*; c) Shot 6 data and the synthetics (4Hz *RickerInt* STF, isotropic) filtered between 4 – 6 Hz; d) Shot 6 data and the synthetics (8 *Hz RickerInt* STF, isotropic) filtered between 6 – 8 *Hz*; e) Shot 1 data and the synthetics (4 *Hz RickerInt* STF, vertical dipole) filtered between 2 – 4 *Hz*; and f) Shot 1 data and the synthetics (4 *Hz RickerInt* STF, vertical dipole) filtered between 4 – 6 *Hz*.

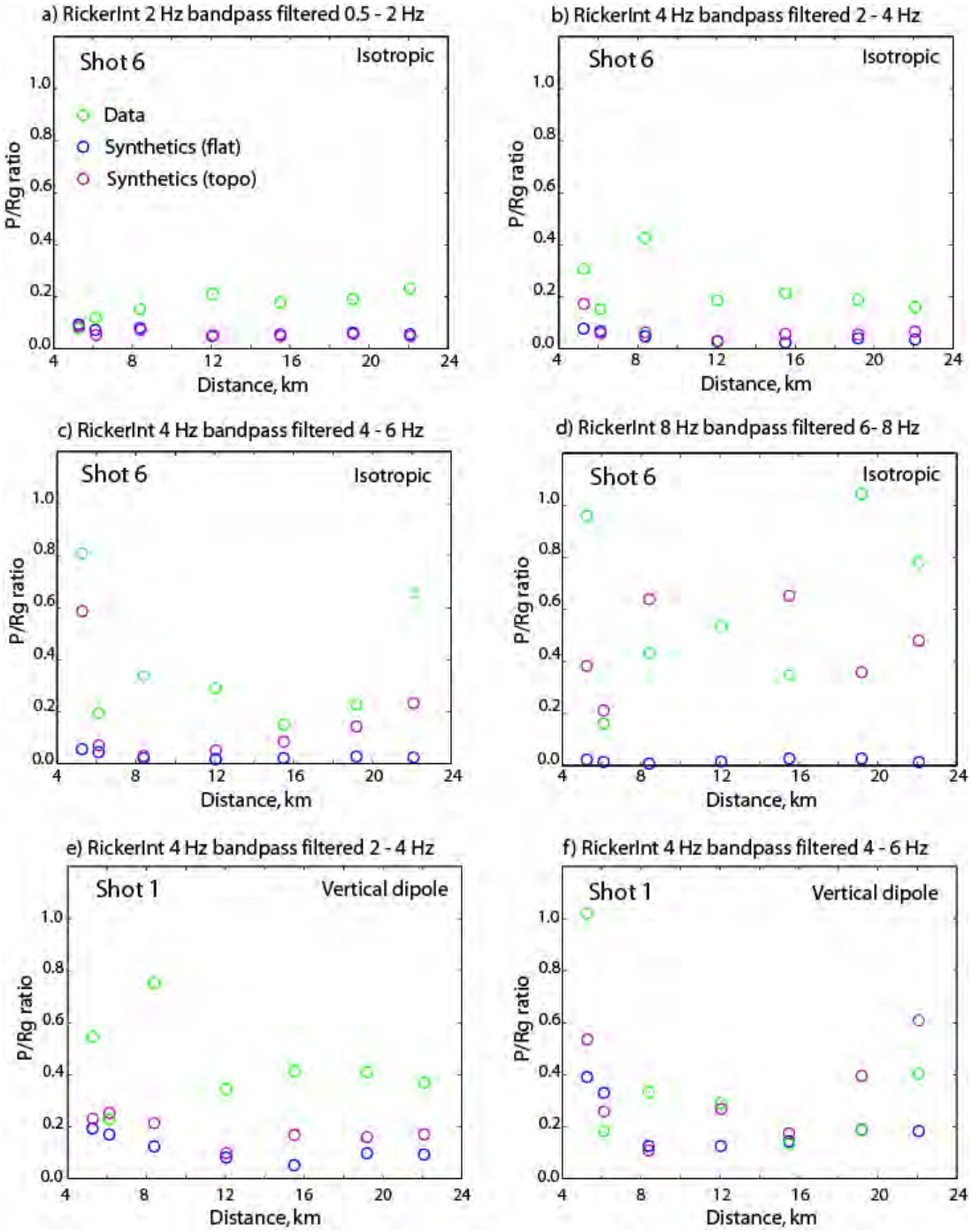


Figure 6. ***P/Rg*** **amplitude ratios plotted against the distance for the data (green), flat synthetics (blue), and the synthetics with topography (purple): a) Shot 6 data and the synthetics (2** ***Hz RickerInt*** **STF, isotropic) filtered between 0.5 – 2** ***Hz*****; b) Shot 6 data and the synthetics (4** ***Hz RickerInt*** **STF, isotropic) filtered between 2 – 4** ***Hz*****; c) Shot 6 data and the synthetics (4** ***Hz RickerInt*** **STF, isotropic) filtered between 4 – 6** ***Hz*****; d) Shot 6 data and the synthetics (8 Hz** ***RickerInt*** **STF, isotropic) filtered between 6 – 8** ***Hz*****; e) Shot 1 data and the synthetics (4** ***Hz RickerInt*** **STF, vertical dipole) filtered between 2 – 4** ***Hz*****; and f) Shot 1 data and the synthetics (4** ***Hz RickerInt*** **STF, vertical dipole) filtered between 4 – 6** ***Hz*****.**

To separate the effects of topography we computed the peak amplitudes for *P* and *Rg* phases for both the data and the synthetics in various frequency bands. Theoretically the geometrical spreading for the body waves in homogeneous medium is proportional to $1/r$, however in the layered medium it is influenced by the variations of the reflection coefficient as a function of angle. For the surface waves the geometrical spreading in 1D medium is proportional to $1/r^{1/2}$ (e.g., Lay and Wallace, 1995). Figure 5 shows the peak amplitudes as a function of range for the isotropic source (Figure 5a–d) and the vertical dipole (Figure 5e, f). For the flat free surface case the *Rg* amplitude decrease with distance is in a good agreement with the predicted rate for all frequency bands. In the rough topography case the *Rg* amplitudes follow the predicted trend for the frequencies below 4 *Hz* (Figure 5a, b). At higher frequencies (4–6 *Hz*) the *Rg* amplitudes become significantly affected by the topography, as shown in Figure 5c-d. Above 6 *Hz* the *Rg* amplitudes approach the *P*-wave amplitudes in the same frequency range. The *Rg* amplitudes computed for the vertical dipole source are significantly lower than for the isotropic source, given the same range and the frequency band.

Figure 6 shows *P/Rg* amplitude ratios for the same frequency bands as shown in Figure 5. At lower frequencies the amplitude ratios for the observed data exceed the synthetic ratios computed suing the isotropic sources (Figure 6 a–c). At frequencies above 6 *Hz* the synthetic amplitude ratios become similar to the observed ratios. The amplitude ratios produced by the dipole source are higher than for the isotropic source in the same frequency bands. The match between the observed and the computed *P/Rg* ratios is reached in the frequency band between 4–6 *Hz*, while for the isotropic source the synthetic amplitude ratios became close to the observed above 6 *Hz*. Notice also higher observed amplitude ratios for Shot 1 compared to Shot 6 in the lower frequency band (2–4 *Hz*). Shot 1 was conducted at shallower depth than Shot 6, and was unconfined. A large vertical dipole component produced by an unconfined shot may explain the differences at the low frequencies.

CONCLUSIONS AND FUTURE WORK

We conducted numerical simulations of wave propagation in layered media with surface topography. The results of the simulations indicate that the observed data at lower frequencies (0.5–2 *Hz*) exhibit normal amplitude decay with distance, which can be explained by the geometrical spreading ($1/r$ rate for *P*-waves and $1/r^{1/2}$ for the surface waves). The synthetic seismograms computed using an isotropic source show similar trends, however the ratios between the *P* and *Rg* amplitudes at frequencies below 4 *Hz* are significantly lower for the synthetics. The *P/Rg* amplitude ratios for the observed data significantly exceed the ratio for the synthetic data with flat free surface. Adding topography, however, produces more realistic seismograms with higher *P/Rg* ratios than those produced using flat free-surface model, particularly at higher frequencies (above 6 *Hz*).

These results show that the topography scattering is an effective mechanism of *Rg*-to-*P* scattering for the higher frequencies (above 6 *Hz*). Other mechanisms of scattering (e.g., scattering due to lateral velocity perturbations and variations in layer thickness) may be significant at lower frequencies to explain the *Rg* amplitude reduction and slow *P*-wave decay with distance. Using a vertical dipole source can account for lower *Rg* amplitudes with distance particularly at low frequencies (below 4 *Hz*). Above 4 *Hz* the combined effect of the focal mechanism and the topography over-predicts the amplitude decay rate with distance. We speculate that the vertical dipole component (e.g., due to spall) could be important at low frequencies, while at higher frequencies the isotropic component dominates the source radiation.

Additional calculations need to be performed in order to evaluate the effect of lateral perturbations of velocity, layer thickness and inelastic losses on the evolution of *Rg* amplitudes with range.

ACKNOWLEDGEMENTS

We thank Anna Chabaeva for help in downloading and formatting the digital elevation model data (ASTER).

REFERENCES

Lay, T. and T. Wallace (1995). *Modern Global Seismology*, Academic Press, Amsterdam, 521 p.

Nilsson, S., N.A. Petersson, B. Sjogreen, and H.-O. Kreiss (2007). Stable difference approximation for the elastic wave equation is second order formulation, *SIAM J. Numer. Anal.* **45**, 1902–1936.

Peterson, N.A. and B. Sjogreen (2010). Reference guide to WPP version 2.0, User's manual, LLNL, Livermore, CA.

Stump, B.W., C.T. Hayward, and R-M Zhou (2005). Morenci refraction interpretation, in *Source Phenomenology Experiments in Arizona*, Final Report DOE Contract. DE-FC03-02SF22638**,** pp. 125–203.

Zhou, R-M. , B. W. Stump, and X. Yang (2005). Moment tensor inversions of single-fired mining explosions at a copper mine in Arizona, in *Source Phenomenology Experiments in Arizona*, Final Report DOE Contract. DE-FC03-02SF22638**,** pp. 204–233.

EFFECT OF ROCK DAMAGE ON SEISMIC AMPLITUDES FROM EXPLOSIONS

Anastasia Stroujkova[1], Jessie L. Bonner[1], Mark Leidig[1], Aaron Ferris[1], Won-Young Kim[2], Timothy W. Rath[3], Mario Carnevale[4], and James F. Lewkowicz[1]

Weston Geophysical Corp.[1], LDEO, Columbia University[2], Maxam NE[3], and Hager Geoscience, Inc.[4]

Sponsored by the Defense Threat Reduction Agency

Award No. HDTRA1-11-1-0029

ABSTRACT

Physical understanding of the seismic radiation generated by explosions in low coupling (damaged/fractured) media is extremely important for nuclear monitoring, because source coupling affects both signal detection and yield estimation. Some empirical evidence for seismic amplitude reductions have been noted for nuclear and chemical explosions detonated in fractured media (e.g., Sokolova, 2008). In order to define the physical mechanism responsible for the amplitude reduction and quantify the degree of the amplitude reduction in fractured rocks, Weston Geophysical Corp in collaboration with Lamont Doherty Earth Observatory conducted Phase I of a multi-phase explosion experiment in central New Hampshire. The experiment involved explosions of various yields, including a 46.3 kg explosion (FD3) in the damage/fracture zone of a 231.8 kg explosion (FD1), and a 46.8 kg shot in nearby undamaged rock (FD2). Geophysical surveys were conducted by Hager Geoscience before and after the FD1 explosion in order to measure the physical effects of a subsurface detonation on rock properties in the immediate vicinity of the blast. The surveys included geophysical well logging as well as a seismic tomography. The tomography results have shown significant seismic velocity reduction from approximately 4−6 km/s down to 1.5−4 km/s. This damaged zone was used as an emplacement medium to conduct the damage rock shot (FD3).

The seismic data analysis has shown *P*-wave amplitude reduction for the explosions conducted in damaged rock by a factor of 2–3. The amplitude differences are frequency dependent, as the explosion in the undamaged rock has a higher corner frequency than the explosion in the damaged zone. The reduction in both seismic amplitudes and the corner frequency for the explosion in damaged rock can be attributed to the seismic velocity and density reduction at the source. The overshoot parameter for the shots in undamaged rock is higher than for the explosion in the damaged zone. Additional experiments will be conducted in the near future to further quantify seismic wave characteristics as a function of the depth of burial, type of explosives and other factors.

OBJECTIVES

Possible nuclear explosion evasion scenarios include cavity decoupling and attempting to hide a nuclear test within large delay-fired mining explosions (National Academy of Sciences, 2002). Another scenario involves fracture decoupling: conducting explosions in the damage or fracture zone created by an earlier explosion(s). Limited observational data suggest fracture decoupling may considerably reduce the amplitudes of the subsequent explosions. The decreased seismic amplitudes reduce the probability of detection and the seismically estimated yield of a repeat nuclear explosion. The objectives of the Fracture Decoupling Experiment (FDE) included:

1) Verifying the amplitude reduction for the repeat shots;
2) Defining the physics responsible for causing seismic amplitude reductions; and
3) Quantifying the phenomena in terms of a "decoupling factor" as a function of frequency.

In order to quantify the material damage caused by the initial explosion, we performed extensive characterization of the granite before and after the explosions.

RESEARCH ACCOMPLISHED

In October of 2011 Weston Geophysical Corp. (WGC) in collaboration with Lamont Doherty Earth Observatory (LDEO) conducted a series of explosions to quantify fracture decoupling at a hard rock site in central New Hampshire (Stroujkova et al, 2012). The major rock type at the site is the Kinsman Granodiorite, which formed during late stages of the Acadian orogeny (400 – 390 ma) (Lyons et al, 1997; Allen, 2003) and was intruded by late stage Newfound Lake area pegmatites (Cameron et al, 1954). The rocks are broken by numerous faults and joints serving as conduits for ground water flow at the test site.

Explosions

The parameters of the explosions are summarized in Table 1. The largest (231.8 kg) shot (FD1) resulted in significant containment failure and formation of a large fracture zone with a surface expression diameter of approximately 12 m (Figure 1). Subsequently, we conducted two smaller shots. The first, FD2, was in virgin (undamaged) rock with very few native fractures 35 m from the damaged test region. The second explosion, FD3, designated the "damage zone shot," was located approximately 6.5 m from the FD1 borehole. Both FD2 and FD3 holes were drilled to a depth of 14.94 m.

Table 1. Explosion characteristics

Shot	Yield, kg	Explosive column top/bottom, m	sDOB*, m/kt$^{1/3}$	BH diameter, cm	Emplacement medium	Explosion notes
CAL	0.44	12.65/12.8	1660	10.1	Virgin rock	Some stemming ejection
FD1	231.8	11.19/12.80	195	38.1	Virgin rock	Containment failure, cratering
FD2	46.3	13.66/14.94	398	20.32	Virgin rock	No surface expression
FD3	46.8	13.5/14.94	395	20.32	Fractured rock	Some stemming ejection, cratering

* Scaled Depth of Burial (SDOB) was estimated using the charge centroids.

The medium surrounding FD3 was so damaged, that the upper 10 m of the borehole were drilled using rotary drilling concurrent with installation of steel casing to prevent the hole from collapsing. The casing was carefully removed prior to detonation. The rock between 10–15 m depth was considerably fractured based on the driller reports, but the hole remained open without need for casing. Both FD2 and FD3 holes were loaded with 44.5–45 kg of Heavy Ammonium Nitrate Fuel Oil (HANFO) explosives and 1.8 kg of Composition B (COMP-B) boosters placed in the middle of the charges, then stemmed and blasted. FD2 produced no surface rock breakage, and stemming remained in the shot borehole. FD3 ejected some of the stemming and created a small crater (approximately 2.44 m in diameter and 1.1 m in depth). The scaled depth of burial (sDOB) for both FD2 and FD3 was approximately 400 m/kt$^{1/3}$, which is overburied and should not have produced any surface expressions (e.g., craters or retarc). The crater for FD3 was caused by gas venting up the borehole through the stemming,

entering near-surface air-filled fractures, and then venting to the surface with the small crater formation. This is a secondary effect as video footage of the blasts show the seismic waves have passed the camera prior to stemming ejection or crater formation. A calibration shot (CAL in Table 1) was conducted prior to Shot FD1 at the same depth (12.8 m), to calibrate the medium response to an approximate point source.

Geophysical Site Characterization

Hager GeoScience, Inc. (HGI) conducted a subsurface geophysical survey before and after FD1 explosion. The objective was to measure the physical effects of a subsurface detonation of explosives on bedrock fracture systems and seismic properties in the immediate vicinity of the blast. The survey included: a) caliper measurements; b) optical/acoustic televiewer (ATV/OTV); c) full-waveform sonic; and d) cross-hole seismic tomography. The ATV/OTV study revealed multiple fractures (foliation) dipping toward the southeast, in addition to a larger fracture dipping toward the northwest.

The objective of the seismic tomography survey was to measure the change in velocity (V_p) after the blast. The imaging was performed between the borehole pairs shown in Figure 1: a) SE – NW, b) SW – NE, and c) NW – NE. The source and the receiver spacing was 0.5 m. Figure 2 shows the tomographic results for the SE – NW cross-section acquired before and after the Shot FD1. There is a fault crossing the shot borehole seen as a low velocity zone dipping toward NW on a pre-shot cross-section. Significant velocity reductions after FD1 (pre-shot $V_p \approx 4-6$km/s, post-shot $V_p \approx 1.5-4$km/s) down to a depth of at least 20 m were apparent from the tomogram. The tomography results confirm that the damage from FD1 extends below the shot, as well as laterally significantly beyond the crater zone. Therefore, the designated damage zone shot (FD3) was well within the damage zone.

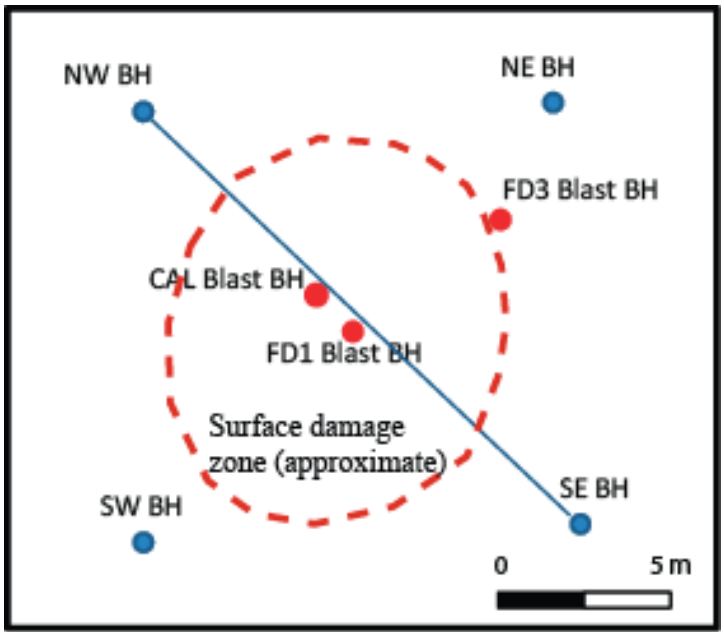


Figure 1. Test bed map showing the near-source geophysical survey geometry and the shot holes. Shot FD2 was located 35 m southeast of FD1.

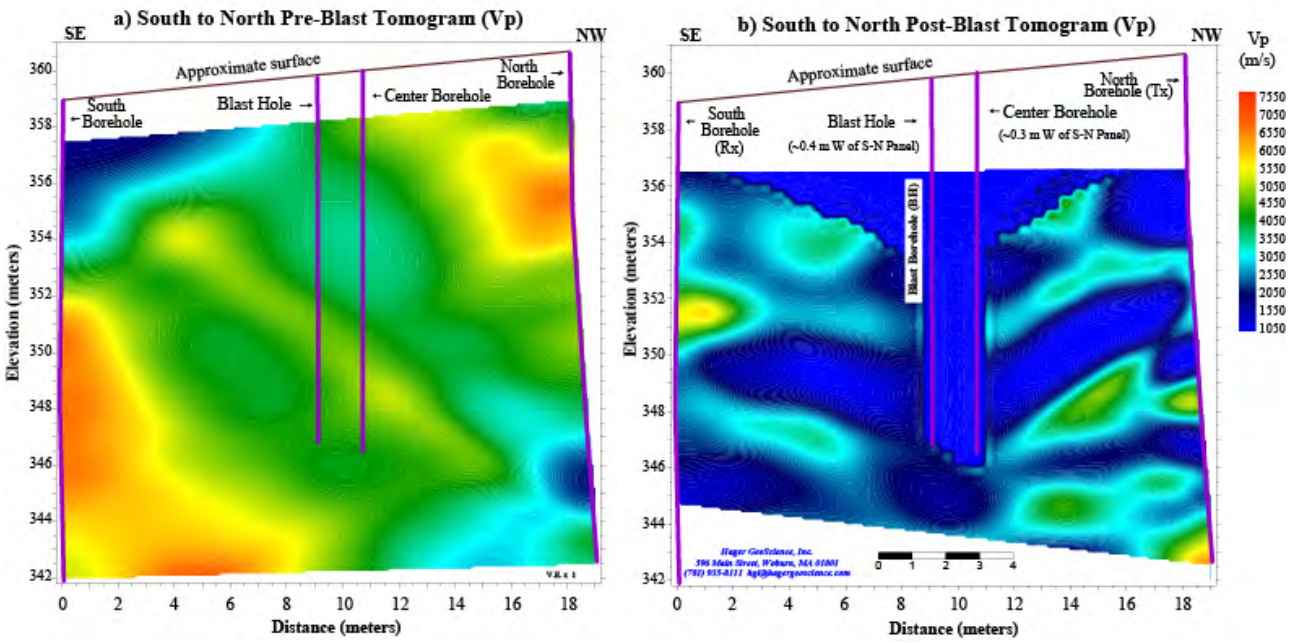


Figure 2. Seismic tomography results from the FDE, showing *P*-velocity before and after FD1 explosion along the SE and NW borehole cross-section (Figure 1).

Seismic Data Analysis

To monitor the explosions we deployed 36 seismic instruments from near field to local distances (between 5 m and 10 km), including short-period seismometers and high-g accelerometers. In the near-field, five Endevco 25g accelerometers and five TerraTech 5g accelerometers were installed in close proximity to the explosions to record the near source ground motions. Figure 3c-d shows the locations of the close-in sensors with respect to the shot locations. All of these instruments recorded three components (3C) of motion at a sampling rate of 1000 samples per second using Reftek 130 (RT130) data loggers. Four of the instruments located within 20 m from the explosion were grouted.

The near-source stations were located at distances between 0.6–1.2 km with 200 m intervals at various azimuths (Figure 3b) on the north side of Spruce Ridge, NH. These stations were equipped with Sercel L22 2Hz 3C sensors. To create a link between the near-source and regional instrumentation, we installed nine stations at local distances between 2 and 10 km. These stations were deployed in the Newfound Lake, NH region. The locations of these stations with respect to the near-source and near-field networks are shown in Figure 3a. With the exception of station GROT, these stations were equipped with a Sercel L-4C-3D 1Hz 3C velocity sensor. Station GROT was equipped with an L22 3C seismometer. Both near-source and local stations recorded continuously with a sampling rate of 500 samples per second on RT130s. The usable frequency band is between 2 and 205 Hz for all stations. The signal-to-noise ratio was on the order of 10^6-10^7 for the near-field and near-source networks and 10^3-10^4 for the local network.

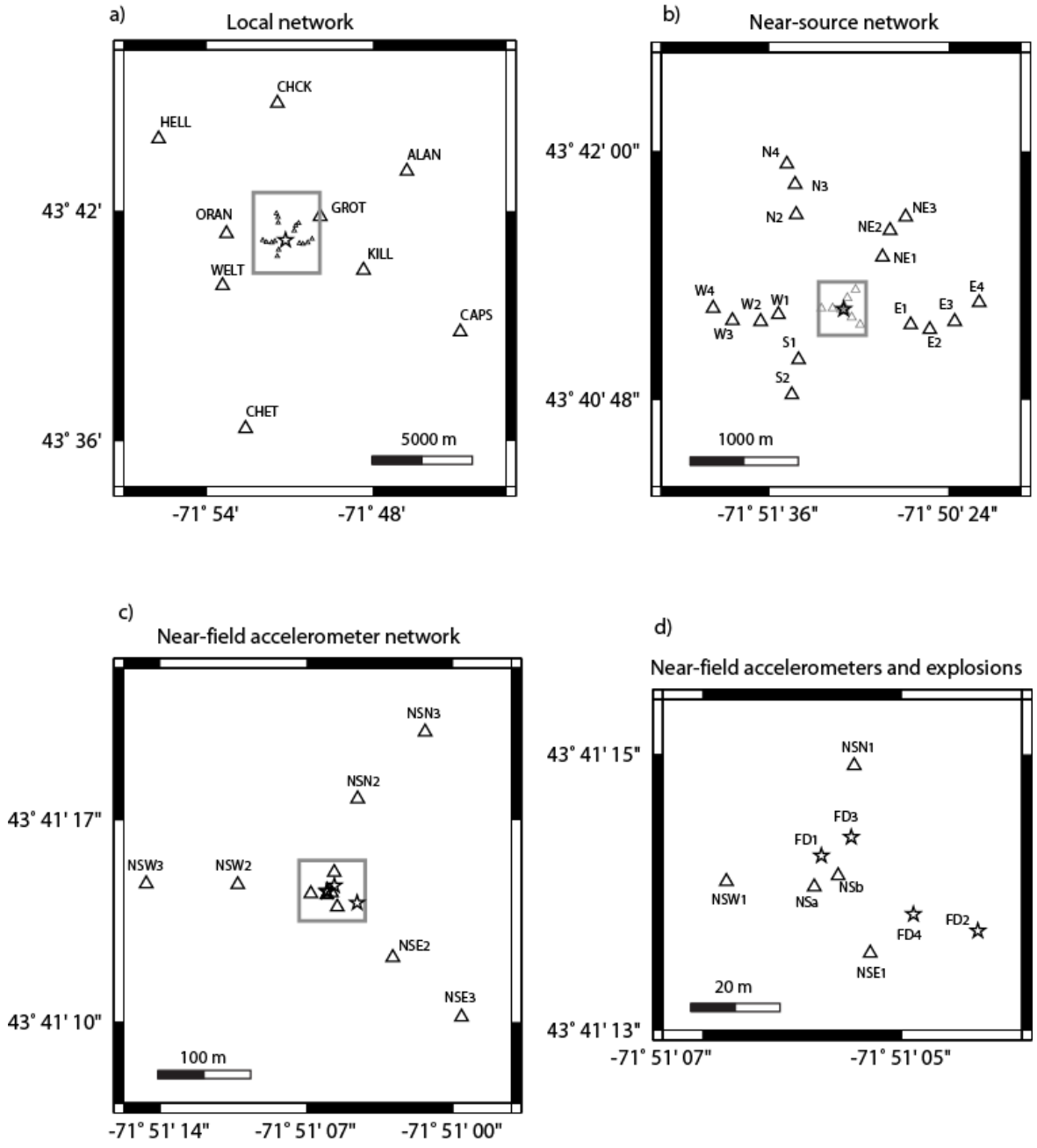


Figure 3. a) Seismic stations deployed at local distances from the Fracture Decoupling Explosions near Newfound Lakes, New Hampshire (USA). Each subplot in a-c shows the area expanded in the following subplot b-d. Triangles show the local stations, the stars show the shot points; the triangles within the rectangle show the near-source seismometer network. The rectangle is enlarged in 1b. b) The near-source network located on Spruce Ridge, New Hampshire. The triangles within the rectangle show the near-field network. The rectangle is enlarged in 1c. c) Enlarged view showing the near-field accelerometers. d) Enlarged view showing the location of the individual explosions.

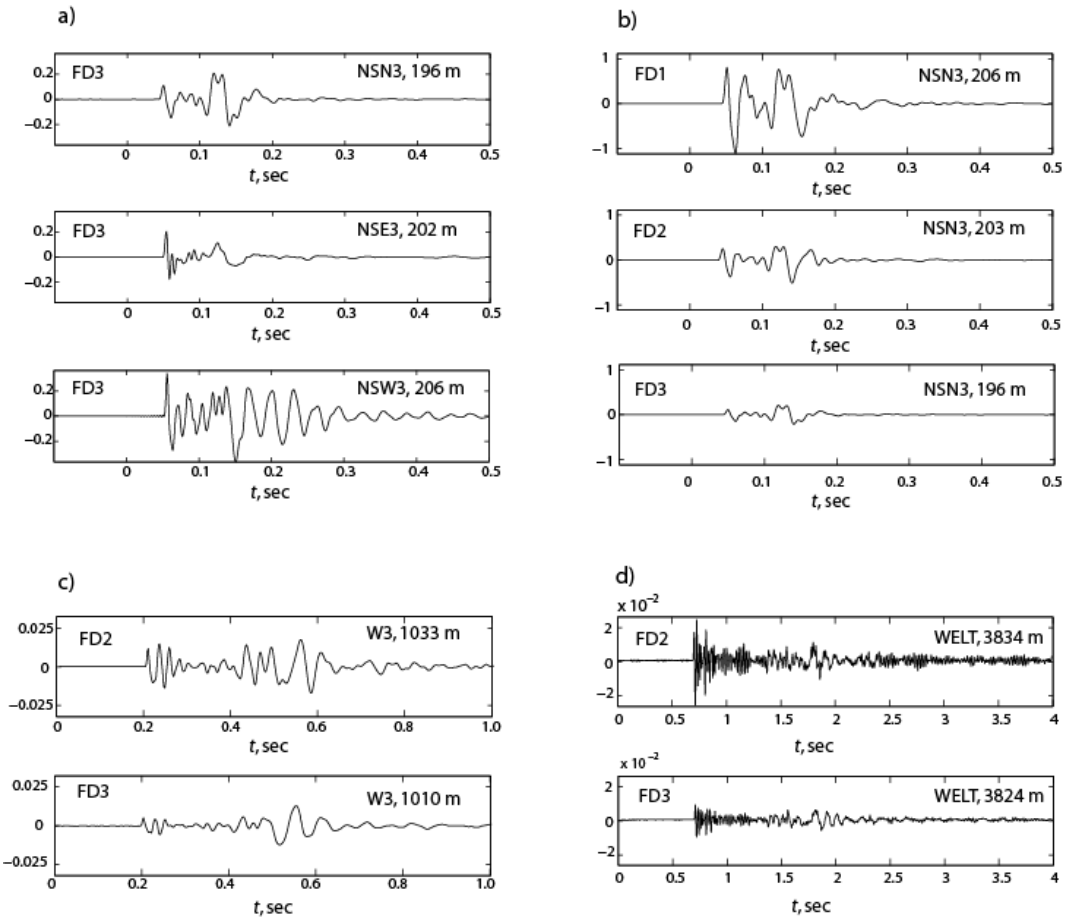


Figure 4. a) Vertical component of the seismic traces for FD3 recorded by the near-field accelerometers (converted to velocities) NSN3, NSE3, and NSW3 located at different azimuths approximately 200 m from the source; b) FD1, FD2 and FD3 recorded by Station NSN3; c) FD2 and FD3 recorded by near-source station W3; and d) FD2 and FD3 recorded by the local station (WELT) located 3000 m away from the explosions. All amplitudes are given in cm/s.

The variations in topography and near-surface geology cause significant variations in the recorded waveforms. Figure 4a shows the seismic traces for FD3 (46.8 kg, fractured rock) recorded by the accelerometers located approximately 200 m from the explosion. Despite similar distances, *P*-wave amplitudes differ by a factor of 3 and the waveforms characteristics vary due to the propagation effects in different directions.

Figure 4b shows a comparison among FD1 (231.8 kg, virgin rock), FD2 (46.3 kg, virgin rock) and FD3 (46.8 kg, fractured zone) recorded by a near-field accelerometer (NSN3) located 200 m away. The yield of FD1 exceeds the yields of FD2 and FD3 by approximately factor of 5. The *P*-wave amplitude ratio between FD1 and FD2 is approximately 2.9, and the ratio between FD1 and FD3 is 7.3. The *P*-wave amplitudes produced by the FD2 explosion exceed the amplitudes produced by FD3 by a factor of 2.5.

A similar trend is observed at all stations of the network. Figure 4c shows FD2 and FD3 waveforms recorded at Station W3 located 1 km away. The FD2 *P*-wave amplitude exceeds the FD3 amplitude by a factor of 3. Notice however, that the *Rg* amplitude for FD2 is greater than the FD3 amplitude by only a factor of 1.5. The signals recorded by local stations (e.g. WELT, Figure 4d) show a similar pattern.

The amplitude differences between different phases can be further observed in Figure 5a and d. The traces for FD2 and FD3 are superimposed, showing similar *Rg* amplitudes and significant reduction in high-frequency *P*-coda amplitude for FD3. The average *P*-wave amplitude reduction for the near-source network is a factor of 2.16 ± 0.19,

while *Rg* is reduced on average by a factor of 1.15±0.20. For the local network these numbers are 2.25±0.43 for *P* and 1.35±0.22 for *Rg*. Thus the decoupling factor for the low frequencies is almost half of the decoupling factor for the high frequencies.

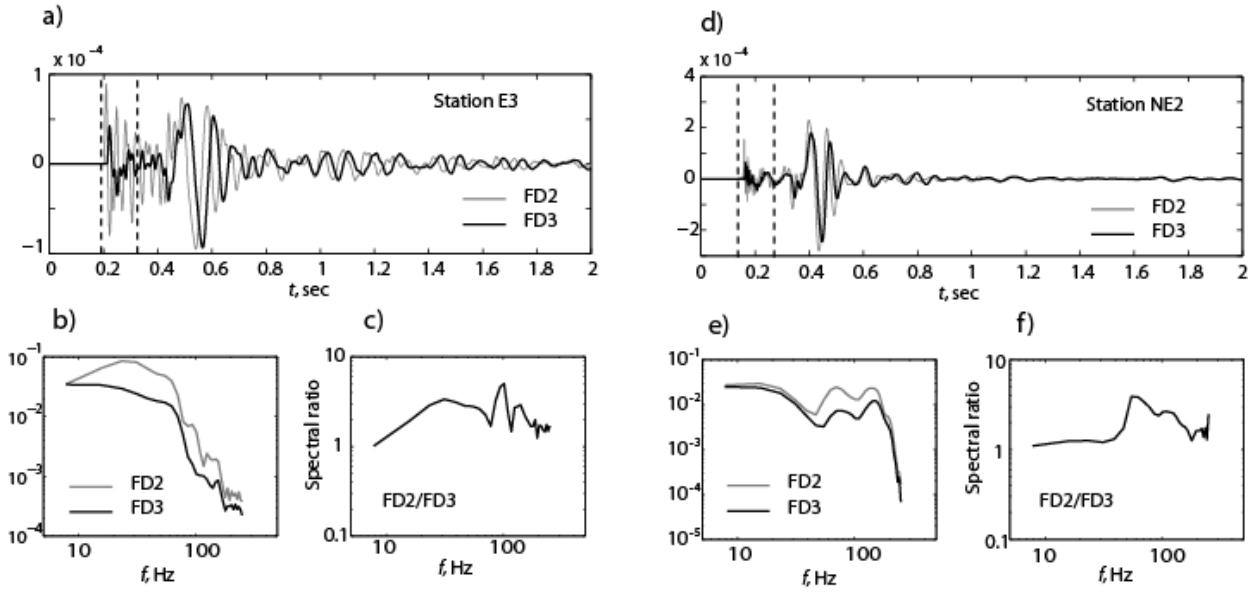


Figure 5. a) Vertical component of the seismic traces recorded by near-source station E3 for FD2 (grey line) and FD3 (black line); b) spectral amplitudes for the traces in a); c) spectral ratios between FD2 and FD3; d) Vertical component of the traces recorded by near-source station NE2 for FD2 (grey line) and FD3 (black line); d) spectral amplitudes for the traces in d); e) spectral ratios between FD2 and FD3.

Figure 5 further illustrates the spectral differences between FD2 and FD3. The spectra were calculated using windowed *P*-waves as shown in Figure 5a,d. FD2 amplitudes exceed FD3 amplitudes at almost all frequencies (Figure 5 b,e). As a result, the spectral ratio between FD2 and FD3 ranges from unity in the low-frequency limit and exceeds 3 above 25 Hz at station E3, and 50 Hz at NE2, as shown in Figure 5 c,f. Notice that the spectra recorded by NE2 show peaks and troughs, different for every station, caused by local site and propagation (different for E3 and NE2) effects.

Since each individual spectrum is affected by propagation and local site effects, we calculated the averaged spectra for different parts of the network. Figure 6a shows the spectra averaged over three groups of sensors: the near-field accelerometers located at a distance of 200 m (NSE3, NSW3, and NSN3 integrated to velocity), the near-source stations located between 600 m and 1200 m (Figure 3b), and the local stations shown in Figure 3a. Notice higher corner frequencies for the near-field stations, which roll-off for the stations beyond 600 m (near-source network) and 1.5 km (local network). All high frequency information about the source is essentially lost at relatively short distances of several kilometers due to inelastic losses.

Figure 6b shows the spectral ratios computed for all stations. The spectral ratios between FD2 and FD3 shots are very similar in all three distance ranges. The amplitude ratios asymptotically approach unity at low frequencies, and reach a factor of 3 between 50 and 100 Hz. Above 100 Hz the amplitudes and ratios become spurious and show larger scatter.

Visual inspection of the spectra shows that the explosion in damaged rock has lower corner frequency and overshoot parameter (e.g. Murphy, 1977). Lower corner frequency for the damaged rock explosion is consistent with the seismic velocity reduction at the source. Further analysis of the corner frequency and the overshoot parameters for the FDE explosions is presented in Stroujkova et al. (2012).

The reduction in seismic velocity can also explain the seismic amplitude reduction. The seismic moment generated by underground explosions is proportional to the squared seismic velocity of the emplacement medium (e.g., Mueller, 1969):

where ρ is the rock density, and is the reduced displacement potential. Based on the tomographic survey results, the seismic velocity is reduced by a factor of 1.5-2.5 (Figure 2). It is also likely that the bulk density of rocks decreased after the explosion due to dilatancy, which would further reduce the seismic moment as well as the observed amplitudes. The limited size of the damage zone (less than 30 m) compared to the wavelength may explain why the lower frequencies were less affected by the fracture zone than the higher frequencies.

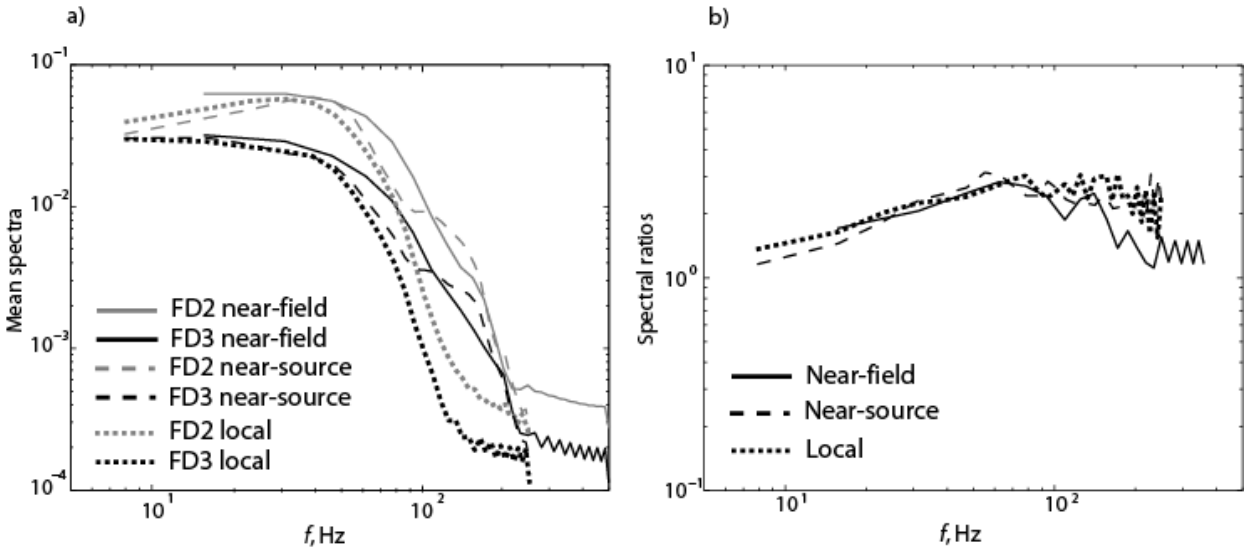


Figure 6. a) Mean spectra for FD2 (grey lines) and FD3 (black lines) computed by averaging the vertical components of the near-field data (stations NSE3, NSN3 and NSW3, solid lines), near-source array data (vertical components, stations shown in Figure 3b, dashed lines), and local station data (stations shown in Figure 3a, dotted lines). b) Spectral amplitude ratios between shots FD2 and FD3 for the near-field stations (solid lines), near-source data (dashed lines), and local stations (dotted lines).

CONCLUSIONS AND RECOMMENDATIONS

We conducted a series of explosions of various yields, including a 46.8 kg explosion in the damage/fracture zone of a 231.8 kg explosion, and a 46.3 kg shot in undamaged rock. The analysis of the seismic data confirms a seismic amplitude reduction from an explosion in damaged rock by a factor of 2-3 as compared to an explosion in undamaged rock. Spectral analysis of the seismic records shows that fractured media reduces the corner frequency; however the frequency roll-off remains approximately the same as for the explosion in the undamaged rocks. Analysis of spectral ratios shows that the low-frequency asymptotes are very close for both explosions. At higher frequencies the amplitudes of the shot in the intact rock exceed the amplitudes of the fractured rock shot by a factor of 2-3. The amplitude reduction can be explained by the reduction in seismic velocity and density of the emplacement medium.

Comparison between the spectra in different distance ranges reveals that the high-frequency source information is lost beyond hundreds of meters to 1 km. Thus the spectral roll-off observed locally or regionally is due to the effects of attenuation rather than the source signature. However, the spectral ratios between the shots in the undamaged and the damaged rocks are similar between the examined distance ranges. Future experiments are planned to conduct more rubble shots at a nearby location in New Hampshire to further quantify fracture decoupling and to evaluate the repeatability of the results.

ACKNOWLEDGEMENTS

We would like to thank our field crew including Jill Franks and Sam Huffstetler. The experiment would not be possible without Skillings and Sons drilling crew led by Bill Conaway. We are grateful to Alan Barnard, Chuck Stata, Larry Kill, the Capsalis family, and the Caron family for giving us permission to place seismic stations on their properties. In addition, Prof. Boettcher of the University of New Hampshire gave us permission to install a seismometer on the University property. We also thank Chuck Stata for providing an ATV to aid the field work. We are grateful to Glen Hansen for the road repairs and restoring the site to its original condition.

REFERENCES

Allen, T. (2003). Bedrock Geology of the Lake Sunapee Area, West-Central New Hampshire, *Guidebook of the 95th Annual New England Intercollegiate Geological Conference (NEIGC), Trip A4*.

Cameron, E., D. Larrabee, A. McNair, J. Page, G. Stewart, and V. Shainin (1954). *Pegmatite Investigations 1942-1945 New England*, Geological Survey Professional Paper 255, US Government Printing Office.

Lyons, J., Bothner, W., Moench, R., and Thompson, J.B. Jr. (1997). *Bedrock Geologic Map of New Hampshire; US Geological Survey, scale 1:250,000*.

Mueller, R. A. (1969). Seismic energy efficiency of underground nuclear detonations, *Bull. Seismol. Soc. Am*. **59**, 2311–2323.

National Academy of Sciences (2002). *Technical issues related to the comprehensive nuclear test ban treaty*, ISBN-13: 978-0-309-08506-9.

Sokolova, I. N. (2008). Investigation of dynamic parameters of seismic records of initial and repeated explosions, (*in Russian*), *NNC RK Bulletin*, **33**(1), 68–73.

Stroujkova, A., J. Bonner, and T. Rath (2012) Effect of fractures on seismic amplitudes from explosions, Submitted to *Bull. Seismol. Soc. Am.*

GEOLOGIC ASSESSMENT OF THE DAMAGE ZONE FROM THE SECOND TEST OF THE SOURCE PHYSICS EXPERIMENT IN NEVADA

Margaret J. Townsend, Heather E. Huckins-Gang, Lance B. Prothro, and Dawn N. Reed

National Security Technologies, LLC

Sponsored by the National Nuclear Security Administration

Award No. DE-AC52-06NA25946/NST11-NCNS-TM-EXP-PD15

ABSTRACT

The National Center for Nuclear Security (NCNS), established by the U.S. Department of Energy, National Nuclear Security Administration, is conducting a series of explosive tests at the Nevada National Security Site (NNSS; formerly the Nevada Test Site) that are designed to increase the understanding of certain basic physical phenomena associated with underground explosions. These tests will aid in developing technologies that might be used to detect underground nuclear explosions in support of verification activities for the Comprehensive Nuclear-Test-Ban Treaty (CTBT). The initial NCNS project is a series of explosive tests, known collectively as the Source Physics Experiment at the NNSS (SPE-N), being conducted in granitic rocks at the Climax stock in northern Yucca Flat. The SPE-N test series is designed to study the generation and propagation of seismic waves. The data will be used to improve the predictive capability of calculational models for detecting and characterizing underground explosions.

The first SPE-N test (SPE-N-1) was a "calibration" shot conducted in May 2011, using 100 kilograms (kg) of explosives at the depth of 54.9 meters (m) (180 feet [ft]) in the U-15n source hole. SPE-N-2 was conducted in October 2011, using 1,000 kg of explosives at the depth of 45.7 m (150 ft) in the same source hole.

Following the SPE-N-2 test, the core hole U-15n#10 was drilled at an angle from the surface to intercept the SPE-N-2 shot point location to obtain information necessary to characterize the damage zone. The desire was to determine the position of the damage zone near the shot point, at least on the northeast side, where the core hole penetrated it. The three-dimensional shape and symmetry of the damage zone are unknown at this time. Rather than spherical in shape, the dimensions of the damage zone could be influenced by the natural fracture sets in the vicinity.

Geologic characterization of the borehole included geophysical logging, a directional survey, and geologic description of the core to document visual evidence of damage. Selected core samples were provided to Sandia National Laboratories (SNL) for laboratory tests (to be reported by SNL).

A significant natural fault zone was encountered in the U-15n#10 angle core hole between the drilled depths of 149 and 155 ft (straight-line distance or range station [RS] from the shot point of 7.5 to 5.7 m). However, several of the fractures observed in the U-15n#10 hole are interpreted as having been caused by the explosion. These fractures are characterized by a "fresh," mechanically broken look, with uncoated and very irregular surfaces. They tend to terminate against natural fractures and have orientations that differ from the previously defined natural fracture sets.

The most distant fracture from the shot point that could be interpreted as having been caused by the explosion was seen at approximately RS 10.0 m. No other possibly explosion-induced fractures are apparent above the fault, but are common starting at RS 5.4 m, which is below the fault. It is unknown how the fault zone might have affected the propagation of seismic waves or how the materials in the fault zone (altered granite, breccia, gouge) were affected by the explosion. From RS 3.3 m to the end of the recovered core at RS 1.6 m, some of the core samples are softer and lighter in color, but do not appear to be weathered. It is thought this could be indicative of the presence of distributed microfracturing.

OBJECTIVES

The NCNS is conducting studies that are designed to increase the understanding of certain basic physical phenomena associated with underground explosions and to develop technologies that might be used to detect underground nuclear explosions in support of verification activities for the CTBT. The initial NCNS project consists of conducting a series of explosive tests, known collectively as SPE-N, in granitic rock at the Climax stock in northern Yucca Flat at the NNSS (Figure 1). The SPE-N test series is specifically designed to study the generation and propagation of seismic waves. Los Alamos National Laboratory (LANL), Lawrence Livermore National Laboratory, Sandia National Laboratories, (SNL), and the Defense Threat Reduction Agency, in conjunction with National Security Technologies, LLC (NSTec), the Management and Operations contractor at the NNSS, are designing and conducting these tests, and will use the data obtained to improve the predictive capability of calculational models for detecting and characterizing underground explosions. It is considered a high priority to obtain geologic data for site models being developed to improve the understanding of how seismic waves propagate through both the natural-state and damaged media.

The first SPE-N test (SPE-N-1) was a "calibration" shot conducted in May 2011, using 100 kg of explosives at the depth of 54.9 meters (m) (180 feet [ft]) in the U-15n source hole. SPE-N-2 was conducted in October 2011, using 1,000 kg of explosives at the depth of 45.7 m (150 ft). The U-15n#10 core hole was drilled to the SPE-N-2 shot point in December 2011, to obtain data on the character of the medium of the next shot, which is planned for the same depth as SPE-N-2.

RESEARCH ACCOMPLISHED

The Climax stock was selected as the site of the first set of SPE-N tests because its granite lithology provides a relatively "homogenous" medium and because, as the site of historical underground nuclear testing, abundant geologic, seismic, and ground shock data are available for comparison to expected SPE-N test data. The assessment of the SPE-N-2 damage zone was accomplished primarily through geologic evaluation of rock samples and geophysical logs from the U-15n#10 core hole, and comparison with pre-test geologic characteristics.

Core hole U-15n#10 was drilled at an angle from the surface to intercept the SPE-N-2 shot point location. The path of the borehole was surveyed, geophysical logs were run in the borehole, and geologists described the core to document visual evidence of damage. The geologists also assisted SNL personnel in selecting core samples for laboratory tests, the results of which will be reported by SNL.

Pre-Test Geologic Characterization Data

The Climax stock area has been extensively characterized through surface geologic mapping (e.g., Houser and Poole, 1960; Barnes et al., 1963) and at depth in support of the three underground nuclear tests and other projects conducted there (see Maldonado, 1977; Orkild et al., 1983; Blouin et al., 2003). See further discussion of the geologic setting of the SPE site in NSTec (2012). Basic geologic characteristics of the SPE-N site are also provided in NSTec (2012), and are summarized below.

Physical and mechanical properties were measured by the SNL Geomechanics Department (Broome and Pfeiffle, 2011) on 10 samples from a core hole drilled at the location of the U-15n source hole prior to any explosive tests. Five of these samples came from the region that is 12.8 m (42 ft) above to 12.8 m (42 ft) below the SPE-N-2 shot point, and some basic properties for these samples are listed in Table 1.

A fracture analysis for the pre-test SPE-N medium was conducted using data from the first seven holes drilled at the site. All fractures were ranked into six categories based on their degree of openness and continuity, and only the higher-ranked fractures were used in the analysis (NSTec, 2012). The most ubiquitous fracture set (50 percent of all higher-ranked fractures) is a group of low-angle fractures (dips 0 to 30 degrees). Fractures with dips of 60 to 90 degrees account for 38 percent of high-ranked fractures, and the remaining 12 percent are fractures with moderate dips (30 to 60 degrees). The higher-angle fractures are further subdivided into three sets based on their dip direction: fractures of Set 1 dip to the north-northeast, and fractures of Set 2 dip to the south-southwest. Set 3 consists of high-angle fractures that dip to the southeast and strike northeast. Most of the low-angle fractures dip eastward and are designated Set 4. Fracture frequency does not appear to change substantially with depth. True fracture spacing averages 0.9 to 1.2 m (3 to 4 ft) for high-angle Sets 1, 2, and 3, and 0.6 m (2 ft) for Set 4.

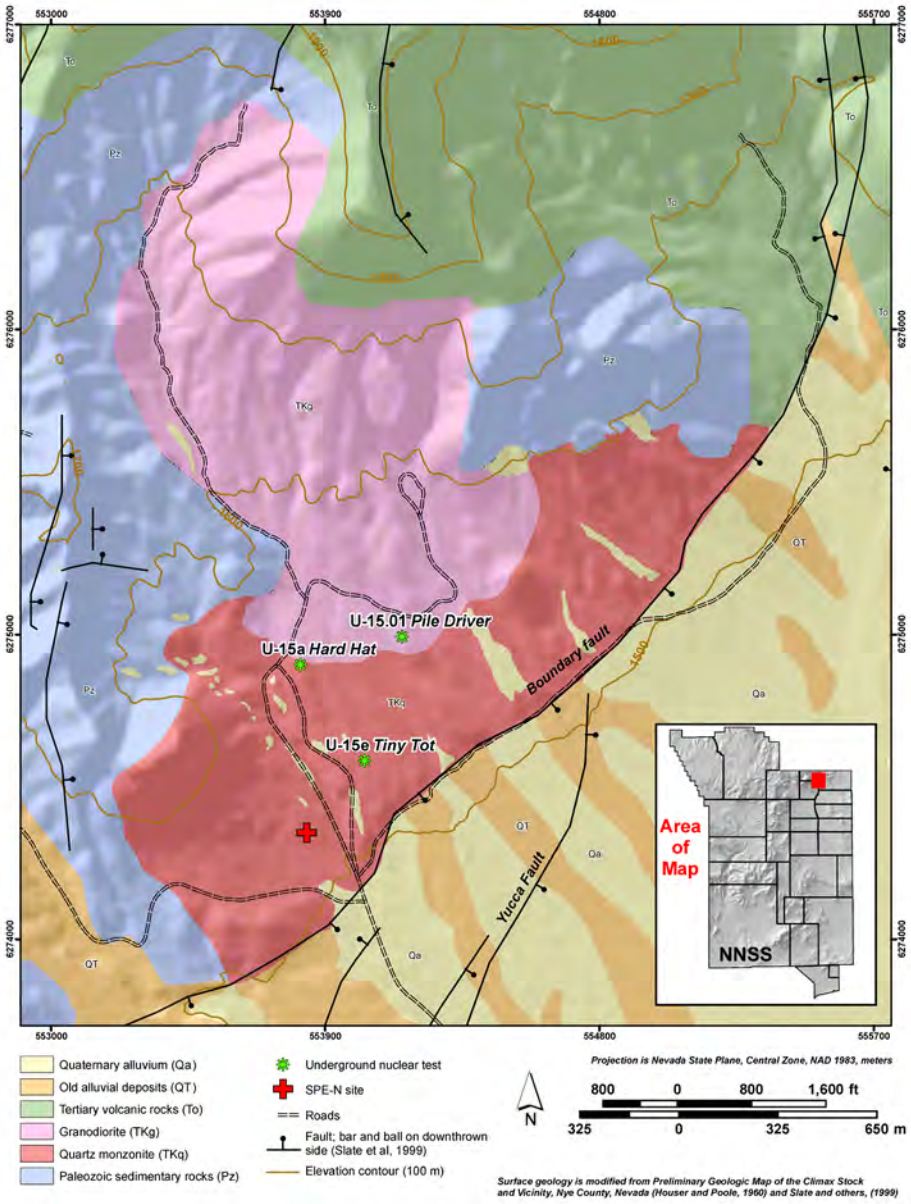


Figure 1. Geologic map of SPE-N site at climax stock.

Table 1. Properties Measured on Core from the U-15n Source Hole Location

Sample Depth (m [ft])	**Density** (g/cc)	**Unconfined Compressive Strength** (MPa)	**Compressional Velocity** (m/s)	**Shear Velocity** (m/s)
32.9 [108]	2.64	210.2	5,802	3,525
40.2 [132]	2.63	205.4	5,820	3,500
46.9 [154]	2.64	195.8	5,928	3,449
53.9 [177]	2.64	227.8	5,888	3,367
58.5 [192]	2.65	165.8	5,908	3,574
Average	**2.64**	**200.4**	**5,869**	**3,483**

Notes:

g/cc = grams per cubic centimeter; MPa = megapascals; m/s = meters per second
Measurements by SNL Geomechanics Department (Broome and Pfeifle, 2011)

Two significant faults were observed in the core from the pre-test U-15n core hole. Severe fracturing and alteration associated with these faults were encountered in the 36-inch (in.) diameter source hole in the depth intervals 17.7 to 24.4 m (58 to 80 ft) and 32.0 to 37.8 m (105 to 124 ft). The upper of these two faults dips 80 degrees to the north-northeast and thus is related to the Set 1 fractures. The lower fault dips 79 degrees to the south-southwest and is related to SPE-N Set 2 fractures. Neither fault has an identifiable surface trace.

Construction of Core Hole U-15n#10

The collar of Core Hole U-15n#10 was set at distance of 26.2 m northeast of the U-15n source hole along an azimuth of 018 degrees, and targeted at the location of the SPE-N-2 shot point, at an angle of 60 degrees from horizontal (30 degrees from vertical) (Figure 2). The planned drilled length for the core hole to intersect the source hole at the SPE-N-2 shot point (at a true vertical depth of 45.7 m) was approximately 175 ft (we use English units to refer to drilled depths in the core hole, and metric units for other lengths such as distance from the shot point).

The position of the borehole was measured every 10 ft during drilling from the depth of 10 ft to 163 ft using a single-shot gyro system. After drilling was complete, but with the drill pipe still in the borehole, the technician ran a final survey with measurement points every 10 ft from the depth of 164 up to 4 ft. A projection of the path of the hole for the last 10 ft (to the total depth [TD] of 174 ft) indicates that the borehole stayed very close to its target path, passing approximately 0.4 m southeast of the SPE-N-2 shot point at closest approach at the drilled depth of 173.6 ft in the core hole. At its TD the core hole is approximately 0.4 m below and southwest of the shot point, approximately within the pre-shot dimensions of the 36-in. source hole (Figure 3).

Geologic Data Collection

The entire U-15n#10 core hole was drilled in quartz monzonite from the top of cement in the conductor casing at 6.3 ft to the TD of 174 ft. All core from U-15n#10 was delivered to the U.S. Geological Survey (USGS) Data Center and Core Library in Mercury, Nevada. USGS personnel photographed each core box, and these photos can be found on the website listed below. Figure 4 shows a photograph of typical undamaged rock core from U-15n#10.

http://nevada.usgs.gov/imagefolio/cgi-bin/ImageFolio43/imagefolio.cgi?direct=NTS_Area15/U-15n10

The geophysical borehole logs listed below were run in the borehole by the NSTec subcontractor Colog, Inc. (a division of Layne Christensen Company) to obtain quantitative data on fundamental rock properties, including properties of discontinuities.

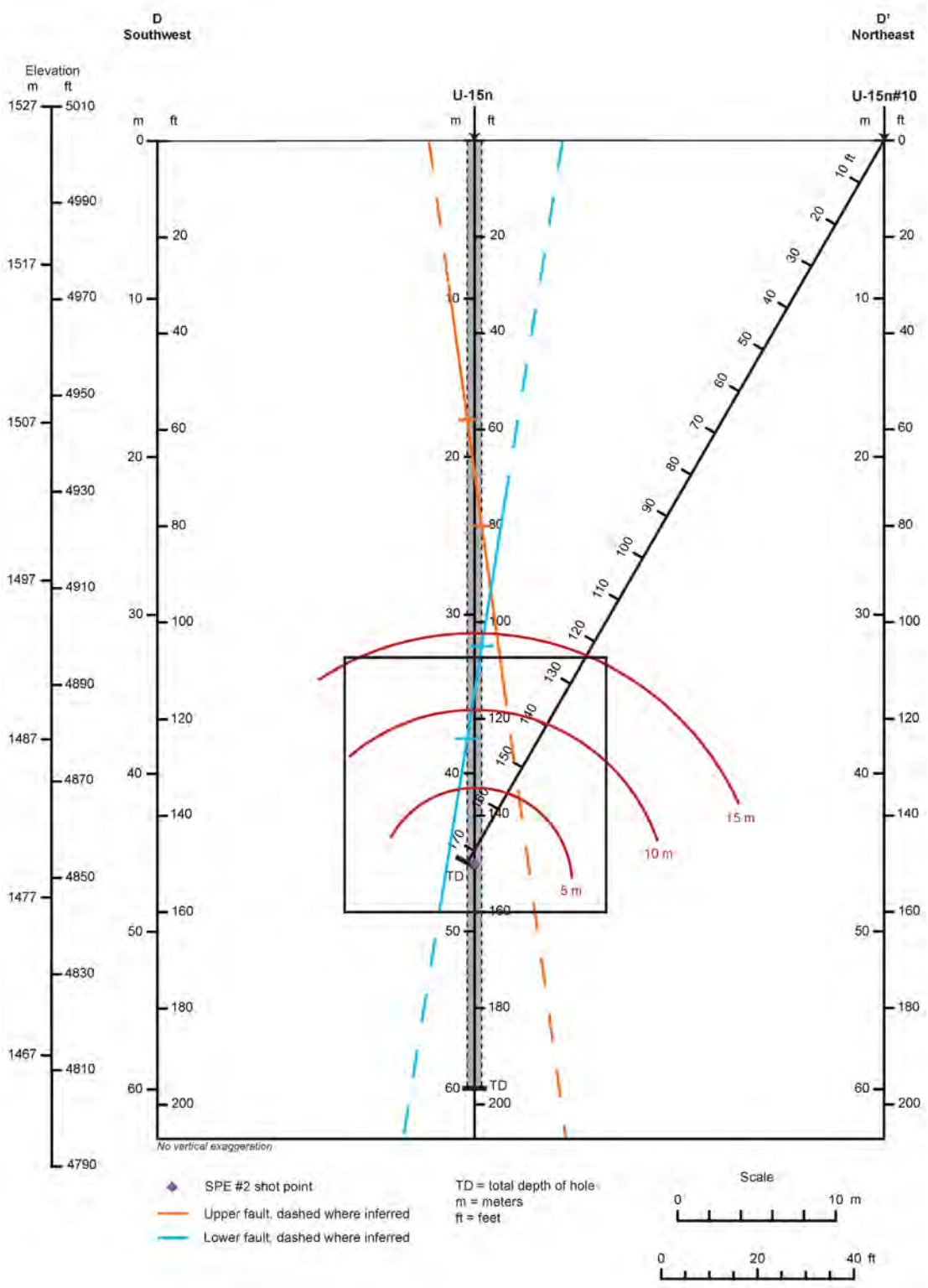
- Deviation (measured on 10-ft spacings during drilling)
- Natural Gamma/1-arm Caliper/Compensated Density
- Full-wave Sonic/Travel Time
- Acoustic Televiewer
- Optical Televiewer

Geologists logged the core to record visible geologic features and collected data required for calculation of Rock Quality Designation (RQD), which is a standard, internationally accepted means of estimating rock quality for engineering purposes (Deere and Deere, 1988).

Logging of discontinuities such as fractures and faults was done on the core recovered from U-15n#10. The core was not oriented, so the strikes of the discontinuities cannot be determined from core data alone. Because the hole is not vertical and fracture strikes are unknown, the true dip magnitudes are also unknown from core data alone. However, the televiewer logs provide orientation data for all discontinuities identified in the images, and it was possible to match features observed in the core with specific discontinuities in the televiewer logs.

Thirty-five dry and preserved samples from the U-15n#10 core hole were selected in March 2012 by personnel from SNL and NSTec for laboratory testing by the SNL Geomechanics Laboratory. The measurements that SNL plans to perform on this collection of samples are listed below. Two samples from the region closest to the SPE-N-2 shot point that are unsuitable for mechanical testing were selected for microscopy and imaging studies by LANL. These investigations are still in progress.

- Unconfined compressive strength
- Triaxial compression
- Direct shear (fracture)
- Brazilian disc tension
- Bulk density
- Velocity



Note: Red arcs represent distances in meters from the shot point. See closer view of area inside box near shot point in Figure 8.

Figure 2. Section view of the SPE-N site showing the relative positions of the U-15n source hole, SPE-N-2 shot point, and path of core hole U-15n#10.

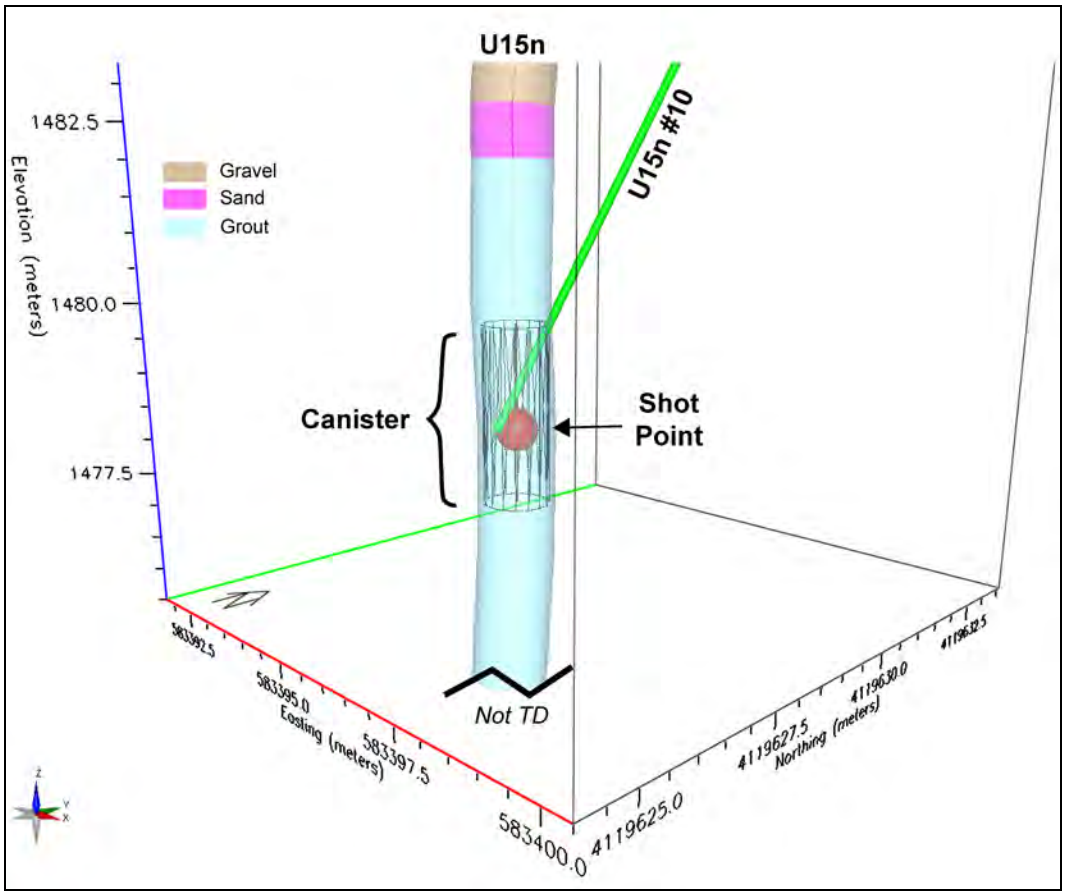


Figure 3. Three-dimensional view of the path of the U-15n#10 angle core hole showing penetration through the pre-shot position of the SPE-N-2 shot point region.



Note: This interval is approximately 24.8 to 26.8 m below ground surface, and 24.3 to 21.9 m from the SPE-N-2 shot point. Core was photographed wet to show detail. Brown sample is preserved in beeswax. Orange paint marks indicate where core was broken by rig-site geologist to fit in box. Photo by U.S. Geological Survey, December 13, 2011.

Figure 4. Photograph of depth interval 94.0 to 101.8 ft from the U-15n#10 core hole.

Geologic Data Summary

The RQD for the U-15n#10 core hole was fairly variable in the upper 45 ft of the hole, but averaged a relatively high 87 down to the drilled depth of 149 ft. This value is similar to the RQD in the correlative portion of the pre-shot U-15n core hole. The RQD values begin to decline at the drilled depth of 134 ft, and then drop dramatically starting at 149 ft (Figure 5).

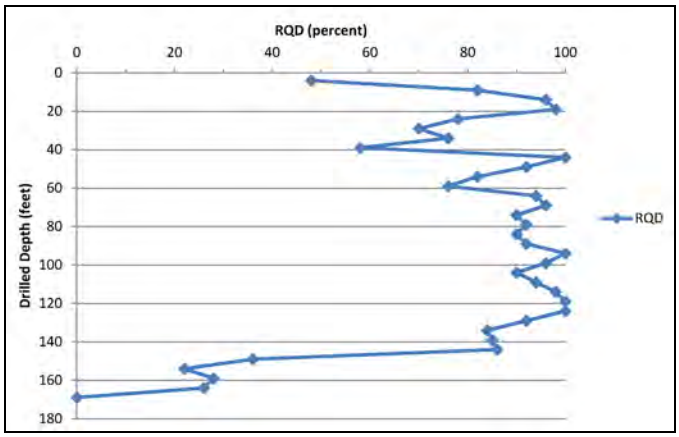


Figure 5. Plot of RQD data versus drilled depth for the U-15n#10 core hole.

Of the 266 discontinuities logged in the core, 12 are considered likely natural faults, including 4 planes within what is thought to be a single fault zone. These features are characterized by the presence of clayey fill, breccia, evidence of shearing, and/or alteration of adjacent rock surfaces. The most significant fault is a zone encountered between the drilled depths of 149.0 and 155.0 ft. This entire zone is characterized by the presence of breccia, gouge, and slickensided surfaces in recovered core.

Analysis of dip directions from the televiewer logs indicates that the high-angle group of fractures in U-15n#10 consists of two main and distinct fracture sets defined on the basis of dip direction (Figure 6). These two fracture sets correlate to Fracture Sets 1 and 2 observed in the pre-shot fracture analyses. Set 3 fractures as defined pre-shot are very poorly represented in the U-15n#10 core hole because fractures in this set strike sub-parallel to the trajectory of the borehole. Most of the ubiquitous low-angle fractures (Set 4) dip eastward, which is consistent with Set 4 fractures in the pre-shot holes. Fracture frequency does not appear to change substantially with depth when all fractures are considered.

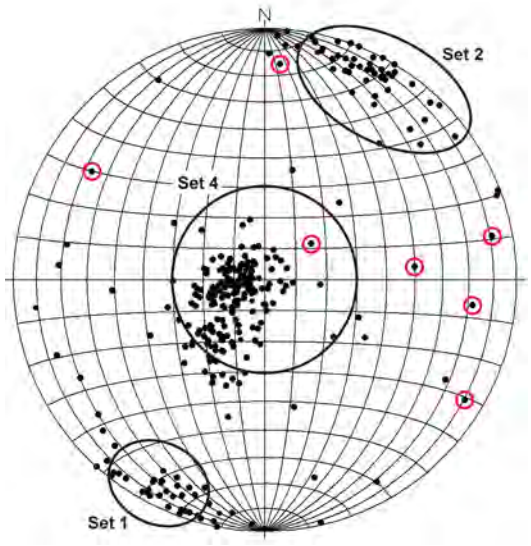
Several fractures near the bottom of the U-15n#10 angle hole are interpreted to be explosion-induced fractures, and are distinctive in both the recovered core and in the televiewer logs. These fractures appear fresh, with no associated secondary staining or alteration, and have rougher fracture surfaces and more irregular shapes (Figure 7) than the clearly natural fractures observed in the hole. They also tend to terminate against the natural fractures. The explosion-induced fractures are observed only below the drilled depth of 141 ft. Most of the induced fractures observed in the borehole televiewer logs have orientations different than those in the established fracture sets, which suggests that the explosion-induced fractures formed in a stress field that is different than that associated with the majority of natural fractures (Figure 6).

Damage Discussion

We attempted to determine the position of the damage zone around the SPE-N-2 shot point, using drilling data, visual data from core logging, borehole geophysical log data, and limited information from videos made in the source hole after the stemming material was removed following the SPE-N-2 shot. Laboratory measurements on core samples (currently in progress at SNL) might provide more quantitative data for the nature of damage in the granite.

The drillers reported a void and loss of fluid circulation between the drilled depths of 168 and 172 ft. The upper edge of the void is about 0.2 m outside the pre-shot source hole, and approximately 1.8 m from the shot point location (assumed to be in the center of the source hole at the vertical depth of 45.7 m (150 ft). Circulation was

regained at 172 ft (within the 36-in. source hole, approximately 0.6 m beyond the shot point), but the core hole was sloughing in at that point, and the sand used as stemming material in the source hole was running into the core hole.



Note: Fractures are plotted on a lower-hemisphere Schmidt net. Natural fractures grouped as Sets 1, 2, and 4 are circled in black. Explosion-induced fractures are circled in red.

Figure 6. Stereonet diagram of all fractures identified in the U-15n#10 televiewer logs, showing the orientations of explosion-induced fractures.

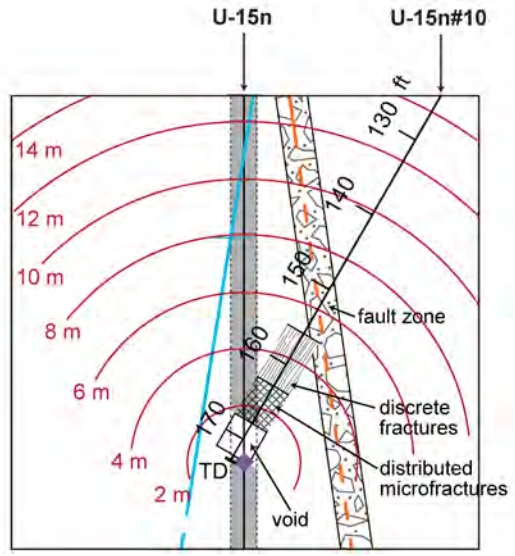


Note: Apparent explosion-induced fractures present in middle and lower rows, between the drilled depths of approximately 156 and 159 ft (approximately RS 5.4 to 4.5 m). Core was photographed wet to show detail. Brown sample with plastic cover is preserved in beeswax. Orange paint marks indicate where core was broken by rig-site geologist to fit in box. Photo by USGS, December 13, 2011.

Figure 7. Photograph of depth interval 154.0 to 159.0 ft from the U-15n#10 core hole.

Evaluation of the position of the damage zone around the SPE-N-2 shot point as determined from fracture data from the U-15n#10 core hole is complicated by the presence of the natural fault zone encountered between the drilled depths of 149 and 155 ft. This fault zone is believed to correlate with the upper Set 1 fault encountered in the source hole pre-shot (Figure 8).

The most distant of the fractures interpreted to have been caused by the explosion was logged at the depth of 141 ft (RS 10.0 m). No others are apparent from drilled depth of 141 ft to and through the natural fault zone. The complex alteration and faulting in this zone may obscure evidence of any other explosion-induced fractures. This zone may also have locally attenuated the seismic waves beyond it. The next apparent explosion-induced fracture is observed at the drilled depth of 156 ft, at approximately RS 5.4 m (Figure 7), and similar interpreted explosion-induced fractures are prevalent from 156 ft to the depth of approximately 163 ft, at approximately RS 3.3 m.



Note: See Figure 2 for location of boxed area. Red arcs represent distances from the SPE-N-2 shot point in meters.

Figure 8. Illustration of features logged in core for angle hole U-15N#10, relative to location of SPE-N source hole.

From the depth of 163 ft to the end of the recovered core at the depth of 168.4 ft (approximately RS 1.6 m), many pieces of the core have a white, chalky, damaged look, and the naturally occurring feldspar crystals are highly fractured (Figure 9). This zone may be a region of distributed microfractures; the SNL and LANL studies currently in progress may provide more definitive data for this region.



Note: Red line is approximately 2.5 centimeters long.

Figure 9. Photo showing fractured feldspar crystal in sample from drilled depth of 168 ft in core hole U-15n#10, approximately 1.8 m from the SPE-N-2 shot point.

Evaluation of post-shot videos of the 36-in. source hole shows increased fracturing of the borehole wall (compared to pre-shot) starting at the depth of approximately 42.7 m, about 3 m above the shot point. At the depth of approximately 45.1 to 45.7 m, within 0.6 m of the shot point, the source hole appears to be somewhat enlarged. The

amount of enlargement could not be measured, but appeared to be less than 0.6 m across the diameter of the hole. Below the depth of 47.2 m, approximately 1.5 m below the shot point, the borehole becomes smoother and more rounded, similar to its original configuration.

CONCLUSIONS AND RECOMMENDATIONS

The primary indicator of damage to the granite medium from SPE-N-2 evaluated to date is fracturing that is distinct in character from abundant natural discontinuities in the SPE-N test bed. One core hole has been drilled into the northeast side of the shot point region, and the most distant fracture that could be interpreted as having been caused by the explosion was seen at approximately 10 m from the shot point. The presence of a large altered zone associated with a natural fault encountered in the core hole between 5.7 and 7.5 m from the shot point likely influenced the creation of new fractures in the vicinity, and no explosion-induced fractures are recognized in the altered interval. Starting at approximately 5.4 m from the shot point, explosion-induced fractures are abundant. At approximately 3.3 m from the shot point to the end of the recovered core at 1.6 m from the shot point, some of the core samples have a damaged appearance, which may indicate a zone of distributed microfractures. Tests of mechanical properties and microscopy studies of samples from the shot zone are currently underway and will likely provide more quantitative data on the damage zone.

ACKNOWLEDGEMENTS

Dr. Catherine Snelson, Test Director for the SPE-N shots and NSTec Program Manager for Treaty Verification R&D, provided valuable support and advice during planning of this research and evaluating its results. Jennifer Mercadante (NSTec) assisted with illustrations. Curtis Obi (NSTec) assisted with determinations of borehole locations.

REFERENCES

Barnes, H., F. N. Houser, and F. G. Poole (1963). Geologic map of the Oak Spring Quadrangle, Nye County, Nevada, U.S. Geological Survey Map GQ-214. Scale: 1:24,000. Washington, D.C.

Broome, S. T. and T. Pfeifle, 2011. Written communication prepared for the U.S. Department of Energy, National Security Administration Nevada Site Office. Subject: “Phase 1 Mechanical Testing Results on Core from Borehole U-15n, Nevada National Security Site, in Support of NCNS Source Physics Experiment.” Sandia National Laboratories Report dated June 8, 2011.

Blouin, S., L. Costin, and K. Wohletz (2003). Geotechnical site characteristics for HARD HAT and PILE DRIVER in *Hard Rock Database Review: Final Report and Proceedings of the HRDR Workshop; Volume 1, Unclassified Material*. Prepared by Defense Threat Reduction Information Analysis Center, DTRIAC-SR-03-V1, July 2003. Kirtland Air Force Base, NM.

Deere, D. U. and D. W. Deere (1988). The rock quality designation (RQD) index in practice, in *Proceedings of Symposium on Rock Classification Systems for Engineering Purposes.* ASTM Special Technical Publication 984, Philadelphia, pp. 91–101.

Houser, F. N. and F. G. Poole (1960). Preliminary geologic map of the Climax Stock and Vicinity, Nye County, Nevada. U.S. Geological Survey, Miscellaneous Geologic Investigations Map I-328. Washington, D.C.

Maldonado, F. (1977). *Summary of the Geology and Physical Properties of the Climax Stock, Nevada Test Site.* Open-File Report 77–356. U.S. Geological Survey, Denver, CO.

National Security Technologies, LLC (2012). *Geology of the Source Physics Experiment Site, Climax Stock, Nevada National Security Site.* DOE/NV/25946--1448. Las Vegas, NV.

NSTec, see National Security Technologies, LLC, above.

Orkild, P. P., D. R. Townsend, M. J. Baldwin, D. L. Healey, G. D. Bath, C. E. Jahren, and J. G. Rosenbaum (1983). *Geologic and Geophysical Investigations of Climax Stock Intrusive, Nevada*. Open-File Report 83–377. U.S. Geological Survey, Denver, CO.

U.S. Geological Survey. USGS/DOE Cooperative Studies in Nevada Website: Rock Sample Images (Core from U-15n#10). http://nevada.usgs.gov/imagefolio/cgi-bin/ImageFolio43/imagefolio.cgi?direct=NTS_Area15/U-15n10 Last accessed on April 4, 2012.

2012

Proceedings of the 2012 Monitoring Research Review:
Ground-Based Nuclear Explosion Monitoring Technologies

Proceedings of the 2012 Monitoring Research Review: Ground-Based Nuclear Explosion Monitoring Technologies

September 18–20, 2012

Albuquerque, New Mexico

Volume II

Hydroacoustic Monitoring
Radionuclide Monitoring
Infrasound Monitoring
Data Processing and Analysis

Approved for Public Release; further dissemination unlimited.

National Nuclear Security Administration

LA-UR-12-24325

Table of Contents - Volume II

4. Hydroacoustic Monitoring 563

4-01 **Ray, T. and P. Grenard**
Installing a Hydroacoustic Station at the Crozet Islands 565

5. Radionuclide Monitoring 575

5-01 **Biegalski, S., M. Deinert, J. Lowrey, and C. Perez**
Radioxenon Transport in Geologic Media 577

5-02 **Ely, J., J. Hayes, D. Haas, W. Harper, J. Madison, A. Ringbom, and K. Elmgren**
Technology Goals for a Next Generation Radioxenon Monitoring System 586

5-03 **Farsoni, A., B. Alemayehu, A. Alhawsawi, and E. Becker**
Real-Time Pulse Shape Discrimination and Radioxenon Measurement in Field-Programmable Gate Array 594

5-04 **Harper, W., M. Cooper, J. Hayes, and L. Lidey**
A Treatment of the Measurement Uncertainty for Xenon Volume Quantification 607

5-05 **Hennig, W., C. Cox, S. Asztalos, H. Tan, P. Franz, A. Xiang, P. Grudberg, W. Warburton, A. Huber, S. Biegalski, A. Brand, and D. Haas**
Radioxenon Measurements with a Coincidence Silicon Detector System 615

5-06 **Jordan, A., J. MacCarthy, P. Stauffer, G. Zyvoloski, M. Person, and D. Anderson**
Simulation of Radionuclide Gas Breakthrough from Underground Nuclear Explosions 625

5-07 **Keillor, M., C. Aalseth, A. Day, L. Erikson, B. Glasgow, E. Hoppe, T. Hossbach, L. Mizouni, J. Merriman, A. Myers, C. Overman, N. Overman, A. Seifert, and T. Stavenger**
A Germanium Array for Sample Measurements: Recent Results and New Analysis Methods 635

5-08 **McIntyre, J., M. Cooper, J. Ely, D. Haas, and B. Schrom**
A Robust Absolute Detection Efficiency Calibration Method Utilizing Beta/Gamma Coincidence Signatures and Isotopically Purified Neutron Activated Radioxenon Isotopes 643

5-09 **Warburton, W., W. Hennig, J. Bertrand, S. George, and S. Biegalski**
Alpha-Al2O3 Diffusion Barriers to Eliminate the Radioxenon Memory Effect in Phoswich Detectors 653

6. Infrasound Monitoring 663

6-01 **Arrowsmith, S., R. Whitaker, A. Le Pichon, Y. Cansi, N. Brachet, M. Charbit, J. Park, B. Stump, and I. Che**
Development and Validation of Infrasound Data Processing Algorithms 665

6-02 **Belyashova, N., S. Baher, N. Mikhailova, Z. Sinyova, A. Smirnov, and A. Velikanov**
Seismic and Infrasound Studies Carried Out at the Institute of Geophysical Research of Kazakhstan in Cooperation with the US National Data Center 676

6-03 **Hale, J., J. Park, K. Pankow, S. Arrowsmith, R. Burlacu, B. Stump, C. Hayward, and S. Taylor**
Infrasound Signal Characteristics from Small Earthquakes 687

6-04 **Jones, K., R. Whitaker, and S. Arrowsmith**
Infrasound Observations from the Source Physics Experiment (Tests 1 and 2) at the Nevada National Security Site 700

6-05 **Koch, K.**
Regional Infrasound Observations from Recent Rocket Engine Tests in Southern Germany 710

6-06 **Marcillo, O., S. Arrowsmith, R. Whitaker, and D. Anderson**
Enhancements to the Bayesian Infrasound Source Location Method 721

6-07 **Waxler, R., J. Lonzaga, and J. Assink**
Non-linear Infrasound Signal Distortion and Yield Estimation from Stratospheric and Thermospheric Returns 729

6-08 **Whitaker, R.**
Infrasound Sensor Calibration and Response 735

7. Data Processing and Analysis 743

7-01 **Ballard, S., J. Hipp, A. Encarnacao, C. Young, and B. Kraus**
A Generalized Earth Model Software Utility 745

7-02 **Bobrov, D., J. Coyne, J. Given, U. Khukhuudei, I. Kitov, K. Sitnikov, S. Spiliopoulos, and L. Zerbo**
Sumatera 2012 Aftershocks: Reviewed Event vs. Waveform Cross-Correlation Bulletin 754

7-03 **Chipman, V., C. Snelson, D. Emer, M. Townsend, and P. Lee**
An Overview of Comprehensive Inspection Technologies under Investigation at the Nevada National Security Site in Support of the Comprehensive Nuclear-Test-Ban Treaty 764

7-04 **Ferris, A., R. Herrmann, and J. Bonner**
A Software Toolbox for Systematic Evaluation of Seismometer-Digitizer Responses 768

7-05 **Kværna, R., S. Gibbons, D. Harris, and D. Dodge**
Adapting Pipeline Architectures to Track Developing Aftershock Sequences and Recurrent Explosions 776

7-06 **Merchant, B. and D. Hart**
Next Generation Analysis Software and Test Equipment for Component Evaluation 786

7-07 **Pitarka, A., R. Mellors, A. Rodgers, S. Ford, P. Harben, J. Wagoner, W. Walter, M. Pasyanos, A. Petersson, O. Vorobiev, H. Xu, S. Ruppert, S. Myers, E. Matzel, and D. Dodge**
Analysis and Simulation of Far-Field Seismic Data from the Source Physics Experiment 796

7-08 **Slinkard, M., S. Heck, D. Carr, R. Eckert, and C. Young**
Broad Area Event Detection Using Waveform Correlation and Distributed Computing 806

Appendices 817

Acronyms, etc. 819

Guide to Seismic Phases 821

Hydroacoustic Monitoring

INSTALLING A HYDROACOUSTIC STATION AT THE CROZET ISLANDS

Terrill W. Ray[1] and Patrick Grenard[2]

United States State Department[1] and Comprehensive Nuclear-Test-Ban Treaty Organization[2]

Sponsored by the United States State Department

Award No. NDF – 288

ABSTRACT

The Comprehensive Nuclear-Test-Ban Treaty (CTBT) International Monitoring System (IMS) includes a network of eleven hydroacoustic stations for monitoring the Earth's oceans, six of which are hydrophone stations, while the remaining six are on-land seismometer-based stations. The efficient propagation of acoustic energy through the Sound Fixing and Ranging (SOFAR) channel makes it possible to effectively monitor large ocean areas with a small number of stations. Ten of the eleven stations in this network have been installed and certified. The remaining station is designated HA04 and is located in the Crozet archipelago, a French territory in the southwestern Indian Ocean. While the location of this site provides unique monitoring capabilities for the IMS, the site presents significant design and installation challenges because of the environmental conditions in the area. This paper addresses some of the main challenges associated with the establishment of HA04 that have been identified based upon the experiences of the prior installation and of a more recent design and feasibility study. These results will be used to move forward with the design and installation of the station.

OBJECTIVES

The CTBT IMS has the objective of providing global monitoring to detect nuclear explosions in any environment. The eleven stations comprising the hydroacoustic network principally look for explosions in the water column of the Earth's oceans and above the ocean surface. The efficient transmission of acoustic energy through the SOFAR channel allows a small number of stations to effectively cover most of the world's oceans. Six of the IMS stations are hydrophone stations, where moored hydrophones float in the SOFAR channel suspended above the seafloor on vertical risers suspended by submerged buoys. Such stations require major installation efforts because of the remote sites where they are deployed and the challenges of deep undersea cable laying operations. Five of the six hydrophone stations in the IMS have been certified and four are currently part of IDC operations. One of the two stations not in operation is HA03 in Juan Fernandez, Chile, which is awaiting repair after having been destroyed by a Tsunami in 2010. The other station, designated HA04 and located on Ile de la Possession in the Crozet archipelago in the southwestern Indian Ocean, will be re-established after having suffered damages during repair and successive anchoring incidents. The re-establishment requires removal of the previous equipment and reinstallation of an entirely new shore component, trunk cables and hydrophone triplets. Given the particularly harsh conditions that prevail in the area, the successful installation of a sustainable certified International Monitoring System hydrophone station at Crozet requires careful consideration of the particular environment in the area.

RESEARCH ACCOMPLISHED

The Crozet Islands are a sub-Antarctic archipelago of small islands that are part of the French Southern and Antarctic Lands (Terres Australes et Antarctiques Françaises, labeled TAAF). The largest island in the group is the 150 km^2 Possession Island located at 46°24′ S, 51°46′ E. The Island is of volcanic origin and sits atop the Del Cano Plateau, which has an average water depth of 2,000 m. The island is uninhabited except for the staff of the Alfred Faure scientific research station, which can provide local support for the IMS station. There is no harbor or airstrip, but there is a small dock facility on the Baie du Marin to accommodate cargo deliveries by lighter vessels (Figure 1). The CTBTO Provisional Technical Secretariat (PTS) and France worked together on the first installation of HA04 since 1999. Similarly to other IMS hydrophone stations situated on islands, two triplets were deployed in 2000, one approximately 40 km North of the island and one approximately 50 km South of it. By February 2006, the station ceased permanently to send data due to technical issues and ship-anchoring incidents that damaged both the North and the South trunk cables in shallow waters. Nevertheless, much useful data on ambient acoustic noise at Crozet, as well as valuable experience on performing installation operations around Crozet, was accumulated through this previous work. It should be noted, that HA04 was the first cabled installation ever attempted at these latitudes.



Figure 1. Photograph showing Alfred Faure base and the only limited available shore landing facility on Ile de la Possession. Part of the colony of penguins which live on the island can be clearly seen.

A hydroacoustic station at Crozet in the Southwestern Indian Ocean, at a latitude south of the Cape of Good Hope, provides important contributions to the IMS monitoring capabilities. First, it increases the azimuthal coverage for events in the Indian Ocean especially between Africa and India compared to that offered by the other IMS hydroacoustic stations in the Indian Ocean at the British Indian Ocean Territories (BIOT) and Cape Leeuwin, Australia. This provides an improvement in location capability in that region. Secondly, its southerly location provides additional monitoring capability into parts of the South Atlantic, as well as improved location capabilities in that area, since the only Atlantic hydrophone station is HA10 on Ascension Island. Third, the location is uniquely placed to give the IMS coverage into the Madagascar Strait, which is not afforded by other locations. Finally, the station location is relatively close to the Antarctic convergence zone and will improve detectability of sources south of the convergence zone. Figure 2 shows the improvements in event detection capability when the IMS includes a station at Crozet Island. However, the location at the high southern latitudes presents multiple challenges. These challenges and their implications on the work to be carried out are discussed below.

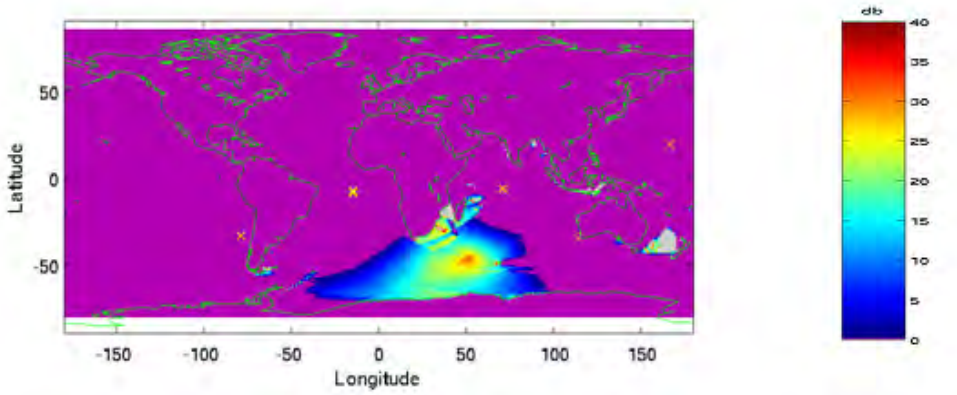


Figure 2. The figure above shows the improvement in hydroacoustic network signal-to-noise ratio (SNR) detectability for a one kiloton surface explosion when the Crozet Is. station is added to the network. Purple indicates areas where the SNR is essentially unchanged when Crozet is added. Note that the grey regions are where there is no detectability without the Crozet Is. station. An "x" is a station location.

The first challenge concerns the selection of the appropriate hydrophone depths. In principle, placing the hydrophones near the axis of the SOFAR channel would give the best performance. The depth of the SOFAR channel axis depends primarily on the temperature in the water column and the hydrostatic pressure. Figure 3 shows the locations of IMS hydroacoustic stations in the Indian Ocean and the annual average depth of the SOFAR channel axis. At Crozet the SOFAR channel effectively extends from near the sea surface down to approximately 700 m and its axis varies significantly depending on the season and somewhat depending on location. The sound-speed gradient is less strong and the SOFAR channel is less well defined in this region compared to other latitudes. However, at the shallow depths at which the channel axis is at Crozet, the disturbance from wave action noise and especially currents could be substantial.

Figure 4 shows noise models for the hydroacoustic stations, derived from long-term averages of the available data. The figure shows that the northern triplet at Crozet Island proved to be the quietest site in the Indian Ocean, while the southern site proved to be the second-noisiest. Further analysis of the characteristics of the noise on timescales of hours, confirm that the noise at the south triplet of the Crozet station is substantially higher than the noise at the north triplet.

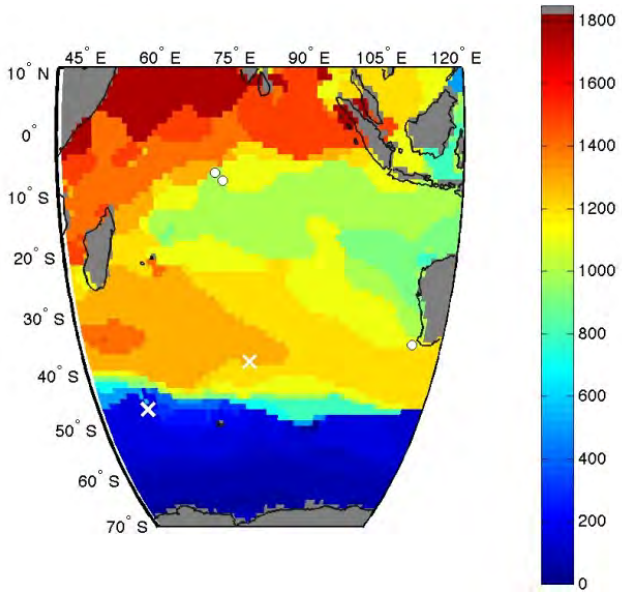


Figure 3. Map of the Indian Ocean from (Mallin, 2012), showing HA01 Cape Leeuwin (rightmost white circle), HA08 BIOT-Diego Garcia (top white circles) and the Crozet archipelago (lower left cross). The colorscale shows the annual averaged depth of the SOFAR channel axis (in m).

Two independent analyses of the noise at HA04 using available data, carried out by CEA (Piserchia et al., 2003) and by CTBTO IDC and IMS in 2012, suggest that currents could be responsible for the high noise level at the South site. Bursts of high noise spectral levels, which last for hours at a time and appear to be related to the tidal cycles, are found consistently in the South triplet data around 10 Hz. Those levels can be up to 50 dB higher than the levels at the North triplet. The North hydrophones were at a depth between 281 m and 290 m, and the South hydrophones were at a depth between 310 m and 350 m. The explanation being considered as the most plausible one is that these noise bursts are caused by strong tide-related sub-surface currents flowing past the hydrophones. Current induced pseudo-noise was first discussed in detail in a journal paper by (Strasberg, 1979). Peaks most likely associated with cable strumming are also visible in the lower part of the noise spectrum in these cases. Besides causing high levels of noise, such currents represent a potential danger to the long-term sustainability of the system, since they may expose the hydrophone risers and moorings to excessive mechanical stresses in the long run. In order to mitigate these risks, the hydrophones need to be placed at locations where the currents do not present any concern. For this reason, a study of the surface and sub-surface currents in the likely deployment area will be undertaken. The study will be performed using state-of-the-art three-dimensional (3-D) ocean modelling tools, and it will provide information which will be crucial for designating hydrophone deployment locations and for the planning of cable deployment operations. As part of this effort, historical ocean, current, sea state and meteorological data as well as available bathymetric and other data will be collected and compiled in a report which will provide a comprehensive picture of the local environment.

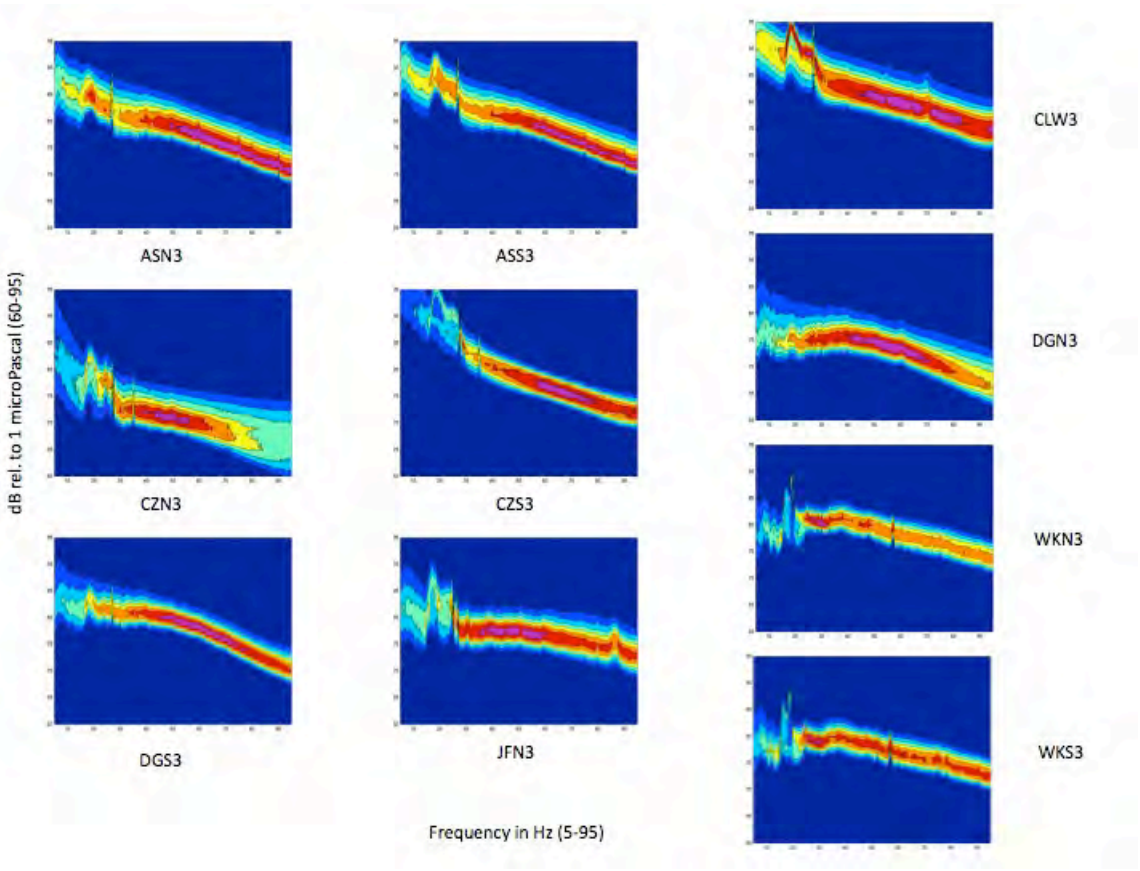


Figure 4. Noise models based on power spectral density (PSD) as a function of frequency for the third sensor in the triplet for the full IMS hydroacoustic network . The naming convention is: AS, CZ, DG, JF, CL, WK for Ascension Is., Crozet Is., Diego Garcia, Juan Fernandez, Cape Leeuwin, Wake Is., respectively. N, S, and W refer to the north arm, south arm, or only arm respectively. The models were constructed using most of the continuous data recorded by all stations from inception through 2009. In the case of Crozet, the models are based on 71% (for the north arm) and 78% (for the south arm) of all data recorded (5000-6000 hours of continuous data). Note that CZN3 and CZS3 models differ by more than any other station arms and that CZN3 has the lowest average noise (and highest variability) of the IMS stations while CZS3 is one of the higher noise stations. Noise model differences between individual sensors forming a triplet proved to be minimal, as one would expect.

When the SOFAR channel axis is sufficiently deep, the amplitude of the low-order acoustic modes is maximal at this depth and hydrophones located near this axis will be most sensitive to the long-range signals of interest for monitoring purposes. In the case of Crozet, where the SOFAR channel is near the surface, the SOFAR channel axis may no longer be the depth of maximum amplitude for low-order modes.

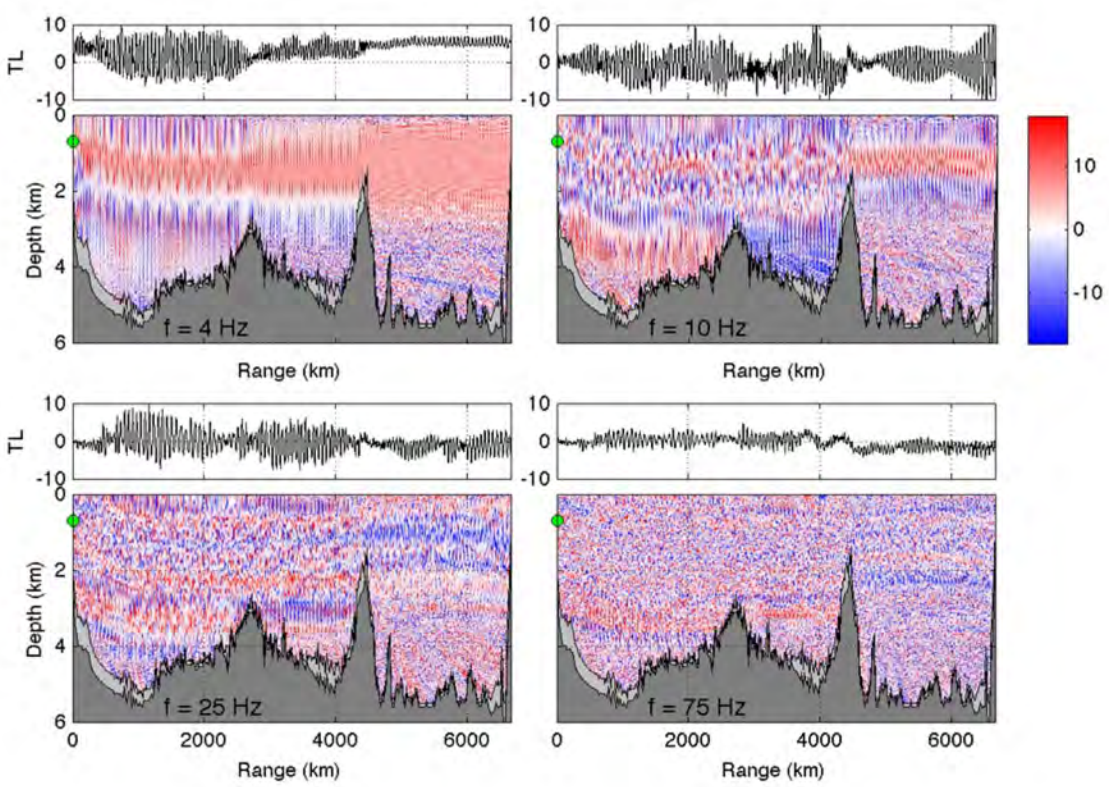


Figure 5. Difference between transmission loss, TL (dB), for a hydrophone at 200 m depth (i.e., at the depth of the SOFAR channel axis at HA04), compared to a hydrophone at 700 m depth, for four different frequencies. The green circles represent the 700 m deep hydrophone. Range 0 km corresponds to the HA04 location. The line-plots show the average TL within the first km depth as a function of range. A positive difference implies an improved reception, whereas a negative difference implies a worse reception. [Figure and caption material from (Mallin, 2012)]

Figure 5 shows the results of a first analysis of transmission loss for the indicated signal path to a potential hydrophone site at Crozet (Mallin, 2012). The analysis shows that the zone of minimum transmission loss is somewhat deeper than the SOFAR channel axis. The depth of the minimum transmission loss varies by frequency and also by season. Taking these variations into account, the optimal depth for the hydrophones deployed in the area is between 500 m and 600 m.

However, the strong sub-surface currents, which could subject the vertical moorings to excessive mechanical stress over the long term and the hydrophones to flow-induced noise, may require that some hydrophones and their respective floats be placed even deeper. Placing the hydrophones further away from the optimal depths has implications on the acoustic performance of the system, and therefore one needs also to bear in mind the tradeoffs associated with an increased transmission loss in this case. Another aspect which is likely to complicate the decisions regarding the South triplet is that most acoustic rays reaching the station from the South are likely to travel through large areas where the sound speed profile is an upward refracting arctic profile (represented by the deeper blue areas in Figure 3). These issues will be addressed in an upcoming high-fidelity long range (at ocean basin scales) propagation modelling effort, through which the acoustic performance of the station as a function of hydrophone location and depth will be carefully evaluated.

Despite Crozet's remoteness, ships do visit and anchor offshore. This includes the visiting resupply vessels and roughly monthly visits by a patrol vessel. Crozet also provides one of the few somewhat sheltered anchorages available for longliner fishing vessels. Possession Island has a designated anchorage zone near Baie du Marin, which is the only site where the cable for the shore recording facility can be landed. Anchorage represents the biggest hazard for the underwater cables and for the entire hydroacoustic station. The segment of the cable nearest to shore

is generally surrounded by an iron split-pipe conduit to protect the cable from near shore hazards. Nevertheless, the anchors of some larger ships can damage the cable regardless of the split-pipe protection.
While there is a designated anchorage and maps showing areas where anchoring is not permitted are available to mariners, this is not a complete solution. In stormy conditions, anchored ships can drift, potentially dragging the anchor into the cable route. Under such conditions, the ship's master will give priority to the safety of the ship and personnel on board, so the best approach, beyond proper cable armoring and protection, is the routing of the cable as far as possible from the anchorage zones or from zones where anchors could be dragged into the cable. This will require the use of improved techniques of controlling and guiding the cable as it falls to depth. Such techniques were not readily available at the time of the initial installation effort at Crozet, but they are available now.

The location of Crozet exposes it to a nearly unlimited fetch contributing to frequent strong storms and high sea states even during the austral summer and to very rapidly changing conditions. This has significant consequences for station design and deployment. During the earlier installation efforts, winds were found to frequently exceed 35 knots. In general, strong winds can appear in the area abruptly and reach speeds of 80 knots in less than a couple of hours, and sometimes exceed 140 knots. The resulting sea states are such that cable-laying operations cannot continue. To operate in such conditions, frequently updated and accurate weather forecasts are needed. This will require training and validating an ad-hoc model with regularly updated meteorological data for a few seasons in advance of the deployment operations, so that a reliable forecasting service can be available during deployment.

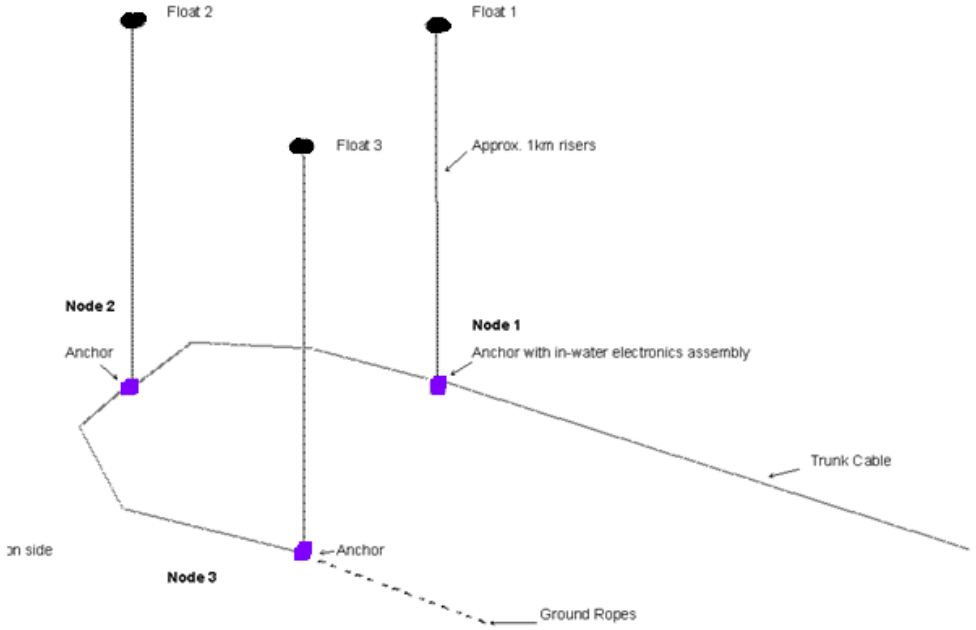
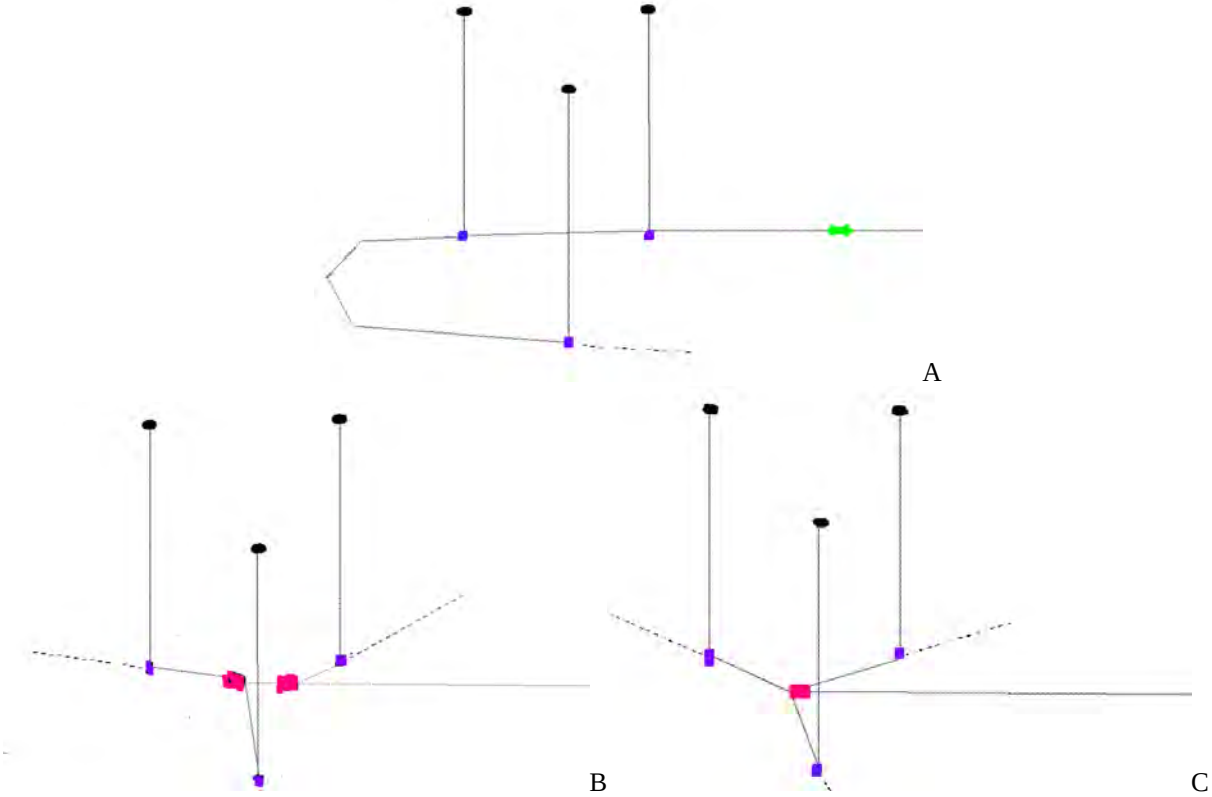


Figure 6. Linear station layout used at other IMS hydroacoustic stations. The three nodes are tied directly to the single trunk cable. (Figure from Mallin, 2012).

A linear layout was used for the current IMS hydrophone station triplets, where three hydrophone nodes are spliced directly onto the trunk cable. The cable is then laid with the three hydrophone nodes deployed as an equilateral triangle with a turn in the cable between each node (Figure 6). This avoids the need for connectors and branching units, but the design also requires that the deployment be done as one continuous process. Weather interruptions cannot be easily handled with this approach. The hydrophone node packages consist of an anchor package on the trunk cable, a riser cable for the hydrophone, the hydrophone, and a float. Once the packages are on the seabed, pyrotechnic fasteners are triggered to release the hydrophone so that the float can raise the hydrophone to the intended depth. The pyrotechnic fastener is also designed to corrode in seawater over some tens of hours to provide a backup release mechanism. This limits the amount of time that the hydrophone package can be in the water before it reaches its intended deployment position. If the hydrophone package is in the water for a longer period of time it would have to be repaired, refurbished, or replaced before redeployment to the intended location. Complete deployment of a trunk cable and its associated triplet would typically be expected to require an uninterrupted good (or reasonable) weather window of 36 hours.

Modular designs may offer a means for subdividing the installation tasks into a series of shorter tasks, for example by separating the laying of the trunk cable from the deployment of the hydrophone triplet. This could be done with the triplet connected into a single junction box, which would be connected to the main trunk cable (Figure 7A), or a configuration involving the use of one or more branching units (Figures 7B and 7C). All of these configurations require connectors between segments, which until recently had to be mated on deck before the system was deployed into the water (dry mating). The configurations using branching units are complex to lay, requiring highly accurate positioning and station keeping techniques.



- **Figure 7. Three alternate hydrophone layouts using a modular approach. A) Linear layout with triplet connected to trunk cable with connector (green). B) Layout utilizing two branching units (red). C) Layout using sinle branching unit. (Figures from [Mallin, 2012])**

The layout with the single junction box connection and the linear one where the trunk cable is continuous share the same difficulties for maintenance of the hydrophones: the entire triplet must be recovered and replaced as a single unit. The slack and loops in the cable between the hydrophone nodes makes damage of this cable segment likely during recovery as well. Dry-mateable connectors require that both the hydrophone unit needing repair and the branching unit to which it connects be brought to the surface.

More recently, wet-mateable connectors have come into use. These allow the connections to be made underwater with a remotely operated vehicle (ROV). This would help avoid many of the complex surface-handling activities required for the configurations involving dry-mateable connectors, as elements could be separately deployed to their mooring positions on the seafloor and then subsequently connected using an ROV. Similarly, in cases where maintenance is needed on individual hydrophone nodes or branching units, an ROV could be used to disconnect the unit underwater allowing that single item to be recovered, repaired/replaced, and reset. The ROV would then be used to reconnect the elements.

The complexities of ROV operation should not be underestimated, as these require specialized operators and deployment and recovery are limited by sea state. This could cause substantial delays and problems if the sea state rises to a level where the ROV cannot be recovered in time and the ship cannot hold station. Further issues which

need to be addressed regarding wet-mateable connectors are power limitations for the connectors, which may require a dry-mateable connector at the junction of the branching unit with the trunk cable towards the shore, and maintenance issues with the underwater connectible junction boxes, which are more complex and in some designs contain components which require periodic servicing.

In general, modular designs can improve the resilience of the system by eliminating single-points-of-failure that compromise the functionality of other components. Breaking deployment efforts into sub-tasks makes it possible to mitigate weather risks and deployment related equipment damage risks.

CONCLUSIONS AND RECOMMENDATIONS

Installing a hydrophone station at Crozet Island is a very significant and challenging undertaking. While the location has important advantages for the capabilities of the IMS network, the remoteness of the location and the environmental challenges will require careful consideration to design a station for reliable deployment and sustainable operation. Planning and preparation will be key to a successful installation. Preliminary bathymetric, oceanographic and acoustic studies are instrumental in this sense. Thorough testing of the equipment to be installed before integration and deployment is essential. Whatever final design configuration is implemented, the vessel used must be suitable for the weather conditions which may be encountered during the deployment operations. Further research of modular design solutions and state-of-the-art subcomponents is warranted as these could significantly decrease maintenance and sustainability challenges for HA04 and other future cabled ocean systems.

ACKNOWLEDGEMENTS

We would like to thank Mario Zampolli, Jeremy Stanley and Georgios Haralabus at the CTBTO and Phil Harben at Lawrence Livermore National Laboratories for their assistance in preparing this paper.

REFERENCES

Mallin Consultants Ltd. (2012). Feasibility and Desktop Studies Regarding HA04, Report.

Piserchia, P.F., Cansi, Y. and J.L. Plantet (2003). Analysis of data from the hydrophone station of Crozet HA04 for 6 months of operation, Characterization of the noise and preliminary evaluation of the detection capability, *CEA working document*.

Strasberg, M. (1979). Nonacoustic noise interference in measurements of infrasonic ambient noise, *J. Acoust. Soc. Am.* **66**, 1487–1493.

Radionuclide Monitoring

RADIOXENON TRANSPORT IN GEOLOGIC MEDIA

Steven R. F. Biegalski, Mark Deinert, Justin D. Lowrey, and Carlos Rios Perez

The University of Texas at Austin

Sponsored by the National Nuclear Security Administration

Award No. DE-AC52-09NA28608
Proposal No. BAA09-57

ABSTRACT

Radioxenon isotopes are produced with high yield in nuclear fission. Since xenon is a noble gas, it has a high leakage probability in comparison to other fission products that are more chemically reactive. This work represents advances in the development of the Underground Transport of Environmental Xenon (UTEX) code as well as work to experimentally measure the diffusion of noble gasses in experimentally controlled conditions. The UTEX code tracks ^{131m}Xe, ^{133m}Xe, ^{133}Xe, and ^{135}Xe as it is produced and transported underground after a nuclear explosion. The results show significant variations in the radioxenon signature resulting from differential isotopic transport, as well as source mixing. The experiments utilize prompt gamma activation analysis to assess the diffusive transport of noble gasses through a one meter test column.

OBJECTIVES

This work aims to further develop the understanding of radioxenon transport in an underground environment. With this understanding, transport times and forensic signatures are calculated. This work encompasses both computational as well as experimental efforts.

RESEARCH ACCOMPLISHED

Progress in this research was accomplished on two fronts. One development was that of the UTEX code. The second development was the measurement of xenon diffusion through a porous media matrix via prompt gamma activation analysis (PGAA).

Modeling of Radioxenon Production and Release Pathways

UTEX is a numerical code derived from a *double porosity* model of underground geology with gas flow driven by an evolving barometric surface pressure at the surface of the system (Nilson et al., 1991). The model simulates the transport of subsurface radioxenon from beneath the ground to the surface by considering the flow of different xenon isotopes having slightly different masses based on diffusion as well as bulk advective flow. This latter process is termed barometric pumping – as the atmospheric pressure above the surface rises and falls due to normal weather changes, the volume below the surface experiences a literal pumping phenomena in which gas is drawn up and down through fractures in the media. The double porosity model considers homogeneous slabs of bulk matrix media characterized by a porosity $\phi_{m,}$ and a permeability k_m, embedded with vertical fractures of width $\delta_{f,}$ and separated by an average distance δ_m. An initial distribution of contaminating gas is assumed to be distributed uniformly throughout the matrix medium below the interface line. Above the contaminated zone lies an assumedly partially-saturated fresh air buffer zone; saturation effects in this model are presumed to be accounted for in the values of ϕ_m and k_m.

Since the simulated system is symmetric with respect to fractures and matrix slabs, the vertical transport model considers the transport within a single representative unit cell. The vertical transport code that models the flow of gas proceeds as follows: at each time step, the pressure response throughout the system due to surface variation at the surface is calculated; the subsequent advective flow at each point is calculated from the pressure response; coupled transport equations are solved to give the flow of contaminant at each point; gas reaching the surface of the system is assumed to escape as outflow and is therefore removed; radionuclides concentrations remaining are decayed before the next time step; the process is repeated for the next time step. The coupled transport equations describing gas concentration $C(x,y)$ at each point in the system are given in Equation 1. More detail on how these equations are employed and solved can be found in Biegalski et al. (2011).

$$\begin{aligned}\phi_f \frac{\partial C}{\partial t} + \frac{\partial}{\partial x}(Cu) &= -\int_0^{\delta_m/2} \phi_m \frac{\partial C}{\partial t} dy + \frac{\partial}{\partial x}\left(\phi_f D \frac{\partial C}{\partial x}\right) - \phi_f \lambda C \\ \phi_m \frac{\partial C}{\partial t} + \frac{\partial}{\partial y}(Cv) &= \frac{\partial}{\partial y}\left(\phi_m D \frac{\partial C}{\partial y}\right) - \phi_m \lambda C\end{aligned} \quad (1)$$

Major work was conducted in early 2011 to overhaul the structure of UTEX – the code was rewritten in a highly modularized and more efficient form to streamline component-by-component debugging and benchmarking. Then a number of mesh reduction studies were undertaken to evaluate the precision of the numerical calculations within the model with respect to choices in mesh size. The most important of these studies was a comparison of the modeled pressure response to an analytical solution. At each time step, the pressure in the system is calculated from a set of coupled equations similar to those of Equation 1 except there are no bulk advection terms (on the left-hand side of Equation 1). In the case of the pressure response,

these equations may be solved analytically for a simple choice of the driving surface pressure. This analytical solution was used to benchmark the numerically calculated pressure response in UTEX as the mesh spacings were varied. Some of the results for the numerical deviations at points deep within the system are plotted in Figure 1. Even though the left plot for the vertical discretization appears to decrease more slowly than for the right plot of horizontal discretization, note the order of magnitude difference in the scales of both axes. Results of these and other studies led to an eventual choosing of an optimal system discretization of $N \times M = 100 \times 200$, that is 100 mesh points vertically and 200 horizontally.

In addition to the above mesh reduction study, a large number of studies to benchmark the transport results of UTEX were undertaken to verify that the numerical code was actually calculating what it was supposed to be calculating. The transport equations (Equation 1) are analytically intractable as a whole. To make analytical solutions possible, the different transport mechanisms were examined individually. For example, by turning off the pressure variations (or forcing the flow velocities, u and v in Equation 1, to be zero) and setting decay constants to zero, it is possible to reduce the transport equations to simple one-dimensional diffusion equations that have analytical solutions. Similarly, diffusion can be turned off and the flow velocities forced to remain constant to again obtain a tractable set of transport equations. Numerical accuracies for these cases were all of the order 0.01% compared to the analytical solutions, but more interesting is that these accuracies are dependent on the specified values for the geologic input parameters discussed in the *background* section above. This is related to the concept of the Courant number, which places a confidence bound on mesh spacing for a given length of time step and flow velocity.

Lastly, since the transport equations (Equation 1) in their coupled, unsimplified forms cannot be solved analytically for more generalized benchmarking scenarios, the results for the whole-system pressure and isotopic concentrations computed by the tri-diagonal Gaussian elimination numerical scheme were verified with two separate numerical solution methods. First, Newton's method was used to iterate on fracture and matrix concentrations simultaneously and it was found that the results converged after fewer than six iterations, and that the UTEX numerical solution to Equation 1 was satisfied to machine precision. Additionally, a simultaneous solution method was also implemented which formulated the fracture-matrix system as a large, sparse block-diagonal matrix. The $N \times M$ pressure matrix was written as a column vector $\mathbf{p}$ of length $N \times M$, and the matrix equation $A\mathbf{p} = \mathbf{f}$ was solved using Gaussian elimination. In both cases, the computed concentrations of the three solution methods agreed to within machine precision. As such, the veracity of the tridiagonal matrix solver utilized in UTEX was verified.

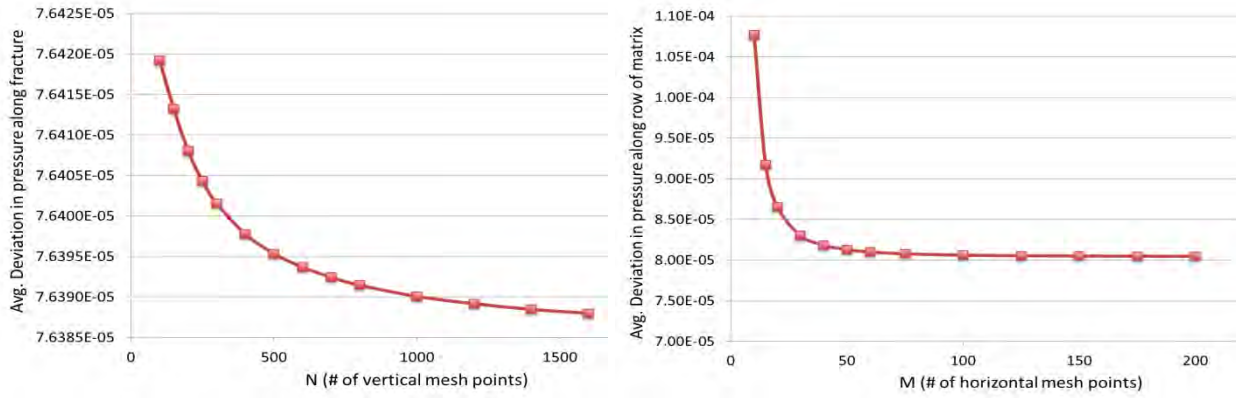


Figure 1. Numerical deviations in pressure from analytical solution for varying vertical (left) and horizontal (right) mesh spacing.

UTEX Sensitivity Study

As a first application of UTEX to consider the ability of geologic transport to affect isotopic fractionation in a subsurface nuclear detonation scenario, a large scale sensitivity study was undertaken to look at how varying the major geologic input parameters can result in fractionation. A survey of available Nevada Test Site geological data was conducted to determine a large parameter space of possible geologies that might be found there; these data are summarized in Table 1 along with the selected values that were considered in the study (McCord, 2007). The atmospheric pressure used to drive the model at each time step was compiled from the weather history at Mercury, NV. The pressure data were chosen to coincide with the 55 days succeeding the March 26, 1992 US test of a device at Pahute Mesa of the Nevada Test Site.

Table 1. NTS geological parameter space

	NTS Geological Range	Parameter Space
Detonation Depth (m)	450-600	{450,525,600}
Matrix Porosity	0.01-0.05 and 0.35-0.45	{0.01,0.05,0.1,0.3,0.37,0.45}
Matrix Permeability (m^{-2})	1E-17 to 1E-15	{1E-17,1E-16,1E-15}
Fracture Spacing (m)	1.0-15.0	{1.0,2.5,5.0,10,15}
Fracture Width (mm)	0.005-1.5	{0.01,0.1,1.0}

In total, 810 separate UTEX simulations were run spanning the parameter space of Table 1 and the isotopic ratios compiled from successive 24-hour samples of released gas are plotted as a multi isotopic ratio correlation (MIRC) plot in Figure 2. Looking at this plot, time is not an explicit parameter, but data points are colored based on the time of outflow and time runs roughly from the top right of the plot to the bottom left. While much of the simulation data fall between the assumed non-fractioned and fully-fractioned bounds, there are in fact many instances in which radioxenon releases give ratios far removed from this domain. Note that the largest deviations from the red and blue (non- and fully-fractioned) bounds occur at times corresponding to the largest drops in atmospheric pressure. It is clear from these data that the vertical transport of radioxenon gas from an underground nuclear explosion may significantly affect the isotopic signature.

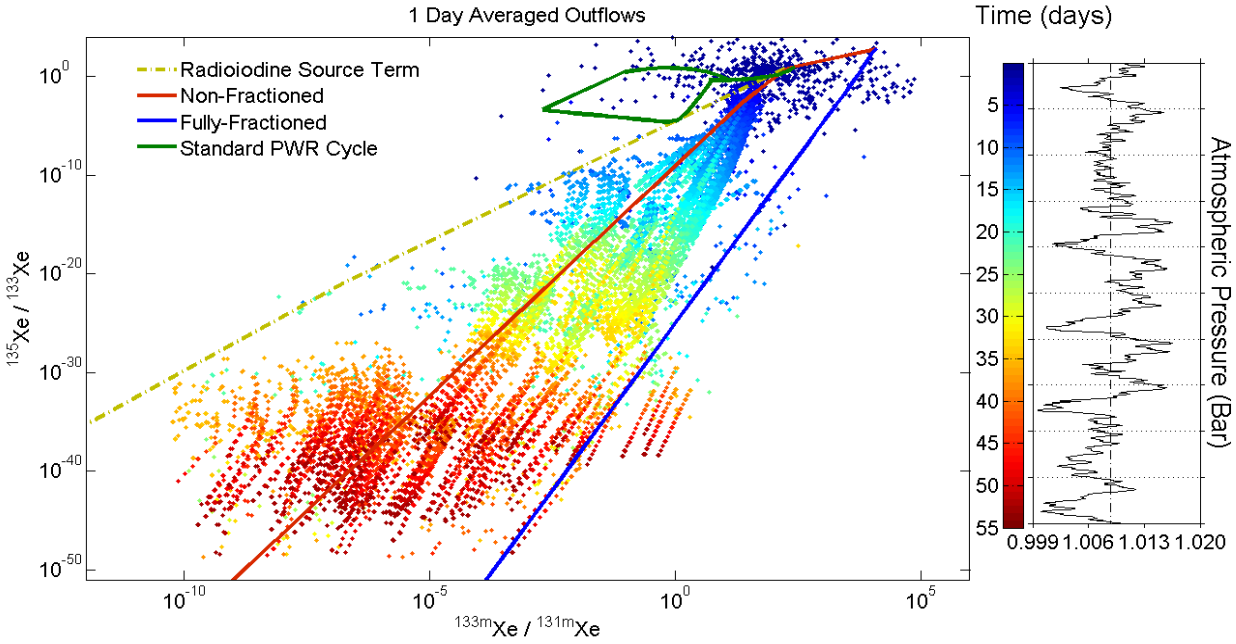


Figure 2. Results of UTEX model sensitivity study plotted in a MIRC plot showing the isotopic ratios exceeding the currently-accepted bounds.

Experimental Diffusion Measurements

The objective of the present project is to obtain experimental data that reveals variation in the isotopic concentration of xenon as it migrates through a porous media as a consequence of the transport mechanisms involved (Lowrey et al., 2012; Carrigan et al., 1996). Previous work conducted at The University of Texas at Austin analyzed the diffusion of xenon through a porous media, and showed the viability of using prompt gamma activation analysis to quantify variations on the concentration of a noble gas after it diffuses through a porous media (Rios Perez et al. 2012). The present work summarizes the latest results regarding the calculation of detection limits utilizing the prompt gamma facility employed, the results of the diffusion experiments conducted using argon (surrogate gas) and xenon, and the numerical model used to estimate the diffusion coefficient of these noble gases.

As part of the experimental methodology development, it is necessary to calibrate the detection system (energy and total count efficiency calibration), and to estimate the detection limits of a xenon and argon gas sample using the prompt gamma activation analysis facility at the Nuclear Engineering Teaching Laboratory. The concentration and pressure detection limits ($L_{D(conc)}$ and $L_{D(press)}$) of the system employed give us the minimum amount of xenon and argon that our prompt gamma facility is capable to detect with its current configuration. Table 2 shows the pressure and concentration detection limits utilizing the Currie method (Currie, 1968; Currie, 1995; Biegalski et al,. 2007). The detector efficiency for this system was calculated utilizing a ^{152}Eu source with activity traceable to the National Institute of Standards and Technology.

Table 2. **Prompt gamma counting rates and detection limits for ^{40}Ar, ^{129}Xe and ^{131}Xe (* ^{131}Xe and ^{129}Xe present peaks at 670.02 keV and 668.59 keV respectively).**

Isotope	*Energy {keV}*	*σ_γ{b}*	*Efficiency (4.02% error)*	*Detection Limit $\times 10^6$ {mol/cm^3}*	*Detection Limit {torr}*
^{40}Ar	166.3	0.22	0.002494	3.681±0.22	66.5 ±0.53
	1185.8	0.14	0.001353	6.367±0.38	115.2±1.49
^{129}Xe	536.17	1.71	0.001724	0.436±0.03	7.9±0.03
	586.17	0.48	0.001688	1.708±0.10	30.9±0.22
	1482.06	0.112	0.001215	10.889±0.66	196.9±3.15
^{131}Xe	630.29	1.41	0.001658	0.607±0.04	10.9±0.04
	667.79*	6.7	0.001635	0.113±0.01	2.1±0.01
	772.72	1.78	0.001572	0.476±0.03	8.6±0.03

Due to the relatively long analysis times required to obtain the detection limits shown in Table 2, the experimental procedure proposed would measure the variation of the argon/xenon concentration at the noble gas source after a diffusion experiment has been conducted. The proposed procedure is performed in three major steps: porous media column venting, noble gas sample preparation, and diffusion of argon in nitrogen. During the first step, a minimum of 120 liters of nitrogen (12 times the empty set-up volume) flows through the experimental set-up at 1.5 liter/min and at 0.5 liter/min (1 hour or more each flow rate) to displace any trace of a noble gas from previous experiments. After this, the experimental set-up is pressurized with nitrogen up to *c.a.* 1,000 Pa.

The preparation of the noble gas sample also requires the extraction of any undesirable trace gas from previous experiments. This includes a series of pump and flush cycles of the 1 liter sample cylinder with the desired noble gas until 99.5% of the gas in the sample cylinder corresponds to argon or xenon. The aluminum cylinder is then pressurized up to 105 kPa (absolute) in a different room than where the media column is located. The gas sample cylinder is taken to the prompt gamma facility and its pressure is set to match the pressure of the porous media test chamber. Flow and pressure are measured utilizing a ¼ inch stainless steel low-flow metering valve from Swagelok® and a PX653-05D5V differential pressure transducer from OMEGA®, respectively.

Before connecting the cylinder to the porous media, the argon/xenon sample is analyzed using prompt gamma with the reactor operating at 950 kW. Then, the sample cylinder is connected to the experimental set-up by a full-flow quick connector from Swagelok® allowing the noble gas diffuse through the experimental set-up for a predetermined time. Once the target diffusion time has elapsed, the sample cylinder is detached from the porous media and analyzed with the reactor operating at 950 kW. The diffusion time would vary on every experiment in order to obtain the change in noble gas concentration after various diffusion times. The results of the argon and xenon diffusion experiments are shown in Figure 3. The non-intuitive lower ratios of xenon concentrations (argon has a larger diffusivity and should be depleted faster) might be caused by the larger difference in molecular weight between the species diffusing in the xenon-nitrogen case. This larger difference in molecular weights may cause a transient pressure gradient as the nitrogen molecules move faster than xenon molecules temporally producing the advection of xenon out of the sample cylinder.

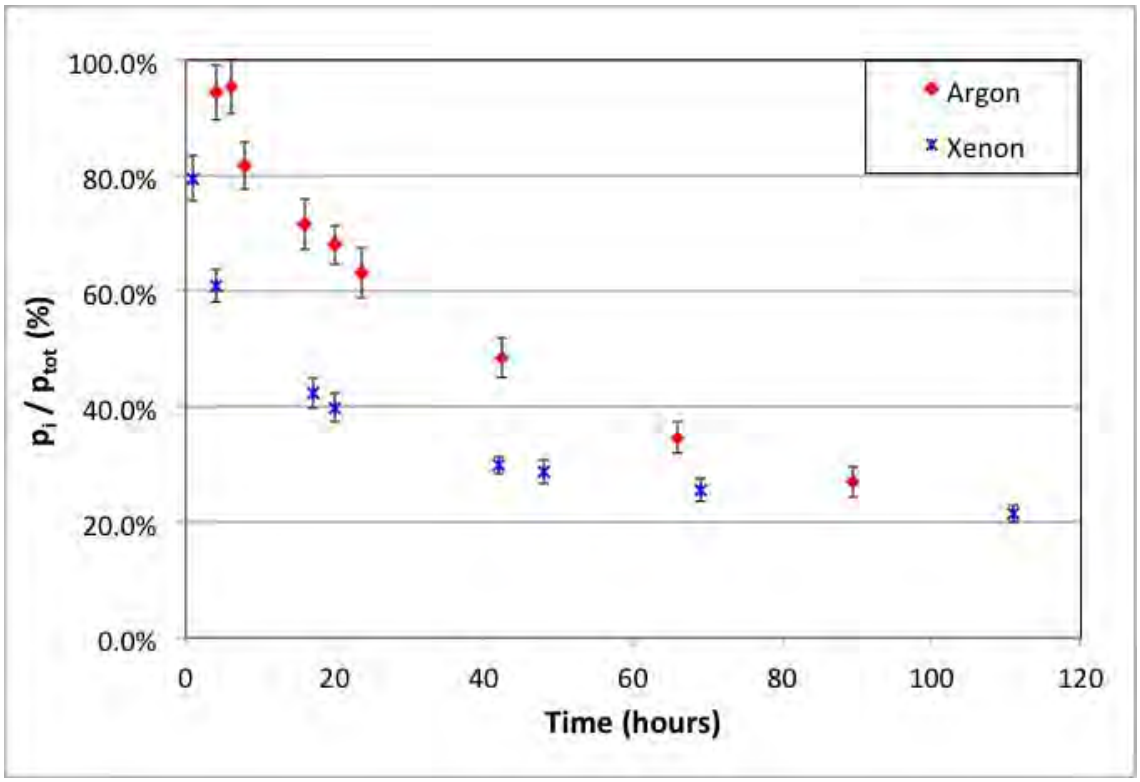


Figure 3. Ratios of argon and xenon concentrations within the gas sample cylinder to initial concentration after diffusing the noble gas through the experimental set-up for different periods of time.

In the proposed methodology, the binary diffusion coefficient of a noble gas migrating through nitrogen within a porous media is estimated by comparison of experimental data with the predictions of a numerical method. This section introduces the model and boundary conditions formulated assuming a 1-D diffusion process of a finite amount of noble gas in a closed system within a 1 m long porous media. For this model, the transient pressure gradient caused by the interdiffusion of species with different molecular weights is neglected. Therefore, a concentration gradient dominated process would be assumed.

The general equation to describe this model and its boundary conditions are shown in Equations 2 and 3:

$$\frac{\partial C_{Ar}}{\partial t} = \frac{\partial}{\partial x}\left(-D_a \frac{\partial C_{Ar}}{\partial x}\right) \tag{2}$$

$t=0,\ x \le L_{CYL}$: $C_{Ar} = Co$ $\qquad t, x = 0 : \frac{\partial C_{Ar}}{\partial x} = 0$

(3)

$t=0,\ x > L_{CYL}$: $C_{Ar} = 0$ $\qquad t, x = L_{TOT} : \frac{\partial CAr}{\partial x} = 0$

where L_{TOT} (m) and L_{CYL} (m) are the total experimental set-up and sample gas cylinder length respectively, Co is the initial molar concentration in the cylinder (mol·cm^{-3}), and D_a (cm^2·s^{-1}) is the apparent or effective diffusivity. Because of the variation in diameter and presence of sections without sand, the experimental set-up was divided in four sections listed in Table 3. The length of the pipe fittings section was calculated, as a first approximation, by using the equivalent length method to calculate its head minor-losses (Fox, 2004). The model proposed in Equation 3 was solved numerically using an explicit second-order finite difference method. The effective diffusion coefficient of argon in nitrogen within the experimental set-up of this project was estimated varying the apparent diffusivity in the numerical model, comparing its results with experimental data, and choosing the value that minimizes the sum of the square errors.

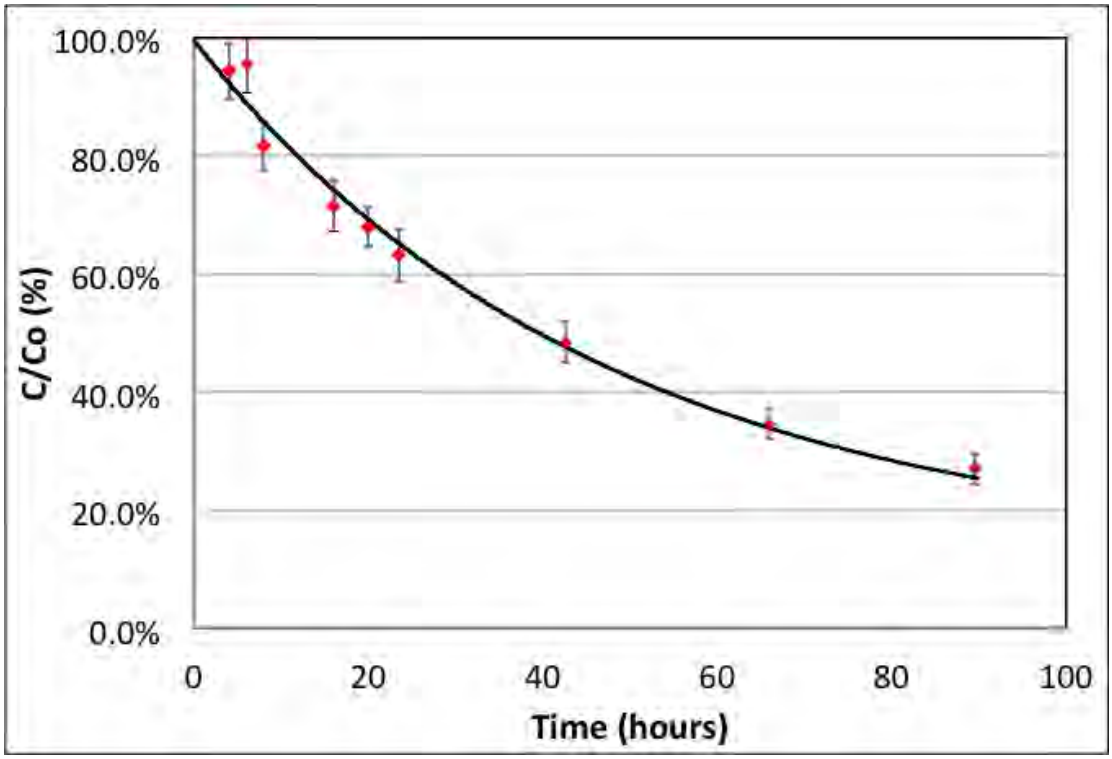


Figure 4. Comparison of the noble gas ratio concentration after various diffusion experiments obtained experimentally and from the numerical model developed.

The apparent diffusivity estimated with the procedure outline here was 0.0572 (cm^2s^{-1}) with a mean square error of 0.0079. Figure 4 shows the good agreement between experimental data and numerical model results for the argon data. However, the experimental results of xenon could not be matched with the numerical model. A possible explanation for this disagreement is the potential presence of advection as an important mechanism of mass transfer. The likely appearance of pressure gradients might be caused by the larger difference in molecular weights between xenon and nitrogen. In order to estimate the diffusion coefficient of xenon, the numerical model needs to be modified to include this effect.

Finally, the variation of the sample isotopic composition was evaluated. The energy peaks selected for this comparison were 536.17 and 772.72 keV for ^{129}Xe and ^{131}Xe respectively due to their smaller detection limits as shown in Table 2. The results, shown in Table 3, only exhibit a higher depletion of ^{129}Xe than ^{131}Xe (with a percentage difference larger than the measurement errors) in the 1-hour diffusion experiment. For all the other cases, the measurement errors overlap the difference in concentration ratios for these two isotopes. Future work could try to improve the accuracy of the measurements by improving the shielding of the prompt gamma activation facility, or use radioactive isotopes with a larger molecular weight difference to produce a bigger fractionation of xenon isotopes.

Table 3. Variations of the ^{129}Xe and ^{131}Xe concentrations after various diffusion experiments.

Diffusion Time (hours)	*ISOTOPE*	*C/Co*	*error*
1	^{129}Xe	78.7%	0.8%
	^{131}Xe	80.0%	0.7%
4	^{129}Xe	61.4%	0.9%
	^{131}Xe	61.5%	1.0%
17	^{129}Xe	42.1%	1.3%
	^{131}Xe	41.1%	1.4%
20	^{129}Xe	38.7%	1.2%
	^{131}Xe	38.0%	1.3%
42	^{129}Xe	29.6%	1.5%
	^{131}Xe	30.1%	1.7%
48	^{129}Xe	28.4%	1.6%
	^{131}Xe	28.1%	1.7%
69	^{129}Xe	25.3%	1.7%
	^{131}Xe	27.1%	1.8%
111	^{129}Xe	22.1%	2.1%
	^{131}Xe	21.6%	2.5%

CONCLUSIONS AND RECOMMENDATIONS

This work shows results from both the modeling efforts conducted with the UTEX code and the experimental diffusion measurements. The UTEX code results show that a wide range of radioxenon signatures may possibly be measured at the surface after an underground nuclear explosion. The local geology plays a major role in the noble gas transport as well as the surface atmospheric pressure. This work has shown that tracking the radioxenon source term from parent fission products as a function of decay time is essential to proper understanding of source signatures that may be present at the time of an On-Site Inspection.

The noble gas diffusion measurements show that argon travels through as porous medium as predicted from classical diffusion theory modeling. The xenon gas, however, travels faster than a simple diffusion model predicts. The difference could be due to advection or due to the presence of micro crack structures present in the porous media. Future work is needed to fully understand the xenon transport results.

ACKNOWLEDGEMENTS

We would like to extend our gratitude to the staff of the Nuclear Engineering Teaching Laboratory at the University of Texas at Austin for experimental support.

REFERENCES

Biegalski SR, Green TC, Alvarez E, Aghara S (2007). Background characterization of The University of Texas PGAA Facility, *J. Radioanal. Nuc. Chem.* **271** (2), 413–417. doi:10.1007/s10967-007-0224-z

Biegalski S., Deinert M., Lowrey J., Rios Perez C. (2011). Radioxenon signatures from underground transport and radiopharmaceutical facilities, in *Proceedings of the 2011 Monitoring Research Review: Ground-Based Nuclear Explosion Monitoring Technologies*, LA-UR-11-04823, Vol. 2, pp. 616–625.

Carrigan CR, Heinle RA, Hudson GB, Nitao JJ, Zucca JJ (1996). Trace gas emissions on geological faults as indicators of underground nuclear testing, *Nature* **382**, 528–531.

Currie LA (1968). Limits for qualitative detection and quantitative determination, application to radiochemistry, *Anal. Chem.* **40** (3), 586–593. doi:10.1021/ac60259a007.

Currie LA (1995). Nomenclature in Evaluation of Analytical Methods Including Detection and Quantification Capabilities, *Pure Appl. Chem.* **67** (10), 25.

Fox RW, McDonald AT, Pritchard PJ (2004). *Introduction to fluid mechanics*. 6th Edn. Wiley, Hoboken, N.J.

Lowrey JD, Biegalski SR, Deinert MR (2012). UTEX modeling of radioxenon isotopic fractionation resulting from subsurface transport, submitted to *J. Radioanal. Nuc. Chem.*

McCord, J (2007). Phase I Contaminant Transport Parameters for the Groundwater Flow and Contaminant Transport Model of Corrective Action Unit 97: Yucca Flat/Climax Mine, Nevada Test Site, Nye County, Nevada, Revision 0. Report No. S-N/99205--096.

Nilson R. H., E. W. Peterson, K. H Lie, N. R. Buckhard, and J. R. Hearst (1991). Atmospheric pumping: a mechanism causing vertical transport of contaminated gases through fractured permeable media, *J. Geophy. Res.* **96**(B13), 21,933–21,948.

Rios Perez C, Lowrey J, Biegalski S, Deinert M (2012) Xenon diffusion studies with prompt gamma activation analysis, *Journal of Radioanalytical and Nuclear Chemistry* **291** (1):261–265.

TECHNOLOGY GOALS FOR A NEXT GENERATION RADIOXENON MONITORING SYSTEM

James H. Ely[1], James C. Hayes[1], Derek A. Haas[1], Warren W. Harper[1],
Jill C. Madison[1], Anders Ringbom[2], and Klas Elmgren[2]

Pacific Northwest National Laboratory[1] and the Swedish Defense Research Agency[2]

Sponsored by the US Department of State

Award No. DOS-IAA-12-ISN-NDF_02

ABSTRACT

A decade of radioxenon sampler operation, primarily in the International Noble Gas Experiment (INGE), has illuminated areas for improvement in operations and verification of continuous field measurements of radioxenon gas escaping from an underground nuclear detonation. These opportunities include measurement sensitivity, sample throughput time, system uptime, and data availability. Increasing measurement sensitivity allows for finer discrimination between manmade radioxenon signals (from sources such as medical isotope production facilities) and radioxenon signals that result from fission in a nuclear weapon. Measurement sensitivity can be increased with techniques such as halving the sample processing time or increasing the quantity of xenon extracted from the atmosphere. Additionally, improvements in gas processing technology and control system software can improve the uptime and data availability. This paper will discuss the technical requirements as well as the system and operational specifications which will be the groundwork for a next-generation radioxenon monitoring system called Xenon International.

OBJECTIVES

Detection of radioxenon isotopes is a proven and important method for detecting nuclear explosions, in particular, for undeclared underground testing. Xenon isotopes are produced in large quantities during fission in a nuclear explosion, and being noble gases, are nonreactive and can escape in measurable quantities from underground detonations. The radioxenon isotopes ^{131m}Xe, ^{133}Xe, ^{133m}Xe and ^{135}Xe are of particularly high-value in identifying nuclear explosions. Four such systems that collect and measure radioxenon automatically were tested in the International Noble Gas Experiment (INGE) which started in 1999: Russia's Analyzer of Xenon Radioisotopes (ARIX), the United States' Automated Radioxenon Sampler/Analyzer (ARSA) the Swedish Automatic Unit for Noble gas Acquisition (SAUNA) and France's Systéme de Prélèvements et d'Analyse en Ligne d'Air pour quantified le Xenon (SPALAX) (Dubasov et al., 2005; Bowyer et al., 1998 and 1999; Fontaine et al., 2004; Ringbom et al., 2003).

Trial evaluations, and initial phase of INGE, were held in Freiburg Germany starting in 1999 to demonstrate the state of development of the four samplers (Auer et al., 2004). After completion of the initial demonstrations, the next phase of the INGE was the deployment of each system to different parts of the world to understand international measurement challenges. Today, still as part of the INGE, stations around the world are being populated mainly by commercially available samplers from France and Sweden and from State produced systems from Russia–systems that are mostly based on the original system designs demonstrated in phase I of the INGE. The INGE now uses data from these samplers to understand operational challenges such as system lifetime, the impact of regional meteorology on radioxenon signatures, and anthropogenic radioxenon background sources.

Past INGE studies led to many lessons learned which can be incorporated into next generation radioxenon measurement systems. INGE not only identified ways to improve monitoring technology, but also discovered the existence of significant radioxenon backgrounds from medical and industrial isotope production. New approaches to distinguishing these backgrounds from nuclear explosions have been and are being investigated, including ratios of the various isotopic concentrations (Kalinowski et al., 2010). A challenge with the ratio approach is the difference in typical concentrations for the isotopes; in particular, the metastables ^{131m}Xe and ^{133m}Xe, tend to have lower concentrations compared to ^{133}Xe and ^{135}Xe. Next generation systems will therefore need to have increased sensitivity especially for the minor xenon isotopes. In addition, studies with atmospheric modeling and plume tracking have indicated that sampling at shorter periods than the current 12 or 24 hours would improve the information learned from positive radioxenon detections. Shorter sampling times would provide more acute timing information for input into the atmospheric modeling, and help provide a more accurate tracking to the source location. Shorter sampling times would provide higher resolution data on the plume, supporting more accurate estimates of the initial release, which will be important for estimating the yield of nuclear explosions. Finally, although the radioxenon sampling systems have been fairly reliable, there remains room for improvement in reliability. Many of the locations are remote with challenging access; higher reliability would reduce downtime and operational costs leading to a more effective monitoring system. Reducing system consumables, or switching to less costly alternatives, would also reduce costs for maintaining remote locations.

The next generation system will need to improve the confidence of identifying nuclear explosions through increased sensitivity to minor xenon isotopes, increased sampling frequency, and improved system reliability and uptime. This paper describes the technology goals needed for the next generation radioxenon systems that will lead to functional improvements and requirements.

RESEARCH ACCOMPLISHED

Increasing Sensitivity

One of the primary goals of a next generation system will be to increase the sensitivity to the radioxenon isotopes. There are benign sources of radioxenon in the form of nuclear reactors and medical isotope production facilities that continuously emit and replenish radioxenon into the atmosphere. Due to this background and the change in concentrations due to mixing in the atmosphere and radioactive decay prior to being collected, it is not possible to distinguish sources of radioxenon using single isotope concentrations, unless the concentrations are much higher than reactor or medical isotope production releases. Ratios of the various isotopes can be helpful in that the

atmospheric mixing is the same for each of the isotopes measured at a specific location. However, the ratios do change with time, depending on the relative life-times of the radioxenons used, and ratios between two isotopes (single isotopic ratios) do not provide discrimination power in many cases. The power of the single isotope ratio is dependent on the source to sampler distance and the atmospheric conditions and which isotopes are measured. The best approach uses all four radioxenons in a multiple isotopic ratio analysis, or if only three isotopes are above the minimal detectable quantity, a three isotope analysis (Kalinowski et al., 2010). However, typically only ^{133}Xe is detected in locations where medical isotope production or nuclear reactor emissions are routinely measured. Periodically, the ^{133}Xe is measured with ^{133m}Xe or ^{135}Xe, and very rarely with ^{131m}Xe. Therefore, in many cases where radioxenon (primarily ^{133}Xe) is detected, multiple isotope analysis is not achievable. Limits on the ratios can be made by using the minimal detectable concentration (MDC) of the system, but reduces the discrimination power of this approach. The need to measure radioxenon isotopes at lower levels for multiple isotope ratio analysis drives the technology goal of increased sensitivity for the next generation radioxenon monitoring system.

The current systems were designed to have a MDC of 1 milliBecquerel per meter cubic meter (mBq/m^3) for ^{133}Xe for a sample of air collected for less than 24 hours. All three (SPALAX, SAUNA, and ARIX) systems exceed this requirement, and have MDCs that range between 0.2-0.6 mBq/m^3 for ^{133}Xe. The SPALAX system samples the atmosphere for slightly under 24 hours, while the SAUNA and ARIX systems have collection periods of 12 hours. A goal on the next generation system would be to exceed the sensitivity capabilities for the same collection time. Since the SAUNA and ARIX have short collection times, the goal should be to improve upon 0.2 mBq/m^3 for ^{133}Xe for a 12-hour collection.

The SAUNA and ARIX systems both use dual nuclear detectors where the beta and gamma are measured in coincidence. Coincidence counting reduces the background and correspondingly the MDC from using just a single detector. For the beta-gamma detector systems the MDC is typically calculated for a single radioxenon isotope as:

$$MDC\left(\frac{mBq}{m^3 air}\right) = \left(\frac{2.71 + 4.65\sigma_0}{\varepsilon_\gamma \varepsilon_\beta \gamma_{BR} \beta_{BR}}\right) \frac{\lambda^2 * T_C}{(1-\exp(-\lambda T_C))\exp(-\lambda T_P)(1-\exp(-\lambda T_A))} \left(\frac{1000}{V_{Air}}\right) \quad (1)$$

where the first term takes into account the typical MDC expression using the standard deviation of the measured blank sample (σ_0) with the gamma and beta detector efficiencies and branching fractions respectively (ε_γ, ε_β, γ_{BR}, β_{BR}), the second term accounts for the decay of the xenon isotope during the collection time (T_C), the processing time (T_P) and the nuclear acquisition time (T_A) using the decay constant for the specific isotope (λ), and the final third term accounts for the volume of air measured (V_{air}) and conversion to milliBecquerel.

To reduce the MDC, the above equation can be used to identify the pertinent variables. The background uncertainty can be reduced (σ_0), the detector efficiency can be increased, the times reduced for decay corrections (specifically the collection time), or the volume increased. Reducing the background uncertainty can be accomplished by extending the count time or reducing the overall background. The background uncertainty is proportional to the square root of both the background counts (B) and acquisition time:

$$\sigma_0 \propto \sqrt{BT_A} \quad (2)$$

Reducing the overall background is the best approach, but is typically challenging to further increase the current shielding in the systems. The count time can be increased, for example, by increasing the number of detectors, so the each sample can be counted longer, but is somewhat offset by the decay correction, and therefore the advantage is less the square root increase in the acquisition time. However, increasing the number of detectors is one of the most straightforward approaches to increased sensitivity.

Reducing the collection and processing times will improve the MDC especially for the short lived isotopes such as ^{135}Xe (nine hour half-life). For example, reducing the collection time from 12 hours to 6 hours can reduce the MDC by ~20% for ^{135}Xe, with less of an effect for the other longer-lived isotopes. Reducing the times to increase the sensitivity is not the most efficient approach, however, reducing the collection time has other advantages (see following section) so is worthwhile to consider for the next generation systems.

As the volume term enters into the MDC equation linearly, increase the sampling volume, or more specifically, the amount of xenon being assayed in the nuclear detector, is the most efficient manner to increase the sensitivity. There are two areas of possible improvement for increasing the amount of xenon in the nuclear detector; sampling a larger volume of air, or increasing the efficiency of the processing. The SAUNA system has a fairly high processing efficiency on the order of 80%, and will be challenging to improve upon. A more direct method is to increase the amount of gas sampled. The SAUNA system samples air at a rate of 1.2 m^3/hr which equates to 20 liters per minute (Auer, 2010). A next generation system could have more sensitivity by increasing the amount of air sampled and processed through the system.

Since the sampled volume, collection times, and acquisition times are interconnected, it is useful to calculate the MDC while varying these parameters. For the following ^{133}Xe example shown in Figure 1, a multiple detector system (containing four detectors) built at PNNL (Cooper et al., 2005 and 2007) was used. The background was measured for ~ two days, and the rate and standard deviation calculated for the ^{133}Xe region of interest. Although it was assumed that there was no interference or memory effect of other radioactive gas in the ^{133}Xe region of interest, the uncertainties associated with those possible contaminations were taken into account. Three different air sampling rates were chosen, and an 80% processing efficiency assumed.

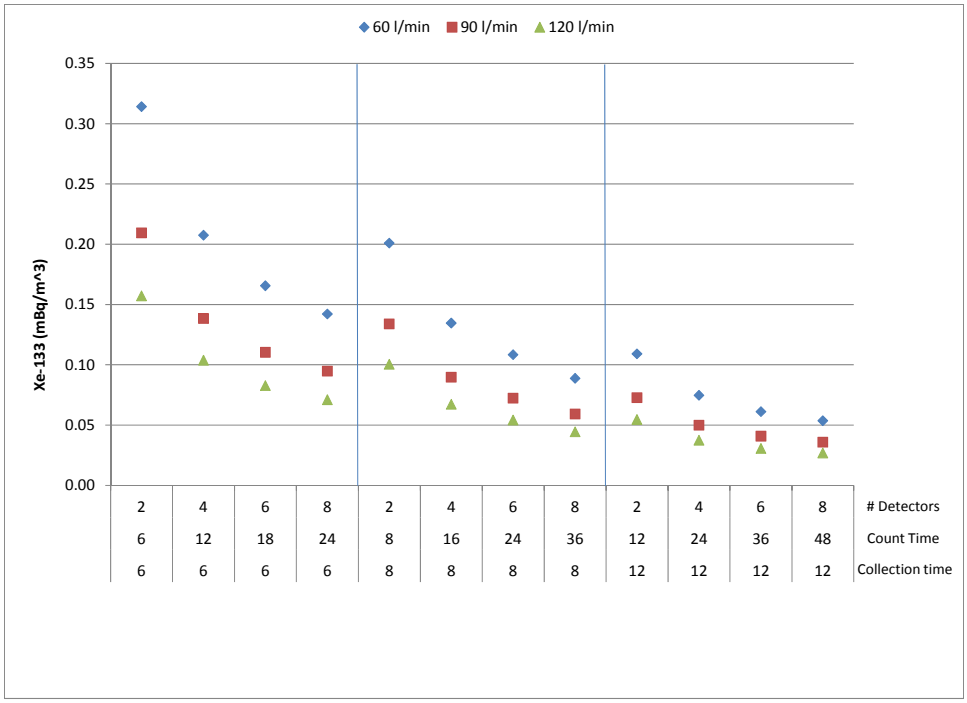


Figure 1. Calculations of the MDC for variations in the count (number of detectors) and collection times, based on the PNNL beta-gamma detector system for three air sampling rates.

As shown in Figure 1, the MDC decreases as the count time increases (number of detector increases), or the air sampling rate increases. Doubling the air sampling reduces the MDC by ½, but doubling the count time only reduces the MDC by ~30%, consistent with the expectations based on the MDC equation: increasing the air sampling is the most efficient method to reduce the MDC and increase the sensitivity. Increasing the collection time at the same air sampling rate (and number of detectors) allows for increased counting time and reduces MDC. However, that is assuming a single sample, and shortening the collection time allows for more samples to be collected for a given period of time. To directly compare the MDC for different collection times, one needs to combine the shorter samples together. For example, taking the 6- and 12-hour collection, one should add two of the 6-hour collections to compare to a single 12-hour collection, in which the MDC would be equal for the same air collected.

Increasing Sampling Frequency

Increased sampling frequency is another technology goal for the next generation radioxenon monitoring system. Increasing the frequency of the samples would provide higher fidelity time information on the plume and detected isotopes. This would provide better input into atmospheric transport models allowing for tighter bounds on source location and activity release estimates. As more stations are installed, the average source-sampler distances are reduced, and plumes will be less dispersed before being sampled; higher sampling frequency would provide better information on plumes sampled for short times.

The current assumption for the radioxenon concentration calculation is that the source activity is constant over the collection period. This provides the basis for the decay correction during the collection time, which is the same as in the MDC equation above. This is a good assumption if the activity is essentially constant as it might be for a very distant source, but is less accurate when the activity is changing as the plume arrives or leaves, or the concentration in the plume changes. A higher sampling frequency can reduce the amount of change during a single sample, and thereby provide a more accurate calculation of the concentration.

However, the same (or greater) sensitivity needs to be maintained for the shorter sampling cycle, in order to detect the low level concentrations of radioxenon. Simply changing the sampling time would not provide much benefit as the fluctuations in the data would be large from smaller Xe collections and perhaps short counting times leading to increase in MDCs. The goal of the next generation system would be to have increased sampling frequency with the same (or increased) sensitivity for the shorter sampling period.

In order to accomplish the same sensitivity in a shorter time period, the radiation detection sensitivity of the system needs to be increased, or the amount of xenon collected and processed increased. As described in the section above, increasing the radiation detection sensitivity of the system can be accomplished by reducing the background in the detector, or increasing the acquisition time, which is most easily accomplished by adding in more detectors when increasing the sampling frequency. Increasing the amount of air flow is the most efficient means to maintain or increase sensitivity while decreasing the collection time (increasing the sampling frequency).

However, the sampling frequency cannot be increased simply by reducing the collection time and increasing the air flow at the system intake. These systems are designed for specific flow rates, total volumes, and specific collection times; increasing the rate and total volume of air processed can be a significant challenge and could require a complete redesign of the system. In addition to being able to handle the increased air volume, the systems will also need to be ready to process the next sample more quickly, which means the time for regeneration and cooling processes will need to decreased as well. These considerations drive toward a more efficient system design which will likely increase the complexity of the system. For example, the current SAUNA system uses an ambient temperature collection process, which requires a rather large amount of absorber material which requires time to heat and cool. Absorbers are more efficient when cooled; one approach would be to use cooling to reduce the volume of material and hence cooling and heating time. The processing at each step needs to be designed and optimized to handle the increased air flow and reduce overall processing time. The goal of the next generation system would be to have increased sampling frequency with a system that is more cost-effective and utilizes a smaller footprint. In other words, selection of the sampling frequency requires a comprehensive examination of the impacts to system cost, sensitivity, resources, and reliability.

Improving System Reliability

The stations are located to provide as uniform coverage of the world as possible. In order to do so, many of the stations are located in remote areas with limited access. The current systems are designed to be automated and operate with minimal maintenance and repair, and the next generation system will improve on the reliability as well. The systems should have minimal occurrences of unscheduled maintenance, as some locations require extensive travel and logistical challenges to reach the location, adding significantly to the downtime. A goal of the next generation systems would be to minimize operation and maintenance costs by maximizing reliability.

In addition to maximizing the reliability, the systems should minimize the consumables required, especially one requiring shipment and replacement. For example, the SAUNA system requires helium gas (as a carrier gas) for processing, which must be replaced periodically. A preferred approach would be to use an alternative such as

nitrogen, which could be generated on-site with a nitrogen generator from the local air. However, a nitrogen generator requires power, which may be in short supply at some locations as well, so the next generation system should optimally be flexible to operate with bottled or generated gas in this case. Other consumables may include absorbent material that requires replacement after some period of use. The next generation system would minimize consumable to as great extent as possible to reduce operational costs.

One of the best outcomes of INGE is the wealth of operational data collected. For example, station reliability has been analyzed and the various downtime causes categorized over the operation period from July 2004-July 2008 (Auer et al., 2010). During that period of time, the operational systems had a downtime of ~26%. The largest fraction (0.31) was associated with issues with the detector system, mostly with the cooling of the high purity germanium (HPGe) detector on the SPALAX system. The next largest fraction (0.27) was associated with the sampling and processing, with the third largest (0.16) being issues with the computer and software. Although the frequency of the detector issues were not as high as some of the other issue categories, logistics of repairs and replacement parts often caused the system to be down for months. The computer and software issues on the other hand could often be resolved by the station operator in short order, reducing the overall downtime. Since the study above, the reliability of the systems has improved considerably. However, these issues indicate that the systems need to be very reliable, with little or no failure between scheduled maintenance periods. Encouragingly, since the time of Auer et al. (2010), the uptime has increased to over 90% for both the SAUNA and SPALAX. Part of this achievement rests on an improved concept of providing spares and improvements in commercial HPGe detector reliability. However, the most important factor is the expense of labor hours and travel by maintenance staff. Improving the inherent reliability of design and component selections will lead to greater operational effectiveness at lower cost.

While HPGe detectors are improving, the next generation system may increase reliability by choosing the beta-gamma coincidence detection instead. PNNL has reported improvements in beta-gamma coincidence systems over the last decade, and has developed a compact four-detector system with minimal complexity (Cooper et al., 2005 and 2007) that might be a good design baseline for the next generation system. This ‘quad’ detector is operated by a commercial data acquisition system (DAQ) that is also capable of operating an entire xenon system, and this control system has shown good reliability for both DAQ function and xenon system control.

Updates in software functionality and reliability are an area of opportunity for the next generation system. Current approaches have used a mixture of commercially developed products and customized software on a variety of platforms. One approach to increased reliability might be to have a complete customized software system, developed in a modular way, that operate on a real time operating system such as Linux to minimize reliability issues and maximize maintainability. Robust software has been developed for a variety of critical applications, and these approaches can be utilized and incorporated into the next generation radioxenon monitoring system to minimize downtime.

Finally, reducing the size, weight, and power requirements of the system will be helpful in supporting the logistics and infrastructure needs for current and future installations. These will also be useful in operation and maintenance of the systems. And there is a possibility to use this next generation system for transportable or mobile applications as well if the reduction is significant.

System Goals

The goals in terms of the sensitivity, sampling frequency, and reliability should significantly enhance the capability of the next generation system over the current one, yet will need to be balanced by the limits of technology, cost, and complexity. As a result of the drivers and investigation discussed above, the next generation system should have the goals for key system attributes as listed in Table 1 which extend the capability of current generation systems. The sampling frequency should be increased, and less than eight hours should be achievable. The sensitivity needs to be increased and the MDC needs to be lower than 0.3 mBq/m^3 for the shorter sampling time. Reducing the MDC is challenging by itself, but even more challenging to decrease within a shorter time period. For reliability, the system needs to have a robust automatic state of health collection and reporting to support troubleshooting and timely maintenance. The goal should be to minimize downtime to less than 2 weeks a year, with a single period no more than one week. The system would benefit from having a small footprint and reduction in weight and power

requirements. Although these are targeted goals, not all of these may be realizable, and may need to be modified as on-going research matures.

Table 1. Next generation system goals for various attributes.

Attribute	Next Generation Goal
Sampling Time	< 8 h
Minimum Detectable Concentration (per sample)	< 0.3 mBq/m^3 for ^{133}Xe
State of Health	Automated with daily reporting
Down Time	< 7 consecutive days; < 14 days annually
Size	1×1× 2 m (3.3×3.3×6.6 ft.)
Weight	< 1000 kg (2200 lbs.)
Power	< 3 kW (peak)

CONCLUSIONS AND RECOMMENDATIONS

Technology goals have been investigated for the next generation radioxenon monitoring systems based on lessons learned during the INGE demonstrations for noble gases. The primary goals for the next generation systems should be increased sensitivity, sampling frequency, and reliability. The increased sensitivity will be important to support better discrimination of detection of reactors and medical isotope production releases and nuclear explosions. This increased sensitivity is primarily for the minor xenon isotopes (^{133m}Xe and ^{131m}Xe), although the requirements have typically been provided in terms of ^{133}Xe sensitivity. Increased sampling frequency will be helpful to support better source location and release estimates by providing a higher fidelity in the plume time and profile at the sampling location. Both the increased sensitivity and sampling frequency are best accomplished by development of a system with increased air processing and increasing the number of nuclear detectors. Increasing reliability while decreasing consumables is another primary goal of the next generation systems that will reduce overall operation and maintenance costs while providing a better overall detection capability. Utilization of highly reliable and proven approaches will be a good path to obtain better reliability.

The goals will provide the basis for the functions and requirements of the next generation radioxenon monitoring systems that will lead toward a system that is better able to accomplish the overall goal of detecting nuclear explosions. These considerations should be expanded upon and developed more fully into a set of requirements.

REFERENCES

Auer M., Axelsson A., Blanchard X., Bowyer T.W., Brachet G., Bulowski I, Dubasov Y., Elmgren K., Fontaine J.P., Harms W., Hayes J.C., Heimbigner T.R., Mcintyre J.I., Panisko M.E., Popov Y., Ringbom A., Sartorius H., Schmid S., Schulze J., Schlosser C., Taffary T., Weiss W., and Wensperger B. (2004). Intercomparison experiments of systems for the measurement of xenon radionuclides in the atmosphere, *Appl. Radiat. Isot.* **60**, 863–877.

Auer M., Kumberg T., Sartorius H., Wernsperger B., and Schlosser, C. (2010). Ten years of development of equipment for measurement of atmospheric radioactive xenon for the verification of the CTBT, *Pure Appl. Geophys*. **167,** 471–486.

Bowyer, T.W., Abel, K.H., Hubbard, C.W., et al. (1998). Automated separation and measurement of radioxenon for monitoring a comprehensive test-ban treaty, *J. Radioanal. Nucl. Chem.* **235** (1–2), 77.

Bowyer, T.W., K.H. Abel, C.W. Hubbard, M.E. Panisko, P.L. Reeder, R.C. Thompson, and R.A. Warner (1999). Field testing of collection and measurement of radioxenon for the Comprehensive Nuclear-Test-Ban Treaty*J. Radioanal. Nucl. Chem.*, **240** (1).

Cooper M.W., et al. (2005). Improved β-γ coincidence detector for radioxenon detection, in *Proceedings of the 27th Seismic Research Review: Ground-Based Nuclear Explosion Monitoring Technologies*, LA-UR-05-6407, Vol. 2, pp. 779–786.

Cooper, M. W., J. I. McIntyre, T. W. Bowyer, A. J. Carman, J. C. Hayes, T. R. Heimbigner, C. W. Hubbard, L. Lidey, K. E. Litke, S. J. Morris, M. D. Ripplinger, R. Suarez, and R. Thompson (2007). Redesigned Beta-Gamma Radio-Xenon Detector, *Nucl. Instr. & Meth. A*, **579**, 426–430.

Dubasov, Yu.V., Popov, Yu.S., Prelovskii, V.V., et al. (2005). The ARIX-03F mobile semiautomatic facility for measuring low concentrations of radioactive xenon isotopes in air and subsoil gas, *Prib. Tekh. Eksp.* **3**, 108 (*Instrum. Exp. Tech.* [engl. Transl.] **3**, 373).

Fontaine, J.P., Pointure, F., Blachard, X., and Taffary, T. (2004). Atmospheric xenon radioactive isotope monitoring, *J. Environ. Radiat.* **72**, pp. 129–135.

Kalinowski, M.B., Axelsson, A., Bean, M., Blanchard, X., Boeyer, T.W., Brachet, G., Hebel, S., McIntyre, J.I., Peters, J., Pistner, C., Raith, M., Ringbom, A., Saey, P., Schlosser, C., Stocki, T.J., Taffary, T., and Ungar, R.K. (2010). Discrimination of nuclear explosions against civilian sources based on atmospheric xenon isotopic activity ratios, in Becker, A., Schurr, B., Kalinowski, M.B., Koch, K., Brown, D. (Hrsg.): Recent advances in nuclear explosion monitoring, *Pure Appl. Geophys*., Topical Volume, **167** (4-5. S.), 517–539.

Ringbom A, Larson T, Axelsson A, Elmgren K, and Johansson C (2003). SAUNA-a system for automatic sampling, processing, and analysis of radioactive xenon, *Nucl. Instr. Meth*. A **508**, 542–553.

REAL-TIME PULSE SHAPE DISCRIMINATION AND RADIOXENON MEASUREMENT IN FIELD-PROGRAMMABLE GATE ARRAY

Abi T. Farsoni, Bemnet Alemayehu, Abdulsalam Alhawsawi, and Eric M. Becker

Oregon State University

Sponsored by the National Nuclear Security Administration

Contract No. DE-AC52-09NA29324
Proposal No. BAA09-27

ABSTRACT

Beta-gamma coincidence is a technique employed to measure ultra-low concentrations of radioxenon in the atmosphere with the lowest sensitivity to background radiation. Several radioxenon detectors have been developed based on this technique. In a standard radioxenon detection system, separate beta and gamma detectors are built into one detection assembly. Phoswich technology is an alternative approach for detecting beta-gamma coincidence events from xenon radioisotopes. A phoswich detector has a simple design: two or more scintillation layers are optically coupled to a single photomultiplier tube (PMT) in a compact configuration. The multiple layers are specifically chosen for their different characteristic material properties in order to distinguish between different interaction scenarios. Although use of the phoswich detector simplifies radioxenon coincidence measurements, its complicated signal output naturally requires a much more involved pulse processing method.

In the past, we developed a new phoswich detector with Compton suppression capability, called the Actively-Shielded Phoswich Detector (ASPD), and an off-line digital pulse processing algorithm for measuring xenon radioisotopes. The three scintillation layers chosen for this detector were BC400, CsI(Tl) and BGO. The Compton suppression mechanism is integrated into the phoswich design and does not need any additional detector.

To enhance the ASPD system in detecting beta-gamma coincidence events and measuring xenon radioisotopes, a real-time digital pulse processing firmware was developed and implemented in a Field-Programmable Gate Array (FPGA). The firmware utilizes the FPGA's multiple dual-port Block RAMs to implement beta and gamma energy histograms. The beta and gamma histograms (32-bit/4096-channel) are updated through a Moore state machine when a beta-gamma coincidence event is detected in the phoswich detector. In this paper, we report on the detail of the FPGA firmware, the pulse shape discrimination method, and the system's operational modes. In addition, our initial real-time radioxenon measurement results with the ASPD are presented.

OBJECTIVES

Measuring elevated concentrations of the four xenon radioisotopes (^{133m}Xe, ^{131m}Xe, ^{133}Xe and ^{135}Xe) along with their relative concentration ratios in the atmosphere will enable the International Monitoring System (IMS) to monitor nuclear weapon testing around the world. One proved efficient and highly sensitive radioxenon measurement method is the well-known beta-gamma coincidence technique. The Automated Radioxenon Sampler and Analyzer (ARSA, Reeder et al., 1998) and the Swedish Automated Unit of Noble gas Acquisition (SAUNA, Ringbom et al., 2003) are two radioxenon detection systems which have been designed based on this technique. Both systems employ two separate detection channels, one for measuring beta particles (or conversion electrons) and one for gamma rays (or X-rays). Employing multiple detection channels in these systems requires separate pulse processing electronics for each channel and, eventually, sophisticated energy calibration and gain matching procedures.

In order to reduce the number of detection channels and consequently to simplify the beta-gamma coincidence measurements, several phoswich detectors have been developed and tested for radioxenon measurements (Ely et al., 2003; Hennig et al., 2005; Farsoni et al., 2011). A phoswich detector has a simple design: two or more scintillation layers are optically coupled to a single photomultiplier tube (PMT) in a compact configuration. The multiple scintillating layers are specifically chosen for their different characteristic material properties (e.g., decay time) in order to distinguish between different interaction scenarios. Although use of the phoswich detector simplifies radioxenon coincidence measurements, its complicated signal output requires a much more involved pulse processing method.

We have developed a novel phoswich detector with Compton suppression capability for radioxenon measurements. One important feature of this detector in enhancing radioxenon detection is its capability to identify and reject Compton scattering events in its gamma detection layer. The phoswich detector has been designed with three scintillation layers. Beta-gamma coincidence events from radioxenon isotopes are identified when a coincidence energy absorption is detected from the first (plastic, BC-400) and second (CsI(Tl) crystal) scintillation layers. To identify and reject scattered photons, the CsI(Tl) crystal is surrounded by a BGO scintillation layer. If a photon triggers responses in both layers, the event is rejected.

In the past, we characterized our phoswich detector in measuring xenon radioisotopes using a PC-based digital pulse processing algorithm (off-line analysis). To enhance the ASPD system's portability in measuring beta-gamma coincidence events, a real-time digital pulse processing firmware was developed and implemented in a Field-Programmable Gate Array (FPGA).

In this paper, we will describe our FPGA design structure by which the system is triggered, phoswich pulse shapes are discriminated, beta/gamma coincidence events are identified, associated energy releases are measured and finally separated and local beta and gamma energy histograms are updated. In addition, our recent real-time test results in measuring coincidence events from ^{133}Xe and ^{135}Xe, produced at the Oregon State University's TRIGA reactor, are presented.

RESEARCH ACCOMPLISHED

Digital Processing of Detector Pulses in FPGA Devices

FPGAs are an array of programmable logic cells interconnected by a network of wires and configurable switches. A FPGA has a large number of these cells available to form multipliers, registers, adders, accumulators and so forth in complex digital circuits. FPGAs can be infinitely reprogrammed in-circuit in only a small fraction of a second. Modern FPGAs have revolutionized digital signal processing in radiation detection as new FPGA devices are replacing their traditional competitors such as Digital Signal Processors (DSPs) and even Application-Specific Integration Circuits (ASICs) in numerous digital radiation measurement applications (Bolic et al., 2002; Schiffer et al., 2011). ASICs can inherently provide greater clock speeds with lower power requirements, but the high cost of designing and manufacturing ASICs, particularly in small quantities, make FPGAs a more cost-effective choice in many applications.

In modern digital pulse processing systems for radiation spectroscopy, the processing of radiation pulses is performed either in a FPGA/DSP system or entirely in a single FPGA device. In both approaches, after an analog conditioning stage, detector pulses are sampled by a high-speed, free-running Analog-to-Digital Convertor (ADC), and then the stream of digital samples is fed into a FPGA device.

In a typical FPGA/DSP-based pulse processing system, generally only those digital functions that should be performed with ADC's clock speed, such as triggering, pileup detection/rejection, pulse capturing (in a circular buffer) and digital pulse shaping, are implemented in the FPGA device. The rest, including pulse amplitude measurement and histogram construction, are performed in a slower sequential algorithm in the DSP device. The DSP processing algorithm must be implemented with much higher clock frequency to maximize the system throughput since the detection system accumulates dead time while the DSP performs the sequential calculations in its algorithm. One other drawback of this approach is the need for code development and troubleshooting for two different devices/platforms which dramatically increases the development time and overall cost.

In the FPGA-based radiation pulse processing system, all the pulse processing functions including energy measurement and histogram construction are realized in a single FPGA device. In addition, new FPGA devices provide integrated memory components. This feature further simplifies the system design in constructing energy histograms inside the FPGA without using external memory. Since all the computation functions are executed in parallel in the hardware, a minimal dead time can be achieved using a single FPGA for real-time measurements. Since only one processing device is employed, developing codes for FPGA-based pulse processors are much easier and less time consuming.

Phoswich Detector and Pulse-Shape Analysis

A phoswich detector (Figure 1) with three scintillation layers has been designed and constructed for measuring xenon radioisotopes via a beta/gamma coincidence method (Farsoni et al., 2011). The phoswich detector consists of a thin plastic scintillator (BC-400) to detect beta and conversion electrons, a CsI(Tl) crystal for measuring X-rays and gamma-rays, and a BGO crystal, which surrounds the CsI(Tl) layer, to identify scattered photons and ultimately to reduce Compton continuum in the gamma energy spectrum.

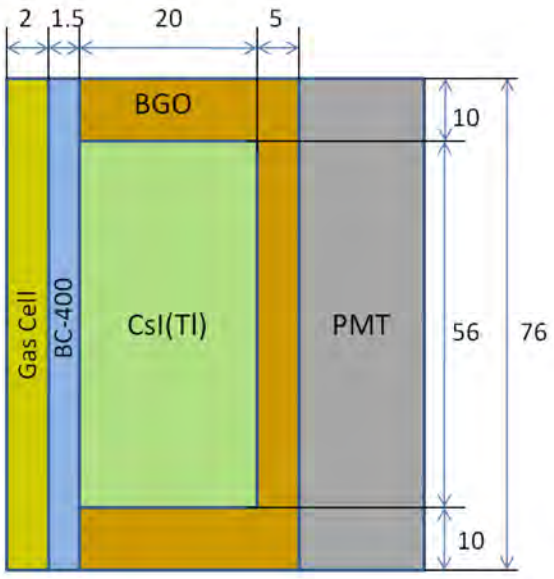


Figure 1. Schematic diagram of the Actively-Shielded Phoswich Detector (ASPD). All dimensions are in mm.

In the past, for prototyping purposes, we developed an offline algorithm in MATLAB to digitally process pulses from phoswich detectors. In the offline algorithm, to discriminate between different pulse shapes, each anode pulse was integrated over three time intervals (T_1, T_2 and T_3, shown in Figure 2) using three digital triangular filters with appropriate peaking times. The output amplitudes of these filters, S_1, S_2 and S_3, represent the integration or sum of each pulse over the T_1, T_2 and T_3 time intervals, respectively. Using these sums, two ratios, the Fast Component Ratio (FCR) and Slow Component Ratio (SCR), were calculated from each captured pulse. The FCR and SCR were calculated using the following equations:

$$FCR = S_1/S_2 \quad (1)$$

$$SCR = (S_2-S_1) / (S_3-S_1) \quad (2)$$

Since sum S_1 is a fraction of sum S_2 and sum S_2 is a fractions of sum S_3, the FCR and SCR defined in Equations 1 and 2 can range from zero to unity. Our previous offline analysis (Farsoni et al., 2011) showed that depending on how the incident radiation releases its energy within each layer of the phoswich detector, seven possible regions are populated in the FCR-SCR scatter plot. Figure 3 shows a two-dimensional scatter plot of the FCR and SCR from our offline analysis when the phoswich detector was exposed to 662 keV of a ^{137}Cs source. In this Figure, regions 1, 2 and 4 represent single events in plastic (BC-400), CsI(Tl) and BGO scintillators, respectively. Regions 3 and 5 show coincidence events of CsI(Tl)-plastic and BGO-plastic, respectively. Region 6 accommodates Compton scattering events between CsI(Tl) and BGO. When either all three timing components appear in the pulse or the shape of pulse is unknown, corresponding event appears in region 7.

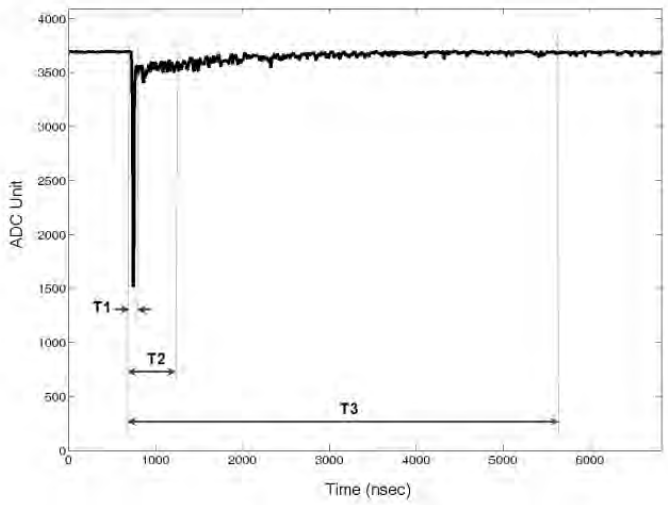


Figure 2. A typical coincidence pulse from the phoswich detector. In order to discriminate pulses from different events, each valid pulse is integrated over three time intervals (T_1, T_2 and T_3).

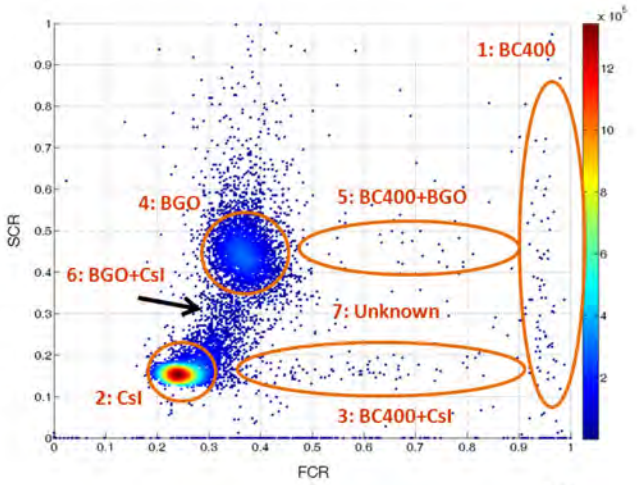


Figure 3. Scatter of the Fast and Slow Component Ratios using 662 keV of ^{137}Cs calculated using an off-line pulse shape-analysis. Seven marked regions correspond to seven pulse shapes, indicating how gamma-rays interact with the three layers of phoswich detector.

The same sum values are used to calculate the corresponding pulse areas A_g and A_b (proportional to the number of scintillation photons generated in the CsI(Tl) and BC400, respectively) and subsequently to measure coincidence energy deposition in the CsI(Tl) and BC400 layers. The A_g and A_b are calculated using the following equations:

$$A_g = S_3 - S_1 \qquad (3)$$

$$A_b = S_1 - K\,(S_3 - S_1) \qquad (4)$$

The product term *"$K\,(S_3 - S_1)$"* in Equation 4 is the contribution of CsI(Tl)'s scintillation component in the T_1 integration interval. The fraction coefficient *"K"* can be determined experimentally using pulses detected in region 2 (CsI(Tl) single events).

We have employed the same pulse shape analysis approach in our real-time pulse processing algorithm discussed in the following sections.

FPGA Operational Modes

To be suitable in both real-time measurements and prototyping stages, the FPGA pulse processing algorithm was developed for operation in four modes: (1) Scope, (2) Pulse-Shape Analysis (PSA), (3) Coincidence Event (CE), and (4) Multichannel Analyzer (MCA) modes. In addition, a MATLAB program was developed to control the digital pulse processor unit, set pulse processing parameters and display measurement results on the PC's screen. The function of each mode is described below.

In the Scope mode, individual anode pulses are captured in a circular buffer (1,024 samples) and transferred to the PC for either displaying on the screen or an off-line analysis. Using this mode, a user can conveniently monitor the health of anode pulses and set the optimum pulse capture parameters such as amplification gain and offset level by the MATLAB program. This mode provides no pulse processing on the phoswich anode pulses.

An anode pulse is identified as a beta-gamma coincidence pulse only if its measured pulse-shape parameters, FCR and SCR, are inside the boundaries of region 3 (BC400+CsI coincidence events) shown in Figure 3. The PSA mode is used to plot a FCR-SCR scatter graph from individual phoswich pulses and to determine the boundaries of region 3. This region is defined by four level values: Fast Ratio Lower Level (FRLL), Fast Ratio Upper Level (FRUL), Slow Ratio Lower Level (SRLL), and Slow Ratio Upper Level (SRUL). These level values should be determined and set before running the pulse processing algorithm in the other two coincidence modes such as the CE and MCA modes.

In the CE mode, for each detected coincidence pulse, two pulse areas (A_g and A_b) are calculated in real-time and transferred to the PC to construct a 3-D beta/gamma coincidence energy spectrum. This type of coincidence spectrum should be built from individual coincidence events and cannot be made from histogram data collected in the MCA mode.

The MCA mode is used to collect separate beta particle and gamma-ray histograms. Both histograms are updated only if the measured FCR and SCR values of the pulse are identified to be in the region 3 (BC400+CsI(Tl) coincidence events). If the gamma-ray undergoes a Compton scattering in the CsI(Tl) and the scattered photon is fully absorbed or re-scattered in the BGO, even if it is in coincidence with beta absorption in the BC400, that event will be outside the region 3 and therefore it will be automatically rejected.

FPGA Hardware Design and Implementation

To realize the four operational modes, the FPGA hardware design was developed with a hierarchical structure including three main modules: Trigger, Scope, and Histogram modules. The Scope mode is realized in the Scope module including two state machines and a circular buffer to capture and transfer sampled pulses to the PC. Since no digital processing is performed in this module, the detail of its hardware implementation will not be discussed here.

Trigger Module

A block diagram of the Trigger module is given in Figure 4. This module has a simple structure and generates a trigger input to other modules. The Trigger module was realized by employing a fast digital triangular filter. The peaking time of this filter was initially set to 100 nsec. Since the triggering function is based on a differential sum computation (triangular filtering), detecting a valid radiation pulse above the noise level is independent of the baseline offset. In this module, the ADC samples are fed into the triangular filter then from there to a comparator. A dedicated state machine (the Trigger State Machine) continually monitors the output of this comparator and issues a one-cycle logic pulse (trigger output) when the filter output is larger than a predetermined threshold level.

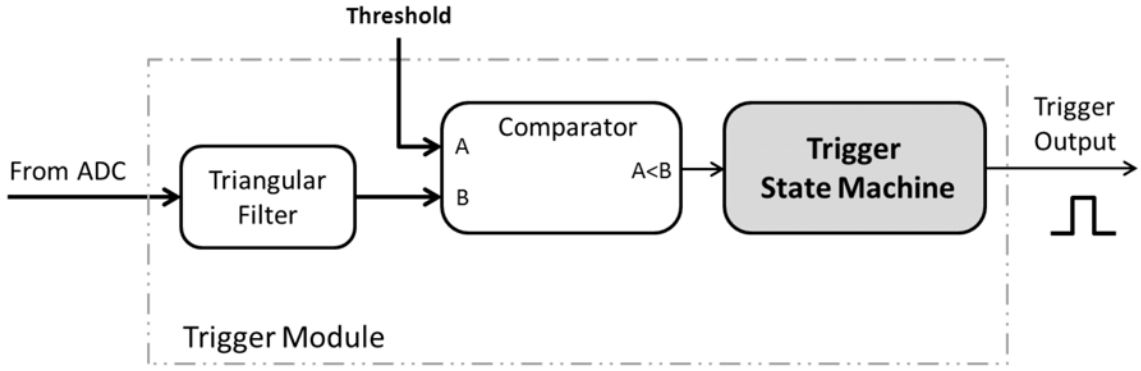


Figure 4. Block diagram of the Trigger module.

Histogram Module

Except the Scope mode, the other three modes are realized in the Histogram module illustrated in Figure 5. To enhance timing performance of the Histogram module, all combinational components implemented in this module were registered leading to a fully pipelined hardware design. As depicted in Figure 5, the Histogram module receives detector sample data directly from the ADC (12 bits). It also receives a trigger signal from the trigger module. Our simulations using the Xilinx ISE Design Suite software shows that there is a 12-cycle latency for the trigger signal when a step function is applied to the Trigger module. To compensate for this latency, the ADC data are delayed by a variable delay unit made by RAM-based shift registers (a Xilinx IP core).

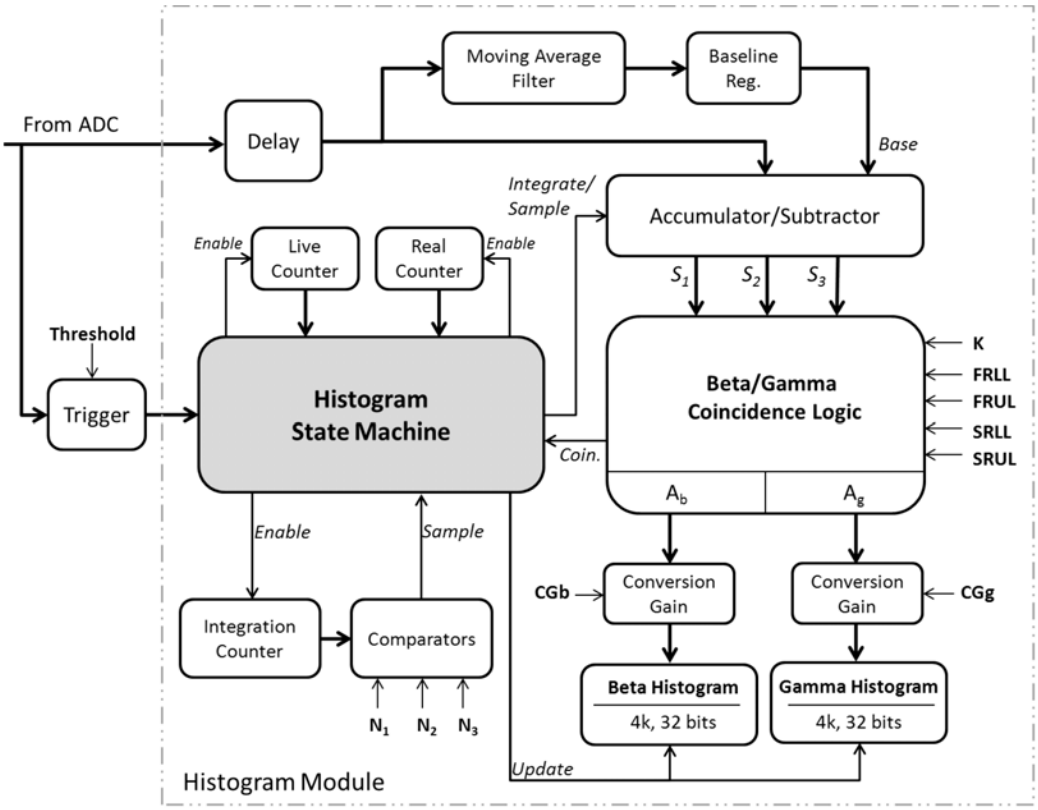


Figure 5. A block diagram of the Histogram module implemented in the FPGA device for real-time pulse-shape discrimination and beta/gamma coincidence measurements. To simplify the diagram, only the data processing path for the MCA mode is shown.

In order to estimate the areas under each phoswich pulse, an average of the pulse's baseline, right before the trigger point, needs to be taken. The average Base is computed using a simple moving average filter. In the current design, the Base is an average of the pulse baseline over eight ADC samples before a radiation pulse arrives. A register is used at the output of this filter to sample the average Base for the accumulation process. Delayed ADC samples are also fed into the Accumulator/Subtractor unit. A single counter (Integration Counter) and three comparators schedule the integration process in the Accumulator/Subtractor unit to estimate the three sums, S_1, S_2 and S_3, defined mathematically by Equations 5-9:

$$y[n] = y[n-1] + x[n] \quad (5)$$

$$b[n] = b[n-1] + Base \quad (6)$$

$$S1 = b[N1] - y[N1] \quad (7)$$

$$S2 = b[N2] - y[N2] \quad (8)$$

$$S3 = b[N3] - y[N3] \quad (9)$$

where "n" is the sample index, x[n] is the delayed ADC sample, y[n] and b[n] are accumulator outputs, "Base" is the averaged baseline, and N_1, N_2 and N_3 are the number of ADC clock cycles within the three integration intervals T_1, T_2 and T_3, respectively.

The three calculated sums (S_1, S_2 and S_3) are fed into the Beta/Gamma Coincidence Logic (BGCL) unit in which (1) coincidence pulses are identified through a real-time pulse-shape analysis (defined by Equations 1 and 2) and (2) corresponding pulse areas A_g and A_b are calculated (defined by Equations 3 and 4). The BGCL unit was realized using three substractors, two dividers, one multiplier, four comparators, and one four-input AND gate (Figure 6).

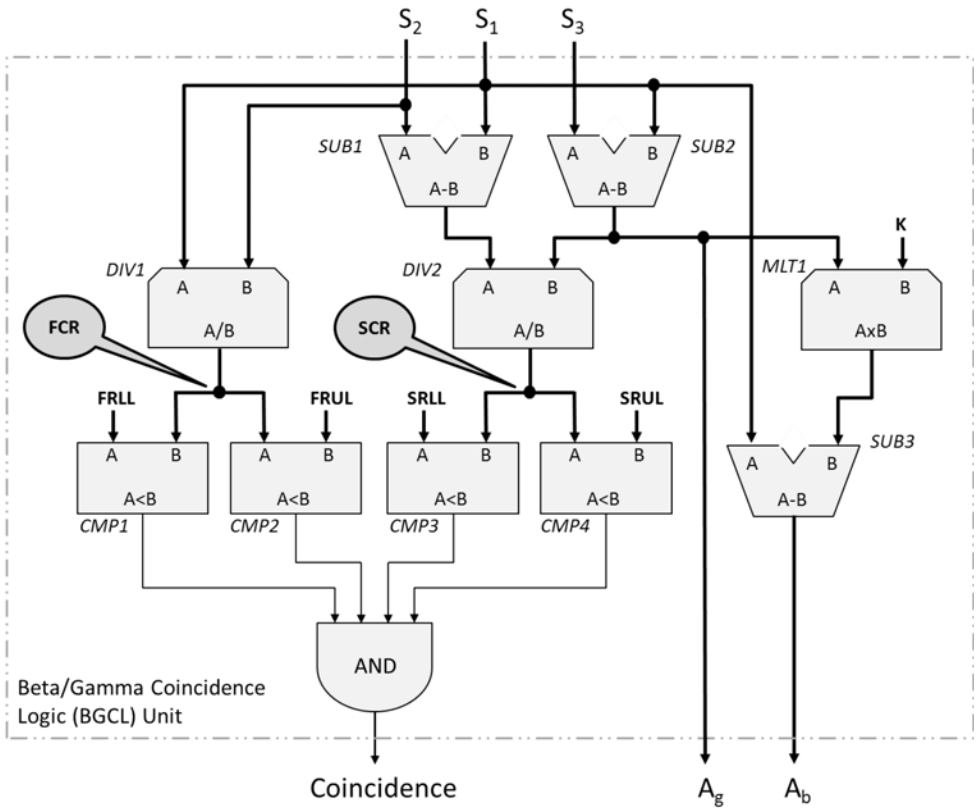


Figure 6. Block diagram of the Beta/Gamma Coincidence Logic (BGCL) unit. It performs real-time pulse-shape discrimination and coincidence pulse-height measurements in hardware.

The Coincidence signal output in BGCL unit (Figure 6) goes "High" if the measured pulse-shape parameters of the pulse (FCR and SCR) are identified to be in the region 3 defined by its predetermined four boundaries (FRLL, FRUL, SRLL and SRUL).

In order to reconstruct the beta particle/conversion electrons and gamma-ray/X-ray energy spectra in real-time, two separate histograms were implemented in our FPGA design. The Gamma and Beta Histograms, shown in Figure 5, were implemented using dual-port Block RAM memories available in SPARTAN-3 FPGA devices. Sixteen Block RAM's were used to implement these two 4k, 32-bit histograms. Two Conversion Gain units are employed to scale and locate appropriate channel addresses in the two histograms. CG_b and CG_g are gamma and beta conversion gain parameters, respectively. These parameters can horizontally scale the beta and gamma energy histograms in 16 scaling steps.

As shown in Figure 5, to measure elapsed real and live times and to perform real-time quantitative measurements, two counters (Live Counter and Real Counter) were implemented in the Histogram module. They were made of two 49-bit counters. These counters are clocked with the ADC's clock frequency, f_{adc}. Since only 32 most significant bits of these counters are used to measure the time, the time measurement resolution is $2^{17}/f_{adc}$.

Histogram State Machine

The histogram state machine, shown in Figure 5, sequentially controls the pulse processing algorithm in the Histogram module. This state machine is clocked with the ADC's clock frequency (f_{adc}). A simplified state diagram is presented in Figure 7. To simplify the diagram, some states such as mode selection/directing states are not shown.

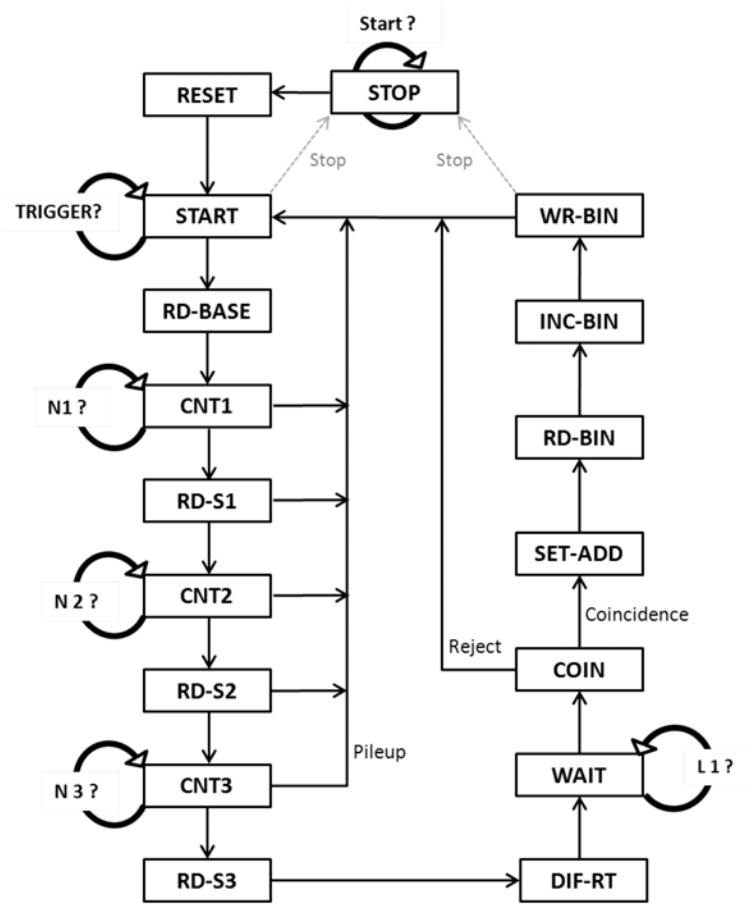


Figure 7. A simplified state diagram of the Histogram State Machine implemented in the FPGA device. This state machine controls our real-time pulse processing algorithm in the Histogram module.

The state machine will move from its idle state, the STOP state, to the RESET state and start processing incoming pulses when it receives a one-cycle signal, Start, initiated from the MATLAB program. The RESET state resets the two time measuring counters, Real and Live Time Counters. Then the state machine stays at the START state until it receives a Trigger signal from the Trigger module. The average baseline, Base, is sampled in the next state, the RD-BASE state. The Integration Counter is also reset in the same state.

The state machine starts integrating incoming pulses by enabling the Integration Counter and Accumulator/Subtractor units in the CNT1 state. It moves to the RD-S1 state when the counter reaches at its first sampling point, at N_1. In the *RD-S1* state, the first sum, S_1, is calculated and sampled in the Accumulator/Subtractor unit. The integration process will continue in the next four states (CNT2, RD-S2, CNT3 and RD-S3) to calculate sums S_2 and S_3. During the integration process, the state machine continually checks the Trigger signal for any pileup event. If a pileup event is detected, the state machine will move to the START state without performing any further pulse processing or histogram updating.

Sums S_1, S_2 and S_3 are provided to the BGCL unit in the DIFF-RT state. Since divider components implemented in the BGCL unit require 34 clock cycles to complete their division operations, the state machine moves to the WAIT state and stays there for L_1=34 clock cycles. The pulse areas A_g and A_b, and the Coincidence signal will be valid for further actions in the COIN state. In the PSA or CE modes, only calculated data such as FCR, SCR, A_g and A_b are transmitted to the PC and no extra processing function will be performed in the hardware. In the MCA mode, however, the two histograms will be updated in the following states if a coincidence event is identified.

If the Coincidence signal level is “LOW” indicating a non-coincidence event has occurred, the state machine will “reject” the event and will move to the START state. Otherwise, it will move to the SET-ADD state where the A_g

and A_b values locate and set the appropriate bin addresses in the two corresponding histograms. In the RD-BIN state, current contents of the two histograms at the located addresses (bins) are read. The current contents (counts) are incremented by one in the INC-BIN state. At the final histogram updating process in the WR-BIN state, the incremented counts are written into the corresponding histograms. At this point, the state machine will stop processing additional phoswich pulses if a stop request is received from the PC side. Otherwise, it will move to the START state and will wait for the next trigger signal.

The Real and Live Counters, shown in Figure 5, are handled differently to account for any dead time caused in the pulse processing algorithm. Both counters are disabled in the STOP state. Whereas the Real Counter is enabled in all other states, the Live Counter is only enabled in the "live states" from the START to the CNT3 states.

Synthesis and Implementation

The real-time pulse processing algorithm, described in the above sections, was synthesized and implemented using Xilinx's ISE WebPack software. The FPGA design was tailored to run in Xilinx's SPARTAN-3 FPGA (1000k equivalent gate) available in the RX1200 (200 MHz/12-bit digital pulse processor, Avicenna Instruments LLC). With the current FPGA design, we achieved a maximum sampling rate of 150 MHz (f_{adc}).

Real-Time Measurements

The following real-time test results were obtained with the phoswich anode output connected directly to the RX1200. First, the PSA mode was used to test the performance of our real-time algorithm in pulse-shape discrimination and determine the four boundary levels (FRLL, FRUL, SRLL and SRUL) for the region 3. Figure 8 shows a 3-D surface plot of FCR/SCR when the phoswich detector was exposed to a ^{137}Cs source. During this experiment, the ^{137}Cs source was shielded against beta and conversion electrons. Six major regions which were observed in our offline analysis (Figure 3) can be identified in this Figure as well. Using this plot, the four boundary levels of the region 3 were initially determined and set for the rest of measurements.

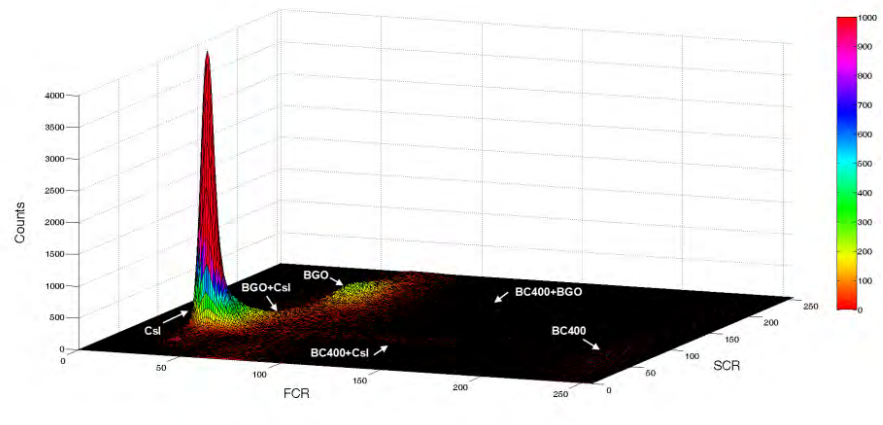


Figure 8. Real-time FCR/SCR 3-D surface plot from 662 keV of ^{137}Cs. Five major pulse-shape discrimination regions are indicated in this plot. Data were collected in real-time using the "Pulse-Shape Analysis" mode.

The real-time FPGA-based processing algorithm was tested for measuring ^{135}Xe and ^{133}Xe through beta/gamma coincidence technique. Radioxenon gases were produced by activating small volumes (3 ml) of stable and enriched (>99%) isotopes of xenon, ^{134}Xe and ^{132}Xe, in the thermal column of the TRIGA reactor for two hours. The resulting 3-D beta/gamma coincidence energy spectra from ^{135}Xe and ^{133}Xe are shown in Figures 9 and 10, respectively. The spectral data in these Figures were collected in real-time using the Coincidence Event mode. In this mode, coincidence events in region 3 (BC400-CsI(Tl) coincidence events) are discriminated then the corresponding pulse areas, A_g and A_b, are transferred to the PC. As it can be seen in these Figures, 250 keV, 30 keV and 80 keV gamma-rays/X-ray lines are clearly populated and extended up to the maximum energy of beta particles from ^{135}Xe and ^{133}Xe.

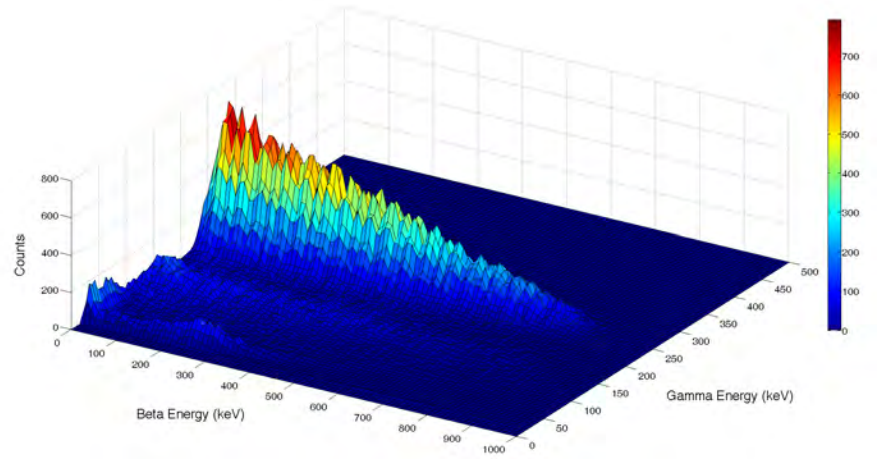


Figure 9. ^{135}Xe 3-D beta/gamma coincidence energy spectra. Data were collected in real-time using the "Coincidence Event" mode.

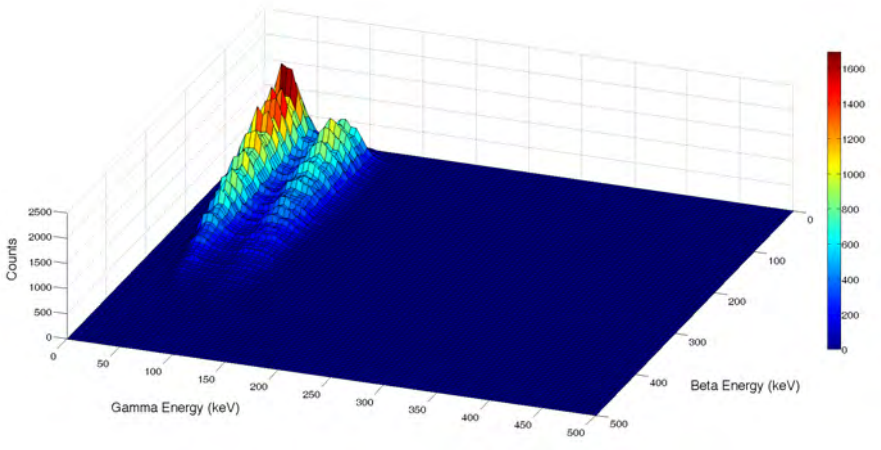


Figure 10. ^{133}Xe 3-D beta/gamma coincidence energy spectra. Data were collected in real-time using the "Coincidence Event" mode.

Separate real-time beta and gamma coincidence energy spectra from ^{135}Xe and ^{133}Xe were collected by running the processing algorithm in the MCA mode. The resulting energy spectra are presented in Figures 11 and 12. The energy resolution for the 250 keV, 30 keV and 80 keV photopeaks were measured to be 16.7%, 56.6% and 37.1%, respectively. Beta and gamma energy spectra for both xenon radioisotopes are in good agreement with their radiological characteristics. However, some abnormal events are seen in low-energy parts of these spectra. These might be due to mischaracterization of BGO events in region 3 in which coincidence events are identified and processed. Our pulse-shape analysis (Figures 3 and 8) shows that events possessing a BGO component are less localized than other events and as a result they are more susceptible to be mischaracterized. Discrimination of BGO events becomes even more difficult when low-energy radiation is absorbed in the BGO. Using high-gain PMTs and enhancing light collection efficiency are two solutions that potentially can improve overall discrimination performance of the phoswich system.

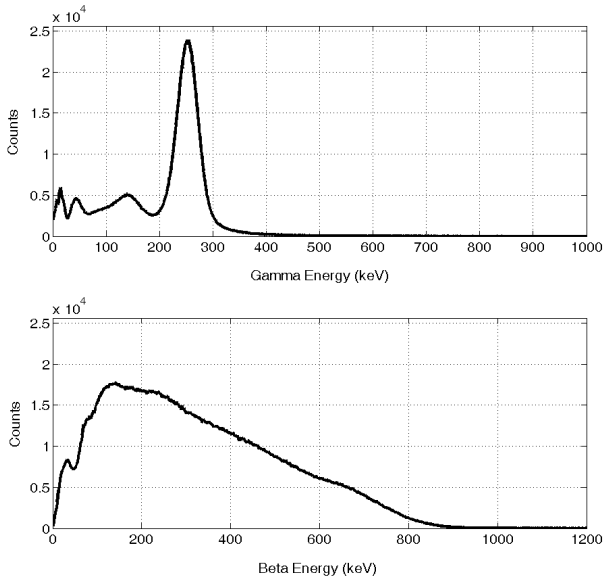


Figure 11. Gamma (top) and beta (bottom) energy spectra from ^{135}Xe. Data were collected in real-time using the "MCA" mode.

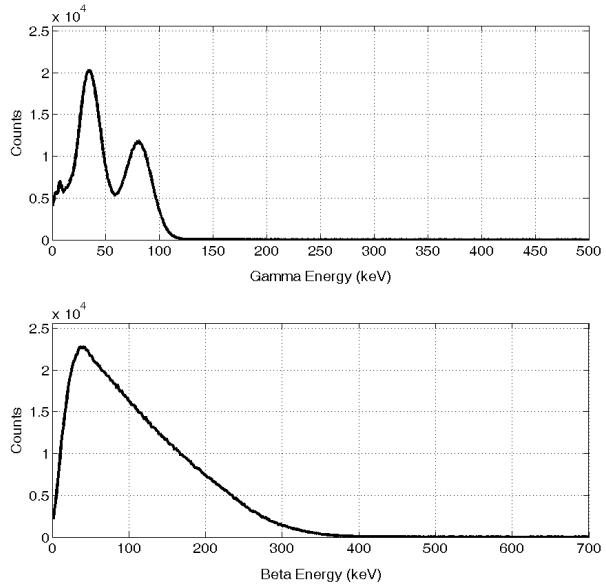


Figure 12. Gamma (top) and beta (bottom) energy spectra from ^{133}Xe. Data were collected in real-time using the "MCA" mode.

CONCLUSIONS AND RECOMMENDATIONS

In this paper we described the principles and development of a real-time FPGA-based digital pulse processing algorithm for our previously developed phoswich detector to discriminate pulse shapes and measure xenon radioisotopes via a beta/gamma coincidence technique. All the digital pulse processing functions including system triggering, pulse-shape discrimination, beta/gamma coincidence event detection, pileup rejection, energy measurements, and updating beta/gamma histograms were entirely realized in a single FPGA device. To be useful in both real-time measurements and prototyping stages, the pulse processing algorithm was developed for operation in four modes: (1) Scope, (2) Pulse-Shape Analysis, (3) Coincidence Event, and (4) Multichannel Analyzer modes. The performance of our digital pulse processing algorithm was tested through real-time measurements of ^{135}Xe and ^{133}Xe produced in the Oregon State University's TRIGA reactor.

Implementation of sophisticated digital processing tasks in Field-Programmable Gate Array has brought significant advantages to analyzing pulses from our phoswich detector. These include: pulse processing performed in real-time with minimal dead time; no external memory needed to construct energy histograms; a processing algorithm that is easily changed without changing hardware; accurate quantitative measurements are possible since the live time is measured in hardware; and code development made easier and less time consuming by employing only one processing device.

REFERENCES

Bolić, M. and V. Drndarević (2002). Digital gamma-ray spectroscopy based on FPGA technology, *Nucl. Instrum. Meth. Phys. Res Sec. A*, **482**, 761–766.

Ely, J. H., C. E. Aalseth, J. C. Hayes, T. R. Heimbigner, J. I. McIntyre, H. S. Miley, M. E. Panisko, and M. Ripplinger (2003). Novel Beta-gamma coincidence measurements using phoswich detectors, in *Proceedings of the 25th Seismic Research Review—Nuclear Explosion Monitoring: Building the Knowledge Base*, LA-UR-03-6029, Vol. 2, pp. 533–541.

Farsoni, A. T., B. Alemayehu, and A. Alhawsawi (2011). Preliminary measurements with a Compton-suppressed phoswich detector, in *Proceedings of the 2011 Monitoring Research Review: Ground-Based Nuclear Explosion Monitoring Technologies*, LA-UR-11-04823, Vol. 2, pp. 671–680.

Hennig, W., H. Tan, W. K. Warburton, and J. I. McIntyre (2005). Digital pulse shape analysis with phoswich detectors to simplify coincidence measurements of radioactive xenon, in *Proceedings of the 27th Seismic Research Review: Ground-Based Nuclear Explosion Monitoring Technologies*, LA-UR-05-6407, Vol. 2, pp. 787–794.

Reeder, P. L., T. W. Bowyer, and R. W. Perkins, (1998). Beta-gamma counting system for Xe fission products, *J. Radioanal. Nuc. Chem.* **235** (1–2), 89–94.

Ringbom, A., T. Larson, A. Axelson, K. Elmgren, and C. Johansson (2003). SAUNA—a system for automatic sampling, processing and analysis of radioactive xenon, *Nucl. Instrum. Meth. Phys. Res. A* **508**, 542–553.

Schiffer, R. T., M. Flaska, S. A. Pozzi, S. Carney, and D. D. Wentzloff (2011). A scalable FPGA-based digitizing platform for radiation data acquisition, *Nucl. Instrum. Meth. Phys. Res. A* **652**, 491–493.

A TREATMENT OF THE MEASUREMENT UNCERTAINTY FOR XENON VOLUME QUANTIFICATION

Warren W. Harper, Matthew W. Cooper, James C. Hayes, and Lance S. Lidey

Pacific Northwest National Laboratory

Sponsored by the National Nuclear Security Administration

Award No. DE-AC05-RLO1830/PL11-MRVL12-NDD05

ABSTRACT

Treaty monitoring gas measurement systems that measure radioxenon typically report results as an activity concentration, which is the measured radioxenon activity divided by the amount of stable xenon present. While the nuclear activity uncertainty has been studied in detail and is driven primarily by counting statistics, the uncertainty for the volume measurement has been considered in less detail. A framework for a more complete consideration of the uncertainty for the volume measurement has been developed. This type of analysis can help drive the system requirements for the volume quantification while the system is still being developed or added to advanced fielded systems. Depending on the accuracy requirements for the activity concentration, the volume quantification measurement and analysis can be developed to a suitably high level of accuracy. Nominally, it is best to have the activity concentration uncertainty limited by the uncertainty of the activity measurement because it tends to be fundamentally limited by the counting statistics. Volume quantification should be performed more accurately so that the activity concentration uncertainty is not degraded from the counting statistics. This paper will describe in detail a stable gas quantification uncertainty analysis for a xenon monitoring system.

OBJECTIVE

The objective of this work is to provide an example calculation of the uncertainty for a system that analyzes gas samples for radioactive decay, in particular for radioxenon analysis. While the specifics vary for any given system, a universal requirement is to be able to quantify the volume of xenon being processed along with how much of the xenon is introduced into the responsive part of a nuclear detector. The nuclear activity measurement is typically combined with the delivered volume to determine the activity concentration, which is a critical measurement result for many systems. As the measurement systems become more sophisticated and have more stringent requirements for the reported results, it becomes increasingly important to determine the level of accuracy of the nuclear measurement and the volume measurement. An analysis of the nuclear activity has been studied previously (Cooper et al., 2012) and is also the subject of continuing consideration. The goal for volume measurements in a field system that has limited size and limited count time is to have a relative uncertainty that is better than the nuclear activity measurement so that the activity concentration uncertainty is not significantly degraded due to the quality of the volume measurement. This situation is desirable because with due diligence the volume measurement can be done with better relative uncertainty than the activity measurement for most field systems. We find that if the relative uncertainty of the volume measurement is better than about a third of the relative uncertainty of the nuclear activity, there is a minimal increase in the relative uncertainty of the activity concentration. The research and analysis presented here details how we have augmented our methodology to make better xenon volume measurements and robust estimates of the uncertainty of the measurement.

RESEARCH ACCOMPLISHED

System Overview

Systems for xenon analysis are beyond the scope of this paper, and for clarity, discussions presented here are for a simplified model system as shown in Figure 1. While this system is simplified, it still contains all of the important components related to quantification, and then transferring to a nuclear detector. In this case, quantification is performed prior to delivery of the sample in the nuclear detector. Additionally, in this study case, the xenon sample has low levels of impurities and is not diluted in a carrier gas while in the quantification region. The sample is manipulated in the processing manifold to monitor and increase the xenon purity if necessary. After processing, the sample is cryo-transferred into the transfer trap using both the small and large traps to efficiently move the entire xenon sample. This approach is similar to what has been discussed previously (Harper et al. 2011). Once the sample is fully in the transfer traps, the quantification region can be isolated and the sample is warmed. After sufficient warming, the xenon sample is vaporized and distributed throughout the quantification region volume. The quantification volume is subdivided into an appropriate number of sub-volumes: pressure transducer (V_P), quantification manifold (V_{Qman}), large trap (V_{LT}), and small trap (V_{ST}). This subdivision is done so that each sub-volume can be regarded as having a uniform temperature. For more complicated systems, or higher levels of accuracy, it may be necessary to subdivide into additional volumes. The xenon gas volume can now be quantified using the measured pressure (P), volumes, and temperatures as will be discussed in the next section. After quantification, the sample is 'recollected' into the small trap so that it can be volumetrically expanded into a detector, via the detector manifold, which can be used to select multiple detector cells. The recollection step is a key component so that the volumetric expansion has much higher efficiency of moving xenon to the detector cell. After the volumetric expansion, the detector cell is closed off and a nuclear activity measurement is initiated. Note that we have specifically separated V_{Count}, which is the volume of the counting part of the detector from V_{Det}, which is the detector plus the line volume from the detector manifold. The volume of xenon introduced into the detector is based on the quantification volume, recollection efficiency, and transfer efficiency to the detector.

Quantification Equations

Before attempting to analyze the uncertainty of the volume quantification measurement, it is first necessary to develop the appropriate quantification equation and measurement assumptions. For our case, we typically state our xenon volumes in terms of STP conditions using the NIST definition (273.15K and 760 Torr). It is important to note that there are a variety of other 'standard conditions' such as the IUPAC definition (273.15K and 100kPa), NPT, and other definitions that may use different temperature and pressure references. The volumes that are called out in Figure 1 can be premeasured to suitably high levels of accuracy after the system is fully assembled and operational. These volumes are stable and do not change appreciably for the life of the system. Provided these volumes (and uncertainties) are known, it is possible to determine the standard volume of xenon by measuring the pressure and temperatures of the various subcomponents of the quantification region. Volumes for the model system are given in

Table 1. The pressure can continue to change during the measurement, but it is equilibrated throughout the quantification region (all subcomponents have the same pressure). The expression for the xenon volume is given by Equation (1).

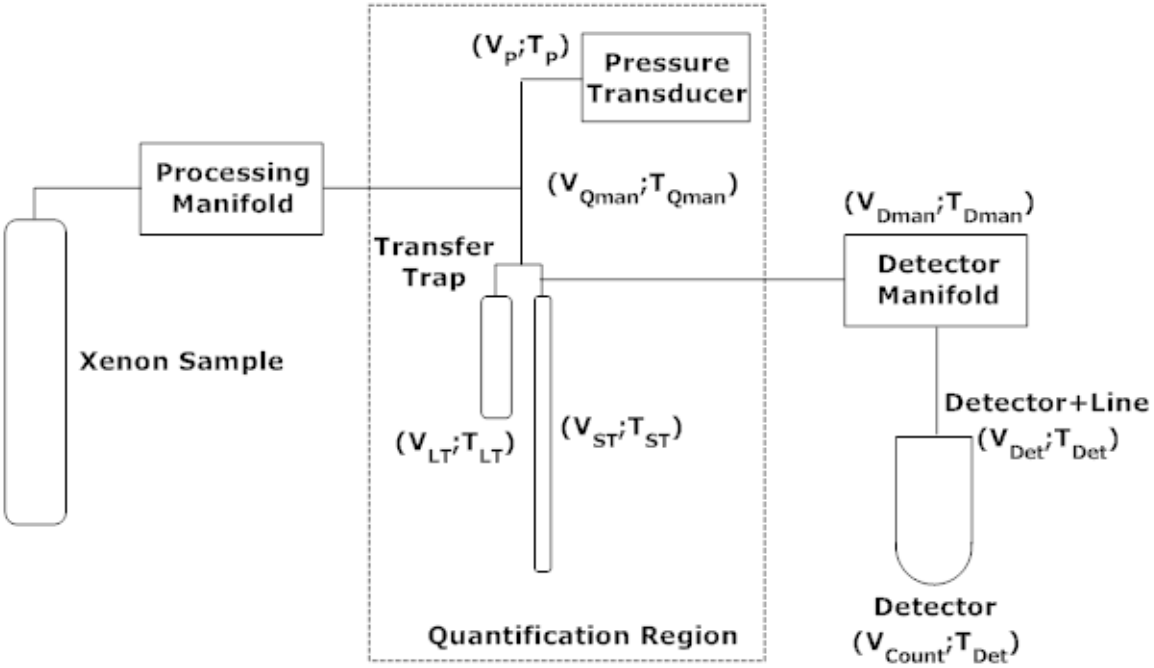


Figure 1. Model Xenon processing system.

Table 1. Model system volumes and uncertainties.

Volume Section	Volume (cc)	Uncertainty (cc)
V_p	1.4584	0.0030
V_{Qman}	1.1698	0.0026
V_{LT}	1.3897	0.0023
V_{ST}	0.0905	0.0009
V_{Dman}	0.3836	0.0018
V_{Det}	4.1862	0.0055
V_{Count}	3.9643	0.0101

$$V_{STP} = \frac{\chi T_{STP}}{P_{STP}} \sum_i \frac{PV_i}{T_i} = \frac{\chi P T_{STP}}{P_{STP}} \left[\frac{V_P}{T_P} + \frac{V_{Qman}}{T_{Qman}} + \frac{V_{LT}}{T_{LT}} + \frac{V_{ST}}{T_{ST}} \right] \quad (1)$$

In general, it is necessary to subdivide the quantification region into sufficient components such that each component can be represented adequately by an average temperature over that subcomponent. For instance, the small and large trap may have been cooled with liquid nitrogen and continue to warm to room temperature slowly

and may be at a significantly different temperature than the pressure transducer volume. This effect will cause the pressure in the quantification region to gradually rise. Equation (1) ignores the gas compressibility, which can be a significant factor for high-quality measurements and is fairly easy to include if needed. The xenon compressibility is about 0.9988 for conditions typically used in our current system and is therefore a small factor. Equation (1) also includes χ representing the mole fraction of xenon present, which can be measured with a variety of techniques.

After quantification of the xenon, the sample is recollected into the small trap and volumetrically expanded into the detector cell. As with any volumetric expansion, there will be some xenon left behind in the quantification region that does not make it into the detector. Equation (2) gives the expression for the volume of xenon making it into the detector cell and includes the volumetric transfer efficiency as well as the recollect efficiency (E_{recoll}). E_{recoll} is the fraction of xenon that is recollected into the small trap, which gives the opportunity to account for residual xenon left in the quantification region. Typically E_{recoll} is better than 0.99 (i.e., between 0.99 and 1.00).

$$V_{STP,detector} = V_{STP} E_{recoll} \frac{\left(\frac{V_{Count}}{T_{Det}} \right)}{\left(\frac{V_{ST}}{T_{ST}} + \frac{V_{Dman}}{T_{Dman}} + \frac{V_{Det}}{T_{Det}} \right)} \tag{2}$$

Equation (2) is often referred to as the 'stable volume', as it is dominated by non-radioactive (stable) xenon. The two quantification formulae can now be used in the uncertainty analysis and determine an uncertainty estimate for the respective volume. For this discussion, we will focus on Equation (2) because it is directly used in the activity concentration calculation and represents the amount of xenon that arrives in the counting part of the detector cell.

Uncertainty Analysis

For uncertainty analysis we have chosen to follow the *U.S. Guide to the Expression of Uncertainty in Measurement* (ANSI/NCLS Z540-2-1997(R2007)), commonly referred to as the U.S.GUM. The U.S.GUM is an adaptation of the International Organization for Standardization (ISO) *Guide to the Expression of Uncertainty in Measurement*, which describes the notation, terminology, and methodology for consideration of the uncertainty of measurement. This is an internationally recognized standard that many laboratories have adopted.

To proceed with the uncertainty analysis, it is first necessary to define the measurands—in this case, the volume of xenon in the quantification region (V_{STP}) and the volume of xenon delivered to the detector ($V_{STP,detector}$). The method of measurement is to measure the pressure and temperature of the xenon sample in the known volume of the quantification region ($V_P+V_{Qman}+V_{ST}+V_{LT}$) and use the appropriate quantification formula. Typically, it is also necessary to define the measurement procedure and conditions with sufficient detail so that the measurement can be repeated. Generally, a higher precision measurement requires a more detailed description of the procedure and conditions. For automated systems that are typically used for manipulating xenon samples, much of this detail is already included into the processing logic and hardware. These details may include waiting for a sample to thermally equilibrate, amount of xenon being processed, averaging for a particular amount of time, and other experimental procedures and requirements.

A measurand is typically defined as a function of all variables that are needed to adequately determine what is being measured. In Equation (3) Y is the measurand and f is a function of multiple variables X_i. Each X_i in the case of this paper will be a temperature, pressure, or other variable, and will have a respective uncertainty of $u(X_i)$. Each $u(X_i)$ may be estimated from multiple uncertainty terms appropriate for describing that uncertainty.

$$Y = f\left(X_1, X_2, \cdots, X_N\right) \tag{3}$$

The uncertainty estimate for a measurand is called the combined standard uncertainty, u_c. This estimate is found by combining all of the uncertainties for each of the parameters X_i.

$$u_c^2(y) = \sum_1^N \left(\frac{\partial f}{\partial x_i} \right)^2 u^2(x_i) \tag{4}$$

In this equation, there are terms for each variable and the equation is simply the 'law of propagation of uncertainty'. The partial derivative terms are also referred to as sensitivity coefficients (c_i). Strictly by this equation, there should be only N terms—that is, one for each parameter in the function f. We take a broader approach to this to consider a larger number of terms that may be associated with an individual parameter. For instance, when considering a temperature parameter, there can be uncertainties associated with the uncertainty of a thermocouple, uncertainty of the readout device, uncertainty of whether the temperature is completely uniform, as well as other factors. In principle, all of these could be collected into a single estimate of the uncertainty ($u(x_i)$) of the specific temperature measurement and included as one of the N terms in Equation (4). We find that it can be more useful to expand the meaning of N in Equation (4) to mean over all considered uncertainty terms. The equation is still valid because the individual terms associated with a given parameter could still be collected as they have the same partial derivative. The advantage of keeping them separated is that you can easily evaluate each contribution to $u_c^2(y)$ from each considered uncertainty.

The U.S.GUM recommends subdividing the uncertainties being considered into two categories that are based on their method of evaluation: A-type and B-type. This distinction is useful for a variety of considerations, but those considerations are beyond the scope of this report. A-type uncertainties are obtained from statistical treatment of repeated observations, such as using a thermocouple to read many temperature measurements. That series of measurements can then be used to estimate the (statistical or A-type) uncertainty of reading a particular temperature. B-type uncertainties are estimated from other methods including available knowledge, datasheets, calibration data, etc. This B-type uncertainty is often larger than the corresponding A-type uncertainty for sensors such as thermocouples and pressure sensors. While we do characterize different uncertainty terms as A-type and B-type, the distinction is not important when determining the combined standard uncertainty.

For the xenon system model displayed in Figure 1, we have chosen not to independently consider each of the A-type uncertainties into our analysis; however, for a more detailed analysis, this can be quite useful. Our approach was to instead repeat the volume measurement many times using an automated procedure so that we can evaluate the A-type uncertainty of the volume measurand. This includes the A-type components from each of the experimental variables and is a measure of the repeatability of the measurement. Based on a detailed analysis we have found that the A-type components are significantly smaller than the B-type components for our system. If some of the A-type components were larger, it would be useful to consider them separately. In the automated experiments, we also added the capability to perform an independent volume measurement as a check on the system reported volume. The repeatability data is shown in Figure 2, and a couple of key points are evident. Foremost, there is good agreement between the determined volumes and the independent volume check to within the 1σ error bars. Second, it turns out that the determined volumes are quite stable, which is reflected in the stability of the volume from run to run (blue data). In fact, the relative standard deviation of the determined volumes was only 0.04%, which is an indication that our system is set up for excellent repeatability. Error bars for the determined volumes have not been included in this plot, as they are still to be estimated below.

To estimate the uncertainty of the volume measurement, we have constructed Table 2 that lists each of the uncertainty components that are considered in Equation (4). This table can easily be augmented if more uncertainty terms are needed and provides an easy way to see the individual contributions to the combined uncertainty. Also in Table 2 are the parameter units, parameter estimate (x_i), uncertainty estimate ($u(x_i)$), sensitivity coefficients, and contribution to the measurand ($V_{STP,detector}$) variance. At the bottom of the table is the combined standard uncertainty found by adding all of the variance contributions and taking the square root to get $u(V_{STP,detector})$. Note that we have included estimates for the parameters for nominal system performance, which turned out to be slightly different than the performance characteristics of the modified system during the autorun collections in Figure 1.

Each temperature that appears in Equations (1) and (2) are considered to have uncertainty components for the manufacturer's specification, as well as an estimate for the temperature non-uniformity. Temperature non-uniformity is an estimate for the amount of temperature variation over a specific sub-section of the quantification region. Uncertainties in the volumes from Table 1 were also treated. The mole fraction has been found to be close to 0.999 and we included an uncertainty estimate based on variations in the mole fraction during quantification for repeated runs. Similarly, the recollect efficiency was monitored over repeated runs and we included the typical efficiency and an estimate of its uncertainty. A repeatability term was added with a sensitivity coefficient of unity, which experimentally accounts for all of the A-type uncertainties in our measurement. The contribution to the combined uncertainty from this term is small, and it is not useful to separate into more terms. The last column in Table 2 gives the contribution to the variance of $V_{STP,detector}$ and inspection shows which terms are most important. In particular the V_{Count} term is dominate at about 4.2×10^{-6} $(cm^3)^2$, while most other terms are less than 1×10^{-6} $(cm^3)^2$.

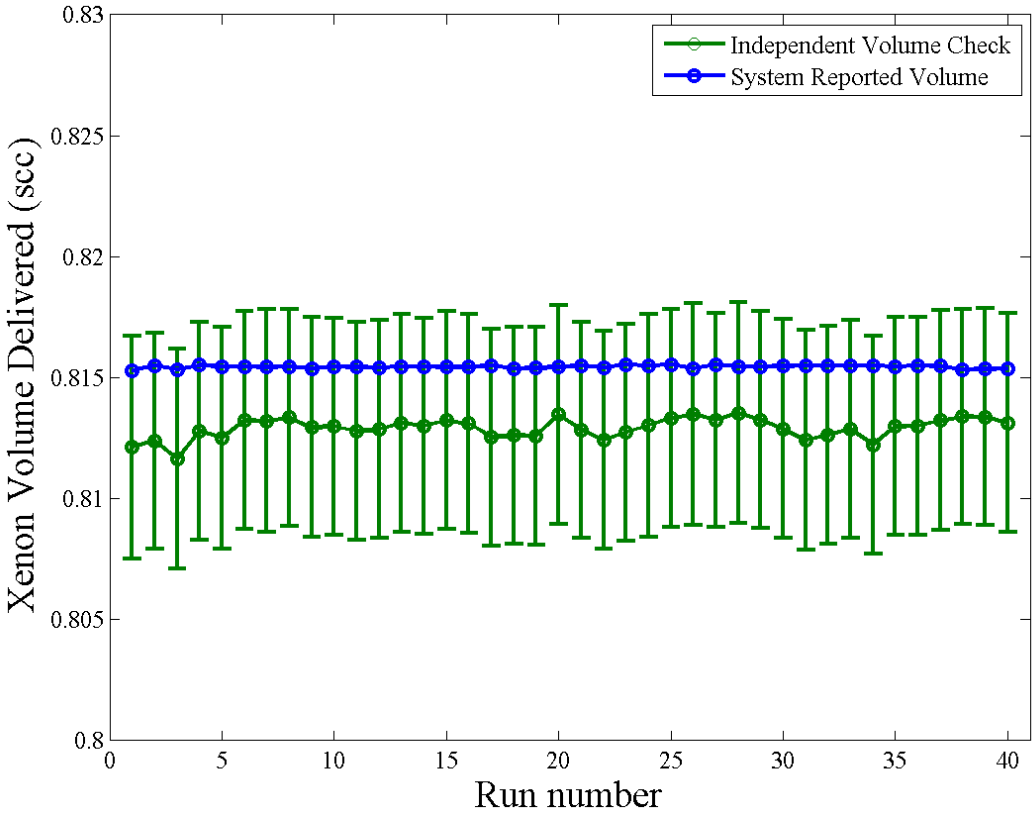


Figure 2. Repeatability Data.

The combined variance results from adding all of the elements in the contributions *to* $u^2(V_{stp})$ column, and the combined standard uncertainty is simply the square root of the combined variance. For purposes of this paper, all uncertainties have been given as 1-σ values, and it is important to mention this with reported uncertainties in general. Different labs have various conventions on reporting uncertainties: 1σ, 2σ, 95% confidence, etc. The U.S.GUM specifies reporting these differences as an expanded uncertainty, where *k* is a coverage factor. By reporting the uncertainty and the coverage factor, it is possible to easily compare between reported measurands and uncertainties in an appropriate manner.

$$U = ku_c(y) \tag{5}$$

For the data that we see in Table 2, it is evident that the measured volume was 0.8013 cm^3, with a combined standard uncertainty of 0.0031 cm^3 at the 1σ level. That would indicate that there is a 0.39% relative uncertainty, which would be quite good for volume measurement in a nuclear activity measurement system. For actual systems, evaluation of the uncertainty can be more complicated, mainly by adding more terms to Table 2. Application to more complicated systems is straightforward, and the primary consideration is what additional terms need to be included. There can be cases where there is disagreement between multiple systems (reproducibility) that is significantly outside of the uncertainty estimate and coverage factor. For those cases, the analyst is being prompted to revisit the uncertainty model to determine what significant contributors have been omitted from the uncertainty model.

Activity Concentration

The activity concentration is given by Equation (6). A_n is the nuclear activity, which has an associated uncertainty $u(A_c)$, and $V_{STP,detector}$ is the xenon volume delivered to the detector; there is also an uncertainty $u(V_{STP,detector})$.

$$A_c = \frac{A_n}{V_{STP,detector}} \tag{6}$$

Table 2. Uncertainty terms and contributions to the combined uncertainty.

Uncertainty	Units	Estimate (x_i)	Standard Uncertainty $u(x_i)$	Sensitivity Coefficient c_i	Contribution to $u^2(V_{STP,detector})$
Pressure					
P	Torr	190	0.15	0.004218	4.0031E-07
Temperature					
T_P non-uniformity	K	298	1	-0.000951	9.0440E-07
Specification	K		0.1	-0.000951	9.0440E-09
T_{Qman} non-uniformity	K	305	1	-0.000728	5.2998E-07
Specification	K		0.1	-0.000728	5.2998E-09
T_{LT} non-uniformity	K	290	1	-0.000957	9.1585E-07
Specification	K		0.1	-0.000957	9.1585E-09
T_{ST} non-uniformity	K	290	1	-0.000007	5.3290E-11
Specification	K		0.1	-0.000007	5.3290E-13
T_{Dman} non-uniformity	K	290	1	0.000233	5.4289E-08
Specification	K		0.1	0.000233	5.4289E-10
T_{Det} non-uniformity	K	298	1	-0.00028	7.8400E-08
Specification	K		0.1	-0.00028	7.8400E-10
Volume					
V_P	cm^3	1.4584	0.0030	0.194190	3.3939E-07
V_{Qman}	cm^3	1.1698	0.0026	0.189733	2.4335E-07
V_{LT}	cm^3	1.3897	0.0023	0.199547	2.1064E-07
V_{ST}	cm^3	0.0905	0.0009	0.023527	4.4835E-10
V_{Dman}	cm^3	0.3836	0.0018	-0.176020	1.0039E-07
V_{Det}	cm^3	4.1862	0.0055	-0.171295	8.8759E-07
V_{Count}	cm^3	3.9643	0.0101	0.201933	4.1597E-06
Mole Fraction					
χ	-	0.999	0.0005	0.800524	1.6021E-07
Recollect Efficiency					
E_{Recoll}	-	0.997	0.00075	0.801326	3.6119E-07
Repeatability	-	-	0.000417	1	1.7364E-07
			$V_{STP,detector}$	0.801326	**Combined std. uncertainty** 0.003089
					Rel. comb std. uncertainty 0.003855

The nuclear activity and the xenon volumes are reported along with their uncertainties, and the activity concentration is reported. The uncertainty model for the activity concentration is given by Equation (7).

$$u(A_c) = A_c \left[\left(\frac{1}{A_n} \right)^2 u^2(A_n) + \left(\frac{1}{V_{STP,detector}} \right)^2 u^2(V_{STP,detector}) \right]^{\frac{1}{2}} \quad (7)$$

In this form, it is easy to see that the uncertainty for the activity concentration is directly related to adding the relative uncertainties of the activity and the volume in quadrature. If the relative uncertainty of the volume $(u(V_{STP,detector})/V_{STP,detector})$ is less than one third of the relative uncertainty of the activity concentration ($u(A_n)/A_n$), then the contribution from the volume part will be quite small and the uncertainty will be dominated by the nuclear activity measurement. This is the recommended situation such that the volume measurement does not degrade the activity concentration uncertainty. In general, for normal samples, it is not excessively difficult to reach this situation and this expression can be used to drive the level of effort directed toward the sophistication of the volume quantification. We note that in the case for calibration samples where count rates can be exceedingly high, it will likely not be possible to match the relative uncertainty of the counting statistics of the nuclear activity measurement.

CONCLUSIONS AND RECOMMENDATIONS

Treaty monitoring gas measurement systems that measure radioxenon typically report results as an activity concentration. The reported data is the measured radioxenon activity divided by the amount of stable xenon present. While the nuclear activity uncertainty has been studied in detail and is driven primarily by counting statistics, the uncertainty for the volume measurement has been considered in less detail. A framework for a more complete consideration of the uncertainty for the volume measurement has been developed. This type of analysis can help drive the system requirements for the volume quantification while the system is still being developed or for advanced fielded systems. Depending on the accuracy requirements for the activity concentration, the volume quantification measurement and analysis can be developed to a suitably high level of accuracy. Nominally, it is best to have the activity concentration uncertainty limited by the uncertainty of the activity measurement because it tends to be fundamentally limited by the counting statistics. Therefore, it is best to have the volume quantification performed more accurately so that the activity concentration uncertainty is not degraded.

REFERENCES

Cooper, M., J Ely, D Haas, J Hayes, J McIntyre, L Lidey, and B Schrom (2012). Absolute efficiency calibration of a beta-gamma detector, in *2012 IEEE SORMA WEST 2012*. PNNL-SA-88667, Pacific Northwest National Laboratory, Richland, WA.

Harper, W., M. Cooper, J. Hayes, and L. Lidey (2011). Limitations using small volume cryotraps, in *Proceedings of the 2011 Monitoring Research Review: Ground-Based Nuclear Explosion Monitoring Technologies*, LA-UR-11-04823, Vol. 2, pp. 689–694.

U.S. Guide to the Expression of Uncertainty in Measurement, ANSI/NCLS Z540-2-1997 (R2007). National Conference of Standards Laboratories International.

RADIOXENON MEASUREMENTS WITH A COINCIDENCE SILICON DETECTOR SYSTEM

Wolfgang Hennig[1], Christopher E. Cox[1], Stephen J. Asztalos[1], Hui Tan[1], Patrick J. Franz[1], Ann Xiang[1], Peter M. Grudberg[1], William K. Warburton[1], Alan Huber[2], Steve Biegalski[3], Alex Brand[3], and Derek Haas[4]

XIA LLC[1], Amptek Inc[2], The University of Texas at Austin[3], and Pacific Northwest National Laboratory[4]

Sponsored by the National Nuclear Security Administration

Award No. DE-SC0004272 Phase II

ABSTRACT

The radioxenon detectors currently used in applications related to nuclear explosion monitoring have a very high sensitivity to detect very small amounts of radioxenon. However, to better distinguish the radioxenon background created by nuclear power plants and medical isotope facilities from a nuclear explosion, an improved discrimination of Xe isotopes is desirable. Silicon detectors have a number of advantages over the existing detectors (high resolution, low background, sensitivity to both photons and electrons, and no memory effect) and thus have the potential to outperform them in isotope discrimination.

In the work reported here, a radioxenon detector based on silicon PIN diodes has been designed, assembled, and tested. In Si-Si coincidence measurements with various Xe isotopes, resolutions were ~0.7 keV for 30 keV X-rays and 1.3-2.5 keV for conversion electrons at 129-232 keV. The presence of metastable Xe isotopes can easily be detected by observing conversion electron peaks in the energy spectra. The efficiency for detecting higher energy gamma rays is low, but backgrounds are practically zero so that overall the minimum detectable concentration is estimated to be well below 1 mBq/m^3 for a Si detector system with 100 mm^2 active area on each of the six sides of a cubic Xe cell.

OBJECTIVES

One of the tools used in nuclear explosion monitoring is the detection of atmospheric radioxenon. Existing radioxenon detectors, e.g., the SAUNA system (Ringbom et al., 2003), the PhosWatch detector (Hennig et al., 2009) and the SPALAX system (Fontaine et al., 2004), have a very high sensitivity to detect small amounts of radioxenon and can distinguish four key Xe isotopes. Because isotope ratios can be used to separate nuclear explosions from other sources like nuclear power plants and radiopharmaceutical facilities (Saey et al., 2010), better determination of isotope ratios emerges as a desirable feature in future developments. Besides generally improving the sensitivity (i.e., lowering the background or increasing the efficiency of the detector), distinction between isotopes can also be achieved by improving the detector's energy resolution so that key X-ray lines from the different isotopes no longer overlap in the energy spectra.

Silicon-based X-ray detectors such as silicon drift detectors (SDD) and PIN diodes have very high resolution at these X-ray lines. In addition, they can detect conversion electrons (CE) with high efficiency and excellent energy resolution, are sensitive to additional L X-rays, require no or simple cooling (with Peltier elements), show no memory effect, and have very low background even without lead shielding. Consequently, silicon based beta/X-ray coincidence detectors are a potential alternative to the existing scintillator based coincidence beta/gamma detectors or germanium based gamma only detectors.

In the work reported here, our objectives were to build a prototype of a silicon coincidence detector, test it with several Xe isotopes, and conduct a preliminary analysis of the data to estimate isotope activities.

RESEARCH ACCOMPLISHED

Si Detector System

In previously reported work (Cox et al., 2011, Hennig et al., 2011) we studied the response of Si detectors to electrons and photon at key Xe energies with test measurements and radiation transport simulations. It was concluded that both PIN diodes and SDDs are suitable for radioxenon detection, with the main difference that SDD achieve better resolution at higher temperatures and larger detector areas, but – at this time – with significantly higher cost. For our first prototype, we therefore chose to use PIN diodes with Peltier cooling. Two 25 mm^2 PIN diodes mounted on 1 cm^2 ceramic substrates were glued to two open sides of a ~1 cm^3 Cu cubic frame. A 1/16 inch stainless steel tube was attached on a third side, allowing evacuation of air and insertion of Xe. A two-stage Peltier cooler and mounting bracket was attached on a fourth side. The detector assembly and preamplifiers were mounted in an airtight box ($5 \times 4 \times 10$ cm^3 with feedthroughs for gas and electrical connections) and flushed with dry N_2 gas to prevent water condensation at an operating temperature of ~276 K. Pictures of the detector assembly are shown in Figures 1 and 2. The detectors were read out with an XIA xMAP spectrometer module, acquiring time-stamped list mode data from which coincidences were extracted offline.

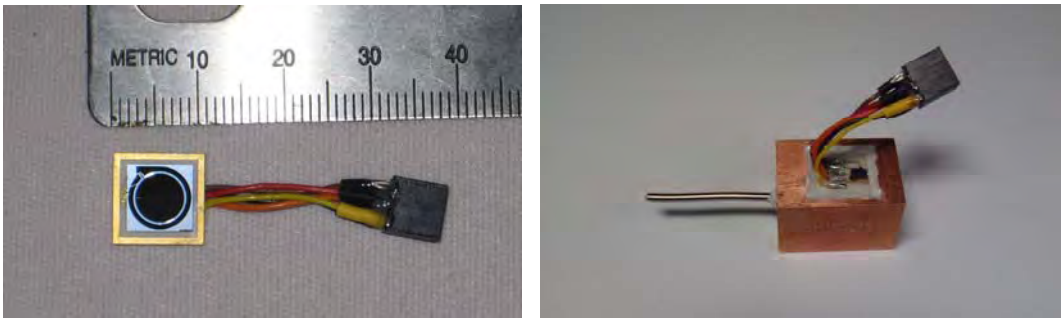


Figure 1. (Left) Picture of Si detector on ceramic substrate. (Right) Picture of Si detector glued into the copper cube acting as Xe cell (with filling tube)

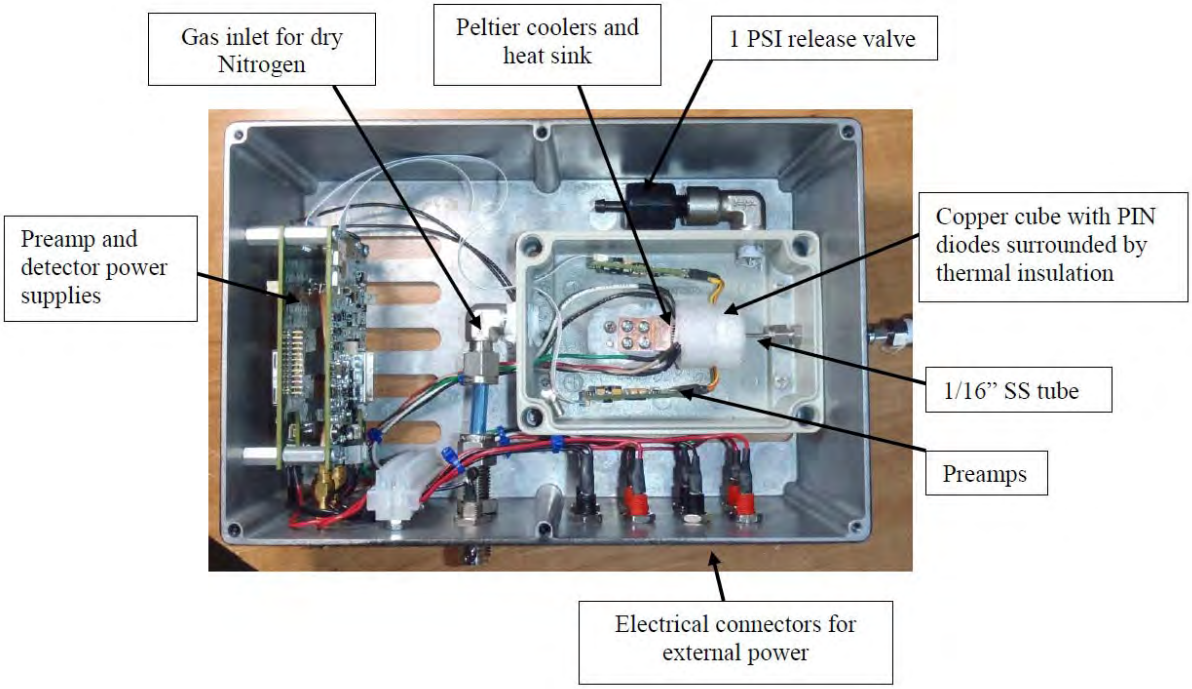


Figure 2. Picture of Si detector assembly. Inner box contains Si detector in foam wrapping, Xe filling tube to right, preamps above and below. Outer box contains HV and preamp power boards and associated wiring, as well as tubing for dry N_2 used to flush inner box from moisture.

Test Measurements

Figure 3 shows the energy spectra acquired in Xe measurements at the University of Texas at Austin, where a mixture of ^{133m}Xe and ^{133}Xe was obtained by the method of irradiating stable ^{132}Xe (Haas et al., 2009). The ^{133}Xe creates betas with energies up to 346 keV; ~4, 31, and 35 keV X-rays; 81 keV gamma-rays; ~25 keV Auger electrons; and 45 and 75-80 keV CEs, producing beta/CE, beta/X-ray, beta/gamma, and CE/X-ray coincidences. The ^{133m}Xe creates ~4, 30, and 34 keV X-rays; ~25 keV Auger electrons; and 199 and 228-233 keV CEs, producing CE/X-ray and CE/Auger coincidences. Coincidences with the variable energy beta absorbed in one detector and the fixed energy particle in the other detector form horizontal and vertical lines in the 2D spectrum. CE/X-ray coincidences from ^{133m}Xe form peaks at (4 keV/199 keV), (30 keV/199 keV), and (4 keV/228 keV). Auger/CE coincidences from ^{133m}Xe form a peak at (21 keV/199 keV), shifed from the nominal value by energy loss of the Auger electron in the Si dead layer and the Xe gas. Scattering of CEs from one detector to the other form diagonal lines with constant sum energy. As both detectors detect photons and electrons, the resulting spectrum is symmetric about the diagonal. Energy resolutions are listed in Table 1. At ≥30 keV, ^{133m}Xe coincidence peaks separate from the ^{133}Xe coincidence lines by the difference in their X-ray energies. The total count rate per detector was ~331 counts/s (~7 counts/s coincident). When the Xe was pumped out again, the total count rate was ~0.1 counts/s, (~0.001 counts/s coincident).

Figure 4 (left) shows the energy spectra acquired in ^{131m}Xe measurements at PNNL. Features are similar to ^{133m}Xe, only the CE energies are smaller. The total count rate per detector was ~22 counts/s (~0.32 counts/s coincident). Energy resolutions are listed in Table 1. A subsequent measurement with the Xe pumped out of the detector resulted in the background spectrum shown in Figure 4 (right). The total count rate per detector was ~0.2 counts/s (~0.0015 counts/s coincident). At the 159/4 keV peak, there were 0 counts in 24h, compared to ~500 counts in 16h in the Xe measurement.

The post-Xe measurements demonstrate the low background and neglible memory effect in Si detectors. We note that measured coincidence backgrounds (BG_{coinc}) are higher than expected from the simple assumption that BG_{coinc} is the product of the background in each detector and the coincidence window. For the PNNL measurement, the

expected BG_{coinc} would be ~10^{-8} counts/s compared to the measured value of ~10^{-3} counts/s. Some of the additional background can be attributed to ^{125}I, a decay product of ^{125}Xe used in a previous test. With a new detector never exposed to internal sources, we obtain BG_{coinc} = 2.0x10^{-4} cps from a 1 week measurement (120 coincident counts). This is still higher than expected; further studies are under way to understand the source of this backgound and to develop possible ways of eliminating it.

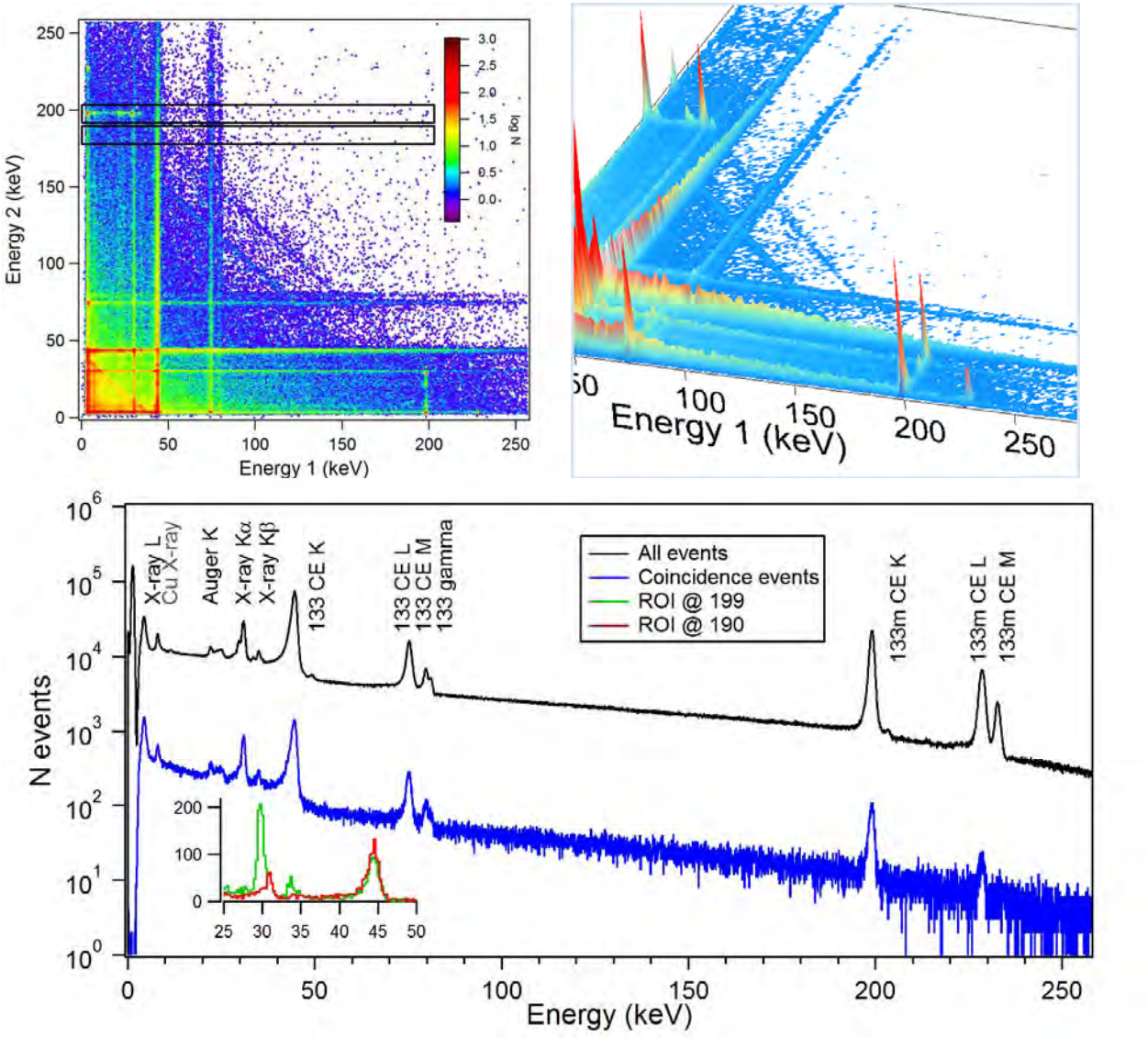


Figure 3. $^{133}Xe/^{133m}Xe$ energy spectra with Si prototype detector. Upper left: Conventional 2D plot colored by number of events in bin. Upper right: 3D surface plot of the same data, better visualizing the sharp CE peaks. Below: 1D histograms (projection to bottom axis) of all events and coincidence events of one detector. The inset shows the spectra from the ROI indicated by boxes in the 2D plot.

The resolution of the CE peaks varies in different measurements. In previous measurements at UT (Hennig et al., 2011), a single PIN test detector in a ~ 5 cm^3 cell made from Conflat vacuum flanges achieved better resolution than the current 1 cm^3 cell 2-PIN prototype. Both measurements used about the same amount of stable Xe for irradiation (about 0.56 cm^3), expanded into cell and manifold tubing. We attribute the lower resolution in 2012 to a) the higher gas pressure in the cell and/or b) small amounts of N_2 leaking into the cell from the surrounding box. In PNNL measurements, the Xe sample contained c) a "filler" of N_2 for better handling, which may have raised the pressure in the cell, and again there is a possibility of leaking. Since CE peaks are well separated, this peak broadening does not

significantly affect the sensitivity of the detector. In fact, it can be used to estimate the amount of sample gas (if leaking is eliminated).

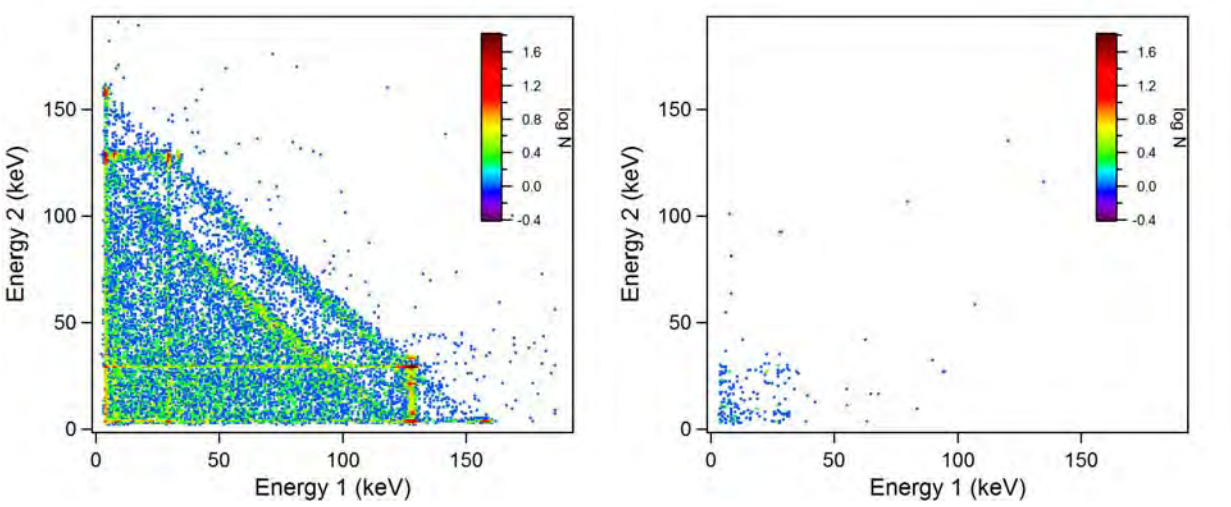


Figure 4: ^{131m}Xe spectrum (16h) and post ^{131m}Xe background (24h).

Table 1. Energy resolution in Xe measurements. UT 2011 measurements from (Hennig et al., 2011) used a single PIN (7 mm^2) test cell, UT 2012 and PNNL 2012 measurements used the 2-PIN prototype (25 mm^2 each).

Energy (keV)	Isotope / Particle	Measurement	Resolution (keV)	Comment
4	131m L Xray 133m/133 L Xray	PNNL 2012 UT 2012	0.75 1.0-1.1	doublet 2 doublets
30	133m K Xray	UT 2011 PNNL 2012 UT 2012	0.6 0.72 1.0	doublet
31	133 K Xray	UT 2011 UT 2012	0.6 0.8-0.9	doublet
45	133 K CE	UT 2011 UT 2012	0.99 1.5	
75	133 L CE	UT 2011 UT 2012	1.1 1.4	
129	133m K CE	PNNL 2012	3.1	
159	133m L CE	PNNL 2012	2.8	
199	133m K CE	UT 2011 UT 2012	1.14 1.3 - 1.6	
228	133m L CE	UT 2011 UT 2012	1.4 1.5-1.9	Several lines in peak

Preliminary Quantitative Analysis

To estimate activities from measured spectra, we developed a simple analysis routine that sums the counts in specific regions of interest (ROI) of the 1D histograms, factors in efficiencies, branching ratios, acquisition time and decay during acquisition, and returns the activity at the beginning of the measurement for each isotope. As this is intended for quick results only, only 2-3 ROIs per isotope are used, no effort is made to correct for coincidences or

electrons interacting in more than one detector, and CE peaks are only corrected by subtracting an equivalent neighboring ROI of the ^{133}Xe beta continuum. No statistical errors or MDCs are computed at this time.

Detection efficiencies are taken from Monte Carlo simulations of the detector geometry used, see Figure 5 (left). The detector was modeled as a pure Cu block with overall dimensions of 1.4 × 1.4 × 2.0 cm^3 with 1.1 × 1.1 cm^2 openings for SiO_2 substrates. Two 25 mm^2 PIN detectors 0.45 mm thick and 1.0 cm apart were placed at the center of opposing SiO_2 substrates with Xe gas at STP uniformly filling the detector volume. A million events were simulated for each of several key energies and particles. The detection efficiency was defined as the number of events that deposited full energy versus the total number of simulated particles. An energy spectrum of 199 keV electrons interacting with a single PIN diode is shown in Figure 5 (right). The *full* energy efficiencies for electrons depend only slightly on the energy and are 3.1-3.3% for 45-199 keV (~6.5% for interactions depositing *any* energy), compared to a geometric active area fraction of 4.2%. *Full* energy efficiencies for photons are 3.7%, 0.5% and ~0.025% at 4 keV, 30 keV and 81 keV, respectively.

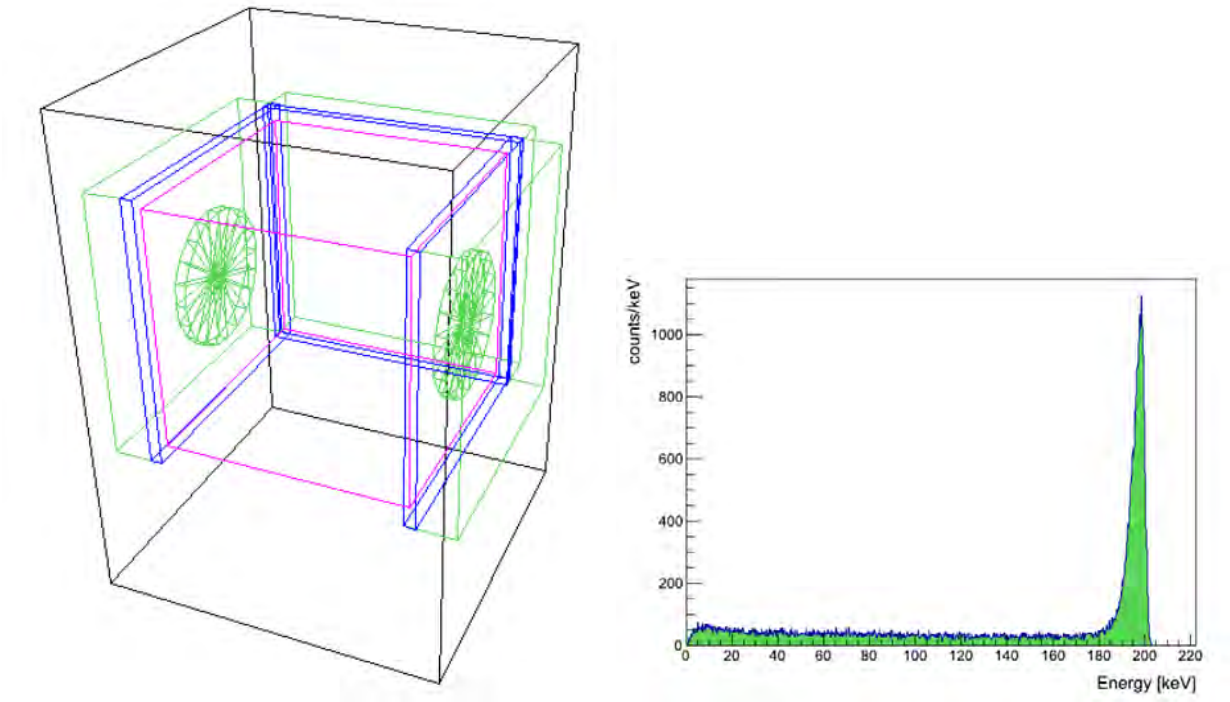


Figure 5. (Left) Side view of the PIN diode detector geometry used for efficiency simulations. Black defines the Cu body, magenta the Xe cell (interior), blue the SiO^2 wafers and hatched green the 25 mm^2 PIN diodes. (Right) Simulated energy spectrum of 199 keV conversion electrons uniformly emitted within the Xe volume.

Table 2 summarizes the analysis results for the Xe and background measurements at UT and PNNL. Activities computed from different ROIs agree well. The data shown in Table 2 are consistent with the expected activities of the sample from irradiation, assuming a 15% transfer efficiency between the created sample and detector cell. This is reasonable considering the volumetric differences and the losses in the transfer lines in the test setup. The ^{133m}Xe/^{133}Xe ratio is also commensurate with the expected value. Figure 6 shows the radioxenon activities as a function of time for the measured sample.

Table 2. Net Counts in 1D ROIs and corresponding activity (in mBq) at start of measurement. Bold fields indicate the major isotopes in each Xe sample.

Isotope	ROI (keV)	Net counts UT 2012	Activity UT 2012	Net counts PNNL 2012	Activity PNNL 2012	Net counts PNNL 2012 background	Activity PNNL 2012 background
131m	129 158-163	-2,441 4,699	-1k 6k	**289,755** **191,979**	**267k** **286k**	22 30	0 0
133m	199 228 232-233	**642,213** **210,611** **46,221**	**567k** **559k** **548k**	-9 50 -7	0 0 0	5 -8 6	0 0 0
133g	45 75	**2,093,114** **346,155**	**2,157k** **2,354k**	5050 273	5k 1k	-72 6	0 0

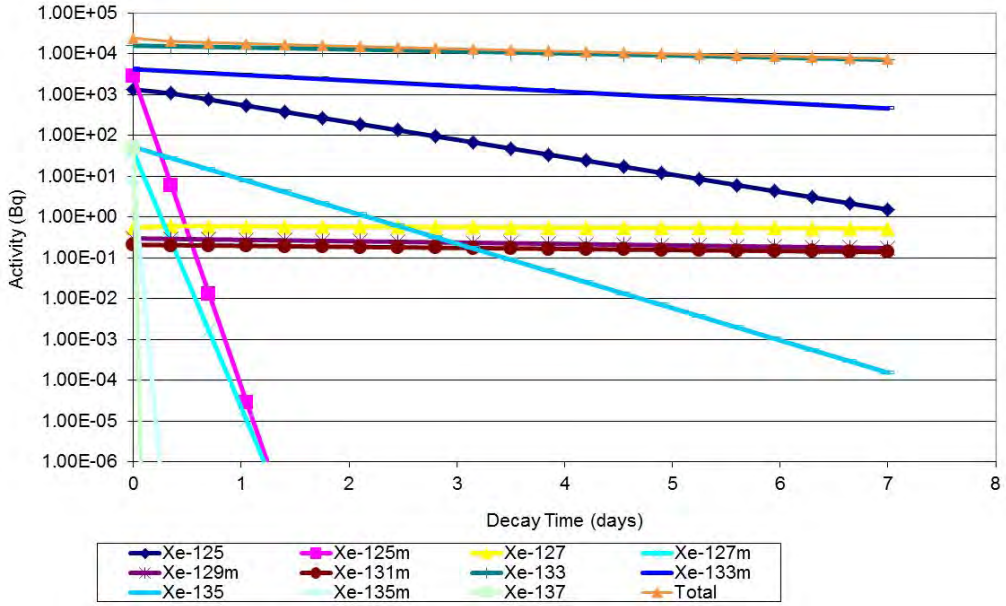


Figure 6. Radioxenon activites as a function of decay time for 0.56 cm^3 enriched (99.9%) ^{133}Xe sample (100 kW for 1 hour in UT TRIGA reactor).

With a large number of ROIs, including overlapping ROIs for beta isotopes and metastables at 4 keV, the above analysis is tedious and error prone. Future analysis with employ the Spectral Deconvolution Analysis Tool (SDAT) analysis tool (Biegalski et al., 2008). SDAT utilizes the standard spectrum method for spectrum analysis where the contribution of each radionuclide is fit within the spectrum. Library vectors containing pure spectra of the following six components are necessary for radioxenon analysis: ^{131m}Xe, ^{133m}Xe, ^{133}Xe, ^{135}Xe, radon, and detector background. The library vectors are fit to the sample spectrum via a least-squares algorithm to determine the magnitude of each spectral component. SDAT was developed for the analysis of β-γ coincidence spectra from detectors with BC-404 plastic scintillators as the β detector. Adaptations of the tool are now in progress at UT Austin so that spectra from the coincidence Si detector may be utilized.

Estimated Sensitivity

Using backgrounds and energy resolution from test measurements and detector efficiencies from simulations, we previously estimated the minimum detectable concentration (MDC) for the four Xe isotopes of interest (Hennig et al., 2011). Simplifying the definition in (Ringbom et al., 2003), as described in (Hennig et al., 2012) we approximate MDC as

$$MDC = (2.71 + 4.65\,\sigma) / (\varepsilon_{\beta\gamma} \times \beta\gamma \times t_{acq} \times V) \qquad (1)$$

Where σ^2 is the number of measured background counts in an ROI, $\varepsilon_{\beta\gamma}$ is the coincidence detection efficiency for the ROI, $\beta\gamma$ is the branching ratio into the ROI from literature (Browne and Firestone, 1986), V is the collected air volume, and t_{acq} is the measurement time, assumed to be 24 h. In the case of multiple ROIs, the background σ and product $\varepsilon_{\beta\gamma} \times \beta\gamma$ are replaced by their sums over the individual ROIs. For the specific case of two ROIs, Equation 1 becomes

$$MDC = (2.71 + 4.65\,\sigma_t) / ((\varepsilon_{\beta\gamma 1} \times \beta\gamma_1 + \varepsilon_{\beta\gamma 2} \times \beta\gamma_2) \times t_{acq} \times V) \qquad (2)$$

Where σ_t^2 equals $\sigma_1^2 + \sigma_2^2$ - the sum in quadrature of measured background counts in each ROI. For ROI 1, the coincidence detection efficiency is $\varepsilon_{\beta\gamma 1}$ and the branching ratio $\beta\gamma_1$, with $1 \rightarrow 2$ for ROI 2. Since backgrounds are extremely low, the numerator is generally dominated by the term 2.71. Selected results are listed in Table 3, column 3. The detector geometries are as follows (keeping the previous enumeration):

Detector B—A 1 cm^3 cube with a single Si detector (25 mm^2 active area) in each of two active sides. This geometry has two coincidence permutations (electron left, photon right, and vice versa).

Detector C—Same as B but 100 mm^2 detectors in all six sides of the cube (30 coincidence permutations).

Detector D—A 5 cm^3 cube with four Si detectors (25 mm^2 active area each) in each of its six sides (552 coincidence permutations).

Detector B represents the geometry of the prototype. Detectors C and D are examples of high efficiency detectors: Detector C is the ideal case with very large PIN diodes or SDDs and no dead area, which is included for illustration but at current state of the art suffers either from bad resolution (with large PINs) or high cost (with large SDD). Detector D models the geometry of our proposed next prototype, using arrays with four 25 mm^2 PINs on a common 1.7cm x1.7cm substrate with an active area fraction of ~34%.

Following the Xe measurements described above, we can refine the previous MDC estimates in a number of ways: First, from Figure 3 we can see that there are a significant number of ^{133}Xe beta/CE and X-ray/CE coincidences detected at 45 keV and 75 keV, which have not been included in the previously estimated MDC for ^{133}Xe. Adding beta/CE and X-ray/CE ROIs into the MDC calculation and adjusting all ROIs for measured resolutions, we obtain the MDCs in column 4, improved by a factor of about 4-10 for the beta emitter isotopes. The improvement is due to the relatively high value of $\varepsilon_{\beta\gamma} \times \beta\gamma$ for beta/CE coincidences: the combined product for ^{133}Xe ROIs is ~10% for X-ray/beta coincidences, ~7.4% for X-ray/CE coincidences and ~46% for beta/CE coincidences (not including the detector specific active area fraction) For ^{135}Xe, the combined products are ~0.5% for X-ray/beta coincidences, ~0.4% for X-ray/CE coincidences and ~4.1% for beta/CE coincidences. Use of Auger/CE coincidences may further improve the MDC, but are difficult to count due to their low energy and consequent relatively high energy loss in the gas and the Si dead layer.

Second, we previously disregarded cross contamination from isotopes with beta decays into the CE ROIs of metastable isotopes, assuming they can be separated by the X-ray energy. From Figure 3 we can see that this assumption is just about correct for 30/31 keV K X-rays, but not for ~4 keV L X-rays. Assuming a (substantial) ^{133}Xe concentration of 100 mBq/m^3, 10% ROI overlap at 30 keV and 100% ROI overlap at 4 keV, we can compute the number of beta/X-ray coincidences that will fall into the ROIs of metastable isotopes and thus increase the background term. The MDC of metastable isotopes then increases to about 1 mBq/m^3 for the high efficiency detectors (column 5). However, this beta cross contamination can be further suppressed by excluding triple coincidences from the ROI in a system with 3 or more detectors. For example, a ^{133}Xe beta decay followed by a 75 keV CE and 4 keV X-ray may create a count in the ^{133m}Xe ROI at (199 keV/4 keV) if only a beta and X-ray are detected. However, if a third detector detects the 75 keV CE at the same time, it is clear that the event comes from ^{133}Xe and the count can be removed from the ^{133m}Xe ROI. This would reduce the cross contamination by as much as 31% and 66% for detectors B and C (depending on the number of PIN diodes and active area) and thus lower the MDCs listed in column 5. An additional, but smaller suppression of beta background comes from events where CE and X-ray hit the same detector and from events with higher number of particles (e.g., beta + 45 keV CE + 30 keV

X-ray + 4 keV X-ray). Cross contamination of decays from ^{131m}Xe and ^{133m}Xe into ^{133}Xe ROIs is not considered here because the metastables' CE peaks are sufficiently narrow to simply exclude them from ^{133}Xe ROIs.

Third, as noticed above, measured coincidence backgrounds do not agree with our assumption of coincidence background being the product of individual backgrounds and the coincidence window. Using the measured average coincidence background of the uncontaminated detector, we obtain the slightly increased values in column 6. However, this measured background has a very large uncertainty; the measured coincidence background in a particular ROI is often zero. These results are therefore best understood as an upper limit. As noted above, sources and/or removal of this unexpected background are under investigation.

Overall, the estimated MDCs for the high efficiency detectors are typically well below 1 mBq/m^3, which is the requirement for ^{133}Xe detection in IMS monitoring stations. Existing detectors reach between 0.1 and 1 mBq/m^3 in the absence of large memory effects (Bowyer et al., 2011, Hennig et al., 2009, Fontaine et al., 2004).

When distinguishing nuclear explosions from other sources of atmospheric radioxenon, one often employed method is to plot measured isotope ratios and compare them to a "separation line" (Kalinowski et al., 2010). A sample of radioxenon with an initial ratio of isotopes will not cross this line as the isotopes decay over time. Typically a 4-isotope plot is used, which has the advantage that explosions fall on one side of the separation line and all other sources fall on the other. On a 3-isotope plot, a subset of the "other" sources may fall on the "explosion" side of the plot, in an area corresponding to an explosion that has decayed for some time T_D. For ^{135}Xe, CE and X-ray branching ratios are small, which means that Si detectors have lower sensitivity for ^{135}Xe than for the other isotopes – the MDC is about a factor 10 higher (though still in the range of 0.2-2 mBq/m^3). Therefore 4-isotope plots may not be applicable. However, since a) ^{135}Xe is rarely detected from a location not close to an IMS station and b) the time limit T_D is in the order of 50 days for a 3-isotope plot without ^{135}Xe, we believe there is not a significant loss of sensitivity for using only ^{131m}Xe, ^{133}Xe, and ^{133m}Xe for source discrimination with Si detectors.

Table 3. Estimated MDC for Xe isotopes (in mBq/m^3)

Isotope	Detector	Previous estimate (Using X-ray/CE for metatsable isotopes and only X-ray/beta for beta emitters)	Adding CE/beta and X-ray/CE ROIs for beta emitters	With beta cross-contamination (100mBq/m^3 ^{133}Xe) and CE/beta and , X-ray/CE ROIs	Using measured coincidence background and CE/beta and X-ray/CE ROIs
131m	B (2 PIN) C (6 SDD) D (24 PIN)	25.32 0.11 0.16	No change	38.50 0.96 1.20	25.51 0.12 0.17
133m	B C D	23.08 0.10 0.15	No change	35.09 0.87 1.10	23.25 0.11 0.15
133g	B C D	22.28 0.09 0.14	4.04 0.02 0.03	No change	4.60 0.05 0.05
135g	B C D	439.42 1.83 2.75	45.41 0.19 0.29	Not calculated	52.39 0.64 0.53

CONCLUSIONS AND RECOMMENDATIONS

In summary, we built a 2-PIN prototype Si detector for radioxenon detection, tested it with Xe samples, and developed a preliminary quantitative analysis routine. Si detection efficiencies for Xe gamma rays are low, but energy resolutions for X-rays and CE are high and backgrounds are extremely low. With multiple detectors, all sensitive to betas, CEs and photons, Si based detectors can make use of beta/CE coincidences in addition to the photon/beta and photon/CE coincidences employed in existing scintillator based detectors, which increases sensitivity. From the test measurements, upper limits for any Xe memory effect range from 1:3000 to 0:500, i.e., there is practically no memory effect.

In ongoing work, we are building a high efficiency Si detector, consisting of 24 PIN diodes for a total of 100 mm^2 active area on each of the six sides of a cubic Xe cell. The basic mechanical design of this detector is complete, with improved vacuum-tightness to eliminate leaking, and its cooling mechanism has been tested successfully. A custom arrangement of four 25 mm^2 PIN diodes on a common substrate has been designed and is about to be manufactured. The MDC of this detector is estimated to be well below 1 mBq/m^3.

Si detectors thus meet several key requirements for detectors in radioxenon monitoring stations. With their lower complexity, no need for lead shielding, and the ability to detect ^{37}Ar L X-rays in the same detector, they may also be a good match for on-site inspection applications.

REFERENCES

Biegalski KMF, Biegalski SR, and Haas D (2008) Performance Evaluation of Spectral Deconvolution Analysis Tool (β) Software Used for Nuclear Explosion Radionuclide Measurements, *J. Radioanal. Nuc. Chem.* **276**(2), 407–413.

Bowyer T.W., S.R. Biegalski, M.W. Cooper, P.W. Eslinger, D. Haas, J.C. Hayes, H.S. Miley, D.J. Strom, and V.Woods (2011). Elevated radioxenon detected remotely following the Fukushima nuclear accident. *J. Environ. Radioact.* **102**, 681–687.

Browne, E. and R. Firestone (1986). *Table of Radioactive Isotopes*, J. Wiley.

Cox C.E., S.J. Asztalos, W. Hennig, and W.K. Warburton (2011). Electron response in windowless Si(Li), SDD and PIN diode photodetectors *Proceedings of the 2011 IEEE Nuclear Science Symp*, 2074–2080 (paper ID NS45-4).

Fontaine, J-P., F. Pointurier, X. Blanchard, and T. Taffary (2004). Atmospheric xenon radioactive isotope monitoring, *J. Environ. Radioact.* **72**, 129.

Haas, D.A., S.R. Biegalski, and K.M. Foltz Biegalski (2009). Radioxenon production through neutron irradiation of stable xenon gas, *J Radioanal Nucl Chem* **282**, 677–680.

Hennig, W., W. K. Warburton, A. Fallu-Labruyere, K. Sabourov, M. W. Cooper, J. I. McIntyre, A. Gleyzer, M. Bean, E. P. Korpach, K. Ungar, W. Zhang, and P. Mekarski (2009). Development of phoswich detector system for radioxenon monitoring, *J. Radioanal. Nucl. Chem.* **282**, 681.

Hennig, W., C. E. Cox, S. J. Asztalos, H. Tan, P. J. Franz, P. M. Grudberg, and W. K. Warburton (2011). Study of silicon detectors for high-resolutin radioxenon measurements, in *Proceedings of 2011 Monitoring Research Review: Ground-Based Nuclear Explosion Monitoring Technologies*, LA-UR-11-04823, Vol. 2, pp. 695–707.

Hennig, W., C. E. Cox, S. J. Asztalos, H. Tan, P. J. Franz, P. M. Grudberg, W. K. Warburton and A. Huber (2012). submitted to *J Radioanal Nucl Chem.*

Ringbom, A., T. Larson, A. Axelson, K. Elmgren, and C. Johansson (2003). SAUNA—A system for automatic sampling, processing and analysis of radioactive xenon, *Nucl. Instrum. Methods Phys. Res., Sect. A* **508**: 542–553.

Saey P.R.J, T.W. Bowyer, A. Ringbom (2010). Isotopic noble gas signatures released from medical isotope production facilities—Simulations and measurements. *Appl. Rad. And Isotopes* **68** (9), 1846–1854.

SIMULATION OF RADIONUCLIDE GAS BREAKTHROUGH FROM UNDERGROUND NUCLEAR EXPLOSIONS

Amy B. Jordan[1,2], Jonathan K. MacCarthy[1], Philip H. Stauffer[1], George A. Zyvoloski[1], Mark A. Person[2], and Dale N. Anderson[1]

Los Alamos National Laboratory[1] and the New Mexico Institute of Mining and Technology[2]

Sponsored by the Defense Threat Reduction Agency

Award No. BRCALL08-0008: DTRA1-11-4539I

ABSTRACT

The breakthrough of isotopic gas atoms at the surface following an underground nuclear explosion (UNE) depends on the device yield, isotope half life, and migration/attenuation factors for gas transport in the subsurface. Here we present Monte Carlo simulations using a numerical model of gas migration through rock following an UNE, with an emphasis on understanding the primary driving mechanisms for gas transport to the surface and comparison with experimental data from the Nevada National Security Site (NNSS) for model validation purposes. The numerical modeling results will be used to support the development of mathematical representations of the gas migration factor for quick deployment during an on-site inspection (OSI) under the Comprehensive Nuclear-Test-Ban Treaty.

The multiphase Finite Element Heat and Mass transfer code (FEHM) was used to perform Monte Carlo modeling of fractured porous media representing Rainier Mesa tuffs at the NNSS. Breakthrough curves for the tracer gases helium-3 (He-3) and sulfur hexafluoride (SF_6), the gases used in the Non-Proliferation Experiment (NPE), were produced for a range of likely subsurface properties, including rock matrix permeability, porosity, and saturation; fracture aperture; and initial gas distribution. The material was taken to be homogeneous with fractured zones represented using a generalized dual permeability model (GDKM). GDKM was tested against discrete fracture simulations and analytical solutions for pressure propagation in fractured rock to validate the code.

A set of 2000 2-D Cartesian simulations were performed with geologic parameters randomly distributed across a range of rock properties and fracture characteristics and an initial gas distribution corresponding to the uniform filling of a "chimney" of height 84 m from the work point. The tracer gases He-3 and SF_6 both arrive at the surface by 14 months in 758 (38%) of the simulations, with SF_6 breakthrough always preceding He-3. In 32 (1.6%) of the simulations, He-3 and SF_6 arrival times coincide closely with the NPE tracer gas data, which show a separation of almost 11 months in arrival. A wide range of input parameters can result in breakthroughs that match the data. Sensitivity studies were performed to illustrate which parameters were most strongly correlated when the observed separation in arrival time between the two gases was achieved.

For simulations that matched the NPE tracer gas data, Xe-133 transport and decay were simulated and the window of opportunity for detection of this signature radionuclide was estimated. The window of Xe-133 detectability ranges from 0 to 135 days in length and begins anywhere from 13 to 51 days following the explosion. The rock properties for the realizations that most closely matched the NPE breakthrough data were also modeled in 3-D Cartesian coordinates, with a planar fracture intersecting a columnar chimney volume of initially distributed gases. Arrival of SF_6 and He-3 generally occurred earlier in the 3-D simulation than in its corresponding 2-D simulation.

The effects of different initial distributions of gas throughout the volume of rock were also considered in our 2-D model of the NPE. For a given set of geologic properties, sufficient space between the top of the initial gas volume and the surface is required to separate the He-3 and SF_6 gases to the observed arrival times. The width of the initial gas volumes affects the concentrations of the gases, which alters their arrival times as well.

To test the effect of the presence of a rubblized chimney on tracer gas transport, simulations were performed with fixed geologic parameters to approximate the hydraulic properties of the layered tuffs beneath Rainier Mesa, with varying chimney configurations and enhanced permeabilities. The results indicate that the presence of a rubblized chimney decreases the separation in He-3 and SF_6 arrival time for the NPE to a span that does not match the observed data.

OBJECTIVES

Models may be used to predict the timing and amount of radionuclide gas breakthrough at the land surface following an UNE. The calculation of a statistical window of opportunity for gas sampling that includes model error (e.g., uncertainties in the subsurface material properties and structure) is of great importance for the deployment of personnel and equipment for an OSI.

The expected number of isotopic gas atoms arriving at the surface at a time t_1 after an UNE at time t_0 is:

$$N = N_0 P_F P_G \exp\{-(t_1 - t_0) \ln(2)/T_{1/2}\} P_R(t_1 - t_0) \quad (1)$$

Where N_0 is the number of atoms available for fission, depending on yield; P_F is the fraction of atoms that undergo fission; P_G is the fraction of atoms of a particular isotopic gas produced; $T_{1/2}$ is the half-life of the radionuclide of interest; and $P_R(t_1 - t_0)$ is a factor representing the fraction of surviving isotopic gas atoms that migrate to the surface and are available for detection. Gaining insights into the magnitude and form of the gas migration factor P_R, which includes diffusive and advective processes, is the primary objective of this research.

The goals of this project are: (1) to use and validate state-of-the-art numerical modeling tools to understand the relative importance of physical processes for vapor transport following an UNE (e.g., barometric pumping, topographic effects, convection); (2) to predict gas migration from the work point of an UNE to the surface for a variety of geologic materials and to understand the associated errors; (3) to develop a mathematical representation for gas migration through rock; and (4) to calibrate the models (numerical and analytical) against available gas migration data from past and future experiments.

RESEARCH ACCOMPLISHED

2-D Monte Carlo Modeling

Prior studies of gas migration in the subsurface have been performed to model radon transport (e.g., Holford et al., 1993), vapor-phase contamination at polluted sites (e.g., Stauffer et al. 2005), and other topics. For gas transport specifically related to UNEs, Nilson and Lie (1990) and Nilson et al. (1991) perform numerical studies with double-porosity models to show the ability of barometric pumping to bring gases to the surface much faster than diffusion alone. Lagus et al. (1994) report on tracer gas injection experiments at the NNSS in post-shot holes. Carrigan et al., (1996) developed a discrete fracture model that matched experimental data collected during the NPE, a 1 kt chemical explosion detonated ~390 m below ground surface in Rainier Mesa on September 22, 1993. Tracer gases (He-3 and SF_6) were emplaced near the explosion cavity and monitored sporadically at the surface for over a year. As these data provide the best opportunity for model validation with experimental data, our initial work presented here has focused on reproducing NPE data with our numerical models.

We developed a 2-D Cartesian model with a single vertical fracture intersecting a contaminated zone to test tracer gas breakthrough across a range of rock properties (matrix permeability and porosity, fracture aperture, and saturation) and initial tracer gas distribution (volume of space homogeneously filled by gases at the beginning of the simulation; Figure 1). The FEHM code, a multiphase flow and transport model developed at Los Alamos National Laboratory (LANL) (Zyvoloski et al. 1997), was used for all simulations.

To test the sensitivity of gas transport in the NPE environment to fracture and matrix properties, a suite of 2000 realizations were simulated with a fixed initial gas distribution; the parameter suite was constructed by random sampling from uniformly distributed values of rock properties. For these simulations, the domain was homogeneous matrix material intersected by a single vertical fracture, with the following properties varying between realizations: matrix porosity (ϕ_m) varied from 0.1–0.36; matrix permeability (k_m) varied from 10^{-16}–10^{-13} m^2; saturation (S) varied from 0.01–0.5; fracture aperture (δ_f) varied from 0.8–3 mm, and fracture permeability (k_f) was linked to aperture as $\delta_f^{\,2}/12$. The ranges of geologic parameters were chosen as wide bounds for these simulations based on geologic investigations at Rainier Mesa . Fracture apertures were chosen to achieve subsurface air permeabilities within the range suggested in the literature; Burkhard et al. (1989) suggests bulk pneumatic diffusivities of order 0.1–15 m^2/s for volcanic rocks at the NNSS.

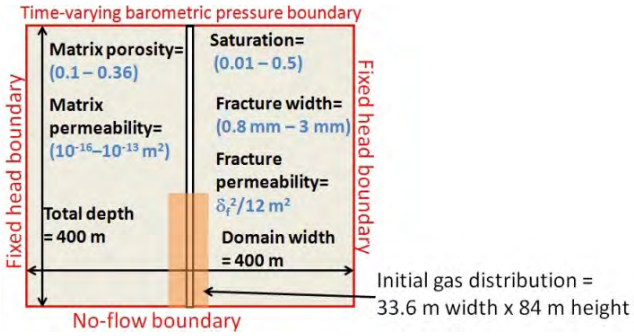


Figure 1. Schematic of 2-D Monte Carlo simulations with fixed initial gas distribution and varying rock properties.

The cavity radius, as determined by the Mueller-Murphy scaling law for tuff given by Mueller and Murphy (1971), is $r_c = (16.3)(1.927)W^{0.29}/h^{0.11}$, where a yield of W = 1.11 kt matched the seismic model of Stump et al. (1999) for the NPE and h = 389 m below ground surface (bgs). In this case, r_c = 16.8 m. A rectangular cavity was modeled in the 2-D simulations with half-width equal to the calculated cavity radius (total width = 33.6 m). The NPE tracer gases (57.3 moles He-3, 357 moles SF_6) were initially distributed in a zone of width $1r_c$ and height $5r_c$ (84 m). The models were run for 500 days with a maximum time step size of 0.1 days.

Concentrations of He-3 and SF_6 for one realization at the end of the simulation (t=500 days) are shown in Figure 2. The greater diffusion coefficient for the smaller He-3 gas results in greater spreading and lower concentrations of the tracer in the vicinity of the fracture at the center of the frame, an effect that would be present even with equal concentrations of the tracers in the initial gas area.

As with Carrigan et al. (1996), our results suggest that, for this simple isothermal model, barometric pumping by the racheting mechanism described in Nilson et al. (1991) is a convincing primary driving mechanism for moving SF_6 and He-3 tracer gases to the surface at their observed arrival times after the explosion. The observed delayed arrival of He-3 (379 days after detonation) compared to SF_6 (49 days after detonation) is then presumed to be caused by their different diffusion coefficients; He-3's higher diffusion coefficient results in more diffusion into the matrix and away from the fracture, where it is less accessible to transport to the fracture during barometric lows.

Breakthrough curves are shown in Figure 3 for 50 of the suite of 2000 simulations. During the NPE, atmospheric pressure data were collected for 83 days prior to the explosion (Carrigan et al., 1996); these data were used to initialize the simulations (t=0–83 days) prior to turning on tracer transport.

In fewer than half of the simulations (758; 38%), both He-3 and SF_6 breakthrough to the surface by t=500 days. Of these, the "best case" scenarios correspond to the 32 simulations where He-3 and SF_6 breakthrough occur during the same barometric lows as they did during sample collection at the NPE. Of the simulations where both He-3 and SF_6 breakthrough at the surface, SF_6 always arrives before He-3, but many realizations do not result in the observed spacing of nearly 11 months between He-3 and SF_6 arrival times. The most common scenario is for He-3 to arrive during earlier barometric lows than observed, whereas SF_6 typically arrives anywhere from early to on-time relative to the NPE breakthrough data (Figure 4).

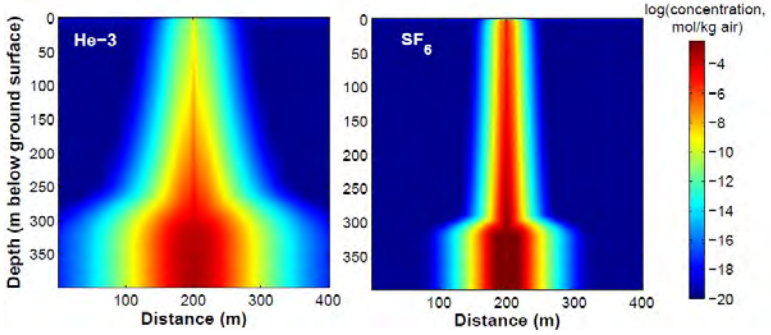


Figure 2. Tracer gas concentrations at t=500 days for one realization of the 2000 2-D Monte Carlo simulations.

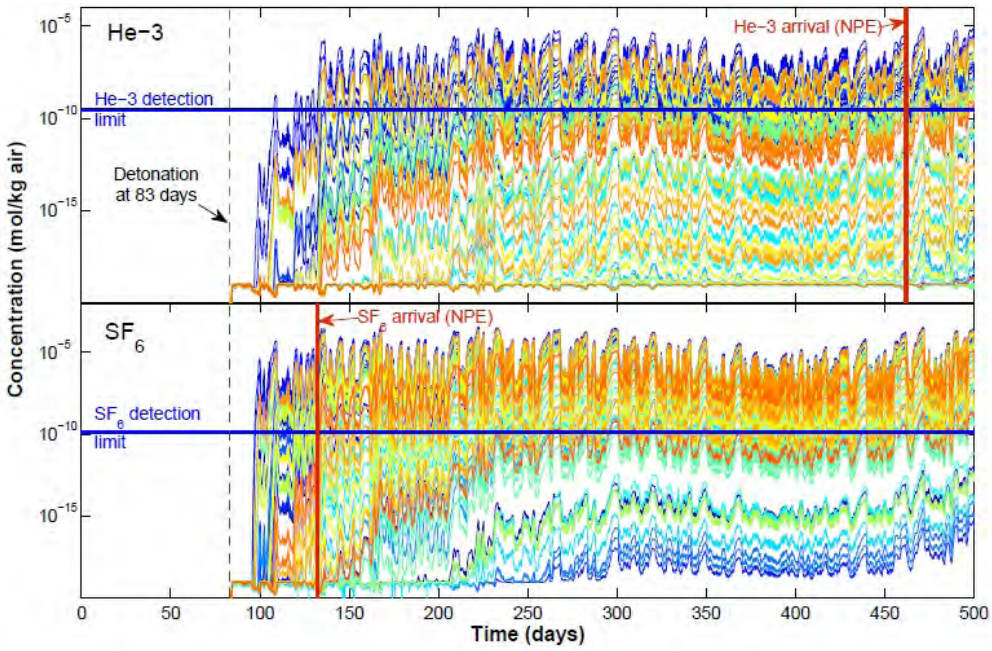


Figure 3. He-3 and SF_6 breakthrough curves for a subset of the 2000 realizations performed with fixed initial gas distribution and varying rock properties (ϕ_m, k_m, S, and δ). Arrival time of the tracer gases during the NPE is also indicated.

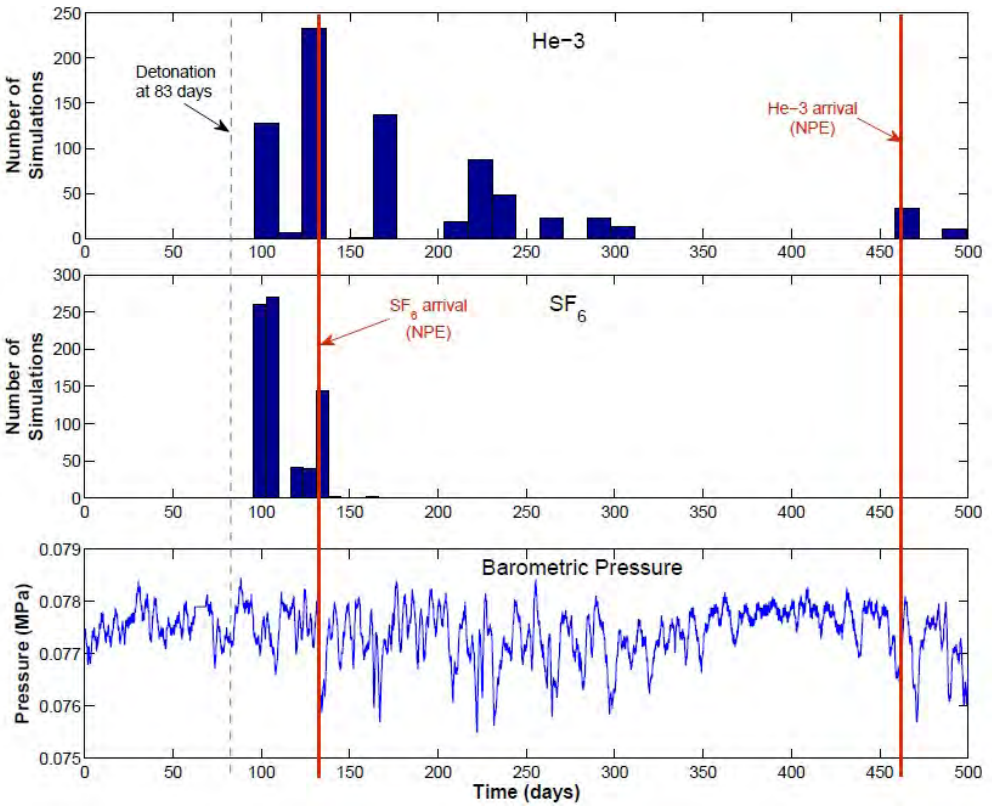


Figure 4. Histograms of arrival time for He-3 and SF_6 showing gas arrivals corresponding to low barometric pressures. Pressure data are from Carrigan et al. (1996).

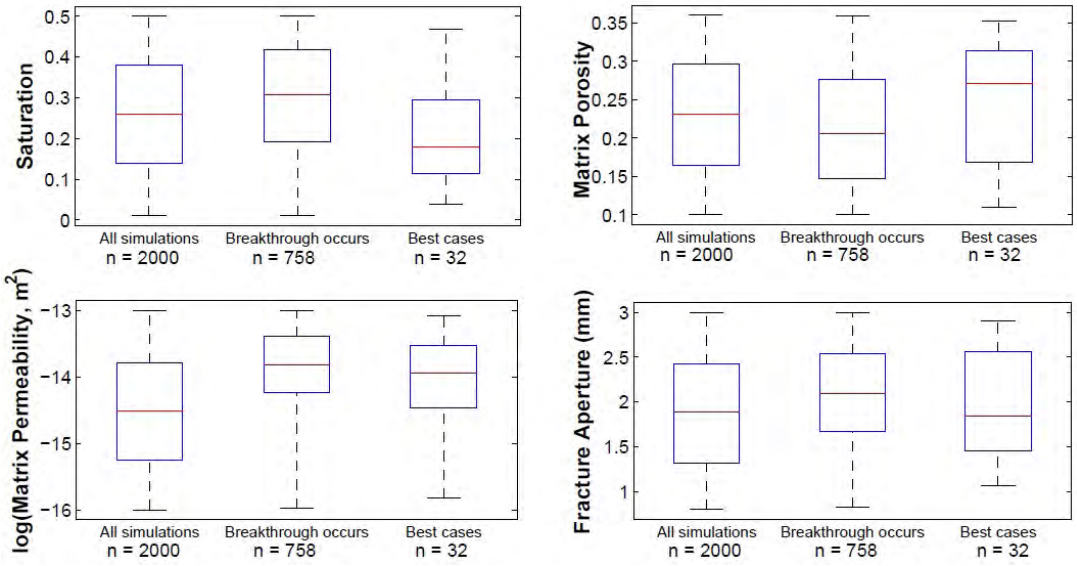


Figure 5. Boxplots of the input parameters for the complete suite of 2000 simulations, for the subset of simulations with breakthrough of both He-3 and SF_6, and for the cases where He-3 and SF_6 breakthrough match the NPE data. Boxes enclose 50% of the suite of parameter values, with the median denoted with a red line; whiskers extend to the full span of the data range.

Boxplots for each of the varied input parameters (S, ϕ_m, k_m, and δ_f) are given in Figure 5 for all simulations (n=2000); for the simulations where breakthrough occurred (n=758); and for the "best case" simulations (n=32). These results suggest that breakthrough and a good match to the data ("best cases") can occur across nearly the full span of variation chosen for the input parameters.

For the 758 cases where breakthrough occurs for both He-3 and SF_6, correlation is used as a tool to summarize the simulations and show physical dependencies between the varied input parameters, further constraining the ranges of realistic parameters (Figure 6). Although the original input data were randomly generated (uncorrelated), among the simulations where breakthrough occurs, S is negatively correlated with k_m and δ_f, and ϕ_m is directly correlated with k_m and δ_f. In both cases, this implies that for a higher gas-filled porosity $n=\phi_m(1-S)$, higher permeabilities (both matrix and fracture) are required to transport the tracer gases to the surface during the time frame of the simulation.

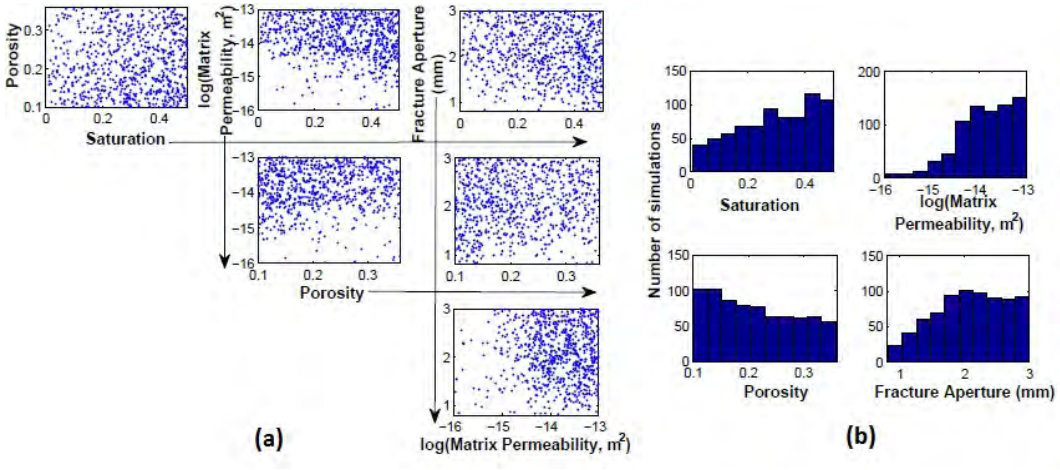


Figure 6. (a) For the subset of 758 simulations with both He-3 and SF_6 breakthrough by t=500 days, a correlation matrix plot illustrates relations between rock property parameters. (b) Histograms of input parameters for these 758 simulations, which were originally sampled from uniform distributions in the complete set (2000 simulations).

The arrival time of the tracer gas He-3 (number of days after the explosion to gas breakthrough) is negatively correlated to *S* and positively correlated to ϕ_m (i.e., higher gas-filled porosity leads to later arrival times). For SF_6, number of days to breakthrough is positively correlated to ϕ_m and uncorrelated to *S*. For both gases, breakthrough time is negatively correlated with k_m and δ_f (decreased permeabilities, both matrix and fracture, lead to increased number of days to gas arrival). The *difference* in breakthrough arrival time for He-3 and SF_6 (number of days after SF_6 arrival until He-3 breakthrough) is also negatively correlated to *S* and positively correlated to ϕ_m, and negatively correlated with k_m and δ_f. This implies that each of the input parameter changes that delays arrival time leads to increased delays for He-3 relative to SF_6 arrival. Any change that results in longer travel time for the gases leads to greater "chromatographic" separation between the two gases of different weights.

For the 32 "best case" scenarios where breakthrough occurs during the same barometric lows as the NPE data, ϕ_m is negatively correlated with δ_f (realizations with low matrix porosities require large fracture apertures to achieve the observed arrival times) (Figure 7a). Matrix porosity is weakly correlated with saturation, such that increased saturation requires increased porosity (i.e., similar air-filled porosity *n*) to achieve the observed breakthrough times.

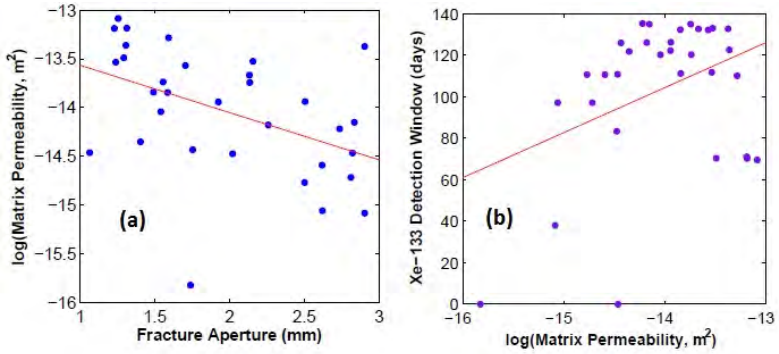


Figure 7. Correlation between k_m and δ_f (a), and window of Xe-133 detectability (b).

One of the gases of potential interest in an OSI scenario is short-lived Xe-133, with half-life 5.243 days. An estimated Xe-133 production of 7.7 x 10^{-3} moles for a 1 kt UNE (Carrigan et al., 1996) was used with the 32 NPE "best case" scenarios above to determine the detectability of Xe-133 under the same conditions as simulations that produced He-3 and SF_6 in good agreement with the NPE data. The detection limit for Xe-133 may be as low as 0.58 mBq/m^3 (~5 x 10^{-22} mol Xe/kg air) (Dresel and Waichler 2004). Although these simulations did not include a baseline of background Xe-133 concentration, any sampling program must take into consideration the statistical comparison of sample concentrations with background levels and other sources of atmospheric Xe-133.

For the simulations that best matched the NPE arrival data, most (30 of 32) resulted in a window of time where Xe-133 would be theoretically detectable. For the simulations where Xe-133 was detectable, arrival times ranged from 13 to 51 days following the explosion. The length of the window of detectability for the simulations with Xe-133 breakthrough ranged from 37 to 135 days. (Although concentrations of Xe-133 may drop below the detection limit and then rise above it, the window of detectability is assumed to end at the time when Xe-133 is no longer continuously detectable.) The length of the window is directly correlated with matrix permeability (Figure 7b).

Changing the height and width of the initial distribution of the tracer gases (with the amount of each gas kept fixed, i.e., 57.3 moles He-3, 357 moles SF_6) affects both the concentration of the gases along the fracture and the available "fresh air" pore space for the barometric racheting mechanism to cause separation between the gases of differing weights. For a given set of geologic parameters, if the gases are concentrated into too small of an initial volume, they may not reach the surface in the 500 days of simulation time. If the gases span to the top of a hypothetical chimney of height $10r_c$ (168 m), the gases may reach the surface without the observed delay in arrival time for He-3.

For 200 realizations with all initial gas distributed to a height of $2r_c$ (33.6 m), width of $2r_c$, and other parameters randomly varied across the same ranges as above for the simulations with gas to $5r_c$, only 47 (23.5%) have both SF_6 and He-3 breakthrough to the surface in 500 days of simulation time, as compared to 38% for the simulations with a

taller initial distribution of gas. However, of the simulations with breakthrough of both gases, 11% result in the observed separation of SF_6 and He-3, as compared with 4% for the taller chimney.
For another set of Monte Carlo realizations, the width and height of the initial gas distribution were randomly varied for 500 simulations, with height ranging from 2–10 times r_c (33.6 m–168 m) and width 1–3 times r_c. The rock properties were fixed, and corresponded to one of the 32 best case scenarios (ϕ_m=0.11, S=0.147, k_m=1.71 x 10^{-15} m^2, and δ_f=2.5 mm).

The minimum initial gas height resulting in breakthrough at the surface for these rock parameters was 82.55 m (Figure 8). From 82.75 m–110.55 m, 28 cases resulted in He-3 and SF_6 arrival during the barometric lows when it was observed during the NPE; however, not all realizations with initial gas distributed between these heights matched the NPE data: the width of the gas distribution, which affects the concentration of the gas, had an important impact on the breakthrough of the tracer gases. The cases with initial gas between 82.75 m–110.55 m that do not breakthrough with the observed separation of the two gases are either distributed in a larger volume (less concentrated; delayed He-3 breakthrough relative to SF_6) or narrower (sooner breakthrough of He-3 relative to SF_6).

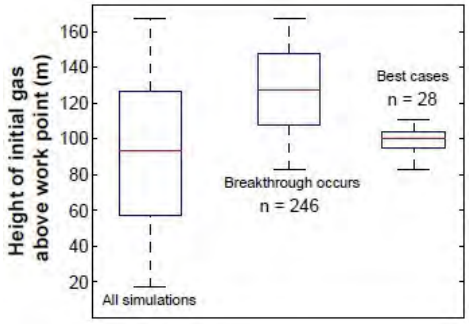


Figure 8. Boxplot showing height of initial gas for all simulations, for the subset of simulations with breakthrough of both He-3 and SF_6, and for the cases where He-3 and SF_6 breakthrough match the NPE data.

To examine the effects of a rubblized chimney on the simulated breakthrough curves, a model was produced with the native rock represented by horizontal tuff layers (Figure 9) with fixed properties resembling the primary zeolitized, vitric, and welded tuff units at Rainier Mesa . The parameters that varied were explosion-related properties such as chimney size and rubblization, with chimney permeability representing bulk fracture/matrix transport based on air permeability measurements of post-shot holes (Burkhard et al., 1989). The initial distribution of gas was the same volume as the rubblized chimney; chimney heights varied from 4–10r_c. The chimney permeability and porosity were varied from 10^{-12}–10^{-10} m^2 and 0.36–0.45, respectively, to represent the potential enhanced diffusivity to air for the rubblized chimney region. As before, the fracture apertures (and corresponding permeabilities) were allowed to vary, from 0.8–3 mm.

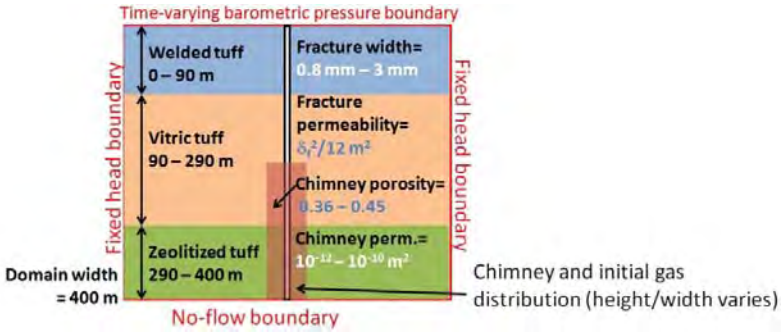


Figure 9. Layout of models performed to test the effect of a rubblized chimney zone on tracer gas transport.

The effect of the rubblized chimney is to shrink the difference in breakthrough time for He-3 and SF_6. Based on the NPE data, which suggest a far earlier arrival of SF_6, and within the limitations of these simple 2-D models, the results suggest that the fractured material that carried the tracer gases to the surface did not intersect a rubblized

zone of higher permeability and porosity than the native rock. This is in agreement with results noted from the 2-D homogeneous case above, where the spacing between SF_6 and He-3 arrival is inversely correlated with k_m; the effect of a high-permeability zone is to diminish the separation in arrival time between the two species of different mass.

Generalized dual permeability model

A discrete fracture model as implemented in 2-D can be done with a tractable number of nodes for many Monte Carlo simulations. However, transitioning to 3-D with mm-sized fractures represented by finely spaced grid nodes results in simulations that require either (a) too many nodes or (b) too large aspect ratios between dimensions, i.e., millimeter grid spacing in the *x* dimension and meter grid spacing in the *z* dimension. The 3-D problem must employ a model for fractured media that allows grid cells to be larger than the fracture itself.

FEHM had previously been used with dual porosity, dual permeability, and equivalent continuum formulations for representing the movement of fluids in fractured media (e.g., Viswanathan et al.; 1998; Robinson et al., 2005), but a new dual permeability model (GDKM) was implemented under this project. GDKM allows the user to specify particular nodes upon which a dual permeability flow regime is desired, while the rest of the domain behaves as single or equivalent continuum material. In GDKM flow behavior is accounted for between matrix-fracture, fracture-fracture, and matrix-matrix.

The input parameters to GDKM are (a) the volume fraction of a cell that is composed of fracture material (f_f) and (b) the length scale between the centerline of the fracture and the center of the matrix material (d_{fm}). Between the fracture and matrix material, the fluid transfer term (gas or liquid) is:

$$q_{fm} = -\left(\frac{k_{fm}\rho R}{\mu}\right)\left(\frac{A_{fm}}{d_{fm}}\right)(P_f - P_m) \quad (2)$$

Where k_{fm} is the permeability between the two differing media (calculated as the harmonic mean of the fracture and matrix permeabilities); ρ and μ are fluid density and viscosity, respectively; R is a relative permeability term calculated based on many available options in FEHM for multiphase flow; A_{fm} is the area separating the fracture and matrix; and P_f and P_m are pressures in the fracture and matrix, respectively. Between like material (matrix-matrix and fracture-fracture), flow and transport are computed normally (Zyvoloski et al., 1997) but modified by a decreased connected area that reflects the fraction of cell volume taken up by the other material.

GDKM has been tested with validation problems in heat and water flow. Additionally, a gas flow problem was developed to test the propagation of a barometric pressure signal at the ground surface through the fractured material to depths of the work point of the NPE. A sinusoidally varying barometric pressure boundary condition with a period of 7 days and amplitude Δp=0.001 MPa was used for the test problem, with a fracture aperture δ_f=1.54 mm, average pressure p_0=0.0774 MPa, matrix air-filled porosity n=0.20 and permeability k_m= 9.1 x 10^{-15} m^2, and large (200 m) fracture spacing to represent a single vertical fracture. The permeability of the fracture is $k_f = \delta_f^{\,2}/12$ and its air-filled porosity is n_f=1.

The test problem was compared to the 2-D analytical solution derived in Nilson et al. (1991) as well as a discrete fracture case using FEHM, as in the 2-D modeling described above. This is done by specifying nodes of high permeability and porosity of 1 (fracture) with a finely-spaced grid in the fracture region such that the widths of the control volumes for fracture nodes is the same as the fracture aperture corresponding to the given permeability.

Plots of pressure versus time for the test problem showing the analytical solution and FEHM solutions for the discrete fracture case and the new GDKM are given in Figure 10a. At depth, the pressure attenuates and lags the surface signal, with pressures at the bottom of the fracture matching the analytical solution well after a short initial period (~3 days). Pressure with depth in the numerical model is compared to the analytical solution in Figure 10b.

3-D Monte Carlo Modeling

For the 3-D simulations, a grid with 108,900 nodes was used, with a planar fracture spanning the domain and no-flow boundaries along the edges of the fracture at the ends of the domain (400 m width). The initial distribution of

tracer gas was in a column of length and width $2r_c$ (33.6 m) and the chimney height was fixed at $5r_c$ (84 m). The rock property parameters for the 32 "best case" realizations were used.

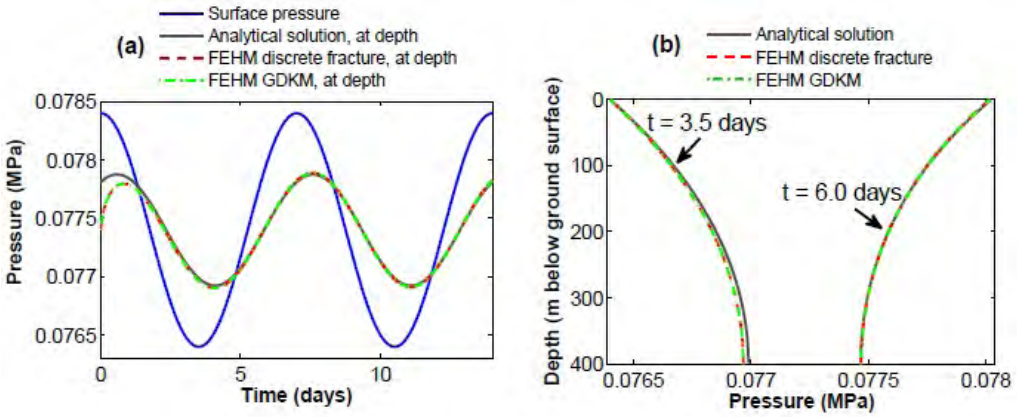


Figure 10. Comparison of the analytical solution of Nilson et al. (1991) with FEHM solutions.

Tracer gas breakthrough generally (though not always) occurred earlier in the 3-D simulation than in its corresponding 2-D simulation. Reasons for this effect could include true differences in the 2-D and 3-D numerical framework (e.g., 2-D simulation assumes infinite planar fracture in the 3rd dimension where 3-D simulation has finite regions), or artificial numerical dispersion from the larger node spacing in the z-dimension for the 3-D model. Additional modeling will be performed to analyze the differences and validate the 3-D model.

CONCLUSIONS AND RECOMMENDATIONS

The research accomplished to date has advanced our understanding of the primary processes and relative importance of unknown parameters in the problem of gas migration to the surface for analysis during an OSI. The numerical models have been tested against the available gas migration data from the NPE, and the models provide excellent agreement with the tracer gas breakthrough data and corroborate prior work on the efficacy of barometric pumping (Nilson et al., 1991; Carrigan et al., 1996).

Sensitivity studies suggest the relative influence of rock parameters in determining the gas migration factor P_R (Equation 1) for radionuclide transport following an UNE. The arrival time of He-3 and SF_6 tracer gases in the Monte Carlo simulations is directly related to gas-filled porosity and inversely related to matrix permeability and fracture aperture. The difference in arrival time, a key piece of information from the NPE data, is heightened by any factor that increases the travel time, including the length of "fresh air" space above the initial contaminated zone and the concentration of the gases around the fracture. The window of detectability for Xe-133 was estimated for a subset of the simulations that provided a good match to the NPE data and showed a wide variability in the length of time that the gas would be consistently detectable (either undetectable or detectable for a span of 37–135 days).

The new GDKM allows the implementation of varying fracture configurations upon a pre-existing grid without requiring large numbers of nodes in 3-D grids. This is a major advantage over discrete fracture formulations and an advancement on previous fracture flow models in FEHM. Initial 3-D results show important differences to the 2-D models and will provide greater confidence in the ability of the model to be of use in predicting hypothetical UNEs.

The next steps for the numerical modeling effort are to improve the model by adding heat; to test the importance of other potential drivers of gas migration, such as seasonal topographic flow; and to perform Monte Carlo modeling on different fracture distributions in 3-D by changing the grid and GDKM parameters. The polished model will be used to predict radionuclide gas (e.g., isotopic xenon) breakthrough for UNEs for different classes of fracture configuration, rock type, and initial gas distribution. In parallel, the project team is constructing an analytical error budget model as suggested by the stochastic numerical modeling efforts. Both the numerical and analytical modeling components of this project are essential and cooperative in the analysis of radioactive gas migration through rock from an UNE.

ACKNOWLEDGEMENTS

The authors would like to thank Edward Kwicklis and Daniel Levitt of LANL for information about Rainier Mesa geology; Yunwei Sun of LLNL for providing the barometric pressure data from the NPE of Carrigan et al. (1996); Carl Gable and Terry Miller of LANL for help with the LaGriT software; and Chris Bradley of LANL for conversations and references related to fracturing caused by UNEs.

REFERENCES

Burkhard, N.R., Hearst, J.R., Peterson, E.W., Nilson, R.H., and K.H. Lie (1989). Containment of cavity gas in fractured or rubblized emplacement media, LLNL Report UCRL-100953, CONF-8909163-4.

Carrigan, C. R., R.A. Heinle, G.B. Hudson, J.J. Nitao, and J.J. Zucca (1996). Trace gas emissions on geological faults as indicators of underground nuclear testing, *Nature* **382**, (6591), 528–531.

Dresel, P.E., and S.R. Waichler (2004). Evaluation of xenon gas detection as a means for identifying buried transuranic waste at the Radioactive Waste Management Complex, Idaho National Environmental and Engineering Laboratory, PNNL-14617.

Holford, D. J., S.D. Schery, J.L. Wilson, and F.M. Phillips (1993). Modeling radon transport in dry, cracked soil, *J. Geophys. Res.* **98**, 567–580.

Lagus, P.L., W.B. McKinnis, J.R. Hearst, N.R. Burkhard, and C.F. Smith (1994). Field measurements of tracer gas transport by barometric pumping, Prepared by S-Cubed, UCRL-CR-119147.

Mueller, R.A. and J.R. Murphy (1971). Seismic characteristics of underground nuclear detonations, *Bull. Seismol. Soc. Am.* **61**, 1675–1692.

Nilson, R.H. and K.H. Lie (1990). Double-porosity modelling of oscillatory gas motion and contaminant transport in a fractured porous medium, *Int. J. Numer. Anal. Meth.* **14** (8), 565–585.

Nilson, R.H., E.W. Peterson, K.H. Lie, N.R. Burkhard, and J.R. Hearst (1991). Atmospheric pumping: A mechanism causing vertical transport of contaminated gases through fractured permeable media, *J. Geophys. Res.* **96** (B13), 21933–21948.

Robinson, B.A., S.G. McLin, and H.S. Viswanathan (2005). Hydrologic behavior of unsaturated, fractured tuff, *Vadose Zone J.* **4** (3), 694–707.

Stauffer, P.H., K.H. Birdsell, M.S. Witkowski, and J.K. Hopkins (2005). Vadose zone transport of 1,1,1-trichloroethane: Conceptual model validation through numerical simulation, *Vadose Zone J.* **4** (3), 760–773.

Stump, B.W., D.C. Pearson, and R.E. Reinke (1999). Source comparisons between nuclear and chemical explosions detonated at Rainier Mesa, Nevada Test Site, *Bull. Seismol. Soc. Am.* **89**, 409–422.

Viswanathan, H.S., B.A. Robinson, A.J. Valocchi, and I.R. Triay (1998). A reactive transport model of neptunium migration from the potential repository at Yucca Mountain, *J. Hydrol* **209**, 251–280.

Zyvoloski, G.A., B.A. Robinson, Z.V. Dash, and L.L. Trease (1997). Summary of models and methods for the FEHM application–A finite element heat- and mass-transfer code, LANL Report LA-13307-MS.

A GERMANIUM ARRAY FOR SAMPLE MEASUREMENTS: RECENT RESULTS AND NEW ANALYSIS METHODS

Martin E. Keillor, Craig E. Aalseth, Anthony R. Day, Luke E. Erikson, Brian D. Glasgow, Eric W. Hoppe, Todd W. Hossbach, Leila K. Mizouni, Jason H. Merriman, Allan W. Myers, Cory T. Overman, Nicole R. Overman, Allen Seifert, and Timothy J. Stavenger

Pacific Northwest National Laboratory

Sponsored by the National Nuclear Security Administration

Award No. DE-AC05-RL01830/PL10-CASCADES-NDD05

ABSTRACT

The Pacific Northwest National Laboratory is finalizing construction of a 14-crystal intrinsic germanium (HPGe) array designed for high detection efficiency, ultra-low-background performance, and sensitive γ-γ coincidence detection. Initial development of a custom software suite capable of automating many of the tasks required to accurately analyze coincident signals within close-geometry detector arrays will also be completed this year. The analysis capability is required to enable rapid interpretation of data collected with the low-background HPGe array. The status of final construction of the second cryostat and the complete system will be discussed, as well as measurement results from independent operation of the first cryostat. Status of the CASCADES analysis development, including cross-talk correction and new techniques for efficiency calibration, are also presented.

OBJECTIVES

A current research effort at Pacific Northwest National Laboratory (PNNL) is focused on developing automated analysis routines to enable rapid, accurate determination of radioisotope activities (and minimum detectable activities) for samples measured in a new 14-crystal low-background germanium array. The first seven crystal array has operated since the summer of 2011, housed in a new shallow underground laboratory facility (Aalseth et al, 2012). All parts and sub-assemblies for the second 7-crystal cryostat are complete, with assembly of the full array planned for the summer of 2012. The design and performance expectations for the instrument have been discussed previously (Keillor et al., 2009). The instrument is designed to take advantage of low background performance, high detection efficiency, and γ–γ coincidence signatures to provide unprecedented gamma spectroscopy sensitivity. This effort is focused on improving gamma analysis capabilities for nuclear detonation detection applications, e.g., nuclear treaty monitoring. The instrument also has the potential to contribute to basic nuclear physics research. For example, the potential for this detector to measure the half-life of predicted rare decay modes of ^{130}Te is being investigated (Mizouni et al., 2011).

RESEARCH ACCOMPLISHED

Cryostat and HPGe Array Assembly

The HPGe array currently operating in the new underground laboratory is described in more detail elsewhere (Keillor, et al., 2011), however is summarized here. The array consists of a single upward-looking cryostat housing seven p-type crystals, each nominally 63 mm diameter by 70 mm height. A matching downward-looking cryostat is in the final stages of construction, and will be installed opposite the first during the Summer of 2012. The cryostats are constructed from pure copper parts (< 1 Bq/kg) electroformed and machined into final form at PNNL. Additional materials are limited to those known to be low in radiological contaminants, or used in sufficiently small quantities to restrict impact on the system background. These include insulator parts from pCTFE and Delrin, small Teflon screws, wiring selected for low background performance, a small quantity of stainless steel wire to form the center contact, and front-end electronics designed with a minimal mass of electronic components.

After brief initial data acquisition, the system was moved from a surface-level laboratory to the new shallow underground facility in the summer and fall of 2010. During the move, the shield design was modified to reduce much of the lead thickness from ~41 cm (16 in.) to ~25 cm (10 in.). Passive shielding consists of the lead, a layer of cadmium foil external to the lead, and ~20 cm (8 in.) of borated polyethylene (a mixture of 5% and 30% sheets that were available). An enclosure surrounds the passive shield for radon exclusion, but this portion of the system is not yet installed around the shield door. Finally, ~5 cm (2 in.) thick BC-408 plastic scintillator paddles surround the passive shield. The shield system, with shield door open and the first cryostat installed, is shown in Figure 1.

Progress on the 2nd cryostat was delayed when thermal testing of a custom commercial dipstick demonstrated that it does not provide sufficient cooling to maintain the crystals at an appropriate operating temperature. With no additional thermal load applied, the dipstick alone stabilizes at 83 K. This is roughly the same temperature that we log at the dewar connection with the full thermal load of the lower cryostat. When an 8.1 W thermal load was applied to the dipstick with a Zener Diode, the temperature stabilized at 135 K. These results indicated that the dipstick would not maintain the HPGe crystals at a sufficiently cold temperature for operation. Efforts to tighten the 90 degree joint between the vertical and horizontal arms of the dipstick did not improve performance. The dipstick design incorporated a 2.54 cm diameter copper rod for the horizontal run, however utilized the manufacturer's standard ¾ in. diameter copper for the vertical section of the cold path. Recent thermal analysis indicates that this ¾ in. diameter run of copper is the limiting factor; unfortunately this deficiency was not noted during the initial design. A new dipstick has been designed and fabricated in-house at PNNL; thermal testing of this assembly is currently underway.

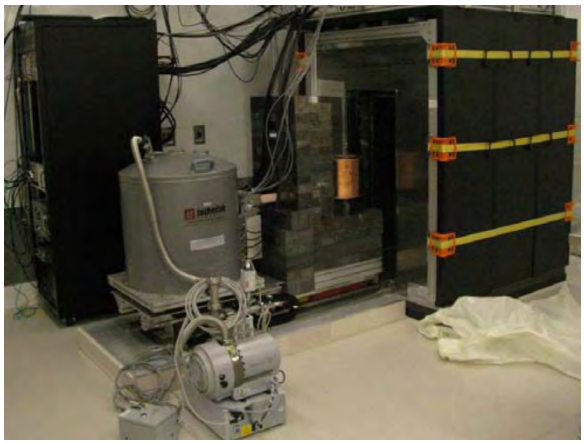


Figure 1. First 7-crystal array installed in the new shallow underground laboratory at PNNL.

System Performance

The current background rate is ~5875 gamma/day/crystal in the range of 40-2700 keV. The background is dominated by the presence of a significant low-energy continuum that we attribute to bremsstrahlung from the high-energy beta decay of ^{210}Bi, the daughter of ^{210}Pb decaying in the lead of the shield (see Figure 2). The shield was designed to accommodate a liner inside of the lead; a 3.8 cm (1.5 in.) thick oxygen free high conductivity (OFHC) copper liner has been built to reduce this bremsstrahlung component of the background – it will be installed during the Summer of 2012. Energy lines associated with radon daughters are also currently prominent in the background; we anticipate full removal of the radon-associated lines after completion of the radon exclusion system. The 511 keV annihilation peak could be reduced slightly by optimization of the anti-cosmic coincidence window. Peaks and features (e.g., "shark fins") associated with neutron interaction in the germanium are observed generally at much lower rates, as are peaks associated with ^{60}Co (~6 counts per day (cpd) in each primary peak) and ^{40}K (~4 cpd in the histogram summed data from all 7 crystals).

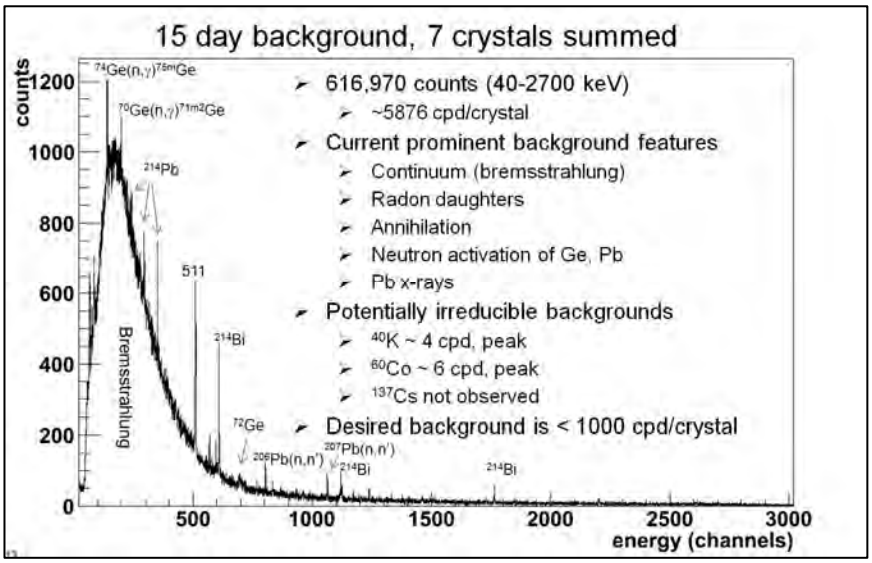


Figure 2. Background features observed in the 7-crystal array.

The first cryostat is consistently performing with excellent energy resolution. This is evidenced by the plot of energy resolution vs. energy provided in Figure 3. Energy resolution of 2.13 keV at 1332 keV has been routinely observed for spectra summed to include all seven crystals. Similar resolution is observed for "add-back" spectra, those spectra that are created by summing energy deposition in the array on an event-by-event basis. The energy resolution of

spectra combining data from the full array shows slight degradation relative to the best performing crystals, being driven by those crystals with poorer energy resolution. Two of the seven crystals in the cryostat are currently run at lower than their preferred bias due to level of leakage current, however they are providing good energy resolution despite the low bias.

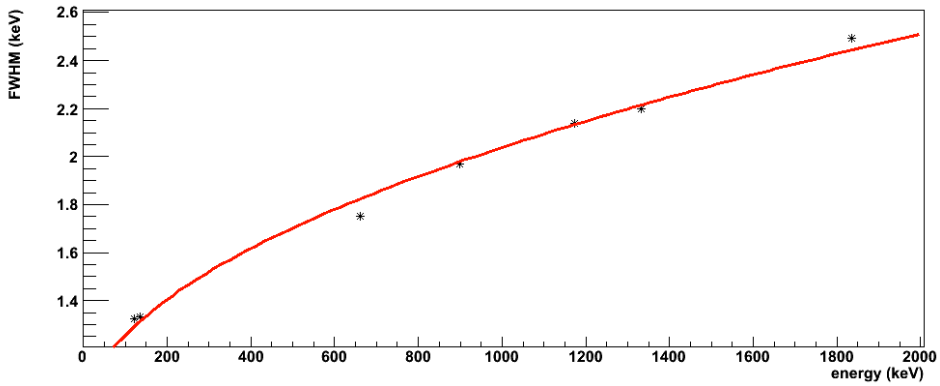


Figure 3. Energy resolution for spectra combining data from all seven crystals by summing the individual histograms. "Add-back," or event-by-event summing reconstruction produces similar energy resolution performance.

A number of observations led to the conclusion that the energy determination for pulses is degraded in the case of coincident events in two or more crystals. In 1-D energy spectra, strong peaks exhibited weak false peaks on the low energy shoulder, or even fully resolved peaks to the low energy side of the main peak. In singles spectra, these false peaks represent a small fraction of the main peak. In the case of spectra constructed from anti-coincident data (only one crystal hit), these false peaks are not observed. The impact is much more pronounced in coincidence data, which are no longer dominated by single crystal events. In coincidence spectra, the Compton ridges display a negative slope, "shadow" or split ridges, and the full energy coincidence peaks are broadened or even observed as doublets or multiplets. Figure 4 shows all of these indicators of crosstalk.

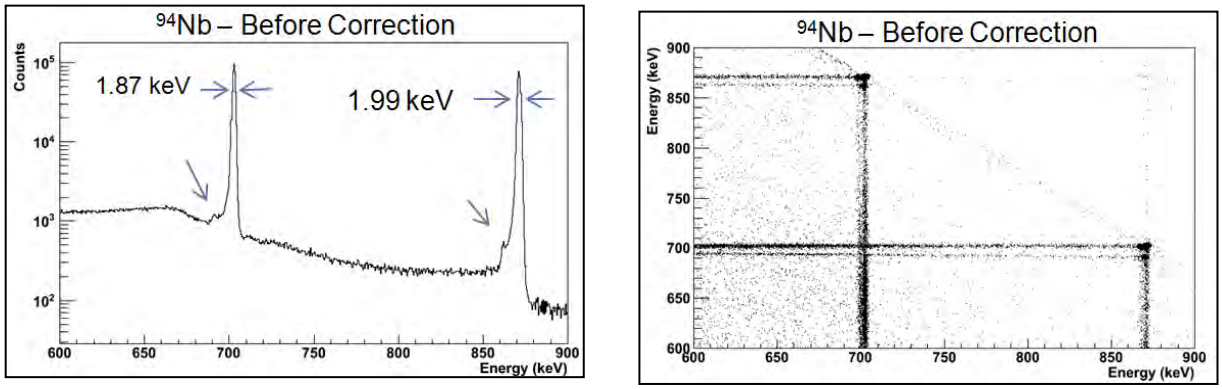


Figure 4. "Singles" and coincidence spectra of ^{94}Nb displaying various indicators of cross talk between channels, including false peaks, split Compton ridges, and peaks split into multiplets in the coincidence plane.

Initial investigation isolated the source of the crosstalk to the cryostat / preamplifier assembly, however significantly more detailed work is required to determine the specific cause. A number of locations where there are short runs of unshielded cable along the signal path are likely candidates, and one of these locations seems likely to be the source of crosstalk. Another possible source is within the preamplifiers; it should be straight-forward to rule out

(or confirm) the preamplifiers as the source of crosstalk. This work has not been completed because we prefer not to dismount the preamplifiers at a time when we have all seven channels operating and performing well.

To first order, the energy reduction observed in one crystal is a linear function of the energy deposited in coincidence in another crystal, and is independent of the energy deposited in the crystal under consideration. Table 1 presents the value of the slope of the Compton ridge determined for crystal pairs in the 7-crystal cryostat; pairs with no appreciable crosstalk are absent from the table. As seen in the table, the slope values are specific to crystal pairs and are not symmetric between the crystals. For example, a recorded energy of 861.5 keV in crystal 1, coincident with a 702.0 keV gamma in crystal 3, is increased by $702.9 \times 1.34542 \times 10^{-2} = 9.44$ keV to produce 870.94 keV. In this example case, the correction to the energy in crystal 3 is an order of magnitude smaller: $861.5 \text{ keV} \times 1.15877 \times 10^{-3} = 1.0$ keV, to produce 703.0 keV in the corrected spectrum. The cross-talk correction is applied to data in native ADC units (rather than energy units used in the example above) during a data preprocessing stage that includes application of anti-Cosmic cuts, determination of coincidence hit patterns, and conversion of the data from the XIA data format (XIA, 2009) into Root data trees (Brun and Rademakers, 1997). Application of this correction produces a slight improvement in energy resolution for the singles spectra, as well as eliminating the false peaks observed on the low energy shoulder of large peaks. The correction makes a very significant improvement in the coincidence plane, removing shadow ridges and collapsing doublet or multiplet peaks back into the expected single peaks (see Figure 5).

Table 1. Slope of Compton ridge in coincidence spectra. The slope is used to correct the observed energy for the crystal in the first column of the table, when observed in coincidence with the crystal in the second column.

Crystal #		Correction (keV/keV)
1	3	1.34542E-02
1	4	8.68312E-04
1	5	1.46387E-03
1	7	1.50914E-03
2	3	6.43439E-04
3	1	1.15877E-03
3	2	1.10909E-03
4	1	4.72709E-03
4	5	1.86198E-03
5	4	1.42031E-03
5	7	2.64189E-04
6	7	1.11181E-03

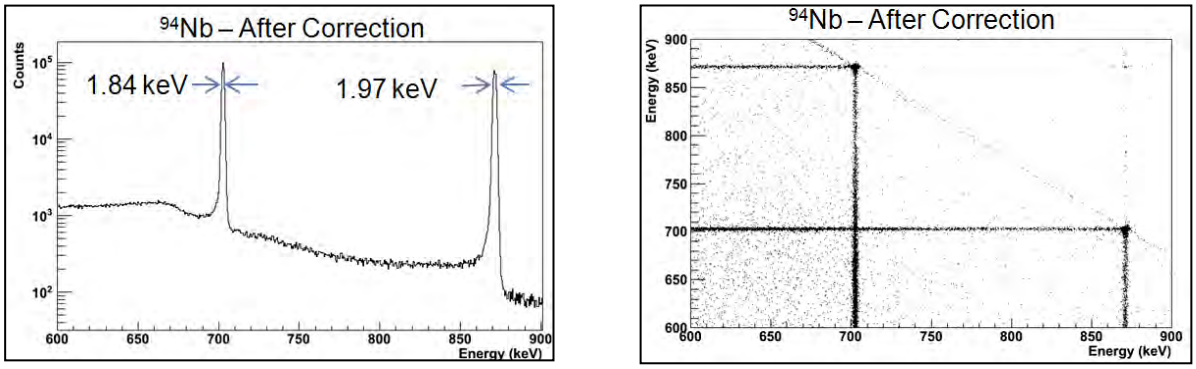


Figure 5. "Singles" and coincidence spectra of ^{94}Nb displaying significantly improved performance after application of the crosstalk correction.

Sample Measurements

To date, a variety of interesting standards and samples have been measured with the array, including standards for the calibrations efforts discussed below, Fukushima-related sea life samples, mixed fission product samples, neutron activation samples, and material samples for assay to determine suitability for use in detector systems for rare event search physics experiments. Results for these sample measurements will be reported elsewhere, as appropriate to the measurement. However, as an example of the current measurement sensitivity, a recent assay of ultra-high-molecular-weight polyethylene indicates that a 7-day measurement provides minimum detectable activities of ~2 mBq for ^{60}Co and ^{137}Cs. We anticipate significant improvement in this capability with the addition of the second cryostat, and further background reduction.

New Analysis Capabilities

The CASCADES detector array uses a new software analysis package developed by PNNL as part of the project's efforts. This system, known as *melusine*, is intended to provide off-line data handling and analysis tools needed for multiple crystal arrays that are not handled by commercial analysis software. While the analysis system directly addresses calculations used in the CASCADES project, it is designed to be easily adapted to the analysis of data generated by other measurement systems that include complicated coincidence detection schemes. While there remains room for significant further development, *melusine* is currently used for most off-line analysis being done on this research project. This includes construction of a wide variety of histograms (with and without cuts on the data), energy and efficiency calibrations, peak search, peak fitting, isotope identification, and activity and decay calculations. Additional features are under development to meet present and future needs, including error propagation, minimum detectable activities (MDAs), and coincidence analysis tools. Details of the software architecture and data flow were presented at the 2011 Monitoring Research Review (Keillor, et al., 2011).

A rather straight forward library-based isotope identification algorithm is now implemented in *melusine*. The code examines a user defined library of isotopes, and identifies isotopes that may be associated with an observed line based on a user-specified centroid energy criterion. Isotope library creation is straight-forward, and is based on nuclear data files written by the Coincidence Lookup Library (Warren et al., 2006). This step provides *melusine* with the nuclear data required for isotope identification, as well as data to complete activity calculations for both singles and coincidence signatures, and half-life data for decay calculations.

Generating reliable detection efficiency calibrations is one of the key challenges to producing accurate activity results with this detector array. The high detection efficiency and close geometry make it impossible to neglect true coincidence summing (TCS) corrections. To address this issue, we are working to create an efficient measurement based technique that produces both peak and total efficiency curves as a function of energy. The goal is to utilize a mixed-isotope standard suitable for the calibration of complex detector arrays using a single measurement. While the initial results presented (Erikson et al., 2012) show potential, additional improvements are required for this approach to produce sufficient accuracy and ease of use. We continue to explore alternative efficiency calibration approaches. For example, the current technique is an absolute method that eliminates dependence on certified standards. However, since well calibrated standards are generally available, a future approach may use the dual-emitter technique to produce only the peak-to-total ratios, while the peak detection efficiencies would be determined using the certificate activity values for the same source. This would still yield a single measurement calibration. Another approach with potential value is use of the peak-to-total ratio based on dual-emitter standards to better inform a Monte Carlo simulation of detection efficiencies.

Doublet and multiplet peak fitting algorithms were developed in the *melusine* code. Logic is included to recognize peaks that are overly broad, and spit those peaks into doublets (Figure 6). The code is also capable of automated multiplet fitting, and interactive peak fitting capabilities allow the user to easily add or remove peaks from the peak search results (Figure 7). At the current time, fits are accomplished with built in ROOT fitting capabilities using Gaussian peaks and a linear background. Tailing functions, stepped backgrounds, and other common enhancements to the functional form would be straight forward to implement into the system, although are not currently available. Recent work incorporated an adaptive region-of-interest algorithm that brought a significant improvement to the background continuum fits on either side of peaks.

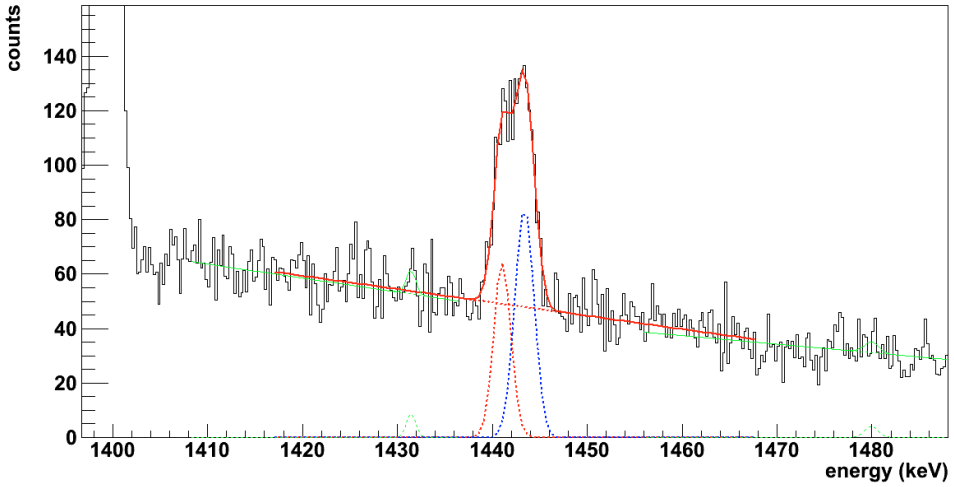


Figure 6. Parameters set by the user restrict the acceptable peak width based on the shape calibration, forcing the system to split this unresolved peak into a doublet. In this case, the sum peak from the 667.73 and 772.68 keV lines of ^{132}I at 1440.41 keV, and the 1442.5 keV line of ^{132}I. The small peaks near 1432 and 1480 keV were identified by the peak search algorithm; however, both were reported as invalid peaks because they did not meet user specified criteria.

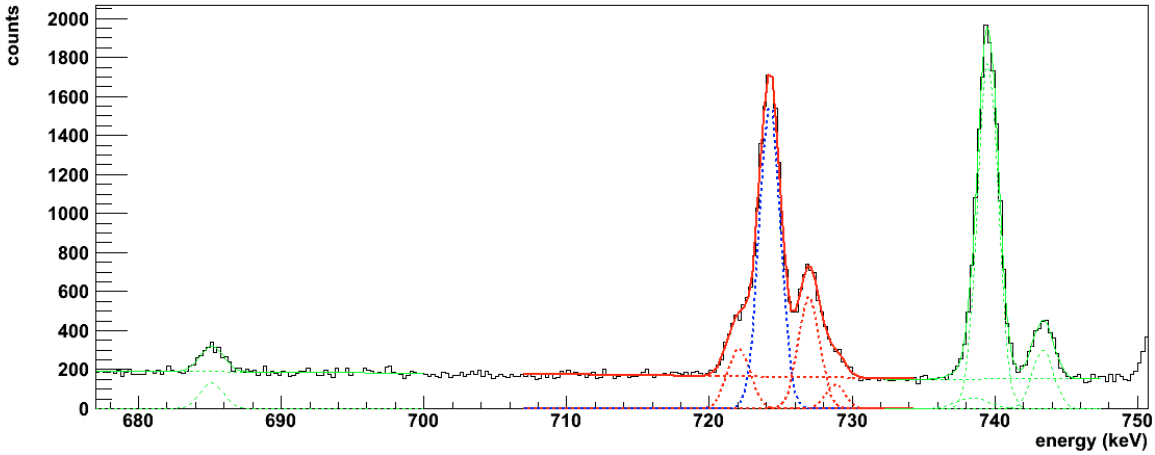


Figure 7. Automated multiplet fitting implemented in the *melusine* code. The multiplet in this figure includes ^{143}Ce, ^{95}Zr, and multiple ^{132}I peaks. In this case, the 721.96 keV peak of ^{143}Ce was not originally identified in the peak search (due to the selected sensitivity parameters). The peak was added to the multiplet fit with a single mouse click. This figure also demonstrates the adaptive fitting ROI implemented in the code, which adjusts the ROI on either side of the peak to avoid poor background continuum fits caused by neighboring peaks. The user interface also highlights the peak sets immediately above and below the peak(s) under consideration, if they are within the displayed energy range (green traces)

Additional capabilities to reduce manual processing steps are especially critical for coincidence analysis involving multiple detectors. Calculations in the coincidence plane require numerous regions of interest for each energy studied and the computer is better suited to the repetitive and calculation-intense tasks involved. The issue is not simply one of identifying peaks but also in calculating the optimal analysis technique to be used. Detailed uncertainty propagation must be carefully developed to allow selection of the most sensitive analysis routine for a given isotope, and to allow calculation of weighted averages from multiple methods where appropriate. While *melusine* is very useful today, many additional labor saving features are currently in the planning or early development stages.

CONCLUSIONS AND RECOMMENDATIONS

A seven-HPGe crystal array has been operated in the new shallow underground laboratory at PNNL over the past year. The array is operating with excellent energy resolution, and nice low background performance. Additional improvements in background are anticipated in the near future and will be realized with completion of the radon suppression system, active anti-cosmic shield, and addition of a copper lining inside the passive shield. Construction of parts and subassemblies for a second array is complete, and assembly of the full system is anticipated in the summer of 2012.

Significant progress has been made on the *melusine* gamma spectroscopy and coincidence analysis system. Capabilities added over the past year include isotope identification, peak fitting, automated doublet and muliplet fitting, adaptive ROIs to improve fits to the background continuum, activity calculation, and decay calculations. Additional features currently in progress include error propogation, MDA calculations, and activity calculations utilizing coincidence signatures. Significant effort was also placed on developing new methods to streamline efficiency calibration of the array. The long-term vision is that the system will be capable of performing multiple parallel analyses to establish the most sensitive data reconstruction for a measurement on an isotope-by-isotope basis.

REFERENCES

Aalseth, C.E., R.M. Bonicalzi, M.G. Cantaloub, A.R. Day, L.E. Erikson, J.B. Forrester, B.D. Glasgow, L.R. Greenwood, E.W. Hoppe, T.W. Hossbach, B.J. Hyronimus, M.E. Keillor, E.K. Mace, J.I. McIntyre, J.H. Merriman, A.W. Myers, C.T. Overman, N. R. Overman, M.E. Panisko, R.C. Runkle, H.A. Seifert, and G.A. Warren (2012). A shallow underground laboratory for low-background radiation measurements and materials development, submitted to *Rev. Sci. Instrum*.

Brun, R. and Rademakers, F. (1997). ROOT – An object oriented data analysis framework, in Proceedings AIHENP-96 Workshop, Lausanne, Sep. 1996, *Nucl. Inst. Meth. Phys. Res*. A **389**, 81–86. See also http://root.cern.ch/

Erikson, L.E., M.E. Keillor, C.E. Aalseth, T.W. Hossbach, L.K. Mizouni, T.J. Stavenger, B.S. McDonald, E. Lepel, L.R. Greenwood, and C. Rutherford (2012). Determining HPGe total detetion efficiency using γ-γ coincidence, submitted to *J. Radioanal. Nuc. Chem*.

Keillor, M.E., C. E. Aalseth, A. R. Day, J. E. Fast, E. W. Hoppe, T. W. Hossbach, B. J. Hyronimus, H. S. Miley and A. Seifert (2009). Design and construction of an ultra-low-background 14-crystal germanium array for high-efficiency and coincidence measurements, *J. Radioanal. Nucl. Chem*. **282** (3), 703–708 (2009).

Keillor, M.E., et al. (2011), in *Proceedings of the 11th International Conference on the Applications of Nuclear Techniques*, AIP Conference Proceedings, **1412**, 208–215.

Mizouni, L. K. , C. E. Aalseth, F. T. Avignone III, L. E. Erikson, T. W. Hossbach, and M. E. Keillor (2011). Search for 2νββ-decay of ^{130}Te to the first excited state of ^{130}Xe with an ultra-low-background germanium crystal array, in *Proceedings of the 11th International Conference on the Applications of Nuclear Techniques*, American Institute of Physics, Melville, NY, (in press).

Warren, G.A., L.E. Smith, C.E. Aalseth, J.E. Ellis, A.B. Valsan, and W. Mengesha (2006). *Trans Nucl Sci* **53,** 351–355.

XIA Digital Gamma Finder (DGF) Pixie-4 User's Manual, (2009), http://www.xia.com/Manuals/Pixie4_UserManual.pdf

A ROBUST ABSOLUTE DETECTION EFFICIENCY CALIBRATION METHOD UTILIZING BETA/GAMMA COINCIDENCE SIGNATURES AND ISOTOPICALLY PURIFIED NEUTRON ACTIVATED RADIOXENON ISOTOPES

Justin I McIntyre, Matthew W. Cooper, James H. Ely, Derek A. Haas, and Brian T. Schrom

Pacific Northwest National Laboratory

Sponsored by the National Nuclear Security Administration

Award No. DE-AC05-RLO1830/PL10-ASAR-NDD05

ABSTRACT

Efforts to calibrate the absolute efficiency of gas cell radiations detectors have utilized a number of methodologies which allow adequate calibration but are time consuming and prone to a host of difficult-to-determine uncertainties. A method that extrapolates the total source strength from the measured beta and gamma gated beta coincidence signal was developed in the 1960's and 1970's. It has become clear that it is possible to achieve more consistent results across a range of isotopes and a range of activities using this method. Even more compelling is the ease with which this process can be used on routine samples to determine the total activity present in the detector. Additionally, recent advances in the generation of isotopically pure radioxenon samples of Xe-131m, Xe-133, and Xe-135 have allowed these measurement techniques to achieve much better results than would have been possible before when using mixed isotopic radioxenon source. This paper will discuss the beta/gamma absolute detection efficiency technique that utilizes several of the beta-gamma decay signatures to more precisely determine the beta and gamma efficiencies. It will than compare these results with other methods using pure sources of Xe-133, Xe-131m, and Xe-135 and a Xe-133/Xe-133m mix.

OBJECTIVES

Efforts to calibrate radiation detectors remains one of the most challenging tasks for manufacturers and operators and is frequently the most significant source of systematic error reported in activity concentration measurements. Calibration methods typically rely on using carefully produced calibration standards and in-depth geometry modeling, both of which are time consuming and, in the case of modeling, use idealized versions of detectors that may differ significantly from the actual detector being calibrated (Keillor, 2009). Other methods to measure the absolute activity use beta-gamma coincidence counting or differential length proportional tubes (NCRP, 1985) to leverage 2 or more parameters to determine the detection efficiency. These techniques frequently are employed to determine the activity of standards which are later used to calibrate other detectors. An ideal solution is to use a source of moderately well-known activity (~±10%) to precisely determine the detector efficiencies, energy range and resolution. While such a generalized technique is applicable across all geometries of detectors and all types of radioactive decays, the extrapolation method for radioxenon discussed in this paper utilizes detectors that subtend very high solid angles, use radioactive isotopes that decay via beta-gamma coincidences and builds upon past efforts in the CTBTO radioxenon community (Axelsson, 2003; Cooper, 2011; Haas, 2009; McIntyre, 2009a). These two elements ensure the spectral extrapolation technique is accurate and easily implemented.

The beta-gamma coincident detectors used at the Pacific Northwest National Laboratory are used to detect very low levels of radio-xenon activities that may be associated with underground nuclear tests (CTBTO, 1999; Auer, 2004; Ringbom, 2003; Fontaine, 2004). The four radio-xenon isotopes are ^{133}Xe, ^{133m}Xe, ^{131m}Xe, and ^{135}Xe. Table 1 shows the dominate decays for the two isotopes investigated in this paper (^{133}Xe, ^{135}Xe). Additionally, ^{222}Rn and its daughter products, ^{214}Pb and ^{214}Bi, are used to calibrate the gamma and beta energy scales. Radon-222 is also used to determine the interference ratios because its daughter products can be an undesirable contaminate in the purified xenon gas samples. Several scheme and hardware modifications have been developed to calibrate the detectors or make the setup and calibration of the detectors easier (Reeder, 2007). The early beta-gamma spectrometer used several photo-multiplier tubes (PMTs) that had to be gain matched for both the gamma/x-ray spectrometer and for the beta and conversion electron (CE) beta cells (Reeder 1998). This hardware setup prevented the detectors from being simultaneously calibrated, and caused cross contamination of samples due to the close proximity of the beta detectors and the 4-well NaI(Tl) saddle detector.

Table 1. Simplified decay scheme for the four radioxenon isotopes (Browne 2004, Firestone 1999). In practice the number of coincident decays for Xe-133 has been determined to be over 5,000,000 for ^{133}Xe, but most are insignificant (Ringbom, 2012).

Nuclide	^{133}Xe	^{135}Xe
Half-life	5.25 d	9.14 h
Gamma-rays		
Energy (keV)	81.0	249.8
Abundance (%)	37.0	90.0
X-rays (K-shell)		
Energy (keV)	30.6-36.0	30.6-36.0
Sum Abundance (%)	48.9	5.2
Beta Spectrum		
Max. Energy (keV)	346.0	905.0
Abundance (%)	99.0	97.0
CE (K-shell)		
Energy (keV)	45.0	214.0
Abundance (%)	54.1	5.7

The improved beta-gamma detectors used independent gamma/x-ray detectors and single PMT beta cells to significantly reduce the detector setup complexity and allow for independent simultaneous calibration of the four detectors (Cooper, 2005). With the development of pure radioxenon samples (^{133}Xe, ^{135}Xe, and ^{131m}Xe) via neutron activation much of the difficulty associated with overlapping beta and gamma signatures from multiple isotopes was minimized or eliminated (Haas, 2009). The interference of the ^{135}Xe isotope was the last of the interference terms to be measured and quantified, and its contribution to the measurement of the ^{133}Xe and ^{133m}Xe concentration has been properly accounted for and reduced (Ely, 2011). The pure radioxenon spikes also allow the use of spectral extrapolation techniques to more accurate determine the beta-gamma efficiency for each of the dominate decays for three of the four radioxenon isotopes

RESEARCH ACCOMPLISHED

An initial investigation of using spectral extrapolation to determine the beta and gamma efficiency for ^{133}Xe and ^{135}Xe was done and has been outlined in a recent paper (McIntyre, 2012). However, more advanced methods have since been employed that provide more consistent results. Figure 1 shows the beta distribution from calibration spectra of ^{131m}Xe, ^{133}Xe, and ^{135}Xe and figure 2 shows the gamma distributions for the same isotopes.

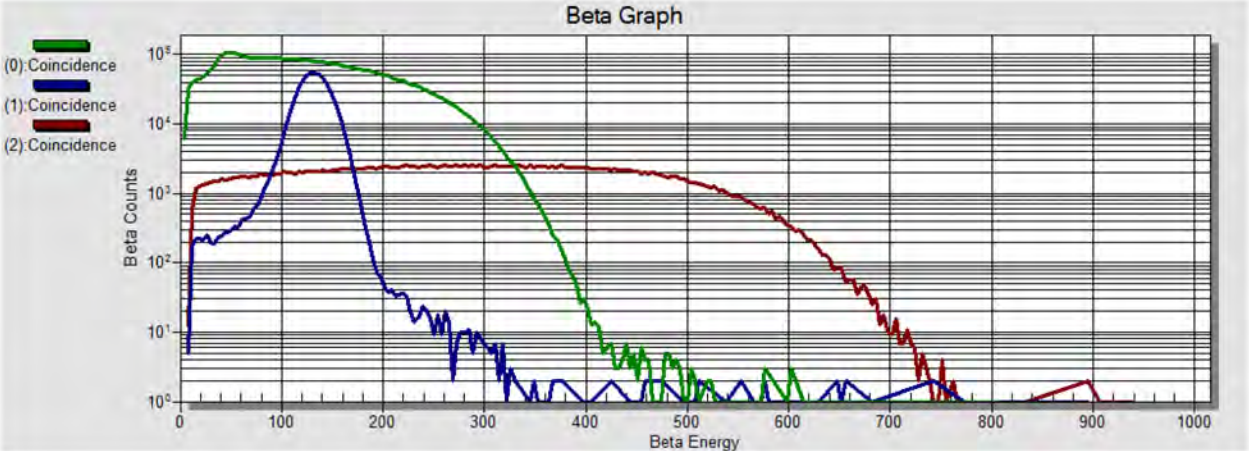


Figure 1. Histogram of the beta energy distributions for three of the four isotopes measued, ^{133}Xe is green, ^{135}Xe is brown and ^{131m}Xe is blue.

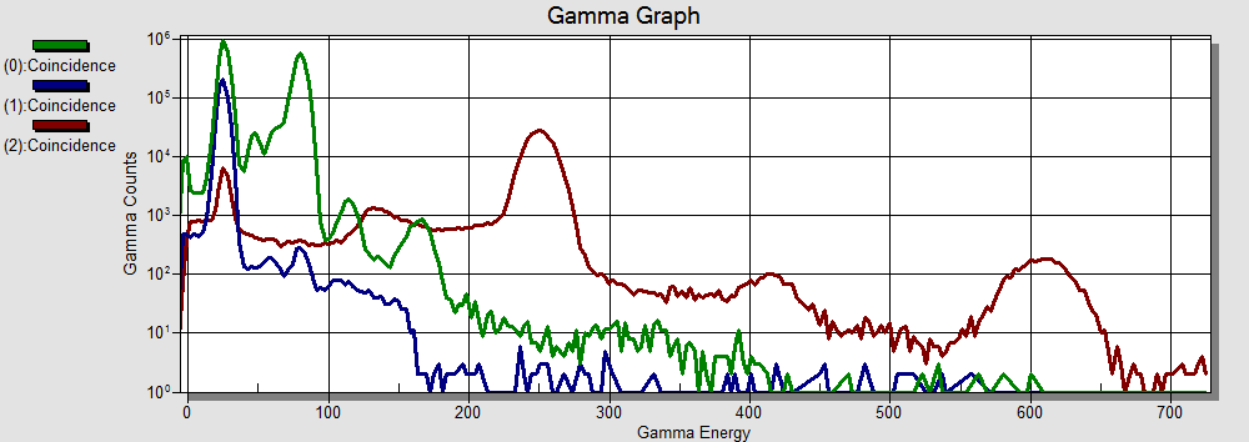


Figure 2. Histogram of the gamma energy distributions for three of the four isotopes measued, ^{133}Xe is green, ^{135}Xe is brown and ^{131m}Xe is blue. Not all of the peaks are used for quantification of the xenon concentrations.

Note that the log scale clearly shows additional gamma peaks that are not used neither in the analysis nor in the determination of the concentrations as they are normally too small to be seen. The ^{131m}Xe beta distribution shows the CE peak that is in coincidence with the ~30-keV x-rays. The ^{133}Xe beta distribution shows a small CE peak at 45-keV on top of a beta distribution that is associated with the 30-keV x-ray emission. The ^{135}Xe beta distribution on the other hand is a pure beta distribution that starts at 0-keV and extends to the beta end point (910-keV) or the maximum beta energy deposited in the 2.0 mm beta cell (~ 750-keV as seen).

Current Calibration Approach

The current approach to calibration of the beta-gamma detectors is using high activity samples of individual isotopes to determine the efficiency of the beta and gamma detectors for the regions of interest for each isotope. The primary region of interest for ^{135}Xe is the 250-keV gamma ray peak. For the ^{133}Xe, the primary regions of interest are the 80-keV gamma peak and ~ 30-keV areas for the x-rays. The beta regions of interest extend from the lowest measureable response to the beta endpoint energies. The background-subtracted counts N for each region are related to the total activity A by the efficiency ε for each detector, and the branching ratio (BR*)* into the specific region of interest:

$$A = \frac{N_\beta}{\varepsilon_\beta BR_\beta} = \frac{N_\gamma}{\varepsilon_\gamma BR_\gamma} = \frac{N_{\beta\gamma}}{\varepsilon_{\beta\gamma} BR_{\beta\gamma}} \quad (1)$$

where the subscripts designate the beta, gamma, and beta-gamma coincidences. It is important to note that this equation is a simplification and is only applicable to simple decay scheme such as the four radioxenon isotopes. With the assumptions that each detector only detects specific radioactivity (i.e., electrons or photons only) and that the beta-gamma efficiency or branching ratio is simply the product of the individual beta and gamma efficiency or branching ratio, the above equations can be rearranged to provide the beta and gamma detector efficiency for the specific region of interest:

$$\varepsilon_\beta = \frac{N_{\beta\gamma}}{N_\gamma BR_\beta}; \quad \varepsilon_\gamma = \frac{N_{\beta\gamma}}{N_\beta BR_\gamma}; \quad (2a,b)$$

This method provides a fairly simple methodology to determine the detector efficiencies without requiring prior knowledge of the activity of the sample, which is challenging to do because the radioxenon samples are a gas and short lived. The efficiencies derived in this fashion have some uncertainty associated with them due to the fact that the beta detectors are not 100% efficient and, in addition to betas, they also detect conversion electrons and low energy x-rays with different efficiencies.

1-Dimensional Extrapolation Approach

Following the formalism developed by Baerg (1973) and others the more general form of the relationship between the net counts and activity becomes more complicated. For example, the relationship between the counts in the beta detector (all counts) is related to the total activity by:

$$N_\beta = A\sum BR_r\left[\varepsilon_{\beta r} + \left(1-\varepsilon_{\beta r}\right)\left(\frac{\alpha\varepsilon_{CE} + \varepsilon_{\beta\gamma}}{1+\alpha}\right)_r\right] \quad (3)$$

Where the BR_r is the beta branching ratio for the r^{th} branch, α is the total internal conversion coefficient, and the efficiencies are for the betas (β), conversion electrons (CE) and for the beta detector to detect gammas (γ). There are similar complicated expressions for the gamma and coincidence count relationships to the total activity, and it becomes challenging to determine the effective efficiency, especially since there are multiple efficiencies for each of the detector types.

To provide a more precise detector calibration for the radioxenons a different approach was investigated. This approach is to use the one dimensional extrapolation method developed several decades ago for absolute activity

measurements with beta-gamma detectors (Baerg, 1973). This approach assumes the counts are all related by a function *F* that can be extrapolated to obtain the total activity:

$$N_\beta = F\left(N_{\beta\gamma} / N_\gamma\right), \quad N_\beta \to \left[F(1) = A\right] \quad as \quad N_{\beta\gamma} / N_\gamma \to 1 \qquad (4)$$

The benefit of this approach is that the various efficiencies, coefficients or branching ratios do not need to be known beforehand. The total activity can be calculated by fitting the distribution of counts from the beta detector as a function of the ratio of coincidence to gamma counts, typically with a low order polynomial, and then extrapolating the result to 1. The distribution is generated by changing the beta detector efficiency, and for this investigation, the data was collected with multichannel analyzers and the lower energy cutoff in the beta detector varied to change the beta efficiency. The changes to the lower energy cut off was done by analysis rather than changing the physical lower level discriminator of the multi-channel analyzer. With the known activity from the extrapolation, the effective efficiency for beta-gamma coincidences determined for each specific region of interest can then be

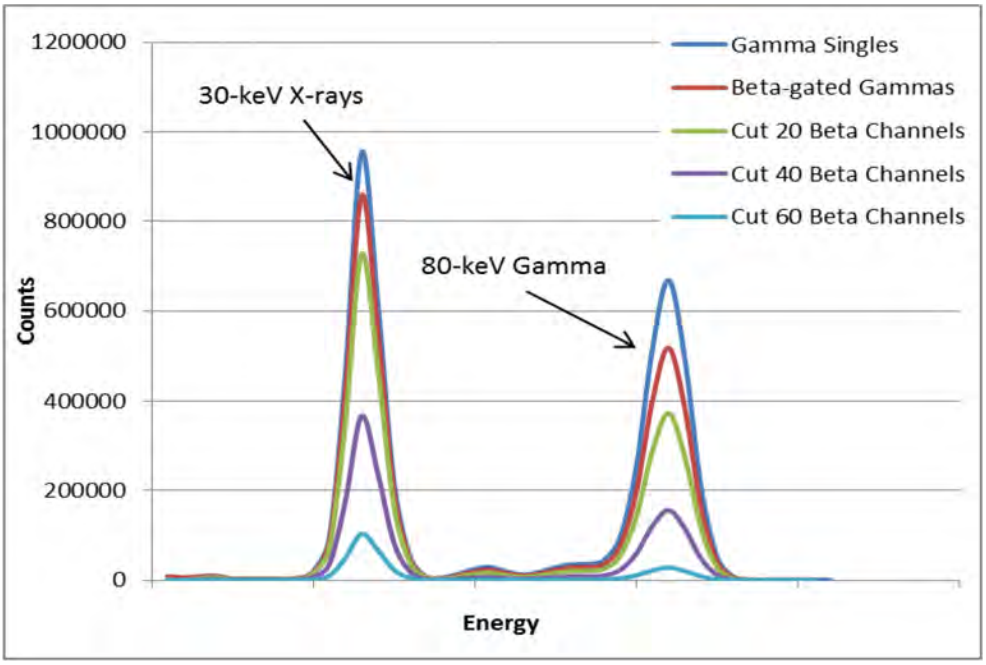


Figure 3. Histogram showing the different beta-gated gamma curves for differing beta detection efficiency (see text for further details).

determined for an accurate calibration of the detector system. Figure 3 shows the simulated gamma singles spectrum (blue curve), along with the beta-gated gamma spectrum (red curve) and additional beta-gated gamma spectra with increasing software cuts on the beta distribution data for a ^{133}Xe sample (green, purple and light blue curves). This is shown in figure 3 as the green, purple and light blue curves where an increasing number of the beta channels are excluded in the sum of the beta-gated gamma's.

Figure 4 shows the results for the one-dimensional analysis extrapolation for a simulated ^{133}Xe sample using the GEANT4 code (Agostinelli, 2003). The y-axis is the number of beta singles, N_β, and the x-axis is the term 1- $N_{\beta\gamma}$ / N_γ. The y-intercept on the graph (or when the beta efficiency is 100%) for each of the distributions then becomes the total activity. As can be seen from the graph the 30 and 80-keV distributions are nonlinear and only the sum is linear which provides a very accurate estimate of the total activity of ^{133}Xe in the sample which was chosen to be 1,000,000 decays. The nonlinear elements in 30-keV and the 80-keV only curves arise from the difference between the 30- and 80-keV gated beta distributions $N_{\beta\gamma 30,80}$ and the total beta distribution N_β which is the combination of at

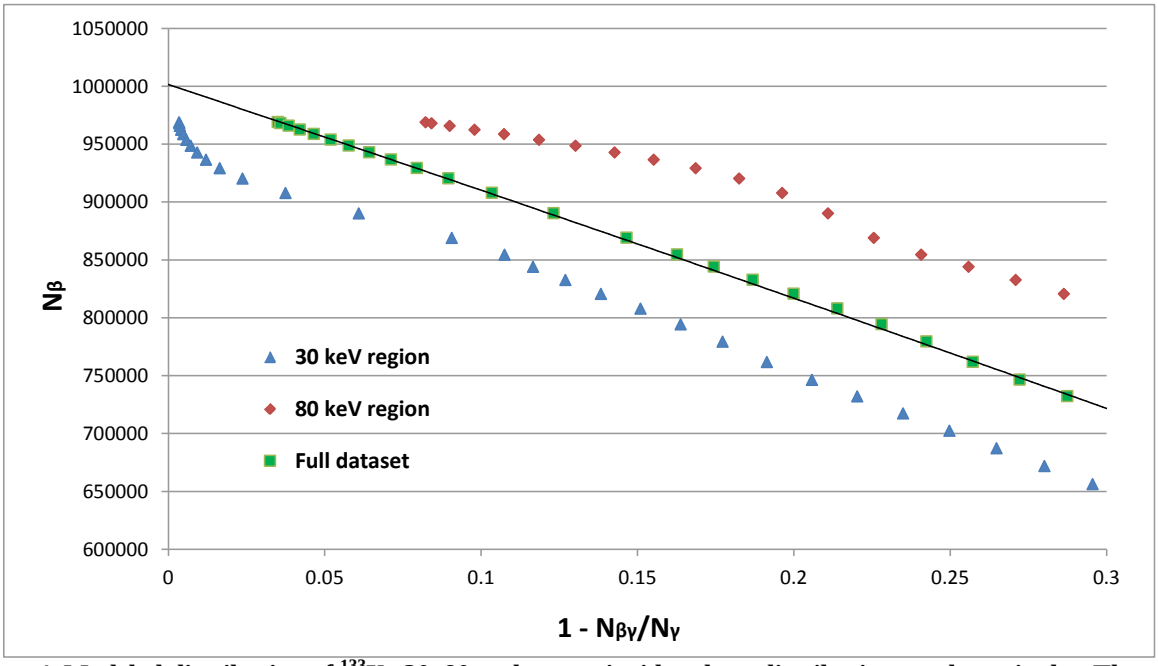


Figure 4. Modeled distribution of ^{133}Xe 30, 80 and sum coincident beta distributions vs. beta singles. The sum distribution has been fit with a 2nd order polynomial extrapolation line to show the extrapolation of *A* when the beta efficiency is 100%.

least three different beta/CE distributions. For example an 80-keV *CE* from the 80-keV gamma in coincidence with the beta. The green data points, which represents the sum of the 30- and 80-keV coincidence data sets, demonstrates that the coincidence sum is a much better representation of the beta singles distribution and as such is nearly linear. The y-axis interception point is within 0.2% of the source strength (1,000,000 decays) and thus shows the power of the 1-D extrapolation technique. Similar results for the activity were obtained for ^{135}Xe, but because the decay is dominated by the 250-keV gamma-line decay (90.0%) the coincident 250-keV results very closely matched (within 0.1%) the coincident beta sum (which included a 5% BR for a 30-keV x-ray).

2-Dimensional Extrapolation Approach

From the 1-D analysis, it is clear that the nonlinear nature of the various beta + CE coincident distributions arises from variations in the beta singles distribution from those found for the gamma-gated distributions. This aspect suggests that, if a method were developed that could remove from the beta singles the contributions from each of the different decay processes, a very linear plot could be generated as seen in Figure 4 for the coincident sum data sets. The y-axis intercept then becomes an estimate of the activity that is associated with the coincident beta distribution under investigation. This estimate (which is now a scalar activity number $A_{distribution}$) can be added back into the coincident distribution to provide a linear and hence better estimate of the overall value of *A*. This technique was developed by Smith (1975) and has since been called the 2-Dimensional extrapolation technique.

For ^{133}Xe there are three dominate distributions to consider, the 30-keV coincident beta-distribution, the 80-keV coincident beta distribution, and a 80-keV CE beta distribution ($N_{\beta CE80}$). The $N_{\beta CE80}$ distribution is a coincidences measurement but there is no photon in coincidence with it so it shows up in the beta-singles distribution and not as a beta-gamma distribution like the other two decay signatures. There are other decays but these are have BR less than 0.2% and tend to generate L-shell x-rays (>5-keV) which are detected in the beta cell but not the NaI(Tl) well detector and so contribute to the beta singles distribution. Figure 5 shows the four beta distributions and gives an indication of the difference in the overall shapes.

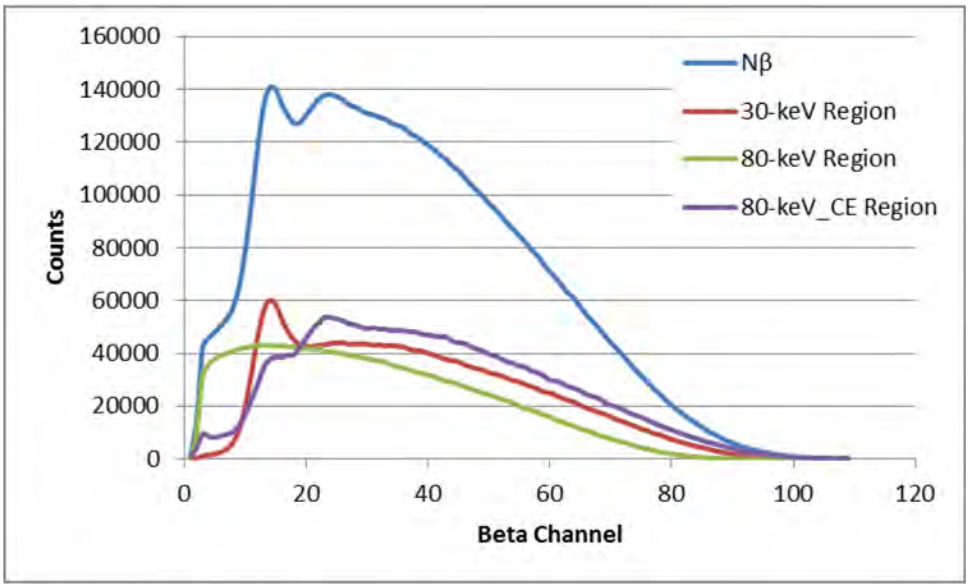


Figure 5. The raw beta distributions. Note that the beta-singles curve (N_β) is the sum of the other three distributions. The 30 and 80-keV curves are measured via coincidence with their repsective gamma-lines. The 80-keV CE curve is the result of subtrating the 30 and 80-keV curves from N_β.

The beta distributions for $N_{\beta\gamma 30}$ and $N_{\beta\gamma 80}$ are estimated from the measured coincident distributions. The $N_{\beta CE80}$ distribution is estimated as the result of subtracting $N_{\beta\gamma 30}$ and $N_{\beta\gamma 80}$ from N_β. There now three plots with different y-axis labels for figure 4. One for each of the new separate N_β distributions:

$$N_\beta - N_{\beta\gamma 80} - N_{\beta CE80} \text{ vs. } N_{\beta\gamma 30}; \quad (6)$$

$$N_\beta - N_{\beta\gamma 30} - N_{\beta CE80} \text{ vs. } N_{\beta\gamma 80}; \quad (7)$$

$$N_\beta - N_{\beta\gamma 30} - N_{\beta\gamma 80} \text{ vs. } N_{\beta CE80}; \quad (8)$$

Figure 6 shows two of the graphs that are produced from these calculations and it is seen that each one can be fit with a simple linear fit. It can also be seen that both the slope of the line and the y-intercept are identical, as would be expected. Essentially, the 2-D extrapolation technique is plotting each of the coincident beta distributions against itself and so the result should be identically linear. It is important to also realize that while the y-intercepts (the value of A when the beta efficiency is 100%) for each of the graphs is an estimate for the activity of that decay signature (A_{30}, A_{80}, and A_{80CE}) it will not be the absolute activity for the decay signature. It is the sum of each of the sub activities that produces the absolute activity A (i.e, $A = A_{30} + A_{80} + A_{80CE}$), which can be added back into equations 6–8.

$$N_\beta - N_{\beta\gamma 80} - N_{\beta CE80} + A_{80} + A_{80CE} \text{ vs. } N_{\beta\gamma 30}; \quad (9)$$

$$N_\beta - N_{\beta\gamma 30} - N_{\beta CE80} + A_{30} + A_{80CE} \text{ vs. } N_{\beta\gamma 80}; \quad (10)$$

$$N_\beta - N_{\beta\gamma 30} - N_{\beta\gamma 80} + A_{30} + A_{80} \text{ vs. } N_{\beta CE80}; \quad (11)$$

The offset of the linear fit for each of these graphs is than the same value and is the new best estimate of A. The slope for each of the linear fits do not change and is still an estimate of that beta distribution's contribution to A.

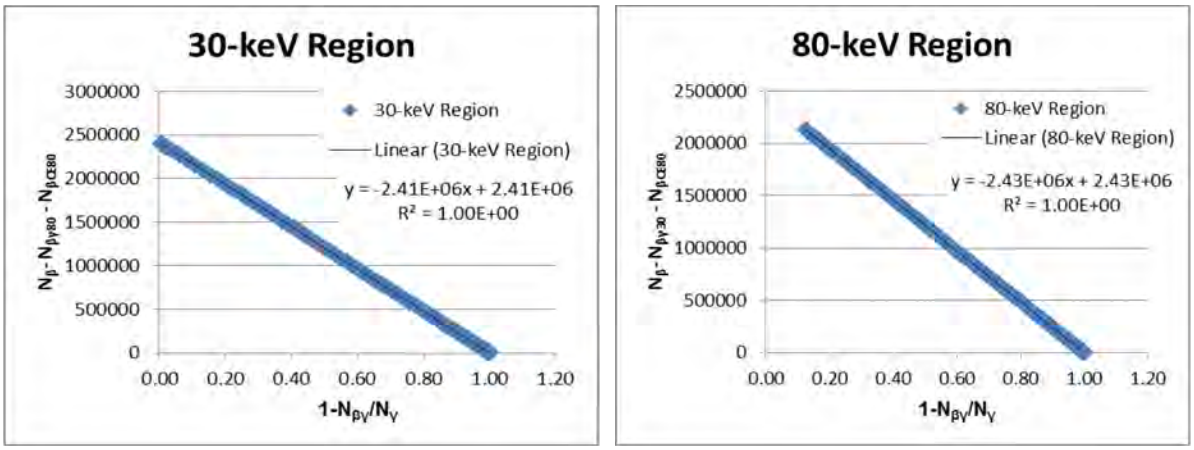


Figure 6A and B. Graphs of the 30-keV (right) and 80-keV (left) efficiencies vs. N_β minus the other beta distributions. The curves have been fit with a line and the slope and offset are identical in magnitude. The graphs show that the response is identically linear however the offsets are different as expected for a pure linear fit. The 30-keV data set (A) lies very close to the y-axis and the extrapolation to 100% efficiency (x=0) is minimal. The 80-keV data set (B) lies much further from the y-axis and the power of extrapolating to 100% efficiency gives a much better estimate of A_{80}.

The extrapolation technique lends itself easily to automated analysis as the generation of the extrapolation plots does not require analyst intervention and the fits to the data plots are simple linear plots. There are also a number of cross correlation checks that can be made to indicate whether a problem has occurred in the analysis, such as the slope and intercept for the individual beta distributions. The linearity of the fit can be checked as well by fitting the distributions with a quadratic fit, and the second order parameter provides a measure of the goodness of the linear fit, large values indicate a poor linear fit and small values indicate a good linear fit. For the data presented here the second-order parameters were of the order 10^{-7} and so were very small.

It is very important that the energy scales be accurate prior to analysis so that the energy ranges for the gamma/x-rays are appropriate and that the beta distributions cover the full range of detection. Also of importance is the large number of counts needed to attain the high accuracy that this method can achieve (typically < 0.5%). Table 2 shows the good agreement between the detector efficiencies that were obtained with the extrapolation method vs. the current standard method.

Table 2. Comparison of the detector efficiency's using the standard calibration method and the extrapolation method.

	Standard	Extrapolation
30-keV Gamma Efficiency	0.6514 ± 0.0124	0.6532 ± 0.0052
30-keV Region Beta Efficiency	0.9869 ± 0.0021	0.9931 ± 0.0078
80-keV Gamma Efficiency	0.7878 ± 0.0015	0.8016 ± 0.0069
80-keV Region Beta Efficiency	0.8921 ± 0.0031	0.8749 ± 0.0070
250-keV Gamma Efficiency	0.6312 ± 0.0015	0.6110 ± 0.0049
250-keV Region Beta Efficiency	0.9113 ± 0.0019	0.9060 ± 0.0073

CONCLUSIONS AND RECOMMENDATIONS

Using the extrapolation technique to determine the total source activity agrees well with the standard calibration method. The technique can be automated within the Java-based calibration program currently under development at PNNL (McIntyre, 2009b). In conclusion, the use of the extrapolation technique is both simple and robust and will allow non-experts to quickly and accurately calibrate sophisticated beta/gamma detectors. Additional work is ongoing to apply the technique to the two meta-stable isotopes ^{131m}Xe and ^{133m}Xe. However the nuclear decays for these two isotopes are covered by the detector efficiency calibrations using ^{133}Xe and ^{135}Xe. The use of ^{222}Rn for a full calibration of the beta-gamma detectors has been investigated but current work indicates that the extrapolation technique is not suited to ^{222}Rn and its several daughter products.

REFERENCES

A Handbook of Radioactivity Measurements Procedures (1985). NCRP Report No. 58, 2nd edition, National Council on Radiation Protection and Measurements, Bethesda, MD, 74–93.

Agostinelli S, et al. (2003). Geant4—a simulation toolkit, *Nucl. Instr. Meth. A* **506**, 250–300.

Auer M, et al. (2004). Intercomparison experiments of systems for the measurement of xenon radionuclides in the atmosphere, *Appl. Radiat. Isot.* **60**(6):863–877.

Axelsson, A. and Ringbom A. (2003). Xenon air activity concentration analysis from coincidence data, Swedish Defence Research Agency report, FOI-R-0913-SE.

Baerg, AP (1973). The Efficiency Extrapolation Method in Coincidence Counting, *Nucl. Instr. Meth*. **112,** 143–150

Browne, Edgardo, Firestone (2004). WWW Table of Radioactive Isotopes Version 2.1. http://ie.lbl.gov/toi/index.asp

Cooper M. W, AJ Carman, JC Hayes, TR Heimbigner, CW Hubbard, KE Litke, JI McIntyre, SJ Morris, MD Ripplinger, and R Suarez, (2005). Improved β-γ coincidence detector for radioxenon detection, in *Proceedings of the 27th Seismic Research Review: Ground-Based Nuclear Explosion Monitoring Technologies*, LA-UR-05-6407, Vol. 2, pp. 779–786.

Cooper MW, JI McIntyre, TW Bowyer, AJ Carman, JC Hayes, TR Heimbigner, CW Hubbard, LS Lidey, KE Litke, SJ Morris, MD Ripplinger, R Suarez, and RC Thompson, (2007). Redesigned Beta-Gamma Radioxenon Detector, *Nucl. Instr. Meth. A* **579(1)**:426–430.

Cooper M, CE Aalseth, DA Haas, and JC Hayes, (2011). Initial Beta-Gamma Nuclear Detector Background Study, in *Proceedings of the 2011 Monitoring Research Review: Ground-Based Nuclear Explosion Monitoring Technologies*, LA-UR-11-04823, Vol. 2, pp. 659–663.

CTBTO Operational Manual for Radionuclide and the International Exchange of Radionuclide Data (1999) Preparatory Commission for Comprehensive Nuclear-Test-Ban-Treaty Organization, CTBT/WGB/TL-11/5/Rev. 4

Ely J, MW Cooper, DA Haas, JC Hayes, TR Heimbigner, and BT Schrom (2011). Interference Terms for Xenon-135, *Proceedings 33rd Monitoring Research Review, Ground-Based Nuclear Explosion Monitoring Technologies*, LA-UR-11-04823, Vol. 2, pp. 664–670.

Firestone, RB, Chu SYF, and Baglin CM (1999). *Table of Isotopes* CD_ROM 8th edn. Wiley, New York

Fontaine, J. P., F. Pointurier, X. Blanchard, and T. Taffary (2004). Atmospheric xenon radioactive isotope monitoring, *J. Environ. Radioact*. **72,** 129–135.

Haas DA, SR Biegalski, and KM Foltz Biegalski (2009). Radioxenon production through neutron irradiation of stable xenon gas *J. Radioanalytical and Nuclear Chemistry* **282** (3), 677–680.

Keillor ME, Cooper MW, Hayes JC, and McIntyre JI (2009). Degradation of 81 keV ^{133}Xe gamma-rays into the 31 keV x-ray Peak in CsI scintillators, *J. Radioanal. Nuc. Chem.* **282**(3), 699–702.

McIntyre JI, MW Cooper, AJ Carman, TW Bowyer, AR Day, DA Haas, JC Hayes, TR Heimbigner, CW Hubbard, KE Litke, MD Ripplinger, and R Suarez (2009a). Concentration independent calibration of a β-γ coincidence detector using ^{131m}Xe and ^{133}Xe, *J. Radioanal. Nucl. Chem*. **282**(3), 755–759.

McIntyre JI, BT Schrom, MW Cooper, DA Haas, and JC Hayes (2009b). Beowulf - beta-gamma detector calibration graphical user interface, in *Proceedings of the 2009 Monitoring Research Review: Ground-Based Nuclear Explosion Monitoring Technologies*, Los Alamos National Laboratory, LA-UR-09-05276, Vol. 2, pp. 779–787.

McIntyre JI, JH Ely, MW Cooper, DA Haas, BT Schrom, and GA Warren, (2012). Further developments of a robust absolute calibration method utilizing beta/gamma coincidence techniques. Accepted for publication in *J. Radioanal. Nuc. Chem.,* PNNL-SA-86583, Pacific Northwest National Laboratory, Richland, WA.

Reeder PL, TW Bowyer, RW Perkins (1998). Beta-gamma counting system for Xe fission products, *J. Radioanal. Nuc. Chem*. **235** (1–2), 89–94.

Ringbom A, T Larson, A Axelsson, K Elmgren, and C Johansson (2003), SAUNA—a system for automatic sampling, processing, and analysis of radioactive xenon, *Nucl. Instr. Meth. A***, 508**, 542–553.

Ringbom A, (2012), Calculation of electron–photon coincidence decay of ^{131m}Xe and ^{133m}Xe including atomic relaxation, Appl. Radiat. Isot. **70**(8), 1499–1508.

Smith D, and LEH Stuart (1975). An extension of the 4πβ-γ coincidence technique: two dimensional extrapolation, *Metrologia* **11**, 67–72.

α-Al_2O_3 DIFFUSION BARRIERS TO ELIMINATE THE RADIOXENON MEMORY EFFECT IN PHOSWICH DETECTORS

W. K. Warburton[1], Wolfgang Hennig[1], Jacob A. Bertrand[2], Steven M. George[2], and Steven Biegalski[3]

XIA LLC[1], University of Colorado, Boulder[2], The University of Texas at Austin[3]

Sponsored by the National Nuclear Security Administration

Award No. DE-NA000486
Proposal BAA10-73

ABSTRACT

Well designed scintillator detectors, including such examples as ARSA, SAUNA, and XIA's "PhosWatch", can readily achieve the state of the art radioxenon detection limits required for nuclear explosion monitoring. They are also reliable, robust detectors that do not require cryogenic cooling for operation. All three employ the principle of beta-gamma coincidence detection to reduce background counting rates, using a BC-404 plastic scintillator to detect the betas and a CsI or NaI scintillator to detect the gamma-rays. As a consequence of this commonality of design, all three also display a "memory effect" arising from the diffusion of Xe into BC-404. Thus, when one sample is pumped out of the detector, a fraction remains behind, embedded in the BC-404, where it artificially raises the signal counting rate for the next sample. While this is not a fatal flaw in scintillator detectors, developing a method to eliminate the memory effect would significantly enhance their utility.

In this work we have been working to develop thin, amorphous Al_2O_3 films, deposited by atomic layer deposition (ALD) to act as diffusion barriers on the BC-404 surfaces exposed to radioxenon. Originally, film thicknesses between 2 and 10 nm were investigated, but were found to still exhibit the memory effect using radon as a substitute for Xe. We then tried 20 and 30 nm films, which were found to eliminate the radon memory effect completely. However, when then tested with radioxenon, they were still found to exhibit large memory effects.
We draw two important conclusions from this result: first that it will be necessary to develop an improved method for depositing thicker ALD Al_2O_3 films at lower temperatures while still retaining high film quality; and, second, that we need a method of testing the memory effect using Xe that does not require radio-isotopes to facilitate rapid sample testing.

OBJECTIVES

XIA, supported by the DOE's SBIR program, developed a "PhosWatch" phoswich radioxenon detector (Hennig, 2006) intended for use in verification operations by the Comprehensive Nuclear-Test-Ban Treaty Organization (CTBTO) (Hennig, 2009). The PhosWatch, like the SAUNA (Ringbom et al., 2003) and ARSA (McIntyre et al., 2001) detectors, is a beta-gamma coincidence detector that uses a fast plastic scintillator BC-404 sample cell to detect beta particles and conversion electrons. It differs from these detectors in that the BC-404 is formed as a spherical shell embedded in and optically coupled to a cylinder of CsI(Tl) that is read out by a single PMT, and beta-gamma coincidences are detected by pulse shape analysis of the single PMT output, rather than by timing analysis of multiple PMT outputs. This approach has been shown to achieve minimum detection limits similar to SAUNA and ARSA, but is cheaper, less complex and easier to operate and keep calibrated in the field. (Hennig**,** 2009)

However, because the PhosWatch shares the same BC-404 sample cell material with the SAUNA and ARSA detectors, it also suffers from the same radioxenon memory effect (McIntyre et al., 2001; Seifert, 2005), which is attributed to the diffusion of radioxenon into the BC-404 plastic (polyvinyltoluene) during the 24 hour counting period. Thus, when a new sample is introduced, some fraction of the previous sample remains, embedded in the BC-404 and contributing to the new count rate. In the present CTBTO protocol, some attempt to mitigate this effect is made by taking a background count between samples (Kalinowski, 2008; Auer et al., 2010) but there is currently an ongoing informal discussion in the community about how to do this correctly, since the sample cell is sealed during the background count but then pumped again before the new sample is introduced, thereby removing the unknown part of the memory gas that diffuses back into the sample volume during the measurement. Therefore it would be far preferable to instead develop means for eliminating the memory effect.

In this work we proposed to eliminate the memory effect by coating the inside of the BC-404 sample cell with a thin vapor barrier made of amorphous aluminum oxide (α-Al_2O_3) deposited by atomic layer deposition (ALD) (George, 2010). Al_2O_3 was chosen because first, it is a dense inorganic material which should not have large internal free volumes to allow the diffusion of Xe atoms; second, it is transparent in thin sections and so will not interfere with light collection within the PhosWatch geometry; and third, it is chemically very inert, which is desirable for the long term stability of the treatment. The amorphous form was chosen because grain boundaries are known fast diffusion channels and are extremely numerous in thin crystalline films, which are almost invariably polycrystalline with grain boundary separations commensurate with the film thickness. We selected ALD to deposit the films because the the technique can operate at relatively low temperatures while producing α-Al_2O_3 films of high density and perfection (Groner et al., 2004) that have been used as vapor barriers for several gases (Groner et al., 2006), and it has been shown to be capable of depositing α-Al_2O_3 films that adhere well to a variety of polymers (Wilson, 2005).

In our previous year's work (Warburton et al., 2011) we reported the following work. First, we developed a collaboration between XIA and the University of Colorado, Boulder (UCB) to use their ALD equipment to deposit α-Al_2O_3 films on a series of BC-404 samples, varying both film thickness and deposition temperature. Second, we built and tested an apparatus for dosing BC-404 with radon. We selected radon as a substitute for xenon in our initial research because: 1: it is also a noble gas whose atomic radius is only slightly larger than xenon's and so should diffuse similarly; 2: it is much easier to obtain commercially than xenon; and, 3: it also has a reported memory effect in BC-404 (McIntyre et al., 2001). Third, we developed a phoswich detector that would allow us to carry out both singles and coincidence counting, using the same pulse shape analysis method as for our PhosWatch detector, for either xenon or radon. Fourth, by the time of the 2011 MRR meeting we had conducted initial measurements to show that our methods were working successfully.

Our major objectives in this year's effort were therefore to:

- Conduct measurements to study the memory effect as a function of film thickness and growth temperature;
- Identify a film growth process that would produce a film that eliminated the radon memory effect;
- Test films grown using this process to measure their xenon memory effect; and
- If a film eliminating the memory effect in xenon could be found, apply this film to a BC-404 shell in a PhosWatch detector and demonstrate the resulting reduction in memory effect. in a full scale detector.

RESEARCH ACCOMPLISHED

EXPERIMENTAL METHODS

Radon measurement



Figure 1. BC-404 with its Al dosing cap.

Our experimental methods have been described in detail (Warburton et al., 2011) and will only be summarized briefly here. First, we constructed a specialized CsI(Tl)-BC-404 phoswich detector that would allow the BC-404 to be exposed to either radon or radioxenon *in situ*. This was accomplished by attaching the BC-404 to an aluminum dosing cap (see Figure 1), placing the BC-404 in contact with one window of a two window container housing a CsI(Tl) crystal, and connecting the other window to a PMT, which was thereby optically coupled to both the CsI(Tl) crystal and to the BC-404. The entire assembly was enclosed in a light-tight housing. An external pumping/dosing system allowed the face of the BC-404 away from the CsI(Tl) crystal to be exposed to either radon or radioxenon for arbitrary periods of time. The PMT signal was processed using a Pixie-4 PXI module from XIA (Hennig, 2007) and the same Igor software and algorithms developed at XIA to process PhosWatch signals (Hennig, 2006). All counting was done in a small lead cave whose background counting rate was about 5 cps with no sign of radon contamination.

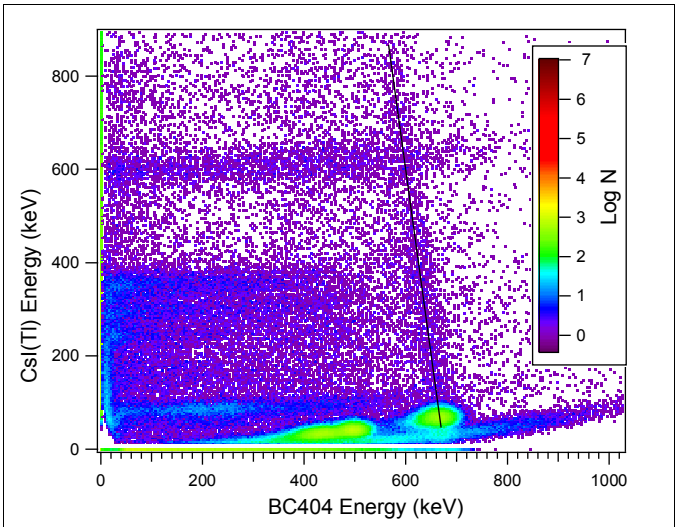


Figure 2. Typical Rn spectrum collected by the test jig.

Figure 2 presents a typical radon "coincidence" spectrum produced by our equipment. The y-axis shows the "gamma-ray energy" that the pulse shape analysis software detects in the CsI(Tl) crystal, while the x-axis shows the "electron energy" that it detects in the BC-404. Both axes have been approximately calibrated using the peak and Compton scattering created by 662 keV gamma-rays from a ^{137}Cs source. In looking at Figure 2, it is important to remember that these energies are inferred by an analysis method that assumes that the PMT pulse shape is composed of a superposition of two shapes, one generated by an electron stopping in BC-404 and one generated by a gamma-ray being absorbed in CsI(Tl). When the actual pulse shape is generated by a different mechanism, specifically by the absorption of an alpha particle in BC-404, the program decomposes it into these two shape terms and "finds" a small "gamma-ray" term. Thus, even though the alpha particles are not actually in coincidence with anything, they still show up in a 2-D coincidence plot such as Figure 2. Further, because of quenching along the alpha particle's track within the BC-404, the reported "electron" energy is smaller by almost an order of magnitude than the alpha particle's actual energy. Thus the three bright spots at the bottom of Figure 2 are alpha particles emitted by radon and its daughters: ^{222}Rn (at ~430 keV), ^{218}Po (at ~500 keV), and ^{214}Po (at ~670 keV), whose actual energies are 5.49, 6.00, and 7.69 MeV respectively. The horizontal lines in Figure 2 below 100 keV and between 200 and 400 keV come from the ^{214}Pb daughter isotope emitting K x-rays and gamma-rays in coincidence with either a beta or an EC electron. The horizontal line at about 600 keV is similarly from ^{214}Bi's 609 keV gamma in coincidence with a beta. At this time we do not have a clear explanation for either the nearly vertical line that appears to terminate on the ^{214}Po alpha peak or the bright line underlying the alpha particle peaks. We are not unduly concerned about these features since the device is not intended to function as a high quality spectrometer and needs only be sensitive to the presence of radon to be useful.

Because the 2-D radon spectrum is complex, we did not attempt to isolate sections of it due solely to ^{222}Rn and instead chose to record total counts/sec, depending upon the fact that ^{222}Rn reaches secular equilibrium with all of

its daughters above ^{210}Pb in less than 2.5 hours. Thus, in our measurements, we exposed the BC-404 to radon for about 24 hours, while counting, and then evacuated the sample volume. We continued to count for another 24 to 72 hours while pumping continuously. By developing a model, further described below, of the expected counting rate throughout the complete dosing-pumping cycle we showed that we could extract the xenon memory effect by fitting the curve during the pumping phase using a two exponential fitting function. Of these two exponentials, the shorter one describes the decay of the non-volatile Rn daughters left in the sample cell after the Rn is evacuated, while the longer one corresponds, approximately to the decay time of any Rn remaining trapped in the sample. The amplitude of the second term therefore reflects the amount of memory effect in the sample being analyzed.

Sample Preparation

Our sample preparation methods have also been described earlier (Warburton et al., 2011). Briefly, disks of BC-404 were obtained from St. Gobain and coated with different thicknesses of α-Al_2O_3 films at several deposition temperatures using existing ALD equipment at the Departments of Chemistry and Chemical Engineering at the University of Colorado, Boulder. (George, 2010 and references therein). To avoid sample deformation and bubbling, all samples were out-gassed overnight at 70 ºC while supported on polished Si wafers. The film thicknesses and deposition temperatures are shown in Table 1. As shown, the samples were prepared in two batches, one with thicknesses between 2 and 10 nm and a second with thicknesses of 20 and 30 nm after the first batch proved incapable of completely blocking the Rn memory effect, as we discuss below.

Table 1: Sample deposition schedule

Temperature (°C)	Thickness (nm)	Quantity
First sample set		
75	7	4
85	7	4
100	2	4
100	5	4
100	7	4
100	10	4
Second sample set		
100	20	4
100	30	4

All samples were produced in a flow reactor by alternately dosing the sample with TMA (tri-methyl-aluminum: $Al(CH_3)_3$) and water vapor (H_2O) with purge times in between to completely remove each reactant before introducing the next. The standard conditions are: 100 sccm of Ar carrier gas at a base pressure of about 1 Torr; TMA dose time of 1.0 sec.; TMA purge time of 120 sec for sample thicknesses of 10 nm or less, 90 seconds for thicker films; water dose time of 0.5 sec; water purge times same as TMA purge times. The pressure rise during dosing was 400 – 500 mTorr. Dosing times had been previously established using quartz crystal microbalances (QCM's), as was the deposition rate of 0.128 nm/cycle. The number of deposition cycles was established by dividing the desired thickness by the known deposition rate/cycle. All of the samples were deposited above BC-404's 70 ºC softening point (Saint-Gobain Data Sheet) and minor amounts of sample sagging were observed, particularly for the longer deposition times, which approach 8 hours for the 30 nm sample. Some of the thicker sample also showed areas with some "frostiness" which we presume to come from additional Al_2O_3 deposition by chemical vapor deposition (CVD) arising from incomplete H_2O removal during the shorter H_2O purge times. Only areas without visible frostiness were selected for memory effect testing. But the presence of CVD suggests that these samples may not have been as atomically perfect as the best ALD films that can be produced.

Radioxenon Measurements

Radioxenon memory effect tests were performed at the University of Texas at Austin in two ways. The first was the same as the radon method described above, but instead exposing the BC-404 to radioxenon. In the second method, the BC-404 sample and its aluminum holder were removed from the phoswich counting assembly and filled directly with radioxenon and held for 24 hours. The sample was then placed on top of an HPGe gamma-ray spectrometer and its spectrum collected and the counting rate in the 80 keV ^{133}Xe line recorded. The sample was then evacuated for 24 hours, resealed, replaced in exactly the same position on the gamma-ray spectrometer and the counting rate in the 80 keV ^{133}Xe line recorded as second time. The ratio of the two was used directly as an upper bound measurement of the memory effect without correcting for ^{133}Xe's 5 day half life.

EXPERIMENTAL RESULTS AND ANALYSIS

The Radon 1-D Finite Element Dosing Model

At a general conceptual level, the interaction of radon with a BC-404 sample coated with a diffusion barrier is fairly straightforward. During dosing, two regions containing radon and its daughters are visible to the counting system: the volume over the sample and the sample volume itself, with the two separated by the diffusion barrier. When the radon is first introduced, there are no daughters and, as time goes on, secular equilibrium is eventually established. Because the radon is mobile and the daughters are not, the latter remain where they are generated, while the radon penetrates the diffusion barrier and moves into the BC-404 at a rate governed by its diffusivity. When pumping begins, all radon is removed from the volume over the sample. Some of the radon within the sample now begins to diffuse out through the diffusion barrier, to be pumped away, while the remainder continues to diffuse further into the BC-404 bulk. Any daughters created during the dosing process continue to be counted until they decay away, while the radon within the BC-404 continues to generate new daughter products.

Because this process is controlled by several kinetic coefficients, including 1) the coefficients for Rn sticking to and evaporating from the diffusion barrier; 2) the radon diffusivity across the barrier; and, 3) the diffusivity of radon within the BC-404, it is much more difficult to predict exactly what will occur in any given circumstance. We therefore developed a 1-D finite element model to explore the possibilities, assuming that the radon in the sample was always well below its saturation density. The model includes both diffusion and radioactive decay.

The “elements” in the model were: 1) the volume over the BC-404; 2) the sample surface; 3) a 'barrier” layer with Rn diffusivity kBar; and, 4) 100 layers of BC-404 with Rn diffusivity kDiff. The proportionality constants for the Rn depositing on the surface and evaporating from it were kDep and kEvap. Standard finite difference equations were then written to describe the motion of the Rn out of the gas and through the sample. At each time step the decay of Rn and each of its daughters was calculated using their known lifetimes, both to adjust the concentration profiles appropriately and to find the total observable counting rate. The model is heuristic in the sense that the diffusion coefficients are all treated as unknowns and adjusted to produce output counting curves that mimicked those actually observed.

Figure 3 shows concentration profiles in uncoated BC-404 during dosing (red), which are typical of diffusion with a pinned surface concentration and after pumping starts at 24 hours (purple), during which some of the Rn returns to the surface and is pumped, but a large fraction continues to diffuse inward. This is an important result: all the Rn (or Xe) cannot be removed by pumping since the interior is also technically a vacuum and any given atom is as likely to move toward the interior as toward the surface. Because we are pumping, any Rn reaching the surface is removed, which shortens the Rn activity's apparent decay time from its natural half life.

Figure 4 shows the time dependence of total activity with barriers ranging from none (kBar = kDiff) to one with kBar = 0.01*kDiff. These curves during pumping can be fit well with a double exponential, the first one modeling the decay of the Rn daughters, the second modeling the Rn leaving the BC-404 by both diffusion and radioactive decay. The first time constant is typically of order 1 hour, the second of order 1-3 days. Examining the decay

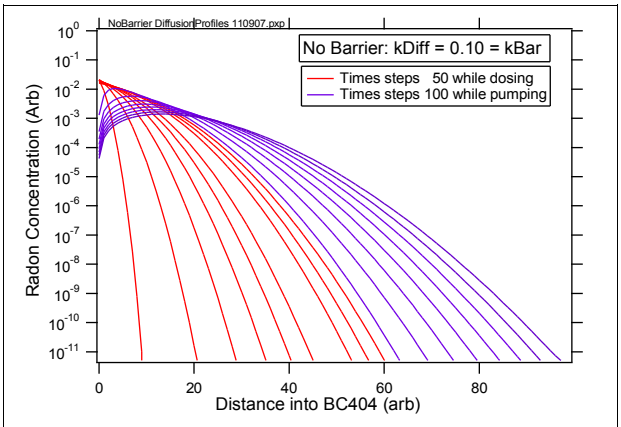


Figure 3. Rn concentration profiles in BC-404 as a function of time with no surface absorption barrier.

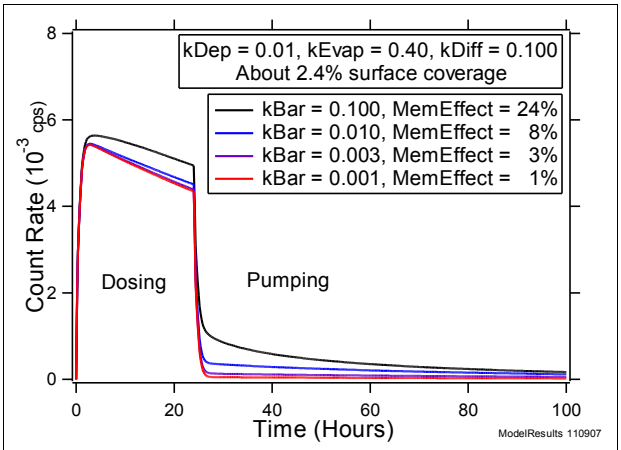


Figure 4. Modeled count rate vs time and barrier value.

curves as a function of increasing diffusion barrier reveals two results of interest: first, as expected, the memory effect is reduced as Rn is prevented from entering the BC-404; and, second, the post-removal decay time increases because better barriers also trap Rn inside the BC-404 where its concentration can be reduced only by radioactive decay with its natural 3.82 day half life.

In this work we compute the "memory effect" as the ratio of the slow term amplitude to the sum of the two amplitudes. This sum represents the total activity in the cell and sample the instant before the gaseous Rn charge is pumped away. This definition overestimates the amount that would be present after a typical 24 hour pump, but we use it both because it is well defined in this analysis and because it sets an upper bound on the effect we will be trying to minimize. Figure 4 also shows that, when the barrier is porous (memory effect 24%) the reduction in memory effect with barrier diffusivity is sub-linear: decreasing kBar by a factor of 10, from 0.100 to 0.010 only reduces the memory effect by a factor of 3. However, as the barrier improves, the memory effect becomes more nearly linear in kBar, reducing from 3% to 1% as kBar decreases from 0.003 to 0.001. These results suggest that we will have to produce a barrier film whose Xe diffusivity is of order 1000 times lower than the diffusivity of Xe in BC-404 in order for it to be effective.

Radon measurements on the first set of BC-404 samples

The first set of samples was intended to explore the α-Al_2O_3 layer's ability to block Rn diffusion as a function of its thickness and deposition temperature. Since our experience has been that α-Al_2O_3 layers of a few nanometers effectively block water diffusion (Carcia et al., 2006) and water molecules are smaller in size than either Xe or Rn atoms, we began, as shown in Table 1, with a set of film thicknesses between 2 and 10 nm. In selecting an optimum growth temperature, we considered both the 70 °C softening point of BC-404 and the observation that α-Al_2O_3 film densities increase with increasing deposition temperature (Groner et al., 2004). Since we expect the film's barrier efficiency to increase as its free volume drops (density rises), we selected temperatures slightly above the softening point, hoping that excess deformation would not occur during deposition. Because this was an exploratory study, we did not undertake a detailed study to determine optimum dosing and purging times, but instead used values in the range that produced good water barrier films on other plastics. (Groner et al., 2004 & 2006)

As described in the experimental section, each tested sample resulted in a record of total count versus time over a period that included a 24 hour background count, a 24 hour Rn exposure, and a count of 24 to 72 hours under vacuum. Figure 5 shows a typical curve, taken on a 5 nm film that was deposited at 100 °C. The fit parameters of the two exponential fit are also shown, together with the calculated memory effect ME in percent:

$$ME = 100\,\frac{A2}{A1+A2} \quad . \qquad (1)$$

Note that, because ME is found from a fit to data, the value of A2 can be negative, even though such a result is not physically possible. For such a situation to occur, A2 would have to be small compared to fluctuations in the background rate.

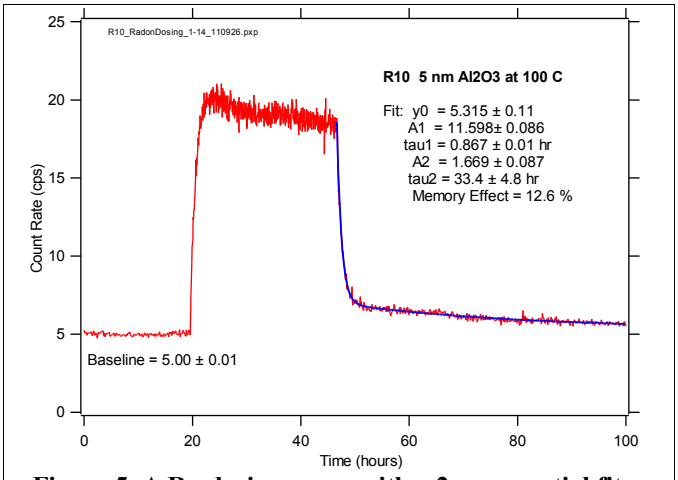


Figure 5. A Rn dosing curve with a 2-exponential fit.

Figure 6 shows the dosing and decay portions of curves from four samples that illustrate the range of memory effects that we measured on these samples. The observed memory effects range for about 3 to 21%, where the largest value is for an uncoated sample and the smallest for a 10 nm film. In the latter case the second exponential region was sufficiently flat that it could not be fit using both A2 and Tau2 as independent parameters. When Tau2 was forced to the half life of Rn, then values for A2 between 3 and 4% were found, depending on the precise fitting range selected.

Figure 7 shows the values of the memory effect that we obtained from this set of samples, which are all the values with film thicknesses of 10 nm or less. It is worth noting that these values cannot be directly compared to values seen for radioxenon. This is primarily because a measured memory effect value depends not only on the solubility and diffusivity of the radio-isotope in BC-404 but also on the sample volume and surface area. Thus, if one starts

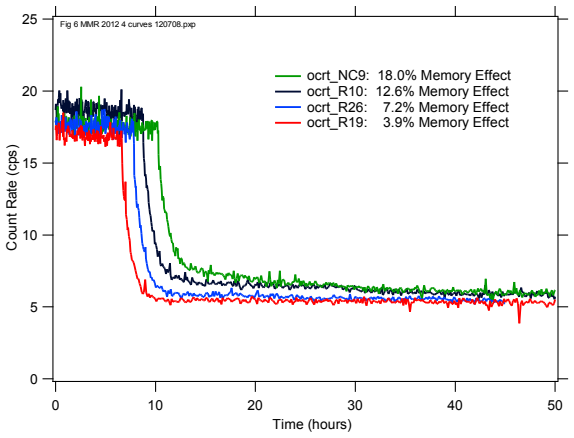


Figure 6. Four dosing curves showing a range of memory effect values.

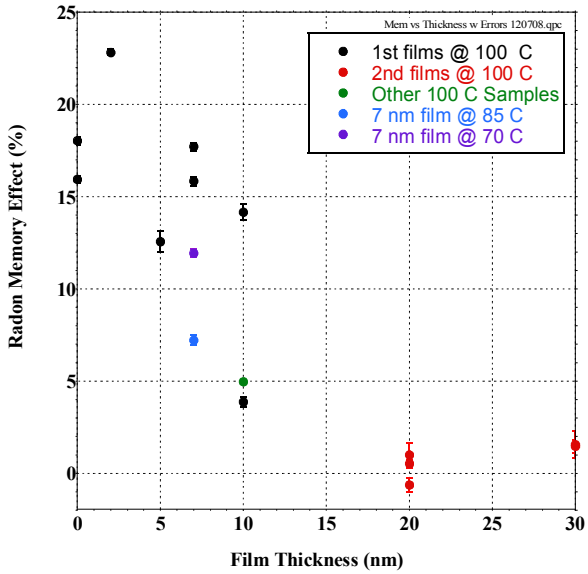


Figure 7. Measured memory effect values.

with N atoms and D of them diffuse into the BC-404, the memory effect will be D/N. Here D varies with the sample area, BC-404 diffusivity and solubility, and barrier efficiency, while N varies with sample cell volume and pressure. Because, in our experiments, we keep everything constant except the barrier efficiency, we can directly compare our results to the uncoated case to obtain barrier efficiencies. But we cannot make quantitative comparisons to experiments made under other conditions. The sole exception to this rule was the 2 nm sample, which was dosed for 48 hours instead of the usual 24 hours and, as a result, shows a distinctly larger memory effect. The remainder of the samples that were nominally dosed for 24 hours were all actually dosed for this time with an accuracy of about 1 hour. The two uncoated samples were dosed for 89,100 and 91,200 seconds, a difference of 2.4%, which is not sufficient to account for their 2% memory effect difference if an extra 24 hours (86,400 sec) raises the memory effect of the 2 nm sample by perhaps 6%.

All the data points in Figure 7 have error bars obtained from the fitting parameters, although in some cases they are smaller than the point sizes. Looking at the data, then, we can conclude that, while there is a general trend to smaller memory effect values as the film thickness increases, the measurements have other sources of error that are large compared to the fitting errors. While there is some fluctuation in the measurement technique itself, primarily due to fluctuations in background counting rate, it is not large enough to account for the discrepancies seen. In particular, we measured several samples twice and obtained answers that typically agreed within about 0.5%.

As an example of these discrepancies, consider the values at 7 nm: the films deposited at higher temperatures, which should be denser, actually have the largest memory effect. The trend for all four samples is exactly opposite from what one would physically expect. Similarly, the two measurements at 10 nm are widely separated. The green point at 10 nm is the same sample that produced the 4% memory effect, but with 2" of Teflon tape introduced into the sample volume to see if the small amounts of pipe tape in the system would contribute to our measured values. But this value reproduced within 1%, showing that this sample is indeed significantly different from the one with a 14% memory effect.

Radon Measurements on the Second Set of BC-404 Samples

One possible explanation is that α-Al_2O_3 films are known not to reliably nucleate on certain plastic substrates (Wilson, 2005) and may take up to 10 mn before they begin growing at a rate that is no longer influenced by the substrate material. To test this hypothesis, we deposited two more sets of samples at 100 °C of thicknesses 20 and 30 nm. The dosing curves for three of the 20 nm samples are shown in Figure 8. In all three cases, once the Rn was pumped out, the only activity remaining was the decay of Rn daughters in the sample cell. The curves could be fit to two exponentials only by fixing the decay time of the slow component to the half live of Rn. The resulting slow component amplitudes were small and, in one case, negative, suggesting that the true value is zero with a standard deviation of less than 1% determined by fluctuations in the background counting rate. The values for the two 30 nm samples were also quite small, at the 1.5% level. These five points are shown in red in Figure 7. It therefore appears

that either a 20 or 30 nm α-Al_2O_3 film makes a Rn barrier that reduces the memory effect by a minimum factor of at least 10.

Radioxenon Measurements on the 30 nm ALD Films

Having produced films that provided a good Rn barrier, we proceeded to test them with radioxenon produced by irradiating natural Xe in a reactor at The University of Texas at Austin (UTA). The results, however, were disappointing. We first tested at 20 nm films, sample R32 (see Fig. 8), with the only changes in our experimental measurement program being, first, the substitution of radioxenon for Rn, and, second, the addition of a quick release valve to the fill tube on our phoswich detector because the Xe gas handling equipment was in a different room from the counting laboratory at UTA.

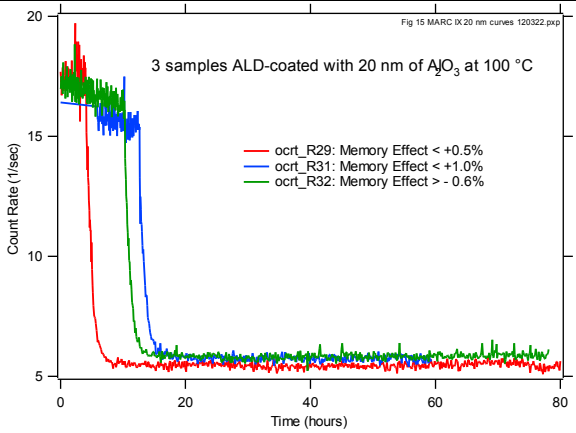


Figure 8. Rn dosing curves for three 20 nm films, showing no memory effect.

Figure 9 shows a the first radioxenon spectrum, which demonstrates that, while still uncalibrated, our phoswich detector is working correctly. The initial counting rate was fairly high, at about 5,000 cps. The Xe and Cs Kα x-ray lines near 30 keV, are clearly visible and show peaks from conversion electrons captured in the BC-404.

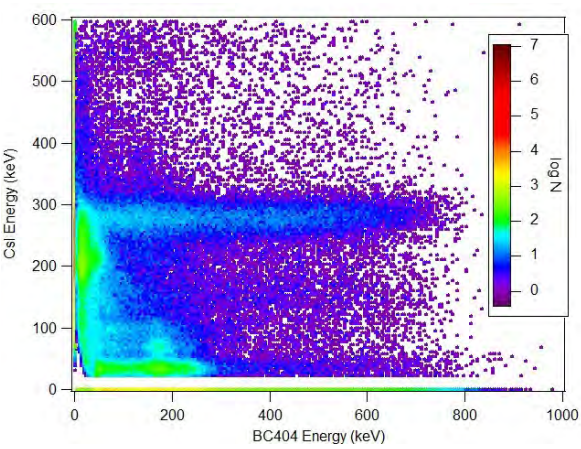


Figure 9. 2-D spectrum from irradiated natural Xe.

We recorded the counting rate for 19.6 hours, by which time it had dropped to about 87 cps, a reduction factor of almost 60. We then pumped out the Xe, which dropped the counting rate to about 16 cps, which would correspond to a memory effect of about 18%. We cannot, however, account for the factor of 60 reduction in count rate over 24 hours without invoking a leak in the system because the reduction factor of the shortest half life Xe isotope (^{135g}Xe - 9.14 h) is only 8.5 over 19.6 hours. We therefore do not regard this memory effect measurement as reliable since, in the presence of a leak it is easier for free Xe to escape from the cell volume than it is for absorbed Xe to escape from the BC-404 sample.

We therefore measured a 30 nm film using the second method for measuring the radioxenon memory effect described above. 24 hours after filling the cell with radioxenon, it took 299.3 seconds to obtain 12,480 ± 119 counts in the 81 keV ^{133}Xe peak (41.70 ± 0.40 cps). The radioxenon was then removed with four pump and flush cycles and the cell counted again, taking 14,400 seconds to obtain 16,323 ± 138 counts in the 81 keV ^{133}Xe peak (1.13 ± 0.01 cps). The memory effect is the ratio of the two counting rates and is 2.70 ± 0.0035 %, where we have not made the small correction for the 5.25 day ^{133}Xe half life. Since the Xe memory effect is typically reported to be about 5 % (McIntyre et al., 2001; Auer et al., 2010; Bläckberg et al., 2011), the 30 nm α-Al_2O_3 coating reduces it by about 50%. This is in agreement with the absolute memory effect results reported by Bläckberg et al. (2011).

DISCUSSION

Rn and Xe clearly behave quite differently in relation both to BC-404 and to the α-Al_2O_3 ALD films with which we are attempting to reduce the memory effect. Thus, while Rn has a factor of 4 larger memory effect than Xe in BC-404, 20 % compared to 5 %, Xe clearly has a much higher diffusivity through α-Al_2O_3, considering that a 30 nm film blocks the one nearly completely but barely hinders the other. Several factors may be contributing here.

First, under the growth conditions that produced our ALD α-Al_2O_3 films, it is known that the film density increases with increasing deposition temperature, from 2.5 g/cm^3 at 35 °C to 3.0 g/cm^3 at 177 °C, being about 2.7 g/cm^3 at 100 °C. This compares to 3.97 g/cm^3 for crystalline Al_2O_3 (corundum). Since interstitial diffusivity rates are

controlled by the passage of atoms through the small holes between the interstices, they are quite sensitive to the dimension of the atom compared to the dimension of the connecting holes. Thus, if the holes are slightly smaller than the diameter of one diffusing species and slightly larger than the diameter of another, then the first may move quite freely while the second may be essentially blocked. In addition, it is known that growing ALD α-Al_2O_3 films at lower temperatures incorporates varying amounts of hydrogen (Groner et al., 2004), which might also influence diffusion rates by modifying the growth structure through bond termination.

Second, in both this work and that of Bläckberg et al., (2011) there is significant sample to sample variation that remains unexplained. Bläckberg suggests that this might be due to variations in surface roughness, which is not currently a controlled or varied parameter. However, in our research we have noted that there appears to be some kind of volatile solvent in the BC-404 samples that cause bubbling when the samples were coated at 100 °C or above and which we removed by baking the samples overnight at 70 °C prior to coating. Our working assumption, which needs to be verified, is that this is water. If true, then this provides an H_2O reservoir to chemically react with TMA during the TMA exposures in the ALD cycle. This process would produce CVD α-Al_2O_3, which lacks the film perfection of ALD grown oxide. Differing amounts of water, sample to sample could then produce variable results, independent of surface roughness variations.

Third, the growth of α-Al_2O_3 by ALD as a function of dose times, purge times and temperature on BC-404 has not been carefully studied or optimized as it has been in certain cases. (Wilson, 2005) In particular, the purge times to adequately remove water vapor have not been demonstrated, while it is known that inadequate removal of water vapor can be deleterious to film quality. It is thus likely that the currently grown films are not of optimal quality.

CONCLUSIONS AND RECOMMENDATIONS

In summary, we developed a method for testing the memory effect of Rn on BC-404 samples coated with α-Al_2O_3 by ALD, using Rn as a substitute for Xe due to the difficulties in making large numbers of measurements without ready access to either a reactor or a commercial source of radioxenon. We found that coatings of 20 or 30 nm, deposited at 100 °C effectively blocked the memory effect for Rn, but only reduced it by half for Xe. In the future, then, the films will have to be tested using Xe. Because the pressures involved are large, it may be possible to make useful measurements using natural Xe and accurate pressure gauges, reserving tests with radio-isotopes for only the best samples. The uncertainties we and others have found in memory effect measurements are currently not well understood, which suggests that it would be worthwhile to carry out more fundamental studies on the ALD process used to produce the films in order to produce a better understanding of the relationship between growth parameters and the measures of film quality, such as density, that may be important to its role as a diffusion barrier. Methods for reducing purge times while avoiding CVD during low temperature ALD would be particularly useful since significant sample deformation occurred during even the shorter depositions at 100 °C and it would be preferable to be able to deposit the Al_2O_3 films at temperatures below BC-404's softening point without simultaneously reducing film density.

Finally, the view that Xe diffusion rates in both BC-404 and the Al_2O_3 films are controlled by free volume suggests a different line of research that may be interesting to pursue, the use of crystalline fast organic scintillators as a replacement for BC-404. Recent work has shown that such materials as Stilbene, which is an fast organic scintillator with a much higher light output that BC-404, can be grown in large single crystals. (Zaitseva et al., 2011) Being crystalline, these materials do not possess the large free volumes found in cast plastics like BC-404, which are thought to form fast diffusion channels for Xe, and therefore, conceptually, should have significantly reduced memory effects.

REFERENCES

Auer, M., Kumberg, T., Sartorius, H., Wernsperger, B., and Schlosser, C. (2010). Ten years of development of equipment for measurement of atmospheric xenon for the verification of the CTBT, *Pure Appl. Geophys.* **167,** 471−486.

Bläckberg, L., Fay, A., Jogi, I., Biegalski, S., Boman, M., Elmgren, K., Fritioff, T., Johansson, A., Mårtensson, L., Nielsen, F., Ringbom, A., Rooth, M. Sjöstrand, and Klintenberg, M. (2011). Investigations of surface coatings to reduce memory effect in plastic scintillator detectors used for radioxenon detection, *Nucl. Instr. Meth. Phys. Res.* A **656,** 84−91.

Carcia, P.F., McLean, R.S., M.H. Reilly, M.D. Groner, and S.M. George (2006). Ca test of Al_2O_3 gas diffusion barriers grown by atomic layer deposition on polymers, *Appl. Phys. Lett*. **89,** 031915.

George, S.M. (2010). Atomic Layer Deposition: An Overview, *Chem. Rev*. **110**, 113–131.

Groner, M.D., Fabreguette, F.H., Elam, J.W., and George, S.M. (2004). Low-Temperature Al_2O_3 Atomic Layer Deposition, *Chem. Mat.* **16**, 639−645.

Groner, M.D., George, S.M., McLean, R.S., and Carcia, P.F. (2006). Gas diffusion barriers on polymers using Al_2O_3 atomic layer deposition, *Appl. Phys. Lett.* **88,** 051907-1 to 3.

Hennig, W., H.Tan, W. K. Warburton, and J. I. McIntyre (2006). Single channel beta-gamma coincidence detection of radioactive Xenon using digital pulse shape analysis of phoswich detector signals, *IEEE Trans. Nucl. Sci.* **53**, 620−624.

Hennig, W., Chu, Y.X., Tan, H., Fallu-Labruyere, A., Warburton, W.K., and Grzywacz, R. (2007). The DGF Pixie-4 spectrometer – compact digital readout electronics for HPGe clover detectors, *Nucl. Instr. Meth. Phys. Res.* B **263,** 175−178.

Hennig, W., W. K. Warburton, A. Fallu-Labruyere, K. Sabourov, M.W. Cooper, J. I. McIntyre, A. Gleyzer, M. Bean, E.P. Korpach, K. Ungar, W. Zhang, and P. Mekarski (2009), Development of phoswich detector system for radioxenon monitoring*, J. Radioanal. Nucl. Chem.* **282**, 681−685.

Kalinowski, M.B., Becker, A., Saey, P.R.J., Tuma, M.P., and Wotowa, G. (2008). The Complexity of CTBT Verification. Taking Noble Gas Monitoring as an Example, *Complexity* **14**, 89−99.

McIntyre, J.I., Abel, K.H., Bowyer, T.W., Hayes, J.C., Heimbigner, T.R., Panisko, M.E., Reeder, P.L. and Thompson, R.C.(2001). Measurements of ambient radioxenon levels using the automated radioxenon sampler/analyzer (ARSA), *J. Radioanal. Nucl. Chem.* **248**, 629–635.

Ringbom, A., T. Larson, A. Axelson, K. Elmgren, and C. Johansson (2003). SAUNA—a system for automatic sampling, processing and analysis of radioactive xenon, *Nucl. Instr. Meth. Phys. Res.*, A **508,** 542–553.

Saint-Gobain Data Sheet, *BC-400, BC-404, BC-408, BC-412, BC-416 Premium Plastic Scintillators,* from www.detectors.saint-gobain.com.

Seifert, C.E., J.I. McIntyre, K.C. Antolick, A.L. Carman, M.W. Cooper, J.C. Hayes, T.P. Heimbigner, C.W. Hubbard, K.E. Litke, M.D. Ripplinger, and R. Suarez (2005). Mitigation of memory effects in beta scintillation cells for radioactive gas detection, in *Proceedings of the 27th Seismic Research Review: Ground-Based Nuclear Explosion Monitoring Technologies*, LA-UR-05-6507, Vol. II, pp. 804–814.

Warburton, W.K., S.J. Asztalos, and W. Hennig, (2011). Alpha-Al2O3 Diffusion Barriers to Eliminate Radio-Xenon Memory Effect in Phoswich Detectors, in *Proceedings of the 2011 Monitoring Research Review: Ground-Based Nuclear Explosion Monitoring Technologies*, Vol. II, pp. 731−740.

Wilson, C.A., R.K. Grubbs, and S.M. George (2005). Nucleation and Growth during Al_2O_3 Atomic Layer Deposition on Polymers, *Chem. Mater*.**17,** 5625–5634.

Zaitseva, N., Carman, L., Glenn, A., Newby, J., Faust, M., Hamel, S., Cherepy, N., and Payne, S. (2011). *Application of solution techniques for rapid growth of organic crystals*, *J. Crystal Growth* **314**, 163−170.

Infrasound Monitoring

DEVELOPMENT AND VALIDATION OF INFRASOUND DATA PROCESSING ALGORITHMS

Stephen J. Arrowsmith[1], Rod W. Whitaker[1], Alexis Le Pichon[2], Yves Cansi[2], Nicolas Brachet[2], Maurice J. C. Charbit[3], Junghyun Park[4], Brian W. Stump[4] and Il-Young Che[5]

Los Alamos National Laboratory[1], CEA/DAM/DIF F91297 Arpajon France[2], Telecom ParisTech[3], Southern Methodist University[4], Korea Institute of Geoscience and Mineral Resources[5]

Sponsored by the National Nuclear Security Administration

Award No. DE-AC52-06NA25396/LA12-Signal_Analysis-NDD02

ABSTRACT

We report on progress in infrasound detection, association, and location algorithms for autonomous infrasound data processing and on the application of these techniques to both synthetic and real datasets. We highlight the latest version of *InfraMonitor* software with example results obtained using regional data. We next summarize a new framework that has been agreed upon by multiple institutions to validate such algorithms, focusing first on the detection problem. To this end, we outline a strategy for evaluating different detectors using Receiver Operating Characteristic (ROC) curves and summarize a new pseudo-synthetic dataset that is being developed to adequately capture real signals and noise in a controlled setting. Our experimental procedure is allowing us to properly calculate the probability of detection and the probability of false alarm using real-world data.

OBJECTIVES

The purpose of this effort is to rigorously evaluate and compare different infrasound data processing methodologies. Two complete autonomous systems for processing infrasound data exist at LANL and at CEA. Many institutions utilize components of these algorithms for infrasound data processing. For example, PMCC is widely used by a number of institutions worldwide, including the International Data Centre (IDC); *InfraMonitor* algorithms, developed under recent NNSA program funding, are currently being used by a number of institutions in the US community. This collaborative effort is motivated by the desire to compare existing methods in order to ultimately develop improved approaches that minimize the number of false alarms while ensuring that important events are not missed by automatic techniques. Here, we review the methodologies we intend to evaluate and, focusing on the detection problem initially, discuss a new framework for performing these evaluations in a systematic way.

RESEARCH ACCOMPLISHED

1. Infrasound data processing: Existing methodologies

1.1 Overview of LANL methods.

During the last five years at LANL we have been working on the development of an infrasound data processing system for automatically generating event catalogs using data from infrasound arrays. The focus of this effort has been on the application to regional monitoring scales using regional networks of infrasound arrays; however, the same techniques can be exported to global scale problems. The key methodology comprises an array-based signal detection method that uses an adaptive F-detector (AFD) (Arrowsmith et al., 2008), an association method that is based on a grid search technique (Arrowsmith et al., 2008), and a Bayesian infrasound source location technique (BISL) that appropriately accounts for model uncertainty (Modrak et al., 2010). Each algorithm continues to be developed and enhanced (see for example the paper by Marcillo et al., these Proceedings), and we plan to make a software package containing all the algorithms – *InfraMonitor* – available through the BSD Open Source license later this year. Here, these techniques are illustrated through application to an example event: the 26 January 2011 Sayarim explosion. This 76.8 ton explosion conducted in Israel was intended to contribute to the understanding of the infrasound propagation and improve International Monitoring Station (IMS) monitoring capabilities. It produced clear signals that have been recorded at regional and continental ranges up to a distance of 6266 km (Gitterman et al., 2011).

1.1.1 Station Processing. Nine hours of data from three IMS arrays, which were listed as detecting the event by the Reviewed Event Bulletin (REB) of the IDC, were processed using a single set of detection parameters developed for broadband data filtered from 0.5 – 5 Hz. The detections are shown in Figure 1; we note that H_0 is frequently violated at I31KZ. The only detection criterion used by AFD is the F-statistic. To avoid using an arbitrary threshold we utilize a p-value test based on the ambient background noise. Since the F-statistic follows a known statistical distribution, we can utilize a p-value test that controls the false alarm rate assuming the null hypothesis is an adequate representation of the background noise. The null hypothesis is automatically adapted to the background noise (Figure 2) by scaling the distribution by a constant (as shown by Shumway et al., 1999, the theoretical F-distribution for correlated noise is simply the standard F-distribution multiplied by a constant).

1.1.2 Categorization Algorithm. Given our background at LANL in processing data from relatively high-density, regional networks, the categorization algorithm used by *InfraMonitor* is relatively simple as compared with the CEA approach (see Section 1.2.2), which has been developed for processing sparse IMS events. *InfraMonitor* categorizes arrivals as either first arrivals ('I' phases) or later arrivals ('Ix' phases). Only I-phases are used in the subsequent network processing algorithms (we note that this approach is analogous to the metafamily approach used by CEA). We use two criteria to determine if an arrival is a first arrival: (1) arrival time – the difference in arrival time between any pair of arrivals from an individual event should be less than some threshold, $T_{\max}$ and (2) backazimuth – the difference in backazimuth between any pair of arrivals from an event should be less than some threshold, $\Delta\phi$. If an individual arrival is not associated with any preceding arrivals, it is automatically flagged as a first arrival ('I'). $T_{\max}$ can be empirically determined for each array from the predicted time difference between the fastest and slowest arrivals, taken for the most distant grid node from that array (where the grid is defined for network processing as discussed below). A limitation with this approach is that signals from sources repeating with intervals less than $T_{\max}$ become associated. There is only one free parameter that needs to be explicitly defined: $\Delta\phi$.

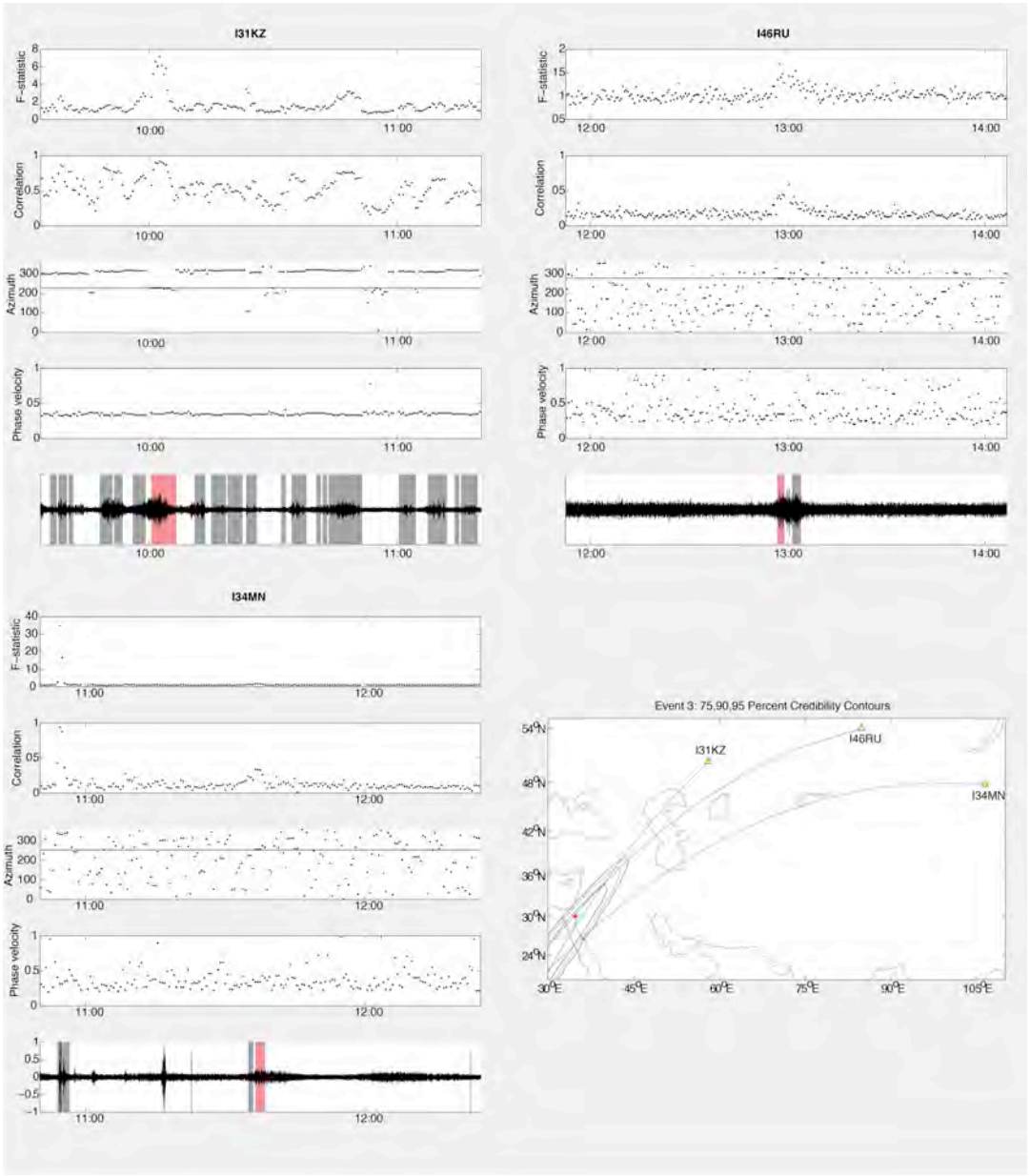


Figure 1. ***InfraMonitor*** **analysis of the January 26, 2011 Sayarim explosion. The top two panels and bottom left panel show the station processing results. Automatic detections are superimposed on the beamformed waveform as gray boxes (unassociated arrivals) and red boxes (associated arrivals). Great-circle backazimuths are represented on the azimuth panels as horizontal gray lines. The bottom right figure shows the Bayesian Infrasound Source location (BISL) location (75%, 90%, and 95% credibility contours) and ground-truth location (red star). The backazimuths of the measured signals at I31KZ, I46RU, and I34MN have not been corrected for wind bias. The localization uses a simple uniform prior PDF on group velocity with limits at 0.22 and 0.34 km/s. For each array the processing parameters are: Frequency band = 0.5-5 Hz, Time window = 60 s, Overlap = 50, p-value = 0.01.**

1.1.3 Network Processing. The association technique performs a grid search over the region of interest. For the Sayarim event we do a grid search over a large region (20-55°N, 30-110°E) using a grid spacing of 1 degree. For each grid node, great circle backazimuths in addition to minimum and maximum predicted delay times between each pair of arrays are calculated. Thus, for each grid node, we calculate $\mathbf{F} = \left[\phi_1, \phi_2, \ldots, \phi_n\right]$, $\mathbf{dT_{max}} = \left[\frac{(d_1 - d_2)}{0.22}, \frac{(d_1 - d_3)}{0.22}, \ldots\right]$, and $\mathbf{dT_{min}} = \left[\frac{(d_1 - d_2)}{0.34}, \frac{(d_1 - d_3)}{0.34}, \ldots\right]$ where there are n arrays and $\frac{n!}{2(n-2)!}$ elements in $\mathbf{dT_{max}}$ and $\mathbf{dT_{min}}$. Assuming appropriate uncertainties in backazimuth and arrival time, we search for groups of arrivals at all arrays that fit these predictions at any given grid node. For each grid node, the algorithm searches for groups of n arrivals where the set of delay-times (**dt**) lie within the minimum and maximum allowed bounds for the given grid node ($\mathbf{dT}_{\min}$ and $\mathbf{dT}_{\max}$) and where the set of backazimuths (Φ) are within $\pm\Delta\phi^{\circ}$ of the great-circle backazimuths (**F**) for the given grid node. A given event may be associated with a number of grid nodes, which map out the corresponding localization uncertainty region (this binary region is then refined and converted to gradational credibilities by BISL). The association scheme is iterative; first, detection pairs for each pair of arrays are associated, and then these are then merged for progressively higher numbers of arrays until no more array associations are found. We set a threshold for Sayarim that a minimum of three arrays must detect the event. Given these constraints, one event is found corresponding to the Sayarim event (Figure 3). We note, however, that for routine IDC processing, given the sparseness of the network, a threshold of two arrays is chosen.

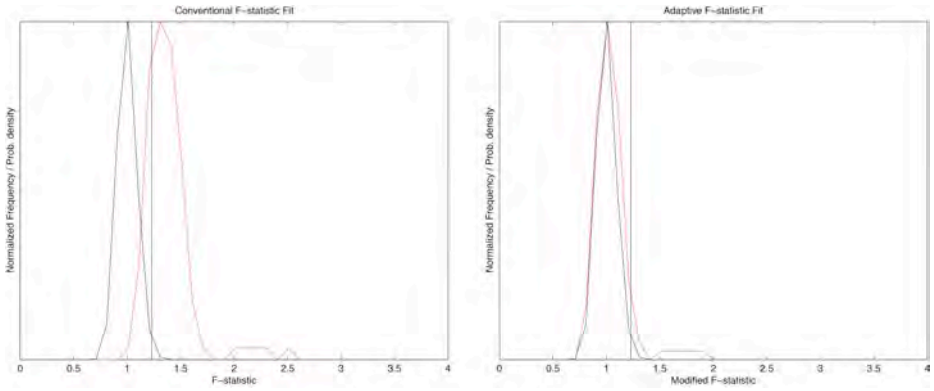


Figure 2. The AFD method adaptively updates the null hypothesis by scaling the calculated F-statistics by a constant such that the measured F-distribution (shown by the red curve) is appropriately scaled to account for correlated noise. Shown here are the comparisons between the measured and theoretical F statistics before scaling (left panel) and after scaling (right panel) for the Sayarim data at I34MN.

As the final part of our processing, the BISL technique is applied to events identified in the network association. This technique is described in detail in the accompanying paper by Marcillo et al. (2012, these Proceedings).

1.2 Overview of CEA methods.

For consistency with Section 1.1, this section presents infrasound algorithms leading to a complete processing flowchart that starts at the station level (signal detection and arrival categorization) and ends at the network level (arrival association and event building).

1.2.1 Station Processing. Progressive Multi-Channel Correlation (PMCC), originally developed by the CEA/DASE (Cansi, 1995), is an antenna technique that is commonly used by the scientific community for detecting coherent signals recorded on infrasound arrays. The processing is performed in consecutive frequency bands on a broad frequency spectrum typically between 0.02 and 4 Hz (standard frequencies recorded by IMS infrasound sensors), and adjacent time windows, to process signals of interest (e.g. Brachet et al., 2010). In 2004, the algorithm was implemented in the operational system of the International Data Centre (IDC) of the Comprehensive Nuclear-Test-Ban Treaty Organization (CTBTO). Since then, collaboration exchanges have continued between the IDC and CEA/DASE, and several changes have been made to enhance the PMCC source code and tune the

configuration parameters. PMCC uses correlation in the time domain to determine the time delays between sensors. The consistency $c_{ijk} = Dt_{ij} + Dt_{jk} + Dt_{ki}$ in time delays is the detection criterion. c_{ijk} values close to 0 (so called "closure relation") indicate a coherent wave front propagating across the array of sensors; this contrasts with noise which leads to a nearly-random set of time-delays. In order to mitigate the risk of aliasing, a progressive computation of consistency is implemented. PMCC initiates the detection processing with sub-arrays of close enough sensors. More distant sensors are progressively incorporated into the solution, by searching the local maximum of cross-correlation guided by predicted time delays. Finally, a grouping algorithm (so called "family grouping") highlights stable parts of the signal by gathering elementary detections that have similar characteristics in time, frequency, azimuth and slowness. PMCC parameters must be optimized to obtain a reasonable compromise between detection and false alarm levels. The duration of the processing window as well as the bandwidths depend on the frequency. A new implementation of the PMCC algorithm allows the full frequency range of interest (0.02-4 Hz) to be processed efficiently in a single computational run. It benefits from the implementation of an adaptive processing window duration and log-spaced frequency bands (Le Pichon et al., 2010). Figure 3 shows an example of PMCC processing of signals produced by the M9.0 Japan earthquake of March 11, 2011 and recorded by the IMS station IS30 near Tokyo. Situated 385 km away from the epicenter, the array clearly recorded seismic arrivals from the main shock (group 1) and series of aftershocks (group 3) identified by high velocity values. The recordings also show late arrivals (group 2) corresponding to ground-to-air coupled infrasound signals diffracted by high mountain ranges. Infrasound signals produced by a large fire which occurred at the Ichihara oil refinery are also well detected between 07:40 and 10:15 UT (group 4).

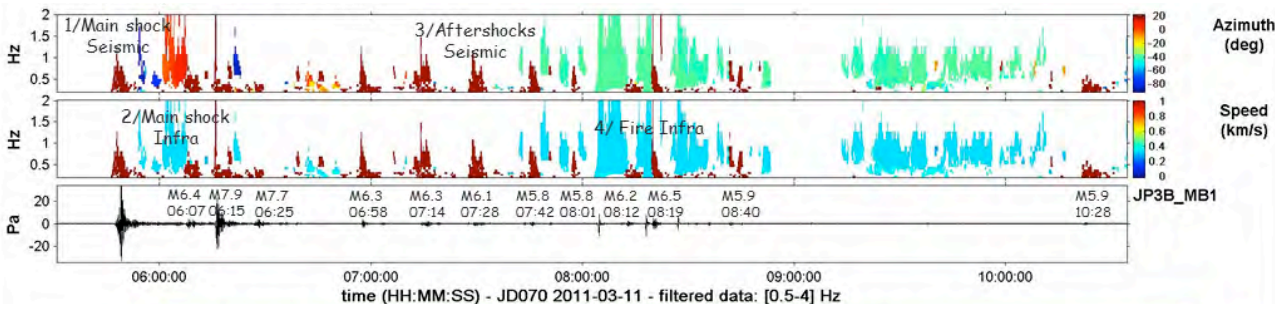


Figure 3. PMCC processing results at IMS station IS30 (Japan) in the 0.02-2 Hz log-scaled band.

1.2.2 Categorization algorithm. Categorization has a direct impact on the event building. Before associating signals, it is important to remove detections that are not of interest (categorized as "noise"). Detections falling in the noise category are typically associated to long duration phenomena – e.g., microbaroms, industrial or surf noise, high-frequency transient signals related to local sources (thunderstorms, quarry blasts). CEA/DASE has been using a categorization procedure that is similar to the one that is implemented at the IDC (Brachet et al., 2010). However, the method sometimes exhibits some limitations in categorizing microbaroms. If too many noise detections are retained, the number of combinations in the association algorithm dramatically increases with higher probability of false associations leading to bogus events. On the other hand, detections incorrectly tagged as noise, subsequently discarded by the association process, may lead to missed events.

The IDC categorization method uses a "cleaning" strategy at two levels:

- Single detection review: local sources are removed (detections with a dominant frequency greater than 2 Hz; signal duration below 50 s; horizontal trace velocities outside the typical range for long propagation range, 0.3 to 0.45 km/s), and
- Metafamily review: metafamilies are clusters of detections that have similar characteristics in azimuth, trace velocity, frequency and time. Threshold values may be configured according to the sensitivity of each array to their respective environment. Long duration clusters, typically more than 1800 s, are likely related to recurrent sources of signals and therefore categorized as noise. For typical IMS infrasound stations, about 85% of the detections are categorized as noise and therefore discarded in the subsequent network processing stage.

A new algorithm has been recently developed at the CEA/DASE in order to improve the metafamily review. This method filters out 85 to 95% of the detections (mainly microbaroms and local industrial activity) from the bulletins, and the remaining detections are kept as inputs for network processing. Whereas the IDC procedure uses fixed threshold values adapted to each station, this new statistical approach is able to adapt automatically to the data. This

allows one to significantly reduce the number of configuration parameters. The main assumption relies on the normal distribution and the independence of the azimuth and frequency detection parameters associated to the noise sources (Le Pichon et al., 2011).

1.2.3 Network Processing. The phase association procedure is based on a uniform atmosphere assuming a constant celerity equal to 0.3 km/s, typical of infrasonic waves propagating in the ground to stratosphere waveguide (Brown et al., 2002). The event building follows a systematic exploration of all possible associations obtained by cross bearing between categorized detection bulletins, satisfying a geophysical criterion based on the used velocity model. The quality of each association is quantified by two scores: the "geophysical" and "signal" scores. The geophysical score is a measure of the gap between the calculated celerities and the initial velocity model. The signal score quantifies the consistency of the signal features relatively to the pre-location obtained by cross bearing, in term of detected mean frequency (Brachet et al., 2010). On-going studies implement other signal features such as peak-to-peak amplitudes and detection durations but still need to be validated. The pre-location is calculated assuming a point-like source and using multi-station measurements where both onset time and back-azimuth are taken into account. The location is initiated by cross bearing, and iteratively modified using a non-linear iterative least squares inversion scheme. In case of conflict (one arrival at one station can be associated to more than one arrival at the other stations), the number of stations and/or the score (in case of equality) decides between all candidates. In order to take into account errors in the origin time estimates due to location uncertainty (because of azimuth deviation added to measure uncertainties) and additional propagation types (e.g. stratospheric and thermospheric), the score thresholds are adjusted to decrease the missed-event rate. Figure 4 presents an example of the 2009 Sayarim calibration event reviewed by the Netinfra interactive tool developed by CEA/DASE. Here, recordings of 12 infrasound stations in central Europe and Middle East are associated to locate the explosion. The analysts use Netinfra to interactively check and revise all the different stages of the automatic event building, from the detection to the location, including the categorization. Information about the atmospheric conditions (stratospheric wind speed and direction) and network detection capability is provided to help in the decision to validate/reject automatic events. Finally, the event is relocated using travel-time curves and azimuthal corrections obtained by tau-p ray-tracing method (Garcés et al., 1998) through realistic European Centre for Medium-Range Weather Forecases (ECMWF) atmospheric specifications (www.ecmwf.int).

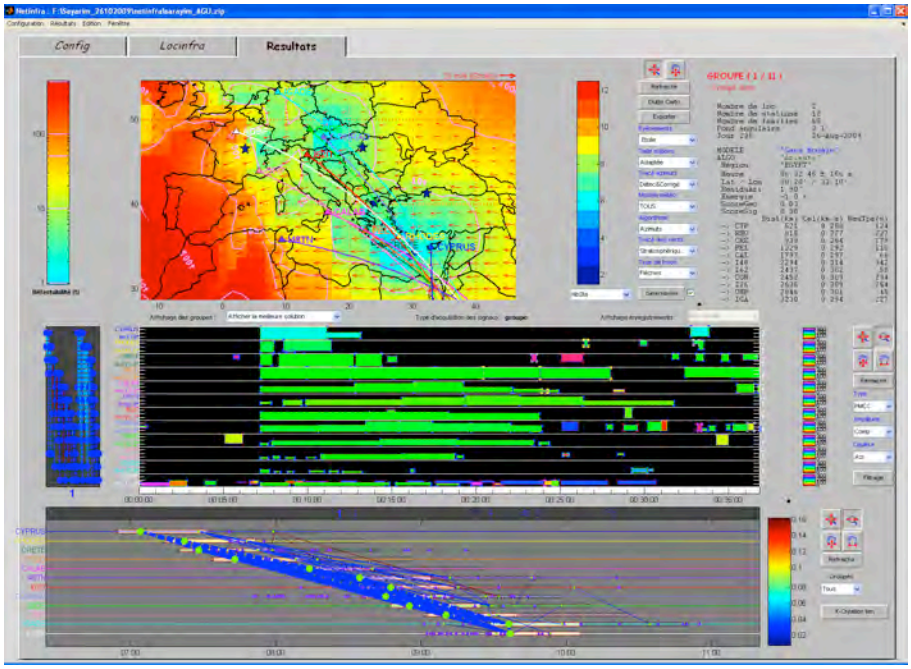


Figure 4. Example of processing an event using the Netinfra interactive tool. The upper panel shows the minimum detectable energy predicted at the time of the event using the LANL empirical yield-amplitude scaling relationship (Whitaker et al., 2003) with two-station coverage. The panel in the middle presents the PMCC detections in the time-frequency domain aligned on relative time-scale. The lower panel details the detections that have been associated as well as "noise" detections rejected by categorization.

2. Assessment and validation of methods

We have begun a collaborative effort to rigorously evaluate and compare the different station processing, categorization, and network processing methods discussed above. The first component of this evaluation focuses on the station processing. Sections 2.1 to 2.5 below outline a preliminary study to evaluate different detectors through the construction of Receiver Operating Characteristic (ROC) curves. While this study focuses on a more limited and idealized scenario, it does provide the basic formalism that will be used for the evaluation of infrasound detectors using suites of realistic signal and noise sequences, as discussed in Section 3.

2.1 Summary of overall goal to assess detection algorithms. One of the main issues is to detect the incoming signal and estimate its direction of arrival (DOA), which comprises both backazimuth and inclination angle. A detection procedure is characterized by a binary test that takes the value 0 or 1, depending whether the signal of interest (SOI) is absent or present. In addition to the AFD and PMCC methodologies (presented above), other methods include the maximum cross-correlation mean (MCCM) (Wilson et al., 2003), the Fisher statistic (Shumway, 2001; 2006) and the Generalized Likelihood Ratio Test (GLRT) (Charbit et al., 2012). To compare test performances, the standard way is to compute their Receiver Operating Characteristic (ROC) curves, which give the true detection probability as a function of the false-alarm probability. In most cases, no closed form expressions of these probabilities are available. Therefore, typically the evaluation protocol are based on simulated data. In Section 2.2, a signal model is first presented by considering plane wave propagation through a non dispersive channel with additive gaussian noise. Then, in Sections 2.3 – 2.5 the GLRT is derived and compared to other decision rules in term of ROC curves.

2.2 Signal model. We consider a station with *M* sensors and one signal of interest (SOI). It is assumed that the source is far enough from the station to consider the propagation of a planar wavefront. In the first stage, a distortionless propagation channel is assumed. Therefore, to reconstruct signals at all array elements, the SOI can simply be time delayed, applying an arbitrary attenuation factor and additive noise. Under these conditions, the signal on sensor m can be written as

$$x_m(t) = g_m s(t - \tau_m(\theta)) + b_m(t) \tag{1}$$

where $s(t)$ denotes the SOI and g_m the attenuation factor of the sensor. The delay

$$\tau_m(\theta) = \frac{1}{c}(-p_{m,1}\sin(a)\cos(e) + p_{m,2}\cos(a)\cos(e) + p_{m,3}\sin(e))$$

is related to the sound velocity *c*, to the 3D-location $(p_{m,1}, p_{m,2}, p_{m,3})$ of the sensor *m* in a given coordinate system (e.g. the sensor 1 can be chosen at the origin) and to the DOA characterized by the couple $\theta = (a, e)$, where $a \in (0, 2\pi)$ and $e \in (0, \pi/2)$ are the back-azimuth and inclination angle, respectively. $b_m(t)$ represents a gaussian, stationary, zero-mean, white, additive noise.

2.3 Maximum Likelihood function. One of the most frequently used model based approach in signal processing is the maximum likelihood (ML) technique. This approach requires a statistical framework for the data generation process. Two different assumptions about the source signal are usually considered: the deterministic ML and the stochastic ML, depending on whether *s* is assumed to be deterministic or random (Capon, 1969; Krim and Viberg, 1996). Here, we consider the stochastic model and assume that $s(t)$ is a zero-mean, gaussian stationary random process. $b(t)$ and $s(t)$ are assumed to be statistically independent.

The observed signals are sampled at $F_s = 1/T_s$. In the following, *N* denotes the number of observations. For a given value of the couple $\theta = (a, e)$, we let $x_{m,n}(\theta) = x(nT_s + \tau_m(\theta))$, i.e. the sampled version of $x_m(t)$ delayed by $-\tau_m$ which can be performed from the sequence $x_m(nT_s)$ thanks to the interpolation formula. By concatenation, we write the associated length-*M* vector $x_n(\theta) = \left[\begin{array}{ccc} x_{1,n}(\theta) & \ldots & x_{M,n}(\theta) \end{array} \right]^t$.

From equation (1) we can write:

$$x_n(\theta) = g s_n + w_n \tag{2}$$

where $s_n = s(nT_s)$, $g = \begin{bmatrix} g_1 & \dots & g_M \end{bmatrix}^t$ and $w_n = \begin{bmatrix} w_1(nT_s) & \dots & w_M(nT_s) \end{bmatrix}^t$ with $w_m(t) = b_m(t+\tau_m)$. Using the previous assumption, we have $E\left[s_n^2\right] = s^2$ and $E\left[w_n w_n^t\right] = \sigma^2 I_M$. We assume that s^2 and σ^2 are unknown. Therefore the log-likelihood associated to these N observations is

$$\ell(\mu) = -\frac{1}{2} M \log(2\pi) - \frac{1}{2} M \log(\sigma^2) - \frac{1}{2}\log(1 + s^2/\sigma^2) - \frac{1}{2\sigma^2}\mathrm{Tr}\left[R_N(\theta)\right] + \frac{1}{2\sigma^2}\frac{s^2}{\sigma^2}\frac{g^t R_N(\theta) g}{1 + s^2/\sigma^2} \tag{3}$$

where

$$R_N(\theta) = \frac{1}{N}\sum_{n=1}^{N}(x_n(\theta) - \overline{x})(x_n(\theta) - \overline{x})^t \tag{4}$$

with $\overline{x} = N^{-1}\sum_{n=1}^{N} x_n(\theta)$ and

$$\mu = \left\{\theta, s^2, g, \sigma^2\right\} \in M = (0, 2\pi) \times (0, \pi/2) \times R^+ \times G \times R^+ \tag{5}$$

Because both s^2 and g are unknown, in the presence of SOI, $g^t g = 1$, unless $g = \vec{0}$ where $\vec{0}$ denotes the null vector. In conclusion, $G = \{g \in R^M : \text{s.t. } g^t g = 1\} \cup \{\vec{0}\}$. Often in statistics, θ is called the parameter of interest (POI) whereas σ^2, s^2 or g are considered as nuisance parameters.

2.4 Generalized Likelihood Ratio Test. A detection processing method consists of a critical function of the observations taking the values 0 or 1. To build such functions from a statistical model, we consider the H_0 hypothesis defined as any non-empty subset of the parameter set. In this study H_0 denotes the subset characterized by *at least one sensor only receives noise*. The counter-hypothesis H_1 indicates that all sensors receive the SOI. Mathematically, H_0 is

$$H_0 = \left\{\mu \quad s.t. \quad g \in \Gamma_0\right\} \tag{6}$$

where Γ_0 is the subset of G where g has at least *one null component*. The critical function of the generalized likelihood ratio test (GLRT) is defined by

$$T : \text{signal} \mapsto \max_{\mu \in M} \ell(\mu) - \max_{\mu \in H_0} \ell(\mu) \tag{7}$$

and the one-sided test consists in deciding

$$\begin{cases} H_0 & \text{if } T \le \eta \\ H_1 & \text{if } T > \eta \end{cases}$$

where η is a given threshold value. The performances of the test are commonly characterized by the ROC curve which gives the detection probability as function of the false alarm probability. We denote by P_0, respectively P_1, the probability distribution of the scalar statistic T given H_0, respectively H_1. For a one-sided test, the false alarm probability is

$$P_{fa} = \int_{\eta}^{+\infty} P_0(dt) \tag{8}$$

and the detection probability

$$P_d = \int_{\eta}^{+\infty} P_1(dt) \tag{9}$$

When η goes from $-\infty$ to $+\infty$, the couple (P_{fa}, P_d) describes the ROC curve. This curve is always above the diagonal line. The closer to the point the ROC curve is, the better is the test.

In the following, we have only implemented (7) for *M=3*. We have also considered the F-statistic of Fisher (Shumway, 2001; Blandford, 2002; Arrowmith et al., 2008)

$$F : \text{signals} \mapsto \frac{u^t \hat{R}_N u}{\text{Tr}\left[\hat{R}_N\right]} \tag{10}$$

where $\hat{R}_N$ is the covariance matrix of the time-aligned signals (delays are obtained by intercorrelation maximization). The expression (7) is different to (10) for at least two reasons: (i) F-statistic corresponds to the case where all components of g are either 0 or 1, (ii) the covariance matrix in (7) is derived from the maximization with respect to θ and hence is different to the covariance matrix in (10) where no constraint is imposed on the delays given the geometry of the sensor locations. We have also consider the statistic *MCCM* whose expression is given by

$$C : \text{signals} \mapsto (C_{12} + C_{13} + C_{23})/3 \tag{11}$$

where C_{ij} is the maximum of intercorrelation between signals $x_i(t)$ and $x_j(t)$. We notice that, if the SOI is present on all sensors without noise, $C = 1$. On the other hand, a small value of C indicates a likely absence of the SOI on one of the three sensors (H_0 hypothesis).

2.5 Preliminary synthetic dataset. Simulations have been carried out with the following evaluation protocol: the station consists of three sensors located at the vertices of an equilateral triangle within a circle of radius 200 m. A reference signal is selected at one sensor of the IMS station IS31 (Kazakhstan). This continuous signal is produced by flares from gas and oil fields about 200 km south of the station. The signal has been sampled at 20 Hz. Taking into account the frequency band of the SOI, a 0.5-4 Hz pass-band filter (Chebyshev, order 4) is applied to the recordings. Time windows are 10 s in duration. Signals are delayed with respect to the sensor locations and the selected parameters. They are multiplied by some chosen gains and embedded in additive noise provided by a pseudo-random generator with a gaussian white spectral distribution. The gain of each sensor is determined so that the SNR has a fixed given value in the frequency bandwidth from 0.5 to 4 Hz. The signal should be time shifted with a sufficiently high precision in order to minimize delay quantization which may introduce bias in the estimator. To delay the signal, we can either (i) interpolate the signal with a sufficiently high sampling rate, then shift it with the appropriate integer value of sampling period, and decimate it, or (ii) use the interpolation formula to reconstruct the true delay. In the simulations, we have considered ~10,000 windows of 10 s for each hypothesis. In this context, we have calculated the ROC curves for the three tests, given by the expressions (7), (10) and (11). The results are reported in Figure 5. The curve labelled 'Fisher-Scov' is related to the expression (10) where we have replaced the covariance matrix by taking into account the geometrical constraint. To quantitatively compare these curves, we may consider the area under the ROC curve (AUC) of the intersection with the bisectrix giving the Equal Error Rate (EER). As expected, the GLRT works better than the two other tests. The F-statistic seems to provide better results than the MCCM based test for the semi-synthetic signals which are used. However, if we take into account the calculation load, the best trade off seems to be given by the F-statistic.

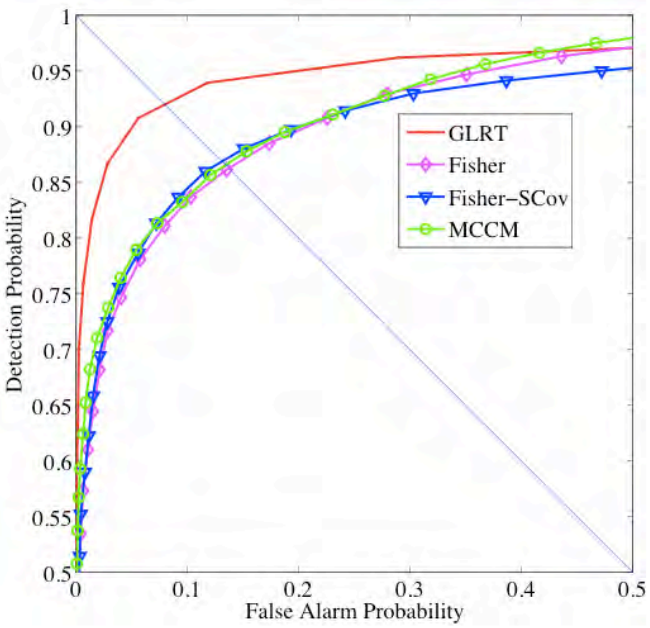


Figure 5. ROC curves for the different tests.

3. Future Work

In the numerical experiments presented here, the reference signal is delayed assuming a perfect propagating planar wavefront in order to construct signals at all array elements of any arbitrary station. However, such an approach has clear limitations due to the lack of realistic propagation model. A compromise approach where we can control signals and noise, and also array configuration using real world examples should be considered. We propose to develop a realistic dataset comprising representative examples of signals and noise. The following scenarios would allow multiple possibilities of experiments where true detections and false alarms rate could be calculated:

- Use one reference signal at one sensor and construct other signals by delaying it assuming planar wave propagation given any array configuration and wave parameters, and add an empirical transfer function between two sensors such like the one proposed by Mack and Flinn (1971),
- Use records and noise sequences for all sensors at a specific array (real propagation effects are considered); such a scenario will not allow exploring different array configurations and wave parameters.

By combination of signal and noise sequences, a pseudo-synthetic dataset will thus be constructed with different array configurations, SNR, wave parameters. Different types of reference signals (transient, long duration, emergent, etc.) and noise (correlated or not, stationary or not) will allow exploring many representative situations. Reference signals will come from the IRED dataset of the CTBTO, the DTRA Ground-truth database in addition to datasets at LANL, CEA, SMU, and KIGAM. ROC curves will then be calculated using these dataset for the detection methods described above.

Regarding association methods, we propose to test different association techniques using a similar ROC curve approach. Such comparisons will be done on both (i) synthetic and (ii) real datasets (e.g., the Infrasound Reference Event Database (IRED) of the IDC or the UTAH event lists).

(i) Both repeating source and station configurations (number and coordinates) can be specified. Sources could generate signals at a random set of stations. Uncertainties in the propagation models are perfectly controlled (errors in azimuths and travel times). This exercises should be done separately for regional and global scales.

(ii) For IRED and UTAH event lists, we can distribute the origin times into different time periods in order to assess the robustness of the association procedures.

For the location, we propose to work on better characterizing both prior probabilities for propagation models. The dataset (i) and (ii) could be used as a test-bed for assessing location, accuracy and precision.

CONCLUSIONS AND RECOMMENDATIONS

The work presented in this paper represents the beginning of a multi-institution effort to rigorously evaluate different infrasound data processing methodologies. This paper has outlined some of these techniques and also laid out the basic framework that will be used to quantify different methodologies. This paper represents a starting point for the evaluation of our different techniques using representative signals and noise.

REFERENCES

Arrowsmith, S. J., R. Whitaker, S. R. Taylor, R. Burlacu, B. Stump, M. Hedlin, G. Randall, C. Hayward, and D. ReVelle (2008). Regional monitoring of infrasound events using multiple arrays: application to Utah and Washington State, *Geophys. J. Int.* **175**, 291–300.

Blandford, R. (2002). Detection and azimuth estimation by infrasonic arrays as a function of array aperture and signal coherence, Air Force Technical Applications Center.

Brachet, N., D. Brown, R. Le Bras, P. Mialle, and J. Coyne (2010). Monitoring the Earth's atmosphere with the Global IMS Infrasound Network, in *Infrasound Monitoring for Atmospheric Studies, Springer Geosciences*, ISBN: 978-1-4020-9507-8, 745 p.

Brown, D. J., C. N. Katz, R. Le Bras, M. P. Flanagan, J. Wang, and A. K. Gault (2002). Infrasonic signal detection and source location at the Prototype International Data Centre, *Pure Appl. Geophys*. **159**, 1081–1125, DOI: 10.1007/s00024-002-8674-2.

Cansi, Y. (1995). An automatic seismic event processing for detection and location: The PMCC method, *Geophys. Res. Lett.* **22**, 1021–1024.

Capon, J. (1969). High-Resolution frequency-wavenumber spectrum analysis, in *Proceedings of the IEEE*, **57**(8).

Charbit, M., P. Gaillard, and A. Le Pichon (2012). Evaluating the performance of infrasound detectors, European Geosciences Union General Assembly 2012, abstract EGU2012-7350, 22-27 April 2012, Vienna, Austria.

Garcés, M. A., R. A. Hansen, K. Lindquist (1998). Travel times for infrasonic waves propagating in a stratified atmosphere. *Geophys. J. Int.* **135**, 255–263.

Gitterman, Y., J. Given, J. Coyne, R. Waxler, J. Bonner, L. Zerbo, and R. Hofstetter (2011). Large-scale controlled surface explosions at Sayarim, Isarael, at different weather patterns, for infrasound calibrations of the International Monitoring System, in *Proceedings of the 2011 Monitoring Research Review: Ground-Based Nuclear Explosion Monitoring Technologies*, LA-UR-11-04823, Vol. 2, pp. 766–777.

Krim, H. and M. Viberg (1996). Two decades of array signal processing research: The parametric approach, in *IEEE Signal Process. Mag.* **13**, 67–94.

Le Pichon, A., R. Matoza, N. Brachet, and Y. Cansi (2010). Recent enhancements of the PMCC infrasound signal detector, *Inframatics Newsletter*, **26**, www.inframatics.org.

Le Pichon, A., J. Vergoz, N. Brachet, P. Gaillard, Y. Cansi, and J. Guilbert (2011). A description of the infrasound data processing at the French CEA/DASE, in *Proceedings of the 2011 Monitoring Research Review: Ground-Based Nuclear Explosion Monitoring Technologies*, LA-UR-11-04823, Vol. 2, pp. 787–797.

Mack, H. and E. A. Flinn (1971). Analysis of the spatial coherence of short-period acoustic-gravity waves in the atmosphere, *J. Geophys. Int.*, DOI: 10.1111/j.1365-246X.1971.tb03399.x.

Marcillo, O., S. Arrowsmith, R. Whitaker, and D. Anderson (2012). Enhancements to the Bayesian infrasound source location method, these Proceedings.

Modrak, R. T., S. J. Arrowsmith, and D. N. Anderson (2010). A Bayesian framework for infrasound location, *Geophys. J. Int.*, doi: 10.1111/j.1365-246X.2010.04499.x.

Shumway, R. H., S-E. Kim, and R. R. Blandford (1999). Nonlinear estimation for time series observed on arrays, in *Asymptotics, Nonparametrics and Time Series*, Ghosh, S. (Editor), Marcel Dekker, New York.

Shumway, R. H. (2001). Detection and location capabilities of multiple infrasound arrays, in *Proceedings of the 23rd Seismic Research Review: Worldwid Monitoring of Nuclear Explosions*, LA-UR-01-4454, Vol. 1, pp. 160–167.

Shumway, R. H. (2006). Advances in mixed signal processing for regional and teleseismic arrays, in *Proceedings of the 28th Seismic Research Review: Ground-Based Nuclear Explosion Monitoring Technologies*, LA-UR-06-5471, Vol. 1, pp. 503–509.

Whitaker, R. W., T. D. Sandoval, and J. P. Mutschlechner (2003). Recent infrasound analysis, in *Proceedings of the 25th Seismic Research Review—Nuclear Explosion Monitoring: Building the Knowledge Base*, LA-UR-03-6029, Vol. 2, pp. 646–654.

Wilson, C. R., J. V. Olson, D. L. Oborne, and A. Le Pichon (2003). Infrasound from Erebus Volcano at I55US in Antarctica, Inframatics Newsletter, www.inframatics.org.

SEISMIC AND INFRASOUND STUDIES CARRIED OUT AT THE INSTITUTE OF GEOPHYSICAL RESEARCH OF KAZAKHSTAN IN COOPERATION WITH US NATIONAL DATA CENTER

Nadezhda N. Belyashova[1], Shirley Baher[2], Natalya N. Mikhailova[1], Zlata I. Sinyova[1], Aleksandr A. Smirnov[1], and Aleksandr E Velikanov[1].

Institute of Geophysical Research of Kazakhstan[1] and the Air Force Technical Applications Center[2]

ABSTRACT

For several years, the Institute of Geophysical Research of Kazakhstan has carried out scientific studies related to nuclear monitoring activity. These studies include the following:

a) Analysis of characteristics of the new seismic arrays ABKAR and KKAR. During the study we estimated azimuth and slowness residuals for the regional (Pn, Pg, Sn, Lg) and teleseismic (P) phases, as well as filters, producing the best array gain and signal to noise ratio for ABKAR array.

We also compared time residuals observed at ABKAR and KKAR arrays during location of regional events with different regional and global velocity models.

b) Compilation of the ground truth database of the mining/quarry explosions. During works on this project, field trips were made to collect information on industrial blasts in the Western Kazakhstan, Southern Kazakhstan and in the area near the Semipalatinsk test site. These trips allowed us to identify the active quarries, underground mine workings and other units at which industrial explosions are conducted. Location and coordinates of active quarries and underground mine workings were compiled in the table format.

c) Development of techniques of quarry blasts localization accuracy enhancement by fusing infrasound and seismic data. Long-term investigations of the seismic signals caused by explosions in quarries in Western Kazakhstan show that due to the large number of different active quarries in this region, correct and accurate identification of the quarry where explosion was made basing on seismic data only was not always possible. To enhance the localization accuracy, we suggested the use of additional source of information, i.e., the data received from IS31 infrasound array. In our study we demonstrated the enhancement of mining explosion location accuracy after adding infrasound data to seismic ones.

RESEARCH ACCOMPLISHED

Introduction

Three seismic arrays—Makanchi, Karatayu, and Akbulak—were constructed and put into operation on the territory of Kazakhstan since 1999. Makanchi station is included into the primary stations network of the International Monitoring System. These stations transmit data to the USNDC and KNDC in real time. During last years, KNDC conducts some investigations under financial support and by order of Air Force Research Laboratory aimed at enhancing of seismic monitoring efficiency. The investigations had different tasks to be solved. Seismic part of the investigations included the study of characteristics of two new seismic arrays: ABKAR and KKAR. For the ABKAR array in particular, we estimated azimuth and slowness residuals for the regional (Pn, Pg, Sn, Lg) phases, as well as filters, producing the best array gain and signal to noise ratio. Using data of KKAR array, comparison of localization accuracy of regional seismic events with different regional and global velocity models was conducted. For the IS31 infrasound station, a technique of its infrasound data integration with seismic data of Akbulak array was developed to enhance localization accuracy of blasts sources at a quarry. The third part of investigations is connected with information acquisition about ground-truth explosions at quarries which will make identification of recorded events nature more reliable. Below are brief results on three directions of the investigations.

1. Analysis of Some Characteristics of the New Seismic Arrays ABKAR and KKAR

1.1. Estimation of Azimuth and Slowness Residuals for the ABKAR Array

ABKAR array was installed in 2003. It is located in the western part of Kazakhstan (see Figure 1). ABKAR array has nine vertical seismometers and one three-component seismometer. Diameter of the array is about 4 kilometers. Since ABKAR is the new array, the following information about this array is necessary to be determined, in order to use this array effectively during seismic data analysis.

First, what kind of filters are preferred during processing of various regional phases and what kind of filters are preferred during processing of teleseismic phases from events occurred in different regions of the world?

Second, how much can we trust f-k analysis during determination of azimuth and slowness of signal? It is known that some seismic arrays have so large deviations in azimuth determination and especially slowness of signal that these parameters can not be used during location of events.

On the first stage of the work, the database of regional events was created on the basis of the following catalogues: regional seismic catalogue of the Institute of Seismology of Kazakhstan, seismic catalogue of the Seismological Bureau of Xinjiang (China), catalogue of the GS RAS (Russia), bulletin IDC REB. The following time period was used: January 1, 2004–August 1, 2004. The map of selected events is shown in Figure 1.

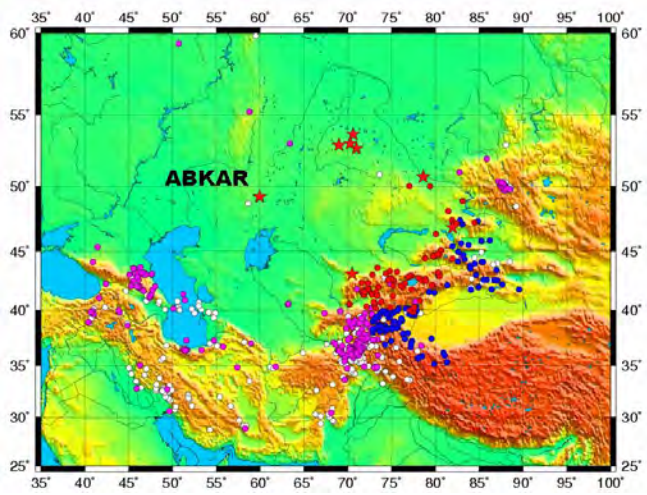


Figure 1. Map of the regional events database. red circles—events from KazIS catalogue (68 events); blue circles—events from China catalogue (123 events); magenta circles—events from GSE Russia catalogue (250 events); white circles—events from REB (IDC Vienna) catalogue (322 events).

Signal to noise ratio, array gain, azimuth residuals and slowness residuals for each filter were computed for each of the selected phases: The following set of filters was used:

0.2–2 Hz ; 0.2–5 Hz ; 0.5–1.5 Hz ; 0.5–2.0 Hz ; 0.6–3.0 Hz; 0.6–4.5 Hz; 0.75–2.25 Hz; 0.8–5.0 Hz ; 1.0–2.0 Hz; 1.0–2.5 Hz; 1.0–3.0 Hz; 1.0–4.0 Hz; 1.0–5.0 Hz; 1.5–3.0 Hz; 2.0–4.0 Hz; 2.0–5.0 Hz; 3.0–6.0 Hz; 4.0–8.0 Hz.

Azimuth and slowness of the signals were computed by the f-k analysis using the EP program (NORSAR). Azimuth and slowness of the signals were computed for every one out of 18 filters . In addition, we used three different time windows. For regional phases we used 3 seconds, 4 seconds and 5 seconds time windows.

We summarize the obtained results for each of the regional phases of the study below.

Pn Phase.

The total number of 422 Pn phases were associated from the regional events database. The best array gain and highest signal/noise ratio are observed for filter at 1.5–3.0 Hz. Constant azimuth residuals were not revealed. Systematic negative deviation of slowness of about -1 s/deg is observed.

After that the maps of azimuth residuals (Figure 2a) and slowness residuals (Figure 2b) were plotted. Data for these maps were prepared in the following way. The region around ABKAR array was divided on squares with the size 0.5x0.5 degrees. After that, for each of these cells we determined median value of azimuth (for the map on Figure 2a) or slowness (for the map on Figure 2b) residuals among all events, which fall into this cell. This operation was made in order to reveal systematic deviations in the spatial distribution of azimuth and slowness residuals. Similar maps we plotted for all other regional seismic phases.

Looking at the map of slowness residuals, we can see for event coming from Hindu Kush and Caucasus areas significantly low values of observed slowness if compare with theoretical ones, and close to the slowness of the P wave. Azimuth residuals are less distinctive. However, there are significant negative azimuth deviations in the area of Caspian Sea.

a) map of spatial distribution of azimuth residuals

b) map of spatial distribution of slowness residuals

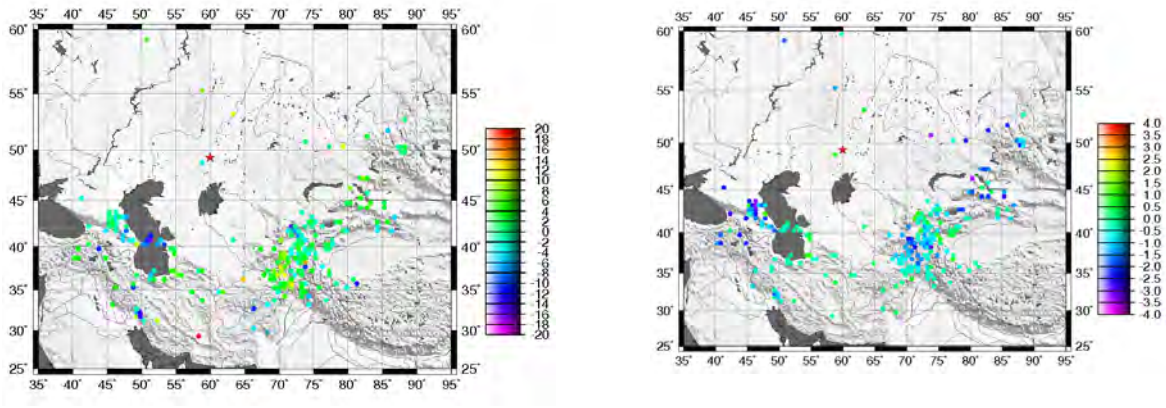


Figure 2. Spatial distribution of azimuth (a) and slowness (b) residuals.

Sn Wave

308 Sn phases were associated with events from regional events database. The best array gain is observed for filter at 1.0–5.0 Hz and 1.0–2.0 Hz. The best signal/noise ratio is observed for 1.5–3.0 Hz filte. Insignificant (about 2 degrees) constant positive azimuthal deviation is observed. Constant negative deviation of slowness which varies for different filters from -1.5 to -2 s/deg was revealed.

Maps of azimuth and slowness residuals were computed in the same way, as for the Pn phase. Filter 1.0–5.0 Hz, 4 seconds time window were applied during computation of azimuth and slowness by the f-k analysis.

For slowness residuals, we also observed significant negative values (which means higher apparent velocities) in the Caucasus area, similar to the slowness residuals of the Pn wave. However, the area of negative residuals for the Hindu Kush events is located farther from the station, than that for the Pn wave slowness residuals.

Lg Wave

There are 55 Lg phases associated with events from the regional events database. For Lg waves, the best signal-to-noise ratio is observed for filter at 1.0–2.0 Hz. The best array gain is observed for the filter at 1.0–5.0 Hz. Systematic azimuthal deviations were not revealed. However, systematic and significant deviations of slowness were observed, about -4–5 s/deg for various filters. In addition, slowness values show large scattering. Thus, it is recommended to avoid using Lg waves during processing of regional events for the ABKAR station.

P Phase

There were 92 P phases associated with the events from the regional events database. The best array gain was observed at filter 1.5–3.0 Hz. The best SNR values were also observed at filter 1.5–3.0 Hz. Significant systematic azimuth residuals were not observed. However, .moderate systematic negative deviation of slowness of about -1 s/deg is observed. For P waves, we did not observe any systematic spatial variations of azimuth and slowness residuals.

S Phase

The total number of 70 S phases were associated. The best array gain was observed on filter 1.0–5.0 Hz. The best SNR was observed at filter 1.0–2.0 Hz. Moderate positive azimuth deviations (about 8 degrees) were observed. Slowness deviations are strongly dependent on the filters applied. In general, medians of slowness residuals have small negative values, about -0.3–0.6 s/deg, depending on filter.

1.2. Comparison of Different Velocity Models for the KKAR Array

Karatayu seismic array is located in southern Kazakhstan. This region is characterized by high seismic activity. On the basis of conducted researches three seismic regions (Central, Eastern, and Southern Kazakhstan) for which generalized 1-D velocity models were constructed were defined (see Figure 3).

Region I. – covers the territory of Central, Eastern and South-East Kazakhstan. Tectonically, this region is represented by southern platform part of Eurasian plate with Kazakh shield in the center. As for velocity characteristics the crust is typical for platform areas. Figure 3a shows velocity model kaz1 constructed for this region (in grey color).

Region II. – borders in the south to region I and is represented by the crust of highly seismic Central Asian Tien Shan including Northern Tien Sha. For this region kaz2 model was constructed (shown in Figure 3b).

Region III – territory of Central Kazakhstan on the transfer zone from Kazakh shield to Torgay depression. Figure 3c shows kaz3 model constructed for this region.

In addition, it was decided to use velocity model constructed by IGR NNC RK staff on the basis of data from chemical calibration explosions conducted on the territory of Semipalatinsk Test Site in 1997 – 2000 [1,2]. This velocity model in Figure 3 is marked with blue color. Hereinafter this model is named kaz_calib.

In addition, it was also decided to use velocity model M1 constructed in 1993 by Roecker et al. [3] on the basis of data obtained during join tomographic experiment conducted by scientists from Kyrgyzstan, Russia and the USA. This model is shown in Figure 4. Hereinafter this model is called kyrgyz. Travel-time tables included into Datascope software have already been constructed for this model.

Thus, during work under the Contract the following velocity models were used: kaz1, kaz2, kaz3, kaz_calib, and kyrgyz. The iasp91 model (Seatools and CTBTO version) was used as a ground-truth model.

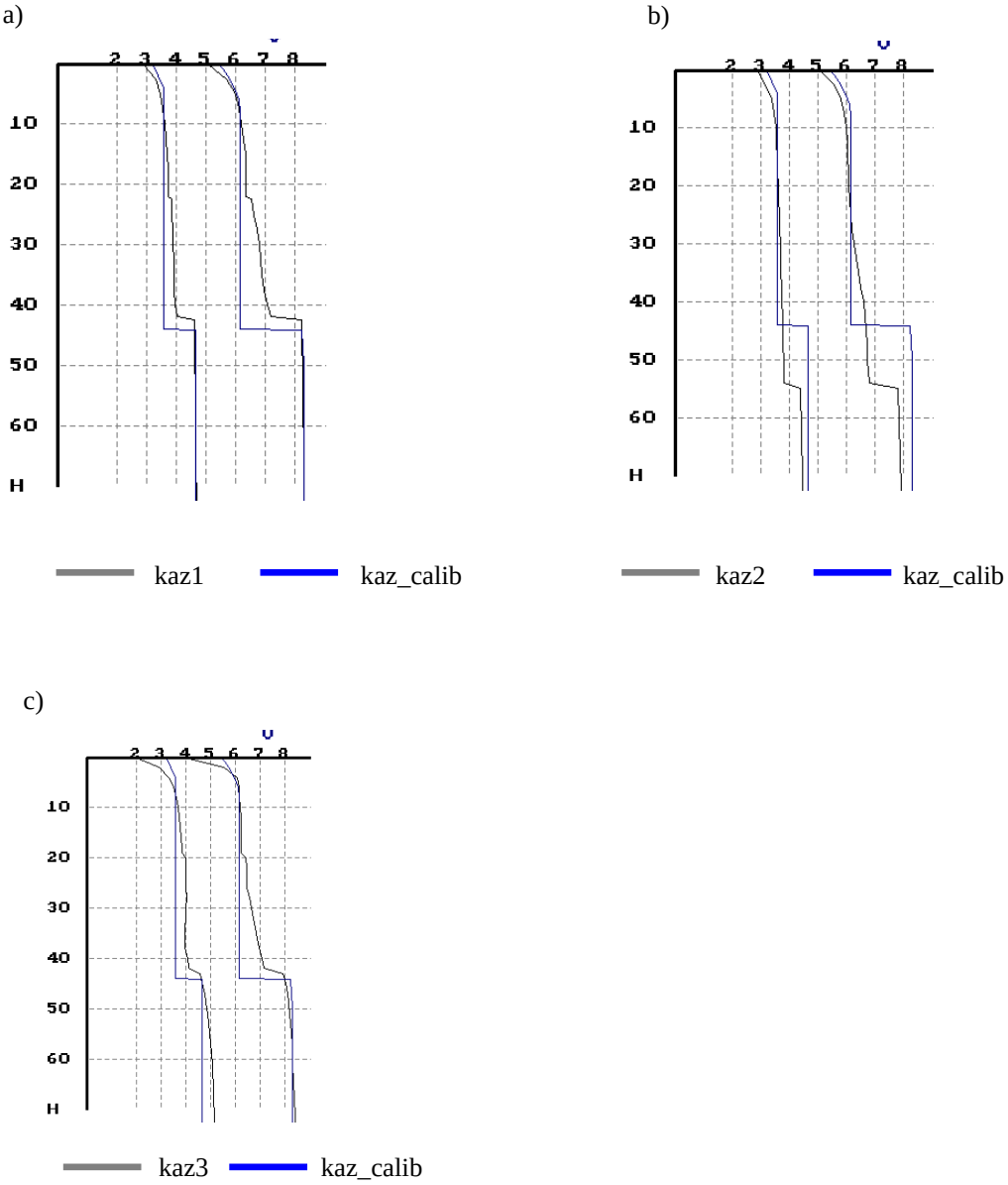


Figure 3. Velocity models kaz1 (a), kaz2 (b) and kaz3 (c) are shown. In addition, each chart shows kaz_calib model (blue color).

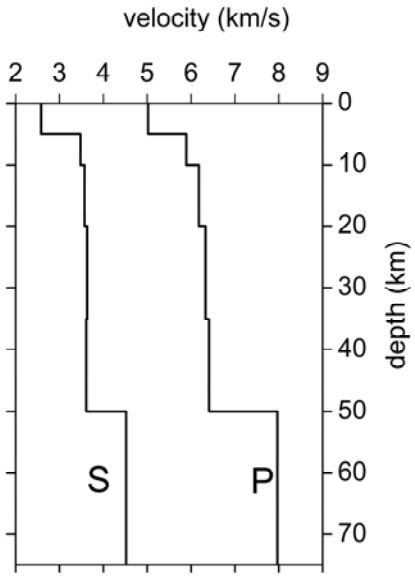


Figure 4. Velocity model for the Northern Tian-Shan by Roecker et al. [3].

All velocity models were tested on the events located on regional distance from KKAR arrays and included into ISC catalogue for the period 2002–2007. The total number of 227 events was selected. Since the investigated area distinguishes by complex depth structure of earth crust and high level of seismic activity it was decided to divide it into six different seismic zones:

1. Tien Shan (nearest to KKAR station),
2. Pamir and Hindu Kush
3. Caspian area and Caucasus
4. Northern part of India and Pakistan
5. Tibet
6. Dzungaria and Altay

Table 1 shows the results of selection of the best velocity models for each of investigated regional phases separately for each zone. It was concluded, that for the nearest to the station Tien Shan region the best accordance shows kaz_calib travel-time curve for the majority phases. For the rest regions along with kaz_calib travel-time curve, the iasp91 travel-time curve also fits well.

Table 1. Velocity models with the smallest time residuals

Zone 1. Tien Shan

Phase	best velocity model	mean, sec	median, sec
Pn	**kaz_calib**	**0.682**	**0,655**
	kyrgyz	-0.897	-0,944
Pg	**IASP91**	**0.665**	**0.886**
	kaz_calib	0.883	0.909
Pb	**kyrgyz**	**0,003**	**-0,006**
Sn	**kaz_calib**	**0,145**	**0,525**
	IASP91	0,550	1,192
Lg	**kaz2**	2,545	**0,914**
	kaz_calib	**-0,564**	-1,507

Zone 2. Pamir and Hindu Kush.

Phase	best velocity model	mean, sec	median, sec
Pn	**kyrgyz**	**-0,173**	**-0,01**
Sn	**kaz_calib**	**1,002**	1,27
	IASP91	-1,235	**-0,795**
Lg	**IASP91**	**1,289**	**0,672**

Zone3. Caspian region and Caucasus

Phase	best velocity model	mean, sec	median, sec
Pn	**kaz1**	**-0,158**	**-0,040**
	iasp91	-0,160	-0,580
Sn	**kaz_calib**	**1,109**	**0,312**

Zone 4. Northern part of India and Pakistan

Phase	best velocity model	mean, sec	median, sec
Pn	**iasp91**	**0,399**	0,701
	kaz1	0,731	**0,252**
Sn	**iasp91**	**-1,876**	**-2,493**

Zone 5. Tibet

Phase	best velocity model	mean, sec	median, sec
Pn	**kaz_calib**	**-0,404**	**0,051**
Sn	**kaz1**	**0,801**	**-0,389**

Zone 6. Dzungaria and Altay

Phase	best velocity model	mean, sec	median, sec
Pn	**kaz_calib**	**0,221**	0,622
	iasp91	-0,615	**-0,513**
Sn	**kaz_calib**	**2,079**	**1,5**
Lg	**kaz_calib**	**2,6272**	**2,093**

2. Combined Use of Seismic and Infrasound Data to Enhance Localization Accuracy of Quarry Blasts Sources

Long-term experience of seismic signals investigation from explosions at quarries in the north-west of Kazakhstan shows that actual accuracy of a source localization is poor using regular seismic data processing techniques. The large number of different active quarries in this region does not allow accurate identification of a quarry where an explosion was conducted as recorded by the stations. Localization uncertainties are often comparable with the distance between the quarries. Infrasound is generated by quarry blasts, next to seismic signals, that travels over long ranges through the atmosphere since this low frequency sound is hardly attenuated. To enhance localization accuracy it is suggested to use records of the IS31 infrasound station as an additional source of information.

An approach allowing the improvement of localization of explosions epicenters is described below. Experience with investigations of infrasound signals from quarry blasts showed [4], that infrasound arrays allows us to identify station-to-source azimuth quite accurately, i.e., within a couple of degrees. However, azimuth identification alone is not enough for localization of explosion epicenter; it is also necessary to identify the epicentral distance. Epicentral distance can be found by multiplication of complete time of infrasound propagation by average velocity. Although infrasound celerity depends on many factors, usually its value is close to 0.3 km/s [5]. Time of infrasound wave propagation was defined by difference of infrasound arrival to the station and origin time that was known accurately by seismic data. Thus, epicenter location can be found by azimuth and epicentral distance values. The obtained value will not be accurate, but can be considered as first approximation. To fix its location precisely, modeling of infrasound propagation trajectory using tau-p method [6] was applied. As a result, the modeled azimuth and horizontal velocity can be precisely measured. Relocalization with the observed and modeled data should provide a more accurate source.

Consider application of suggested method for the Chromatau quarry. The quarry is located 31 km away from IS31 station. The station to quarry azimuth is 107°. For one year period the IS31 infrasound station detected 66 events from more than 80 events recorded by the NNC seismic network at the region. Seismic signals from explosions were mainly recorded by the Akbulak array; the distance from the station to the explosions source is more than 200 km. We managed to model a trajectory of infrasound propagation from the source to the station for 31 events. Figure 5 shows three variants of explosions localization for the Chromtau quarry: by data of NNC RK seismic network only (slanting crosses); using data of seismic and infrasound methods without précising back-azimuths; and with average infrasound velocity by data of two methods with precision of celerity and back azimuth by modeling of rays propagation. It is clearly seen that stars form more compact cluster than slanting crosses, i.e., usage of additional information on infrasound narrows the area of possible epicenters scattering. However, relative location of these epicenters cluster and actual quarry testifies availability of a systematic error in values of back azimuths and epicentral distances. This systematic error is caused by influence of atmospheric winds on infrasound signal and difference between actual infrasound velocity and used average value of celerity. The group of crosses is the most compact. There is no doubt that these events are epicenters of explosions at the Chromtau quarry.

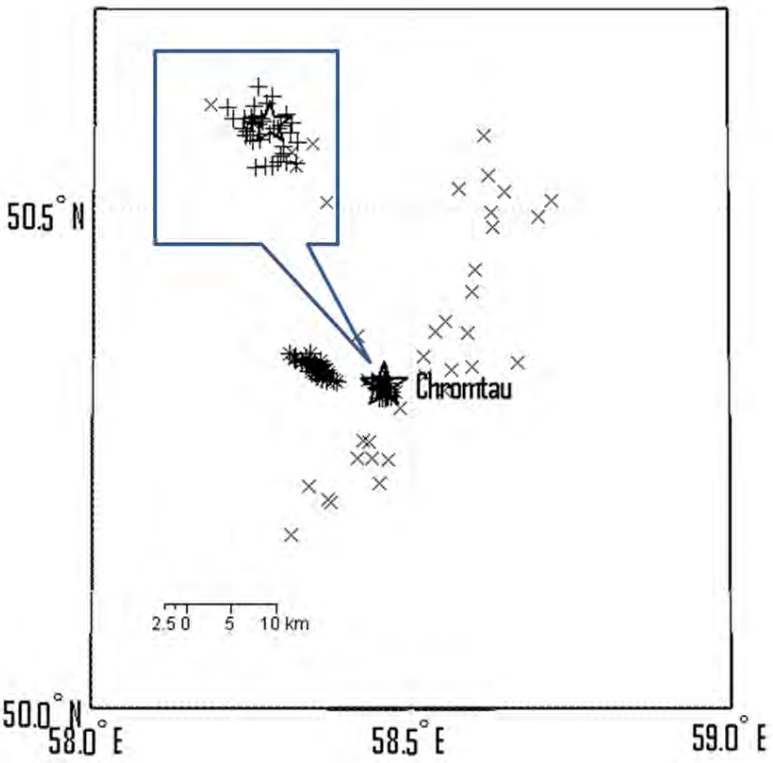


Figure 5. The map of explosions epicenters by three variants of their localization. Slanting crosses—by seismic network only; stars—by seismic and infrasound data; crosses—by seismic and infrasound data taking into account results of signal propagation paths modeling from the source to the station. The large star is the location of the Chromtau quarry.

Thus, the following can be concluded. Large number of active quarries on the one hand, and availability of long-term seismic and acoustic observations on another, allowed to obtain a method of precise localization of quarry explosions epicenters. Even simple integration of seismic and infrasound data allows to enhance significantly the localization accuracy. Application of modeling results of infrasound propagation allows to reach more accurate localization.

3. Investigation of Industrial Blast Sources on the Territory of Kazakhstan and Compilation of the Ground-Truth Events Database

Since 2007 the Institute of Geophysical Researches NNC RK conducts detailed investigations of industrial blasts sources on the territory of Kazakhstan. Suitability of these works is due to necessity to identify the nature of large number of events recorded yearly by a network of permanent high-sensitive seismic stations of the NNC RK while seismic monitoring of the Republic territory. This task is especially urgent for territories of Northern, Western and Central Kazakhstan. Daily routine data processing showed that total number of processed and licalized seismic events in these zones is about several thousands per year, major part of which is not connected with natural seismicity, but with industrial blasts. Often, blasts and earthquakes are located close to each other, thus for Kazakhstan solving the issue on enhancing the identification accuarcy of recorded events nature is of high importance taking into account the activity of blasting operations at ore and construction materials production increasing each year.

Investigation object of industrial blasts on the territory of Kazakhstan is mainly quarry blasts, sometimes underground explosions in shafts and tunnels when explosive mass exceeds 1 – 3 tons. Quarry blasts are conducted for rocks ripping to conduct stripping operations and minerals production (ore, coal and construction materials). Underground explosions in shafts and tunnels with mass of 1 ton and more are conducted for ore falling and lowering-failure of exhausted horizons. There are also temporary objects of industrial blasts connected with laying of car roads, pipelines, construction of industrial facilities, and elimination of ice jams in spring, and other (for example, military explosions at military sites). The work on industrial blasts investigation was conducted in stages; each year during field season the objects located on a distinct part of Kazakhstan territory included one to three adjacent areas were studied.

A technique of information acquisition on industrial blasts consisted of two stages: 1) preliminary analysis of materials on investigating territory to reveal potentially active quarries, and 2) field trips to investigated areas. At preliminary stage, the map of Kazakhstan minerals scaled 1:1000000 issued by the Committee of Geology of the Ministry for Energy and Mineral Resources of RK in 2002, reference literature on ore deposits in Kazakhstan, and information from the Internet about Mining Enterprises were analyzed. Materials of LANDSAT space images were used to make sure that the coordinates of ore opencast objects were precise. Catalogues and epicenters maps of events recorded by seismic stations within investigated area were analyzed for the last three years. Special attention was paid on spatial concentration of epicenters and origin time of the events. The results of preliminary analysis were used to construct a preliminary scheme of active quarries in the investigated region. However, the preliminary analysis of materials can not provide complete information about industrial blasts at revealed quarries.



Figure 6. A block of drilling and blasting operations at western side of Kosmyuryn quarry.

The most reliable and detailed information about industrial blasts is collected by visiting Mining Enterprises located at the investigated area, meetings with administration of mines and quarries, and with specialists of Organizations conducting drilling and blasting operations. At this, location of active quarries and other objects of industrial blasts is précised. Information about technique of drilling and blasting operations and explosions parameters for a certain period (1–1.5 years) indicating date, time and place of explosion, blasting blocks dimension, deployment geometry (boreholes grid) and explosive mass is acquired. After that, final tables and schemes of active quarries location and other objects of industrial blasts location for a certain period of 1–2 years are constructed indicating their activity by number of explosions per year and peak explosion yield on the background of average yield for individual quarries, and parameters of drilling and blasting operations for individual industrial blasts. Figure 6 shows a block of drilling and blasting operations at western side of Kosmyuryn quarry located southward of the Semipalatinsk Test Site.

At the present time, field investigations on detailed study of industrial blasts sources in Kazakhstan were conducted on the territory of the former Semipalatinsk Test Site and adjacent territories (2007), in Northern Kazakhstan on the territory of Kostanay and Aktyubinsk areas (2008), in Southern Kazakhstan on the territory of Zhambyl, South-Kazakhstan and Kyzylorda areas (2009), in Central Kazakhstan on the territory of Karaganda area (2010), and in North-East Kazakhstan on the territory of north-Kazakhstan, Akmola and Pavlodar areas (2011). Detailed investigations of industrial blasts were not conducted on the territory of East-Kazakhstan and Almaty areas (Figure 7). In total, from 2007–2011, the IGR NNC RK seismic stations network revealed on the investigated areas the following objects of industrial blasts: 267 quarries, 11 underground mines (shafts, tunnels), and 15 other objects (pipeline laying, construction of industrial facilities, elimination of ice jams in rivers, military sites).

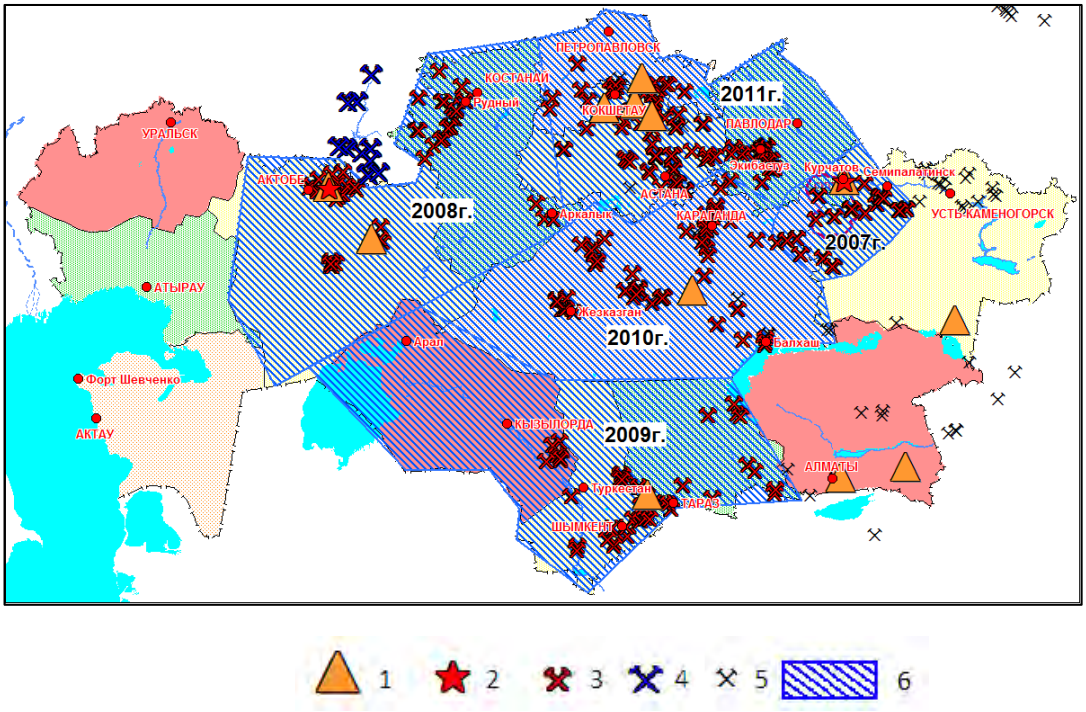


Figure 7. The map of Kazakhstan with territory covered by detailed investigations of industrial blasts for 2007–2011. 1 – NNC RK seismic stations; 2 – infrasound stations; 3 – examined and investigated quarries and objects of industrial blasts; 4 – quarries of Russia which explosions are recorded by the NNC RK stations; 5 – possible unexamined quarries; 6 – the territory covered by detailed investigations of industrial blasts.

At present time the main sources of industrial blasts are active quarries of Mining Enterprises and production of construction materials with activity at some of them up to 50–100 and more explosions per year. At large number of ore and non-ore quarries, and other objects, number of industrial blasts is about 5–10 per year. At active quarries the average explosions yield varies within 15–40 tons of explosive, rarely reaches 70–80 tons. However, at individual giant quarries, such as Zhitikara asbestos or at iron-ore quarries of Sokolov-Sarbay Association even average yield of mass explosions reaches 100 and 200 tons, and maximal explosions yield may reach 578 and 625 tons.

Significant part of industrial explosions recorded by the NNC RK seismic stations network belongs to Mining Enterprises of neighboring countries, especially Russia. Information on them is collected mainly from literature, Internet and by space images. Figure 8 shows mass explosions at chromite ore quarry Mirniy of Donskoy Mining and Processing Enterprise and iron ore quarry Sarbay of Sokolov-Sarbay Industrial Association.



a



b

Figure 8. (a) Mass explosions at chromite ore quarry Mirniy of Donskoy Mining and Processing Enterprise, and (b) at iron ore quarry Sarbay of Sokolov-Sarbay Industrial Association.

All collected data on quarries and explosions is reduced to a unified format and entered into a database of industrial blasts at active quarries and other objects. The database was developed and realized in Microsoft Access of Microsoft Windows, providing storage, accumulation and fast and convenient view of the information. Collected material allows to solve successfully tasks on identification of nature of recorded seismic events to divide them into industrial blasts and earthquakes. Special attention is paid to search of ground-truth explosions for which there are precise parameters of blasting, binding to a definite quarry and corresponding records at the stations. Data on ground-truth explosions are used to investigate velocity characteristics of geological environment, to enhance localization accuracy of events, and examination of monitoring stations network capabilities. A database of ground-truth events was created using results of ground-truth records analysis. At present time, a technique of identification of recorded seismic events nature is improved; in prospect the technique will allow to run automated division of events into industrial blasts and earthquakes.

REFERENCES

1. Mikhailova N.N., Germanova T.I., and Aristova I.L (2002). Seismic waves travel-time curve on the basis of the results signal records from chemical explosions. Geophysics and non-proliferation problems. Vestnik NNC RK. Vol.2.

2. Belyashova N.N., Shacilov V.I., Mikhailova N.N., Komarov I.I., Sinyova Z.I., Belyashov A.V., and Malakhova M.N. (2001). On the use of calibration explosions at the former Semipalatinsk Test Site for computing a travel-time model of the crust and upper mantle. *Pure Appl. Geophys.***158**, N1-2, 193–209.

3. Roecker, S.W., T. M. Sabitova, L.P. Vinnik, Y.A. Burmakov, M.I. Golyanov, R. Mamatlhanova, and L. Munirova (1993). Three-dimensional elastic wave structure of the western and central Tien Shan., *J. Geophys. Res*. **98**, 15779–15795.

4. Il-Young Che, Brian W. Stump, and Hee-Il Lee (2011). Experimental characterization of seasonal variations in infrasonic traveltimes on the Korean Peninsula with implications for infrasound event location, *Geophys. J. Int*. **185**, 190–200.

5. Brown, D. J., Katz, C. N., Le Bras, R., Flanagan, M. P., Wang, J. and Gault, A. K. (2002). Infrasonic signal detection and source location at the Prototype Data Centre, *Pure Appl. Geophys*. **159**, 1081–1125.

6. Garces, M. A., R. A. Hansen, and K. G. Lindquist (1998). Traveltimes for infrasonic waves propagating in a stratified atmosphere, *Geophys. J. Int*. **135**, 255–263.

INFRASOUND SIGNAL CHARACTERISTICS FROM SMALL EARTHQUAKES

J. Mark Hale[1], Junghyun Park[2], Kristine L. Pankow[1], Stephen J. Arrowsmith[3], Relu Burlacu[1], Brian W. Stump[2], Chris T. Hayward[2], and Steven R. Taylor[4]

University of Utah[1], Southern Methodist University[2], Los Alamos National Laboratory[3], and Rocky Mountain Geophysics[4]

Sponsored by the National Nuclear Security Administration

Award No. DE-AR52-09NA29325 and DE-AC52-06NA25396
Proposal No. BAA09-49

ABSTRACT

This work focuses on the utilization of regional infrasound signals for the purposes of characterizing the source of the signals with particular focus and linkage to small earthquakes. Research reported in this paper focuses on the assessment of regional infrasound signals in a network environment. The primary data component of this study comes from nine infrasonic arrays operated by the University of Utah Seismograph Stations (UUSS). The arrays are composed of four elements with an approximate aperture of ~150 m, with one element being co-located with a seismic station. Two distinct research activities are reported. The first documents a systematic search for evidence of epicentral infrasound associated with earthquakes in the western United States between April 2007 and December 2011. We have identified 19 $M \geq 3$ earthquakes from the UUSS catalog and 56 $M \geq 4$ earthquakes from the Western US Advanced National Seismic System (ANSS) catalog that generated epicentral infrasound. An infrasound signal generated by an earthquake is defined here to have an array correlation value ≥ 0.5, an azimuthal deviation $\leq 8°$ from the epicenter, and an appropriate group velocity for the distance and time of the event. Additionally, there must be detections at two or more arrays with crossing backazimuths near the expected source (azimuthal deviation $\leq 8°$) for an association with an earthquake. These data associated with earthquakes are in turn used to make amplitude and duration measurements that consistently extend the results of Mutschlecner and Whitaker (2005) and Le Pichon et al. (2006) to lower magnitudes. The second research activity has focused on the production of a western US regional infrasound catalog for the time period of April 2011 to March 2012. Data from the UUSS infrasonic arrays are supplemented with data from three additional arrays in Nevada. An automated detection procedure based on an adaptive F-detector (Arrowsmith and Whitaker, 2008) is used with the Bayesian Infrasonic Source Location (BISL, Modrak et al. 2010). The infrasonic catalog consists of 963 events for the one-year time period with indication of repeated events from a number of locations. These automated locations are utilized to trigger detailed studies of the repeated events. There is significant commonality between this new map and the western US infrasound catalog published by Walker et al. (2011) that utilized infrasound signals detected on seismometers while the USArray stations were deployed in the western US during 2007 and 2008. Both this earlier result and the new one document that the vast majority of events occur during working hours, Monday through Friday, suggesting a human cause.

OBJECTIVES

A wide range of natural and man-made source types generate seismo-acoustic signals. To associate and locate the source of such signals requires recordings from multiple arrays. The analysis of both the seismic and infrasound signals accompanying these sources provides an opportunity for signal characterization. A primary focus in this research is on earthquakes as sources of infrasound that extends previous studies of medium to large earthquakes recorded at distances greater than 220 km (e.g., Kim et al., 2004, Mutschlecner and Whitaker, 2005, and Le Pichon et al., 2006). This research study is designed to extend the magnitude range to small earthquakes recorded at distances less than 220 km and to provide a basis for constraining models of earthquake generated infrasound including source parameters such as depth, source mechanism and local strong ground motions. Studies of medium to large earthquakes (M > 4) suggest a linear relationship between earthquake magnitude and stratospheric return duration as well as the log of the amplitude of stratospheric returns corrected for winds and scaled to a reference distance (Mutschlecner and Whitaker, 2005 and Le Pichon et al., 2006). In addition to these tasks, the collection of infrasound data from a network of regional arrays provides the opportunity to explore the production of regional infrasound event bulletins.

The first steps in this work have been related to the acquisition of seismo-acoustic data in a network setting in order to determine whether small earthquakes generate seismo-acoustic signals (Stump et al., 2009; Hale et al., 2010). Multiple seismo-acoustic arrays are necessary in order to assess the impact of propagation path effects on the observations. Processing schema and rules for defining detections and amplitude and duration measurements have been established. Also, in a detailed analysis of the January 3, 2011 Circleville, Utah earthquake (M_w 4.6) an infrasound modeling procedure was developed that used the Rayleigh integral to model the near-field acoustic wavefield constrained by an epicentral ground motion model based on a 3D finite difference simulation scaled by peak acceleration estimates from ShakeMap. This source term provided the initial conditions for time domain parabolic equation modeling which predicts the acoustic waveform at the receivers. This work demonstrated that the infrasound recorded from the Circleville earthquake at six of the UUSS infrasonic arrays is consistent with a 'baffled piston' model for the generation of infrasound from earthquakes (Arrowsmith et al., 2012b).

In this work, we report on two new and distinct accomplishments resulting from this contract over the last year: (1) systematic array processing of epicentral time windows for earthquakes in the UUSS and the ANSS earthquake catalogs and comparison of duration and amplitude measurements to the linear relationships developed by Mutschlecner and Whitaker (2005) and (2) development of a bulletin of infrasound events for the western United States.

RESEARCH ACCOMPLISHED

Summary of Seismo-Acoustic Network

Building upon more than four decades of seismic station infrastructure, maintenance, and technical expertise, nine real-time telemetered infrasonic arrays (Figure 1, blue triangles) have been integrated into the regional seismic network in Utah for continuous data recording (Burlacu et al., 2010). Emphasizing cost effectiveness, the integration allows: (1) sharing of existing seismic data telemetry solutions and data acquisition capabilities, (2) exchanging infrasonic data with partners, using an established operational system based on Earthworm software (import/export modules), and (3) archiving the infrasonic data at the IRIS DMC, using Earthworm waveservers dedicated to both seismic and acoustic data. Although the experiment is on-going, the embargo on the data at the IRIS DMC will be removed and the data will be available in near-real-time to the research community.

Each infrasonic array, with an aperture of ~150 m, consists of four sensors with one of the elements co-located with a seismic sensor that is part of the Utah regional seismic network. Co-locating acoustic and seismic sensors was part of the design plan to characterize and understand problems related to seismic-to-acoustic and acoustic-to-seismic energy coupling. The arrays are equipped with microphones (Chaparral 2, Chaparral 2.5, or IML ST) each fitted with eight or ten hoses, for noise reduction. Data recorders (REFTEK 130, Quanterra Q330) are used to digitize data at 100 sps. The microphones are provided by Southern Methodist University (SMU) and the data recorders are from SMU and PASSCAL. PASSCAL also supplied solar panels and cell modems for telemetry.

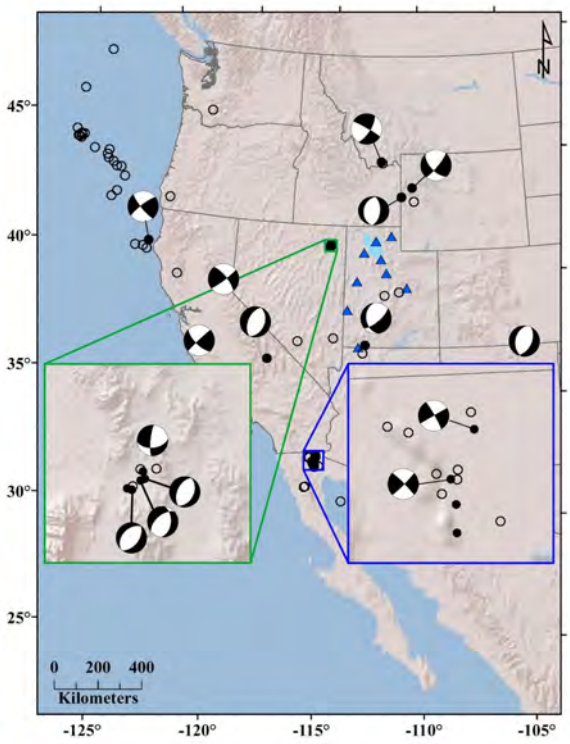


Figure 1. Combined ANSS and UUSS earthquake catalogs. Closed black circles and moment tensors (Herrmann et al., 2011; Whidden and Pankow, 2012; NEIC, 2012; NCEDC, 2012; and SCSN, 2012) are earthquakes with detections at two or more arrays for which amplitude and duration measurements could be made. Open circles are events detected at two or more arrays but the signal to noise ratio was inadequate to make amplitude and duration measurements. The blue triangles represent the UUSS infrasonic arrays.

Table 1. Measured events

Origin Time	Latitude	Longitude	Depth	Magnitude	Detections†	Catalog
02/21/2008 14:16:02	41.153	-114.867	6.7	6.0	*BGU*/EPU/NOQ	UUSS
02/21/2008 14:34:41	41.150	-114.868	5.7	4.5	*BGU*/EPU/NOQ	UUSS
02/22/2008 01:50:05	41.128	-114.874	8.1	4.0	BGU/*NOQ*	UUSS
02/22/2008 23:24:03	41.108	-114.915	7.9	3.6	BGU/*NOQ*	UUSS
02/22/2008 23:27:45	41.106	-114.900	7.4	4.5	BGU/EPU/NOQ	UUSS
04/01/2008 13:16:17	41.229	-114.840	11.0	4.1	BGU/EPU	UUSS
01/16/2009 04:15:34	43.214	-111.013	1.4	4.1	*BGU*/EPU	UUSS
10/03/2009 01:10:26	36.386	-116.868	3.6	4.9	BGU/EPU	ANSS
12/30/2009 18:48:57	32.464	-115.189	6.0	5.8	*BGU*/EPU/*NOQ*	ANSS
01/10/2010 00:27:39	40.650	-124.690	29.3	6.5	BGU/EPU/NOQ	ANSS
02/12/2010 22:37:09	37.092	-112.892	11.9	3.0	*EPU*/NOQ	UUSS
04/04/2010 22:40:41	32.260	-115.290	10.0	7.2	BGU/EPU/NOQ	ANSS
08/05/2010 14:59:27	43.598	-110.414	0.1	4.3	HWU/WMU	UUSS
12/11/2010 12:52:26	32.160	-115.260	13.1	4.9	LCM/PSU/WMU	ANSS
01/03/2011 12:06:36	38.247	-112.340	5.4	4.6	BGU/BRP/EPU/HWU/WMU	UUSS
01/12/2011 08:51:03	36.771	-121.496	8.0	4.5	BRP/*FSU*/HWU/*PSU*	ANSS
02/20/2011 19:34:39	32.047	-115.252	10.0	4.5	BRP/LCM	ANSS
04/05/2011 07:05:24	44.663	-112.165	0.9	4.6	HWU/*PSU*	UUSS
08/23/2011 05:46:18	37.063	-104.701	4.0	5.4	BRP/FSU/LCM/*PSU*	ANSS
10/15/2011 11:42:29	37.899	-118.572	8.2	4.3	BRP/HWU/*LCM*/PSU	ANSS
10/27/2011 06:37:08	39.611	-120.475	16.0	5.0	BGU/BRP/FSU/*HWU*/LCM/*PSU*/WMU	ANSS

† Italicized detections not measured due to poor signal-to-noise ratio

Table 2. InfraMonitor batch input parameters

Catalog	Window (seconds)	Window Overlap (%)	Adaptive Window (seconds)	P-value	Filter Band (Hz)
UUSS	20	50	7200	0.01	1-5
ANSS	20	50	7200	0.01	0.5-5

Systematic Search for Evidence of Epicentral Infrasound

Available infrasound data from arrays located in Utah for all M ≥ 3 earthquakes (N = 276) in the UUSS earthquake catalog (http://www.quake.utah.edu/EQCENTER/LISTINGS/utahregion.htm), and M ≥ 4 earthquakes (N = 871) in the ANSS earthquake catalog within 1750 km of the UUSS infrasound network centroid (http://www.ncedc.org/anss/catalog-search.html), from January 1, 2007 through December 31, 2011 were evaluated for epicentral infrasound using InfraMonitor 3.0 (Arrowsmith et al., 2008; Arrowsmith, 2012a). InfraMonitor uses an adaptive noise hypothesis when correlating array components in order to account for time varying coherent noise sources. To establish the coherent background noise level, each waveform includes 45-minute data buffers on each side of the event window. The event window is defined here as extending from the earthquake origin time to the expected arrival time for epicentral thermospheric returns (0.22 km/s). The InfraMonitor input parameters for the batch processing of each catalog are detailed in Table 2.

For the purpose of this study, detections must occur within the time-window for epicentral infrasound (0.35-0.22 km/s), and are defined when the correlation coefficient is ≥ 0.5 and the azimuthal deviation from the epicenter reported in the catalog is ≤ 8º. For completeness, UUSS catalog detections with azimuthal deviation between 8º and 20º are also reviewed. Of the 276 events in the UUSS catalog 19 had epicentral time-window detections from two or more arrays. Of those, eight had detections of sufficient quality for measuring duration and amplitude. For the ANSS catalog 56 events had detections at two or more arrays. Of those, 15 events are of sufficient quality for measuring duration and amplitude. Solid symbols and moment tensors in Figure 1 (detailed in Table 1) indicate the location of the earthquakes generating infrasound of sufficient quality to measure amplitude and durations.

To measure the duration and amplitudes of the detection, the detections are reviewed using the InfraMonitor GUI and the following processing steps are applied:

- Inspection of the spectrogram of raw data in order to optimize the bandpass filter. For example, based on the spectrogram in Figure 2a the data would be filtered using a 4-pole Butterworth from 1 to 10 Hz. In cases where there is no clear peak in the signal the corners are set at the corresponding filter band used in batch processing (Table 2).
- The beam is formed using the backazimuth and group velocity corresponding to the highest correlation window. The fk plot (slowness in seconds-per-degree; Figure 2b) from the highest correlation window (Figure 2c) is reviewed to assess the quality of the detection. The beam is displayed along with phase velocity, azimuth, correlation, and f-statistic values for each time window (Figure 2c). The beam is also output for further analysis including the measurement of the amplitude and duration of the detection.
- Durations are calculated in Matlab by applying the Hilbert transform to the beam (Figure 3a). The start and end times (blue lines) are defined as the locations where the 0.001 Hz low-pass Hilbert transform exceeds the background noise levels.
- Three separate amplitude measurements are made from the beam: a maximum peak-to-peak amplitude (Figure 3b), a 10-second root-mean-square (RMS) amplitude centered at the middle of the peak-to-peak amplitude (Figure 3c), and the RMS calculated over the duration of the signal, as determined from the Hilbert transform analysis (Figure 3c).
- Amplitude measurements are converted from counts to micro-bars using the array response.
- The group velocity (Figure 4) is used to identify the atmospheric layer where the energy turns. Using this information, stratospheric wind corrections are applied for group velocities between 0.28 and 0.31 km/s (Ceplecha et al., 1998) and all detections are normalized using the same constant R_s as Mutschlecner and Whitaker (2005).

$$A_n = A_o 10^{-kV_d} \left(\frac{R}{R_s}\right)^s \qquad (1)$$

Where A_n is the amplitude in μbars, k = 0.018 s/m, V_d is the stratospheric wind component from source to array, R is the distance to the epicenter, R_s = 1000 km, and S = 1.45. In this preliminary analysis the wind corrections depend solely on the mean stratospheric wind component.

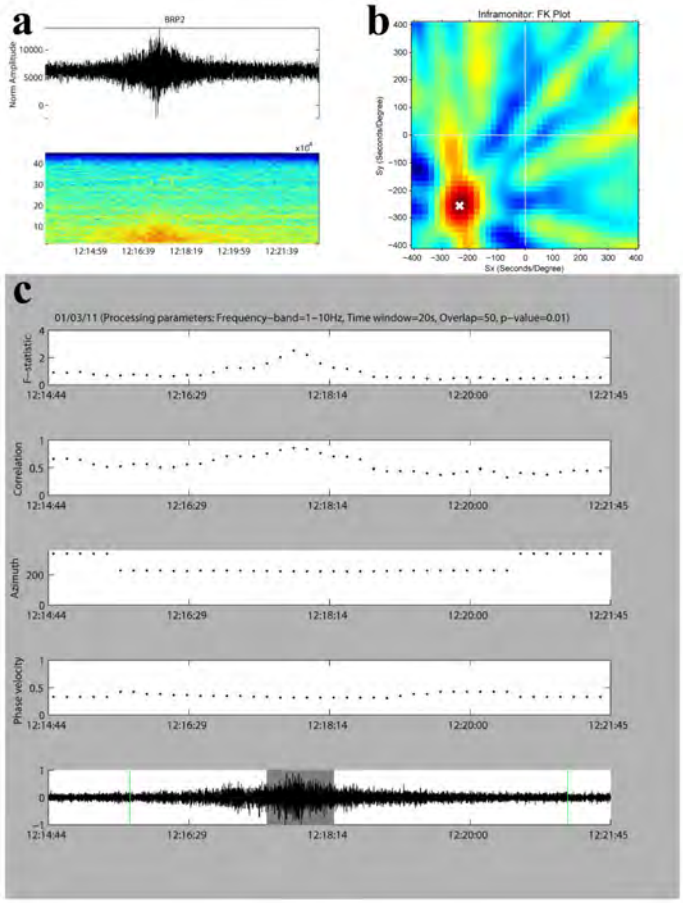


Figure 2. InfraMonitor3 GUI mode processing of a detection at array BRP of the January 3, 2011 Mw 4.6 Circleville, Utah earthquake. (a)—Raw trace of channel BRP2 (top) and spectrogram of the epicentral time window (bottom). (b)—fk plot (seconds/degree) of the highest correlation window shown in (c). (c)—Screenshot of the GUI showing the F-statistic, correlation, azimuth (°), phase velocity (km/s), and the BRP2 waveform.

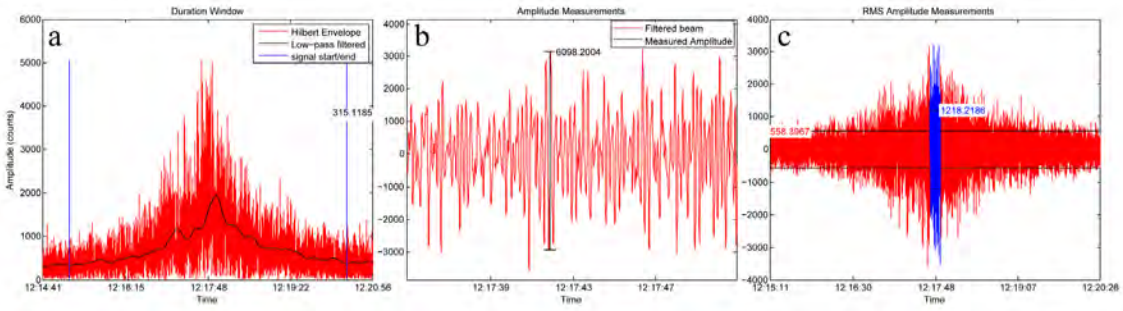


Figure 3. (a) Hilbert transform applied to the beam and the low-pass (0.001 Hz) of the Hilbert transform are used to determine duration (marked by vertical blue lines). (b) Maximum peak-to-peak amplitude measurement of the beam in counts. (c) 10-second RMS amplitude measurement centered on the peak amplitude (blue) and RMS amplitude for the detection duration (red). Black lines show the location of the displayed values.

This study adds 33 measurements (Figure 5a, red symbols) to the log(duration) versus magnitude plot, primarily from M < 5.5 earthquakes. A new regression including measurements from this study combined with data from Mutschlecner and Whitaker, 2005 (blue lines and points) show consistent results from M > 4.5 earthquakes. For earthquakes with M < 5, there is increased scatter in the distribution of the measurements, including those from Mutschlecner and Whitaker (2005). Nine of the new measurements for these smaller magnitude earthquakes were recorded within the zone-of-silence (distances < 220 km) and potentially tropospheric ducting (not stratospheric returns) could be responsible for the increased scatter and low log(duration) values. It is also possible that the scaling differs for smaller magnitudes. Ray-tracing will be used to further investigate this change in duration for smaller earthquakes.

This study almost doubles the number of log(amplitude) measurements (n=45; Figure 5b, red symbols), again primarily from M < 5.5 earthquakes. Compared to the duration measurements there is more scatter in these observations, especially for the smaller magnitude events. One notable difference between the two studies is a difference in how the measurements were made. In an attempt to standardize the measurements, we use the amplitude determined by calculating the RMS over a 10-second window. Mutschlecner and Whitaker (2005) report measuring an average of significant features over an approximate 10-second window with a focus on peak amplitudes. The RMS measurements might then be expected to have slightly lower amplitudes, which is what we see. The other two measures of amplitude will be investigated in the next phase of our research. There are two significant outliers, labeled A and B on Figure 5b. Outlier A is from an M 3.0 earthquake near the Utah-Arizona border, recorded at a distance of 401 km. Outlier B represents measurements from an offshore M 6.5 earthquake along the Mendocino fracture zone, recorded at a distance of 1062 km. Although there is scatter, the final regression is similar to Mutschlecner and Whitaker (2005). However, like in the duration results, there is an indication that there might be a change in the relation of magnitude versus amplitude for smaller earthquakes.

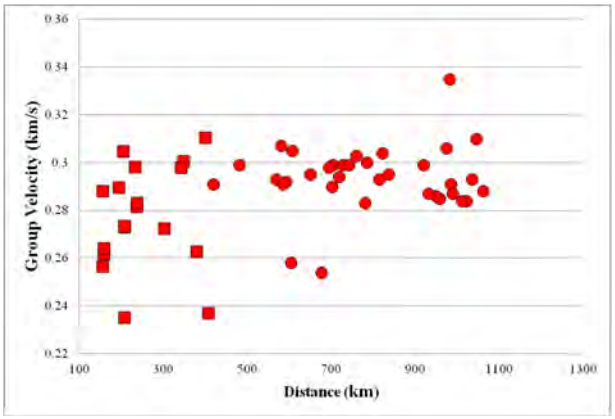


Figure 4. Group velocities for earthquakes from the ANSS catalog (circles) and the UUSS catalog (squares) plotted as a function of distance. Note the number of UUSS measurements within the zone of silence (distances < 220 km).

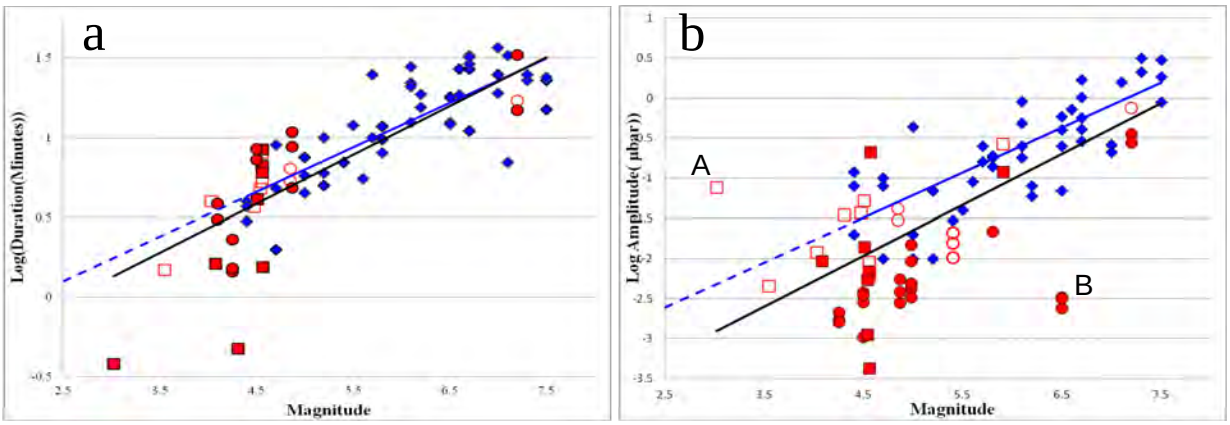


Figure 5. (a)—Log of signal duration (minutes) versus magnitude. Mutschlecner and Whitaker (2005) measurements shown in blue, this study shown in red. Earthquakes from the UUSS catalog (squares) and from the ANSS catalog (circles). Stratospheric (closed symbols) and non-stratospheric (open symbols) returns based on group velocities following Ceplecha et al., 1998). (b)—Log(wind corrected 10-second RMS amplitude) as a function of magnitude. Mutschlecner and Whitaker (2005) measurements (blue diamonds). Measurements from this study (red symbols): corrected using equation 1 (closed symbols) and corrected without the wind component from equation 1 (open symbols). Regression lines are shown for the Mutschlecner and Whitaker (2005; blue lines dashed portion extrapolated using their scaling relation) and the combined regression (black).

Western US Regional Infrasound Catalog

The long-term operation of the infrasound arrays in Utah with data from additional arrays in near-by Nevada (independently supported at SMU) provides an opportunity to supplement the focused earthquake catalogs and subsequent analysis with an independent and automated network infrasound bulletin. Walker et al. (2011), using a reverse time migration method, have reported on a similar effort to produce a regional infrasound bulletin using the seismic stations from the USArray that were deployed in the western US from 2007 to 2008. In the analysis reported here, the 12 infrasound arrays shown in Figure 6 provide the basis for analysis and subsequent formation of a network infrasound bulletin (Stump et al., 2012).

The first step in the production of the bulletin is the development of a set of event detections from the observational datasets. Robust detection for infrasound relies on separating signals from noise using a variety of correlation techniques applied to array data. Included among these procedures are the progressive multi-channel correlation (PMCC) algorithm (Cansi, 1995) as well as simpler correlation detectors found in InfraTool and MatSeis-1.7 (Hart and Young, 2002). Based on a preliminary study of detectors (Stump et al., 2012), we use the modified F-statistic as proposed by Arrowsmith et al.,2009 which accounts for temporal changes in noise by using an adaptive window to assess the changing noise environment and remap the detection distribution as time progresses.

The adaptive F-detector was tuned in the frequency band of 1 to 5 Hz based on practical experience with the regional infrasound signals as well as the optimal signal to noise ratios found in the observations. The time duration of the detector window was 30 s, with a 50% overlap. A 1-hour adaptive window was used to capture the changing noise environment. A p-value of 0.01 minimized the number of false alarms. A summary of a one-year-dataset that includes the infrasound arrays BGU, BRP, DNIAR, EPU, FNIAR, FSU, HWU, NOQ, and WMU was used to produce an initial set of detections (Figure 7).

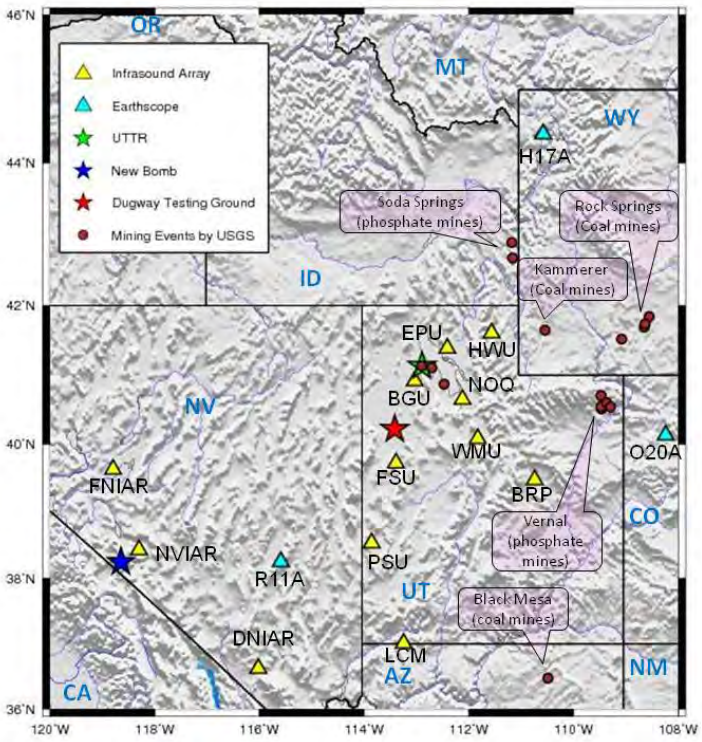


Figure 6. Location of the infrasound arrays that are used to produce the regional infrasound bulletin. A number of known sites where near-surface explosions occur are noted. Mining events near and in Utah from April 2011 through March 2012 are also plotted (data from USGS/NEIC, 2012).

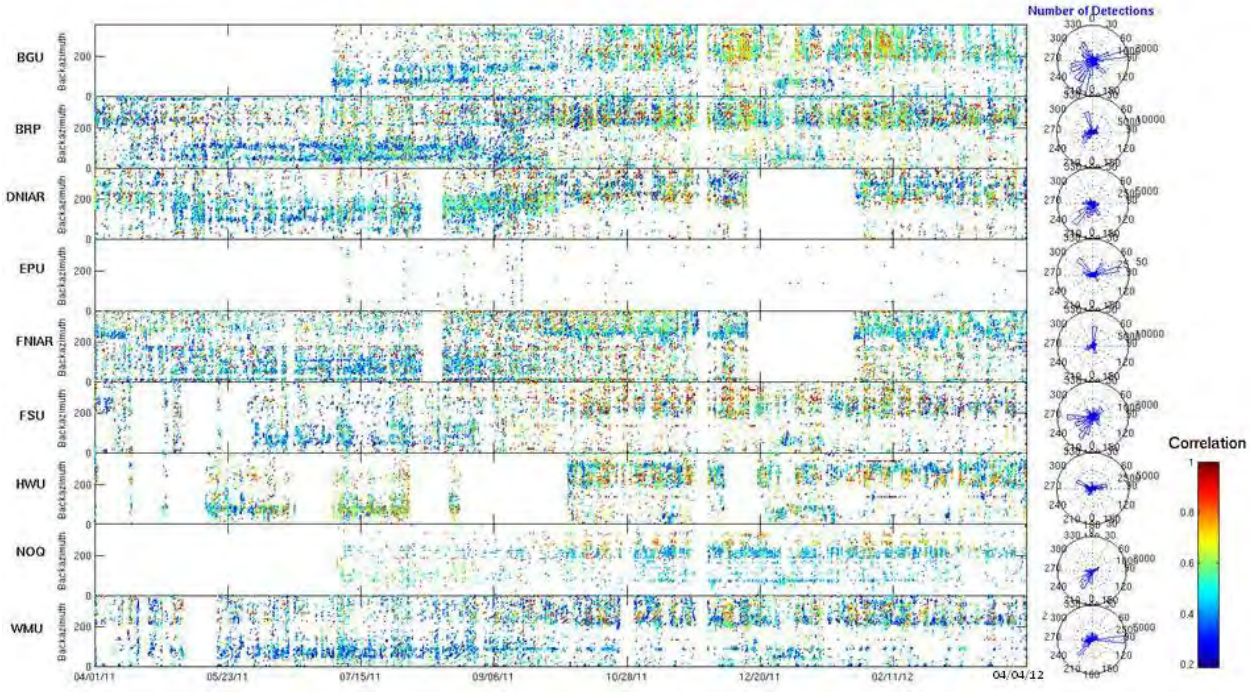


Figure 7. Summary of automated detection results for the western US for the time period 04/01/2011 through 04/03/2012. The color of the individual detections represents the correlation value and is plotted against azimuth and time. The rose diagrams to the right summarize the total number of detections as a function of azimuth for the entire time period.

There are many station centric differences documented in the detection summary. For instance, EPU has relatively few detections (the EPU array experienced telemetry outages during the time period of the analysis). Stations close to one another, such as BGU, FSU, NOQ and WMU (located in the northern part of the network) have many detections from the southeast and west. There are a large number of detections from the southwest of FNIAR and DNIAR. One can also track seasonal variations in the details of the detections, with consistent changes in the average detection directions as well as their correlation values. For instance, station BGU in Figure 7 has a large number of low correlation detections from the NE during the summer months that move to the SW, W and NW during the fall and winter. Similar trends are apparent for many of the arrays suggesting that these data may provide constraints on temporal variations in the atmosphere and that the resulting bulletin may be seasonally variable.

The association and event locations based on the detections were made using InfraMonitor (Arrowsmith et al., 2008; Arrowsmith, 2012a). The specific location algorithm follows Modrak et al., 2010, the Bayesian Infrasonic Source Location (BISL). This algorithm accounts for the fact that there are significant source-to-array path effects by adding a random component to the infrasonic group velocity. Likelihood functions for backazimuth and travel-time are utilized to estimate a combined likelihood value for the location parameters.

The infrasonic events located in the Western US for the one-year time period are summarized in Figure 8. A total of 963 events are included in the map. Comparison of this map with the published results of Walker et al. (2011) suggests that the two bulletins have significant commonality, although for different time periods. These studies document common regions where infrasound sources are located, including an explosive detonation site in Nevada designated as New Bomb in Figure 6, the Utah Test and Training Range (UTTR), Dugway, as well as areas in central Nevada and southwest Idaho. There are many infrasound events in the southwest part of the study area, mostly occurring from October 2011 to March 2012, during the winter. Infrasound event distribution in this area is similar to the infrasound hot spots identified and associated with military activities by (Walker et al., 2011). A number of infrasound events occurred near the site of New Bomb from July 2011 to March 2012 and reflect the regular detonation of explosives at this site (Figure 9a). The infrasound event clusters (April to June 2011), north of FNIAR, may also represent human activity based on the analysis by Walker et al. (2011). Events in Utah between BGU and EPU may be associated with UTTR (Figure 9b). Many infrasound events occurred near the Dugway Testing Ground (between BGU and FSU), mostly during two time periods, July - September 2011 and January - March 2012 (Figure 9b), correlating with the seasonal variations identified in the detection results. These events have smaller uncertainty estimates and seem to form a linear cluster.

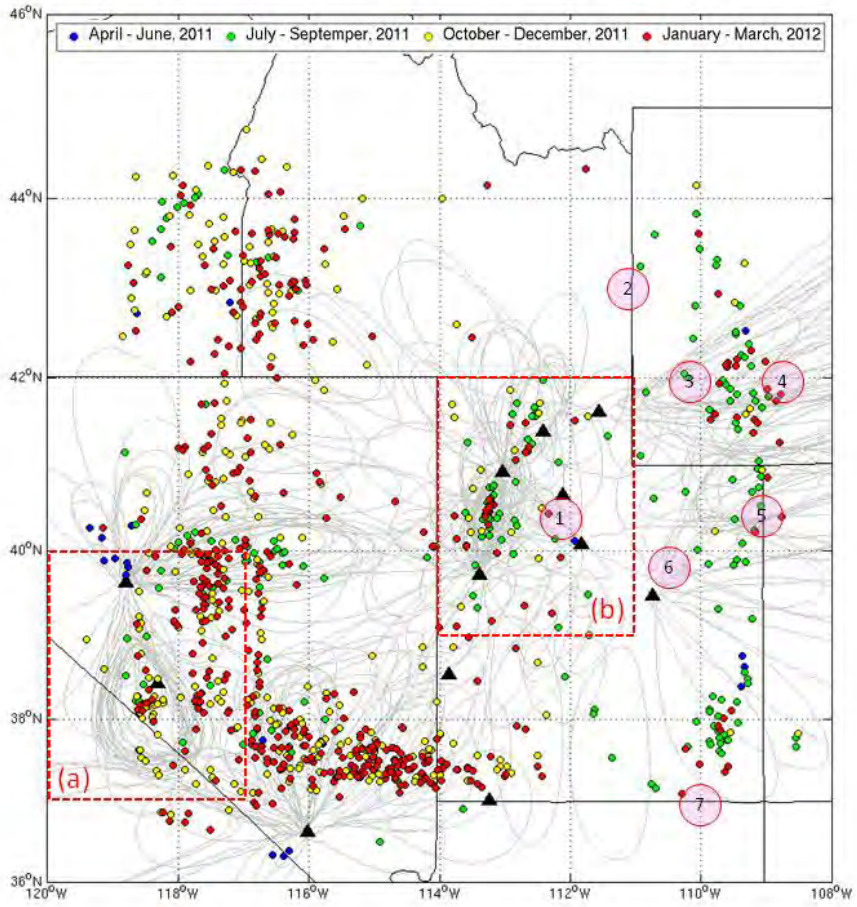


Figure 8. Automated infrasound events for the time period April 2011 through March 2012 are color coded by time. Uncertainty estimates less than 25,000 km^2 are included as the light grey contours. Mining regions denoted by USGS are represented by pink circles (1: Copperton, 2: Soda Springs, 3: Kemmerer, 4: Rock Springs, 5: Vernal, 6: Price, and 7: Kayenta). Regions inside the red boxes (a) and (b) are expanded in Figure 9.

Comparison of the infrasound locations with the USGS mining regions suggests that the number of located infrasound events, that might be associated with these mines over the course of a year, is small. This lack of correlation may reflect a combination of the seasonal variations in the winds, the limited station distribution, as well as the possibility of reduced atmospheric infrasound coupling from some types of mining explosions. In comparison, Figure 8 suggests that sites known to conduct surface detonations of explosives may be regularly detected and located. These surface explosions provide the opportunity to develop ground truth for characterizing the seasonal variation in atmospheric propagation.

There is strong evidence that a large proportion of the events located in this study are related to human activities. A histogram of the number of events as a function of time of the day and day of the week is shown in Figure 10; the vast majority of events occur during work days and hours.

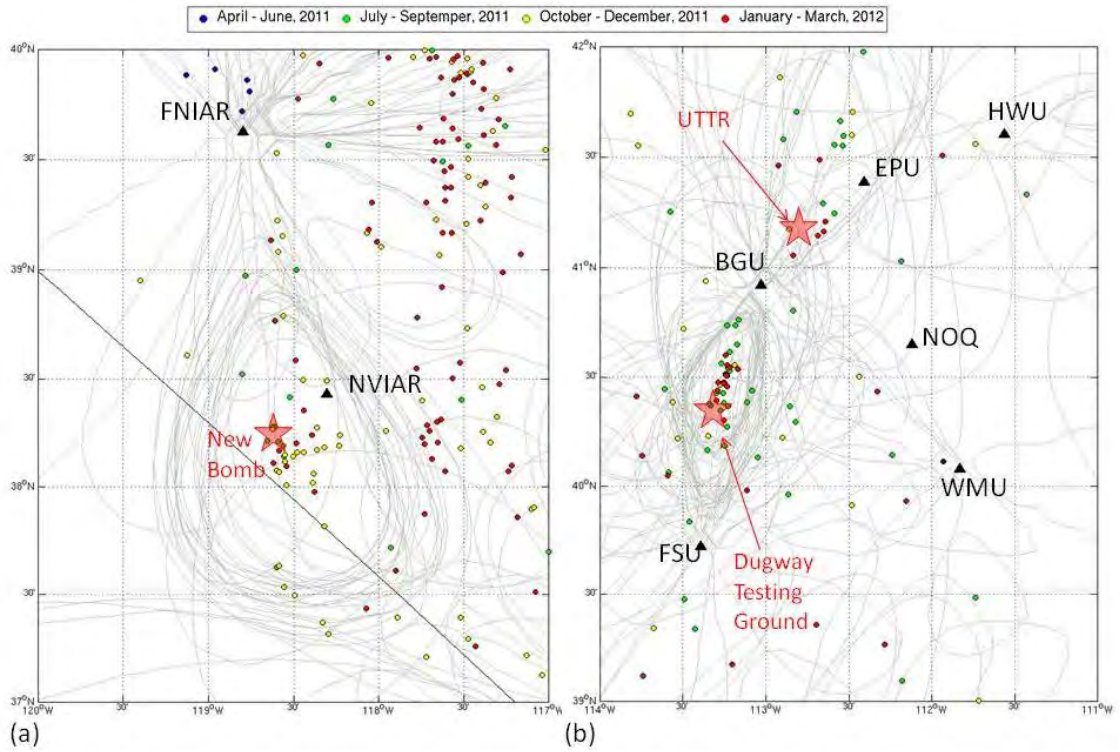


Figure 9. Automatic events from the two focus areas depicted in Figure 8. (a)—The area of New Bomb in Nevada that regularly detonates explosive ordnance; and (b)—The large number of events located in the region around the Dugway Testing Ground as well as UTTR. Uncertainty estimates less than 25,000 km^2 are represented by the grey error contours.

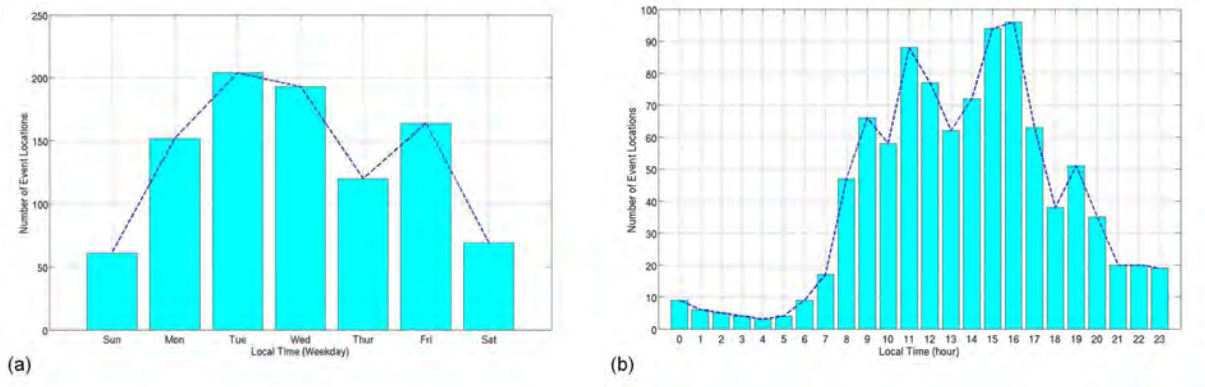


Figure 10. Histogram of source times for located events for the one-year dataset. The rate of occurrence versus (a) weekday and (b) hour of the day suggests that many of the detected events may be related to human activities.

CONCLUSIONS AND RECOMMENDATIONS

A network of nine infrasound arrays has been co-located with existing seismic stations that are part of UUSS and are being operated in near real-time. Time series from these stations are beginning to provide a dataset for automated signal detection, association, and location of events within the Intermountain Seismic Belt. This region produces many moderate sized earthquakes and is a source of active near-surface and underground mining as well as a region with military activity that can generate acoustic signals. Initial results have been presented summarizing possible earthquakes that may have generated infrasound. Although the number of possible sources is modest, these results

suggest that infrasound may accompany moderate sized earthquakes. The results also suggest a possible change in amplitude and duration scaling as a function of magnitude between moderate-to-large earthquakes and smaller earthquakes. Development of the scaling relations requires further analysis.

The infrasound arrays in Utah supplemented by data from three arrays in Nevada have been used to develop a one-year network infrasound bulletin. Detections were formed using the adaptive F-detector (Arrowsmith et al., 2009). The detection database documents important seasonal variations that merit further exploration. These variations suggest that the detection data may be useful in documenting time variation in the atmosphere. Additionally, these characteristics suggest that the network bulletin may also be seasonally variable.

Association of detections and event locations were formed using the BISL procedure (Modrak et al., 2010). Using this approach a total of 963 events were located. Analysis of this network bulletin for April 2011 through March 2012 illustrates a number of locations with a high density of events. Comparison with a similar bulletin produced by Walker et al. (2011) for the time periods of 2007 to 2008, using EarthScope seismic data and a reverse time migration method suggests that a small number of infrasonic arrays or a large number of single sensors (seismometers in the Walker example) can be used to produce location estimates for network bulletins. A natural conclusion is that some hybrid technique that utilizes a combination of arrays and single stations, possibly seismometers, might be worth exploring.

The initial bulletin for the western US has a relatively small number of events near known mining regions. This lack of correlation may be an effect of the station distribution relative to the seasonal variations of the atmospheric winds. Alternatively, it might reflect reduced atmospheric coupling of mining explosions in comparison to surface explosions. The bulletin results motivate further study of these issues.

It is clear that the vast majority of infrasound events occur during working hours. This result suggests that a large portion of the bulletin is related to human activities. The detailed earthquake study suggests that moderate size earthquakes are also a source of infrasound. Additional analysis is needed to assess the frequency of human and natural events and determine the implications for using infrasound for event identification.

ACKNOWLEDGEMENTS

Dataloggers and materials support were provided by PASSCAL.

REFERENCES

Arrowsmith, S. J., and R. Whitaker (2008). InfraMonitor: A Tool for Regional Infrasound Monitoring, in *Proceedings of the 2008 Monitoring Research Review: Ground-Based Nuclear Explosion Monitoring Technologies*, LA-UR-08-05261, Vol. 2, pp. 837–843.

Arrowsmith, S. J., R. Whitaker, S.R. Taylor, R. Burlacu, B. Stump, M. Hedlin, G. Randall, C. Hayward, and D. ReVelle, (2008). Regional Monitoring of Infrasound Events Using Multiple Arrays: Application to Utah and Washington State, *Geophys. J. Int.* **175**(1), 291–300.

Arrowsmith, S.J., R. Whitaker, C. Katz, and C. Hayward (2009). The F-detector revisited: An improved strategy for signal detection at seismic and infrasound arrays, *Bull. Seismol. Soc. Am.* **99(**1), 449–453.

Arrowsmith, S.J. (2012a). Users Guide of InfraMonitor3.1 (beta version).

Arrowsmith, S.J., R. Burlacu, K. Pankow, B. Stump, R. Stead, R. Whitaker, and C. Hayward (2012b). A seismoacoustic study of the 2011 January 3 Circleville earthquake, *Geophys. J. Int.* **189**, 1148–1158, doi:10.1111/j.1365-246X.2012.05420.x.

Burlacu, R., S. Arrowsmith, K. Pankow, M. Hale, C. Hayward, and B. Stump (2010). A network of infrasonic arrays in Utah, 2010 Fall Meeting, AGU, San Francisco, California, 13–17 December.

Ceplecha, Z., J. Borovicka,W. G. Elford, D. O. ReVelle, R. L. Hawkes, V. Porubcan, and M. Simek (1998). Meteor phenomena and bodies, *Space Sci. Rev.* **84**, 327–471.

Cansi, Y. (1995). An automated seismic event processing for detection and location: the P.M.C.C. method, *Geophys. Res. Lett*. **22**, 1021–1024.

Hale, J., S. Arrowsmith, C. Hayward, R. Burlacu, K. Pankow, B. Stump, G. Randall, and S. Taylor (2010). Infrasound Signal Characteristics for Small Earthquakes, *Proceedings of the 2010 Monitoring Research Review: Ground-Based Nuclear Explosion Monitoring Technologies*, LA-UR-10-05578, Vol. 2, pp. 720–730.

Hart, D. H. and Chris J. Young (2002). MatSeis User Manual version 1.7, Sandia National Laboratories.

Herrmann, R. B., H. Benz, and C. J. Ammon (2011). Monitoring the Earthquake Source Process in North America *Bull. Seismol. Soc. Am* **101**, 2609–2625, doi:10.1785/0120110095

Kim, T.S., C. Hayward and B. Stump (2004). Local infrasound signals from the Tokachi-Oki Earthquake, *Geophys. Res. Lett.* **31** (20), L20605 10.1029/2004GL021178

Le Pichon, A., P. Mialle, J. Guilbert, and J. Vergoz (2006). Multistation infrasonic observations of the Chilean earthquake of 2005 June 13, *Geophys. J. Int.* **167**, 838–844.

Modrak, R. T., S. J. Arrowsmith, and D. N. Anderson (2010). A Bayesian framework for infrasound location, *Geophys. J. Int* **181**:399–405.

Mutschlecner, J. P. and R. W. Whitaker (2005). Infrasound from earthquakes, *J. Geophys. Res.* 110:D01108, doi:10.1029/2004JD0050067.

NCEDC, (2012). Moment tensor catalog, http://www.ncedc.org/ncedc/mt.html

NEIC, (2012). Source parameter catalog, http://earthquake.usgs.gov/earthquakes/eqarchives/sopar/

SCSN, (2012). Moment tensor catalog, http://www.data.scec.org/eq-catalogs/CMTsearch.php

Stump, B. W., J. Park, C. Hayward, S. Arrowsmith and I.-L. Che (2012). *Performance Assessment of Multi-Array Processing with Ground Truth for Infrasonic, Seismic and Seismo-acoustic Events*, Air Force Research Laboratory, AFRL-RV-PS-TR-2012-xxxx, *i*n draft 24-05-2012.

Stump, B., R. Burlacu, C. Hayward, K. Pankow, S. Nava, J. Bonner, S. Hock, D. Whiteman, A. Fisher, T.S. Kim, R. Kubacki, M. Leidig, J. Britton, D. Drobeck, P. O'Neill, K. Jensen, K. Whipp, G. Johnson, P. Roberson, R. Read, R. Brogan and S. Masters (2007). *Seismic and Infrasonic Energy Generation and Propagation at Local and Regional Distances: Phase I – Divine Strake Experiment*, Air Force Research Laboratory, AFRL-RV-HA-TR-2007-1188, 11 October 2007.

Stump, B., Hayward C., Arrowsmith S., Randall G., Pankow K., Burlacu R., and Taylor S. R (2009). Infrasound from earthquakes: signal characterizations, in *Proceedings of the 2009 Monitoring Research Review: Ground-Based Nuclear Explosion Monitoring Technologies*, LA-UR-09-05276, Vol. 2, pp. 742–749.

USGS/NEIC, 2012, Mining event catalog, http://earthquake.usgs.gov/earthquakes/eqarchives/mineblast/.

Walker, K. T., R. Shelby, M. A. H. Hedlin, C. de Groot-Hedlin and F. Vernon, 2011, Western U.S. Infrasonic Catalog: Illuminating infrasonic hot spots with the USArray, J. *Geohys. Res.*, **116**, B12305, doi:10.1029/2011JB008579/.

Whidden, K.M., and K.L. Pankow (2012). A Catalog of Regional Moment Tensors in Utah from 1998 to 2011, *Seismol. Res. Lett.* **83**(5), in press.

INFRASOUND OBSERVATIONS FROM THE SOURCE PHYSICS EXPERIMENT (TESTS 1 AND 2) AT THE NEVADA NATIONAL SECURITY SITE

Kyle R. Jones[1], Rod W. Whitaker[2], and Stephen J. Arrowsmith[2]

Sandia National Laboratory[1] and Los Alamos National Laboratory[2]

Sponsored by the National Nuclear Security Administration

Award No. DE-AC52-06NA25946/NST11-NCNS-TM-EXP-PD15

ABSTRACT

The overall mission of the National Center for Nuclear Security (NCNS) Source Physics Experiment (SPE-N) at the Nevada National Security Site (NNSS) near Las Vegas, Nevada is to improve upon and develop new physics based models for underground nuclear explosions using scaled, underground chemical explosions as proxies. Infrasound has been used for many years to study explosive sources both above and below ground. For most of these studies, the explosions were single shot events located in different areas. With the SPE-N series of explosions, we have the unique and rare opportunity to study infrasound generated by a well-characterized source from the same borehole. This reduces the number of variables that must be accounted for when generating models using the acoustic data. At the time of submission, the first two explosive tests (SPE-N-1 and SPE-N-2) were successfully conducted on May 3 and October 25, 2011, respectively. SPE-N-1 had a yield of 0.1 tons at a depth of 60 m with a scaled depth of burial of 1,026 m. This explosion was used as a calibration shot as it was the first in the series. SPE-N-2 had a yield of 1 ton at a depth of 45 m, corresponding to a scaled depth of burial of 357 m. The acoustic amplitudes ranged from ~0.5 Pa at 225 m, to not being detected after 1 km for the 0.1 ton shot; and ~14 Pa at 225 m, to ~0.1 Pa at 5 km for the 1 ton shot. This paper will focus on detailed acoustic observations from both of these tests as well as describe future work, including detailed modeling of infrasound generation at the surface in the area above the explosion.

OBJECTIVES

The objective of this research is to use the SPE-N at the NNSS to study infrasound generated by underground explosions that occur at a well-characterized site. A primary goal of the project is to produce physics-based models to better understand and analyze explosive sources both above and belowground. At the time of submission, the first two explosive tests (SPE-N-1 and SPE-N-2) were successfully conducted on May 3 and October 25, 2011, respectively. This paper will focus on detailed acoustic observations from both of these tests as well as describe future work, including modeling of infrasound generation at the surface in the region above the explosion.

RESEARCH ACCOMPLISHED

Background

We will discuss infrasound data collected during the first two underground explosions conducted for the SPE-N at the NNSS. These series of explosions are intended such that only one variable is changed at a time, so that the data from each shot can be analyzed for subtle differences stemming from these changes. The first seven explosions will occur in "simple" granite geology at the same location as the previous nuclear experiments Hard Hat (5.7 kt; 2/15/1962) and Pile Driver (62 kt; 6/2/1966) (DOE/NV-209, 1994). Several more shots will be conducted in a "complex" geologic setting (yet to be determined). For each series (simple and complex) we will re-occupy our station and sensor locations for each subsequent explosion. It is important to note that the primary purpose of the source physics experiment is to study the seismic waves generated from explosions in both damaged and undamaged rock and that the observed infrasound is a fortuitous side effect of those explosions.

Infrasound, while not the primary goal, is still an important component to the SPE-N series of experiments because infrasound signals can still be detected, even though there is little visible surface expression of the shots. The data can be analyzed to determine yield, extent of the surface expression (spall), and energy coupled to the atmosphere. With the ground truth information available from these experiments, we will be able to further our understanding of the previously developed empirical relationships among shot size, emplacement depth and source area to evaluate what factors affect infrasound generation from underground explosions.

The IML-ST infrasound sensor, manufactured by Inter-Mountain Labs, was used for both of the first two tests. This sensor has an approximately flat response between 2 and 30 Hz with a sensitivity of 0.20 Volts/Pa (http://www.intermountainlabs.com/pdf/IML_ModelSTDataSheet.pdf). The Sandia National Laboratory Facility for Acceptance, Calibration and Testing (FACT) Site conducted an independent and detailed evaluation/characterization of this sensor (Hart, 2007). The primary purpose of the IML sensor (model SS) is to detect avalanches (Comey and Mendnhall, 2004) but has been redesigned (model ST) to study different infrasound sources, from earthquakes to explosions (Stump et al., 2007; Hale et al., 2010). The IML contains 20 small electret condenser microphones that are summed to produce an improved signal-to-noise output signal. Depending on the model, either four or eight hose connector ports are used to attach porous hoses for wind noise reduction. The output from the sensors was digitized on a Reftek RT-130 digitizer set to a gain of 32 with a sampling rate of 500 samples per second (500 Hz).

For the first two experiments, seven stations were distributed azimuthally about ground zero at ~230 m with stations extending Southeast at distances of 1, 2 and 5 km (Figure 1). Each station had five IML-ST infrasound sensors. Four sensors had 50 ft. porous hoses for wind reduction and one sensor was left open to the elements. They were arranged in a roughly triangular geometry with one sensor North, two Southeast and Southwest, respectively, and two in the center. Each leg is approximately 30 m away from center. One of the center sensors was the one without porous hoses and was approximately co-located with the center sensor. For this paper, only data recorded at the sensors with the wind reductions systems will be discussed. All figures, except where noted, were produced with data that have been broadband filtered between 1 and 10 Hz using a four-pole Butterworth filter.

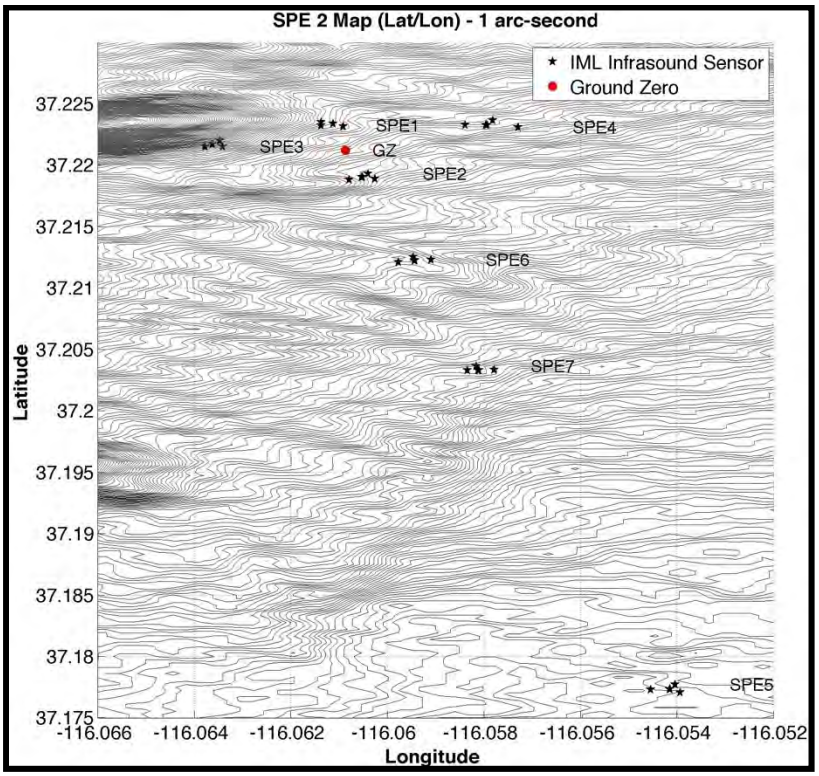


Figure 1. Topographic map showing each infrasound sensor (black star) at the seven SPE-N station locations and ground zero (red circle). The station locations remained the same for SPE-N-1 and SPE-N-2.

SPE-N Shot 1

The first explosion, conducted May 3, 2011, at 22:00:00 UTC, had a yield of 0.1 tons at 60 m depth of burial (DOB), corresponding to a scaled depth of burial (SDOB) of 1,026 m. This first explosion was designed to be a calibration shot to determine, empirically, the Green's functions for the surrounding rock. The shot plan called for a line of Det-Cord to be emplaced from the working point to the surface, as a secondary means of detonation should the electronic detonation fail. The Det-Cord was wrapped around several sandbags at the surface, above the hole and again buried with more sandbags. During the shot, the primary electronic detonator worked as planned and set off the Sensitized Heavy Ammonium Nitrite and Fuel Oil (SHANFO). This in turn ignited the Det-Cord resulting in an explosion at the surface. After the Det-Cord exploded, the weld on a line-of-sight pipe, that goes from the working point to the surface, failed and ejected out of the hole. A review of the acoustic data show that there was little to no significant acoustic energy released into the atmosphere, at least not sufficient enough to interfere with the detection of the primary explosion. In this case, the dominant source of the infrasound is the vertical ground motion from the detonation of the SHANFO with an estimated spall size of ~50 m in diameter. However, even with the stemming failure, the observed amplitudes for this shot are very low due to the yield (<<1 Pa at the closest station – Table 1), compared to the ~14 Pa observed for SPE-N-2 (Table 2).

Table 1. Station number, mean peak amplitude (Pa) (i.e. peak amplitudes from all sensors at each station are averaged) and mean distance (km). Note – the stations have been ordered according to distance. The amplitudes marked with a (*) are noise estimates since the signal-to-noise is too low to measure an amplitude of the signal.

Station	Mean Peak Amplitude (Pa)	Mean Distance (km)
1	0.30	0.24
2	0.35	0.25
3	0.41	0.25
4	0.23	0.35
6	0.13*	0.99
7	0.07*	2
5	0.10*	5

For this shot, only the four closest stations (0.25 km) recorded the explosion with decent signal-to-noise ratios. The station located at 1 km recorded the signal but with a much reduced amplitude, while the two farthest stations, 2 and 5 km respectively, did not record the shot with sufficient signal strength. We normalized and cross-correlated each recorded signal with the observed signal from station 1, sensor 1 and stacked and summed the results (Figure 2A). It is clear that only the closest stations provide any benefit to the stacking. The preceding seismic signal is shown on the plot occurring at 60 seconds followed by a clear acoustic pulse. This can also be seen in detail in Figure 2B. The "m" shape of the pulse is a result of filtering and the propagation of the signal being recorded off-axis to the movement of the distributed source region.

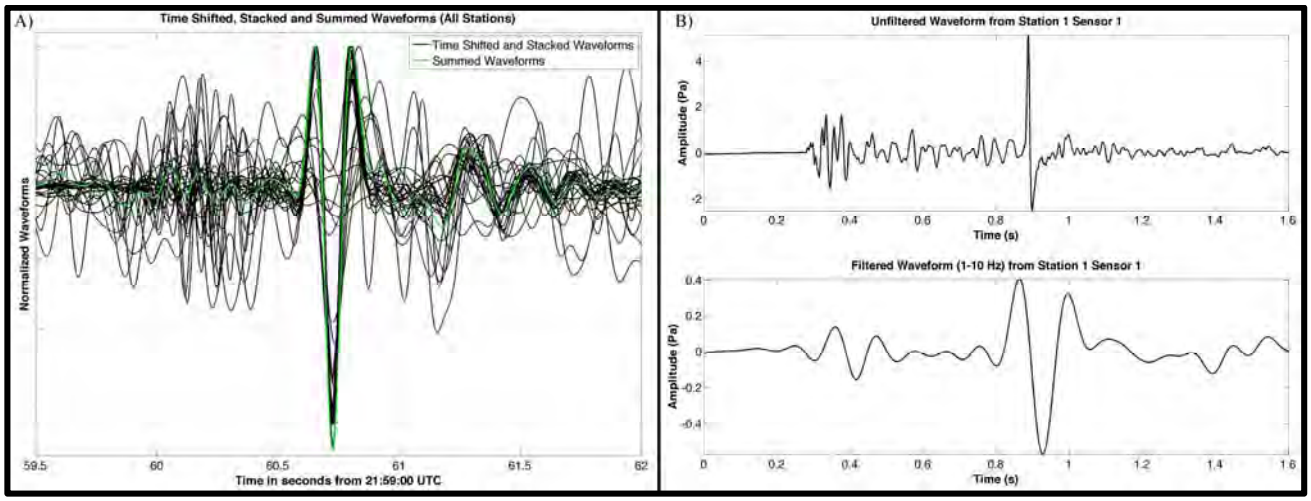


Figure 2. A) Time shifted, stacked (black) and summed (green) waveforms from all SPE-N-2 infrasound sensors. The variability in the waveforms around 60 seconds corresponds to the seismic component of the explosion signal recorded with the infrasound sensors. The rest of the variability comes from low signal-to-noise for the stations 1 km and beyond. B) Waveforms from sensor 1, station 1 shown unfiltered (top) and filtered (bottom) between 1 and 10 Hz using a 4-pole, Butterworth filter.

As shown above, the explosion was not large enough for the acoustic wave to propagate to the entire network. The waveforms from the four closest stations show the seismic signal followed by the acoustic pulse, but significantly decays to the point of not being detected at all past 1 km (Figure 3).

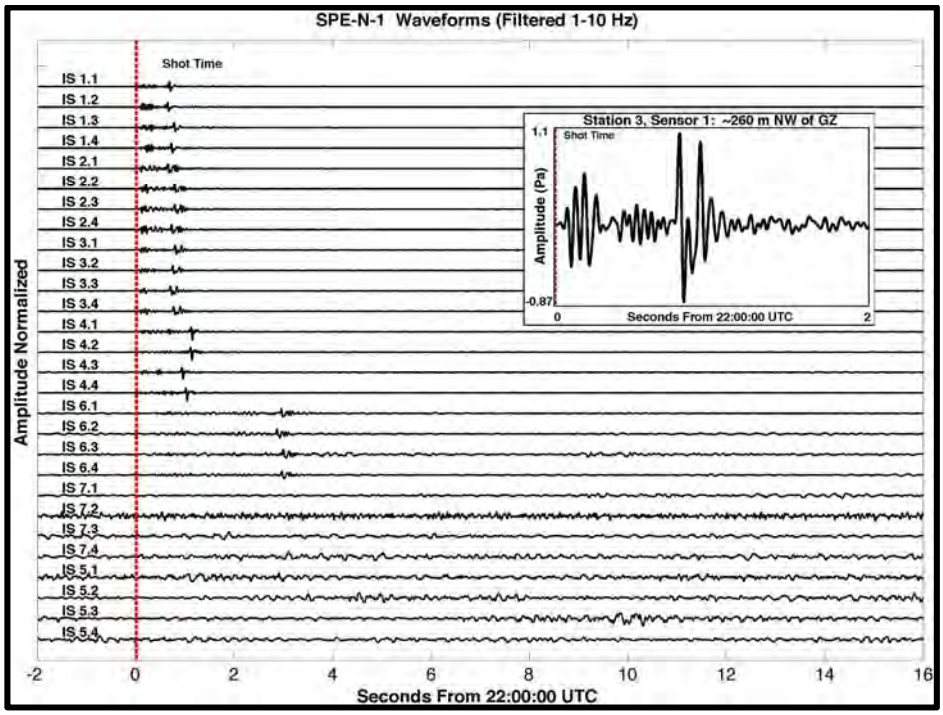


Figure 3. Normalized waveform plot showing all the infrasound sensors with an inset showing a detailed waveform from station 1, sensor 1.

For the sensors at stations 1 - 4, the close-in stations, we are able to determine if the recorded amplitudes decay according to the standard model of 1 over the distance. The American National Standards Institute (ANSI) describes the decay rate of a point source explosion to be $\frac{1}{r^{1.1}}$ (ANSI, 1983). This is to say that as distance (r) increases, the amplitude will decay at a rate of $\frac{1}{r^{1.1}}$ (Figure 4 – Red Line). This relationship generally works well for most explosions that are in the free field and directly perturbing the atmosphere. For the SPE-N series of explosions we find that since they are not in the free field, the standard model of $\frac{1}{r^{1.1}}$ doesn't fit as well as simply approximating the decay rate as $\frac{1}{r}$. Unfortunately, due to the much decreased signal-to-noise for stations 5, 6, and 7. We plot signals from only the four closest stations. Not surprisingly, the amplitudes generally fit the $\frac{1}{r}$ decay rate with some sensor variability at each station. This variability will be discussed in more detail later in the SPE-N-2 section.

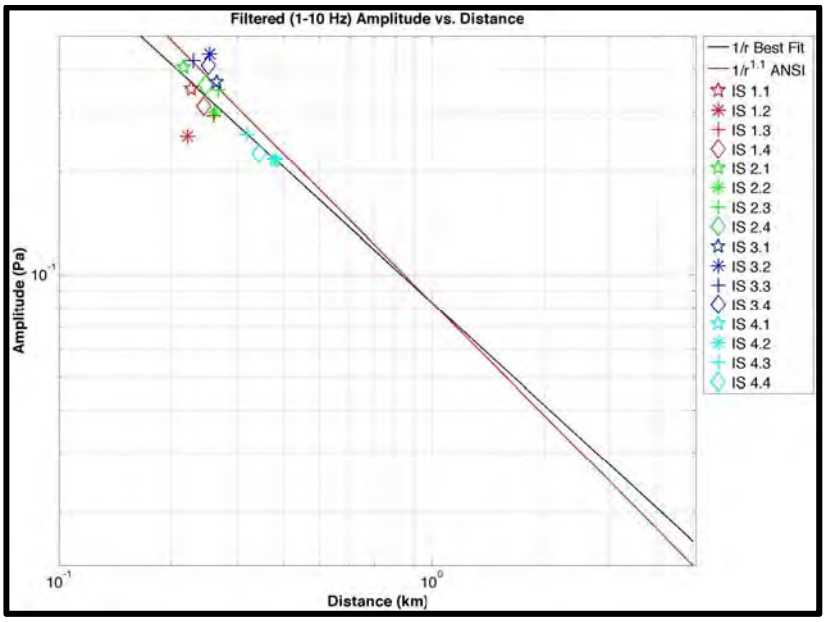


Figure 4. Amplitude vs. distance for each infrasound sensor at four of the seven stations with $\frac{1}{r}$ and ANSI $\frac{1}{r^{1.1}}$ best-fit lines. The signal-to-noise for the stations >1 km was too low to get an accurate amplitude measurement.

SPE-N Shot 2

The second explosion, conducted October 25, 2011 at 19:00:00 UTC, had a yield of 1 ton at a depth of 45 m, corresponding to a SDOB of 357 m. This shot was completely contained and resulted in a small dust cloud at the surface. The spall region was estimated to be ~90 m in diameter. The station locations and sensors were identical to those used in the SPE-N-1 experiment. The primary difference between SPE-N-1 and SPE-N-2, in terms of observed infrasound, is that all of the stations detected the SPE-N-2 explosion (Figure 6), largely due to the higher yield. The observed amplitudes ranged from ~0.2 to 13.4 Pa (Table 2).

Table 2. Station number, mean peak amplitude (Pa) (i.e., peak amplitudes from all sensors at each station are averaged) and mean distance (km). Note – the stations have been ordered according to distance.

Station	Mean Peak Amplitude (Pa)	Mean Distance (km)
1	7.68	0.24
2	10.05	0.25
3	13.44	0.25
4	6.83	0.35
6	2.01	0.99
7	0.77	2
5	0.20	5

Since SPE-N-2 had a much larger signal-to-noise ratio for the event, the resulting signal correlation, summation and stack of the recorded signals resulted in a much cleaner signal (Figure 5A). Again, preceding the event, the seismic signal is observed followed by the acoustic "N-wave" (Figure 5B). There is some variability between waveforms from each sensor, which could be related to propagation, but overall, the acoustic portion of the waveform is very similar.

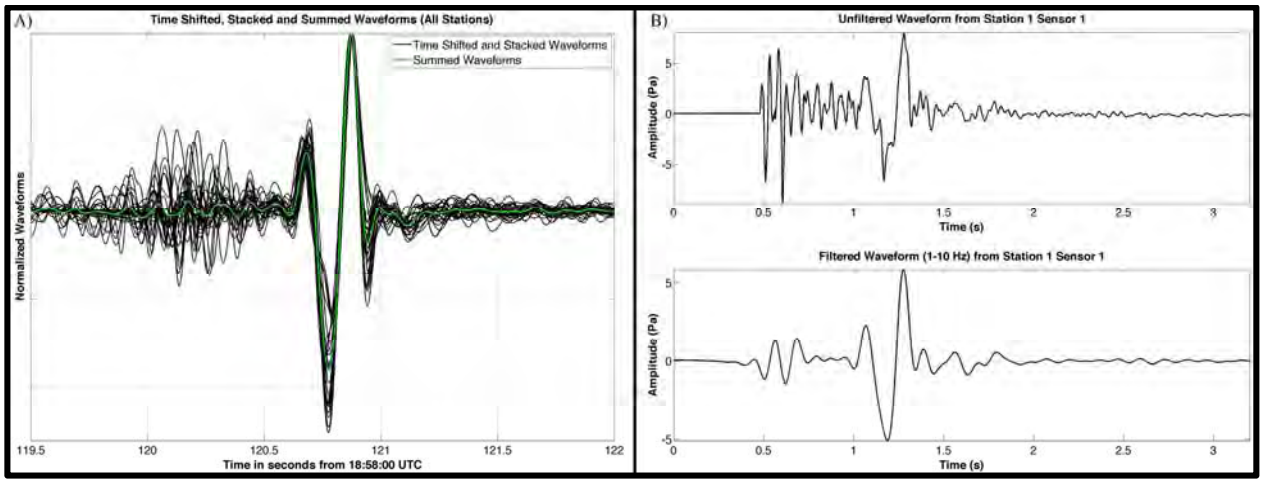


Figure 5. A) Time shifted, stacked (black) and summed (green) waveforms from all SPE-N-2 infrasound sensors. The variability in the waveforms around 120 seconds corresponds to the seismic component of the explosion signal recorded with the infrasound sensors, followed by the acoustic arrival ("N" wave). B) Waveforms from sensor 1, station 1 shown unfiltered (top) and filtered (bottom) between 1 and 10 Hz using a 4-pole, Butterworth filter.

The acoustic pressure wave from the explosion propagated across the entire network and to each sensor with the potential to have been detected to some distance past 5 km, though, not far, as the amplitude at 5 km was 0.2 Pa (Figure 6). The observed seismic signal is present on the closest stations (1 – 4) but starts to become less evident past 1 km.

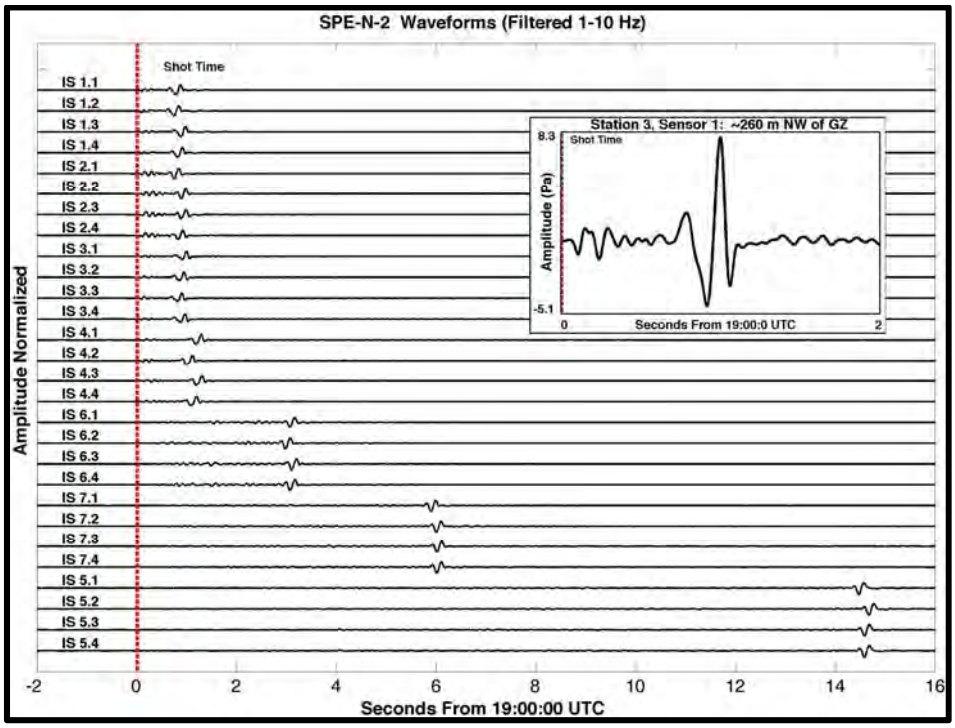


Figure 6. Normalized waveform plot showing all the infrasound sensors with an inset showing a detailed waveform from station 1, sensor 1.

As with SPE-N-1, we are able to determine the amplitude decay rate. SPE-N-2 was ten times larger than SPE-N-1, resulting in the acoustic pressure wave being observed across the entire network. We were able to use every sensor

at every station to plot the amplitude versus distance decay for the entire network (Figure 7). We again plot both the $\frac{1}{r}$ best fit and the ANSI $\frac{1}{r^{1.1}}$ solutions. In this case the $\frac{1}{r}$ solution fits more of the stations than the ANSI solution, however, the ANSI solution better follows the actual trend of the data.

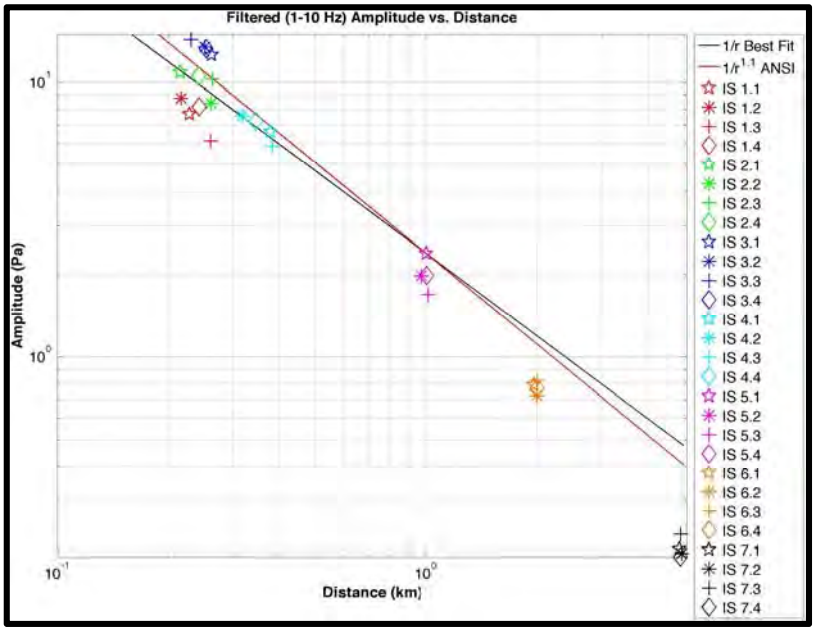


Figure 7. Amplitude vs. distance for each infrasound sensor at all seven stations with $\frac{1}{r}$ and ANSI $\frac{1}{r^{1.1}}$ best-fit lines.

There are several reasons for the variation in sensor amplitudes at each station. Wind can affect the propagation of acoustic signals (Figure 8). During the time of the shot, the wind was blowing from the Southeast to the Northwest at ~3 m/s, potentially causing the lower amplitudes observed at the more distant stations (5, 6, and 7). This may not entirely account for the variation in the near stations (1, 2, 3, and 4). In this case, it is possible that the amplitude variations are due to the placement of each sensor. Although the sensor spacing is only ~30 m, the topography is not flat in this region. This results in sensors that do not have line-of-sight (LOS) to ground zero. The sensors are also subject to some level of variability as they rely on multiple electret condenser microphones that each have their own response. The microphones are selected and the sensors are tuned to minimize this effect, but it is still a potential source of variability. Interestingly, for both SPE-N-1 and SPE-N-2, the first three stations all vary in amplitude in a similar manner; i.e., in both cases, station 3 is has a larger amplitude than station 2, and station 2 has a larger amplitude than station 1. This could potentially be caused by the topography, but future SPE-N tests are needed to further constrain the cause of the amplitude variations.

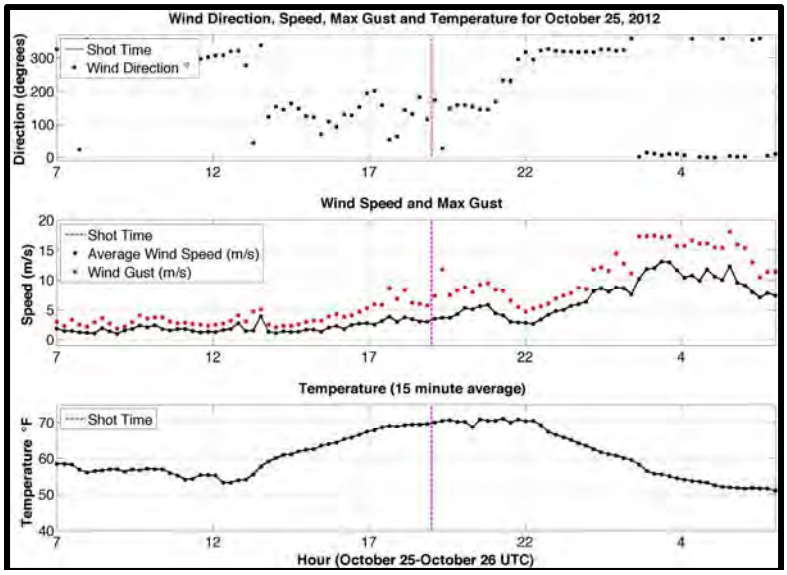


Figure 8. Onsite meteorological observations including: wind direction, wind speed, max wind gust, and temperature on a 15-minute average. The time of the shot is denoted with vertical dashed line.

Despite the sensor variability, we were able to use the infrasound sensors at each station as mini-arrays, to calculate the back azimuth to ground zero. For this analysis we use the regional infrasound monitoring software, InfraMonitor (Arrowsmith and Whitaker, 2008). Using the back azimuths (Figure 9A) from each station we use the Bayesian infrasonic source location (BISL) technique (Modrak, 2010) built into InfraMonitor to calculate a location solution. The calculated location solution agrees very well with the actual location of ground zero to within a ~35x35 m area with 95% confidence (Figure 9C).

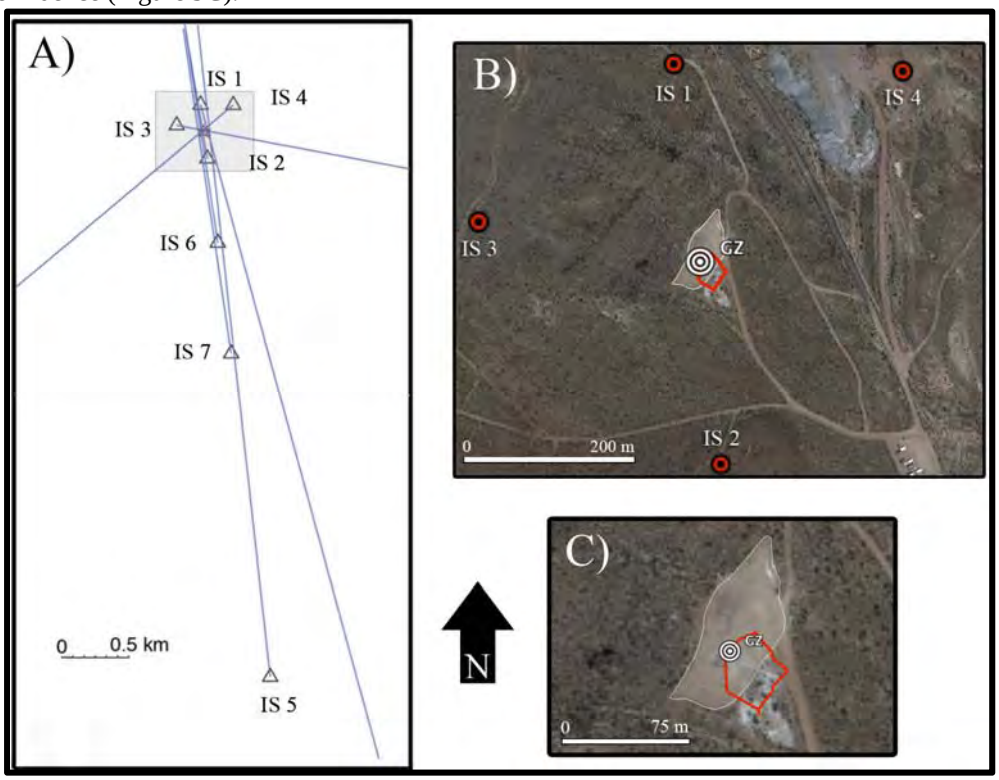


Figure 9. A) BISL location solution using the InfraMonitor detection and location software in shaded square represents enlarged area (B). B) Map of the four closest stations (1 – 4) and ground zero (white target) with a 95% confidence location solution (red). C) Close up view of the explosive pad (white), ground zero (white target) and the 95% confidence location solution (red).

CONCLUSIONS AND RECOMMENDATIONS

The explosions conducted at the NNSS, as part of the Source Physics Experiment, are invaluable to the ongoing study and understanding of infrasound generation by underground explosive events. With the level of ground truth knowledge in terms of yield, location and rock characteristics, we are able to begin to constrain specific properties of infrasound generation and propagation.

Future Work

Currently, we are working on modeling the infrasound generated from the underground explosions using several surface accelerometers located at ground zero. With the accelerometer data we can create and compare synthetic infrasound waveforms using the Rayleigh Integral Method (Whitaker, 2008; Arrowsmith et al., 2012). This will help to better understand what parameters are dominant in producing acoustic pressure waves from underground explosions.

ACKNOWLEDGEMENTS

The authors are grateful to Bobby Corbell and Chris Jones for the initial deployment and collection of the data for both shots and to Cathy Snelson, Bob White, and Ryan Emmitt for their support at NNSS.

REFERENCES

ANSI (1983). Estimating airblast characteristics for single point explosions in air with a guide to evaluation of atmospheric propagation and effects, ANSI S2.20-1983.

Arrowsmith, S. J., et al. (2012). A Seismoacoustic Study of the 2011 January 3 Circleville Earthquake. *Geophys. J. Int.* **189,** 31148–1158.

Arrowsmith, S. J. and Whitaker, R. (2008). InfraMonitor: a tool for regional infrasound monitoring, in *Proceedings of the 2008 Monitoring Research Review*: *Ground-Based Nuclear Explosion Monitoring Technologies,* LA-UR-08-05281, Vol. 2, pp. 837–843.

Comey, R. H. and Mendenhal, T. (2004). Recent studies using infrasound sensors to remotely monitor avalanche activity, in Proceedings of the 2004 International Snow Science Workshop, Jackson Hole, Wyoming.

DOE/NV-209 (1994). United States Nuclear Tests: July 1945 through September 1992. Rev. 14:p16, 26

Hale, J. M., et al. (2010). Infrasound signal characteristics from small earthquakes, in *Proceedings of the 2010 Monitoring Research Review*: *Ground-Based Nuclear Explosion Monitoring Technologies,* LA-UR-10-05578, Vol. 2, pp. 720–730.

Hart, D. M. (2007). Evaluation of inter-mountain labs infrasound sensors July 2007. Sandia National Laboratory Report, SAND2007-7020.

Inter-Mountain Labs Model ST Infrasound Sensor Datasheet. (2012) http://www.intermountainlabs.com/pdf/IML_ModelSTDataSheet.pdf

Modrak, R. T., et al. (2010). A Bayesian framework for infrasound location. *Geophys. J. Int.* **181**, 399–405.

Stump, B., et al. (2007). Seismic and infrasonic energy generation and propagation at local and regional distances: phase 1 – Divine Strake experiment, in *Proceedings of the 2007 Monitoring Research Review: Ground-Based Nuclear Explosion Monitoring Technologies,* LA-UR-07-5613, Vol. 1, pp. 674–683.

Whitaker, R., W. (2008). Infrasound signals from ground motion sources, in *Proceedings of the 2008 Monitoring Research Review: Ground-Based Nuclear Explosion Monitoring Technologies,* LA-UR-08-05281, Vol. 2, pp. 912–920.

REGIONAL INFRASOUND OBSERVATIONS FROM RECENT ROCKET ENGINE TESTS IN SOUTHERN GERMANY

Karl Koch

Federal Institute for Geosciences and Natural Resources

Sponsored by the German National Data Centre

ABSTRACT

The European Space Agency's ARIANE-5 main engine has undergone numerous development and acceptance tests in the late 1990s and early years of the 21st century. These engine tests from a facility of the German Aerospace Agency (DLR) in Southern Germany, near the city of Heilbronn, represent, as well-controlled sources, an excellent ground-truth source for studies of infrasound propagation to local and regional distances. As such, a considerable number of engine tests have previously been identified at the International Monitoring System (IMS) station IS26 in the Bavarian Forest, which is located at a distance of about 320 km in an east-southeasterly direction, following its establishment in 1999. In a previous study it was found that signals emanating from the propulsion tests could regularly be detected at IS26 during winter months, but not for tests during summer months, thus reflecting the changes in atmospheric conditions in Central Europe between winter and summer.

In 2011, DLR prepared for a new series of seven propulsion tests which eventually started in November 2011. With interim times of 3-4 weeks between tests, the last test was planned for late March 2012. However, near the end of the testing series two additional tests were scheduled and the last test was then carried out on 14 May 2012. With the favorable infrasound propagation conditions during this time period in the direction of IMS station IS26 a set of six mobile infrasound recorders available at BGR were deployed at local and regional distances to capture the infrasonic wavefield along the path to IS26. The mobile stations were set up at distances as close as 20 km from the source and stretched profile lengths of 100-130 km for a maximum distance of 240 km. Our aim with these measurements is to study sound propagation from direct paths mainly involving the tropospheric layer through the "zone of silence" to the range for IS26, where paths through the stratosphere are followed.

Preliminary results show a strongly varying wavefield from test to test. During the initial field campaign on 19 December 2012 with mobile recording up to 120 km distance, infrasound signals were only observed to some 40 km from the source. In the next two campaigns with the same station arrangement, the only signal was found at the largest distance. No seismo-acoustic signals could be detected at distances as close as 20 km, where the nearest seismographic station is located. Three tests in March and April showed consistent but highly varying signal levels between 120 and 200 km. This is in contrast to the last test in May, where there were no infrasound signals observable at distances from 80 to 180 km. Besides these engine tests, an incidental explosion in the Grand Duchy of Luxemburg was recorded on 16 February 2012 several hours prior to an engine test, where the event occurred nearly on the great-circle path from Heilbronn to the Bavarian Forest. The mobile stations deployed at distances between about 250 and 350 km as well as IS26 at 560 km showed clear multi-pathed infrasound arrivals and, thus, provide a good opportunity to study infrasound propagation to even larger regional distances.

OBJECTIVES

To study the propagation of infrasound to local and regional distances and in particular within the so-called zone of silence, ground-truth sources are of special interest. One such well-controlled source has previously been identified in Southern Germany from development and acceptance propulsion tests of the European Space Agency's ARIANE-5 main engine (Koch, 2005, 2010). This source near Heilbronn, Germany, was repeatedly observed at the IMS stations IS26 about 320 km to the east-southeast of the source location. The previous research with data from the years 2000-2004 has indicated that the significant changes between the state of and the processes within the atmosphere between winter and summer months result in the presence or absence of infrasound signals at IS26, consistent with the findings by Le Pichon et al. (2008).

The research work reported here was carried out to address a number of topics of interest in the propagation of infrasound to local and regional distances. When we obtained the information on a series of seven propulsion tests of the ARIANE-5 engine to be conducted from fall 2011 to spring 2012 we aimed at acquiring infrasound recordings from these sources from close-in (local) distances, as low as 20 km, to a range of nearly 250 km. This configuration allows us to gather a representative sample of reception and signals characteristics over the distance range to IMS station IS26. Due to the well-known characteristics of the ground-truth events, we are able to study how the corresponding atmospheric conditions affect the observations obtained in the near-regional distance range. Of special use is the information on propulsion start and duration for signal identification in the presence of noise, and the fact that the temporal extent of the test of up to 12 minutes allows us to study very short-term variations of propagation conditions.

RESEARCH ACCOMPLISHED

In previous work Koch (2005, 2010) has studied infrasound signals from similar tests of the ARIANE-5 main engine, the VULCAIN-2 engine type, that had been carried out in the years 2000-2004. The observations were made at the IMS station IS26 at a distance of about 320 km in the east-southeasterly direction in the Bavarian Forest (see Figure 1). In 2010, after a test in January 2010 completing the previous testing campaign at the rocket engine testing facility of the DLR near the city of Heilbronn, Southern Germany, information was obtained that a subsequent testing campaign should commence in the second half of 2011. As these rocket tests are frequently observed at IS26, at least during winter months, we planned to deploy a number of mobile infrasound stations at local and regional distance, filling in between the testing site and the IMS station in the Bavarian forest. One advantage of the source, compared to explosive types of sources, is that it can have a duration of 10 minutes or more. When using a single-element infrasound station configuration lacking the ability for bearing measurements, it can easily be verified that a particular signal is indeed consistent with this source.

Temporary Field Deployments of Mobile Infrasound Stations

The testing campaign eventually was announced to start in November 2011 and to extend through March 2012. A set of six mobile systems were available for deployment along the path to IMS station IS26. With the announced number of seven tests we prepared for the deployment of the equipment at distances as close as 20 km and with inter-station spacing of about 20 km. To cover the nearly entire range to IS26 the mobile stations were first installed in the distance range from 20 to 120 km for a total of three tests and later in the distance range of 120-240 km for another four tests as shown in Figure 1. From the initial seven tests we could not deploy the systems for the first two due to logistical problems. After the seventh test, however, two additional tests were announced by DLR and the campaign finally ended in mid-May 2012 (see Table 1). For the very last of these tests we relocated the farthest mobile stations to intermediate distances of 80 and 100 km.

Of the total nine propulsion tests, seven exceeded durations of 10 minutes. Only one test was significantly shorter with a duration of less than 5 minutes.

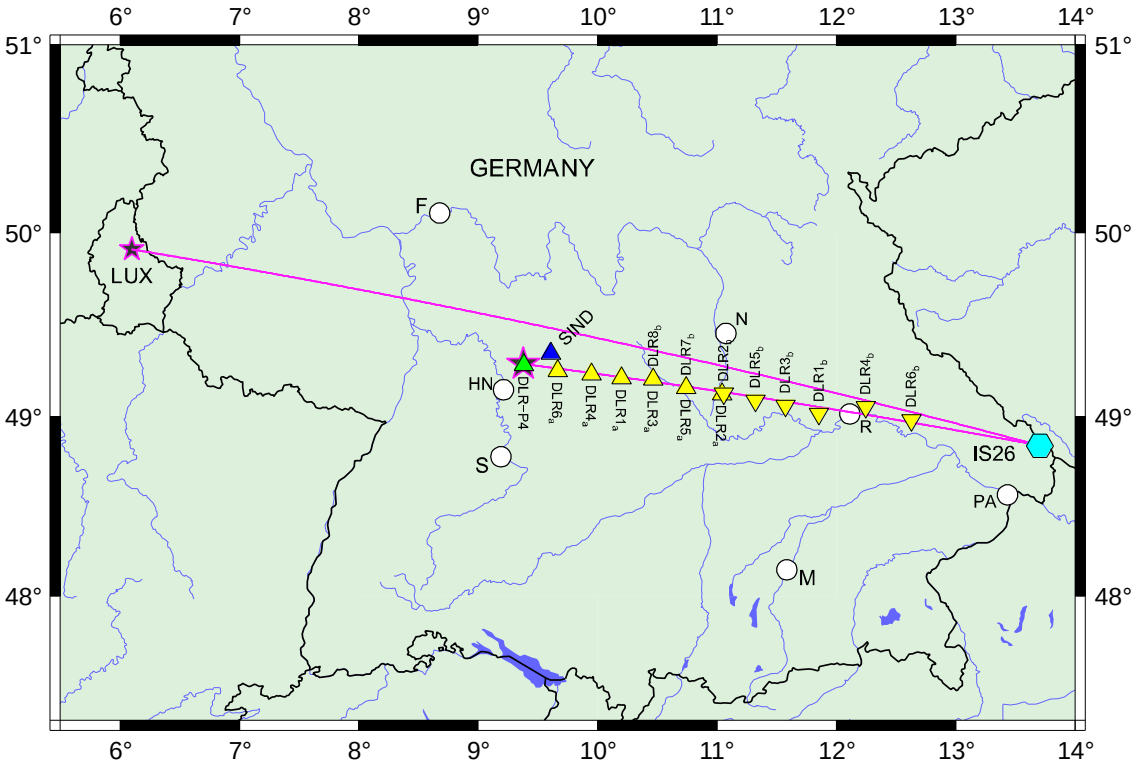


Figure 1. Geographical location of the ground truth source near Heilbronn, Southern Germany, and the deployment of mobile infrasound stations along the path to IMS station IS26. The source is from propulsion tests of the VULCAIN-2 engine (ARIANE-5 main engine) at the propulsion testing facility of DLR (star). The mobile stations are indicated by triangles and inverted (yellow) triangles. A seismometer was installed at a distance of about 150m from the testing facility (green triangle). The State Seismological Survey of Baden-Württemberg operates the seismic station SIND at a distance of 18 km from the source. Also shown are the locations of an explosion in Luxemburg which was recorded along the profile of mobile stations and major cities in Southern Germany (F-Frankfurt, M-Munich, N-Nuremberg, R-Regensburg, S-Stuttgart, HN-Heilbronn, PA-Passau).

The mobile infrasound equipment, as sketched in Figure 2, consisted of Reftek digitizers and MB-2000/2005 microbarometers and included power supply systems and GPS antennas. In addition we also installed Lennartz 3D seismometers for stations close to the rocket testing facility at distances of 20 and 40 km in the first deployment. These installations were triggered by the seismo-acoustic recordings obtained at the seismic station SIND of the State Seismological Survey of Baden-Württemberg. This station is at a distance of about 18 km from the DLR site.

The seismo-acoustic signals were digitized with a sampling frequency of 100 Hz. At the close-in seismometer station, installed after the 19 December 2011 test, a sampling frequency of 500 Hz was used. This station was switched on a few hours before a test and shut down hours afterwards.

For reducing wind noise for our installations in harsh fall and winter conditions we connected porous hoses to the microbarometers. These hoses of some 5-8m length were terminated in two different configurations. In the first deployment in December 2011 we used a closed loop of about 1 m diameter at all stations. Due to the lack of signals beyond the distance of 40 km during this initial deployment and the advent of snow coverage due to the season, we later used a T-end configuration with a end-leg length of about 2-3 m and the ends completely open.

Table 1. Ground-truth information on propulsion tests carried out at the testing facility of DLR near Heilbronn, Southern Germany. The ground-truth source is near the geographic location of 49.3°N and 9.4°E. The distance to IS26 is 320 km.

No.	Date	Start time (local time)	Duration (s)	Recording range
1	18-11-2011	16:50	600	IS26
2	08-12-2011	16:30	668	IS26
3	19-12-2011	16:17	646	20-120 km, IS26
4	16-01-2012	17:43	285	20-120 km, IS26
5	16-02-2012	14:28	720	20-120 km, IS26
6	07-03-2012	16:53	700	120-240 km, IS26
7	22-03-2012	16:31	696	120-240 km, IS26
8	27-04-2012	16:39	653	120-240 km, IS26
9	14-05-2012	17:21	530	80-180 km, IS26

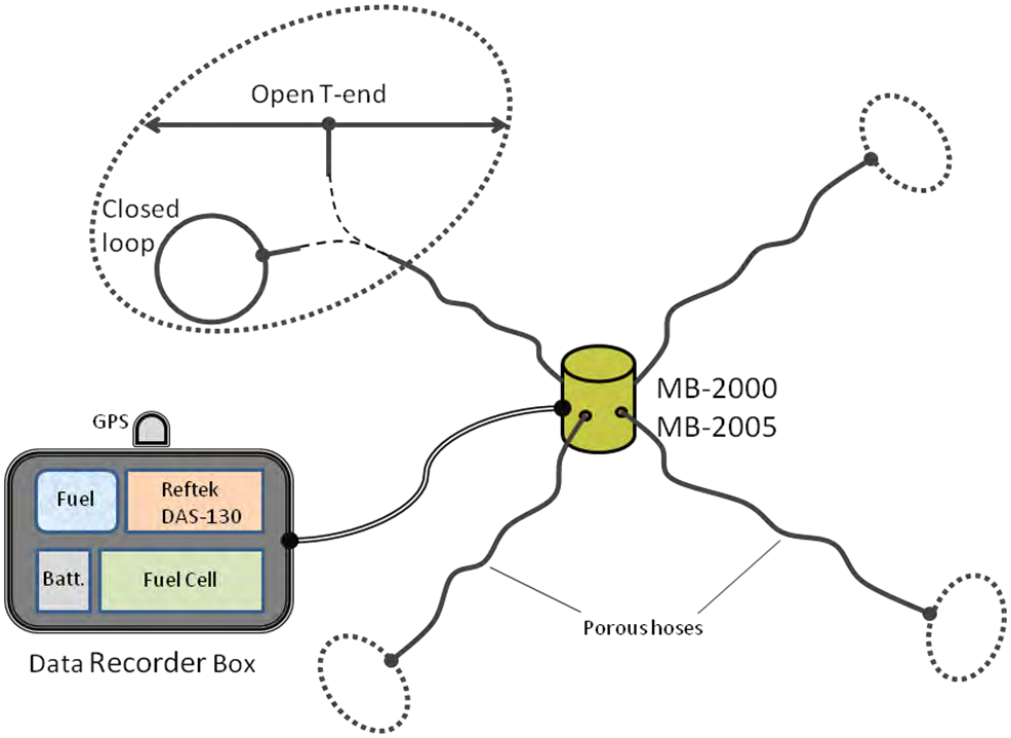


Figure 2. Overview of the mobile infrasound station installation. Two different noise filter layouts with porous hoses were used. One consisted of a closed loop and the other had a T-shaped end with hose ends open. Not sketched are the seismometers attached to the acquisitions systems as used at two stations in the first deployment.

Infrasound Observations at IMS Station IS26

Infrasound observations at IMS station IS26 were obtained from all nine tests of the testing campaign. As the campaign was carried out in winter months this could be expected except for the last test in May 2012. For the first test on 18 November 2011, the observed signals are shown in Figure 3 (a) along with the results of the frequency-wavenumber (FK) analysis . The signal-to-noise ratio observed here was highest for all tests. The results of the FK analysis are consistent with stratospheric returns and the location of the source. The signals arrive after a travel time of about 18 minutes.

As found by Koch (2010), propulsion tests at DLR are commonly observed between October and April. Therefore it is somewhat unexpected that the test on 14 May 2012 could be found in the IS26 data, even though exhibiting a small signal to noise ratio in the selected frequency band above 2 Hz. As such it is also surprising that these signals provided sufficiently good results in the FK-analysis.

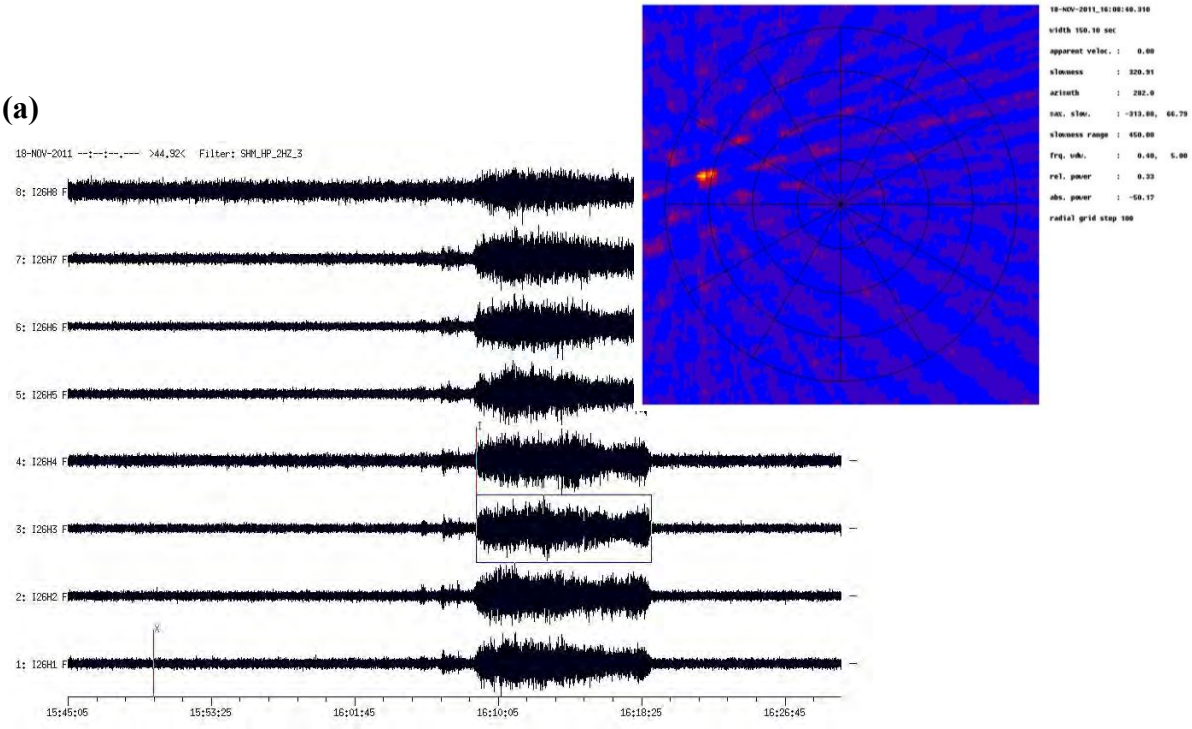


Figure 3. (a) Infrasound signals observed at the eight elements of IS26 from the engine test on 18 November 2011 at 15: 50UT and results of the FK analysis for an analysis window of about 150 s at the beginning of the signal. The data were high-pass filtered at 2Hz. The FK frequency band extended from 0.4-5Hz.

(b)

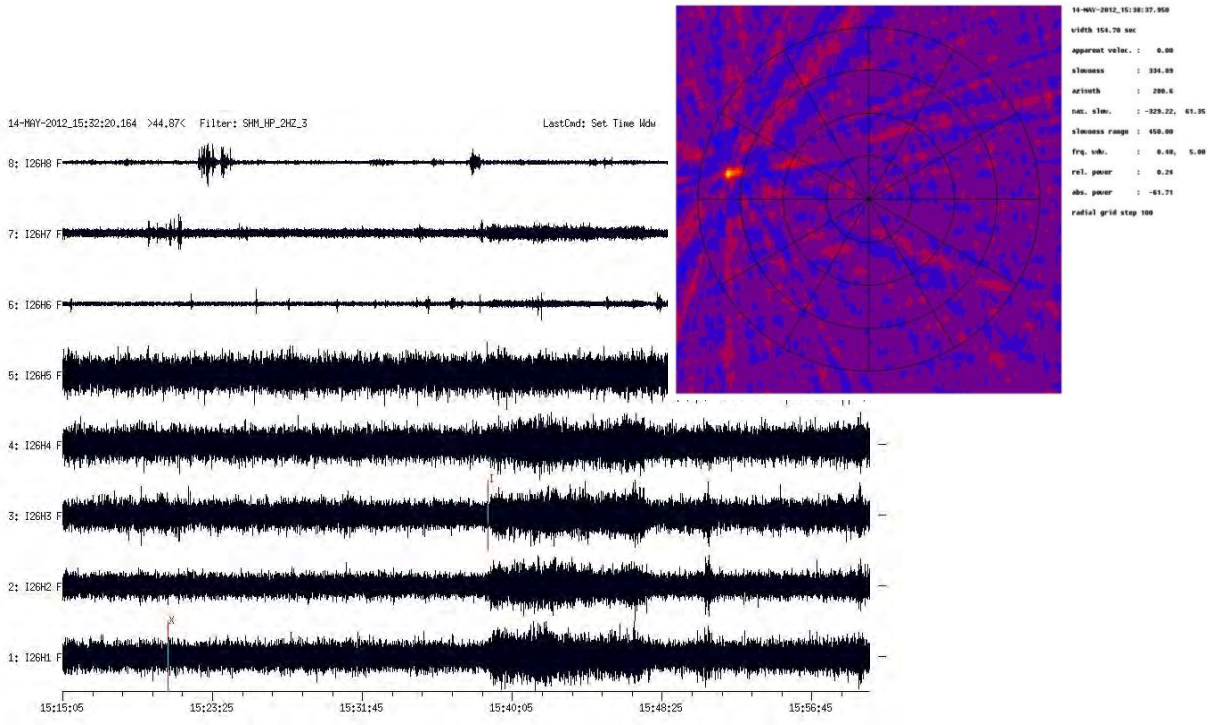


Figure 3 (cont'd). (b) Infrasound signals and FK analysis results for the test on 14 May 2012 at 15:21UT. For the filtering and processing parameters, see (a).

Infrasound Observations from the Mobile Infrasound Stations at Distances between 20 and 240 km

The initial three deployments for the tests on 19 December 2011 and January and February 2012 covered the distance range between 20 and 120 km. For the engine test on 19 December, the stations at distances of 20 km and 40 km equipped with both microbarometers and three-component seismometers showed seismo-acoustic signals. Stations beyond 40 km did not show any signals. For the next test, there were only marginal infrasound signals seen at 20 km and no signals visible at larger distances except at 120 km, where a strong signal was observed. Unfortunately, the station at 100 km was not operational, which could have indicated an even shorter range for the emergence of infrasound signals. The same pattern was observed for the test on 16 February 2012 (see Figure 4). Again, the only clear infrasound signal could be seen at 120 km. In this case it is interesting that there is a significant structure within the recorded signal, which is not related to the source excitation. Since the excitation is nearly constant throughout the propulsion test, the variation within the observation must clearly be a short-term path effect.

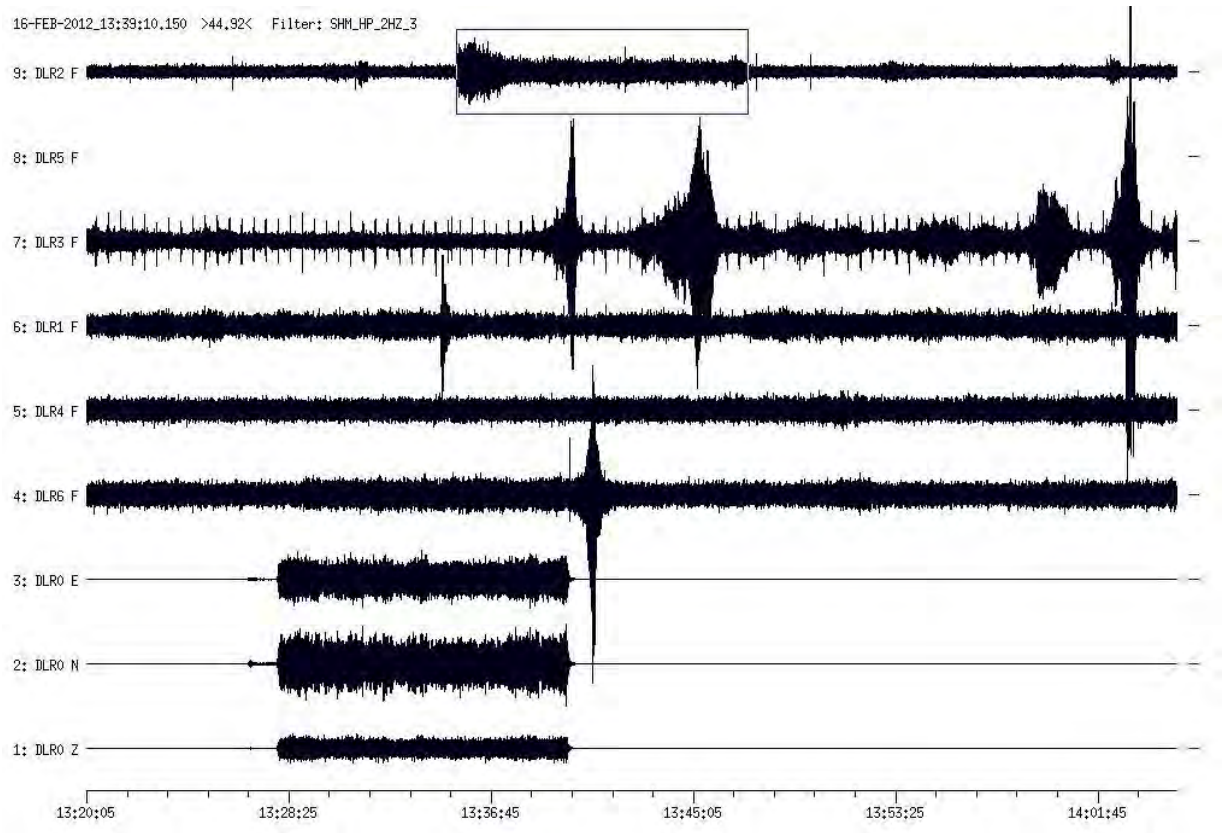


Figure 4. Infrasound signals observed on a recording profile of mobile infrasound stations between 20 and 120 km for the propulsion test on 16 February 2012 at 13:28UT (upper six traces; traces are ordered according to distance – top trace is the signal at 120km; no data were recorded at 100 km). The length of the box on the top trace corresponds to the source duration. Also shown are the three-component seismic records from a seismometer located next to the ground-truth source (lower traces). The instrument was installed to prove the consistency of the source excitation.

After the engine test in February 2012, the mobile infrasound stations were removed and redeployed at the larger distance range, however, re-occupying the range at 120 km which previously showed clear infrasound signals. In this larger distance range we consistently observed infrasound signals from the following three tests, i.e., through late April 2012. The data example shown in Figure 5 may be the most impressive record though.

For the final test, the farthest stations at distances of 210 and 240 km were removed and relocated to previous locations at ranges of less than 120 km. This test on 14 May 2012 could not be identified on any of the mobile stations between 80 and 180 km distance, even though a marginal signal could be observed at IS26 (see Figure 3b).

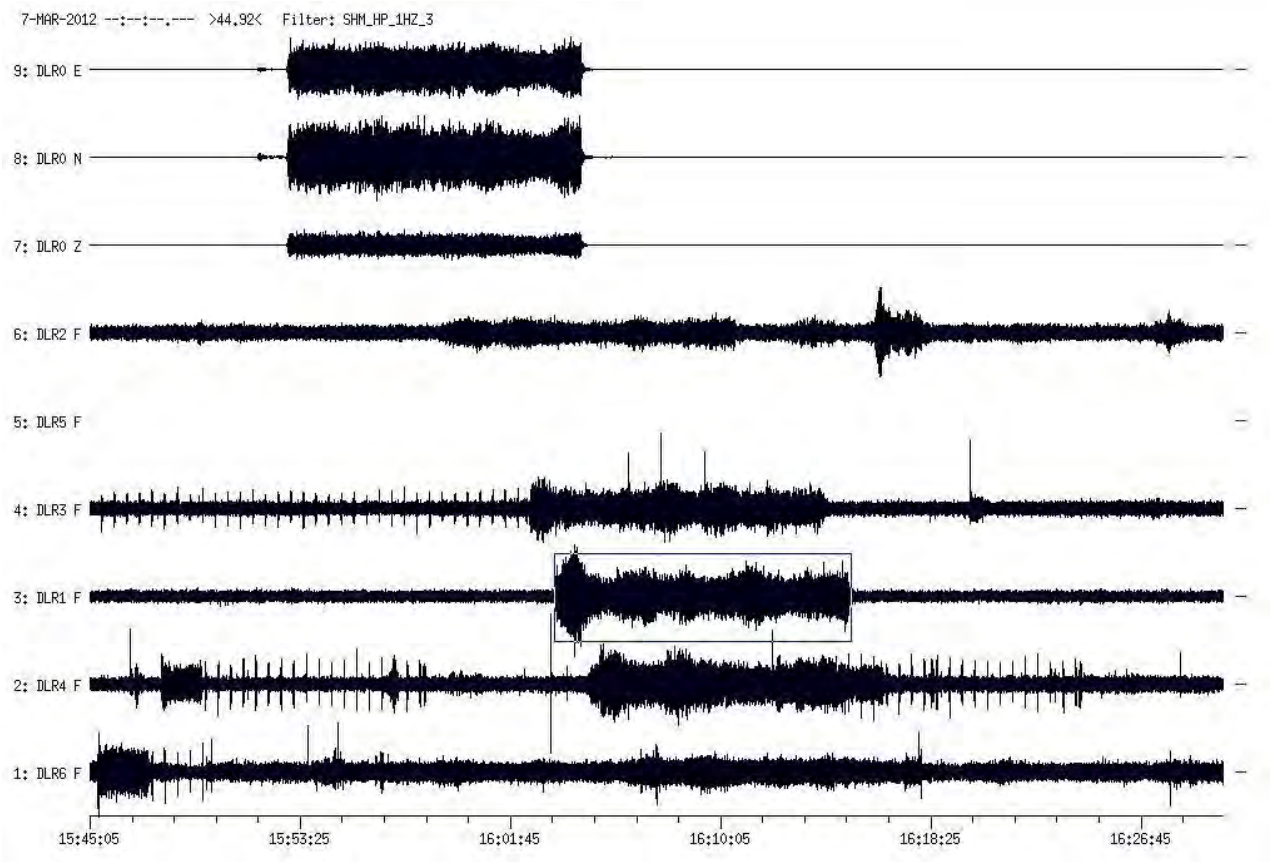


Figure 5. Infrasound signals observed on a recording profile of mobile infrasound stations between 120 and 240 km from the propulsion test on 7 March 2012 at 15:53 UT (lower six traces; traces are (inversely) ordered according to distance with the bottom trace being the signal at 240 km distance; no data were recorded at 140 km) . Also shown are seismic records from the close-in seismometer (top three traces). This is the only seismic signal which indicates a certain degree of source variability in the last quarter of the source time function. Note the distinct modulation of the infrasound signal at 180 km (see box corresponding to the source duration), which is different from the source.

Infrasound Observations from an Explosion in Luxemburg

Besides the projected recordings from the propulsion tests, we were able to record infrasound signals from an accidental explosion that occurred on 16 February 2012 a few hours prior to one of the propulsion tests. The explosion occurred in the Grand-Duchy of Luxemburg about 240 km further to the west-northwest of Heilbronn and, thus, nearly on the great circle path between IS26, the mobile infrasound stations and the DLR source location (see Figure 1). This explosion source is of great interest to our study of regional infrasound propagation: first, the recordings from this event confirm the proper operation of the stations located within the zone of silence and, second, it extends the range of infrasound recordings to more than 550 km when combining the observations from the propulsion test and the explosion that occurred both on 16 February 2012 (unless atmospheric condition would have changed significantly within the few hours between these two events).

The mobile stations and IS26 recorded the signals from this explosion as displayed in Figure 6. The closest mobile station at 240 km from the source showed a fairly simple waveform for this event, while waveforms at the farther stations show progressively more complex signals, with the stations beyond 300 km clearly showing three distinct arrivals. These arrivals develop beyond 250 km distance. A similar complexity is also seen at IS26, which is more than 560 km from the source.

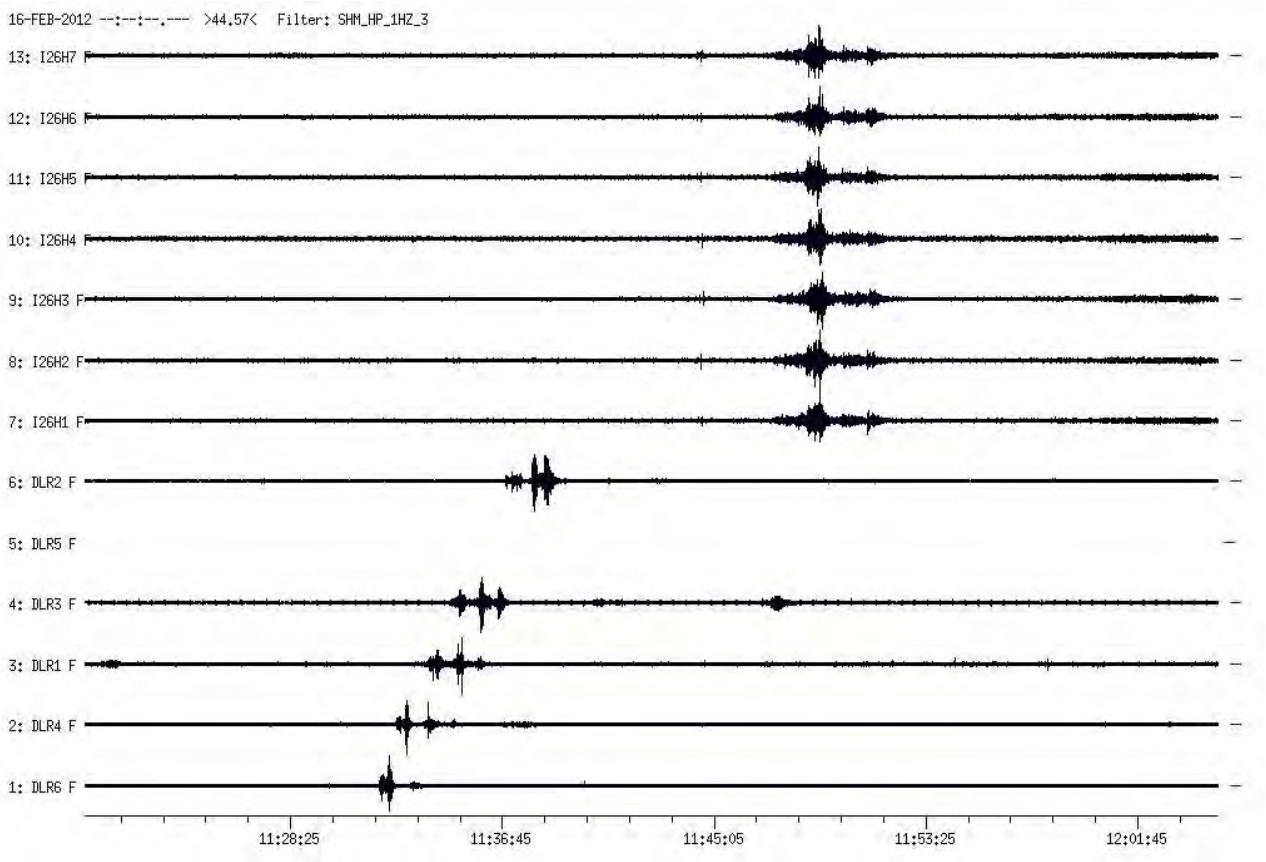


Figure 6. Infrasound signals from an explosion that occurred in Luxemburg on 16 February 2012 shortly after noon local time (about 11:15UT) on the recording profile of mobile infrasound stations located 20 to 120 km east-southeast of Heilbronn and at IMS station IS26. The traces are ordered according to distance. The former stations are between 250 and 345 km from the explosion site (lower six traces – no data recorded at 330 km), while IS26 is about 565 km away (top seven traces – I26H8 not shown due to strong instrumental noise). The data were high-pass filtered at 1 Hz.

Discussion

With the infrasound data collected from the series of propulsion tests at the DLR testing facility near Heilbronn, Southern Germany, we analyzed the signal strength of the noise and the signals in those cases where they could distinctly be observed. Stations in the distance range 60-100 km did not show identifiable signals and signals from stations at closer distance were marginal. These stations therefore only provided noise data, while most signals were found in the range beyond 120 km and mainly for the two tests in March 2012. For the last two tests in April and May no data were read because of the sparseness or lack of signals.

The corresponding analysis results are shown in Figure 7. For the 7 March 2012 data the signals yield a peak in amplitudes near 180 km. For the test on 22 March 2012 the most pronounced signal is seen at 120 km, beyond which the amplitudes decrease rapidly until 200 km distance. For four out of the shown five tests the station at 120 km showed signal amplitudes markedly above the background noise. In the case of IS26 at a distance of about 320km the background noise is lowest, obviously by means of the sophisticated noise reduction filter. Signal levels are up to four times higher, with the strongest signals for the 19 December 2011 test (see also Figure 3a).

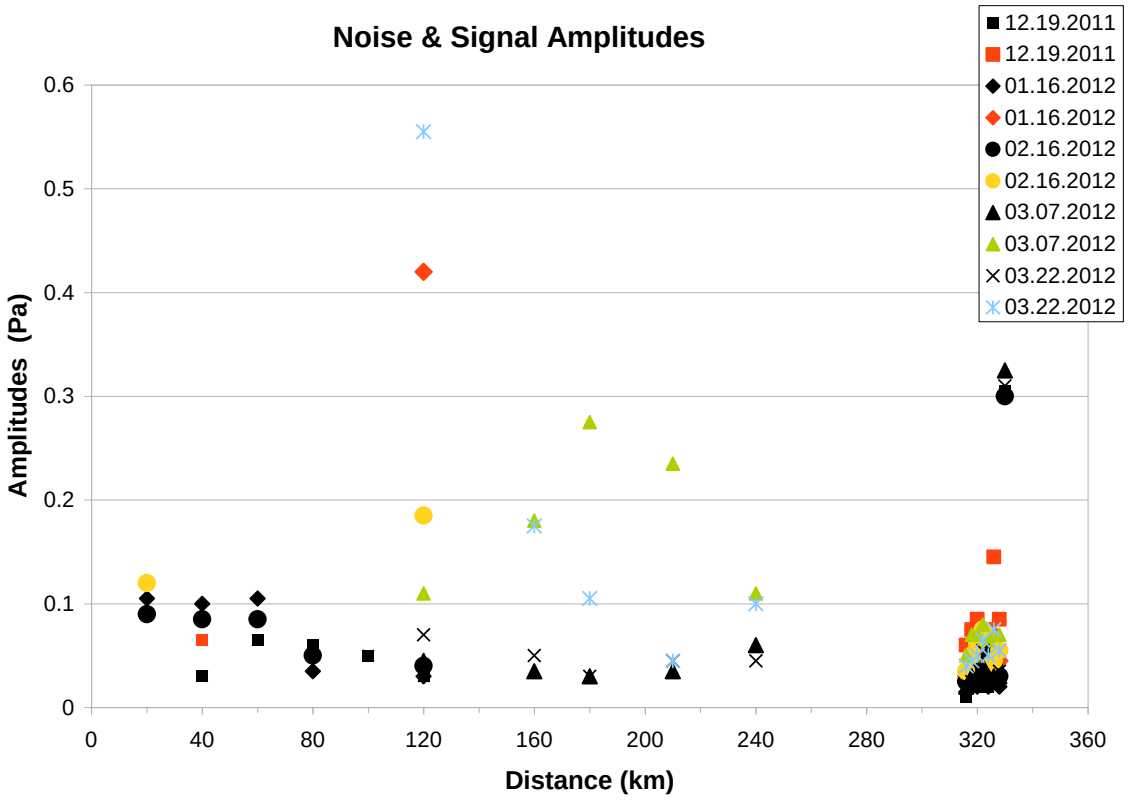


Figure 7. Measurements of noise and signal amplitudes from the data recorded at the mobile stations and at IS26. The amplitudes were determined for frequencies above 2 Hz and show fairly consistent values for the noise from December 2011 to March 2012. The data for IS26 are not given at the true distance, but at distances between 316km (I26H1) and 330 km (I26H8) for plotting purposes. Black symbols mark the noise values, while color symbols represent signal amplitudes.

The multi-pathing effects so clearly observed in the data from the Luxemburg explosions seem not observable in the data from the propulsion tests. Since the pattern is observed on 16 February 2012 at distances beyond 250 km, it should be expected to be seen at IS26 (at 320 km) for the propulsion test a few hours later as well. Whether any such effect is hidden in the rather complex waveforms is unclear; however, the consistency between source duration and observed signal length argues otherwise.

CONCLUSIONS AND RECOMMENDATIONS

From November 2011 to May 2012 the DLR carried out a total of nine tests at their propulsion test facility for the ARIANE-5 main engine. Six mobile infrasound stations were deployed on a profile towards IMS stations IS26 to cover a range of local and regional distances and to study infrasound propagation through the so-called zone of silence. While this zone was indeed found for distances between 40 and 120 km, significant signals were observed for shorter distances and for distances beyond 120 km as well as at IS26, which is 320 km from the source. The pattern of signal observations is highly variable and reflects the significant changes of the atmosphere over this time period. Most striking however is the observation of a marginal signal at IS26 for the last test in May 2012. Previously (see Koch, 2010) no signal could be identified from tests that were carried out later in a year than April and before October.

The work presented here has generated a set of infrasound observations that will be used in a future modeling exercise to study and understand the propagation of infrasound waves at local and near-regional distances and, in particular, through the so-called zone of silence.

ACKNOWLEDGEMENTS

The cooperation of the P5 testing facility team at DLR Lampoldshausen (K.Fröhlke) is gratefully acknowledged. This work would not have been possible without the assistance and support of the engineering staff at the Seismological Central Observatory section of BGR who provided the support to get the equipment ready for deployment and to recover and reformat the data. Particular thanks go to my colleagues E. Wetzig and U. Stelling who helped to field the equipment in more or less severe winter conditions. Data displays and FK analysis results were generated with the Seismic Handler software package (Stammler, 1993).

REFERENCES

Koch, K. (2005). Data analysis of infrasound recordings at IS26 from ARIANE-5 engine tests (abstract), 65th Annual Meeting of the German Geophysical Society, Graz, Austria, 21-25 February 2005.

Koch, K (2010). Analysis of signals from an unique ground-truth infrasound source observed at IMS station IS26 in Southern Germany, *Pure Appl. Geophys*. **167**, 401–412

Le Pichon, A., Vergoz, J., Herry, P., and Ceranna, L. (2008). Analyzing the detection capability of infrasound arrays in Central Europe, *J. Geophys. Res*. **113**, D12115, doi:10.1029/2007JD009509

Stammler, K. (1993). SeismicHandler - Programmable multichannel data handler for interactive and automatic processing of seismological analyses, *Computers & Geosciences* **19**, 135–140.

ENHANCEMENTS TO THE BAYESIAN INFRASOUND SOURCE LOCATION METHOD

Omar E. Marcillo, Stephen J. Arrowsmith, Rod W. Whitaker, and Dale N. Anderson

Los Alamos National Laboratory

Sponsored by the National Nuclear Safety Administration

Award No. DE-AC52-06NA25396/LA12-Signal Propagation-NDD02

ABSTRACT

We report on R&D that is enabling enhancements to the Bayesian Infrasound Source Location (BISL) method for infrasound event location. The focus of this effort is on improving BISL through the development and implementation of physics-based priors. Phase identification in BISL is incorporated through a prior probability density function on group velocity. We report on the development of a distance-dependent prior through a massive simulation effort that will be validated by a ground-truth data analysis effort. In addition to providing constraints for the prior Probability Density Function (PDF), this coupled effort is also providing constraints on the probability distributions that are used in the likelihood equations in BISL. We assess the enhancement in location precision using a dynamic prior, instead of the previous uniform prior, for some example events. Finally, we discuss efforts to improve the numerical implementation of BISL using Monte Carlo integration.

OBJECTIVES

This research aims to enhance infrasound event localization by utilizing both empirical observations and model-based propagation constraints in the BISL algorithm (Modrak et al., 2010) in the form of prior information.

The specific objectives of this research are discussed below:

Modeling infrasound propagation under a comprehensive set of atmospheric scenarios.
To first order, vertical variations in atmospheric temperatures, wind speeds, and wind directions determine the effective velocity and thus propagation paths at regional and global distances. To capture the variability of acoustic propagation in time and space, multi-year multi-scale atmospheric specification datasets are used to run the numerical modeling with rays propagating at representative directions and elevation angles covering regional and global distances.

Extracting information from modeling, and generating and implementing prior information into BISL.
By modeling infrasound propagation, we can classify ray paths that return to ground with the respective velocities, ranges, and maximum elevation. This information leads to the generation of propagation catalogs that can be used for the generation of prior information that is fed into the localization algorithm to constrain the solution to physically meaningful scenarios.

Estimating accuracy and precision for standard and enhanced prior PDF for BISL implementation.
Measuring the successfulness of the enhanced localization requires the introduction of metrics that account for the precision and accuracy of the solution. The BISL localization algorithm is applied to global and regional ground-truth events to estimate the 95% credibility area and the offset between estimated and real events to assess the precision and the accuracy of the algorithms.

Exploring further enhancements for localization schemes.
Our planned mathematical manipulation of the BISL framework will allow further enhancements by allowing the likelihood density function to probe more complex parameter spaces.

RESEARCH ACCOMPLISHED

Overview of the BISL and Theory of Enhancement.

The BISL method estimates the most likely source location and origin time by performing a grid search over a 4D parameter space (Modrak et al., 2010). This multidimensional space includes the two Cartesian coordinates (x_0 and y_0), velocity (v), and time (t_0). In the Bayesian framework, the posterior probability density function (posterior PDF $P(m \mid d)$) assesses the probability of a model under certain model parameters ($m \equiv \{x_0, y_0, v, t_0\}$) given a specific dataset ($d \equiv \{t_i, \theta_i\}$ arrival times t_i and back azimuth θ_i) and is written as:

$$P(m \mid d) = c(d)P(m)P(d \mid m) \qquad \textbf{(1)}$$

Where, $P(m)$ is the prior PDF, $P(d \mid m)$ the likelihood PDF and $c(d)$ a normalization function. $P(d \mid m)$ is the joint distribution of the errors in back azimuth $\Theta_i(\theta_i \mid m)$ and origin time $\Phi_i(\theta_i \mid m)$ between the data and the forward model evaluated in each point of the parameter space (Modrak et al., 2010):

$$P(d \mid m) = \prod_{i=1}^{n} \Theta_i(\theta_i \mid m)\Phi_i(\theta_i \mid m) \qquad \textbf{(2)}$$

where, n is the number of stations in the network, $\Theta_i(\theta_i \mid m) = \frac{1}{\sqrt{2\pi\sigma_\theta^2}} \exp\left[-\frac{1}{2}\left(\frac{\gamma_i}{\sigma_\theta} \right)^2 \right]$ and $\Phi_i(t_i \mid m) = \frac{1}{\sqrt{2\pi\sigma_\phi^2}} \exp\left[-\frac{1}{2}\left(\frac{\varepsilon_i}{\sigma_\phi} \right)^2 \right]$ the error distribution of back azimuths and arrival times, σ_θ and σ_ϕ the corresponding variances, $\gamma_i = \theta_i - \tilde{\theta}_i$, $\varepsilon_i = t_i - \tilde{t}_i$, $\tilde{\theta}_i$ and $\tilde{t}_i$ the back azimuth and arrival time at station i of a candidate source of the parameter space. $P(m)$ accounts for potential prior information that can be used to constrain the parameters. The prior distribution can be written as:

$$P(m) = p(x_0, y_0)p(t_0)p(v) \quad \textbf{(3)}$$

Marginalization

The posterior PDF ((1) can be marginalized over any dimension of the parameter space. BISL marginalizes over the velocity (v), and time or origin (t_o) and obtains a new posterior PDF over the probable event location $\{x_0, y_0\}$:

$$\begin{aligned} P\left(\{x_0, y_0\} \mid d\right) &= \int_{t_0, v} c(d)P(m)P(d \mid m) \\ &= p(x_0, y_0) \int_{t_0, v} p(t_0)p(v)P\left(d \mid \{x_0, y_0, t, v\}\right) \\ &= c'(d)p(x_0, y_0)P\left(d \mid \{x_0, y_0\}\right) \end{aligned} \quad \textbf{(4)}$$

where, $c'(d)$ is the new normalization function. The marginalization process, integration over specific dimensions, allows the assimilation of prior information in the form of the prior PDF ((3). Earlier implementations of BISL (Arrowsmith and Whitaker, 2008) use very basic priors that just constrain upper and lower limits of the sound propagation (0.35 to 0.22 km/s, respectively) and assign flat probabilities to the velocities within this range. This velocity range is selected to assess group velocity of rays refracting in the thermosphere (0.22-0.24 km/s), stratosphere (0.28-0.31 km/s), and troposphere (0.30-0.34 km/s) (Ceplecha et al., 1998). The approach taken here is to create prior PDFs for group velocity that assign different probabilities to sub-regions of the 0.22-0.35 km/s interval. By performing numerical simulations of infrasound propagation using a comprehensive set of atmospheric scenarios, we create propagation catalogs that are used to evaluate the probability of occurrence of group velocity for a specific range (r_a), azimuth (ϕ_a), and time (t_a) such that:

$$p(v) = K(v, r_a, \phi_a, t_a) \quad \textbf{(5)}$$

where, K is a function that retrieves and normalizes information from the propagation catalogs such that $\int_v K(v, r_a, \phi_a, t_a)dv = 1$. Assuming that there is not prior information for the location and time of origin of the event, we can write $p(x_0, y_0)p(t_0) = 1$. Using (5, (3 can be written as:

$$P(m) = K(v, r_a, \phi_a, t_a).$$

Networks (groups of sensor arrays) can have complete or partial azimuthal coverage while recording an event. Networks with arrays located at similar distances and azimuths may see similar atmospheric conditions, and therefore a unique prior PDF can be assigned to them. On the other hand, networks with good azimuthal coverage may see very different atmospheric conditions depending on the highly anisotropic wind field. In the latter case, a

unique prior PDF based on a single azimuth, range, and time is not adequate to provide information to the entire network. Below we discuss future implementations of BISL that will properly account for such scenarios. For now, a more appropriate prior PDF can be formed by averaging the prior PDFs for each array of the network into a general prior PDF:

$$P(m) = k\sum_{i=1}^{n} K_i(v, r_a, \phi_a, t_a) \qquad \textbf{(6)}$$

where, n is the number of arrays in the system, and $k = 1 \Big/ \int_v \left(\sum_{i=1}^{n} K_i \right) dv$ a new normalization coefficient.

Azimuth Dependent Celerity-Range Histograms and Prior PDF Generation.

We generated two propagation catalogs using model-based regional and global atmospheric specifications. Infrasound can propagate at local (few 10s km), regional (100s km), and/or global distances (1000s km). At very local (few kilometers) and local distances, topography and source geometry can play a significant role in propagation. On the other hand, propagation at regional and global distances is mainly driven by the atmospheric structure. These specifications are generated by the NRL-G2S atmospheric model (Drob et al., 2003) and include air temperature, and zonal and meridional wind from the ground to 140 km. The regional dataset comprises atmospheric specifications every 6 hours for eleven years for a location centered at the Utah. The global dataset comprises atmospheric specifications taken within a one-year period for locations randomly distributed around the entire surface of the Earth. Ray tracing uses the tau-p method (Garcés et al., 1998; Drob et al., 2003) for rays launched at azimuths covering 360° in steps of 30°, and elevation angles between 1° and 50° at 2° interval and extending out to 2000km and 12000 km horizontal distance for regional and global catalogs. As a result of these simulations, we extract celerity, maximum elevation, and range for multiple bounces for rays that are refracted to the ground. To display these results, we introduce the Celerity Range Histogram (CRH), which displays the ratio between the number of rays that reach the ground and the number of profiles at specific ranges and celerities. The CRHs use: 1) an evenly discretized range, from 0 to 2000 km and 0 to 10000 km for regional and global catalogs respectively, with 50 km interval, and 2) evenly spaced celerities from 0.2 to 0.35 km/s with 0.01 km/s interval.

As the propagation of acoustic energy is controlled by the highly anisotropic vertical effective velocity profiles, we developed azimuth dependent CRHs by grouping ray-path features in four groups (quadrants) depending on launch azimuth. Quadrants covering 315-45 and 135-225 degrees are used to capture the influence of meridional winds in propagation. The 45-135 and 225-315 quadrants are expected to capture the influence of zonal winds. In order to capture the variability in time of the propagation, mainly related to changes in the stratospheric winds (Whitaker and Mutschlecner, 2008), different CRHs were computed for different parts of the year. Figure 1 shows two regional azimuth dependent CRHs for the summer and winter of 2005. The two main components in the histograms (0.29-0.32 km/s and 0.22-0.26 km/s) correspond to the expected thermospheric and stratospheric returns. Seasonal variability (summer-winter) is noted specially for stratospheric returns at azimuths influenced by zonal winds.

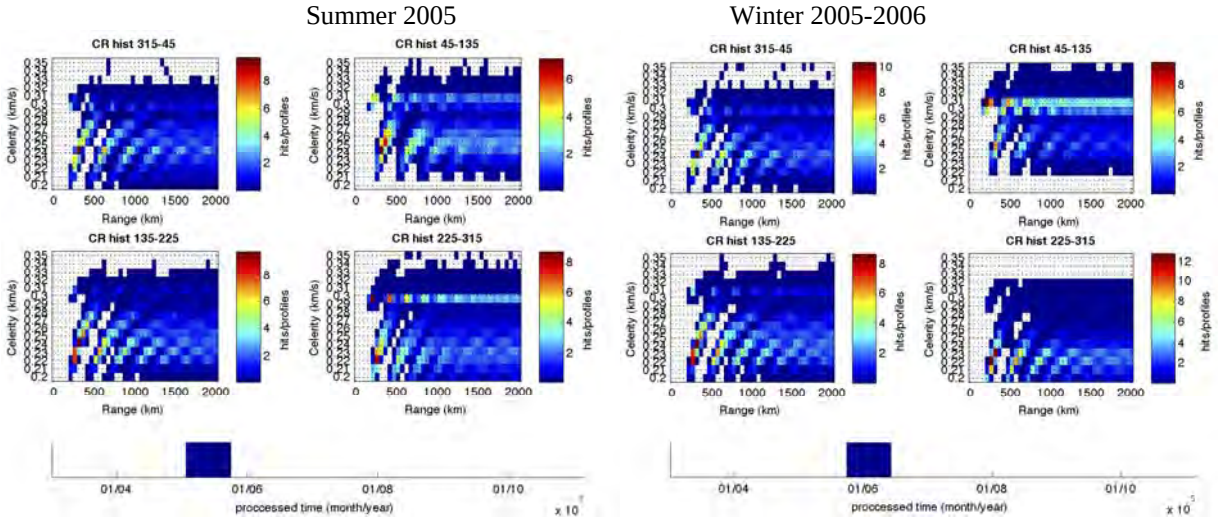


Figure 1. Azimuth dependent Celerity Range Histograms for Winter 2005-2006 (panel a) and Summer 2005 (panel b). CRHs display the ratio (color axis) between the number of rays that return to ground and the associated number of profiles (used in the propagation modeling) at specific celerities (y-axis) and ranges (x-axis).

Figure 2 shows azimuth dependent CRHs for the global catalog. It is interesting to notice that for distances above 1000 km the histograms are very homogenous and seasonal variation is weaker than the effect for regional distances. This effect can be related to the random distribution of the locations used to get the specifications, as the seasonal wind patterns in northern and southern hemispheres have opposite behaviors.

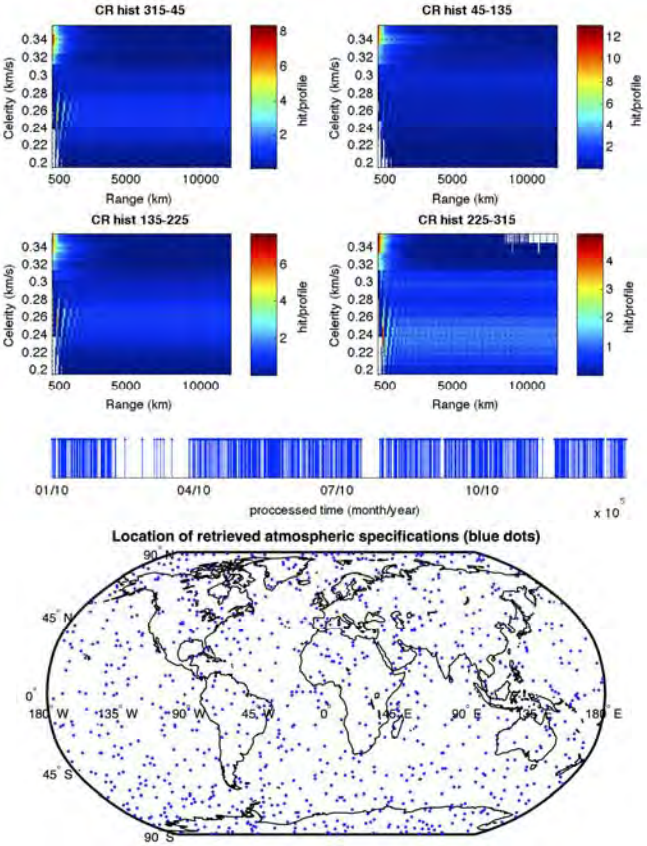


Figure 2. Global azimuth dependent CRH.

Using CRH-based Prior PDF to Enhance BISL.

Every point of the $\{x_0, y_0\}$ parameter sub-space has CRH-based prior PDFs for each element of the network. Station-specific prior PDFs are averaged into one celerity distribution that is used to marginalize the celerity axis. We tested the performance of BISL with both uniform and CRH-based prior PDFs using a surface explosion. This event was a 100-ton ANFO explosion conducted at the Sayarim Military Range, Negev desert in Israel on January 26, 2011 (Gitterman et al., 2011). The event was recorded for three stations of the International Monitoring System (IMS) in I31KZ, I46RU, and I34MN, with distances of up to 6300 km. Figure 3a shows the localization of the detecting IMS stations and Sayarim, this figure also shows the results of using flat and CRH-based prior PDFs for localization using BISL. These results show a significant enhancement in the localization precision (decrease in the 95% credibility area). However, both results display an offset between estimated and actual event location (red star) that can be related to the influence of wind in long-range propagation. In the current implementation of the BISL algorithm back (θ) and launch (ϕ) azimuths correspond geometrically, such that $\theta = \phi + \pi$. However, wind can introduce propagation offsets perpendicular to the launch angle and change the expected back azimuth. We are exploring optimal techniques to correct for this effect.

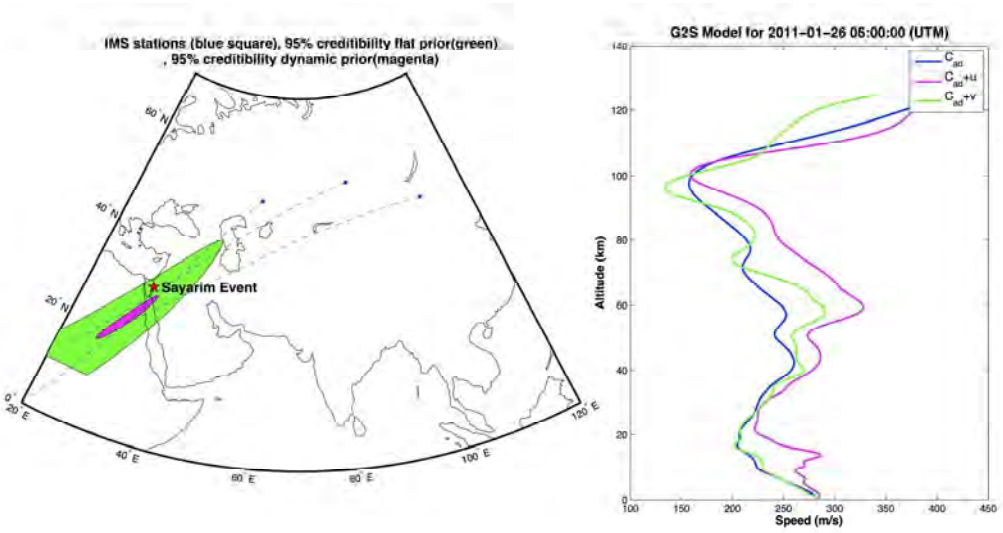


Figure 3. Using uniform and CRH-based prior PDFs for localization using BISL. a) Location of the three stations of the IMS (blue squares) that recorded and identified the Sayarim event (red star), 95% credibility areas using flat (green) and CRH-based (magenta) priors. b) NRL-G2S based atmospheric profiles at the location of the explosion.

Analytical Expression for Model-Based CRH

We are exploring the generation of analytical CRHs based on the decomposition of model-based CRHs. We form vertical cross-sections of an analytical CRH (celerity distributions for specific ranges, azimuths, and times) by linear combination of three probability density functions (PDFs) each characterizing thermospheric (f_H), stratospheric (f_S) and tropospheric (f_T) celerity distributions:

$$\Psi(v, r_a, \phi_a, t_a) = \eta_T f_T(\mu_T, \sigma_T) + \eta_S f_S(\mu_S, \sigma_S) + \eta_H f_H(\mu_H, \sigma_H), \qquad (7)$$

where, μ_X and σ_X are mean and standard deviation of an interval X, and η_X a weight coefficient for the same function in (0,1) and the sum of weight functions equal to one. (7 is commonly known as a mixed PDF. This decomposition of elements is intended to provide a physical view of the CRHs, which can be interpreted as the superposition of the three main atmospheric ducts. The parameters and coefficients required for this decomposition are estimated using model-based CRHs. First, the celerity is regrouped in three intervals: 1) 0.22-0.27 km/s,

2) 0.28-0.31 km/s, and 3) 0.30-0.34 km/s. Second, the hit/profile ratios for these new intervals are added, and mean and standard deviation are estimated. These nine parameters (three for each interval) are passed to the (7 to generate Ψ which is the analytic version of K. The function f can have various distribution shapes. We used the normal distribution in this study; however, further analysis should determine the most appropriate shape distribution for f. Figure 4 shows the analytic version of the CRH of Figure 1b. The intensity and width of the thermospheric and stratospheric returns are well recovered in this analytic CRH compared to the model-based one.

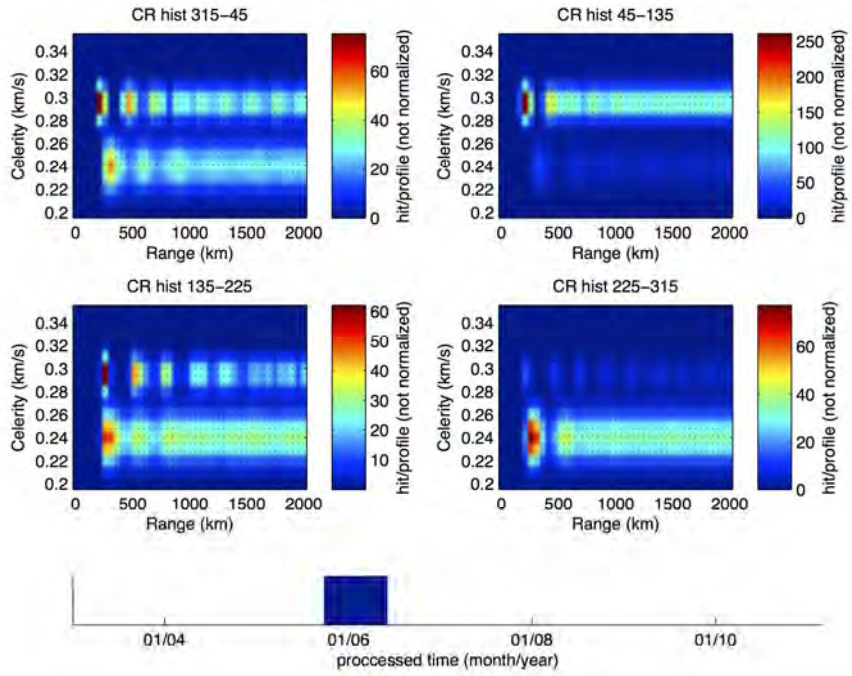


Figure 4. Analytic version of the CRH. This figure is the analytic version of the summer version of the CRH showed in Figure 1.

CONCLUSIONS AND RECOMMENDATIONS

Implementing azimuth and range dependent prior information for group velocity in the BISL algorithm can significantly enhance the precision of event localization. The azimuth dependent CRHs prove to be an effective tool to display and summarize the results of ray propagation modeling. Extracting and normalizing cross-sections of the CRH can easily generate prior PDFs for specific ranges. By using CRH-based prior PDFs we were able to locate an event and determine a 95% confidence area that is significantly smaller than the one using flat priors. Our ongoing research is focused now on studying further enhancements in the application and generation of prior information. Several mathematical representations of the weighting proportions η_X in Equation 7 are under development.

The implementation of the BISL algorithm described here assumes a uniform CRH-based prior PDF for the entire network (averaged version of the array-specific prior PDFs). However, even at regional distances each station of the network has different pictures of the atmosphere between source and receivers. This BISL implementation cannot accommodate for station specific prior information as it sees the network as a whole entity in the 4D parameter space. Further work would require the manipulation of the BISL mathematical framework to include station-specific priors. This work may require probing more complex parameter space that can include expanding the velocity from a parameter to a vector of parameters, with one velocity parameter for each array. This expansion would allow applying array-specific prior PDFs, however, this will increase the dimensions of the parameter space and the corresponding marginalization can slow the application of the algorithm. Our on-going research also includes code development for Monte Carlo integration of the BISL posterior kernel to efficiently probe these more complex spaces and to enable real-time or near real-time applications.

ACKNOWLEDGEMENTS

We would like to acknowledge David Green (AWE Blacknest) and Alexis Le Pichon (CEA) for the helpful discussions that motivated the approach taken in this document.

REFERENCES

Arrowsmith, S. J. and R. Whitaker (2008). Inframonitor: A tool for regional infrasound monitoring, in *Proceedings of the 2008 Monitoring Research Review Proceedings: Ground-Based Nuclear Explosion Monitoring Technologies*, LA-UR-08-05261, Vol 2, pp. 837–843.

Ceplecha, Z., J. Borovička, W. Elford, D. ReVelle, R. Hawkes, V. Porubčan, and M. Šimek (1998). Meteor phenomena and bodies. *Space Science Reviews* **84**(3), 327–471.

Drob, D. P., J. M. Picone, and M. Garcés (2003). Global morphology of infrasound propagation. *J. Geophys. Res.* **108**(D21), 4680.

Garcés, M. A., R. A. Hansen, and K. G. Lindquist (1998). Traveltimes for infrasonic waves propagating in a stratified atmosphere, *Geophys. J. Int.* **135**(1), 255–263.

Gitterman, Y., J. Given, J. Coyne, R. Waxler, J. Bonner, L. Zerbo and R. Hofstetter (2011). Large-scale controlled surface explosions at sayarim, israel, at different weather patterns, for infrasound calibration of the international monitoring system. in *Proceedings of the 2011 Monitoring Research Review: Ground-Based Nuclear Explosion Monitoring Technologies*, LA-UR-11-04823, Vol. 2, pp. 766–777.

Modrak, R. T., S. J. Arrowsmith, and D. N. Anderson (2010). A bayesian framework for infrasound location. *Geophys. J. Int.* **181**(1), 399–405.

Whitaker, R. W. and J. P. Mutschlecner (2008). A comparison of infrasound signals refracted from stratospheric and thermospheric altitudes. *J. Geophys. Res.* **113**(D8), D08117.

NON-LINEAR INFRASOUND SIGNAL DISTORTION AND YIELD ESTIMATION FROM STRATOSPHERIC AND THERMOSPHERIC RETURNS

Roger Waxler, Joel Lonzaga, and Jelle Assink

National Center for Physical Acoustics at the University of Mississippi

Sponsored by the Army Space and Missile Defense Command

Award No. W9113M-06-C-0029

ABSTRACT

The propagation of sound through gasses and fluids is intrinsically non-linear, although for sufficiently small signal amplitudes the propagation is well modeled by the linear approximation. The degree of non-linearity increases, however, as the density of the propagation medium decreases. As a consequence, signals travelling through the upper atmosphere undergo severe non-linear distortion. This distortion takes two forms: waveform steepening and period lengthening. Both processes are always in evidence; however, waveform steepening is generally associated with stratospheric returns, for which the decreased density of the atmosphere causes shock fronts to begin to form in regions of steep positive pressure gradients, while period lengthening is generally associated with thermospheric returns where severe attenuation prevents significant shock formation but severe non-linearity causes significant period lengthening. Since non-linear effects increase with increasing signal amplitude, it is possible to use non-linear distortion to estimate signal source strength. Uncertainties in propagation path and in thermospheric attenuation will limit the accuracy of this approach. Using a non-linear propagation model, the fundamental limits of this approach are investigated. Comparisons with available data will be made.

OBJECTIVES

The objective of this work is to develop improved methods, and to estimate the uncertainties associated with the methods, for explosive source yield determination from infrasonic signals. The philosophy being taken is based on the identification of the different signal phases in the infrasonic wave train with different atmospheric propagation paths and on the discrimination between propagation characteristics of the different paths. In the work presented here, we report on investigations of the signal distortion produced by non-linear propagation.

The predominant propagation paths through the atmosphere can be separated in three categories based on the altitude at which the path turns back towards the earth. These are tropospheric, stratospheric and thermospheric. A qualitative model for the temperature and wind velocity profiles in the Northern Hemisphere in spring and summer is shown in Figure 1. In Figure 2 eastward and westward propagation of a 0.5 Hz signal in the atmosphere of Figure 1 is modeled in the linear approximation. Note that to the east there are tropospheric (staying below 15 km) and thermospheric (propagating up to 100 km or more) paths. To the west there are predominantly stratospheric (up to 60 km or so) paths, with some thermospheric energy visible.

The linear approximation to the equations of acoustic propagation fails for sufficiently large signals and for sufficiently small density. Near to a large, explosive infrasonic source, signals are typically shock waves. As the signal propagates outwards, its amplitude decreases due to geometrical spreading and attenuation. At some distance from the source, depending on source magnitude and atmospheric conditions, the signal becomes small enough for the propagation to be well described by the linear approximation. However, as the signal propagates into the upper atmosphere, the density of the atmosphere decreases dramatically, and deviations from the linear approximation become significant.

In the linear approximation, the different frequency components of an acoustic signal propagate independently and no energy flows from one frequency component to another while the signal propagates. The rate at which energy is attenuated by the atmosphere does depend on frequency, increasing with the square of the frequency. Further, attenuation depends on the atmospheric density, increasing with decreasing density. Deviations from the linear approximation cause energy to flow into both higher and lower frequencies. For a transient signal, the high-frequency generation is manifested as waveform steepening and shock formation while the low-frequency generation is manifested as period lengthening. Signals shock and stretch as they propagate through the upper atmosphere. For signals that return to earth from the stratosphere, shocking is more evident than stretching. In the thermosphere, the severe attenuation prevents significant shock formation; however, signals returning to earth from the thermosphere exhibit significant signal stretching. In all cases, the signal distortion is greater the greater the signal amplitude.

The notion of using the non-linear distortion of a signal to estimated source strength goes back at least to Kulichkov (2002). The primary difficulty is related to attenuation in the thermosphere. The accepted models for atmospheric attenuation (Sutherland and Bass, 2004) are known to significantly overestimate attenuation in the thermosphere. This makes direct prediction of the amplitudes of thermospheric returns problematic. However, we will see that does not significantly influence period lengthening. Further, if one may assume that, near to the source, the signal waveform is that of a point explosion and satisfies the well-established period-amplitude scaling laws, then the number of independent source parameters reduces to one, making it possible, in principle, to determine the source parameters from the period of a thermospheric return alone.

RESEARCH ACCOMPLISHED

A weak shock theory model, similar to those developed by Robinson (1991) and Gainville (2008), has been developed and coded in C++. Model propagated waveforms for stratospheric and thermospheric paths are shown in Figure 3. Note the severe waveform steepening for the stratospheric returns and the severe period lengthening for the thermospheric returns. In Figure 4 some modeled waveforms are compared to recorded data, showing reasonable qualitative agreement.

The greatest sources of uncertainty in determining source parameters from long-range infrasonic signals are the determination of the atmospheric winds, which influence the propagation paths, and the uncertainties associated with the attenuation in the thermosphere. To study the influence of the thermospheric attenuation on yield estimation, a modification of the attenuation coefficient was introduced in which the Bass-Sutherland attenuation coefficient is used below 100 km and a constant, while above 100 km the Bass-Sutherland coefficient is multiplied by a constant to artificially reduce the attenuation. A value of 0.1 was used for this constant to obtain the model output shown in Figure 3. This gives roughly correct signal amplitude. In Figure 5 the influence of changing the attenuation on the relation between period and yield is studied. Note that the degree of pulse stretching is largely insensitive to the thermospheric attenuation.

The atmospheric winds are a different matter. These influence the propagation path, which causes the signal to pass through more or less dense air and thus can have a large effect on the amount of nonlinear distortion. In Figure 6, a test case is considered. A mesospheric wind jet with wind speeds up to 50 m/s is added centered at 100 km altitude. The upper two plots show the wind speed model for three wind jet perturbations and the effective sound speeds (sound speed plus horizontal wind speed in the direction of propagation) corresponding to the wind jet perturbations. The lower two plots show the corresponding eigenrays and the source-amplitude/duration curves for the three eigenrays. Note that for a given pulse duration, deviations of about 25% in predicted signal amplitude at 1 km are predicted. In Figures 7 and 8 a similar analysis is performed for thermospheric returns seen in data collected during the 2011 Sayarim campaign and for stratospheric returns captured during rocket motor fuel elimination events at the UTTR. Deviations of no more than about 30% are predicted.

CONCLUSIONS AND RECOMMENDATIONS

Initial results for the estimation of effective signal source strength at 1 km from both thermospheric and stratospheric signal duration are optimistic. The research should continue in several directions. More data from ground truth experiments needs to be analyzed to characterize the accuracy of the method. Classical near-field analysis needs to be performed to allow the determination of source explosive yield from the effective source signal strength.

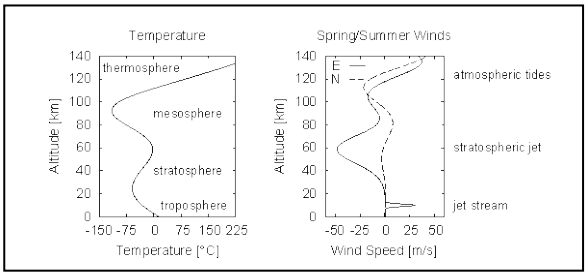


Figure 1. Model atmospheric profiles for the Northern Hemisphere in spring and summer.

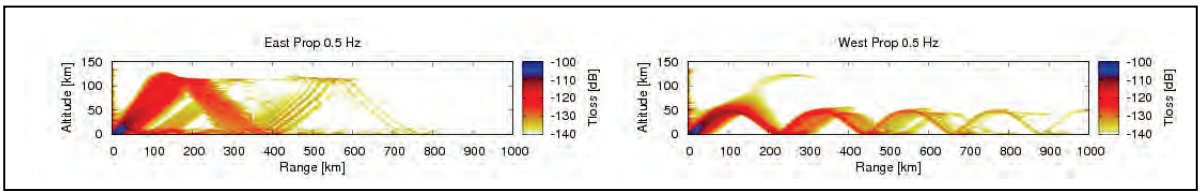


Figure 2. Transfer function magnitude for linear propagation in the model atmosphere of Figure 1 to the East, showing thermospheric and tropospheric paths, and to the West, showing predominantly stratospheric paths.

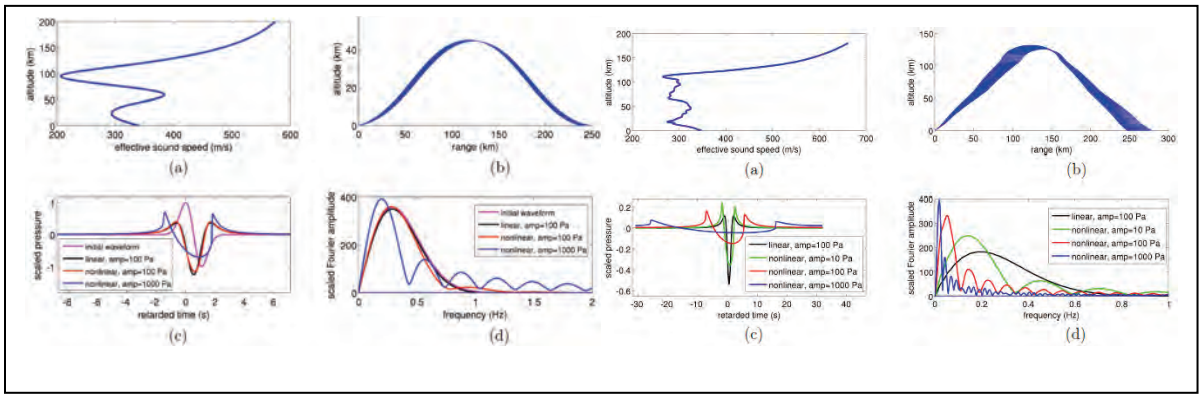


Figure 3. Stratospheric ray paths and waveforms on the left and thermospheric on the right. (a) is an effective sound speed profile along the direction of propagation of a ray bundle shown in (b). (c) shows the waveform near the source as well as the waveforms after linear and nonlinear propagations with corresponding spectral amplitudes shown in (d).

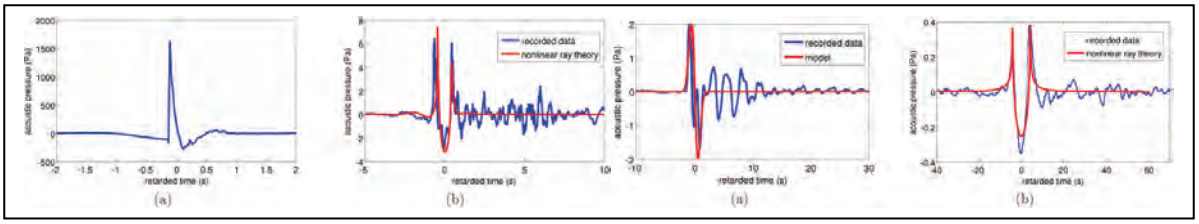


Figure 4. Recorded near field signals and corresponding thermospheric phases compared to recorded data. On the left is a thermospheric arrival recorded in Idaho from a Trident Missile rocket motor fuel elimination event in Utah. On the right is a thermospheric arrival corresponding to an explosive eruption of the Tungurahua volcano in Ecuador.

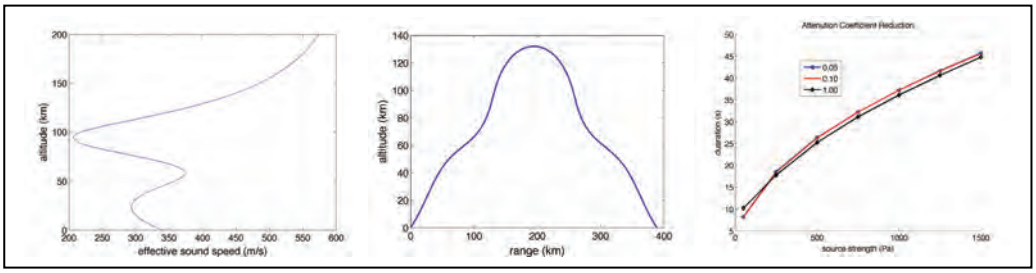


Figure 5. Testing the sensitivity of thermospheric pulse stretching to the atmospheric attenuation in the thermosphere. To the left is the model effective sound speed profile used, in the middle is the ray path considered, and to the right are the duration/source-strength curves for 1, 1/10 and 5/100 of Bass-Sutherland attenuation, above 100 km. Source strengths are peak pressure amplitudes 1 km from the source.

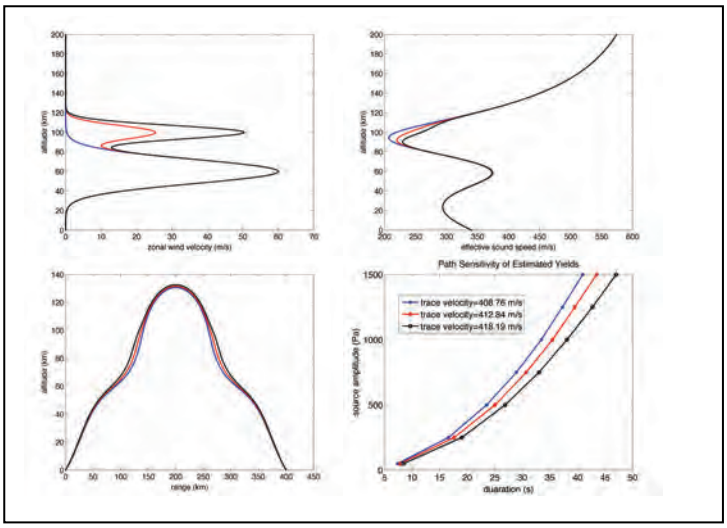


Figure 6. Perturbations of the zonal mesospheric wind model, the corresponding effective sound speeds, and eigenrays from source to a ground point 400 km to the east, and the source-amplitude/duration curves for each ray path. Source amplitudes are peak pressures 1 km from the source.

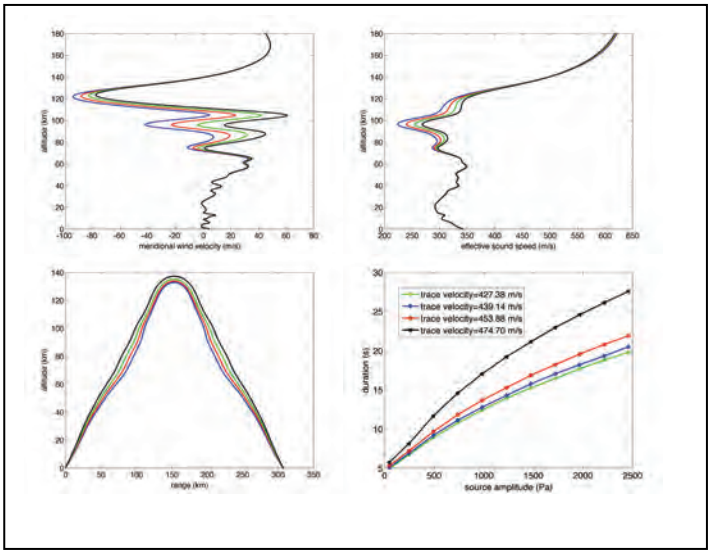


Figure 7. Analysis of data from the 2011 Sayarim experiment. Perturbations of the G2S zonal thermospheric winds, the corresponding effective sound speed and eigenrays from the Sayarim source location to an array deployed in northern Israel and the source-amplitude/duration curves for each ray path. Source amplitudes are peak pressures 1 km from the source.

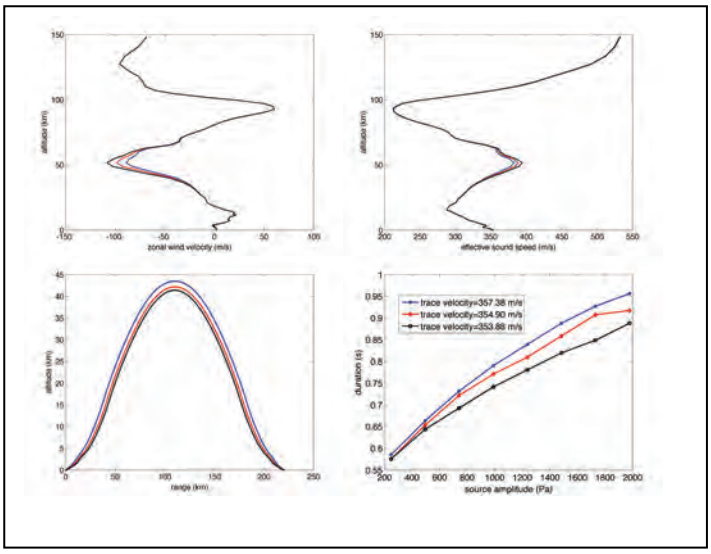


Figure 8. Analysis of data from 2009 UTTR Trident Missile rocket motor fuel elimination events. Perturbations of the zonal winds, the corresponding effective sound speed and eigenrays from the UTTR source location to an array deployed to the west in Nevada, and the source-amplitude/duration curves for each ray path. Here the signals are stratospheric returns. Source amplitudes are peak pressures 1 km from the source.

ACKNOWLEDGEMENTS

This research was sponsored by the US Army Space and Missile Defense Command under Contract W9113 M-06-C-0029. The statements, findings, conclusions, and recommendations are those of the author and do not necessarily reflect the views of the US Army Space and Missile Defense Command.

REFERENCES

Gainville, O. (2008). Modelisation de la propagation atmospherique des ondes infrasonores par une methode de trace de rayons non lineaire, Ph.D. Thesis, L'Ecole Centrale de Lyon, France

Kulichkov, S. N. (2002). Nonlinear acoustic phenomena in atmosphere, in Nonlinear Acoustics at the Beginning of the 21st Century, 16th International Symposium on Nonlinear Acoustics (ISNA Moscow, 2002), edited by O. V. Rudenko and O. A. Sapozhnikov, pp. 251–258, *Fac. of Phys*., Moscow State Univ., Moscow.

Robinson, L. D. (1991). Sonic boom propagation through an inhomogeneous, windy atmosphere, Ph.D. Thesis, University of Texas, Austin, TX.

Sutherland, L. G. and H. E. Bass (2004). Atmospheric absorption in the atmosphere up to 160 km, *J. Acoust. Soc. Am*. **115**, 1012–1032, doi:10.1121/1.1631937.

INFRASOUND SENSOR CALIBRATION AND RESPONSE

Rodney W. Whitaker

Los Alamos National Laboratory

Sponsored by the National Nuclear Security Administration

DE-AC52-06NA25396/LA12-Sensors-NDD02

ABSTRACT

We will report on new developments that add improved functionality to the Los Alamos infrasound calibration chamber. Under separate funding a number of upgrades were made to the chamber. These include a Geotech Smart24 digitizer and workstation, an LVDT sensor for piston phone phase measurement, a Vaisala pressure and temperature sensor package, new motor controller for the mechanical piston phone, and a CLD electro-mechanical piston source, which can be driven by the calibration functions in the Smart24. This work greatly benefited from the expertise and collaboration of R. P. Kromer, Array Information Technology, Albuquerque, NM. We will discuss how the new features improve and extend the usefulness of the chamber for infrasound calibration. Additionally, plans for increased collaboration with Darren Hart, Sandia National Laboratory, on calibration issues and research will be discussed.

OBJECTIVES

This project supports the capability to perform accurate infrasound sensor calibrations using a piston source and large volume chamber whose output has been independently determined and for which the error budget has been accurately assessed. Since the mid 1980s, Los Alamos National Laboratory (LANL) has operated an infrasound sensor calibration chamber that operates over a frequency range of 0.02 to 4 Hz. This chamber has provided sensitivities, volts/Pa, for sensors used by Los Alamos and others. Under the current program we will restore the chamber function, interrupted by an unexpected move, collaborate with researchers at the Sandia National Laboratory (SNL) Facility for Acceptance, Calibration, and Testing (FACT) Site on sensor issues, calibrate sensors as needed and research new methods for sensor response determination.

RESEARCH ACCOMPLISHED

Background

The Los Alamos infrasound calibration chamber, Figure 5, is a large volume concrete and steel, sealable, chamber equipped with a gear-driven, variable speed piston that has a fixed travel distance. The nominal output is a sinusoid of around 3.5 Pa peak –to-peak amplitude, and the larger interior volume is just under 10^6 cm^3. LANL was given the chamber by Ed Bullard, head of the original Chaparral Physics. (In the 1960s and 1970s, Mr. Bullard was involved in a variety of infrasound research and applications work in the El Paso, TX, area. Two of the important organizations were Globe Universal Sciences and Schellenger Research Laboratory at the University of Texas, El Paso.) More than one sensor may be calibrated in the chamber at the same time. The walls of the chamber are 4.5 inches thick and aid in the reduction of low-frequency external signals such as from passing weather systems. One can, from time to time, see effects of strong fronts at the lowest frequencies. This suggests that a better configuration would be to put the chamber in an isolated room inside a building. This provide better isolation.

As a calibration tool, the output of the piston source must be known. The piston output pressure, p, can be written as

$$p = \frac{P_0 \gamma \delta V}{V_0} = C_{ch} P_0 \qquad (1)$$

where P_0 is the ambient pressure, V_0 is the total system volume, γ, is the ratio of specific heats, and δV is the piston volume, depending on the piston area and travel distance, and C_{ch} then is the chamber constant. The equation above is correct as long as the air responds adiabatically and no non-ideal effects are in play. At lower frequencies these become more important. We will discuss this more in a later section. Clearly it is possible to establish the chamber constant through direct measurement of the physical components. A number of years ago we made measurements of the volumes and piston area and piston travel distance to derive the chamber constant.

More Recent Calibration Work

The next step in determining the chamber constant involved the use of an MKS Baratron 698A sensor that had an independent calibration that was verified at the SNL Standards Lab. An output of 0.0 to 10.0 volts corresponded to 0.0 to 0.1 Torr (mm of Hg). The conversion from Pa to Torr is 133.3224 Pa equals 1.0 Torr. The chamber piston was operated at 0.04 Hz, and the signal was measured and recorded at 20 samples per second on a GeoTech Instruments DL 24 digitizer. Fifty cycles of data were fit with the Matlab function NLINFIT that gave the peak amplitude. A sample of the measured and fit data is shown in Figure 1. This gave a value of 4.143E-05 for the chamber constant, C_{ch} at 0.04 Hz. This value was within 2% of the value derived from the first dimensional measurements mentioned above. The Baratron unit could only be used at low frequency. (This work was presented at the 2001 Infrasound Technology Workshop in Hawaii.)

The next calibration measurements were made with a GRAS 40 AN low frequency microphone with an independent calibration from a standards laboratory in England. This unit was used over the frequency range of 1.0 to 4.0 Hz.

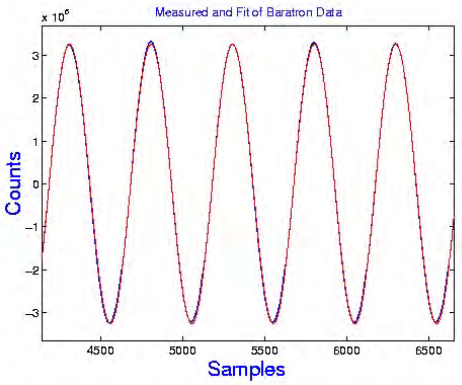


Figure 1: A portion of the measured (blue) and fit (red) MKS Baratron signal at 0.04 Hz, in the form of counts vs samples.

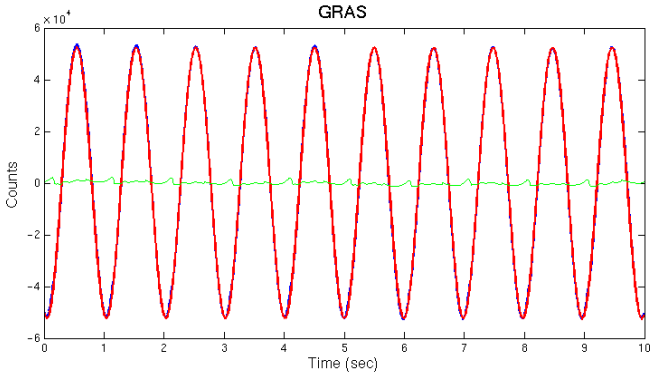


Figure 2: A portion of the calibration record for the GRAS microphone at 1 Hz covering 0 to 10 seconds on the x-axis and ± 60,000 counts on the y-axis. Blue are the data, red is the fit and green is the residual of the fit.

In doing the calibrations with the GRAS unit, we used a Martel calibrated voltage source to establish the bit weights of the DL 24 recorder we used in the runs with the GRAS sensor. The chamber constant at 4 Hz was 4.446E-05 using the calibrated GRAS microphone. This value is a bit larger than that derived with the MKS Baratron sensor, which is likely due to the influence of non-ideal effects that can be more significant at lower frequency.

Around this time Dr Harold Parks of the Primary Standards Laboratory at SNL began working with us to re-determine the chamber constant and to independently estimate the uncertainty in the determination. The first task was a new set of measurements of the chamber dimensions. The interior dimensions were made with an interior micrometer set that had been calibrated at the Sandia Mechanical Calibration Laboratory. Between 5 and 10 measurements were made of the chamber length, height and width and portal length and diameter. The piston travel distance was measured with a depth micrometer that was calibrated against a gauge block by the Sandia Primary Standards Laboratory. In measuring the geared piston, we found that there was a rubber boot (sleeve) around the piston that provided an airtight seal in the cylinder housing in which the piston moved and added a small amount to the piston area, potentially 8% in diameter. In the previous measurement, this small increment had not been included. In Figure 3 we show the four values for the chamber constant, where full boot refers to the most recent dimensional measurements and includes the maximum boot addition to piston area.

Dr Parks examined non-ideal effects and measurement errors and compiled an error budget, Parks (2007). The uncertainty in piston output is the largest contributor to the uncertainty and his summary is shown in Table 1. Adiabatic versus isothermal processes in the chamber were examined. His analysis of thermal conduction, without convection, showed that in the LANL chamber, at its operating frequencies, γ is very close to the adiabatic of 1.4, falling only to 1.38 at 0.02 Hz, and is shown in Figure 4. His analysis followed Gerber (1964a, 1964b), whose work used known solutions to the heat transfer equation by Carslaw and Jaeger (1959) and Hunt (1955).

Chamber Upgrades

While the chamber worked well there were improvements that could be made that would enhance functionality. Some of the upgrades included: a way to determine the position, phase, of the piston, a dedicated digitizer, piston frequency counter, better cabling, chamber pressure and temperature sensors and a variable output piston. In 2010 with support from US Space Missile Defense Command (SMDC) and the National Center for Physical Acoustics (NCPA) of the University of Mississippi, we began to install a series of upgrades to the chamber. The mechanical design and fabrication work were done by Mr. Richard Kromer, of Array Information Technologies, working with LANL under the SMDC support.

The upgrade started with Mr Kromer building a custom Hoffman box to house the new Geotech Instruments Smart24 digitizer/recorder that was linked to a Windows XP workstation with the Geotech software. The Hoffman box was installed with a power and signal distribution blocks, as shown in Figure 5. New sensor cabling was added to three of the chamber side ports and fed to the digitizer. A GPS receiver sends accurate time to the digitizer.

Table 1: Estimates of uncertainty in chamber error analysis.

Component	Uncertainty (1σ)
Piston Area	4.1%
Piston Travel	0.3%
Chamber Empty Volume	0.4%
Sensor Volume Displacement	0.2%
Heat Conduction Correction	0.1% at 1 Hz 2% at 0.02 Hz
Wall Stiffness	0.1%
Non-Ideal Gas Corrections	0.2%
Humidity Correction	0.1%
Noise in the Signal	0.1%
Ambient Pressure	<0.1%
Digitizer Calibration	<0.1%
Chamber Leaks	<0.1%
Total Standard Uncertainty	4.2 - 4.7%

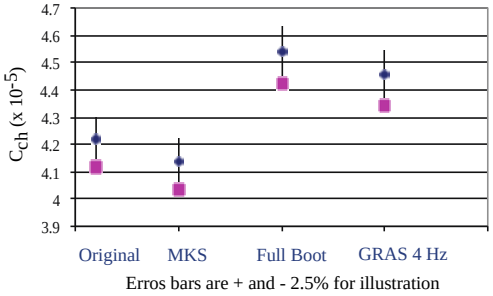


Figure 3: Plots the four values for the chamber constant. The MKS (at 0.04 Hz) value suggests other non-ideal effects may be present.

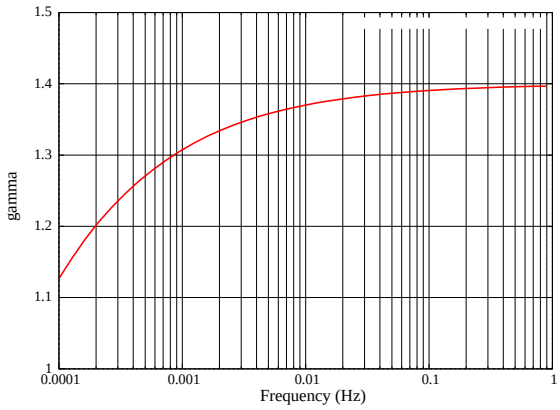


Figure 4: Heat conduction effects on gamma for the LANL chamber with a thermal diffusivity of 2 x 10^{-5} m^2/s.

A Vaisala pressure and temperature sensor package was installed, Figure 7, in one of the chamber side ports to measure the interior conditions and cabled to the digitizer. A Micro-Epsilon LVDT Gaging sensor was installed on the chamber piston, Figure 8, that enables accurate registration of the piston position and is recorded as one of the digitizer channel inputs. A frequency counter was added to the geared piston for frequency determination.

In order to have a variable frequency and amplitude source, we added a CLD Dynamics Model 316 electro-mechanical piston source, similar to that in use at the SNL FACT site. In addition to variable displacement and frequency, this unit can be driven by the calibration functions of the Smart24. The Model 316 was mounted on the back wall of the chamber as seen in Figure 9 and is power by the controller in Figure 10.

We performed a quick linearity test on the CLD piston by using the sensor calibration feature of the Smart24 with a sinusoid source function at 0.5 and 1.0 volts driving voltage and covering the frequency range of 0.02 to 2.0 Hz. These results are shown in Figure 11. The ratio was just under a factor of two.



Figure 5: The Los Alamos infrasound sensor calibration chamber is shown before the upgrades.



Figure 6: The Smart24 digitizer is shown mounted in the Hoffman box.



Figure 7: The Vaisala pressure and temperature display unit is shown mounted on the chamber side wall.

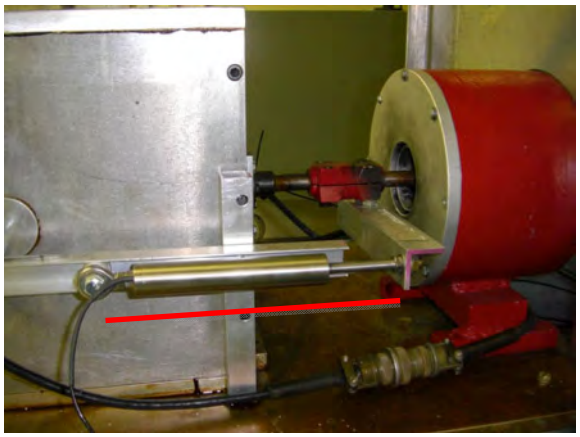


Figure 8: The LVDT sensor, for following the piston position is shown just above the red line.



Figure 9: The CLD Dynamics Model 316 mounted on the back wall of the chamber.



Figure 10: The CLD Dynamics power unit shown on top of the chamber.

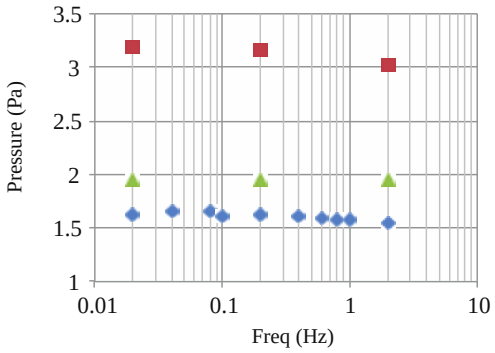


Figure 11 (at left): CLD 316 piston response at 0.5 volt (blue) and 1.0 volt (red) driving voltages. The ratio is displayed by the green triangles.

Direct Sensor Response

We have been interested in how well one could derive the sensor response, amplitude and phase, from a direct measurement of the sensor response to a step input. This could be useful and would supplement the technique of using a reference sensor. The transfer function of a sensor is, in words, the Laplace transform of the sensor output to an impulse or step input divided by the Laplace transform of the input. To approximate a step input, we have used a hypodermic syringe driven quickly by hand. For one of the sensors we calibrated, the output pressure-time history, for this source, was approximately given by

$$p(t) = \left(1.0 - \frac{(t - t_{start})}{\tau}\right) e^{-((t-t_{start})/\tau)} \qquad (2)$$

where the step starts at t_{start} and where the positive phase duration is τ in seconds. Equation (2) is written with unit amplitude. The Laplace transform (LT) of Equation (1) is given by

$$LT(p(t)) = \frac{s}{(s+a)^2} \qquad (3)$$

where a is 1/τ. The Laplace transform of a step is just 1/s, so that the transfer function is then easily given by

$$T(s) = \frac{s^2}{(s+a)^2}. \qquad (4)$$

Equation (4) has a repeated zero of 0.0 and a repeated pole of amplitude of –a. If we substitute 2πfi for s in Equation (4), we can write for the amplitude and phase of the response as a function of frequency, after simplification

$$Amp(f) = \frac{4\pi^2 f^2}{\sqrt{((a^2 - 4\pi^2 f^2)^2 + 16\pi^2 a^2 f^2)}} = \frac{4\pi^2 f^2}{4\pi^2 f^2 + a^2} \qquad (5)$$

$$Phas(f) = \arctan\left(-\frac{4\pi af}{(a^2 - 4\pi^2 f^2)}\right). \qquad (6)$$

In Figure 12 we show the measured sensor response to the step input and the fit given by Equation (2). If one looks closely at the rise of the measured sensor response to the step, one can see that a more rapid step source would be better. In Table 2 we show phase of the sensor response as a function frequency as given by Equation (6) and from measurements. The analytic result compares favorably to actual measurements for this sensor.

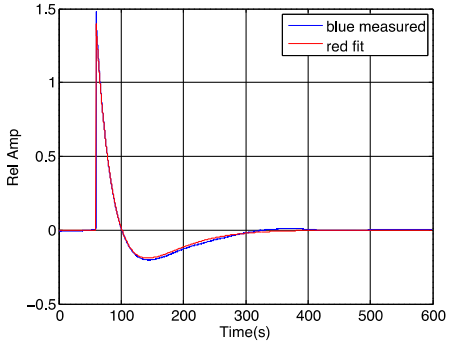


Figure 12: The measured sensor response (blue) and the fit (red) are shown

Table 2: Comparison of response phases

Frequency (Hz)	Phase analytic (degrees)	Phase reference (degrees)
0.02	21.4	20.9
0.04	10.8	11.5
0.05	8.6	9.4
0.06	7.2	7.9
0.1	4.3	4.8
0.2	2.2	2.3

This initial experiment in the derivation of a sensor response from a measured step response has shown some promise. The need for a faster impulse source has been shown. The direct approach here requires that the measured sensor response be fit with an analytic function whose Laplace transform is determinable. This leads directly to a form from which the amplitude and phase are easily obtained or can be found with Maxima or Mathematica.

FUTURE WORK

As mentioned above, we had to move the chamber to a new location at the end of FY11. This move has caused a bit of a delay in our planned work. Two potential locations have proved unworkable; a third is being explored. When the chamber is relocated, we will put it all back together and began a checkout process in order to get back to where

we were before the move. We still need to get the Sensor Testing Software from SNL that we hope to apply to our operation. (At this time it is not quite ready for release.) Then we can get back to doing an annual check on some sensors for SNL. For step function generation, we want to control the CLD Model 316 with the Smart24 step calibration signal to see if faster rise times can be achieved. We will also explore other methods of generating step functions with faster rise times.

SUMMARY

We have documented past work on the determination of the calibration constant of the LANL infrasound sensor calibration chamber done with collaboration of SNL. This included an uncertainty analysis. A summary of equipment upgrades and measurements was provided as well. Finally we discussed some aspects of analytic approaches to sensor response determinations.

ACKNOWLEDGMENTS

The detailed analysis of the chamber output and error budget was supported in part by the US SMDC and the National Center for Physical Acoustics of the University of Mississippi. The upgrades were made possible through a research grant from SMDC and administered by NCPA. Dr. Harold Parks of the Primary Electrical Standards Laboratory at Sandia National Laboratory performed some of the dimensional measurements, performed the detailed error analysis and provided important technical advice. Mr. Richard Kromer, formerly of SNL and now at Array Information Technologies, designed and implemented the upgrades and made other improvements. His contributions were essential to making the upgrade process successful. We thank Dr George Randall for insightful discussions on seismic and infrasonic sensor response and other analysis topics. Finally, thanks to H. V. Parks for information gleaned through personal communication in 2007 regarding his uncertainty analysis and chamber measurements.

REFERENCES

Carslaw, H. S. and J.C. Jaeger (1959). *Conduction of Heat in Solids* 2nd ed., Oxford University Press, London.

Gerber, H. (1964a). Acoustic properties of fluid-filled chambers at infrasonic frequencies in the absence of convection, *J. Acoust. Soc. Am.* **36**, 1427. (Some typos in this paper are noted in Jarvis (1987))

Gerber, H. (1964b). Calculation of dynamic-pressure changes in the presence of free convection, *J. Acoust. Soc. Am.*, **36**, 1435.

Hunt, F. V. (1955). Notes on the Exact Equations Governing the Propagation of Sound in Fluids, *J. Acoust. Soc. Am.* **27**, 1019.

Jarvis, D. R., J. (1987). Acoustical admittance of cylindrical cavities, *J. Sound Vib.* **117**, 390.

Data Processing and Analysis

A GENERALIZED EARTH MODEL SOFTWARE UTILITY

Sandy Ballard, Jim R. Hipp, Andre V. Encarnacao, Chris J. Young, and Brian J. Kraus

Sandia National Laboratories

Sponsored by the National Nuclear Security Administration

Award No. DE-AC04-94AL85000/SL12-SignalPropagation-NDD021

ABSTRACT

Implementation and sharing of 3D Earth models by the seismological research community, and evaluation of those models by global monitoring agencies is hampered by the plethora of model parameterizations and formats that have been implemented by model developers. GeoTess is an attempt to address this issue by providing a common model parameterization for multi-dimensional Earth models and a software support system that deals with the construction, population, storage and interrogation of data stored in the model. GeoTess is not limited to any particular type of data; to GeoTess, the data are just 1D arrays of values associated with each node in the grid. The grid and many of the basic grid manipulation algorithms implemented by GeoTess are described in Ballard et al. (2009).

In this paper, we describe the salient features of the model parameterization and supporting software and describe two example applications. The first is called LibCorr3D, which is an application that manages 3D lookup tables for travel time correction information. With this software, the research community can develop 3D velocity models of the Earth, pre-compute station–phase –specific travel times and travel time uncertainties through their model in any manner they deem appropriate and deliver that information to monitoring agencies in a format that the monitoring agencies are prepared to accept.

The package, including source code, is supplied in Java and C++. There are also interfaces to the C++ version written in C and Fortran90. GeoTess has been tested on multiple platforms, including Linux, SunOS, MacOSX and Windows.

INTRODUCTION

The use of multi-dimensional global Earth models in both the seismological research community and in the operational systems of global monitoring agencies has become increasingly ubiquitous in recent years and is destined to become even more prevalent in the future. This trend is driven by the significantly enhanced fidelity of these models relative to the real Earth structure and composition, resulting in the promise of more accurate predictions of seismic observations and hence to more accurate and precise estimates of seismic event locations and magnitudes. Use of multi-dimensional global models has become feasible in recent years due to the dramatic increase in commercial off-the-shelf computational resources that are readily available.

Efforts to evaluate multi-dimensional models and incorporate them into operational systems are complicated by the unique formats and software support systems that are implemented by each development team (Reiter et al, 2011). This makes evaluation and implementation of 3D models by monitoring agencies difficult and inefficient and reduces the probability that research products developed by the seismological research community will ever find their way into operational systems.

GeoTess is an attempt to address some of these issues by providing a common model format designed to facilitate the implementation and sharing of 3D Earth models. GeoTess is composed of a model parameterization for multi-dimensional Earth models and extensible software that implements the construction, population, storage and interrogation of data stored in the model. GeoTess is not limited to any particular type of data; to GeoTess, the data are just 1D arrays of values associated with each node in the grid. The grid and many of the basic grid manipulation algorithms implemented by GeoTess are described in Ballard et al. (2009).

While many Earth models use regular latitude longitude grids to describe the geographic geometry and topology, GeoTess uses a triangular tessellation. These two approaches are compared in Figure 1. While software algorithms that use regular latitude longitude grids are much more straightforward to develop, the grids suffer from severe unintended variability in cell areas, with cell areas approaching zero near the poles. Software for triangular tessellations, on the other hand, is somewhat more complicated to develop but results in grids with much more uniform cell size and approximately 25% fewer vertices.

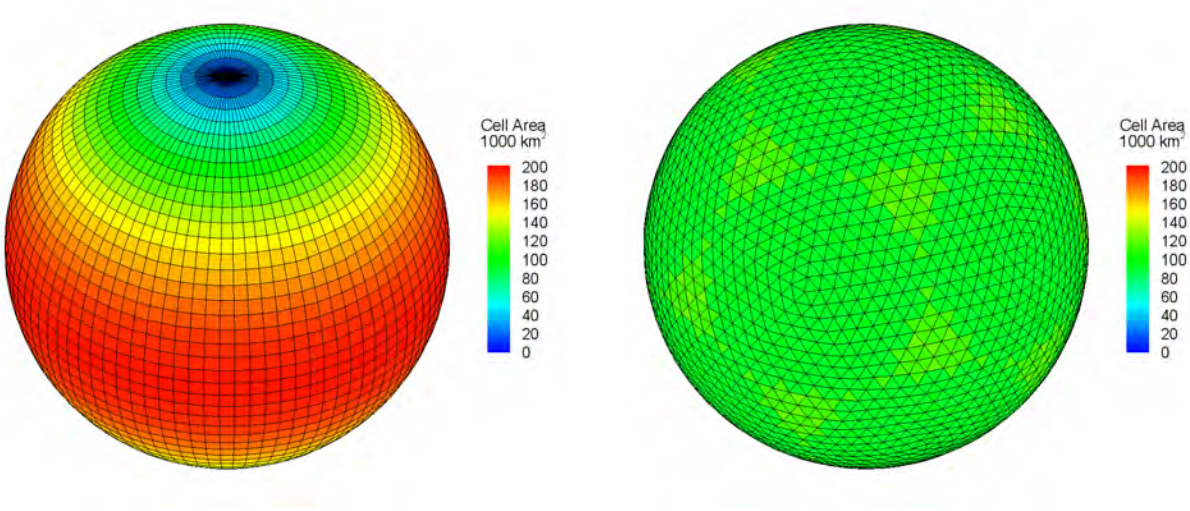


Figure 1. Comparison of a regular latitude longitude grid and a uniform triangular tessellation. In both grids the edge lengths are approximately 4°.

GeoTess software provides tools to perform the following functions:

- Construct the discretized grid of a model by defining the positions of all the nodes (geometry), and the connectivity of the nodes with one another (topology or connectivity) to form non-overlapping triangles that completely span the unit sphere. Construction of grids with variable resolution in both geographic and radial dimensions is supported.
- Query a model grid for information about the nodes, cells or tessellations.
- Associate data structures with the nodes and/or the cells of the geometry.

- Modify the data associated with a node or cell.
- Query the model for the data associated with a specified node or cell.
- Rapidly find arbitrary positions within the grid hierarchy (point searching).
- Given an arbitrary position within the model space that does not correspond to a node of the model geometry, calculate a set of interpolation coefficients that can be applied to data at nearby nodes of the model geometry to obtain an estimate of the data value at the point of interest. GeoTess currently implements linear and natural neighbor interpolation algorithms and may implement additional methods in the future.
- Read models from, and write them to, files in ascii, netcdf and a custom binary formats.

Grid construction is implemented in an application called GeoTessBuilder, which is written in Java and can be run on any computer platform that supports that language. The remaining functions described above are implemented in a software library called GeoTess, which is available in Java and C++ with C and FORTRAN95 interfaces to the C++ library. The libraries have been tested on SunOS, Linux, Mac OSX and Windows operating systems.

MODEL COMPONENTS

A GeoTess model is comprised of the following elements:

- **A set of layers** (Figure 2). Each layer spans the entire 2D geographic extent of the model. The boundaries at the top and bottom of a layer may have topography. Within each layer, model data values are continuous, both geographically and radially. Model data values may be discontinuous across layer boundaries. Layers may have zero thickness at some or all geographic locations. An important limitation of the parameterization used by GeoTess is that layer boundaries may not fold back on themselves, i.e., any radial line emanating from the center of the Earth must intersect each layer boundary exactly one time.

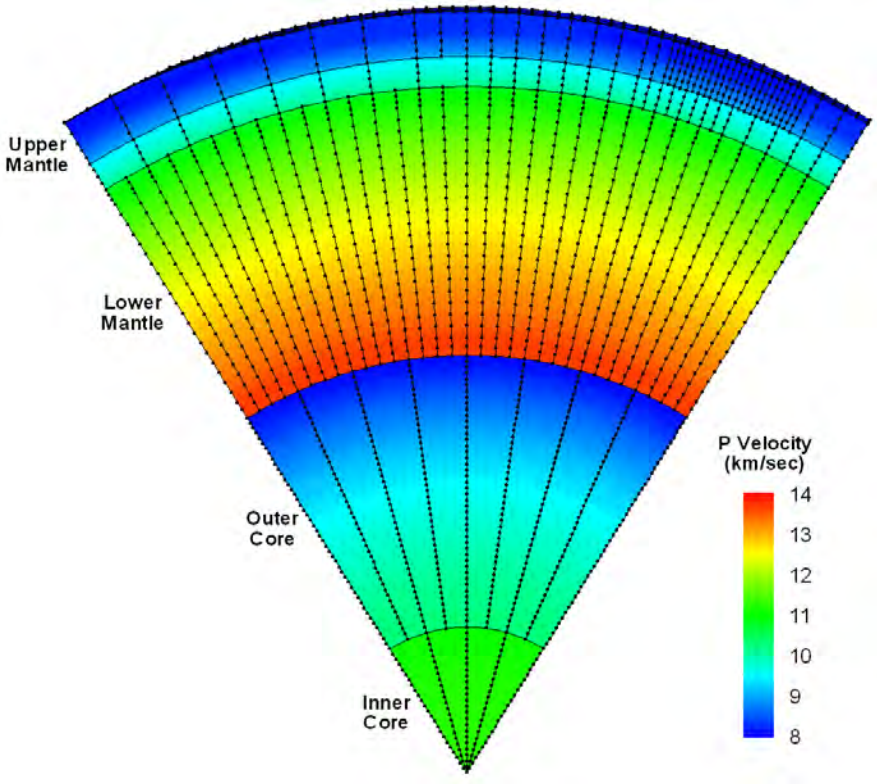


Figure 2. A slice through a 3D P velocity model. The model consists of a number of layers, such as the Inner Core, Outer Core, etc. Each layer is associated with a separate multi-level tessellation, providing variable resolution in the radial direction. Profiles are defined as a set of nodes, all within a single layer of the model, positioned along a line with constant geographic position. Note the variable resolution in the geographic dimensions in the upper mantle.

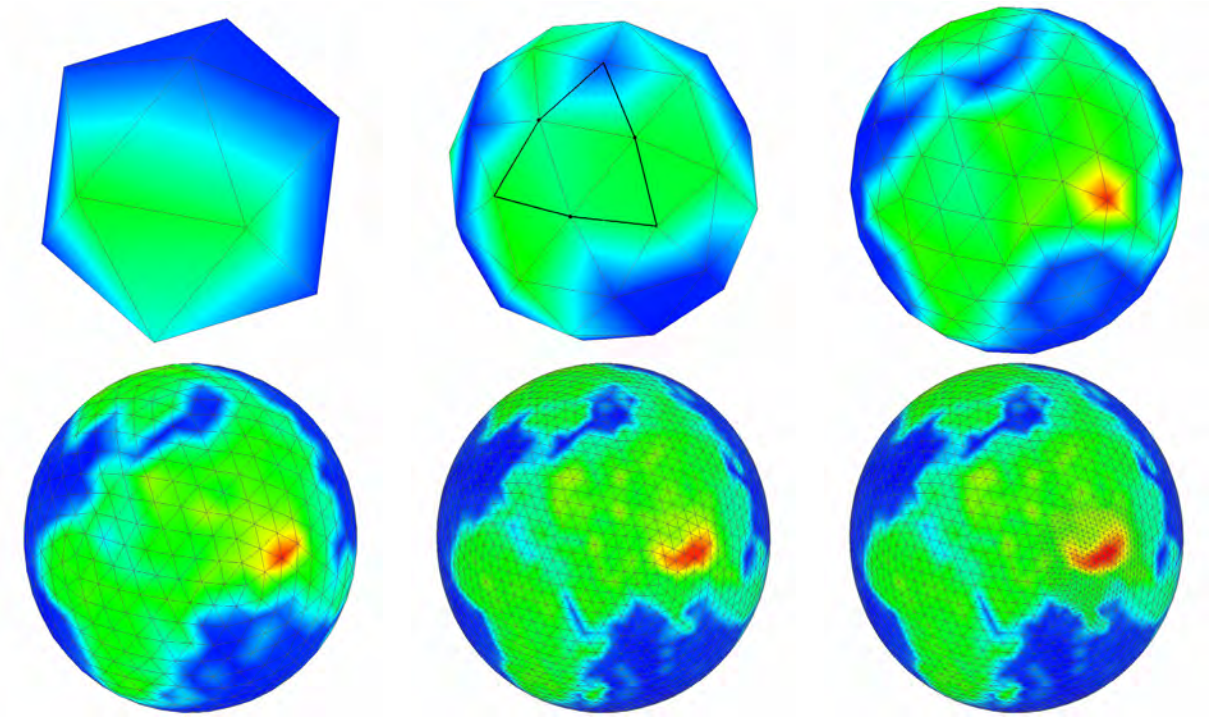


Figure 3. Construction of a multi-level tessellation by iterative subdivision of triangles. Each image represents one level and together the levels comprise a single multi-level tessellation.

- **A set of multi-level tessellations** (Figure 3). Each layer will be associated with one multi-level tessellation but many layers may be associated with each multi-level tessellation, i.e., there is a many-to-one relationship between layers and multi-level tessellations. By associating layers that are deep in the Earth with low resolution multi-level tessellations and layers at shallower levels in the Earth with higher resolution multi-level tessellations, the resolution of the model can be varied radially as necessary to achieve more appropriate sampling.
- **Topology**. The topology of each multi-level tessellation will consist of a set of levels (see Figure 3), with each level consisting of a set of triangles that spans the surface of a unit sphere, without gaps or overlaps. The triangles on a given tessellation level are obtained by subdivision of the triangles on the previous tessellation level, with the first tessellation level being an icosahedron. Each multi-level tessellation may have variable resolution in the geographic dimensions (i.e., the triangles can be subdivided into smaller triangles arbitrarily).
- **Geometry.** The geometry of each multi-level tessellation will consist of a set of vertices that defines the positions of the corners of the triangles. If a model is comprised of more than one multi-level tessellation, they will share common vertices, to the extent possible.
- **Data arrays**. Each data array is a 1D array of data values that may be of type double, float, long, int, short or byte. All the data arrays in the model must be of the same type and must have the same number of elements.
- **Profiles**. Each profile is composed of a set of monotonically increasing radii and a set of data arrays. Each profile is associated with a single vertex and a single layer in the model. The first and last radii in a profile define the bottom and top of the associated layer at the geographic position of the vertex. Several types of profiles are supported:
  - **N-Point profiles** consist of two or more radii and an equal number of data arrays, with one data array associated with each radius.
  - **Constant value profiles** consist of two radii and a single data array that defines the data values for the entire radial span of the profile.

  - **Thin profiles** consist of a single radius and a single data array. They have zero thickness, i.e., the radius of the bottom and top of the profile are equal.
  - **Empty profiles** consist of two radii but no data arrays.
  - **Surface profiles** consist of only a single data array. They have no radius values. These are used to support 2D models.

  The data values within a profile are continuous.

- A **2D array of Profiles** with *nVertices* × *nLayers* elements. The first index refers to one of the vertices of the model geometry and the second index refers to one of the layers of the model. For a given vertex index, the 1D array of profiles contains a profile for each layer of the model, stored in order of increasing radius. The last radius of each profile in a 1D profile array must be equal to the first radius of the next profile in the same 1D profile array. While the data values within a single profile are continuous, data values may be discontinuous across profile (i.e., layer) boundaries.
- **Radial interpolators** that interpolate data values in profiles. These include linear interpolators, cubic spline interpolators, and potentially others.
- **2D interpolators** that interpolate values in the 2 geographic dimensions. These include linear interpolators that interpolate values within a single triangle of the 2D tessellations, and higher order interpolators that provide continuous spatial derivatives of the data values.
- **(2+1)D interpolators** that combine 1D and 2D interpolators to interpolate data in 3D. They first use a 1D interpolator to interpolate values at a specified radius in a neighborhood of profile arrays, and then apply a 2D interpolator to those values to find an interpolated value at the desired 3D location.

GRID GENERATION

As mentioned above, grid generation is accomplished with a software application called GeoTessBuilder, which operates in two fundamental modes. In the first, GeoTessBuilder will construct a new 2D geographic grid from scratch. Specification of the radii and data values along the profiles of the model is performed separately by user-generated software (examples are provided with the code). To build a new grid in this manner, the user first specifies a default grid resolution (the edge length of the triangles, in degrees). If nothing further is specified, then a uniform tessellation with that resolution will be constructed. The user may also specify an arbitrary collection of points, paths and polygons, or any combination thereof. GeoTessBuilder will refine the grid in and around those points, paths, and polygons, to whatever grid resolution the user requests (Figure 4). The points, paths and polygons can be specified in ascii text files, or can be accessed from kmz files generated by Google Earth.

In the second mode of operation, GeoTessBuilder will construct a new 3D grid by refining an existing 3D GeoTess grid. The user supplies an existing grid and a list of grid node indexes. GeoTessBuilder will add additional grid nodes around the specified grid nodes, effectively doubling the spatial resolution around the supplied grid nodes. Refinement is performed in both the geographic and radial dimensions.

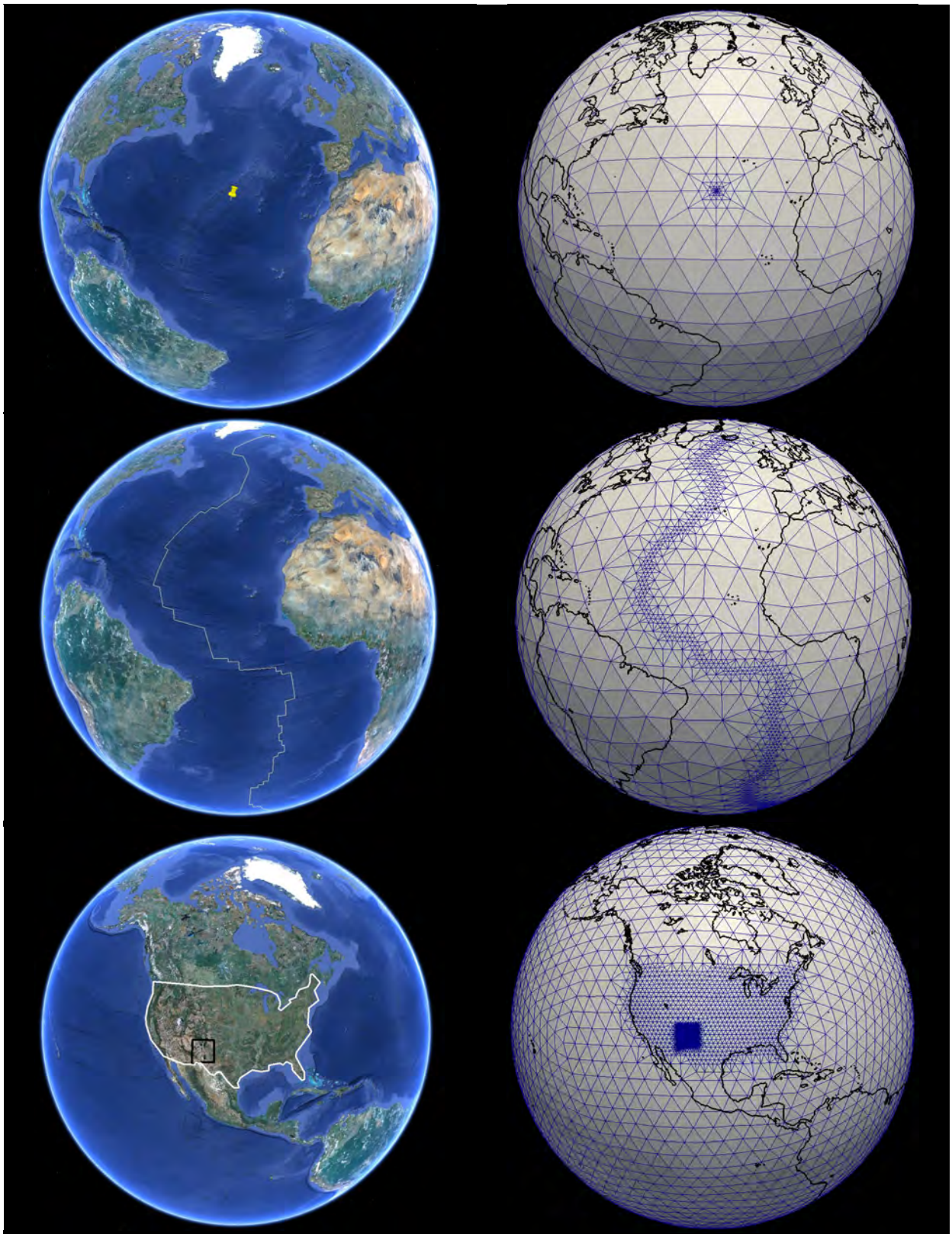


Figure 4. Grid refinement options. On the left are shown points, paths and polygons generated in Google Earth. GeoTessBuilder can read the Google Earth kmz files and refine the grid in or around the points, paths or polygons.

SALSA3D MODEL

We offer two examples of models based on the GeoTess parameterization. The first is SALSA3D, a global P velocity model of the Earth (Begnaud et al., these Proceedings; Begnaud et al., 2011). The SALSA3D model is deployed on a grid that was generated with an adaptive grid refinement algorithm. The starting model consisted of a triangular tessellation with uniform 8° edge lengths (Figure 5a). After an iterative tomographic inversion procedure had converged, the model resolution matrix was computed (Figure 5b). All grid nodes where the diagonal of the model resolution matrix was greater than 0.3 were refined to effectively double the spatial resolution of the model in the vicinity of the nodes with high model resolution. This procedure—tomography followed by model resolution calculation and adaptive grid refinement—was repeated 4 times, at the end of which the grid had spatial resolution as low as ½° (Figure 5c) and the model resolution was everywhere less than 0.3 (Figure 5d). This procedure resulted in a model with approximately an order of magnitude fewer nodes than would have been the case if the spatial resolution had been ½° everywhere.

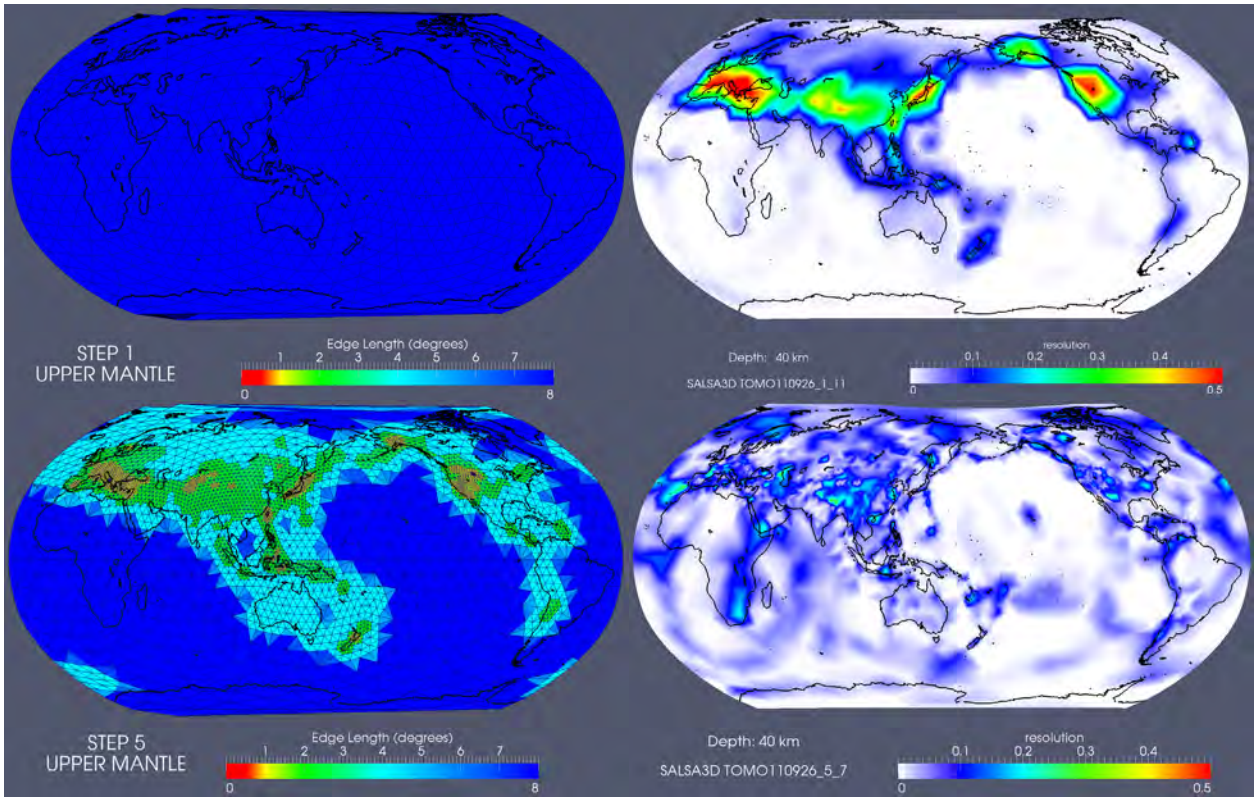


Figure 5. SALSA3D grid refinement.

LIBCORR3D

LibCorr3D is a software library built upon GeoTess that is used to manage station-phase specific predictions of seismic attributes, and uncertainties of those predictions. For every station in a network, every phase of interest, and every attribute of interest (e.g., travel time, horizontal slowness, station-event azimuth, etc.) a separate GeoTess model is generated which stores 2 quantities: the predicted value and the uncertainty of the prediction. A seismic event location code would use these models by looking up predictions and model uncertainties, rather than computing them on the fly. An alternative strategy would be that LibCorr3D would store corrections to values computed with a 1D model, such as ak135, rather than the predictions themselves, and the locator would add the corrections to the values it calculated with the 1D model.

Figure 6 illustrates the contents of a typical model for station GERES located in Germany. The difference in travel time computed using SALSA3D and ak135 is illustrated in the upper left. In the lower left is the uncertainty of the travel time predictions calculated by SALSA3D (see Hipp et al., these Proceedings, for more information). Standard

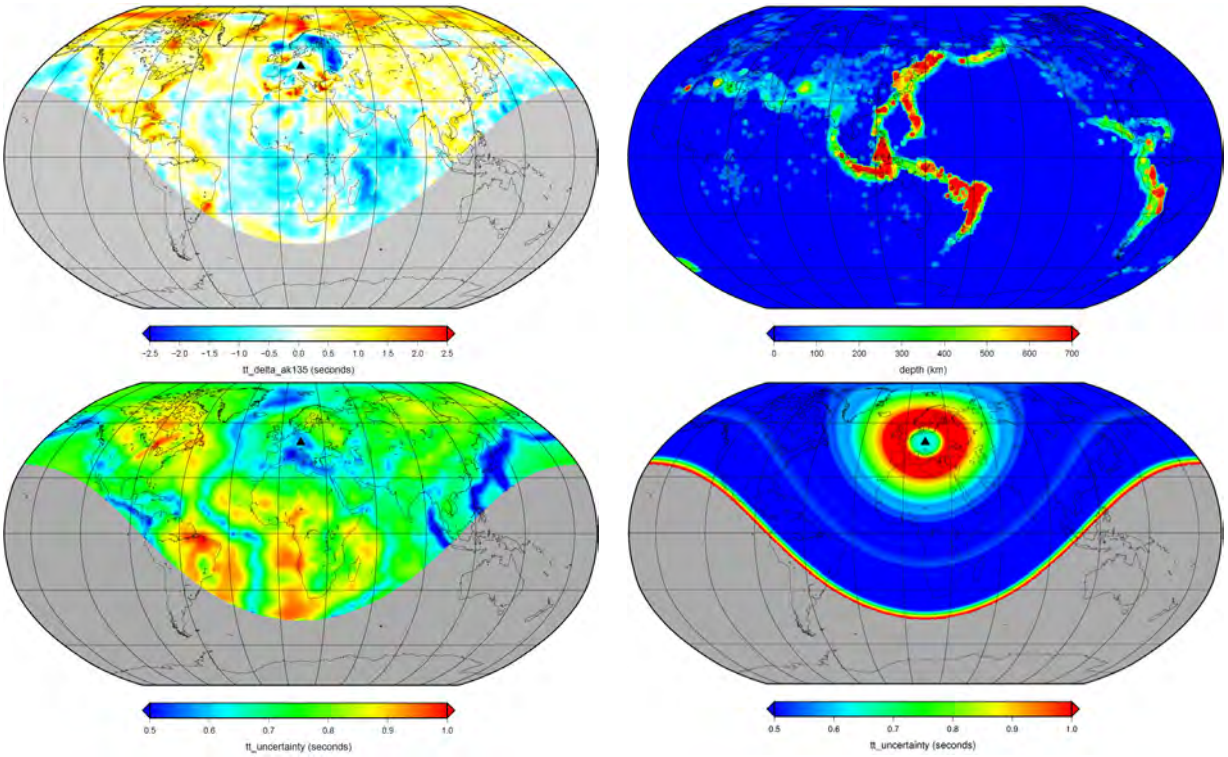


Figure 6. LibCorr3D model for station GERES located in Germany. a) Difference between travel times computed with SALSA3D and ak135. b) Depth of the bottom of all the LibCorr3D models (not stored in the model). c) Path dependent travel time uncertainty. d) 1D distance dependent model uncertainty (for comparison only, not stored in the model).

1D distance dependent travel time uncertainty is shown in the lower right for comparison with the path dependent travel time uncertainties computed with SALSA3D. While the surface values of predicted travel time and uncertainty have been emphasized, it is important to note that these values are stored in a 3D grid. The upper right image in Figure 6 is the depth of the bottom of the LibCorr3D models. Over most of the globe, the model is only one node thick (blue in Figure 6) but the model extends deeper than any recorded earthquake where warranted by recorded seismicity.

This strategy has implications for computational performance. A typical model for a single station-phase-attribute, stored at a resolution of 0.5° horizontally and 30 km radially, will require roughly 50 MB of memory once it is loaded into a computer. For a network of approximately 60 stations, a single phase (first P), and two attributes (travel time and horizontal slowness), this will require approximately 6 GB of RAM to store, which is a modest amount of memory on a modern computer. To meet operational performance requirements, it will be necessary that all the models be loaded into memory and retained there for as long as they are being used. This is because the load time for the models can be substantial (several 10s of seconds up to a minute or so to load an entire 60-station network). Once the models are loaded, the time required to lookup a value in the collection of models is minimal, much less than the time required to compute a 1D or 2½D prediction on the fly. For this strategy to work on a shared computer resource where multiple jobs are running that all require access to the models, it will be desirable to run either the LibCorr3D lookup table facility or the locator itself in a service oriented mode. This implies that a single instance of LibCorr3D (or the locator) is running as a service on a computer and multiple independent jobs running at the same time can access the common lookup table or locator service.

CONCLUSIONS AND RECOMMENDATIONS

GeoTess is a model parameterization and software support library that manages the construction, population, storage and interrogation of data stored in 3D Earth models. It is our hope that monitoring agencies will familiarize themselves with GeoTess and implement the ability to accept 3D models in GeoTess format. If this happens, and members of the research community develop the ability to deliver data products in this format, it would greatly facilitate the sharing of 3D Earth model information between model developers and monitoring agencies and would likely increase the probability that research products are properly evaluated and ultimately implemented by monitoring agencies.

REFERENCES

Ballard, S, J. R. Hipp, and C. J. Young, (2009). Efficient and accurate calculation of ray theory seismic travel time through variable resolution 3D earth models, *Seismol. Res. Lett.* **80**, 989–999.

Begnaud, M. L., S. Ballard, C. J. Young, J. R. Hipp, M. C. Chang, A. V. Encarnacao, C. A. Rowe, W. S. Phillips, and L. K. Steck (2011). A global 3D P-velocity model of the Earth's crust and mantle for improved event location, in *Proceedings of the 2011 Monitoring Research Review: Ground-Based Nuclear Explosion Monitoring Technologies*, LA-UR-11-04823, Vol. 1, pp. 237–248.

Reiter, D., W. Rodi, and S. Myers (2011). Estimating the Uncertainty and Predictive Capabilities of Three-Dimensional Earth Models, in *Proceedings of the 2011 Monitoring Research Review: Ground-Based Nuclear Explosion Monitoring Technologies*, LA-UR-11-04823, Vol. 1, pp. 132–140.

SUMATERA 2012 AFTERSHOCKS: REVIEWED EVENT VS. WAVEFORM CROSS-CORELATION BULLETIN

Dmitry Bobrov, John Coyne, Jeffrey W. Given, Urtnasan Khukhuudei, Ivan Kitov, Kirill Sitnikov, Spilio Spiliopoulos, and Lassina Zerbo

Comprehensive Nuclear-Test-Ban Treaty Organization

Sponsored by the European Union Joint Decision IV

ABSTRACT

Our objective is to assess the performance of a waveform cross-correlation technique, as applied to automatic and interactive processing of the aftershock sequence of the 2012 Sumatera (M_s=8.2) earthquake relative to the Reviewed Event Bulletin (REB) issued by the International Data Centre (IDC). The REB includes ~1200 aftershocks between April 11 and May 25 with (IDC) body wave magnitudes from 3.05 to 6.19. These aftershocks cover a slightly unusual V-shape area. The cross correlation technique allows a flexible approach to signal detection, phase association and event building. To automatically recover the sequence, we selected sixteen aftershocks with m_b(IDC) between 4.5 and 5.0 from the IDC Standard Event List (SEL3) available on April 13. These events sparsely cover the area of the most intensive aftershock activity. After a superficial review, these aftershocks were designated as master events. The selected set of master events is not the best, or even an optimal one, as there was no time or any specific procedure to estimate an event performance as a master. We instead used intuition based on experience. When the sequence is fully analyzed one may design a strict procedure as based on the optimal choice of defining parameters. As an example, the number of stations with template waveforms has to be defined in the very beginning. In this study, waveform templates from only seven array stations with the largest signal-to-noise ratio (SNR) estimated for the signals from the main shock were used to calculate cross-correlation coefficients over the entire period of 44 days with a time step corresponding to the relevant digitization rate. This rate varies among the stations from 40 to 80 samples per second. Approximately 620,000 detections obtained by cross-correlation were then used to build events according to the IDC definition, i.e., at least three primary stations with accurate arrival times, azimuth and slowness estimates.

After conflict resolution between events with similar arrivals built by more than one master all qualified event hypotheses populated the automatic cross-correlation Standard Event List (aXSEL). The total number of hypotheses was 4924. When all events matched by similar arrivals from at least one aftershock in the REB were excluded there were 2763 new hypotheses in the aXSEL. Some events in the aXSEL were built by arrivals in P-coda, with intensive water reflections as the major source of strong arrivals in the coda. Since these reflections-based events have arrivals close in time to those from valid REB events, they were excluded after the comparison of the REB and aXSEL. As a result, the total number of new hypothesis not matched by the REB is not the mechanistic difference between the aXSEL and REB. To evaluate the quality of new events in the aXSEL, we randomly selected a small portion (~10%) from 2763 events and experienced analysts reviewed them according to IDC rules and guidelines. After the interactive review (a portion of) the final product of cross correlation was obtained – the reviewed XSEL. In the ideal case, the aXSEL should be identical to the XSEL, i.e., the automatic part of cross correlation processing should be tuned to provide the most comprehensive seismic bulletin without bogus events. Therefore, we have investigated the influence of many defining parameters (threshold and SNR of cross correlation coefficient, *F*-statistics and *f-k* analysis, azimuth and slowness estimates, relative magnitude, etc.) on the aXSEL. We have constructed relevant frequency and probability density distributions for all detections, all associated detection, and for those which were associated with the aXSEL events. These distributions are also station and master dependent. When applied to the aXSEL from the beginning, these defining parameters would reject a majority of bogus events in the aXSEL, not affecting the creation of valid event hypotheses.

OBJECTIVES

Our principal objective is to assess the performance of the waveform cross correlation technique as applied to automatic and interactive processing of the aftershock sequence of an extremely large (M_s(IDC)=8.2) earthquake as measured by the IDC. Since this technique allows a flexible approach to all defining parameters, our objective is to investigate the effects of correlation time windows, frequency bands, thresholds, signal-to-noise ratio (SNR), relative magnitude and other parameters controlling the flux of detections on the final list of events. In an attempt to optimize the analyst workload we test a reduced set of seven from nineteen International Monitoring System (IMS) array stations reporting P-waves from the studied earthquakes. These seven stations are characterized by the highest SNRs measured from the main shock. The minimum number of associated stations for a valid event hypothesis is three, as required by the IDC event definition criteria (EDC).

RESEARCH ACCOMPLISHED

The IDC is obliged to find all seismic events, which one can retrieve from IMS data. Our experience with waveform cross correlation as an automatic detection and event building technique shows that, currently, the REB likely misses between 50% and 70% of events, some of them having valid arrivals at five and more IMS stations (Bobrov and Kitov, 2011; Bobrov et al., 2011; Bobrov et al., 2012). In addition, a relatively large portion of REB events does not demonstrate any cross correlation with neighbouring events, as expected from their relative locations and other parameters, and thus, look suspicious. These documented deficiencies of the REB have to be studied quantitatively at regional and global levels and a technical solution should be developed for a new automatic and interactive pipeline.

Here we address the problem of optimal defining parameters for detection and event building as based on waveform cross correlation and propose simple recipes for conflict resolution between event hypotheses created by neighbouring master events. To demonstrate the power of cross correlation, we have selected the most complicated case for automatic and interactive processing at the IDC– the aftershock sequence of one of the biggest events in 2012. This sequence includes ~1200 aftershocks with ~350 during the first 16 hours. We aimed at replicating the REB using cross correlation and building new REB-ready events, i.e., the events complying with the EDC. The REB was wholly replicated with an exception a few suspicious events, which are all small, and approximately 2760 new hypotheses were created. Due to the extraordinary large number of new hypothesis and limited human resources (analysts at the IDC are all busy with routine work) we had to carry out a (quasi-) bootstrap exercise – just a small portion of all hypotheses was interactively reviewed, with the set of hypotheses from one master reviewed completely. At the same time, we have reviewed all events with six and seven (from seven used for cross correlation) defining stations because such events should never be missed by the IDC. Unfortunately, we have found five (!) seven-station events during the first 24 hours after the main shock, with the largest m_b(IDC)=4.95. This situation is inacceptable in nuclear test monitoring even for aftershock sequences of extremely large earthquakes. One can easily design an evasion scenario using this lacuna in monitoring.

Theoretically, cross correlation detectors take the advantage of waveform similarity what makes it superior to standard (STA/LTA) seismic signal detectors (Gibbons and Ringdal, 2006; Schaff and Waldhauser, 2010). In practice, the cross-correlation technique has proven to be a powerful tool for detection of similar signals (Harris and Paik, 2006; Bobrov and Kitov, 2011; Bobrov et al., 2012). For 3-C stations, similar signals on vertical channels may come from any azimuth and have any slowness. For P-waves, the use of all three components puts only weak constraints on the difference between azimuth and slowness of arrivals having a high correlation coefficient. For array stations with many individual sensors, similar signals should have similar vector slownesses: the signals from different azimuths and with different apparent velocities across arrays with an aperture of several kilometres are well suppressed by destructive interference. The same effect irons the ambient seismic noise out – the cross correlation coefficient for noise is hardly above a few hundredths. Therefore, even a marginal level of cross correlation around 0.2 usually provides an SNR high enough to detect a signal similar to that in the template waveform. This level of correlation between two time series is slightly counterintuitive for conventional physics, where the level below 0.7 is considered as an insignificant one.

The cross correlation coefficient, *CC*, depends on the relative length of signal and correlation time window. When a signal is short and the window is wide, *CC* is likely underestimated because the noise input dominates. In a very narrow window, all signals look similar and *CC* is biased up. Because the Nuclear-Test Ban Treaty is a

comprehensive one, the IDC has to focus on signals from near-surface events in the (body) magnitude range between 2.5 and 4.5. The coverage of larger events is globally comprehensive as the IDC catalogue demonstrates (Bobrov et al., 2011). Smaller events are hardly seen even by regional networks. Therefore, all waveform templates include several seconds of (P- or Pn-wave) signal and a short time interval before the signal (lead), which provides additional flexibility in onset time.

For signals from low-magnitude events, one may expect the peak signal energy between 0.8 Hz and 6 Hz and the accuracy of *CC* estimates depends on relative frequency content of signals and background noise. A standard way to improve detection is to filter in the frequency band where SNR is the largest. The length of a given window also depends on its frequency band. For the low-frequency (BP, order 3) filter between 0.8 Hz and 2.0 Hz, the length is 6.5 s and includes 1 s before the arrival time. For the high-frequency filter between 3 Hz and 6 Hz, the full length is only 4.5 s. For Pn-waves, the length is 11 s and does not depend on frequency. The Pn templates also include 1 s of preceding noise.

In this study, we first calculate *CC* for each individual channel and then average these *CC*s over the channels to obtain an aggregate *CC* estimate for a given time point. Since we convolve and then average two multichannel ground motion waveforms, i.e., the template and the whole record, the set of several channels is replaced by one *CC*-trace. This trace is used to detect signals with a standard STA/LTA detector and to estimate the peak *CC* for these signals. The length of short-term and long-term windows is flexible; we use 0.8 s and 40 s, respectively. (One may also apply different detectors to the aggregate *CC*-trace and to the multichannel *CC*-traces, e.g., *F*-statistics.) Without loss of generality, we ignore all signals which have $CC < 0.2$ or STA/LTA < 2.8. According to our previous studies, these are conservative thresholds rejecting the majority of inappropriate signals but still allowing some bogus signals in noisy environment. One needs these bogus signals in order to determine statistically justified thresholds for all master/station pairs. These thresholds may balance the rate of missed valid signals and that of bogus signals.

At this stage, all individual *CC*-traces are retained for further analysis. They have the same sampling rate and time shifts relative to the reference sensor as the underlying waveforms. (In that sense, all signals obtained by cross correlation with a given master are well pre-filtered in azimuth and scalar slowness.) The only difference is that the *CC*-traces are normalized and thus do not depend on the relative master/slave size. In addition, the input of noisy channels is heavily suppressed on *CC*-traces since they are not correlating with master waveforms. This advantage of *CC*-traces allows obtaining reliable estimates of azimuth and slowness by standard *f-k* analysis even for very weak signals measured at a few channels. In order to characterize the quality of signals detected with cross correlation coefficient we also estimate *F*-statistics for the multichannel *CC* records. In this study, we compare results obtained using regular waveforms with those from the corresponding *CC*-traces.

When a signal is detected by cross correlation, we calculate all standard IDC attributes such as amplitude, period, azimuth, scalar slowness, standard SNR, quality class, etc. For a given source/station distance, one can calculate body wave magnitude using amplitude and period. Magnitude is a helpful dynamic parameter for global association of seismic phases – only signals in a predefined magnitude range can be associated with one source. Cross correlation provides another statistically reliable dynamic parameter for phase association. To characterized relative sizes of two events having a cross correlation coefficient above some predefined threshold at a given station, we propose to use the ratio of their L^2-norms, $|\boldsymbol{x}| / |\boldsymbol{y}|$, where $\boldsymbol{x}$ and $\boldsymbol{y}$ are the vectors of data for the slave and master event, respectively. In other words, we use the ratio of RMS amplitudes calculated in the same correlation window. The logarithm of the ratio, $RM = \log(|\boldsymbol{x}| / |\boldsymbol{y}|) = \log|\boldsymbol{x}| - \log|\boldsymbol{y}|$, is essentially the magnitude difference or the relative magnitude, *RM*. This difference has a clear physical meaning for close events with similar waveforms, i.e., for events with a higher level of cross correlation. It does not work for remote events because propagation paths and source functions are quite different. Then, one has to use standard magnitude scales. We have already shown that the *RM* is the best dynamic parameter for discrimination between genuine and dynamically inappropriate arrivals for a given event at several stations (Bobrov et al, 2011).

Having a detector based on cross correlation and an extended set of signal attributes, including the relative magnitude, one can process routine IMS data and associate appropriate signals with events, i.e., to build event hypotheses. The association process is much simpler than that realized in the Global Association algorithm (Coyne et al., 2012) currently used at the IDC. Since we are looking for seismic sources very close (0 km to 50 km) to a known set of master events, a local association, *LA*, is possible (Bobrov et al., 2011). The principal assumption

of the *LA* is that the travel times from a given master event to IMS stations are a good first approximation for any slave event, which by definition is close to the master. Therefore, actual travel time residuals for any slave event have to be within a few (say, 6) seconds from those predicted by the master. By projecting actual arrival times back to source with the relevant masters/station travel times, one can obtain a set of origin times associated with several IMS stations. For a true REB-ready slave event, three or more origin times associated with different stations have to group within a short interval (e.g., 8 s) and all attributes of the relevant signals (azimuth, slowness, relative magnitude) should be within station-specific uncertainty bounds (Coyne et al., 2012).

The main shock of the Sumatera April 11, 2012 earthquake was measured by the IDC, which located the event 2.294N and 93.035E with the origin time 08:38:32.23 (UTC). The solution was fixed to surface. Body wave magnitude m_b(IDC)=5.82 is small judging by M_s(IDC)=8.2. This underestimation of m_b for larger events (also relative to other global seismological centres, e.g., the ISC) is well known and is associated with the length of time window for the peak amplitude and period estimation. There were 162 associated and 60 defining phases including two Pn-arrivals and fifty two P-arrivals.

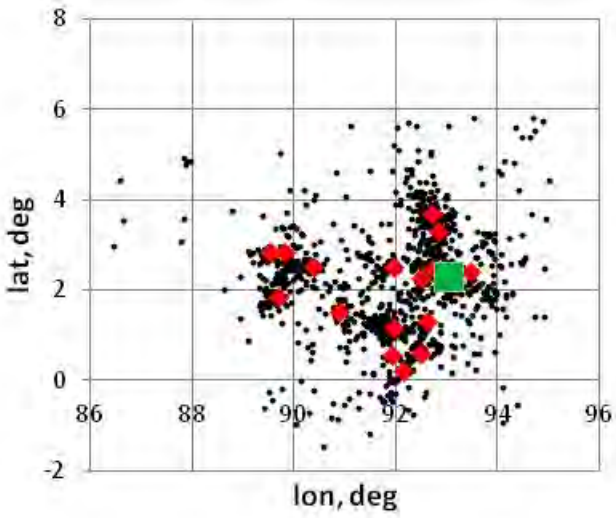


Figure 1. Distribution of REB events (black circles) related to the Sumatera earthquake (green square) between April 11 and May 25, 2012. Sixteen master events are shown by red diamonds. They were preselected using SEL3 available on April 13 and reviewed by an experienced analyst. The events at the far perephery of the aftreshock zone are likely related to low location accuracy for 3 to 5 station events and probable mis-timing/mis-assocaition of low-amplitude arrivals.

Figure 1 demonstrates that one may consider the area of the aftershock zone as constrained by a square between 88.0E and 94.0E, and 1.0S and 4.0N. Thus, the principal area is approximately 500 × 500 km^2. There are many events sparsely distributed far away from the main aftershock zone, which has a slightly unusual V-shape. (Such a shape might correspond to two fault planes.) The events to the west, north and south of the zone are likely mislocated by hundreds kilometres. Some of the events to the east of the zone are likely mislocated but may also be related to the high seismicity zone beyond 95E. Therefore, we have limited our study to the events to the west of 95E. The REB includes 1181 aftershocks which we would like to find using waveform cross correlation.

There were no REB events in the area of the studied earthquake and its aftershocks before the main shock, and no masters could be preselected. Therefore, we had to select a high quality and comprehensive set of master events from the aftershocks during the first day after the main shock. By IDC rules, SEL3 for a given day has to be ready six hours after the data day. There was no plan to recover the aftershock sequence before April 11. The decision to start cross correlation analysis in parallel to the routine automatic processing was made on April 12. On April 13, we examined the SEL3 for days 1 and 2 after the main shock. Without any formal procedure we selected sixteen (approximately) evenly distributed events with m_b(IDC) between 4.34 and 5.06 within the 24-hour interval after the main shock.

In order to select a self-consistent set of waveform templates for the sixteen masters we have inspected P-wave SNR at all IMS array stations from the main shock. Table 1 lists SNRs for 20 IMS array stations in descending order. The highest SNR belongs to MKAR and the lowermost – to PETK, which was excluded from processing because of low sensitivity. Station ILAR also has to be excluded from the list since the event-station distance is on the edge of P-wave existence and some aftershocks may be in the core shadow zone. Thus, from 18 eligible stations, we had to select a set with high SNRs, which is common for all masters. It had also to balance the workload of automatic/ interactive processing and the performance of the cross correlation technique including reliable event building; this small set of stations had to provide a good azimuth distribution. Fortunately, the top seven stations in Table 1 fit these requirements and we initially processed only waveform templates for the following stations: MKAR, WRA, CMAR, SONM, ASAR, ZALV, and GERES. An experienced analyst reviewed all candidate signals and corrected onset times where necessary. Finally, we obtained a set of 16 master events and each of the masters had 7 waveform templates at the best array stations for the main shock. We assumed that the relative amplitudes of signals (and SNRs) from aftershocks at 18 stations follow the same general trend as in Table 1.

Table 1. **IMS array stations, main shock – station distances, arrival times, and signal-to-noise ratios, number of detections as obtained by cross correlation.**

STA	Δ, °	Arrival time, s	SNR	# detections
MKAR	45.30	1334134011.	248.0	170827
WRA	46.16	1334134018.	169.2	104954
CMAR	17.08	1334133751.	113.5	68212
SONM	46.81	1334134023.	99.8	101104
ASAR	47.40	1334134028.	87.6	60634
ZALV	51.93	1334134062.	84.6	48742
GERES	81.26	1334134250.	77.1	66638
KSRS	47.41	1334134029.	73.6	27722
GEYT	47.76	1334134031.	67.2	30430
FINES	77.13	1334134228.	56.2	31524
BRTR	65.31	1334134157.	54.8	66142
ARCES	80.12	1334134243.	54.6	22392
NOA	84.03	1334134263.	54.1	2361
USRK	54.09	1334134080.	48.4	66447
AKASG	71.87	1334134195.	45.9	19430
TORD	90.79	1334134298.	43.2	31109
MJAR	53.80	1334134077.	38.0	37077
ESDC	93.94	1334134314.	33.5	6
ILAR	100.29	1334134341.	18.6	-
PETK	73.17	1334134207.	10.0	-

In order to assess the overall quality of templates, we have averaged all *SNR*s for each master. The highest average *SNR* is 208.4 and the lowermost is 14.6. This is a significant scattering and one might select a better set of masters with higher *SNR_AV* in some optimal procedure. Altogether, we have found 998773 detections at 18 primary array stations during the studied period. (Notice, the input of ESDC is only 6 detections) The selected subset of the best seven stations has given 621111 detections (62.1%). Table 1 lists the distribution of detections over the stations. The highest sensitivity is associated with MKAR, which detected 170827 P-wave arrivals. This is an expected result since MKAR has by far the highest SNR among all stations. Unexpectedly, station NOA gave only 2361 detections while FINES and ARCES, having the very same *SNR* associated with the main shock, reported 31524 and 22392 arrivals, respectively. One should reconsider NOA processing.

Having absolute arrival times for all detections it is possible to calculate approximate origin times by subtracting corresponding master/station travel times. For each master event, one can find all groups of three or more stations

with origin times within 8 s. These groups create zero-level event hypotheses. Apparently, theoretical (master/ station) travel time depends on the accuracy of master location. At the same time, the slave event can be 50 and even more kilometres far from the master. To compensate the influence of the master mislocation and the master/slave distance on the origin time we have introduces a sparse grid of 20 virtual masters at distances 20 km and 40 km from each master event. Effectively, we recalculate travel times for each grid point and subtract them from the same arrival times. Therefore, there are 21 different hypotheses on the origin times and we choose the one with the largest number of stations and the lowermost origin time RMS residual. In other words, we select the tightest group of origin times among the most populated groups. The average origin time is considered as the event origin time for the hypothesis.

When the set of zero-level hypotheses is built, we resolve a number of conflicts between the arrivals in the same hypothesis using amplitude, azimuth and slowness residuals, and obtain a set of REB-consistent hypotheses for each master event. As mentioned above, azimuth and slowness are estimated by *f-k* analysis on *CC*-traces. The deviation of the estimated parameters from their theoretical values has to be within station-dependent bounds: azimuth residual between $\pm 15^{o}$ (large aperture or teleseismic arrays) and $\pm 25^{o}$ (regional arrays), slowness ±2 s/deg for all arrays. This is a simple test, which we actually partly implemented at the detection stage, i.e., all detections are already within some global uncertainty bounds relative to station/master vector slownesses. At the stage of local association, one can apply station dependent limits and this makes the procedure more flexible. The estimation of these limits from the XSEL is one of our main tasks.

There should also be an overall consistency between dynamic parameters of associated arrivals. We have introduced the relative magnitude as a measure of source strength relative to master events. From or previous experience, we have estimated the global level of allowed deviation of a station relative magnitude, *dRM,* from the average value for a given event, i.e., station magnitude residual. For the Chinese aftershock sequence, ninety per cent of these residuals reside within ±0.4 units of magnitude. In this study, we have defined the magnitude residual threshold as 0.7: no absolute deviation from the network average relative magnitude is above 0.7. At the same time, we expect the distribution of *dRM* in the XSEL to have less than 5% of arrivals beyond ±0.4. The relative magnitude is a very efficient parameter to suppress the creation of bogus events for regular seismicity.

When all time-azimuth-slowness-magnitude conflicts between arrivals in a given eight-second-wide interval are resolved there might be more than one event with practically the same origin time. This may often happen in the initial stage of a large aftershock sequence when the rate of aftershocks is very high. We have considered such a situation and allowed new hypotheses to be formulated when the number of un-associated arrivals in the window is 3 or more. It might also happen that the arrivals out of the window may be associated with the leftovers within another eight-second window. We are trying to associate any arrival with a potential REB event considering its kinematic and dynamic attributes. No arrival for a given master can be associated with two or more events.

The number of aftershocks found by 16 master events varies from 1738 to 2636, but concentrates around 2100. At this stage, we obtain a preliminary automatic event list, aXSEL, which has to be as close to the final (reviewed) XSEL as possible. The aXSEL is not a mechanistic sum of all individual masters, however. Only the closest master is able to find smaller slaves, but bigger aftershocks can be built by many masters. There are two effects creating multiple solutions and thus working against the simplicity of local association. First, the correlation distance depends on the vector slowness difference between master and slave and remote stations “see” slaves at larger distances from master. Second effect resulting in multiple event hypotheses is associated with larger seismic events. Their waveforms are much longer than the correlation time windows and the waveform templates may find peak correlation coefficients not in the beginning of the records but later in the wavetrains. This may happen even for signals arriving from different azimuths. In a way, the correlation technique is blinded by bigger events like a night-vision system is blinded by daylight. A simple way to avoid the multiple choices is to separate all bigger events by their relative magnitude and review any of the related hypotheses interactively. There is no case where one can miss the bigger events. Therefore, this issue is not critical for the CTBT.

There are 137274 detections left after the first round of phase association and event building. This is 22 percent of the total number of detections (621111) obtained by seven stations and sixteen master events. For the total number of 34957 built events, one has 3.96 phases per event. Therefore, an average event built by cross correaltion is a 4-station event. Actual numbers are: 17202 3-station events, 8555 4-station, 5073 5-station, 2806 6-station, and 1321 7-station events. Bigger aftershocks have a higher probability to be built by many master events and their best

solutions should be reliable. Three-station events are likely to be bogus because we intentionally put our thresholds rejecting the (kinematically and dynamically) inapproporiate detections too low.

We have developed and tested a tentative procedure to resolve conflicts between events with similar arrivals, which are built by different masters, in order to leave only one best hypothesis in the aXSEL for the further interactive review. To begin with, we check the arrival times at all stations. Obviously, origin times for various masters may vary in a wide range because of travel time differences, but for the same (in physical terms) event all masters have to find the same physical signals, which belong to the sought slave event. When several (from 2 to 16) master events have similar arrivals at the same station, i.e., close (±4 s) arrival times and magnitude estimates (master magnitude + *dRM*), one can consider them as generated by the very same source. Between all hypotheses involving similar arrivals we select those with the highest number of defining stations. This is a natural choice since all master events have the same number of stations. (To populate the master event list, one also should guarantee that SNR at a given station should be similar for all masters. We did not apply this criterion when selected the master events and this might affect the aXSEL.) If two or more master events have the same number of defining stations, we give the priority to that with the highest cumulative *CC*. This completely resolves any conflict between masters having the same set of arrivals and only one event hypothesis left in the aXSEL. Because of the grid search, we also estimate the slave event location relative to its master event.

The entire phase association/event building procedure was developed during the first days after the main shock and we had to test it using the most fresh data. Before analysts started interactive review of the SEL3 for April 11, we had created a preliminary aXSEL for the first three days. Among hundreds of hypotheses, this aXSEL also included 25 new events with seven defining phases. This finding was of importance for monitoring and all 25 hypotheses were included in the interactive review by force. (The IDC should not miss big events even and specifically after the major earthquakes.) Twenty event hypotheses were found associated with reflected/refracted P-waves from very big aftershocks. In the first version of the *LA*, we allowed colocated events spaced by 12 s in origin time. In terms of physics these are imaginary events with properties practically equivalent to those in the relevant true events. In that sense, it is very difficult to distinguish between the imaginary and true events except the former should be observed later in time. At the same time, an evasion scenario is possible when an explosion is mixed with P-wave coda of a large earthquake. Hence, the IDC should not suppress the events based on P-coda. In the initial stage of our investigation, we decided to remove all colocated events within 40 s in order to reduce the workload for the post-mortem interactive analysis. But we remember that no events should be neglected in routine cross correlation processing.

There were five true events absent in the SEL3 and thus potentilly missed by the REB. Analysts confirmed all phases found by the automatic cross correlation detector. However, only one event had more than seven defining phases. The event with the largest magnitude (m_b(IDC)=4.95) occurred in ~13 minuts after the main shock. The hours after the main shock are charaterized by very high flux of arrivals from the same region which is hardly resolved by the *GA*. There were many six- and five-station events for the first day which were not reviewed in the beginning. Some of them were analyzed later.

After the conflict resolution between masters, the aXSEL includes 4924 hypoptheses, i.e., only 14% of hypotheses survive after the conflict resolution. Accordingly, we have two sets of detections: those associated with one of 34957 events build by all masters and a smaller subset of detections associated with the aXSEL. There are no human resources to review all 4900+ hypotheses in the aXSEL and we use this (likely not-perfect) automatic bulletin to estimate various statistic properties of the event defining parameters. The obtained estimates may slightly differ from those associated with the subset of valid REB events in the aXSEL.

The aXSEL can be split is two parts: the events close in time and space to one or several aftershocks in the REB, and those events which are far from any REB aftershock. The latter events are called “new” and define the superiority of the aXSEL. We consider an aXSEL hypotehsis as matching an REB event when two or more respective arrivals are within ±6 s and the difference of body wave magnitudes is less than 0.7. For the aXSEL, the magnitude is the sum of the master event magnitude plus the network avearge *RM*. When all events matched by similar arrivals from at least one aftershock in the REB were excluded there were 2763 new hypotheses left in the aXSEL. Many events in the aXSEL were built by arrivals in P-coda, with intensive water reflections as the major source of strong arrivals in the coda. Since these reflections-based events have arrivals close in time to those from

valid REB events, they were excluded after the comparison of the REB and aXSEL. Therefore, the total number of new hypotheses not matched by the REB is not the simple difference between the aXSEL and REB.

The rate of valid (i.e., REB-ready) and bogus events in the aXSEL can be estimated only by interactive review. Analysts have to check each associated arrival according to IDC rules and quidlines and approve/reject the aXSEL hypotheses. The interactive review is not possible for all aXSEL events, however, despite the REB-ready events are easier to test. All hypotheses include at least three primary stations with arrivals matching azimuth and slowness uncertainty bounds. Therefore, the analyst has just confirm the existence of the arrivals. When the number of approved arrivals is less than three no additional search for arivals at different stations is needed since the hypothesis is already based on the most sensitive stations. The probability to find another station to corroborate the event is negligible. (We do not consider here regional 3-C stations which may help in event building but in small areas.) These are two major problems with the review of SEL3 events, where the search for three primary stations and checking a huge number of alternative solutions for smallest events consume valuable time. In any case, the workload related to this study exceeds the limits of human resources because of routine interactive processing.

There are two posibilities to estimate the true rates. We have reviewed 109 new XSEL events built by one of sixteen master events and found 34 new REB events. Since 13 from 109 events were actually matched by REB counterparts, they were excluded from the set of 109: we cannot define any of these 13 events as new or bogus since they are valid REB events. (The definition of closeness of an aXSEL event to an REB event has to be revised.) After the subtraction of valid REB events, the portion of new events is 34 of 96 or 35%. Assuming a homogeneous distribution of aftershocks over space and similar performance of other 15 masters, one can estimate the number of new events (i.e., missed from the REB) in the sequence as ~850. With all uncertainty in the aftershock distributions and the imperfectness of master event choice and coverage, the number of new (i.e., missed by the REB) events is likely close to the number of REB events. It is highly important that these events are smaller and thus are most challenging for monitoring CTBT. It should be also mentioned that the reviewed aXSEL events are most difficult for interactive analysis since they are characterized by weaker signals and smaller number of stations.

CONCLUSIONS AND RECOMMENDATIONS

We have created an aXSEL for the aftershock sequence of the April 11 Sumatera earthquake. The aXSEL includes 4924 event hypotheses. Almost all of 1181 aftershocks from the REB for the same period are matched by one or more events from the aXSEL. There are more than 2750 event hypotheses extra to the REB, i.e., there are no REB events close in time and space. Resource limits did not allow interactive reviewing these hypotheses according to standard IDC rules and guidelines. We have applied quasi-bootstrap technique in order to statistically characterize the rate of valid and bogus events in the aXSEL.

For one master event, we have conducted a comprehensive review. We have found 34 new REB events from 96 hypotheses. It makes around 850 new events overall. Since the choice of master events was not optimal and we did not apply iterative procedures with increasing number of masters, the true share of missed events in the REB might exceed 100%. We have found many low magnitude events and likely reduced the monitoring threshold for the CTBT by 0.4 units of magnitude. These small events are most difficult to find and review interactively. In order to better estimate the portion of REB-ready events and the rate of false alarms we are going to select a small subset mimicking the distribution of hypothesis over master events and the number of defining stations (from 3 to 7).

Overall, waveform cross correlation has proved its superior performance relative to automatic processing at the IDC. This technique has found more REB-ready events (XSEL) than the REB for the same period. The set of new events included five new aftershocks during the first day after the main shock, which were based on all seven IMS array stations used for cross correlation. These five events have m_b(IDC) between 4.3 and 5.0. The XSEL also excludes those REB events, which do not demonstrate a reliable level of cross correlation with any neighbouring events. Therefore, the quality of XSEL is likely higher than that of the REB.

The exercise with a large aftershock sequence is an important step on the way to global coverage. The cross correlation technique is based on master events which are available only in seismic regions. In practical terms, seismicity is a stationary process with repeating events within well-constrained areas. This makes the choice of masters easy for 99% of events in the REB. We have already selected a set of master events in the North Atlantic after calculation of cross correlation coefficients for all REB events after 2009. This is a working prototype for the

global coverage. The procedure has been tuned and tested to optimise the performance of automatic processing for the purposes of interactive review.

The areas without master events represent a challenge for cross correlation. Fortunately, the method is powerful enough to provide a better monitoring capability even for aseismic areas. There are three possibilities based on the dependence of cross correlation coefficient on signal shape and time delays between individual channels of an array. One can use any master event for relatively large area (e.g., 500 km in radius) just changing theoretical time delays in the master template and studied waveform. This procedure preserves the empirical time shifts between channels, which are the most important advantage of cross correlation. In this regard, we are going to replace all 16 master events for the Sumatera aftershock sequence with one best master. Instead of unevenly distributed empirical masters, we will introduce a uniform rectangular grid with 70 km to 100 km spacing where all waveforms at individual channels are the same but shifted by theoretical times for given grid points and stations. Since the continuous waveforms are shifted by the same theoretical times the calculation of cross correlation coefficient in frequency domain will be reduced to phase change. When the change in time shifts between adjacent grid points (master events) is less than one count (e.g., 1/40 s) and the cross correlation coefficient for a given station does not change the grid spacing can be adjusted. Overall, the use of empirical master events beyond their actual positions allows substantial reduction (orders of magnitude) in computer resources and extends the zone covered by cross correlation by hundreds kilometres.

There are extensive (also continental) aseismic areas where one cannot extrapolate the influence of empirical master events. Then two approaches are feasible. One is based on synthetic seismograms for master/stations pairs. Before it can be used for cross correlation, the accuracy of this method should be tested with actual waveforms in seismic areas. The overall experience with synthetic seismograms is encouraging. Since the most important for cross correlation are relative time delays between individual sensors, which are associated with local velocity structure beneath seismic stations, one can use local seismic events for the calibration of the delays. Then the empirical time shifts could be scaled to any distance by synthetic seismograms.

The second approach was proposed by Harris and Paik (2006). The entire diversity of signal shapes for a given magnitude range can be decomposed into a few orthonormal functions similar to the decomposition into a Fourier series. They also proposed an algorithm for easy implementation. Therefore, one can use the set of orthonormal functions instead of master templates and use the sum of coefficients or the maximum coefficient of the decomposition to best represent the sought signal. Cross correlation coefficient can be calculated accordingly. This procedure should also be tested using actual master events.

The location accuracy is one of the most important characteristics of REB events. This is associated with the area of on-site inspections limited by 1000 km^2. The cross correlation technique includes as a natural part the possibility of double-difference location. The use of regular master event grid and the resolution of conflicts between adjacent masters allows very accurate location even (and especially) for the smallest events. Moreover, confidence ellipses of the corresponding master events are also the ellipses for the slaves. We also envisage the use of nonlinear grid search algorithms based on a dynamic grid adjustment. Regional cross correlation studies documented the location improvement by an order of magnitude and event more for small events. We expect the same effect globally when the cross correlation pipeline becomes operational.

In terms of computer resources, to produce the aXSEL for the studied aftershock sequence one needed only one regular CPU, which can run twenty master events with templates at seven stations in real time. The process of master events selection can be easily optimized and automated to the level of superficial review only. The progress in computer technology (e.g. GPU), the optimization of master event distribution, and the use of synthetic and repeated templates by neighbouring master may reduce the computer resources by orders of magnitude.

The rate of valid and bogus events should be optimized globally. For each master/station pair we have to define a large number of thresholds: time window, frequency bands, *CC*, *CC_SNR*, azimuth and slowness residual, *F*-statistics, *RM*, the distance between sequential detections with similar characteristics. For the *LA*, the event building procedure (i.e., the tightness in time and *RM*) should be tuned to meet the requirement of the most intensive seismicity after catastrophic earthquakes. We have also to define the minimum time between collocated events. The conflict resolution between similar hypotheses obtained by different masters is currently a challenge.

One may try to split larger events with many masters (larger average RM as well) and smaller events with one or a few masters. It is possible to resolve all issues using the machine learning approach, when enough data.

We did no touch upon a number of problems associated with regional stations and phases. Regional velocity structure is characterized by large amplitude variations which reduce waveform similarity and thus cross correlation to several kilometres. Since the IMS seismic network is a regional one with three stations within 20^o from any place within continents, the input of arrays and 3-C stations cannot be neglected. Fortunately, the experience with regional stations and networks is extensive and may be borrowed and implemented directly under the IDC framework.

All these advantages of the cross correlation technique and the absence of significant problems in automatic and interactive processing urge the replacement of the current processing pipeline. As a start point, all aftershock sequences at the IDC could be processed with an aftershock scanner based on cross correlation.

ACKNOWLEDGEMENTS

The authors are grateful to all analysts at the IDC who have built the REB.

REFERENCES

Bobrov, D. and I. Kitov (2011). Analysis of the 2008 Chinese earthquake aftershocks using cross correlation, in *Proceedings of Monitoring Research Review 2011: Ground- Based Nuclear Explosion Monitoring Technologies*, LA-UR-11-04823, Vol. 2, pp. 811–821.

Bobrov, D., I. Kitov, and L. Zerbo (2011). Perspectives of cross correlation in seismic monitoring at the International Data Centre, arXiv:1112.4696v1.

Bobrov, D., J. Coyne, I. Kitov, and R. Pearce (2011). Comparison of recurrence curves from the IDC and ISC catalogues, in *Proceedings of the Science and Technology 2011*: *Earth as a complex system*, Vienna.

Bobrov, D., J. Coyne, I. Kitov, and G. Turiomuruguendo (2012). On comprehensive recovery of an aftershock sequence with cross correlation, Proceeding of the EGU 2012, http://presentations.copernicus.org/EGU2012-5540_presentation.pdf

Coyne, J., D. Bobrov, P. Bormann, E. Duran, P. Grenard, G. Haralabus, I. Kitov, and Yu. Starovoit (2012). Chapter 17: CTBTO: Goals, Networks, Data Analysis and Data Availability. In: New Manual of Seismological Practice Observatory, ed. P. Bormann (forthcoming), doi: 10.2312/GFZ.NMSOP-2_ch17

Gibbons, S. J. and F. Ringdal (2006). The detection of low magnitude seismic events using array-based waveform correlation, *Geophys. J. Int.* **165**, 149–166.

Harris, D. B. and T. Paik (2006). Subspace detectors: Efficient Implementation, Lawrence Livermore National Laboratory technical report UCRL-TR-223177.

Schaff, D. P. and F. Waldhauser (2010). One magnitude unit reduction in detection threshold by cross correlation applied to Parkfield (California) and China seismicity, *Bull. Seismol. Soc. Am.* **100**(6), 3224–3238.

AN OVERVIEW OF COMPREHENSIVE INSPECTION TECHNOLOGIES UNDER INVESTIGATION AT THE NEVADA NATIONAL SECURITY SITE IN SUPPORT OF THE COMPREHENSIVE NUCLEAR-TEST-BAN TREATY

Veraun D. Chipman, Catherine M. Snelson, Dudley F. Emer, Margaret J. Townsend, and Ping Lee

National Security Technologies, Inc.

Sponsored by the National Nuclear Security Administration

Award No. DE-AC52-06NA25946/NST11-NCNS-TM-EXP-PD15

ABSTRACT

Comprehensive Inspection Technologies (CIT) under investigation at the Nevada National Security Site (NNSS) in support of the United States' effort to decide whether or not to ratify the Comprehensive Nuclear-Test-Ban Treaty (CTBT) include the detection of noble gases from clandestine underground nuclear testing, visual observations, hyperspectral imaging, controlled-source and passive-source seismic surveys, and geophysics.

Noble gas detection includes a series of experiments, called the Noble Gas Migration Experiment (NGME) experiments, that explore the fundamental parameters that determine the capability to detect radioxenon isotopes and ^{37}Ar produced in underground nuclear tests that are of interest to both the International Monitoring System (IMS) global monitoring and CTBT On-Site Inspection (OSI) regimes. Through a unique combination of field experiments at the NNSS, radioactive noble gas production, large-scale hydrogeologic computer simulations, and a regimen involving carefully designed field-sampling techniques, the experiments will research the production, release, and sampling challenges that determine the ability to detect these two important Noble gases. The NGMEs are a collaborative effort involving the National Laboratories and National Security Technologies (NSTec), and use a former underground nuclear test site on the NNSS as an initial test bed. The results of this research will be a better understanding of the migration of radioactive noble gases to support OSI efforts. The generation of radioisotopes is an unequivocal signature of a nuclear explosion. Understanding how gaseous and particulate radioisotopes are released from the subsurface and transported into the environment will greatly enhance current national capabilities for treaty verification and inspection.

Other OSI experiments leverage the scientific expertise of the National Laboratories and NSTec, and the unique attributes of the NNSS to develop, test, and demonstrate treaty verification technologies and devices. The NNSS is well suited to support bilateral confidence-building and transparency activities such as integrated field investigations wherein means, methods, and procedures supporting the OSI operational manual can be vetted. The OSI experiments will explore and validate geophysical (controlled-source and passive-source seismic, gravity, electrical, magnetic, etc.) and optical techniques (both visual and instrument-based) that could greatly enhance the understanding of the efficiency of these techniques for OSI. Project goals encompass both technique validation and technology development in order to prepare for future OSI activities. Part of this effort will be to investigate how to better integrate the various technologies with each other (cross sensor analysis) and individually at different physical scales. For the optical techniques this means vertical integration, from ground-based systems to commercial satellite imagery.

OBJECTIVES

Important to ratification of the CTBT are: (1) the integration of a suite of non-intrusive techniques to swiftly delineate a search area for targeted invasive data collection; and (2) the ability to identify noble gases, including radioxenons and ^{37}Ar, that provide an unequivocal signature of an underground nuclear explosion. To this end, CIT are being researched and developed at the NNSS. As to the integration of a suite techniques for OSI, a campaign of visual observation methods, geophysics, controlled- and passive-source seismic surveys, and imaging techniques is being performed at a legacy underground nuclear explosion (UNE) site at the NNSS. At a separate UNE at the NNSS, an NGME is being conducted where chemical and radiological tracers will be injected into the subsurface via a drill-back hole into the UNE cavity and monitored for at the surface.

RESEARCH ACCOMPLISHED

In the event of a suspected underground nuclear test, a typical OSI allows for forty inspectors over a sixty-day period, with an option for an additional ten days. During that short amount of time, inspectors may use a wide range of techniques and tools that are specifically called out in the CTBT to narrow a wide search area to a more focused and detailed site investigation that would ultimately prove, or disprove, that a test had occurred (see Figure 1). This research seeks to advance the understanding, application, and integration of these techniques and tools, along with developing other promising techniques that are currently not specifically called-out in the Treaty. To do so, a legacy UNE site at the NNSS has been selected as a test-bed for researching and developing a comprehensive suite of inspection technologies that could be deployed during an OSI.

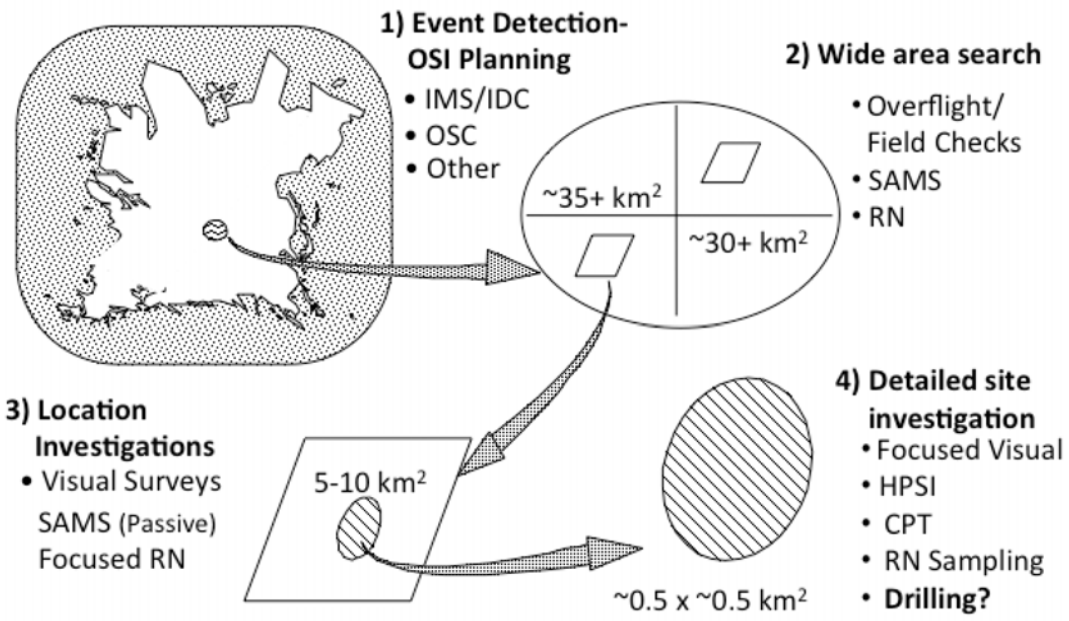


Figure 1. Typical stages of an On-Site Inspection.

At the selected UNE site for CIT research and development, National Security Technologies, Inc. (NSTec), Los Alamos National Laboratory (LANL), Lawrence Livermore National Laboratory (LLNL), and Sandia National Laboratory (SNL) are testing the following techniques and tools during the summer of 2012:

- Visual Observations
- Ground Penetrating Radar
- Ground-Based Gravity Surveys
- Ground-Based Magnetic Surveys
- Electrical Resistivity Surveys
- Passive- and Active-Source Seismic Surveys

- Hyper-Spectral Imaging Surveys
- Light-Detection and Ranging Surveys
- Satellite Synthetic Aperture Radar

Acquired data from the deployment of these techniques at a single UNE test-bed will be analyzed, and a methodology for integrating each of the data sets will be developed, with the expectation that a fully coupled data-set will provide a much clearer picture of the UNE site than any of the techniques listed above could by themselves.

At a second UNE site at the NNSS, a test-bed is being developed for chemical and radiological tracer migration studies, called the Noble Gas Migration Experiments. The first phase of the NGME was to select a legacy UNE site at the NNSS in a geologic formation that had well connectivity with the atmosphere. The degree of connectivity, or "breathing", was determined by monitoring the barometric pressure and the outflow of air from wellheads of the drill-back holes at 2 different sites. As shown in Figure 2, when the barometric pressure rises, a steady flow of air exits the wellhead of the drill-back hole, and when the barometric pressure raises, atmospheric air inflows via the wellhead. Under the right atmospheric conditions, a net upward migration of soil gas from the UNE cavity (now collapsed and forming a rubble chimney) should ratchet to the surface.



Figure 2. Time-histories of barometric pressure and well outflow at the Noble Gas Migration Experiment Site.

At the NGME site, an existing drill-back hole was then prepared by placing packers near the bottom of the hole where it is estimated to have intersected the UNE rubble zone. As shown conceptually in Figure 3, the drill-back hole was stemmed so as to prevent short-circuiting of the tracer gas. An inert chemical tracer gas will be injected into the rubble zone and monitored for by "smart" samplers that autonomously pull soil-gas samples from both the surface and shallow subsurface. LLNL and Pacific Northwest National Laboratory (PNNL) have deployed three different
soil-gas sampling systems around the NGME site. LLNL's system is shown in Figure 4. Soil gas samples will be shipped to an off-site laboratory for analysis. The purpose of the chemical tracer injection is to gauge the transport times and refine the monitoring plan for a later injection of a radiological tracer combined with sulfur-hexafluoride.

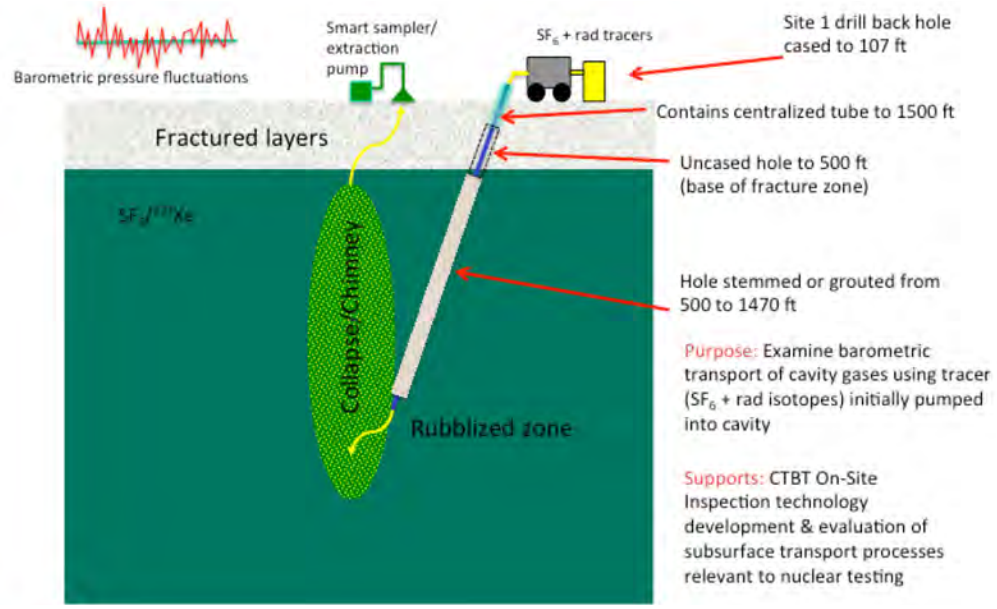


Figure 3. Conceptual depiction of the Noble Gas Migration Experiment.

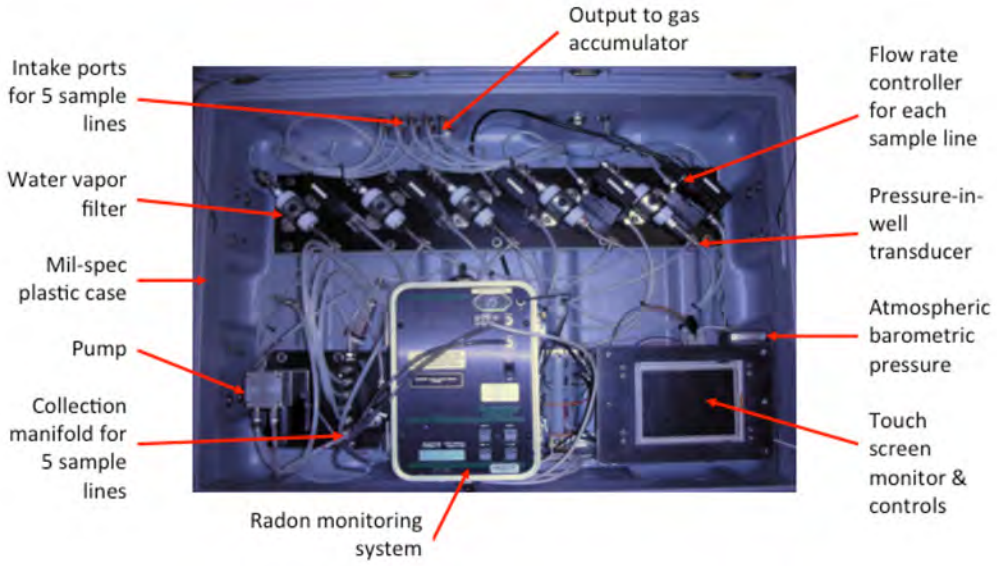


Figure 4. Lawrence Livermore National Laboratory's "Smart" soil gas sampler.

ACKNOWLEDGEMENTS

The author would like to thank all those involved at NSTec, including NSTec's Special Technologies Laboratory (STL), LANL, LLNL, PNNL, and SNL, as well as various subcontractors that have contributed to make this project successful.

A SOFTWARE TOOLBOX FOR SYSTEMATIC EVALUATION OF SEISMOMETER-DIGITIZER RESPONSES

Aaron Ferris[1], Robert B. Herrmann[2], and Jessie L. Bonner[1]

Weston Geophysical Corporation[1] and St. Louis University[2]

Sponsored by the National Nuclear Security Administration

Award No. DE-FG02-09ER85548/Phase II

ABSTRACT

Absolute amplitude and phase measurements of seismic signals require accurate knowledge of the seismometer-digitizer response system. However, for many important datasets, instrument responses or absolute data units are not accurately known or are missing from metadata. We are developing a software suite to evaluate and/or recover the seismometer-digitizer response. For amplitude response information, our approach involves computing an amplitude transfer function between the power-spectral density of seismic noise at a reference station (which has a well-known response) and noise at a candidate station where the response or data units are unknown or require evaluation. The resulting transfer function is a pseudo-amplitude response that can be used for response file evaluation or to correct candidate data to real, absolute units. Phase response recovery is a work-in-progress, but a method under active development isolates the source and path phase effects from instrument effects through a deconstruction of noise cross-correlations between the reference and candidate station. Currently, phase recovery by this method works well at short periods but requires further refinement to adequately recover instrument phase effects at periods > 10 sec.

We have extensively tested our amplitude methodology on multiple datasets to understand its effectiveness and limitations. For example, geospatial variations in amplitude response recovery have been evaluated between 12,500 station pairs from US Array (2009-2011). These studies have shown that the difference between the true responses and our computed pseudo-responses is typically <±0.25 log units (0.01-10 Hz) for reference stations < 250 km from the candidate. We find that much of the error is for frequencies > 1 Hz, where local noise sources can vary strongly between localities. There also appears to be geologic and population effects in the geospatial distribution of response errors. Using a reference station in the Great Plains (e.g., CBKS in Kansas), response recovery error increases (>±0.25 log units) for candidate stations along the Gulf Coast and the Northern Rockies at periods > 10 sec. In these cases, the reference-candidate station distances are typically > 250 km, and it is likely that response recovery is negatively impacted by strong differences in crustal structure between the reference and candidate stations.

Our future research is focused on further method refinement, including improved recovery of the phase component of the response, as well as packing the toolkit into a JAVA-based graphical interface to be shared with the community. One method refinement under development increases the ease of pseudo-response utilization by fitting the pseudo-response files to a pole-zero system. The current implementation inverts 3-parameters of the pseudo-response to generate a pole-zero system: 1) the low-frequency corner, 2) the amplitude gains factor, and a damping factor at the low frequency end. The output is a 2-pole, 2-zero system that can be easily used in common processing software such as Seismic Analysis Code (SAC). Future refinements to the inversion will include an arbitrary number of pole-zeros and include a non-zero phase component.

OBJECTIVES

We are developing a set of software tools that can recover the seismometer-digitizer response function when the response is either unknown or incorrectly known. The software tools work by comparing ambient noise recordings between a reference station, where the response is well known, and a candidate station, where the response is desired. These tools include SACPSD, which computes the Power Spectral Densities (PSD), and NOISETRAN, which estimates the pseudo-amplitude and phase response function. The pseudo-response can be used to convert the candidate station data into real, absolute units calibrated to the reference station or for response file evaluation. The final set of tools will be packed into a JAVA-based graphical interface to be shared with the seismological community. The toolkit will include amplitude and phase recovery functionality, as well as pole-zero output for the recovered response information.

RESEARCH ACCOMPLISHED

Noise Transfer Function for Pseudo-Amplitude Response Estimation

For many important waveform datasets the instrument response or absolute data units are not accurately known or are missing from metadata. We have developed a method, referred to as NOISETRAN, which can estimate the seismometer-digitizer system for such datasets. For the case of amplitude response, the method works by computing the transfer function ($T(\omega)$) between background noise levels recorded at a reference station ($R_1(\omega)$) and the noise levels at the candidate station($R_2(\omega)$), such that

$$R_1(\omega) = R_2(\omega) \cdot T(\omega) + e_r(\omega).$$

In this formulation, the response error ($e_r(\omega)$) mainly occurs from differences in the noise field between the reference and candidate stations, which is frequency dependent. As shown in McNamara and Buland (2004), noise characteristics at periods < 1 sec are strongly influenced by cultural sources, especially near cities. In the microseismic band (4–8 sec), proximity to the oceans is important, and at longer periods the noise characteristics between seismic stations are quite similar. The similarity of the noise field at longer periods is a main justification for the work presented here. We see similar observations in the application of NOISETRAN, and we find that reliable response recovery information is generally attainable for periods > 1 sec and in many cases reliable results are attainable up to 0.1 sec.

NOISETRAN for Amplitude Response Recovery

An example of amplitude response recovery is shown in Figures 1-3. In this example, the reference station (CBKS) and candidate station (Q34A) are both located in the central Great Plains but separated by 242 km. Figure 1 compares the PSDs of the two stations computed using SACPSD. The PSDs of the reference station have been instrument corrected to real units and the PSDs of the candidate station are assumed to be “unknown” units for this test. PSDs for both stations are computed for 1-hour nighttime noise records to minimize the influence of cultural noise on the PSDs. Prior to NOISETRAN processing, the median PSD is computed at each frequency and then used in the analysis.

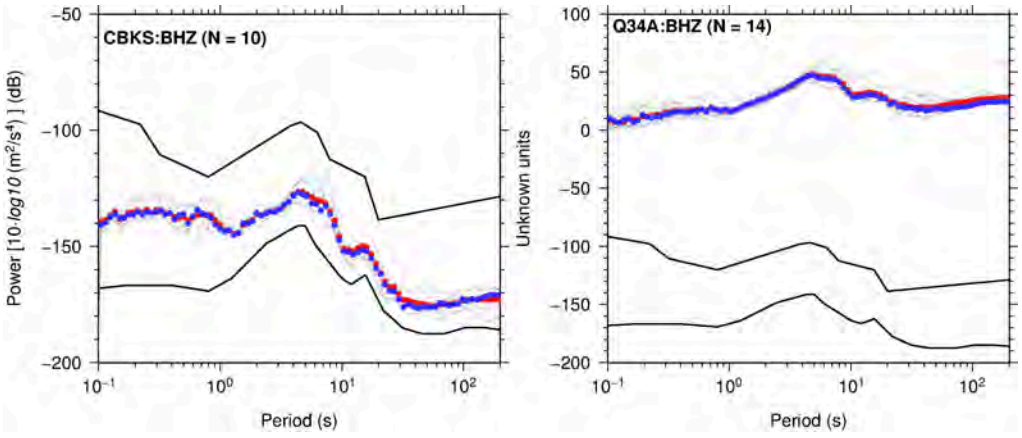


Figure 1. Example PSD functions for the reference station (left; CBKS) and the candidate station (right; Q34A). The PSDs are estimated from 1-hour nighttime noise records and then averaged. The median curve is show in blue and the mean is shown in red. The USGS high/low noise curves are also shown (black; Berger and Ekstrom).

NOISETRAN computes the transfer function as the log difference between the two PSD functions (Figure 2). Once computed, the transfer function (or pseudo-amplitude response) can be used to convert the candidate data into real, absolute units. Since the pseudo-response is calibrated to the reference station, the units will be the same as the reference station. In our test case, the candidate data are actually in raw counts, thus the pseudo-amplitude response should be very similar to the true instrument response. The comparison between the computed pseudo-response and true response is shown in Figure 2 for both velocity and acceleration. In this example, the pseudo-response and true response are in good agreement over the period band of 200–0.1 sec.

Pseudo-Response to Pole-Zero System

While the pseudo-amplitude response can be used in its raw form to convert data to known units or for response file evaluation, we have added functionality to NOISETRAN to invert the pseudo-response for a pole-zero system. A pole-zero representation has several improvements over the raw frequency-amplitude format of NOISETRAN. For example, pole-zero representations are easy to input into programs such as SAC. This permits a convenient means to correct waveform data directly from the output of NOISETRAN. Pole-zero fitting also removes the oscillations and jaggedness of the raw pseudo-response, making them similar to true instrument responses. Adjustments to the pseudo-response, post-NOISETRAN processing, is also more straightforward with a pole-zero system. Gain adjustments can be easily undertaken by modifying a single constant, or the passband or frequency roll off can be adjusted by adding or modifying a pole or zero.

The current implementation of the pole-zero inversion is relatively simplistic by solving for three characteristics of the pseudo-response. These characteristics are the low-frequency corner, the amplitude gains factor, and a damping factor at the low frequency end. An example of the fitting procedure is shown in Figure 2 for our test case example. Future refinements to the inversion will include a semi-arbitrary number of pole-zeros and include a non-zero phase component. The current implementation solves for only 2-poles and 2-zeros, and it assumes a zero-phase component. As the phase-response recovery methodology of NOISETRAN improves, the pseudo-phase response will also be included in the inversion.

In Figure 2, the pole-zero system from the pseudo-response inversion shows remarkable similarity to the true amplitude response. Between the frequency bands of 0.01-0.1 Hz, the RMS misfit is < 0.1 log units. Most of the misfit occurs because of a mismatch between the true low frequency corner and the corner obtained from the fitting routine. This is a common occurrence, and we are researching methods to better estimate the long period portions of the pseudo-response.

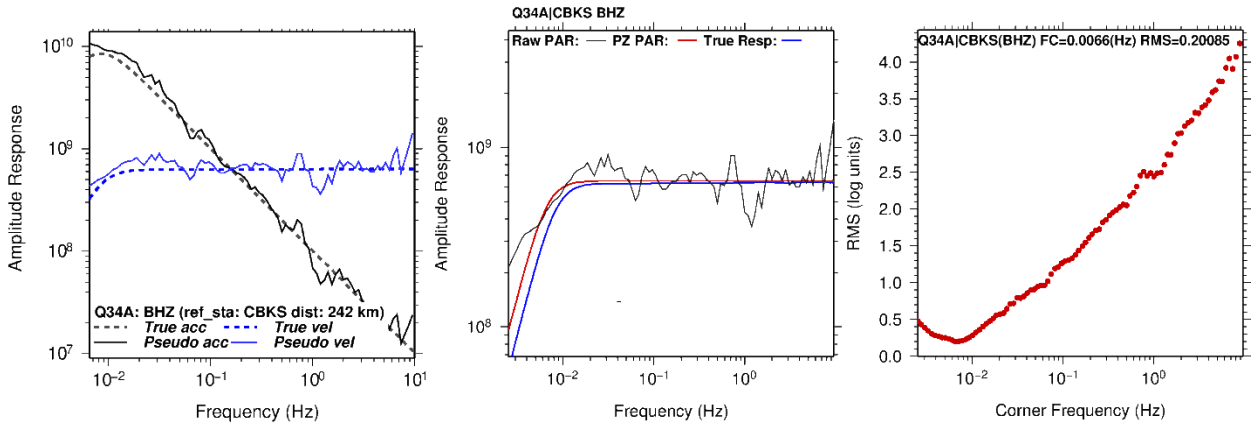


Figure 2. NOISETRAN results for candidate station Q34A. Left: a comparison of the true velocity (blue-dashed) and acceleration (black-dashed) response to the pseudo-response (solid). Middle: a comparison of the raw velocity pseudo-response (black) to the true response (blue) and the response determined from the pole-zero fitting routine (red). Right: The Root Mean Square residual (RMS) from the pole-zero fitting for various corner frequency parameters.

Noise Cross Correlation for Pseudo-Phase Response Estimation

Estimating the phase response is more difficult than estimating the amplitude response. The phase of a recorded signal is a function of source, path, site and instrument effects. One method that shows promise involves analyzing noise cross-correlation between the reference and candidate station. This approach attempts to take advantage of the fact that noise correlations between two stations can reveal the Green's function for the path between the two locations (Campillo and Paul, 2003). Thus, the two-station cross-correlation function is a representation of a source propagating from one station to the other station and vice verse along the same path. The assumption is that the source and path terms can be removed, leaving only the instrument and site effects. For simplicity we are currently ignoring possible site effects from the phase-response estimation.

It is our intent to isolate the instrument phase effects from the source and path effects by comparing two sets of noise correlations. In this analysis, the correlation processing follows the typical practice of Green's function retrieval where a common time window is selected for the reference and candidate station, the amplitudes are normalized by spectral whitening prior to correlation, and the correlations are averaged over a particular time window until the Green's function emerges (Frank et al., 2009). By normalizing the amplitudes, the correlations should be sensitive to the phase of the time series and not amplitude.

To recover the phase response, the first set of correlations are computed between a phase-corrected reference station (i.e., the instrument response is removed) and the candidate station (unknown phase). The second set is computed as the cross correlation between the phase-uncorrected reference station (i.e., the instrument response is not removed) and the candidate station (unknown phase). By comparing the phase difference between these two correlation functions we attempt to estimate the instrument phase response of the candidate station. Since the path and source are the same for the two correlations, it is assumed that the main difference between them is instrument effect (we are ignoring any site effects).

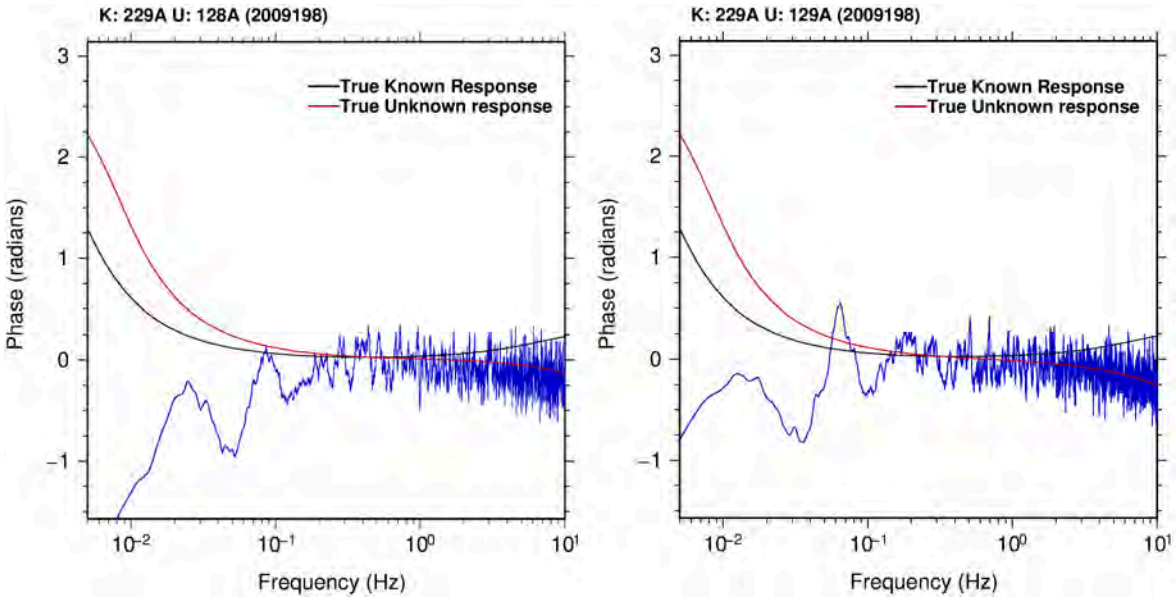


Figure 3. Phase response recovery (blue line) from day long correlation functions. Left: the reference station is 229A, which is instrumented with a Nanometrics Trillium sensor, and the candidate station is 128A, which has a Guralp CMG3-T. Right: the reference station is 229A, and the candidate station is 129A, which has a Streckeisen STS-2. The true phase response of the reference station is shown in black and the true phase response of the candidate station is shown in red.

An example of our progress in phase recovery is shown in Figure 3. Here, we illustrate the results for two closely located reference-candidate station pairs. While the method is still under active development, Figure 3 demonstrates that it appears possible to recover the candidate station phase component for a portion of the frequency band of

interest. In the two cases shown, there is agreement between the recovered phase component and the true phase response between 0.2 – 10 Hz. At frequencies < 0.1 Hz, the recovered response diverges greatly from the true response. This is curious since the amplitude response recovery typically improves at frequencies < 1Hz and is typically degraded at higher frequencies.

The development of the phase recovery has been mostly undertaken with data recorded by USArray broadband seismometers. These sensors (e.g., Trillium, Guralp, and Streckeisen) have very similar phase responses, and the responses between periods of 60 and 0.1 seconds are essentially zero (Figure 4). To further develop and validate this method, more research needs to be undertaken using a better mix of instruments, such as examining the effects of correlating short period to broad bands, as well as accelerometers.

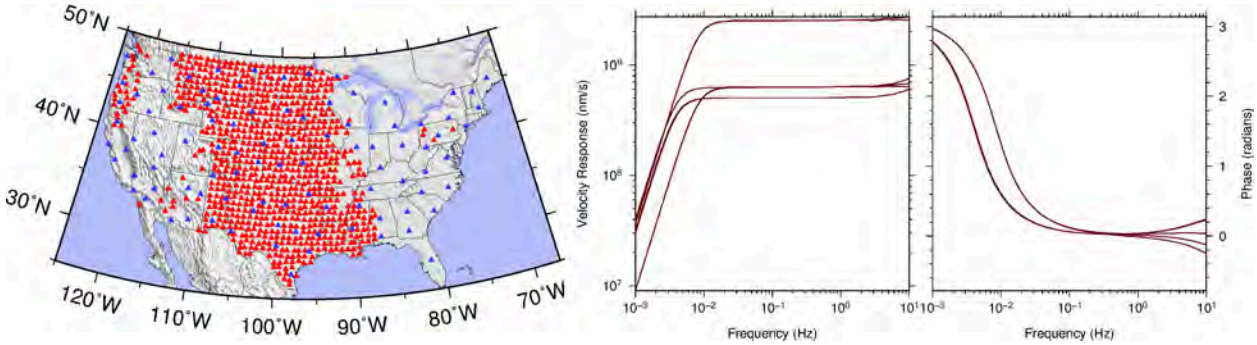


Figure 4. Deployment map of USArray stations operating during 2009-2011. Left: USArray Backbone (blue) and Transportable Array (red) stations used in the evaluation NOISETRAN. Right: amplitude and phase response for the different USArray broad band seismic stations.

Evaluating NOISETRAN with US Array Data

We have extensively tested NOISETRAN on a variety of datasets to improve, validate and understand the limiations of our methodology, particularly regarding amplitude response recovery (Franks et al., 2011). One series of tests focuses on data recorded by the USArray. The massive quantity and spatial extent of USArray data permits the examination of geospatial and distance relations between the reference and candidate stations.

The USArray test includes 107 reference stations from the Backbone network, and 849 candidate stations from the Transportable Array, deployed during 2009 through 2011. Since the amplitude recovery methodology only requires background noise levels, time synchronous records between the reference and candidate station are not required. During 2009-2011, USArray was deployed across the the central US, including the eastern Rockies, the Great Plains, the Central Lowlands and the Gulf Coast (Figure 4). Over 12,500 reference-candidate station pairs are evaulated in this test.

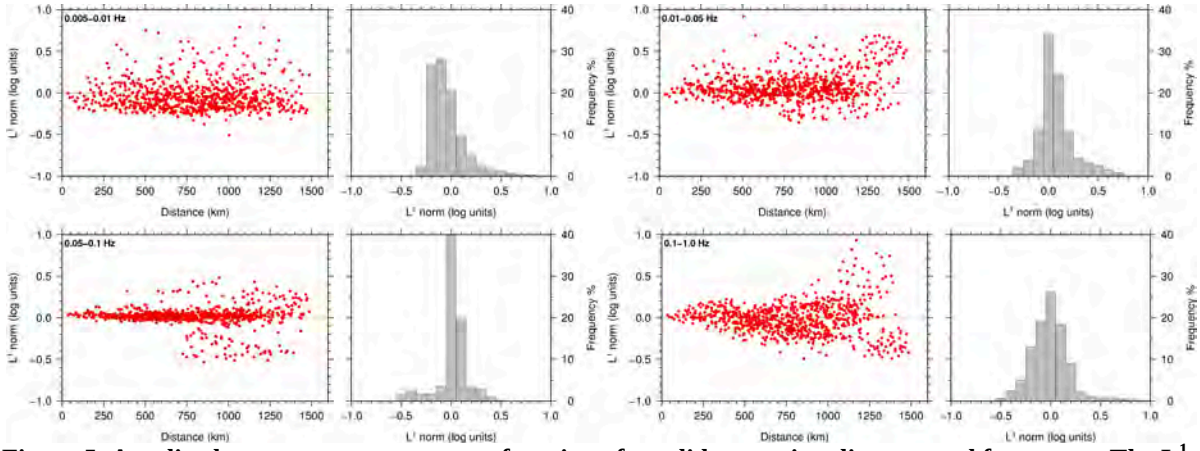


Figure 5. Amplitude response recovery as a function of candidate station distance and frequency. The L^1 norm between the pseudo-response and true response is shown as red dots. The frequency band over which the L^1 norm is computed is labeled. Histograms of the L^1 distribution are also shown.

Power spectral densities are estimated using 1-hour nighttime noise records for 1 day of each month that the stations are in operation. Time periods of large earthquakes are avoided. This produces 10-25 PSD functions for each station. The median PSD of each station is then computed for input into NOISETRAN. Nighttime records are chosen to minimize effects from cultural noise sources near cities, and by sampling noise from each month of station operation, seasonal variations in the noisefield should have less of an impact. The median tends to provide a better estimate over the mean when a limited number of short PSD functions are used, especially in cases where spurious local noise events can elevate a particular PSD function, which can bias the mean.

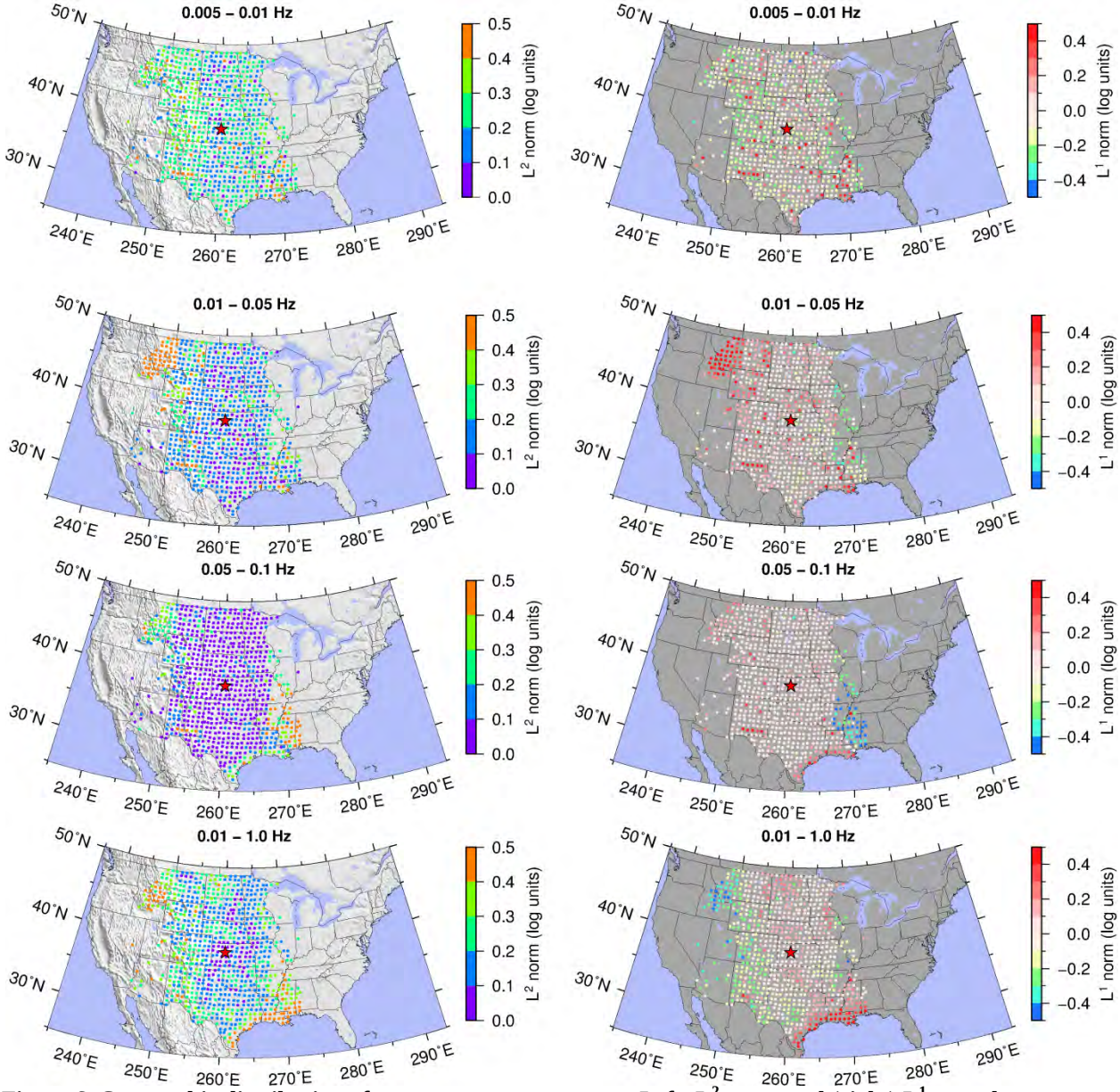


Figure 6. Geographic distribution of response recovery errors. Left: L^2 norm and (right) L^1 norm between pseudo-amplitude responses and the true instrument responses. The location of reference station CBKS is shown (star).

Figure 5 shows amplitude response recovery as a function of distance and frequency for a single reference station. In this case the reference station is CBKS located in western Kansas. The great circle distance from CBKS to the candidate stations ranges between 50–1500 km. For illustration, the results have been divided into four frequency

bands: 0.005–0.01, 0.01–0.05, 0.05–0.1, and 0.1–1.0 Hz. For each of these frequency bands the L^1 norm is computed between the true response and the pseudo-response in log units.

One main conclusion that can be drawn from the USArray test is that amplitude response recovery is frequency dependent. At long periods (0.005–0.01 Hz), the difference between the true-response and the pseudo-response is generally below 0.5 log units and shows a negative bias. The negative bias implies that NOISETRAN over-estimates the amplitude response in this band, at least when using CBKS as the reference station. In the 0.01–0.05 Hz band, a distance dependence begins to emerge. Stations > 750 km from the reference station tend to have larger scatter in the response recovery. At closer distances the average difference between the true and pseudo-response is < 0.3 log units and has a positive bias. In the 0.05–0.1 Hz band, response recovery is generally the best, and in the cases shown, the response difference is generally < 0.1 log units for candidate stations within 750 km of the reference station. At 0.1–1Hz, the response recovery is still acceptable for stations within 750 km of the reference station, but large scatter is observed for stations at a distance > 750 km. Overall, then mean response error for frequencies between 0.01–1 Hz is <±0.25 log units for stations < 750 km from the reference station.

The results shown in Figure 5 are geographically displayed in Figure 6. In this manner geospatial variations in amplitude response recovery become apparent. At long periods (0.005–0.01 Hz), stations along the Rockies exhibit a larger response error than stations to the east. In most of the Great Plains the response error is < 0.25 log units, although it increases to 0.35 log units eastward to the Central Lowlands. At 0.01–0.05 Hz, a large group of stations in the northern Rockies exhibits a positive error (0.5 log units), which decreases to 0.3 log units in the 0.05–0.1 Hz band. From the Colorado Plateau to the Central lowlands most stations exhibit a response error of < 0.3 log units in this band. Also in the 0.05–0.1 Hz band, stations along the Gulf Coast show a negative bias of 0.3 log units. Stations in the Central Lowlands also exhibit a negative bias but of larger magnitude, 0.4 log units. Elsewhere, most stations show a response error of < 0.1 log units. In the 0.1–1.0 Hz band, response errors increase to the west and to the east of the central Great Plains. In summary, a negative response error occurs in stations in the Rockies, and a positive error is exhibited by stations from the Gulf Coast through the Central Lowlands.

Stations that exhibit the largest errors are in the Northern Rockies and along the Gulf Coast. These stations are generally > 750 km from the reference station. However, it is likely that differences in the crustal structure between the candidate and reference stations also contribute to the observed response error. Along the Gulf Coast, proximity to the coast likely has influence on the response recovery error, especially for frequencies near the microseismic band.

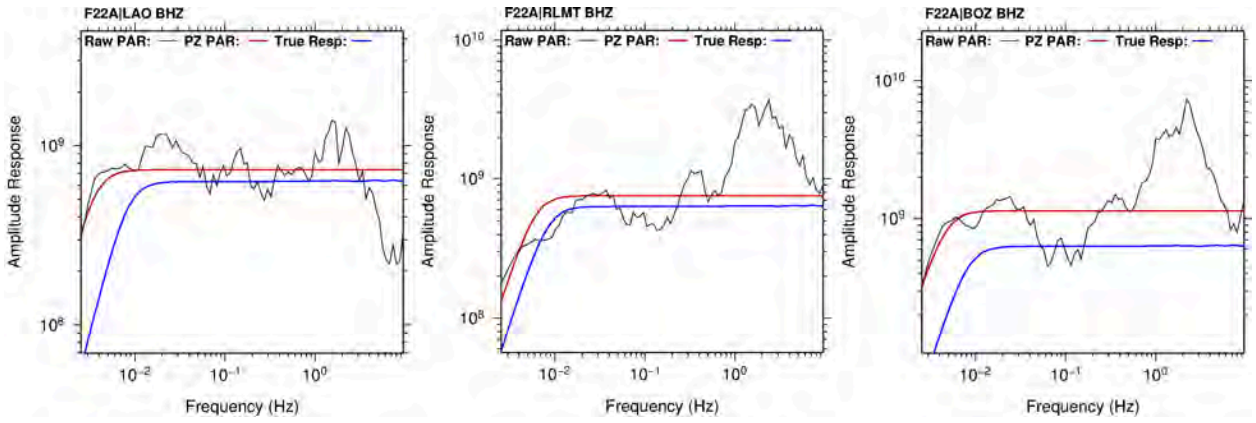


Figure 7. Pole-Zero fit (red line) of the pseudo-amplitude response from NOISETRAN (black line) compared to the true response (blue line). In all 3 panels the candidate station is F22A. Left: reference station LAO is located 101 km from F22A. Middle: reference station RLMT is located 245 km from F22A, and (right) reference stations BOZ is located 417 km from F22A.

The response recovery errors reported in Figures 5 and 6 were computed using the raw pseudo-responses. However, the pseudo-responses were also inverted for pole-zero systems. Examples are shown in Figure 7 for three different reference-candidate station pairs. The station separation distances are 101, 245, and 417 km.

The pole-zero inversion considers frequencies between 0.005-10 Hz. We extend to low frequencies to make sure to capture the low frequency corner of the pseudo-response. In the three examples shown in Figure 7, the

low-frequency corner determined from the inversion misses the true response corner. This is a systematic feature of NOISETRAN where the low frequency corner is almost always over estimated. We are actively investigating this in order to improve NOISETRAN functionality. It appears to be partially a feature of the PSD estimation.

The gain factor determined from the inversion is typically very similar to the true gain. In Figure 7, station pairs F22A-LAO and F22A-RLMT have a gain factor within 0.1 log units of the true gain over the 0.01-10 Hz band. Station pair F22A-BOZ, which has a larger reference-candidate station separation, has gain factor mismatch of 0.4 log units. However, in this case, the gain factor might be improved by discarding frequencies above 1 Hz, where the pseudo-response exhibits large amplitude deviations from the mean.

CONCLUSIONS AND RECOMMENDATIONS

Using the methodology of NOISETRAN it is possible to convert seismic data from unknown units to known units using background noise levels from a nearby reference station. This is accomplished by estimating a transfer function between the reference station, where the response is well known, and a candidate station, where the response is desired. The quality of the transfer function can be improved by averaging the power spectral densities over several hours of data and by using nighttime noise records to minimize cultural noise contamination. The output transfer function is essentially a pseudo-response that converts the candidate station data to the units of the reference station. The pseudo-response can be further refined by inverting it to a pole-zero system. Pole-zero systems are easily input into programs such as SAC and can be used in response file evaluations.
In general the quality of the pseudo-response is influenced by several factors. These factors include the differences in the noise field between the reference and candidate station, the distance between the stations, and physiographic differences between the stations. Response recovery is generally best at periods > 1 sec. At periods < 1 sec, local noise differences can negatively impact the quality of the response recovery. However, in many cases, adequate response recovery is achievable to periods as short as 0.1 sec. Response recovery is also generally best for reference-candidate stations within 250 km of each other. However, tests using USArray data demonstrate that stations separated by 750 km can also yield highly satisfactory results. The USArray tests also revealed that physiographic differences are important. Using a reference station in the Great Plains, candidate stations in the Northern Rockies and the Gulf Coast exhibited higher than average errors in the NOISETRAN response recovery. In the case of the Gulf Coast, differences in crustal structure, as well as proximity to the cost, are likely contributing factors.

Phase response information appears retrievable by deconstructing noise cross correlations between the reference and candidate station. This method takes advantage of Green's function emergence from the two-station noise correlation. It assumes that the instrument phase effects can be isolated from source and path effects by considering cross correlations computed between the candidate and the reference stations, where 1) the reference station instrument response is removed, and 2) the reference station response is not removed.

Future research is focused on improving and validating the phase-response recovery methodology and refining the pole-zero inversion scheme. In the finally phase, the response recovery tools will be packaged in a JAVA-based graphical interface to be shared with the seismological community.

ACKNOWLEDGEMENTS

We thank Jill Franks and Michelle Johnson for their contribution to the data processing and analysis of this project.

REFERENCES

Berger, J. P. Davis, and G Ekstrom (2005). Ambient Earth noise: a survey of the global seismograph network, *J. Geophys. Res.* **109**, B11307.

Campillo, M. and A. Paul (2003). Long-range correlations of diffuse seismic coda, *Science* **299**, 547–550.

Frank, S.D., A. E. Foster, A. N. Ferris, and M. Johnson (2009). Frequency-dependent asymmetry of seismic cross-correlation functions associated with noise directionality, *Bull. Seismol. Soc. Am.* **99,** 462–470.

Franks, J. M., M. Johnson, R. B. Herrmann, J. L. Bonner, and A. Ferris (2011). A software toolbox for systematic evaluation of seismometer-digitizer system responses, in *Proceeding of the 2009 Monitoring Research Review: Ground-Based Nuclear Explosion Monitoring Technologies*, LA-UR-11-04823, Vol. 2, pp. 822–831.

McNamara, D. E. and R. P. Buland (2004). Ambient noise levels in the continental United States, *Bull. Seismol. Soc. Am.* **94,** 1517–1527.

ADAPTING PIPELINE ARCHITECTURES TO TRACK DEVELOPING AFTERSHOCK SEQUENCES AND RECURRENT EXPLOSIONS

Tormod Kværna[1], Steven J. Gibbons[1], David B. Harris[2], and Douglas A. Dodge[3]

NORSAR[1], Deschutes Signal Processing, LLC[2], and Lawrence Livermore National Laboratory[3]

Sponsored by the Air Force Research Laboratory and the National Nuclear Security Administration

Award Nos. FA9453-11-C-0230[1,2] and DE-AC52-07NA27344 [3]
Proposal No. BAA11-26

ABSTRACT

Pattern detectors (e.g., correlation, subspace, and matched field detectors) fuse the signal detection and source identification processes into a single operation. The organization of repeating waveforms for efficient analyst interpretation may result in significant gains in productivity when analyzing extensive aftershock sequences and explosions from repeating sources. Under current practice, pattern detectors run entirely independently of the pipeline signal detectors and the preparation and supervision of pattern detectors is relatively labor-intensive. It is the aim of this two-year study to investigate algorithms for adapting processing pipelines to create and supervise pattern detectors semi-automatically for incoming multi-channel data streams. A functional model of an operational detection pipeline is being constructed with extensions that create and manage pattern detectors under a variety of spawning policies. The system is being tested on two aftershock sequences: that for the 8 October 2005, M=7.6, Kashmir earthquake and that for the 23 October 2011, M=7.1, Eastern Turkey event. Both cases are representative of challenging aftershock sequences given the vast numbers of events and relatively large source regions.

Pattern detectors that are coherent over multiple arrays and 3-component stations can constitute exquisitely sensitive detectors that increase the detection capability greatly for events in the immediate geographical vicinity of the master events. An alternative strategy would be to operate pattern detectors coherently over single arrays or other limited subsets of sensors, and combine the results incoherently across the complete network. This alternative strategy may allow a greater geographical region to be covered by given templates. The merits and limitations of the two strategies are being investigated for a range of different case studies. For correlation detectors on single arrays the validity of detections can be assessed by performing f-k analysis on single-channel detection statistic traces, eliminating enormous numbers of false alarms and allowing a significant reduction in the detection threshold.

Policies for triggering and spawning of correlation detectors are being studied extensively. The simplest trigger is using an STA/LTA detector on an array beam steered towards the slowness of anticipated first P-wave arrival from the source region considered, with the classification of the detected phase being confirmed using classical f-k analysis. This strategy is reinforced significantly when considering multiple observing stations. Considering only detections which are confirmed on multiple stations, with limits on the time-delays determined by the dimensions of the source region, will lead to fewer detectors generated by false triggers.

The most promising triggering algorithm considered so far is the single phase empirical matched field detector (EMFD). This narrow frequency band approach mitigates the effects of, and indeed exploits, the scattering which frequently confounds classical array processing. Correlation detectors using a waveform template from the main event are frequently very unsuccessful at detecting large number of aftershocks, since large spectral differences between the main shock and aftershocks may lead to significantly different waveforms. The empirical matched field processing recognizes the characteristic spatial structure of the incoming wavefronts over the array aperture in each of many narrow frequency bands and this appears to be a more stable characteristic of a given source region than the temporal structure of the waveforms on each sensor. For both the Turkey and Kashmir sequences, the EMFD readily detects many very low signal-to-noise ratio (SNR) signals which are all confirmed by stations in the vicinity of the source region to correspond to real events in the sequences.

OBJECTIVES

This two-year study will investigate the adaptation of processing pipelines to create pattern detectors (i.e., correlation, subspace and matched field detectors) that discover and organize repeating waveforms in data streams from a network of seismic arrays. The monitoring applications of this technology will include real-time responses to major developing aftershock sequences to ameliorate analyst overload, and autonomous discovery of repetitive explosions.

A functioning model of the detection stage of a pipeline implementing conventional beam recipes will be constructed, but extended to create and manage pattern detectors under a variety of spawning policies. This system will be used to test a number of strategies for discovering repeating waveform patterns and organizing detected occurrences for efficient interpretation by analysts. The system will be tested using the four regional Kazakhstan arrays as a network observing the 2005 Kashmir earthquake aftershock sequence. For additional system testing, we also plan to analyze signals from the October 2011 Van sequence in Turkey recorded at the Kazakhstan arrays. For this sequence a bulletin of quite accurate event locations and magnitudes, provided by the local Turkish network, form a good reference for evaluating the pipeline performance.
It will be investigated as to whether pattern detector waveform templates should be limited to individual arrays or extended to coherent operation across the network, and whether templates can be improved as observations accumulate. An autonomous supervisory function will be introduced that keeps track of detector performance, and culls, updates or merges detectors to improve overall system performance. This includes periodic reprocessing of the data stream with the suite of maturing pattern detectors, to be conducted as a parallel operation so as not to slow the main detection process.

Alternative pattern detector spawning policies will be examined, one with new detectors created only from special analyst-designated primary detectors and another with spawning from all of the conventional STA/LTA or F detectors implemented on recipe beams. System performance will be graded, with the ultimate metric being a measure of the consolidation of detections into efficiently-interpreted families. This includes checks to ensure that this autonomous system does not screen events of interest from analyst evaluation, by superimposing waveforms from other events among the Kashmir aftershocks.

RESEARCH ACCOMPLISHED

The Framework

The detection framework that we are building (Figure 1) models the detection front end of many pipelines that process array data, using an object-oriented architecture to allow different types of detectors to be added to the system dynamically and with any number of instances. The heart of the system is a list of detectors that can hold traditional beamformers with STA/LTA detectors and also several types of pattern-matching processors: correlation, subspace and matched-field detectors. The idea behind the system is to allow traditional power detectors (and one type of targeted pattern detector) to spawn new pattern detectors for specific aftershock families as they are detected and add them to the pipeline in real time. These pattern detectors are intended to sweep up some fraction of the aftershocks into groups for efficient interpretation later in the pipeline.

The system supports or will support other innovations, such as the ability to construct pattern detectors that span more than one array in the network and a capability to reprocess older data in a developing aftershock sequence with detectors created late in the sequence. Coherent pattern detectors with a larger network footprint may obviate some association problems that lead to incorrect event formation in automatic associators. They also should build event clusters that may be assumed to be families with a very high degree of confidence, which may lead to strategies for efficient use of analyst resources. The reprocessing capability (complete as of this writing) allows pattern detectors formed late in an aftershock sequence to sweep up similar events early in the sequence. This function may prove useful if analysts get behind by reducing the backlog of events to be reviewed.

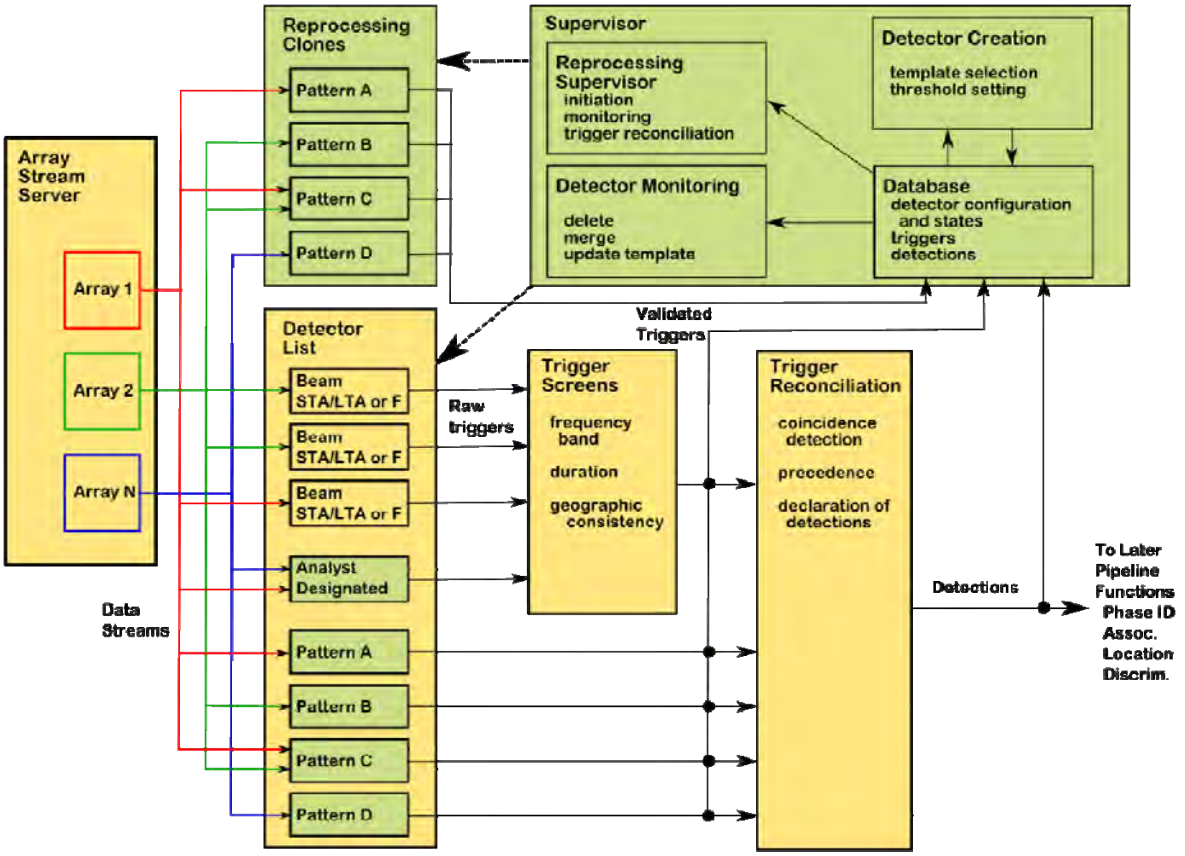


Figure 1. Block diagram of the detection processor being developed to test pattern detector creation and management strategies. The boxes in yellow indicate functions approximately shared with a conventional pipeline detection processor. Those in green represent entirely new functions. Note that some detectors may process data from more than one array, possibly coherently.

To simplify the construction of detectors that span multiple arrays, we have completed an Array Stream Server function that acquires continuous stream data from different types of sources (flat files, database or conceivably real-time streams) and, so to speak, puts it on a common footing. By that we mean it resamples data to a common sampling rate and interpolates all samples to fall on the same time instants. This function simplifies selection of data from disparate stations to be combined (possibly coherently) in a single detector.

The other innovation is a supervisory function that creates detectors and monitors their performance. It incorporates an extensive database archiving the configuration of all detectors either designated by the system operators or created autonomously by the framework, all triggers produced by the detectors and the detections that emerge from a process of reconciliation and ranking of nearly simultaneous triggers. The archive supports tests of policies for updating (and possibly retiring and combining) detectors, as well as extensive post-operation analysis of overall system behavior and the performance of individual detectors. We are contemplating an ability to track and adapt the templates of detectors with new observations as they occur.

The kind of tests that we contemplate performing with this framework might be appreciated from an example. We would like to investigate how a subspace detector might be constructed automatically with a template that spans several arrays. One question is how to choose the receiver aperture of the template, i.e., which arrays to combine. Several possible strategies emerge. In a conservative approach, we might allow the system to operate for a time on a developing aftershock sequence to see if detectors are created among the arrays that have many triggers in common (discovered by examining whether patterns emerge in the relative timing of triggers made by the detectors). The

absolute trigger times and the pattern of observed relative arrival times then could be used to extract waveforms for a correlation template. Alternatively, with a single event detected and under the assumption that we know the approximate location of the aftershock sequence, we could use a trigger time from a single station to predict arrival times at other stations for waveform extraction. We could operate the detector for a while to see whether it performed as well (had as many triggers) as a single-array correlation detector.

Because the pattern detectors we are using have efficient implementations, it may make sense to try fairly liberal spawning policies (such as the one just described), operate a fairly large number (thousands) of detectors, measure their performance and prune off the ones that don't perform well. In this view the system could come to implement a kind of natural selection for empirical detectors.

Single Phase Empirical Matched Field Processing for Spawning Detectors

A pipeline which generates pattern detectors autonomously needs sensitive but robust criteria for spawning new detectors. Harris and Dodge (2011) classified an extensive aftershock sequence effectively by using triggers on an STA/LTA trace for the beam on a single array steered optimally to detect the initial P-arrivals from events in the source region. An ideal strategy for triggering the generation of a new pattern detector would be a correlation detector which simply took a waveform template from the main event and declared a detection on each occasion that the correlation coefficient trace attained a significant value. In practice, for large earthquakes, the contrast in source dimensions, magnitude, and consequent form of the signals usually make the mainshock signals very poor waveform templates for identifying aftershocks. This is demonstrated in the lowermost trace of Figure 2 where a 15 second long template for a teleseismic P-arrival from a magnitude 7.1 earthquake essentially fails to detect any of the aftershocks convincingly in the window displayed. The situation is improved considerably by considering the zero-moveout correlation stack on the array (trace 4) and it is possible that the noise floor could be lowered further by a flattening of the amplitudes in the incoming data stream (Gibbons et al., 2012).

Harris and Kværna (2010) present an application of empirical matched field processing (EMFP) on array signals to identifying the source of mining blasts. EMFP is a narrow frequency band procedure which matches the spatial structure of the incoming wavefield over the set of sensors, rather than the temporal structure of each time-series. EMFP outperforms waveform correlation for most mining sources since the ripple-fired nature of the shots makes the wavetrains from different blasting sequences very dissimilar, whereas the narrow band representations of the waveforms are relatively insensitive to the events' source-time functions and are highly characteristic for a given source region. EMFP also outperforms classical plane wavefront array methods since it takes templates from existing records from the relevant source region, producing pattern detectors which are uniquely calibrated for each source and account for the deviations that heterogeneous Earth structure imposes upon the arriving wavefront.

Wavefronts propagating to a distant array from an aftershock sequence will propagate along a very similar path. Therefore, the characteristic phase and amplitude relations between signals on the different sensors of the array are likely to be very similar from event to event and will comprise a fairly characteristic spatial seismic fingerprint for the sequence. Correlators ideally use the full wavetrain to maximize the signal's time-bandwidth product, and this can be problematic in rapidly unfolding sequences of events when the delay between events is often shorter than the wavetrains. Harris and Kværna (2010) demonstrated that a short window surrounding the initial P-arrival was a highly effective "information carrier" meaning only a short data segment may be required for each event. This will mitigate problems due to overlapping wavetrains. A further possible advantage of EMFP over waveform correlation in relating a large main event to subsequent smaller aftershocks results from the narrowband nature of the procedure. Correlation between the signals generated by the main event and aftershocks will usually be diminished by the significant spectral differences. In EMFP, in which the template is defined by the spatial structure of the wavefield in each narrow frequency band, the spectral content of each incoming wavefront is likely to be less significant.

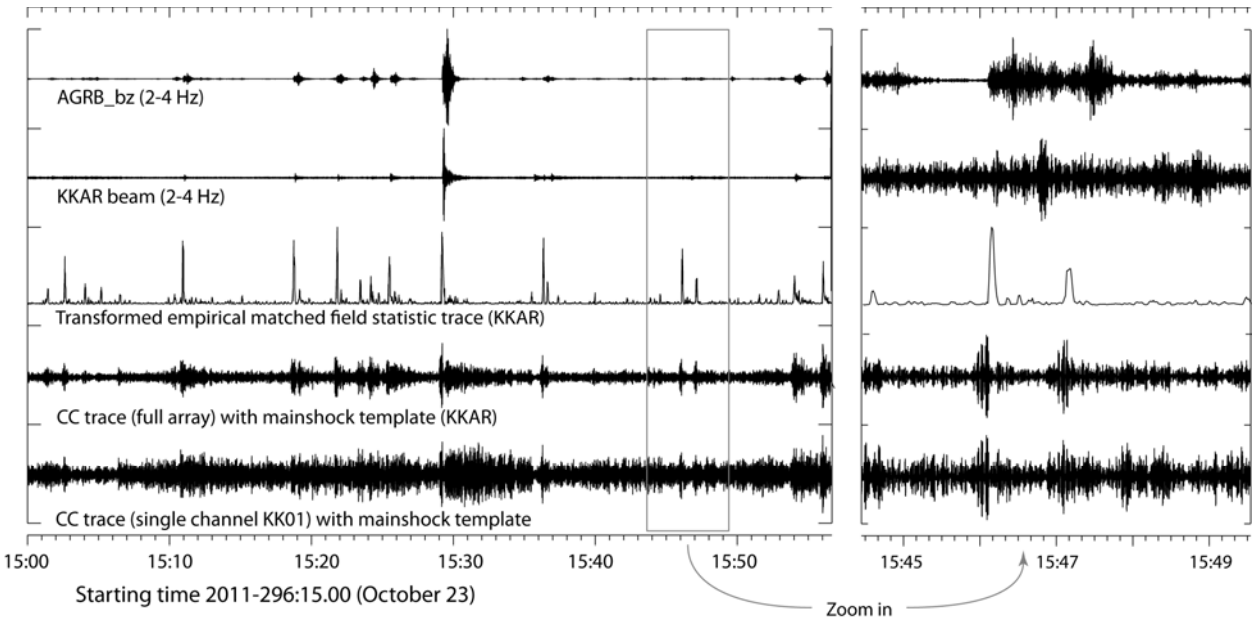


Figure 2. Comparison of empirical matched field and correlation detectors on the KKAR array where both the empirical steering vectors and waveform template are taken from the initial P-arrival at time 2011-296:10.46.04 from the October 23, M=7.1 Van earthquake, Turkey (38.733°N, 43.483°E). The covariance matrix used to calculate the empirical steering vector was calculated using a data segment with 256 samples (6.4 seconds) and 26 narrow frequency bands between 1.09 and 5.00 Hz were used. The waveform correlation calculations were performed with a 15 second waveform template filtered 1-5 Hz. Data from the AGRB station (approximately 1 degree from the mainshock) is delayed by 266 seconds to provide an optimal alignment of initial P arrivals with the P phases at KKAR.

A matched field statistic trace can be evaluated for consecutive windows of incoming data, in a given narrow frequency band, for a given template or empirical steering vector. The third trace in Figure 2 displays the mean over 26 narrow frequency bands of transformed matched field statistic traces, where the transformation (described in Gibbons et al., 2008) results in local maxima at times characterized by an increase. There are numerous clear peaks in this function which can all, on closer inspection, be associated with events visible in data from far closer stations. The zoom panel makes it clear that the matched field statistic, measuring the spatial characteristics of the wavefield over the array, provides a significant improvement in SNR over an optimal beam steered with the appropriate time-delays. Times of arrival are clearer on the matched field traces than the correlation traces and this may be particularly useful if valid event hypotheses are to be validated by observations over multiple arrays.

STA/LTA detectors on a beam return many detections that are unrelated to the source region of interest (a strong signal from a completely different direction is likely to result in an increase of energy on all beams). The same may occur for the matched field detector. Just because sensitivity is optimal for the direction of the template steering vectors, this does not mean that the response to wavefronts arriving from other directions will be negligible. Gibbons and Ringdal (2006) demonstrate how vast numbers of false alarms using correlation detectors on arrays can be eliminated fully automatically by performing f-k analysis on the correlation coefficient traces, essentially testing whether or not directions other than the one corresponding to the master event are preferred. We here demonstrate an equivalent procedure for matched field detections.

Figure 3 shows f-k analysis in two different narrow frequency bands, at 2 Hz and 4 Hz, for the Pn phases for the main October 8, 2005, Kashmir event (left) and a selected aftershock (center). The similarity between the f-k grids strengthens the claim that two earthquakes in the same sequence (in this case separated by over two units of magnitude) will result in wavefronts with similar phase and amplitude relations between sensors in the various narrow bands. As anticipated, the relative beam power at 4 Hz is less than that at 2 Hz with greater sidelobes

resulting from aliasing and incoherence. The differences between the 2 Hz and the 4 Hz slowness grids provide some of the motivation for using EMFP as opposed to the simple plane-wave model.
If a detection is made using a given empirical steering vector, for example from a “mainshock”, then we can scan slowness space in the same way that we do in classical f-k analysis, only that the phase shifts for the theoretical plane-waves are superimposed onto the phase shifts specified by the empirical steering vector.
In the right panels of Figure 3, we map out the f-k spectrum at the time of the Pn arrival at KKAR from the aftershock, relative to the empirical steering vector obtained from the Pn arrival from the mainshock. At both 2 Hz and 4 Hz, the maximum relative beam power is obtained close to the zero slowness vector, indicating that the detected phase is very likely to be from the same direction as the master event phase.

These results suggest that a single-phase empirical matched field primary detector designed from the main or early events of an on-going earthquake sequence would provide a robust and sensitive tool for spawning new pattern detectors. When used in combination with the described screening procedure, this primary detector can operate with a low false-alarm at a low detection threshold.

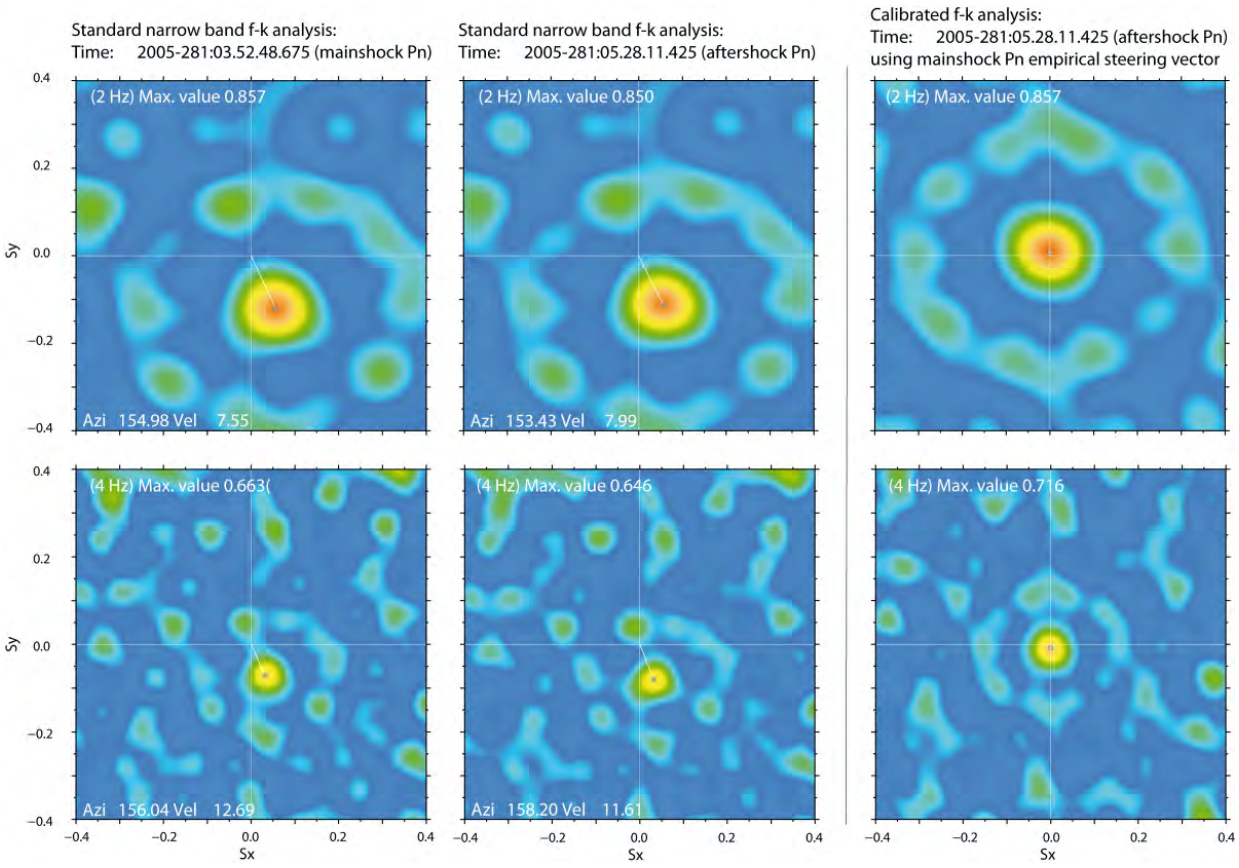


Figure 3. Narrow band f-k analysis performed at the times indicated at 2.0 Hz and 4.0 Hz. The procedure employs the multitaper subroutines of Prieto et al. (2009). In the panels on the right, the phase shifts in the empirical steering vector are imposed and the zero slowness vector indicates that the wavefront observed comes from the same direction as the master signal.

.

The framework operating on aftershocks of the 2005 Kashmir earthquake

Our eventual goal is to enable the framework automatically to create detectors that operate on individual arrays or combinations of arrays. While an algorithm for creating (spawning) individual-array detectors is in place, we are

experimenting with procedures for spawning detectors that operate across a network of arrays. Subspace detectors with a wider geographic footprint (on the receiver end) will have advantages in defining groups of events that are reliably related (families) and may obviate association problems among multiple stations. We are emulating manually parts of the eventual automatic process with tests on a ten-day period (2005:281-290) with data from the Kazakh arrays.

In our initial test, the spawning detectors were power detectors (STA/LTA) operating on beams directed at the backazimuths and slownesses of the initial P phase of the Kashmir mainshock (determined by FK analysis) for stations KKAR and ABKAR. KKAR is 10.5 degrees from the mainshock and ABKAR is 19.4 degrees distant. After some experimentation, we found that a two-pass process works well to define initial groups of correlated events. For example, we performed an initial run of the framework in which the spawned correlators were given a detection threshold of 0.6 (KKAR) and 0.4 (ABKAR) and template lengths of 160 and 310 seconds respectively. Following the initial pass all detectors with fewer than 4 detections (at KKAR) and 2 detections (at ABKAR) were removed from the system, and the framework was run again (with no spawning) with the surviving correlation detectors operating at lower thresholds (0.1).

Table 1 summarizes the number of detections made in the second pass. Statistics are shown only for the detectors that made 4 or more detections on the second pass. We emphasize that the two arrays were treated independently until this point.

Table 1. Numbers of detections made by automatically-created correlation detectors on a second pass.

KKAR Detectors		ABKAR Detectors	
DETECTORID	Detection Count	DETECTORID	Detection Count
52037	631	54422	467
52204	67	54470	14
52150	61	54902	5
52583	44	54442	5
52130	26	54610	5
52181	26	54823	4
52085	21	54512	4
52182	19	54558	4
52090	16		
52349	14		
52264	14		
52424	13		
52101	11		
52128	11		
52135	7		
52199	7		
52139	6		
52369	5		
52681	4		

Figure 4 displays seismograms from the most prolific detectors (52037 at KKAR and 54422 at ABKAR). Although most detail is not visible at the scale of these plots, nonetheless, the arrivals of P and S waves are clear with S-P times of about 110 seconds at KKAR and 210 seconds at ABKAR.

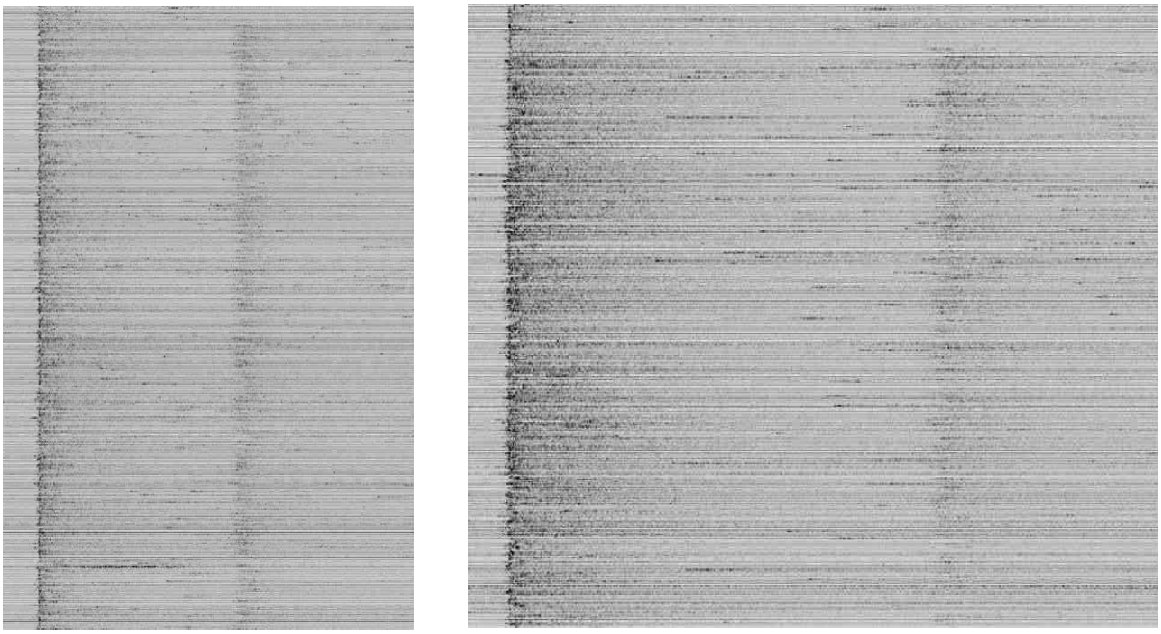


Figure 4. Aftershocks of the 2005 Kashmir event recorded at KKAR (left) and ABKAR (right). The plot at left displays 631 events found by automatically-created detector number 52037 (220 second window of data) and the plot at right displays 467 events found by detector 54422 in a window 320 seconds long.

Our next step was to determine which detectors found events in common. For this purpose, we searched for events with common offsets in trigger times between the arrays, based upon observed P travel times (143 seconds for KKAR and 260 seconds for ABKAR; 117 second offset) on a sample of 10 detected aftershocks. Table 2 shows the result for all pairs of detectors that had more than 4 detections in common (in fact, perhaps twice as many detector pairs had at least one detection in common).

To create a trial joint detector, we used the 172 common detections between KKAR detector 52037 and ABKAR detector 54422. The template was 380 seconds long and included the 9 KKAR SHZ channels and the 9 ABKAR SHZ channels. A subspace detector was built with an energy capture threshold of 0.9, resulting in a very high rank (128) detector. Electing caution in our first attempt, we reprocessed that combined data stream of the two arrays for the ten days 2005:281 – 290 with a conservative detection threshold of 0.2. The detector collected 507 detections, compared with 631 for detector 52037 operating at KKAR alone, with few or no false triggers.

Table 2. Numbers of detections found in common between pairs of independently-created detectors at stations KKAR and ABKAR.

KKAR Detector ID	ABKAR Detector ID	Common detections
52037	54422	172
52204	54422	22
52150	54422	14
52182	54422	11
52090	54422	10
52583	54422	9
52181	54422	8
52085	54422	6
52424	54422	5
52037	54610	5
52349	54422	4
52101	54422	4
52128	54422	4
52369	54422	4

Figure 5 displays plots of the extracted detections first at KK01 and then at ABK01.

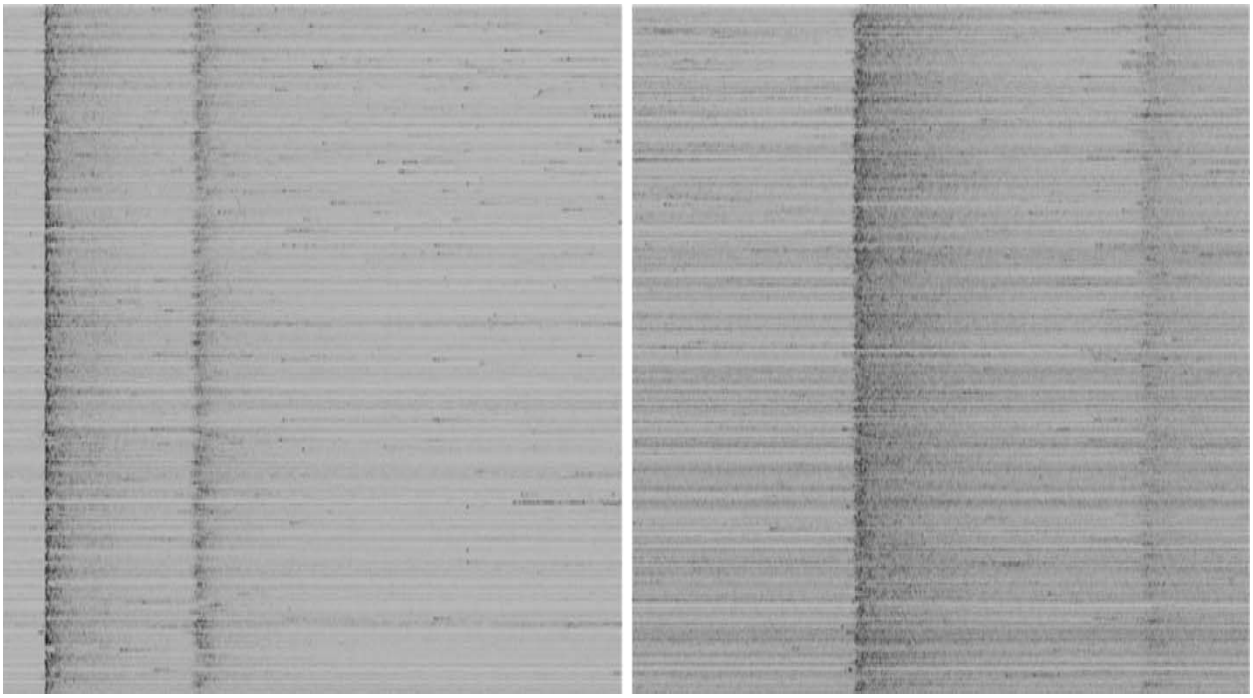


Figure 5. Plots of 507 events at station KK01 (left) and ABK01 (right) detected by the joint subspace detector of rank 128.

CONCLUSIONS AND RECOMMENDATIONS

Correlation and subspace detectors are the principal methods for event detection and grouping. However, correlators using templates from extremely large earthquakes are often ineffective at spawning new pattern detectors for classifying large numbers of far smaller aftershocks. This is due to waveform dissimilarity resulting from the disparity of event magnitudes and source dimensions. While STA/LTA detectors on array beams steered towards the source region of interest, followed by f-k analysis for verification of direction and slowness, constitute an intuitive triggering algorithm for detector spawning, we argue that single-phase EMFP is both a sensitive and robust method for triggering new pattern detectors. EMFP operates on short data segments, which mitigates the problems associated with overlapping signals from consecutive events in a sequence. EMFP is a narrowband procedure, measuring the spatial structure of an incoming wavefront over an array of sensors, and may be less susceptible to differences in the spectral content between the signals from different events. We have demonstrated clear detections of confirmed aftershocks using EMFP for which the signal-to-noise ratio on the beam itself is so low that detection using an STA/LTA detector would not be feasible. It is also noted that false alarms from the EMFP detector are readily screened out by scanning the slowness space relative to the imposed template empirical steering vector.

Our initial trial of a detector operating across two arrays (KKAR and ABKAR) produced a very high-dimension (128) subspace detector that swept up a large number (507) of aftershocks from the 2005 Kashmir sequence. Because the dimension of the detector was so large, we elected to use the detector with a relatively high correlation power threshold (0.2, comparable to 0.45 linear correlation). Probably because the template was so large (TB > 10,000) and encoded very precise and large time delays across the combined aperture of the two arrays, few or no false alarms were detected. This fact suggests that the threshold could be reduced substantially to allow an even larger collection of aftershocks to be swept up in a correlated group. We plan to experiment with lower thresholds and to build joint detectors from additional pairs independently-defined single-station event clusters. We intend to automate the process (manual to this point) of forming joint detectors, experimenting with several different policies for initiating joint detectors.

ACKNOWLEDGEMENTS

We are grateful to the Kazakhstan National Data Center for permission to use the data from the KKAR array. Data from the AGRB station in Turkey was obtained through ORFEUS and is courtesy of the Kandilli Observatory Digital Broadband Seismic Network.

REFERENCES

Gibbons, S. J. and Ringdal, F. (2006). The detection of low magnitude seismic events using array-based waveform correlation, *Geophys. J. Int.* **165**, 149–165.

Gibbons, S. J., Ringdal, F., and Kværna, T. (2008). Detection and characterization of seismic phases using continuous spectral estimation on incoherent and partially coherent arrays, *Geophys. J. Int.* **172**, 405–421.

Gibbons, S. J., Ringdal, F., and Kværna, T. (2012). Ratio-to-moving-average seismograms: a strategy for improving correlation detector performance, *Geophys. J. Int.* **190**, 511–521.

Harris, D. B. and D. Dodge (2011). An autonomous system for grouping events in a developing aftershock sequence. *Bull. Seismol. Soc. Am.* **101**, 763–774.

Harris, D. B. and T. Kvaerna (2010). Superresolution with seismic arrays using empirical matched field processing. *Geophys. J. Int.* **182**, 1455–1477.

Prieto, G. A., Parker, R. L., and Vernon, F. L. (2009). A Fortran 90 library for multitaper spectrum analysis. *Computers and Geosciences* **35**, 1701–1710.

NEXT GENERATION ANALYSIS SOFTWARE AND TEST EQUIPMENT FOR COMPONENT EVALUATION

B. John Merchant and Darren M. Hart

Sandia National Laboratories

Sponsored by the National Nuclear Security Administration

Award No. DE-AC04-94AL85000/SL12-Sensors-NDD02

ABSTRACT

The Component Evaluation project at Sandia National Laboratories supports the Ground-based Nuclear Explosion Monitoring Research and Development program by performing testing and evaluation of the components that are used in seismic and infrasound monitoring systems. In order to perform this work, Component Evaluation maintains a testing facility called the FACT (Facility for Acceptance, Calibration, and Testing) site, a variety of test bed equipment, and a suite of software tools for analyzing test data. Recently, Component Evaluation has successfully integrated several improvements to its software analysis tools and test bed equipment that have substantially improved our ability to test and evaluate components.

The software tool that is used to analyze test data is called TALENT: Test and AnaLysis EvaluatioN Tool. TALENT is designed to be a single, standard interface to all test configuration, metadata, parameters, waveforms, and results that are generated in the course of testing monitoring systems. It provides traceability by capturing in a relational database everything about a test that is required to reproduce the results. TALENT provides a simple, yet powerful, user interface to quickly acquire, process, and analyze waveform test data. The software tool has also been expanded recently to communicate with and control test bed equipment over an Ethernet network. This capability will allow for increased automation of test execution in the future.

In conjunction with the updates to the software analysis tools, several pieces of test bed equipment have been upgraded as well. The most significant new test bed component is the Quanterra Supertonal Signal Source, an ultra-low distortion oscillator and signal generator. This component is expected to be a corner stone of the FACT site test bed by providing very high quality signal generation. Using the new test automation capabilities within TALENT, the Quanterra Supertonal was able to be evaluated much more quickly and to a greater degree than was possible previously.

OBJECTIVES

There are three objectives that are to be achieved for the work described in this paper. The first objective is to upgrade the test bed equipment and infrastructure to better support the desired command and control functions. The second objective is the implementation of functionality within the TALENT test and analysis software tool to be able to command and control the equipment within the test bed. Using this capability to command and control the test bed equipment, TALENT with then be able to automate the execution of many of the tests that are performed. The third and final objective is to employ the test bed automation to perform a thorough evaluation of the new Quanterra Supertonal Signal Source and present of the results of that evaluation.

RESEARCH ACCOMPLISHED

Testbed Upgrade

The goal of upgrading the test bed equipment is to allow it to be controlled remotely, preferably over an Ethernet network connection. One of the key components of our test bed is an Agilent (formerly Hewlett Packard) 3458A high resolution meter. The Agilent 3458A is capable of up to 8.5 digits of resolution and can record a voltage time series with a high degree of accuracy (Agilent Technologies, 2000). This meter is used within the test bed primarily to measure and quantify the reference signals that are generated and fed into various devices under test. In order to ensure its continued accuracy and to provide traceability for our measurements, all of our Agilent 3458A meters are calibrated yearly by Sandia's standards laboratory which is traceable to NIST.



Figure 1. Agilent 3458A high resolution meter.

The Agilent 3458A represents one of the best performing meters commercially available. Its only interfaces are RS232 or GPIB cable connection, a legacy instrumentation data bus. It is considered a mature product by Agilent and will not be considered for feature enhancements. In the past, we have interfaced to the Agilent 3458 using a PCMCIA – GPIB adapter and a stand-alone utility to control the meter and transfer recorded data to a file on disk.

In order to connect to the Agilent 3458A over an Ethernet network, it is necessary to employ an Ethernet – GPIB adapter, such as the Agilent E5810A shown below. Using this adapter, we will be able to control the Agilent 3458A directly from the local Ethernet network and transfer the recorded time series to anywhere on the local network.



Figure 2. Agilent E5810A LAN - GPIB gateway.

The final piece of test bed equipment that we are adding at this time is the new Quanterra Supertonal Signal Source ultra-low distortion oscillator (Quanterra, Inc. 2012). The Component Evaluation project has acquired two of the Supertonals. This evaluation is for one of the units: Serial Number 021204. The Supertonal is capable of generating tonal signals with very little distortion. The Supertonal also has the capability to function as an arbitrary waveform generator and a GPS timing source. All of the signals generated by the Supertonal are time synchronized to a highly accurate GPS timing source. The Supertonal has the potential to become a central part of our test bed and will be replacing several antiquated and custom developed pieces of hardware.

The Supertonal has two differential signal outputs: a low amplitude output and a high amplitude output. The low amplitude output has a maximum signal level of 5.5 Volts peak to peak (2.75 Volts peak). The high amplitude output has a maximum signal level of 44 Volts peak to peak (22 Volts peak). The two lines have identical outputs when a signal is being generated other than a difference of a gain of 8x.



Figure 3. Quanterra Supertonal and GPS timing source.

The Supertonal has a straight forward interface in which waveform files are generated by a Quanterra utility on a desktop computer and then stored on a USB flash drive. The user may select the desired waveform file to play back using a control button on the front face of the Supertonal. Alternatively, the Supertonal has a built in Ethernet connection and embedded Linux operating system that may be used. This is the approach that we are using to transfer the desired waveform file to the flash drive remotely over an FTP connection. The necessary commands to configure the Supertonal and start outputting the waveform file are then issued over a Telnet connection.

Software Upgrades

TALENT is designed to be a single, standard interface to all test configuration, metadata, parameters, waveforms, and results that are generated in the course of testing monitoring systems. It provides traceability by capturing everything about a test that is required to reproduce the results of that test and store that information in a relational database. Individual test modules have been designed for the types of tests (Kromer et al., 2007; Merchant and Hart, 2011) that are conducted on the components that make up a monitoring system.

The TALENT database can store entries for each piece of equipment within the test bed. Each entry contains the necessary information to uniquely identify, connect to, and interface with that piece of equipment.

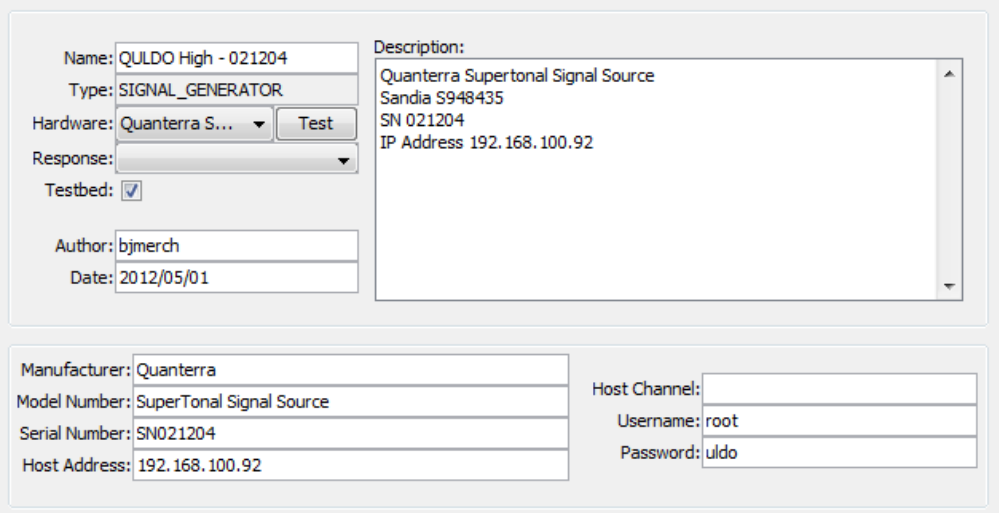


Figure 4. Testbed instrument configuration.

For each instance of the total harmonic distortion (THD) test that is created, the appropriate reference to a signal generator and meter can be selected and associated with that test.



Figure 5. THD test metadata.

Within the THD test viewer, there are also parameters that may be specified to control the desired time series length, signal voltage, and signal frequency that are to be generated.

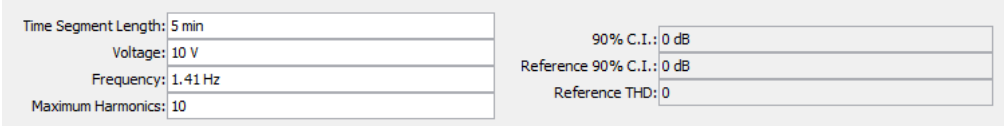


Figure 6. THD signal parameters.

Once the initial THD test has been created and defined, TALENT contains a wizard that will allow users to replicate a selected test over a defined combination of parameter values. For the purpose of this evaluation, specific values for the signal voltages and amplitudes were provided to automatically generate all of the desired tests to be run.

Once the tests have been created, they may be run individually or as a set. As each test is run, TALENT uses the associated reference to the signal generator and the defined signal parameters to command and control the signal generator to output an appropriate signal. TALENT then switches over to the associated meter and configures it to record the signal being generated. Once the signal collection period has completed, the recorded waveform time series is transferred back to TALENT, windowed, and analyzed. The resulting parameters, waveforms, and results are then stored in the TALENT database before completion.

As each test in the selected queue is run, it is flagged within the TALENT table of contents as being executed. If there are any identified problems that prevented the tests execution, then the test would be flagged red. This will allow the user to quickly follow up on any suspected problems.

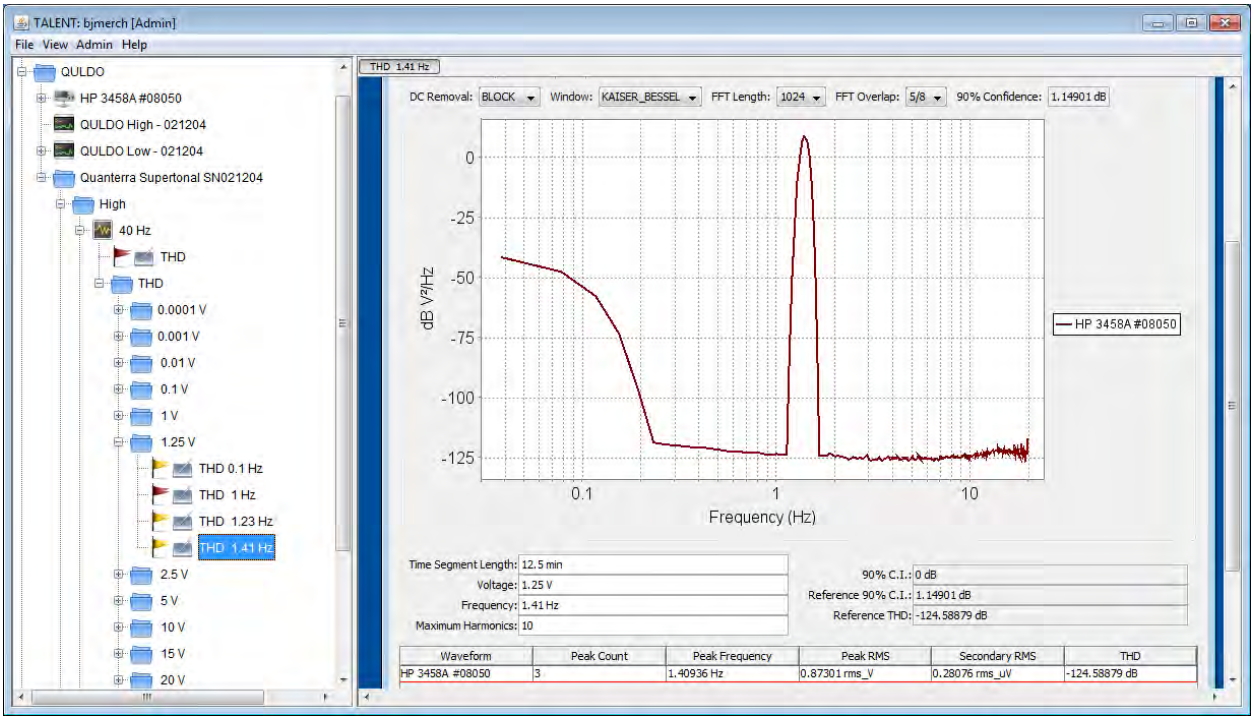


Figure 7. TALENT THD Tests.

Quanterra Supertonal Evaluation

In order for the Quanterra Supertonal to become an integral portion of our test bed, it is necessary to perform a thorough evaluation of its capabilities. Quantifying the Supertonal's performance will involve carrying out many iterations of a variety of tests. Some examples of the capabilities that we are looking to evaluate are described in the table below.

Table 1. Capabilities to evaluate

Test	Description
Source Impedance	Measure the impedance of each of the output lines
Self Noise	Measure output of the 3458 when there is no waveform being generated.
THD	Measure THD at a range of frequencies and amplitudes, recorded on a meter.
DC Accuracy	Measure the DC accuracy on a meter at a range of amplitudes.
Sinusoidal Amplitude & Frequency	Measure the frequency and amplitude accuracy over a range of frequencies and amplitudes on a meter.

Test	Description
Phase Delay	Measure phase delay of sinusoids with a range of frequencies.
Relative Amplifier Noise & Gain	Feed each of the differential legs from the low and high outputs into a separate digitizer channel while generating ½ full scale white noise. Measure the coherence, magnitude response, and phase response between them.
Analog Bandwidth	Record a random white signal at ½ of full scale on the meter. Measure the 3dB roll off point.
Timing Accuracy	Feed timing signals (PPS/PPM/1 Hz sine/original GPS) into a digitizer and estimate variations in timing accuracy.
Timing Drift	Feed timing signals (PPS/PPM/1 Hz sine/original GPS) into a digitizer and estimate the drift in timing over a long period.
Verify Signal Characteristics of other capabilities of Supertonal	Single Tone, Two Tone, Square, Triangle, Random Telegraph, White

Given the length of time required to performing many of these tests, we are focusing first on evaluating the THD. Achieving a very low amount of THD was one of the primary intents for the development of the Supertonal. So, its performance in this regard is of high interest. In the process of performing the THD tests, we will be able to begin demonstrating our command, control, and automation of the test bed.

The procedure for performing a THD test is to configure the Quanterra Supertonal to output a sinusoid with a specific amplitude and frequency. The output of the Supertonal is then connected to the input of the Agilent 3458A meter. The meter then records the sinusoid for as long as the internal memory will allow. A picture of the test configuration is shown below.



Figure 8. Quanterra Supertonal recording on Agilent 3458A.

The THD is then computed from the recorded sinusoid time series. The THD is estimated to be the ratio between the integrated power in the harmonics located at integer multiples of the fundamental frequency and the power in the signal located at the fundamental frequency (Merchant and Hart, 2011). The THD tests will be performed on both

the Low and High amplitude outputs of the Supertonal for the amplitudes and frequencies in the tables shown below. These amplitudes and frequencies span the operating range of the Supertonal and coincide with the range of signals commonly used in our testing.

Table 2 a, b. Range of amplitudes for THD tests

a)

Low Amplitude Output (2.75 Vp max)
0.0001
0.001
0.01
0.1
1
1.25
2.5
2.75

b)

High Amplitude Output (22 Vp max)
0.0001
0.001
0.01
0.1
1
1.25
2.5
5
10
20
22

Table 3. Range of frequencies for THD tests

Sinusoid Frequency (Hz)	Meter Sample Rate (Hz)	Duration (s)	PSD Window Length	PSD 90% Confidence Interval dB
0.1	40	750	8192	3.62704
1.0	40	750	1024	1.14901
1.23	40	750	1024	1.14901
1.41	40	750	1024	1.14901
5	200	150	1024	1.14901
10	200	150	1024	1.14901
15	200	150	1024	1.14901

The amplitudes of the sinusoids were chosen to start from an extreme low of 0.0001 V peak and step, over the decades, up to the full scale output. Additional amplitude values were included for half of nominal full-scale, nominal full-scale, and absolute full-scale. The set of high output amplitudes also includes corresponding amplitudes from the low amplitude set to allow for easy comparisons between them.

The frequencies were similarly chosen. It is typical for most monitoring systems components (digitizers and sensors) to be evaluated at 1 Hz. This is a complication for digitizer evaluations because of the potential for interference from test bed instrumentation at integer multiples of 1 Hz, also often referred to as “integer Hertz” noise. This integer Hertz noise is often due to the refresh rate of panel displays, timing synchronization pulses, etc. The presence of integer Hertz noise can confound the estimation of THD. So, we will often perform THD evaluations at 1.23 or 1.41 Hz so that the introduced harmonics do not overlap with any of the integer Hertz harmonics.

THD testing for the above set of amplitudes and frequencies were performed as described above. This resulted in 133 individual THD tests for all of the combinations of amplitude and frequency for both the low and high amplitude outputs of the Supertonal. This comes to over 18 hours of data that had to be collected. Including a 25% padding of the time series length, time taken to transfer data, and time to compute the THD values, this represents

approximately 24 hours of execution time. Using the newly implemented automation capabilities to command and control the test bed, these tests were able to be executed in two over-night runs without any supervision. The tests for the low level outputs were performed one night and the high level outputs were performed the following night. Using the old procedures that were in place for performing THD tests, this would have taken approximately a week and required the continuous oversight of a staff member to setup and record each test.

The power spectra for a THD performed at 10 V and 1.41 Hz is shown below. There are at least two harmonics, at 2.82 Hz and 4.23 Hz, which are visible above the noise floor of the meter. This corresponds to a THD of -138.389 decibels (dB).

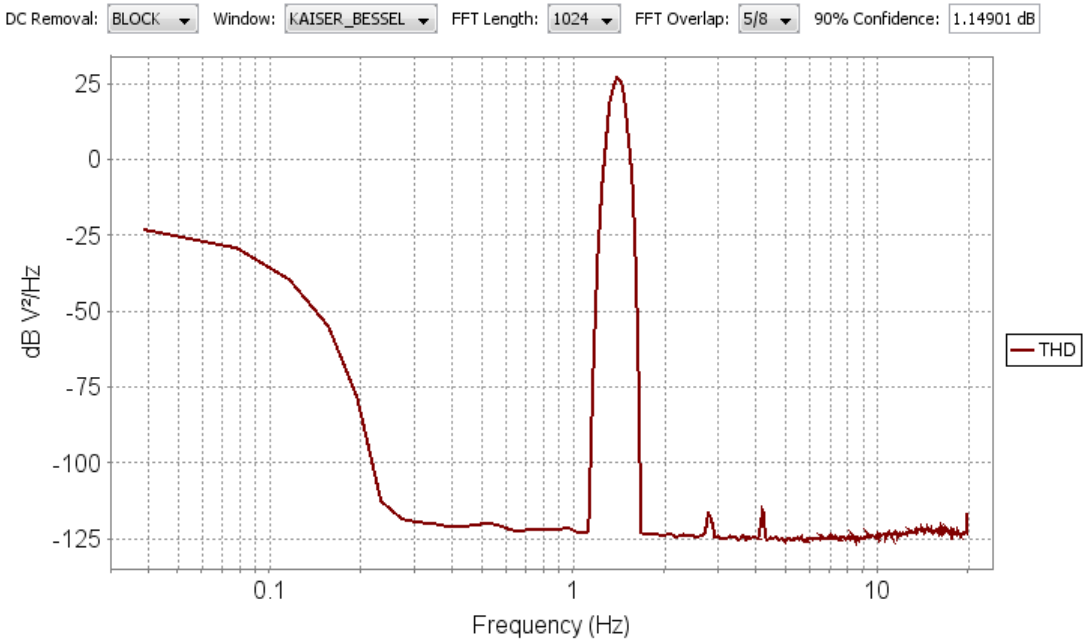


Figure 9. Power spectra of a THD at 10 V and 1.41 Hz with two harmonics

Tables 4 and 5 below contain the THD in decibels for all of the combinations of amplitude and frequency that were performed on both the high and low level outputs. Note that there are a few entries in the tables that are marked with a N/A. These correspond to instances where an error occurred in the automation that resulted in the test data being unable to be acquired for those entries. At a later date, it will be necessary to go back and re-execute those tests.

Table 4. Low level output THD in decibels

	0.1 Hz	1 Hz	1.23 Hz	1.41 Hz	5 Hz	10 Hz	15 Hz
0.0001 V	-59.1038	-60.8845	-63.04766	-66.0643	-32.6789	-31.8664	-29.1876
0.001 V	-76.2836	-74.8832	-80.35851	-85.89	-52.7492	-51.7912	-49.2058
0.01 V	-99.0891	-91.931	-96.02898	-94.1508	-72.719	-71.5757	-69.1476
0.1 V	-118.77	-118.206	-124.3346	-124.418	-93.1977	-91.5826	-89.1313
1 V	-135.352	-136.007	-133.7828	-134.016	N/A	N/A	N/A
1.25 V	-131.295	-133.882	-133.3033	-138.437	-112.786	-110.709	-110.021
2.5 V	-126.674	-127.712	-127.7997	-127.998	-118.021	-116.977	-116.191
2.75 V	-125.263	-126.047	-126.5228	-126.764	-118.802	-117.623	-117.087

Table 5. High level output THD in decibels

	0.1 Hz	1 Hz	1.23 Hz	1.41 Hz	5 Hz	10 Hz	15 Hz
0.0001 V	-43.518	-51.1098	-42.67032	-51.3483	-31.1223	-32.1089	-29.388
0.001 V	-64.9513	-62.2465	-70.92295	-71.84	-52.5209	-52.0722	-49.1474
0.01 V	-83.4704	N/A	-87.22272	-90.5785	-73.4089	-72.1729	-69.2047
0.1 V	-105.12	-96.7232	-99.0676	-99.926	-91.8106	-92.1594	-89.2318
1 V	-123.985	-120.56	-124.0131	-120.327	-112.678	-111.646	-107.773
1.25 V	-125.266	N/A	-131.7895	-124.589	-111.763	-111.181	-110.163
2.5 V	-132.256	-129.742	-128.4607	-138.521	-117.187	-116.884	-116.304
5 V	-138.246	-141.662	-137.204	-135.361	-124.185	-122.713	-121.726
10 V	-140.428	-137.064	-136.1228	-138.389	-126.878	-125.625	-126.148
15 V	-128.614	-130.222	-125.1206	-126.988	-110.561	-109.659	-109.298
20 V	-129.263	-128.392	-126.9684	-127.123	-113.665	-112.348	-111.168
22 V	-131.356	-127.168	-125.3372	-127.001	-113.515	-112.505	-111.634

From the test results above, the THD was minimal at 1.41 Hz for both the Low and High level outputs. The minimum THD at this frequency of approximately -138.4 dB for the low and high level outputs occurred at 1.25 V and 10 V, respectively. These amplitudes both coincide with one-half of the nominal full scale for each output. This corresponds to the expectations stated in the Supertonal documentation.

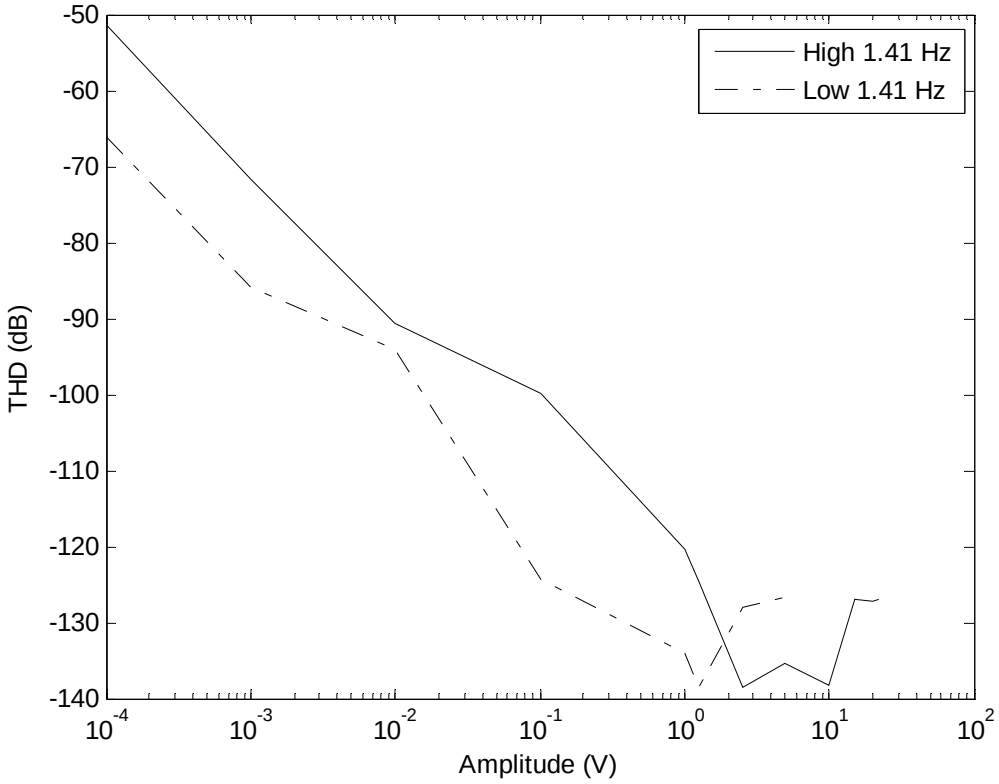


Figure 10. THD for Low and High outputs versus amplitude at 1.41 Hz.

From this data comparing the THD between the Low and High outputs at 1.41 Hz, we can observe that at 1.25 V and below the Low output has a better THD than the High output. Above 1.25 V the High output has a better THD. Much of the increase in THD at lower amplitudes is due to the constant noise floor of the Agilent 3458A meter relative to the decreasing sinusoidal amplitude. Below approximately 1 V on the High output and 0.1 V on the Low output the presence of harmonic distortions are not visible. It may be possible to further reduce the Agilent 3458A noise floor through a combination of meter configuration and test setup changes. Additional investigation on this possibility will be needed to be performed.

CONCLUSIONS AND RECOMMENDATIONS

Introducing the capability to automate the execution of testing for the Component Evaluation project has the potential to dramatically change how components are evaluated. It will be possible to conduct more in-depth testing and complete evaluations much more rapidly than was previously possible. Extending the ability to automate repetitive tasks in other tests will require implementing command and control for additional test bed instruments, meticulous attention to timing details, and configuration control of the test bed. Already work is progressing on implementing the ability to interface to elements of the test bed such as temperature loggers, additional signal generators, digitizer data acquisition systems, network controlled relays, etc. Additional work has also been identified to help in streamlining the software tools to make it easier to define the tests sequences to be performed and to aggregate the test results for easier report generation.

The initial evaluation of the THD performance of the Quanterra Supertonal Signal Source has been successful. The minimum THD of the unit tested is approximately -138.4 dB at 1.41 Hz and half of the full scale voltage. This level of THD is consistent with the specification sheet which quotes a level of better than -130 dB and possibly approaching -140 dB. In addition, evaluating THD across a wide range of frequencies and amplitudes has helped to identify the different performance levels between low and high signal outputs. This will aid us greatly determining how to best utilize the Supertonal in future testing of components.

REFERENCES

Agilent Technologies, Inc. (2000). *Agilent Technologies 3458A Multimeter User's Guide.*

Kromer, R.P., Hart, D.M., and Harris, J.M. (2007). *Test Definitions for the Evaluation of Seismic Sensors*, SAND2007-5025, Sandia National Laboratories, Albuquerque, NM.

Kromer, R.P., Hart, D.M., and Harris, J.M. (2007). *Test Definitions for the Evaluation of Digital Waveform Recorders*, SAND2007-5037, Sandia National Laboratories, Albuquerque, NM.

Kromer, R.P., Hart, D.M., and Harris, J.M. (2007). *Test Definitions for the Evaluation of Infrasound Sensors*, SAND2007-5038, Sandia National Laboratories, Albuquerque, NM.

Merchant, B.J. and Hart, D.M. (2011). *Component Evaluation Test and Analysis Algorithms*, SAND2011-8265, Sandia National Laboratories, Albuquerque, NM.

Merchant, B.J. (2012). *TALENT User's Manual*, SAND2012-0135, Sandia National Laboratories, Albuquerque, NM.

Quanterra, Inc. (2012) *Quanterra Supertonal Signal Source Operation Guide Rev. B.*

Quanterra, Inc. (2012) *Quanterra Supertonal Specification Rev. B.*

ANALYSIS AND SIMULATION OF FAR-FIELD SEISMIC DATA FROM THE SOURCE PHYSICS EXPERIMENT

Arben Pitarka, Robert J. Mellors, Arthur J. Rodgers, Sean R. Ford, Phillip E. Harben, Jeffery L. Wagoner, William R. Walter, Michael E. Pasyanos, Anders Petersson, Oleg Y. Vorobiev, Heming Xu, Stan D. Ruppert, Stephen C. Myers, Eric M. Matzel, and Douglas A. Dodge

Lawrence Livermore National Laboratory

Sponsored by the National Nuclear Security Administration

Award No. DE-AC52-06NA25946/NST11-NCNS-TM-EXP-PD15

ABSTRACT

The Source Physics Experiment (SPE-N) at the Nevada National Security Site (NNSS) provides new data for investigating the excitation and propagation of seismic waves generated by buried explosions. A particular target is the generation of S waves. The far-field ground motions during the first two SPE explosions reveal complex features, such as pronounced azimuthal variations in P- and S-wave arrival times, amplitudes and scattered energy. Substantial energy is observed on the tangential component. We pursue multiple approaches for analyzing the effects of three-dimensional (3D) structure and scattering on wave propagation. These include determinations of the source characteristics, comparisons of waveforms from local earthquakes with the SPE waveforms, refinements of the 3D velocity model, and numerical simulations of the source using both standard moment tensor representations and coupled hydrodynamic codes. A comparison of the SPE waveforms with nearby earthquakes shows clear differences in phase amplitude ratios between the shots and the earthquakes. A full waveform moment tensor inversion using a 1D velocity model and seismograms recorded at a distance of approximately 2 km yielded a poor fit to the tangential components suggesting significant 3D velocity variations. Anelastic finite-difference synthetic seismograms were calculated using the WPP computer program and a 3D seismic model. The 3D seismic model includes surface topography. It is based on regional geological data, with material properties constrained by shallow borehole data. The model was progressively increased in complexity by adding random heterogeneities to evaluate the effect of wave scattering on waveform complexity. Two types of sources were tested: a moment tensor representation and an extended source generated by GEODYN, which is a 3D hydro-dynamic code. Finally we use simulations of the SPE explosions and local earthquakes to examine the frequency behavior of P/S ratios as function of source size and geology.

OBJECTIVES

The SPE-N is a series of chemical explosions intended to enhance our physical understanding and ability to quantitatively model seismic signals from explosions at the NNSS with the goal of improving our nuclear test monitoring capabilities (Brunish et al., 2010). The main objective is to develop comprehensive three-dimensional high fidelity modeling capabilities to enable a transition from the current empirically-based explosion monitoring approach, where accuracy hinges on the availability of calibration data, to a physics-based predictive approach, where seismic observables are correlated to both non-linear physical processes in the near source region, and wave propagation scattering away from the source. To address these issues, we are developing an end-to-end three-dimensional (3D) simulation methodology to model the data collected, including non-linear (shock) motions and linear anelastic motions in the solid earth. We seek to understand the partitioning of energy excited by underground explosions and its propagation in complex 3D geological structure to far-field seismic monitoring stations. The data obtained during the SPE series will be used to validate and calibrate these numerical modeling techniques. Although the entire wavefield will be modeled, particular focus is on the generation of shear waves.

In parallel with the numerical modeling, a comprehensive set of empirical and semi-empirical analysis and discrimination techniques are being applied and will be contrasted with the numerical results. Here we present an overview of the research performed, which included signal analysis of ground motion data recorded at source distances shorter than 1 km, effects of underground structure on ground motion, full waveform moment tensor inversion of far-field motion for the SPE-2 explosion, analysis of P/S ratio as a function of source size using waveforms from SPE and local earthquakes. Finally we present preliminary results of our work on coupling three-dimensional near-field with far-field motion simulated with GEODYN and WPP computer programs developed at Lawrence Livermore National Laboratory.

RESEARCH ACCOMPLISHED

Analysis of Recorded Waveforms

A variety of instruments were deployed in five lines extending radially away from the shot point (Figure 1). Short-period (4.5 Hz) geophones, broad-band sensors, accelerometers and rotational sensors were deployed at selected locations. These instruments were installed on concrete pads set at a shallow depth into the surface.

Figure 2 shows recorded vertical component seismo-grams for two lines, Line 1 (L1) and Line 3 (L3), which show significant differences in amplitude and frequency. L1 is entirely situated on the weathered granite of the Climax Stock, while L3 starts on the granite but is mostly situated on the Quaternary sediments in the northern Yucca Flat basin. Seismograms on L1 show relatively constant moveout and clear Rg waves with a low phase velocity (about 600 m/s). The ground motion recorded along L3 is more complex and likely due to the transition from the granite

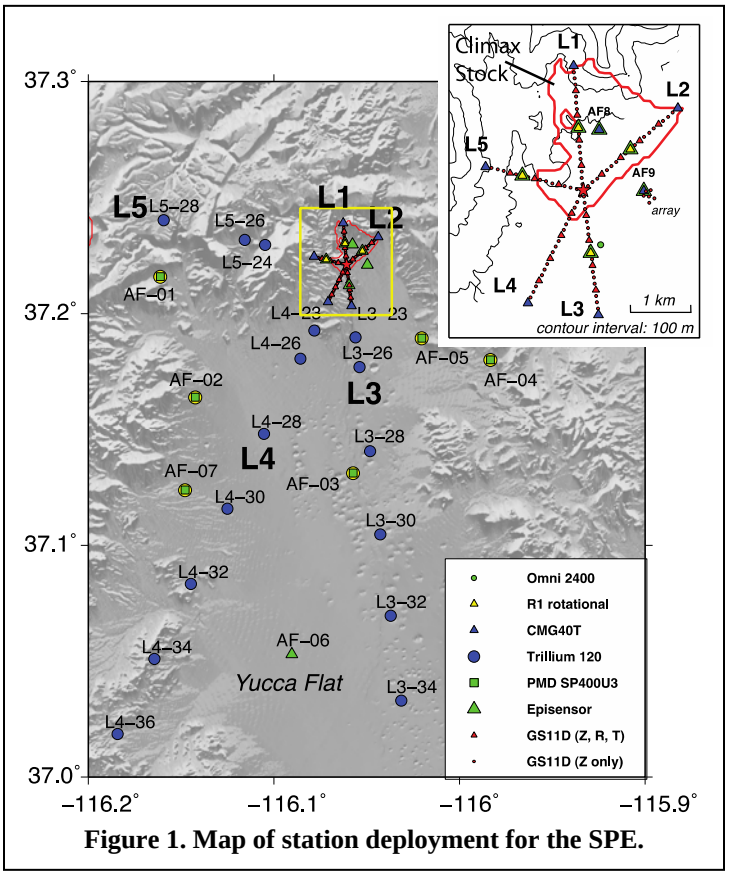


Figure 1. Map of station deployment for the SPE.

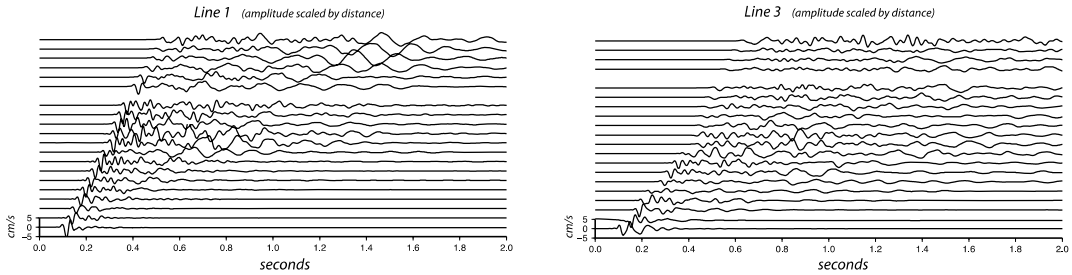


Figure 2. Recorded vertical velocity at L1 (left) and L3 (right).

Climax Stock to the sediments and tuffs of Yucca Flat.

To assist understanding of the waveforms, a polarization filter (Vidale, 1986) is applied to selected waveforms at a distance of 400m (Figure 3). Plots of Strike and Dip are the estimated azimuth and dip angle of the direction of maximum polarization. Angular Polarization P_E measures the degree of ellipticity of motion. P_E is1 for circularly polarized motion, and P_E is 0 for linearly polarized motion. Polarization Strength measures the directionality of the particle motion. Polarization strength is high for motion highly polarized in a single direction.

L1-04 and L2-04 waveforms are similar and show a large amplitude, linearly polarized phase observed in the transverse component, with its peak at 0.15s, travelling with a very small strike angle, which we interpret as a direct S body wave from the source. The second and third arrivals observed on all three components (peak amplitudes at 0.30 s and 0.38 s at L1-04 and L2-04) appears to be an elliptically polarized Rayleigh wave propagating from the source direction as indicated by angular polarization, and low strike angle and dip angles. The fourth significant phase observed in the transversal component which starts at 0.42 s and 0.5 sec at L1-04 and L2-04, respectively is a Love wave. Later phases are scattered surface waves. For L3-04, which is in Yucca Flat, the pattern differs. The first energetic arrival is a strong SV wave immediately followed by a Rayleigh wave. The largest phases at this station are multi-azimuthal Love waves.

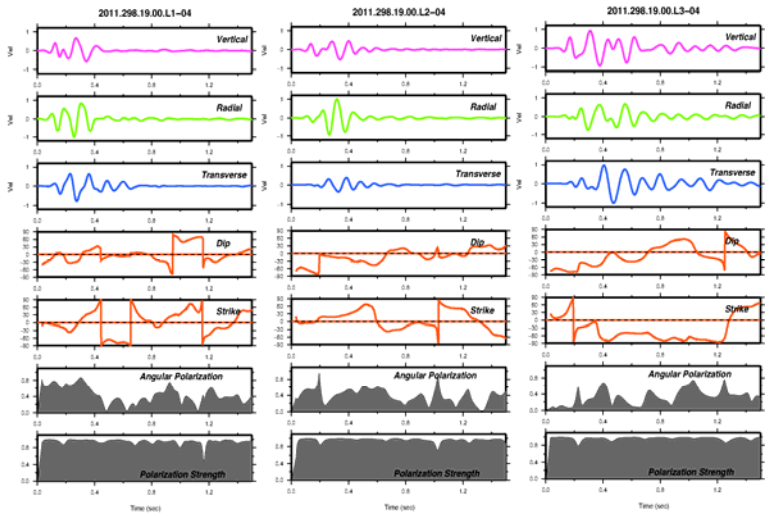


Figure 3. Polarization analysis of the velocity records at stations L1-04, L2-04, and L3-04. The Dip Strike Angular Polarization and Polarization Strength are defined in the text.

Waveform Moment Tensor Inversion

As a preliminary step towards evaluating the source mechanism of the SPE-2 explosion we conducted a full moment-tensor inversion using waveform data recorded by broadband instruments (Guralp CMG-40T and Trillium-120). We applied the inversion technique of Ford et al (2006). Synthetic displacement seismograms are calculated with a frequency-wavenumber integration method. Both computed and recorded displacements were band-pass filtered at 0.5-2Hz. A 1D velocity model was constructed assuming a 20 m thick weathered layer (Vp = 2700 m/s, Vs = 1600, r = 2600 kg/m^3, Q = 300) over granite (Vp = 5000 m/s, Vs = 2700 m/s, r = 2600 kg/m3, Q = 600).

Inversions were conducted using four possible source types: explosion, full moment tensor, deviatoric, and double-couple (Table 1). The explosion source fit the vertical components reasonably well except for station L3-20, which is located on the alluvium and tuffs of Yucca Flat rather than the granite Climax Stock. Radial components appeared similar in shape but with a poor fit to the amplitudes. As expected for a 1D model and isotropic source, no energy was generated on the tangential components. A full moment tensor inversion (Figure 4) provided a slightly better fit with a variance reduction of 49%. The moment tensor is partitioned into 75%, 20% and 5 % isotropic, CLVD and deviatoric components respectively. A constraint solution to only produce the deviatoric component yielded 68% CLVD and 32% DC contributions. None of these solutions fits the tangential displacement satisfactorily. This, combined with the observations of multi-pathing, suggest that a 3D model is required to adequately fit the data even in the low frequency range of 0.5 – 2 Hz.

Table 1. Results from 1D inversion

Source	*Variance reduction*	*Moment*	*Mw*
SPE2			
Explosion	45%	$M_0 6.3\times10^{11}$ N-m	$M_W 1.8$
Full moment tensor	48%	$M_0 2.1\times10^{12}$ N-m	$M_W 2.2$
Deviatoric	42%	$M_0 4.1\times10^{11}$ N-m	$M_W 1.7$
Best double couple	36%	$M_0 3.1\times10^{11}$ N-m	$M_W 1.6$
SPE1			
Explosion		$M_0 6\times10^{10}$ N-m	$M_W 1.2$

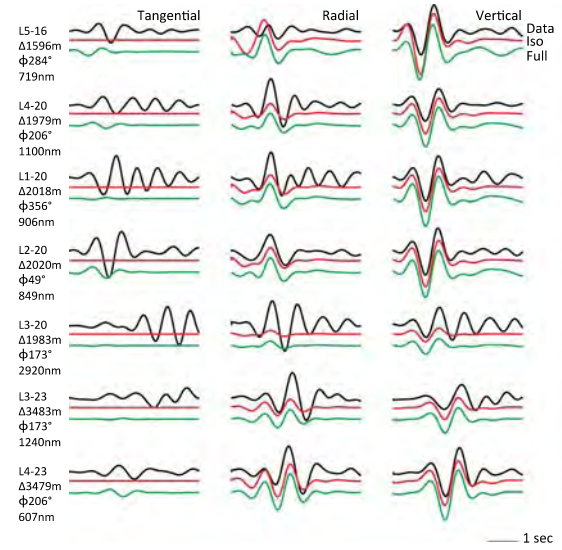


Figure 4. Waveform fits comparing data (black) with inversion results for the full moment tensor (green) and isotropic explosion (red) solution as matched at selected broadband stations.

___ 1 sec line plotted as a 1-sec scale to indicate duration of seismograms.

Iso and Full represent synthetics obtained with the isotropic and full moment tensor source representations.

Local 3D Velocity Model

An important part of our work is the development of a regional three-dimensional velocity model of the SPE site area. The model was used to simulate near-field ground motion from the SPE-2 explosion and perform sensitivity analysis of the simulated motion to shallow structure complexities and surface topography. Our velocity model was based on a geologic model developed with EarthVision, a 3D geologic GIS/visualization program (Figure 5). A set of layers corresponding to the topography, Quaternary alluvium, Tertiary tuffs, pre-Tertiary carbonates, and granite Climax Stock were meshed with an initial grid spacing of 10 m. Each layer was assigned a velocity with a vertical gradient and lateral and vertical variations. We used borehole data from the Climax stock and other locations in the Yucca flat to constrain the velocity gradient and vertical variability of velocity in the alluvium tertiary layer and granite. The horizontal and vertical correlation length of large-scale velocity variations within each layer are 350 m and 20 m respectively, whereas the amount of variability changes within each layer. We used the empirical relationships of Brocher (2005) to estimate the shear wave velocity and density from compressional wave velocity. Figure 6 shows a N-S cross-section of the 3D velocity model. The section passes through the SPE site. 1D profiles of the Vp shown at two locations illustrate the assumed gradient and vertical variation of velocity in the Climax Stock and Yucca flat.

A comprehensive geological study of the Climax stock that includes ample information from borehole data (Townsend et al., 2012) suggests that the granite is highly fractured and its top 30 m highly altered. Recent 2D tomographic models indicate that the thickness of the weathered layer is about 25 m with P wave

velocity of about 1.2 km/s at the surface. Patton et al. (2012) (this proceedings) found that the weathered layer along L1 has a thickness of 22 m, Vp=1300m/s and Vs=700 m/s. To investigate the effects of the weathered granite layer on seismic waveforms, we generated as series of 2.5D finite difference seismograms using an isotropic point source. The assumed velocity profiles and the corresponding simulation results for L1 are shown in Figure 7. Model #4 produces a good fit between the simulated and recorded Rg wave but underpredicts the Rg wave velocities slightly.

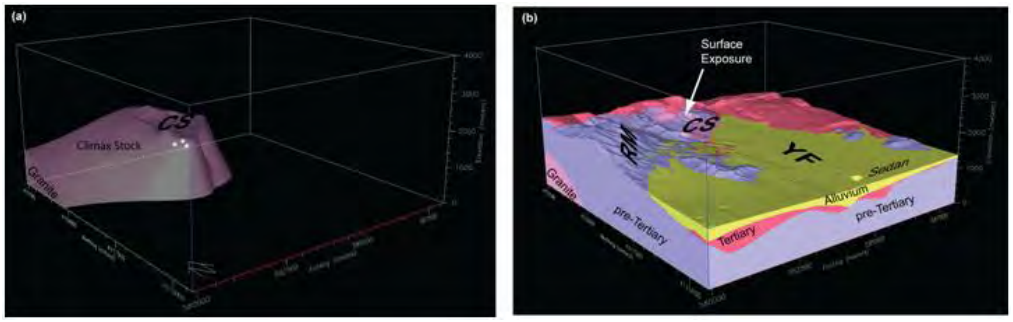


Figure 5. Geologic model used to develop the velocity model showing (a) granite Climax Stock and (b) pre-Tertiary, alluvium and fill in Yucca Flat (Rodgers et al., 2010a).

Finite Difference Simulation of Far-Field Ground Motion

A series of 3D simulations of the far-field wavefield were performed using the WPP finite difference code (Petersson and Sjogreen 2011). WPP is a second-order node-centered code designed specifically for implementation on highly-parallel machines. It models the full wave equation and is capable of handling 3D variations in the material properties, topographic variations on the free-surface (Appelo and Petersson, 2009), and attenuation (Petersson and Sjogreen, 2012). It also includes depth-dependent mesh refinement (Petersson and Sjogreen, 2010). WPP has been previously used to simulate earthquakes (Rodgers et al., 2008) and nuclear explosions (Rodgers et al., 2010b).

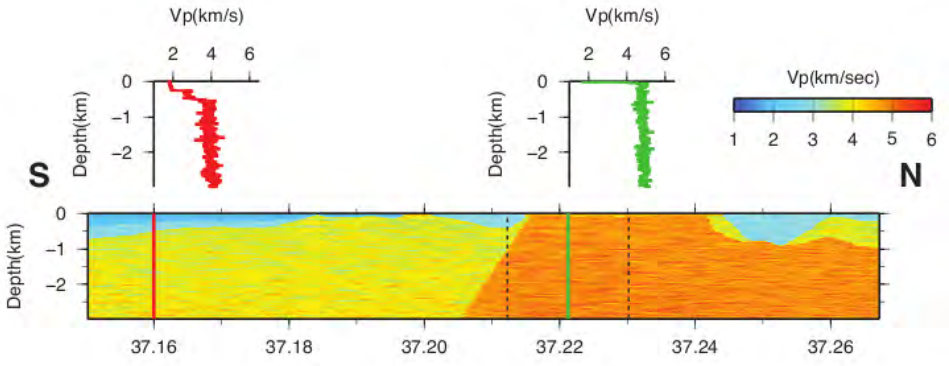


Figure 6. N-S cross-section of the 3D velocity model through the SPE site. Top panels show Vp as a function of depth at Yucca Flat (red line) and SPE site (green line).

The simulations of the SPE2 explosion were conducted on two computational domains, 8×8×5 km and 2×2×4. The grid spacing was variable in the vertical direction, and constant in both horizontal directions. The smallest grid spacing (5 m) corresponded to an upper frequency of about 10 Hz (minimum shear wave velocity was 700 m/s). In all simulations the explosion source was modeled as an isotropic point source with a Gaussian source time function and a seismic moment $Mo=2.0\times10^{12}$ Nm. Several simulations were run to investigate the effect of source time function, velocity variations, and surface topography. Simulations with a Mueller Murphy source time function (Mueller and Murphy, 1971) calculated for granite, source depth=45 m, yield=0.002 kT, Vp=5000m/s, Vs=2900 m/s and density=2.5 g/cm^3 produced the same results as simulations with a Gaussian source time function and a seismic moment $Mo=2.0\times10^{12}$ Nm in the considered frequency range of 0.1-10 Hz.

Figure 8 compares data and synthetics stations on granite along L1 and L2 in the frequency range of 0.1-10 Hz and between distances ranges of 200 m to 1000 m. The amplitude and phase of the Rg waves are very well reproduced for the vertical component. Rg on the radial component has a stronger reverberation in the synthetics than the data. Notice that the shear waves observed in the transverse component are not reproduced by the simulation well, as they arrive much later than the observed shear wave. Our simulation with an isotropic explosion source suggests that wave scattering in the source area did not contribute to the generation of shear waves observed in the transverse component, which may indicate a source contribution.

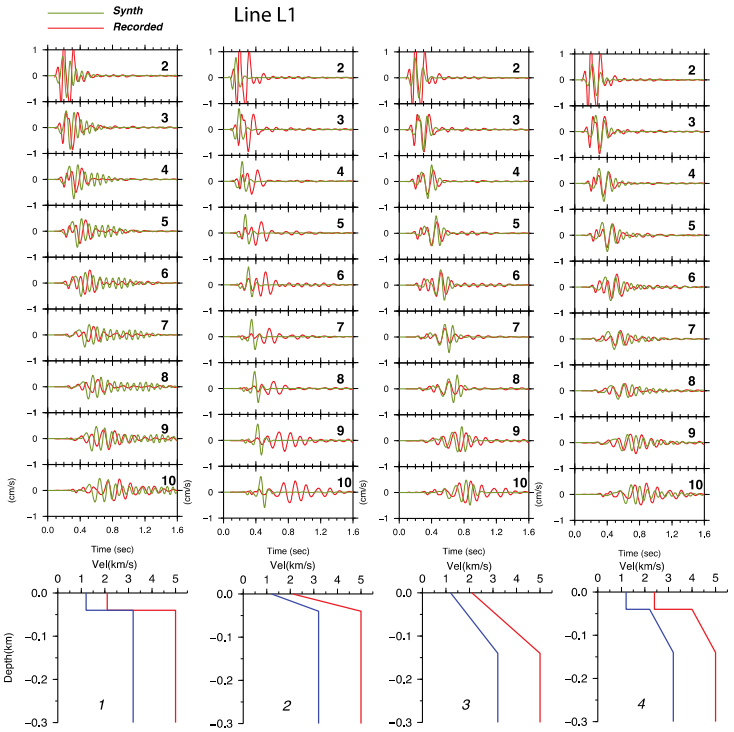


Figure 7. Simulated effects of surface weathering of the Climax stock granite on far-field waveforms (0.1-10 Hz). Each panel compares 2.5D finite difference synthetic seismograms (green) with recorded velocity waveforms (red) at stations along line L1. Bottom panels show the two-dimensional velocity models.

The inclusion of the weathered layer and surface topography has a dramatic effect on the synthetic seismograms. Figure 9 compares synthetics produced with 3D velocity models with and without topography. The topography has an effect on Rg waves observed in the radial and transverse components. The effect of topography is increased by a low velocity weathered layer. Figure 10 shows a snapshot of the wavefield simulated with a 3D velocity model that covers an area of 8 km × 8 km. The simulation shows that the complex geology and topography of the area is expected to cause strong variations in azimuth in both travel-time and waveform. In particular, as the seismic waves propagate to the south and southeast they encounter the low velocities of the Yucca Flat alluvium and underlying tuff. We are working to improve our model in these areas.

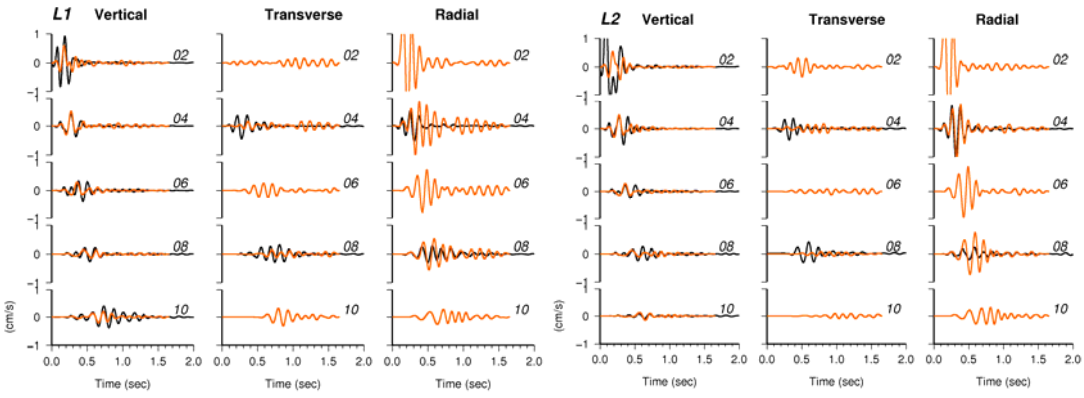


Figure 8. Comparison of data (black) and synthetics (brown) calculated using an isotropic point source model of the SPE-2 shot at stations array L1 (left) and L2 (right) (filtered, 0.1-10 Hz). The synthetics are calculated using a 3D velocity model with surface topography.

Coupling of 3D Hydrodynamic Source Modeling With far-field Anelastic Wave Propagation Modeling

Understanding the partitioning of energy excited by underground explosions as observed in the far-field, requires the ability to model both the near-field, which includes the nonlinear deformation and damage caused by the explosion, and the far-field, which consists of three-dimensional wave propagation in a

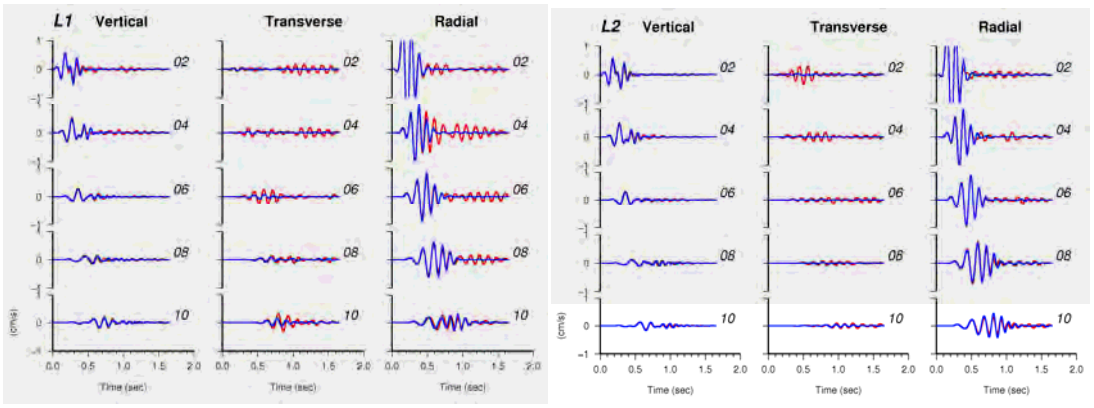


Figure 9. Effects of surface topography. Comparison of synthetic velocity seismograms calculated with surface topography (red traces) and without surface topography (blue traces) band-pass filtered at 0.1-10 Hz.

complex geological structure. We are developing an end-to-end three-dimensional (3D) simulation methodology to handle both near- and far-complex geological structure. The transition between hydrodynamic to seismic motion near the source is performed by coupling GEODYN, an Eulerian hydrodynamics code with adaptive mesh refinement, and WPP a finite-difference computer program.

Figure 11 illustrates an example of synthetic seismograms from an isotropic explosion source calculated with WPP and the coupled 3D-GEODYN-WPP codes using 3D simulations for a half space. The coupling between the two codes is performed on the faces of a cube of 100m × 100 × 100m centered at the source. Our next step is to perform simulations using realistic models of the nonlinear deformation and damage caused by the chemical explosion (Antoun et al., these Proceedings).

Physical Models for P/S Earthquake-explosion Discrimination

The far-field seismic sensors in and around NNSS record natural earthquakes in addition to the SPE chemical explosions. Previously (Mellors et al., 2011), we showed a comparison of the SPE-1 shot to a nearby magnitude 0.7 earthquake at a few of the SPE seismic stations filtered at a high frequency passband of 16-32 Hz. These seismograms show the expected difference in relative P/S amplitude values for closely located and similar sized events, with the explosion having systematically higher P/S amplitudes than the earthquake. This P/S discriminant has shown empirically that it can separate explosions from a background of earthquakes at many locations in the world (e.g., Dysart and Pulli, 1987; Baumgardt and Young, 1990; Walter et al., 1995; Taylor, 1996; Hartse et al., 1997; Battone et al.; 2002; Walter et al., 2007).

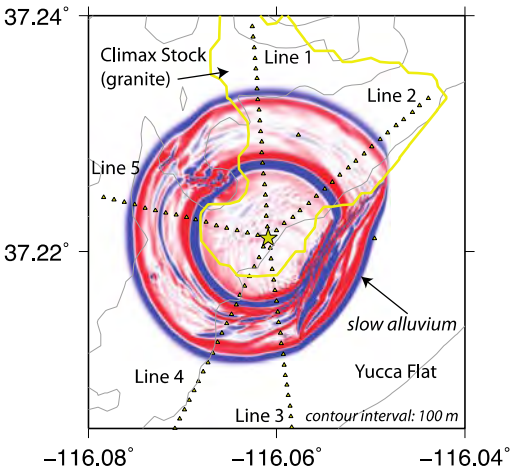


Figure 10. Snapshot of the SPE simulated wavefield using WPP program and a 3D velocity model with surface topography.

For the SPE we are trying to address questions of how and why the P/S discriminant works. This includes investigating any magnitude, frequency, depth or other dependencies that could affect how to use the discriminant in practice. We are also working towards understanding the separate contributions of source and path on the discriminant through the development of physics-based models. A question we are trying to address in the SPE is how much of such observed differences are due to source parameter differences (e.g., mechanism, duration), versus how much is due to path differences (e.g., depth, scattering). In order to apply the P/S discriminant over broad regions we need to be able to model and account for such effects.

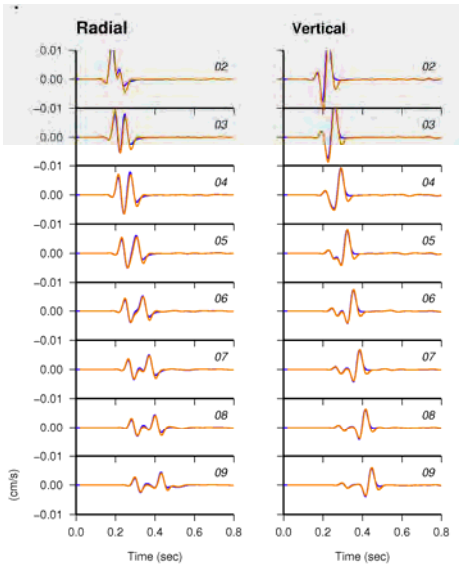


Figure 11. Comparison of synthetic velocity seismograms calculated with WPP code (brown) GEODYN-WPP codes (blue), for a half space velocity model. The seismograms are band-pass filtered at 0.1-13 Hz

We are using the SPE data to test earthquake and explosion models. For example in Figure 12 we show the SPE-1 and SPE-2 data at one of the SPE stations. Note that at low frequency, below the corner frequency of the two events, the seismograms are very well correlated and the amplitude difference is very close to the factor of ten change in the yield. We form spectral ratios based on energy in the P-wave arrival window on the vertical component and the S-wave arrival window on the transverse component. We compare these observed ratios with several explosion source models. For example in Figure 12 we calculate the expected P-wave source spectral ratio for SPE-2 to SPE-1 using the Muller and Murphy (1971) model for granite with the parameters given by Steven and Day (1985). We used the actual depths of the shots and an assumed factor of two enhancement in yield for the chemical explosion (compared to the nuclear explosion for which the model was developed). The match of the model with the observations at one station is reasonable.

We also calculated the expected SPE-2 to SPE-1 ratio for S-waves using the Fisk (2006) conjecture that the S-waves are matched by lowering the Mueller-Murphy corner frequency by the ratio of the P to S wave velocity. The implication of this model is that S-waves are generated close to the source and are tied to the elastic radius similarly to P-waves. As shown in Figure 12, the fit to the ratio of the observed S-wave ratios at this station is poor. It is not clear yet if the observed ratio reflects the true S-wave source or is contaminated at high frequencies by scattered P and other waves. We are actively working to better model and separate path and source effects in order to gain insight into the true source model for explosion S-waves. Such a model is crucial to being able to understand both the basis for the P/S ratio discriminants and the circumstances under which they may not work.

CONCLUSIONS AND RECOMMENDATIONS

Results from our initial analysis of recorded and simulated waveforms from the SPE-2 explosion demonstrate that the waves generated from the explosion have a rich content in shear wave energy. The S-P wave conversion at the surface topography, and affected by the weathered layer in the Climax stock contributed to generation of Rg waves near the source region. However the shear waves observed in the transverse component arrive much earlier than near-source scattered waves. Our interpretation of these results is that the origin of such waves is at the source. We have developed the computational capability that will allow modeling of nonlinear deformation and damage caused by the explosion, as well as three-dimensional wave propagation effect in a complex geological structure. We will use these tools to model near- and far-field data to better distinguish source and path effects. A full suite of other analysis will be conducted. This will include further study of the rotational data and modeling, small array signal processing, examination of the P, S wave spectra and ratios, body and surface wave amplitudes, full moment tensor inversion using 3D Green's functions, interferometry, and comparison with local earthquake data.

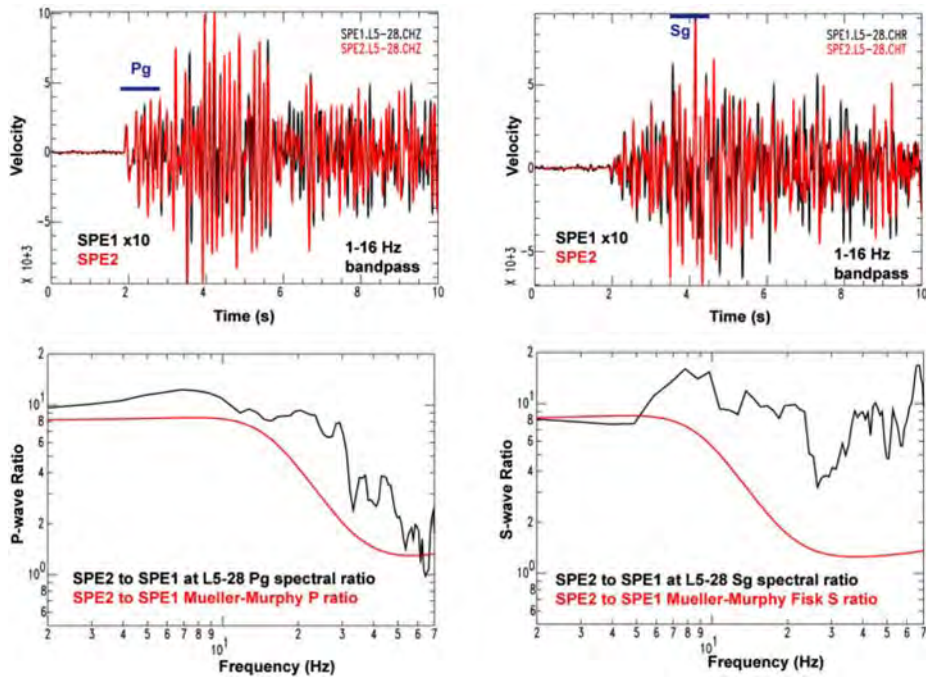


Figure 12. A comparison of the SPE-1 and SPE-2 chemical explosion seismograms at station L5-28 about 9 km away. Upper right shows the vertical component, and the upper left shows the transverse component (SPE-1 L5-28 had an error in the horizontal orientation). Sseismograms are band pass filtered from 1-16 Hz and the 100kg SPE1 data is multiplied by a factor of 10 and correlates very well with the 1000 kg SPE-2 shot. The lower left shows the Pg window spectral ratio for SPE-2/SPE-1 which matches well with the Muller-Murphy prediction but the Sg window spectral ratio (lower right) does not match the Fisk (2006) conjecture prediction well possibly due to scattering and contamination.

ACKNOWLEDGEMENTS

We thank NA-22 and all the SPE participants for all their efforts in planning and carrying out SPE-1 and SPE-2. We thank the group at NSTec and, in particular, Bob White and Catherine Snelson-Gerlicher for their efforts. Rob Abbott and Margaret Townsend were also very helpful. Gabe Plank and Ken Smith assisted with data organization. Numerical simulations were performed on the SIERRA and CAB Linux clusters operated by Livermore Computing using a Computing Grand Challenge Allocation.

REFERENCES

Antoun, T., X. Heming, O. Y. Vorobiev, E. B. Herbold, L. Glenn, and I. Lomov (2012). Analysis and simulation of near-field wave motion data from the source physics explosions, these Proceedings.

Appelo D. and N. A. Petersson (2009). A stable finite difference method for the elastic wave equation on complex geometries with free surfaces, *Comm. Comput. Phys.* **5**, 84–107.

Battone, S., M. D. Fisk and G. D. McCarter (2002). Regional seismic-event characterization using a Bayesian formulation of simple kriging, *Bull. Seismol. Soc. Am.* **92**, 2277–2296.

Baumgardt, D. R. and G. B. Young (1990). Regional seismic waveform discriminants and case-based identification using regional arrays, *Bull. Seismol. Soc. Am.* **80**, 1874–1892.

Brocher, T. M. (2005). Empirical relations between elastic wavespeeds and density in the earth's crust. *Bull. Seismol. Soc. Am.* **95**, 2081–2092.

Brunish, W. N., W. L. Hawkins, D. Coblentz, H. J. Patton, J. J. Zucca, J. J. Sweeney, C. R. Carrigan, T. H. Antoun, C. E. Seifert, K. H. Wohletz, C. R. Bradley, A. J. Sussman, T. W. Bowyer, R. Cirbell, C. M. Snelson, and P. Lee (2010). Source physics experiments at the Nevada Test Site, in *Proceedings of the 2010 Monitoring Research Review: Ground-Based Nuclear Explosion Monitoring Technologies*, LA-UR-10-05578, Vol. 1, pp. 370–390.

Dysart, P. S. and J. J. Pulli (1987). Spectral study of regional earthquakes and chemical explosions recorded at the NORES array. SAIC technical report C87-03.

Fisk, M.D (2006). Source spectral modeling of regional P/S discriminants at nuclear test sites in China and the Former Soviet Union, *Bull. Seismol. Soc. Am.* **96**, 2348–2367.

Ford, S. R., D. S. Dreger, and W. R. Walter (2006). Identifying isotropic events using an improved moment tensor technique, in *Proceedings of the 28th Seismic Research Review: Ground-Based Nuclear Explosion Monitoring Technologies*, LA-UR-06-5471, Vol. 1, pp. 590–596.

Hartse, H., S. R. Taylor, W. S. Phillips, and G. E. Randall (1997). A preliminary study of regional seismic discrimination in Central Asia with an emphasis on Western China, *Bull. Seismol. Soc. Am.* **87**, 551–568.

Mellors, R., A. J. Rodgers, P. E. Harben, W. R. Walter, S. Ford, J. L. Wagoner, N. A. Petersson, B. A. Sjogreen, T. F. Hauk, S. D. Ruppert, Stephen C. Myers, E. M. Matzel, Douglas A. Dodge, M. E. Pasyanos, and J. P. Lewis (2011). Analysis and simulation of far-field seismic data from the Source Physics Experiment explosions, in *Proceedings of the 2011 Monitoring Research Review: Ground-Based Nuclear Explosion Monitoring Technologies*, LA-UR-11-04823, Vol. 1, pp. 503–512.

Mueller, R. A. and J. R. Murphy (1971). Seismic characteristics of underground nuclear detonations. Part I. seismic spectral scaling, *Bull. Seismol. Soc. Am*. **61,** 1675–1692.

Petersson, N.A. and B. Sjogreen (2010). Stable grid refinement and singular source discretization for seismic wave simulations, *Comm. Comput. Phys.* **8**(5), 1074–1110.

Petersson, N.A., B. Sjogreen (2011). User's guide to WPP version 2.1, Lawrence Livermore National Laboratory, LLNL-SM-487431

Petersson, N.A. and B. Sjogreen (2012). Stable and efficient modeling of anelastic attenuation in seismic wave propagation, *Comm. Comput. Phys.* **12**(1), pp. 193-225, DOI: 10.4208.

Rodgers, A., A. Petersson, S. Nilsson, B. Sjogreen and K. McCandless (2008). Broadband waveform Modeling of Moderate Earthquakes in the San Francisco Bay Area to Evaluate the USGS 3D Seismic Velocity Model, *Bull. Seismol. Soc. Am*. **98**, 969–988.

Rodgers, A. J., J. Wagoner, N. A. Petersson, and B. Sjogreen (2010a). Pre-shot simulations of far-field ground motions for the Source Physics Experiment (SPE) explosions at the Climax Stock, Nevada National Security Site, Lawrence Livermore National Laboratory technical report LLNL-TR-461990.

Rodgers, A., N. A. Petersson, B. Sjogreen (2010b). Simulation of topographic effects on seismic waves from shallow explosions near the North Korean Nuclear Test Site with emphasis on shear wave generation, in press *J. Geophys. Res.-B Solid Earth Planets*, doi:10.1029/2010JB007707, LLNL-JRNL-433892.

Taylor, S. (1996). Analysis of high-frequency Pg/Lg ratios from NTS explosions and Western U.S. earthquakes, *Bull. Seismol. Soc. Am.* **86**, 1042–1053.

Townsend, M., L.B. Protho, and C.Obi (2012). Geology of the Source Physics Experiment site Climax stock, Nevada National Security Site. DOE/NV/25946-1448.

Vidale, J.E (1986). Complex polarization analysis of particle motion. *Bull. Seismol. Soc. Am*. **76**, 1393–1405.

Walter, W. R., K. Mayeda, and H. J. Patton, (1995). Phase and spectral ratio discrimination between NTS earthquakes and explosions Part 1: Empirical observations, *Bull. Seismol. Soc. Am.* **85**, 1050–1067.

Walter, W. R., E. Matzel, M. Pasyanos, D. Harris, R. Gok and S. Ford (2007). Empirical observations of earthquake explosion discrimination using P/S ratios and implications for the source of explosion S-waves, in *Proceedings of the 29th Seismic Research Review*: *Ground-Based Nuclear Explosion Monitoring Technologies*, LA-UR-07-5613, Vol. 1, pp. 684–693.

BROAD AREA EVENT DETECTION USING WAVEFORM CORRELATION AND DISTRIBUTED COMPUTING

Megan E. Slinkard, Stephen L. Heck, Dorthe B. Carr, Regina F. Eckert, and Christopher J. Young

Sandia National Laboratories

Sponsored by the National Nuclear Security Administration

Award No. DE-AC04-94AL85000/SL12-SignalAnalysis-ND

ABSTRACT

Waveform correlation techniques have garnered increasing attention in the last few years, as their value in detecting and categorizing repeated events has been demonstrated again and again. In previous work, we, and other researchers, have shown the value of applying waveform correlation techniques to aftershock sequences; in particular, we found that, depending on the source-to-station distance and the characteristics of the sequence, 24%–92% of aftershocks could be detected using waveform correlation.

By porting our code to the 400+ node SNL GNDD distributed computing resource, we now have the ability to assess the effectiveness of waveform correlation for continuous monitoring of a broad region of interest. In this manner, we can gain insight into the total amount of repeated seismicity in a region, and point toward the upper limit of value provided by using waveform correlation for monitoring. We present our results so far towards our goal of monitoring a region which includes most of central Asia, using nearby stations from the IMS network and a large event archive based on several years of the LEB catalog. We test our system against several months of continuous data, and quantify performance by comparison with the LEB catalog. We discuss how our results are affected by various factors related to the details of the correlation processing (phase windowing, correlating single vs. multiple stations, etc.).

OBJECTIVES

Waveform correlation offers a method to identify repeated seismic events such as occur frequently during aftershock sequences and which occur occasionally during periods of normal seismicity. In the monitoring mission, where aftershocks and earthquakes are nuisance events, rapid identification of repeated events improves monitoring efficiency. Over the past several years, Sandia National Laboratories (SNL) has developed and refined a prototype system named the Waveform Correlation Detector (WCD) to evaluate the effectiveness of waveform correlation based event detection techniques, particularly during aftershock sequences where a high rate of repeated events is anticipated. Our WCD runs from the beginning of a user-selected time interval and strives to detect repeated events by comparing incoming waveform data at a station against the waveforms of archived events. Events can be added to the archive as they occur (e.g., during an aftershock sequence). Incoming data is continually compared against this archive to identify repeating events before traditional processing would need to be engaged. Typically, numerous similar events are found, some of which can be linked to events in a reference catalog (i.e., they would have been found using traditional methods), and some, generally smaller events, which are not. Similar events are grouped in families under a master event. In past work we have applied the WCD to various aftershock sequences and found the percentage of repeating events varies widely, depending on the characteristics of the sequence and the distance to the station.

Recently we ported our WCD algorithm to the SNL GNDD distributed computing resource (400+ cores) to improve performance. With this new, more powerful, resource, we have turned our attention to continuous monitoring of a broad region of interest. In this manner, we can gain insight into the total amount of repeated seismicity in a region, and point toward the upper limit of value provided by using waveform correlation for monitoring.

In this paper, we discuss our preliminary results from applying the new WCD to monitoring central Asia using data from nearby IMS stations. Thus far we have analyzed a three month period which includes a small mainshock/aftershock sequence in the Xinjiang-Xizang region of China that began on March 20, 2008 and which is known to have repeated events (Bobrov, 2011); this ensures that our WCD will have some repeated events to find. We processed data from three IMS array stations located in Asia, looking for events similar to those produced by the aftershock sequence. We discuss our results, describe our method of choosing template waveforms, show plots of typical families, and discuss our validation methods, including receiver operating characteristic (ROC) curves.

RESEARCH ACCOMPLISHED

Our WCD is designed to simulate using waveform correlation in an operational monitoring system. Waveform correlation techniques rely on the uniqueness of paths through the earth to declare that waveforms with a high degree of correlation are statistically very likely to be from the same type of source at the same location (Thorbjanrardottir & Pechman, 1987; Harris, 1991; Withers et al., 1999). We refer to the waveform of a known signal, recorded at a specific station, as a template. Future waveform data recorded at that station can be compared via correlation to the template; if the correlation coefficient is high, we say we have found a repeated event. This simple approach is remarkably robust. The high number of repeating events expected during an aftershock sequence suggests that waveform correlation can identify a large percentage of the aftershocks. As stated above, our previous research has validated the potential utility of waveform correlation for identifying aftershock events. Our current efforts focuses on moving away from processing time- and geography-bound aftershock sequences to processing large time periods of data for broad regions of interest, using historical data as templates. Our distributed computation environment allows us to quickly process longer time intervals and permits an increase in our template collection size with a minimal increase in processing time.

Dataset

Though our ultimate goal is broad regional processing of central Asia, we selected a small mainshock/aftershock sequence from 2008 as a starting point because we wanted to begin with a small data set that could be expected to have repeating events over a limited time span. The plan is then to expand both the geographic and time spans until we are monitoring all of central Asia with a rich template library. For our current testing, we ran the WCD on three months of IMS data beginning with the mainshock (LEB parameters: T_0=2008/03/20 22:32:56 GMT, lat= 35.4^o, lon.=81.5^o, depth=0 km, m_b=5.4). Our data were from the three nearby IMS primary network stations that recorded the largest number of aftershock events (MKAR, SONM, and ZALV), according to the analyst-reviewed IDC LEB bulletin. All of these stations were arrays, and we processed the data as arrays, correlating each element separately and averaging the results (e.g., Harris & Dodge, 2011). Our templates were obtained from events that occurred

during the first
48 hours after the mainshock with a lat/lon box which bounded the aftershock sequence. Our dataset parameters are described in Table 1. By containing our templates to a small region, we could assume that for each station the P-S separation of the arrivals and the bandwidth of the incoming signals would be fairly constant. Thus we were able to use a constant window length for the templates at a given station. Combining that with our assumption of a fairly constant signal bandwidth meant our time-bandwidth product could be assumed to be stable. As the correlation threshold should be set according to the time-bandwidth product of the templates, we were then able to assign each station a single correlation threshold for all events in this dataset. This is in contrast to assigning each template its own individual correlation threshold, which we believe will be necessary when the templates are not all from the same tight geographic region. The use of a constant correlation threshold allowed us to study the effect of varying the threshold on detection and false alarm rates for the dataset. The insight we have gained from this analysis will aid our ability to set thresholds properly when we move to the broad regional problem, where we will assign individual correlation thresholds for each station/event pair.

Table 1. Parameters of dataset and WCD run.

Dates WCD Ran	3/20/2008 – 6/20/2008		
Stations used	MKAR	SONM	ZALV
Distance from mainshock to station	11.2 ˚	18.4 ˚	21.9 ˚
Array elements used	9	5	8
Templates: acquisition dates	3/20/2008 22:00:00 -3/22/2008 22:00:00 (48 hours starting from mainshock)		
Templates: lat/lon box	lat : 34-37.5 lon : 79.5 - 82.5		
Correlation Threshold	.4	.5	.4
Filtering	3rd order Butterworth bandpass filter; .5 – 5Hz		

Template selection

Choosing quality templates is one of the most critical parts of setting up a successful waveform correlation run, and should be approached with great caution. The consequences of a poorly selected template can be dramatic, as we show below. On our first attempt to search for repeating events using data from station MKAR, we included in our set of templates taken from the LEB catalog events the seemingly reasonable waveform shown in Figure 1.

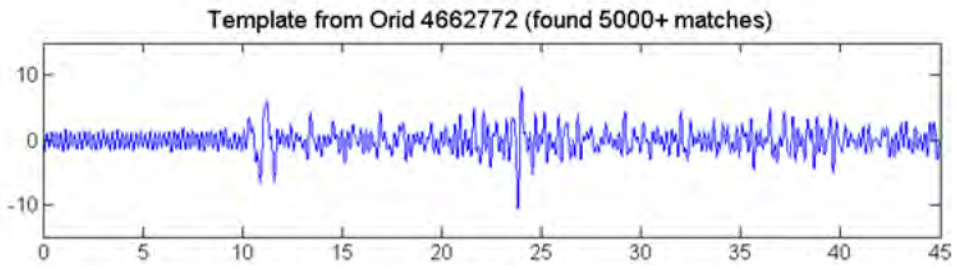


Figure 1. Template which generated over 5000 poor matches, as seen at array element MK01.

Surprisingly, while all the other templates we selected generated a handful of matched events over the three months of monitoring, this template generated more than 5000 matches, all but a few of which seemed to be noise. The reason is the noise source of about 3 Hz very evident prior to the event signal, and continuing throughout the waveform. If this type of noise were isolated to this window, it might not be a problem; unfortunately, the noise was frequently present on MKAR data (i.e. not just during this time window), hence the high number of correlated "events", which were really correlations of 3 Hz noise. Correlating all the elements of the array might be expected to alleviate the problem, but we found that it did not always help and in fact obfuscated the situation. Often only one

array element would have data that contained the noise, yet the high correlation at that element would cause us to detect otherwise dubious matches because that element would have such a high correlation that the average of all elements was still above our threshold. Since detecting noise was not our goal, we decided to add some additional checks to our automatic template selection algorithm

We compared this template to the waveform from a nearby event, which could just easily have been selected as the template for this family (Figure 2). The first waveform (2a) is the same as the one in Figure 1; the second (2b) is clearly very similar to the first but does not have the high frequency noise source superimposed on the event waveform. We then took each of these templates and correlated it with the same 2 days of data, and created historgrams of the correlations for each time window processed (Figure 2). Though the templates capture a very similar type of signal, there is a distinct difference in shape of the historgrams. The top histogram has proiminent tails in correlations below -0.2 and above +0.2. Compare this with the lower histogram for the template without the 3 Hz noise, which has a much simpler shape, with a handful of high correlation values extending to the right, which are the legitimate matched events. Based on this observation, we decided to add a histogram check to our template-selection algorithm by first checking the characteristics of each template's histograms, and rejecting a template if one or more array elements produced an unusual histogram.

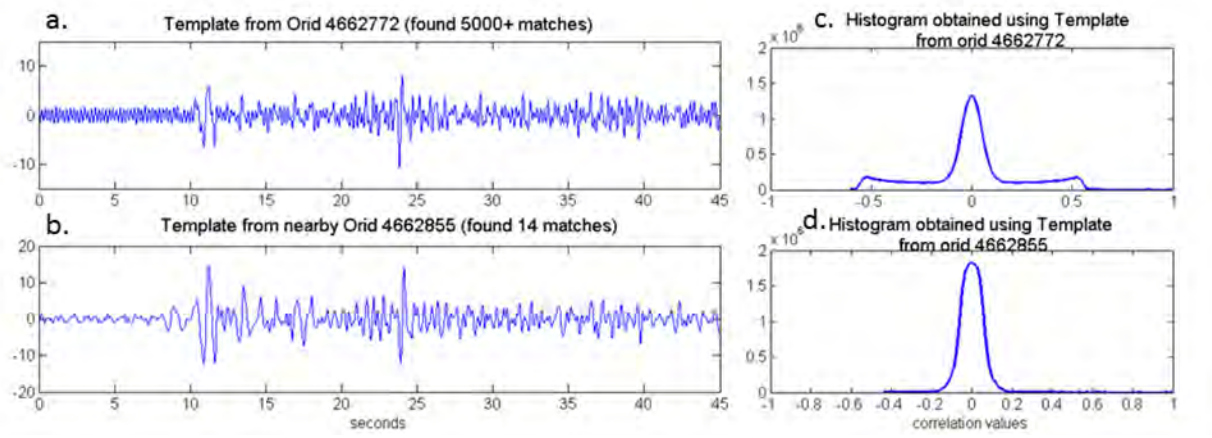


Figure 2. Templates and Histograms generated from two nearby events

Based on this and other experiences with selecting proper templates, we came up with the template selecton methodology shown below (Figure 3).

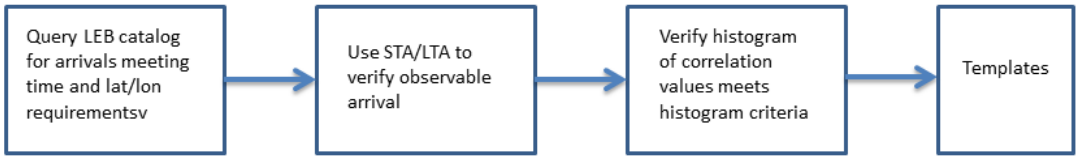


Figure 3. Template Selection Algorithm

To construct out template library, we firsrt query the LEB catalog to find if there was a signal detected at the IMS station of interest; for this dataset we queried for events in the first 48 hours of the aftershock sequence. Since we only want very clean, high signal-to-noise ratio (SNR) signals for templates, we then run an STA/LTA detector to ensure that our candidate template does indeed have a strong arrival. Then we calculate a correlation value histogram using the candidate template on a representative data segment short enough to process quickly, but long enough to develop meaningful statistics (two days of data in this case), and toss out any candidate templates which produced histograms which varied from the expected histogram shape. The remaining candidates were used as our templates. At each of our 3 stations, about half of the LEB arrivals linked to catalog events for the aftershock sequence passed our criteria to become templates. Each station selected its templates independently (e.g., the three stations did not have the same template list). In total, we had 50 templates for MKAR, 39 for SONM, and 33 for ZALV.

Example Families

WCD found families of similar waveforms at all 3 stations. For conciseness, in this paper examples will focus primarily on our MKAR results. We examine our results, and then seek to validate our detections and create a ROC curve showing the effect of threshold on valid detections and false alarm rates.

Figure 4a gives an overview of our detections at MKAR during the 3 month period; the x-axis shows time of day and the y-axis shows days after starttime, i.e. each row shows the results for a single day. At the top (i.e., the first two days), we see the self-detections of the templates marked in blue. Green and red markers shows other events we detected as a match: green is for WCD events that we could associate to LEB catalog events, red is for WCD events that we could not find a match for. To give a sense of context, we also plot all of the LEB arrivals at that station, in gray. We observe that the WCD found matches throughout the entire 3 months, though more were found at the beginning. Figure 4b plots the effectiveness of each template: for each template (y-axis) we show the matches it found, and when (x-axis). Two families that will be discussed in detail have their orids listed on the y axis. We see that two families were particularly prolific, and a few families found nothing, but that most of the families found a handful of matches.

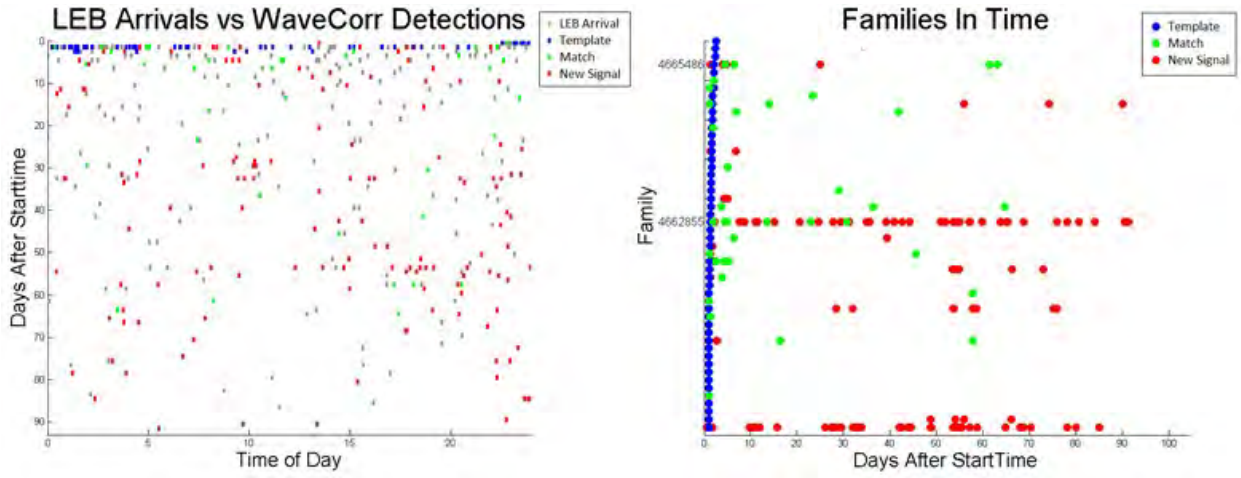


Figure 4. (a) WCD detections for MKAR as a function of day after start time. Blue markers indicate self-detection of the template; green markers indicate detections of LEB catalog events, red markers indicate detection of non-LEB events. (b) WCD detections for MKAR as a function of template/family. Marker colors are the same as in (a).

Figure 5 shows the family (template and matches) created at MKAR from the template generated from orid 4665486, the upper labeled family in Figure 4. As mentioned previously, we correlate each element of the array separately and average the results, but to simplify the presentation for each detection we show a beamed waveform steered in the direction of the template origin and assuming Pn slowness, since we assume that our correlation matches are near the location of the template. This should allow us to see high SNR waveforms for good matches. WCD found 14 matches, 5 of which were linked with arrivals in the LEB catalog, and 9 of which were not found to be listed in the catalog. The top plot is the template; the traces underneath it are plotted in order of correlation score. Note that the template found itself—a useful validation—so the 2nd trace is actually a repeat of the template, and not counted as a match in our statistics. When there was a first P arrival in the LEB catalog within 5 seconds of our computed arrival time, we found the associated LEB origin and calculated the distance to template location and distance to station, using the lat/lon coordinates listed for that origin in the LEB catalog. These results are documented in Table 2. We see that although most of the matches occurred in March, three occurred in late May. Also, we see that for the events that we do link to catalog listings, the catalog locations are close to the template location (maximum distance is 22 km), and the event to station distance is fairly constant. All matches were reviewed by an analyst and evaluated by our automatic validation algorithm (more on this later), and the verdicts are shown in the Validity columns in the table, with a rating of “Good” for a legitimate match or FA for “False Alarm”.

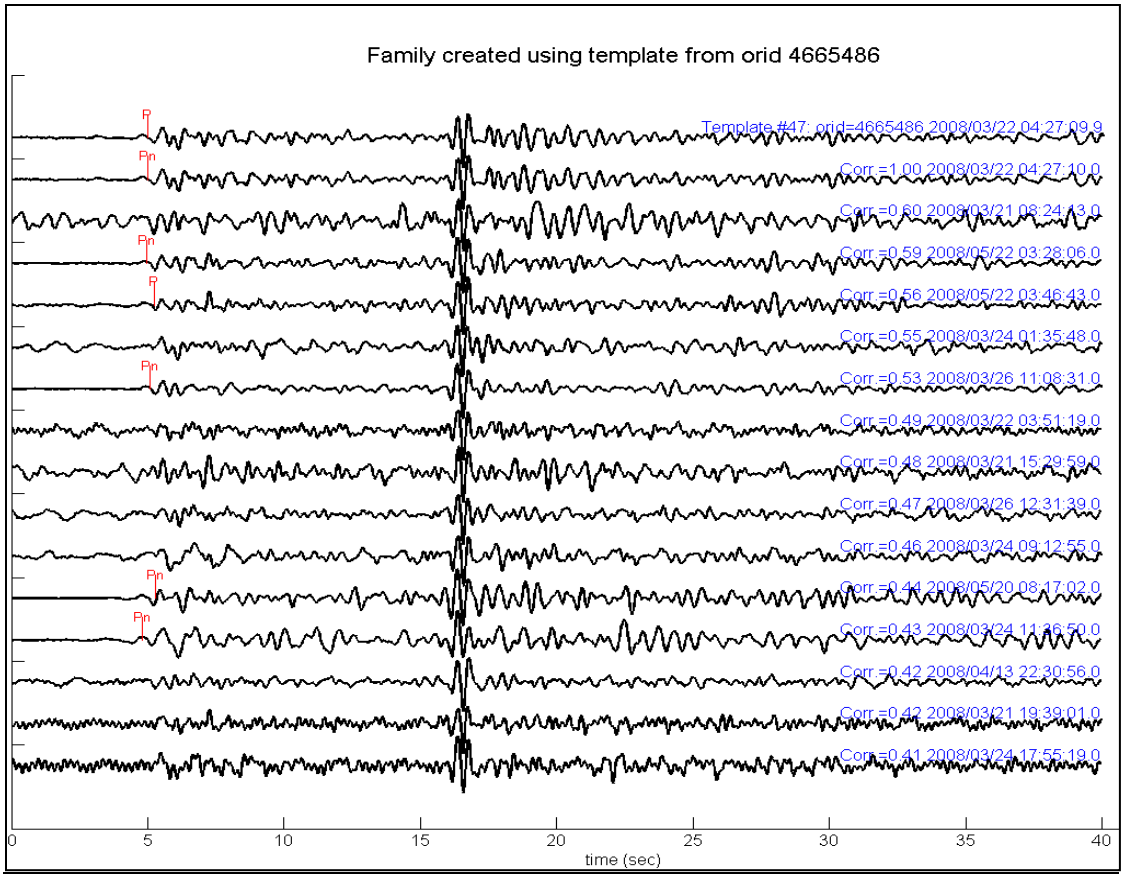


Figure 5. Family create using template from orid 4665486; top trace is template.

Table 2. Information about the family shown in Figure 5.

Correlation	Detection time	LEB Orid	Distance to Template (LEB)	Distance to Station (LEB)	Validity (algorithm)	Validity (analyst)
.6	2008/03/21 08:24:13				Good	Good
.59	2008/05/22 03:28:06	4761388	1km	1235km	FA	Good
.56	2008/05/22 03:46:43				Good	Good
.55	2008/03/24 01:35:48				Good	Good
.53	2008/03/22 03:51:19	4664132	22km	1215km	Good	Good
.49	2008/03/22 03:51:19				FA	Good
.48	2008/03/21 15:29:59				FA	Good
.47	2008/03/26 12:31:39				FA	Good
.46	2008/03/24 09:12:55				FA	Good
.44	2008/05/20 08:17:02	4764116	9km	1240km	Good	Good
.43	2008/03/24 11:36:50	4662561	4km	1239km	Good	Good
.42	2008/04/13 22:30:56				FA	Good
.42	2008/03/21 19:39:01				FA	Good
.41	2008/03/24 17:55:19				FA	Good

Figure 6 shows the first nine matches in another family created at MKAR, from the template generated from orid 4662855. It is important to note that all templates were run with the same correlation threshold for this test (0.4), a significant factor here. For this template, WCD found 52 matches, many of which we determined to be of dubious quality, and only 6 of which we could link to LEB origins. In the figure we can see that several detections match the first P arrival (Pn) at 7 seconds, but lack the secondary phase arrival at 20 seconds. Interestingly, when we perform a cluster analysis on the results, many of the dubious events cluster quite tightly (correlation values > .6) with one another, suggesting that if one of those events been used as a template, it would have created its own distinct family. Nevertheless, the fact all of those events ended up being detected by this template suggests that a correlation value of .4 was too low for this template. The associated table is shown as Table 3, and shows that for the events that are listed in the catalog there is a group of events that are located near the template location, while others thousands of kilometers away, clearly unrelated. This example shows why it is so important to choose the appropriate threshold for each template. Some of the correlation values shown for the template in Figure 6 are actually higher than those in Figure 5, and yet the events found are nowhere near the template event: a score that is considered a good match for one template is not necessarily even a fair match for another template.

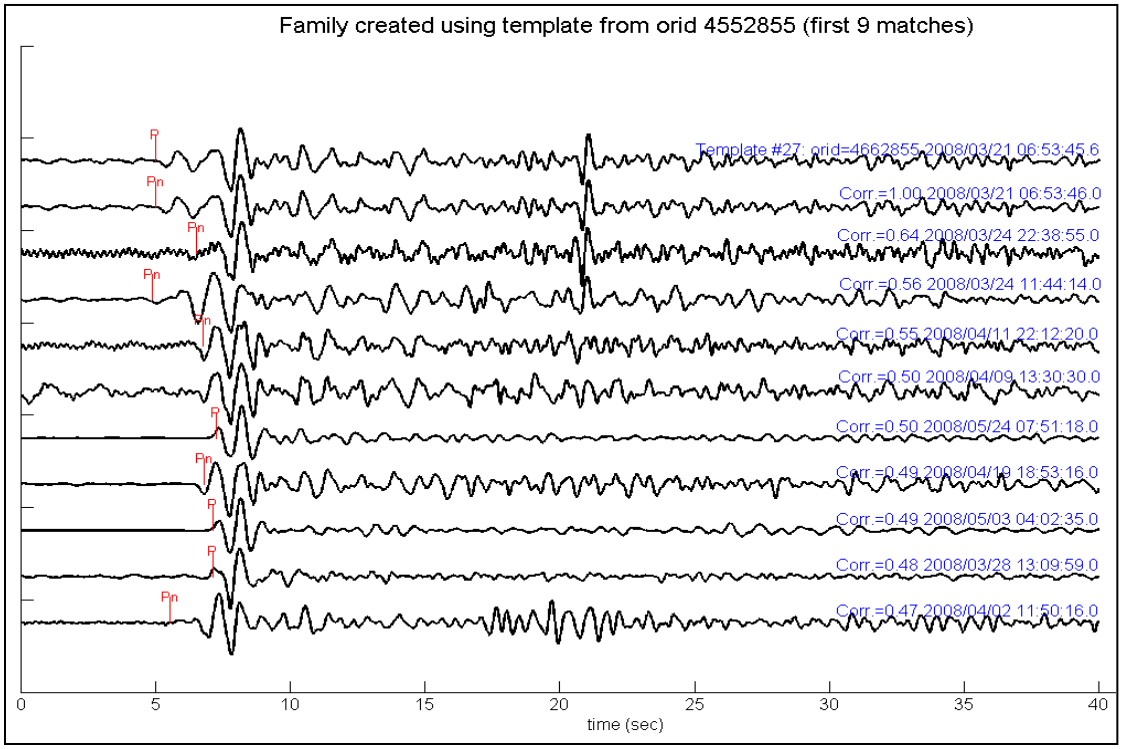


Figure 6. First 9 matches using template from orid 4552855.

Table 3. Information about family in Figure 6.

Correlation	Detection time	LEB Orid	Distance to Template (LEB)	Distance to Station (LEB)	Validity (algorithm)	Validity (analyst)
.64	2008/03/24 22:38:55	4662772	28km	1247km	Good	Good
.56	2008/03/24 11:44:14	4662678	10km	1228km	Good	Good
.55	2008/04/11 22:12:20	4695730	20km	1227km	Good	Good
.50	2008/04/09 13:30:30				Good	Good
.50	2008/05/24 07:51:18	4775216	6650km	7426km	Good	FA
.49	2008/04/19 18:53:16	4700636	38km	1220km	Good	Good
.49	2008/05/03 04:02:35	4720020	4748km	5817km	Good	FA
.48	2008/03/28 13:09:59	4669608	5988km	6882km	Good	FA
.47	2008/04/02 11:50:16	4670845	37km	1228km	Good	Good

Validation

Validating the results of waveform correlation presents significant challenges. First, we must decide what a "good" match is. The answer can vary considerably depending on the application. Is the goal event detection (Bobrov, 2011), or event categorization or relocation (Schaff and Richards, 2011)? Theoretically, for the same source mechanism, lowering the correlation threshold should allow the detection of matches spread over a broader geographical area, but is this desirable? A second challenge is to decide how significant false alarms are, which also varies according to the application. In an operational system, waveform correlation results may be sent to a traditional signal associating event detector to associate detected signals. Knowing the approximate origin location saves the associator time, and likely offsets the costs of a few bad detections (which traditional detection, using STA/LTA, is not immune from either). As long as the end result is increased efficiency, we satisfy our goals. Perhaps the biggest challenge is to validate the tremendous number of events detected using waveform correlation that are not listed in available catalogs. Having an analyst manually verify each detection is practical for small test sets but not for the longer intervals we plan to process.

We are developing an automated algorithm to determine if a match is valid or not, using whatever criteria are appropriate to the application at hand. Our current version applies five validation criteria, at least two of which must be satisfied to declare a valid match:

1) Multi-station validation– is this event seen at another station as well? We calculate theoretical origin times for all our matches, and then see if another station also found a match for the same event with a theoretical origin time within 2 seconds.

2) Catalog match – can we associate this match with an arrival listed in a published catalog? (LEB in this paper)

3) STA/LTA – does this event trigger using STA/LTA at the expected P arrival location?

4) High Correlation – is the correlation value at one station exceptionally high? A sufficiently high correlation at one station can trump all other considerations.

5) Has Friends – does this event correlate well with some of the other events in the family? We observed that well behaved families tend to have events which correlate well with one another, and that poor matches often vary considerably from other events in the family.

Currently our algorithm still does not match the analyst validations to an acceptable level. The algorithm suffers both from declaring as valid matches that the analyst judges to be false (see Table 4) and declaring as invalid matches that the analyst judges to be legitimate (see Table 3). The former problem is generally because of

dubious events triggering on the "STA/LTA" and "Has Friends" criteria, while the latter is because the "Multi-Station" and "High Correlation" criteria don't always work. Both of these problems must be addressed in order for us to use our validation algorithm to generate statistics to evaluate WCD performance. In the meantime, we use our analyst review validations for our evaluations of performance.

To capture the ratio of good matches vs. false alarms, we use a ROC curve. Good matches are those which our analyst said looked like the template waveform and were most likely from an event near the template event location; a false alarm is anything else – noise, an event which just doesn't look enough like the template, etc. The ROC curve for the MKAR dataset (all families) is shown in figure 7a. The curve traces out the effect of changing the correlation threshold for this dataset on the number of false alarms and good matches. We see that at a correlation value of .4 we had 69 good detections, and 114 false alarms. As the correlation threshold is raised, the number of false alarms drops off more quickly than the number of good matches, and at a correlation value of .5 we had 24 good matches and only 1 false alarm. Two families, one of which was the family shown in Figure 6, contributed the vast majority of false alarms. In the discussion of Figure 6 we mentioned that we believe the threshold selection chosen for this dataset, 0.4, was too low for that particular template; these results support that idea, as the false alarm rate plummets as we increase the threshold slightly. If we delete these two problem families from our dataset, we get the ROC curve shown in figure 7b. The fact that one or two poor templates can drastically increase the number of false alarms for a given threshold level reinforces our idea that it will be necessary to set threshold values individually for each template (as well as perhaps have the ability to remove poor performing templates during operation).

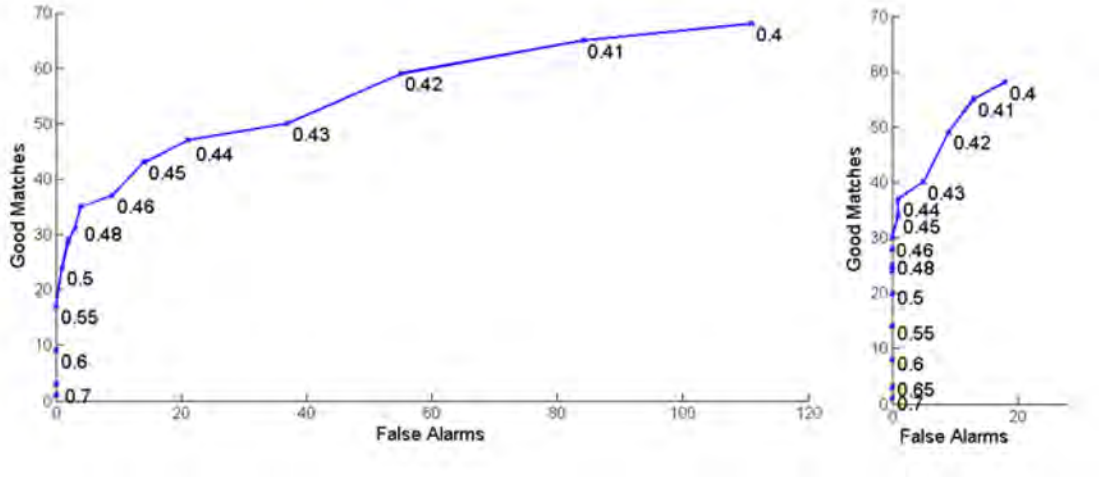


Figure 7. a) ROC curve of MKAR dataset, b) ROC curve after removing 2 families

CONCLUSIONS AND RECOMMENDATIONS

As a preliminary step towards our goal of monitoring all of central Asia using waveform correlation processing of IMS data, we performed waveform correlation monitoring of three IMS stations for a small region in central Asia (lat. 34-37.5, lon. 79.5-82.5) for a duration of three months following a moderately sized earthquake that generated a small aftershock sequence in our region. Our templates for each station were selected from the set of signals at that station associated with aftershock events during the first two days of the sequence. Despite that narrow time window for template selection, and associated small template set, we managed to detect on windows containing 16% of the first P LEB arrivals associated with events in our monitoring region during the 3 month period following the mainshock. Moreover, we found 32 events that were valid matches but not listed in the LEB catalog.

Achieving good results is highly dependent on choosing high-quality templates, meaning templates that will find valid repeating events but not often trigger on noise. Validating waveform correlation output is a difficult problem, and one that we are still addressing. The biggest challenge is classifying detections as valid or false alarms. Catalogs (global, regional, or local) can be used to search for matches, but inevitably waveform correlators will produce additional events that cannot be matched to a catalog. The preferred method for assessing these detections is analyst

review, but this is impractical for large data sets. Once waveform correlation events have been classified, ROC curves can be used to capture the tradeoffs associated with changing the correlation threshold.

Moving forward, we plan to expand our monitoring region and our template timespan. Using templates from a broad area means a single station will have templates from a wide range of distances, thereby requiring varying window lengths and individualized correlation thresholds. We also plan to continue refining our validation techniques, and feed those results into our threshold selection algorithm.

ACKNOWLEDGEMENTS

We are grateful to Paul Richards, David Schaff, Ivan Kitov, and Charlotte Rowe for their encouragement of this research, and valuable conversations.

REFERENCES

Bobrov, D.I. and I.O. Kitov (2011). Analysis of the 2008 Chinese Earthquake Aftershocks using Cross-Correlation, in *Proceedings of the 2011 Monitoring Research and Review: Ground-Based Nuclear Explosion Monitoring Technologies*, LA-UR-11-04823, Vol. 2, pp. 811–821.

Harris, D.B. (1991). A waveform correlation method for identifying quarry explosions, *Bull. Seismol. Soc. Am.* **81** (6), 2395–2418.

Harris, D.B. and D. A. Dodge (2011). An autonomous system for grouping evnets in a developing aftershock sequence, *Bull. Seismol. Soc. Am.* **101** (2), 763–774.

Schaff, D. P. and P. G. Richards (2011). On finding and using repeating events in and near China, *J. Geophys. Res.* **116**, B03309.

Thorbjarnardottir, B.S. and J.C. Pechman (1987). Constraints on relative earthquake locations from cross-correlation of waveforms, *Bull. Seismol. Soc. Am.* **77**(5), 1626–1634.

Withers, M., R. Aster, and C. Young (1999). An automated local and regional seismic event detection system using waveform correlation, *Bull. Seismol. Soc. Am.* **89** (3), 657–669.

Appendices

Acronyms, etc.

Acronym	Definition
3D	three-dimensional
AFRL	Air Force Research Laboratory
AFTAC	Air Force Technical Applications Center
ANFO	ammonium nitrate fuel oil
ARSA	Automated Radioxenon Sampler/Analyzer
BAA	Broad Agency Announcement
CEA	Commissariat à l'Energie Atomique
CLVD	compensated linear vector dipole
CMT	Harvard centroid moment tensor
CORRTEX	Continuous Reflectometry for Radius vs. Time Experiment
CTBT	Comprehensive Nuclear-Test-Ban Treaty
CTBTO	Comprehensive Nuclear-Test-Ban Treaty Organization
DMC	Data Management Center (IRIS)
DOB	depth of burial
DoD	Department of Defense
DOE	Department of Energy
DOS	Department of State
DPRK	Democratic People's Republic of Korea
ECM	Event Categorization Matrix (formerly Event Classification Matrix)
EGF	Empirical Green's Function
EMP	electromagnetic pulse
EOS	equation of state
FACT	Facility for Acceptance, Calibration, and Testing (SNL)
FFT	Fast Fourier Transform
FWHM	full width at half maximum
GIS	geographical information system
GMT	generic mapping tool
GNEMRD	Ground-Based Nuclear Explosion Monitoring Research and Development Program
GPR	ground-penetrating radar
GSN	Global Seismographic Network
GT0	ground truth zero
GTx	ground truth information of accuracy x km
HDC	hypocentroidal decomposition
HE	high explosive
HPGe	high purity germanium
HPXe	high-pressure xenon
HV	high voltage
IAEA	International Atomic Energy Agency
IASPEI	International Association of Seismology and Physics of the Earth's Interior
iasp91	standard earth model
IDC	International Data Centre
IMS	International Monitoring System
INGE	International Noble Gas Experiment
IRIS	Incorporated Research Institutions for Seismology
ISC	International Seismological Centre
LANL	Los Alamos National Laboratory
LEB	Late Event Bulletin
LLNL	Lawrence Livermore National Laboratory

Acronym	Definition
mb	body wave magnitude
MDAC	magnitude and distance amplitude corrections
MDC	minimum detectable concentration
MEMS	microelectromechanical systems
MFA	multiple filter analysis
Ms	surface wave magnitude
MOHO	Mohorovičić discontinuity
Mw	moment magnitude
NA-22	Office of Nonproliferation and Verification Research and Development in NNSA
NDC	National Data Center
NEIC	National Earthquake Information Center
NEM R&D	Nuclear Explosion Monitoring Research and Development
NIST	National Institute of Standards and Technology
NNSA	National Nuclear Security Administration
NNSS	Nevada National Security Site (formerly Nevada Test Site)
NPE	Nonproliferation Experiment
NRL	Naval Research Laboratory
NTS	Nevada Test Site (renamed Nevada National Security Site)
O&M	operations and maintenance
OSI	on-site inspections
PASSCAL	Program for Array Seismic Studies of the Continental Lithosphere
PNE	peaceful nuclear explosions
PNNL	Pacific Northwest National Laboratory
PSD	power spectral density
PTS	Provisional Technical Secretariat
RASA	Radionuclide Aerosol Sampler Analyzer
R&D	research and development
REB	Reviewed Event Bulletin - IDC report
REL	Reference Event List
RMS	root mean square (errors)
RSTT	regional seismic travel-time model
SAUNA	Swedish Automatic Unit for Noble Gas Acquisition
SBIR	Small Business Innovation Research
SEB	Seismic Event Bulletin
SEL	Standard Event List
SLBM	Seismic Location Baseline Model
SMDC	Space Missile Defense Command (Army)
SNL	Sandia National Laboratories
SNR	signal-to-noise ratio
SOFAR	SOund Fixing And Ranging
SPE-A	Source Phenomenology Experiments in Arizona
SPE-N	Source Physics Experiments at NNSS
STA/LTA	short-term average/long-term average
TTBT	Threshold Test Ban Treaty
UNE	underground nuclear explosions
USGS	United States Geological Survey
USNDC	United States National Data Center
VOD	velocity of detonation
WHO	World Health Organization
WMO	World Meteorological Organization

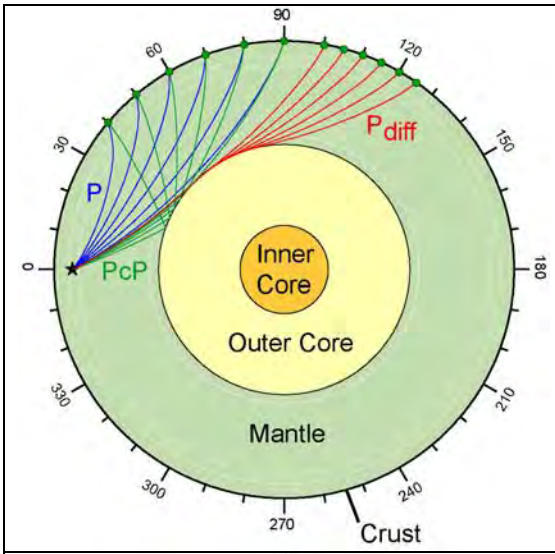
Guide to Seismic Phases

The change of seismic velocities within Earth, as well as the possibility of conversions between compressional (P) waves and shear (S) waves, results in many possible wave paths. Each path produces a separate seismic phase on seismograms. Seismic phases are described with one or more letters, each of which describes a part of the wave path. Upper case letters denote travel through a part of the earth (e.g. P or S), and lower case letters denote reflections from boundaries. A complete, standardized nomenclature for seismic wave paths is available at the web site: http://www.isc.ac.uk/standards/phases. This information has also been published [Storchak, D.A., J. Schweitzer, P. Bormann (2003), "The IASPEI Standard Seismic Phase List", Seismol. Res. Lett. 74, 6, 761-772], and a pdf file of this publication is available from the same web site.

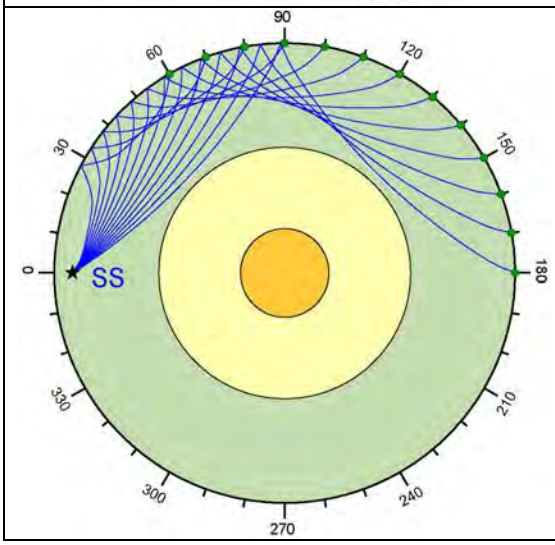
In the verification context, wave propagation in Earth is divided into *teleseismic* (distances greater than 2000 kilometers) paths and *regional* (distances less than 2000 kilometers) paths.

Teleseismic Phases

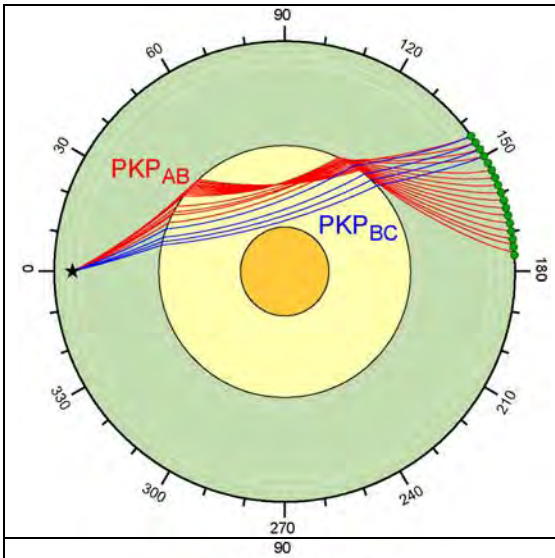
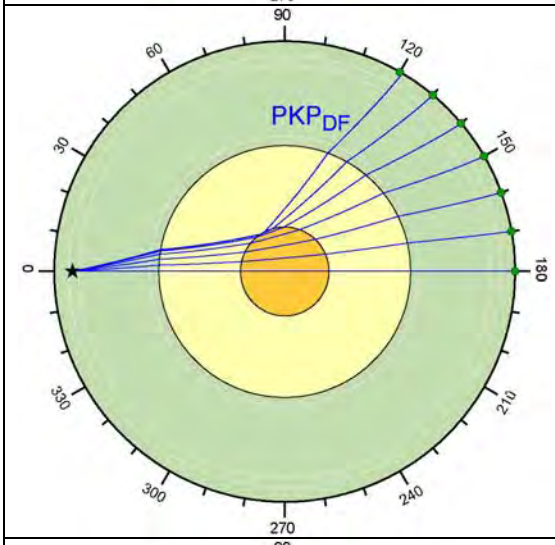
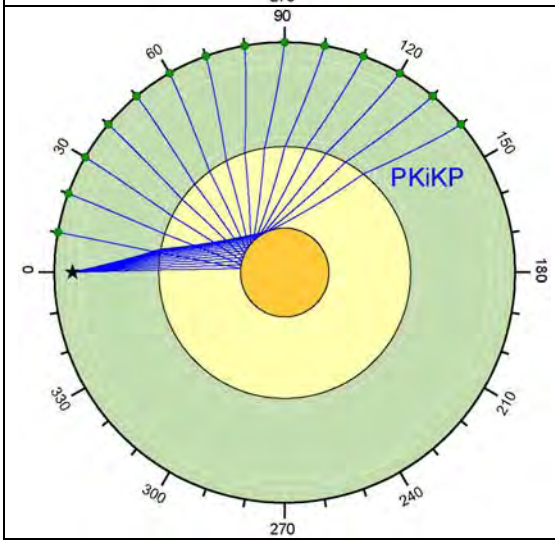
In these plots, the seismic event is at the left, and seismic ray paths are shown to possible stations at several angular distances from the event.



P	A primary (compressional) wave that follows a simple path from event source to the station.
PcP	A P wave that goes downward through the mantle (the first "P"), is reflected from the top of the outer core ("c") and goes upward through the mantle to the station (second "P").
P_{diff}	A P wave that has been bent (diffracted) around the outer core boundary and arrives at a station in the ray "shadow" of the outer core.
S	A secondary (shear) wave that follows a path similar to the P wave (not shown).



SS	A shear wave that has traveled through the mantle ("S"), undergone one reflection from the underside of Earth's surface and traveled again through the mantle (second "S"). Unlike with most other reflected waves, there is no separate letter to denote the reflection at the surface; it is implicit.
PP	A compressional wave that follows paths similar to those of SS (not shown).

	**PKP** A P wave that has traveled through the mantle ("P"), been transmitted across the mantle-outer core boundary and traveled through the outer core ("K"), transmitted back across the outer core-mantle boundary and traveled as a P wave to the station ("P"). Because of the large difference between the P wave velocity in the mantle and the outer core, this wave is bent (refracted) strongly at the boundary. Seismic waves can follow slightly different paths (labeled PKP_{AB}, PKP_{BC}) and still arrive at about the same time.
	**PKIKP** A P wave that has traveled through the mantle ("P"), been transmitted across the mantle-outer core boundary ("K"), crossed the outer-core inner-core boundary and traveled through the inner core as a P wave ("I"), then followed a similar path in reverse to get from the inner core to the station (the second "KP"). An alternate name for this phase is PKP_{DF} (shown in the path illustration).
	**PKiKP** This phase has followed a series of paths similar to the PKIKP phase, except it was reflected off the top of the inner core-outer core boundary (this is the "i" part of the path), rather than being transmitted through the inner core.

Figures courtesy of Ed Garnero, Arizona State University (http://garnero.asu.edu/research_images/index.html)

Depth Phases

A number of "depth" phases are referred to in the proceedings. The paths of these phases are nearly the same as P waves. The depth phases all result from a reflection from the Earth's surface near the epicenter of the event. The

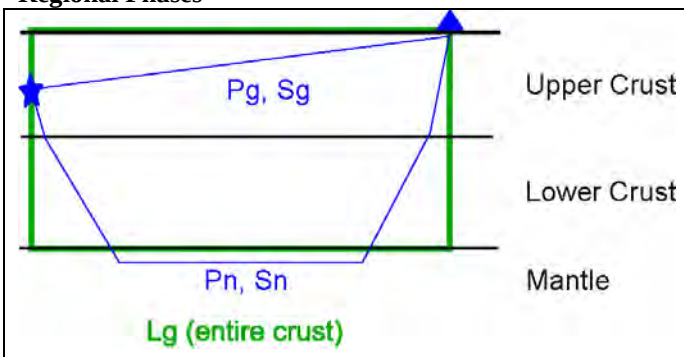
time delay between the P wave and the depth phase is proportional to the depth of the event (hence the term "depth" phase).

pP A P wave that started out upward from the source ("p"), reflected off the Earth's surface, and traveled to the station as a P wave ("P").

sP An S wave that started out upward from the source ("s"), reflected off the earth's surface and also converted to a P wave, which then traveled to the station as a P wave ("P").

pwP Similar to the pP phase. A P wave that started out upward from the source ("p"), reflected off the ocean surface ("w" - water) and traveled to the station as a P wave ("P").

Regional Phases



A highly simplified representation of the crust of Earth, which is seldom so simple and flat. Changes of crustal thickness and velocities can disrupt crustal phases, notably Lg.

Pg (Sg) At short event-station distances, an upgoing P (S) wave from a source in the upper crust (depicted here) or a P (S) wave bottoming in the upper crust. At larger distances the Pg phase includes arrivals resulting from multiple P-wave reverberations within the entire crust that propagate at a group velocity around 5.8 km/s.

Pn (Sn) A P (S) wave bottoming in the uppermost mantle or an upgoing P wave from a source in the uppermost mantle

Lg A wave group observed at larger regional distances and caused by superposition of multiple S-wave reverberations and S to P and/or P to S conversions inside the whole crust. The maximum energy travels with a group velocity around 3.5 km/s